TTI: 0-6955

Texas A&M Transportation Institute

Development of a Strategy to Address Load-Posted Bridges through Reduction in Uncertainty in Load Ratings—Volume 2: Load Testing and Modeling for Refined Load Rating

Technical Report 0-6955-R1-Vol2

Cooperative Research Program

TEXAS A&M TRANSPORTATION INSTITUTE
COLLEGE STATION, TEXAS

sponsored by the
Federal Highway Administration and the
Texas Department of Transportation
https://tti.tamu.edu/documents/0-6955-R1-Vol2.pdf

1. Report No.	2. Government Accession No.	3. Recipient's Catalog No.
FHWA/TX-19/0-6955-R1-Vol2		

4. Title and Subtitle	5. Report Date
DEVELOPMENT OF A STRATEGY TO ADDRESS LOAD-POSTED BRIDGES THROUGH REDUCTION IN UNCERTAINTY IN LOAD RATINGS—VOLUME 2: LOAD TESTING AND MODELING FOR REFINED LOAD RATING	Published: August 2022
	6. Performing Organization Code

7. Author(s)	8. Performing Organization Report No.
Mary Beth Hueste, Stefan Hurlebaus, John Mander, Stephanie Paal, Tevfik Terzioglu, Matthew Stieglitz, and Nuzhat Kabir	Report 0-6955-R1-Vol2

9. Performing Organization Name and Address	10. Work Unit No. (TRAIS)
Texas A&M Transportation Institute The Texas A&M University System College Station, Texas 77843-3135	11. Contract or Grant No. Project 0-6955

12. Sponsoring Agency Name and Address	13. Type of Report and Period Covered
Texas Department of Transportation Research and Technology Implementation Office 125 E. 11th Street Austin, Texas 78701-2483	Technical Report: September 2017–October 2019
	14. Sponsoring Agency Code

15. Supplementary Notes

Project performed in cooperation with the Texas Department of Transportation and the Federal Highway Administration.

Project Title: Development of a Strategy to Address Load-Posted Bridges through Reduction in Uncertainty in Load Ratings

URL: https://tti.tamu.edu/documents/0-6955-R1-Vol2.pdf

16. Abstract

Maintaining the functionality of the transportation infrastructure depends on the successful management of aging bridge assets. Departments of transportation rely on the load rating process to evaluate the sufficiency of the bridge structures in their state, and they post load restrictions if the capacity of a bridge does not meet the maximum load effect based on current legal loads. Removing load postings is always of interest because there can be commerce, traffic, and emergency egress issues due to rerouting of vehicles. Posted structures come in various shapes and sizes, are built in different eras and environments, and exhibit vastly different structural behaviors. Thus, there is no clear-cut single solution for addressing the possibility of removing postings. In this study, strategies were developed to reduce uncertainty in load rating procedures in a safe and appropriate manner to potentially increase or remove the load postings of typical steel and concrete bridges. The Volume 1 report (Hueste et al. 2019a) documented findings that included a review of the state-of-the-practice and state-of-the-art for load rating existing bridges, a review and synthesis of the bridge characteristics of load-posted bridges in Texas, and the basic load rating analysis conducted for selected representative bridges to identify the controlling limit states. This Volume 2 report documents further study for typical bridges, including refined analysis for more accurate prediction of load distribution, load testing, model updating and calibration, and refined load rating analysis. The load testing of the selected load-posted bridges, along with model updating and calibration based on the field measurements, is used to determine refined load ratings to compare with the basic load ratings. The results are reviewed with respect to the implications and opportunities for load rating these bridges and similar bridge structures to potentially increase the posted loads or remove the load restrictions.

17. Key Words	18. Distribution Statement
Finite element method, live load distribution, model calibration, refined load rating, load-posted bridges, steel bridges, concrete bridges, composite action	No restrictions. This document is available to the public through NTIS: National Technical Information Service Alexandria, Virginia http://www.ntis.gov

19. Security Classif. (of this report)	20. Security Classif. (of this page)	21. No. of Pages	22. Price
Unclassified	Unclassified	772	

Form DOT F 1700.7 (8-72) Reproduction of completed page authorized

DEVELOPMENT OF A STRATEGY TO ADDRESS LOAD-POSTED BRIDGES THROUGH REDUCTION IN UNCERTAINTY IN LOAD RATINGS —VOLUME 2: LOAD TESTING AND MODELING FOR REFINED LOAD RATING

by

Mary Beth D. Hueste, Ph.D., P.E.
Research Engineer
Texas A&M Transportation Institute

Stefan Hurlebaus, Ph.D.
Research Scientist
Texas A&M Transportation Institute

John B. Mander, Ph.D.
Research Engineer
Texas A&M Transportation Institute

Stephanie Paal, Ph.D.
Assistant Research Scientist
Texas A&M Transportation Institute

Tevfik Terzioglu, Ph.D.
Postdoctoral Research Associate
Texas A&M Transportation Institute

Matthew Stieglitz
Graduate Assistant Researcher
Texas A&M Transportation Institute

Nuzhat Kabir
Graduate Assistant Researcher
Texas A&M Transportation Institute

Report 0-6955-R1-Vol2
Project 0-6955
Project Title: Development of a Strategy to Address Load-Posted Bridges through Reduction in Uncertainty in Load Ratings

Performed in cooperation with the
Texas Department of Transportation and the
Federal Highway Administration

Published: August 2022

TEXAS A&M TRANSPORTATION INSTITUTE
College Station, Texas 77843-3135

DISCLAIMER

This research was performed in cooperation with the Texas Department of Transportation (TxDOT) and the Federal Highway Administration (FHWA). The contents of this report reflect the views of the authors, who are responsible for the facts and the accuracy of the data presented herein. The contents do not necessarily reflect the official view or policies of FHWA or TxDOT. This report does not constitute a standard, specification, or regulation.

This report is not intended for construction, bidding, or permit purposes. The researcher in charge of the project was Mary Beth D. Hueste. The United States Government and the State of Texas do not endorse products or manufacturers. Trade or manufacturers' names appear herein solely because they are considered essential to the object of this report.

ACKNOWLEDGMENTS

This project was conducted at Texas A&M University (TAMU) and was supported by TxDOT and FHWA through the Texas A&M Transportation Institute (TTI) as part of Project 0-6955, "Development of a Strategy to Address Load-Posted Bridges through Reduction in Uncertainty in Load Ratings." The authors are grateful to the individuals who were involved with this project and provided invaluable assistance, including James Kuhr (TxDOT, project manager), Graham Bettis (TxDOT, project director), and the TxDOT Project Monitoring Committee: Aaron Garza, Courtney Holle, Jesus Alvarez, Jonathan Boleware, and Curtis Rokicki.

The following individuals were instrumental in providing support to ensure the successful completion of the project, and their contributions are appreciated:

- Individuals from TxDOT district offices, including Anthony Garcia, Carlos Neveu, Jody Valero, Paul Cepak, Christopher Niedorf, Jason Scantling, and Alan Ogden, provided assistance during the field testing of the selected bridges.
- Hyeonki Hong and Hungjoo Kwon, graduate students at TAMU, assisted with the instrumentation and load testing of the selected bridges.

TABLE OF CONTENTS

LIST OF FIGURES

Page

LIST OF TABLES

Page

1 INTRODUCTION

1.1 BACKGROUND AND SIGNIFICANCE

An ever-increasing demand on highways exists for improved mobility and connectivity for delivering more goods and services, which increases the importance of reliable, well-maintained transportation infrastructure. Maintaining the functionality and health of the transportation infrastructure depends on the successful management of aging bridge assets. Departments of Transportation rely on the load rating process to evaluate the sufficiency of the bridge structures in their state and post load restrictions if the capacity of a bridge does not meet the maximum load effect based on the current legal loads. According to the National Bridge Inventory (NBI 2016) database, the state of Texas has 2111 bridges that are posted at load levels below the legal limit. Although load postings are generally a management issue, there can be commerce, traffic, and emergency egress issues. Therefore, removing postings is always of interest. However, posted bridges vary greatly in terms of geometry, size, construction style, age, and environmental conditions; their structural behavior can also differ significantly. Thus, there is no clear-cut single solution for addressing the possibility of removing postings.

1.2 OBJECTIVES AND SCOPE

The overall objective of this project is to determine through a reduction in uncertainty appropriate strategies for bridge load rating that can lead to removal of load postings for Texas bridges posted at load levels below the legal limit. Some of the uncertainty and inherent conservatism in the current basic load rating procedures can potentially be minimized by using more accurate material properties, refined modeling, and load testing to understand the in situ structural behavior. The proposed approach to addressing posted bridges begins with developing a strategy to reduce uncertainty in a safe and appropriate manner based on the specific details of a bridge and refinements in the load rating process. The *American Association of State Highway and Transportation Officials* (AASHTO) *Manual for Bridge Evaluation* (MBE) (AASHTO 2018) allows for refined load rating but does not address the challenge of identifying appropriate structures. Therefore, this research project quantifies and characterizes the population of load-posted bridges in Texas and reviews areas of opportunity, including more accurate material

properties and information from bridge inspections, refined modeling for less conservative live load distribution modeling, and load testing for verification of structural response. The load rating calculations using refined information and techniques presented in this research are expected to provide better accuracy in load rating and can potentially eliminate load postings or increase the allowable loads on load-posted bridges.

1.3 RESEARCH PLAN

The outcome of this research study supports the Texas Department of Transportation's (TxDOT's) implementation of refined load rating approaches to potentially remove or increase the posted load limits in the Texas bridge inventory. The following tasks were conducted to accomplish the research objectives:

- Task 1—Project Management and Research Coordination.
- Task 2—Review State of the Art, State of the Practice, and Load-Posted Bridge Inventory.
- Task 3—Conduct Basic Load Ratings and Identify Areas of Opportunity.
- Task 4—Refined Analysis for more Accurate Prediction of Live Load Distribution.
- Task 5—Load Testing, Model Updating and Calibration, and Refined Load Ratings.
- Task 6—Develop Refined Load Rating Guidelines and Examples.

The Volume 1 report (Hueste et al. 2019a) documents the findings of Tasks 2 and 3, which include a summary of the state of the practice and state of the art for load rating of existing bridges, a review and synthesis of the characteristics of load-posted bridges in Texas, and the basic load rating analysis for selected representative bridges to identify the controlling limit states. Volume 3 (Hueste et al. 2019b) discusses the developed guidelines for refined load rating and provides several examples.

This Volume 2 report documents the findings of Tasks 4 and 5, including a refined analysis for more accurate LLDF prediction, load testing, model updating and calibration, and a refined load rating analysis. The investigation of sub-standard for load only (SSLO) bridges that was reported on in Volume 1 found that the significant majority of load-posted bridges in Texas include four main bridge types: (1) steel multi-girder (SM), (2) continuous steel multi-girder (SC), (3) concrete multi-girder (CM), and (4) concrete slab (CS) bridges. One typical bridge from each category was selected for refined finite element analysis and field testing. Refined analysis

includes three-dimensional linear finite element modeling, which can provide a more accurate estimation of load distribution and live load distribution factors (LLDFs). Load testing of the selected bridges, along with model updating and calibration based on the field measurements, is used to determine refined load ratings to compare with the basic load ratings. The results are reviewed with respect to the potential implications and opportunities for load rating these bridges and similar bridge structures.

1.4 REPORT OUTLINE

This Volume 2 report consists of 10 chapters that document the findings of Task 4 and 5.

Chapter 1 presents the background and significance, research objectives and scope of the project, and research plan (including specific tasks) and outlines the Volume 2 research report.

Chapter 2 then provides the finite element method (FEM) modeling approach and analysis results for two selected simple-span steel multi-girder bridges. The purpose of the refined analysis of the simple-span steel multi-girder bridges can be summarized as follows: (1) create a model of the bridge superstructure that can more accurately predict the live load distribution, and (2) investigate the effect of partial composite action on the load distribution behavior of the bridge under service loads.

Chapter 3 presents the FEM modeling approach and analysis results for the selected continuous steel multi-girder bridge in Texas. The effect of the identified parameters has been investigated using three-dimensional linear FEM models that can more accurately capture the bridge behavior. The objectives of FEM analysis of the continuous steel multi-girder bridge are to (1) create a model of the bridge superstructure that can more accurately predict the live load distribution, (2) investigate the effect of partial composite action on the load distribution behavior of the bridge under service loads, and (3) evaluate the effect of deck cracking over the negative moment region.

Chapter 4 summarizes the FEM modeling approach and analysis results for the selected simple-span concrete multi-girder bridge in Texas. The purpose of the of FEM analysis of the simple-span concrete multi-girder bridge is to accurately capture the distribution of live load between girders.

Chapter 5 focuses on the FEM modeling approach and analysis results for the selected simple-span concrete slab bridge in Texas. This chapter provides the basic characteristic of the

selected typical concrete slab bridge, provides details about the FEM modeling procedure, and summarizes the findings of the FEM analysis by focusing on the moment and shear distribution. The objectives of FEM analysis of the simple-span concrete slab bridge can be summarized as follows: (1) create a model of the bridge superstructure to accurately capture the two-way action in the slab, (2) investigate the actual equivalent slab width over which the vehicular loads are distributed for design, and (3) evaluate the effect of integral curbs on the load distribution across the slab width.

Chapter 6 presents the field-test results, provides the FEM model updating and calibration procedure, and compares the FEM predictions with test results for the selected simple-span steel multi-girder bridge. The implications of using the refined modeling approach for refined load rating calculations are discussed.

Chapter 7 summarizes the field-test results, provides the FEM model updating and calibration procedure, and compares the FEM predictions with test results for the selected continuous steel multi-girder bridge. The implications of using the refined modeling approach for refined load rating calculations are discussed.

Chapter 8 documents the field-test results, provides the FEM model updating and calibration procedure, and compares the FEM predictions with test results for the selected simple-span concrete multi-girder bridge. A thorough investigation of the field-test results and the results from the updated and calibrated FEM models is then used to determine a refined load rating for the concrete multi-girder bridge, and potential implications for load posting of similar bridge structures are discussed.

Chapter 9 reports the field-test results, provides the FEM model updating and calibration procedure, and compares the FEM predictions with test results for the selected simple-span concrete slab bridge. A thorough investigation of the field-test results and the results from the updated and calibrated FEM models is used to determine potential updates to the load posting of the concrete slab bridge, and the potential implications for load posting of similar bridge structures are discussed.

Chapter 10 provides a summary of the findings from each of the tasks reported on in this Volume 2 report.

2 ANALYSIS OF SIMPLE-SPAN STEEL MULTI-GIRDER BRIDGES

In the previous tasks, a detailed review and synthesis of the population of load-posted bridges in Texas was conducted, and 25 simple-span steel multi-girder bridges were selected from the inventory of SSLO simple-span steel multi-girder bridges in Texas for basic load rating evaluation. This basic load rating analysis helped identify several areas of opportunity for refined load rating analysis. The refined load rating analysis used in this study investigated the effect of the identified parameters using three-dimensional finite element models that can more accurately capture the bridge behavior. The main objectives of the refined analysis of the simple-span steel multi-girder bridges can be summarized as follows: (1) create a model of the bridge superstructure that can more accurately predict the live load distribution, and (2) investigate the effect of partial composite action on the load distribution behavior of the bridge under service loads.

2.1 INTRODUCTION

Two typical load-posted simple-span steel multi-girder (SM) bridges were selected as representative structures of this type to further investigate the identified objectives. Table 2.1 lists some of the key parameters for the two SM bridges and for the average SSLO simple-span steel multi-girder bridge in Texas. In this table, the Operating HS-20 rating factor (RF) represents the multiple of HS-20 truck loads that is the absolute maximum load that can safely travel on the bridge. The posting evaluation represents the degree to which the operating rating of the bridge is below the maximum legal load. A value of 5 indicates that the operating rating is equal to or above the legal load. The values 0–4 represent that the operating rating is below the legal load by varying degrees, with 4 representing a rating within 10 percent of the legal load and 0 indicating a rating 40 percent or greater below the legal load.

Three-dimensional linear FEM models were developed using the commercial software package CSiBridge (Computers and Structures Inc. 2019), which has the capability to model and analyze complex bridge superstructures while also providing user-friendly pre- and postprocessing tools for bridge structures. The following sections provide the geometric and material properties of the selected simple-span steel multi-girder bridges, describe the FEM modeling approach, and summarize the analysis results.

Table 2.1. Selected SSLO SM Bridges and Average Characteristics

ID	Route Prefix	Year Built	ADT	Max. Span Length (ft)	Deck Width (ft)	Condition Rating			Operating HS-20 Rating Factor	Posting Eval.
						Deck	Super-structure	Sub-structure		
Avg.	–	1974	–	36	20	6	6	6	0.83	3
SM-5	3	1938	300	41	24	7	6	7	0.77	2
SM-21	4	1990	550	53	25	8	7	7	0.99	5

– : Not applicable
Route Prefix: 3 = On-System, 4 = Off-System
Condition Ratings: 6 = Satisfactory, 7 = Good, 8 = Very Good
Posting Evaluation: 2 = 20–29.9% below legal load, 3 = 10–19.9% below legal load, 5 = equal to or above legal load

The models were analyzed with HS-20 truck and designated HL-93 load simulations to obtain deflection profiles, modal properties, and moment and shear values. The deflection and modal property analyses were conducted for comparison to the measured behavior of the bridges in the future field tests. The deflection values and modal characteristics allow for calibration of the FEM models based on the field-test results. For the moment and shear analysis, the main bridge characteristics of interest are the LLDFs. The LLDFs found using the FEM model were compared to those LLDFs determined through field testing and to values from the procedures in the *AASHTO Standard Specifications* (AASHTO 2002) and *AASHTO Load and Resistance Factor Design (LRFD) Specifications* (AASHTO 2017). LLDFs can be calculated as the moment or shear force of an individual girder divided by the sum of moments or shear forces in all of the girders for a one-lane loaded case, as expressed in Equation (2.1):

$$g = m\frac{F_{girder}}{F_{total}} \tag{2.1}$$

where:

g = Live load distribution factor.

F_{girder} = Moment or shear force in the individual girder.

F_{total} = Total moment or shear force on the entire section for one-lane loading.

m = Multiple presence factor per the *AASHTO LRFD Specifications* (AASHTO 2017), 1.2 for one-lane loading and 1.0 for two-lane loading.

2.2 DESCRIPTION OF SELECTED BRIDGES

2.2.1 Bridge SM-5

Simple-span Bridge SM-5 has a 41 ft 4 in. total length and a 40 ft 2 in. center-to-center bearing span length. The total width of the bridge is 24 ft, with a roadway width of 23 ft 6 in.. The girder spacing for SM-5 is 23 in., and lateral bracing is provided at third points along the span. The deck thickness is 6 in. The steel yield strength and the 28-day concrete compressive strength are taken as 33 ksi and 2.5 ksi, respectively, based on values used for load rating noted in TxDOT's inspection reports (TxDOT 2018a). The bridge carries two lanes, one in each direction, and has an average daily traffic (ADT) of 300 vehicles. These properties are tabulated in Table 2.2. Also of note, this bridge has a girder flange embedment of 0.5 in. into the deck, according to the structural drawings (TxDOT 2018a).

Table 2.2. Geometric and Material Properties of SM-5

Characteristic	Measurement
Total Length	41'-4"
Span Length	40'-2"
Deck Width	24'-0"
Roadway Width	23'-6"
Girder Spacing	1'-11"
Lateral Bracing Spacing	13'-5"
Steel Cross-Section Shape	S15x42.9
Steel Yield Strength	33 ksi
Deck Thickness	6"
28-day Concrete Compressive Strength	2.5 ksi
Number of Lanes	2

Bridge SM-5 has a deck condition rating of 7 (Good), a superstructure condition rating of 6 (Satisfactory) with 2 percent beam section loss due to corrosion, and a substructure condition rating of 7 (Good). The steel girder flexure controls the rating of the bridge, which has an inventory gross loading of 17 US tons and an operating gross loading of 28 US tons. Table 2.3 shows the posted loads of Bridge SM-5 for different axle and vehicle configurations. Figure 2.1 shows an elevation view of Bridge SM-5 and a view of the underside of the superstructure. Figure 2.2 shows a transverse section detail of Bridge SM-5.

Table 2.3. Bridge SM-5 Postings

Configuration	Posting (lbs)
Single Axle	20,000
Tandem Axle	34,000
Single Vehicle	47,000
Combination Vehicle	74,000

(a) Elevation view

(b) Underside view

Figure 2.1. Photographs of Bridge SM-5 (TxDOT 2018a)

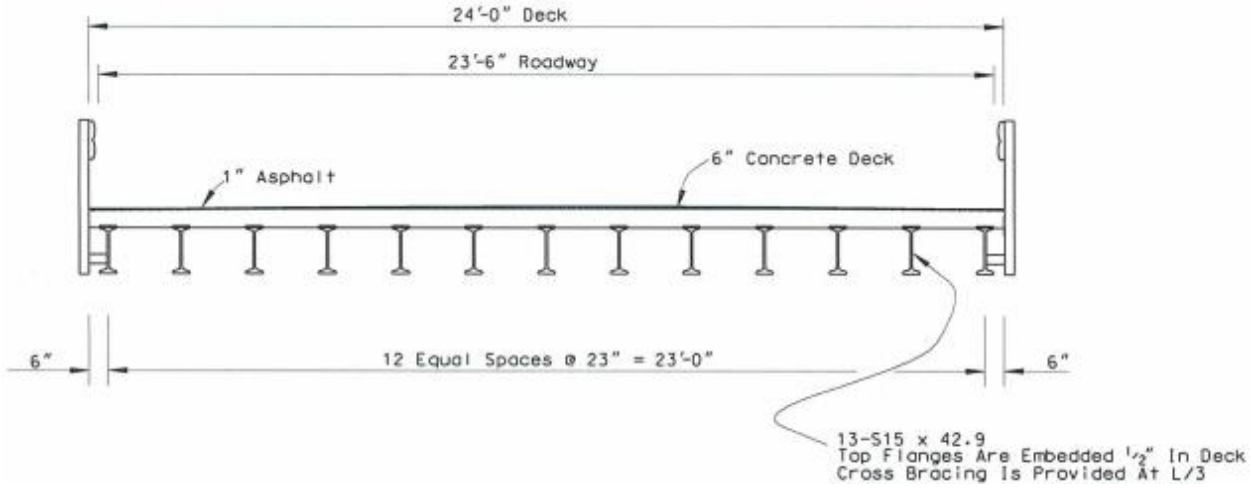

Figure 2.2. Transverse Section of Bridge SM-5 (TxDOT 2018a)

2.2.2 Bridge SM-21

A second steel simple-span bridge was selected for refined analysis to provide a girder spacing that is more typical when compared to the group of bridges for which basic load rating analysis was conducted. The average girder spacing value for this group of bridges, including both simple span and continuous steel multi-girder bridges, is 4 ft 0.5 in. Bridge SM-5 has a girder spacing of 1 ft 11 in., and Bridge SC-12, discussed later, has a girder spacing of 6 ft 8 in. Therefore, Bridge SM-21, with a girder spacing of 4 ft, was chosen to consider a typical girder spacing.

Bridge SM-21 has a total length of 54 ft and a center-to-center bearing span length of 52 ft 10 in. The total width of the bridge is 25 ft, with a roadway width of 24 ft. Lateral bracing is provided at third points along the span. The deck thickness is 6 in. The steel yield strength and the 28-day concrete compressive strength are taken as 33 ksi and 2.5 ksi, respectively, based on values used for load rating noted in TxDOT's inspection reports (TxDOT 2018a). The bridge carries two lanes, one in each direction, and has an ADT of 550 vehicles. These properties are tabulated in Table 2.4.

Table 2.4. Geometric and Material Properties of SM-21

Characteristic	Measurement
Total Length	54'-0"
Span Length	52'-10"
Deck Width	25'-0"
Roadway Width	24'-0"
Girder Spacing	4'-0"
Lateral Bracing Spacing	17'-7"
Steel Cross-Section Shape	W33x130
Steel Yield Strength	33 ksi
Deck Thickness	6"
28-day Concrete Compressive Strength	2.5 ksi
Number of Lanes	2

Bridge SM-21 has a deck condition rating of 8 (Very Good), a superstructure condition rating of 7 (Good) with 2 percent beam section loss due to corrosion, and a substructure condition rating of 7 (Good). The assumed deck rating controls the rating of the bridge, which has an inventory gross loading of 25 US tons and an operating gross loading of 36 US tons. The bridge was once posted for a 28,000 lbs tandem axle and a 52,000 lbs gross vehicle; however, it is no longer posted. Figure 2.3 shows an elevation view of Bridge SM-21 and a view of the underside of the superstructure. Figure 2.4 shows transverse section details of Bridge SM-21.

(a) Elevation view

(b) Underside view

Figure 2.3. Photographs of Bridge SM-21 (TxDOT 2018a)

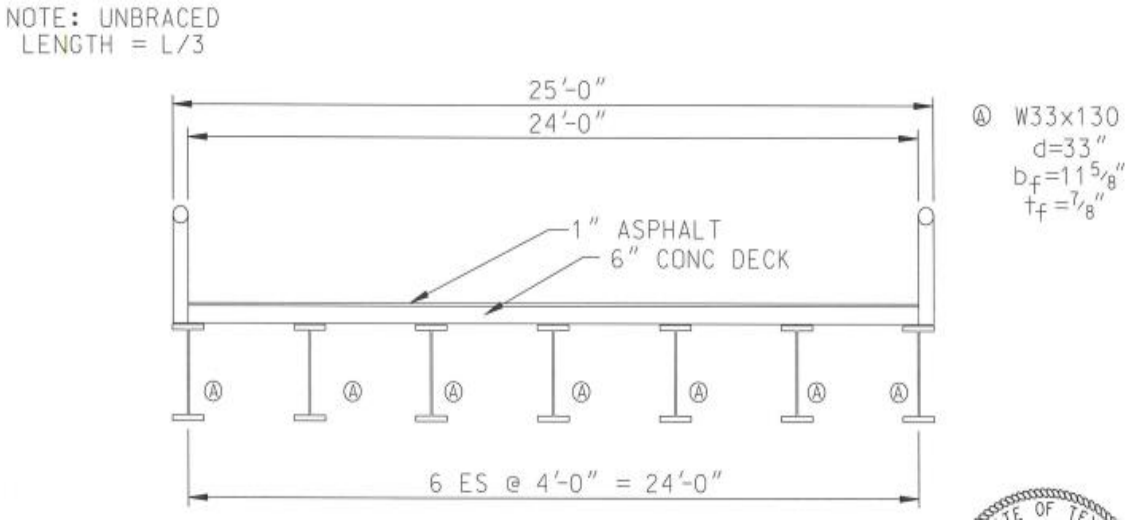

Figure 2.4. Transverse Section of Bridge SM-21 (TxDOT 2018a)

2.3 FEM MODEL DEVELOPMENT

Three-dimensional linear FEM models of the selected simple-span steel multi-girder bridges, SM-5 and SM-21, were developed using the commercial CSiBridge software (Computers and Structures Inc. 2019). The geometry of the bridges was modeled based on information provided in the design drawings and inspection reports for each bridge. The geometric information relevant to the development of the FEM models of these two bridges was presented in the previous sections of this chapter. The following subsection describes the FEM modeling approach, finite element types, and material properties. The next subsection presents the results of the mesh sensitivity study and selection of mesh size. The last subsection provides details about boundary conditions, which are critical for accurately capturing the behavior of the bridge.

2.3.1 Bridge Model Description

The superstructure of a slab-on-girder bridge can be modeled using a variety of finite element types, most of which are available in the CSiBridge software. A significant amount of information in the literature exists that provides guidelines for developing FEM models for slab-on-girder steel bridges (Barnard et al. 2010; Hurlebaus et al. 2018; Puckett et al. 2011). Based on the recommendations provided in the literature and engineering judgement, the FEM models of the selected SM bridges were developed using a combination of four-node linear quadrilateral shell

elements and two-node linear beam elements (frame elements). The superstructures of the selected SM bridges consist of steel I-girders and a reinforced concrete deck. The reinforced concrete deck was modeled using four-node linear shell elements. Table 2.5 shows the relevant material properties for the steel girders and concrete deck used in the FEM models of both bridges, which match the material strength values noted in the TxDOT load rating calculations. Deck reinforcement is not modeled because the linear elastic model will be analyzed under service level loads only, and the superstructure is expected to remain in the linear elastic range. The steel girder webs were also modeled using four-node linear shell elements. Top and bottom flanges of the steel girder and the diaphragms were modeled using two-node linear beam/frame elements. Figure 2.5 shows the meshed FEM model of SM-21 with the components of the model labeled. When creating a meshed analytical model, CSiBridge first partitions the deck along the centerlines of the girders and then meshes based on the selected maximum mesh size. The maximum mesh size is 6 in. for the FEM model of Bridge SM-21, shown in Figure 2.5. Bridge SM-5 was meshed in a similar manner.

The default option for modeling a steel multi-girder bridge with a concrete deck in the CSiBridge software considers the deck and girders as fully composite. In order to model non-composite behavior, an edge release was applied to the bottom surface of the concrete deck. This option removes interface shear restraint between the deck and the girders, thereby creating fully non-composite behavior. Both bridges were modeled and analyzed as fully composite and fully non-composite to allow comparison of the results.

Table 2.5. FEM Model Material Properties

Material	Density (pcf)	Modulus of Elasticity (ksi)	Poisson's Ratio	28-Day Concrete Compressive Strength (ksi)	Steel Yield Strength (ksi)
Steel	490	29,000	0.3	–	33
Concrete	150	2850	0.2	2.5	-

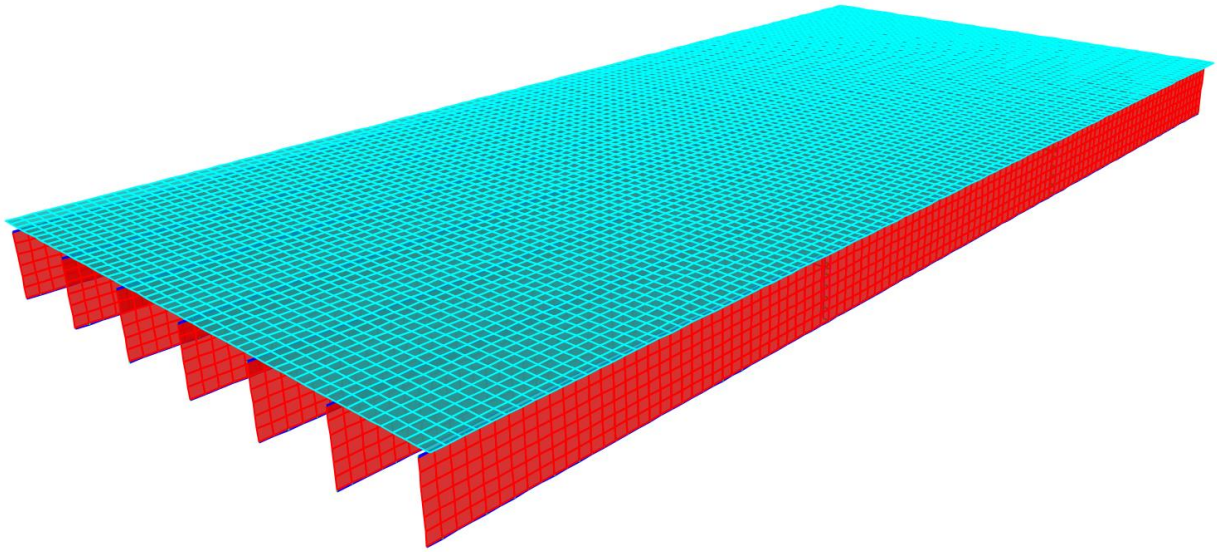

(a) Fully Meshed Superstructure

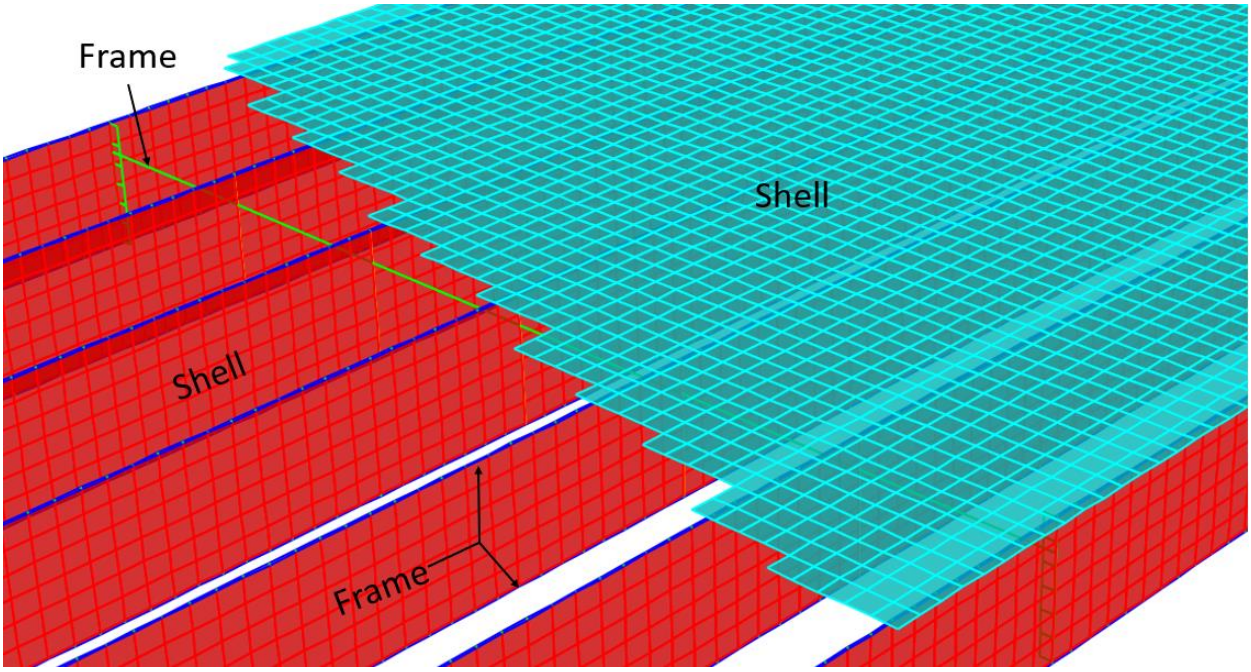

(b) Finite Element Types

Figure 2.5. FEM Model of the SM-21 Bridge (6 in. mesh)

For Bridge SM-5, the FEM models for the composite analysis and for the non-composite analysis were slightly different in an attempt to accurately model the actual geometry of the bridge. The bridge has a 6 in. thick deck, with girder flanges embedded 0.5 in. into the deck. Limitations

with the CSiBridge software do not allow the modeling of flange embedment. Therefore, for the composite bridge, the model consists of a 5.5 in. thick deck on top of the steel girders. This approach results in calculated fully composite centroids, moments of inertia, and section moduli for the entire bridge, an interior girder, and an exterior girder that are very close to values of those properties calculated for the actual bridge cross section, assuming fully composite behavior. For the non-composite bridge, a 6 in. thick deck was used on top of the steel girders. This detail will best represent the load distribution by the deck to the bridge girders, assuming fully non-composite behavior, because the actual bridge deck thickness is 6 in.

2.3.2 Mesh Sensitivity Analysis

To determine the most efficient mesh size to use in the FEM models of each SM bridge, the effect of different mesh sizes on the calculated shear force, moment, and bottom flange bending stress was examined. A model of each bridge was created using maximum mesh sizes of 4 in., 6 in., 12 in., and 18 in. Figure 2.6 shows these different mesh sizes when applied to Bridge SM-5. Each bridge was analyzed using a static multistep analysis of one HS-20 truck driving across it with the interior wheel line 2 ft away from the centerline of the bridge (shown as PATH 3 in Figure 2.13(a) and Figure 2.14(a)).The maximum forces and stresses in the bridge cross-section for each model with different mesh sizes were then compared.

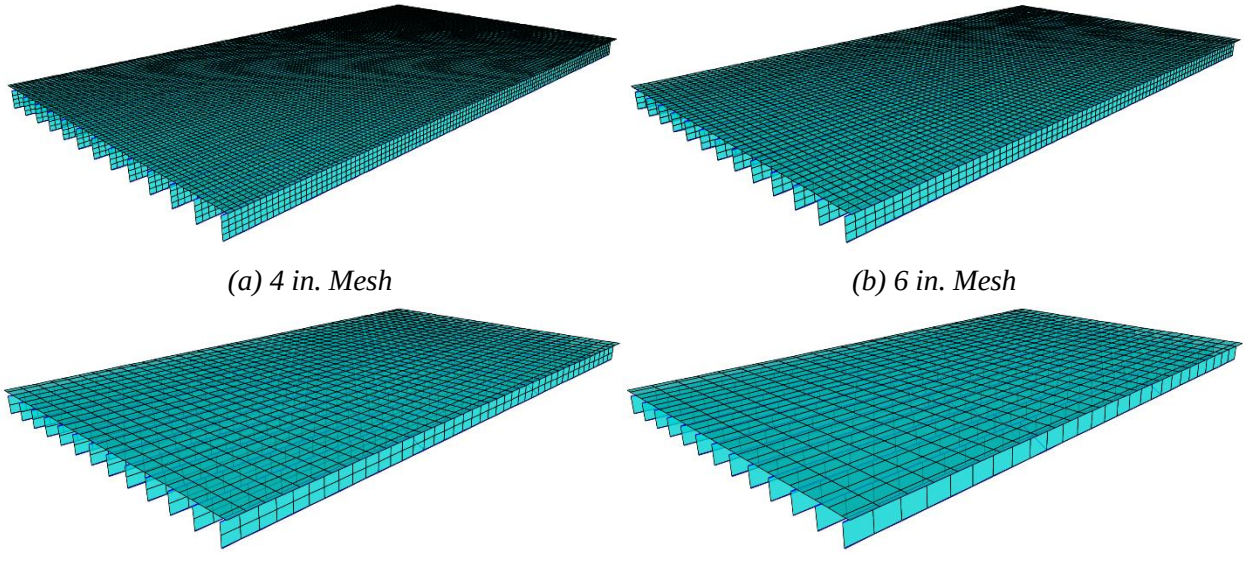

(a) 4 in. Mesh *(b) 6 in. Mesh*

(c) 12 in. Mesh *(d) 18 in. Mesh*

Figure 2.6. FEM Models Showing Different Mesh Sizes for the SM-5 Bridge

Table 2.6 and Table 2.7 show the results of the mesh sensitivity analysis for Bridge SM-5 and SM-21, respectively. There was no difference in the results for the models using a 12 in. mesh and an 18 in. mesh. There was only minimal difference in the results for the models with a 4 in. mesh and a 6 in. mesh, and this difference was deemed to not justify the added computation time. However, a noticeable difference existed in the results between using a 6 in. mesh and a 12 in. mesh. The 6 in. mesh produced more refined results, and for the reasons noted, a 6 in. mesh size was chosen to be used for Bridge SM-5. Figure 2.7 shows the final meshed FEM models that were used for the analysis of the SM-5 and SM-21 bridges.

Table 2.6. Mesh Sensitivity Analysis for Bridge SM-5

Mesh Size (in.)	Maximum Moment in Girder G11 (kip-ft)	Maximum Shear in Girder G11 (kip)	Maximum Bottom Flange Stress in Girder G11 (ksi)
4	64.61	13.68	8.10
6	63.87	13.68	8.07
12	63.62	12.21	7.91
18	63.14	12.10	7.89

Table 2.7. Mesh Sensitivity Analysis for Bridge SM-21

Mesh Size (in.)	Maximum Moment in Girder 6 (kip-ft)	Maximum Shear in Girder 6 (kip)	Maximum Bottom Flange Stress in Girder 6 (ksi)
4	177.97	19.71	4.03
6	177.76	19.59	4.03
12	174.93	19.45	3.98
18	174.21	19.21	3.97

2.3.3 Boundary Conditions

In the absence of more accurate information, the boundary conditions at the supports are defined as pins and rollers. The boundary conditions for both SM bridges were modeled to represent a simply supported condition in which both ends of all of the girders, except one end of one of the girders, are modeled as roller supports. A roller support releases all three rotational degrees of freedom and two translational degrees of freedom in the horizontal plane (two orthogonal in-plane directions parallel to the bridge superstructure) and fully restrains the translational degree of freedom in the vertical direction (perpendicular to the plane of the bridge superstructure). Only

one girder was pinned at one end in order to resist any horizontal forces that develop. A pin support releases all three rotational degrees of freedom and restrains all three translational degrees of freedom.

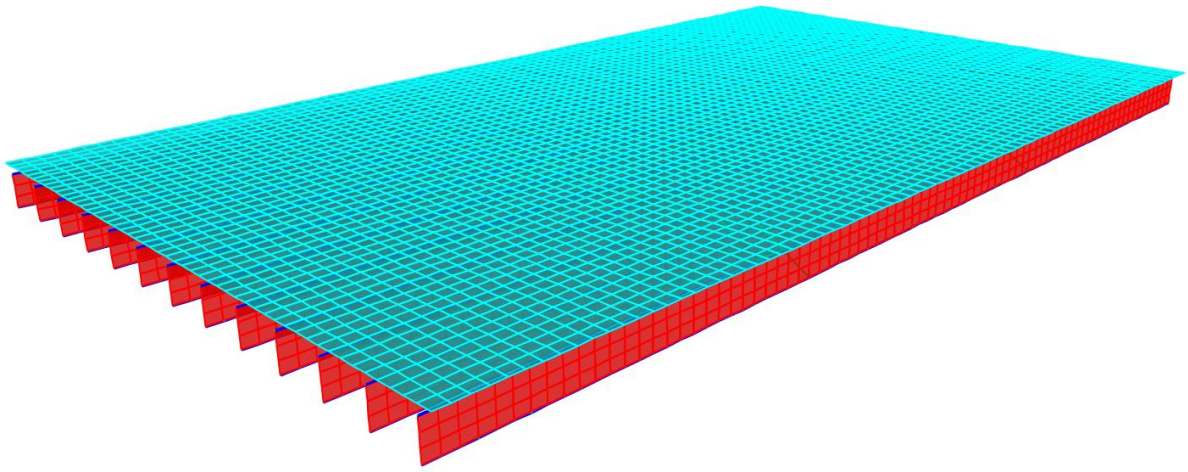

(a) SM-5 Bridge

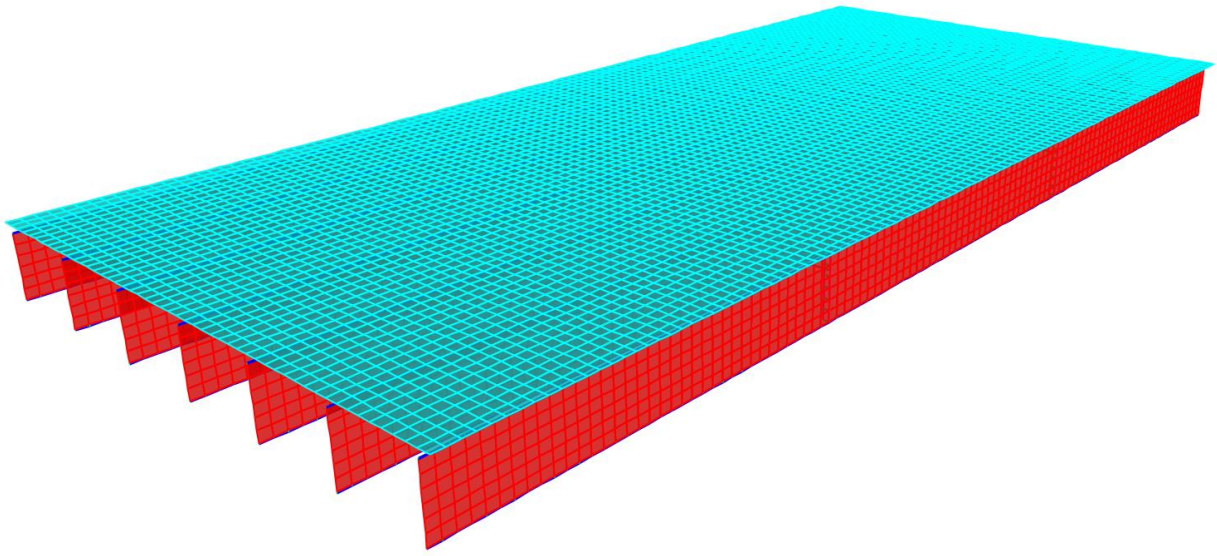

(b) SM-21 Bridge

Figure 2.7. Selected Meshed FEM Models (6 in. mesh)

Accurately modeling the boundary conditions may have a significant effect on the overall behavior of the bridge. Although the boundary conditions are initially modeled as simply supported, the restraint of the supports will be evaluated based on field-test results during the next

phase of this project. Unintended partial end restraint may develop at the supports due to the bearing detail at the supports and/or friction between the bottom surface of the bridge girders and the bearing surface. The presence of partial end restraint will be verified through field testing.

2.4 BASIC VERIFICATION OF FEM MODELS

Some basic loading conditions were simulated to verify that the FEM models were developed correctly. These basic checks were conducted by investigating maximum deflections under a uniformly distributed dead load and absolute maximum moments and support reactions under HS-20 design truck and designated HL-93 loading.

Figure 2.8 shows the characteristics of the HS-20 design truck as specified in the *AASHTO LRFD Specifications* (AASHTO 2017). The front axle has an 8-kip total load and is 14 ft in front of the middle axle, which has a 32-kip total load. The spacing between the middle axle and the rear axle, which also carries a 32-kip total load, varies between 14 ft and 30 ft depending on which distance produces the maximum effect for the force being investigated. The vehicular live load model in the *AASHTO Standard Specifications* (AASHTO 2002) also considers an alternative loading scheme consisting of a uniformly distributed 0.64 kips per linear foot of load lane and a concentrated load of 18 kips when checking moment or 26 kips when checking shear, which should be used if it controls over the HS-20 design truck loading.

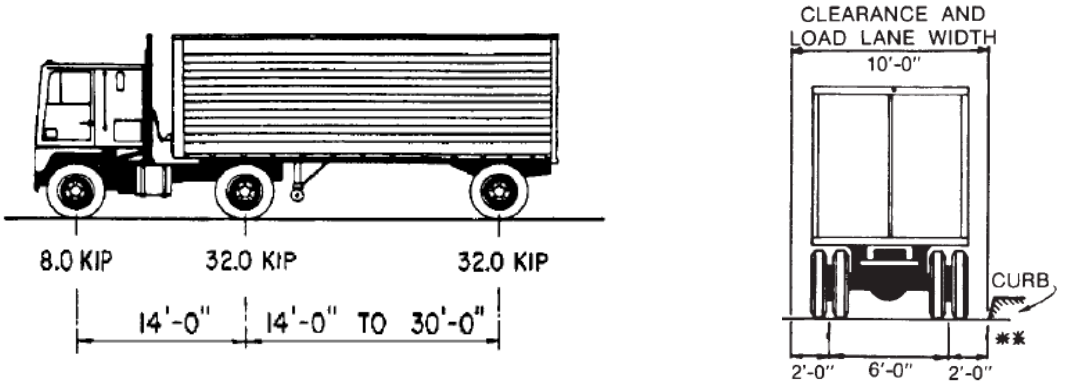

(a) Truck Axle Loadings and Longitudinal Spacings *(b) Truck Transverse Spacing*

Figure 2.8. HS-20 Truck Loading (AASHTO 2002, 2017)

Figure 2.9 shows the designated HL-93 loading with HS-20 truck and tandem loads. The designated HL-93 loading consists of the design truck or design tandem coincident with the design

lane load. The design lane load consists of a 0.64 kip per linear foot uniformly distributed load that is evenly distributed over a 10 ft width. The design truck or design tandem is used depending on which will create the maximum force effects on the span. Figure 2.9(a) shows the HS-20 design truck and the design lane load. The design tandem consists of two 25-kip axle loads spaced 4 ft apart in the longitudinal direction and 6 ft apart in the transverse direction. Figure 2.9(b) shows the design tandem loading with the lane load.

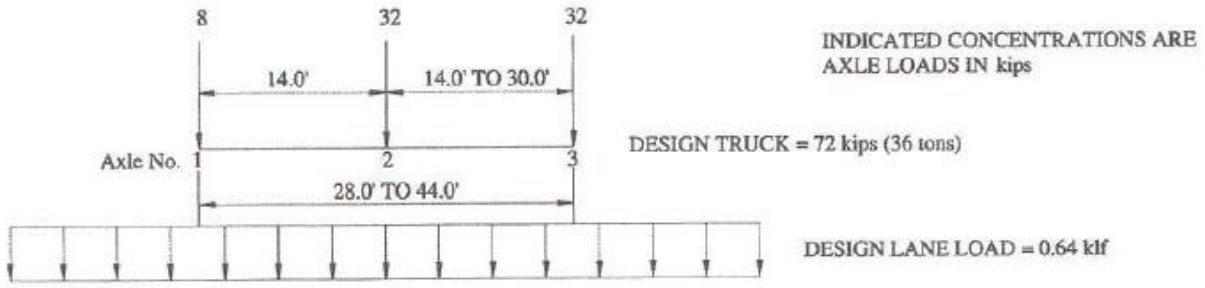

(a) Design Truck and Lane Load

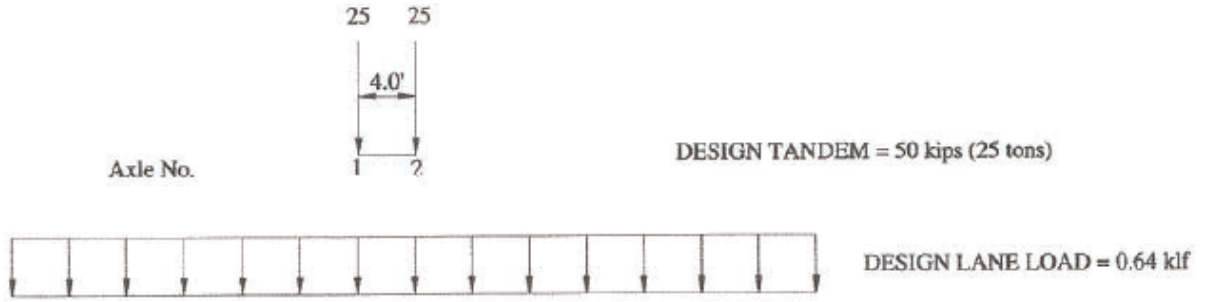

(b) Design Tandem and Lane Load

Figure 2.9. Designated HL-93 Load Model (AASHTO 2018)

2.4.1 Verification of Maximum Deflection

To verify that the structure had been modeled correctly, maximum deflections for the composite and non-composite bridge superstructure under a uniformly distributed dead load were verified against the deflections obtained from theoretical structural analysis. The model was analyzed as both composite and non-composite under dead loads, and the deflection of an interior girder was obtained. The estimated deflection values from FEM analysis were compared to the calculated deflection of an interior girder with tributary width of the deck using theoretical structural analysis.

For Bridge SM-5, assuming fully non-composite action, the equivalent distributed load was calculated as the sum of the weight of the girder, the deck, and the wearing surface. The total uniformly distributed weight can be found as follows:

$$w = w_g + w_d + w_{ws} = 0.209 \text{ kip/ft} \tag{2.2}$$

in which:

w_g = weight of the girder = 0.0429 kip/ft

$$w_d = (\gamma_c)(t_d)(s) = 0.144 \text{ kip/ft} \tag{2.3}$$

$$w_{ws} = (\gamma_{ws})(t_{ws})(s) = 0.0224 \text{ kip/ft} \tag{2.4}$$

where:

w_d = Weight of the deck (kip/ft)

γ_c = Unit weight of concrete = 0.15 kip/ft^3

t_d = Thickness of the concrete deck (ft)

s = Spacing of the steel girders (ft)

w_{ws} = Weight of the wearing surface (kip/ft)

γ_{ws} = Unit weight of the wearing surface = 0.14 kip/ft^3

t_{ws} = Thickness of the wearing surface (ft)

When the section is assumed to be non-composite, the stiffness EI of each component is linearly added for the deflection calculation. The total deflection of the non-composite section under dead loads can be calculated using Equation (2.5) for maximum deflection of a simply supported beam under a uniformly distributed load:

$$\Delta_{non-composite} = \frac{5wL^4}{384(E_s I_g + E_c I_d)} = 0.866 \text{ in.} \tag{2.5}$$

where:

I_g = Moment of inertia of the steel girder = 446 in^4

I_d = Moment of inertia of the deck = 414 in^4

E_s = Modulus of elasticity of steel = 29,000 ksi

E_c = Modulus of elasticity of concrete = $57{,}000\sqrt{f'_c}$ = 2850 ksi

To determine the fully composite deflection of Bridge SM-5, the moment of inertia of the composite section with transformed deck width, I_{tr}, was calculated about the horizontal axis at the centroid of the composite section. The width of the transformed deck, $b_{tr} = 2.3$ in., was determined by dividing the effective width of the deck by the modular ratio, which is approximately 10:

$$I_{tr} = I_g + A_g(y_{bc} - y_b)^2 + I_{d_{tr}} + A_d(y_{bc} - y_d)^2 = 1214 \text{ in}^4 \quad (2.6)$$

where:

A_g = Cross-sectional area of the steel girder = 12.6 in^2

y_{bc} = Distance from the bottom of girder to the centroid of the composite section = 12.99 in.

y_b = Distance from the bottom of girder to the centroid of the steel girder = 7.5 in.

$I_{d_{tr}}$ = Moment of inertia of the transformed deck about its own centroidal axis = 41.4 in^4

A_d = Area of the transformed deck = 13.8 in^2

y_d = Distance from the bottom of girder to the centroid of the transformed deck = 18 in.

Finally, the maximum composite deflection can be found using the same deflection equation and replacing the non-composite moment of inertia with the transformed section moment of inertia.

$$\Delta_{composite} = \frac{5wL^4}{384E_sI_{tr}} = 0.348 \text{ in.} \quad (2.7)$$

A similar analysis was performed for Bridge SM-21 to determine the maximum vertical non-composite and composite deflections due to dead load. Table 2.8 shows the deflections calculated

using each method and the percent difference between them. The FEM deflections matched very closely to the calculated deflections.

Table 2.8. Dead Load Deflection Comparison for Modeled SM Bridges

Bridge ID	Composite/ Non-Composite	FEM Deflection (in.)	Calculated Deflection (in.)	Percent Difference (%)
SM-5	Non-Composite	0.865	0.866	0.12
	Composite	0.349	0.348	0.29
SM-21	Non-Composite	0.427	0.424	0.71
	Composite	0.226	0.221	2.24

2.4.2 Verification of Absolute Maximum Moment

The live load moments obtained from FEM analysis were compared to the moment values obtained from basic structural analysis to verify that the truck loadings were modeled correctly. The following calculations show the analysis for obtaining the absolute maximum moment due to moving loads in a simple span.

*2.4.2.1 **Maximum Moment due to HS-20 Design Truck Loading***

For a simple-span bridge, a 14 ft spacing between the rear and middle axles produces the maximum moment for the HS-20 design truck loading. Three cases can be considered for a bridge under HS-20 truck loading depending on the span length.

1. The first case is placing only the rear axle at the center of the span to produce the maximum moment at the center of the span. This loading governs for spans smaller than 24 ft. The absolute maximum moment at the midspan can be calculated as follows:

$$M = \frac{PL}{4} = 8L \tag{2.8}$$

2. The second case is the application of the rear and middle axles on the span to produce the maximum moment on the span. Figure 2.10(a) show the general loading diagram to determine the location of the truck that produces the maximum moment.

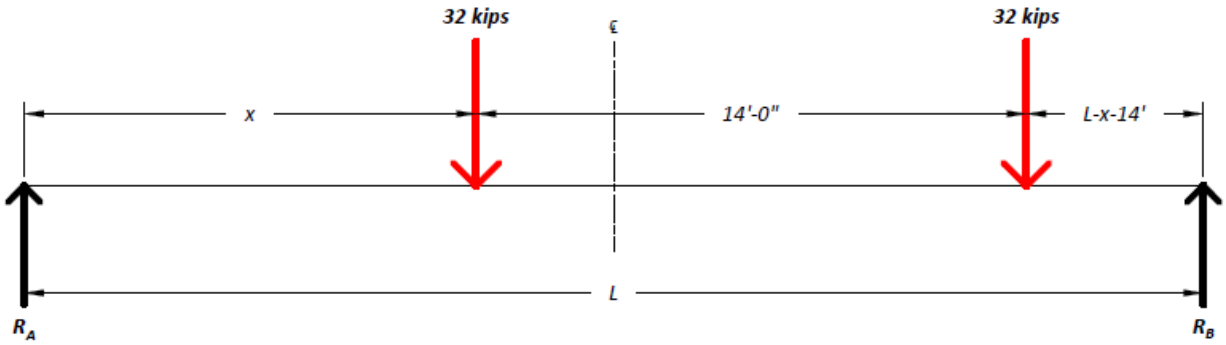

(a) Diagram of Loading Scheme

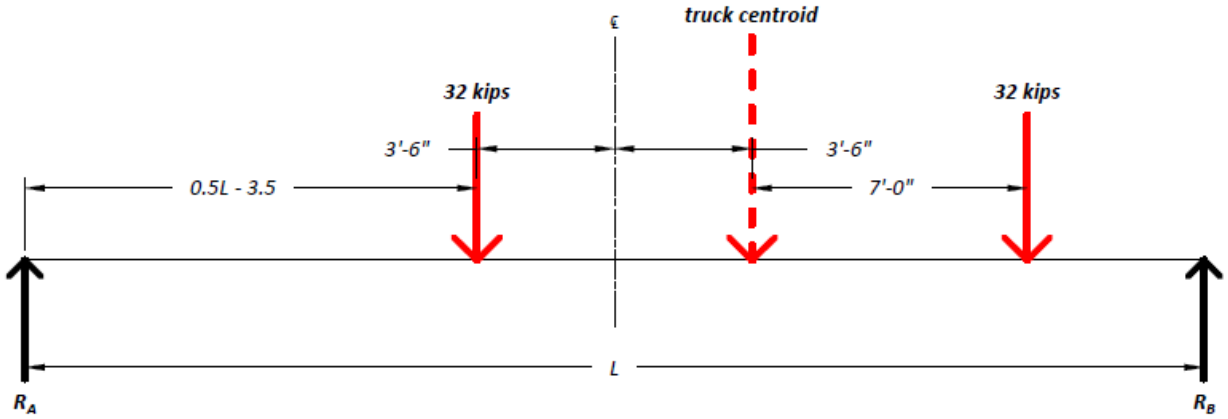

(b) Location of Axles for Maximum Moment

Figure 2.10. Positioning of HS-20 Truck for Maximum Moment for Case 2

The maximum moment occurs under one of the axles when it is located at a distance x from the support. The support reaction and the maximum moment can be calculated as shown in Equations (2.9) and (2.10):

$$R_A = 32\left(\frac{L-x}{L}\right) + 32\left(\frac{L-x-14}{L}\right) = 64 - \frac{64x}{L} - \frac{448}{L} \qquad (2.9)$$

$$M_{at\ x} = R_A x \tag{2.10}$$

The distance x to produce the absolute maximum moment can then be computed by setting the first derivative of the moment equation to zero and solving for x:

$$x = \frac{L}{2} - 3.5 \tag{2.11}$$

By substituting this value for x in Equation (2.10), the value for the absolute maximum moment on the span due to the HS-20 truck loading for Case 2 can be found as follows:

$$M_{max} = (16L) - 224 + \frac{784}{L} \tag{2.12}$$

Note that the maximum moment occurs under one of the axles when this axle and the resultant of the load group are placed equidistant from the centerline of the span. Figure 2.10(b) shows a diagram of this moment critical position of the two 32-kip axle loading. This loading case governs for span lengths between 24 ft and 34 ft.

3. The third case is the application of the full HS-20 design truck on the span to produce the maximum moment on the span. Figure 2.11(a) shows the loading diagram that can be used to determine the location of the truck position that will produce the maximum moment.

   The maximum moment occurs under the middle axle when it is located at a distance $x +$ 14 ft from the support. The support reaction and the maximum moment can be calculated as shown in Equations (2.13) and (2.14):

$$R_A = 32\left(\frac{L-x}{L}\right) + 32\left(\frac{L-x-14}{L}\right) + 8\left(\frac{L-x-28}{L}\right) = 72 - \frac{72x}{L} - \frac{672}{L} \tag{2.13}$$

$$M_{at\ (x+14)} = (R_A x) + (R_A - 32)(14) \tag{2.14}$$

The distance x to produce the absolute maximum moment can then be computed by setting the first derivative of the moment equation to zero and solving for x:

$$x = \frac{L}{2} - 11.67 \tag{2.15}$$

By substituting this value for x in Equation (2.14), the value for the maximum moment on the span due to the HS-20 truck loading can be found as follows:

$$M_{max} = (18L) - 280 + \frac{392}{L} \tag{2.16}$$

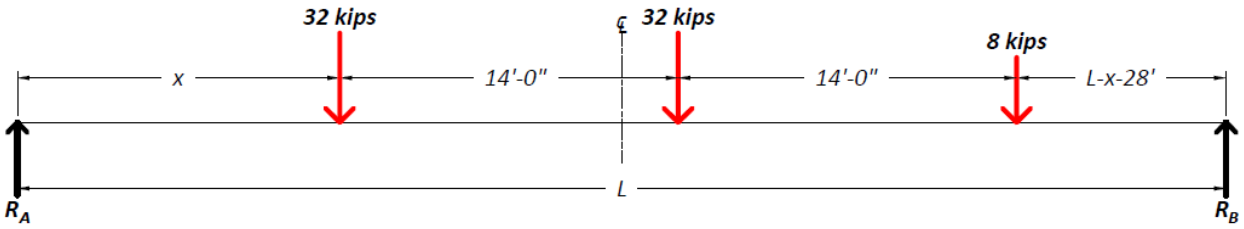

(a) Diagram of loading scheme

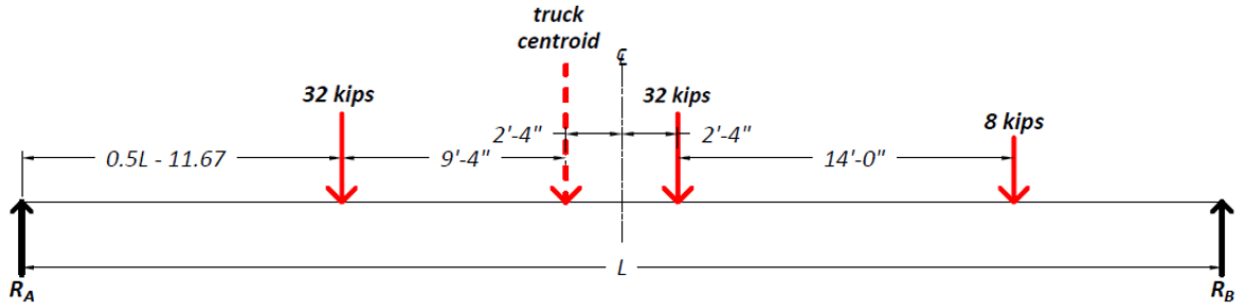

(b) Location of axles for maximum moment

Figure 2.11. Positioning of HS-20 Truck for Maximum Moment for Case 3

Note that the maximum moment occurs under the middle axle when the middle axle and the resultant of the load group are placed equidistant from the centerline of the span. Figure 2.11(b) shows a diagram of this moment critical position of the three-axle loading for the HS-20 truck. This loading case governs for span lengths longer than 34 ft.

Both the SM-5 and SM-21 bridges are longer than 34 ft. Therefore, the absolute maximum moment values due to a one-lane-loaded case were computed using the equation derived for Case 3. The absolute moment values calculated from basic structural analysis and the maximum moment results obtained for the total section from FEM analysis are compared in Table 2.9.

*2.4.2.2 **Maximum Moment due to Designated HL-93 Loading***

The designated HL-93 load model considers the HS-20 design truck or design tandem coincident with a uniformly distributed design lane load. The absolute maximum moment for a simple span due to the combined truck plus lane and tandem plus lane loading was calculated:

1. For the combined loading of the HS-20 design truck and lane loading, shown in Figure 2.12(a), the absolute maximum moment that occurs under the middle axle and the corresponding longitudinal position of the combined loading is calculated by first finding the reaction at Support A and the maximum moment, shown in Equations (2.17) and (2.18):

$$R_A = \left[72 - \frac{72x}{L} - \frac{672}{L}\right] + 0.32L \tag{2.17}$$

$$M_{at\,(x+14)} = \left(72 - \frac{72x}{L} - \frac{672}{L}\right)x + \left(40 - \frac{72x}{L} - \frac{672}{L}\right)(14) + 0.32L(x+14) - 0.32(x+14)^2 \tag{2.18}$$

The distance x to produce the absolute maximum moment can then be computed by setting the first derivative of the moment equation to zero and solving for x.

$$x = \frac{L^2 + 197L - 5250}{2L + 450} \tag{2.19}$$

By substituting this value for x in Equation (2.18) the value for the maximum moment on the span due to the HL-93 design truck and lane loading can be found.

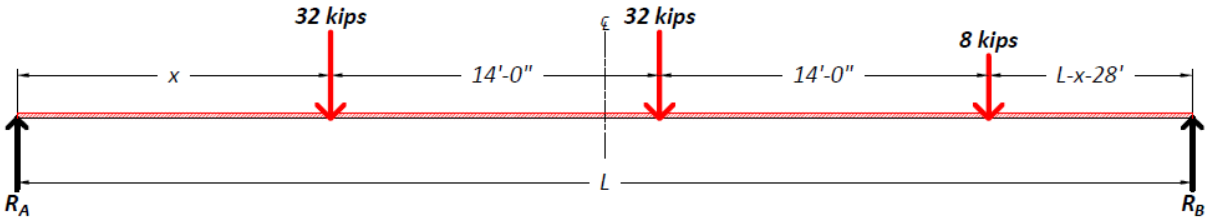

(a) Diagram of Loading Scheme

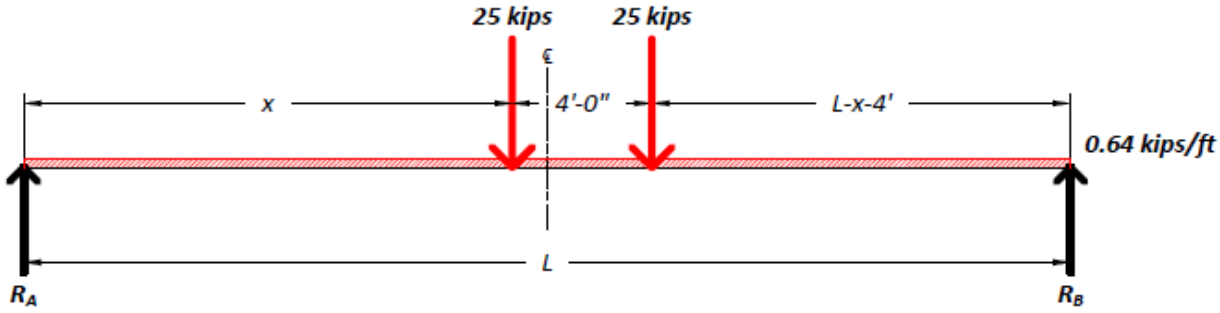

(b) Location of Axles for Maximum Moment

Figure 2.12. Positioning of HL-93 Tandem for Maximum Moment

2. For the combined loading of design tandem and lane loading, shown in Figure 2.12(b), the absolute maximum moment that occurs under the middle axle and the corresponding longitudinal position of the combined loading is calculated by first finding the reaction at Support A and the maximum moment, shown in Equation (2.20) and (2.21):

$$R_A = \left[50 - \frac{50x}{L} - \frac{100}{L}\right] + 0.32L \tag{2.20}$$

$$M_{at\,x} = \left(50 - \frac{50x}{L} - \frac{100}{L}\right)x + 0.32Lx - 0.32x^2 \tag{2.21}$$

The distance x to produce the absolute maximum moment can then be computed by setting the first derivative of the moment equation to zero and solving for x.

$$x = \frac{4L^2 + 625L - 1250}{8L + 1250} \tag{2.22}$$

By substituting this value for x in Equation (2.21), the value for the maximum moment on the span due to the HL-93 design tandem and lane combined loading can be found.

Table 2.9 shows the live load moments calculated using this method, the FEM calculated moments, and the percent difference between them. The FEM live load moments match very closely to the expected live load moments.

Table 2.9. Comparison of Live Load Moment on Composite Section for SM Bridges

Bridge ID	Applied Load	FEM One-Lane Moment on Total Section (kip-ft)	Expected One-Lane Moment on Total Section (kip-ft)	Percent Difference
SM-5	HS-20	452.4	452.8	0.09
	HL-93	581.9	582.1	0.03
SM-21	HS-20	676.7	678.6	0.28
	HL-93	899.3	900.3	0.11

Note: All calculated moments are without the application of the impact factor.

2.4.3 Verification of Maximum Shears

The maximum shears were also verified to ensure that the load models were developed correctly. The FEM models use step-by-step loading for the moving load analysis. The step size of the moving load was adjusted such that the first step with the rear axle of the vehicle on the bridge placed the rear axle approximately one member depth away from the support. The resulting shears from this loading were obtained from the FEM model. These shears were compared with the shears found using classical structural analysis methods by placing the rear axle 1 ft away from the support. Table 2.10 shows the live load shears calculated using this method, the FEM calculated shears, and the percent difference between them. The FEM live load shears matched up very closely to the expected live load shears.

Table 2.10. Comparison of Live Load Shears on Composite Section for SM Bridges

Bridge ID	Applied Load	FEM One-Lane Shear on Total Section (kips)	Expected One-Lane Shear on Total Section (kips)	Percent Difference
SM-5	HS-20	53.5	53.5	0.01
	HL-93	59.0	59.1	0.26
SM-21	HS-20	57.9	57.9	0.00
	HL-93	74.7	74.8	0.21

Note: All calculated shears are without the application of the impact factor.

2.5 SIMULATING VEHICLE LOADS

2.5.1 Simulating HS-20 Truck Loading

The HS-20 truck-loads were placed transversely on the SM bridges per the *AASHTO Standard Specifications* (AASHTO 2002). Both SM bridges are two-lane bridges.

2.5.1.1 ***Bridge SM-5***

Bridge SM-5 has a lane width of 11 ft 9 in. For a one-lane-loaded case, based on the *AASHTO Standard Specifications* (AASHTO 2002), the truck was first placed so that the exterior wheel line was 2 ft away from the edge of the barrier. For each separate load case, the truck was moved transversely 1 ft closer to the interior of the bridge. The third and final load case was only moved 9 in. closer to the centerline of the bridge in order to keep the interior wheel line 2 ft away from the interior edge of the lane. This procedure created three different one-lane-loaded cases, shown in Figure 2.13(a): one with the exterior wheel line 2 ft from the barrier (Path 1), one with the exterior wheel line 3 ft from the barrier (Path 2), and one with the exterior wheel line 3 ft 9 in. from the barrier (Path 3).

For the two-lane-loaded case, the first truck was positioned in the same way as for each one-lane-loaded case. A second truck was placed in the second lane of the bridge, with the interior wheel line 2 ft away from the interior edge of the lane for each load case. This created three separate two-lane-loaded cases: Path 1 + Path 4, Path 2 + Path 4, and Path 3 + Path 4, as shown in Figure 2.13(b).

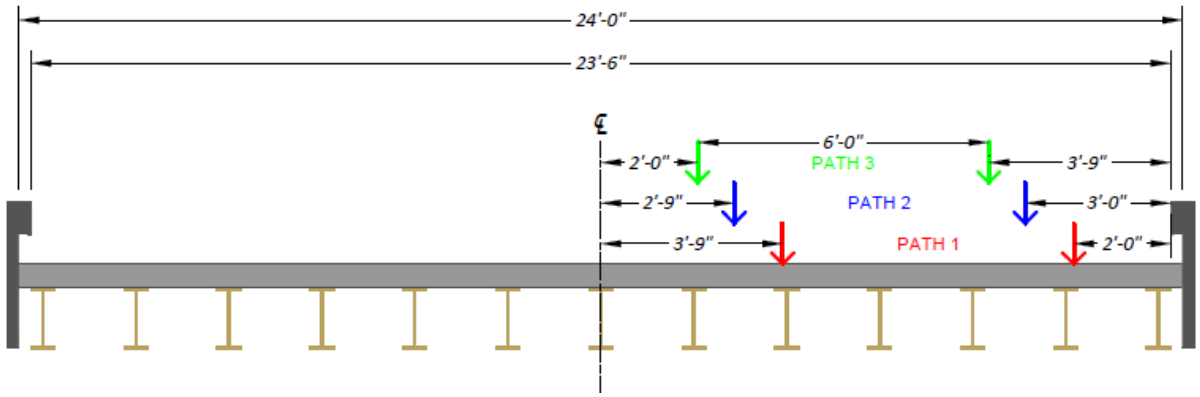

(a) One-Lane Loading Paths

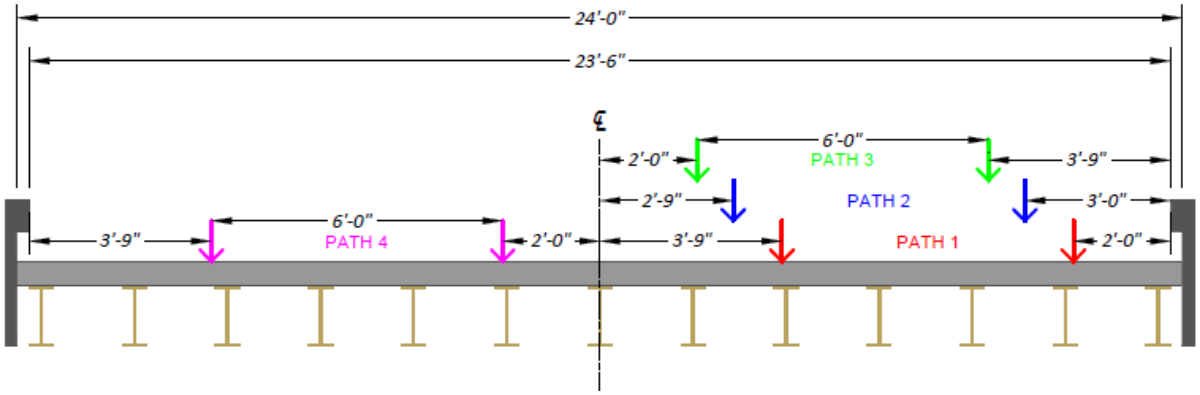

(b) Two-Lane Loading Paths

Figure 2.13. HS-20 Loading Cases for Bridge SM-5

2.5.1.2 ***Bridge SM-21***

Bridge SM-21 has a lane width of 12 ft. For a one-lane-loaded case, based on the *AASHTO Standard Specifications* (AASHTO 2002), the HS-20 design truck was placed at three transverse positions within the first lane, similar to Bridge SM-5. Figure 2.14(a) shows the exact transverse positions of the three paths of the truck in the first lane. The two-lane-loaded cases were also created similarly to Bridge SM-5, which produced three separate two-lane-loaded cases for the bridge, Path 1 + Path 4, Path 2 + Path 4, and Path 3 + Path 4, as shown in Figure 2.14(b).

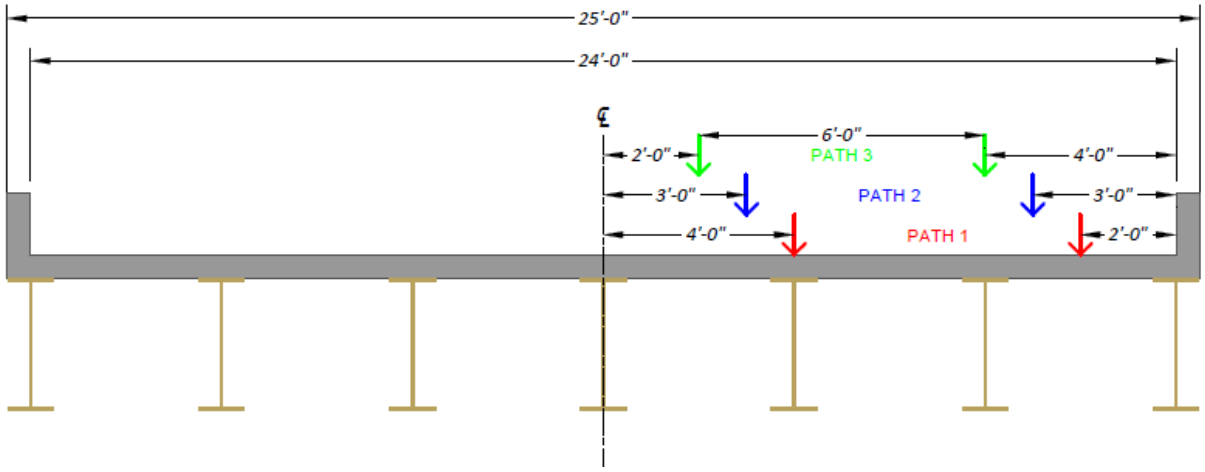

(a) One-Lane Loading Paths

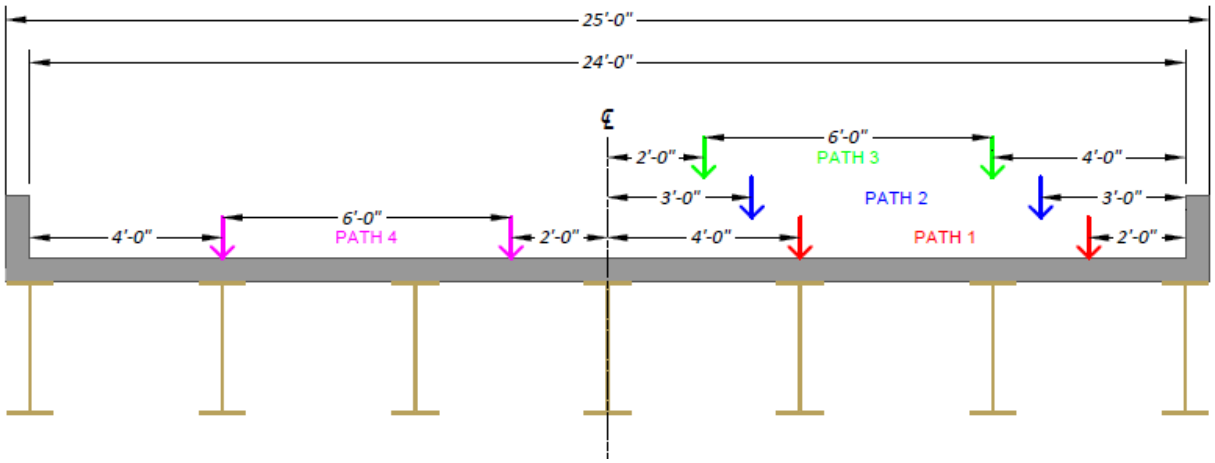

(b) Two-Lane Loading Paths

Figure 2.14. HS-20 Loading Cases for Bridge SM-21

2.5.2 Simulating HL-93 Loading

The HL-93 load model was also placed at different transverse locations on the SM bridges per the *AASHTO LRFD Specifications* (AASHTO 2017).

*2.5.2.1 **Bridge SM-5***

Bridge SM-5 has a lane width of 11 ft 9 in. and a span length of approximately 40 ft 2 in. Since the tandem load configuration controls for spans shorter than 40 ft 6 in., the tandem plus lane load was used for the HL-93 loading of SM-5. The design tandem was placed transversely in the same

manner as described for the HS-20 load. The lane load was added so that the exterior edge of the lane load in Path 1 was immediately adjacent to the railing of the bridge. The exterior edge of the lane load in Path 2 was placed 1 ft away from the railing, and the interior edge of the lane load in Path 3 was placed immediately adjacent to the interior edge of the lane. A total of three different one-lane-loaded cases were created in the first lane, as shown in Figure 2.15(a): (1) one with the exterior wheel line of the tandem 2 ft from the railing and the exterior edge of the lane load against the railing (Path 1), (2) one with the exterior wheel line of the tandem 3 ft from the railing and the exterior edge of the lane load 1 ft from the railing (Path 2), and (3) one with the exterior wheel line of the tandem 3 ft 9 in. from the railing and the interior edge of the lane load adjacent to the interior edge of the lane (Path 3).

For a two-lane-loaded case, the tandem and lane loads were positioned in the same way as for each one-lane-loaded case. A second tandem was placed in the second lane of the bridge, with the interior wheel line 2 ft away from the interior edge of the lane for each load case. A second lane load was placed with its right edge against the interior edge of the lane in the second lane. This created three separate two-lane-loaded cases for the bridge: Path 1 + Path 4, Path 2 + Path 4, and Path 3 + Path 4, as shown in Figure 2.15(b).

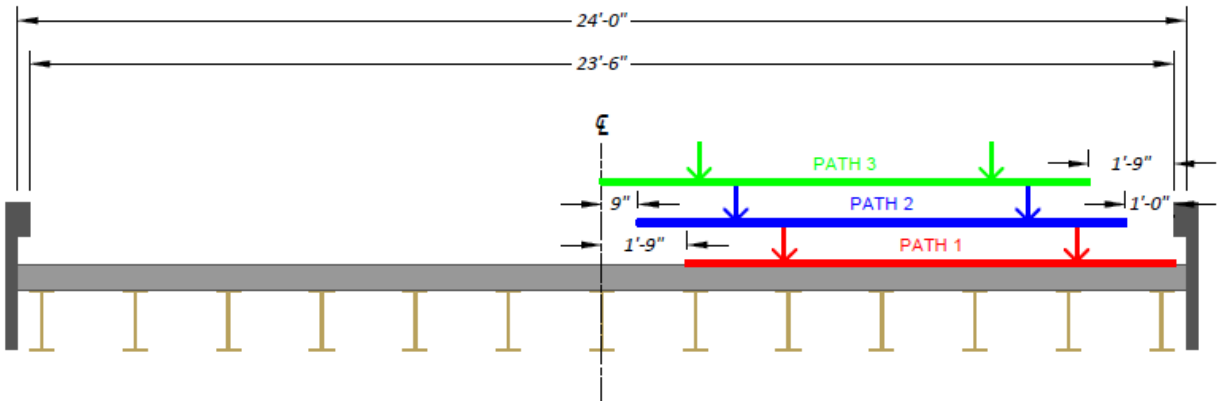

(a) One-Lane Loading Paths

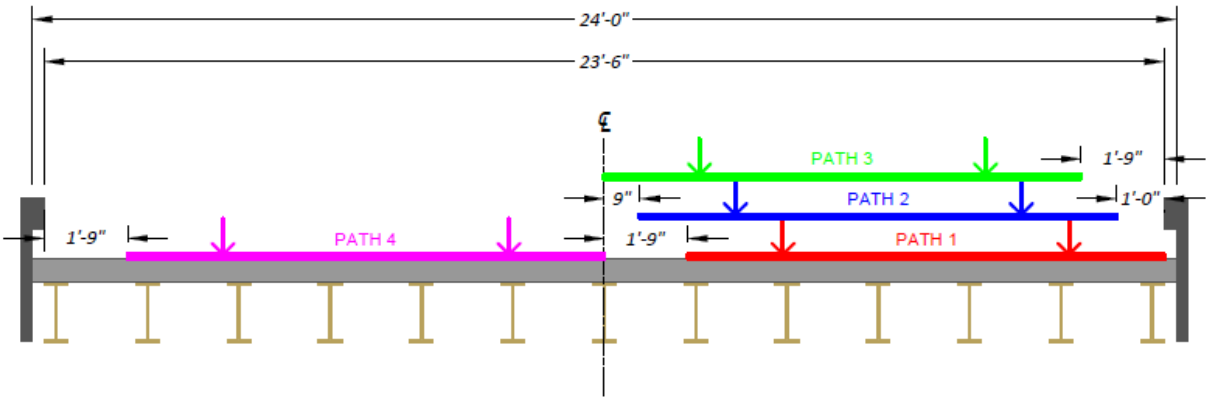

(b) Two-Lane Loading Paths

Figure 2.15. HL-93 Loading Cases for Bridge SM-5

2.5.2.2 ***Bridge SM-21***

Bridge SM-21 has a lane width of 12 ft and a span length of approximately 52 ft 10 in. The HS-20 truck configuration was now used along with the lane load since the tandem no longer controls for span lengths above 40 ft 6 in. For a one-lane-loaded case based on the *AASHTO LRFD Specifications* (AASHTO 2017), the HL-93 loading scheme was placed at three transverse positions within the first lane, similar to the SM-5 bridge. Figure 2.16(a) shows the exact transverse positions of the three paths of the truck and lane load in the first lane. Two-lane-loaded cases were also created similarly to the SM-5 Bridge, which produced three separate two-lane-loaded cases for the bridge: Path 1 + Path 4, Path 2 + Path 4, and Path 3 + Path 4, as shown in Figure 2.16(b).

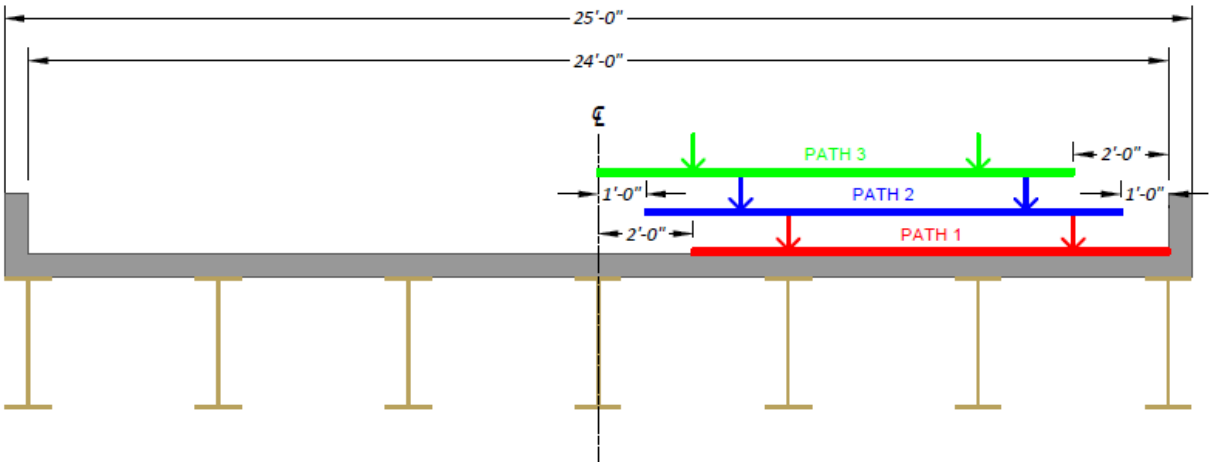

(a) One-Lane Loading Paths

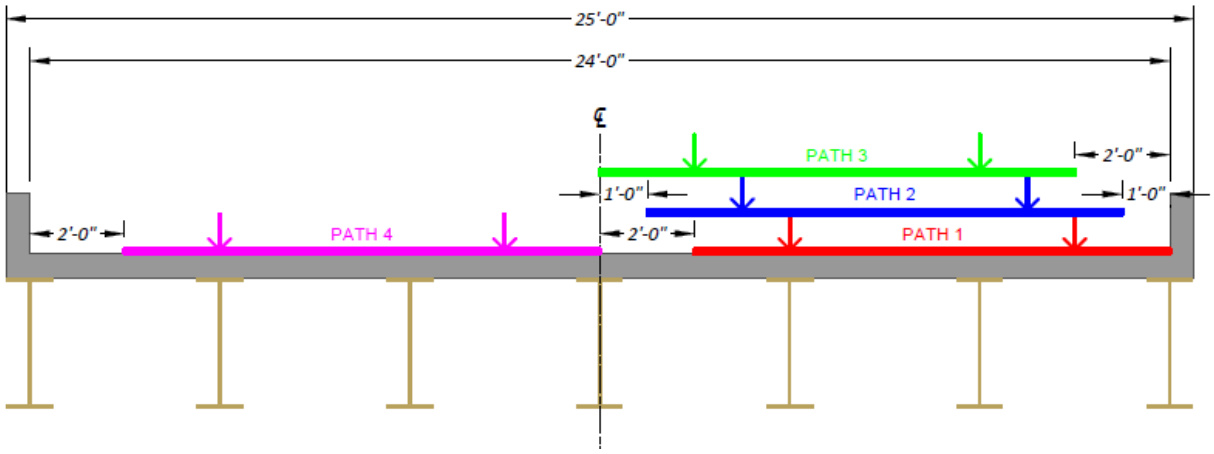

(b) Two-Lane Loading Paths

Figure 2.16. HL-93 Loading Cases for Bridge SM-21

2.6 FEM RESULTS FOR BRIDGE SM-5

Bridge SM-5 was analyzed using the CSiBridge software under the loading scenarios provided in Figure 2.13 through Figure 2.16. Girder displacement profiles were obtained for the load cases that represent the field-test plans. Modal analyses were conducted for both composite and non-composite conditions to determine estimated modal frequencies and mode shapes. Live load moment and shear values were also extracted and analyzed to compare the expected LLDFs with

the LLDFs prescribed in *AASHTO Standard Specifications* (AASHTO 2002) and *AASHTO LRFD Specifications* (AASHTO 2017).

The *AASHTO Standard Specifications* (AASHTO 2002) Article 3.23.2.3.1.4 states, "In no case shall an exterior stringer have less carrying capacity than an interior stringer." The *AASHTO LRFD Specifications* (AASHTO 2017) Article 2.5.2.7.1 states, "Unless future widening is virtually inconceivable, the load carrying capacity of exterior beams shall not be less than the load carrying capacity of an interior beam." In some cases for bridges SM-5 and SM-21, the moment LLDF determined through *AASHTO Standard and AASHTO LRFD Specifications* for the exterior girder is smaller than the moment LLDF for the interior girder. Therefore, interior girder moment LLDFs were used when calculating the exterior girder moment demands to account for any potential future widening of the bridge.

2.6.1 Modal Properties

The first two modes of Bridge SM-5 were identified as the first longitudinal bending mode and the first torsional mode. The frequencies of the non-composite bridge were determined to be 4.04 Hz and 4.70 Hz, respectively. Figure 2.17(a) shows the amplitude contours of the first longitudinal bending mode shape and the normalized amplitudes along the span for the non-composite condition. Figure 2.17(b) shows the amplitude contours for the first torsional mode shape and the normalized amplitudes transverse to the span for the non-composite condition. The frequencies of the longitudinal bending and torsional modes for the composite bridge were determined to be 6.27 Hz and 7.12 Hz, respectively. Figure 2.18(a) shows the amplitude contours of the first longitudinal bending mode shape and the normalized amplitudes along the span for the composite condition. Figure 2.18(b) shows the amplitude contours resulting from the first torsional mode and the normalized amplitudes transverse to the span for composite analysis.

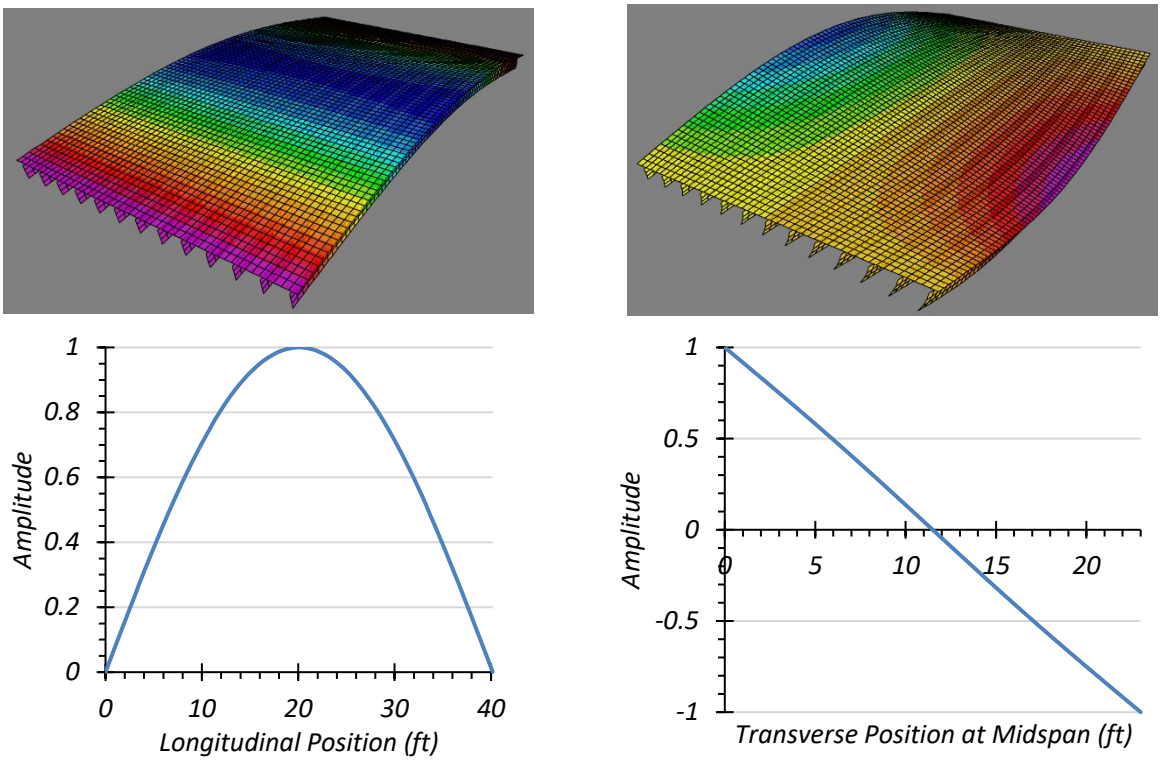

(a) Longitudinal bending Mode (f=4.04 Hz) *(b) Torsional Mode (f=4.69 Hz)*

Figure 2.17. First Two Mode Shapes of Non-Composite Bridge SM-5

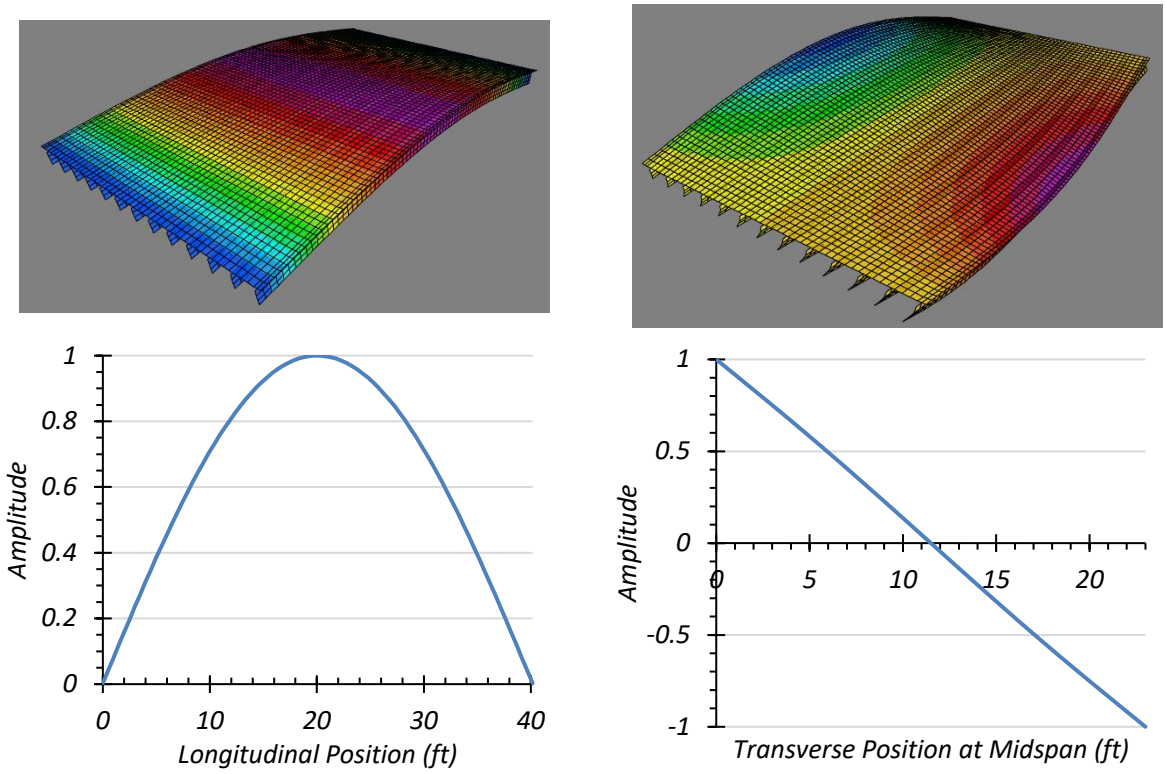

(a) Longitudinal bending Mode (f=6.27 Hz) *(b) Torsional Mode (f=7.12 Hz)*

Figure 2.18. First Two Mode Shapes of Composite Bridge SM-5

2.6.2 HS-20 Live Load Analysis

Bridge SM-5 was first analyzed using the HS-20 design truck presented in the *AASHTO Standard Specifications* (AASHTO 2002). The bridge was analyzed for one-lane- and two-lane-loaded cases along four transverse paths, as shown in Figure 2.13. Deflection, moment, and shear results were obtained.

*2.6.2.1 **Deflection Results***

Figure 2.19 shows the estimated girder deflection profiles and contours along the span for a one-lane HS-20 loading along Path 1 and Path 4 when the bridge is analyzed as fully non-composite. Table 2.11 shows the corresponding maximum deflections for each girder, assuming non-composite action. Load Paths 1 and 4 are the only ones shown because they are the load paths planned for later load tests, and were selected to maximize the forces on an interior girder and on an exterior girder.

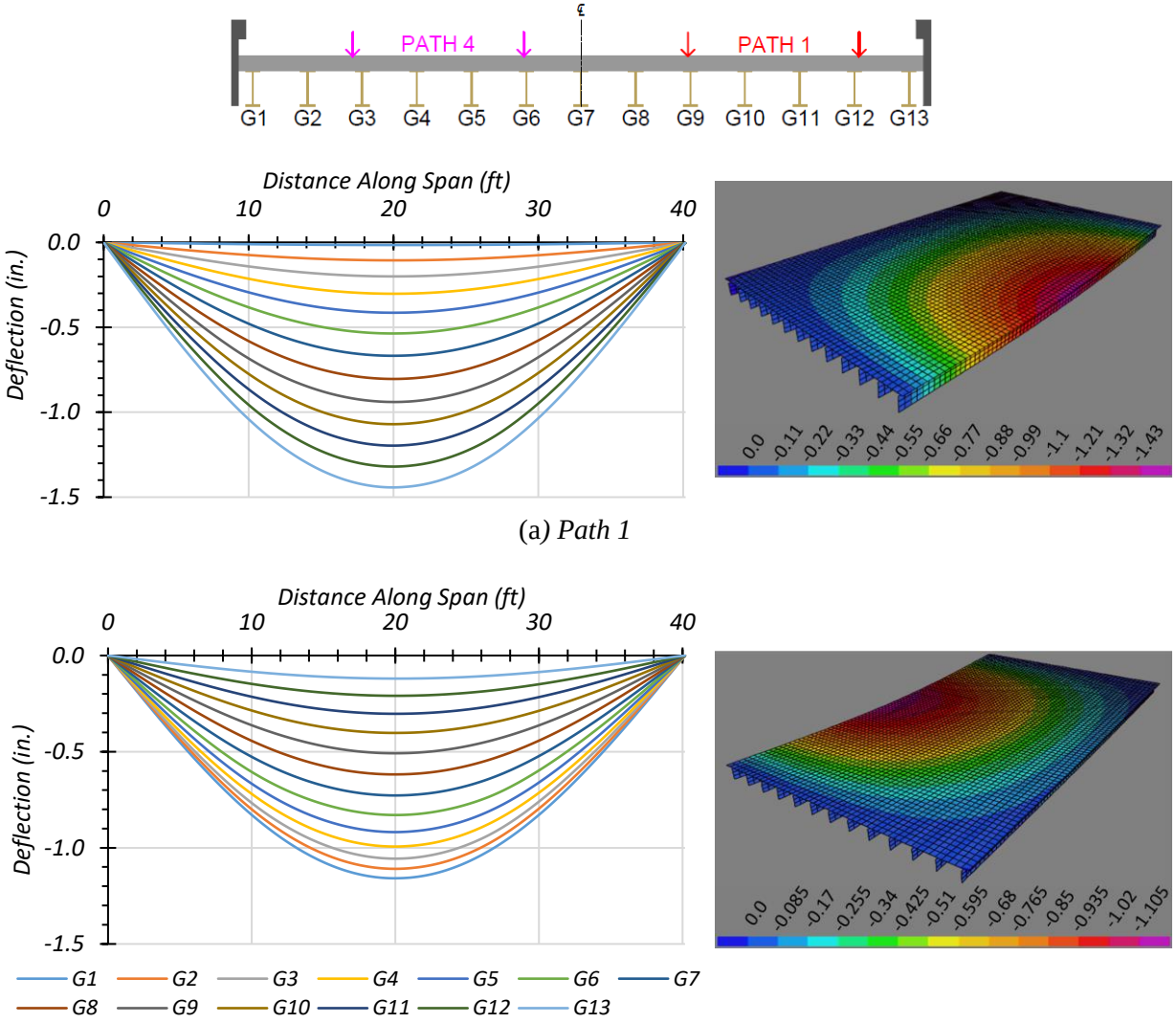

(a) *Path 1*

(b) Path 4

Figure 2.19. Deflection Profiles for Non-Composite Bridge SM-5 with HS-20 Loading

Table 2.11. Maximum Deflections for Non-Composite Bridge SM-5 with HS-20 Loading

Loading	G1	G2	G3	G4	G5	G6	G7	G8	G9	G10	G11	G12	G13
Path 1	−0.016	−0.106	−0.200	−0.302	−0.414	−0.536	−0.668	−0.804	−0.940	−1.070	−1.197	−1.320	−1.442
Path 4	−1.158	−1.109	−1.056	−0.993	−0.918	−0.829	−0.728	−0.618	−0.508	−0.402	−0.303	−0.209	−0.120

Note: G = girder, paths indicate transverse loading positions as shown, deflections have inch units

Figure 2.20 shows the estimated girder deflection profiles and contours along the span for one-lane HS-20 loading along Path 1 and Path 4 when the bridge is analyzed as fully composite. Table 2.12 shows the corresponding maximum deflections for each girder, assuming fully composite action. Load Paths 1 and 4 are the only ones shown because they are the load paths planned for later load tests, and were selected to maximize the forces on an interior girder and on an exterior girder.

For both non-composite and composite cases, the maximum deflections were obtained in Girder G13 (G13) when the HS-20 truck was run along Path 1. The estimated deflections were 1.442 in. and 0.691 in. for the non-composite and composite cases, respectively. This result indicates that the composite bridge is 70.4 percent stiffer in flexure than the non-composite bridge. The maximum deflections obtained when the HS-20 truck was run along Path 4 were in Girder G1 for both the non-composite and composite case. The estimated deflections were 1.158 in. and 0.527 in. for the non-composite and composite cases, respectively. This result indicates that the composite bridge is 74.9 percent stiffer in flexure than the non-composite bridge. The slightly different values of relative stiffness suggest that the relative girder deflection depends on the location of loading and corresponding load distribution.

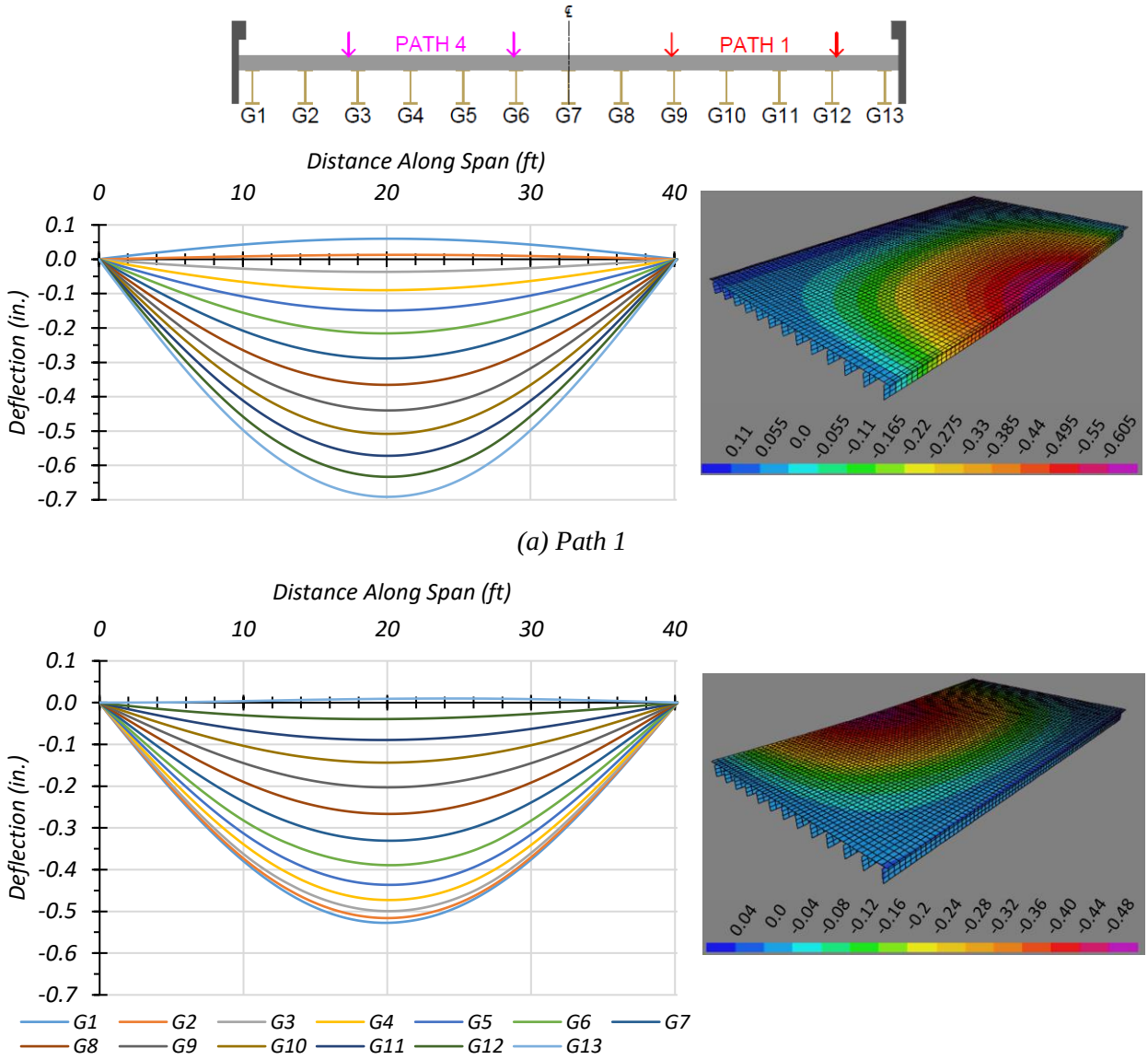

(a) Path 1

(b) Path 4

Figure 2.20. Deflection Profiles for Composite Bridge SM-5 with HS-20 Loading

Table 2.12. Maximum Deflections for Composite Bridge SM-5 with HS-20 Loading

Loading	G1	G2	G3	G4	G5	G6	G7	G8	G9	G10	G11	G12	G13
Path 1	0.060	0.013	−0.037	−0.090	−0.149	−0.216	−0.289	−0.365	−0.440	−0.508	−0.572	−0.633	−0.691
Path 4	−0.527	−0.516	−0.499	−0.473	−0.436	−0.389	−0.331	−0.266	−0.203	−0.144	−0.089	−0.039	0.014
Note: G = girder, paths indicate transverse loading positions as shown, deflections have inch units													

2.6.2.2 ***Moment Results***

One-Lane Loading. Figure 2.21 shows the individual girder moments and moment LLDF results for the non-composite Bridge SM-5 under simulated moving HS-20 loading along three one-lane loading paths. Table 2.13 provides the corresponding maximum moment values of each girder for each loading path. The moment LLDF values are calculated using the estimated moment results from FEM analysis. Table 2.15 shows the governing moment LLDFs found using the FEM analysis and compares them to the AASHTO LLDF values. Compared to the FEM results, the governing moment LLDF value computed using the approximate equations in the *AASHTO Standard Specifications* (AASHTO 2002) is slightly unconservative for interior girders, with a g^m_{AASHTO}/g^m_{FEM} ratio of 0.90, while conservative for exterior girders, with a g^m_{AASHTO}/g^m_{FEM} ratio of 1.12.

Figure 2.22 shows the individual girder moments and moment LLDF results for the fully composite Bridge SM-5 under simulated moving HS-20 loading along three one-lane loading paths.

Table 2.14 provides the corresponding maximum moment values of each girder for each loading path. The moment LLDF values are calculated using the estimated moment results from the FEM analysis. Compared to the FEM results, the governing moment LLDF value computed using the approximate equations in the *AASHTO Standard Specifications* (AASHTO 2002) is unconservative for interior girders, with a g^m_{AASHTO}/g^m_{FEM} ratio of 0.80, while being conservative for exterior girders, with a g^m_{AASHTO}/g^m_{FEM} ratio of 1.12.

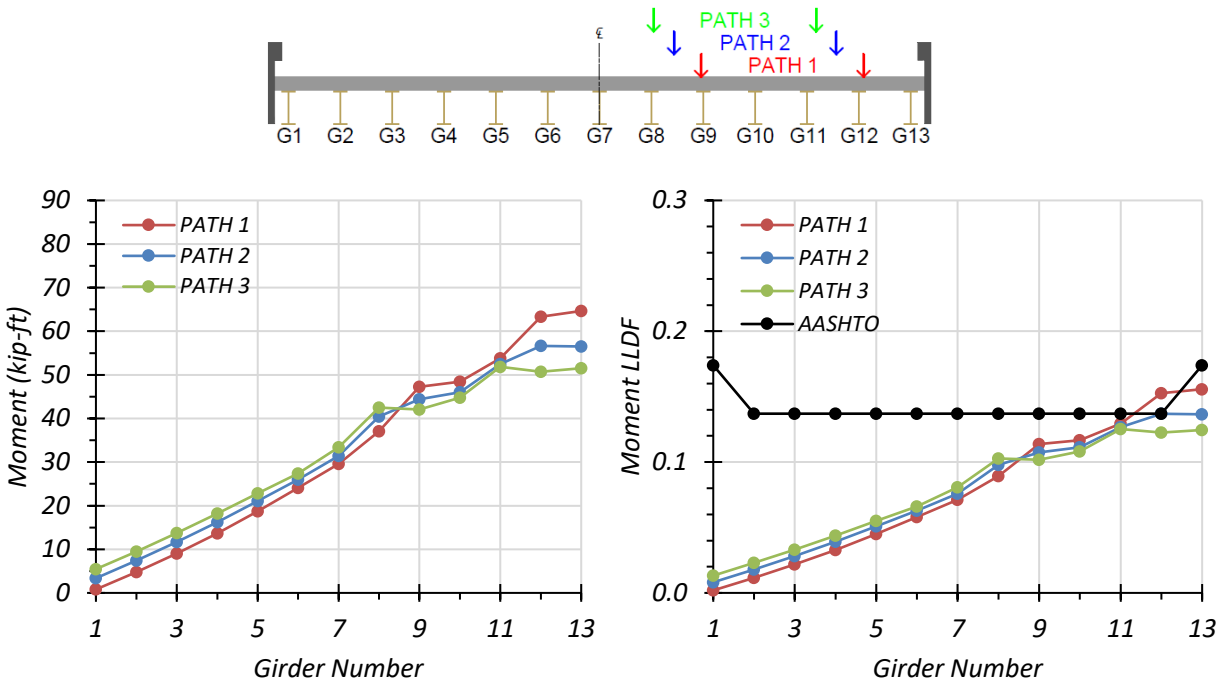

(a) Moment *(b) Moment LLDF*

Figure 2.21. Moment Results for Non-Composite Bridge SM-5 with One-Lane HS-20 Loading

Table 2.13. Maximum Moments for Non-Composite Bridge SM-5 with One-Lane HS-20 Loading

Loading	G1	G2	G3	G4	G5	G6	G7	G8	G9	G10	G11	G12	G13
Path 1	0.8	4.8	9.1	13.7	18.7	24.1	29.6	37.0	47.3	48.4	53.8	63.4	64.7
Path 2	3.4	7.4	11.7	16.2	21.1	26.0	31.4	40.5	44.4	46.0	52.5	56.6	56.5
Path 3	5.5	9.5	13.7	18.2	22.8	27.4	33.4	42.5	42.1	44.8	51.8	50.7	51.5
Note: G = girder, paths indicate transverse loading positions as shown, moments have kip-ft units													

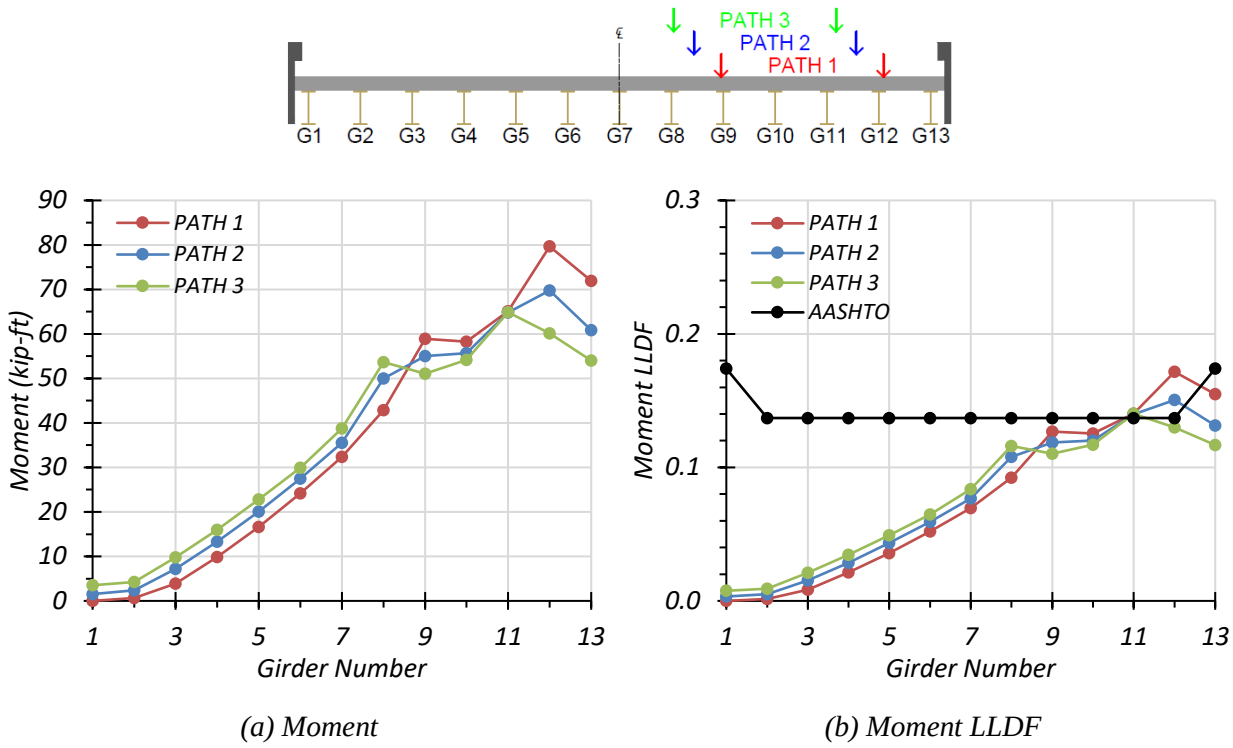

(a) Moment *(b) Moment LLDF*

Figure 2.22. Moment Results for Composite Bridge SM-5 with One-Lane HS-20 Loading

Table 2.14. Maximum Moments for Composite Bridge SM-5 with One-Lane HS-20 Loading

Loading	G1	G2	G3	G4	G5	G6	G7	G8	G9	G10	G11	G12	G13
Path 1	0.0	0.6	3.9	9.9	16.6	24.2	32.3	42.9	58.9	58.3	65.1	79.7	72.0
Path 2	1.5	2.4	7.2	13.3	20.1	27.5	35.5	50.0	55.0	55.7	64.8	69.8	60.9
Path 3	3.5	4.2	9.8	16.0	22.8	29.9	38.8	53.7	51.0	54.2	64.9	60.1	54.0
Note: G = girder, paths indicate transverse loading positions as shown, moments have kip-ft units													

Comparison of governing moment LLDF values computed from FEM results for the composite and non-composite cases reveals that the maximum moment LLDF in an interior girder for the composite bridge is higher than the one for the non-composite bridge, with a $g^m_{composite}/g^m_{non-composite}$ ratio of 1.12. However, the maximum moment LLDF in an exterior girder for the composite bridge is almost the same as the one for the non-composite bridge, with a $g^m_{composite}/g^m_{non-composite}$ ratio of 0.99.

Table 2.15. Governing Moment LLDFs for Bridge SM-5 with One-Lane HS-20 Loading

Type	Girder Location	AASHTO (g^m_{AASHTO})	FEM (g^m_{FEM})	g^m_{AASHTO}/g^m_{FEM}
Non-Composite	Interior	0.137	0.153	0.90
	Exterior	0.174	0.156	1.12
Composite	Interior	0.137	0.172	0.80
	Exterior	0.174	0.155	1.12

Two-Lane Loading. Figure 2.23 shows the individual girder moments and moment LLDF results for the non-composite Bridge SM-5 under simulated moving HS-20 loading along three two-lane loading paths.

Table 2.16 provides the corresponding maximum moment values of each girder for each loading path. The moment LLDF values are calculated using the estimated moment results from FEM analysis. Table 2.18 shows the governing moment LLDFs found using the FEM analysis and compares them to the AASHTO LLDF values. Compared to the FEM results, the governing moment LLDF value computed using the approximate equations in the *AASHTO Standard Specifications* (AASHTO 2002) is almost the same for interior girders, with a g^m_{AASHTO}/g^m_{FEM} ratio of 0.99, and is slightly conservative for exterior girders, with a g^m_{AASHTO}/g^m_{FEM} ratio of 1.03.
Figure 2.24 shows the individual girder moments and moment LLDF results for the fully composite Bridge SM-5 under simulated moving HS-20 loading along three two-lane loading paths.

Table 2.17 provides the corresponding maximum moment values of each girder for each loading path. The moment LLDF values are calculated using the estimated moment results from the FEM analysis. Compared to the FEM results, the governing moment LLDF value computed using the approximate equations in the *AASHTO Standard Specifications* (AASHTO 2002) is slightly unconservative for interior girders, with a g^m_{AASHTO}/g^m_{FEM} ratio of 0.96, and is conservative for exterior girders, with a g^m_{AASHTO}/g^m_{FEM} ratio of 1.12.

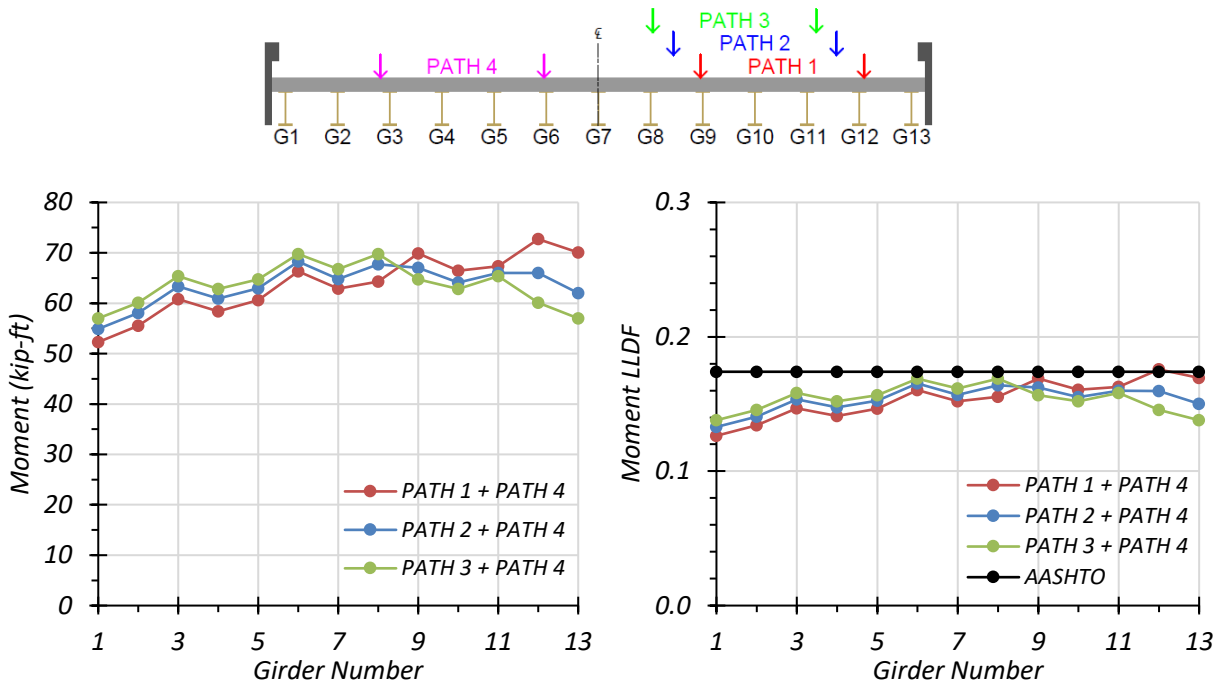

(a) Moment *(b) Moment LLDF*

Figure 2.23. Moment Results for Non-Composite Bridge SM-5 with Two-Lane HS-20 Loading

Table 2.16. Maximum Moments for Non-Composite Bridge SM-5 with Two-Lane HS-20 Loading

Loading	G1	G2	G3	G4	G5	G6	G7	G8	G9	G10	G11	G12	G13
Path 1 + Path 4	52.3	55.5	60.8	58.4	60.6	66.3	62.9	64.3	69.9	66.4	67.3	72.7	70.1
Path 2 + Path 4	54.9	58.1	63.4	60.9	63.0	68.3	64.8	67.7	67.0	64.1	66.0	66.0	62.0
Path 3 + Path 4	57.0	60.1	65.4	62.8	64.7	69.8	66.7	69.8	64.7	62.8	65.4	60.1	57.0
Note: G = girder, paths indicate transverse loading positions as shown, moments have kip-ft units													

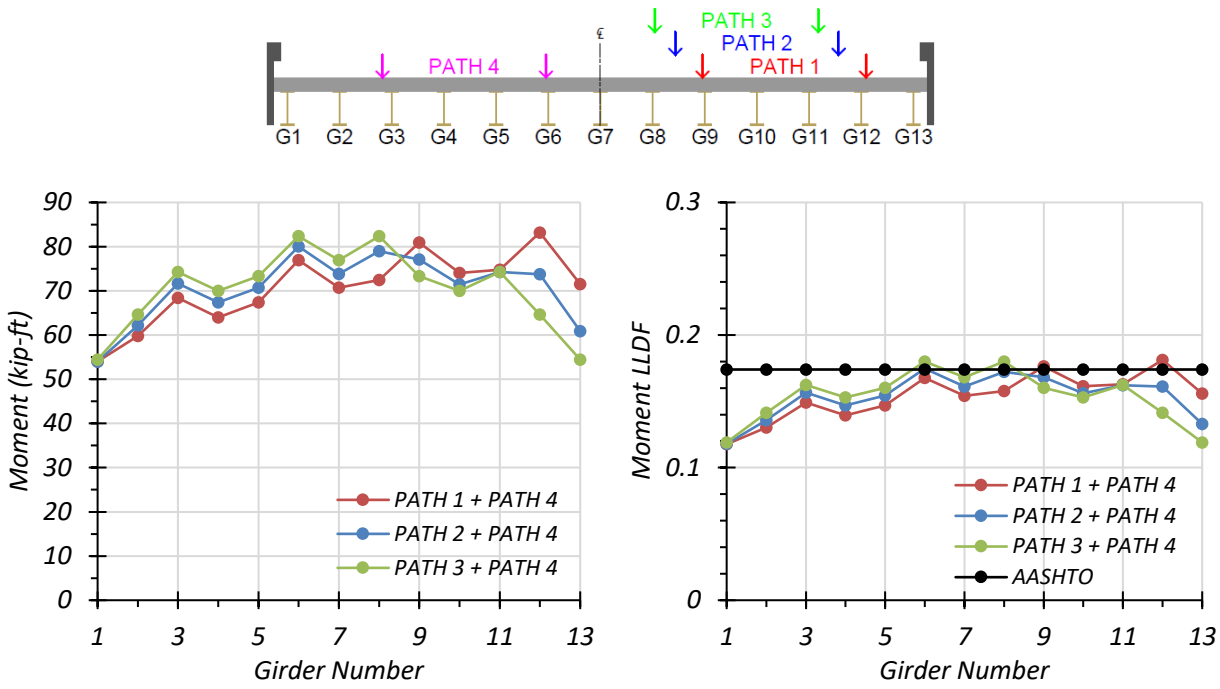

(a) Moment *(b) Moment LLDF*

Figure 2.24. Moment Results for Composite Bridge SM-5 with Two-Lane HS-20 Loading

Table 2.17. Maximum Moments for Composite Bridge SM-5 with Two-Lane HS-20 Loading

Loading	G1	G2	G3	G4	G5	G6	G7	G8	G9	G10	G11	G12	G13
Path 1 + Path 4	54.0	60.1	68.6	63.9	67.4	77.5	70.9	72.6	81.5	74.1	74.7	83.6	72.0
Path 2 + Path 4	54.0	61.6	71.8	67.3	70.9	80.9	74.3	79.7	77.6	71.5	74.3	73.7	60.9
Path 3 + Path 4	54.1	64.0	74.4	70.0	73.6	83.4	77.5	83.4	73.6	70.0	74.4	64.0	54.1
Note: G = girder, paths indicate transverse loading positions as shown, moments have kip-ft units													

Comparison of governing moment LLDF values computed from FEM results for the composite and non-composite cases reveals that the maximum moment LLDF in an interior girder for the composite bridge is higher than the one for the non-composite bridge, with a $g^m_{composite}/g^m_{non-composite}$ ratio of 1.03. However, the maximum moment LLDF in an exterior girder for the composite bridge is lower than the one for the non-composite bridge, with a $g^m_{composite}/g^m_{non-composite}$ ratio of 0.92.

Table 2.18. Governing Moment LLDFs for Bridge SM-5 with Two-Lane HS-20 Loading

Type	Girder Location	AASHTO (g^m_{AASHTO})	FEM (g^m_{FEM})	g^m_{AASHTO}/g^m_{FEM}
Non-Composite	Interior	0.174	0.176	0.99
	Exterior	0.174	0.169	1.03
Composite	Interior	0.174	0.182	0.96
	Exterior	0.174	0.156	1.12

*2.6.2.3 **Shear Results***

One-Lane Loading. Figure 2.25 shows the individual girder shears and shear LLDF results for the non-composite Bridge SM-5 under simulated moving HS-20 loading along three one-lane loading paths.

Table 2.19 provides the corresponding maximum shear values of each girder for each loading path. The shear LLDF values are calculated using the estimated shear results from the FEM analysis. Table 2.21 shows the governing shear LLDFs found using the FEM analysis and compares them to the AASHTO LLDF values. Compared to the FEM results, the governing shear LLDF value computed using the approximate equations in the *AASHTO Standard Specifications* (AASHTO 2002) is unconservative for interior girders, with a g^v_{AASHTO}/g^v_{FEM} ratio of 0.75, and is conservative for exterior girders, with a g^v_{AASHTO}/g^v_{FEM} ratio of 1.21.

Figure 2.26 shows the individual girder shears and shear LLDF results for the fully composite Bridge SM-5 under simulated moving HS-20 loading along three one-lane loading paths. Table 2.20 provides the corresponding maximum shear values of each girder for each loading path. The shear LLDF values are calculated using the estimated shear results from the FEM analysis. Compared to the FEM results, the governing shear LLDF value computed using the approximate equations in the *AASHTO Standard Specifications* (AASHTO 2002) is very unconservative for interior girders, with a g^v_{AASHTO}/g^v_{FEM} ratio of 0.59, and is very conservative for exterior girders, with a g^v_{AASHTO}/g^v_{FEM} ratio of 1.31.

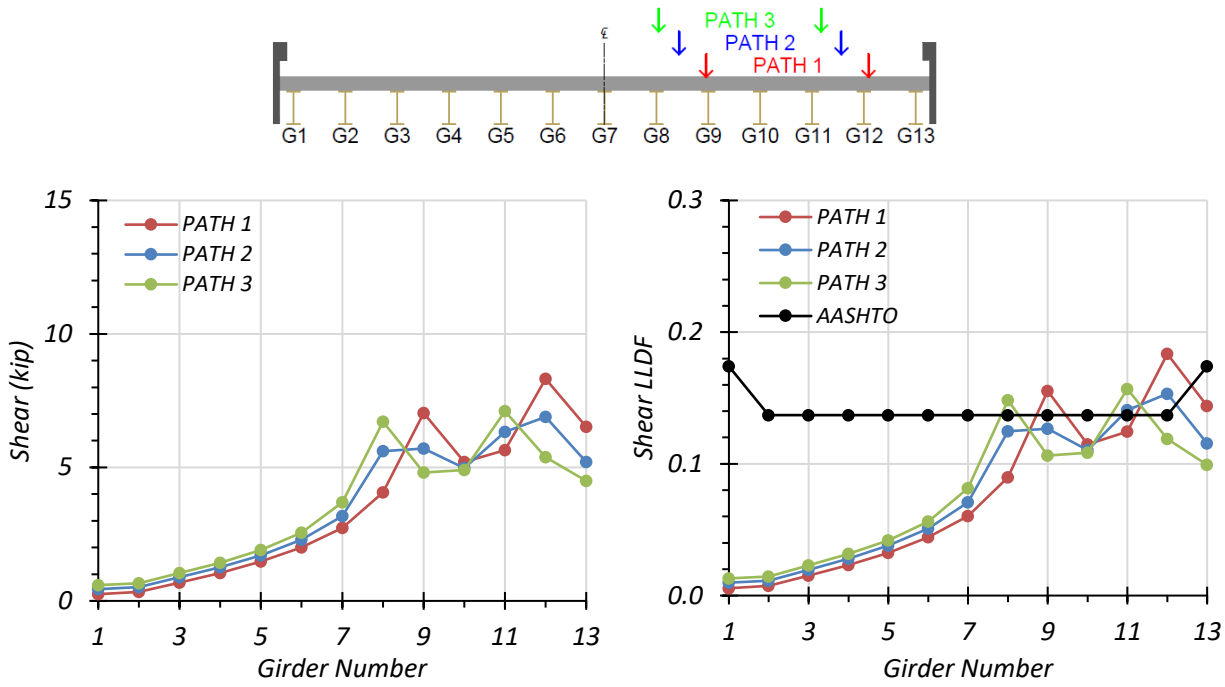

(a) Shear *(b) Shear LLDF*

Figure 2.25. Shear Results for Non-Composite Bridge SM-5 with One-Lane HS-20 Loading

Table 2.19. Maximum Shears for Non-Composite Bridge SM-5 with One-Lane HS-20 Loading

Loading	G1	G2	G3	G4	G5	G6	G7	G8	G9	G10	G11	G12	G13
Path 1	0.3	0.3	0.7	1.0	1.5	2.0	2.7	4.1	7.0	5.2	5.6	8.3	6.5
Path 2	0.4	0.5	0.9	1.3	1.7	2.3	3.2	5.6	5.7	5.0	6.3	6.9	5.2
Path 3	0.6	0.7	1.0	1.4	1.9	2.6	3.7	6.7	4.8	4.9	7.1	5.4	4.5
Note: G = girder, paths indicate transverse loading positions as shown, shears have kip units													

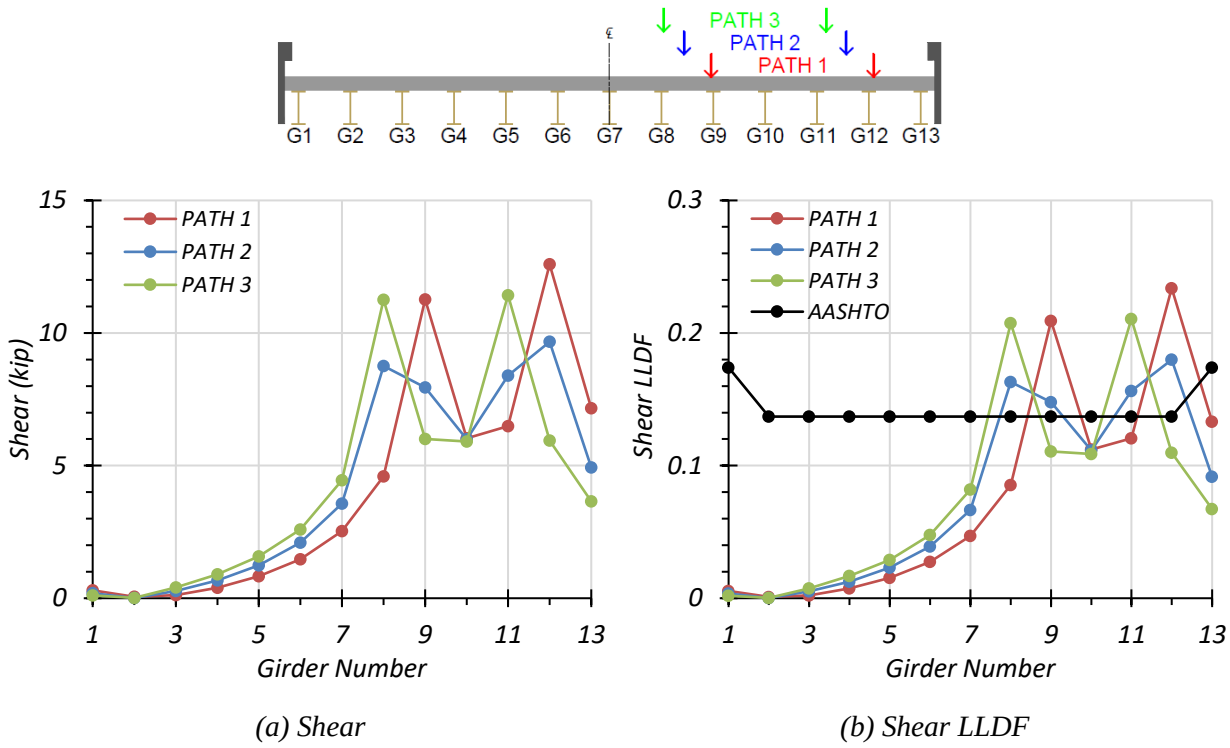

(a) Shear *(b) Shear LLDF*

Figure 2.26. Shear Results for Composite Bridge SM-5 with One-Lane HS-20 Loading

Table 2.20. Maximum Shears for Composite Bridge SM-5 with One-Lane HS-20 Loading

Loading	G1	G2	G3	G4	G5	G6	G7	G8	G9	G10	G11	G12	G13
Path 1	0.3	0.1	0.1	0.4	0.8	1.5	2.5	4.6	11.3	6.0	6.5	12.6	7.2
Path 2	0.2	0.0	0.3	0.7	1.2	2.1	3.6	8.8	7.9	6.0	8.4	9.7	4.9
Path 3	0.1	0.0	0.4	0.9	1.6	2.6	4.4	11.3	6.0	5.9	11.4	6.0	3.7
Note: G = girder, paths indicate transverse loading positions as shown, shears have kip units													

Comparison of governing shear LLDF values computed from FEM results for the composite and non-composite cases reveals that the maximum shear LLDF in an interior girder for the composite bridge is higher than the one for the non-composite bridge, with a $g^v_{composite}/g^v_{non-composite}$ ratio of 1.28. However, the maximum shear LLDF in an exterior girder for the composite bridge is lower than the one for the non-composite bridge, with a $g^v_{composite}/g^v_{non-composite}$ ratio of 0.92.

Table 2.21. Governing Shear LLDFs for Bridge SM-5 with One-Lane HS-20 Loading

Type	Girder Location	AASHTO (g^v_{AASHTO})	FEM (g^v_{FEM})	g^v_{AASHTO}/g^v_{FEM}
Non-Composite	Interior	0.137	0.183	0.75
	Exterior	0.174	0.144	1.21
Composite	Interior	0.137	0.234	0.59
	Exterior	0.174	0.133	1.31

Two-Lane Loading. The same procedure for one-lane loading was conducted for two-lane loading. Figure 2.27 shows the individual girder shears and shear LLDF results for the non-composite Bridge SM-5 under simulated moving HS-20 loading along three two-lane loading paths.

Table 2.22 provides the corresponding maximum shear values of each girder for each loading path. The shear LLDF values are calculated using the estimated shear results from the FEM analysis. Table 2.24 shows the governing shear LLDFs found using the FEM analysis and compares them to the AASHTO LLDF values. Compared to the FEM results, the governing shear LLDF value computed using the approximate equations in the *AASHTO Standard Specifications* (AASHTO 2002) is unconservative for interior girders, with a g^v_{AASHTO}/g^v_{FEM} ratio of 0.84, and is conservative for exterior girders, with a g^v_{AASHTO}/g^v_{FEM} ratio of 1.12.

Figure 2.28 shows the individual girder shears and shear LLDF results for the fully composite Bridge SM-5 under simulated moving HS-20 loading along three one-lane loading paths.

Table 2.23 provides the corresponding maximum shear values of each girder for each loading path. The shear LLDF values are calculated using the estimated shear results from the FEM analysis. Compared to the FEM results, the governing shear LLDF value computed using the approximate equations in the *AASHTO Standard Specifications* (AASHTO 2002) is very unconservative for interior girders, with a g^v_{AASHTO}/g^v_{FEM} ratio of 0.68, and is very conservative for exterior girders, with a g^v_{AASHTO}/g^v_{FEM} ratio of 1.31.

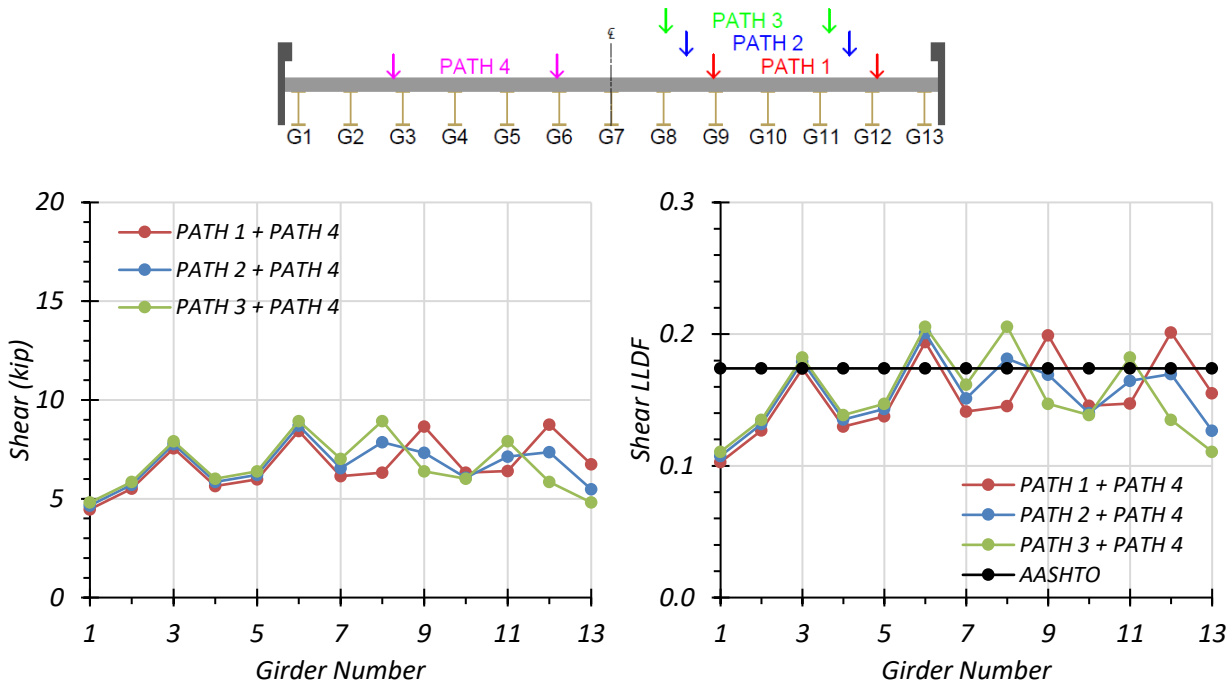

(a) Shear *(b) Shear LLDF*

Figure 2.27. Shear Results for Non-Composite Bridge SM-5 with Two-Lane HS-20 Loading

Table 2.22. Maximum Shears for Non-Composite Bridge SM-5 with Two-Lane HS-20 Loading

Loading	G1	G2	G3	G4	G5	G6	G7	G8	G9	G10	G11	G12	G13
Path 1 + Path 4	4.5	5.5	7.6	5.6	6.0	8.4	6.1	6.3	8.7	6.3	6.4	8.8	6.7
Path 2 + Path 4	4.7	5.7	7.8	5.9	6.2	8.7	6.6	7.9	7.3	6.1	7.1	7.4	5.5
Path 3 + Path 4	4.8	5.9	7.9	6.0	6.4	8.9	7.0	8.9	6.4	6.0	7.9	5.9	4.8
Note: G = girder, paths indicate transverse loading positions as shown, shears have kip units													

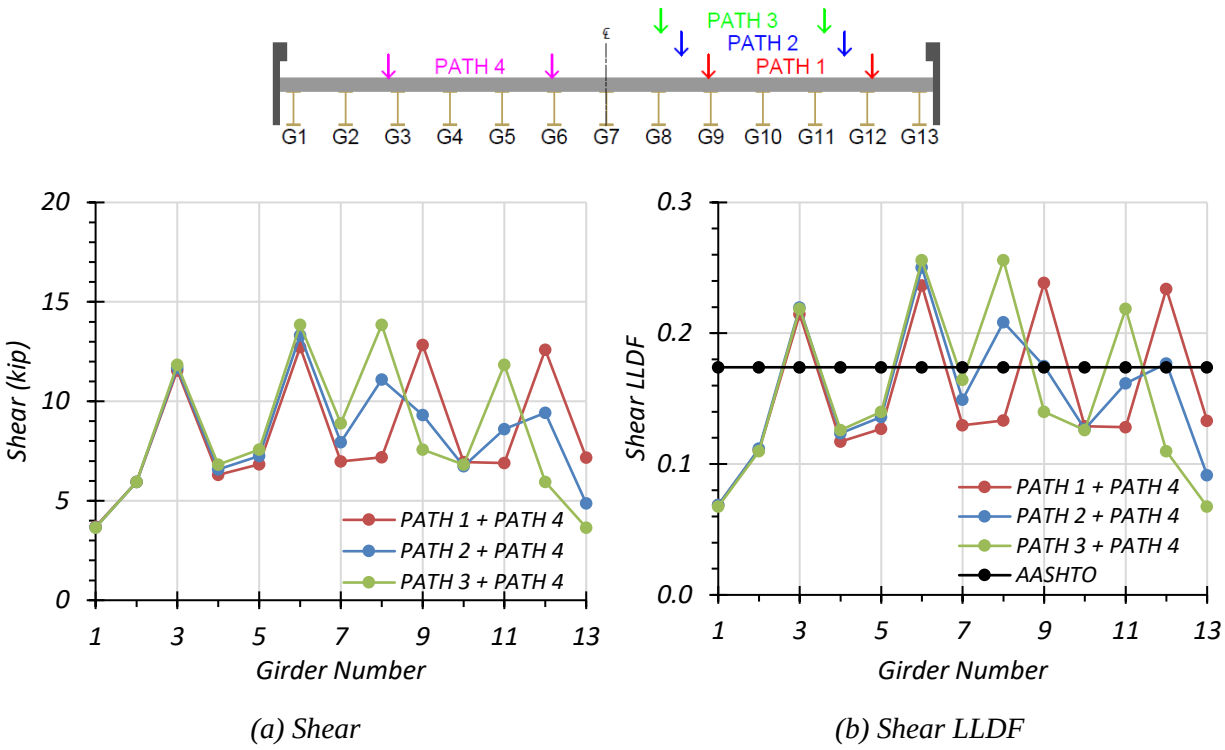

(a) Shear *(b) Shear LLDF*

Figure 2.28. Shear Results for Composite Bridge SM-5 with Two-Lane HS-20 Loading

Table 2.23. Maximum Shears for Composite Bridge SM-5 with Two-Lane HS-20 Loading

Loading	G1	G2	G3	G4	G5	G6	G7	G8	G9	G10	G11	G12	G13
Path 1 + Path 4	3.7	6.0	11.5	6.3	6.8	12.7	7.0	7.2	12.8	6.9	6.9	12.6	7.2
Path 2 + Path 4	3.7	6.0	11.7	6.6	7.2	13.3	7.9	11.1	9.3	6.7	8.6	9.4	4.9
Path 3 + Path 4	3.7	6.0	11.8	6.8	7.6	13.8	8.9	13.8	7.6	6.8	11.8	6.0	3.7
Note: G = girder, paths indicate transverse loading positions as shown, shears have kip units													

Comparison of governing shear LLDF values computed from FEM results for the composite and non-composite cases reveals that the maximum shear LLDF in an interior girder for the composite bridge is higher than the one for the non-composite bridge, with a $g^v_{composite}/g^v_{non-composite}$ ratio of 1.24. However, the maximum shear LLDF in an exterior girder for the composite bridge is lower than the one for the non-composite bridge, with a $g^v_{composite}/g^v_{non-composite}$ ratio of 0.86.

Table 2.24. Governing Shear LLDFs for Bridge SM-5 with Two-Lane HS-20 Loading

Type	Girder Location	AASHTO (g^v_{AASHTO})	FEM (g^v_{FEM})	g^v_{AASHTO}/g^v_{FEM}
Non-Composite	Interior	0.174	0.206	0.84
	Exterior	0.174	0.155	1.12
Composite	Interior	0.174	0.256	0.68
	Exterior	0.174	0.133	1.31

2.6.3 HL-93 Live Load Analysis

Bridge SM-5 was also analyzed using the HL-93 design loading presented in the *AASHTO LRFD Specifications* (AASHTO 2017). The bridge was analyzed for one-lane- and two-lane-loaded cases along four transverse paths, as shown in Figure 2.15. Deflection, moment, and shear results were obtained.

2.6.3.1 ***Deflection Results***

Figure 2.29 shows the estimated girder deflection profiles and contours along the span for one-lane HL-93 loading along Path 1 and Path 4 when the bridge is analyzed as fully non-composite. Table 2.25 shows the corresponding maximum deflections for each girder, assuming non-composite action. Load Paths 1 and 4 are the only ones shown because they are the load paths planned for later load tests, and were selected to maximize the forces on an interior girder and on an exterior girder.

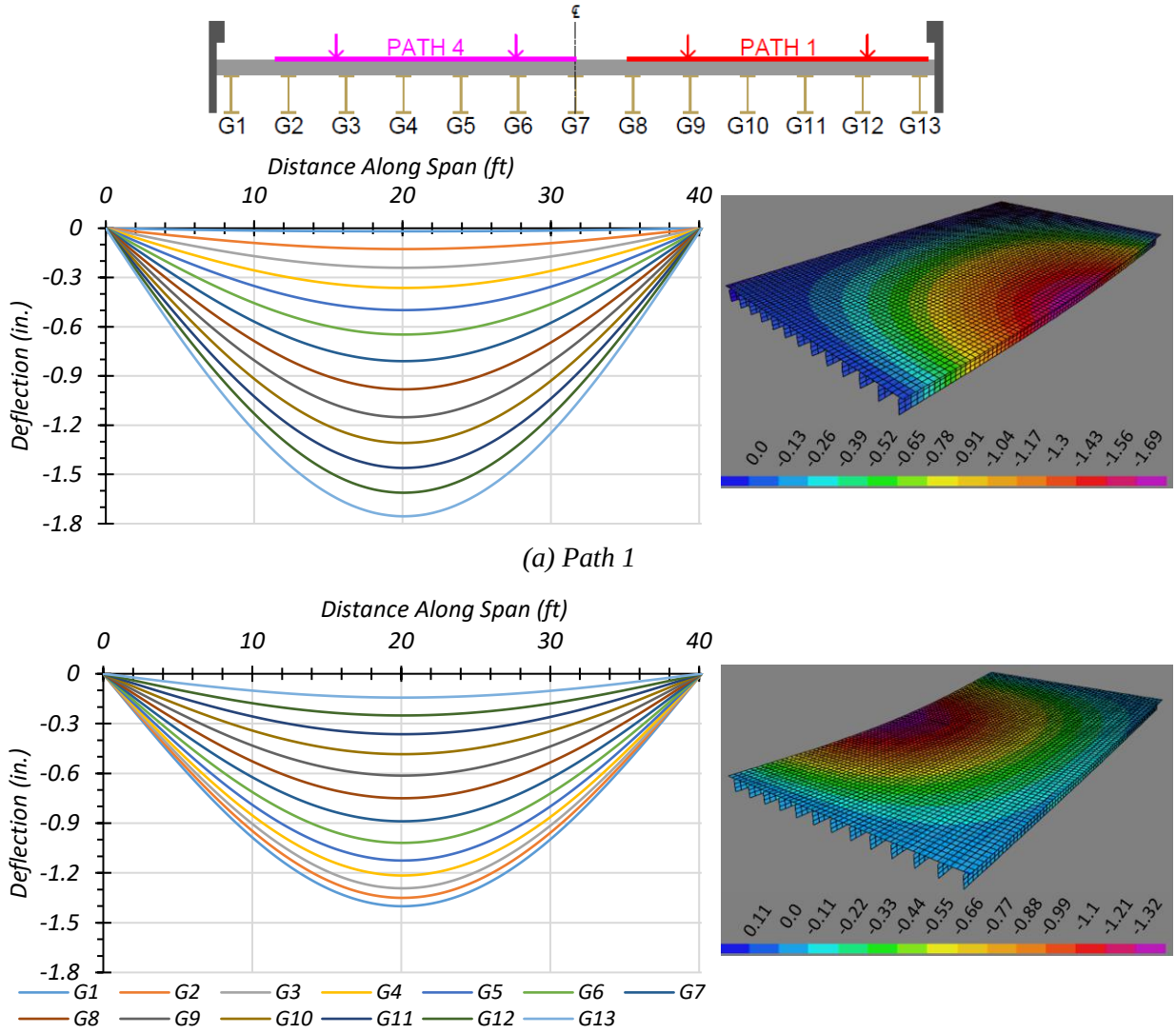

Figure 2.29. Deflection Profiles for Non-Composite Bridge SM-5 with HL-93 Loading

Table 2.25. Maximum Deflections for Non-Composite Bridge SM-5 with HL-93 Loading

Loading	G1	G2	G3	G4	G5	G6	G7	G8	G9	G10	G11	G12	G13
Path 1	−0.018	−0.127	−0.241	−0.364	−0.499	−0.647	−0.810	−0.981	−1.151	−1.308	−1.460	−1.611	−1.755
Path 4	−1.401	−1.350	−1.292	−1.215	−1.125	−1.019	−0.889	−0.750	−0.613	−0.484	−0.364	−0.251	−0.143
Note: G = girder, paths indicate transverse loading positions as shown, deflections have inch units													

Figure 2.30 shows the estimated girder deflection profiles and contours along the span for one-lane HL-93 loading along Path 1 and Path 4 when the bridge is analyzed as fully composite.

Table 2.26 shows the corresponding maximum deflections for each girder, assuming fully composite action. Load Paths 1 and 4 are the only ones shown because they are the load paths planned for later load tests, and were selected to maximize the forces on an interior girder and on an exterior girder.

For both non-composite and composite cases, the maximum deflections were obtained in Girder G13 when the HL-93 truck was run along Path 1. The estimated deflections were 1.755 in. and 0.840 in. for the non-composite and composite cases, respectively. This result indicates that the composite bridge is 70.5 percent stiffer than the non-composite bridge. The maximum deflections obtained when the HL-93 truck was run along Path 4 were in Girder G1 for both the non-composite and composite case. The estimated deflections were 1.401 in. and 0.635 in. for the non-composite and composite cases, respectively. This result indicates that the composite bridge is 75.2 percent stiffer than the non-composite bridge. The slightly different values of relative stiffness suggest that the relative girder deflection depends on the location of loading and corresponding load distribution.

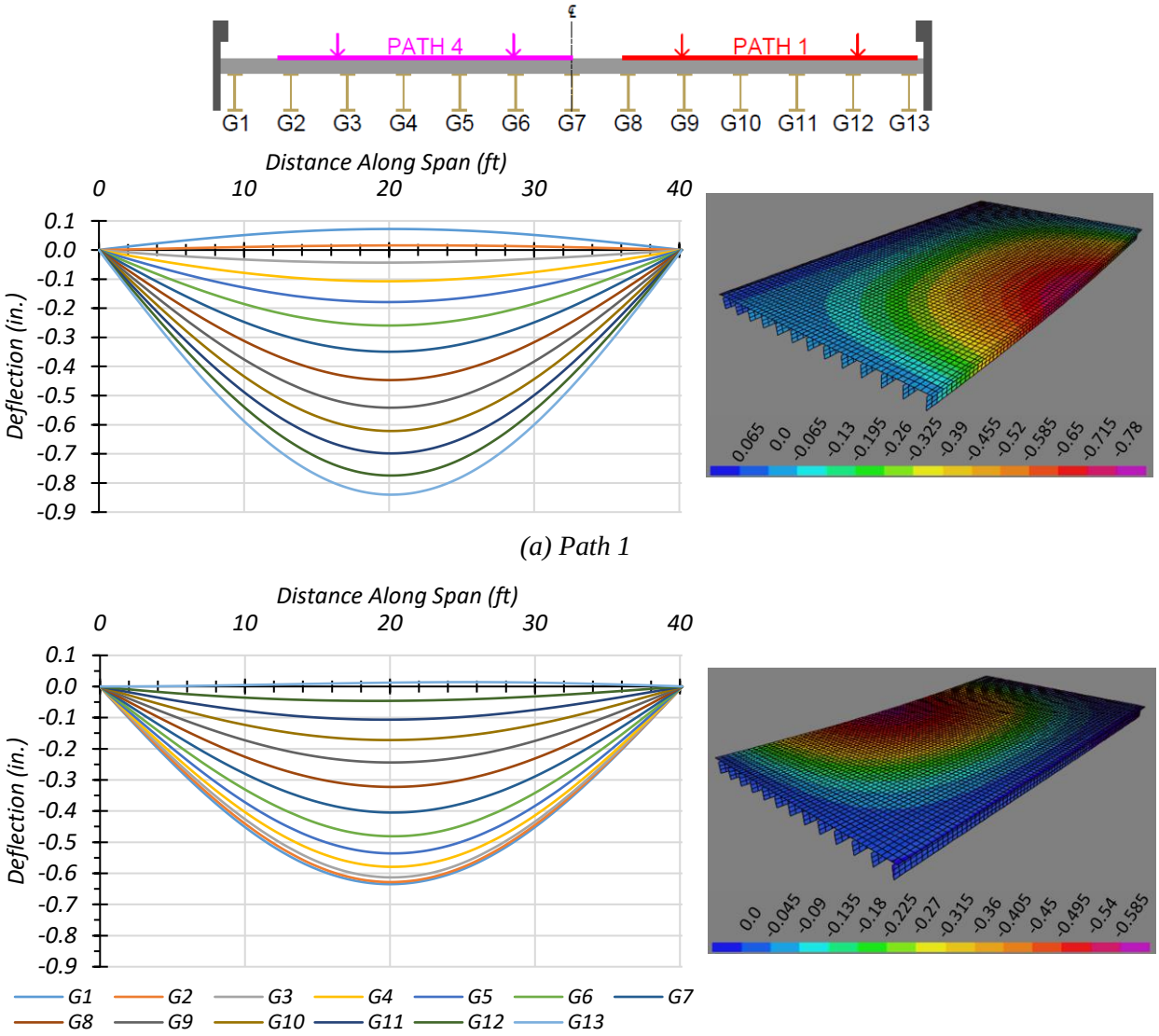

Figure 2.30. Deflection Profiles for Composite Bridge SM-5 with HL-93 Loading

Table 2.26. Maximum Deflections for Composite Bridge SM-5 with HL-93 Loading

Loading	G1	G2	G3	G4	G5	G6	G7	G8	G9	G10	G11	G12	G13
Path 1	0.072	0.016	-0.043	-0.107	-0.179	-0.259	-0.349	-0.447	-0.541	-0.621	-0.698	-0.774	-0.840
Path 4	-0.635	-0.628	-0.613	-0.579	-0.536	-0.481	-0.405	-0.323	-0.244	-0.172	-0.107	-0.046	0.014
Note: G = girder, paths indicate transverse loading positions as shown, deflections have inch units													

2.6.3.2 ***Moment Results***

One-Lane Loading. Figure 2.31 shows the individual girder moments and moment LLDF results for the non-composite Bridge SM-5 under simulated moving HL-93 loading along three one-lane loading paths.

Table 2.27 provides the corresponding maximum moment values of each girder for each loading path. The moment LLDF values are calculated using the estimated moment results from the FEM analysis. Table 2.29 shows the governing moment LLDFs found using the FEM analysis and compares them to the AASHTO LLDF values. The first AASHTO LLDF value is calculated using the simplified stiffness parameter. The second AASHTO LLDF value is calculated using the analytical stiffness parameter calculated for the specific bridge. Compared to the FEM results, the governing moment LLDF value computed using the approximate equations and the simplified stiffness parameter in *AASHTO LRFD Specifications* (AASHTO 2017) is quite conservative for interior girders, with a $g^m_{AASHTO\_S}/g^m_{FEM}$ ratio of 1.36, and is conservative for exterior girders, with a g^m_{AASHTO}/g^m_{FEM} ratio of 1.28. Compared to the FEM results, the governing moment LLDF value computed using the approximate equations and the analytical stiffness parameter in *AASHTO LRFD Specifications* (AASHTO 2017) is conservative for interior girders, with a $g^m_{AASHTO\_K}/g^m_{FEM}$ ratio of 1.18, and is slightly conservative for exterior girders, with a $g^m_{AASHTO\_K}/g^m_{FEM}$ ratio of 1.10. Figure 2.32 shows the individual girder moments and moment LLDF results for the fully composite Bridge SM-5 under simulated moving HL-93 loading along three one-lane loading paths.

Table 2.28 provides the corresponding maximum moment values of each girder for each loading path. The moment LLDF values are calculated using the estimated moment results from the FEM analysis. Compared to the FEM results, the governing moment LLDF value computed using the approximate equations and the simplified stiffness parameter in *AASHTO LRFD Specifications* (AASHTO 2017) is conservative for both interior and exterior girders, with a $g^m_{AASHTO\_S}/g^m_{FEM}$ ratio of 1.22 and 1.29, respectively. Compared to the FEM results, the governing moment LLDF value computed using the approximate equations and the analytical stiffness parameter in *AASHTO LRFD Specifications* (AASHTO 2017) is slightly conservative for interior girders, with a $g^m_{AASHTO\_K}/g^m_{FEM}$ ratio of 1.05, and conservative for exterior girders, with a $g^m_{AASHTO\_K}/g^m_{FEM}$ ratio of 1.12.

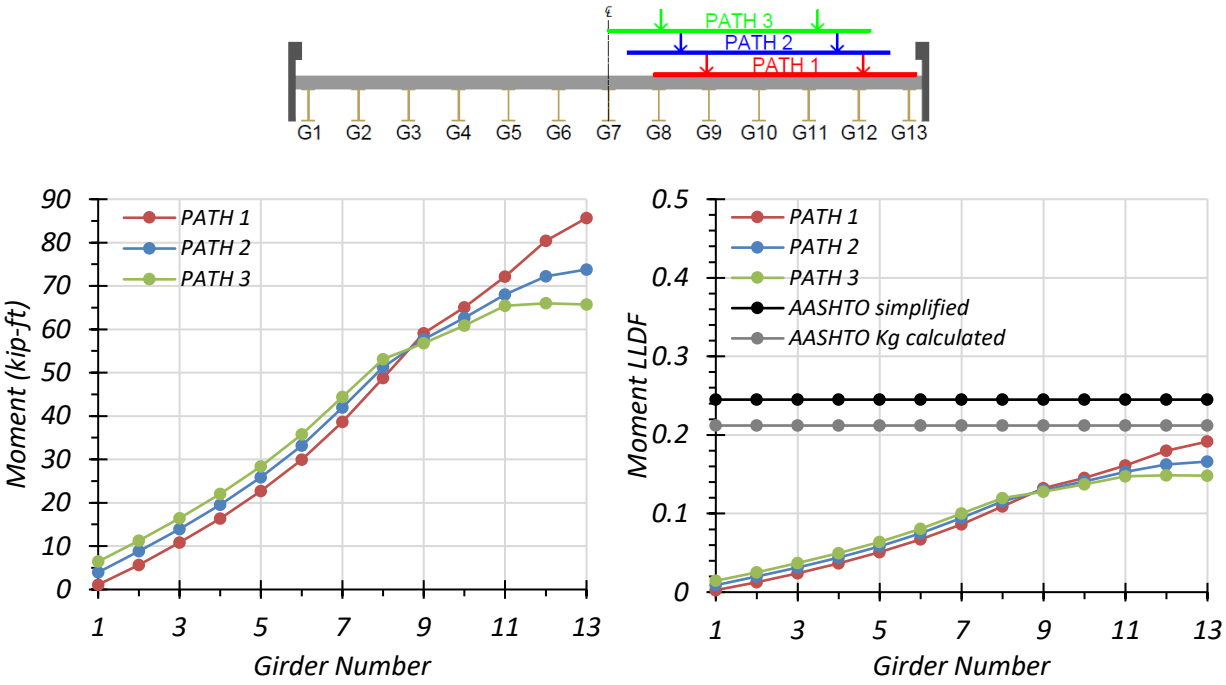

(a) Moment *(b) Moment LLDF*

Figure 2.31. Moment Results for Non-Composite Bridge SM-5 with One-Lane HL-93 Loading

Table 2.27. Maximum Moments for Non-Composite Bridge SM-5 with One-Lane HL-93 Loading

Loading	G1	G2	G3	G4	G5	G6	G7	G8	G9	G10	G11	G12	G13
Path 1	1.1	5.7	10.8	16.4	22.7	30.0	38.6	48.8	59.1	65.1	72.2	80.4	85.7
Path 2	3.9	8.8	13.9	19.5	25.8	33.2	41.9	51.3	57.7	62.6	68.0	72.2	73.8
Path 3	6.4	11.3	16.4	22.0	28.4	35.8	44.4	53.1	56.8	60.9	65.4	66.0	65.8
Note: G = girder, paths indicate transverse loading positions as shown, moments have kip-ft units													

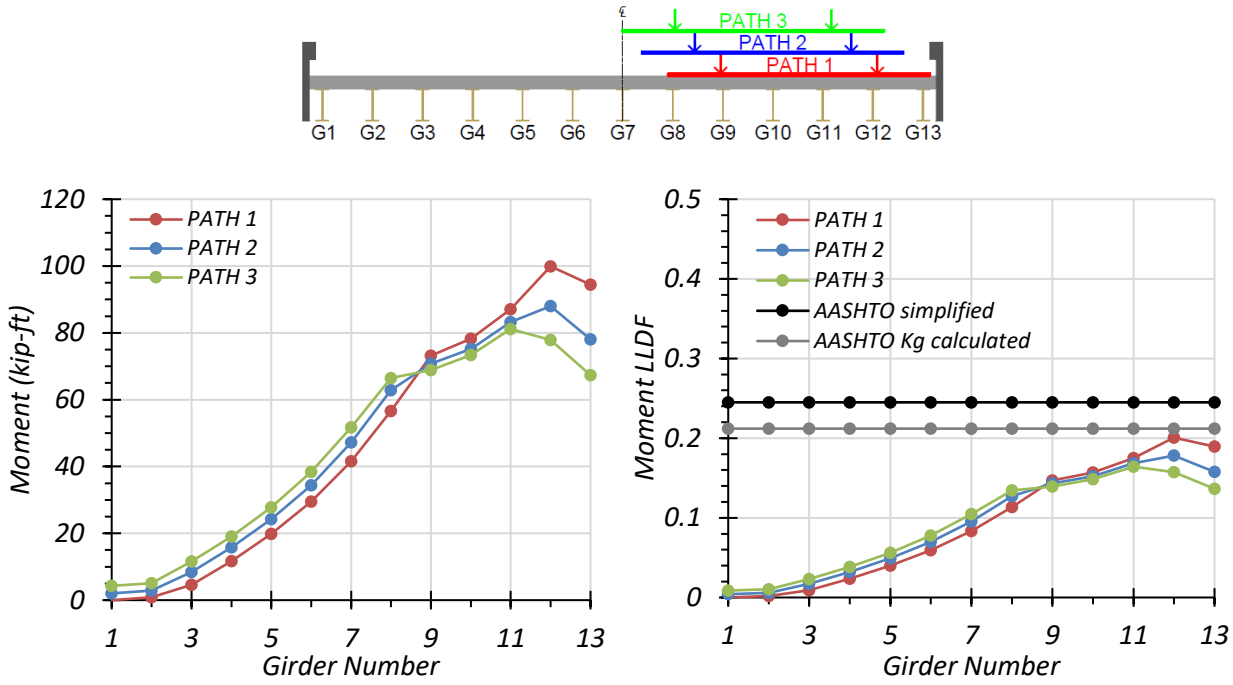

(a) Moment *(b) Moment LLDF*

Figure 2.32. Moment Results for Composite Bridge SM-5 with One-Lane HL-93 Loading

Table 2.28. Maximum Moments for Composite Bridge SM-5 with One-Lane HL-93 Loading

Loading	G1	G2	G3	G4	G5	G6	G7	G8	G9	G10	G11	G12	G13
Path 1	0.0	0.9	4.6	11.7	19.9	29.5	41.6	56.6	73.1	78.2	87.0	99.9	94.4
Path 2	2.0	2.8	8.4	15.8	24.3	34.4	47.2	62.8	70.8	75.2	83.2	88.0	78.0
Path 3	4.3	5.1	11.5	19.1	27.8	38.4	51.7	66.5	68.9	73.4	81.2	77.9	67.4
Note: G = girder, paths indicate transverse loading positions as shown, moments have kip-ft units													

Comparison of governing moment LLDF values computed from FEM results for the composite and non-composite cases reveals that the maximum moment LLDF in an interior girder for the composite bridge is higher than the one for the non-composite bridge, with a $g^m_{composite}/g^m_{non-composite}$ ratio of 1.12. However, the maximum moment LLDF in an exterior girder for the composite bridge is lower than the one for the non-composite bridge, with a $g^m_{composite}/g^m_{non-composite}$ ratio of 0.99.

Table 2.29. Governing Moment LLDFs for Bridge SM-5 with One-Lane HL-93 Loading

Type	Girder Location	AASHTO Simplified ($g^m_{AASHTO\_S}$)	AASHTO K_g Calculated ($g^m_{AASHTO\_K}$)	FEM (g^m_{FEM})	$g^m_{AASHTO\_S}/g^m_{FEM}$	$g^m_{AASHTO\_K}/g^m_{FEM}$
Non-Composite	Interior	0.245	0.212	0.180	1.36	1.18
	Exterior	0.245	0.212	0.192	1.28	1.10
Composite	Interior	0.245	0.212	0.201	1.22	1.05
	Exterior	0.245	0.212	0.190	1.29	1.12

Two-Lane Loading. Figure 2.33 shows the individual girder moments and moment LLDF results for the non-composite Bridge SM-5 under simulated moving HL-93 loading along three two-lane loading paths. Table 2.30 provides the corresponding maximum moment values of each girder for each loading path. The moment LLDF values are calculated using the estimated moment results from the FEM analysis. Table 2.32 shows the governing moment LLDFs found using the FEM analysis and compares them to the AASHTO LLDF values. The first AASHTO LLDF value is calculated using the simplified stiffness parameter. The second AASHTO LLDF value is calculated using the analytical stiffness parameter calculated for the specific bridge. Compared to the FEM results, the governing moment LLDF value computed using the approximate equations and the simplified stiffness parameter in *AASHTO LRFD Specifications* (AASHTO 2017) is quite conservative for both interior and exterior girders, with a $g^m_{AASHTO\_S}/g^m_{FEM}$ ratio of 1.67 for both. Compared to the FEM results, the governing moment LLDF value computed using the approximate equations and the analytical stiffness parameter in *AASHTO LRFD Specifications* (AASHTO 2017) is quite conservative for both interior and exterior girders, with a $g^m_{AASHTO\_K}/g^m_{FEM}$ ratio of 1.45 for both.

Figure 2.34 shows the individual girder moments and moment LLDF results for the fully composite Bridge SM-5 under simulated moving HL-93 loading along three two-lane loading paths. Table 2.31 provides the corresponding maximum moment values of each girder for each loading path. The moment LLDF values are calculated using the estimated moment results from the FEM analysis. Compared to the FEM results, the governing moment LLDF value computed using the approximate equations and the simplified stiffness parameter in *AASHTO LRFD Specifications* (AASHTO 2017) is quite conservative for both interior and exterior girders, with a $g^m_{AASHTO\_S}/g^m_{FEM}$ ratio of 1.62 and 1.80, respectively. Compared to the FEM results, the governing

moment LLDF value computed using the approximate equations and the analytical stiffness parameter in *AASHTO LRFD Specifications* (AASHTO 2017) is quite conservative for both interior and exterior girders, with a $g^m_{AASHTO\_K}/g^m_{FEM}$ ratio of 1.40 and 1.56, respectively.

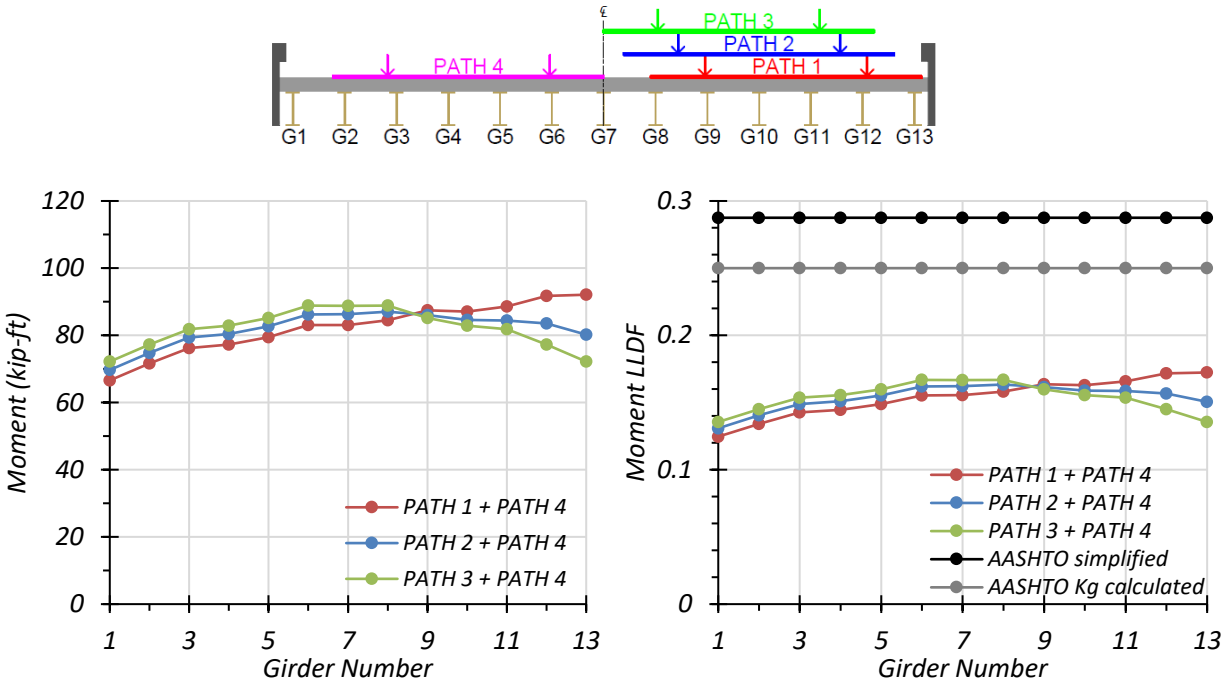

(a) Moment *(b) Moment LLDF*

Figure 2.33. Moment Results for Non-Composite Bridge SM-5 with Two-Lane HL-93 Loading

Table 2.30. Maximum Moments for Non-Composite Bridge SM-5 with Two-Lane HL-93 Loading

Loading	G1	G2	G3	G4	G5	G6	G7	G8	G9	G10	G11	G12	G13
Path 1 + Path 4	66.6	71.7	76.2	77.2	79.5	83.0	83.0	84.5	87.4	87.1	88.6	91.7	92.1
Path 2 + Path 4	69.7	74.8	79.3	80.4	82.7	86.3	86.3	87.0	86.0	84.6	84.4	83.5	80.2
Path 3 + Path 4	72.2	77.3	81.8	82.9	85.2	88.9	88.8	88.9	85.2	82.9	81.8	77.3	72.2
Note: G = girder, paths indicate transverse loading positions as shown, moments have kip-ft units													

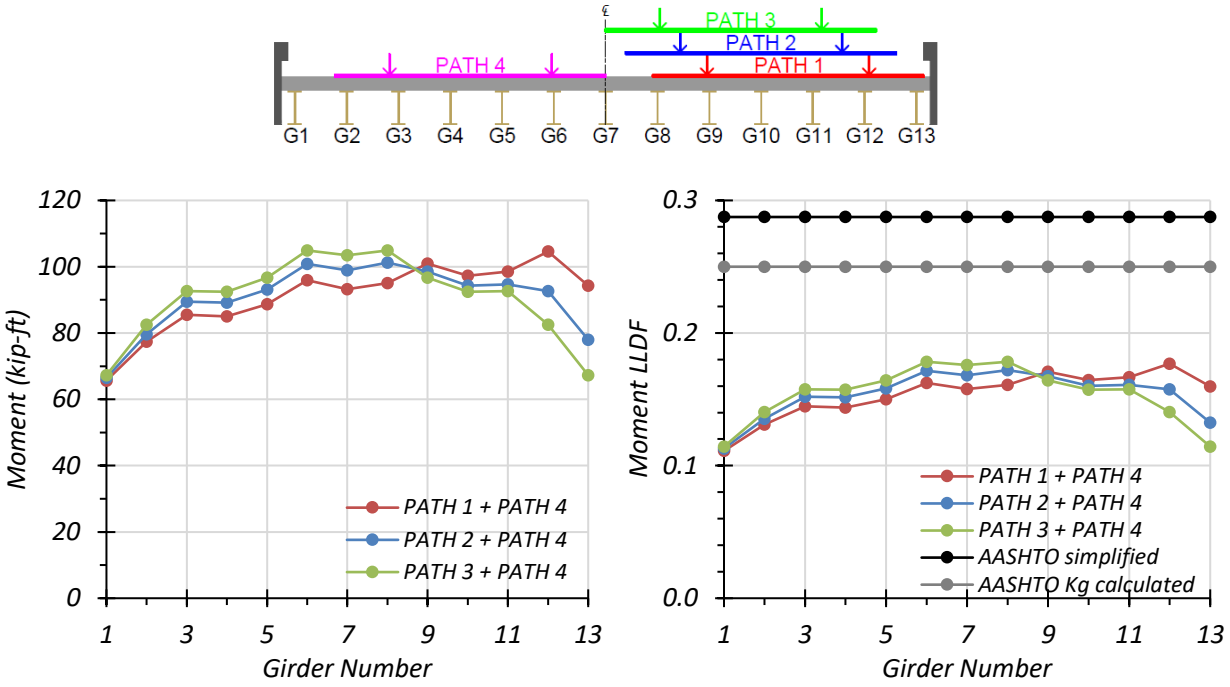

(a) Moment *(b) Moment LLDF*

Figure 2.34. Moment Results for Composite Bridge SM-5 with Two-Lane HL-93 Loading

Table 2.31. Maximum Moments for Composite Bridge SM-5 with Two-Lane HL-93 Loading

Loading	G1	G2	G3	G4	G5	G6	G7	G8	G9	G10	G11	G12	G13
Path 1 + Path 4	65.7	77.4	85.5	85.0	88.7	96.0	93.3	95.0	100.9	97.3	98.5	104.6	94.3
Path 2 + Path 4	66.5	79.6	89.5	89.2	93.1	100.9	99.0	101.2	98.5	94.3	94.7	92.6	77.9
Path 3 + Path 4	67.3	82.5	92.6	92.5	96.7	104.9	103.4	104.9	96.7	92.5	92.6	82.5	67.3
Note: G = girder, paths indicate transverse loading positions as shown, moments have kip-ft units													

Comparison of governing moment LLDF values computed from FEM results for the composite and non-composite cases reveals that the maximum moment LLDF in an interior girder for the composite bridge is higher than the one for the non-composite bridge, with a $g^m_{composite}/g^m_{non-composite}$ ratio of 1.03. However, the maximum moment LLDF in an exterior girder for the composite bridge is lower than the one for the non-composite bridge, with a $g^m_{composite}/g^m_{non-composite}$ ratio of 0.93.

Table 2.32. Governing Moment LLDFs for Bridge SM-5 with Two-Lane HL-93 Loading

Type	Girder Location	AASHTO Simplified ($g^m_{AASHTO\_S}$)	AASHTO K_g Calculated ($g^m_{AASHTO\_K}$)	FEM (g^m_{FEM})	$g^m_{AASHTO\_S}/g^m_{FEM}$	$g^m_{AASHTO\_K}/g^m_{FEM}$
Non-Composite	Interior	0.288	0.250	0.172	1.67	1.45
	Exterior	0.288	0.250	0.172	1.67	1.45
Composite	Interior	0.288	0.250	0.178	1.62	1.40
	Exterior	0.288	0.250	0.160	1.80	1.56

*2.6.3.3 **Shear Results***

One-Lane Loading. Figure 2.35 shows the individual girder shears and shear LLDF results for the non-composite Bridge SM-5 under simulated moving HL-93 loading along three one-lane loading paths.

Table 2.33 provides the corresponding maximum shear values of each girder for each loading path. The shear LLDF values are calculated using the estimated shear results from the FEM analysis. Table 2.35 shows the governing shear LLDFs found using the FEM analysis and compares them to the AASHTO LLDF values. Compared to the FEM results, the governing shear LLDF value computed using the approximate equations in *AASHTO LRFD Specifications* (AASHTO 2017) is quite conservative for both interior and exterior girders, with a g^v_{AASHTO}/g^v_{FEM} ratio of 2.14 and 2.46, respectively.

Figure 2.36 shows the individual girder shears and shear LLDF results for the fully composite Bridge SM-5 under simulated moving HL-93 loading along three one-lane loading paths. Table 2.34 provides the corresponding maximum shear values of each girder for each loading path. The shear LLDF values are calculated using the estimated shear results from the FEM analysis. Compared to the FEM results, the governing shear LLDF value computed using the approximate equations in *AASHTO LRFD Specifications* (AASHTO 2017) is quite conservative for both interior and exterior girders, with a g^v_{AASHTO}/g^v_{FEM} ratio of 1.71 and 2.68, respectively.

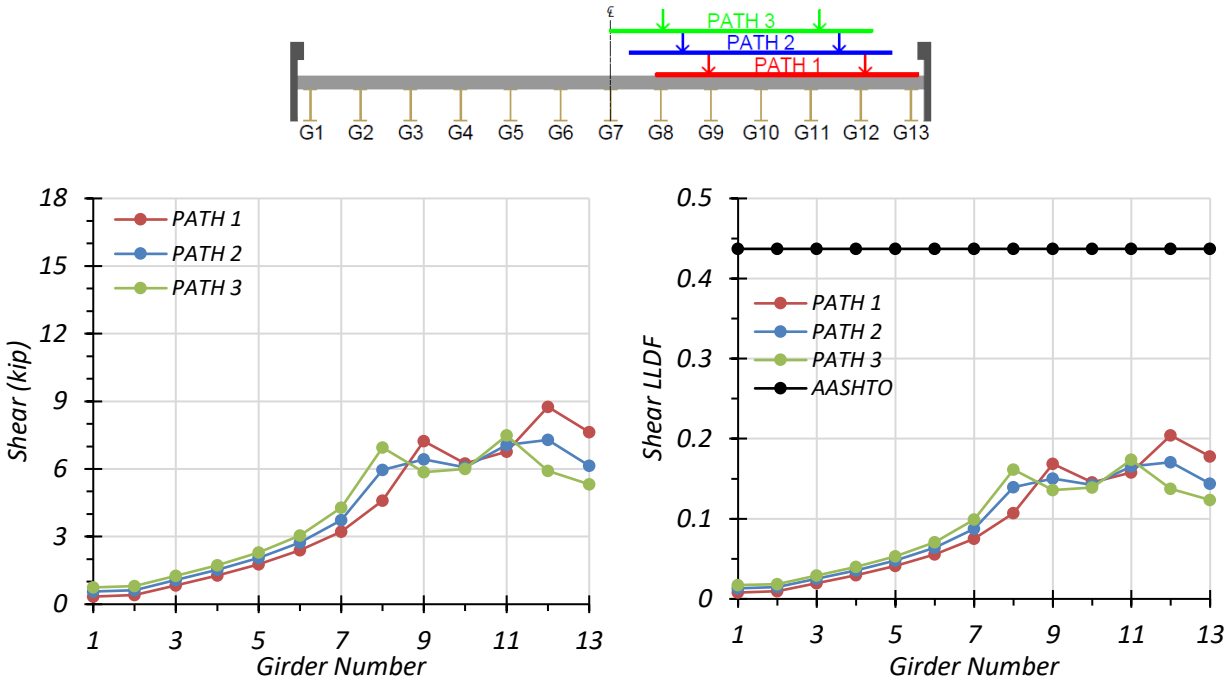

(a) Shear *(b) Shear LLDF*

Figure 2.35. Shear Results for Non-Composite Bridge SM-5 with One-Lane HL-93 Loading

Table 2.33. Maximum Shears for Non-Composite Bridge SM-5 with One-Lane HL-93 Loading

Loading	G1	G2	G3	G4	G5	G6	G7	G8	G9	G10	G11	G12	G13
Path 1	0.3	0.4	0.8	1.3	1.8	2.4	3.2	4.6	7.2	6.2	6.8	8.8	7.6
Path 2	0.6	0.6	1.1	1.5	2.1	2.7	3.7	6.0	6.4	6.1	7.1	7.3	6.1
Path 3	0.7	0.8	1.3	1.7	2.3	3.1	4.3	7.0	5.9	6.0	7.5	5.9	5.3
Note: G = girder, paths indicate transverse loading positions as shown, shears have kip units													

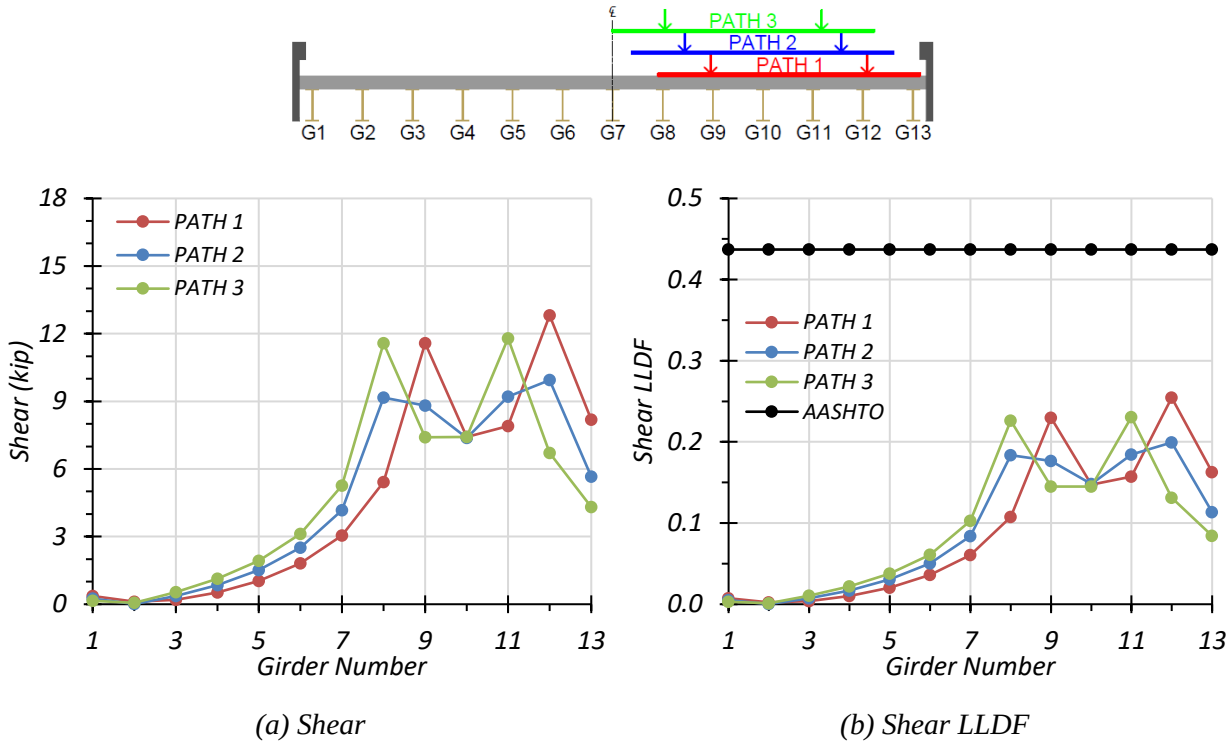

(a) Shear *(b) Shear LLDF*

Figure 2.36. Shear Results for Composite Bridge SM-5 with One-Lane HL-93 Loading

Table 2.34. Maximum Shears for Composite Bridge SM-5 with One-Lane HL-93 Loading

Loading	G1	G2	G3	G4	G5	G6	G7	G8	G9	G10	G11	G12	G13
Path 1	0.4	0.1	0.2	0.5	1.0	1.8	3.0	5.4	11.6	7.4	7.9	12.8	8.2
Path 2	0.2	0.0	0.4	0.8	1.5	2.5	4.2	9.2	8.8	7.4	9.2	9.9	5.7
Path 3	0.2	0.1	0.5	1.1	1.9	3.1	5.3	11.6	7.4	7.4	11.8	6.7	4.3
Note: G = girder, paths indicate transverse loading positions as shown, shears have kip units													

Comparison of governing shear LLDF values computed from FEM results for the composite and non-composite cases reveals that the maximum shear LLDF in an interior girder for the composite bridge is higher than the one for the non-composite bridge, with a $g^v_{composite}/g^v_{non-composite}$ ratio of 1.25. However, the maximum shear LLDF in an exterior girder for the composite bridge is lower than the one for the non-composite bridge, with a $g^v_{composite}/g^v_{non-composite}$ ratio of 0.92.

Table 2.35. Governing Shear LLDFs for Bridge SM-5 with One-Lane HL-93 Loading

Type	Girder Location	AASHTO (g^v_{AASHTO})	FEM (g^v_{FEM})	g^v_{AASHTO}/g^v_{FEM}
Non-Composite	Interior	0.437	0.204	2.14
	Exterior	0.437	0.178	2.46
Composite	Interior	0.437	0.255	1.71
	Exterior	0.437	0.163	2.68

Two-Lane Loading. The same procedure was conducted for two-lane loading. Figure 2.37 shows the individual girder shears and shear LLDF results for the non-composite Bridge SM-5 under simulated moving HL-93 loading along three two-lane loading paths.

Table 2.36 provides the corresponding maximum shear values of each girder for each loading path. The shear LLDF values are calculated using the estimated shear results from the FEM analysis. Table 2.38 shows the governing shear LLDFs found using the FEM analysis and compares them to the AASHTO LLDF values. Compared to the FEM results, the governing shear LLDF value computed using the approximate equations in *AASHTO LRFD Specifications* (AASHTO 2017) is quite conservative for both interior and exterior girders, with a g^v_{AASHTO}/g^v_{FEM} ratio of 2.25 and 2.71, respectively.

Figure 2.38 shows the individual girder shears and shear LLDF results for the fully composite Bridge SM-5 under simulated moving HL-93 loading along three one-lane loading paths. Table 2.37 provides the corresponding maximum shear values of each girder for each loading path. The shear LLDF values are calculated using the estimated shear results from the FEM analysis. Compared to the FEM results, the governing shear LLDF value computed using the approximate equations in *AASHTO LRFD Specifications* (AASHTO 2017) is quite conservative for both interior and exterior girders, with a g^v_{AASHTO}/g^v_{FEM} ratio of 1.82 and 3.24, respectively.

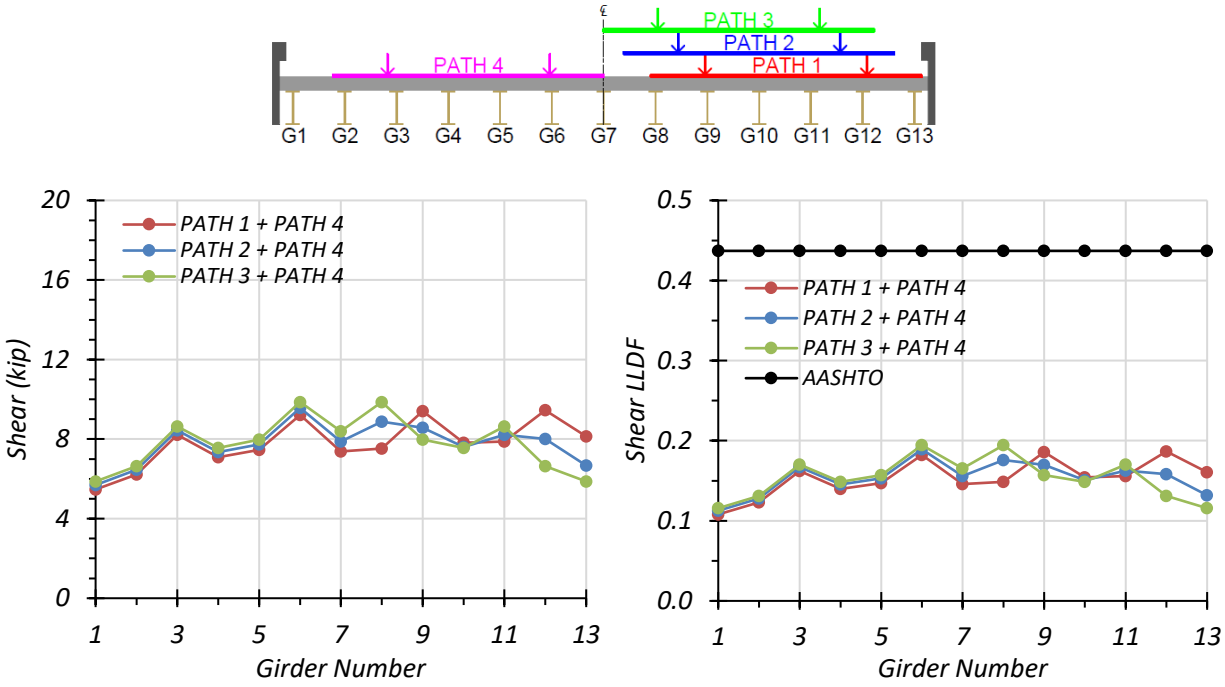

(a) Shear *(b) Shear LLDF*

Figure 2.37. Shear Results for Non-Composite Bridge SM-5 with Two-Lane HL-93 Loading

Table 2.36. Maximum Shears for Non-Composite Bridge SM-5 with Two-Lane HL-93 Loading

Loading	G1	G2	G3	G4	G5	G6	G7	G8	G9	G10	G11	G12	G13
Path 1 + Path 4	5.5	6.2	8.2	7.1	7.5	9.2	7.4	7.5	9.4	7.8	7.9	9.5	8.1
Path 2 + Path 4	5.7	6.5	8.5	7.3	7.7	9.6	7.9	8.9	8.6	7.6	8.2	8.0	6.7
Path 3 + Path 4	5.9	6.6	8.6	7.6	8.0	9.9	8.4	9.9	8.0	7.6	8.6	6.6	5.9
Note: G = girder, paths indicate transverse loading positions as shown, shears have kip units													

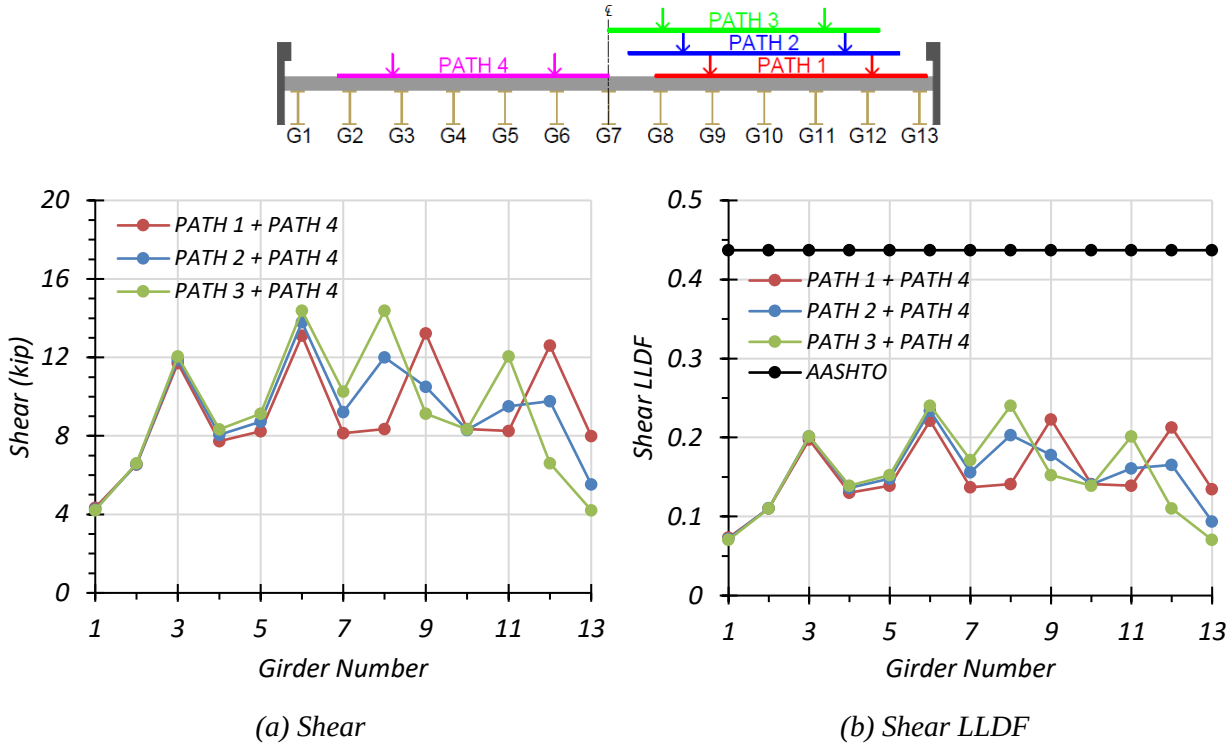

(a) Shear *(b) Shear LLDF*

Figure 2.38. Shear Results for Composite Bridge SM-5 with Two-Lane HL-93 Loading

Table 2.37. Maximum Shears for Composite Bridge SM-5 with Two-Lane HL-93 Loading

Loading	G1	G2	G3	G4	G5	G6	G7	G8	G9	G10	G11	G12	G13
Path 1 + Path 4	4.3	6.5	11.7	7.7	8.2	13.1	8.1	8.4	13.2	8.4	8.3	12.6	8.0
Path 2 + Path 4	4.3	6.5	11.9	8.1	8.7	13.8	9.2	12.0	10.5	8.3	9.5	9.8	5.5
Path 3 + Path 4	4.2	6.6	12.1	8.3	9.1	14.4	10.3	14.4	9.1	8.3	12.1	6.6	4.2
Note: G = girder, paths indicate transverse loading positions as shown, shears have kip units													

Comparison of governing shear LLDF values computed from FEM results for the composite and non-composite cases reveals that the maximum shear LLDF in an interior girder for the composite bridge is higher than the one for the non-composite bridge, with a $g^v_{composite}/g^v_{non-composite}$ ratio of 1.24. The maximum shear LLDF in an exterior girder for the composite bridge is also lower than that for the non-composite bridge, with a $g^v_{composite}/g^v_{non-composite}$ ratio of 0.84.

Table 2.38. Governing Shear LLDFs for Bridge SM-5 with Two-Lane HL-93 Loading

Type	Girder Location	AASHTO (g^v_{AASHTO})	FEM (g^v_{FEM})	g^v_{AASHTO}/g^v_{FEM}
Non-Composite	Interior	0.437	0.194	2.25
	Exterior	0.437	0.161	2.71
Composite	Interior	0.437	0.240	1.82
	Exterior	0.437	0.135	3.24

2.7 FEM RESULTS FOR BRIDGE SM-21

Bridge SM-21 was analyzed using the CSiBridge software under the loading scenarios provided in Figure 2.13 through Figure 2.16. Girder displacement profiles were obtained for the load cases that represent the field load testing plans. Modal analyses were conducted for both composite and non-composite conditions to determine estimated modal frequencies and mode shapes. Live load moment and shear values were also extracted and analyzed to compare the expected LLDFs with the LLDFs prescribed in *AASHTO Standard Specifications* (AASHTO 2002) and *AASHTO LRFD Specifications* (AASHTO 2017).

As stated for Bridge SM-5, because of articles in the *AASHTO Standard Specifications* (AASHTO 2002) and *AASHTO LRFD Specifications* (AASHTO 2017) and the way in which they are interpreted, in some cases for Bridge SM-21, the LLDF determined through AASHTO for the exterior girder is controlled by the LLDF determined for the interior girder.

2.7.1 Modal Properties

The first two modes of Bridge SM-21 were identified as the first longitudinal bending mode and the first torsional mode. The frequencies of longitudinal bending and torsional modes for the non-composite bridge were determined to be 6.29 Hz and 6.41 Hz, respectively. Figure 2.39(a) shows the amplitude contours of the first longitudinal bending mode shape and the normalized amplitudes along the span for the non-composite condition. Figure 2.39(b) shows the amplitude contours for the first torsional mode shape and the normalized amplitudes transverse to the span for the non-composite condition. The frequencies of the longitudinal bending and torsional modes of the composite bridge were determined to be 8.04 Hz and 8.33 Hz, respectively. Figure 2.40(a) shows the amplitude contours of the first longitudinal bending mode shape and the normalized amplitudes along the span for the composite condition. Figure 2.40(b) shows the amplitude contours resulting

from the first torsional mode and the normalized amplitudes transverse to the span for composite analysis.

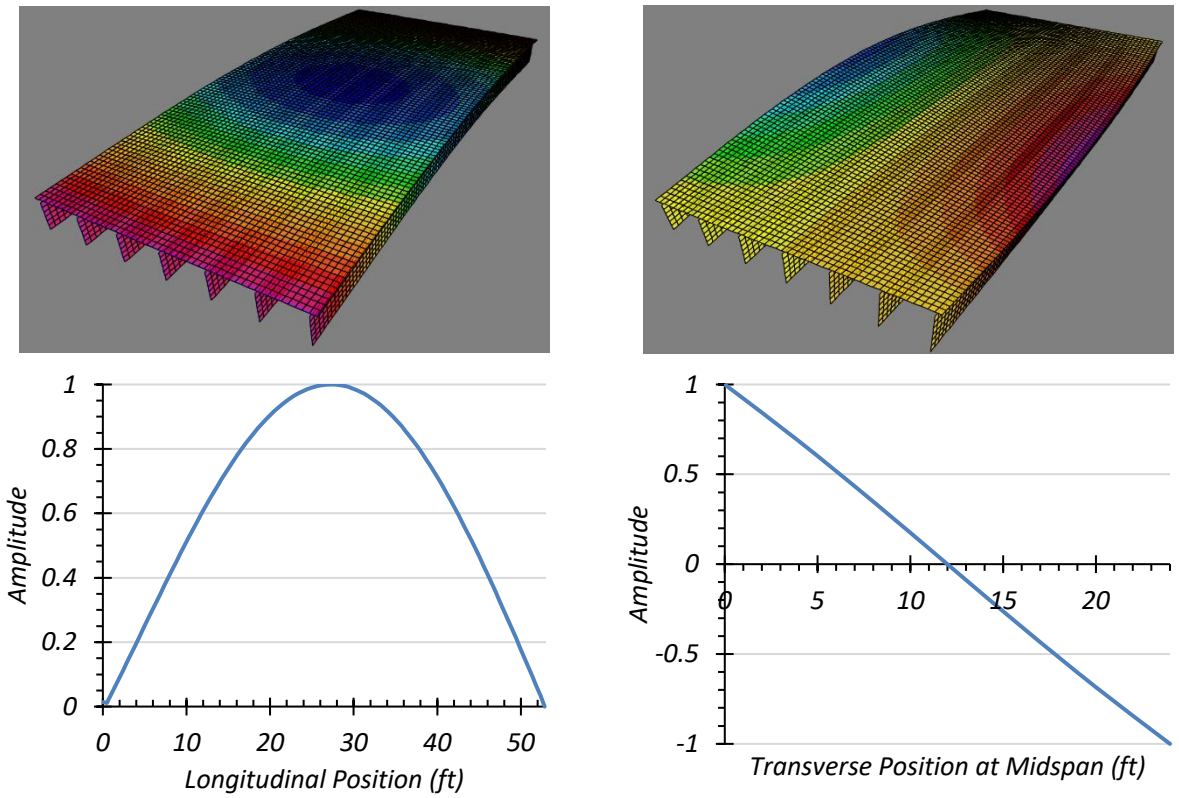

(a) Longitudinal bending Mode (f=6.29 Hz) *(b) Torsional Mode (f=6.41 Hz)*

Figure 2.39. First Two Mode Shapes of Non-Composite Bridge SM-21

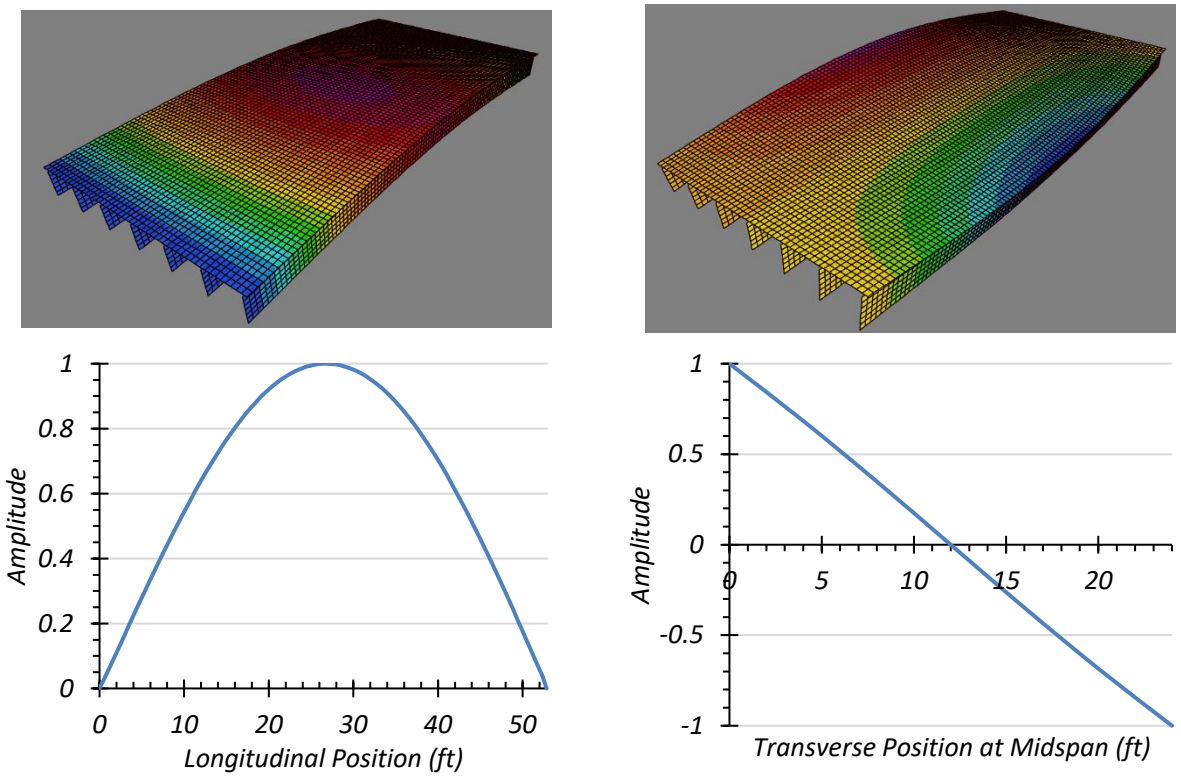

(a) Longitudinal bending Mode (f=8.04 Hz) *(b) Torsional Mode (f=8.33 Hz)*

Figure 2.40. First Two Mode Shapes of Composite Bridge SM-21

2.7.2 HS-20 Live Load Analysis

Bridge SM-21 was first analyzed using the HS-20 design truck presented in the *AASHTO Standard Specifications* (AASHTO 2002). The bridge was analyzed for one-lane- and two-lane-loaded cases along four transverse paths, as shown in Figure 2.13. Deflection, moment, and shear results were obtained.

2.7.2.1 ***Deflection Results***

Figure 2.41 shows the estimated girder deflection profiles and contours along the span for the one-lane HS-20 loading along Path 1 and Path 4 when the bridge is analyzed as fully non-composite. Table 2.39 shows the corresponding maximum deflections for each girder, assuming non-composite action. Load Paths 1 and 4 are the only ones shown because they are the load paths planned for later load tests, and were selected to maximize the forces on an interior girder and on an exterior girder.

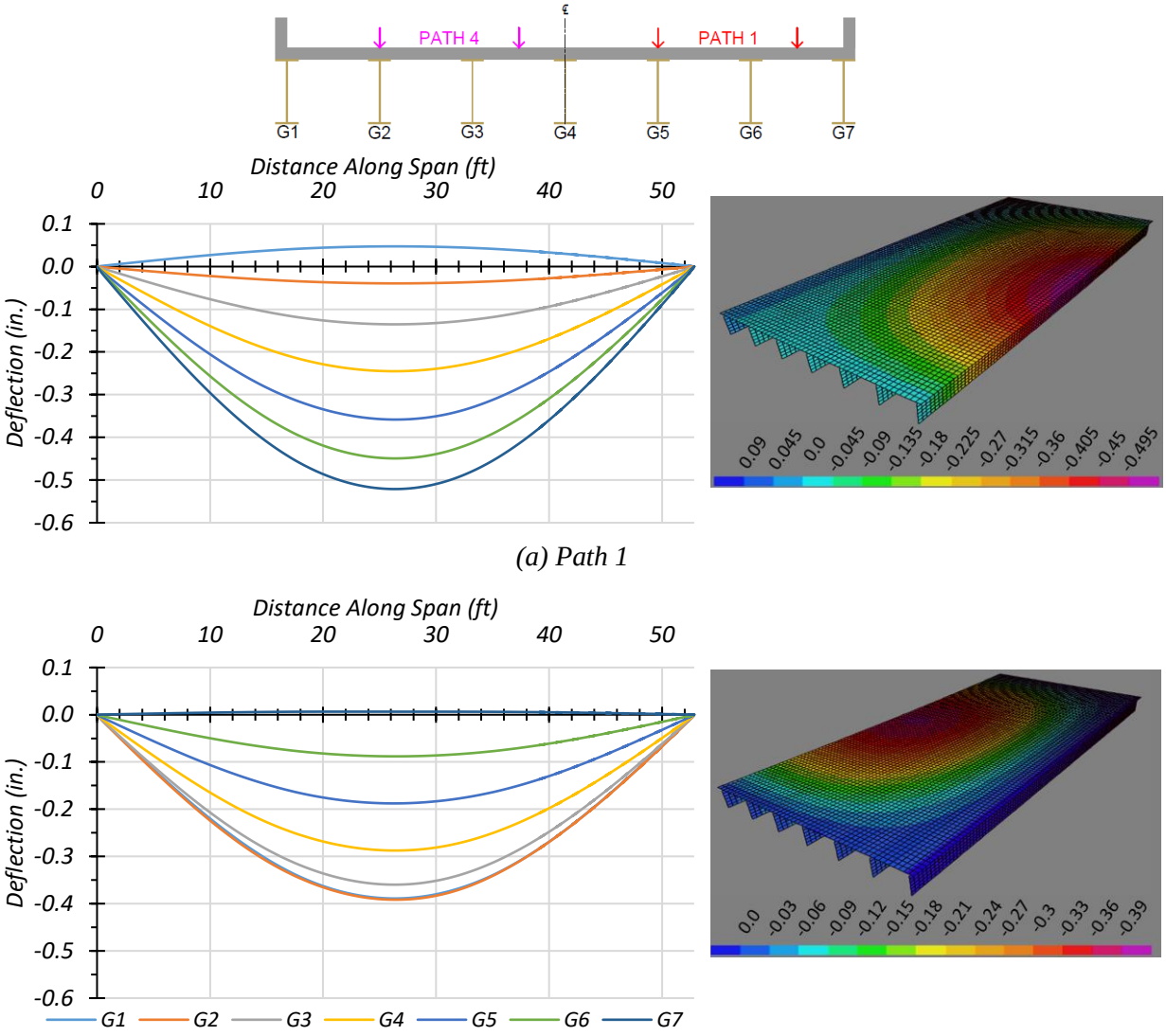

Figure 2.41. Deflection Profiles for Non-Composite Bridge SM-21 with HS-20 Loading

Table 2.39. Maximum Deflections for Non-Composite Bridge SM-21 with HS-20 Loading

Loading	G1	G2	G3	G4	G5	G6	G7
Path 1	0.047	−0.039	−0.135	−0.245	−0.358	−0.449	−0.521
Path 4	−0.453	−0.421	−0.361	−0.267	−0.162	−0.063	0.007
Note: G = girder, paths indicate transverse loading positions as shown, deflections have inch units							

Figure 2.42 shows the estimated girder deflection profiles and contours along the span for one-lane HS-20 loading along Path 1 and Path 4 when the bridge is analyzed as fully composite. Table 2.40 shows the corresponding maximum deflections for each girder, assuming fully composite action. Load Paths 1 and 4 are the only ones shown because they are the load paths planned for later load tests, and were selected to maximize the forces on an interior girder and on an exterior girder.

For both non-composite and composite cases, the maximum deflections were obtained in Girder G7 when the HS-20 truck was run along Path 1. The estimated deflections were 0.521 in. and 0.297 in. for non-composite and composite cases, respectively. This result indicates that the composite bridge is 54.8 percent stiffer than the non-composite bridge. The maximum deflections obtained when the HS-20 truck was run along Path 4 were in Girder G1 for both the non-composite and composite case. The estimated deflections were 0.453 in. and 0.225 in. for non-composite and composite cases, respectively. This result indicates that the composite bridge is 67.7 percent stiffer than the non-composite bridge. The slightly different values of relative stiffness suggest that the relative girder deflection depends on the location of loading and corresponding load distribution.

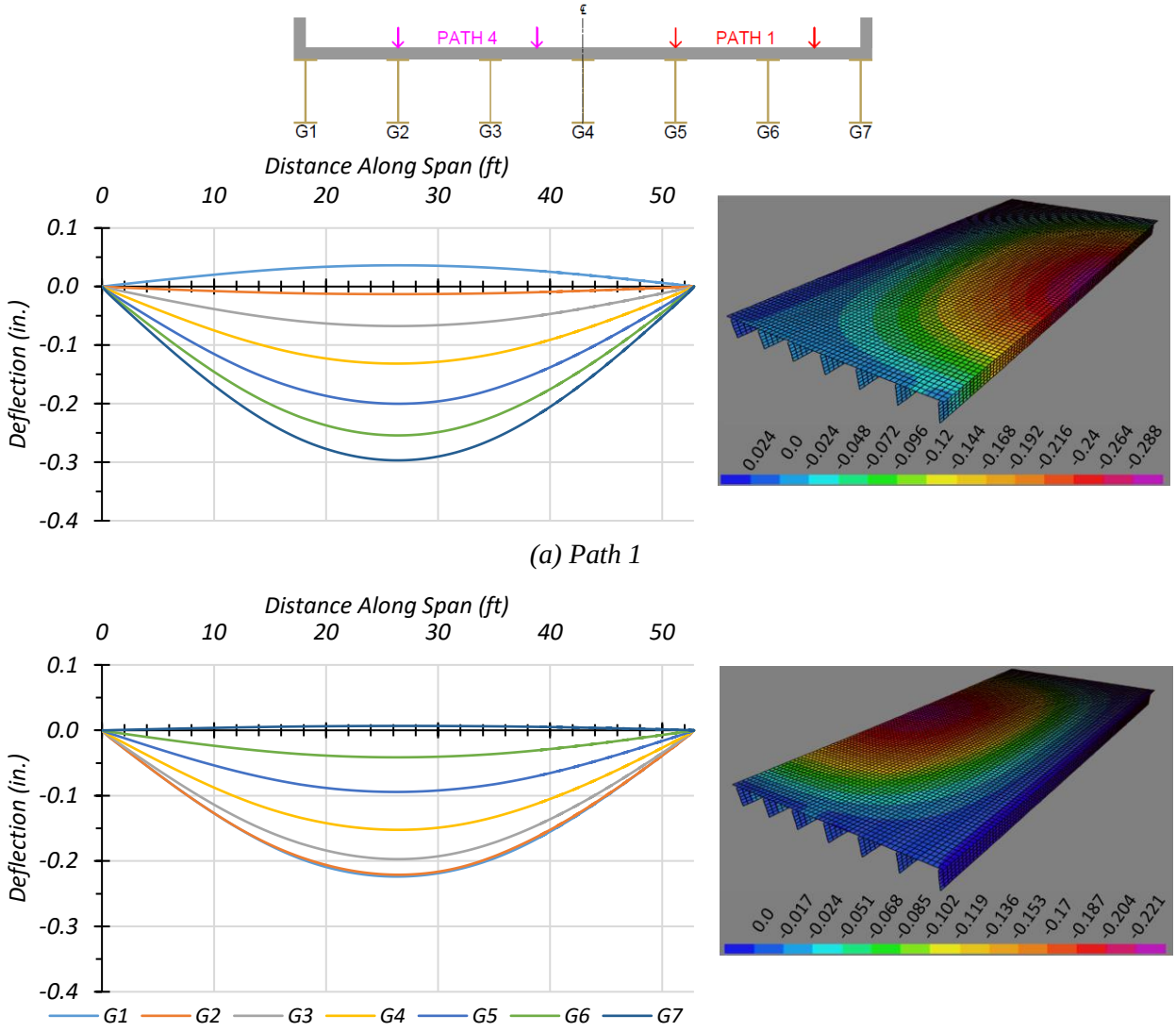

Figure 2.42. Deflection Profiles for Composite Bridge SM-21 with HS-20 Loading

Table 2.40. Maximum Deflections for Composite Bridge SM-21 with HS-20 Loading

Loading	G1	G2	G3	G4	G5	G6	G7
Path 1	0.036	−0.013	−0.067	−0.132	−0.200	−0.254	−0.297
Path 4	−0.224	−0.221	−0.197	−0.152	−0.094	−0.041	0.007
Note: G = girder, paths indicate transverse loading positions as shown, deflections have inch units							

2.7.2.2 ***Moment Results***

One-Lane Loading. Figure 2.43 shows the individual girder moments and moment LLDF results for the non-composite Bridge SM-21 under simulated moving HS-20 loading along three one-lane loading paths. Table 2.41 provides the corresponding maximum moment values of each girder for each loading path. The moment LLDF values are calculated using the estimated moment results from FEM analysis. Table 2.43 shows the governing moment LLDFs found using the FEM analysis and compares them to the AASHTO LLDF values. Compared to the FEM results, the governing moment LLDF value computed using the approximate equations in the *AASHTO Standard Specifications* (AASHTO 2002) is slightly conservative for interior girders, with a g^m_{AASHTO}/g^m_{FEM} ratio of 1.10, and is conservative for exterior girders, with a g^m_{AASHTO}/g^m_{FEM} ratio of 1.25.

Figure 2.44 shows the individual girder moments and moment LLDF results for the fully composite Bridge SM-21 under simulated moving HS-20 loading along three one-lane loading paths. Table 2.42 provides the corresponding maximum moment values of each girder for each loading path. The moment LLDF values are calculated using the estimated moment results from the FEM analysis. Compared to the FEM results, the governing moment LLDF value computed using the approximate equations in the *AASHTO Standard Specifications* (AASHTO 2002) is slightly conservative for interior girders, with a g^m_{AASHTO}/g^m_{FEM} ratio of 1.03, and is quite conservative for exterior girders, with a g^m_{AASHTO}/g^m_{FEM} ratio of 1.34.

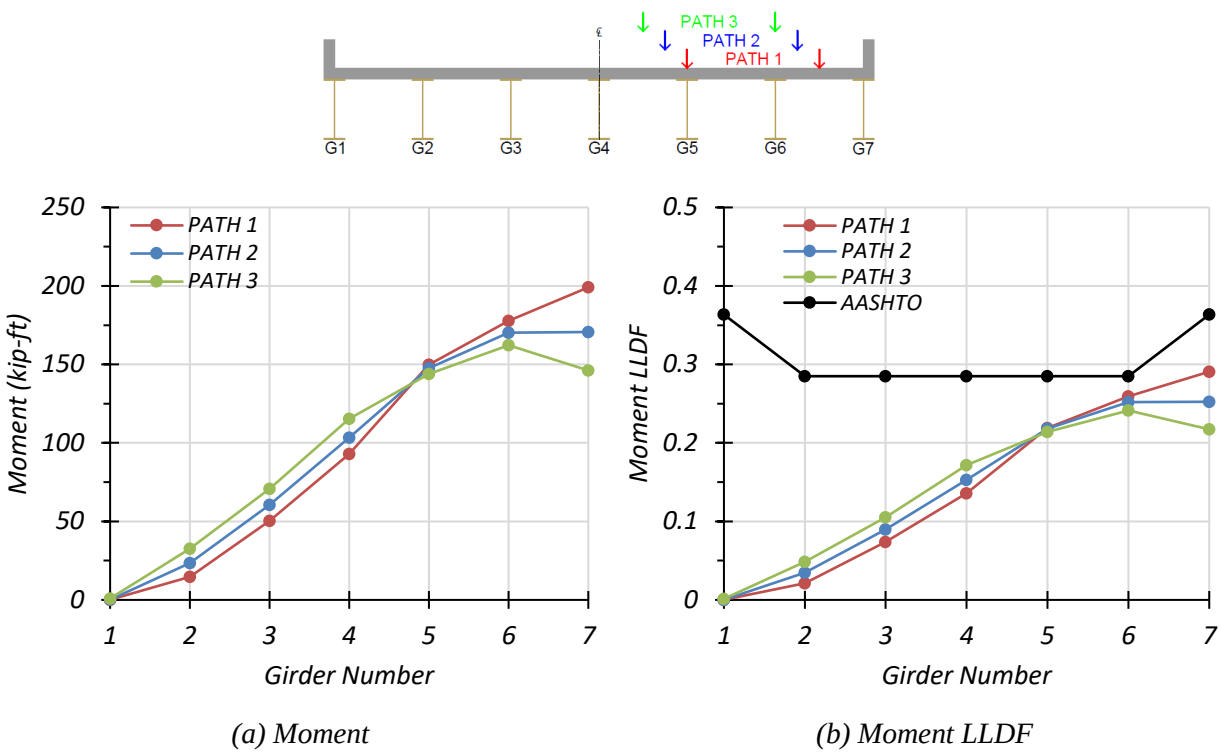

(a) Moment *(b) Moment LLDF*

Figure 2.43. Moment Results for Non-Composite Bridge SM-21 with One-Lane HS-20 Loading

Table 2.41. Maximum Moments for Non-Composite Bridge SM-21 with One-Lane HS-20 Loading

Loading	G1	G2	G3	G4	G5	G6	G7
Path 1	0.1	14.6	50.5	93.0	149.8	177.7	199.1
Path 2	0.1	23.5	60.6	103.3	147.5	170.3	170.6
Path 3	0.9	32.7	70.8	115.5	144.0	162.2	146.1
Note: G = girder, paths indicate transverse loading positions as shown, moments have kip-ft units							

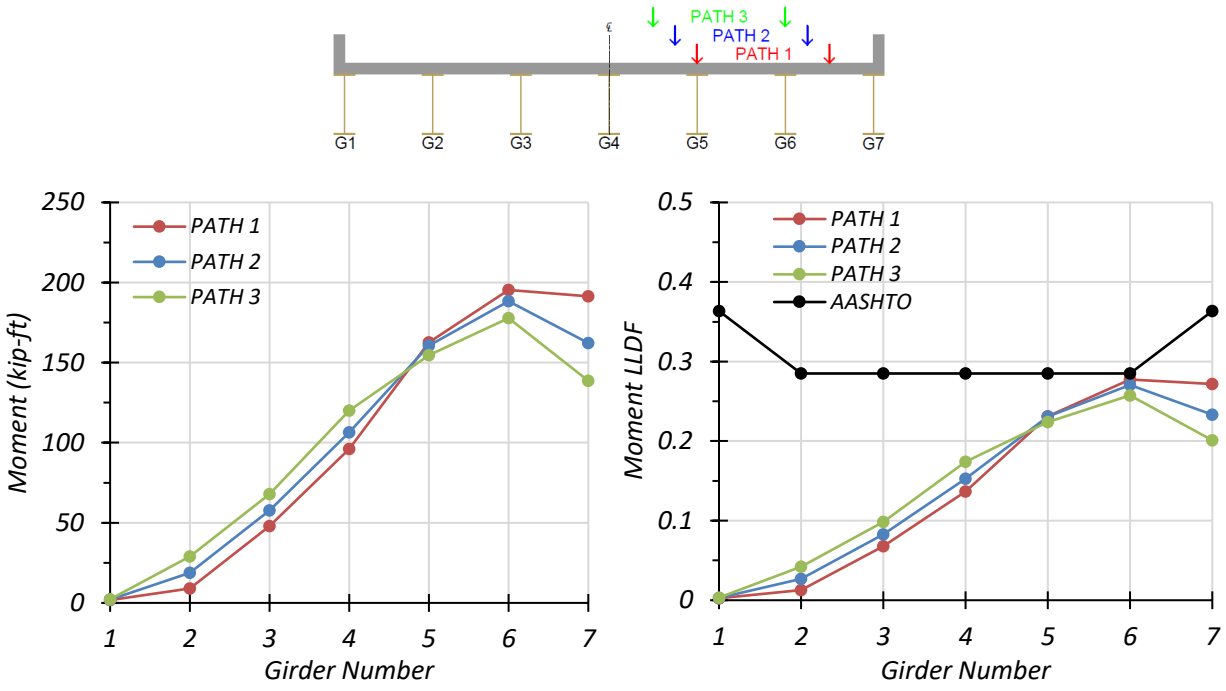

(a) Moment *(b) Moment LLDF*

Figure 2.44. Moment Results for Composite Bridge SM-21 with One-Lane HS-20 Loading

Table 2.42. Maximum Moments for Composite Bridge SM-21 with One-Lane HS-20 Loading

Loading	G1	G2	G3	G4	G5	G6	G7
Path 1	1.8	9.0	47.9	96.1	162.7	195.4	191.4
Path 2	2.0	18.7	57.7	106.4	160.7	188.3	162.2
Path 3	2.3	29.0	68.0	120.0	154.6	177.8	138.7
Note: G = girder, paths indicate transverse loading positions as shown, moments have kip-ft units							

Comparison of governing moment LLDF values computed from FEM results for the composite and non-composite cases reveals that the maximum moment LLDF in an interior girder for the composite bridge is higher than the one for the non-composite bridge, with a $g^m_{composite}/g^m_{non-composite}$ ratio of 1.07. However, the maximum moment LLDF in an exterior girder for the composite bridge is lower than the one for the non-composite bridge, with a $g^m_{composite}/g^m_{non-composite}$ ratio of 0.93.

Table 2.43. Governing Moment LLDFs for Bridge SM-21 with One-Lane HS-20 Loading

Type	Girder Location	AASHTO (g^m_{AASHTO})	FEM (g^m_{FEM})	g^m_{AASHTO}/g^m_{FEM}
Non-Composite	Interior	0.285	0.259	1.10
	Exterior	0.364	0.291	1.25
Composite	Interior	0.285	0.277	1.03
	Exterior	0.364	0.272	1.34

Two-Lane Loading. Figure 2.45 shows the individual girder moments and moment LLDF results for the non-composite Bridge SM-21 under simulated moving HS-20 loading along three two-lane loading paths. Table 2.44 provides the corresponding maximum moment values of each girder for each loading path. The moment LLDF values are calculated using the estimated moment results from FEM analysis. Table 2.46 shows the governing moment LLDFs found using the FEM analysis and compares them to the AASHTO LLDF values. Compared to the FEM results, the governing moment LLDF value computed using the approximate equations in the *AASHTO Standard Specifications* (AASHTO 2002) is slightly conservative for interior girders, with a g^m_{AASHTO}/g^m_{FEM} ratio of 1.06, and is conservative for exterior girders, with a g^m_{AASHTO}/g^m_{FEM} ratio of 1.24.

Figure 2.46 shows the individual girder moments and moment LLDF results for the fully composite Bridge SM-21 under simulated moving HS-20 loading along three two-lane loading paths. Table 2.45 provides the corresponding maximum moment values of each girder for each loading path. The moment LLDF values are calculated using the estimated moment results from the FEM analysis. Compared to the FEM results, the governing moment LLDF value computed using the approximate equations in the *AASHTO Standard Specifications* (AASHTO 2002) is slightly conservative for interior girders, with a g^m_{AASHTO}/g^m_{FEM} ratio of 1.04, and is quite conservative for exterior girders, with a g^m_{AASHTO}/g^m_{FEM} ratio of 1.32.

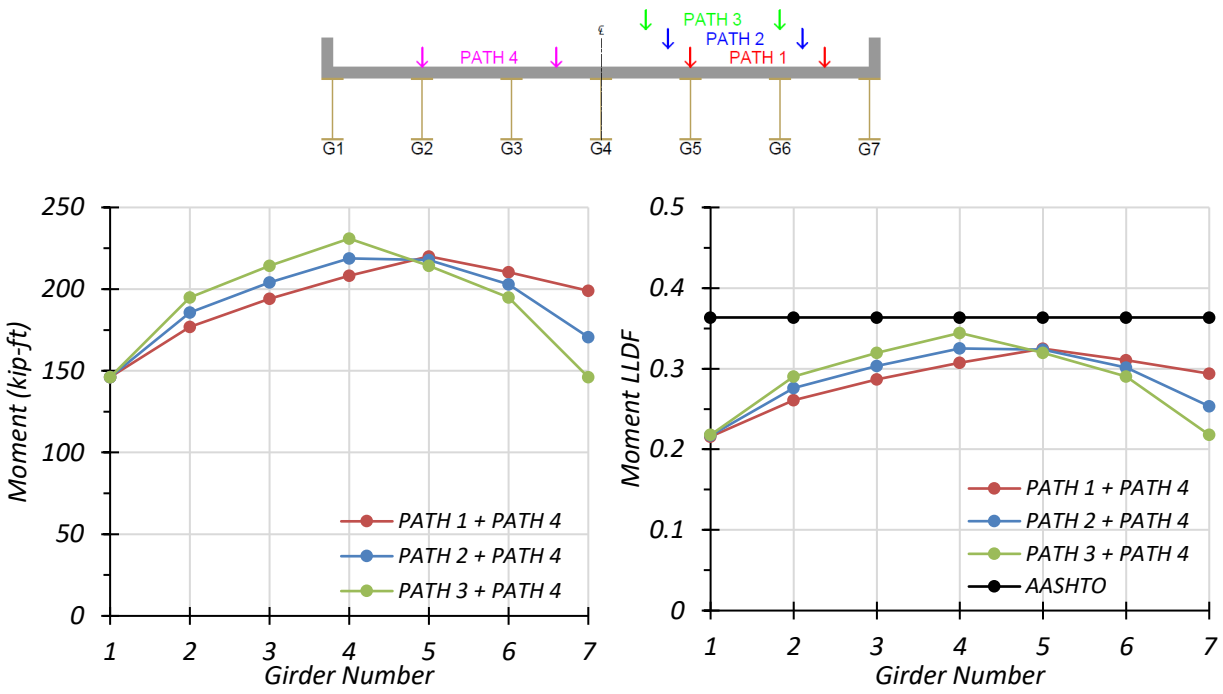

(a) Moment *(b) Moment LLDF*

Figure 2.45. Moment Results for Non-Composite Bridge SM-21 with Two-Lane HS-20 Loading

Table 2.44. Maximum Moments for Non-Composite Bridge SM-21 with Two-Lane HS-20 Loading

Loading	G1	G2	G3	G4	G5	G6	G7
Path 1 + Path 4	146.1	176.8	194.2	208.2	220.0	210.3	199.1
Path 2 + Path 4	146.1	185.6	204.1	218.8	217.8	202.9	170.6
Path 3 + Path 4	146.1	194.8	214.3	230.9	214.3	194.8	146.1
Note: G = girder, paths indicate transverse loading positions as shown, moments have kip-ft units							

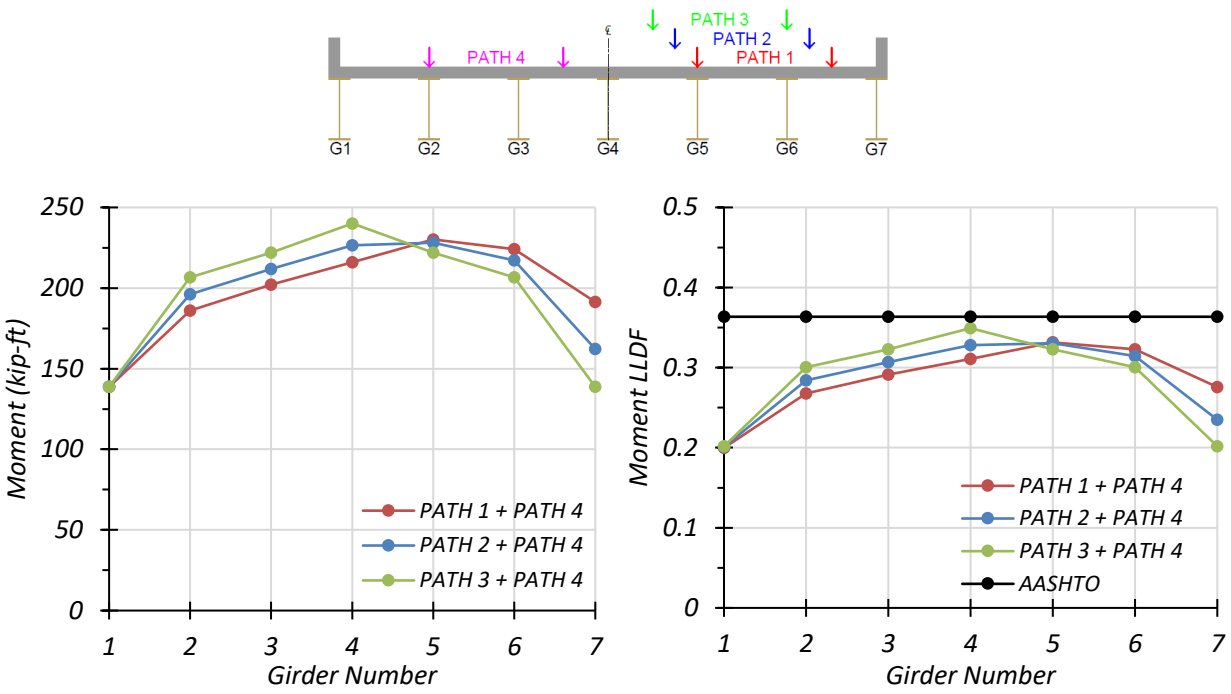

(a) Moment *(b) Moment LLDF*

Figure 2.46. Moment Results for Composite Bridge SM-21 with Two-Lane HS-20 Loading

Table 2.45. Maximum Moments for Composite Bridge SM-21 with Two-Lane HS-20 Loading

Loading	G1	G2	G3	G4	G5	G6	G7
Path 1 + Path 4	138.7	186.0	202.2	215.9	230.1	224.2	191.4
Path 2 + Path 4	138.7	196.1	211.8	226.4	228.1	217.1	162.2
Path 3 + Path 4	138.7	206.6	222.0	240.1	222.0	206.6	138.7
Note: G = girder, paths indicate transverse loading positions as shown, moments have kip-ft units							

Comparison of governing moment LLDF values computed from FEM results for the composite and non-composite cases reveals that the maximum moment LLDF in an interior girder for the composite bridge is almost the same as the one for the non-composite bridge, with a $g^m_{composite}/g^m_{non-composite}$ ratio of 1.01. However, the maximum moment LLDF in an exterior girder for the composite bridge is lower than the one for the non-composite bridge, with a $g^m_{composite}/g^m_{non-composite}$ ratio of 0.94.

Table 2.46. Governing Moment LLDFs for Bridge SM-21 with Two-Lane HS-20 Loading

Type	Girder Location	AASHTO (g^m_{AASHTO})	FEM (g^m_{FEM})	g^m_{AASHTO}/g^m_{FEM}
Non-Composite	Interior	0.364	0.344	1.06
	Exterior	0.364	0.294	1.24
Composite	Interior	0.364	0.349	1.04
	Exterior	0.364	0.276	1.32

*2.7.2.3 **Shear Results***

One-Lane Loading. Figure 2.47 shows the individual girder shears and shear LLDF results for the non-composite Bridge SM-21 under simulated moving HS-20 loading along three one-lane loading paths. Table 2.47 provides the corresponding maximum shear values of each girder for each loading path. The shear LLDF values are calculated using the estimated shear results from the FEM analysis. Table 2.49 shows the governing shear LLDFs found using the FEM analysis and compares them to the AASHTO LLDF values. Compared to the FEM results, the governing shear LLDF value computed using the approximate equations in the *AASHTO Standard Specifications* (AASHTO 2002) is almost the same for interior girders, with a g^v_{AASHTO}/g^v_{FEM} ratio of approximately 1.00, and very conservative for exterior girders, with a g^v_{AASHTO}/g^v_{FEM} ratio of 1.44.

Figure 2.48 shows the individual girder shears and shear LLDF results for the fully composite Bridge SM-21 under simulated moving HS-20 loading along three one-lane loading paths. Table 2.48 provides the corresponding maximum shear values of each girder for each loading path. The shear LLDF values are calculated using the estimated shear results from the FEM analysis. Compared to the FEM results, the governing shear LLDF value computed using the approximate equations in the *AASHTO Standard Specifications* (AASHTO 2002) is slightly unconservative for interior girders, with a g^v_{AASHTO}/g^v_{FEM} ratio of 0.91, and very conservative for exterior girders, with a g^v_{AASHTO}/g^v_{FEM} ratio of 1.44.

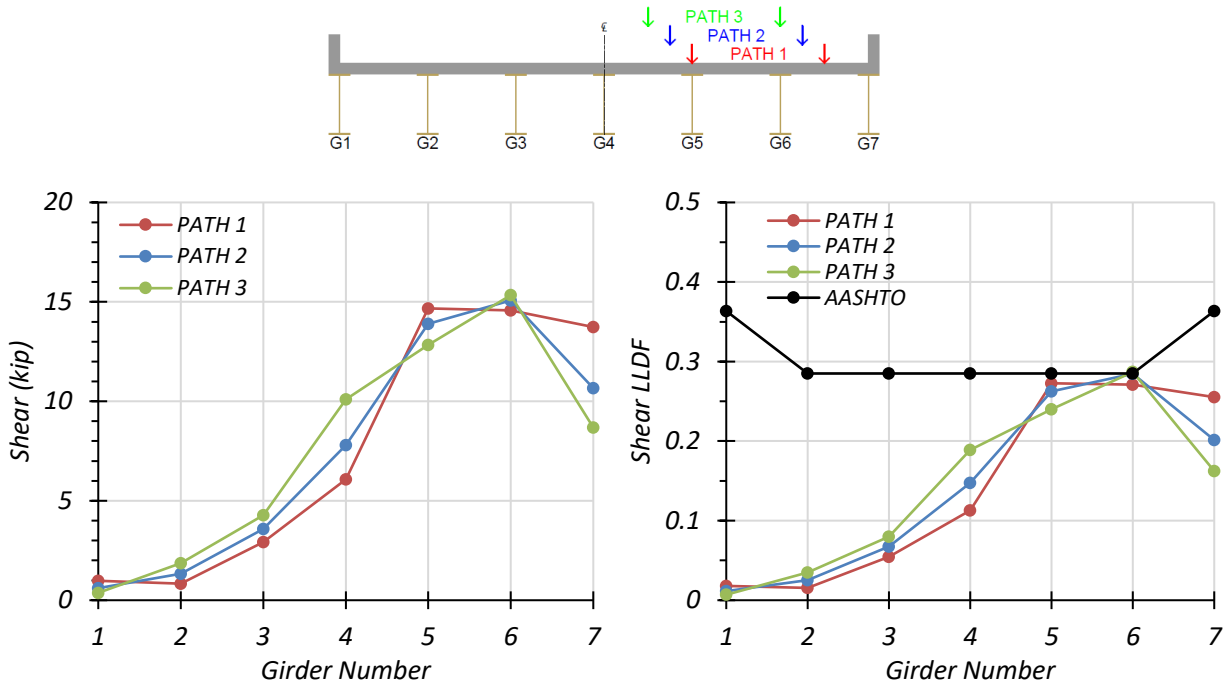

(a) Shear *(b) Shear LLDF*

Figure 2.47. Shear Results for Non-Composite Bridge SM-21 with One-Lane HS-20 Loading

Table 2.47. Maximum Shears for Non-Composite Bridge SM-21 with One-Lane HS-20 Loading

Loading	G1	G2	G3	G4	G5	G6	G7
Path 1	1.4	0.8	2.9	6.1	14.7	14.6	13.7
Path 2	1.0	1.3	3.6	7.8	13.9	15.1	10.7
Path 3	0.6	1.9	4.3	10.1	12.8	15.3	8.7
Note: G = girder, paths indicate transverse loading positions as shown, shears have kip units							

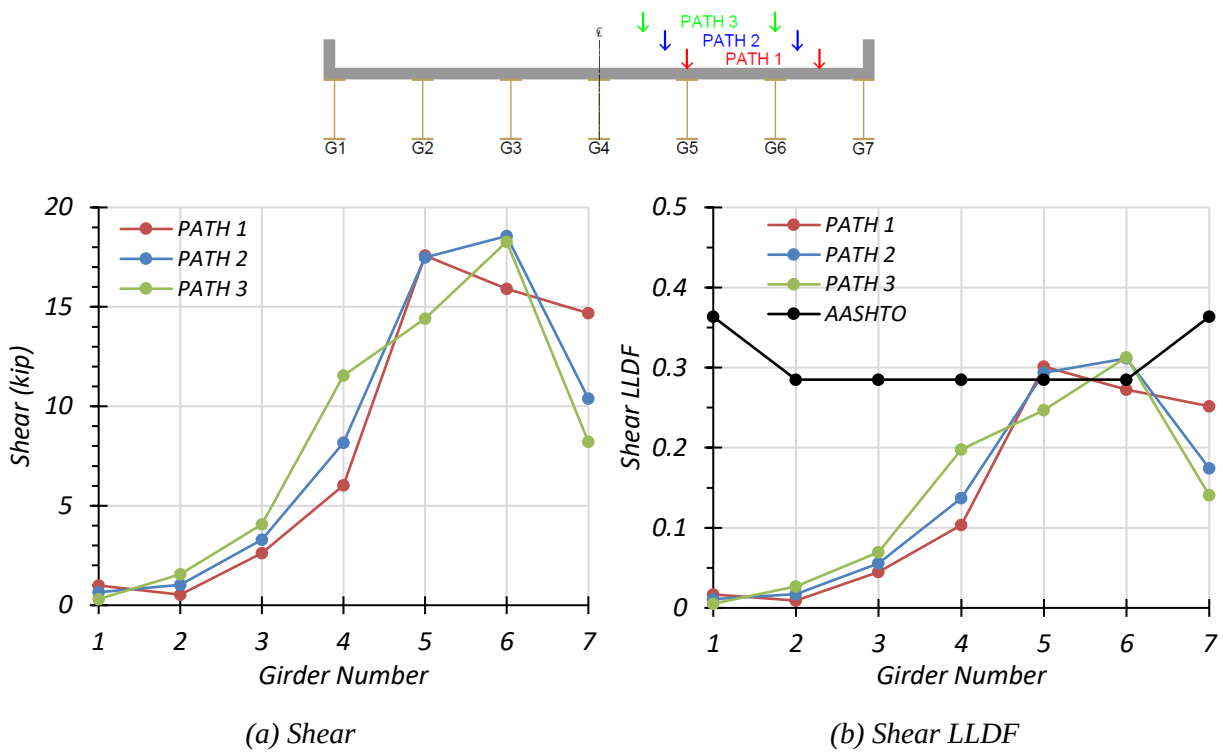

(a) Shear *(b) Shear LLDF*

Figure 2.48. Shear Results for Composite Bridge SM-21 with One-Lane HS-20 Loading

Table 2.48. Maximum Shears for Composite Bridge SM-21 with One-Lane HS-20 Loading

Loading	G1	G2	G3	G4	G5	G6	G7
Path 1	1.0	0.5	2.6	6.0	17.6	15.9	14.7
Path 2	0.7	1.0	3.3	8.2	17.5	18.6	10.4
Path 3	0.4	1.6	4.1	11.6	14.4	18.3	8.2
Note: G = girder, paths indicate transverse loading positions as shown, shears have kip units							

Comparison of governing shear LLDF values computed from FEM results for the composite and non-composite cases reveals that the maximum shear LLDF in an interior girder for the composite bridge is higher than the one for the non-composite bridge, with a $g^v_{composite}/g^v_{non-composite}$ ratio of 1.09. However, the maximum shear LLDF in an exterior girder for the composite bridge is about the same as the one for the non-composite bridge, with a $g^v_{composite}/g^v_{non-composite}$ ratio of 1.00.

Table 2.49. Governing Shear LLDFs for Bridge SM-21 with One-Lane HS-20 Loading

Type	Girder Location	AASHTO (g^v_{AASHTO})	FEM (g^v_{FEM})	g^v_{AASHTO}/g^v_{FEM}
Non-Composite	Interior	0.285	0.286	1.00
	Exterior	0.364	0.253	1.44
Composite	Interior	0.285	0.313	0.91
	Exterior	0.364	0.252	1.44

Two-Lane Loading. The same procedure was conducted for two-lane loading. Figure 2.49 shows the individual girder shears and shear LLDF results for the non-composite Bridge SM-21 under simulated moving HS-20 loading along three two-lane loading paths. Table 2.50 provides the corresponding maximum shear values of each girder for each loading path. The shear LLDF values are calculated using the estimated shear results from the FEM analysis. Table 2.52 shows the governing shear LLDFs found using the FEM analysis and compares them to the AASHTO LLDF values. Compared to the FEM results, the governing shear LLDF value computed using the approximate equations in the *AASHTO Standard Specifications* (AASHTO 2002) is slightly unconservative for interior girders, with a g^v_{AASHTO}/g^v_{FEM} ratio of 0.96, and very conservative for exterior girders, with a g^v_{AASHTO}/g^v_{FEM} ratio of 1.40.

Figure 2.50 shows the individual girder shears and shear LLDF results for the fully composite Bridge SM-21 under simulated moving HS-20 loading along three one-lane loading paths. Table 2.51 provides the corresponding maximum shear values of each girder for each loading path. The shear LLDF values are calculated using the estimated shear results from the FEM analysis. Compared to the FEM results, the governing shear LLDF value computed using the approximate equations in the *AASHTO Standard Specifications* (AASHTO 2002) is slightly unconservative for interior girders, with a g^v_{AASHTO}/g^v_{FEM} ratio of 0.91, and very conservative for exterior girders, with a g^v_{AASHTO}/g^v_{FEM} ratio of 1.43.

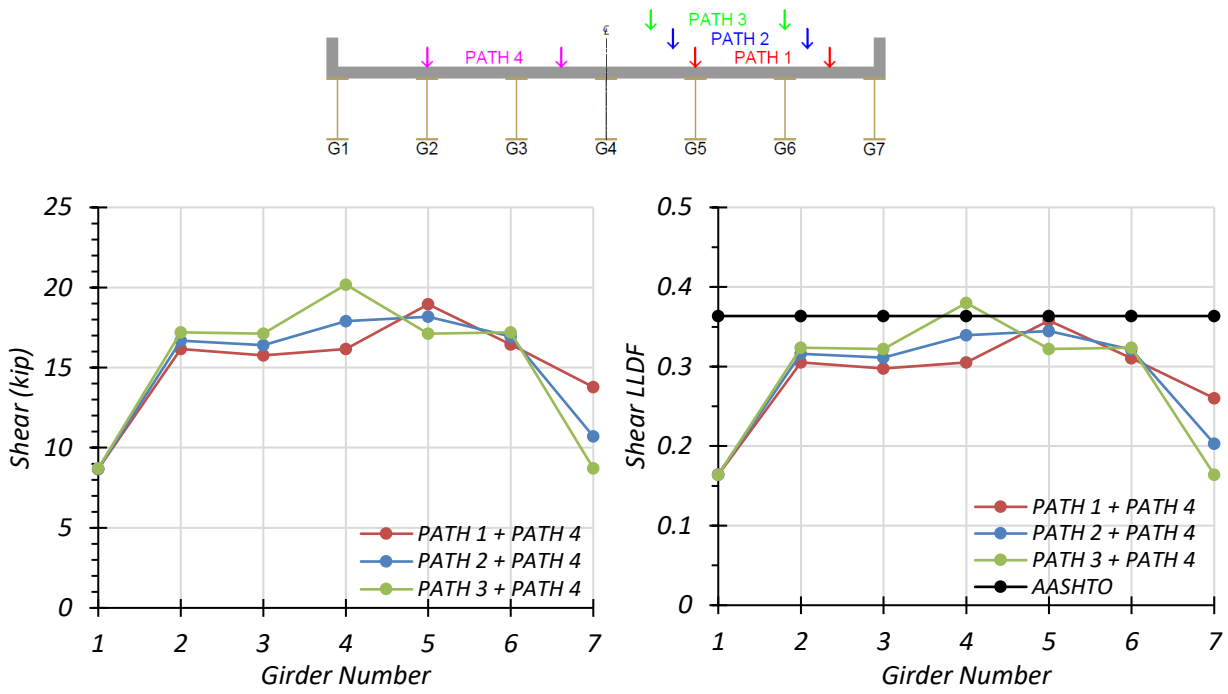

(a) Shear *(b) Shear LLDF*

Figure 2.49. Shear Results for Non-Composite Bridge SM-21 with Two-Lane HS-20 Loading

Table 2.50. Maximum Shears for Non-Composite Bridge SM-21 with Two-Lane HS-20 Loading

Loading	G1	G2	G3	G4	G5	G6	G7
Path 1 + Path 4	8.7	16.2	15.8	16.2	19.0	16.4	13.8
Path 2 + Path 4	8.7	16.7	16.4	17.9	18.2	16.9	10.7
Path 3 + Path 4	8.7	17.2	17.1	20.2	17.1	17.2	8.7
Note: G = girder, paths indicate transverse loading positions as shown, shears have kip units							

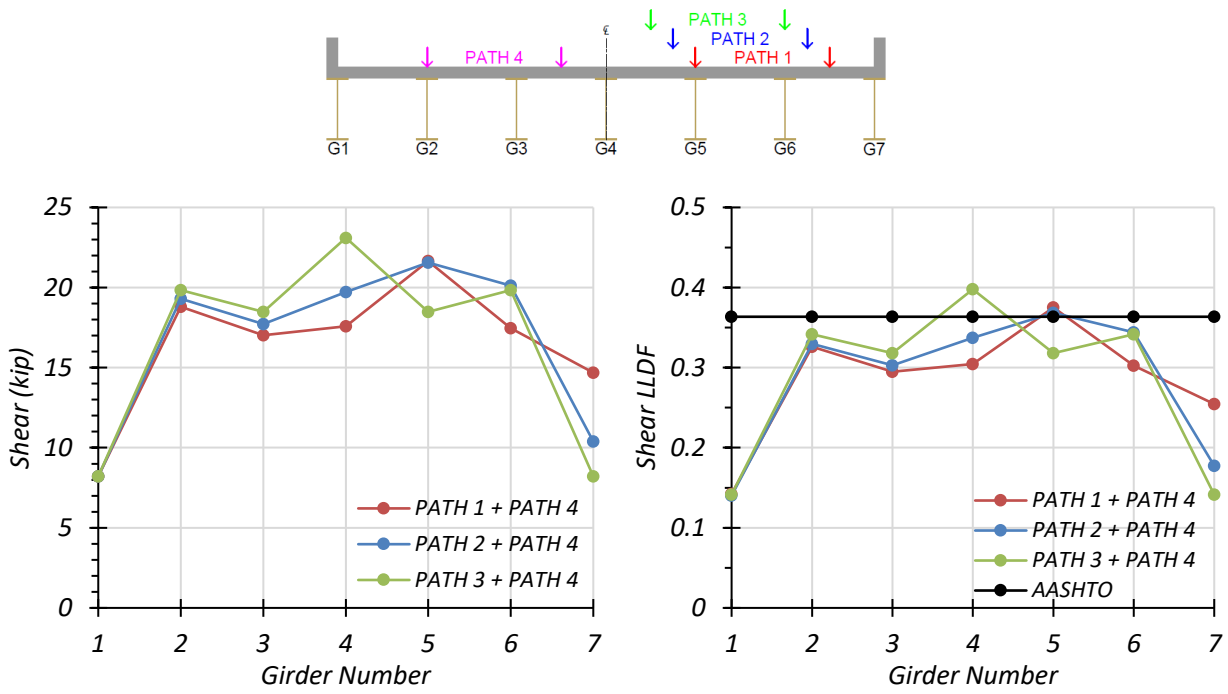

(a) Shear *(b) Shear LLDF*

Figure 2.50. Shear Results for Composite Bridge SM-21 with Two-Lane HS-20 Loading

Table 2.51. Maximum Shears for Composite Bridge SM-21 with Two-Lane HS-20 Loading

Loading	G1	G2	G3	G4	G5	G6	G7
Path 1 + Path 4	8.2	18.8	17.0	17.6	21.6	17.5	14.7
Path 2 + Path 4	8.2	19.3	17.7	19.7	21.6	20.1	10.4
Path 3 + Path 4	8.2	19.8	18.5	23.1	18.5	19.8	8.2
Note: G = girder, paths indicate transverse loading positions as shown, shears have kip units							

Comparison of governing shear LLDF values computed from FEM results for the composite and non-composite cases reveals that the maximum shear LLDF in an interior girder for the composite bridge is higher than the one for the non-composite bridge, with a $g^v_{composite}/g^v_{non-composite}$ ratio of 1.05. However, the maximum shear LLDF in an exterior girder for the composite bridge is almost the same as the one for the non-composite bridge, with a $g^v_{composite}/g^v_{non-composite}$ ratio of 0.98.

Table 2.52. Governing Shear LLDFs for Bridge SM-21 with Two-Lane HS-20 Loading

Type	Girder Location	AASHTO (g^v_{AASHTO})	FEM (g^v_{FEM})	g^v_{AASHTO}/g^v_{FEM}
Non-Composite	Interior	0.364	0.380	0.96
	Exterior	0.364	0.260	1.40
Composite	Interior	0.364	0.398	0.91
	Exterior	0.364	0.255	1.43

2.7.3 HL-93 Live Load Analysis

Bridge SM-5 was also analyzed using the HL-93 design loading presented in the *AASHTO LRFD Specifications* (AASHTO 2017). The bridge was analyzed for one-lane- and two-lane-loaded cases along four transverse paths, as shown in Figure 2.15. Deflection, moment, and shear results were obtained.

*2.7.3.1 **Deflection Results***

Figure 2.51 shows the estimated girder deflection profiles and contours along the span for one-lane HL-93 loading along Path 1 and Path 4 when the bridge is analyzed as fully non-composite. Table 2.53 shows the corresponding maximum deflections for each girder, assuming non-composite action. Load Paths 1 and 4 are the only ones shown because they are the load paths planned for later load tests, and were selected to maximize the forces on an interior girder and on an exterior girder.

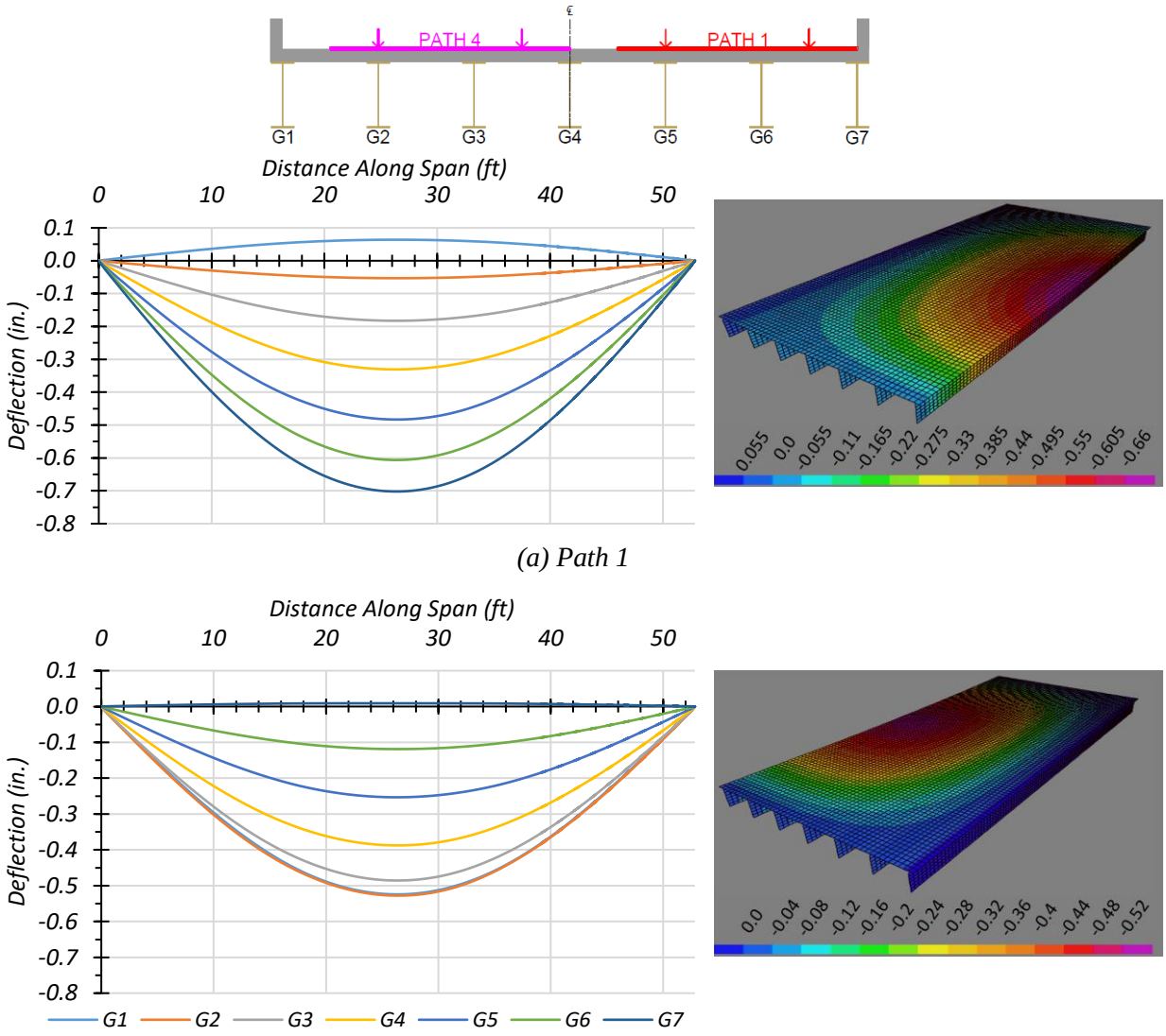

Figure 2.51. Deflection Profiles for Non-Composite Bridge SM-21 with HL-93 Loading

Table 2.53. Maximum Deflections for Non-Composite Bridge SM-21 with HL-93 Loading

Loading	G1	G2	G3	G4	G5	G6	G7
Path 1	0.064	−0.053	−0.183	−0.331	−0.483	−0.606	−0.702
Path 4	−0.524	−0.528	−0.486	−0.388	−0.253	−0.119	0.009
Note: G = girder, paths indicate transverse loading positions as shown, deflections have inch units							

Figure 2.52 shows the estimated girder deflection profiles and contours along the span for one-lane HL-93 loading along Path 1 and Path 4 when the bridge is analyzed as fully composite. Table 2.54 shows the corresponding maximum deflections for each girder, assuming fully composite action. Load Paths 1 and 4 are the only ones shown because they are the load paths planned for later load tests, and were selected to maximize the forces on an interior girder and on an exterior girder.

For both non-composite and composite cases, the maximum deflections were obtained in Girder G7 when the HL-93 truck was run along Path 1. The estimated deflections were 0.702 in. and 0.400 in. for the non-composite and composite cases, respectively. This result indicates that the composite bridge is 54.8 percent stiffer than the non-composite bridge. The maximum deflections obtained when the HL-93 truck was run along Path 4 were in Girder G1 for both the non-composite and composite case. The estimated deflections were 0.524 in. and 0.302 in. for the non-composite and composite cases, respectively. This result indicates that the composite bridge is 50.1 percent stiffer than the non-composite bridge. The slightly different values of relative stiffness suggest that the relative girder deflection depends on the location of loading and corresponding load distribution.

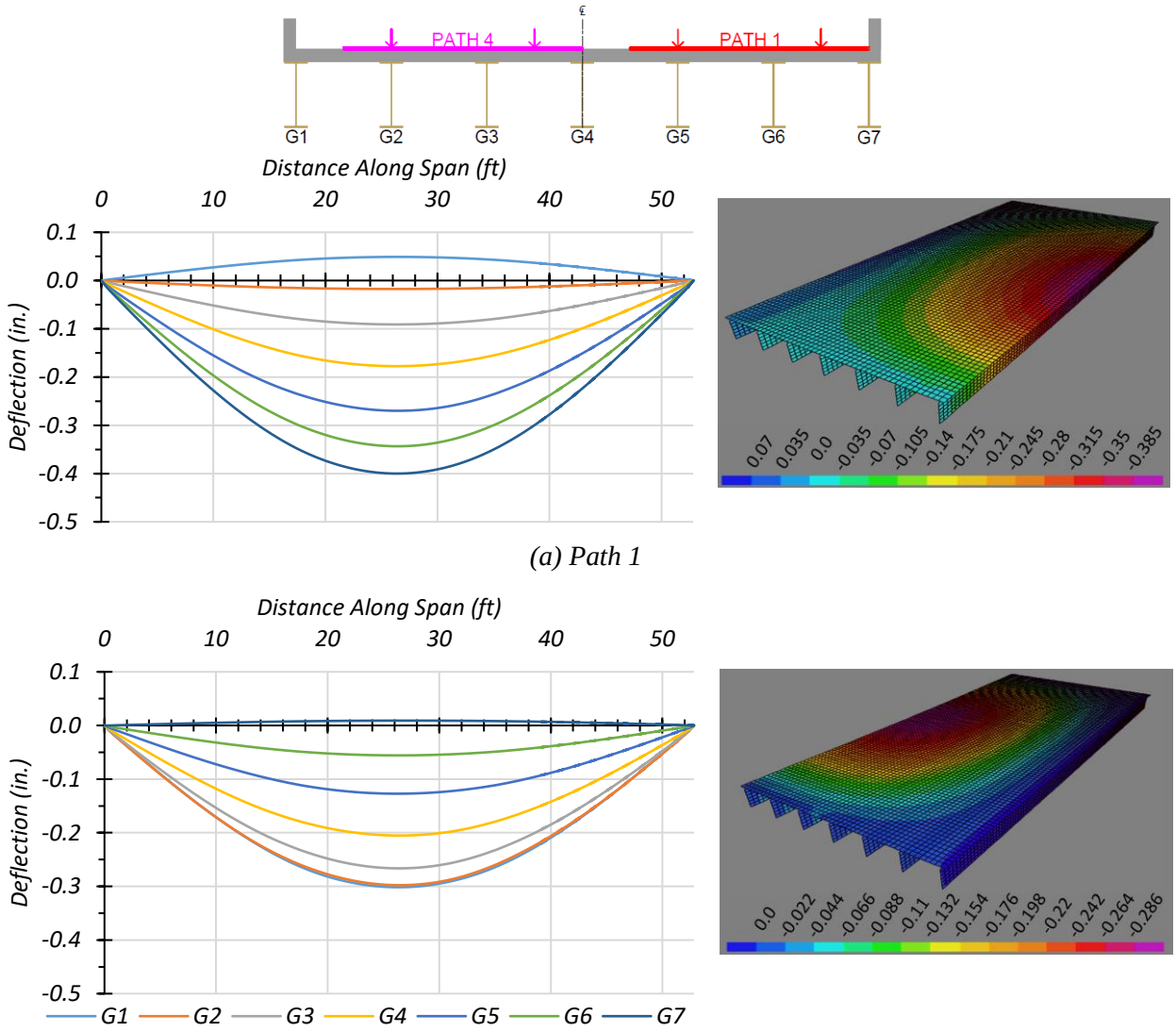

Figure 2.52. Deflection Profiles for Composite Bridge SM-21 with HL-93 Loading

Table 2.54. Maximum Deflections for Composite Bridge SM-21 with HL-93 Loading

Loading	G1	G2	G3	G4	G5	G6	G7
Path 1	0.049	−0.017	−0.091	−0.177	−0.270	−0.343	−0.400
Path 4	−0.302	−0.298	−0.266	−0.205	−0.127	−0.056	0.009
Note: G = girder, paths indicate transverse loading positions as shown, deflections have inch units							

2.7.3.2 ***Moment Results***

One-Lane Loading. Figure 2.53 shows the individual girder moments and moment LLDF results for the non-composite Bridge SM-21 under simulated moving HL-93 loading along three one-lane loading paths. Table 2.55 provides the corresponding maximum moment values of each girder for each loading path. The moment LLDF values are calculated using the estimated moment results from the FEM analysis. Table 2.57 shows the governing moment LLDFs found using the FEM analysis and compares them to the AASHTO LLDF values. The first AASHTO LLDF value is calculated using the simplified stiffness parameter. The second AASHTO LLDF value is calculated using the analytical stiffness parameter calculated for the specific bridge. Compared to the FEM results, the governing moment LLDF value computed using the approximate equations and the simplified stiffness parameter in *AASHTO LRFD Specifications* (AASHTO 2017) is conservative for interior girders, with a $g^m_{AASHTO\_S}/g^m_{FEM}$ ratio of 1.11, and is also conservative for exterior girders, with a $g^m_{AASHTO\_S}/g^m_{FEM}$ ratio of 1.10. Compared to the FEM results, the governing moment LLDF value computed using the approximate equations and the analytical stiffness parameter in *AASHTO LRFD Specifications* (AASHTO 2017) is conservative for both interior and exterior girders, with a $g^m_{AASHTO\_K}/g^m_{FEM}$ ratio of 1.13 and 1.12, respectively.

Figure 2.54 shows the individual girder moments and moment LLDF results for the fully composite Bridge SM-21 under simulated moving HL-93 loading along three one-lane loading paths. Table 2.56 provides the corresponding maximum moment values of each girder for each loading path. The moment LLDF values are calculated using the estimated moment results from the FEM analysis. Compared to the FEM results, the governing moment LLDF value computed using the approximate equations and the simplified stiffness parameter in *AASHTO LRFD Specifications* (AASHTO 2017) is slightly conservative for both interior and exterior girders, with a $g^m_{AASHTO\_S}/g^m_{FEM}$ ratio of 1.04 and 1.06, respectively. Compared to the FEM results, the governing moment LLDF value computed using the approximate equations and the analytical stiffness parameter in *AASHTO LRFD Specifications* (AASHTO 2017) is slightly conservative for both interior and exterior girders, with a $g^m_{AASHTO\_K}/g^m_{FEM}$ ratio of 1.06 and 1.08, respectively.

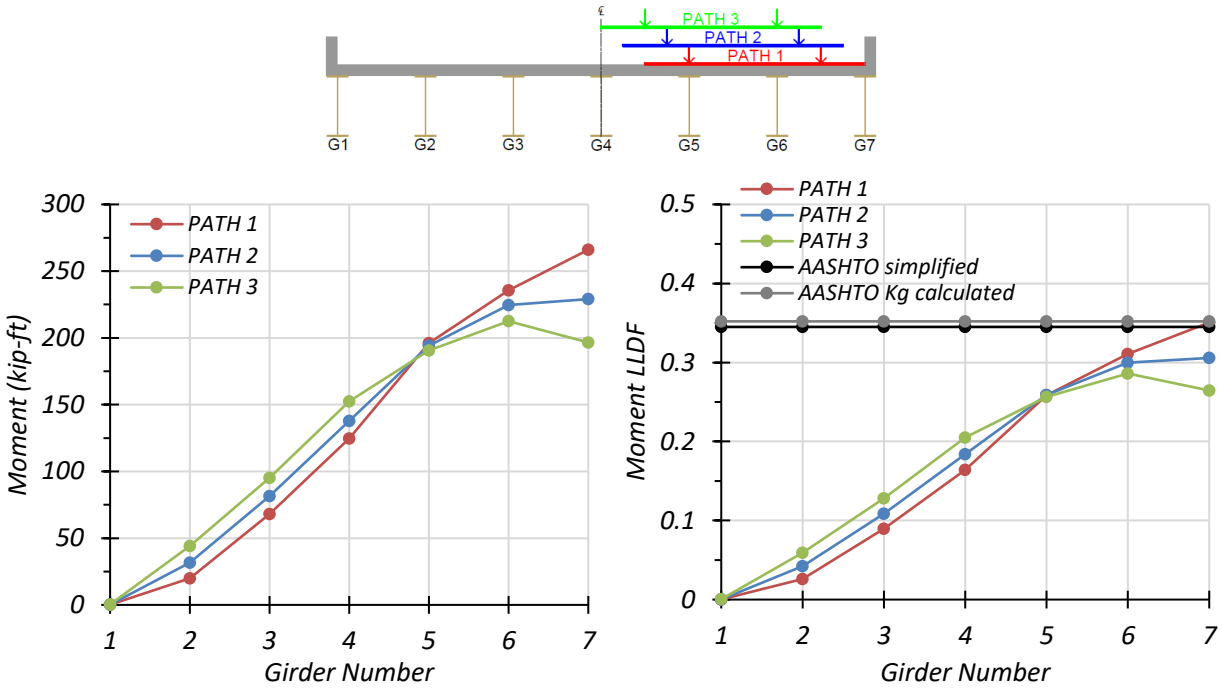

(a) Moment *(b) Moment LLDF*

Figure 2.53. Moment Results for Non-Composite Bridge SM-21 with One-Lane HL-93 Loading

Table 2.55. Maximum Moments for Non-Composite Bridge SM-21 with One-Lane HL-93 Loading

Loading	G1	G2	G3	G4	G5	G6	G7
Path 1	0.2	19.8	68.1	124.7	196.0	235.8	266.1
Path 2	0.4	44.2	95.1	152.5	190.5	212.5	196.5
Path 3	0.2	31.7	81.5	137.8	194.1	224.7	229.1
Note: G = girder, paths indicate transverse loading positions as shown, moments have kip-ft units							

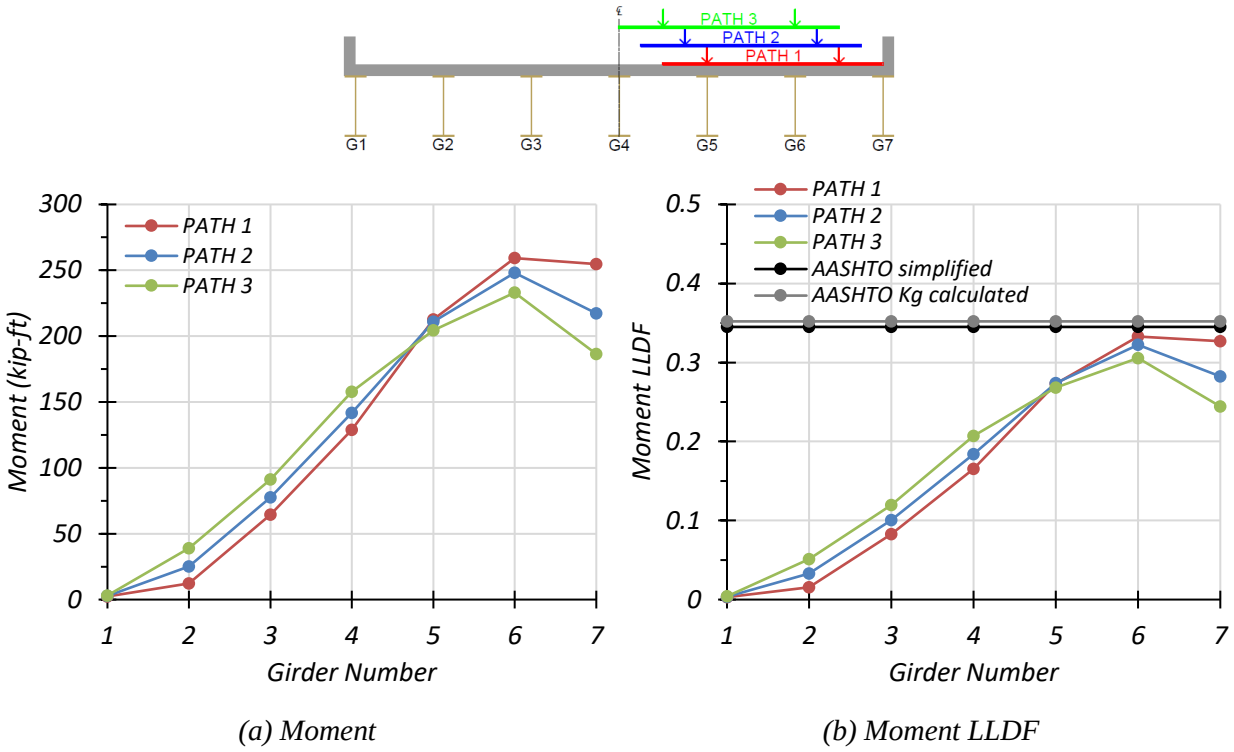

(a) Moment *(b) Moment LLDF*

Figure 2.54. Moment Results for Composite Bridge SM-21 with One-Lane HL-93 Loading

Table 2.56. Maximum Moments for Composite Bridge SM-21 with One-Lane HL-93 Loading

Loading	G1	G2	G3	G4	G5	G6	G7
Path 1	2.4	12.2	64.5	128.9	212.8	259.2	254.7
Path 2	2.8	25.2	77.6	141.7	210.9	248.1	217.3
Path 3	3.1	39.0	91.2	157.8	204.4	233.0	186.4
Note: G = girder, paths indicate transverse loading positions as shown, moments have kip-ft units							

Comparison of governing moment LLDF values computed from FEM results for the composite and non-composite cases reveals that the maximum moment LLDF in an interior girder for the composite bridge is higher than the one for the non-composite bridge, with a $g^m_{composite}/g^m_{non-composite}$ ratio of 1.07. The maximum moment LLDF in an exterior girder for the composite bridge is also higher than that for the non-composite bridge, with a $g^m_{composite}/g^m_{non-composite}$ ratio of 1.04.

Table 2.57. Governing Moment LLDFs for Bridge SM-21 with One-Lane HL-93 Loading

Type	Girder Location	AASHTO Simplified ($g^m_{AASHTO\_S}$)	AASHTO K_g Calculated ($g^m_{AASHTO\_K}$)	FEM (g^m_{FEM})	$g^m_{AASHTO\_S}/g^m_{FEM}$	$g^m_{AASHTO\_K}/g^m_{FEM}$
Non-Composite	Interior	0.345	0.352	0.311	1.11	1.13
	Exterior	0.345	0.352	0.315	1.10	1.12
Composite	Interior	0.345	0.352	0.333	1.04	1.06
	Exterior	0.345	0.352	0.327	1.06	1.08

Two-Lane Loading. Figure 2.55 shows the individual girder moments and moment LLDF results for the non-composite Bridge SM-21 under simulated moving HL-93 loading along three two-lane loading paths. Table 2.58 provides the corresponding maximum moment values of each girder for each loading path. The moment LLDF values are calculated using the estimated moment results from the FEM analysis. Table 2.60 shows the governing moment LLDFs found using the FEM analysis and compares them to the AASHTO LLDF values. The first AASHTO LLDF value is calculated using the simplified stiffness parameter. The second AASHTO LLDF value is calculated using the analytical stiffness parameter calculated for the specific bridge. Compared to the FEM results, the governing moment LLDF value computed using the approximate equations and the simplified stiffness parameter in *AASHTO LRFD Specifications* (AASHTO 2017) is conservative for interior girders, with a $g^m_{AASHTO\_S}/g^m_{FEM}$ ratio of 1.27, and is quite conservative for exterior girders, with a g^m_{AASHTO}/g^m_{FEM} ratio of 1.48. Compared to the FEM results, the governing moment LLDF value computed using the approximate equations and the analytical stiffness parameter in *AASHTO LRFD Specifications* (AASHTO 2017) is quite conservative for both interior and exterior girders, with a $g^m_{AASHTO\_K}/g^m_{FEM}$ ratio of 1.30 and 1.51, respectively.

Figure 2.56 shows the individual girder moments and moment LLDF results for the fully composite Bridge SM-21 under simulated moving HL-93 loading along three two-lane loading paths. Table 2.59 provides the corresponding maximum moment values of each girder for each loading path. The moment LLDF values are calculated using the estimated moment results from the FEM analysis. Compared to the FEM results, the governing moment LLDF value computed using the approximate equations and the simplified stiffness parameter in *AASHTO LRFD Specifications* (AASHTO 2017) is conservative for interior girders, with a $g^m_{AASHTO\_S}/g^m_{FEM}$ ratio of 1.26, and is quite conservative for exterior girders, with a g^m_{AASHTO}/g^m_{FEM} ratio of 1.58.

Compared to the FEM results, the governing moment LLDF value computed using the approximate equations and the analytical stiffness parameter in *AASHTO LRFD Specifications* (AASHTO 2017) is conservative for interior girders, with a $g^m_{AASHTO\_K}/g^m_{FEM}$ ratio of 1.29, and is quite conservative for exterior girders, with a g^m_{AASHTO}/g^m_{FEM} ratio of 1.61.

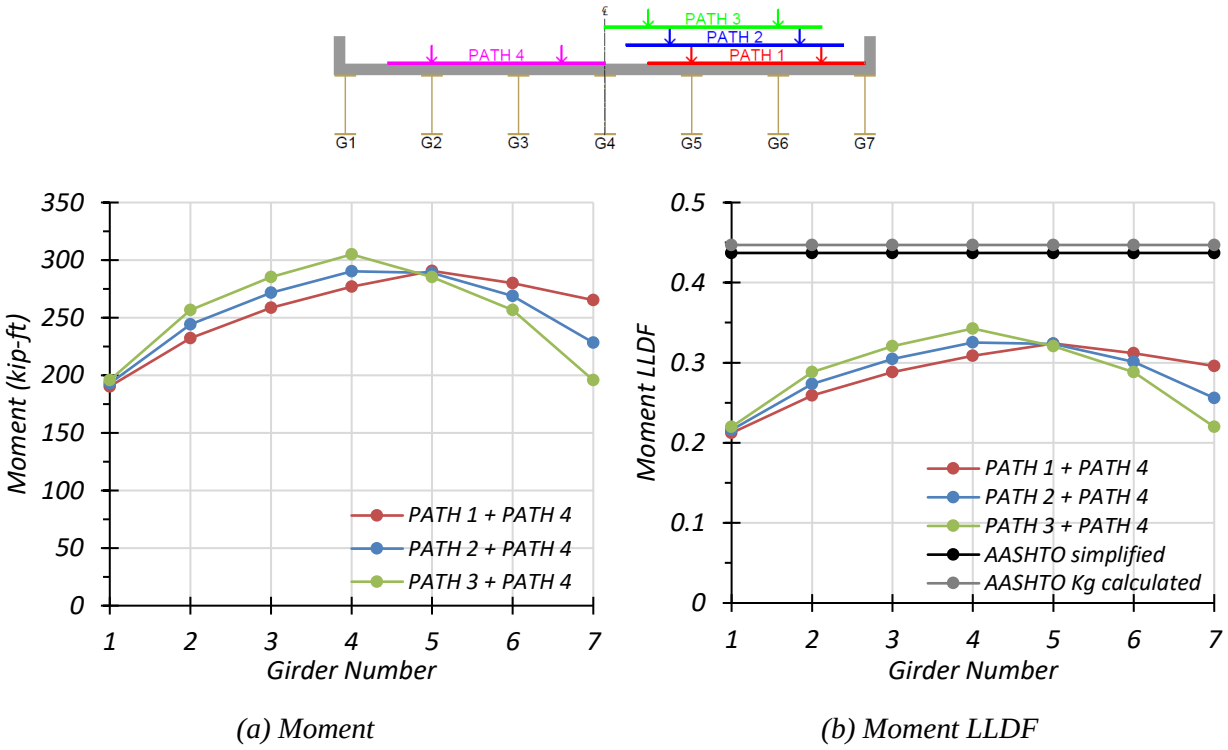

(a) Moment *(b) Moment LLDF*

Figure 2.55. Moment Results for Non-Composite Bridge SM-21 with Two-Lane HL-93 Loading

Table 2.58. Maximum Moments for Non-Composite Bridge SM-21 with Two-Lane HL-93 Loading

Loading	G1	G2	G3	G4	G5	G6	G7
Path 1 + Path 4	190.4	232.3	258.5	276.9	290.6	279.9	265.3
Path 2 + Path 4	192.9	244.2	271.8	290.3	288.8	268.8	228.3
Path 3 + Path 4	195.7	256.6	285.2	305.0	285.2	256.6	195.7
Note: G = girder, paths indicate transverse loading positions as shown, moments have kip-ft units							

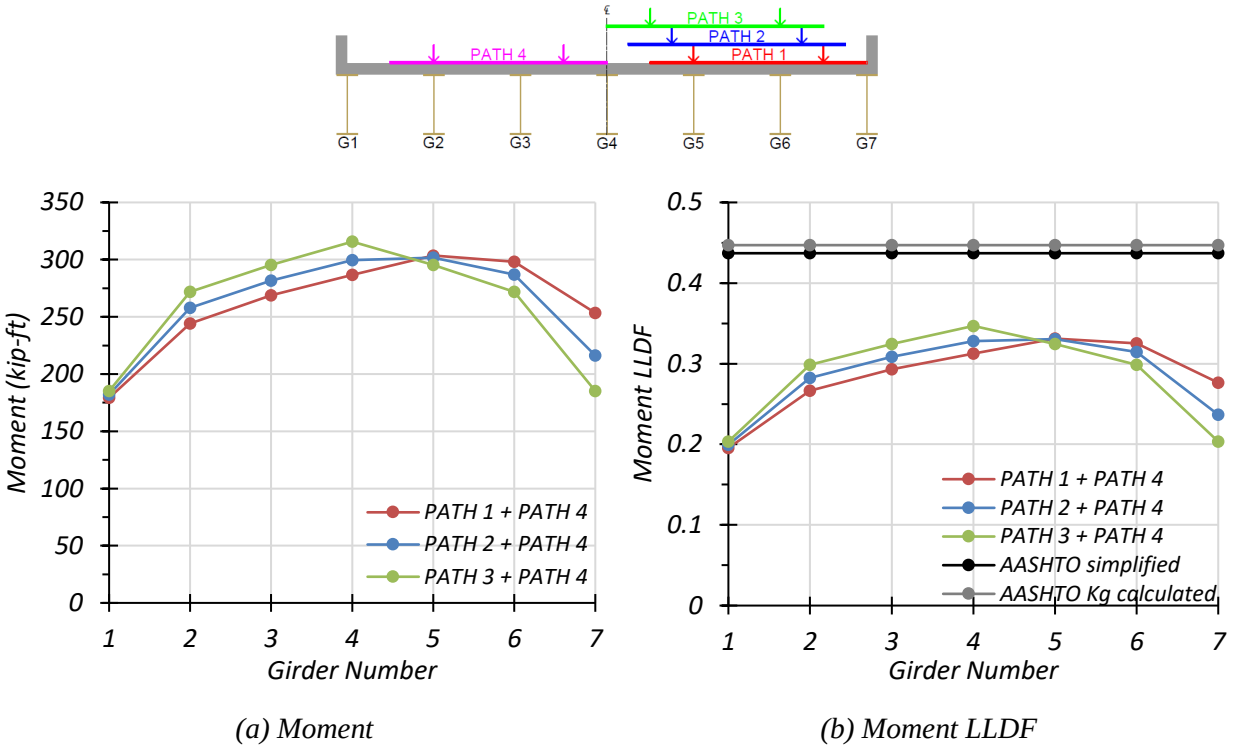

(a) Moment *(b) Moment LLDF*

Figure 2.56. Moment Results for Composite Bridge SM-21 with Two-Lane HL-93 Loading

Table 2.59. Maximum Moments for Composite Bridge SM-21 with Two-Lane HL-93 Loading

Loading	G1	G2	G3	G4	G5	G6	G7
Path 1 + Path 4	179.2	244.2	268.7	286.6	303.6	298.1	253.5
Path 2 + Path 4	182.1	257.8	281.7	299.5	301.7	287.0	216.2
Path 3 + Path 4	185.2	271.9	295.3	315.7	295.3	271.9	185.2
Note: G = girder, paths indicate transverse loading positions as shown, moments have kip-ft units							

Comparison of governing moment LLDF values computed from FEM results for the composite and non-composite cases reveals that the maximum moment LLDF in an interior girder for the composite bridge is almost the same as the one for the non-composite bridge, with a $g^m_{composite}/g^m_{non-composite}$ ratio of 1.01. However, the maximum moment LLDF in an exterior girder for the composite bridge is lower than the one for the non-composite bridge, with a $g^m_{composite}/g^m_{non-composite}$ ratio of 0.96.

Table 2.60. Governing Moment LLDFs for Bridge SM-21 with Two-Lane HL-93 Loading

Type	Girder Location	AASHTO Simplified ($g^m_{AASHTO\_S}$)	AASHTO K_g Calculated ($g^m_{AASHTO\_K}$)	FEM (g^m_{FEM})	$g^m_{AASHTO\_S}/g^m_{FEM}$	$g^m_{AASHTO\_K}/g^m_{FEM}$
Non-Composite	Interior	0.437	0.447	0.343	1.27	1.30
	Exterior	0.437	0.447	0.296	1.48	1.51
Composite	Interior	0.437	0.447	0.347	1.26	1.29
	Exterior	0.437	0.447	0.277	1.58	1.61

*2.7.3.3 **Shear Results***

One-Lane Loading. Figure 2.57 shows the individual girder shears and shear LLDF results for the non-composite Bridge SM-5 under simulated moving HL-93 loading along three one-lane loading paths. Table 2.61 provides the corresponding maximum shear values of each girder for each loading path. The shear LLDF values are calculated using the estimated shear results from the FEM analysis. Table 2.63 shows the governing shear LLDFs found using the FEM analysis and compares them to the AASHTO LLDF values. Compared to the FEM results, the governing shear LLDF value computed using the approximate equations in *AASHTO LRFD Specifications* (AASHTO 2017) is quite conservative for both interior and exterior girders, with a g^v_{AASHTO}/g^v_{FEM} ratio of 1.57 and 1.68, respectively.

Figure 2.58 shows the individual girder shears and shear LLDF results for the fully composite Bridge SM-21 under simulated moving HL-93 loading along three one-lane loading paths. Table 2.62 provides the corresponding maximum shear values of each girder for each loading path. The shear LLDF values are calculated using the estimated shear results from the FEM analysis. Compared to the FEM results, the governing shear LLDF value computed using the approximate equations in *AASHTO LRFD Specifications* (AASHTO 2017) is quite conservative for both interior and exterior girders, with a g^v_{AASHTO}/g^v_{FEM} ratio of 1.43 and 1.69, respectively.

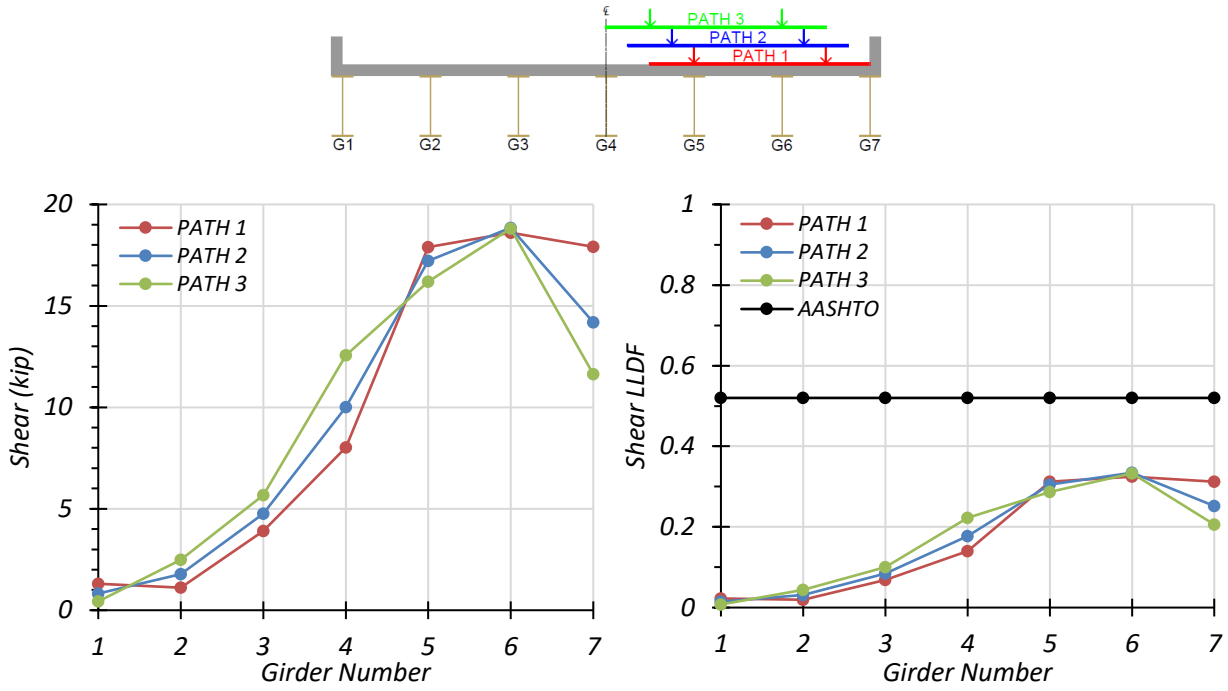

(a) Shear *(b) Shear LLDF*

Figure 2.57. Shear Results for Non-Composite Bridge SM-21 with One-Lane HL-93 Loading

Table 2.61. Maximum Shears for Non-Composite Bridge SM-21 with One-Lane HL-93 Loading

Loading	G1	G2	G3	G4	G5	G6	G7
Path 1	1.9	1.1	3.9	8.0	17.9	18.6	17.9
Path 2	0.8	2.5	5.7	12.6	16.2	18.8	11.6
Path 3	1.4	1.8	4.8	10.0	17.2	18.9	14.2
Note: G = girder, paths indicate transverse loading positions as shown, shears have kip units							

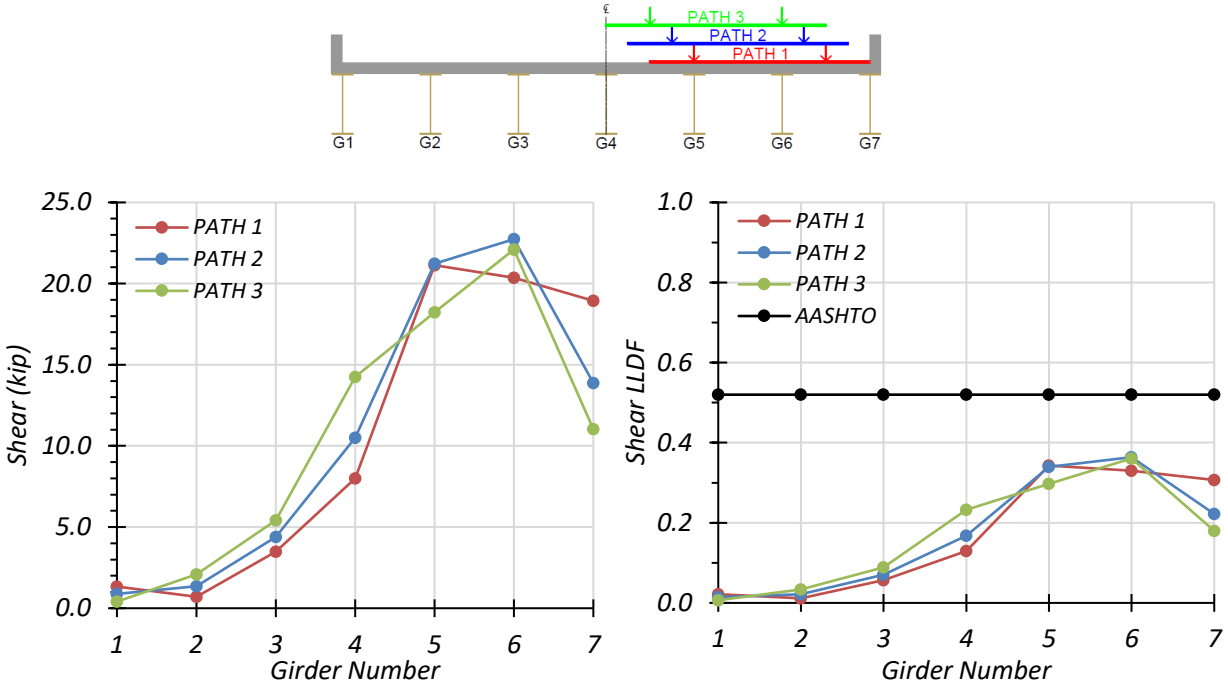

(a) Shear *(b) Shear LLDF*

Figure 2.58. Shear Results for Composite Bridge SM-21 with One-Lane HL-93 Loading

Table 2.62. Maximum Shears for Composite Bridge SM-21 with One-Lane HL-93 Loading

Loading	G1	G2	G3	G4	G5	G6	G7
Path 1	1.3	0.7	3.5	8.0	21.1	20.4	18.9
Path 2	0.9	1.4	4.4	10.5	21.2	22.7	13.9
Path 3	0.4	2.1	5.4	14.2	18.2	22.1	11.0
Note: G = girder, paths indicate transverse loading positions as shown, shears have kip units							

Comparison of governing shear LLDF values computed from FEM results for the composite and non-composite cases reveals that the maximum shear LLDF in an interior girder for the composite bridge is higher than the one for the non-composite bridge, with a $g^v_{composite}/g^v_{non-composite}$ ratio of 1.10. However, the maximum shear LLDF in an exterior girder for the composite bridge is almost the same as the one for the non-composite bridge, with a $g^v_{composite}/g^v_{non-composite}$ ratio of 0.99.

Table 2.63. Governing Shear LLDFs for Bridge SM-21 with One-Lane HL-93 Loading

Type	Girder Location	AASHTO (g^v_{AASHTO})	FEM (g^v_{FEM})	g^v_{AASHTO}/g^v_{FEM}
Non-Composite	Interior	0.520	0.332	1.57
	Exterior	0.520	0.310	1.68
Composite	Interior	0.520	0.364	1.43
	Exterior	0.520	0.307	1.69

Two-Lane Loading. The same procedure was conducted for two-lane loading. Figure 2.59 shows the individual girder shears and shear LLDF results for the non-composite Bridge SM-21 under simulated moving HL-93 loading along three two-lane loading paths. Table 2.64 provides the corresponding maximum shear values of each girder for each loading path. The shear LLDF values are calculated using the estimated shear results from the FEM analysis. Table 2.66 shows the governing shear LLDFs found using the FEM analysis and compares them to the AASHTO LLDF values. Compared to the FEM results, the governing shear LLDF value computed using the approximate equations in *AASHTO LRFD Specifications* (AASHTO 2017) is quite conservative for both interior and exterior girders, with a g^v_{AASHTO}/g^v_{FEM} ratio of 1.39 and 1.95, respectively.

Figure 2.60 shows the individual girder shears and shear LLDF results for the fully composite Bridge SM-21 under simulated moving HL-93 loading along three one-lane loading paths. Table 2.65 provides the corresponding maximum shear values of each girder for each loading path. The shear LLDF values are calculated using the estimated shear results from the FEM analysis. Compared to the FEM results, the governing shear LLDF value computed using the approximate equations in *AASHTO LRFD Specifications* (AASHTO 2017) is quite conservative for both interior and exterior girders, with a g^v_{AASHTO}/g^v_{FEM} ratio of 1.33 and 2.01, respectively.

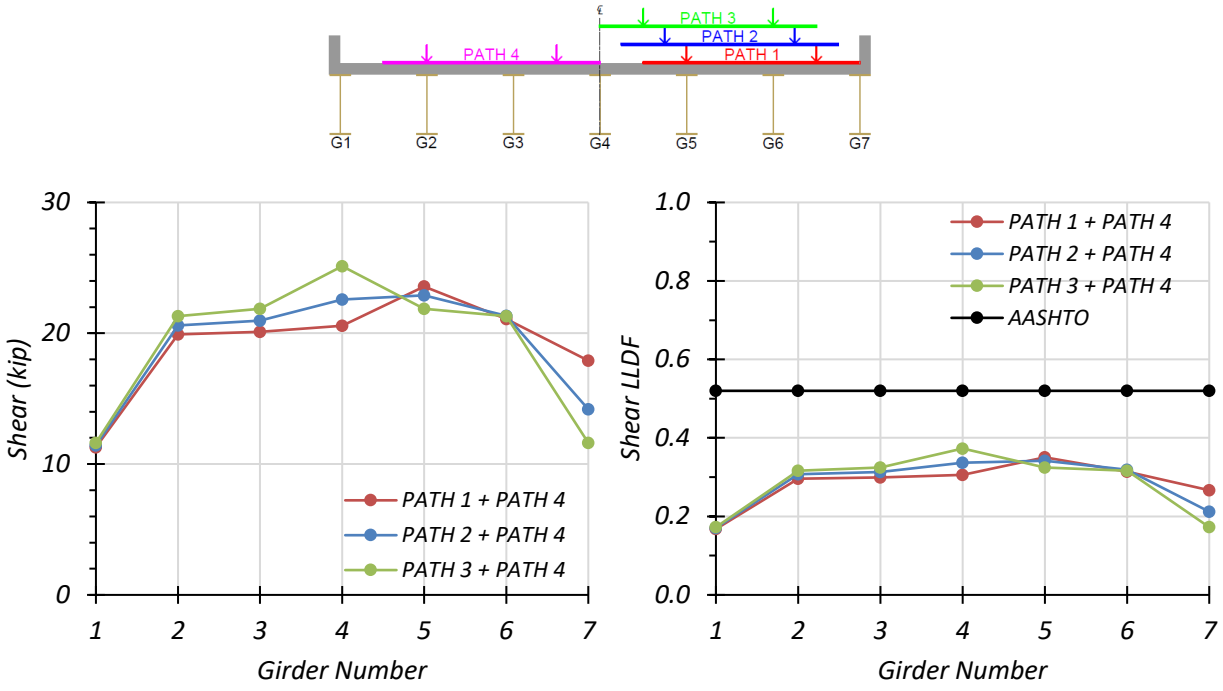

(a) Shear *(b) Shear LLDF*

Figure 2.59. Shear Results for Non-Composite Bridge SM-21 with Two-Lane HL-93 Loading

Table 2.64. Maximum Shears for Non-Composite Bridge SM-21 with Two-Lane HL-93 Loading

Loading	G1	G2	G3	G4	G5	G6	G7
Path 1 + Path 4	11.3	19.9	20.1	20.6	23.6	21.1	17.9
Path 2 + Path 4	11.4	20.6	21.0	22.6	22.9	21.3	14.2
Path 3 + Path 4	11.6	21.3	21.9	25.1	21.9	21.3	11.6
Note: G = girder, paths indicate transverse loading positions as shown, shears have kip units							

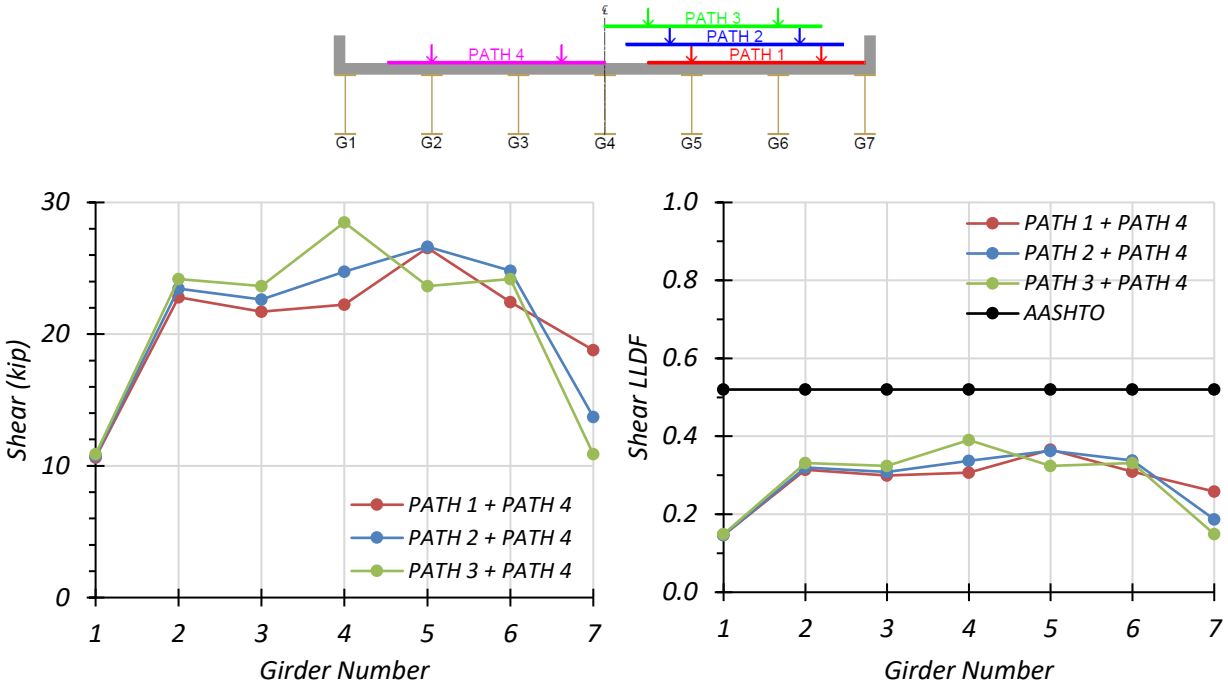

(a) Shear *(b) Shear LLDF*

Figure 2.60. Shear Results for Composite Bridge SM-21 with Two-Lane HL-93 Loading

Table 2.65. Maximum Shears for Composite Bridge SM-21 with Two-Lane HL-93 Loading

Loading	G1	G2	G3	G4	G5	G6	G7
Path 1 + Path 4	10.6	22.8	21.7	22.2	26.6	22.4	18.8
Path 2 + Path 4	10.8	23.5	22.6	24.7	26.6	24.8	13.7
Path 3 + Path 4	10.9	24.2	23.6	28.5	23.6	24.2	10.9
Note: G = girder, paths indicate transverse loading positions as shown, shears have kip units							

Comparison of governing shear LLDF values computed from FEM results for the composite and non-composite cases reveals that the maximum shear LLDF in an interior girder for the composite bridge is higher than the one for the non-composite bridge, with a $g^v_{composite}/g^v_{non-composite}$ ratio of 1.05. However, the maximum shear LLDF in an exterior girder for the composite bridge is slightly lower than the one for the non-composite bridge, with a $g^v_{composite}/g^v_{non-composite}$ ratio of 0.97.

Table 2.66. Governing Shear LLDFs for Bridge SM-21 with Two-Lane HL-93 Loading

Type	Girder Location	AASHTO (g^v_{AASHTO})	FEM (g^v_{FEM})	g^v_{AASHTO}/g^v_{FEM}
Non-Composite	Interior	0.520	0.373	1.39
	Exterior	0.520	0.266	1.95
Composite	Interior	0.520	0.390	1.33
	Exterior	0.520	0.259	2.01

2.8 CONCLUSIONS

2.8.1 Live Load Distribution Factors

2.8.1.1 AASHTO Standard Specifications LLDFs

The FEM analysis of the selected simple-span steel multi-girder bridges has shown that, in general, the current LLDF equations given in the *AASHTO Standard Specifications* (AASHTO 2002) provide accurate, slightly conservative LLDF values in flexure for the selected bridges. The g_{AASHTO}/g_{FEM} ratio for flexure ranges from 0.80 to 1.34; however, in most cases it is slightly above 1.0. This result will likely not significantly affect the rating of this bridge type.

Meanwhile, for the shear LLDF values obtained from the FEM analysis, the g_{AASHTO}/g_{FEM} ratio for shear ranges from 0.59 to 1.44, producing a larger variation in results. In order to better capture the wide range, the shear LLDFs could be changed; however, the shear RFs for the larger group of selected bridges are already quite high, as shown in Technical Memorandum 3, and changing the LLDF is not expected to significantly change RFs and corresponding load postings.

2.8.1.2 AASHTO LRFD Specifications LLDFs

The FEM analysis of the selected simple-span steel multi-girder bridges has shown that, in general, the current LLDF equations given in the *AASHTO LRFD Specifications* (AASHTO 2017) provide conservative—with some variability in accuracy—LLDF values in flexure for the selected bridges. The g_{AASHTO}/g_{FEM} ratio for flexure using the simplified stiffness parameter ranges from 1.04 to 1.80, and in every case is above 1.0. The g_{AASHTO}/g_{FEM} ratio for flexure using the calculated stiffness parameter ranges from 1.05 to 1.61, and in every case is above 1.0. These LLDFs are

accurate and only slightly conservative for one-lane loaded cases. However, for two-lane loaded cases they are significantly conservative. Using more accurate LLDFs for two-lane HL-93 loading cases would likely help increase load and resistance factor ratings (LRFRs).

For the shear LLDF values obtained from the FEM analysis, the g_{AASHTO}/g_{FEM} ratio for shear ranges from 1.31 to 3.24, again producing very conservative results. As with the LRFD flexure LLDFs, the shear LLDFs could be modified in order to improve the LRFR shear RFs of bridges.

2.8.2 Composite Action

Regarding the effect of analyzing the bridge as fully composite or fully non-composite on the LLDFs, the FEM analysis did not find a significant difference. For the most part, the LLDFs were very similar; however, the non-composite bridge seemed to produce more uniform LLDF profiles across the bridge transverse section.

An examination of HS-20 loading showed the $g_{composite}/g_{non-composite}$ ratio for flexure ranged from 0.92 to 1.12, and the $g_{composite}/g_{non-composite}$ ratio for shear ranged from 0.86 to 1.28. The $g_{composite}/g_{non-composite}$ ratio for an interior girder was always above 1.0, while it was always below 1.0 for an exterior girder except for in one case—the one-lane shear for Bridge SM-21.

For HL-93 loading, the $g_{composite}/g_{non-composite}$ ratio for flexure ranged from 0.93 to 1.12, and the $g_{composite}/g_{non-composite}$ ratio for shear ranged from 0.84 to 1.25. The $g_{composite}/g_{non-composite}$ ratio for an interior girder was always above 1.0, while it was always below 1.0 for an exterior girder except in one case—the one-lane flexure for Bridge SM-21. Between the HS-20 loading and the HL-93 loading, the ratios did not significantly change for the same number of lanes loaded and force being examined.

In terms of LLDFs, composite action does not seem to have a major effect; however, it is known that composite action or partial composite action significantly affects the capacity of the bridge. This effect was noticed in the FEM analysis through the stress values computed for the girders. The effect of partial composite action on load rating will be further explored in the next task, wherein any partial composite measured during field testing will be used to help calibrate the FEM models, which will be used to develop a more refined load rating of the bridge.

2.8.3 End Fixity

During the FEM modeling process, it was noted that end springs to provide partial restraint can be added to the girder supports in the model. If any partial fixity is measured during the field testing to take place during the next task, it will be accounted for in the calibrated model. Partial end fixity would help improve the load rating by reducing the applied positive moment in the span.

2.8.4 Additional Comments

Additional results from the FEM modeling will be used to calibrate the FEM model after field testing is complete. The results presented in this report for deflections and dynamic characteristics will be compared to those found in the field to determine if the girders are acting compositely or non-compositely.

3 ANALYSIS OF A CONTINUOUS STEEL MULTI-GIRDER BRIDGE

In the previous tasks, a detailed review and synthesis of the population of load-posted bridges in Texas was conducted, and 16 continuous steel multi-girder bridges were selected from the inventory of SSLO continuous steel multi-girder bridges in Texas for basic load rating evaluation. This basic load rating analysis helped identify several areas of opportunity for refined load rating analysis. The refined load rating analysis used in this study investigated the effect of the identified parameters using three-dimensional finite element models that can more accurately capture the bridge behavior. The main objectives of FEM analysis of the continuous steel multi-girder bridge can be summarized as follows: (1) create a model of the bridge superstructure that can more accurately predict the live load distribution, (2) investigate the effect of partial composite action on the load distribution behavior of the bridge under service loads, and (3) evaluate the effect of deck cracking over the negative moment region.

3.1 INTRODUCTION

A typical load-posted continuous steel multi-girder (SC) bridge was selected as a representative structure of this type to further investigate the identified objectives. Table 3.1 lists some of the key parameters for the selected continuous steel multi-girder bridge (SC-12) and for the average SSLO continuous steel multi-girder bridge in Texas. In this table, the Operating HS-20 RF represents the multiple of HS-20 truck loads that is the absolute maximum load that can safely travel on the bridge. The posting evaluation represents the degree to which the operating rating of the bridge is below the maximum legal load.

A three-dimensional linear FEM model was developed using the commercial software package CSiBridge (Computers and Structures Inc. 2019), which has the capability to model and analyze complex bridge superstructures while also providing user-friendly pre- and postprocessing tools for bridge structures. The following sections provide the geometric and material properties of the selected continuous steel multi-girder bridge, describe the FEM modeling approach, and summarize the analysis results.

Table 3.1. Selected SSLO SC Bridge and Average Characteristics

ID	Route Prefix	Year Built	ADT	Max. Span Length (ft)	Deck Width (ft)	Condition Rating			Operating HS-20 Rating Factor	Posting Eval.
						Deck	Super-structure	Sub-structure		
Avg.	–	1962	–	25	20	6	6	6	0.85	3
SC-12	3	1959	260	75	26	6	7	7	0.88	4
Route Prefix: 3 = On-System Condition Ratings: 6 = Satisfactory, 7 = Good Posting Evaluation: 3 = 10-19.9% below legal load, 4 = 0.1-9.9% below legal load										

The models were analyzed with HS-20 truck and designated HL-93 load simulations to obtain deflection profiles, modal properties, and moment and shear values. The deflection and modal property analysis were conducted for comparison to the measured behavior of the bridges in the future field tests. The deflection values and modal characteristics allow for calibration of the FEM models based on the field-test results. For the moment and shear analysis, the main bridge characteristics of interest are the LLDFs. The LLDFs found using the FEM model are to be compared to those determined through the field testing and values from the procedures in the *AASHTO Standard Specifications* (AASHTO 2002) and *AASHTO LRFD Specifications* (AASHTO 2017). LLDFs can be calculated as the moment or shear force of an individual girder divided by the sum of moments or shear forces in all of the girders for a one-lane loaded case, as shown in Equation (2.1) in Chapter 2.

3.2 DESCRIPTION OF SELECTED BRIDGE

The selected continuous steel multi-girder bridge to be modeled has a total length of 195 ft consisting of three continuous spans. The center-to-center of bearing span length of the middle span is 75 ft, which controls the load ratings. The length of both end spans is 60 ft. The total width of the bridge is 25 ft 6 in., with a roadway width of 24 ft and a 6 in. thick deck. The girder spacing is 6 ft 8 in., and lateral bracing is provided at quarter points of each span. The steel yield strength and the 28-day concrete compressive strength are taken as 33 ksi and 2.5 ksi, respectively, based on values used for load rating noted in TxDOT's inspection reports (TxDOT 2018a). The bridge carries two lanes, one in each direction, and has an ADT of 260 vehicles. These properties are tabulated in Table 3.2.

Table 3.2. Load Rating Characteristics for SC-12

Characteristic	Measurement
Total Length	195'-0"
Controlling Span Length	75'-0"
Deck Width	25'-6"
Roadway Width	24'-0"
Girder Spacing	6'-8"
Lateral Bracing Spacing	18'-9"
Steel Cross-Section Shape	W30x108
Steel Yield Strength	33 ksi
Deck Thickness	6"
28-day Concrete Compressive Strength	2.5 ksi
Number of Lanes	2

Bridge SC-12 has a deck condition rating of 6 (Satisfactory), a superstructure condition rating of 7 (Good) without beam section loss due to corrosion, and a substructure condition rating of 7 (Good). The girder flexure controls the rating of the bridge, which has an inventory gross loading of 19 US tons and an operating gross loading of 32 US tons. Table 3.3 shows the posted loads of Bridge SC-12 for different axle and vehicle configurations. Figure 3.1 shows an elevation view of Bridge SC-12 and a view of the underside of the superstructure. Figure 3.2 shows transverse section details of Bridge SC-12.

Table 3.3. Bridge SC-12 Postings

Configuration	Posting (lbs)
Single Axle	20,000
Tandem Axle	34,000
Single Vehicle	58,000
Combination Vehicle	75,000

(a) Elevation view

(b) Underside view

Figure 3.1. Photographs of Bridge SC-12 (TxDOT 2018a)

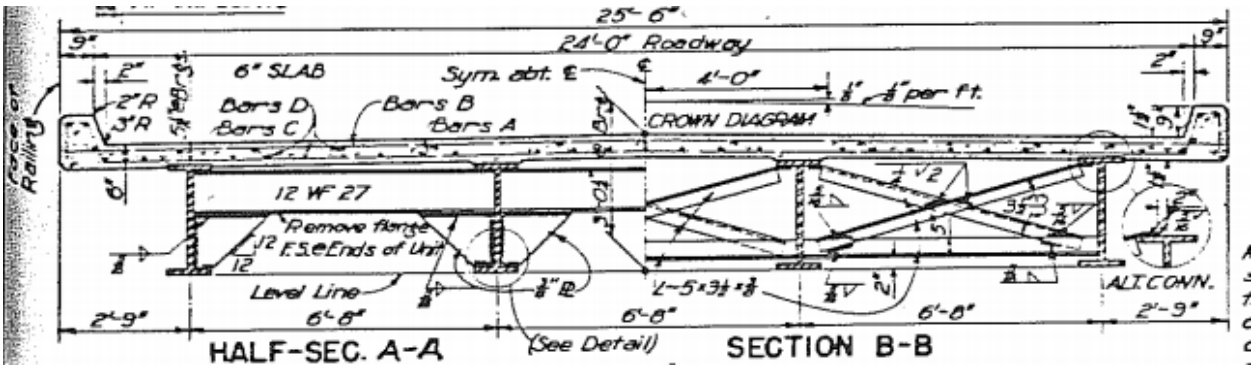

Figure 3.2. Bridge SC-12 Transverse Section (TxDOT 2018a)

3.3 FEM MODEL DEVELOPMENT

A three-dimensional linear FEM model of the selected continuous steel multi-girder bridge, SC-12, was developed using the commercial CSiBridge software (Computers and Structures Inc. 2019). The geometry of the bridge was modeled based on information provided in the design drawings and inspection reports. The geometric information relevant to the development of the FEM model was presented in the previous section of this chapter. The following subsection describes the FEM modeling approach, finite element types, and material properties. The next subsection describes the selection of mesh size. The last subsection provides details about boundary conditions, which are critical for accurately capturing the behavior of the bridge.

3.3.1 Bridge Model Description

The superstructure of a slab-on-girder bridge can be modeled using a variety of finite element types, most of which are available in the CSiBridge software. A significant amount of information exists in the literature that provides guidelines for developing FEM models for slab-on-girder steel bridges (Barnard et al. 2010; Hurlebaus et al. 2018; Puckett et al. 2011) Based on the recommendations provided in the literature and engineering judgement, the FEM models of the selected SC bridge were developed using a combination of four-node linear quadrilateral shell elements and two-node linear beam elements (frame elements). The superstructure of the selected SC bridge consists of steel I-girders and a reinforced concrete deck. The reinforced concrete deck was modeled using four-node linear shell elements. Table 3.4 shows the relevant material properties for the steel girders and concrete deck used in the FEM models of the bridge, which

match the material strength values noted in the TxDOT load rating calculations. Deck reinforcement is not modeled because the linear elastic model will be analyzed under service level loads only, and the superstructure is expected to remain in the linear elastic range. The steel girder webs were also modeled using four-node linear shell elements. Top and bottom flanges of the steel girders and the diaphragms were modeled using two-node linear beam/frame elements. Figure 3.3 shows the meshed FEM model of SC-12 with the components of the model labeled. When creating a meshed analytical model, CSiBridge first partitions the deck along the centerlines of the girders and then meshes based on the selected maximum mesh size. The maximum mesh size is 6 in. for the FEM model of Bridge SC-12 shown in Figure 3.3.

The default option for modeling a steel multi-girder bridge with a concrete deck in CSiBridge software considers the deck and girders as fully composite. In order to model non-composite behavior, an edge release was applied to the bottom surface of the concrete deck. This option removes interface shear restraint between the deck and the girders, thereby creating fully non-composite behavior. Bridge SC-12 was modeled and analyzed as fully composite and fully non-composite to allow comparison of the results.

Table 3.4. FEM Model Material Properties

Material	Density (pcf)	Modulus of Elasticity (ksi)	Poisson's Ratio	28-Day Concrete Compressive Strength (ksi)	Steel Yield Strength (ksi)
Steel	490	29,000	0.3	–	33
Concrete	150	2850	0.2	2.5	–

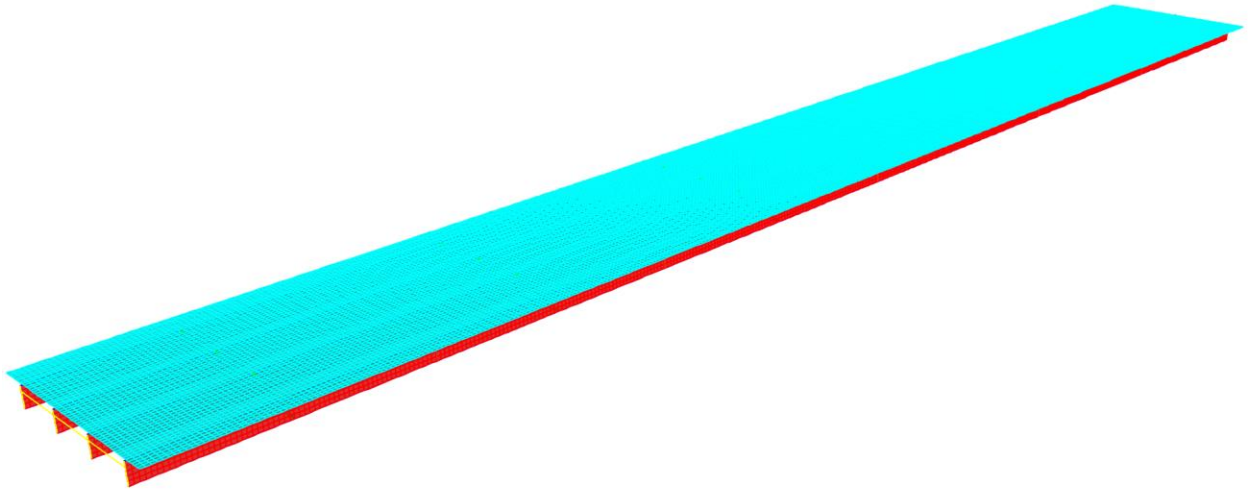

(a) Fully Meshed Superstructure

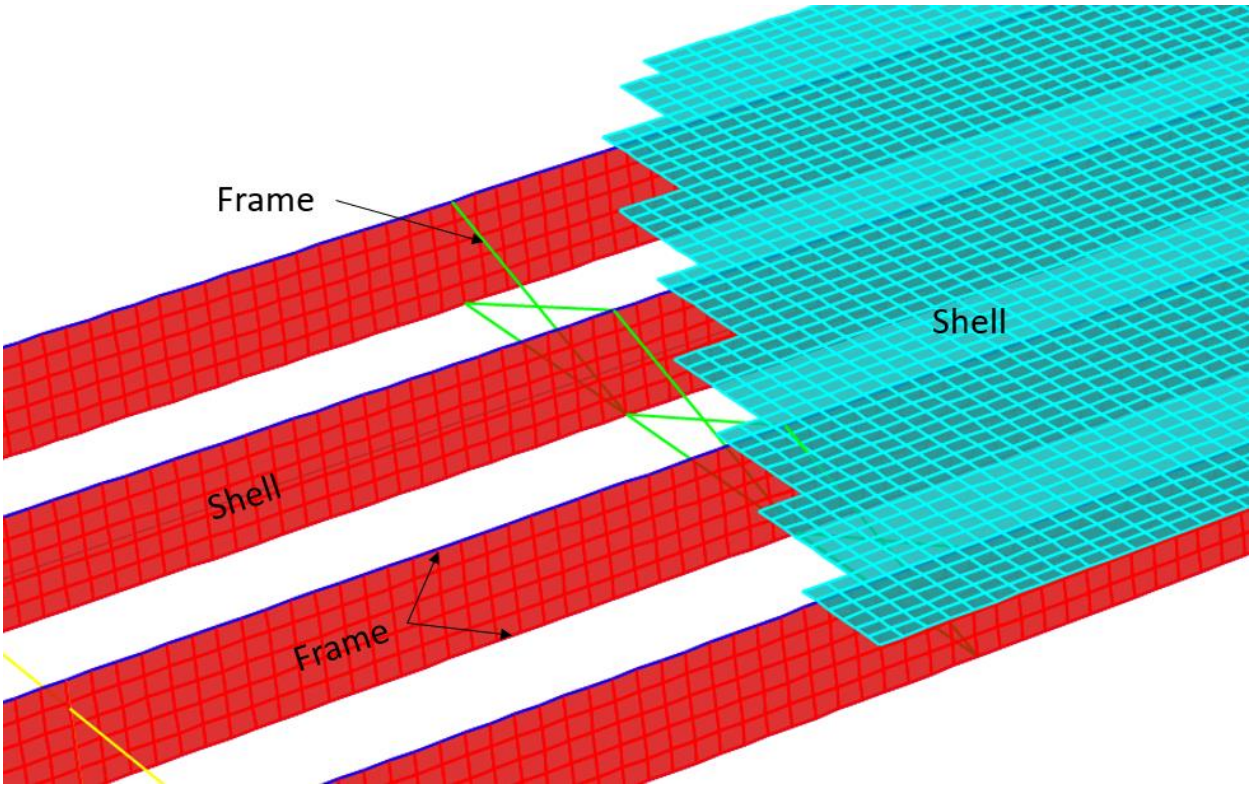

(b) Finite Element Types

Figure 3.3. FEM Model of the SC-12 Bridge (6 in. mesh)

3.3.2 Mesh Sensitivity Analysis

A mesh sensitivity analysis was conducted on the SM bridges and is presented in the first chapter of this report. This analysis found that a 6-in. mesh was the optimal mesh size to use. A mesh sensitivity analysis for Bridge SC-12 was not expected to produce different results from the previous analysis performed for the SM bridges. Therefore, a mesh size of 6 in. was chosen for the FEM analysis of Bridge SC-12.

3.3.3 Boundary Conditions

In the absence of more accurate information, the boundary conditions at the supports are defined as pins and rollers. The boundary conditions for Bridge SC-12 were modeled to represent a three-span continuous condition. Roller supports were used under the girders for all exterior and interior supports except for one exterior support on one girder, which was modeled as a pin support. A roller support releases all three rotational degrees of freedom as well as two translational degrees of freedom in the horizontal plane (two orthogonal in-plane directions parallel to the bridge superstructure) and fully restrains the translational degree of freedom in the vertical direction (perpendicular to the plane of the bridge superstructure). Only one girder was pinned at one end in order to resist any horizontal forces that develop. A pin support releases all three rotational degrees of freedom and restrains all three translational degrees of freedom.

Accurately modeling the boundary conditions has significant effect on the overall behavior of the bridge. Although the boundary conditions are initially modeled as simply supported, the restraint of the supports will be evaluated based on field-test results during the next phase of this project. Unintended partial fixity may develop at the end supports due to the bearing detail at the supports and/or friction between the bottom surface of the bridge girders and the bearing surface. Thus, the presence of partial fixity will be verified through field testing.

3.4 BASIC VERIFICATION OF FEM MODELS

The three-span continuous FEM model of Bridge SC-12 was verified through a comparison with a single beam analysis conducted in RISA 3D software (RISA Tech Inc 2016). The bridge was modeled as a single beam in RISA 3D, with three spans and continuous over the interior supports. For verification of HS-20 loading, the HS-20 truck configuration was moved along the beam using static step loading at 6 in. increments. A similar loading approach was used for HL-93 loading verification, with the addition of the lane load onto the appropriate spans to obtain the maximum

moment and shear reactions. To obtain maximum moment and shear, the lane load was applied to the center span, while for the negative moment the HS-20 truck train was used, and the lane load was applied to the center span and one adjacent span. When using the truck train, both the trucks and lane load were multiplied by a factor of 0.9, per the *AASHTO LRFD Specifications* (AASHTO 2017).

3.4.1 Verification of Absolute Maximum Moment

Table 3.5 shows the live load moments calculated using the RISA verification model, the FEM calculated moments, and the percent difference between them. The FEM live load moments match up very closely to the expected live load moments obtained from RISA.

Table 3.5. Comparison of Live Load Moment on Composite Section for Bridge SC-12

Bridge ID	Positive/ Negative Moment	Applied Load	FEM One-Lane Moment on Total Section (kip-ft)	Expected One-Lane Moment on Total Section (kip-ft)	Percent Difference
SC-12	Positive	HS-20	658.7	664.0	0.8
	Positive	HL-93	901.7	909.2	0.8
SC-12	Negative	HS-20	441.3	438.3	0.7
	Negative	HL-93	892.6	887.6	0.6
Note: All calculated moments are without the application of the impact factor.					

3.4.2 Verification of Shear Forces

The maximum shear force was also verified to ensure that the load models were developed correctly. The FEM models use step-by-step loading for the moving load analysis. The step size of the moving load was adjusted such that the first step with the rear axle of the vehicle on the bridge placed the rear axle 3 ft away from the support, which is equivalent to one member depth. The resulting shear forces at 3 ft away from the support were obtained from the FEM model. These forces were compared with the shear forces found using RISA by placing the rear axle 3 ft away from the support. Table 3.6 shows the live load shears calculated using the RISA verification model, the FEM calculated shears, and the percent difference between them. The FEM live load shears match very closely to the expected live load shears.

Table 3.6. Comparison of Live Load Shear Forces on Composite Section for Bridge SC-12

Bridge ID	Applied Load	FEM One-Lane Shear on Total Section (kips)	Expected One-Lane Shear on Total Section (kips)	Percent Difference
SC-12	HS-20	61.9	61.8	0.2
	HL-93	85.6	85.7	0.1
Note: All calculated shears are without the application of the impact factor.				

3.5 SIMULATING VEHICLE LOADS

3.5.1 Simulating HS-20 Truck Loading

The HS-20 truck loads were placed transversely on the SC bridge per the *AASHTO Standard Specifications* (AASHTO 2002). Bridge SC-12 is a two-lane bridge with a lane width of 12 ft. For a one-lane-loaded case based on the *AASHTO Standard Specifications*, the truck was first placed so that the exterior wheel line was 2 ft away from the edge of the barrier. For each separate load case, the truck was moved transversely 1 ft toward the centerline of the bridge. For the third and final load case, the interior wheel line was placed 2 ft away from the interior edge of the lane. This process created three different one-lane-loaded cases, shown in Figure 3.4(a): one with the exterior wheel line 2 ft from the barrier (Path 1), one with the exterior wheel line 3 ft from the barrier (Path 2), and one with the exterior wheel line 4 ft from the barrier (Path 3).

For the two-lane-loaded case, the first truck was positioned in the same way as for each one-lane-loaded case. A second truck was placed in the second lane of the bridge with the interior wheel line 2 ft away from the interior edge of the lane for each load case. This created three separate two-lane-loaded cases: Path 1 + Path 4, Path 2 + Path 4, and Path 3 + Path 4, as shown in Figure 3.4(b).

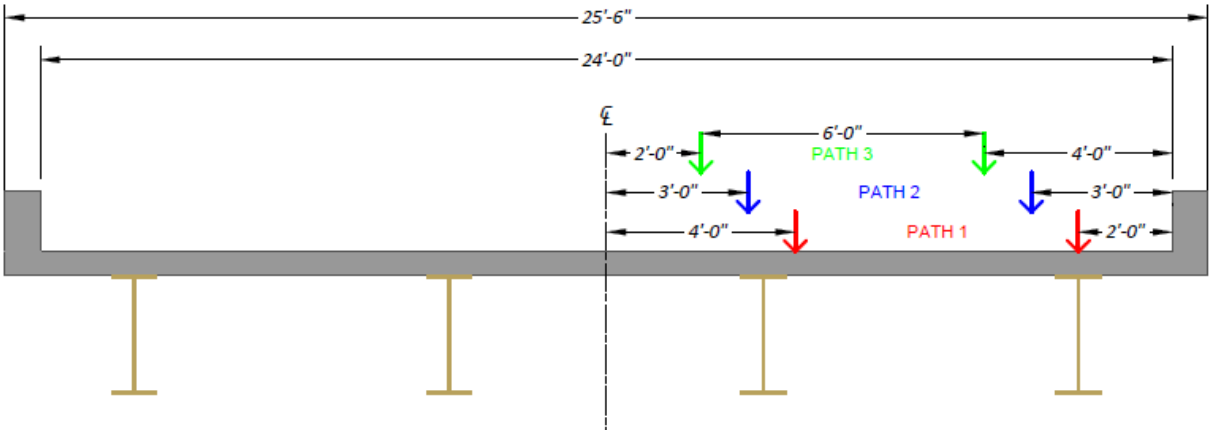

(a) One-Lane Loading Paths

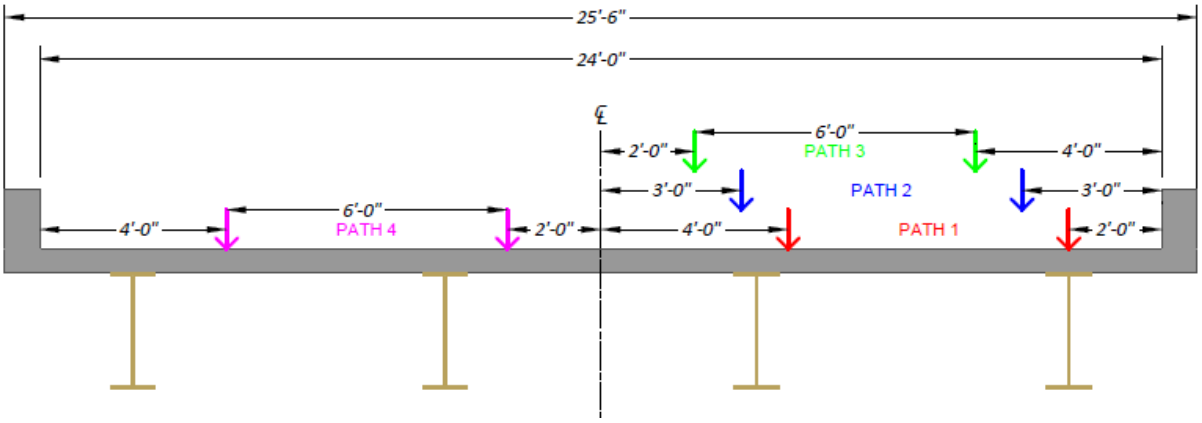

(b) Two-Lane Loading Paths

Figure 3.4. HS-20 Loading Cases for Bridge SC-12

3.5.2 Simulating HL-93 Loading

The HL-93 load model was also placed at different transverse locations on the SC bridge per the *AASHTO LRFD Specifications* (AASHTO 2017). It has a lane width of 12 ft and a maximum span length in the center span of approximately 75 ft. Since the truck load configuration controls for spans longer than 40 ft 6 in., the truck plus lane load was used for the HL-93 loading of Bridge SC-12. The design truck was placed transversely in the same manner as described for the HS-20 load. The lane load was added so that the exterior edge of the lane load in Path 1 was against the railing of the bridge. The exterior edge of the lane load in Path 2 was placed 1 ft away from the railing, and the interior edge of the lane load in Path 3 was placed against the interior edge of the

lane. A total of three different one-lane-loaded cases were created in the first lane, as shown in Figure 3.5(a): (1) one with the exterior wheel line of the truck 2 ft from the railing and the exterior edge of the lane load immediately adjacent to the railing (Path 1), (2) one with the exterior wheel line of the truck 3 ft from the railing and the exterior edge of the lane load 1 ft away from the railing (Path 2), and (3) one with the exterior wheel line of the truck 4 ft from the railing and the interior edge of the lane load immediately adjacent to the interior edge of the lane (Path 3).

For a two-lane-loaded case, the tandem and lane loads were positioned in the same way as for each one-lane-loaded case. A second truck was placed in the second lane of the bridge with the interior wheel line 2 ft away from the interior edge of the lane for each load case. A second lane load was placed with its right edge against the interior edge of the lane in the second lane. This created three separate two-lane-loaded cases for the bridge: Path 1 + Path 4, Path 2 + Path 4, and Path 3 + Path 4, as shown in Figure 3.5(b).

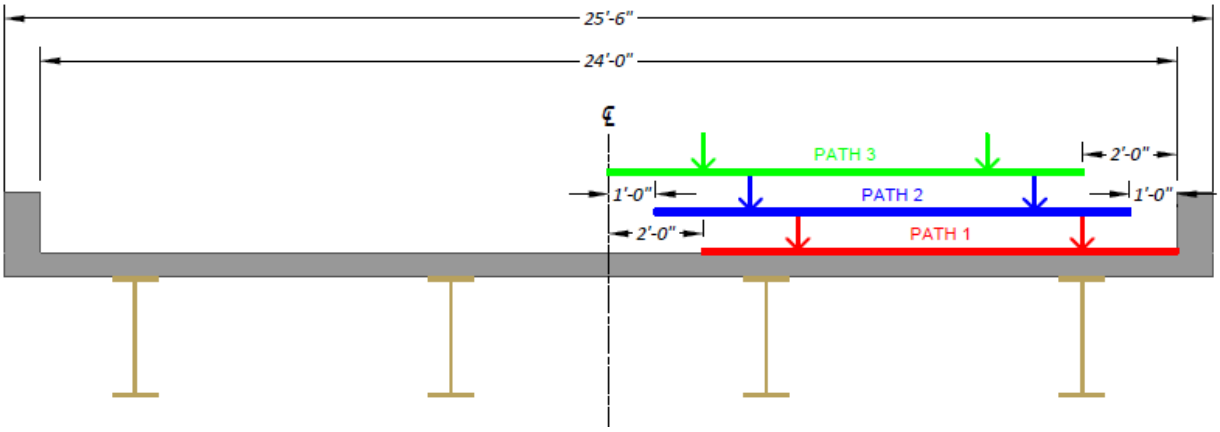

(a) One-Lane Loading Paths

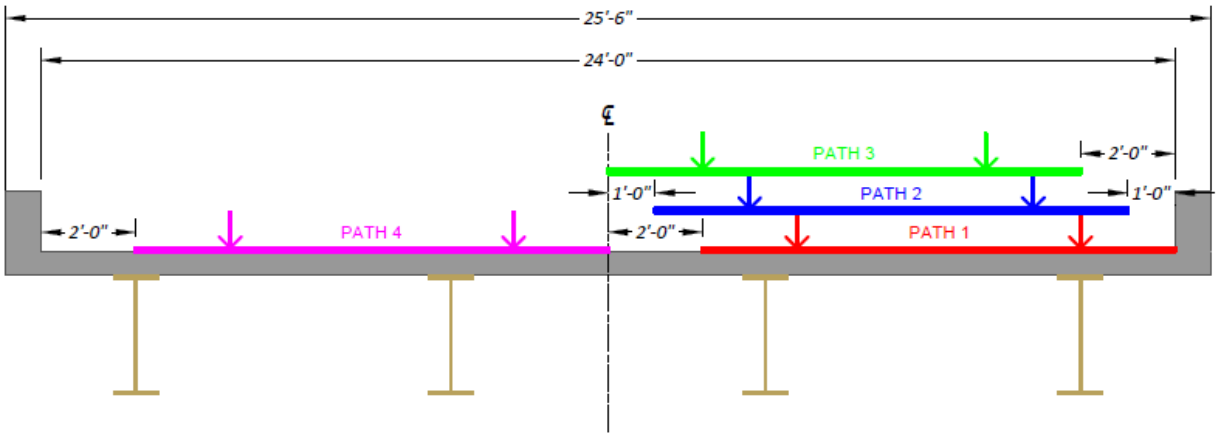

(b) Two-Lane Loading Paths

Figure 3.5. HL-93 Loading Cases for Bridge SC-12

3.6 FEM RESULTS FOR BRIDGE SC-12

Bridge SC-12 was analyzed using the CSiBridge software under the loading scenarios provided in Figure 3.4 and Figure 3.5. Girder displacement profiles were obtained for the load cases that represent the field load testing plans. Modal analyses were conducted for both composite and non-composite conditions to determine estimated modal frequencies and mode shapes. Live load moment and shear values were also extracted and analyzed to compare the expected LLDFs with the LLDFs prescribed in the *AASHTO Standard Specifications* (AASHTO 2002) and the *AASHTO LRFD Specifications* (AASHTO 2017).

The *AASHTO Standard Specifications* (AASHTO 2002) Article 3.23.2.3.1.4 states, "In no case shall an exterior stringer have less carrying capacity than an interior stringer." The *AASHTO LRFD Specifications* (AASHTO 2017) Article 2.5.2.7.1 states, "Unless future widening is virtually inconceivable, the load carrying capacity of exterior beams shall not be less than the load carrying capacity of an interior beam." In most cases for Bridge SC-12, the moment LLDF determined through the *AASHTO Standard Specifications* and *AASHTO LRFD Specifications* for the exterior girder is smaller than the moment LLDF for the interior girder. Therefore, interior girder moment LLDFs were used when calculating the exterior girder moment demands.

It is also important to note that for calculation of the negative moment LLDFs, Table 4.6.2.2.1-2 in the *AASHTO LRFD Specifications* (AASHTO 2017) prescribes the use of the average length of the two adjacent spans over the support of interest to be used as the variable *L* in the LLDF equations.

3.6.1 Modal Properties

The first two modes of the Bridge SC-12 were identified as the first longitudinal bending mode and the first torsional mode. The frequencies of the longitudinal and torsional modes for the non-composite bridge were determined to be 2.31 Hz and 2.72 Hz, respectively. Figure 3.6(a) shows the amplitude contours of the first longitudinal bending mode shape for half of the bridge length and the normalized amplitudes along the span for the non-composite condition. Figure 3.6(b) shows the amplitude contours for the first torsional mode shape for half of the bridge length and the normalized amplitudes transverse to the center span for the non-composite condition.

The frequencies of the first longitudinal bending and the first torsional modes of the composite bridge were determined to be 3.23 Hz and 3.41 Hz, respectively. Figure 3.7(a) shows the amplitude contours of the first longitudinal bending mode shape for half of the bridge and the normalized amplitudes along the span for the composite condition. Figure 3.7(b) shows the amplitude contours resulting from the first torsional mode for half of the bridge and the normalized amplitudes transverse to the center span for composite analysis.

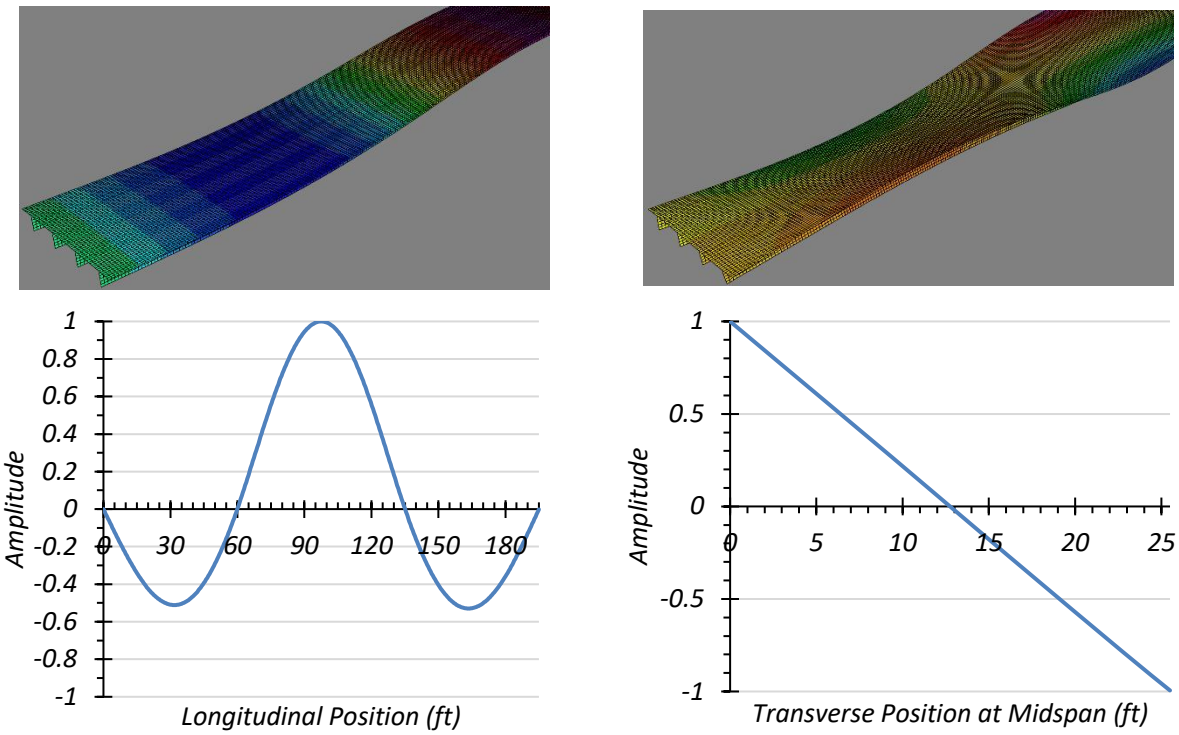

(a) Longitudinal bending Mode (f=2.31 Hz) *(b) Torsional Mode (f=2.72 Hz)*

Figure 3.6. First Two Mode Shapes of Non-Composite Bridge SC-12

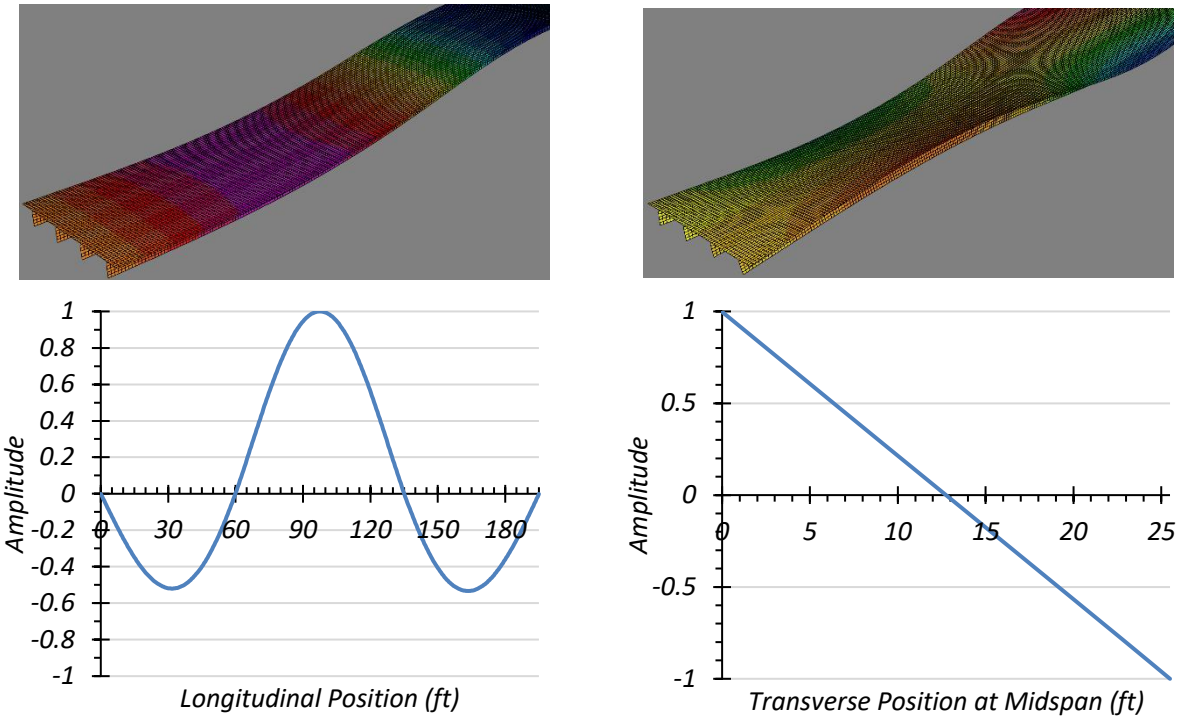

(a) Longitudinal bending Mode (f=3.23 Hz) *(b) Torsional Mode (f=3.41 Hz)*

Figure 3.7. First Two Mode Shapes of Composite Bridge SC-12

3.6.2 HS-20 Live Load Analysis

Bridge SC-12 was first analyzed using the HS-20 design truck presented in the *AASHTO Standard Specifications* (AASHTO 2002). The bridge was analyzed for one-lane- and two-lane-loaded cases along four transverse paths, as shown in Figure 3.4. Deflection, moment, and shear results were obtained.

*3.6.2.1 **Deflection Results***

Figure 3.8 shows the estimated girder deflection profile envelopes for the full length of the bridge and contours of the half length of the bridge for one-lane HS-20 loading along Path 1 and Path 4 when the bridge is analyzed as fully non-composite. Table 3.7 shows the corresponding positive (downward) and negative (upward) deflections for each girder, assuming non-composite action. Load Paths 1 and 4 are the only ones shown because they are the load paths planned for later load tests, and were selected to maximize the forces on an interior girder and on an exterior girder.

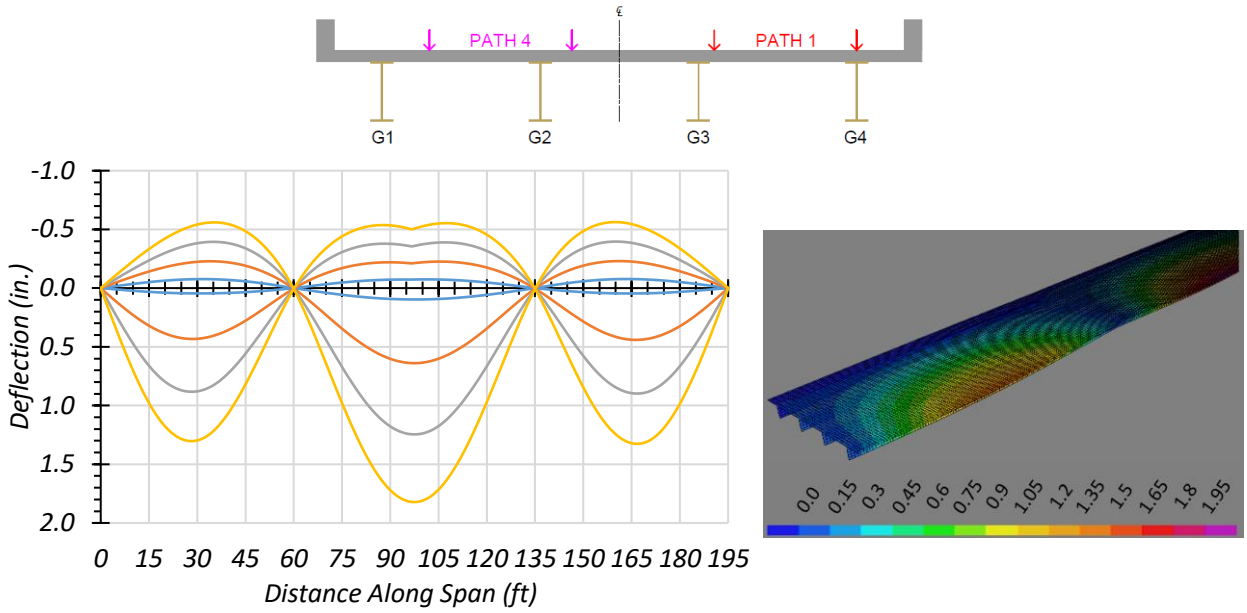

(a) Path 1

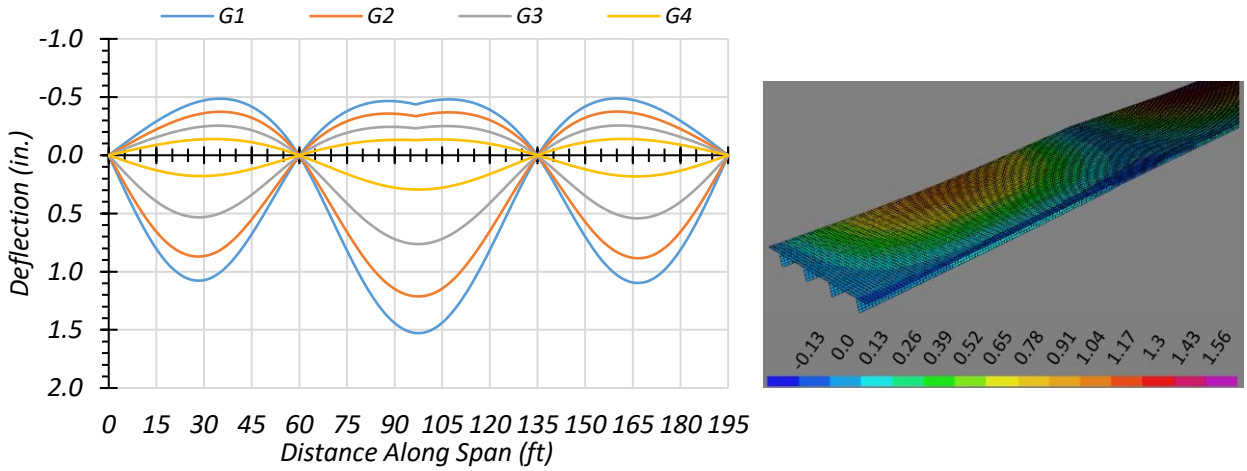

(b) Path 4

Figure 3.8. Deflection Profiles for Non-Composite Bridge SC-12 with HS-20 Loading

Table 3.7. Maximum Deflections for Non-Composite Bridge SC-12 with HS-20 Loading

Loading	Deflection Positive/Negative	G1	G2	G3	G4
Path 1	Positive	0.097	0.639	1.246	1.822
Path 1	Negative	−0.077	−0.230	−0.396	−0.562
Path 4	Positive	1.528	1.212	0.763	0.295
Path 4	Negative	−0.489	−0.375	−0.256	−0.141
Note: G = girder, paths indicate transverse loading positions as shown, deflections have inch units					

Figure 3.9 shows the estimated girder deflection profile envelopes for the full length of the bridge and contours of the half length of the bridge for one-lane HS-20 loading along Path 1 and Path 4 when the bridge is analyzed as fully composite. Table 3.8 shows the corresponding positive (downward) and negative (upward) deflections for each girder, assuming fully composite action. Load Paths 1 and 4 are the only ones shown because they are the load paths planned for later load tests, and were selected to maximize the forces on an interior girder and on an exterior girder.

For both non-composite and composite cases, the maximum negative deflections were obtained in Girder G4 when the HS-20 truck was run along Path 1. The estimated deflections were 1.82 in. and 0.84 in. for the non-composite and composite cases, respectively. This result indicates that the composite bridge is 74 percent stiffer than the non-composite bridge. The maximum deflections were obtained in Girder G1 when the HS-20 truck was run along Path 4 for both the non-composite and composite case. The estimated deflections were 1.53 in. and 0.69 in. for the non-composite and composite cases, respectively. This result indicates that the composite bridge is 76 percent stiffer than the non-composite bridge. The slightly different values of relative stiffness suggest that the relative girder deflection depends on the location of loading and corresponding load distribution.

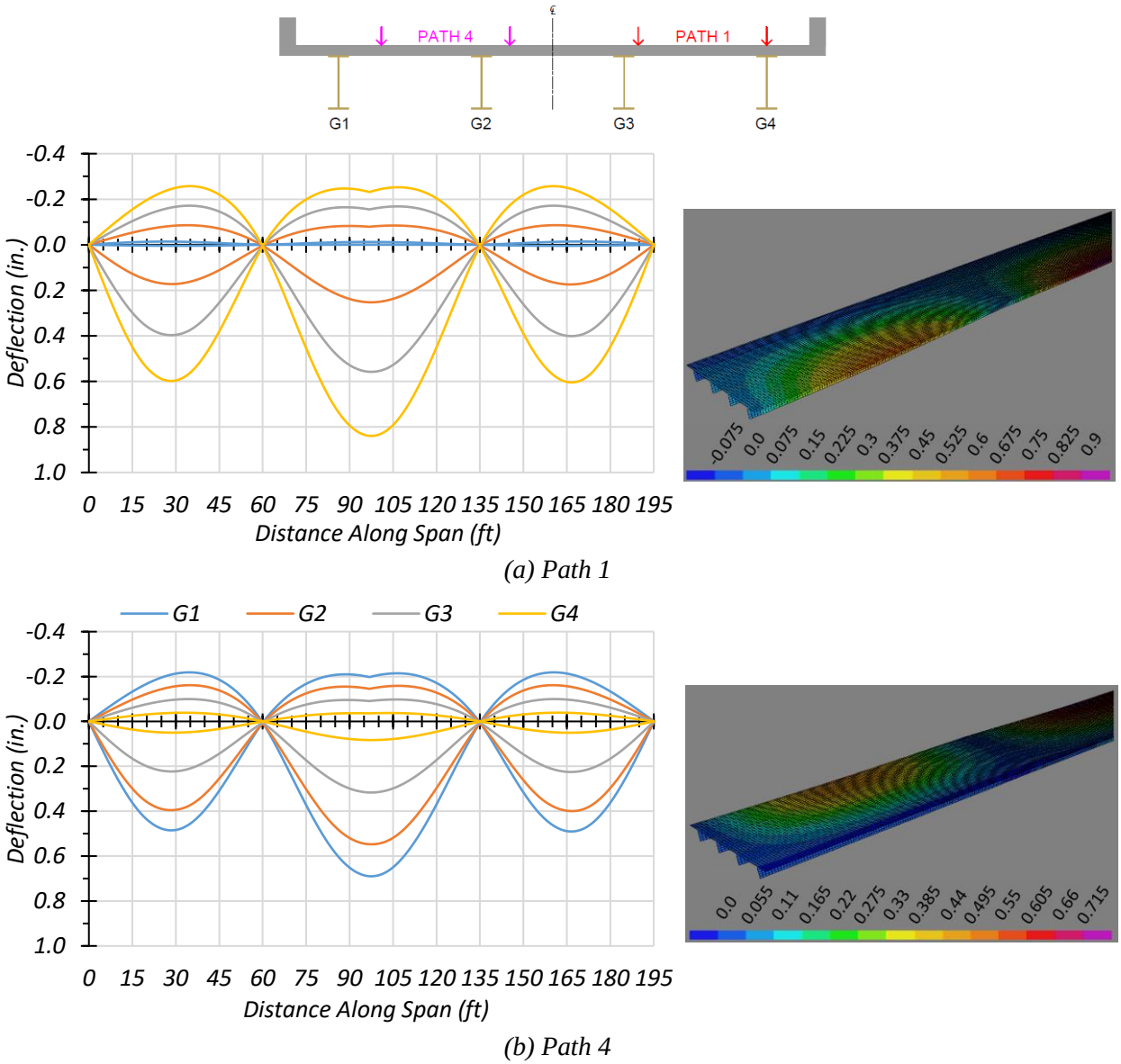

(a) Path 1

(b) Path 4

Figure 3.9. Deflection Profiles for Composite Bridge SC-12 with HS-20 Loading

Table 3.8. Maximum Deflections for Composite Bridge SC-12 with HS-20 Loading

Loading	Deflection Positive/Negative	G1	G2	G3	G4
Path 1	Positive	0.005	0.253	0.558	0.839
Path 1	Negative	−0.014	−0.086	−0.171	−0.257
Path 4	Positive	0.690	0.547	0.317	0.083
Path 4	Negative	−0.219	−0.161	−0.100	−0.039
Note: G = girder, paths indicate transverse loading positions as shown, deflections have inch units					

3.6.2.2 ***Positive Moment Results***

One-Lane Loading. Figure 3.10 shows the individual girder positive moment and positive moment LLDF results for the non-composite Bridge SC-12 under simulated moving HS-20 loading along three one-lane loading paths. Table 3.9 provides the corresponding maximum positive moment values of each girder for each loading path. The positive moment LLDF values are calculated using the estimated positive moment results from the FEM analysis. Table 3.11 shows the governing positive moment LLDFs found using the FEM analysis and compares them to the AASHTO LLDF values. Compared to the FEM results, the governing positive moment LLDF value computed using the approximate equations in the *AASHTO Standard Specifications* (AASHTO 2002) is quite conservative for interior girders, with a g^m_{AASHTO}/g^m_{FEM} ratio of 1.43, and is conservative for exterior girders, with a g^m_{AASHTO}/g^m_{FEM} ratio of 1.22.

Figure 3.11 shows the individual girder positive moment and positive moment LLDF results for the fully composite Bridge SC-12 under simulated moving HS-20 loading along three one-lane loading paths. Table 3.10 provides the corresponding maximum positive moment values of each girder for each loading path. The positive moment LLDF values are calculated using the estimated positive moment results from the FEM analysis. Compared to the FEM results, the governing positive moment LLDF value computed using the approximate equations in the *AASHTO Standard Specifications* (AASHTO 2002) is quite conservative for interior girders, with a g^m_{AASHTO}/g^m_{FEM} ratio of 1.31, and is conservative for exterior girders, with a g^m_{AASHTO}/g^m_{FEM} ratio of 1.19.

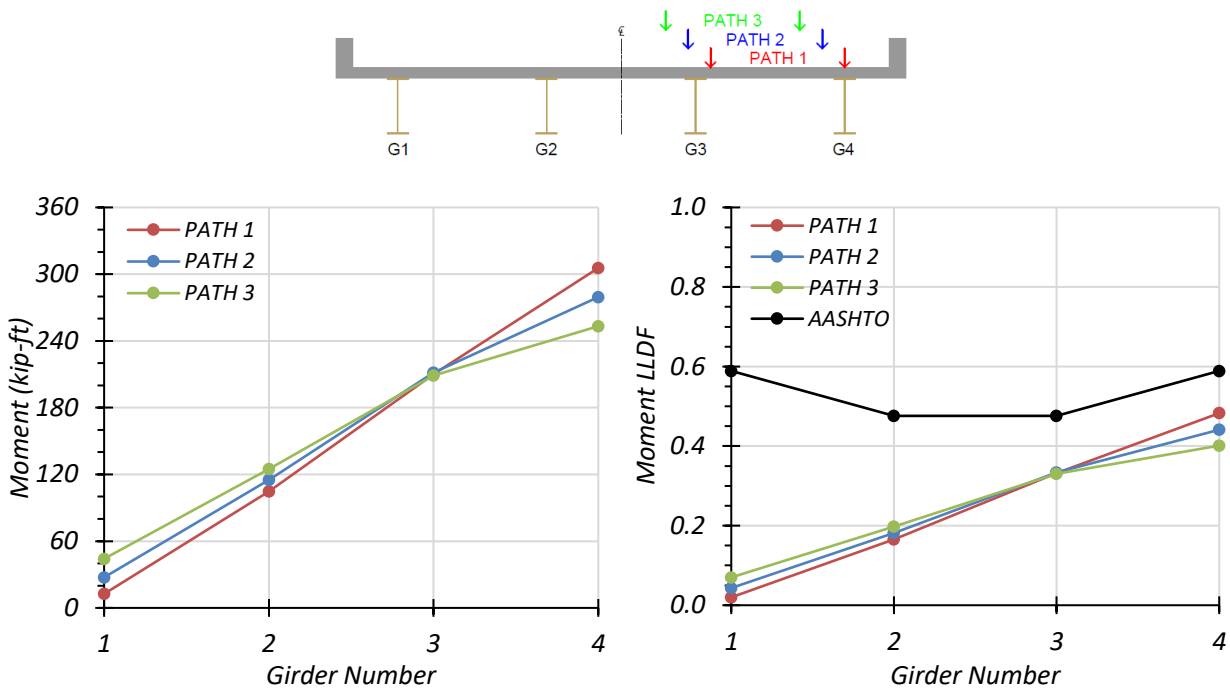

(a) Moment *(b) Moment LLDF*

Figure 3.10. Positive Moment Results for Non-Composite Bridge SC-12 with One-Lane HS-20 Loading

Table 3.9. Maximum Positive Moments for Non-Composite Bridge SC-12 with One-Lane HS-20 Loading

Loading	G1	G2	G3	G4
Path 1	12.6	104.8	209.9	305.6
Path 2	27.4	115.1	211.5	279.4
Path 3	44.2	125.0	208.8	253.2
Note: G = girder, paths indicate transverse loading positions as shown, moments have kip-ft units				

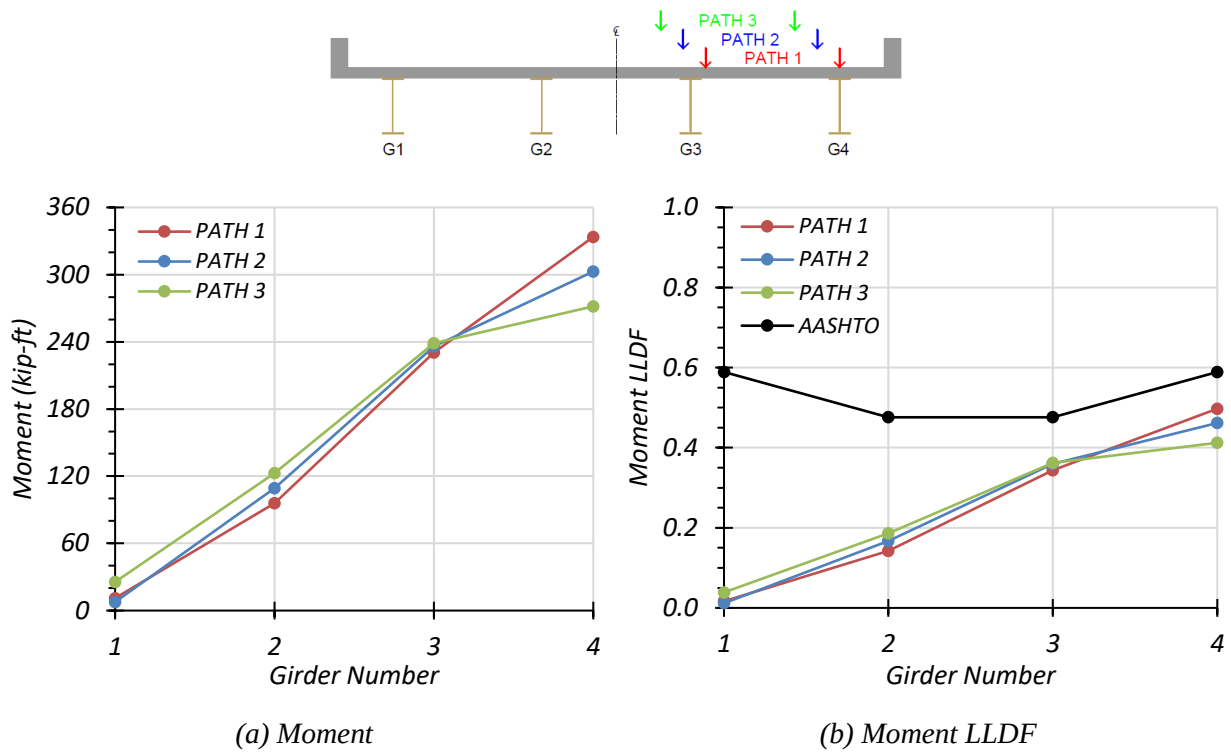

(a) Moment *(b) Moment LLDF*

Figure 3.11. Positive Moment Results for Composite Bridge SC-12 with One-Lane HS-20 Loading

Table 3.10. Maximum Positive Moments for Composite Bridge SC-12 with One-Lane HS-20 Loading

Loading	G1	G2	G3	G4
Path 1	11.1	95.7	230.4	333.7
Path 2	7.7	109.4	236.0	302.8
Path 3	25.5	122.8	238.7	271.7
Note: G = girder, paths indicate transverse loading positions as shown, moments have kip-ft units				

Comparison of governing positive moment LLDF values computed from FEM results for the composite and non-composite cases reveals that the maximum positive moment LLDF in an interior girder for the composite bridge is slightly higher than the one for the non-composite bridge, with a $g^m_{composite}/g^m_{non-composite}$ ratio of 1.08. The maximum positive moment LLDF in an exterior girder for the composite bridge is also slightly higher than the one for the non-composite bridge, with a $g^m_{composite}/g^m_{non-composite}$ ratio of 1.03.

Table 3.11. Governing Positive Moment LLDFs for Bridge SC-12 with One-Lane HS-20 Loading

Type	Girder Location	AASHTO (g^m_{AASHTO})	FEM (g^m_{FEM})	g^m_{AASHTO}/g^m_{FEM}
Non-Composite	Interior	0.476	0.334	1.43
	Exterior	0.589	0.483	1.22
Composite	Interior	0.476	0.362	1.31
	Exterior	0.589	0.497	1.19

Two-Lane Loading. Figure 3.12 shows the individual girder positive moments and positive moment LLDF results for the non-composite Bridge SC-12 under simulated moving HS-20 loading along three two-lane loading paths. Table 3.12 provides the corresponding maximum positive moment values of each girder for each loading path. The positive moment LLDF values are calculated using the estimated positive moment results from the FEM analysis. Table 3.14 shows the governing positive moment LLDFs found using the FEM analysis and compares them to the AASHTO LLDF values. Compared to the FEM results, the governing positive moment LLDF value computed using the approximate equations in the *AASHTO Standard Specifications* (AASHTO 2002) is conservative for interior girders, with a g^m_{AASHTO}/g^m_{FEM} ratio of 1.14, and is slightly conservative for exterior girders, with a g^m_{AASHTO}/g^m_{FEM} ratio of 1.09.

Figure 3.13 shows the individual girder positive moments and positive moment LLDF results for the fully composite Bridge SC-12 under simulated moving HS-20 loading along three two-lane loading paths. Table 3.13 provides the corresponding maximum positive moment values of each girder for each loading path. The positive moment LLDF values are calculated using the estimated positive moment results from the FEM analysis. Compared to the FEM results, the governing positive moment LLDF value computed using the approximate equations in the *AASHTO Standard Specifications* (AASHTO 2002) is conservative for interior girders, with a g^m_{AASHTO}/g^m_{FEM} ratio of 1.11, and is also conservative for exterior girders, with a g^m_{AASHTO}/g^m_{FEM} ratio of 1.10.

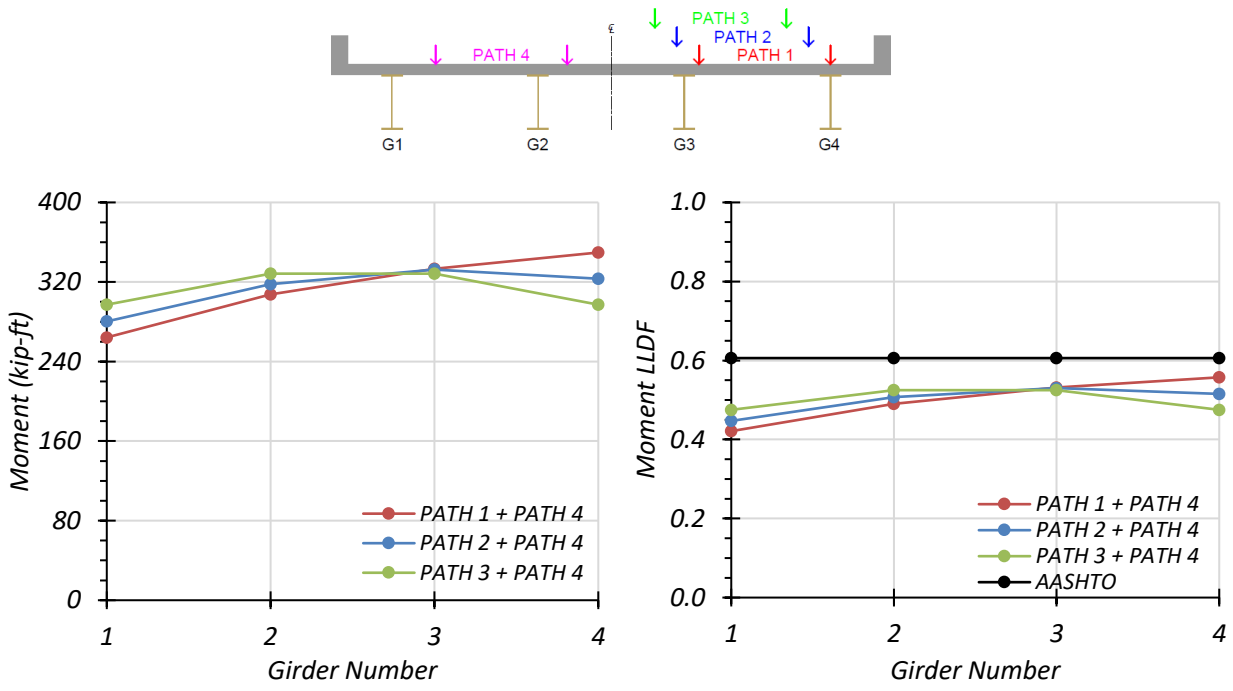

(a) Moment *(b) Moment LLDF*

Figure 3.12. Positive Moment Results for Non-Composite Bridge SC-12 with Two-Lane HS-20 Loading

Table 3.12. Maximum Positive Moments for Non-Composite Bridge SC-12 with Two-Lane HS-20 Loading

Loading	G1	G2	G3	G4
Path 1 + Path 4	264.2	307.5	333.3	349.6
Path 2 + Path 4	280.3	318.0	332.5	323.4
Path 3 + Path 4	297.2	328.4	328.4	297.2
Note: G = girder, paths indicate transverse loading positions as shown, moments have kip-ft units				

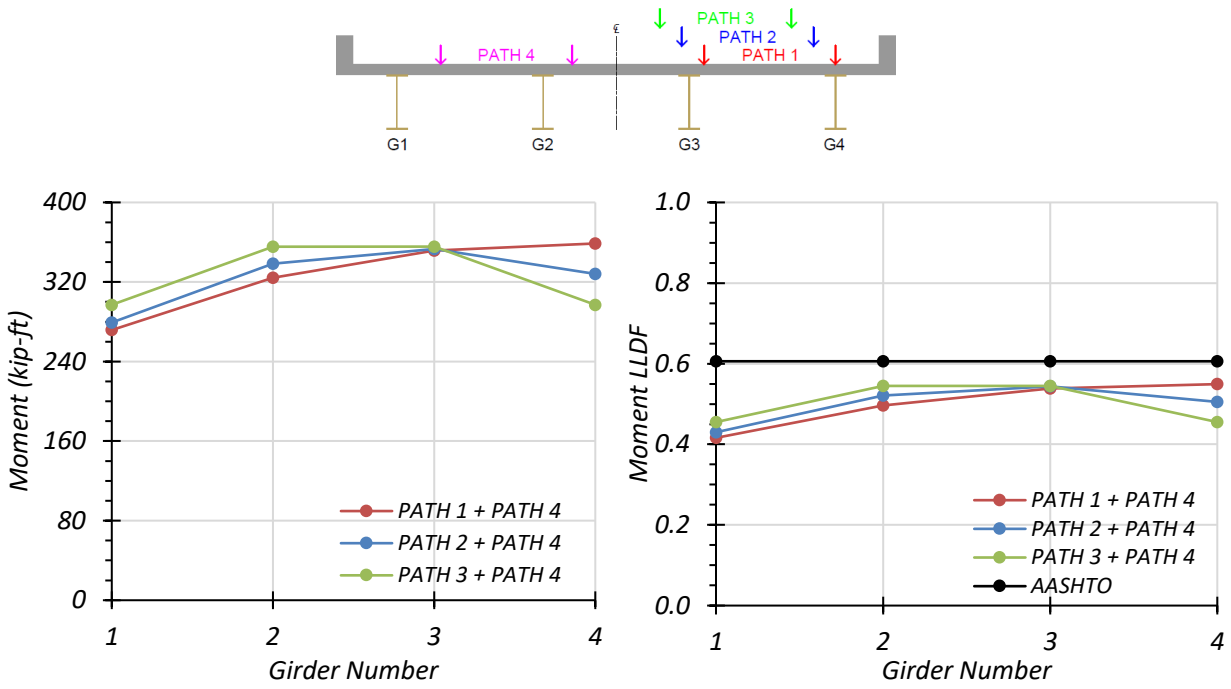

(a) Moment *(b) Moment LLDF*

Figure 3.13. Positive Moment Results for Composite Bridge SC-12 with Two-Lane HS-20 Loading

Table 3.13. Maximum Positive Moments for Composite Bridge SC-12 with Two-Lane HS-20 Loading

Loading	G1	G2	G3	G4
Path 1 + Path 4	271.7	324.1	351.6	358.7
Path 2 + Path 4	279.2	338.5	353.1	328.2
Path 3 + Path 4	297.1	355.6	355.6	297.1
Note: G = girder, paths indicate transverse loading positions as shown, moments have kip-ft units				

Comparison of governing positive moment LLDF values computed from FEM results for the composite and non-composite cases reveals that the maximum positive moment LLDF in an interior girder for the composite bridge is higher than the one for the non-composite bridge, with a $g^m_{composite}/g^m_{non-composite}$ ratio of 1.03. The maximum positive moment LLDF in an exterior girder for the composite bridge is slightly lower than the one for the non-composite bridge, with a $g^m_{composite}/g^m_{non-composite}$ ratio of 0.96.

Table 3.14. Governing Positive Moment LLDFs for Bridge SC-12 with Two-Lane HS-20 Loading

Type	Girder Location	AASHTO (g^m_{AASHTO})	FEM (g^m_{FEM})	g^m_{AASHTO}/g^m_{FEM}
Non-Composite	Interior	0.606	0.531	1.14
	Exterior	0.606	0.557	1.09
Composite	Interior	0.606	0.545	1.11
	Exterior	0.606	0.549	1.10

3.6.2.3 Negative Moment Results

One-Lane Loading. Figure 3.14 shows the individual girder negative moment and negative moment LLDF results for the non-composite Bridge SC-12 under simulated moving HS-20 loading along three one-lane loading paths. Table 3.15 provides the corresponding maximum negative moment values of each girder for each loading path. The negative moment LLDF values are calculated using the estimated negative moment results from FEM analysis. Table 3.17 shows the governing negative moment LLDFs found using the FEM analysis and compares them to the AASHTO LLDF values. Compared to the FEM results, the governing negative moment LLDF value computed using the approximate equations in the *AASHTO Standard Specifications* (AASHTO 2002) is quite conservative for interior girders, with a g^m_{AASHTO}/g^m_{FEM} ratio of 1.40, and is conservative for exterior girders, with a g^m_{AASHTO}/g^m_{FEM} ratio of 1.19.

Figure 3.15 shows the individual girder negative moment and negative moment LLDF results for the fully composite Bridge SC-12 under simulated moving HS-20 loading along three one-lane loading paths. The HS20 design truck with 14 ft axle spacing between 32-kip axles was used for the analyses because it was found to control the negative moment for the bridge. Table 3.16 provides the corresponding maximum negative moment values of each girder for each loading path. The negative moment LLDF values are calculated using the estimated negative moment results from the FEM analysis. Compared to the FEM results, the governing negative moment LLDF value computed using the approximate equations in the *AASHTO Standard Specifications* (AASHTO 2002) is conservative for both interior and exterior girders, with a g^m_{AASHTO}/g^m_{FEM} ratio of 1.27 and 1.16, respectively.

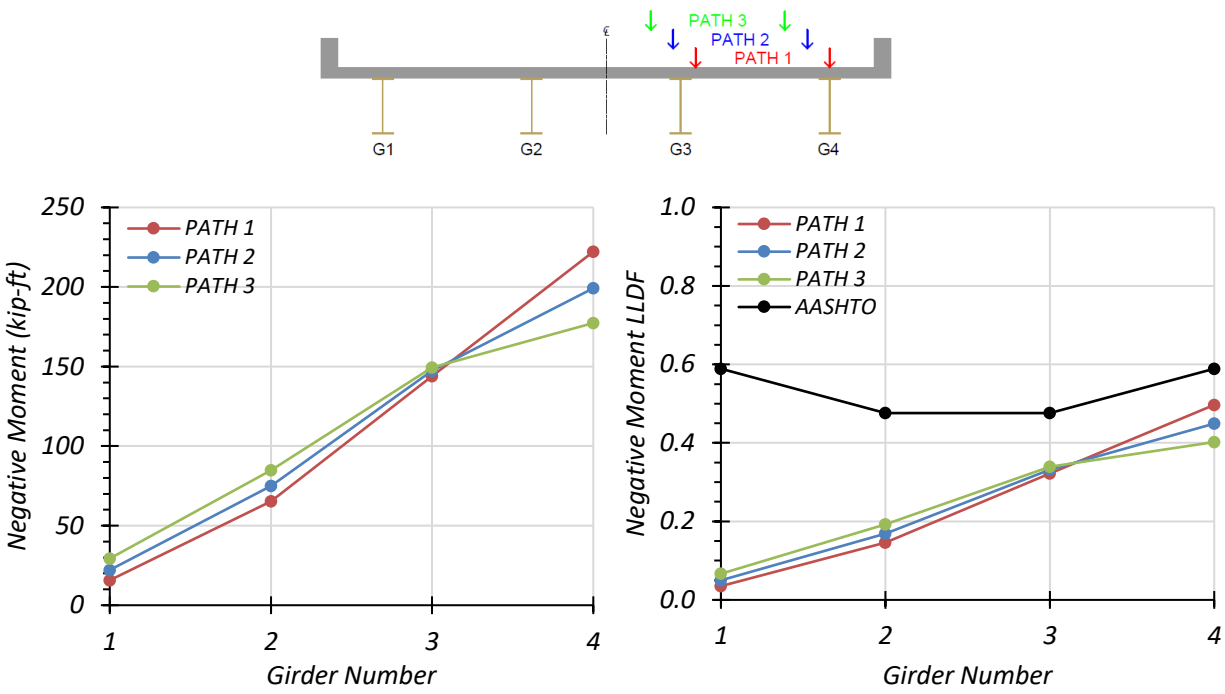

(a) Moment *(b) Moment LLDF*

Figure 3.14. Negative Moment Results for Non-Composite Bridge SC-12 with One-Lane HS-20 Loading

Table 3.15. Maximum Negative Moments for Non-Composite Bridge SC-12 with One-Lane HS-20 Loading

Loading	G1	G2	G3	G4
Path 1	15.7	65.3	144.0	222.2
Path 2	22.1	74.9	147.3	199.2
Path 3	29.4	84.8	149.4	177.3
Note: G = girder, paths indicate transverse loading positions as shown, moments have kip-ft units				

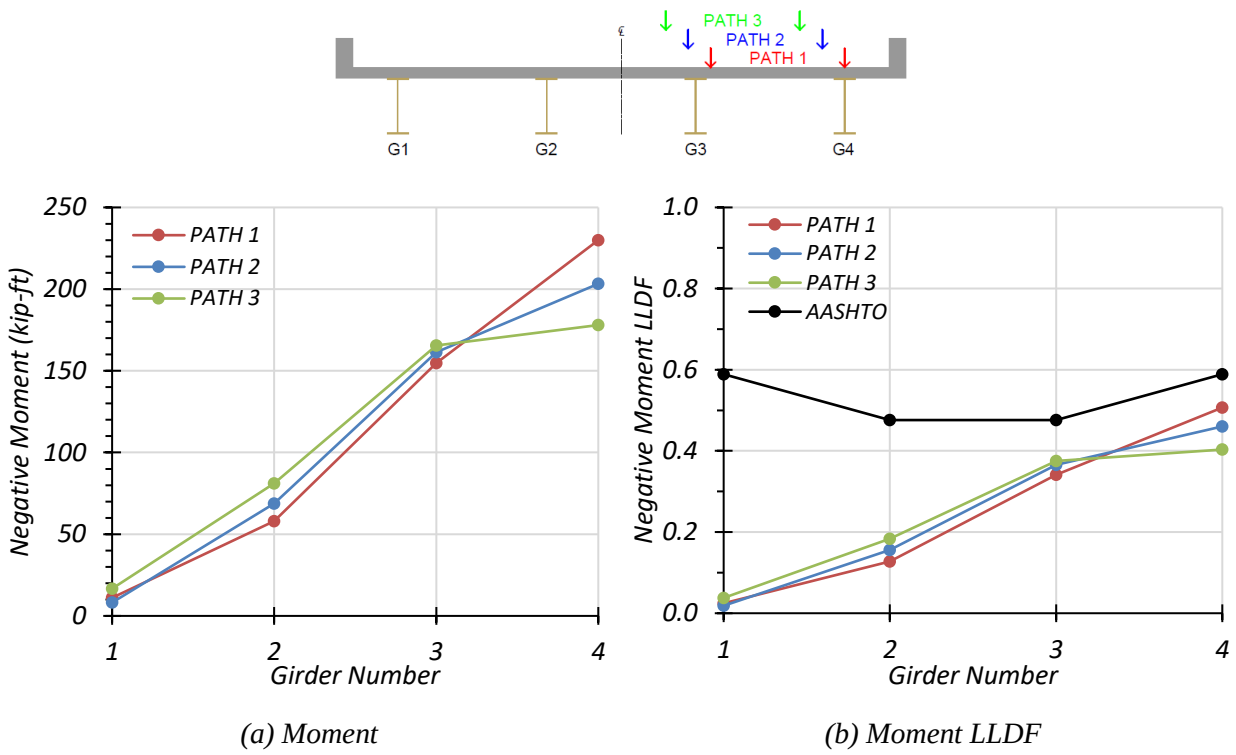

(a) Moment *(b) Moment LLDF*

Figure 3.15. Negative Moment Results for Composite Bridge SC-12 with One-Lane HS-20 Loading

Table 3.16. Maximum Negative Moments for Composite Bridge SC-12 with One-Lane HS-20 Loading

Loading	G1	G2	G3	G4
Path 1	11.1	57.9	154.8	230.0
Path 2	8.2	68.8	161.3	203.3
Path 3	16.7	81.1	165.5	178.0
Note: G = girder, paths indicate transverse loading positions as shown, moments have kip-ft units				

Comparison of governing negative moment LLDF values computed from FEM results for the composite and non-composite cases reveals that the maximum negative moment LLDF in an interior girder for the composite bridge is higher than the one for the non-composite bridge, with a $g^m_{composite}/g^m_{non-composite}$ ratio of 1.11. The maximum negative moment LLDF in an exterior girder for the composite bridge is also slightly higher than the one for the non-composite bridge, with a $g^m_{composite}/g^m_{non-composite}$ ratio of 1.02.

Table 3.17. Governing Negative Moment LLDFs for Bridge SC-12 with One-Lane HS-20 Loading

Type	Girder Location	AASHTO (g^m_{AASHTO})	FEM (g^m_{FEM})	g^m_{AASHTO}/g^m_{FEM}
Non-Composite	Interior	0.476	0.339	1.40
	Exterior	0.589	0.497	1.19
Composite	Interior	0.476	0.375	1.27
	Exterior	0.589	0.507	1.16

Two-Lane Loading. Figure 3.16 shows the individual girder negative moment and negative moment LLDF results for the non-composite Bridge SC-12 under simulated moving HS-20 loading along three two-lane loading paths. Table 3.18 provides the corresponding maximum negative moment values of each girder for each loading path. The negative moment LLDF values are calculated using the estimated negative moment results from the FEM analysis. Table 3.20 shows the governing negative moment LLDFs found using the FEM analysis and compares them to the AASHTO LLDF values. Compared to the FEM results, the governing negative moment LLDF value computed using the approximate equations in the *AASHTO Standard Specifications* (AASHTO 2002) is conservative for interior girders, with a g^m_{AASHTO}/g^m_{FEM} ratio of 1.11, and is slightly conservative for exterior girders, with a g^m_{AASHTO}/g^m_{FEM} ratio of 1.09.

Figure 3.17 shows the individual girder negative moment and negative moment LLDF results for the fully composite Bridge SC-12 under simulated moving HS-20 loading along three different two-lane loading paths. Table 3.19 provides the corresponding maximum negative moment values of each girder for each loading path. The negative moment LLDF values are calculated using the estimated negative moment results from the FEM analysis. Compared to the FEM results, the governing negative moment LLDF value computed using the approximate equations in the *AASHTO Standard Specifications* (AASHTO 2002) is slightly conservative for interior girders, with a g^m_{AASHTO}/g^m_{FEM} ratio of 1.07, and is conservative for exterior girders, with a g^m_{AASHTO}/g^m_{FEM} ratio of 1.11.

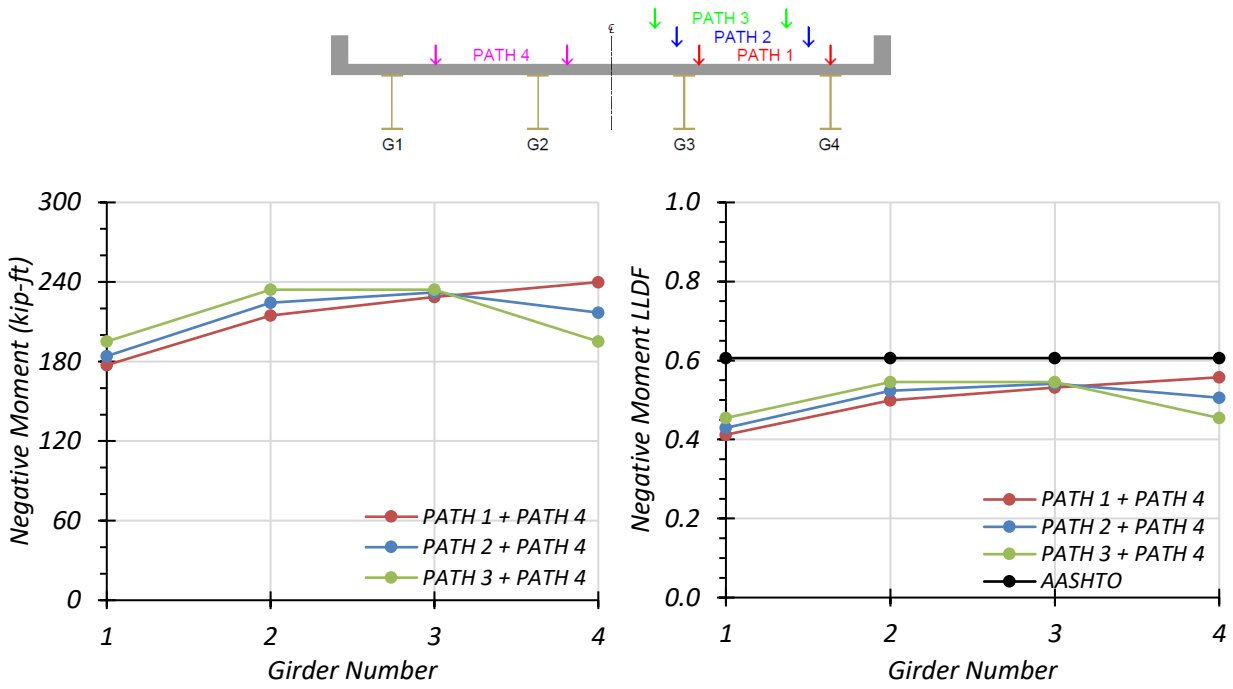

(a) Moment *(b) Moment LLDF*

Figure 3.16. Negative Moment Results for Non-Composite Bridge SC-12 with Two-Lane HS-20 Loading

Table 3.18. Maximum Negative Moments for Non-Composite Bridge SC-12 with Two-Lane HS-20 Loading

Loading	G1	G2	G3	G4
Path 1 + Path 4	177.3	214.7	228.8	239.9
Path 2 + Path 4	184.1	224.3	232.1	217.0
Path 3 + Path 4	195.1	234.2	234.2	195.1
Note: G = girder, paths indicate transverse loading positions as shown, moments have kip-ft units				

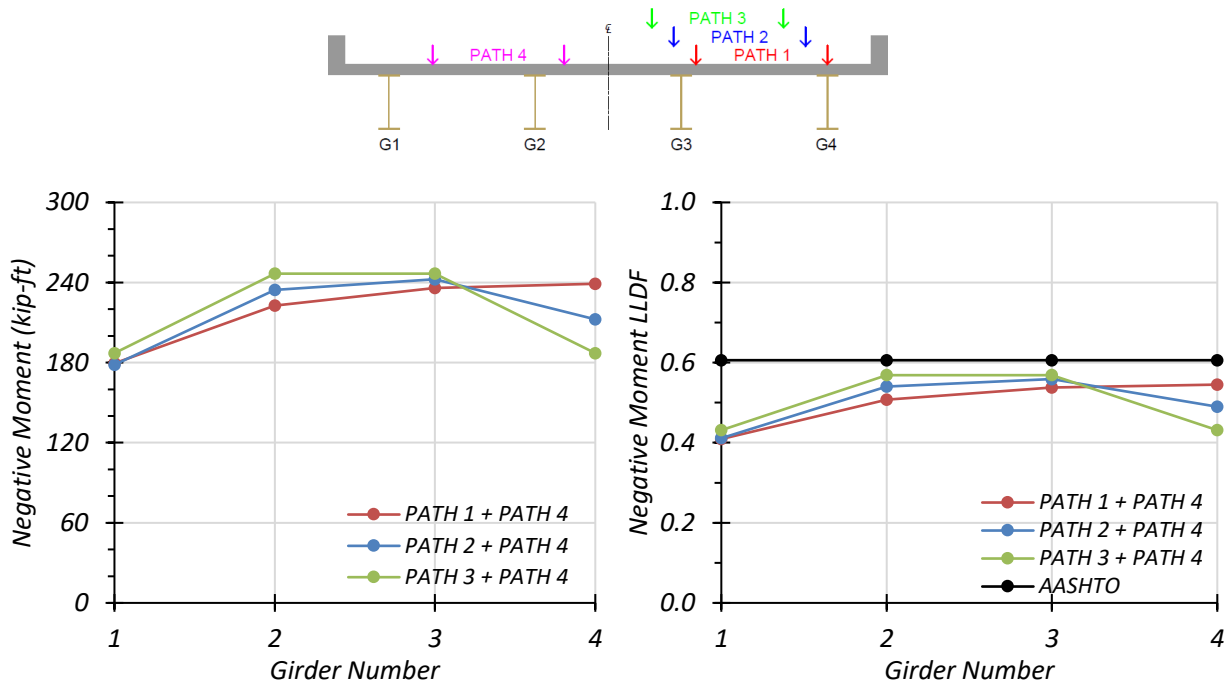

(a) Moment *(b) Moment LLDF*

Figure 3.17. Negative Moment Results for Composite Bridge SC-12 with Two-Lane HS-20 Loading

Table 3.19. Maximum Negative Moments for Composite Bridge SC-12 with Two-Lane HS-20 Loading

Loading	G1	G2	G3	G4
Path 1 + Path 4	179.5	222.7	235.9	239.1
Path 2 + Path 4	178.4	234.3	242.4	212.3
Path 3 + Path 4	187.1	246.7	246.7	187.1
Note: G = girder, paths indicate transverse loading positions as shown, moments have kip-ft units				

Comparison of governing negative moment LLDF values computed from FEM results for the composite and non-composite cases reveals that the maximum negative moment LLDF in an interior girder for the composite bridge is higher than the one for the non-composite bridge, with a $g^m_{composite}/g^m_{non-composite}$ ratio of 1.04. However, the negative moment LLDF in an exterior girder for the composite bridge is slightly lower than the one for the non-composite bridge, with a $g^m_{composite}/g^m_{non-composite}$ ratio of 0.98.

Table 3.20. Governing Negative Moment LLDFs for Bridge SC-12 with Two-Lane HS-20 Loading

Type	Girder Location	AASHTO (g^m_{AASHTO})	FEM (g^m_{FEM})	g^m_{AASHTO}/g^m_{FEM}
Non-Composite	Interior	0.606	0.546	1.11
	Exterior	0.606	0.557	1.09
Composite	Interior	0.606	0.569	1.07
	Exterior	0.606	0.545	1.11

*3.6.2.4 **Shear Results***

One-Lane Loading. Figure 3.18 shows the individual girder shear forces and shear LLDF results for the non-composite Bridge SC-12 under simulated moving HS-20 loading along three one-lane loading paths. Table 3.21 provides the corresponding maximum shear values of each girder for each loading path. The shear LLDF values are calculated using the estimated shear results from the FEM analysis. Table 3.23 shows the governing shear LLDFs found using the FEM analysis and compares them to the AASHTO LLDF values. Compared to the FEM results, the governing shear LLDF value computed using the approximate equations in the *AASHTO Standard Specifications* (AASHTO 2002) is conservative for both interior and exterior girders, with a g^v_{AASHTO}/g^v_{FEM} ratio of 1.15 and 1.17, respectively.

Figure 3.19 shows the individual girder shears and shear LLDF results for the fully composite Bridge SC-12 under simulated moving HS-20 loading along three one-lane loading paths. Table 3.22 provides the corresponding maximum shear values of each girder for each loading path. The shear LLDF values are calculated using the estimated shear results from the FEM analysis. Compared to the FEM results, the governing shear LLDF value computed using the approximate equations in the *AASHTO Standard Specifications* (AASHTO 2002) is slightly conservative for interior girders, with a g^v_{AASHTO}/g^v_{FEM} ratio of 1.06, and is conservative for exterior girders, with a g^v_{AASHTO}/g^v_{FEM} ratio of 1.15.

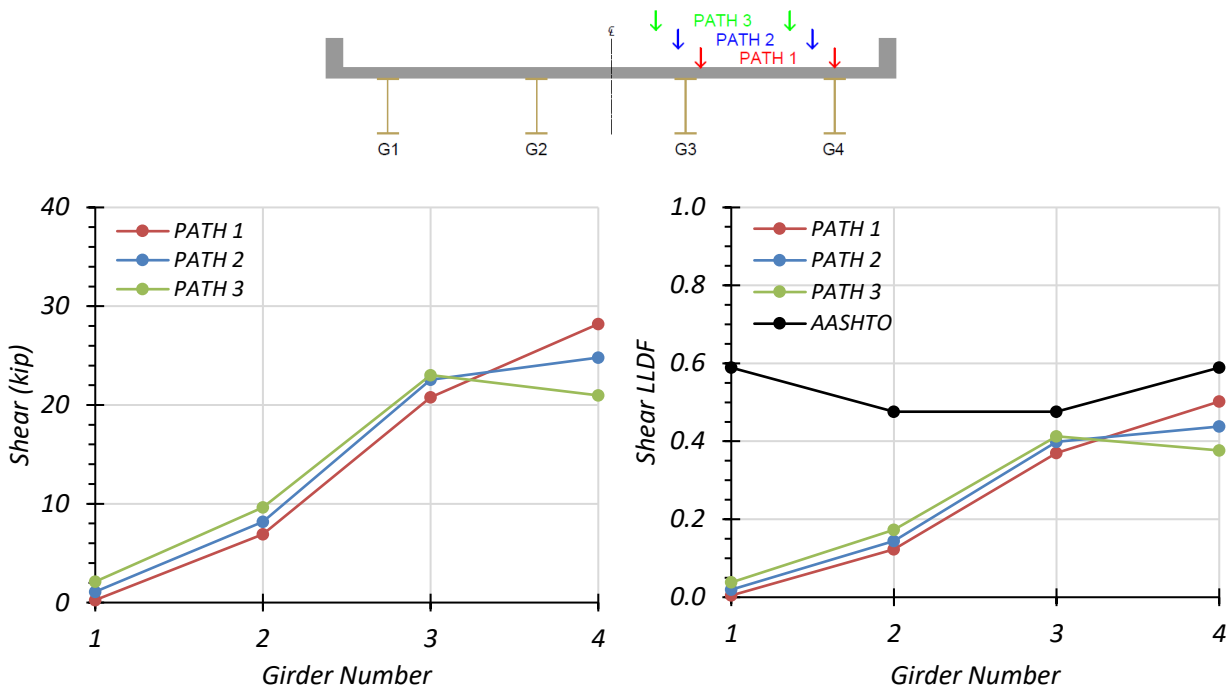

(a) Shear *(b) Shear LLDF*

Figure 3.18. Shear Results for Non-Composite Bridge SC-12 with One-Lane HS-20 Loading

Table 3.21. Maximum Shears for Non-Composite Bridge SC-12 with One-Lane HS-20 Loading

Loading	G1	G2	G3	G4
Path 1	0.3	6.9	20.8	28.2
Path 2	1.1	8.2	22.6	24.8
Path 3	2.1	9.6	23.0	21.0
Note: G = girder, paths indicate transverse loading positions as shown, shears have kip units				

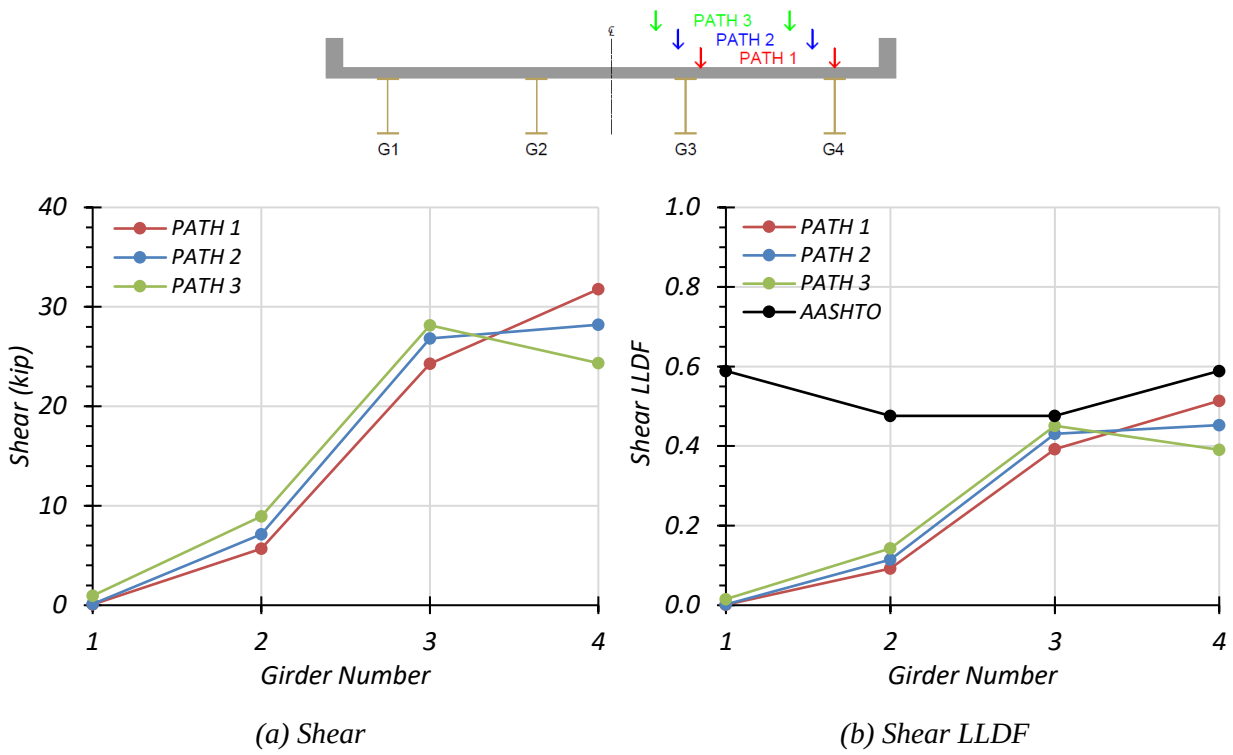

(a) Shear *(b) Shear LLDF*

Figure 3.19. Shear Results for Composite Bridge SC-12 with One-Lane HS-20 Loading

Table 3.22. Maximum Shears for Composite Bridge SC-12 with One-Lane HS-20 Loading

Loading	G1	G2	G3	G4
Path 1	0.1	5.7	24.3	31.8
Path 2	0.1	7.1	26.8	28.2
Path 3	1.0	8.9	28.1	24.4
Note: G = girder, paths indicate transverse loading positions as shown, shears have kip units				

Comparison of governing shear LLDF values computed from FEM results for the composite and non-composite cases reveals that the maximum shear LLDF in an interior girder for the composite bridge is higher than the one for the non-composite bridge, with a $g^v_{composite}/g^v_{non-composite}$ ratio of 1.09. The maximum shear LLDF in an exterior girder for the composite bridge is also higher than the one for the non-composite bridge, with a $g^v_{composite}/g^v_{non-composite}$ ratio of 1.02.

Table 3.23. Governing Shear LLDFs for Bridge SC-12 with One-Lane HS-20 Loading

Type	Girder Location	AASHTO (g^v_{AASHTO})	FEM (g^v_{FEM})	g^v_{AASHTO}/g^v_{FEM}
Non-Composite	Interior	0.476	0.413	1.15
	Exterior	0.589	0.502	1.17
Composite	Interior	0.476	0.451	1.06
	Exterior	0.589	0.514	1.15

Two-Lane Loading. The same procedure was conducted for two-lane loading. Figure 3.20 shows the individual girder shears and shear LLDF results for the non-composite Bridge SC-12 under simulated moving HS-20 loading along three two-lane loading paths. Table 3.24 provides the corresponding maximum shear values of each girder for each loading path. The shear LLDF values are calculated using the estimated shear results from the FEM analysis. Table 3.26 shows the governing shear LLDFs found using the FEM analysis and compares them to the AASHTO LLDF values. Compared to the FEM results, the governing shear LLDF value computed using the approximate equations in the *AASHTO Standard Specifications* (AASHTO 2002) is slightly conservative for interior girders, with a g^v_{AASHTO}/g^v_{FEM} ratio of 1.04, and is conservative for exterior girders, with a g^v_{AASHTO}/g^v_{FEM} ratio of 1.11.

Figure 3.21 shows the individual girder shears and shear LLDF results for the fully composite Bridge SC-12 under simulated moving HS-20 loading along three one-lane loading paths. Table 3.25 provides the corresponding maximum shear values of each girder for each loading path. The shear LLDF values are calculated using the estimated shear results from the FEM analysis. Compared to the FEM results, the governing shear LLDF value computed using the approximate equations in the *AASHTO Standard Specifications* (AASHTO 2002) is slightly conservative for interior girders, with a g^v_{AASHTO}/g^v_{FEM} ratio of 1.02, and is conservative for exterior girders, with a g^v_{AASHTO}/g^v_{FEM} ratio of 1.14.

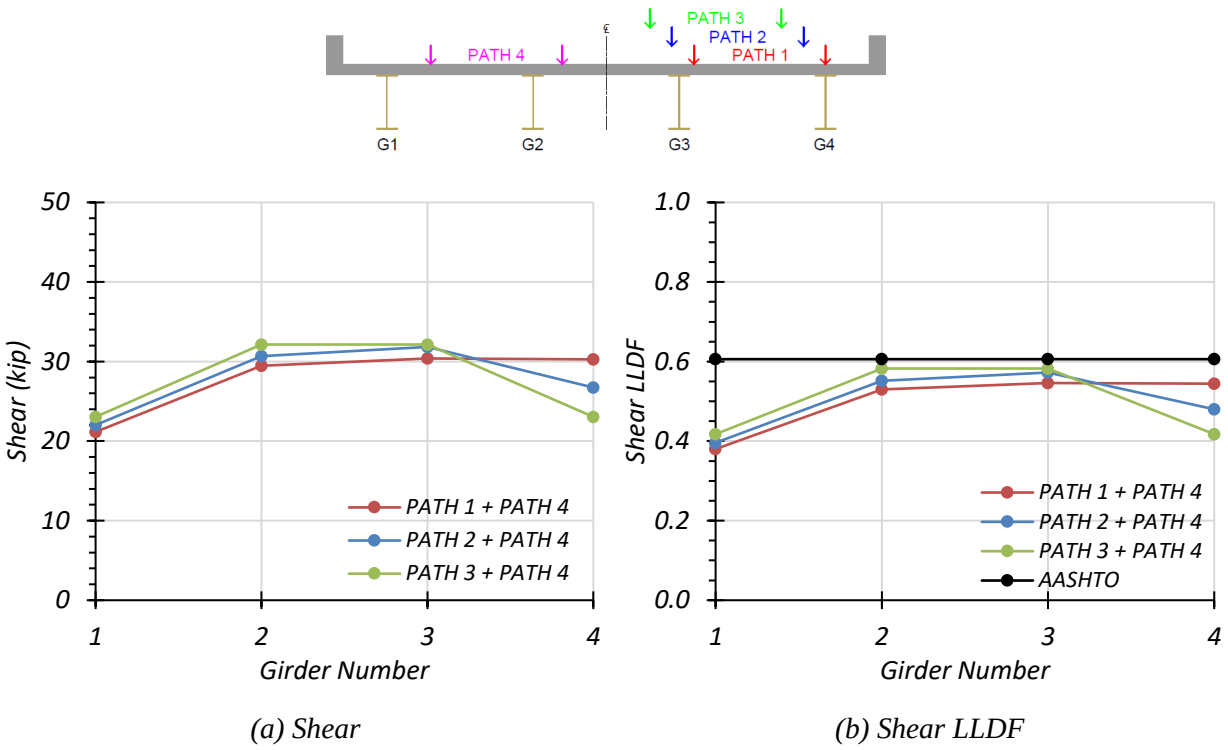

(a) Shear *(b) Shear LLDF*

Figure 3.20. Shear Results for Non-Composite Bridge SC-12 with Two-Lane HS-20 Loading

Table 3.24. Maximum Shears for Non-Composite Bridge SC-12 with Two-Lane HS-20 Loading

Loading	G1	G2	G3	G4
Path 1 + Path 4	21.2	29.5	30.4	30.3
Path 2 + Path 4	22.0	30.7	31.8	26.7
Path 3 + Path 4	23.0	32.1	32.1	23.0
Note: G = girder, paths indicate transverse loading positions as shown, shears have kip units				

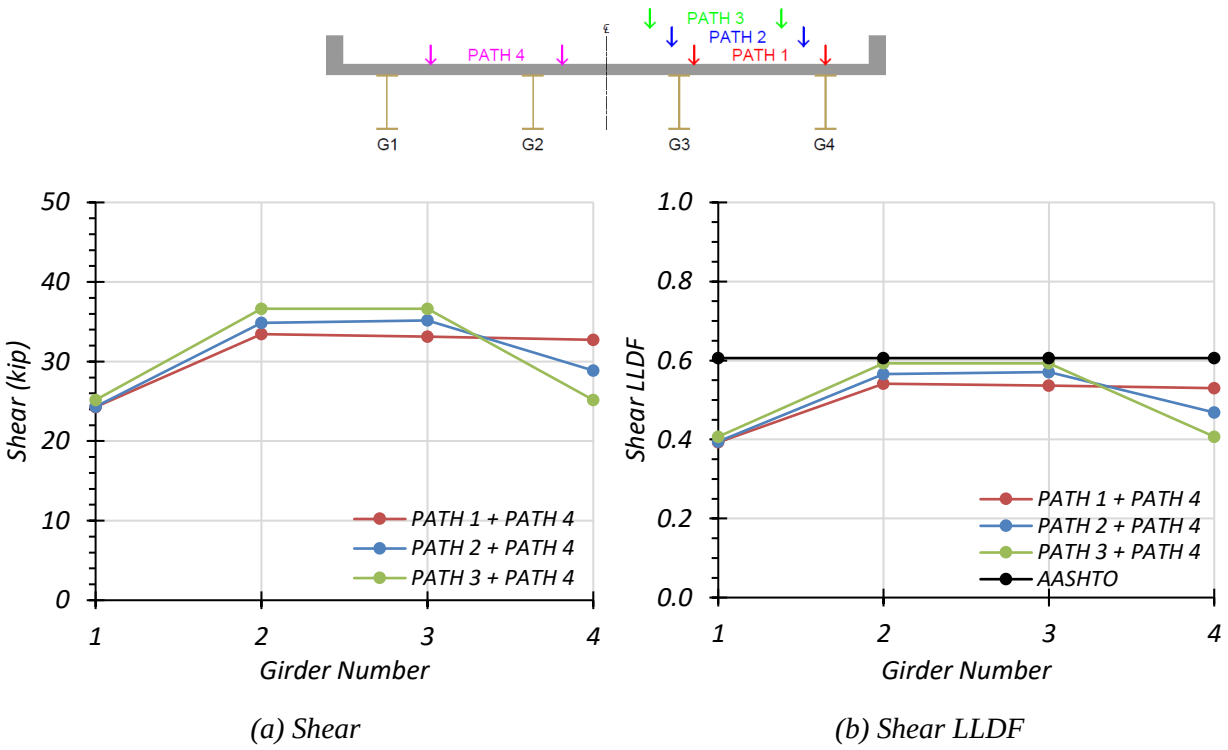

(a) Shear *(b) Shear LLDF*

Figure 3.21. Shear Results for Composite Bridge SC-12 with Two-Lane HS-20 Loading

Table 3.25. Maximum Shears for Composite Bridge SC-12 with Two-Lane HS-20 Loading

Loading	G1	G2	G3	G4
Path 1 + Path 4	24.3	33.4	33.1	32.7
Path 2 + Path 4	24.3	34.9	35.2	28.9
Path 3 + Path 4	25.2	36.6	36.6	25.2
Note: G = girder, paths indicate transverse loading positions as shown, shears have kip units				

Comparison of governing shear LLDF values computed from FEM results for the composite and non-composite cases reveals that the maximum shear LLDF in an interior girder for the composite bridge is higher than the one for the non-composite bridge, with a $g^v_{composite}/g^v_{non-composite}$ ratio of 1.02. However, the maximum shear LLDF in an exterior girder for the composite bridge is lower than the one for the non-composite bridge, with a $g^v_{composite}/g^v_{non-composite}$ ratio of 0.97.

Table 3.26. Governing Shear LLDFs for Bridge SC-12 with Two-Lane HS-20 Loading

Type	Girder Location	AASHTO (g^v_{AASHTO})	FEM (g^v_{FEM})	g^v_{AASHTO}/g^v_{FEM}
Non-Composite	Interior	0.606	0.582	1.04
	Exterior	0.606	0.544	1.11
Composite	Interior	0.606	0.593	1.02
	Exterior	0.606	0.530	1.14

*3.6.2.5 **Stiffness Adjustment Results***

During the analysis of SC-12, it was determined that an additional analysis should be performed considering a reduction of stiffness in the negative moment regions. If the bridge is acting compositely and experiences a large enough negative moment over the interior supports, the concrete deck will experience tension cracking. This will reduce the stiffness of the deck in that region and could possibly influence the distribution of positive and negative moment along the length of the bridge and the LLDFs for each girder. This analysis was only conducted for HS-20 loading because that is the loading that TxDOT uses to rate this bridge and all of their bridges not designed using LRFD.

In order to determine the area in which the stiffness of the deck should be adjusted, the cracking moment of the composite section was determined. The modulus of rupture of concrete was determined using Article 8.15.2.1.1 in the *AASHTO Standard Specifications* (AASHTO 2002), which is given as follows:

$$f_r = 7.5\sqrt{f'_c} \tag{3.1}$$

where:

f_r = Modulus of rupture of concrete (psi).

f'_c = Specified compressive strength of concrete (psi).

By using the modulus of rupture of concrete, the calculated section modulus of the composite section for an interior girder, and the modular ratio, the cracking moment was determined to be approximately 310 kip-ft. Therefore, the stiffness of concrete would need to be adjusted in the regions where the negative moment exceeds a magnitude of 310 kip-ft. Accounting for dead load as well, these regions were determined using the moment diagram for a two-lane HS-20 load case

with trucks along Paths 1 + 4 because this case produced the maximum possible negative moment in an individual girder. Figure 3.22 shows the moment envelope along the bridge length for this load case, considering dead load and live load, as well as the calculated cracking moment in the negative moment region.

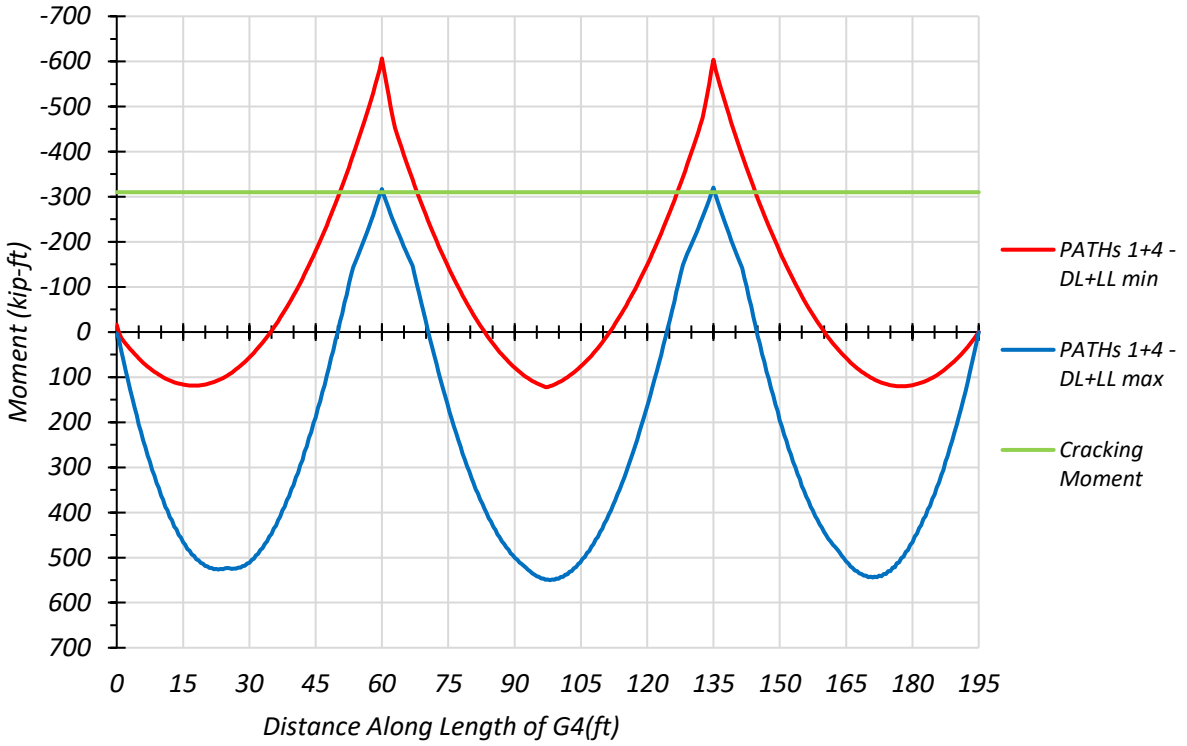

Figure 3.22. Maximum Moment Envelope for SC-12 from HS-20 Loading

By using this moment envelope, the regions where the magnitude of negative moment exceeded the cracking moment were determined to be approximately between 50 ft 6 in. and 68 ft and between 127 ft and 144 ft 6 in. along the total length of the bridge. The stiffness adjustment was determined by taking the ratio of the area of a cracked element to the area of an uncracked element and considering the 6 in. wide by 6 in. thick elements used in the FEM analysis. The area of an uncracked element is therefore 36 in^2 using the gross concrete area. To determine the area of a cracked element, the amount of steel reinforcement in that element was determined. The construction drawings from the TxDOT inspection reports (TxDOT 2018a) show #5 bars top and bottom but do not provide a spacing for the longitudinal bars in the deck. Therefore, the spacing

of the transverse bars in the deck, given as 12.25 in., was used. Multiplying by the modular ratio gives a cracked element area of 3.04 in^2. Dividing 3.04 by 36 gives a stiffness adjustment ratio of 0.0844. The MOE of concrete was multiplied by this ratio in the negative moment regions with a moment demand greater than the cracking moment.

An analysis was conducted using the updated FEM model, and it was determined that the LLDFs for the individual girder did not significantly change due to the stiffness reduction. However, the positive moment and negative moment distribution along the length of the bridge did change. Figure 3.23 shows the moment envelope before the stiffness adjustment, in dashed lines, and after the stiffness adjustment, in solid lines, for exterior girder G4 under HS-20 loading along the Paths 1 + 4. Figure 3.24 shows the moment envelope before the stiffness adjustment, in dashed lines, and after the stiffness adjustment, in solid lines, for interior girder G3 under HS-20 loading along the Paths 3 + 4.

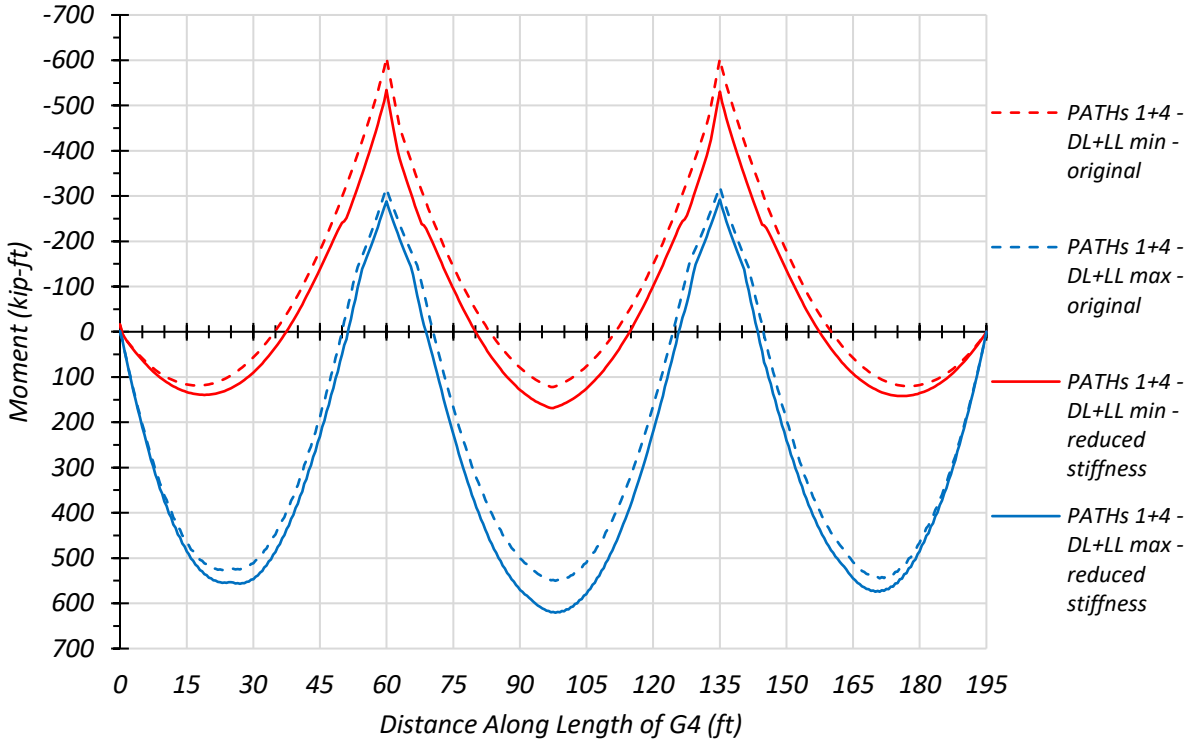

Figure 3.23. Original vs. Reduced Stiffness Moment Envelopes for Exterior Girder

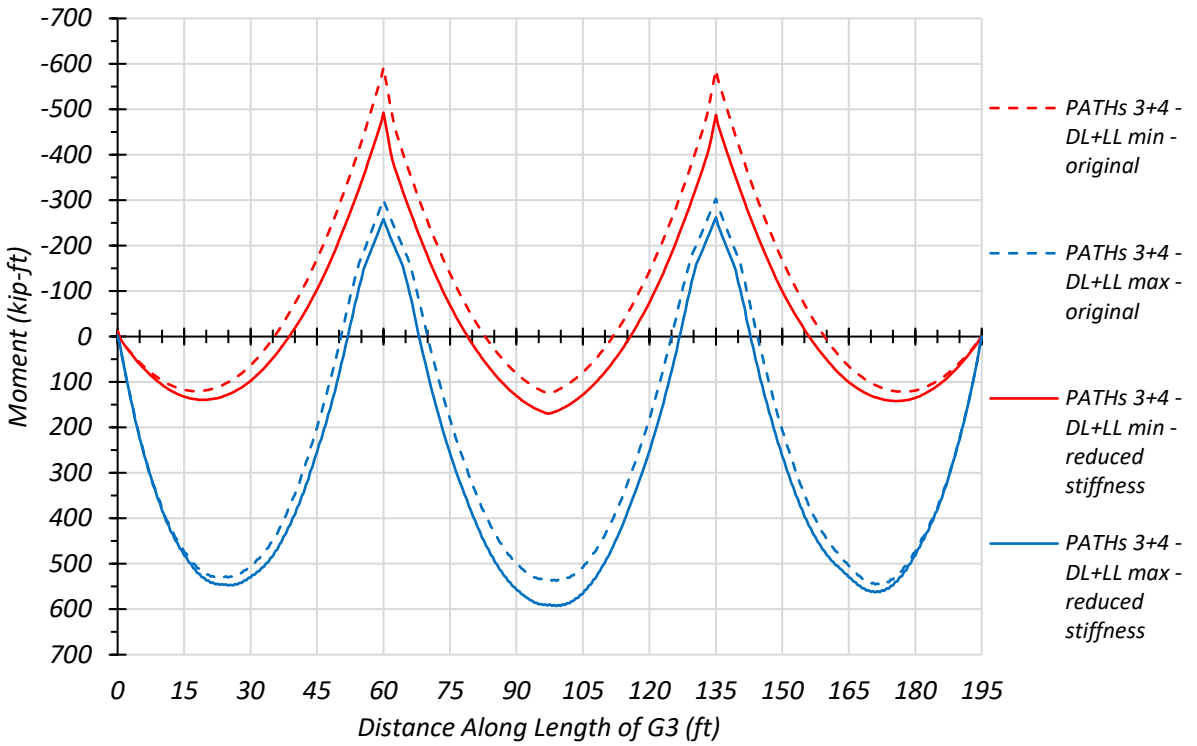

Figure 3.24. Original vs. Reduced Stiffness Moment Envelopes for Interior Girder

The reduction in stiffness of the deck to account for cracking over the negative moment region increased the maximum applied positive moment and decreased the maximum applied negative moment for both the interior and exterior girders. Table 3.27 shows the maximum positive and negative moment values for an interior and exterior girder, as well as the ratio of the original moment, using the uncracked deck to the moment calculated by considering the reduced deck stiffness due to cracking. This ratio is 0.92 for the positive moment and 1.20 for the negative moment for an interior girder, while the ratio is 0.89 for the positive moment and 1.14 for the negative moment for an exterior girder. This analysis has implications on the load rating process because it shows that if the deck in the negative moment region exhibits cracking, then the applied moments used for the rating process could change. During the field testing of Bridge SC-12, the potential impact of deck cracking in the negative moment region will be explored further if test results confirm that the bridge is acting compositely and that there may be cracking over the interior supports.

Table 3.27. Positive Moment and Negative Moment Changes Due to Cracked Deck Section

Girder Location	Maximum Moment Region	Original Moment (kip-ft)	Reduced Stiffness Moment (kip-ft)	Original/Reduced Stiffness Moment
Interior	Positive	545.9	593.0	0.92
	Negative	591.9	492.6	1.20
Exterior	Positive	550.2	620.8	0.89
	Negative	606.5	534.3	1.14

3.6.3 HL-93 Live Load Analysis

Bridge SC-12 was also analyzed using the HL-93 design loading presented in the *AASHTO LRFD Specifications* (AASHTO 2017). The bridge was analyzed for one-lane and two-lane-loaded cases along four transverse paths, as shown in Figure 3.5. Deflection, moment, and shear results were obtained.

*3.6.3.1 **Deflection Results***

Figure 3.25 shows the estimated girder deflection profile envelopes along the full length of the bridge and contours of the half length of the bridge for one-lane HL-93 loading along Path 1 and Path 4 when the bridge is analyzed as fully non-composite. Table 3.28 shows the corresponding positive (downward) and negative (upward) deflections for each girder, assuming non-composite action. Load Paths 1 and 4 are the only ones shown because they are the load paths planned for later load tests, and were selected to maximize the forces on an interior girder and on an exterior girder.

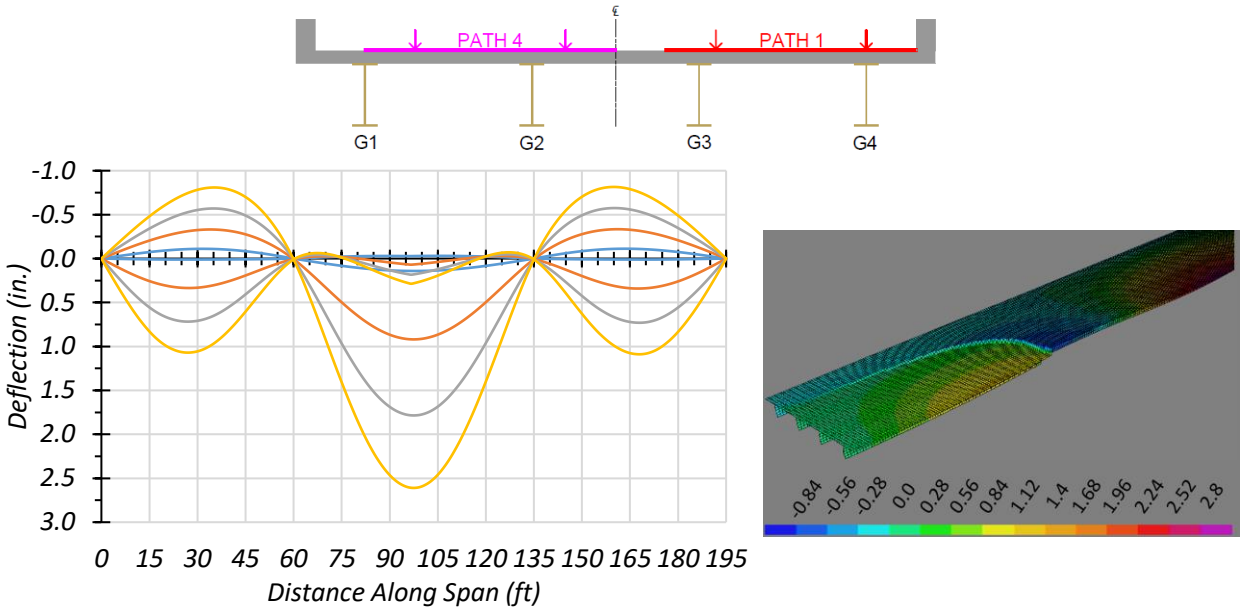

(a) Path 1

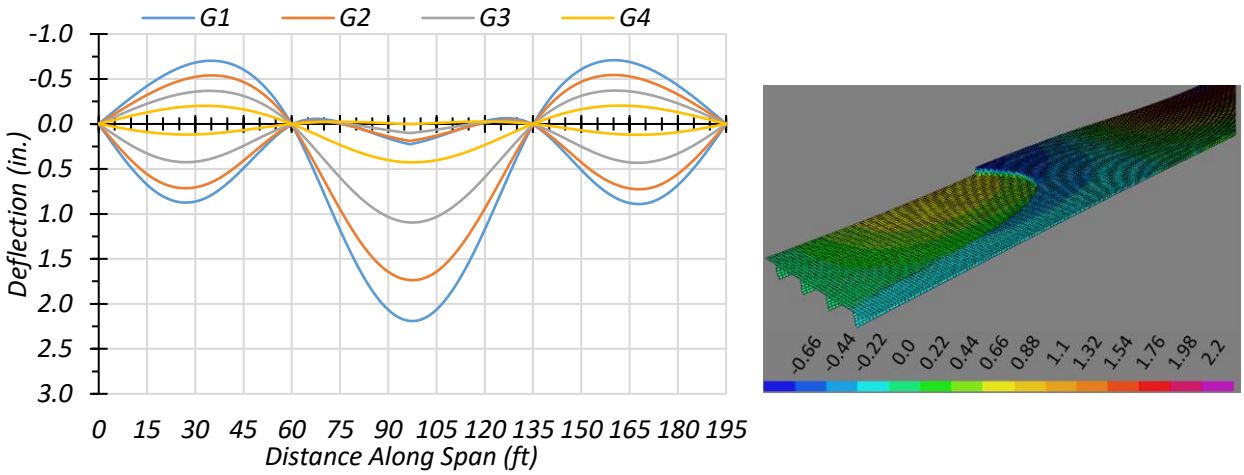

(b) Path 4

Figure 3.25. Deflection Profiles for Non-Composite Bridge SC-12 with HL-93 Loading

Table 3.28. Maximum Deflections for Non-Composite Bridge SC-12 with HL-93 Loading

Loading	Deflection Positive/Negative	G1	G2	G3	G4
Path 1	Positive	0.141	0.920	1.785	2.610
Path 1	Negative	−0.112	−0.334	−0.575	−0.815
Path 4	Positive	2.191	1.736	1.096	0.427
Path 4	Negative	−0.709	−0.544	−0.371	−0.204
Note: G = girder, paths indicate transverse loading positions as shown, deflections have inch units					

Figure 3.26 shows the estimated girder deflection profile envelopes along the full length of the bridge and contours of the half length of the bridge for one-lane HL-93 loading along Path 1 and Path 4 when the bridge is analyzed as fully composite. Table 3.29 shows the corresponding positive (downward) and negative (upward) deflections for each girder assuming fully composite action. Load Paths 1 and 4 are the only ones shown because they are the load paths planned for later load tests, and were selected to maximize the forces on an interior girder and on an exterior girder.

For both the non-composite and composite cases, the maximum negative deflections were obtained in Girder G4 when the HL-93 truck was run along Path 1. The estimated deflections were 2.61 in. and 1.20 in. for non-composite and composite cases, respectively. This result indicates that the composite bridge is 74 percent stiffer than the non-composite bridge. The maximum deflections obtained when the HL-93 truck was run along Path 4 were in Girder G1 for both the non-composite and composite case. The estimated deflections were 2.19 in. and 0.99 in. for the non-composite and composite cases, respectively, indicating that the composite bridge is 76 percent stiffer than the non-composite bridge. The slightly different values of relative stiffness suggest that the relative girder deflection depends on the location of loading and corresponding load distribution.

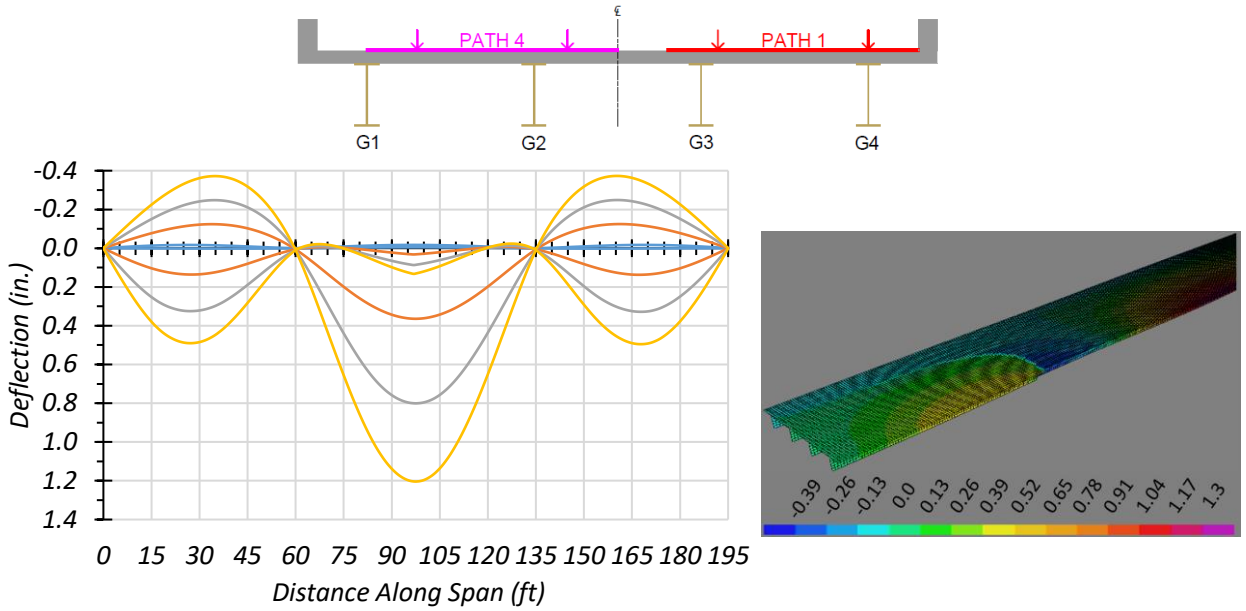

(a) Path 1

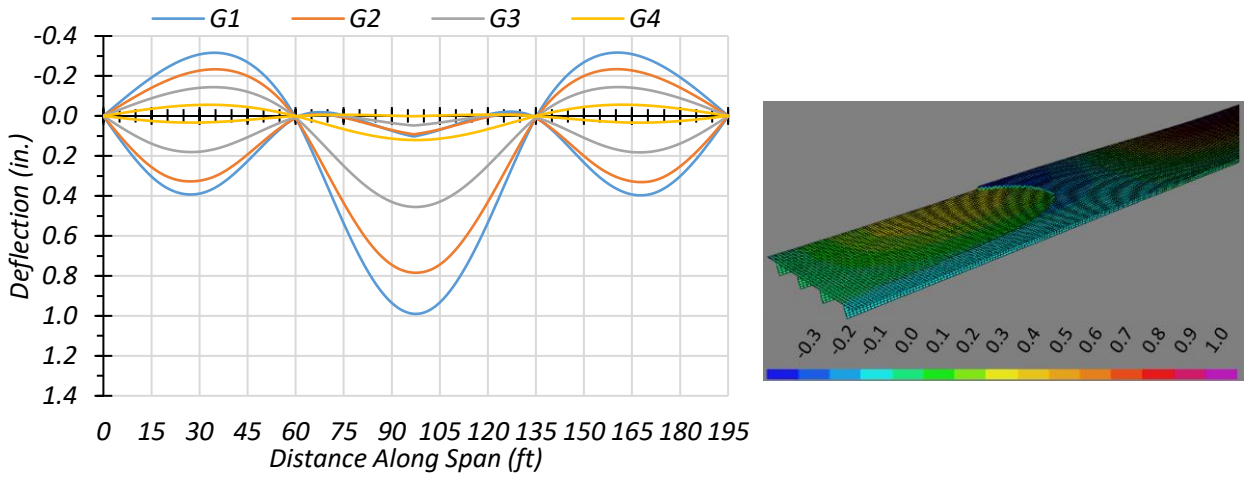

(b) Path 4

Figure 3.26. Deflection Profiles for Composite Bridge SC-12 with HL-93 Loading

Table 3.29. Maximum Deflections for Composite Bridge SC-12 with HL-93 Loading

Loading	Deflection Positive/Negative	G1	G2	G3	G4
Path 1	Positive	0.002	0.364	0.801	1.204
Path 1	Negative	−0.017	−0.125	−0.249	−0.373
Path 4	Positive	0.990	0.784	0.455	0.120
Path 4	Negative	−0.317	−0.234	−0.144	−0.056
Note: G = girder, paths indicate transverse loading positions as shown, deflections have inch units					

3.6.3.2 ***Positive Moment Results***

One-Lane Loading. Figure 3.27 shows the individual girder positive moment and positive moment LLDF results for the non-composite Bridge SC-12 under simulated moving HL-93 loading along three different one-lane loading paths. Table 3.30 provides the corresponding maximum positive moment values of each girder for each loading path. The positive moment LLDF values are calculated using the estimated positive moment results from the FEM analysis. Table 3.32 shows the governing positive moment LLDFs found using the FEM analysis and compares them to the AASHTO LLDF values. The first AASHTO LLDF value is calculated using the simplified stiffness parameter. The second AASHTO LLDF value is calculated using the analytical stiffness parameter calculated for the specific bridge. Compared to the FEM results, the governing positive moment LLDF value computed using the approximate equation and the simplified stiffness parameter in *AASHTO LRFD Specifications* (AASHTO 2017) is slightly conservative for interior girders, with a $g^m_{AASHTO\_S}/g^m_{FEM}$ ratio of 1.05, and conservative for exterior girders, with a $g^m_{AASHTO\_S}/g^m_{FEM}$ ratio of 1.14. Compared to the FEM results, the governing positive moment LLDF value computed using the approximate equations and the analytical stiffness parameter in *AASHTO LRFD Specifications* (AASHTO 2017) is almost the same for interior girders, with a $g^m_{AASHTO\_K}/g^m_{FEM}$ ratio of 1.01, and conservative for exterior girders, with a $g^m_{AASHTO\_K}/g^m_{FEM}$ ratio of 1.14.

Figure 3.28 shows the individual girder positive moment and positive moment LLDF results for the fully composite Bridge SC-12 under simulated moving HL-93 loading along the three one-lane loading paths. Table 3.31 provides the corresponding maximum positive moment values of each girder for each loading path. The positive moment LLDF values are calculated using the estimated positive moment results from the FEM analysis. Compared to the FEM results, the governing positive moment LLDF value computed using the approximate equation and the simplified stiffness parameter in *AASHTO LRFD Specifications* (AASHTO 2017) is almost the same for interior girders, with a $g^m_{AASHTO\_S}/g^m_{FEM}$ ratio of 1.01, and slightly conservative for exterior girders, with a $g^m_{AASHTO\_S}/g^m_{FEM}$ ratio 1.10. Compared to the FEM results, the governing positive moment LLDF value computed using the approximate equations and the analytical stiffness parameter in *AASHTO LRFD Specifications* (AASHTO 2017) is slightly unconservative

for interior girders, with a $g^m_{AASHTO\_K}/g^m_{FEM}$ ratio of 0.97, and slightly conservative for exterior girders, with a $g^m_{AASHTO\_K}/g^m_{FEM}$ ratio of 1.10.

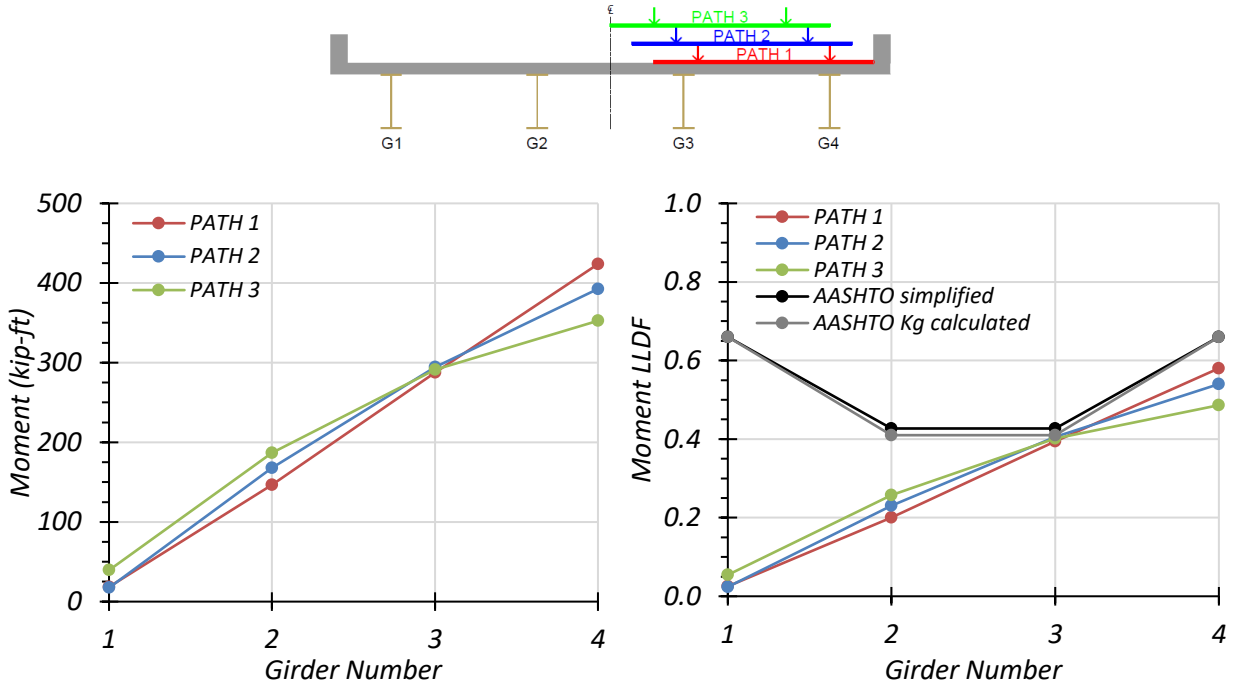

(a) Moment *(b) Moment LLDF*

Figure 3.27. Positive Moment Results for Non-Composite Bridge SC-12 with One-Lane HL-93 Loading

Table 3.30. Maximum Positive Moments for Non-Composite Bridge SC-12 with One-Lane HL-93 Loading

Loading	G1	G2	G3	G4
Path 1	18.4	146.6	287.6	423.7
Path 2	17.4	167.8	294.5	392.6
Path 3	39.4	186.8	291.1	352.6
Note: G = girder, paths indicate transverse loading positions as shown, moments have kip-ft units				

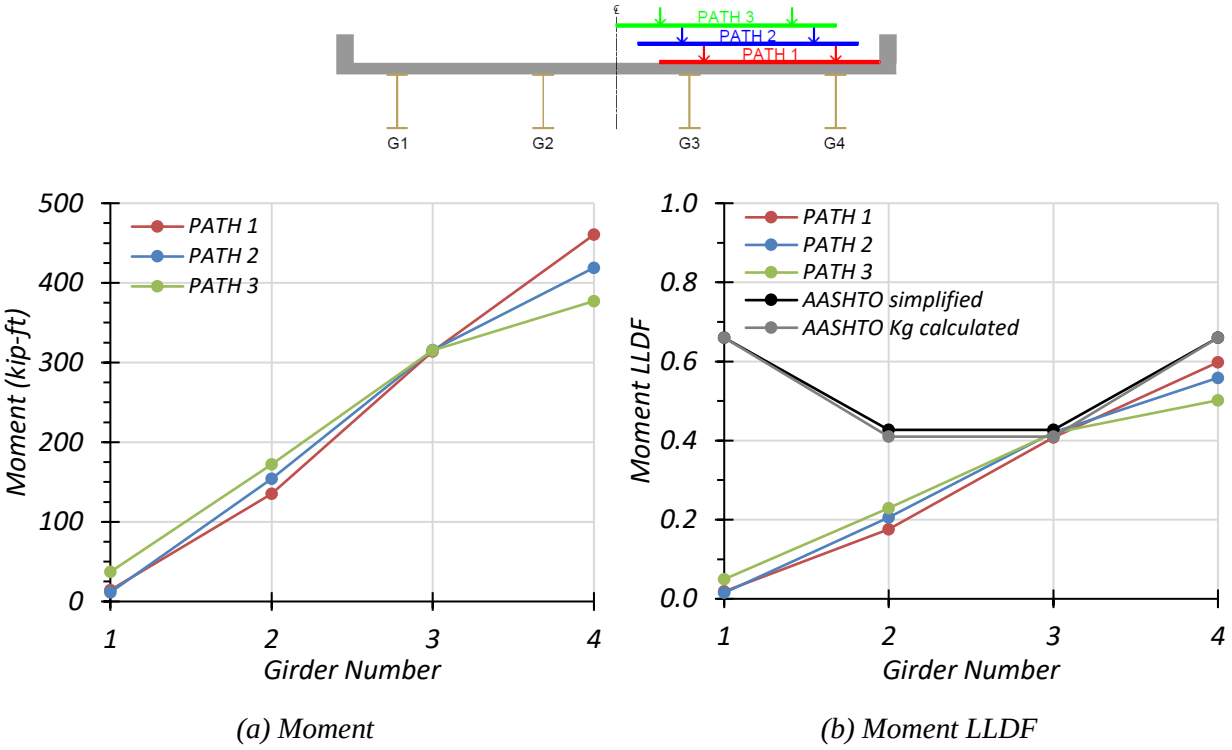

(a) Moment *(b) Moment LLDF*

Figure 3.28. Positive Moment Results for Composite Bridge SC-12 with One-Lane HL-93 Loading

Table 3.31. Maximum Positive Moments for Composite Bridge SC-12 with One-Lane HL-93 Loading

Loading	G1	G2	G3	G4
Path 1	14.3	135.4	313.9	460.5
Path 2	11.4	154.1	315.4	419.0
Path 3	37.1	172.3	315.1	377.1
Note: G = girder, paths indicate transverse loading positions as shown, moments have kip-ft units				

Comparison of governing positive moment LLDF values computed from FEM results for the composite and non-composite cases reveals that the maximum positive moment LLDF in an interior girder for the composite bridge is slightly higher than the one for the non-composite bridge, with a $g^m_{composite}/g^m_{non-composite}$ ratio of 1.04. The maximum positive moment LLDF in an exterior girder for the composite bridge is also slightly higher than the one for the non-composite bridge, with a $g^m_{composite}/g^m_{non-composite}$ ratio of 1.03.

Table 3.32. Governing Positive Moment LLDFs for Bridge SC-12 with One-Lane HL-93 Loading

Type	Girder Location	AASHTO Simplified ($g^m_{AASHTO\_S}$)	AASHTO K_g Calculated ($g^m_{AASHTO\_K}$)	FEM (g^m_{FEM})	$g^m_{AASHTO\_S}/g^m_{FEM}$	$g^m_{AASHTO\_K}/g^m_{FEM}$
Non-Composite	Interior	0.427	0.410	0.405	1.05	1.01
	Exterior	0.660	0.660	0.580	1.14	1.14
Composite	Interior	0.427	0.410	0.421	1.01	0.97
	Exterior	0.660	0.660	0.598	1.10	1.10

Two-Lane Loading. Figure 3.29 shows the individual girder positive moment and positive moment LLDF results for the non-composite Bridge SC-12 under simulated moving HL-93 loading along three two-lane loading paths. Table 3.33 provides the corresponding maximum positive moment values of each girder for each loading path. The positive moment LLDF values are calculated using the estimated positive moment results from the FEM analysis. Table 3.35 shows the governing positive moment LLDFs found using the FEM analysis and compares them to the AASHTO LLDF values. The first AASHTO LLDF value is calculated using the simplified stiffness parameter. The second AASHTO LLDF value is calculated using the analytical stiffness parameter calculated for the specific bridge. Compared to the FEM results, the governing positive moment LLDF value computed using the approximate equations and the simplified stiffness parameter in *AASHTO LRFD Specifications* (AASHTO 2017) is slightly conservative for interior girders, with a $g^m_{AASHTO\_S}/g^m_{FEM}$ ratio of 1.10, and conservative for exterior girders, with a $g^m_{AASHTO\_S}/g^m_{FEM}$ ratio of 1.18. Compared to the FEM results, the governing positive moment LLDF value computed using the approximate equations and the analytical stiffness parameter in *AASHTO LRFD Specifications* (AASHTO 2017) is slightly conservative for interior girders, with a $g^m_{AASHTO\_K}/g^m_{FEM}$ ratio of 1.05, and conservative for exterior girders, with a $g^m_{AASHTO\_K}/g^m_{FEM}$ ratio of 1.18.

Figure 3.30 shows the individual girder positive moment and positive moment LLDF results for the fully composite Bridge SC-12 under simulated moving HL-93 loading along three two-lane loading paths. Table 3.34 provides the corresponding maximum positive moment values of each girder for each loading path. The positive moment LLDF values are calculated using the estimated positive moment results from the FEM analysis. Compared to the FEM results, the governing positive moment LLDF value computed using the approximate equations and the

simplified stiffness parameter in *AASHTO LRFD Specifications* (AASHTO 2017) is slightly conservative for interior girders, with a $g^m_{AASHTO\_S}/g^m_{FEM}$ ratio of 1.08, and conservative for exterior girders, with a $g^m_{AASHTO\_S}/g^m_{FEM}$ ratio of 1.19. Compared to the FEM results, the governing positive moment LLDF value computed using the approximate equations and the analytical stiffness parameter in *AASHTO LRFD Specifications* (AASHTO 2017) is slightly conservative for interior girders, with a $g^m_{AASHTO\_K}/g^m_{FEM}$ ratio of 1.04, and conservative for exterior girders, with a $g^m_{AASHTO\_K}/g^m_{FEM}$ ratio of 1.19.

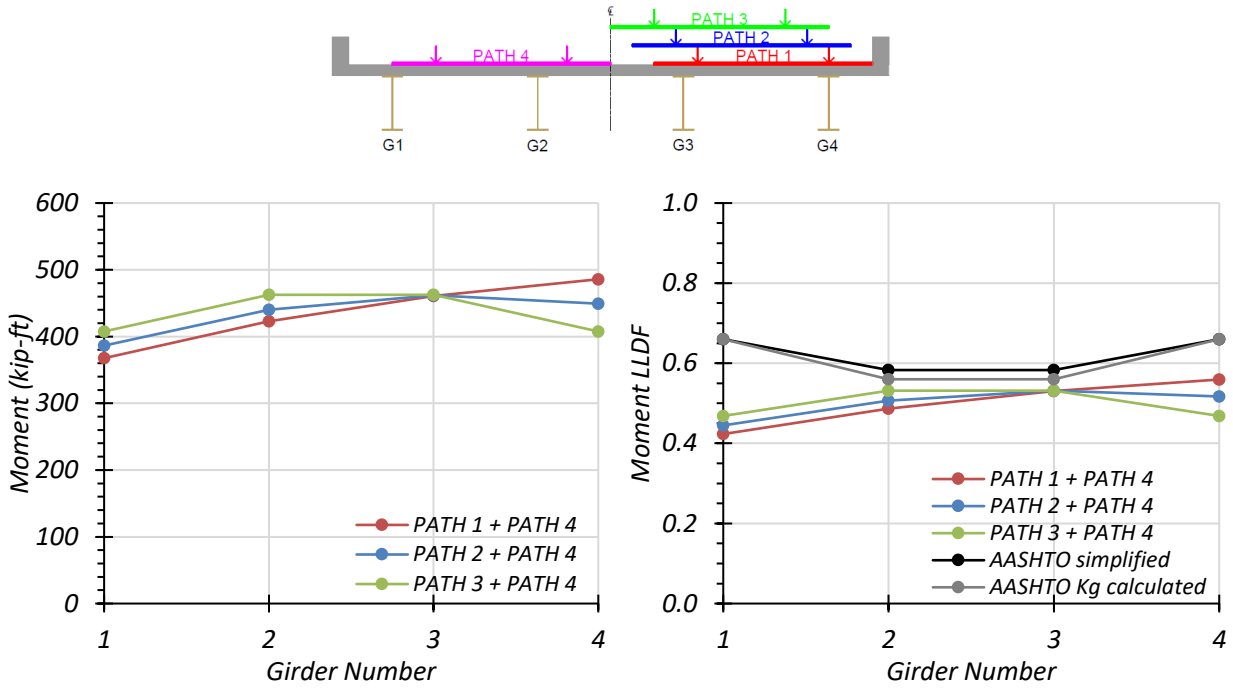

(a) Moment *(b) Moment LLDF*

Figure 3.29. Positive Moment Results for Non-Composite Bridge SC-12 with Two-Lane HL-93 Loading

Table 3.33. Maximum Positive Moments for Non-Composite Bridge SC-12 with Two-Lane HL-93 Loading

Loading	G1	G2	G3	G4
Path 1 + Path 4	367.6	423.0	460.7	485.9
Path 2 + Path 4	386.5	440.1	461.8	449.1
Path 3 + Path 4	407.6	462.5	462.5	407.6
Note: G = girder, paths indicate transverse loading positions as shown, moments have kip-ft units				

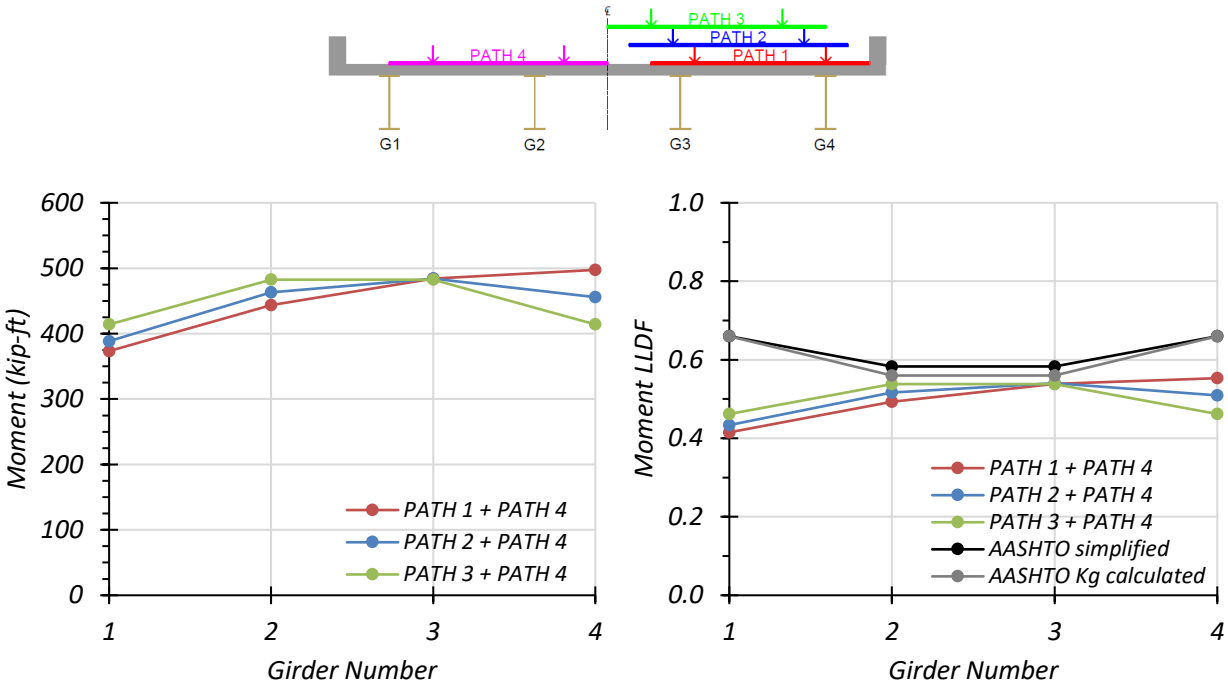

(a) Moment *(b) Moment LLDF*

Figure 3.30. Positive Moment Results for Composite Bridge SC-12 with Two-Lane HL-93 Loading

Table 3.34. Maximum Positive Moments for Composite Bridge SC-12 with Two-Lane HL-93 Loading

Loading	G1	G2	G3	G4
Path 1 + Path 4	373.3	443.6	484.1	497.4
Path 2 + Path 4	388.4	462.9	484.1	456.0
Path 3 + Path 4	414.1	482.4	482.4	414.1
Note: G = girder, paths indicate transverse loading positions as shown, moments have kip-ft units				

Comparison of governing positive moment LLDF values computed from FEM results for the composite and non-composite cases reveals that the maximum positive moment LLDF in both interior and exterior girders for the composite bridge is almost the same as the one for the non-composite bridge, with a $g^m_{composite}/g^m_{non-composite}$ ratio of 1.02 and 0.99, respectively.

Table 3.35. Governing Positive Moment LLDFs for Bridge SC-12 with Two-Lane HL-93 Loading

Type	Girder Location	AASHTO Simplified ($g^m_{AASHTO\_S}$)	AASHTO K_g Calculated ($g^m_{AASHTO\_K}$)	FEM (g^m_{FEM})	$g^m_{AASHTO\_S}/g^m_{FEM}$	$g^m_{AASHTO\_K}/g^m_{FEM}$
Non-Composite	Interior	0.583	0.560	0.532	1.10	1.05
	Exterior	0.660	0.660	0.559	1.18	1.18
Composite	Interior	0.583	0.560	0.540	1.08	1.04
	Exterior	0.660	0.660	0.553	1.19	1.19

3.6.3.3 Negative Moment Results

One-Lane Loading. Figure 3.31 shows the individual girder negative moment and negative moment LLDF results for the non-composite Bridge SC-12 under simulated moving HL-93 loading along three one-lane loading paths. Table 3.36 provides the corresponding maximum negative moment values of each girder for each loading path. The negative moment LLDF values are calculated using the estimated negative moment results from the FEM analysis. Table 3.38 shows the governing negative moment LLDFs found using the FEM analysis and compares them to the AASHTO LLDF values. The first AASHTO LLDF value is calculated using the simplified stiffness parameter. The second AASHTO LLDF value is calculated using the analytical stiffness parameter calculated for the specific bridge. Compared to the FEM results, the governing negative moment LLDF value computed using the approximate equations and the simplified stiffness parameter in *AASHTO LRFD Specifications* (AASHTO 2017) is slightly conservative for both interior and exterior girders, with a $g^m_{AASHTO\_S}/g^m_{FEM}$ ratio of 1.04 and 1.08, respectively. Compared to the FEM results, the governing negative moment LLDF value computed using the approximate equations and the analytical stiffness parameter in *AASHTO LRFD Specifications* (AASHTO 2017) is almost the same for interior girders, with a $g^m_{AASHTO\_K}/g^m_{FEM}$ ratio of 1.00, and slightly conservative for exterior girders, with a $g^m_{AASHTO\_K}/g^m_{FEM}$ ratio of 1.08.

Figure 3.32 shows the individual girder negative moment and negative moment LLDF results for the fully composite Bridge SC-12 under simulated moving HL-93 loading along three one-lane loading paths. Table 3.37 provides the corresponding maximum negative moment values of each girder for each loading path. The negative moment LLDF values are calculated using the estimated negative moment results from the FEM analysis. Compared to the FEM results, the governing negative moment LLDF value computed using the approximate equation and the simplified stiffness parameter in the *AASHTO LRFD Specifications* (AASHTO 2017) is almost the same for interior girders, with a $g^m_{AASHTO\_S}/g^m_{FEM}$ ratio of 0.99, and is slightly conservative for exterior girders, with a $g^m_{AASHTO\_S}/g^m_{FEM}$ ratio of 1.07. Compared to the FEM results, the governing negative moment LLDF value computed using the approximate equation and the analytical stiffness parameter in *AASHTO LRFD Specifications* (AASHTO 2017) is slightly unconservative for interior girders, with a $g^m_{AASHTO\_K}/g^m_{FEM}$ ratio of 0.96, and slightly conservative for exterior girders, with a $g^m_{AASHTO\_K}/g^m_{FEM}$ ratio of 1.07.

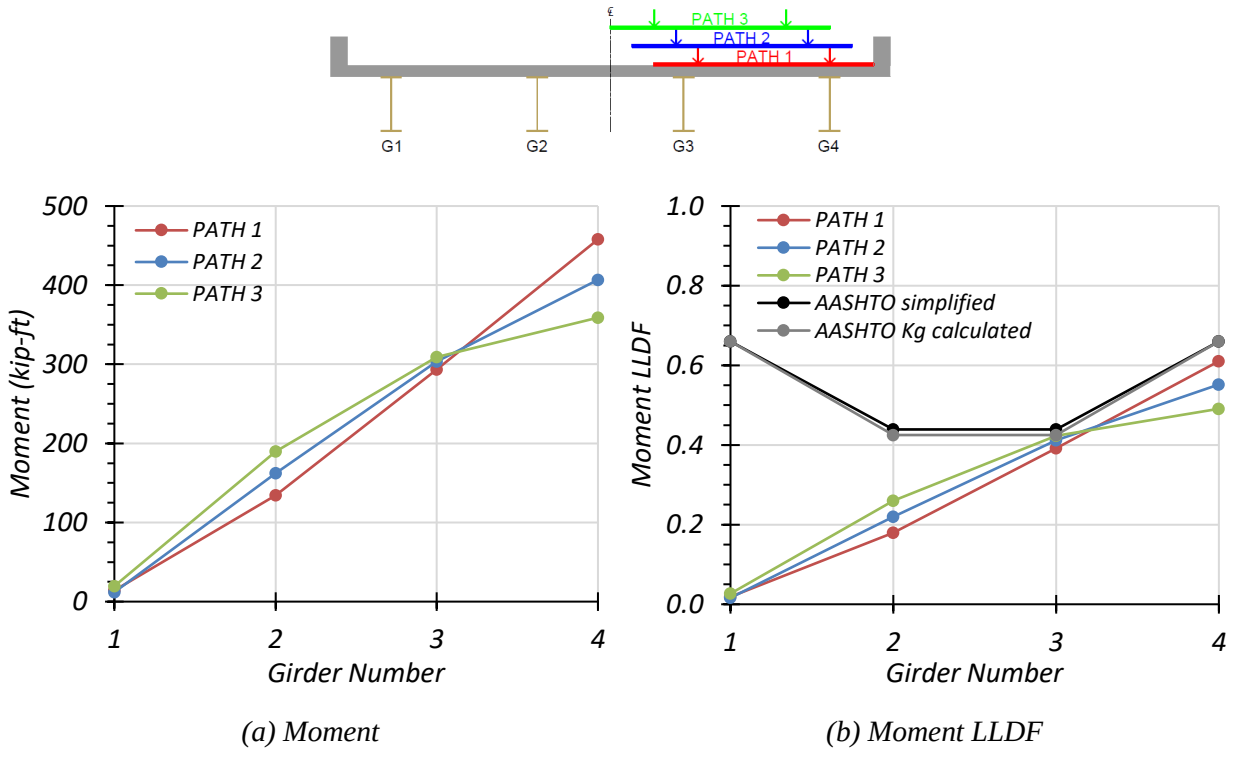

(a) Moment *(b) Moment LLDF*

Figure 3.31. Negative Moment Results for Non-Composite Bridge SC-12 with One-Lane HL-93 Loading

Table 3.36. Maximum Negative Moments for Non-Composite Bridge SC-12 with One-Lane HL-93 Loading

Loading	G1	G2	G3	G4
Path 1	14.1	134.5	293.5	457.8
Path 2	11.9	162.1	303.6	406.8
Path 3	19.6	189.8	309.1	358.9
Note: G = girder, paths indicate transverse loading positions as shown, moments have kip-ft units				

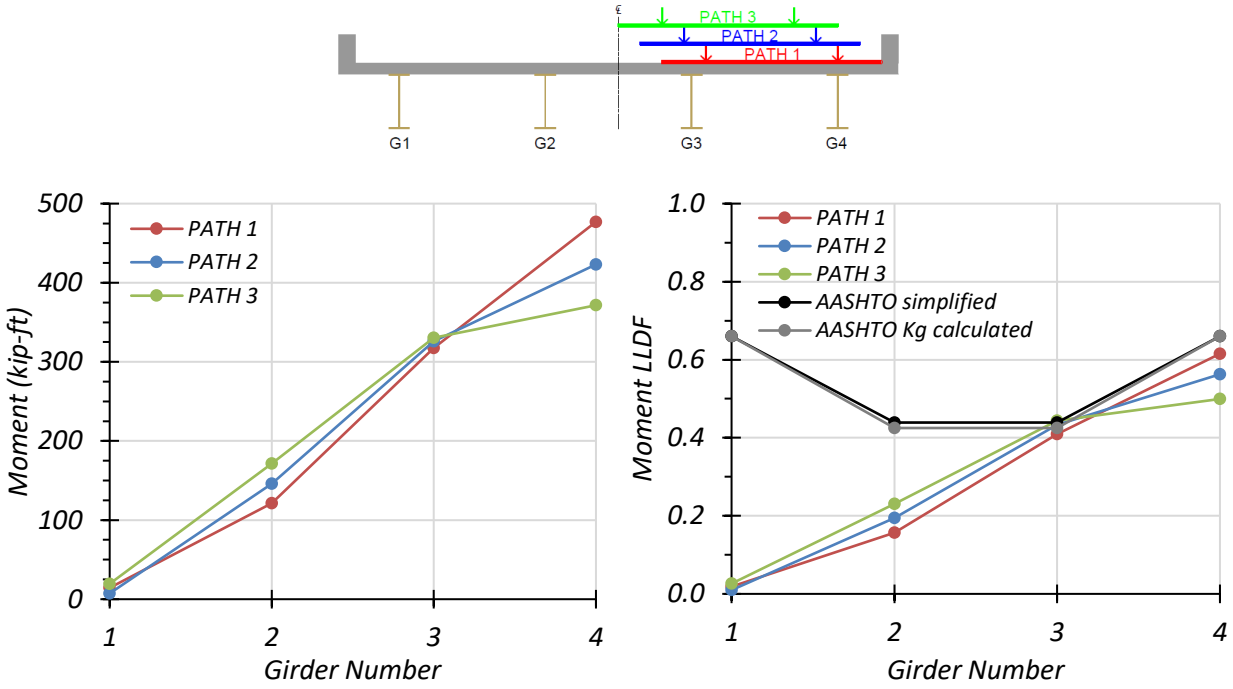

(a) Moment *(b) Moment LLDF*

Figure 3.32. Negative Moment Results for Composite Bridge SC-12 with One-Lane HL-93 Loading

Table 3.37. Maximum Negative Moments for Composite Bridge SC-12 with One-Lane HL-93 Loading

Loading	G1	G2	G3	G4
Path 1	14.4	121.4	317.4	477.0
Path 2	7.3	146.0	325.8	423.1
Path 3	19.5	171.3	330.3	371.5
Note: G = girder, paths indicate transverse loading positions as shown, moments have kip-ft units				

Comparison of governing negative moment LLDF values computed from FEM results for the composite and non-composite cases reveals that the maximum negative moment LLDF in an interior girder for the composite bridge is higher than the one for the non-composite bridge, with a $g^m_{composite}/g^m_{non-composite}$ ratio of 1.05. The maximum negative moment LLDF in an exterior girder for the composite bridge is almost the same as the one for the non-composite bridge, with a $g^m_{composite}/g^m_{non-composite}$ ratio of 1.01.

Table 3.38. Governing Negative Moment LLDFs for Bridge SC-12 with One-Lane HL-93 Loading

Type	Girder Location	AASHTO Simplified ($g^m_{AASHTO\_S}$)	AASHTO K_g Calculated ($g^m_{AASHTO\_K}$)	FEM (g^m_{FEM})	$g^m_{AASHTO\_S}/g^m_{FEM}$	$g^m_{AASHTO\_K}/g^m_{FEM}$
Non-Composite	Interior	0.439	0.425	0.423	1.04	1.00
	Exterior	0.660	0.660	0.610	1.08	1.08
Composite	Interior	0.439	0.425	0.444	0.99	0.96
	Exterior	0.660	0.660	0.615	1.07	1.07

Two-Lane Loading. Figure 3.33 shows the individual girder negative moments and negative moment LLDF results for the non-composite Bridge SC-12 under simulated moving HL-93 loading along three two-lane loading paths. Table 3.39 provides the corresponding maximum negative moment values of each girder for each loading path. The negative moment LLDF values are calculated using the estimated negative moment results from the FEM analysis. Table 3.41 shows the governing negative moment LLDFs found using the FEM analysis and compares them to the AASHTO LLDF values. The first AASHTO LLDF value is calculated using the simplified stiffness parameter. The second AASHTO LLDF value is calculated using the analytical stiffness parameter calculated for the specific bridge. Compared to the FEM results, the governing negative moment LLDF value computed using the approximate equations and the simplified stiffness parameter in *AASHTO LRFD Specifications* (AASHTO 2017) is slightly conservative for interior girders, with a $g^m_{AASHTO\_S}/g^m_{FEM}$ ratio of 1.07, and is conservative for exterior girders, with a $g^m_{AASHTO\_S}/g^m_{FEM}$ ratio of 1.18. Compared to the FEM results, the governing negative moment LLDF value computed using the approximate equations and the analytical stiffness parameter in *AASHTO LRFD Specifications* (AASHTO 2017) is slightly conservative for interior girders, with

a $g^m_{AASHTO\_K}/g^m_{FEM}$ ratio of 1.04, and is conservative for exterior girders, with a $g^m_{AASHTO\_K}/g^m_{FEM}$ ratio of 1.18.

Figure 3.34 shows the individual girder negative moment and negative moment LLDF results for the fully composite Bridge SC-12 under simulated moving HL-93 loading along three two-lane loading paths. Table 3.40 provides the corresponding maximum negative moment values of each girder for each loading path. The negative moment LLDF values are calculated using the estimated negative moment results from the FEM analysis. Compared to the FEM results, the governing negative moment LLDF value computed using the approximate equations and the simplified stiffness parameter in *AASHTO LRFD Specifications* (AASHTO 2017) is slightly conservative for interior girders, with a $g^m_{AASHTO\_S}/g^m_{FEM}$ ratio of 1.06, and conservative for exterior girders, with a $g^m_{AASHTO\_S}/g^m_{FEM}$ ratio of 1.20. Compared to the FEM results, the governing negative moment LLDF value computed using the approximate equations and the analytical stiffness parameter in *AASHTO LRFD Specifications* (AASHTO 2017) is almost the same for interior girders, with a $g^m_{AASHTO\_K}/g^m_{FEM}$ ratio of 1.02, and is conservative for exterior girders, with a $g^m_{AASHTO\_K}/g^m_{FEM}$ ratio of 1.20.

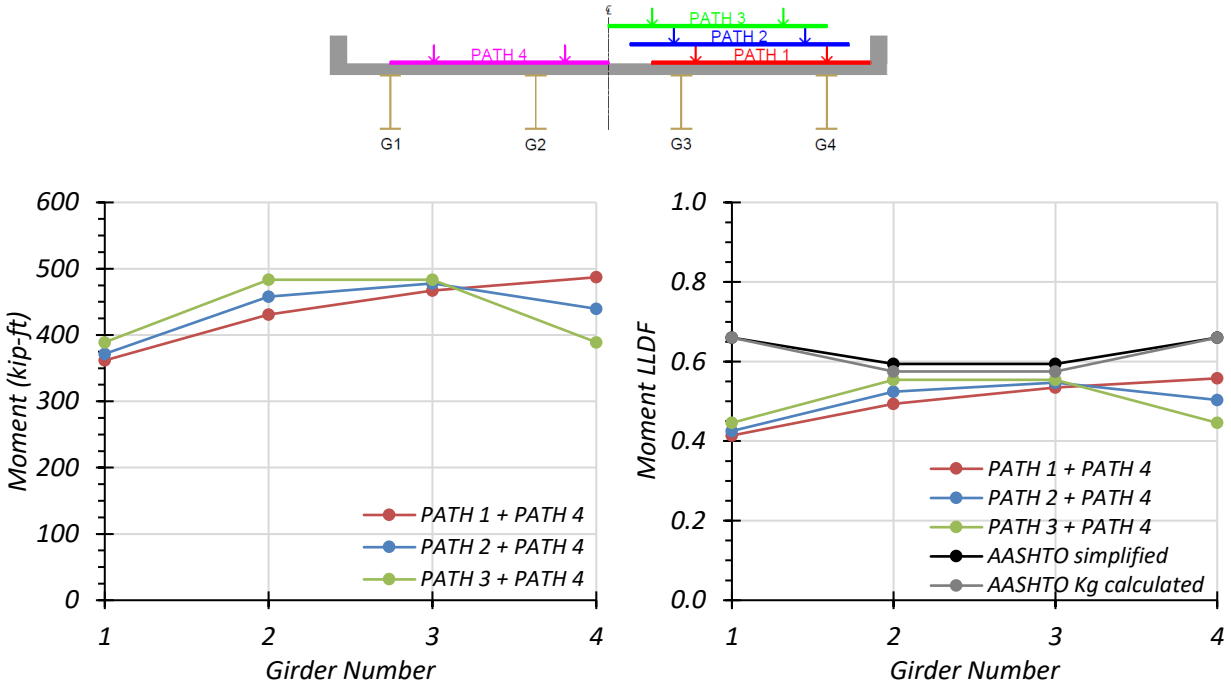

(a) Moment *(b) Moment LLDF*

Figure 3.33. Negative Moment Results for Non-Composite Bridge SC-12 with Two-Lane HL-93 Loading

Table 3.39. Maximum Negative Moments for Non-Composite Bridge SC-12 with Two-Lane HL-93 Loading

Loading	G1	G2	G3	G4
Path 1 + Path 4	361.7	430.9	466.9	487.1
Path 2 + Path 4	371.6	458.1	477.8	439.3
Path 3 + Path 4	389.1	483.4	483.4	389.1
Note: G = girder, paths indicate transverse loading positions as shown, moments have kip-ft units				

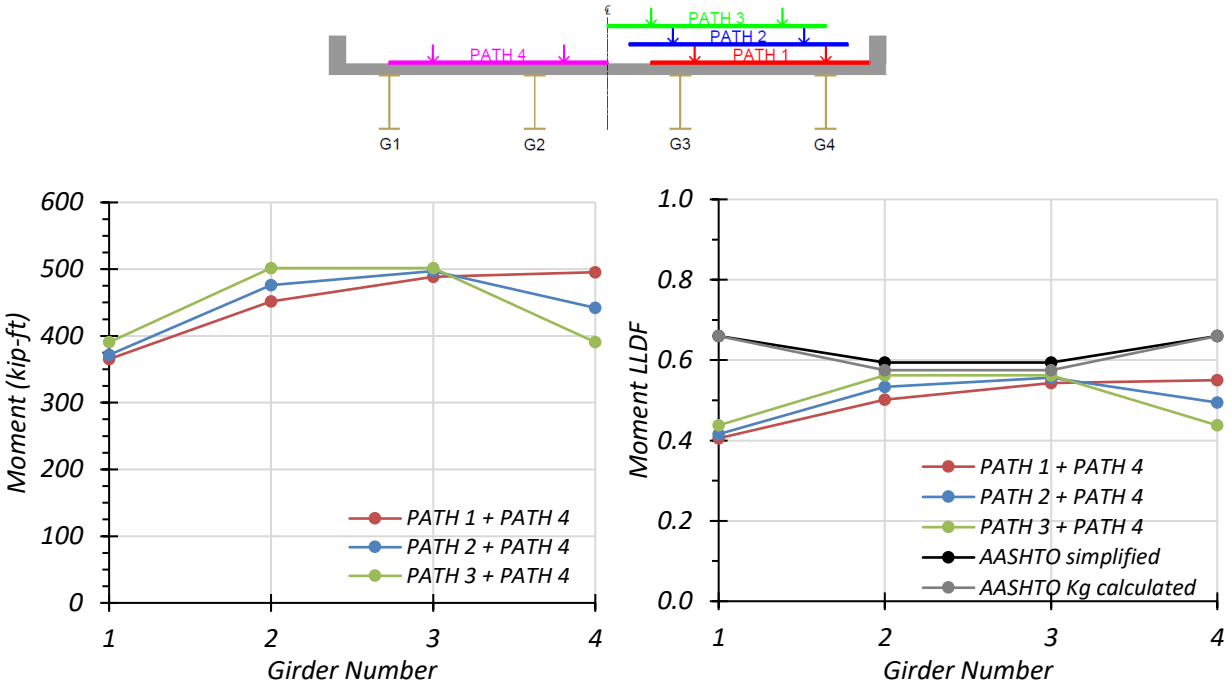

(a) Moment *(b) Moment LLDF*

Figure 3.34. Negative Moment Results for Composite Bridge SC-12 with Two-Lane HL-93 Loading

Table 3.40. Maximum Negative Moments for Composite Bridge SC-12 with Two-Lane HL-93 Loading

Loading	G1	G2	G3	G4
Path 1 + Path 4	365.3	451.7	488.7	495.5
Path 2 + Path 4	371.5	476.3	497.1	441.9
Path 3 + Path 4	390.6	501.6	501.6	390.6
Note: G = girder, paths indicate transverse loading positions as shown, moments have kip-ft units				

Comparison of governing negative moment LLDF values computed from FEM results for the composite and non-composite cases reveals that the maximum negative moment LLDF in an interior and exterior girder for the composite bridge is almost the same as the one for the non-composite bridge, with a $g^m_{composite}/g^m_{non-composite}$ ratio of 1.01 and 0.99, respectively.

Table 3.41. Governing Negative Moment LLDFs for Bridge SC-12 with Two-Lane HL-93 Loading

Type	Girder Location	AASHTO Simplified ($g^m_{AASHTO\_S}$)	AASHTO K_g Calculated ($g^m_{AASHTO\_K}$)	FEM (g^m_{FEM})	$g^m_{AASHTO\_S}/g^m_{FEM}$	$g^m_{AASHTO\_K}/g^m_{FEM}$
Non-Composite	Interior	0.594	0.575	0.554	1.07	1.04
	Exterior	0.660	0.660	0.558	1.18	1.18
Composite	Interior	0.594	0.575	0.562	1.06	1.02
	Exterior	0.660	0.660	0.550	1.20	1.20

*3.6.3.4 **Shear Results***

One-Lane Loading. Figure 3.35 shows the individual girder shears and shear LLDF results for the non-composite Bridge SC-12 under simulated moving HL-93 loading along three different one-lane loading paths. Table 3.42 provides the corresponding maximum shear values of each girder for each loading path. The shear LLDF values are calculated using the estimated shear results from the FEM analysis. Table 3.44 shows the governing shear LLDFs found using the FEM analysis and compares them to the AASHTO LLDF values. Compared to the FEM results, the governing shear LLDF value computed using the approximate equations in *AASHTO LRFD Specifications* (AASHTO 2017) is conservative for interior girders, with a g^v_{AASHTO}/g^v_{FEM} ratio of 1.24, and is slightly conservative for exterior girders, with a g^v_{AASHTO}/g^v_{FEM} ratio of 1.07.

Figure 3.36 shows the individual girder shears and shear LLDF results for the fully composite Bridge SC-12 under simulated moving HL-93 loading along three one-lane loading paths. Table 3.43 provides the corresponding maximum shear values of each girder for each loading path. The shear LLDF values are calculated using the estimated shear results from the FEM analysis. Compared to the FEM results, the governing shear LLDF value computed using the approximate equations in *AASHTO LRFD Specifications* (AASHTO 2017) is conservative for interior girders, with a g^v_{AASHTO}/g^v_{FEM} ratio of 1.16, and is slightly conservative for exterior girders, with a g^v_{AASHTO}/g^v_{FEM} ratio of 1.06.

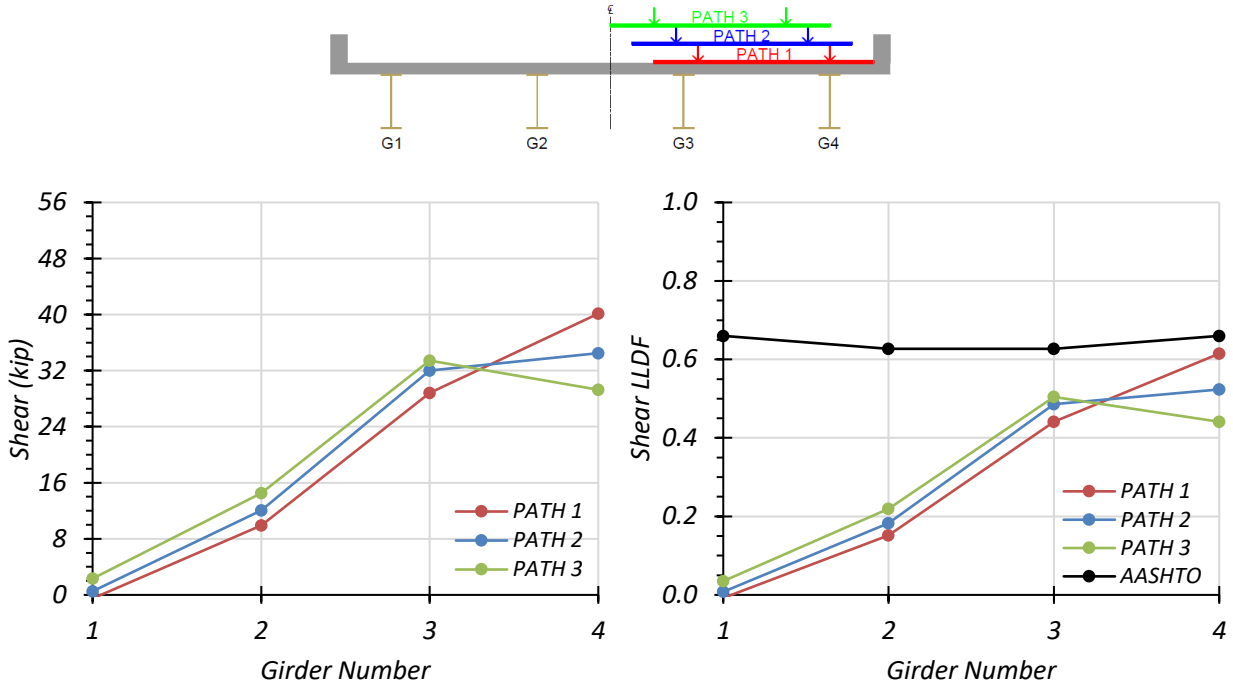

(a) Shear *(b) Shear LLDF*

Figure 3.35. Shear Results for Non-Composite Bridge SC-12 with One-Lane HL-93 Loading

Table 3.42. Maximum Shears for Non-Composite Bridge SC-12 with One-Lane HL-93 Loading

Loading	G1	G2	G3	G4
Path 1	-0.5	9.9	28.8	40.1
Path 2	0.5	12.0	32.0	34.5
Path 3	2.3	14.5	33.4	29.3
Note: G = girder, paths indicate transverse loading positions as shown, shears have kip units				

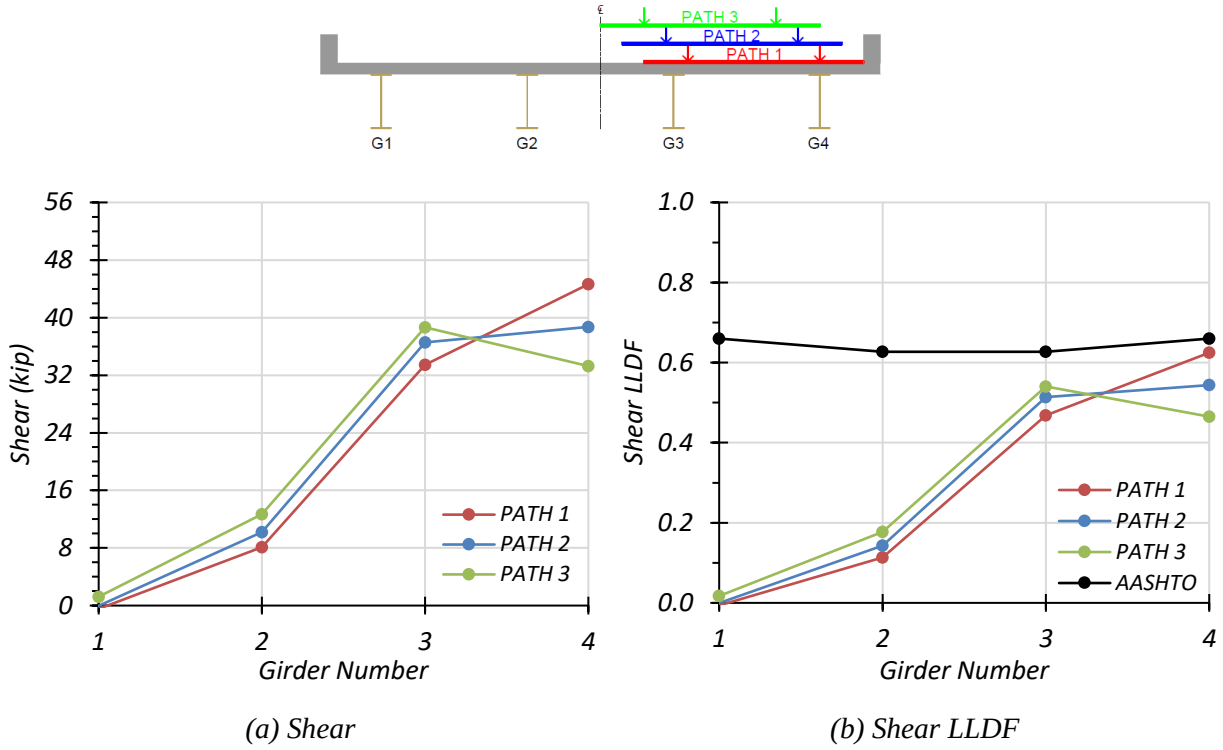

(a) Shear *(b) Shear LLDF*

Figure 3.36. Shear Results for Composite Bridge SC-12 with One-Lane HL-93 Loading

Table 3.43. Maximum Shears for Composite Bridge SC-12 with One-Lane HL-93 Loading

Loading	G1	G2	G3	G4
Path 1	−0.5	8.1	33.4	44.6
Path 2	0.0	10.2	36.5	38.7
Path 3	1.2	12.7	38.6	33.3
Note: G = girder, paths indicate transverse loading positions as shown, shears have kip units				

Comparison of governing shear LLDF values computed from FEM results for the composite and non-composite cases reveals that the maximum shear LLDF in an interior girder for the composite bridge is slightly higher than the one for the non-composite bridge, with a $g^v_{composite}/g^v_{non-composite}$ ratio of 1.07. The maximum shear LLDF in an exterior girder for the composite bridge is almost the same as the one for the non-composite bridge, with a $g^v_{composite}/g^v_{non-composite}$ ratio of 1.02.

Table 3.44. Governing Shear LLDFs for Bridge SC-12 with One-Lane HL-93 Loading

Type	Girder Location	AASHTO (g^v_{AASHTO})	FEM (g^v_{FEM})	g^v_{AASHTO}/g^v_{FEM}
Non-Composite	Interior	0.627	0.504	1.24
	Exterior	0.660	0.615	1.07
Composite	Interior	0.627	0.540	1.16
	Exterior	0.660	0.625	1.06

Two-Lane Loading. The same procedure was conducted for two-lane loading. Figure 3.37 shows the individual girder shears and shear LLDF results for the non-composite Bridge SC-12 under simulated moving HL-93 loading along the three two-lane loading paths. Table 3.45 provides the corresponding maximum shear values of each girder for each loading path. The shear LLDF values are calculated using the estimated shear results from the FEM analysis. Table 3.47 shows the governing shear LLDFs found using the FEM analysis and compares them to the AASHTO LLDF values. Compared to the FEM results, the governing shear LLDF value computed using the approximate equations in *AASHTO LRFD Specifications* (AASHTO 2017) is conservative for interior girders, with a g^v_{AASHTO}/g^v_{FEM} ratio of 1.20, and is quite conservative for exterior girders, with a g^v_{AASHTO}/g^v_{FEM} ratio of 1.32.

Figure 3.38 shows the individual girder shears and shear LLDF results for the fully composite Bridge SC-12 under simulated moving HL-93 loading along three one-lane loading paths. Table 3.46 provides the corresponding maximum shear values of each girder for each loading path. The shear LLDF values are calculated using the estimated shear results from the FEM analysis. Compared to the FEM results, the governing shear LLDF value computed using the approximate equations in *AASHTO LRFD Specifications* (AASHTO 2017) is conservative for interior girders, with a g^v_{AASHTO}/g^v_{FEM} ratio of 1.20, and is quite conservative for exterior girders, with a g^v_{AASHTO}/g^v_{FEM} ratio of 1.34.

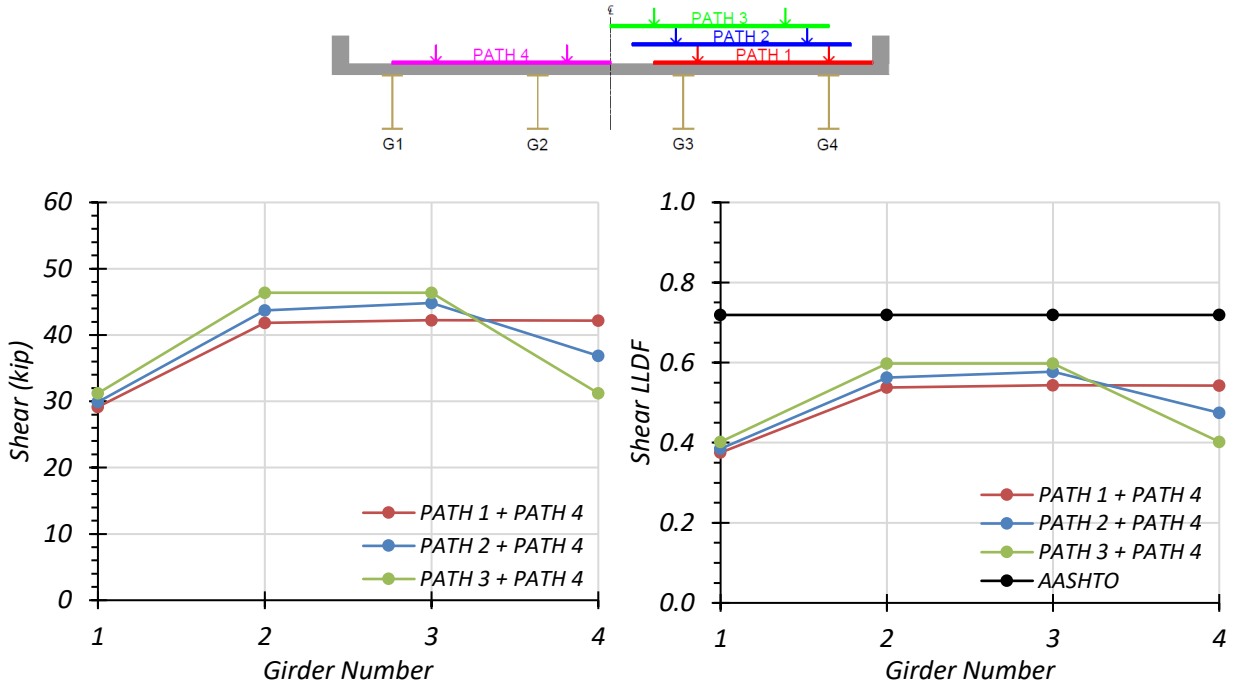

(a) Shear *(b) Shear LLDF*

Figure 3.37. Shear Results for Non-Composite Bridge SC-12 with Two-Lane HL-93 Loading

Table 3.45. Maximum Shear Forces for Non-Composite Bridge SC-12 with Two-Lane HL-93 Loading

Loading	G1	G2	G3	G4
Path 1 + Path 4	29.2	41.8	42.2	42.2
Path 2 + Path 4	29.9	43.7	44.8	36.9
Path 3 + Path 4	31.2	46.4	46.4	31.2
Note: G = girder, paths indicate transverse loading positions as shown, shears have kip units				

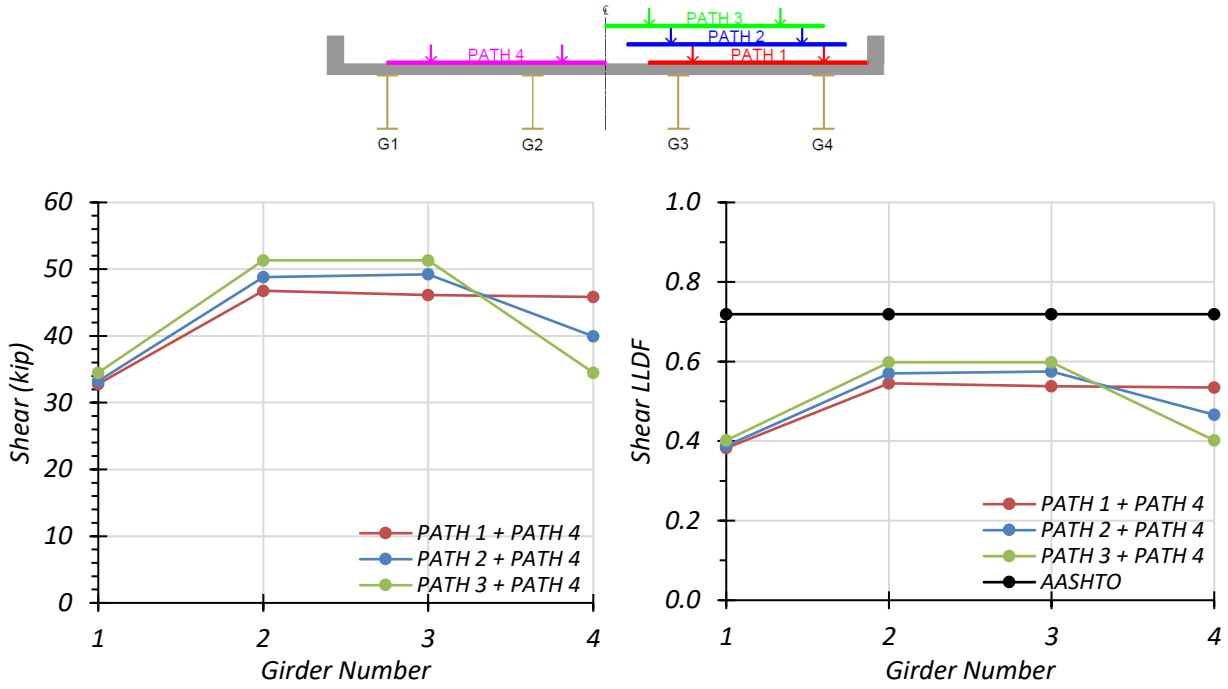

(a) Shear *(b) Shear LLDF*

Figure 3.38. Shear Results for Composite Bridge SC-12 with Two-Lane HL-93 Loading

Table 3.46. Maximum Shear Forces for Composite Bridge SC-12 with Two-Lane HL-93 Loading

Loading	G1	G2	G3	G4
Path 1 + Path 4	32.8	46.8	46.1	45.8
Path 2 + Path 4	33.2	48.8	49.2	39.9
Path 3 + Path 4	34.5	51.3	51.3	34.5
Note: G = girder, paths indicate transverse loading positions as shown, shears have kip units				

Comparison of governing shear LLDF values computed from FEM results for the composite and non-composite cases reveals that the maximum shear LLDF in an interior girder for the composite bridge is the same as the one for the non-composite bridge, with a $g^v_{composite}/g^v_{non-composite}$ ratio of 1.00. However, the maximum shear LLDF in an exterior girder for the composite bridge is also almost the same as the one for the non-composite bridge, with a $g^v_{composite}/g^v_{non-composite}$ ratio of 0.99.

Table 3.47. Governing Shear LLDFs for Bridge SC-12 with Two-Lane HL-93 Loading

Type	Girder Location	AASHTO (g^v_{AASHTO})	FEM (g^v_{FEM})	g^v_{AASHTO}/g^v_{FEM}
Non-Composite	Interior	0.719	0.598	1.20
	Exterior	0.719	0.543	1.32
Composite	Interior	0.719	0.598	1.20
	Exterior	0.719	0.535	1.34

3.7 CONCLUSIONS

3.7.1 Live Load Distribution Factors

3.7.1.1 AASHTO Standard Specifications LLDFs

The FEM analysis of the selected continuous steel multi-girder bridge has shown that, in general, the current LLDF equations given in the *AASHTO Standard Specifications* (AASHTO 2002) provide conservative, mostly accurate LLDF values in positive flexure for the selected bridge. The g_{AASHTO}/g_{FEM} ratio for positive flexure ranges from 1.09 to 1.43, with most cases within 0.25 of 1.0. The negative LLDF values obtained from the FEM analysis produce a very similar result, with the g_{AASHTO}/g_{FEM} ratio ranging from 1.07 to 1.40, with most cases between 0.80 and 1.20. Because these results are conservative—but not overly conservative for the most part—possible changes to the LLDFs are not likely to significantly affect HS-20 load ratings of this bridge type.

For the shear LLDF values obtained from the FEM analysis, the g_{AASHTO}/g_{FEM} ratio ranges from 1.02 to 1.17, producing a lower range of results than for flexure. Again, this result is unlikely to significantly change HS-20 load ratings.

3.7.1.2 AASHTO LRFD Specifications LLDFs

The FEM analysis of the selected continuous steel multi-girder bridge has shown that, in general, the current LLDF equations given in the *AASHTO LRFD Specifications* (AASHTO 2017) provide fairly accurate LLDF values in positive flexure for the selected bridge. The g_{AASHTO}/g_{FEM} ratio for positive flexure using the simplified stiffness parameter ranges from 1.01 to 1.19, and in every case is above 1.0. The g_{AASHTO}/g_{FEM} ratio for positive flexure using the calculated stiffness parameter ranges from 0.97 to 1.19 and is only below 1.0 for one case. A similar trend holds true

for negative flexure. The g_{AASHTO}/g_{FEM} ratio for negative flexure using the simplified stiffness parameter ranges from 0.99 to 1.20 and is only below 1.0 for one case. The g_{AASHTO}/g_{FEM} ratio for negative flexure using the calculated stiffness parameter ranges from 0.96 to 1.20 and is only below 1.0 for one case. Because these results are accurate for most cases, potential changes to LLDFs are not likely to significantly affect HL-93 load ratings for this bridge type.

For the shear LLDF values obtained from the FEM analysis, the g_{AASHTO}/g_{FEM} ratio ranges from 1.06 to 1.34, producing slightly conservative results. The LRFR shear LLDFs could possibly be modified in order to increase the LRFR shear RFs of bridges.

3.7.2 Composite Action

In regard to the effect of analyzing the bridge as fully composite or fully non-composite with respect to LLDFs, the FEM analysis did not find a significant difference. For the most part, the LLDFs found were very similar; however, the non-composite bridge seemed to exhibit more uniform LLDF profiles across the bridge transverse section.

For HS-20 loading, the $g_{composite}/g_{non-composite}$ ratio for positive flexure ranged from 0.96 to 1.08, the $g_{composite}/g_{non-composite}$ ratio for negative flexure ranged from 0.98 to 1.11, and the $g_{composite}/g_{non-composite}$ ratio for shear ranged from 0.97 to 1.09. The $g_{composite}/g_{non-composite}$ ratio for an interior girder was always above 1.0. For an exterior girder, it was always above 1.0 for one-lane loading and below 1.0 for two-lane loading.

An examination of HL-93 loading showed the $g_{composite}/g_{non-composite}$ ratio for positive flexure ranged from 0.99 to 1.04, the $g_{composite}/g_{non-composite}$ ratio for negative flexure ranged from 0.99 to 1.05, and the $g_{composite}/g_{non-composite}$ ratio for shear ranged from 0.99 to 1.07. The $g_{composite}/g_{non-composite}$ ratio for an interior girder was always above 1.0. For an exterior girder, it was always above 1.0 for one-lane loading and below 1.0 for two-lane loading. Between the HS-20 loading and the HL-93 loading, the ratios did not significantly change for the same number of lanes loaded and force being examined.

In terms of LLDFs, composite action does not seem to have a major effect; however, it is known that composite action or partial composite action significantly affects the positive moment capacity of the bridge. This effect was noticed in the FEM analysis through the stress values computed for the girders. The effect of partial composite action on load rating will be further

explored in the next task, wherein any partial composite measured during field testing will be used to help calibrate the FEM models, which can then be used to develop a more refined load rating of the bridge.

3.7.3 Additional Comments

Additional results reported from the FEM modeling will be used to calibrate the FEM model after field testing is complete. The results presented in this report for deflections and dynamic characteristics will be compared to those found in the field to determine if the girders are acting compositely or non-compositely.

The results of the stiffness adjustment analysis are also useful in identifying the effects of deck cracking on the maximum positive and negative moments that may occur in the actual bridge. If, during testing, the bridge exhibits behavior that indicates a reduced stiffness due to deck cracking, a stiffness reduction could be used in the calibrated FEM model to further investigate the impact on load rating.

4 ANALYSIS OF A SIMPLE-SPAN CONCRETE MULTI-GIRDER BRIDGE

In the previous tasks, a detailed review and synthesis of the population of load-posted bridges in Texas was conducted, and 14 simple-span concrete multi-girder (CM) bridges were selected from the inventory of SSLO concrete multi-girder bridges in Texas for basic load rating evaluation. This basic load rating analysis helped to identify several areas of opportunity for refined load rating analysis. Refined load rating analysis investigates the effect of the identified parameters using three-dimensional finite element models that can more accurately capture the actual bridge behavior. The main objective of FEM analysis of the simple-span concrete multi-girder bridge is to accurately capture the distribution of live load between girders.

4.1 INTRODUCTION

A typical load-posted simple-span concrete multi-girder bridge was selected as a representative case study to further investigate the identified objectives. Table 4.1 lists some of the key parameters for the selected bridge to be modeled and for the average SSLO simple-span concrete multi-girder bridge in Texas. In this table, the Operating HS-20 RF represents the multiple of HS-20 truck loads that is the absolute maximum load that can safely travel on the bridge at once. The posting evaluation represents the degree to which the operating rating of the bridge is below the maximum legal load. A 5 indicates the operating rating is equal to or above the legal load. Values of 0–4 represent varying ranges for which the operating rating is below the legal load, with 4 being within 10 percent of the legal load and 0 being 40 percent or greater below the legal load.

A three-dimensional FEM model was developed using the commercial software package CSiBridge, which has the capability to model and analyze complex bridge superstructures while also providing user-friendly pre- and postprocessing tools for bridge structures. The following sections provide the geometric and material properties of the selected simple-span concrete multi-girder bridge and a description of the FEM modeling approach and summarize the analysis results.

Table 4.1. Selected SSLO CM Bridge and Average Characteristics

ID	Route Prefix	Year Built	ADT	Max. Span Length (ft)	Deck Width (ft)	Condition Rating			Operating HS-20 Rating Factor	Posting Eval.
						Deck	Super-structure	Sub-structure		
Avg.	–	1964	–	34	28	7	7	6	0.99	5
CM-5	4	1950	150	29	22	7	7	5	0.99	5

–: Not applicable
Route Prefix: 3 = On-System
Condition Ratings: 6 = Satisfactory, 7 = Good
Posting Evaluation: 3 = 10–19.9% below legal load, 4 = 0.1–9.9% below legal load

Modal analysis was conducted to obtain modal properties, including modal frequencies and mode shapes. The model was also analyzed with HS-20 truck and designated HL-93 load simulations to obtain deflection profiles, moment, and shear results. The deflection and modal analyses were conducted for comparison to the measured behavior of the bridge in the future field tests. The deflection values and modal characteristics will allow for calibration of the FEM model based on field-test results. The main bridge characteristics of interest for the moment and shear analyses are the LLDFs. A comparison of the LLDFs found using the FEM model will be carried out with those determined from field testing and those found using the procedures outlined in the *AASHTO Standards Specifications* (AASHTO 2002) and *AASHTO LRFD Specifications* (AASHTO 2017). LLDFs can be calculated as the moment or shear force of an individual girder divided by the sum of moments or shear forces in all of the girders for a one-lane-loaded case, as given in Equation (2.1).

4.2 DESCRIPTION OF THE BRIDGE

The selected Bridge CM-5 is made up of eight pan girders, each 24 in. deep. The bridge has a total length of 30 ft. The simply supported bridge is 21 ft 7.5 in. wide and has a center-to-center of bearing span length of 29 ft. The steel yield strength and the 28-day concrete compressive strength are taken as 33 ksi and 2.5 ksi, respectively, according to the AASHTO MBE (AASHTO 2018) guidelines. The bridge carries two lanes, one in each direction, and has an ADT of 150 vehicles. These properties are tabulated in Table 4.2.

Table 4.2. Geometric and Material Properties for Bridge CM-5

Characteristic	Measurement
Total Length	30'-0"
Controlling Span Length	29'-0"
Deck Width	21'-7.5"
Roadway Width	21'-0"
Girder Spacing	3'-0"
Slab + Beam Depth	2'-0"
Steel Yield Strength	33 ksi
Slab Thickness	8"
28-day Concrete Compressive Strength	2.5 ksi
Number of Lanes	2

Bridge CM-5 carries CR 119 and traverses Small Creek near Caldwell, Texas, approximately 2.5 mi east of State Highway 36. It has a deck condition rating of 7 (Good), a superstructure condition rating of 7 (Good), and a substructure condition rating of 5 (Fair). The concrete pan girders control the rating of the bridge, which has an inventory gross loading of 26 US tons and an operating gross loading of 36 US tons. The bridge is posted for a 24,000 lbs tandem axle. Figure 4.1 shows an elevation view and an underside view of Bridge CM-5, and Figure 4.2 shows a longitudinal section detail obtained from TxDOT inspection reports (TxDOT 2018a).

(a) Elevation view

(b) Underside view

Figure 4.1. Photographs of Bridge CM-5 (TxDOT 2018a)

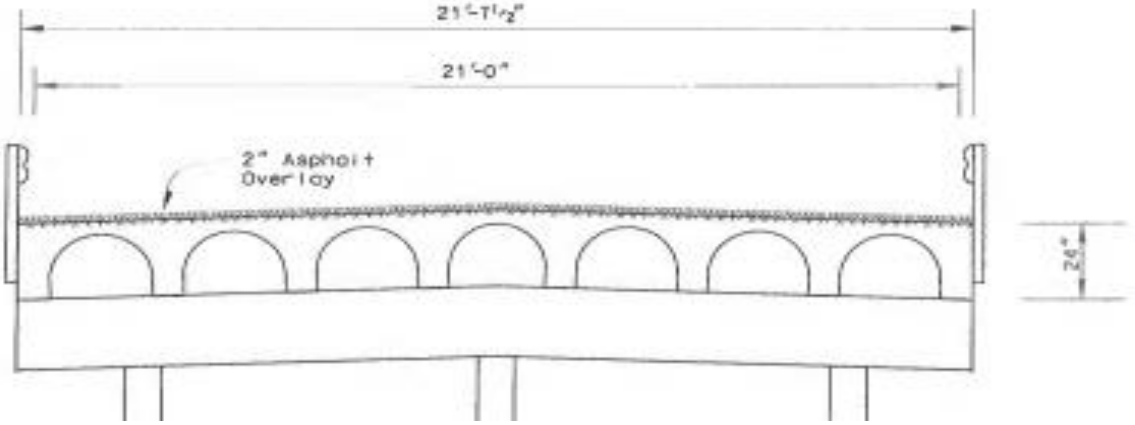

Figure 4.2. Bridge CM-5 Longitudinal Section (TxDOT 2018a)

4.3 FEM MODEL DEVELOPMENT

A three-dimensional linear FEM model of the selected simple-span concrete pan girder bridge was developed using the commercial CSiBridge software (Computers and Structures Inc. 2019). The bridge geometry was modeled based on information provided in the structural design drawings and TxDOT inspection reports (TxDOT 2018a). The geometric information relevant to the development of the FEM model for Bridge CM-5 was presented in the previous sections of this chapter. The following subsection describes the FEM modeling approach, finite element types, and material properties. The next subsection presents the results of the mesh sensitivity study and selection of mesh size. The last subsection provides details about boundary conditions, which are critical for accurately capturing the behavior of the bridge.

4.3.1 Bridge Model Description

A realistic model of the bridge superstructure requires appropriate finite element types, boundary conditions, and a sufficiently refined mesh. Ample information exists that provides recommendations about FEM modeling for various concrete bridge superstructures (Davids et al. 2013; Hueste et al. 2015). Based on recommendations provided in the literature and engineering judgement, a three-dimensional linear finite element model of Bridge CM-5 was developed using the commercial software CSiBridge (Computers and Structures Inc. 2019). Due to the absence of structural drawings for this specific bridge, the bridge geometry was modeled according to the standard drawing provided on the TxDOT website titled “CG 30'-4" Spans” (TxDOT 2005). The

standard drawing called for nine pan girders. However, photographs and sketches documented in TxDOT inspection reports (TxDOT 2018a) for this bridge showed the bridge has eight girders. The slab in this bridge did not extend beyond the edge girders, as was shown in the standard drawing. Due to complications in modeling the semicircular profile of the pan girders, a trilinear geometry was adopted for each girder. The geometry of the trilinear model was determined by keeping the depth (24 in.) and bottom width of the girder web (8.25 in.) the same as shown in the standard drawing. All other dimensions of the pan girder were modified until the gross section moment of inertia (I_{xx}) matched the original value, with an approximate 5 percent tolerance. The bridge superstructure was modeled using 3-D eight-node linear solid brick elements. The reinforcement was not modeled because the linear elastic model is analyzed under service level loads only, and the superstructure is expected to remain in the linear elastic range. Figure 4.3 shows the finite element model for Bridge CM-5.

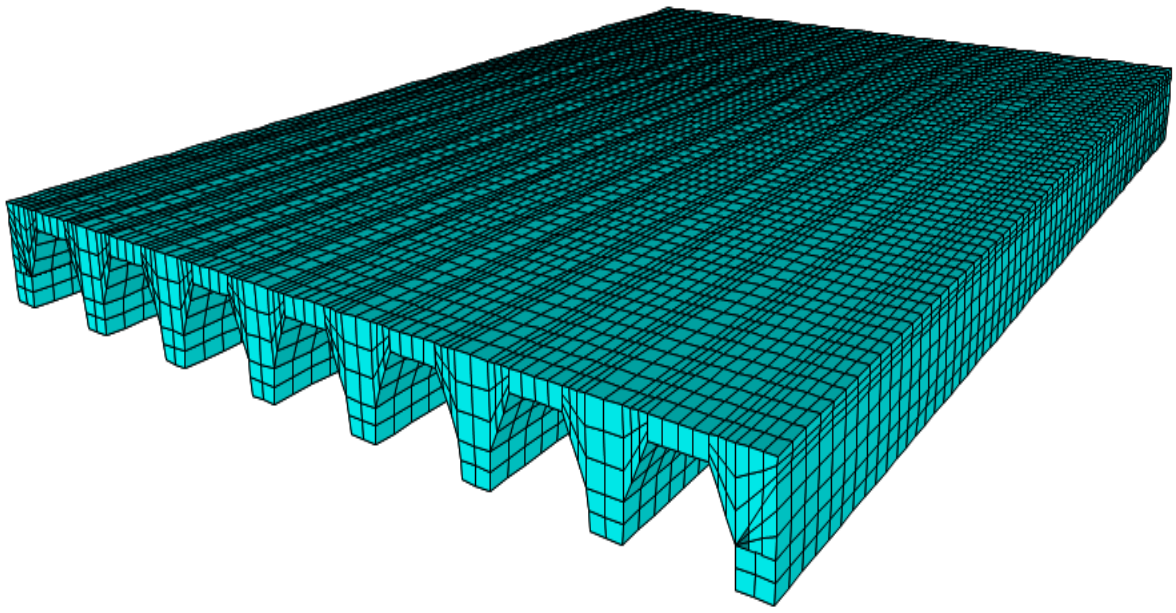

Figure 4.3 FEM Model of Bridge CM-5 (6 in. mesh)

In the absence of any record of the specified material strengths for Bridge CM-5, the steel yield strength and the 28-day concrete compressive strength are taken in accordance with the

AASHTO MBE guidelines (AASHTO 2018). Table 4.3 lists the material properties adopted for the FEM model.

Table 4.3. Material Properties for Bridge CM-5

Bridge	28-Day Concrete Compressive Strength	Modulus of Elasticity	Concrete Unit Weight
	(ksi)	(ksi)	(pcf)
CM-5	2.5	3031	150

The MOE, E_c, for concrete was calculated using Equation (4.1), as stated in the *AASHTO LRFD Specifications* (AASHTO 2017). This equation is valid for normal weight concrete with unit weights between 0.09 and 0.155 kcf and design compressive strength up to 15.0 ksi:

$$E_c = 33{,}000 K_1 w_c^{1.5} \sqrt{f_c'} \quad (4.1)$$

where:

E_c = Elastic modulus of concrete, ksi

K_1 = Correction factor for source of aggregate, to be taken as 1.0 unless determined by physical test

w_c = Unit weight of concrete, kcf

f_c' = Compressive strength of concrete, ksi

4.3.2 Mesh Sensitivity Analysis

A mesh sensitivity study was undertaken for several models with different mesh sizes (4 in., 6 in., 12 in., and 18 in.) in order to determine the optimal mesh size for the three-dimensional linear finite element model of Bridge CM-5. The effect of different mesh sizes on the calculated shear force, moment, and bending stress was examined. Figure 4.4 shows these different mesh sizes when applied to Bridge CM-5.

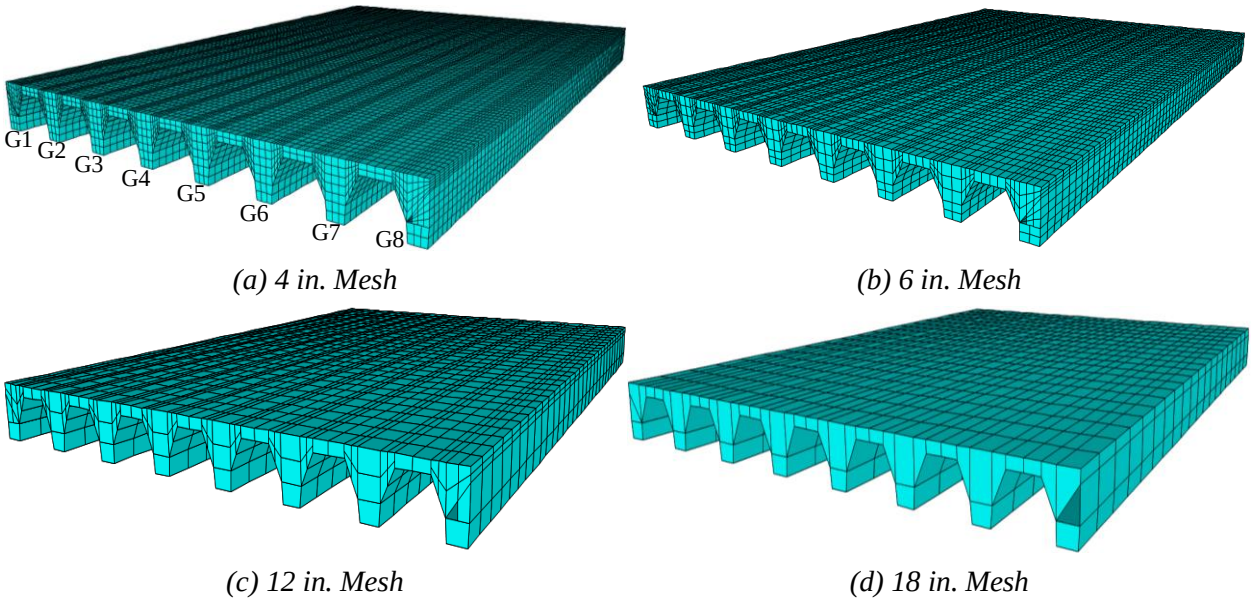

(a) 4 in. Mesh *(b) 6 in. Mesh*

(c) 12 in. Mesh *(d) 18 in. Mesh*

Figure 4.4. FEM Models Showing Different Mesh Sizes for Bridge CM-5

The FEM results for shear force, bending moment, and stress for the Bridge CM-5 models are listed in Table 4.4. All the results correspond to the case of a single HS-20 truck pass through the right lane, 2 ft from the centerline of the bridge (Path 2 in Figure 4.6). The accuracy of the results increases with decreasing mesh size. However, reducing the mesh size to 4 in. does not significantly increase the accuracy when compared to the results obtained from the model with a mesh size of 6 in. Thus, a 6 in. mesh size was chosen to be used for Bridge CM-5. With this mesh size and discretization points, an accurate FEM model of the bridge with an efficient computation time was created in CSiBridge. The final meshed FEM model used for analysis of Bridge CM-5 is shown in Figure 4.5.

Table 4.4. FEM Results for CM-5 with Different Mesh Sizes

Mesh Size (in.)	Maximum Moment in Girder 3 (kip-ft)	Maximum Shear in Girder 3 (kip)	Maximum Stress in Girder 3 (ksi)
4	52.56	9.35	0.366
6	52.55	9.12	0.366
12	52.56	8.64	0.366
18	52.35	8.22	0.366

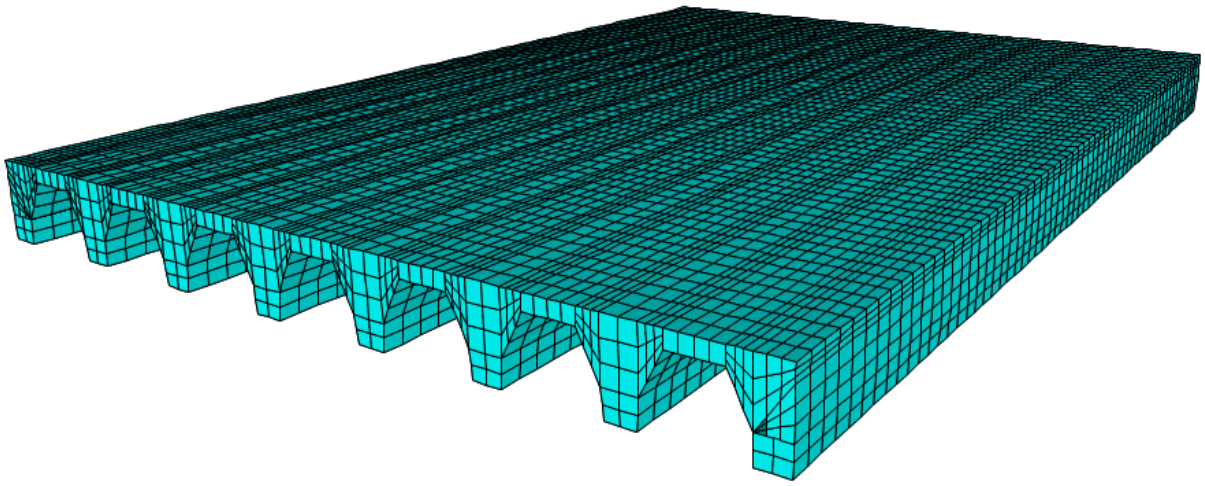

Figure 4.5. Selected FEM Model (6 in. mesh)

4.3.3 Boundary Conditions

In the absence of more accurate information, the boundary conditions at the supports were modeled as simply supported with pins and rollers. One end of each girder was modeled with roller supports, while the other end was modeled with pin supports. The roller support releases all three rotational degrees of freedom and two translational degrees of freedom in the horizontal plane (two orthogonal in-plane directions parallel to the bridge superstructure) and fully restrains the translational degree of freedom in the vertical direction (perpendicular to the plane of the bridge superstructure). The pin support releases all three rotational degrees of freedom and restrains all three translational degrees of freedom.

Accurately modeling the boundary conditions may have a significant effect on the overall behavior of the bridge. Although the boundary conditions are initially modeled as simply supported, the level of restraint will be assessed based on experimental results during the next task. Unintended partial fixity may develop at the supports due to the bearing detail at the supports and/or friction between the bottom surface of the bridge and the bearing surface.

4.4 BASIC VERIFICATION OF FEM MODELS

Some basic loading conditions were simulated to verify that the FEM model was providing expected results. These basic checks were conducted by investigating maximum deflections under

a uniformly distributed dead load and maximum moments and shears under HS-20 truck load and designated HL-93 loading.

The characteristics of the HS20 design truck as specified in *AASHTO LRFD Specifications* (AASHTO 2017) is shown in Figure 2.8. The total load in the front axle is 8 kips and is 14 ft away from the middle axle, which has a total load of 32 kips. The rear axle has a total load of 32 kips and may be spaced between 14 ft and 30 ft from the middle axle, depending on which creates the maximum force effect being investigated. An alternative loading scheme consisting of a uniformly distributed load of 0.64 kip/ft and a concentrated load of 18 kips when checking moment or 26 kips when checking shear is also considered in *AASHTO Standard Specifications* (AASHTO 2002).

The designated HL93 loading consisting of the design truck or design tandem coincident with the design lane load is shown in Figure 2.9. The design lane load consists of a 0.64 kip/ft uniformly distributed load over a 10 ft width. Two 25-kip axle loads spaced 4 ft apart longitudinally and the wheel lines spaced 6 ft apart transversely constitute the design tandem load. The design truck or design tandem is used depending on which will create the maximum force effect on the span.

4.4.1 Verification of Maximum Deflection

The maximum deflection for the bridge superstructure under a uniformly distributed dead load was verified against the deflections obtained from basic structural analysis. The estimated deflections for an interior girder obtained from FEM analysis were compared to the calculated deflections. The equivalent distributed load was calculated as the sum of the weight of the girder, the deck, and wearing surface. The total uniformly distributed weight can be found in Equation 4.2:

$$w = w_g + w_{ws} = 1.272 \text{ kip/ft} \tag{4.2}$$

in which:

w_g = weight of girders (including slab) = 0.408 kip/ft

$$w_{ws} = (\gamma_{ws})(t_{ws})(s) = 0.864 \text{ kip/ft} \tag{4.3}$$

where:

γ_c = unit weight of concrete = 0.15 kip/ft^3

s = spacing of the pan girders (ft)

w_{ws} = weight of wearing surface (kip/ft)

γ_{ws} = unit weight of the wearing surface = 0.144 kip/ft^3

t_{ws} = thickness of the wearing surface (ft)

The midspan deflection of the pan girder bridge can be calculated using Equation (4.4) for a simply supported beam under a uniformly distributed load:

$$\Delta = \frac{5wL^4}{384E_cI} = 0.413 \text{ in.} \tag{4.4}$$

where:

I = Moment of inertia of an interior pan girder section = 18,501 in^4

E_c = MOE of concrete = 3031 ksi

Table 4.5 shows the deflections calculated using each method and the percent difference relative to the calculated deflection. The FEM deflections are within two percent of the calculated deflection.

Table 4.5. Dead Load Deflection Comparison for Bridge CM-4

Bridge ID	FEM Deflection (in.)	Calculated Deflection (in.)	Percent Difference (%)
CM-5	0.420	0.413	1.69

4.4.2 Verification of Absolute Maximum Moment

To verify that the truck loadings were modeled correctly, the live load moments were compared to the live load moments obtained from basic structural analysis. The model was analyzed under HS-20 truck and HL-93 loading. In Chapter 2, calculations for obtaining the maximum moment due to moving loads in a simple span are presented in Section 2.4.2.

Table 4.6 shows the calculated live load moments, the FEM moments, and the percent difference between them. The FEM live load moments matched up very closely to the expected live load moments.

Table 4.6. Live Load Moment on the Comparison for Bridge CM-5

Bridge ID	Applied Load	FEM One-Lane Moment on Total Section (kip-ft)	Expected One-Lane Moment on Total Section (kip-ft)	Percent Difference (%)
CM-5	HS-20	281.6	282.1	0.18
	HL-93	398.35	398.4	0.01

Note: All calculated moments are without the application of the impact factor

4.4.3 Verification of Maximum Shears

To verify that the structural supports have been modeled correctly, maximum shears corresponding to the live loads were verified against the shear forces obtained from the basic structural analysis. Step-by-step loading is employed by FEM for the moving load analysis. The step size of the moving load was adjusted so that the first step with the rear axle of the truck on the bridge positioned the rear axle 2 ft away from the support. The resulting support reactions were obtained from the FEM model and compared with those calculated using classical structural analysis methods. Table 4.7 shows the support reactions calculated using each method and the percent difference between them. The FEM support reactions matched up very closely to the calculated reactions.

Table 4.7. Live Load Shears Comparison for the Bridge CM-5

Bridge ID	Applied Load	FEM One-Lane Shear on Total Section (kip)	Expected One-Lane Shear on Total Section (kip)	Difference (%)
CM-5	HS-20	46.9	47.2	0.57
	HL-93	54.4	54.6	0.29

Note: All calculated shears are without the application of the impact factor.

4.5 SIMULATING VEHICLE LOADS

The truck loads and lane loads were placed transversely on Bridge CM-5 as per the *AASHTO Standard Specifications* (AASHTO 2002) and *AASHTO LRFD Specifications* (AASHTO 2017). Bridge CM-5 has two lanes, each 10.85 ft wide.

A linear static moving load analysis was performed with each truck moving along the length of the bridge in approximately 1 ft increments. It should be noted that although it would be an unlikely event, for the two-lane-loaded cases both trucks traveled along the bridge in the same direction in order to produce the maximum possible effect on the bridge.

4.5.1 Simulating HS-20 Truck Loading

For a one-lane-loaded case based on the *AASHTO Standard Specifications,* the truck was placed so that the exterior wheel line was 2 ft away from the edge of the barrier (Path 1). Due to the narrow lane width, the only other loading scenario considered was placing the interior wheel line 2 ft from the centerline of the bridge (Path 2). For a two-lane-loaded case, one truck was positioned in Path 1, and a second truck was positioned in Path 2. This process created two separate one-lane-loaded cases and one two-lane-loaded case. Figure 4.6 shows the different HS-20 truck loading cases along the transverse section of Bridge CM-5. The red and blue arrows represent the wheel lines of the truck, and the black dashed line is the centerline (CL) of the bridge.

4.5.2 Simulating HL-93 Loading

For loading based on the AASHTO LRFD specifications, the tandem configuration and lane load were added to the already created load cases. The tandem configuration was used for HL-93 loading since it controls over the truck configuration for short span bridges less than 40.5 ft long.

The design tandem was placed transversely in the same manner as described for the HS-20 truck. The lane load was placed immediately adjacent to the edge of the barrier for Path 1. For Path 2, the lane load was placed immediately adjacent to the centerline of the bridge. For the two-lane-loaded case, the lane load was kept adjacent to the centerline of the bridge in the second lane. Figure 4.7 shows the different HL-93 loading cases along the transverse section of Bridge CM-5. The red and blue arrows represent the wheel lines of the truck, the red and blue cross-hatched regions represent the lane load distributed over the lane width, and the black dashed line is the centerline (CL) of the bridge.

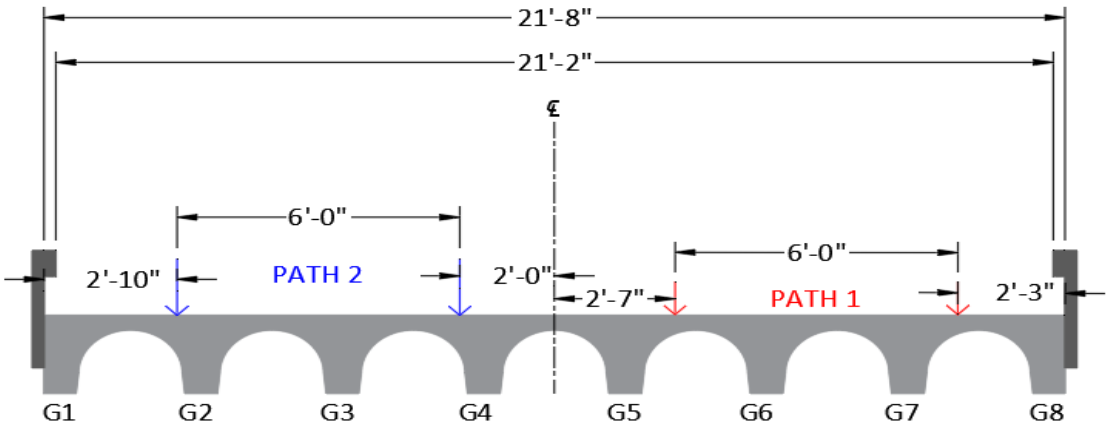

Figure 4.6. HS-20 Truck Loading Cases for Bridge CM-5

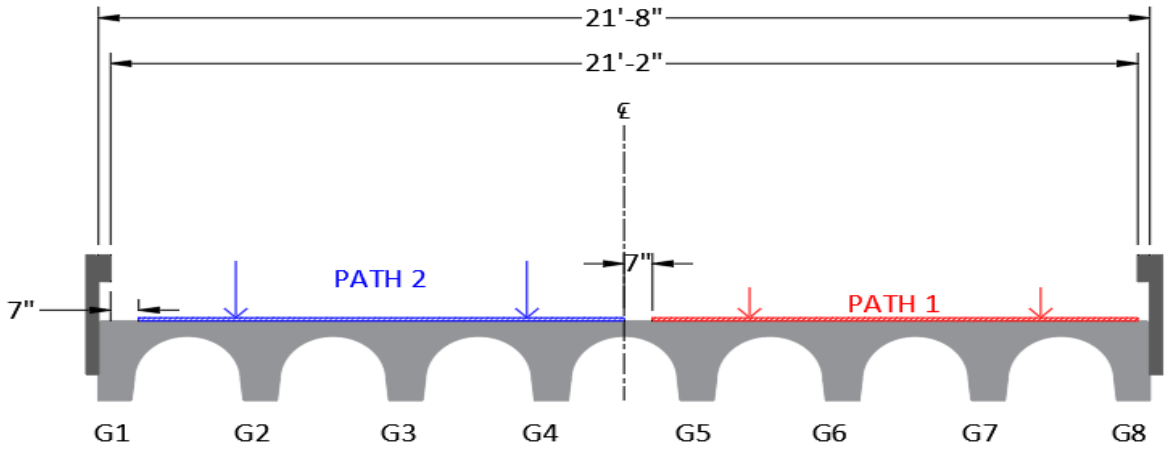

Figure 4.7. HL-93 Loading Cases for Bridge CM-5

4.6 FEM RESULTS

Bridge CM-5 was analyzed using the FEM software CSiBridge under the loading scenarios provided in Figure 4.6 and Figure 4.7. Girder displacement profiles were obtained for both one-lane-loaded and two-lane-loaded cases. Modal analysis was conducted to determine estimated modal frequencies and mode shapes. Live load moment and shear values were also extracted and analyzed to compare the expected LLDFs with the LLDFs prescribed in *AASHTO Standard Specifications* (AASHTO 2002) and *AASHTO LRFD Specifications* (AASHTO 2017).

4.6.1 Modal Properties

The first longitudinal bending mode and the first torsional mode constitute the first two modes of Bridge CM-5. The frequency for the longitudinal bending mode was determined to be 9.42 Hz, and for the torsional mode it was 11.58 Hz. The contours of the longitudinal bending mode shape along with the normalized amplitudes along the span of the bridge are shown in Figure 4.8(a). Figure 4.8(b) shows the contours of the torsional mode shape along with the normalized amplitudes transverse to the span.

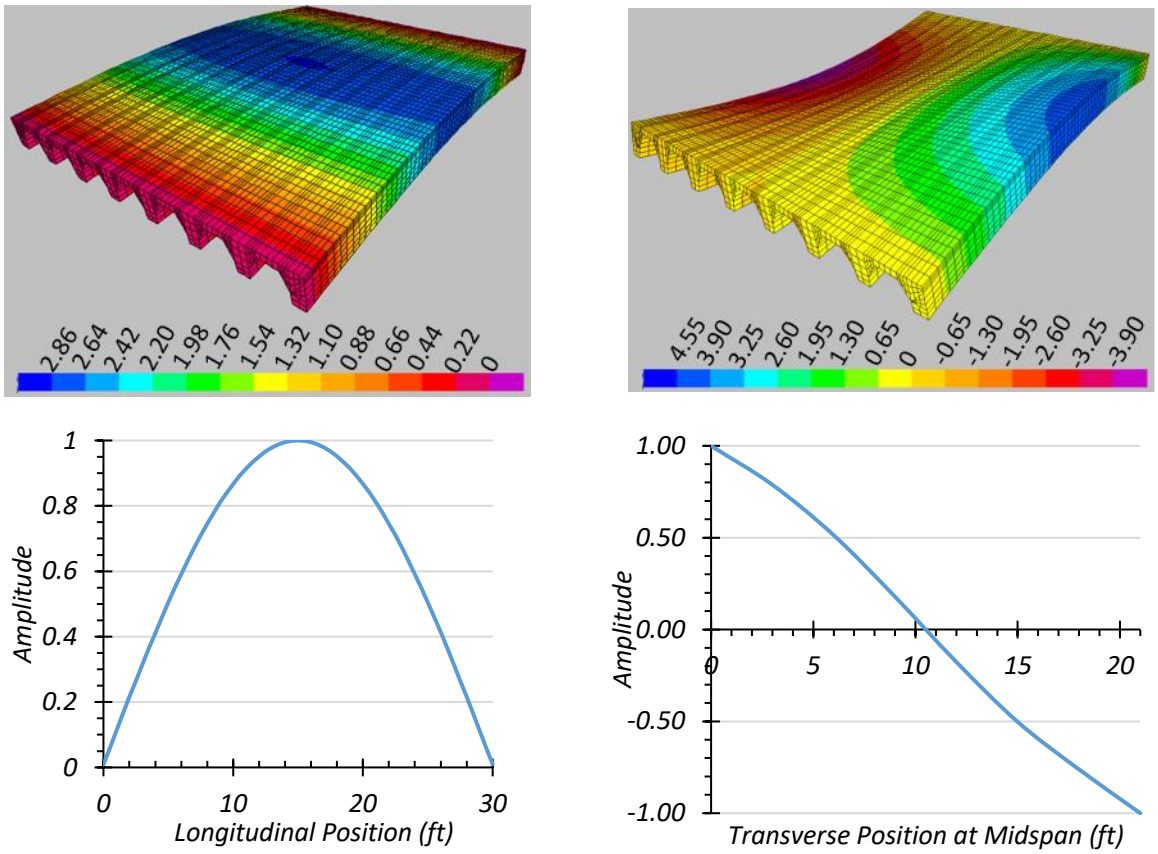

(a) Longitudinal Bending Mode (f=9.42 Hz) *(b) Torsional Mode (f=11.58 Hz)*

Figure 4.8. First Two Mode Shapes of Bridge CM-5

4.6.2 HS-20 Live Load Analysis

Bridge CM-5 was subjected to the design HS-20 truck load as defined in the *AASHTO Standard Specifications* (AASHTO 2002). The paths defined in Figure 4.6 were prescribed in FEM for analysis. The following sections discuss the deflections, bending moment, and shear values obtained from the FEM model.

*4.6.2.1 **Deflection Results***

The estimated girder deflection profiles and contours along the span for one-lane HS-20 loading along Path 1 and Path 2 are shown in Figure 4.9. The maximum deflections under HS-20 loading for each loaded path is tabulated in Figure 4.8. The maximum deflection under one-lane HS-20 loading was observed at the edge girders, with 0.19 in. at Girder G1 under Path 1 loading.

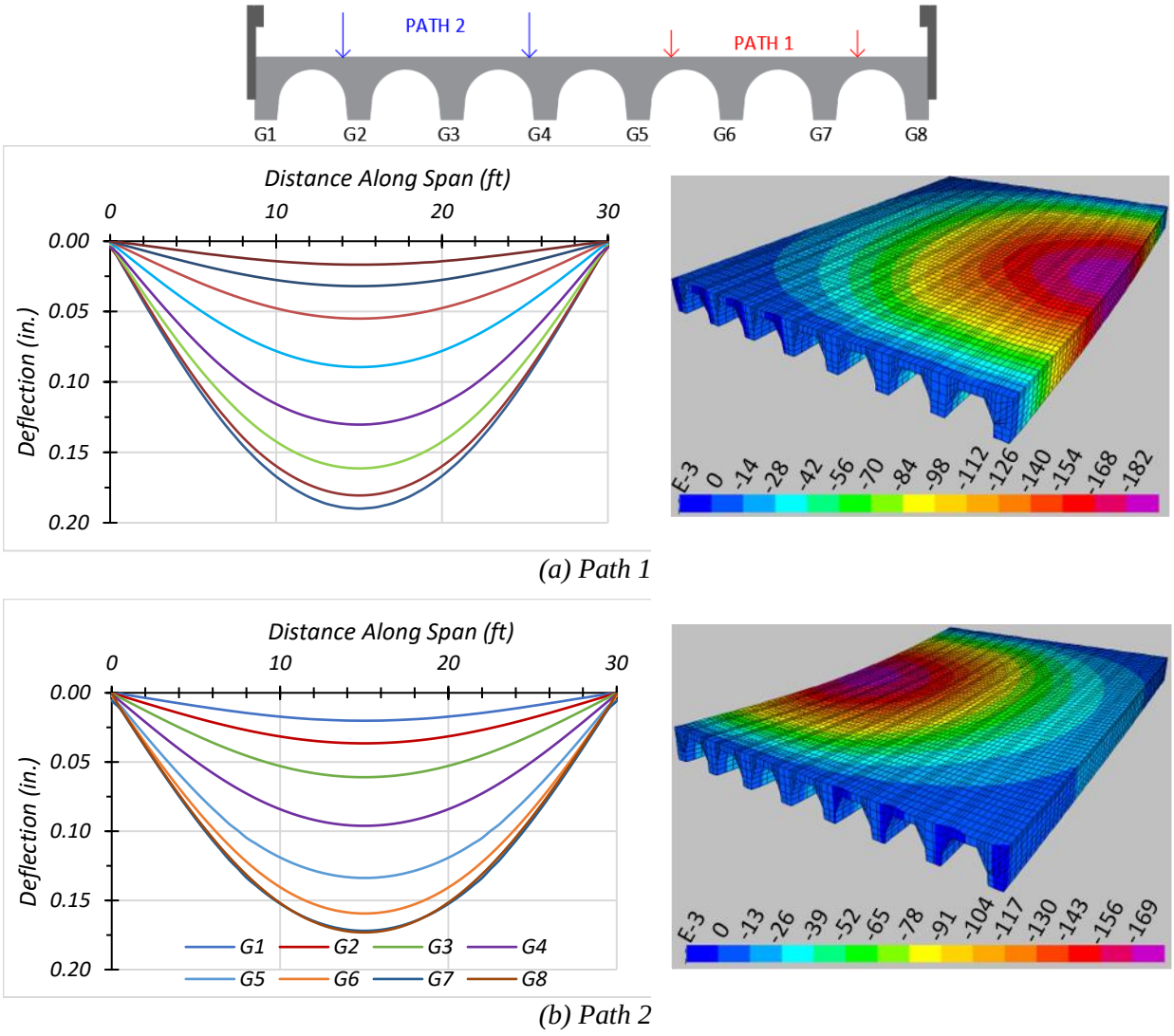

Figure 4.9. Deflection Profiles under HS-20 Loading

Table 4.8. Maximum Deflections under HS-20 Loading

Loading	G1	G2	G3	G4	G5	G6	G7	G8
Path 1	0.190	0.181	0.161	0.130	0.089	0.055	0.032	0.017
Path 2	0.020	0.036	0.061	0.096	0.134	0.159	0.172	0.173

Note: G = girder, paths indicate transverse loading positions as shown, deflections have inch units

4.6.2.2 *Moment Results*

The moments corresponding to each girder and the corresponding LLDFs for the one-lane and two-lane HS-20 loading paths are shown in Figure 4.10. The corresponding maximum moments for each girder and path are listed in Table 4.9. Maximum Moments under HS-20 LoadingThe estimated moment results from the FEM model were used to calculate the moment LLDFs. A comparison of the estimated moment LLDFs obtained from the FEM model and those calculated using the approximate equations in the *AASHTO Standard Specifications* (AASHTO 2002) is provided in Table 4.10. The AASHTO moment LLDF is slightly conservative for the interior girder, $g^m_{AASHTO}/g^m_{FEM} = 1.02$, and very conservative for the exterior girder, $g^m_{AASHTO}/g^m_{FEM} = 1.33$, for a one-lane HS-20 loading scenario. For the two-lane HS-20 loading case, the AASHTO prediction is unconservative, with a g^m_{AASHTO}/g^m_{FEM} ratio of 0.87 for the interior girder, and conservative for the exterior girder, with $g^m_{AASHTO}/g^m_{FEM} = 1.27$.

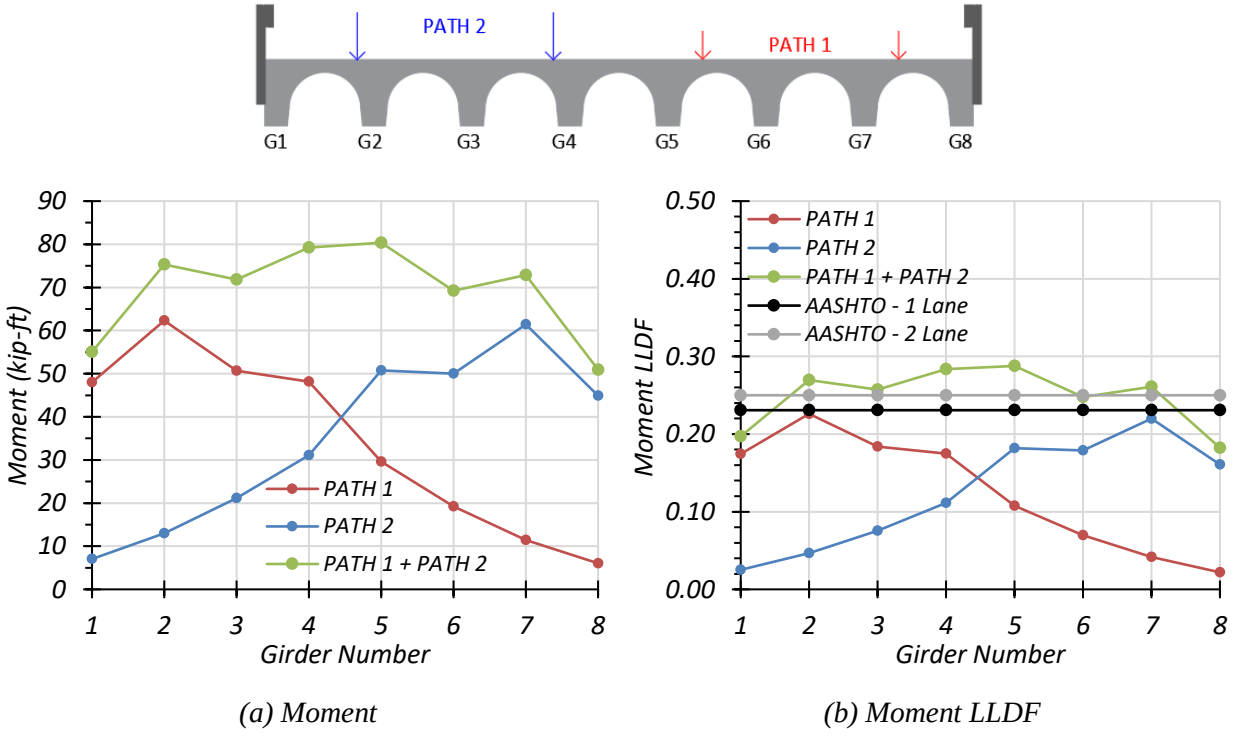

(a) Moment *(b) Moment LLDF*

Figure 4.10. Moment Results under HS-20 Loading

Table 4.9. Maximum Moments under HS-20 Loading

Loading	G1	G2	G3	G4	G5	G6	G7	G8
Path 1	48.03	62.30	50.71	48.14	29.62	19.25	11.44	6.04
Path 2	7.03	13.03	21.13	31.07	50.75	49.99	61.42	44.89
Path 1 + Path 2	55.06	75.33	71.84	79.21	80.37	69.24	72.86	50.93

Note: G = girder, paths indicate transverse loading positions as shown, moments have kip-ft units

Table 4.10. Governing Moment LLDF Values for HS-20 Loading

Loading	Girder Location	AASHTO (g^m_{AASHTO})	FEM (g^m_{FEM})	g^m_{AASHTO}/g^m_{FEM}
One-lane	Interior	0.231	0.226	1.02
	Exterior	0.231	0.174	1.33
Two-lane	Interior	0.250	0.288	0.87
	Exterior	0.250	0.197	1.27

*4.6.2.3 **Shear Results***

The shear forces in each girder and the corresponding shear LLDFs for the one-lane and two-lane HS-20 loading paths are shown in Figure 4.11. The corresponding maximum support reactions for each girder and path are listed in Table 4.11. Maximum Shears under HS-20 LoadingA comparison of the estimated shear LLDFs calculated from the FEM support reactions and those calculated using the approximate equations in the *AASHTO Standard Specifications* (AASHTO 2002) is provided in Table 4.12. Governing Shear LLDF Values for HS-20 LoadingThe AASHTO shear LLDF is conservative for the exterior girder with $g^v_{AASHTO}/g^v_{FEM} = 1.38$, while being unconservative for the interior girder with $g^v_{AASHTO}/g^v_{FEM} = 0.84$, for a one-lane HS-20 loading scenario. Similarly, for the two-lane HS-20 loading case, g^v_{AASHTO}/g^v_{FEM} has an unconservative value of 0.75 for the interior girder and a conservative ratio of 1.42 for the exterior girder.

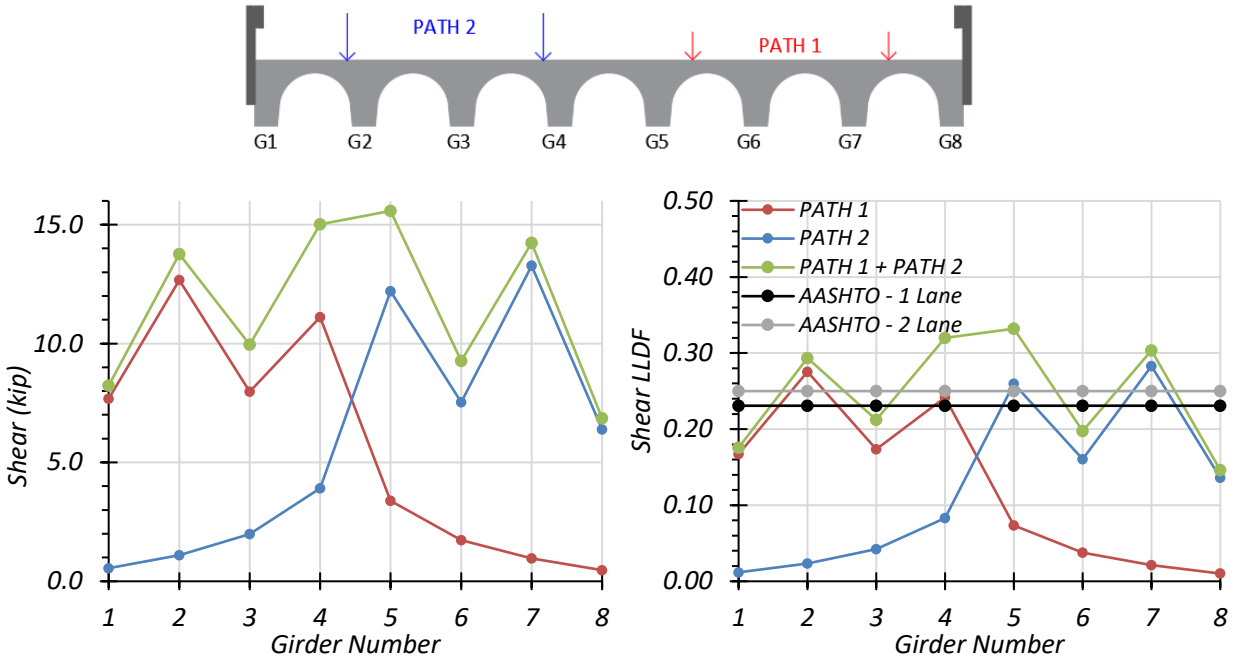

(a) Shear *(b) Shear LLDF*

Figure 4.11. Shear Results under HS-20 Loading

Table 4.11. Maximum Shears under HS-20 Loading

Loading	G1	G2	G3	G4	G5	G6	G7	G8
Path 1	7.68	12.67	7.97	11.11	3.38	1.73	0.97	0.47
Path 2	0.55	1.10	1.98	3.91	12.20	7.53	13.27	6.39
Path 1 + Path 2	8.24	13.77	9.95	15.01	15.58	9.26	14.24	6.85

Note: G = girder, paths indicate transverse loading positions as shown, shears have kip units

Table 4.12. Governing Shear LLDF Values for HS-20 Loading

Loading	Girder Location	AASHTO (g^v_{AASHTO})	FEM (g^v_{FEM})	g^v_{AASHTO}/g^v_{FEM}
One-lane	Interior	0.23	0.28	0.84
	Exterior	0.23	0.17	1.38
Two-lane	Interior	0.25	0.33	0.75
	Exterior	0.25	0.18	1.42

4.6.3 HL-93 Live Load Analysis

Bridge CM-5 was subjected to the HL-93 design loading as defined in the *AASHTO LRFD Specifications* (AASHTO 2017). The paths defined in Figure 4.7 were prescribed in FEM for analysis. The following sections discuss the deflections, bending moment, and shear values obtained from the FEM model.

4.6.3.1 ***Deflection Results***

The estimated girder deflection profiles and contours along the span for one-lane HL-93 loading along Path 1 and Path 2 are shown in Figure 4.12. The maximum deflections under HL-93 loading for each loaded path is tabulated in Table 4.13. The maximum deflection under one-lane HL-93 loading was observed at the edge girders, with 0.248 in. at Girder G1 under loading Path 1.

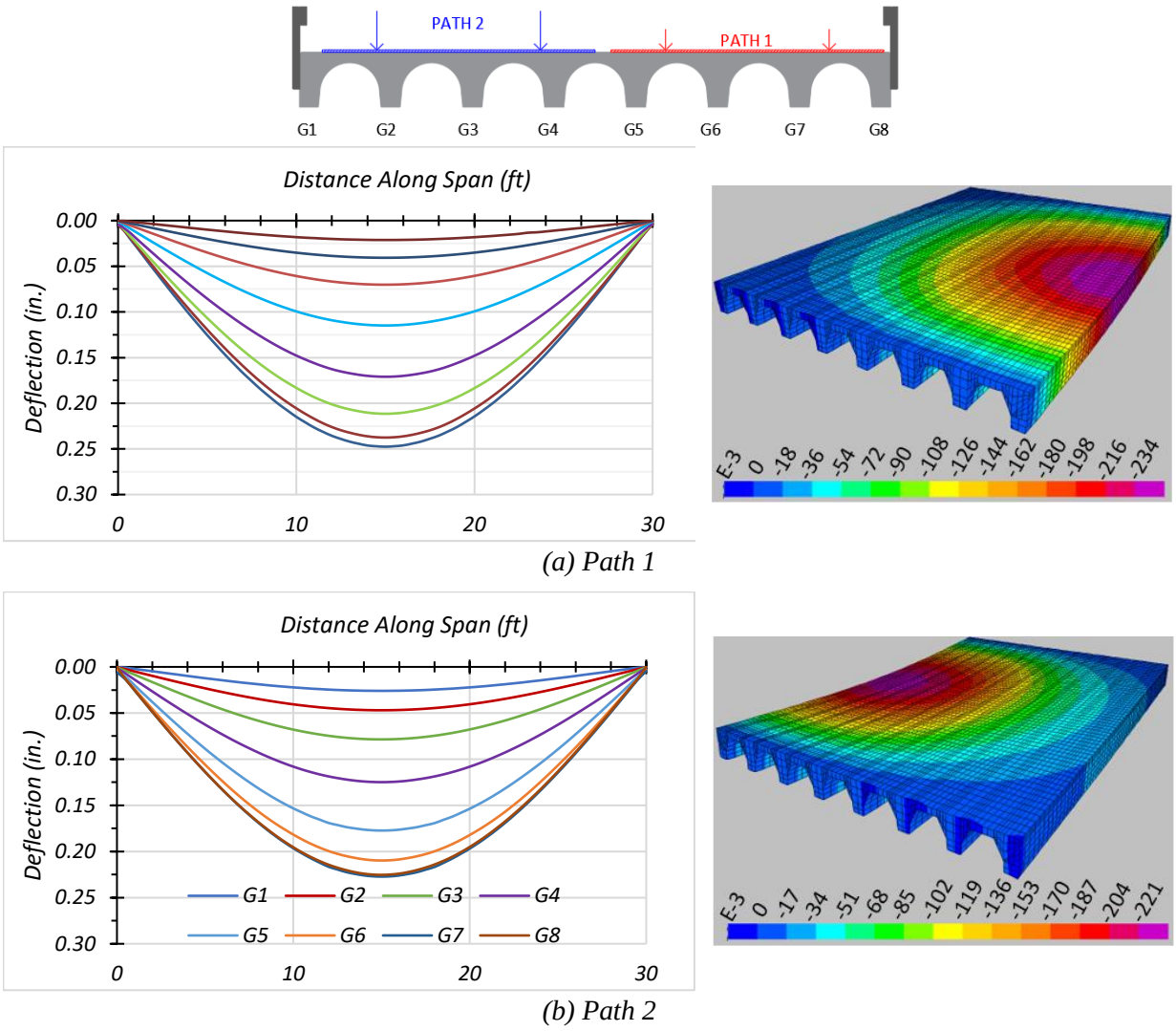

Figure 4.12. Deflection Profiles under HL-93 Loading

Table 4.13. Maximum Deflections under HL-93 Loading

Loading	G1	G2	G3	G4	G5	G6	G7	G8
Path 1	0.248	0.238	0.212	0.171	0.115	0.070	0.041	0.021
Path 2	0.026	0.047	0.079	0.125	0.177	0.210	0.227	0.225

Note: G = girder, paths indicate transverse loading positions as shown, deflections have inch units

*4.6.3.2 **Moment Results***

The moments corresponding to each girder and the corresponding LLDFs for the one-lane and two-lane HL-93 loading paths are shown in Figure 4.13. The corresponding maximum moments

for each girder and path are listed in Table 4.14. The estimated moment results from the FEM model were used to calculate the moment LLDFs. A comparison of the estimated moment LLDFs obtained from the FEM model and those calculated using the approximate equations in the *AASHTO LRFD Specifications* (AASHTO 2017) is provided in Table 4.15. AASHTO LRFD approximate LLDF values were calculated using two different methods: (1) using the simplified stiffness parameter, and (2) using the more accurate analytical stiffness parameter. Both methods gave almost the same LLDFs, as shown in Figure 4.13. The AASHTO LRFD moment LLDF is very conservative for the interior girder, with $g^m_{AASHTO}/g^m_{FEM} = 1.49$, and conservative for the exterior girder, with $g^m_{AASHTO}/g^m_{FEM} = 1.29$, for a one-lane HL-93 loading scenario. For the two-lane HL-93 loading case, the AASHTO LRFD prediction is very conservative, with a g^m_{AASHTO}/g^m_{FEM} ratio of 1.43 for the interior girder and 1.57 for the exterior girder.

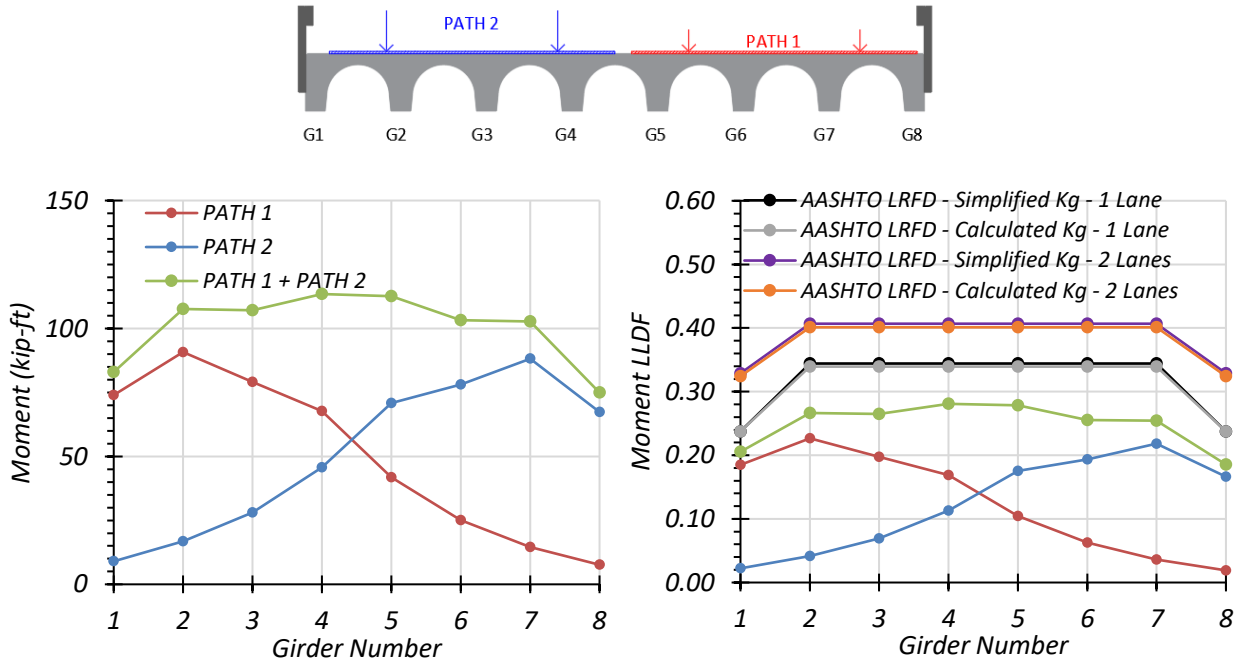

(a) Moment *(b) Moment LLDF*

Figure 4.13. Moment Results under HL-93 Loading

Table 4.14. Maximum Moments under HL-93 Loading

Loading	G1	G2	G3	G4	G5	G6	G7	G8
Path 1	74.03	90.78	79.04	67.70	41.77	25.06	14.55	7.64
Path 2	9.00	16.79	28.04	45.75	70.81	78.15	88.17	67.28
Path 1 + Path 2	83.03	107.57	107.08	113.45	112.58	103.21	102.72	74.92

Note: G = girder, paths indicate transverse loading positions as shown, moments have kip-ft units

Table 4.15. Governing Moment LLDF Values for HL-93 Loading

Loading	Girder Location	AASHTO (g^m_{AASHTO})	FEM (g^m_{FEM})	g^m_{AASHTO}/g^m_{FEM}
One-lane	Interior	0.37	0.23	1.49
	Exterior	0.27	0.19	1.29
Two-lane	Interior	0.40	0.28	1.43
	Exterior	0.32	0.21	1.57

4.6.3.3 ***Shear Results***

The shear forces in each girder and the corresponding shear LLDFs for the one-lane and two-lane HL-93 loading paths are shown in Figure 4.13. The corresponding maximum support reactions for each girder and path are listed in Table 4.16. A comparison of the estimated shear LLDFs calculated from the FEM support reactions and those calculated using the approximate equations in the *AASHTO LRFD Specifications* (AASHTO 2017) is provided in Table 4.17. In comparison to the FEM results, the AASHTO LRFD shear LLDF for a one-lane HL-93 loading scenario is conservative for the exterior girder, with $g^v_{AASHTO}/g^v_{FEM} = 1.36$, while the $g^v_{AASHTO}/g^v_{FEM} = 2.20$ for the interior girder. For the two-lane HL-93 loading case, g^v_{AASHTO}/g^v_{FEM} has a value of 1.44 for the interior girder and 1.53 for the exterior girder.

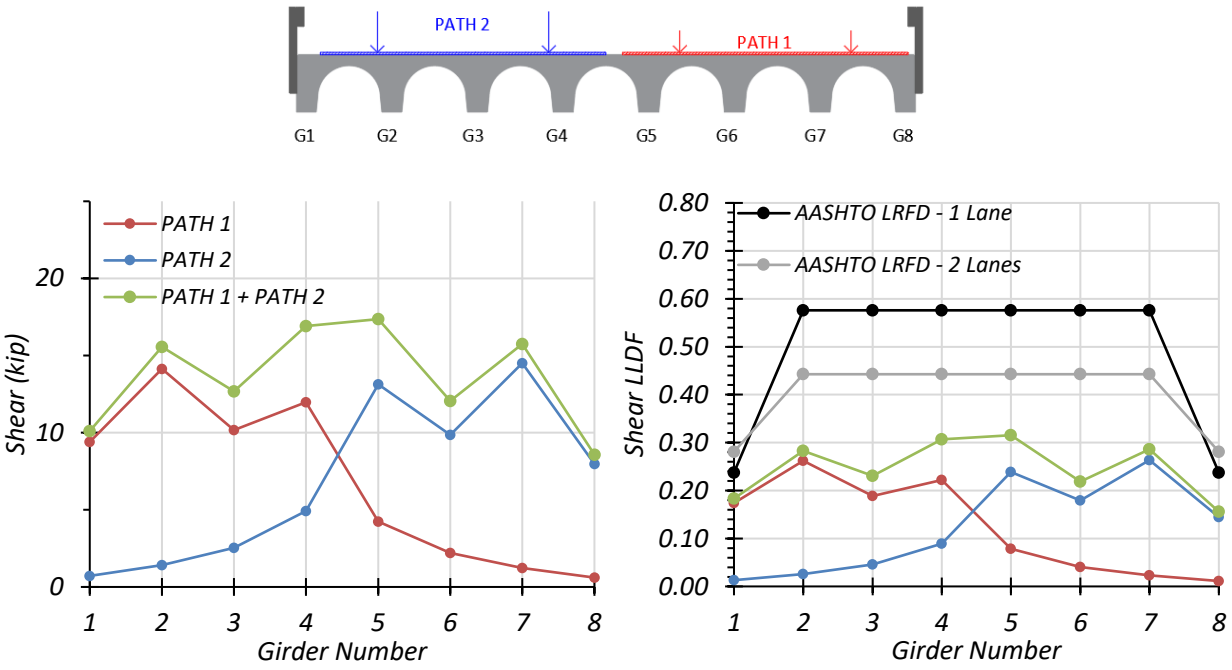

(a) Shear *(b) Shear LLDF*

Figure 4.14. Shear Results with HL-93 Loading

Table 4.16. Maximum Shears with HL-93 Loading

Loading	G1	G2	G3	G4	G5	G6	G7	G8
PATH 1	9.39	14.14	10.16	11.98	4.23	2.20	1.24	0.61
PATH 2	0.72	1.42	2.53	4.92	13.13	9.86	14.51	7.97
PATH 1 + PATH 2	10.11	15.56	12.69	16.91	17.36	12.05	15.75	8.58

Note: G = girder, paths indicate transverse loading positions as shown, shears have kip units

Table 4.17. Governing Shear LLDF Values for HL-93 Loading

Loading	Girder Location	AASHTO (g^v_{AASHTO})	FEM (g^v_{FEM})	g^v_{AASHTO}/g^v_{FEM}
One-lane	Interior	0.576	0.262	2.20
	Exterior	0.238	0.174	1.36
Two-lane	Interior	0.443	0.307	1.44
	Exterior	0.281	0.184	1.53

4.7 SUMMARY AND CONCLUSIONS

Finite element analysis of the selected simple-span concrete multi-girder bridge, Bridge CM-5, was conducted for various vehicular load configurations. Live load moment and shear values were extracted and analyzed to compare the expected LLDFs with the LLDFs prescribed in the *AASHTO Standard Specifications* (AASHTO 2002) and *AASHTO LRFD Specifications* (AASHTO 2017).

In general, the *AASHTO Standard Specifications* moment LLDF is accurate and slightly conservative for one-lane loading scenarios for Bridge CM-5. The governing g_{AASHTO}/g_{FEM} ratio for flexure is above 1.0 for both interior and exterior girders. However, the g_{AASHTO}/g_{FEM} ratios for flexure are 0.87 and 1.27 for interior and exterior girders for the two-lane-loaded scenario. A similar trend is also observed for the AASHTO shear LLDF. The g_{AASHTO}/g_{FEM} ratios for shear are 0.84 and 1.38 for interior and exterior girders for one-lane loading and 0.75 and 1.42 for two-lane loading. These results will not significantly affect the load rating of this bridge type.

The current AASHTO LRFD moment and shear LLDF equations provide highly conservative LLDF values for Bridge CM-5. The AASHTO LRFD moment LLDFs values obtained using the simplified stiffness parameter and calculated stiffness parameter are similar. For the two-lane-loaded case, the governing g_{AASHTO}/g_{FEM} ratios for flexure are 1.43 and 1.57 for interior and exterior girders, respectively. A similar trend is also observed for the AASHTO LRFD shear LLDFs, with g_{AASHTO}/g_{FEM} ratios of 1.44 and 1.53 for the interior and exterior girders, respectively. Using more accurate LLDFs for HL-93 loading cases would likely help increase LRFR ratings.

In a subsequent task, the selected Bridge CM-5 was field-tested using the posted load limit. The bridge was instrumented with strain gages, string potentiometers, and accelerometers to record the required data and the in-situ behavior of the bridge. The experimental results were then compared with the FEM analysis results to validate and calibrate the FEM model.

5 ANALYSIS OF A CONCRETE SLAB BRIDGE

In previous tasks, a detailed review and synthesis of the population of load-posted bridges in Texas was conducted, and 23 simple-span concrete slab (CS) bridges were selected from the inventory of SSLO simple-span concrete slab bridges in Texas for basic load rating evaluation. This basic load rating analysis helped to identify several areas of opportunity for refined load rating analysis. Refined load rating analysis investigates the effect of the identified parameters using three-dimensional finite element models that more accurately capture the actual bridge behavior. The main objectives of FEM analysis of the simple-span concrete slab bridge can be summarized as follows: (1) create a model of the bridge superstructure to accurately capture the two-way action in the slab, (2) investigate the actual equivalent strip width over which vehicular loads are distributed, and (3) evaluate the effect of integral curbs to the load distribution across the slab width.

5.1 INTRODUCTION

A typical load-posted simple-span concrete slab (CS) bridge was selected as a representative case study to further investigate the identified objectives. Table 5.1 lists some of the key parameters for the selected bridge to be modeled and for the average SSLO simple-span concrete slab bridge in Texas. In this table, the Operating HS-20 RF represents the multiple of HS-20 truck loads that is the absolute maximum load that can safely travel on the bridge. The posting evaluation represents the degree to which the operating rating of the bridge is below the maximum legal load. A 5 indicates the operating rating is equal to or above the legal load. Values of 0–4 represent varying ranges for which the operating rating is below the legal load, with 4 being within 10 percent of the legal load and 0 being 40 percent or greater below the legal load.

A three-dimensional FEM model was developed using the commercial software package CSiBridge, which has the capability to model and analyze complex bridge superstructures while also providing user-friendly pre- and postprocessing tools for bridge structures. The following sections provide the geometric and material properties of the selected simple-span concrete slab bridge, a description of the FEM modeling approach, and summarize the analysis results.

Table 5.1. Selected SSLO Concrete Slab Bridge and Characteristics

ID	Route Prefix	Year Built	ADT	Max. Span Length (ft)	Deck Width (ft)	Condition Rating			Operating HS-20 Rating Factor	Posting Eval.
						Deck	Super-structure	Sub-structure		
Avg.	–	1949	795	22	28	6	6	6	0.98	4
CS-9	3	1948	30	25	21	6	6	7	0.94	2

Note:
– : Not Applicable
Route Prefix: 3 = On-System
Condition Ratings: 6 = Satisfactory, 7 = Good
Posting Evaluation: 3 = 10–19.9% below legal load, 4 = 0.1–9.9% below legal load

The model was analyzed with HS-20 truck and designated HL-93 load simulations to obtain modal properties, deflection profiles, moment, and shear results. The deflection and modal analyses were conducted for comparison to the measured behavior of the bridge in future field tests. The deflection values and modal characteristics allow for calibration of the FEM model based on field-test results. The equivalent strip width over which the vehicular loads are distributed is calculated using the bending moment and shear results. A comparison of the equivalent strip widths found using the FEM model will be carried out with those determined from field testing and those found using the procedures outlined in the *AASHTO Standard Specifications* (AASHTO 2002) and *AASHTO LRFD Specifications* (AASHTO 2017).

5.2 DESCRIPTION OF THE BRIDGE

The selected Bridge CS-9 is a cast-in-place concrete slab bridge with integral curbs—also referred to as an FS (Farm Service Road) bridge in the TxDOT bridge drawings. According to the *TxDOT Rate Spreadsheet User Guide* (TxDOT 2001), such slabs have structural curbs that contribute to the load carrying capacity of the bridge. Thus, these curbs are considered in the FEM model.

The selected bridge has a total length of 75 ft, consisting of three simply supported spans. Each span is 21 ft 4 in. wide and has a center-to-center bearing span length of 25 ft. The integral curbs are trapezoidal in shape, with a bottom width of 1 ft 0.5 in. and a top width of 8 in. and a height of 1 ft 6 in. The steel yield strength and the 28-day concrete compressive strength are taken as 33 ksi and 2.5 ksi, respectively, according to the values used for load rating calculations noted

in TxDOT inspection reports (TxDOT 2018a). The bridge carries two lanes, one in each direction, and has an ADT of 30 vehicles. These properties are tabulated in Table 5.2.

Table 5.2. Geometric and Material Properties for Bridge CS-9

Characteristic	Measurement
Total Length	75'-0"
Controlling Span Length	25'-0"
Deck Width	21'-4"
Roadway Width	20'-0"
Curb Height	1'-6"
Curb Top Width	0'-8"
Curb Bottom Width	1'-5"
Steel Yield Strength	33 ksi
Slab Thickness	11"
28-day Concrete Compressive Strength	2.5 ksi
Number of Lanes	2

Bridge CS-9 carries FM 216 and traverses Flag Creek near Walnut Springs, Texas, approximately 7.0 mi north of FM 927. It has a deck condition rating of 6 (Satisfactory), a superstructure condition rating of 6 (Satisfactory), and a substructure condition rating of 6 (Satisfactory). The concrete slab controls the rating of the bridge, which has an inventory gross loading of 16 US tons and an operating gross loading of 33.7 US tons. The bridge is posted for a 28,000 lbs tandem axle. Figure 5.1 shows a transverse section detail obtained from TxDOT inspection reports (TxDOT 2018a), and Figure 5.2 shows an elevation view and an underside view of Bridge CS-9.

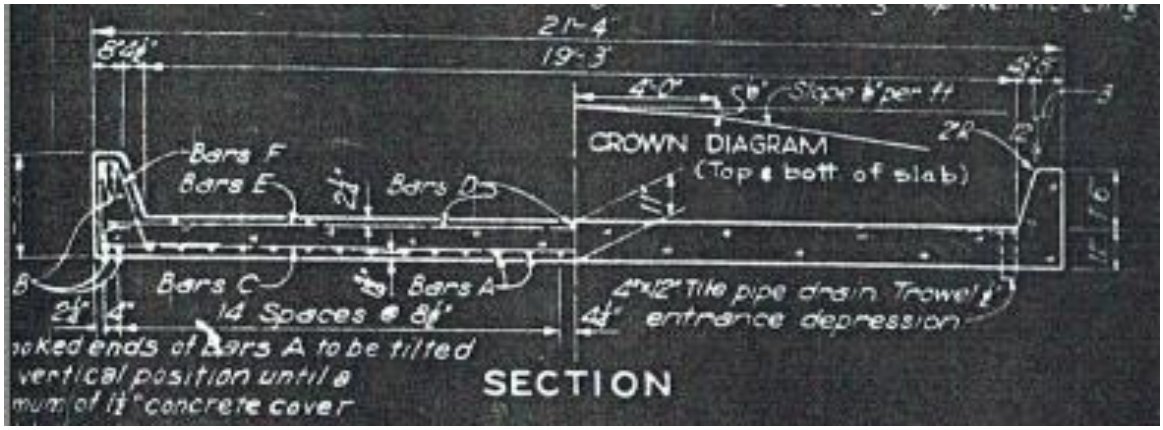

Figure 5.1. Bridge CS-9 Transverse Section (TxDOT 2018a)

(a) Elevation View

(b) Underside View

Figure 5.2. Photographs of Bridge CS-9 (TxDOT 2018a)

5.3 APPROXIMATE ANALYSIS METHODS FOR SLAB TYPE BRIDGES

5.3.1 Equivalent Strip Width Methods

The *AASHTO Standard Specifications* (AASHTO 2002) Article 3.24.3.2 predicts the wheel load distribution width *E* (ft) for both single-lane-loaded and multi-lane loaded cases as follows:

$$E = 4 + 0.06S \tag{5.1}$$

where:

E = Slab width over which a wheel load is distributed (ft)

S = Effective span length (ft)

The live load moments and shears are distributed over the equivalent strip width *E* (in.) defined in *AASHTO LRFD Specifications* Article 4.6.2.3, where Equation (5.2) corresponds to a single-lane-loaded situation, while Equation (5.3) is for a multi-lane-loaded condition:

$$E = 10.0 + 5.0\sqrt{L_1 \times W_1} \tag{5.2}$$

$$E = 84.0 + 1.44\sqrt{L_1 \times W_1} \leq \frac{12.0W}{N_L} \tag{5.3}$$

where:

E = Equivalent width for a truck load (in.)

L_1 = Modified span length (ft), minimum of actual span or 60 ft

W_1 = Modified edge-to-edge width of bridge, minimum of actual width or 60 ft for multi-lane loading, or 30 ft for single-lane loading (ft)

W = Actual edge-to-edge width of bridge (ft)

N_L = Number of design lanes

Amer et al. (1999) used the grillage analogy method to identify the main parameters influencing the equivalent width of slab bridges, compared the equivalent widths of slab bridges defined in the standard *AASHTO Standard* and *AASHTO LRFD Specifications* with those based on field tests and analyses, and proposed a simple design formula for the effective width of solid slab bridges. The main parameters considered in this study were the span length, bridge width, slab thickness, edge beam, and number of lanes. A parametric study was carried out using the AASHTO HS-20 standard truck. Based on the parametric studies, Amer et al. (1999) proposed the following equation to calculate the equivalent width *E* (ft) over which the truck load is assumed to be uniformly distributed:

$$E = 6.89 + 0.23L \leq \frac{W}{N_L} \tag{5.4}$$

where:

E = Equivalent width for a truck load (ft)

L = Span length (ft)

W = Bridge width (ft)

N_L = Number of design lanes

This equation is limited to spans of up to 40 ft (12.2 m) and slab thicknesses of up to 14 in. (360 mm). The effect of any edge beam, if present, is taken into account by multiplying Equation (5.4) with the factor C_{edge}, defined as follows:

$$C_{edge} = 1.0 + 0.5\left(\frac{d_1}{3.28} - 0.15\right) \geq 1.0 \tag{5.5}$$

where:

d_1 = Edge beam depth above slab thickness (ft)

In 2012, researchers at the University of Delaware were tasked by the Delaware Department of Transportation (DelDOT) to load test a selection of slab bridges and determine their actual effective width, with the goal of developing new effective width formulas to be used in Delaware (Jones and Shenton 2012). In this study, a diagnostic load test was conducted on six slab bridges in the state of Delaware. Longitudinal strain versus transverse transducer location plots were developed for each bridge using the data collected from the field tests. The area under the

curve of these plots was used to convert the plot to one that had a constant strain with the same area under the graph. From this new plot, the measured effective width was found as one half of the width of the constant strain graph. A schematic representation of the idealized strain distribution and effective width is shown in Figure 5.3.

The following equations for equivalent width were proposed, where Equation (5.6) corresponds to the equivalent width for a single-lane loaded situation, and Equation (5.7) corresponds to a multi-lane loaded scenario:

$$E = 10.0 + 5.8\sqrt{L_1 W_1} \tag{5.6}$$

$$E = 84.0 + 2.06\sqrt{L_1 W_1} \leq \frac{12.0 W_1}{N_L} \tag{5.7}$$

where:

- E = Equivalent or effective width for truck load (in.)
- L_1 = Modified span length (ft) taken equal to the lesser of the actual span length or 60 ft
- W_1 = Modified edge-to-edge width (ft) of the bridge taken to be equal to the lesser of the actual width or 60 ft for multilane loading, or 30 ft for single-lane loading
- W = Physical edge-to-edge width of the bridge (ft)
- N_L = Number of design lanes

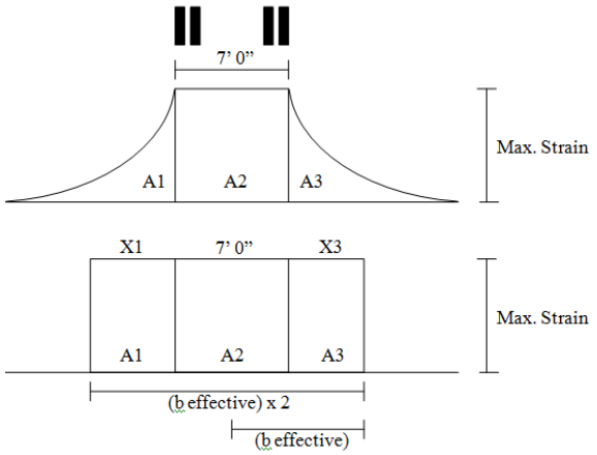

Figure 5.3. Schematic Representation of Strain Distribution and Effective Width (Jones and Shenton 2012)

5.3.2 Illinois Bulletin Method

A modified version of these constant depth slab bridges with monolithically poured curbs/parapets were called Type FS bridges in TxDOT standard drawings. These integrated structural curbs/parapets were designed based on simplified guidelines established with findings from research conducted at the University of Illinois (Jenson et al. 1943). It was found that by adopting integrated structural curbs (Type FS) that act as an edge girder, the slab could be designed thinner than standard CS bridges, thereby making FS bridges more economical. Several analytical and experimental research findings related to the design of FS bridges in Illinois were provided in a series of documents, starting with Illinois Bulletin 346, and thus the method of analysis for FS bridges is termed Illinois Bulletin 346 Method (IB346).

In the simplified analysis method, the cross-section of an FS bridge is divided into two parts: the slab and the edge curb/beam. The total static live load moment resisted by the curb and slab in a FS simply supported bridge is given as follows:

$$M_{static} = m\frac{Pa}{4} \tag{5.8}$$

where:

m = Number of rear wheel loads (e.g., m = 4 for a two-lane-loaded bridge)

P = Magnitude of real wheel load (impact factor not included for comparison with other methods)

a = Span of bridge from center-to-center of bearing areas

The live load moment in the curb is assumed to be reduced by 25 percent when the loads are shifted transversely. Therefore, the moment resisted by each curb can be calculated using Equation (5.9):

$$M_{curb} = \frac{m}{2} 0.75 C_1 \frac{Pa}{4} \tag{5.9}$$

where:

C_1 = Dimensionless coefficient that is defined by the following empirical equation:

$$C_1 = \left(\frac{12}{2.5 + G}\right) \frac{\left(4 - \frac{v}{a}\right)}{\left(4 + 28\left(\frac{v}{a}\right)\right)}$$

in which:

$$G = \frac{ah^3}{12I}$$

G = Dimensionless stiffness factor, ratio of slab stiffness to curb stiffness

I = Moment of inertia of curb gross section outside the roadway width (ft^4)

h = Slab thickness (ft)

v = Axle width, center-to-center of truck tires (6 ft)

Therefore, the total live load moment resisted by the slab alone is the difference between the total moment on the bridge and two curbs:

$$M_{slab} = M_{total} - 2M_{curb} \tag{5.10}$$

The average live load moment per unit width of slab can then be calculated as:

$$M_{slab,avg} = \frac{M_{slab}}{b} \tag{5.11}$$

where:

b = Width of roadway between curbs (ft)

5.4 FEM MODEL DEVELOPMENT

A three-dimensional linear FEM model of the selected simple-span concrete slab bridge was developed using the commercial CSiBridge software (Computers and Structures Inc. 2019). The bridge geometry was modeled based on information provided in the structural design drawings and TxDOT inspection reports (TxDOT 2018a). The next subsection describes the FEM modeling approach, finite element types, and material properties. The following subsection presents the results of the mesh sensitivity study and selection of mesh size. The last subsection provides details about boundary conditions, which are critical for accurately capturing the behavior of the bridge.

5.4.1 Bridge Model Description

A realistic model of the bridge superstructure requires appropriate finite element types, boundary conditions, and a sufficiently refined mesh. There is ample information providing recommendations about FEM modeling for various concrete bridge superstructures (Davids et al. 2013; Hueste et al. 2015). Based on the recommendation found in the literature, a three-dimensional linear finite element model of Bridge CS-9 was developed. The bridge geometry is modeled exactly as in the actual bridge drawings, including the integral curbs, without any simplification based on information gathered from structural drawings and inspection reports. The bridge superstructure, including the curbs, were modeled using 3D eight-node linear solid brick elements. The slab and curb reinforcement were not modeled because the linear elastic model will be analyzed under service level loads only, and the superstructure is expected to remain in the linear elastic range. Figure 5.4 shows the finite element model for Bridge CS-9.

In the absence of any record of the specified material strengths for Bridge CS-9, the steel yield strength and the 28-day concrete compressive strength are taken in accordance with AASHTO MBE guidelines (AASHTO 2018). These figures are consistent with the values used in TxDOT load rating calculations (TxDOT 2018a). Table 5.3 lists the material properties adopted for the FEM model.

The MOE, E_c, for concrete was calculated using Equation (5.12), as stated in the *AASHTO LRFD Specifications* (AASHTO 2017). This equation is valid for normal weight concrete with unit weights between 0.09 and 0.155 kcf and design compressive strength up to 15.0 ksi:

$$E_c = 33{,}000 K_1 w_c^{1.5} \sqrt{f_c'} \quad (5.12)$$

where:

E_c = Elastic modulus of concrete, ksi

K_1 = Correction factor for source of aggregate, to be taken as 1.0 unless determined by physical test

w_c = Unit weight of concrete, kcf

f_c' = Compressive strength of concrete, ksi

Table 5.3. Material Properties for Bridge CS-9

Bridge	**Concrete Strength (f_c')**	**Modulus of Elasticity (E_c)**	**Concrete Unit Weight (w_c)**
	(psi)	**(ksi)**	**(pcf)**
CS-9	2.5	3031	150

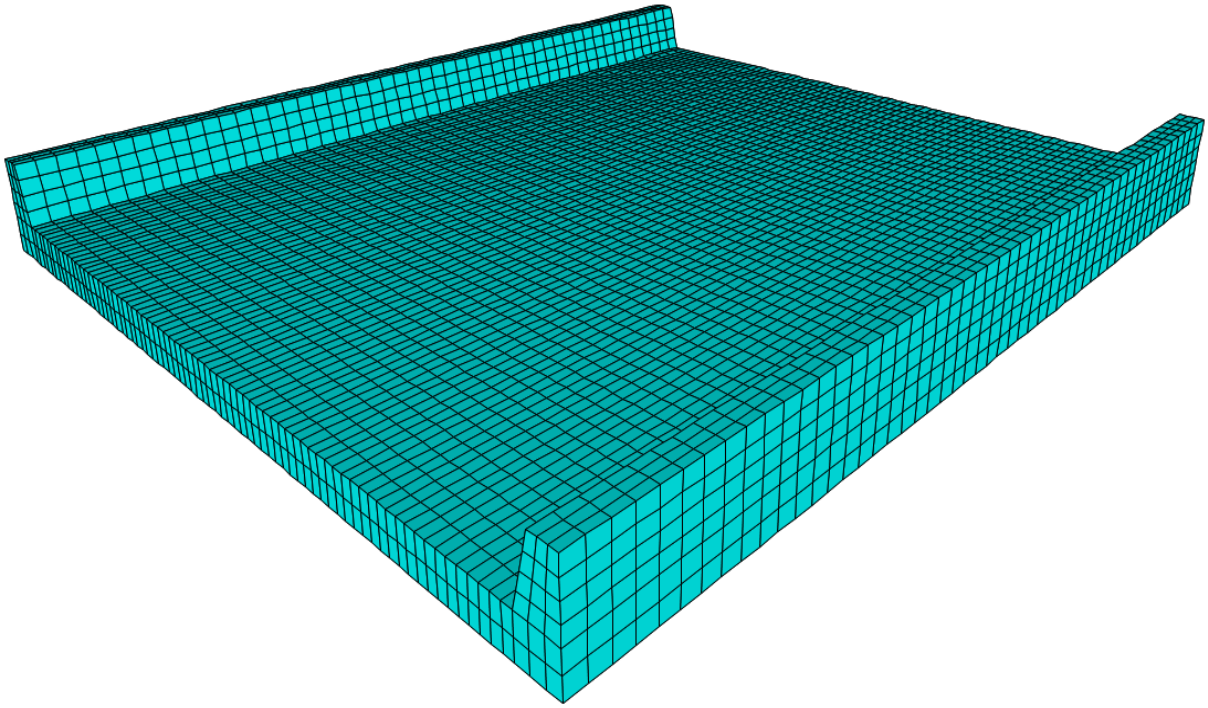

Figure 5.4 FEM Model of Bridge CS-9 (6 in. mesh)

5.4.2 Mesh Sensitivity Analysis

A finite element mesh was generated for the model with consistently spaced nodes. A mesh sensitivity study was undertaken for several models with different mesh sizes (4 in., 6 in., 12 in., and 18 in.) in order to determine the optimal mesh size for the three-dimensional linear finite element model of Bridge CS-9. The effect of different mesh sizes on the calculated shear force, moment, and bending stress was examined. Figure 5.5 shows these different mesh sizes when applied to Bridge CS-9.

The FEM results for shear force, bending moment, and stress for Bridge CS-9 model are listed in Table 5.4. All the results correspond to the case of a single HS-20 truck pass through the right lane, 2 ft from the centerline of the bridge (Path 2 in Figure 5.6). The accuracy of the results increases with decreasing mesh size from 18 in. to 12 in. However, reducing the mesh size to 4 in. does not significantly increase the accuracy when compared to the results obtained from the model with a mesh size of 6 in. Thus, a 6 in. mesh size was chosen to be used for Bridge CS-9. With these mesh size and discretization points, an accurate FEM model of the bridge with an efficient computation time was created in CSiBridge.

Table 5.4. FEM Results for CS-9 with Different Mesh Sizes

Mesh Size (in.)	Maximum Moment (kip-ft)	Maximum Shear (kip)	Maximum Stress (ksi)
4	197.33	15.36	0.277
6	200	16	0.277
12	199.36	15.36	0.277
18	195.76	14.72	0.269

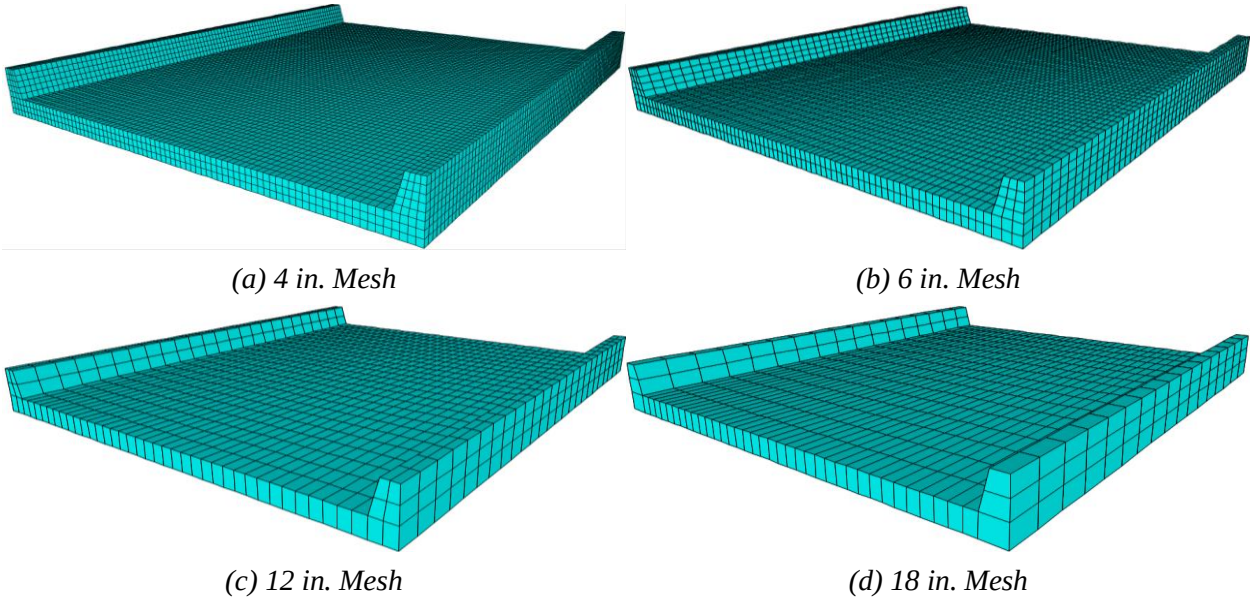

(a) 4 in. Mesh *(b) 6 in. Mesh*

(c) 12 in. Mesh *(d) 18 in. Mesh*

Figure 5.5. FEM Models Showing Different Mesh Sizes for Bridge CS-9

5.4.3 Boundary Conditions

In the absence of more accurate information, the boundary conditions at the supports were modeled as simply supported with pins and rollers. One end of the slab bridge was modeled with roller supports, while the other end was modeled with pin supports. The roller support releases all three rotational degrees of freedom and two translational degrees of freedom in the horizontal plane (two orthogonal in-plane directions parallel to the bridge superstructure) and fully restrains the translational degree of freedom in the vertical direction (perpendicular to the plane of the bridge superstructure). The pin support releases all three rotational degrees of freedom and restrains all three translational degrees of freedom.

Accurately modeling the boundary conditions may have a significant effect on the overall behavior of the bridge. Although the boundary conditions are initially modeled as simply supported, the level of restraint will be assessed based on experimental results from the next task. Unintended partial fixity may develop at the supports due to the bearing detail at the supports and/or friction between the bottom surface of the bridge and the bearing surface.

5.5 BASIC VERIFICATION OF FEM MODELS

Some basic loading conditions were simulated to verify that the FEM model was providing expected results. These basic checks were conducted by investigating maximum deflections under a uniformly distributed dead load and maximum moments and support reactions under the HS-20 truck and HL-93 loading.

The characteristics of the HS-20 design truck as specified in the *AASHTO LRFD Specifications* (AASHTO 2017) are shown in Figure 2.8. The total load in the front axle is 8 kips and is 14 ft away from the middle axle, which has a total load of 32 kips. The rear axle has a total load of 32 kips and may be spaced between 14 ft and 30 ft from the middle axle, depending on which creates the maximum force effect being investigated. An alternative loading scheme consisting of a uniformly distributed load of 0.64 kip/ft and a concentrated load of 18 kips when checking moment or 26 kips when checking shear is also considered in *AASHTO Standard Specifications* (AASHTO 2002).

The designated HL-93 loading consisting of the design truck or design tandem coincident with the design lane load is shown in Figure 2.9. The design lane load consists of a 0.64 kip/ft uniformly distributed load over a 10 ft width. Two 25-kip axle loads spaced 4 ft apart longitudinally and 6 ft apart transversely constitute the design tandem load. The design truck or design tandem is used, depending on which will create the maximum force effect on the span.

5.5.1 Verification of Maximum Deflection

The maximum deflection for the bridge superstructure under a uniformly distributed dead load was verified with the deflections obtained from theoretical structural analysis. The estimated deflections for the slab bridge obtained from FEM analysis were compared to the calculated deflections. The equivalent distributed load was calculated as the sum of the weight of the slab,

the deck, and wearing surface. The total uniformly distributed weight is determined from Equation (5.13):

$$w = w_s + w_{ws} + 2 \times w_{CURB} = 4.02 \text{ kip/ft} \tag{5.13}$$

in which:

w_s = weight of slab = 2.65 kip/ft

w_{CURB} = weight of curb = 0.34 kip/ft

$$w_{ws} = (\gamma_{ws})(t_{ws})(b) = 0.69 \text{ kip/ft} \tag{5.14}$$

where:

γ_c = unit weight of concrete = 0.15 kip/ft^3

b = clear slab width between curbs (ft)

w_{ws} = weight of wearing surface (kip/ft)

γ_{ws} = unit weight of the wearing surface = 0.144 kip/ft^3

t_{ws} = thickness of the wearing surface (ft)

The midspan deflection of the concrete slab bridge can be calculated using Equation (5.15) for a simply supported beam under a uniformly distributed load:

$$\Delta = \frac{5wL^4}{384E_cI} = 0.116 \text{ in.} \tag{5.15}$$

where:

I = Moment of inertia of transverse section = 100,702 in^4

E_c = MOE of concrete = 3031 ksi

Table 5.5 shows the deflections calculated using each method and the percent difference between them. The FEM deflections are closely matched to the calculated deflections.

Table 5.5. Dead Load Deflection Comparison for Bridge CS-9

Bridge ID	FEM Deflection (in.)	Calculated Deflection (in.)	Percent Difference (%)
CS-9	0.121	0.116	4.31

5.5.2 Verification of Absolute Maximum Moment

To verify that the truck loadings were modeled correctly, the live load moments were compared to the live load moments obtained from theoretical influence line analysis. The model was analyzed under an HS-20 truck load and HL-93 loading. In Chapter 2, calculations for obtaining the maximum moment due to moving loads in a simple span are presented in Section 2.4.2. Table 5.6 shows the calculated live load moments, the FEM moments, and the percent difference between them. Again, the model provides a close match to the expected values.

Table 5.6. Live Load Moment on the Comparison for Bridge CS-9

Bridge ID	Applied Load	FEM One-Lane Moment on Total Section (kip-ft)	Expected One-Lane Moment on Total Section (kip-ft)	Percent Difference (%)
CS-9	HS-20	200	200	0
	HL-93	310.63	302.56	2.67
Note: All calculated moments are without the application of the impact factor				

5.5.3 Verification of Maximum Shear Forces

To verify that the structural supports have been modeled correctly, maximum shears corresponding to the live loads were verified against the shear obtained from basic structural analysis. Step-by-step loading is employed by FEM for the moving load analysis. The step size of the moving load was adjusted so that the first step with the rear axle of the truck on the bridge positioned the rear axle 1 ft away from the support. The resulting support reactions were obtained from the FEM model and compared with those calculated using classical structural analysis methods. Table 5.7 shows the support reactions calculated using each method and the percent difference between them. The FEM shear forces match very closely with the calculated shear forces.

Table 5.7. Live Load Support Reactions Comparison for Bridge CS-9

Bridge ID	Applied Load	FEM One-Lane Shear on Total Section (kip)	Expected One-Lane Shear on Total Section (kip)	Percent Difference (%)
CS-9	HS-20	43.5	43.5	0.0
	HL-93	51.5	52.00	1.0
Note: All calculated shears are without the application of the impact factor.				

5.6 SIMULATING VEHICLE LOADS

The truck loads and lane loads were placed transversely on Bridge CS-9 as per the *AASHTO Standard Specifications* (AASHTO 2002) and *AASHTO LRFD Specifications* (AASHTO 2017). Bridge CS-9 has two lanes, each 9.625 ft wide.

A linear static moving load was applied, with each truck moving along the length of the bridge in approximately 1 ft increments. It should be noted that although it would be an unlikely event, for the two-lane-loaded cases, both trucks traveled along the bridge in the same direction in order to produce the maximum possible load effect on the bridge.

5.6.1 Simulating HS-20 Truck Loading

For a one-lane-loaded case based on the *AASHTO Standard Specifications*, the truck was placed so that the exterior wheel line was 2 ft from the nominal face of the curb, which is 2 ft 10 in. from the edge of the bridge (Path 1). Due to the narrow lane width, the only other loading scenario considered was where the interior wheel line was 1 ft 10 in. from the centerline of the bridge (Path 2). For a two-lane-loaded case, one truck was positioned in Path 1 and another truck in Path 2. This created two separate one-lane-loaded cases and one two-lane-loaded case. Figure 5.6 shows the different HS-20 truck loading cases across the transverse section of Bridge CS-9. The red and blue arrows represent the wheel lines of the truck and the black dashed line is the centerline of the bridge.

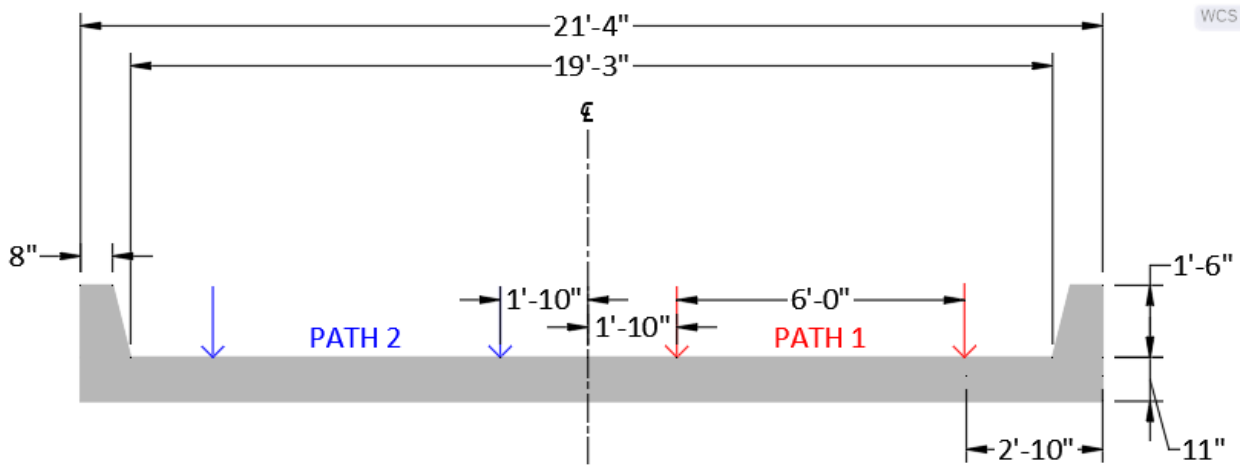

Figure 5.6. HS-20 Truck Loading Cases for Bridge CS-9

5.6.2 Simulating HL-93 Loading

For loading based on the AASHTO LRFD Specifications, the tandem configuration and lane load were added to the already created load cases. The tandem configuration was used for HL-93 loading since it controls over the truck configuration for short span bridges less than 40.5 ft long. The design tandem was placed transversely in the same manner as described for the HS-20 truck. The lane load was placed immediately adjacent to the edge of the barrier for both Path 1 and Path 2. Because the lanes are less than 10 ft wide, the lane load was distributed over the lane width of 9 ft 7.5 in. Figure 5.7 shows the different HL-93 loading cases across the transverse section of Bridge CS-9. The red and blue arrows represent the wheel lines of the truck, the red and blue cross-hatched regions represent the lane load distributed over the lane width, and the black dashed line is the centerline of the bridge.

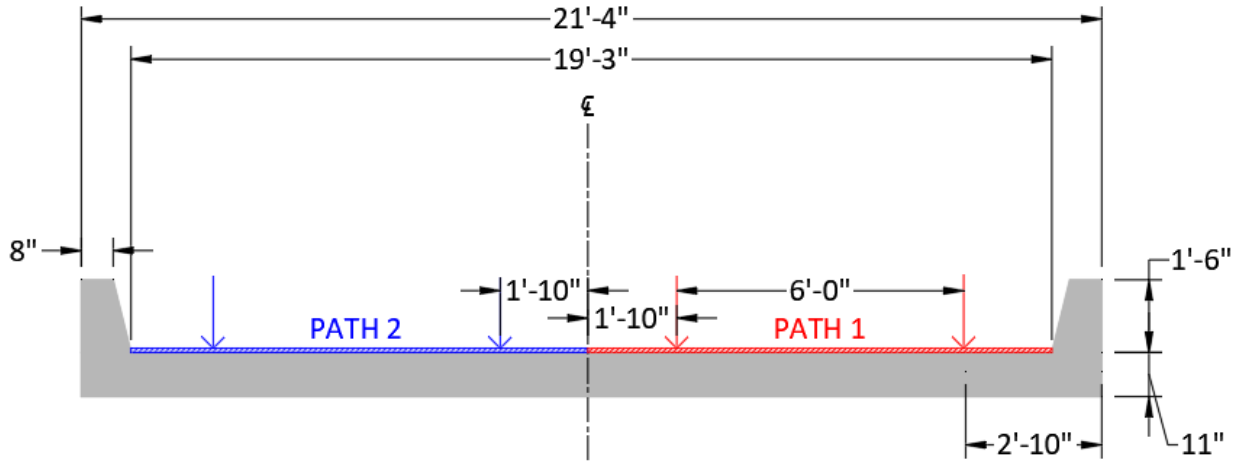

Figure 5.7. HL-93 Loading Cases for Bridge CS-9

5.7 FEM RESULTS

Bridge CS-9 was analyzed using the FEM software CSiBridge under the loading scenarios provided in Figure 5.6 and Figure 5.7. Slab displacement profiles were obtained for loading along both paths. Modal analysis was conducted to determine estimated modal frequencies and mode shapes. Live load moment and shear values were also extracted and analyzed to compare the expected LLDFs with the LLDFs prescribed in *AASHTO Standard Specifications* (AASHTO 2002) and *AASHTO LRFD Specifications* (AASHTO 2017).

5.7.1 Modal Properties

The first longitudinal bending mode and the first torsional mode constitute the first two modes of Bridge CS-9. The frequency for the first longitudinal bending mode was determined to be 10.11 Hz, and the frequency for the first torsional mode was 12.11 Hz. The contours of the first longitudinal bending mode shape, along with the normalized amplitudes along the span of the bridge, are shown in Figure 5.8(a). Figure 5.8(b) shows the contours of the first torsional mode shape and the normalized amplitudes transverse to the span.

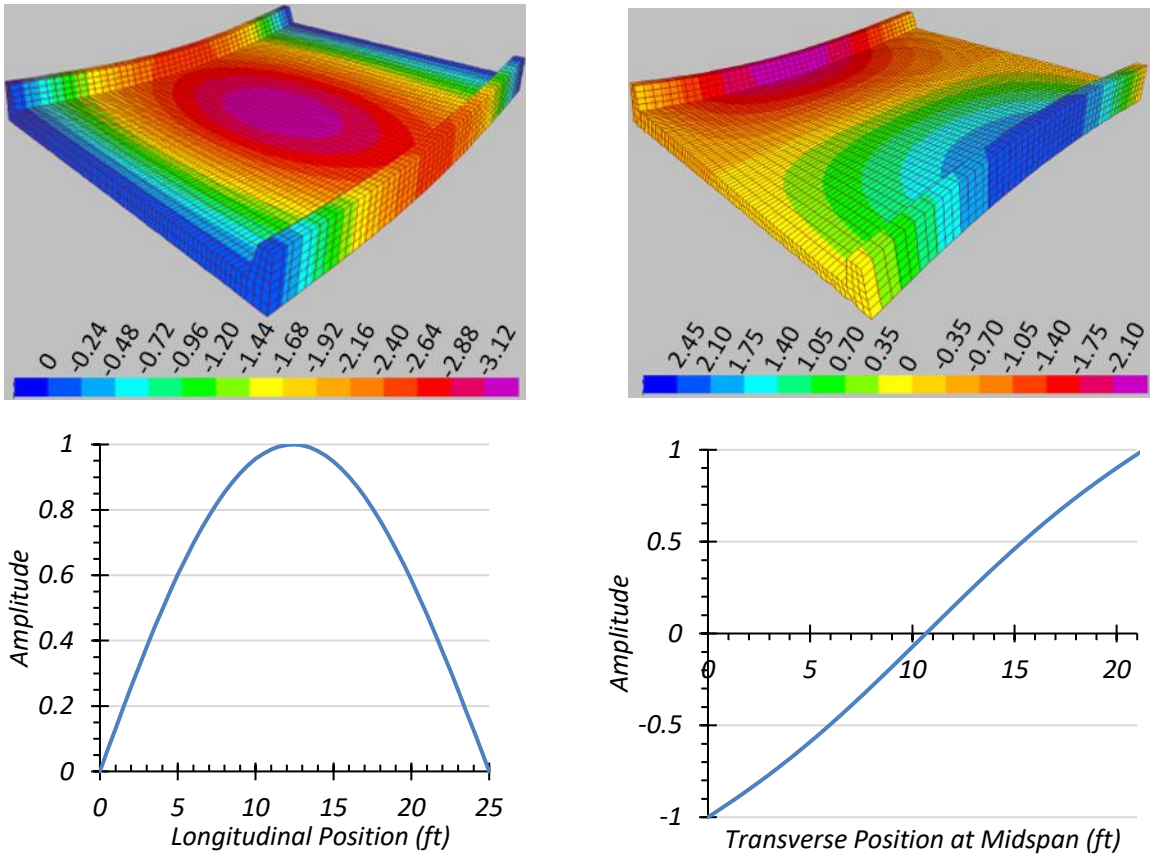

(a) Longitudinal Bending Mode (f=10.11 Hz) *(b) Torsional Mode (f=12.11 Hz)*

Figure 5.8. First Two Mode Shapes of Bridge CS-9

5.7.2 HS-20 Live Load Analysis

Bridge CS-9 was subjected to the design HS-20 truck load as defined in the *AASHTO Standard Specifications* (AASHTO 2002).The paths defined in Figure 5.6 were prescribed in FEM for analysis. The slab bridge was divided into 10, 20, and 38 transverse sections, and the corresponding bending moment and LLDFs were compared. The exterior transverse sections for each group consisted of the two curbs, each 12.5 in. wide at the base of the curb. The clear roadway width of 19 ft 3 in. was divided into 8, 18, and 36 interior transverse sections for 10, 20, and 38 groups, respectively. The LLDF for each transverse section was defined to be the ratio of the corresponding bending moment of the section to the total bending moment of the whole bridge section due to one-lane loading. Similarly, the LLDFs for the curbs were calculated as the ratio of the curb bending moment to the total bending moment due to one-lane loading. The bending moment and

corresponding LLDFs for the various groups were compared, as shown in Figure 5.9. Table 5.8 tabulates the maximum moment for each transverse section in each group. The results corresponding to 20 transverse sections (12.8 in. elements) provide sufficient refinement in the transverse direction to capture the transverse distribution of vehicle load. Thus, results corresponding to 20 transverse sections are presented in the following subsections. The equivalent width for the interior slab portion between curbs was calculated as the inverse of per ft share of the maximum LLDF occurring within the interior slab portion.

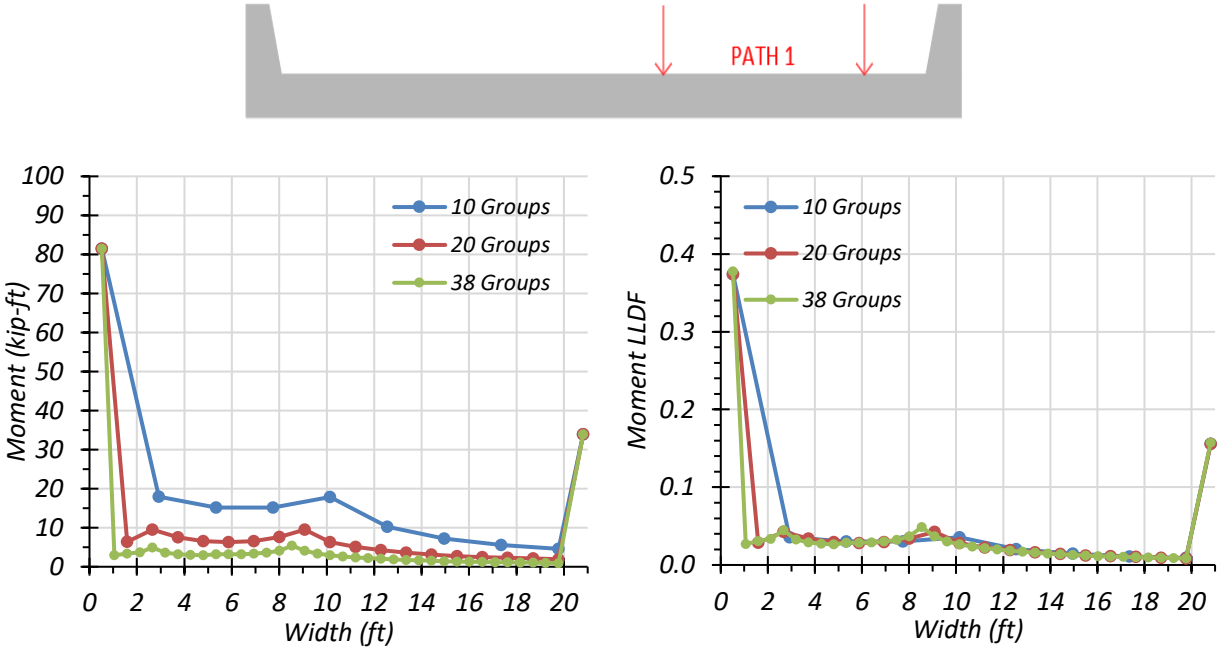

(a) Moment *(b) Moment LLDF*

Figure 5.9. Comparison of Bending Moment Results for Different Number of Sections

Table 5.8. Maximum Moments under HS-20 Loading for Different Number of Transverse Sections

Group	S1	S2	S3	S4	S5	S6	S7	S8	S9	S10	S11	S12	S13	S14	S15	S16	S17	S18	S19	S20
10	81.5	18.0	15.1	15.2	17.9	10.2	7.2	5.5	4.6	33.9										
20	81.5	6.4	9.5	7.6	6.5	6.3	6.6	7.6	9.5	6.3	5.0	4.2	3.6	3.2	2.7	2.5	2.3	2.1	1.9	33.9
38	81.5	3.0	3.4	3.7	4.9	3.6	3.2	3.0	3.0	3.2	3.2	3.2	3.3	3.6	4.1	5.4	4.1	3.3	2.9	2.6
	S21	**S22**	**S23**	**S24**	**S25**	**S26**	**S27**	**S28**	**S29**	**S30**	**S31**	**S32**	**S33**	**S34**	**S35**	**S36**	**S37**	**S38**		
	2.4	2.2	2.0	1.9	1.8	1.6	1.5	1.4	1.3	1.3	1.2	1.2	1.1	1.1	1.0	1.0	0.9	33.9		

Note: Moments have kip-ft units and load is along Path 1.

*5.7.2.1 **Deflection Results***

The estimated slab deflection profiles and contours along the span for one-lane loading along Path 1 and Path 2 are shown in Figure 5.10. The maximum deflections under HS-20 loading for each loaded path is tabulated in

Table 5.9. The maximum deflection under one-lane HS-20 loading was observed to be 0.12 in. for both Path 1 and Path 2.

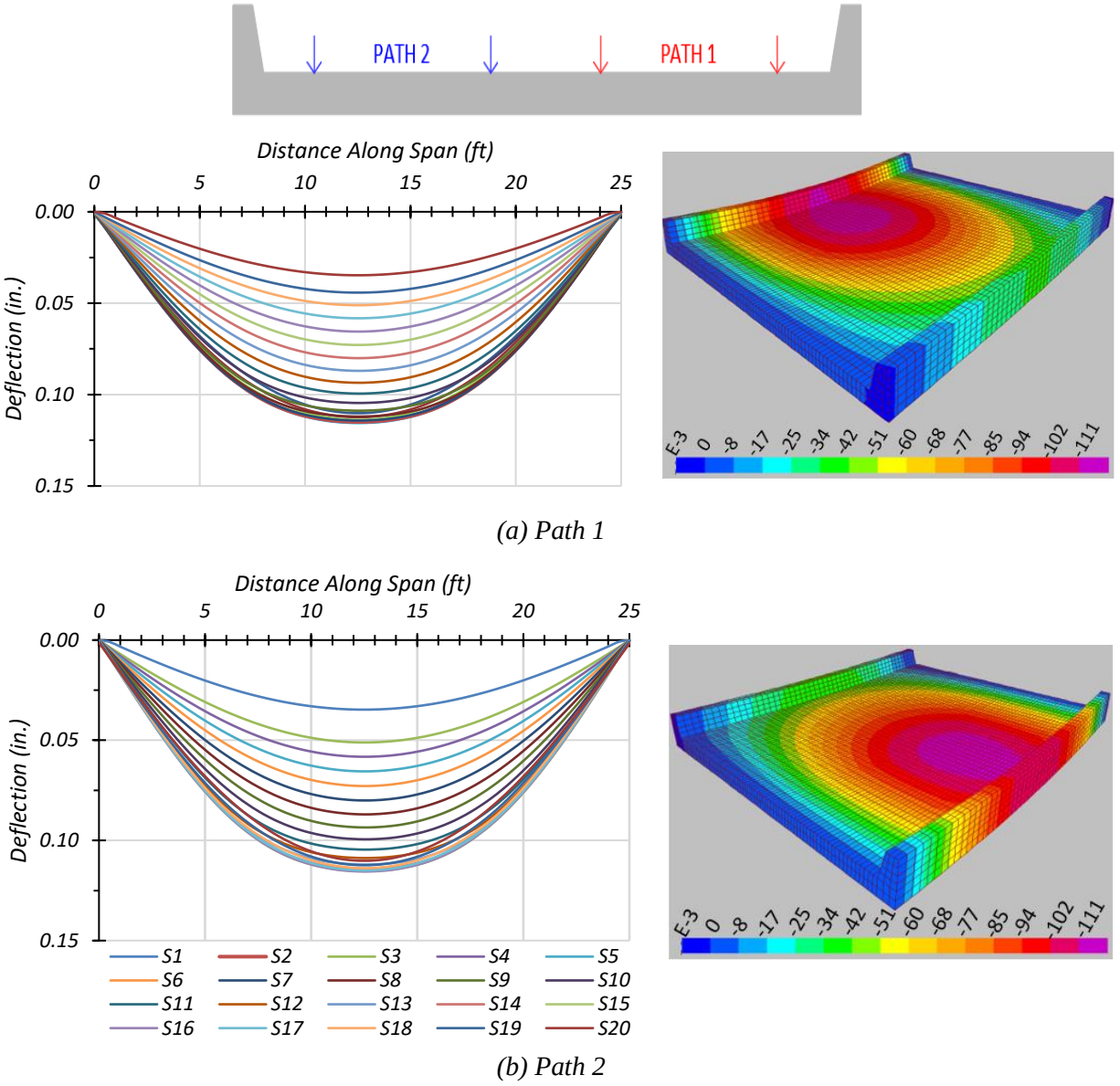

Figure 5.10. Deflection Profiles with HS-20 Loading

Table 5.9. Maximum Deflections with HS-20 Loading

Loading	S1	S2	S3	S4	S5	S6	S7	S8	S9	S10	S11	S12	S13	S14	S15	S16	S17	S18	S19	S20
Path 1	0.11	0.11	0.11	0.11	0.12	0.12	0.11	0.11	0.11	0.10	0.10	0.09	0.09	0.08	0.07	0.07	0.06	0.05	0.04	0.03
Path 2	0.03	0.04	0.05	0.06	0.07	0.07	0.08	0.09	0.09	0.10	0.10	0.11	0.11	0.11	0.12	0.12	0.11	0.11	0.11	0.11
Note: S = transverse section, paths indicate transverse loading positions as shown, deflections have inch units																				

*5.7.2.2 **Moment Results***

The moments corresponding to each transverse section and the corresponding LLDFs for the one-lane and two-lane HS-20 loading paths are shown in Figure 5.11. The corresponding maximum moments for each transverse section and path are listed in Table 5.10. The estimated moment results from the FEM model were used to calculate the equivalent widths for the slab portion and LLDFs for the curbs. Equivalent width for the slab portion is calculated as the inverse of the maximum LLDF of 1 ft slab sections. A comparison of the estimated equivalent width for the interior slab portion obtained from the FEM model for the two-lane-loaded scenario and those calculated using the approximate equations in the *AASHTO Standard Specifications* (AASHTO 2002) and *AASHTO LRFD Specifications* (AASHTO 2017) is provided in Table 5.11. Comparison with studies such as Amer et al. (1999) and Jones and Shenton (2012) was also carried out, as shown in Figure 5.12, based on the two-lane-load case. All the equivalent widths were conservative in comparison to the FEM results.

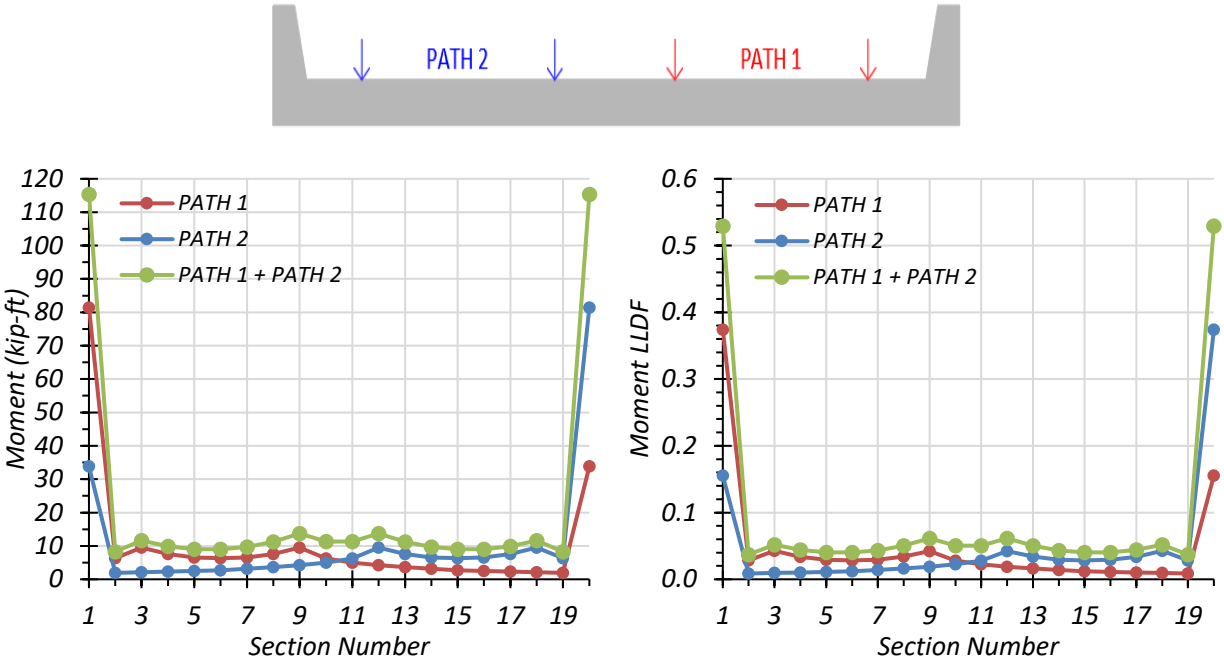

(a) Moment *(b) Moment LLDF*

Figure 5.11. Moment Results with HS-20 Loading

Table 5.10. Maximum Moments with HS-20 Loading

Loading	S1	S2	S3	S4	S5	S6	S7	S8	S9	S10	S11	S12	S13	S14	S15	S16	S17	S18	S19	S20
Path 1	81.5	6.4	9.5	7.6	6.5	6.3	6.6	7.6	9.5	6.3	5.0	4.2	3.6	3.2	2.7	2.5	2.3	2.1	1.9	33.9
Path 2	33.9	1.9	2.1	2.3	2.5	2.7	3.2	3.6	4.2	5.0	6.3	9.5	7.6	6.6	6.3	6.5	7.6	9.5	6.4	81.5
Path 1 + Path 2	115.4	8.3	11.6	9.9	9.0	9.1	9.7	11.3	13.7	11.3	11.3	13.7	11.3	9.7	9.1	9.0	9.9	11.6	8.3	115.4
Note: S = section, paths indicate transverse loading positions as shown, moments have kip-ft units																				

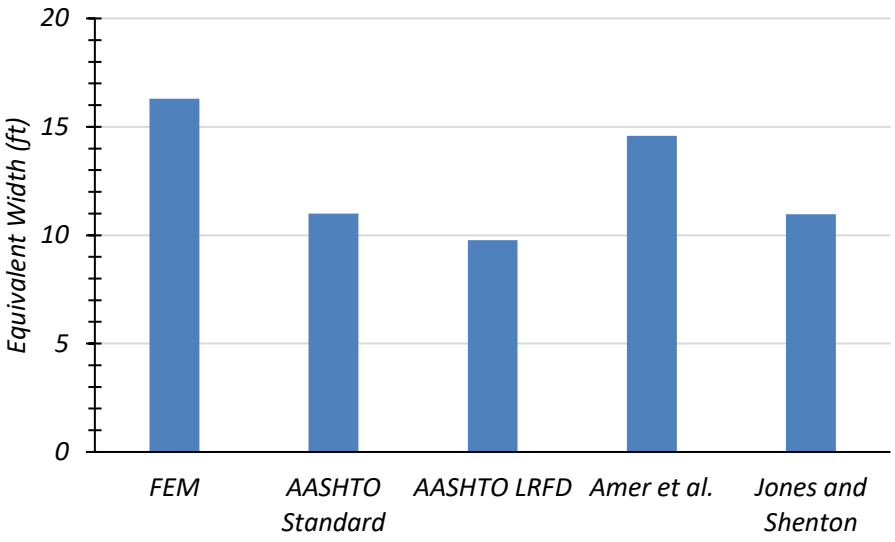

Figure 5.12. Comparison of Equivalent Width with Various Models for HS-20 Loading

Table 5.11. Governing Moment Equivalent Width (ft) for HS-20 Loading for Interior Slab

Loading	FEM (E^m_{FEM})	AASHTO (E^m_{AASHTO})	AASHTO LRFD (E^m_{LRFD})	Amer et al. (E^m_{Amer})	Jones and Shenton ($E^m_{Jones\ \&\ Shenton}$)
One-lane	23.5	11.0	10.5	14.6	12.0
Two-lane	16.3	11.0	9.8	14.6	11.0

Table 5.12 compares the curb moment and the interior slab moment per ft width from the FEM model with the respective moments obtained using the simplified analysis method outlined in IB346. For a one-lane-loaded case, the bending moment obtained from IB346 tends to be highly unconservative for the slab portion, while it is slightly unconservative for the curb. For a two-lane-loaded case, the bending moment obtained from IB346 is highly unconservative for the slab and conservative for the curb.

Table 5.12. Comparison of FEM Moment with HS-20 Loading with IB346

Loading	Component	FEM Moment	IB346 Moment	IB/FEM
One-lane	Curb	81.5	80.7	0.99
	Slab	8.9	2.4	0.27
Two-lane	Curb	115.4	161.4	1.40
	Slab	12.8	4.8	0.37
Note: Curb moment have kip-ft units and slab moment have kip-ft/ft units.				

5.7.2.3 ***Shear Results***

The shear forces in each transverse section and the corresponding shear LLDFs for the one-lane and two-lane HS-20 loading paths are shown in Figure 5.13. The corresponding maximum moments for each section and path are listed in Table 5.13. The estimated shear results from the FEM model were used to calculate the equivalent widths for the slab portion and LLDFs for the curbs. A comparison of the estimated equivalent width for the interior slab portion obtained from the FEM model and those calculated using the approximate equations in the *AASHTO Standard Specifications* (AASHTO 2002) and *AASHTO LRFD Specifications* (AASHTO 2017) is provided in Table 5.14. Comparisons with studies such as Amer et al. (1999) and Jones and Shenton (2012) were also carried out. All the equivalent widths were conservative in comparison to the FEM results.

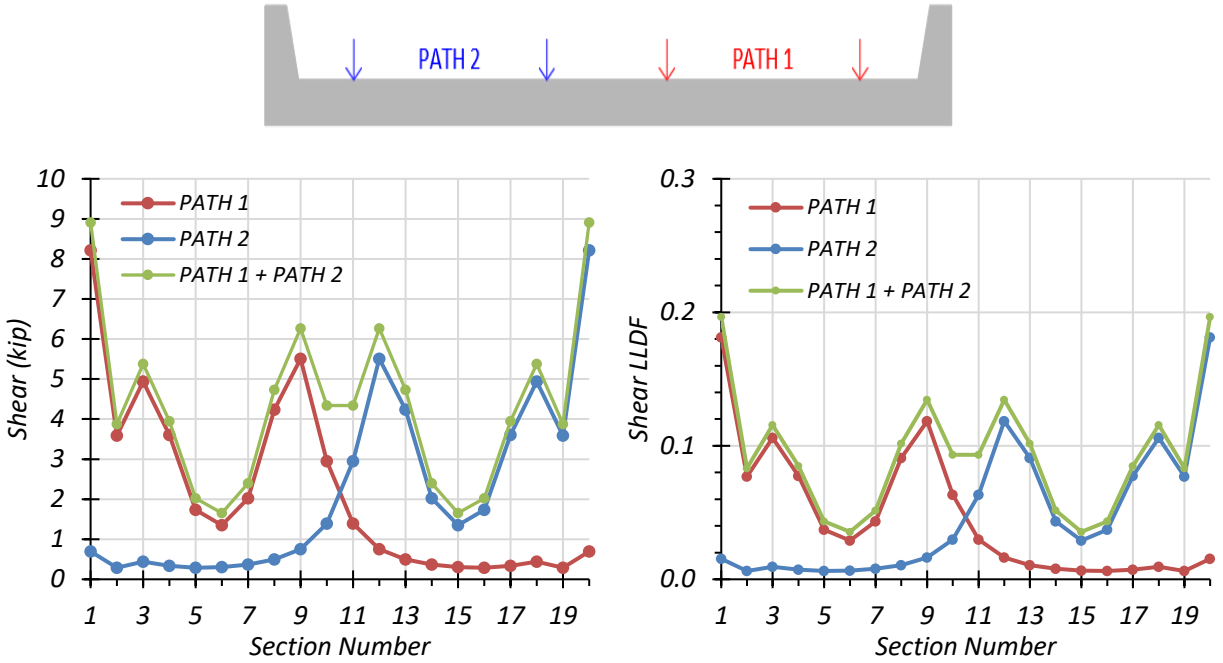

(a) Shear *(b) Shear LLDF*

Figure 5.13. Shear Results with HS-20 Loading

Table 5.13. Maximum Shears with HS-20 Loading

Loading	S1	S2	S3	S4	S5	S6	S7	S8	S9	S10	S11	S12	S13	S14	S15	S16	S17	S18	S19	S20
Path 1	8.2	3.6	4.9	3.6	1.7	1.3	2.0	4.2	5.5	3.0	1.4	0.8	0.5	0.4	0.3	0.3	0.3	0.4	0.3	0.7
Path 2	0.7	0.3	0.4	0.3	0.3	0.3	0.4	0.5	0.8	1.4	3.0	5.5	4.2	2.0	1.3	1.7	3.6	4.9	3.6	8.2
Path 1 + Path 2	8.9	3.9	5.4	3.9	2.0	1.7	2.4	4.7	6.3	4.3	4.3	6.3	4.7	2.4	1.7	2.0	3.9	5.4	3.9	8.9
Note: S = section, paths indicate transverse loading positions as shown, shears have kip units																				

Table 5.14. Governing Shear Equivalent Width (ft) for HS-20 Loading for Interior Slab

Loading	FEM (E^v_{FEM})	AASHTO (E^v_{AASHTO})	AASHTO LRFD (E^v_{LRFD})	Amer et al. (E^v_{Amer})	Jones and Shenton ($E^v_{Jones\ \&\ Shenton}$)
One-lane	8.4	11.0	10.5	14.6	12.0
Two-lane	7.4	11.0	9.8	14.6	11.0

5.7.3 HL-93 Live Load Analysis

Bridge CS-9 was subjected to the HL-93 design loading as defined in the *AASHTO LRFD Specifications* (AASHTO 2017). The paths defined in Figure 5.7 were prescribed in FEM for analysis. The following sections discuss the deflections, bending moment, and shear values obtained from the FEM model.

5.7.3.1 ***Deflection Results***

The estimated girder deflection profiles and contours along the span for one-lane HL-93 loading along Path 1 and Path 2 are shown in Figure 5.14. The maximum deflections under HL-93 loading for each loaded path is tabulated in Table 5.15. The maximum deflection under one-lane HL-93 loading was observed to be 0.174 in. for both Path 1 and Path 2.

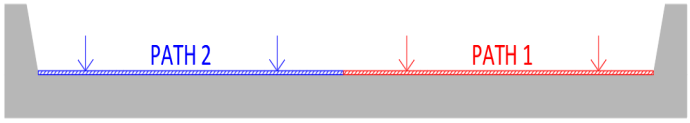

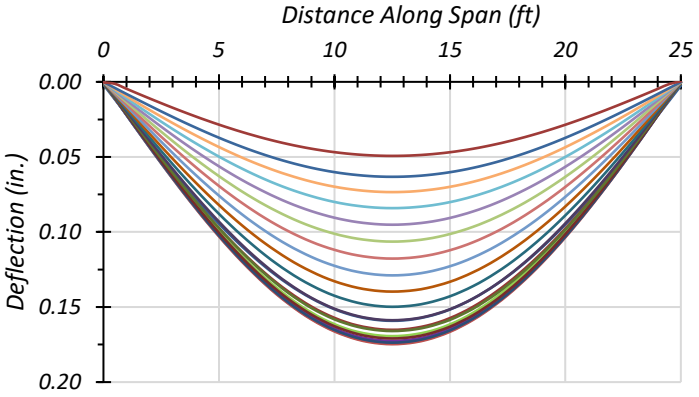

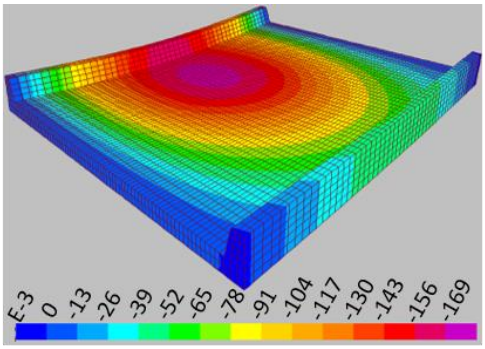

(a) Path 1

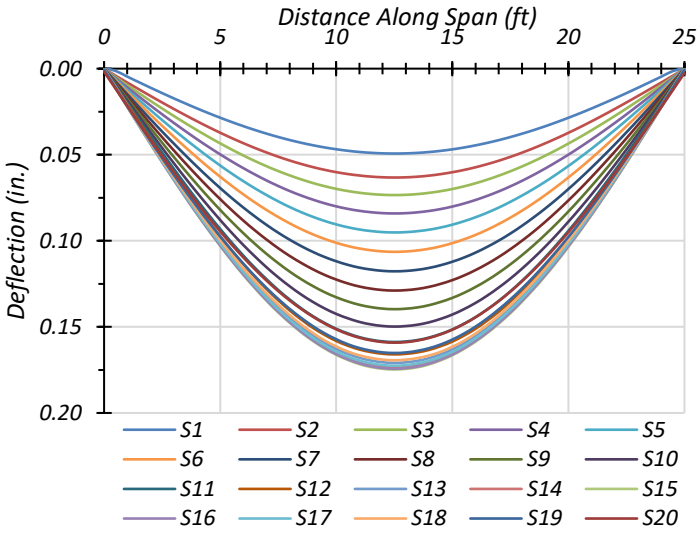

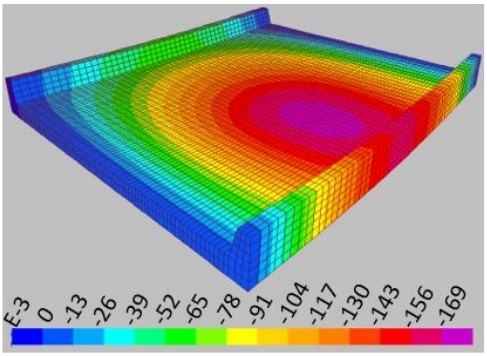

(b) Path 2

Figure 5.14. Deflection Profiles with HL-93 Loading

Table 5.15. Maximum Deflections with HL-93 Loading

Loading	S1	S2	S3	S4	S5	S6	S7	S8	S9	S10	S11	S12	S13	S14	S15	S16	S17	S18	S19	S20
Path 1	0.16	0.17	0.17	0.17	0.17	0.17	0.17	0.17	0.17	0.16	0.15	0.14	0.13	0.12	0.11	0.10	0.08	0.07	0.06	0.05
Path 2	0.05	0.06	0.07	0.08	0.10	0.11	0.12	0.13	0.14	0.15	0.16	0.17	0.17	0.17	0.17	0.17	0.17	0.17	0.17	0.16
Note: S = transverse section, paths indicate transverse loading positions as shown, deflections have in. units																				

5.7.3.2 *Moment Results*

The moments corresponding to each transverse section and the corresponding LLDFs for the one-lane and two-lane HL-93 loading paths are shown in Figure 5.15. The corresponding maximum moments for each section and path are listed in Table 5.16. The estimated moment results from the FEM model were used to calculate the equivalent widths for the slab portion and LLDFs for the curbs. A comparison of the estimated equivalent width for the interior slab portion obtained from the FEM model and those calculated using the approximate equations in the *AASHTO Standard Specifications* (AASHTO 2002) and *AASHTO LRFD Specifications* (AASHTO 2017) is provided in Table 5.17. Comparisons with studies such as Amer et al. (1999) and Jones and Shenton (2012) were also carried out, as shown in Figure 5.16, based on the two-lane-load case. All the equivalent widths were conservative in comparison to the FEM results.

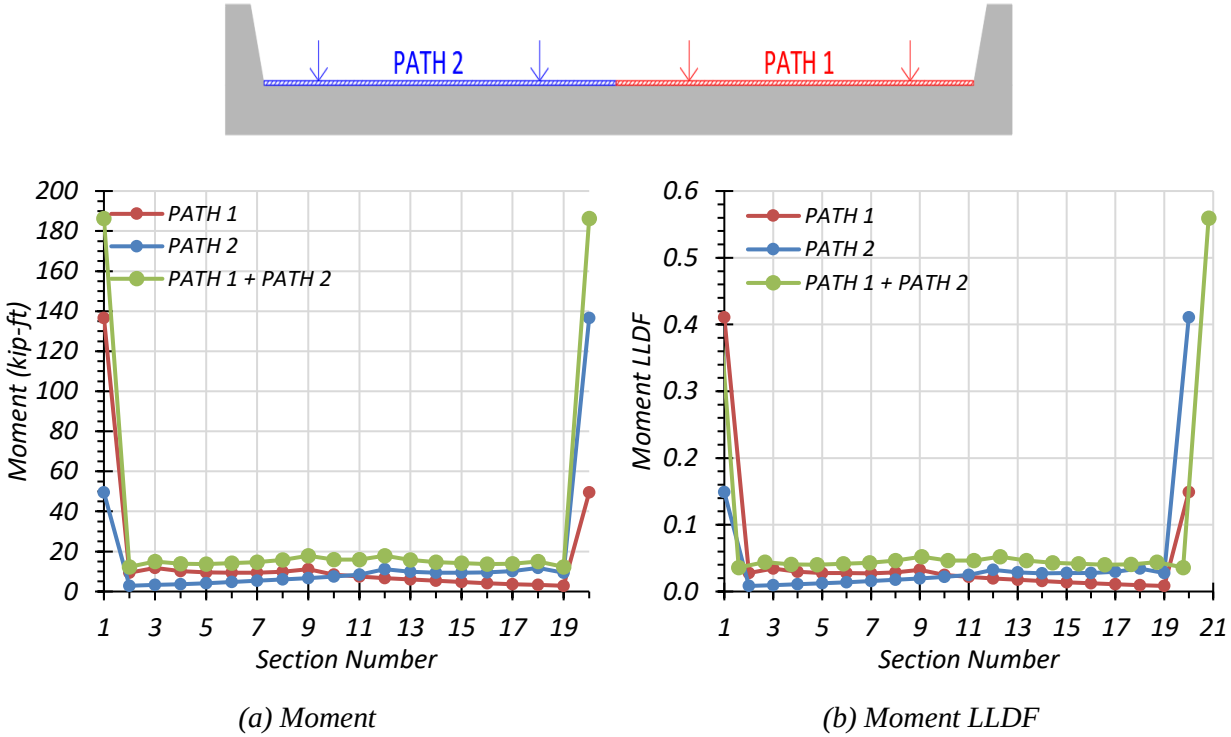

(a) Moment *(b) Moment LLDF*

Figure 5.15. Moment Results with HL-93 Loading

Table 5.16. Maximum Moments with HL-93 Loading

Loading	S1	S2	S3	S4	S5	S6	S7	S8	S9	S10	S11	S12	S13	S14	S15	S16	S17	S18	S19	S20
Path 1	136.7	9.5	11.8	10.2	9.5	9.4	9.4	9.8	11.1	8.5	7.5	6.7	6.0	5.3	4.7	4.2	3.7	3.3	2.9	49.6
Path 2	49.6	2.9	3.3	3.7	4.2	4.7	5.3	6.0	6.7	7.5	8.5	11.1	9.8	9.4	9.4	9.5	10.2	11.8	9.5	136.7
Path 1 + Path 2	186.2	12.3	15.0	13.9	13.7	14.2	14.7	15.8	17.8	15.9	15.9	17.8	15.8	14.7	14.2	13.7	13.9	15.0	12.3	186.2
Note: S = section, paths indicate transverse loading positions as shown, moments have kip-ft units																				

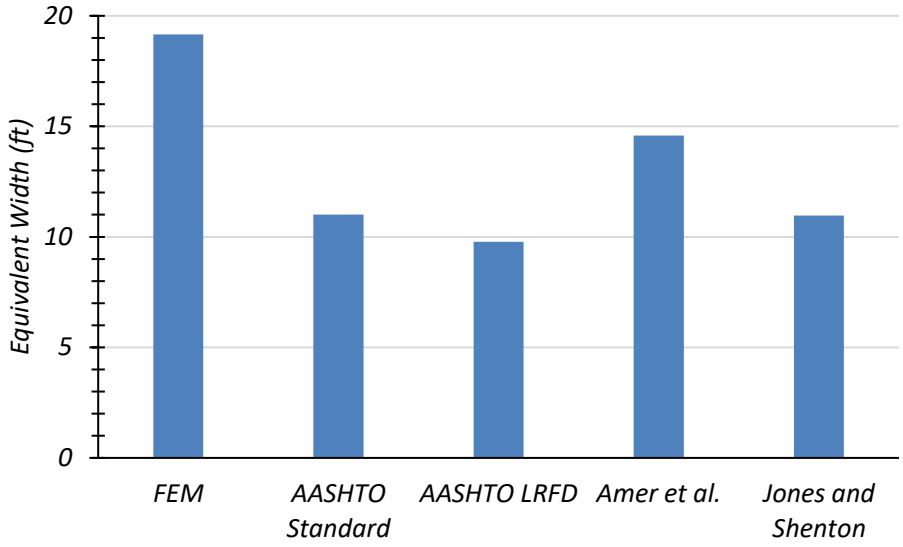

Figure 5.16. Comparison of Equivalent Width with Various Models for HL-93 Loading

Table 5.17. Governing Moment Equivalent Width (ft) for HL-93 Loading for Interior Slab

Loading	FEM (E^m_{FEM})	AASHTO (E^m_{AASHTO})	AASHTO LRFD (E^m_{LRFD})	Amer et al. (E^m_{Amer})	Jones and Shenton ($E^m_{Jones\ \&\ Shenton}$)
One-lane	29	11.0	10.5	14.6	12.0
Two-lane	19.2	11.0	9.8	14.6	11.0

5.7.3.3 ***Shear Results***

The shear forces in each transverse section and the corresponding shear LLDFs for the one-lane and two-lane HL-93 loading paths are shown in Figure 5.17. The corresponding maximum moments for each section and path are listed in Table 5.18. The estimated shear results from the FEM model were used to calculate the equivalent widths for the slab portion and LLDFs for the curbs. A comparison of the estimated equivalent width for the interior slab portion obtained from

the FEM model for a two-lane-loaded case and those calculated using the approximate equations in the *AASHTO Standard Specifications* (AASHTO 2002) and *AASHTO LRFD Specifications* (AASHTO 2017) is provided in Table 5.19. Comparison with studies such as Amer et al. (1999) and Jones and Shenton (2012) was also carried out. The *AASHTO LRFD Specifications* (AASHTO 2017) was slightly unconservative for both the one-lane and two-lane-loaded scenario, while the *AASHTO Standard Specifications* (AASHTO 2002), Amer et al. (1999), and Jones and Shenton (2012) equivalent widths were unconservative for both scenarios.

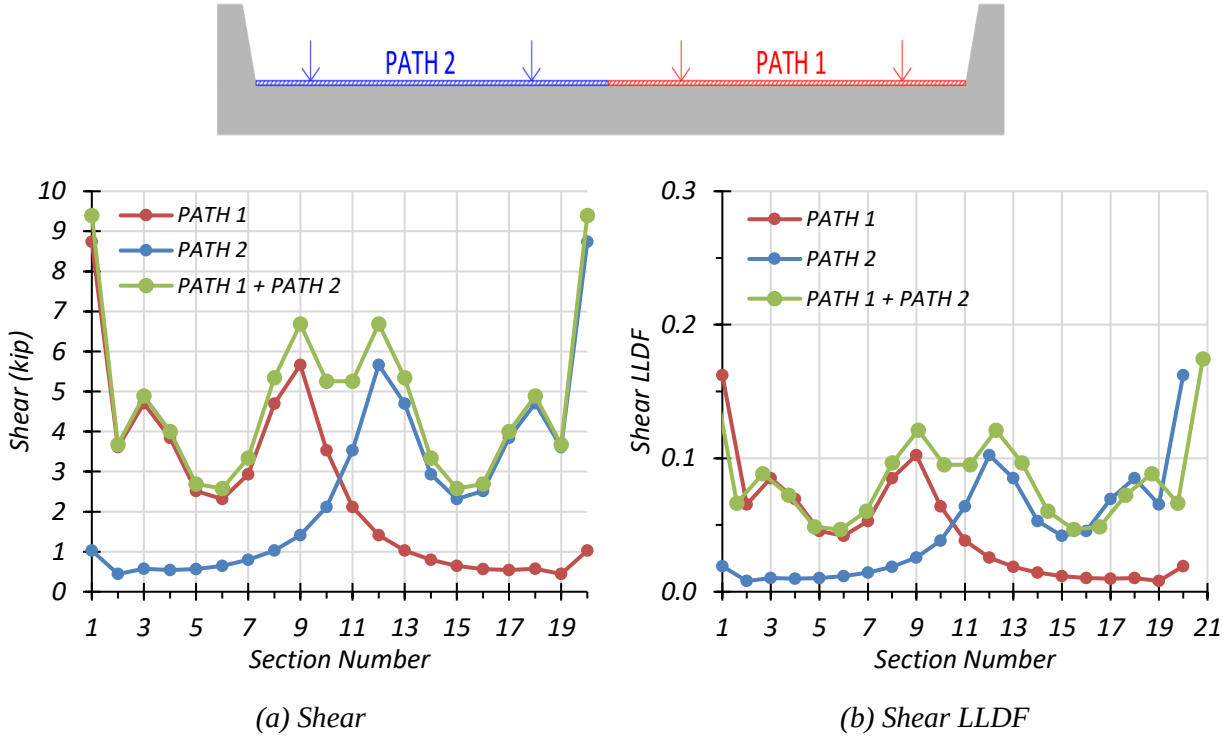

(a) Shear *(b) Shear LLDF*

Figure 5.17. Shear Results with HL-93 Loading

Table 5.18. Maximum Shears with HL-93 Loading

Loading	S1	S2	S3	S4	S5	S6	S7	S8	S9	S10	S11	S12	S13	S14	S15	S16	S17	S18	S19	S20
Path 1	8.7	3.6	4.7	3.8	2.5	2.3	2.9	4.7	5.7	3.5	2.1	1.4	1.0	0.8	0.6	0.6	0.5	0.6	0.4	1.0
Path 2	1.0	0.4	0.6	0.5	0.6	0.6	0.8	1.0	1.4	2.1	3.5	5.7	4.7	2.9	2.3	2.5	3.8	4.7	3.6	8.7
Path 1 + Path 2	9.4	3.7	4.9	4.0	2.7	2.6	3.3	5.3	6.7	5.3	5.3	6.7	5.3	3.3	2.6	2.7	4.0	4.9	3.7	9.4
Note: S = section, paths indicate transverse loading positions as shown, shears have kip units																				

Table 5.19. Governing Shear LLDF Values for HL-93 Loading

Loading	FEM (E^v_{FEM})	AASHTO (E^v_{AASHTO})	AASHTO LRFD (E^v_{LRFD})	Amer et al. (E^v_{Amer})	Jones and Shenton ($E^v_{Jones\ \&\ Shenton}$)
One-lane	9.8	11.0	10.5	14.6	12.0
Two-lane	8.3	11.0	9.8	14.6	11.0

5.8 SUMMARY AND CONCLUSIONS

Finite element analysis of Bridge CS-9 was conducted for various vehicular load configurations. The equivalent strip width over which the vehicular loads are distributed was calculated using the bending moment and shear results. A comparison of the equivalent strip widths found using the FEM model was carried out with those determined using the procedures outlined in the *AASHTO Standard Specifications* (AASHTO 2002) and *AASHTO LRFD Specifications* (AASHTO 2017).

For all loading scenarios, the equivalent widths for the interior slab portion of Bridge CS-9 calculated as per *AASHTO Standard Specifications* (AASHTO 2002) and *AASHTO LRFD Specifications* (AASHTO 2017) are conservative in comparison to the equivalent widths obtained from the FEM bending moment results. This trend is also observed with the equivalent widths proposed by Amer et al. (1999) and Jones and Shenton (2012). However, the equivalent widths obtained from the FEM shear force results are unconservative for all loading scenarios when compared with those corresponding to *AASHTO Standard Specifications* (AASHTO 2002), *AASHTO LRFD Specifications* (AASHTO 2017), Amer et al. (1999), and Jones and Shenton (2012).

The bending moments for the curb and slab calculated using the simplified approach outlined in IB346 (Jenson et al. 1943) are less than the bending moments extracted from the FEM model for one-lane HS-20 loading, with the curb moment being slighty less and the slab moment being much lower using IB346. For the two-lane HS-20 loading, the calculated moments using IB346 are conservative for the curb and highly unconservative for the slab when compared to the FEM values.

In a subsequent task, the selected bridge, CS-9, will be field-tested for the posted load limit. The bridge will be instrumented with strain gages, string potentiometers and accelerometers to record the required data and in situ behavior of the bridge. The experimental results will be compared with the FEM analysis results to validate and calibrate the FEM model.

6 EXPERIMENTAL TESTING OF BRIDGE SM-5

6.1 INTRODUCTION

Nondestructive load testing of Bridge SM-5 was conducted to gather information about the in-situ behavior of the bridge under vehicular loading. The load test results provide evidence of whether partial composite action or end fixity is present in the structure and measurements of the actual live load distribution between girders. The load test results are also used to update and calibrate the FEM model of the bridge, with which refined analysis is conducted. These results help to determine if the bridge posting can be increased or removed.

Various non-destructive material tests were also performed on Bridge SM-5. Ground Penetrating Radar (GPR) was used to locate steel reinforcing bars in the concrete deck. Ultrasonic Pulse Velocity (UPV) testing, as well as Original Schmidt Hammer and Silver Schmidt Hammer tests, were performed to determine the compressive strength of the concrete deck.

6.2 GENERAL DESCRIPTION OF BRIDGE SM-5

Bridge SM-5 has a deck condition rating of 7 (Good), a superstructure condition rating of 6 (Satisfactory) with 2 percent beam section loss due to corrosion, and a substructure condition rating of 7 (Good). The steel girders control the rating of the bridge, which has an inventory gross load rating of 17 US tons and an operating gross load rating of 28 US tons. The bridge is posted for a 20,000 lbs single axle, a 34,000 lbs tandem axle, a 47,000 lbs single vehicle, and a 74,000 lbs combination vehicle. Table 6.1 shows the posted loads of Bridge SM-5 for different axle and vehicle configurations. Figure 6.1 shows photographs of an elevation view of Bridge SM-5 and a view of the underside of the superstructure. Figure 6.2 shows a transverse section detail of Bridge SM-5.

Table 6.1. Bridge SM-5 Postings

Configuration	Posting (lbs)
Single Axle	20,000
Tandem Axle	34,000
Single Vehicle	47,000
Combination Vehicle	74,000

(a) Elevation view

(b) Underside view

Figure 6.1. Photographs of Bridge SM-5 (TxDOT 2018a)

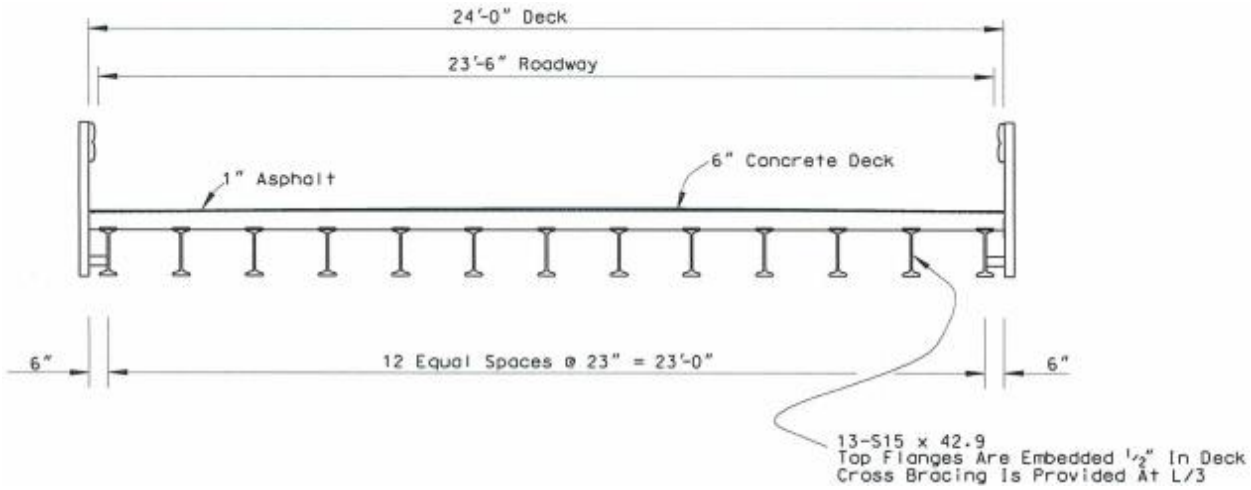

Figure 6.2. Transverse Section of Bridge SM-5 (TxDOT 2018a)

6.3 IN-SITU MEASUREMENTS AND OBSERVATIONS AND NDE RESULTS

6.3.1 In-Situ Measurements and Observations

In-situ measurements of the geometric details of the Bridge SM-5 were taken during field testing. The bridge span measured 41 ft 7 in. from back wall to back wall, and the deck measured 24 ft wide. The abutments were 39 ft 9 in. apart (face-to-face), and an approximately 10 in. length of each girder sat on the concrete abutments, leaving an average gap of approximately 1 in. between the end of the girder and the back wall of the abutment. After taking the simply supported bearing position to be half of the girder bearing length, the center-to-center span length of Bridge SM-5 was determined to be 40 ft 7 in. instead of the 40 ft 2 in. span length shown in the drawings.

It was also observed that the top flanges of the girders were indeed embedded into the concrete deck, as the drawings show and that the deck concrete around the embedment exhibited no signs of cracking, which would indicate the potential for composite action between the girders and deck, although the bridge girders were not originally designed as composite members. Figure 6.3 shows a photo taken in the field verifying this observation. The presence of composite action is further evaluated during the load testing.

Figure 6.3. Observation of Girder Flange Embedment with No Signs of Cracking

6.3.2 NDE Results

Four different nondestructive material tests were performed on Bridge SM-5 in order to obtain more information about the concrete deck and steel girder strength. The first test performed was a UPV test that measures the time it takes for an ultrasonic wave to travel through a known thickness of concrete, which was conducted in accordance with ASTM C597 standard test method for pulse velocity through concrete (ASTM C597 2016). The compressive strength of the concrete can then be estimated based on the measured velocities. For Bridge SM-5, measurements were taken between the bottom and top of the concrete deck, which had a measured thickness of 6.125 in. The wave travel times for the two tests were 31.6 microseconds and 32.4 microseconds. This correlates to an average wave velocity of 4863 m/s. Considering the wave velocity only, and using equations given in Trtnik et al. (2009), the compressive strength can be found as 6.5 ksi. However, as stated in Huang et al. (2011), using wave velocity alone is not a reliable method to obtain concrete compressive strength. Therefore, the SonReb method was performed. By using the wave velocity, the rebound number found using the Original Schmidt Hammer, and equations given in Huang et al. (2011), the concrete compressive strength was found to be 11.3 ksi.

The second NDE material test performed on Bridge SM-5 was the Original Schmidt Hammer, which was conducted in accordance with ASTM C805 standard test method for rebound number of hardened concrete (ASTM C805 2018). In this test, a device is pushed against the concrete surface and uses the rebound of a spring-loaded mass to estimate the compressive strength

of the concrete. For Bridge SM-5, the average rebound value produced by ten Original Schmidt Hammer measurements was 48. From the conversion chart shown in Figure 6.4, the compressive strength of the deck was determined to be 7.4 ksi.

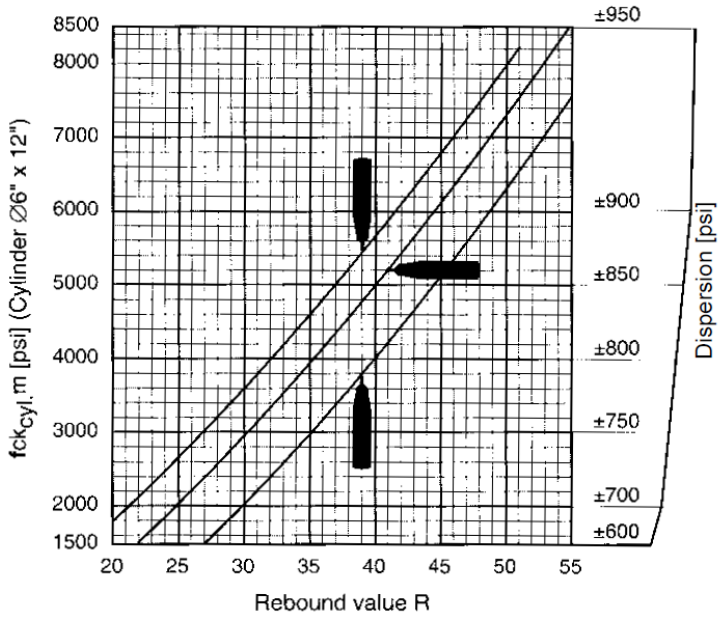

Figure 6.4. Original Schmidt Hammer Conversion Chart (Proceq 2017a)

The third NDE test performed on Bridge SM-5 was the Silver Schmidt Hammer. The procedure for performing this test is very similar to that of the Original Schmidt Hammer. For Bridge SM-5, the average Q value produced by 10 Silver Schmidt Hammer measurements was 65. From the conversion chart shown in Figure 6.5, the compressive strength of the deck was determined to be 7.2 ksi.

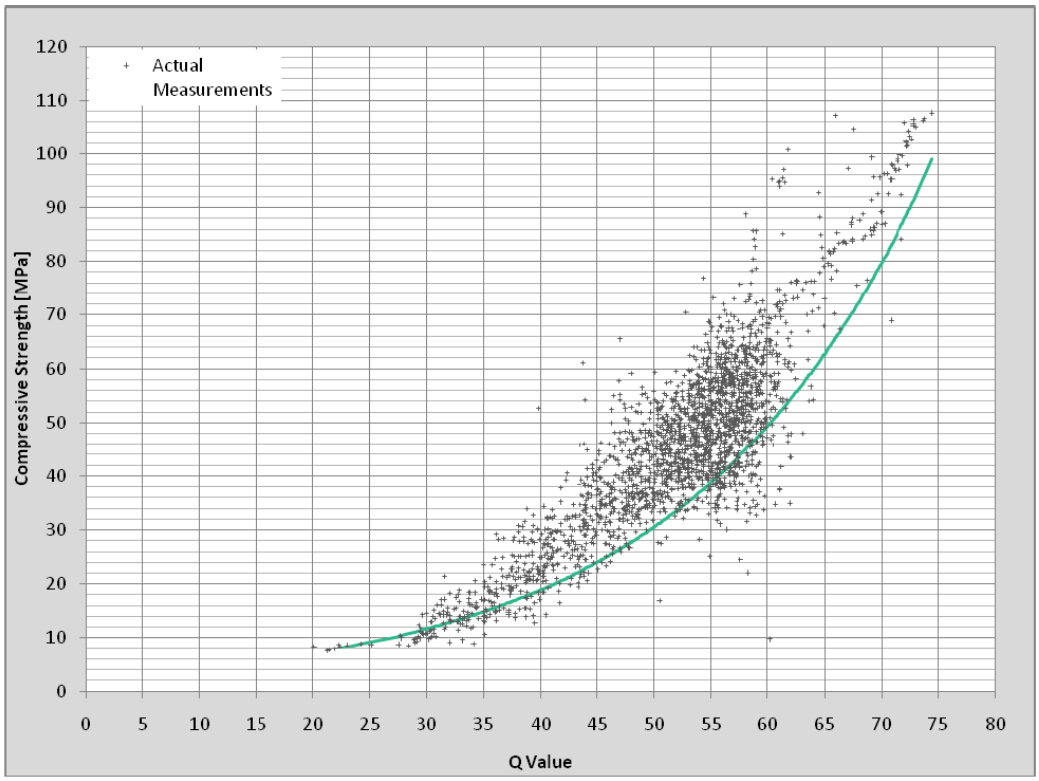

Figure 6.5. Silver Schmidt Hammer Conversion Chart (Proceq 2017b)

The fourth NDE test performed on Bridge SM-5 was the use of GPR in order to determine the spacing of the steel reinforcement in the deck. The GPR device was only run along the underside of deck because the asphalt layer on the deck prevented it from being used on the top of the deck. Thus, the spacing of the lower longitudinal bars was determined to be 12 in., and the spacing of the lower transverse bars was determined to be 7.5 in. There are no structural drawings for Bridge SM-5 that show the deck reinforcement; therefore, this information could not be compared.

Out of the three NDE tests performed to measure the compressive strength of the concrete deck, the lowest compressive strength value produced by a reliable method was 7.2 ksi. This value was used in updated FEM models to perform post-test analysis for comparison of other test values. The measured rebar spacing will also be helpful if an analysis of the concrete deck is performed.

6.4 DATA ACQUISITION AND INSTRUMENTATION FOR BRIDGE SM-5

The instrumentation plan for field testing of Bridge SM-5 was developed based on the objectives of the research project. Three types of instrumentation were used and are shown in Figure 6.8. Strain gauges, string potentiometers, and accelerometers were installed on the bridge to measure its response under the nondestructive vehicular load tests.

6.4.1 Instrumentation Plan for Bridge SM-5

The installed instrumentation and their locations on the bridge were selected in order to obtain specific data to understand the true behavior of the bridge—such as the load sharing between girders, composite action, and end fixity— and determine if its posting can be increased or removed.

Figure 6.6 shows the full instrumentation layout for Bridge SM-5, with plan and cross-section views. Figure 6.7 shows the labeling system used for the instrumentation, and Table 6.2 shows the instrumentation labels and corresponding DAQ channels.

Strain gauges were installed on the bottom face of the top flange and the top face of the bottom flange as close as possible to the girder web at three longitudinal locations for a selected interior girder and exterior girder. The strain gauges were installed at the midspan location and at an average of 9 in. away from the bearing centerline at each girder end for the selected interior and exterior girders. Several goals were identified in determining the instrumentation types and locations, as follows:

- The strain gauge locations were selected to collect data pertaining to the midspan moments, to determine neutral axis values to check for potential composite action, and to evaluate possible end fixity of the girders.
- The string potentiometer locations were selected to measure midspan deflections and infer experimental LLDFs to compare with the estimated values from the FEM model of Bridge SM-5.
- The accelerometers were selected to collect dynamic property information, thereby allowing for comparison with estimated dynamic properties from the FEM model of the bridge.

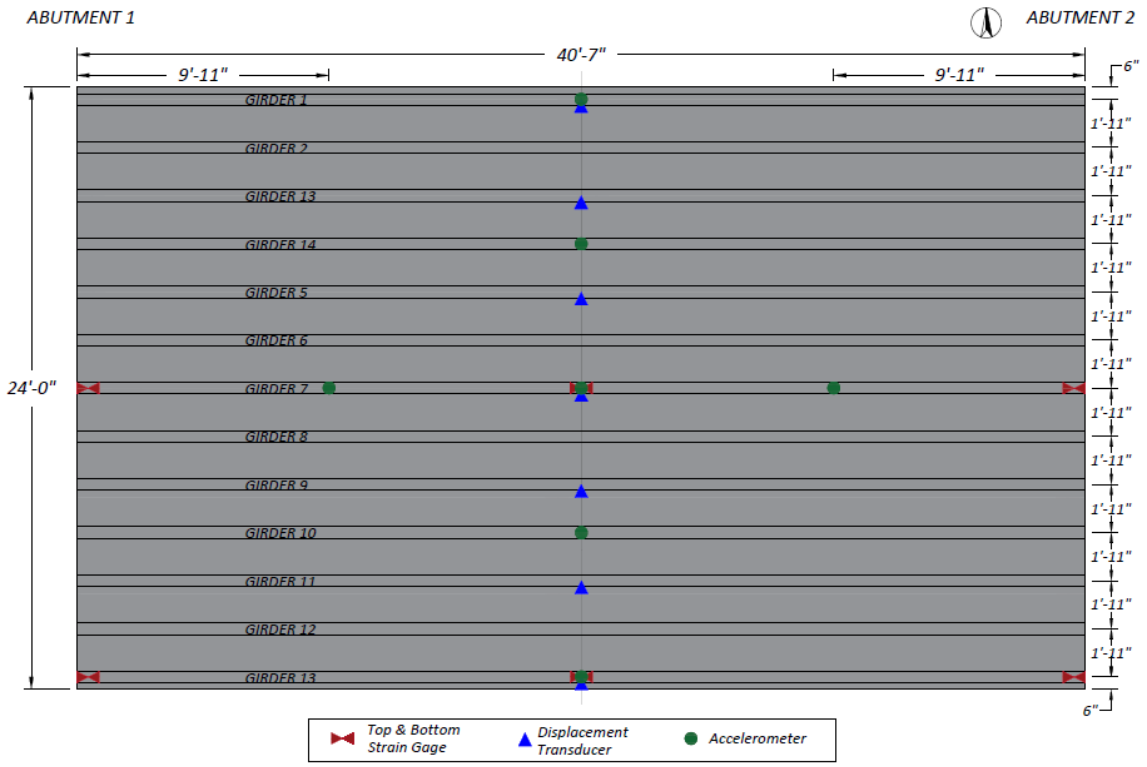

(a) Plan View

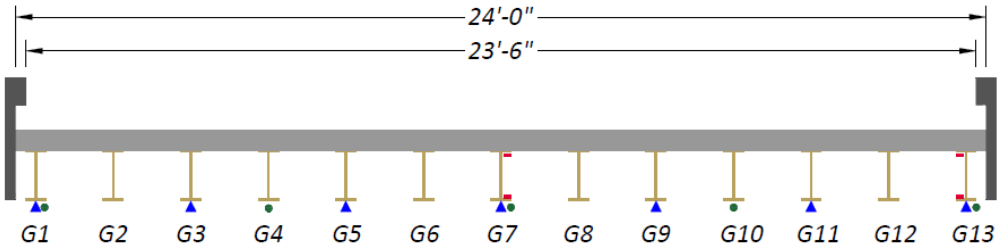

(b) Midspan Section

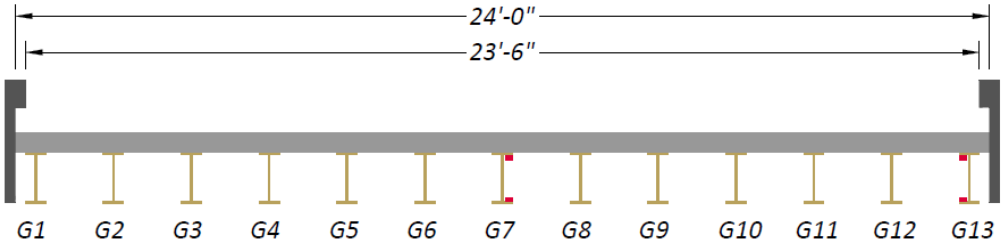

(c) End Section

Figure 6.6. Instrumentation Layout for Bridge SM-5

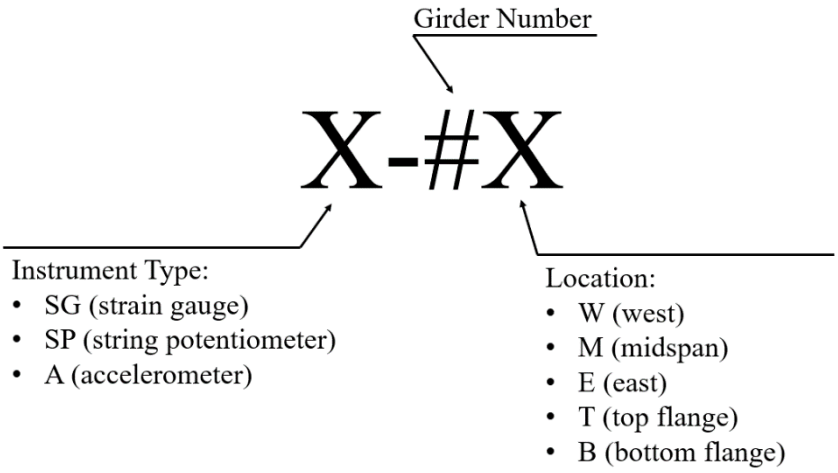

Figure 6.7. Instrumentation Labeling System Used for Field Testing

Table 6.2. Instrumentation Labels for Bridge SM-5

DAQ Box	Channel	Label	Type	DAQ Box	Channel	Label	Type
Strain Book	CH1	SG-13WT	FLA-6	WBK 16-3	CH25	SP-1M	SM1-2
	CH2	SG-13WB	FLA-6		CH26	–	–
	CH3	SG-13MT	FLA-6		CH27	–	–
	CH4	SG-13MB	FLA-6		CH28	–	–
	CH5	SG-13ET	FLA-6		CH29	–	–
	CH6	SG-13EB	FLA-6		CH30	–	–
	CH7	SG-7WT	FLA-6		CH31	–	–
	CH8	SG-7WB	FLA-6		CH32	–	–
WBK 16-1	CH9	SG-7MT	FLA-6	WBK 18	CH57	A-13M	4507IEPE
	CH10	SG-7MB	FLA-6		CH58	A-10M	4507IEPE
	CH11	SG-7ET	FLA-6		CH59	A-7M	4507IEPE
	CH12	SG-7EB	FLA-6		CH60	A-4M	4507IEPE
	CH13	–	–		CH61	A-1M	4507IEPE
	CH14	–	–		CH62	A-7W	4507IEPE
	CH15	–	–		CH63	A-7E	4507IEPE
	CH16	–	–		CH64	-	
WBK 16-2	CH17	–	–				
	CH18	–	–				
	CH19	SP-13M	SM1-2				
	CH20	SP-11M	SM1-2				
	CH21	SP-9M	SM1-2				
	CH22	SP-7M	SM1-2				
	CH23	SP-5M	SM1-2				
	CH24	SM-3M	SM1-2				

6.4.2 Data Acquisition System and Instrument Details

*6.4.2.1 **Data Acquisition System***

A total of 24 strain gauges (using half-bridge circuits at 12 measurement locations), seven string potentiometers, and seven accelerometers were installed onto Bridge SM-5. Twenty-six channels were used in the data acquisition (DAQ) system, which consisted of a Measurement Computing StrainBook main DAQ unit and WBK16 extension modules for recording the strain gauge and string potentiometer data, and a WBK18 extension module for recording accelerometer data. Figure 6.8(a) shows the main box and extensions modules of the DAQ system.

Strainbook WBK16 WBK18

(a) Main Data Acquisition Box and Extension Modules (MCC 2014)

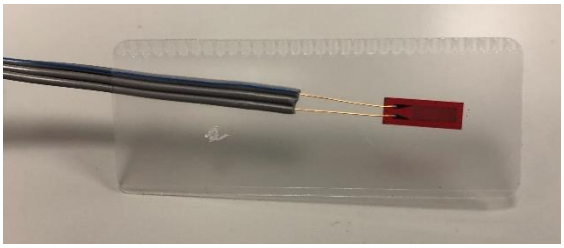

(b) Tokyo Measuring Instruments Lab FLA-6-11-3LJCT Strain Gauges

(c) Celesco SM1-2 String Potentiometer

(d) Brüel & Kjær IEPE Accelerometer

Figure 6.8. Data Acquisition System and Instrumentation

*6.4.2.2 **Strain Gauges***

In order to obtain longitudinal strain data during testing, 24 strain gauges were installed at 12 measurement locations on the steel girders of the bridge. Two strain gauges were installed at each measurement location: a main gauge in the longitudinal direction to obtain longitudinal strain data and a secondary gauge in the transverse direction to compensate for any temperature changes experienced during testing. Figure 6.9 shows a close-up of the installation of the strain gauges. The strain gauges used were selected with ease of installation in mind and because the testing being conducted was short-term and took place over the span of a couple hours. Figure 6.8(b) shows the Tokyo Measuring Instruments Lab FLA-6-11-3LJCT strain gauges used during testing.

Figure 6.9. Close-Up of Strain Gauge Installation

6.4.2.3 ***String Potentiometers***

Seven string potentiometers were installed at midspan of every other girder of the 13-girder Bridge SM-5 to obtain midspan girder deflections. All string potentiometers used were Celesco SM1-2 string potentiometers with a 2.5 in. stroke. Figure 6.8(c) shows the Celesco SM1-2 string potentiometers used during testing.

6.4.2.4 ***Accelerometers***

To obtain dynamic properties of the bridge, such as natural frequency and mode shapes, seven piezoelectric accelerometers were installed on the bridge. Accelerometers were installed at midspan on the bottom of every third girder, as well as at quarter-span locations on the bottom of the middle girder. The accelerometers used were selected because their resonance frequency of 18 kHz is far from the bridge natural frequency and because they are highly sensitive and low in mass and size. Figure 6.8(d) shows the Brüel & Kjær IEPE accelerometers used during testing.

6.5 LOAD TESTING PROCEDURE FOR BRIDGE SM-5

A comprehensive test program was conducted to evaluate the performance and behavior of Bridge SM-5. The test program consisted of two parts: (1) static load tests, which consisted of stop

location tests and crawl speed tests, and (2) dynamic load tests. The testing took place on March 7, 2019.

6.5.1 Test Vehicle

The TxDOT Huntsville Maintenance Office provided a Sterling LT 9500 dump truck to be used for the nondestructive load testing of Bridge SM-5. The truck was loaded with asphalt base material such that the rear tandem axles weighed approximately the same as the posted limit of the bridge (posted as 34,000 lb tandem axle). The truck was weighed using portable scales provided by the TxDOT Bryan District Office. The wheel loads and wheel and axle spacings of the dump truck used for testing are shown in Figure 6.10.

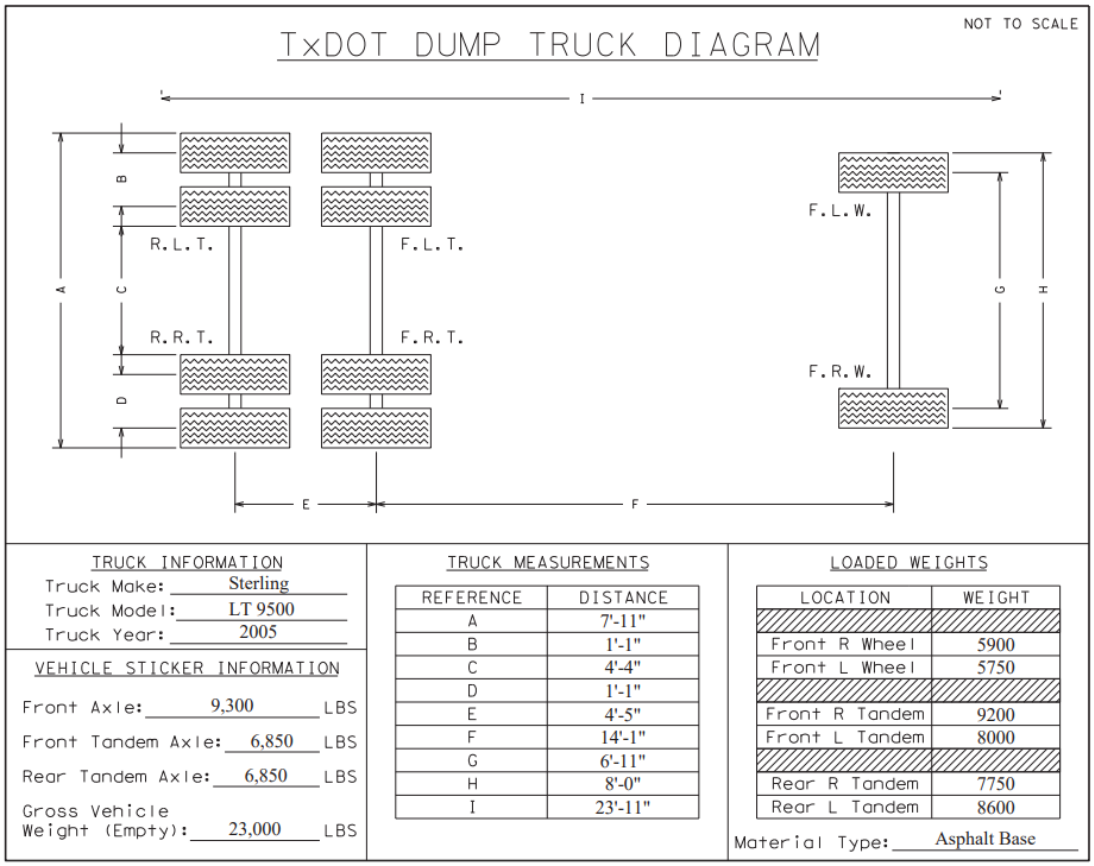

Figure 6.10. Wheel Weights and Spacings of the Loaded Dump Truck

6.5.2 Vehicle Positioning

In order to investigate the transverse load distribution between the bridge girders, three paths were determined that would be used during testing. The first path, designated Path 1, was at a location such that the centerline of the adjacent rear tires would be 2 ft from the bridge guardrail. The second path, designated Path 2, was in the opposite lane at a location such that the centerline of the adjacent rear tires would be 2 ft from the centerline of the bridge. The third and final path, designated the Middle Path, was at a location such that the truck was straddling the centerline of the bridge. All three testing paths are shown in the bridge cross-section in Figure 6.11.

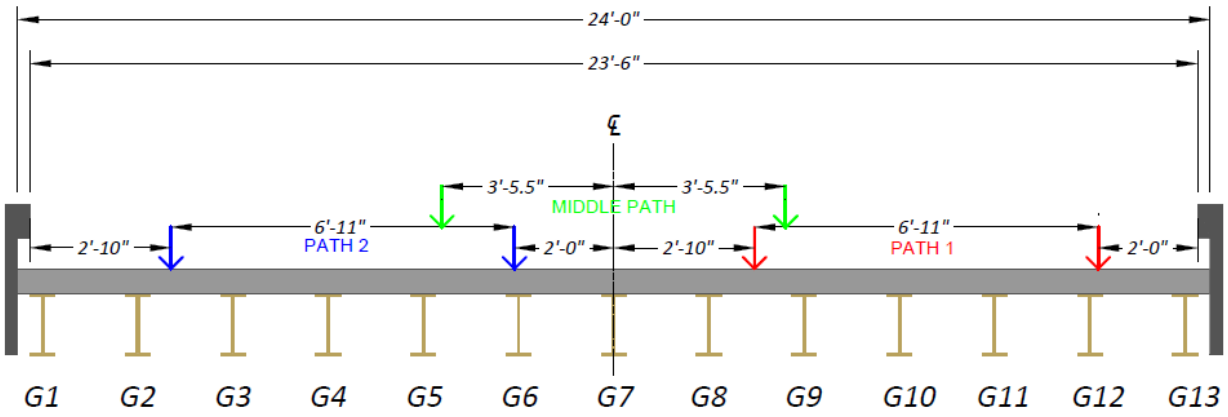

Figure 6.11. Load Test Paths for Bridge SM-5

For the static load tests, it was desired for the truck to be placed approximately at the location at which maximum moment would occur in the girders since the moment LLDFs are one of the key parameters of interest. Therefore, the truck was placed such that the front axle was 16 ft 3.5 in. from the midspan of the bridge, resulting in the rear axles straddling the midspan of the bridge. This longitudinal position was used for the static tests conducted. For the crawl speed tests and the dynamic tests, the truck was driven across the bridge without stopping.

6.5.3 Test Protocol

*6.5.3.1 **Static Tests***

Two types of static load tests were performed on Bridge SM-5—stop location tests and crawl speed tests. The stop location load tests began with the truck stopped before entering the bridge to record a reference data file that serves as a baseline. The truck then proceeded onto the bridge and was stopped at the longitudinal moment critical position previously described. Once the truck was stopped, data were recorded for a period of approximately five seconds. This procedure was used along each load path. Two different static tests were performed along Path 1 and Path 2: (1) the truck engine was running, and (2) the truck engine was shut off. For the static test along the Middle Path, the test was performed while the truck engine was shut off. The static test results presented in this chapter are only the ones with the engine shut off. During the static tests in which the engine

was running, there was a possibility that, due to the truck dynamics with the engine running, unwanted vibrations could be introduced in the measurements.

The crawl speed load tests began with the truck stopped before entering the bridge to record a reference data file that serves as a baseline. The truck then proceeded at an idle speed of approximately 2 mph across the full length of the bridge while data were recorded for the entire time. This procedure was used along each load path.

6.5.3.2 ***Dynamic Tests***

The dynamic tests began with the truck stopped some distance away from the bridge. At this time, a reference data file was recorded. The truck then proceeded at a specific speed across the entire length of the bridge while data were recorded during the passage of the vehicle. This procedure was used along each load path. Two different dynamic tests were performed along Path 1 and Path 2. The first dynamic test was performed at approximately 30 to 35 mph, and the second dynamic test was performed at approximately 23 mph. Only one dynamic test, at 35 mph, was performed along the Middle Path. These speeds were chosen based on a variety of factors including the speed limit of the road (35 mph), the estimated speed at which a heavy vehicle might drive over the bridge, and the comfort level of the truck driver going at certain speeds along the predefined load paths.

6.5.3.3 ***Impact Tests***

In order to obtain more information about the dynamic properties of the bridge, a sledgehammer was used to strike the top of the bridge deck in three different transverse locations (north edge of the bridge, at the centerline of the bridge, and at the south edge of the bridge) at the midspan. Although all the instruments were in place while data were being recorded during these three impact tests, only accelerometer measurements were used to identify dynamic characteristics. The impact excitation provides a more accurate way of measuring bridge dynamic characteristics because, unlike a vehicle excitation, the impact excitation does not introduce additional mass and dynamic interaction with the bridge. Table 6.3 summarizes all the tests that were performed on Bridge SM-5.

Table 6.3. Test Protocol for Bridge SM-5 Testing

Test Number	Test Location	Test Type
1	Path 1	Static—Stop Location (Engine Running)
2	Path 2	Static—Stop Location (Engine Running)
3	Path 1	Static—Crawl Speed (5 mph)
4	Path 2	Static—Crawl Speed (2 mph)
5	Path 1	Dynamic (30 mph)
6	Path 2	Dynamic (35 mph)
7	Path 1	Dynamic (23 mph)
8	Path 2	Dynamic (22 mph)
9	Path 1	Static—Stop Location (Engine Stopped)
10	Path 2	Static—Stop Location (Engine Stopped)
11	Path 1	Static—Crawl Speed (2 mph)
12	Path 2	Static—Crawl Speed (2 mph)
13	Middle Path	Static—Stop Location (Engine Stopped)
14	Middle Path	Static—Crawl Speed (2 mph)
15	Middle Path	Dynamic (34 mph)
16	North Edge	Sledgehammer
17	Centerline	Sledgehammer
18	South Edge	Sledgehammer

6.5.4 Test Operations

The test program for Bridge SM-5 occurred from March 5, 2019, to March 7, 2019 and included all instrumentation installation, load testing, and instrumentation removal.

The clearance height of Bridge SM-5 is approximately 14 ft. Therefore, scaffolding platforms were set up below the bridge to provide a working platform for instrumentation installation. To install strain gauges, an approximately 2 in. by 4 in. area at the desired location of

the strain gauge was ground using an angle grinder to remove any loosely bonded adherent, such as paint, rust, and oxides. This location was then sanded using 150- and 220-grit sandpaper to obtain a smooth surface. Conditioner (acetone) was applied repeatedly and the surface scrubbed with paper towels until a clean tip was no longer discolored by the scrubbing. Liberally applying acetone brought the surface condition back to an optimum alkalinity of 7.0 to 7.5pH for ideal bonding of the glue. The strain gauges were then glued using CN (Cyanoacrylate) adhesive. Figure 6.12(a) shows an example of installed strain gauges on the girder. String potentiometers were attached to small pieces of 2 in. x 4 in. wood, which were then clamped to the bottom flanges of the girders at the midspan location. The string potentiometers were fixed by attaching fishing wire to metal hooks attached to wooden posts driven into the stream bed. Accelerometers were also attached to the bottom flange of the appropriate girders using magnets. Figure 6.12(b) shows an example of an installed string potentiometer and accelerometer on the bridge.

The load testing took place on March 7, 2019. Traffic control was provided by the TxDOT Bryan District through the Huntsville Maintenance Office while the testing took place. The dump truck was loaded and weighed at the TxDOT Huntsville Maintenance Office in the morning while members of the research team marked the test paths and the static test stop locations on the bridge using tape and spray paint. The previously described tests in the test protocol were performed while data from the installed instruments were recorded during each test period. Once the testing was completed, traffic control ceased, and the instrumentation was removed from the bridge. Figure 6.13(a) shows the scaffolding setup for instrumentation installation and Figure 6.13(b) shows the test truck on the bridge during a load test.

(a) Installed Strain Gauges at an End Location of a Girder

(b) Installed String Potentiometer and Accelerometer at Midspan of a Girder

Figure 6.12. Installed Instrumentation on Bridge SM-5

(a) Instrumentation of Bridge SM-5

(b) Test Truck at the Stop Location for Path 1

Figure 6.13. Instrumentation and Testing of Bridge SM-5

6.6 TEST RESULTS FOR BRIDGE SM-5

Two types of diagnostic tests were conducted following the guidelines provided in AASHTO MBE (AASHTO 2018): (1) static load tests using stationary loads to obtain static strains and deflections and infer composite action and LLDFs, and (2) dynamic load tests with moving loads that excite vibrations in the bridge to measure modes of vibration, frequencies, and dynamic amplification.

The data obtained during testing were compiled, processed, and analyzed. Strains were measured using strain gauges, which allowed stresses to be inferred. Deflections were measured using string potentiometers, which were used to infer transverse load distribution. Accelerations were measured using accelerometers, which were processed to obtain natural frequencies and mode shapes of the bridge. Videos taken during testing were used to determine deflections using computer vision and were compared with the string potentiometer measurements. NDE results were also compiled to obtain the in-situ compressive strength of the concrete bridge deck and reinforcement locations in the deck.

6.6.1 Static Load Tests on Bridge SM-5

Two types of static load tests were conducted: (1) stop location tests—by parking the vehicle at the moment critical longitudinal position for each selected path on the bridge, and (2) crawl speed tests—by moving the truck at low speeds (approximately 2 mph) along the same predefined paths.

6.6.1.1 Strain Measurements and Composite Action

After obtaining strain gauge data from the load testing, the maximum bottom flange strains were plotted along with their corresponding top flange strains at the same time step. In all strain figures shown in this section, the measured strain values are shown by a colored dot symbol. The colored line connecting two dot symbols represents the strain diagram at this cross-section based on an assumption that the plane section remains plane. The blue plot shows the strain results for the west end, the red plot shows the strain results for the east end, and the green plot shows the strain results for the midspan of the girder.

Interior Girder G7. Figure 6.14 through Figure 6.16 provide plots of the measured strains for interior Girder G7 during static load testing. The strains measured for Girder G7 during the Path 1 static tests are shown in Figure 6.14. Figure 6.14(a) shows the maximum strains observed during the stop location test for Girder G7 at each end of the girder. Figure 6.14(b) shows the

maximum strains observed during the stop location test for Girder G7 at the midspan. Figure 6.14(c) shows the maximum strains observed during the crawl speed test for Girder G7 at each end of the girder. Figure 6.14(d) shows the maximum strains observed during the crawl speed test for Girder G7 at the midspan. The corresponding observed midspan stresses for Girder G7 are 2.14 ksi for the stop location test and 2.10 ksi for the crawl speed test. The observed neutral axis locations at the midspan are 13.95 in. from the bottom of the girder for the stop location test and 13.37 in. from the bottom of the girder for the crawl speed test.

The strains measured for Girder G7 during the Path 2 static tests are shown in Figure 6.15. Figure 6.15(a) shows the maximum strains observed during the stop location test for Girder G7 at each end of the girder. Figure 6.15(b) shows the maximum strains observed during the stop location test for Girder G7 at the midspan. Figure 6.15(c) shows the maximum strains observed during the crawl speed test for Girder G7 at each end of the girder. Figure 6.15(d) shows the maximum strains observed during the crawl speed test for Girder G7 at the midspan. The corresponding observed midspan stresses for Girder G7 are 2.41 ksi for the stop location test and 2.51 ksi for the crawl speed test. The observed neutral axis locations at the midspan are 14.08 in. from the bottom of the girder for the stop location test and 13.77 in. from the bottom of the girder for the crawl speed test.

The strains measured for Girder G7 during the Middle Path static tests are shown in Figure 6.16. Figure 6.16(a) shows the maximum strains observed during the stop location test at each end of the girder. Figure 6.16(b) shows the maximum strains observed during the stop location test at the midspan. Figure 6.16(c) shows the maximum strains observed during the crawl speed test for Girder G7 at each end of the girder. Figure 6.16(d) shows the maximum strains observed during the crawl speed test for Girder G7 at the midspan. The corresponding observed midspan stresses for Girder G7 are 2.96 ksi for the stop location test and 2.95 ksi for the crawl speed test. The observed neutral axis locations at the midspan are 15.05 in. from the bottom of the girder for the stop location test and 13.80 in. from the bottom of the girder for the crawl speed test.

For all three paths, there is evidence of restraint at the girder ends causing a negative moment to occur, which is seen by the bottom flange end strain gauges being in compression. Also of note, the measured neutral axes show signs of significant composite behavior occurring, which will be discussed later in this chapter.

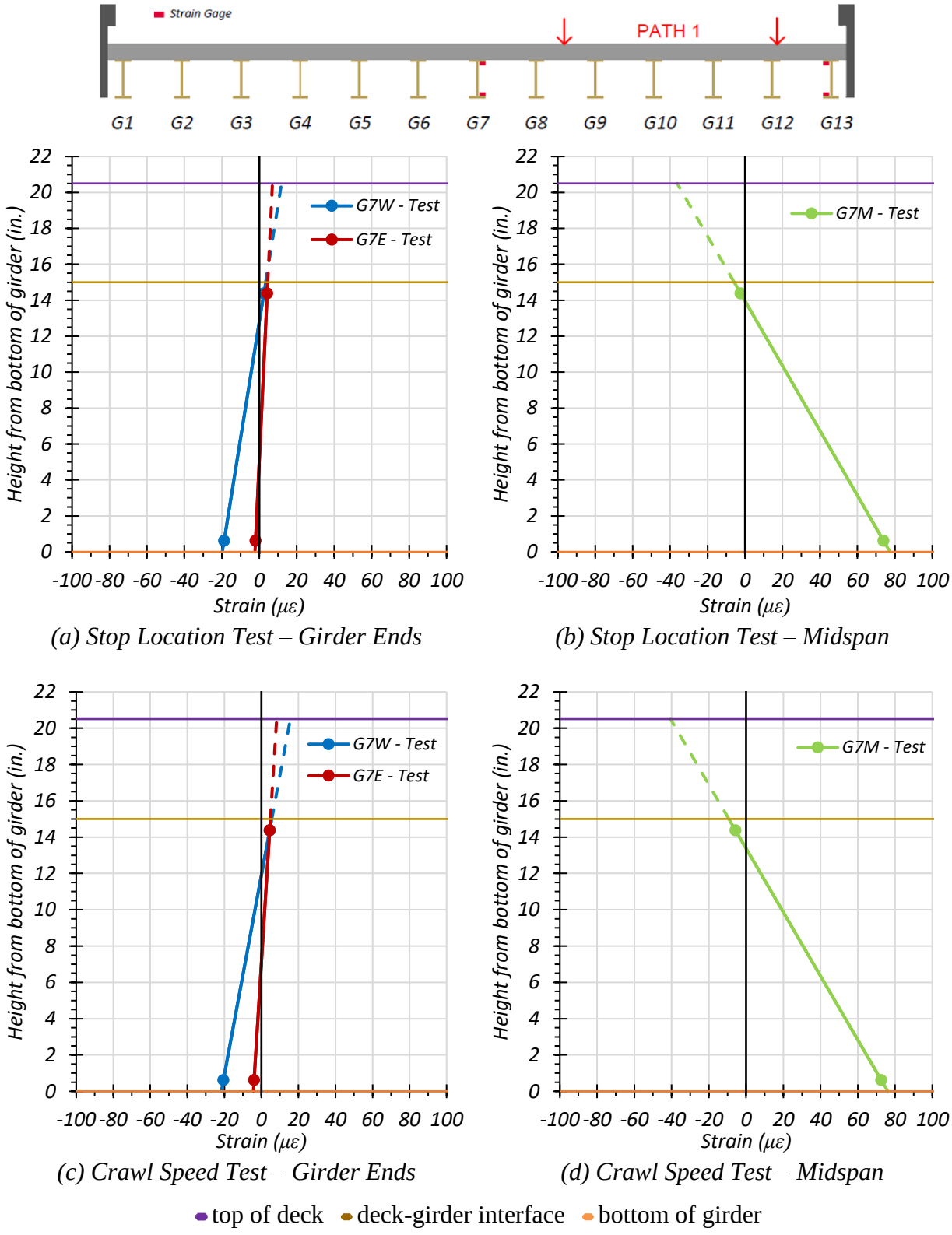

Figure 6.14. Static Strains for Interior Girder G7—Path 1

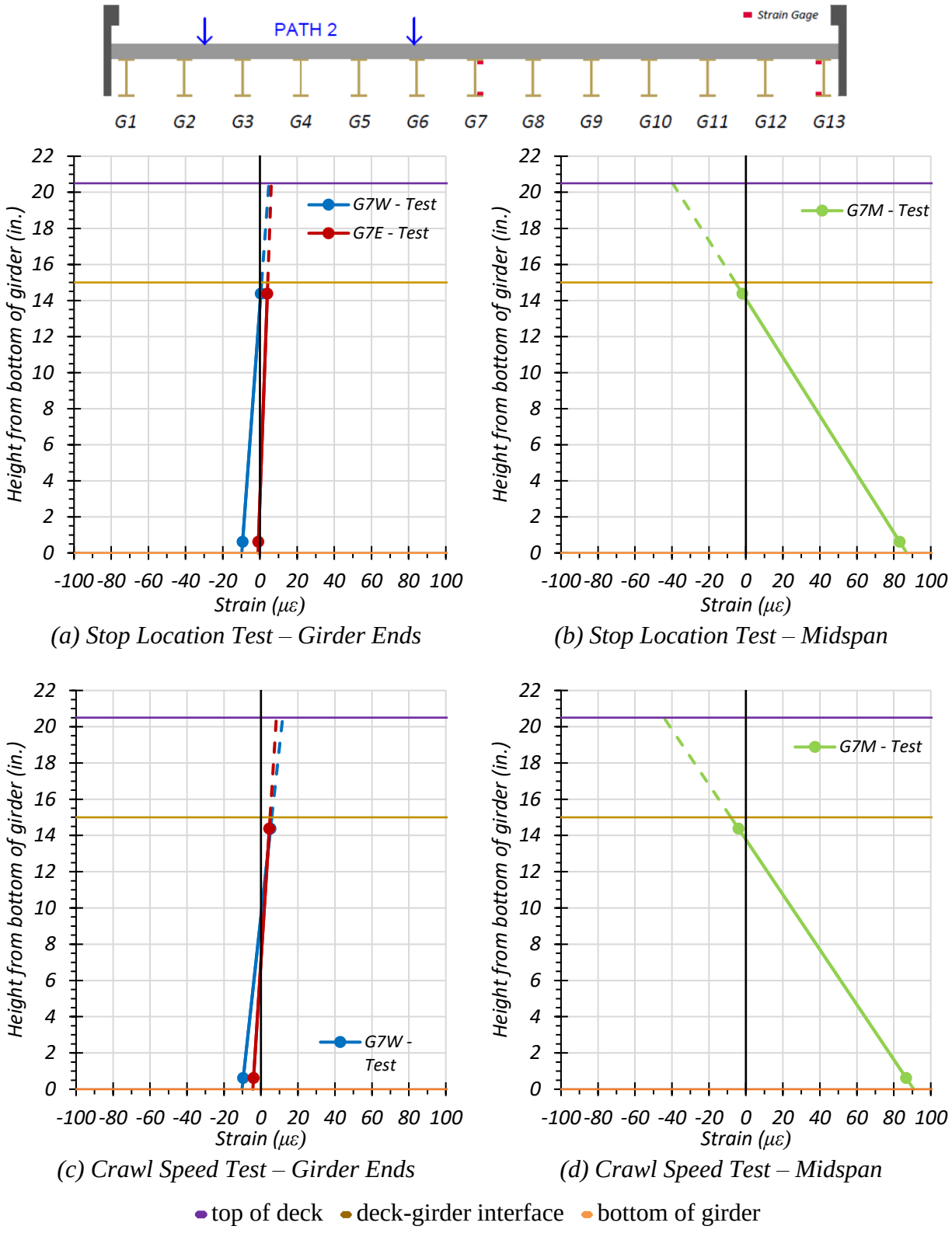

(a) Stop Location Test – Girder Ends

(b) Stop Location Test – Midspan

(c) Crawl Speed Test – Girder Ends

(d) Crawl Speed Test – Midspan

Figure 6.15. Static Strains for Interior Girder G7—Path 2

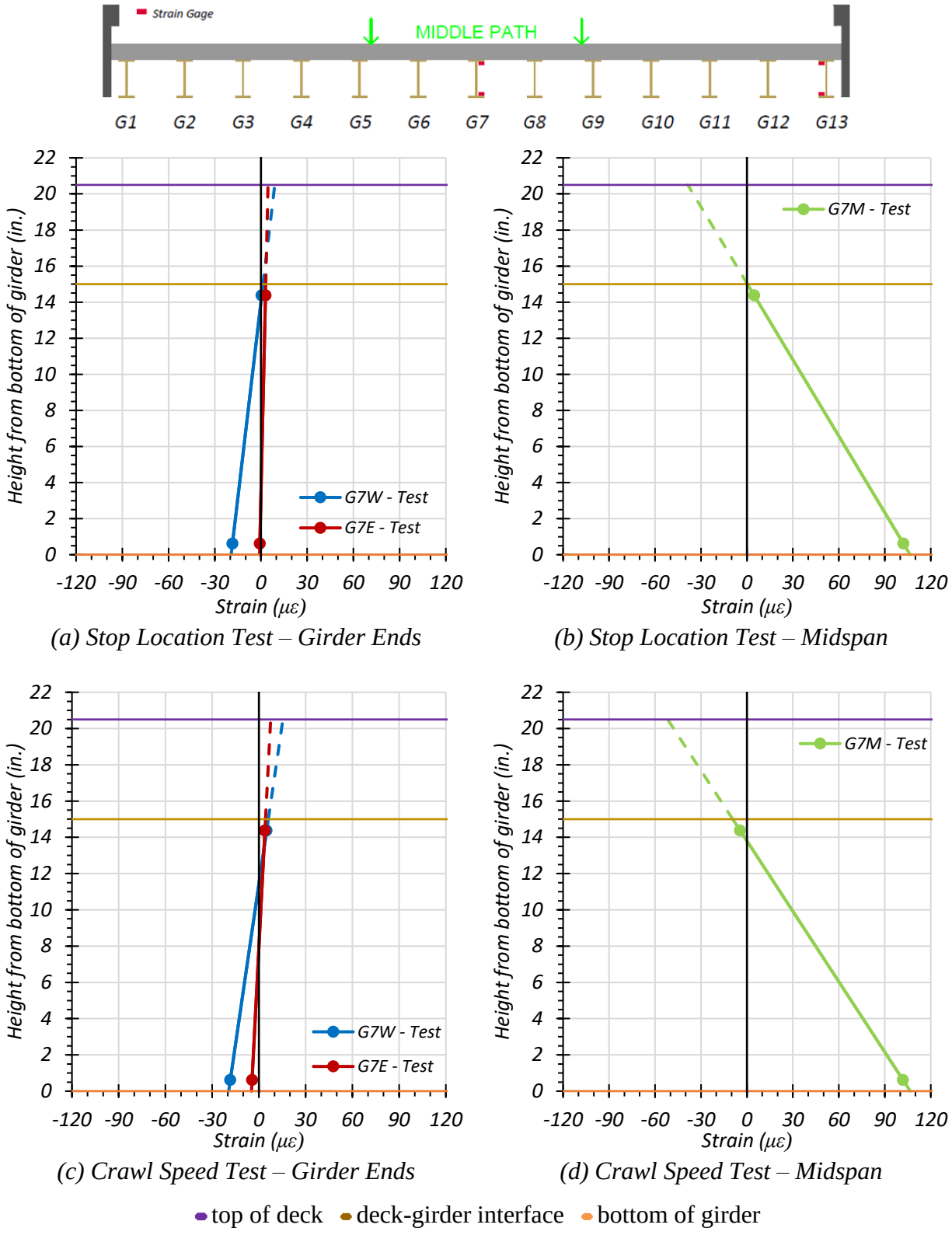

Figure 6.16. Static Strains for Interior Girder G7—Middle Path

Exterior Girder G13. Figure 6.17 through Figure 6.19 provide plots of the measured strains for exterior Girder G13 during static load testing. The strains measured for Girder G13 during the Path 1 static tests are shown in Figure 6.17. Figure 6.17(a) shows the maximum strains observed during the stop location test for Girder G13 at each end of the girder. Figure 6.17(b) shows the maximum strains observed during the stop location test for Girder G13 at the midspan. Figure 6.17(c) shows the maximum strains observed during the crawl speed test for Girder G13 at each end of the girder. Figure 6.17(d) shows the maximum strains observed during the crawl speed test for Girder G13 at the midspan. The corresponding midspan stresses at the bottom flange for Girder G13 are 4.70 ksi for the stop location test and 5.05 ksi for the crawl speed test. The observed neutral axis locations are 13.96 in. from the bottom of the girder for the stop location test and 14.04 in. from the bottom of the girder for the crawl speed test.

The strains measured for Girder G13 during the Path 2 static tests are shown in Figure 6.18. Figure 6.18(a) shows the maximum strains observed during the stop location test for Girder G13 at each end of the girder. Figure 6.18(b) shows the maximum strains observed during the stop location test for Girder G13 at the midspan. Figure 6.18(c) shows the maximum strains observed during the crawl speed test for Girder G13 at each end of the girder. Figure 6.18(d) shows the maximum strains observed during the crawl speed test for Girder G13 at the midspan. The corresponding observed midspan stresses for Girder G13 are 0.27 ksi for the stop location test and 0.34 ksi for the crawl speed test. The observed neutral axis locations are 12.39 in. from the bottom of the girder for the stop location test and 10.79 in. from the bottom of the girder for the crawl speed test.

The strains measured for Girder G13 during the Middle Path static tests are shown in Figure 6.19. Figure 6.19(a) shows the maximum strains observed during the stop location test for Girder G13 at each end of the girder. Figure 6.19(b) shows the maximum strains observed during the stop location test for Girder G13 at the midspan. Figure 6.19(c) shows the maximum strains observed during the crawl speed test for Girder G13 at each end of the girder. Figure 6.19(d) shows the maximum strains observed during the crawl speed test for Girder G13 at the midspan. The corresponding observed midspan stresses for Girder G13 are 1.36 ksi for the stop location test and 1.47 ksi for the crawl speed test. The observed neutral axis locations are 12.70 in. from the bottom of the girder for the stop location test and 13.17 in. from the bottom of the girder for the crawl speed test.

As expected, Girder G13 saw a higher level of stress than Girder G7 during the Path 1 loading; however, it saw lower stress levels than Girder G7 during the Path 2 and Middle Path loading. For all three paths, there is also evidence of restraint at the girder ends causing a negative moment to occur, which is seen by the bottom flange end strain gauges being in compression. Also of note, the measured neutral axes show signs of significant composite behavior occurring, which will be discussed later in this chapter.

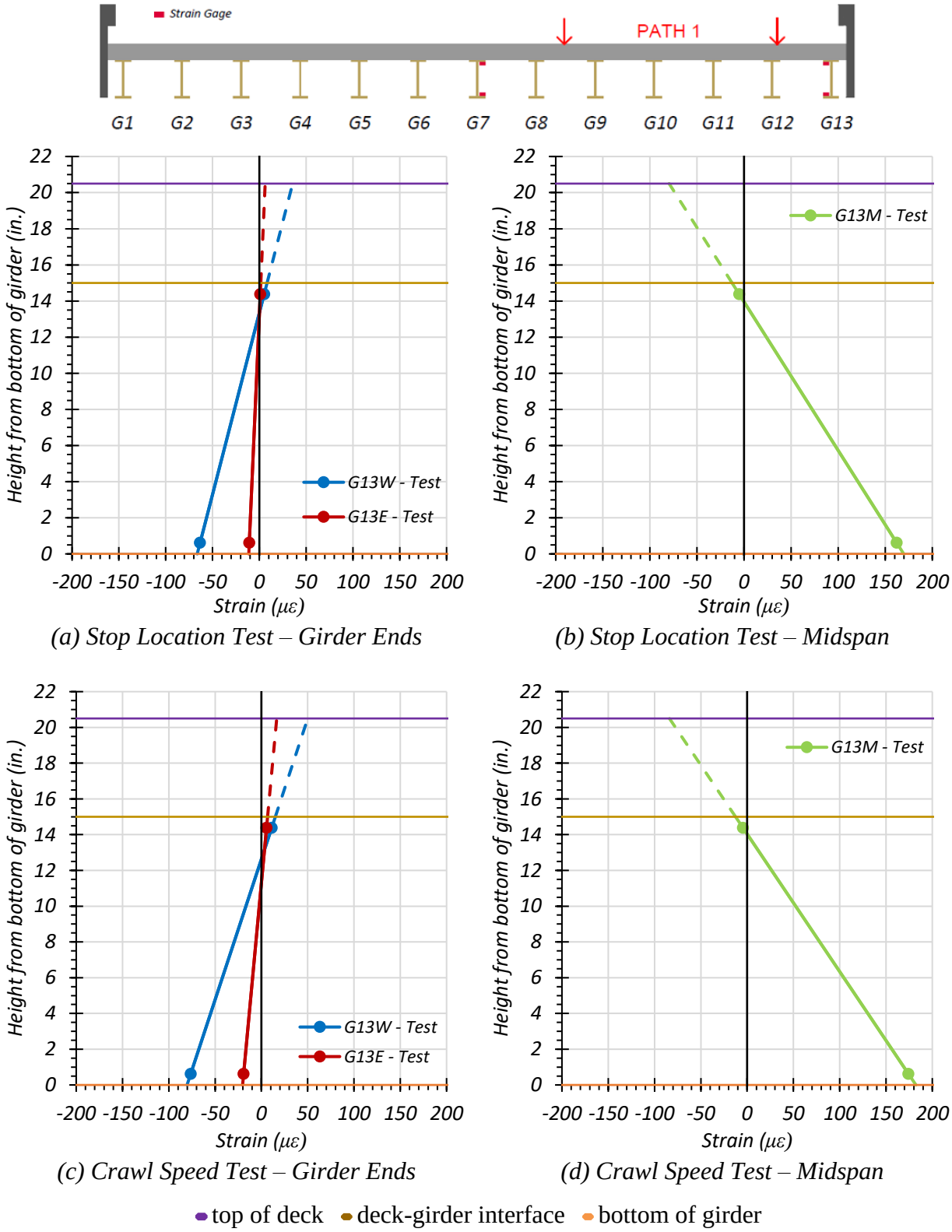

Figure 6.17. Static Strains for Exterior Girder G13—Path 1

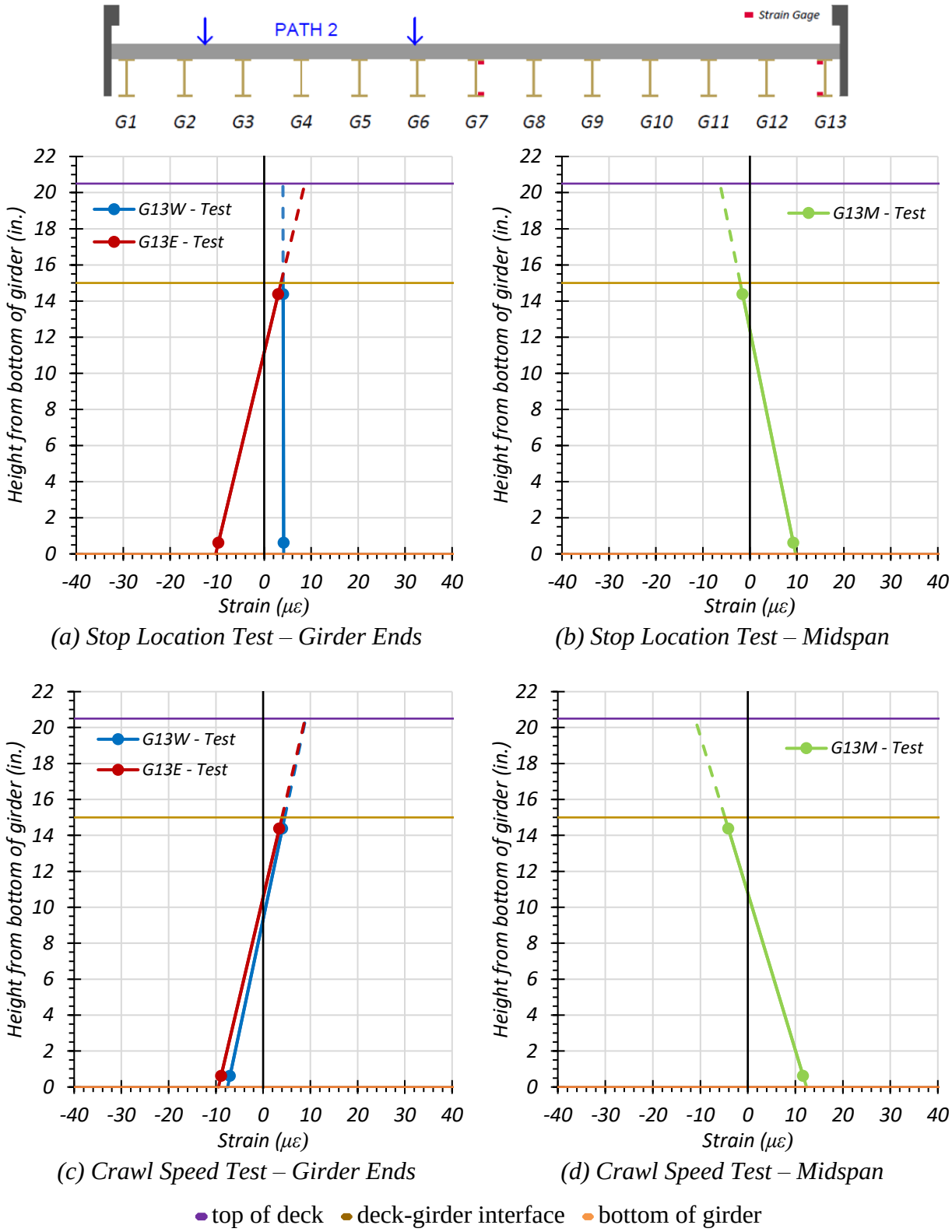

(a) Stop Location Test – Girder Ends

(b) Stop Location Test – Midspan

(c) Crawl Speed Test – Girder Ends

(d) Crawl Speed Test – Midspan

Figure 6.18. Static Strains for Exterior Girder G13—Path 2

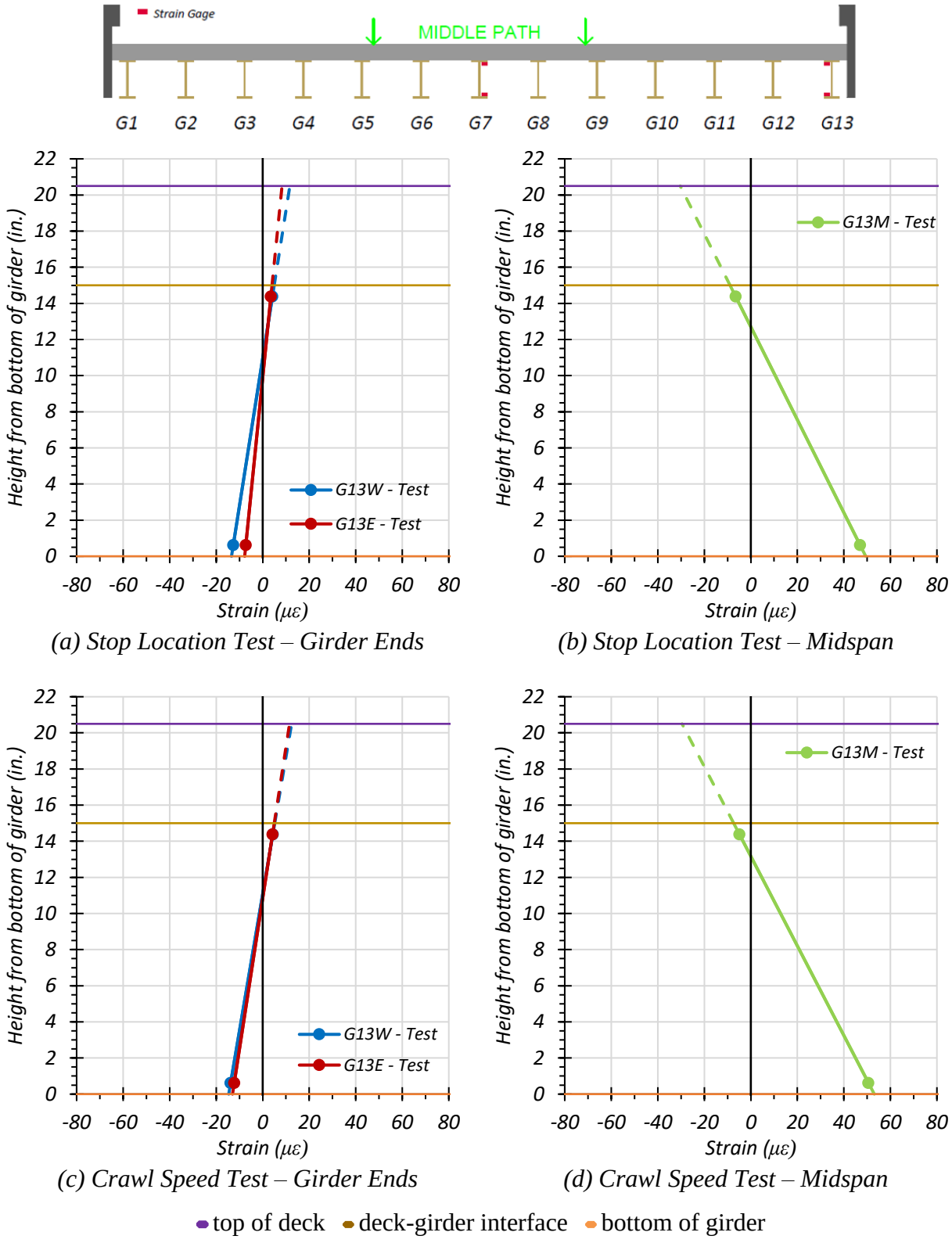

(a) Stop Location Test – Girder Ends

(b) Stop Location Test – Midspan

(c) Crawl Speed Test – Girder Ends

(d) Crawl Speed Test – Midspan

Figure 6.19. Static Strains for Exterior Girder G13—Middle Path

Comparison of Measured Strain Results. Table 6.4 and Figure 6.20 show the observed neutral axis locations based on the strain measurements for all static load tests. The average neutral axis locations were 12.84 in. from the bottom of the girder for Girder G13 and 14.00 in. from the bottom of the girder for Girder G7. The test neutral axes tend to be significantly closer to the theoretical composite neutral axis than to the theoretical non-composite neutral axis. This result is based on use of the parallel axis theorem using the updated geometric and material properties determined during testing described in Section 6.3, which includes an f_c' of 7.2 ksi and a corresponding MOE of 4836 ksi. The effective deck width used for an interior girder is 23 in. and for an exterior girder is 17.5 in., determined using Article 10.38.3 in the *AASHTO Standard Specifications* (AASHTO 2002). Reinforcing steel is not included in this calculation. This analysis indicates that Bridge SM-5 likely has significant horizontal load transfer between the deck and girders and is nearly fully composite.

Table 6.4. Measured Neutral Axis Locations for All Static Load Tests

Test	G7 Neutral Axis Location (in. from bottom of girder)	G13 Neutral Axis Location (in. from bottom of girder)
Path 1 – Stop Location	13.95	13.96
Path 1 – Crawl Speed	13.37	14.04
Path 2 – Stop Location	14.08	12.39
Path 2 – Crawl Speed	13.77	10.79
Middle Path – Stop Location	15.05	12.70
Middle Path – Crawl Speed	13.80	13.17
Theoretical Non-Composite	7.50	7.50
Theoretical Composite	14.28	13.60

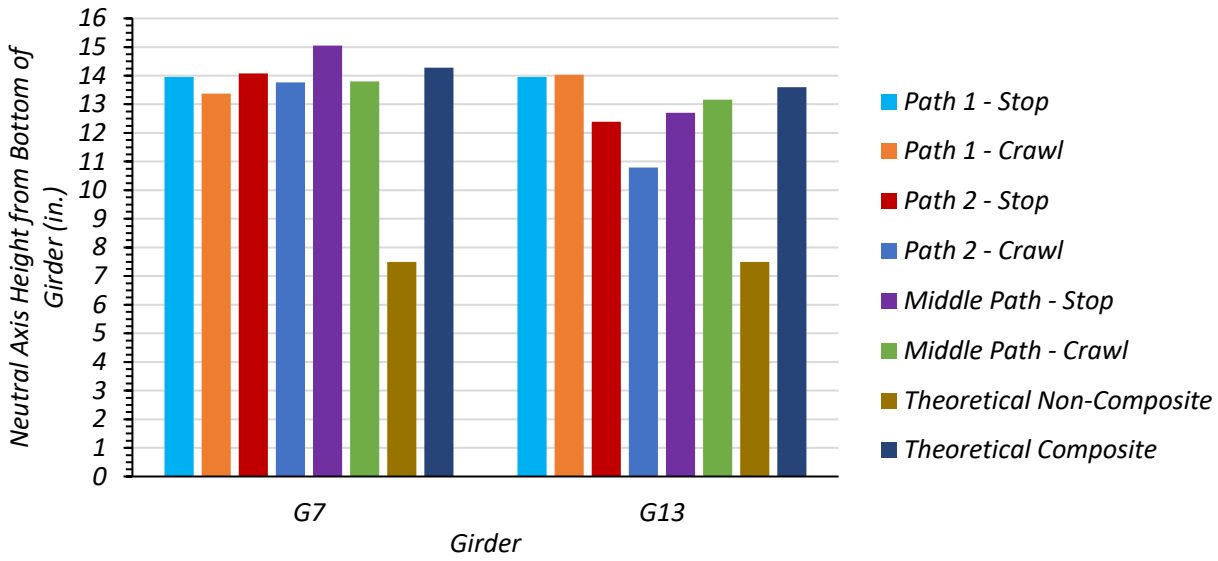

Figure 6.20. Test Neutral Axis Locations

Table 6.5 and Figure 6.21 show the measured bottom flange stress observed during the static load testing. The maximum stress in interior Girder G7 was 3.09 ksi from the Middle Path stop location and crawl speed tests. The maximum stress in exterior Girder G13 was 5.29 ksi from the Path 1 crawl speed test.

Table 6.5. Maximum Static Test Bottom Flange Stresses (ksi)

Load Path	Interior Girder G7		Exterior Girder G13	
	Stop Location Test	Crawl Speed Test	Stop Location Test	Crawl Speed Test
Path 1	2.24	2.21	4.92	5.29
Path 2	2.52	2.63	0.28	0.36
Middle Path	3.09	3.09	1.43	1.54

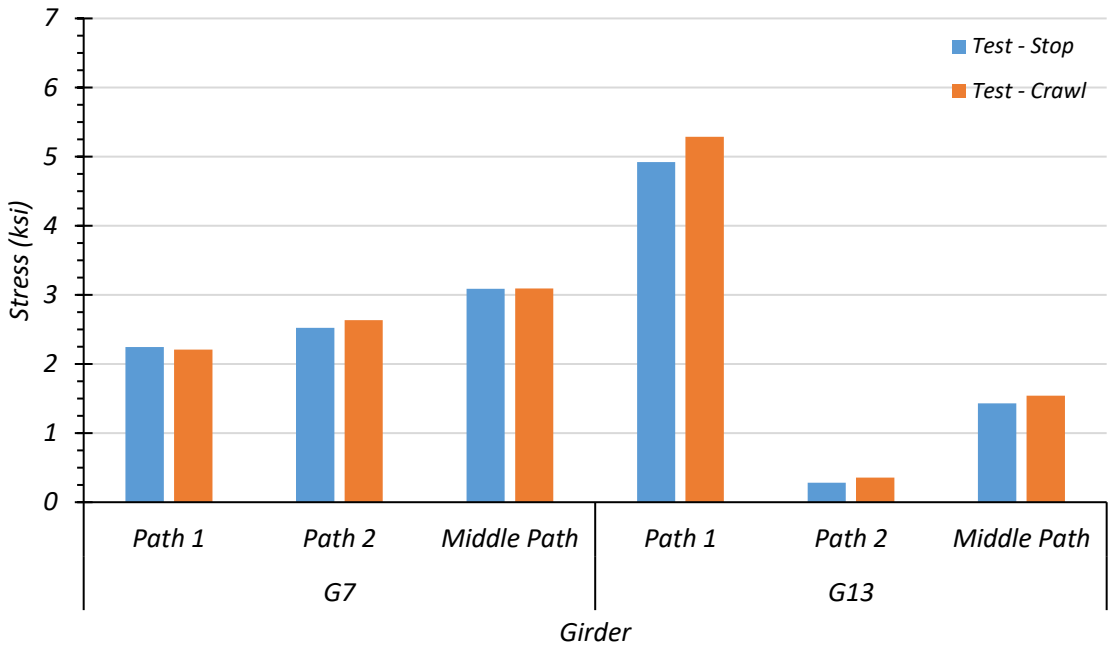

Figure 6.21. Comparison of Maximum Test Bottom Flange Stresses

6.6.1.2 Deflection Measurements and LLDFs

Path 1 Loading. Table 6.6 shows the measured girder deflections during testing for the stop location test and crawl speed test along Path 1. Deflection data for every other girder were recorded; therefore, deflections for the intermediate girders have been interpolated. The associated LLDFs, determined using the measured midspan deflections, are also provided.

Table 6.6. Experimental Midspan Deflections and LLDFs for Path 1 Loading

Girder	G1	G2*	G3	G4*	G5	G6*	G7	G8*	G9	G10*	G11	G12*	G13
Stop Location Test Disp. (in.)	−0.009	0.007	0.023	0.045	0.067	0.091	0.114	0.143	0.173	0.195	0.218	0.263	0.307
Stop Location Test LLDF	0.005	0.004	0.014	0.027	0.041	0.055	0.069	0.087	0.104	0.118	0.132	0.159	0.186
Crawl Speed Test Disp. (in.)	−0.013	0.002	0.017	0.040	0.063	0.088	0.112	0.142	0.172	0.197	0.222	0.273	0.324
Crawl Speed Test LLDF	0.008	0.001	0.010	0.024	0.038	0.053	0.068	0.085	0.103	0.118	0.133	0.164	0.195

Note: 1 – G = girder, Disp. = Displacement, * = displacement results have been interpolated using test results
2 – LLDF values are based on the midspan deflections.

Table 6.7 compares the maximum experimental LLDFs based on midspan deflections to those calculated using the *AASHTO Standard Specifications*, the *AASHTO LRFD Specifications* using the simplified stiffness parameter, and the *AASHTO LRFD Specifications* using the analytical stiffness parameter (AASHTO 2002, 2017). Note that the LLDF expressions in the *AASHTO LRFD Specifications* (AASHTO 2017) consider a multiple presence factor m of 1.2 for one-lane loading and 1.0 for two-lane loading. For this reason, the LLDF values computed for interior girders were divided by 1.2 for comparison to the *AASHTO Standard Specifications* LLDFs and measured LLDFs, which are for a one-lane loaded condition. The maximum g_{AASHTO_Std}/g_{test} ratio ranges from 0.84 to 0.94, indicating the *AASHTO Standard Specifications* estimate is not always conservative. The maximum g_{AASHTO_S}/g_{test} ratios were always above 1.0, ranging from 1.05 to 1.28, indicating good estimates of the measured LLDFs, while and g_{AASHTO_K}/g_{test} ratios are slightly unconservative for exterior girders.

Table 6.7. LLDF Comparison with AASHTO for Path 1 Loading

Test and Girder Type	AASHTO Standard Specs ($g^m_{AASHTO\_Std}$)	AASHTO LRFD Simplified ($g^m_{AASHTO\_S}$)	AASHTO LRFD K_g Calculated ($g^m_{AASHTO\_K}$)	Test (g^m_{test})	$g^m_{AASHTO\_Std}/g^m_{test}$	$g^m_{AASHTO\_S}/g^m_{test}$	$g^m_{AASHTO\_K}/g^m_{test}$
Stop Location Interior	0.137	0.204	0.177	0.159	0.86	1.28	1.11
Stop Location Exterior	0.174	0.204	0.177	0.186	0.94	1.10	0.95
Crawl Speed Interior	0.137	0.204	0.177	0.164	0.84	1.24	1.08
Crawl Speed Exterior	0.174	0.204	0.177	0.195	0.89	1.05	0.91

Figure 6.22(a) and Figure 6.22(c) show the Path 1 stop location and crawl speed girder deflection profiles. Figure 6.22(b) and Figure 6.22(d) show the Path 1 stop location and crawl speed LLDFs compared to relevant AASHTO values. The governing LLDFs observed during testing are slightly higher than the LLDFs provided by the *AASHTO Standard Specifications* and very close to the *AASHTO LRFD Specifications* LLDFs with the simplified stiffness parameter. The measured

LLDFs are slightly higher than the *AASHTO LRFD Specifications* LLDFs determined using the simplified stiffness parameter.

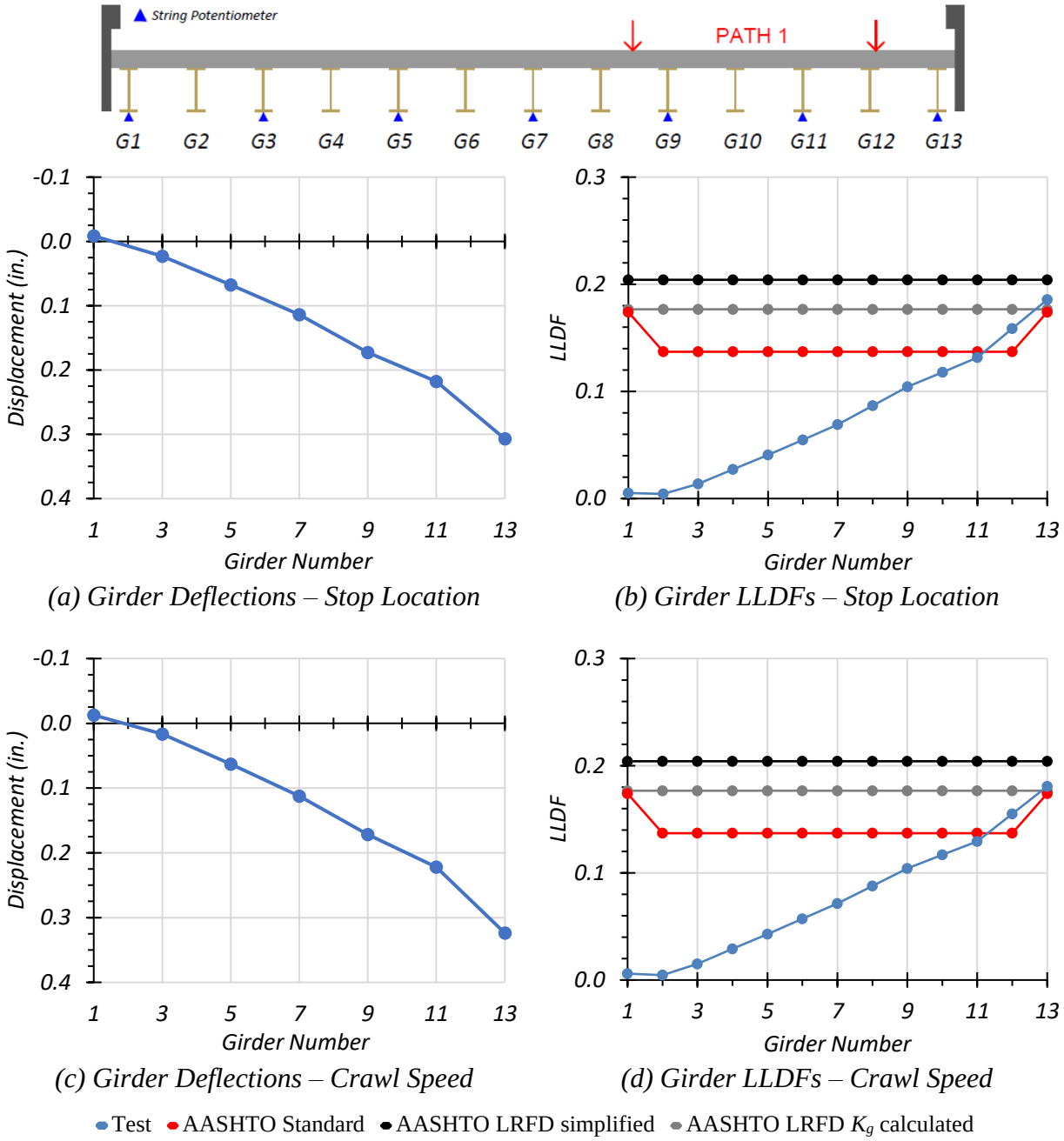

(a) Girder Deflections – Stop Location

(b) Girder LLDFs – Stop Location

(c) Girder Deflections – Crawl Speed

(d) Girder LLDFs – Crawl Speed

Figure 6.22. Static Deflection Results for Path 1 Loading

Path 2 Loading. Table 6.8 shows the measured girder deflections during testing for the stop location test and crawl speed test along Path 2. Deflection data for every other girder were

recorded; therefore, deflections of the intermediate girders have been interpolated. The associated LLDFs, determined using the measured midspan deflections, are also provided.

Table 6.8. Experimental Midspan Deflections and LLDFs for Path 2 Loading

Girder	G1	G2*	G3	G4*	G5	G6*	G7	G8*	G9	G10*	G11	G12*	G13
Stop Location Test Disp. (in.)	0.212	0.202	0.192	0.179	0.166	0.145	0.124	0.101	0.078	0.056	0.035	0.020	0.006
Stop Location Test LLDF	0.140	0.133	0.127	0.118	0.109	0.096	0.082	0.067	0.051	0.037	0.023	0.013	0.004
Crawl Speed Test Disp. (in.)	0.205	0.197	0.189	0.179	0.168	0.148	0.127	0.104	0.081	0.060	0.039	0.025	0.010
Crawl Speed Test LLDF	0.134	0.129	0.124	0.117	0.110	0.097	0.083	0.068	0.053	0.039	0.026	0.016	0.007
Note: G = girder, Disp. = Displacement, * = displacement results have been interpolated using test results													

Table 6.9 compares the maximum experimental LLDFs based on midspan deflections to those calculated using the *AASHTO Standard Specifications*, the *AASHTO LRFD Specifications* using the simplified stiffness parameter, and *AASHTO LRFD Specifications* using the analytical stiffness parameter (AASHTO 2002, 2017). Note that the LLDF expressions in the *AASHTO LRFD Specifications* (AASHTO 2017) consider a multiple presence factor m of 1.2 for one-lane loading and 1.0 for two-lane loading. For this reason, the LLDF values computed for interior girders were divided by 1.2 for comparison to the *AASHTO Standard Specifications* LLDFs and measured LLDFs, which are for a one-lane loaded condition. The g_{AASHTO_Std}/g_{test} ratio was always above 1.0, ranging from 1.03 to 1.30, indicating that the *AASHTO Standard Specifications* LLDFs are slightly conservative for interior girder while being quite conservative for exterior girder for this load path. The g_{AASHTO_S}/g_{test} and g_{AASHTO_K}/g_{test} ratios were also always above 1.0, ranging from 1.26 to 1.58, indicating even more conservative estimates of the measured LLDFs.

Table 6.9. LLDF Comparison with AASHTO for Path 2 Loading

Test and Girder Type	AASHTO Standard Specs ($g^m_{AASHTO\_Std}$)	AASHTO LRFD Simplified ($g^m_{AASHTO\_S}$)	AASHTO LRFD K_g Calculated ($g^m_{AASHTO\_K}$)	Test (g^m_{test})	$g^m_{AASHTO\_Std}/g^m_{test}$	$g^m_{AASHTO\_S}/g^m_{test}$	$g^m_{AASHTO\_K}/g^m_{test}$
Stop Location Interior	0.137	0.204	0.177	0.133	1.03	1.53	1.33
Stop Location Exterior	0.174	0.204	0.177	0.140	1.24	1.46	1.26
Crawl Speed Interior	0.137	0.204	0.177	0.129	1.06	1.58	1.37
Crawl Speed Exterior	0.174	0.204	0.177	0.134	1.30	1.52	1.32

Figure 6.23(a) and Figure 6.23(c) show the Path 2 stop location and crawl speed girder deflection profiles. Figure 6.23(b) and Figure 6.23(d) show the Path 2 stop location and crawl speed LLDFs compared to relevant AASHTO values. The governing LLDFs observed during testing are slightly lower than the LLDFs provided by the *AASHTO Standard Specifications*. They are significantly lower than the *AASHTO LRFD Specifications* LLDFs with both the analytical stiffness parameter and with the simplified stiffness parameter.

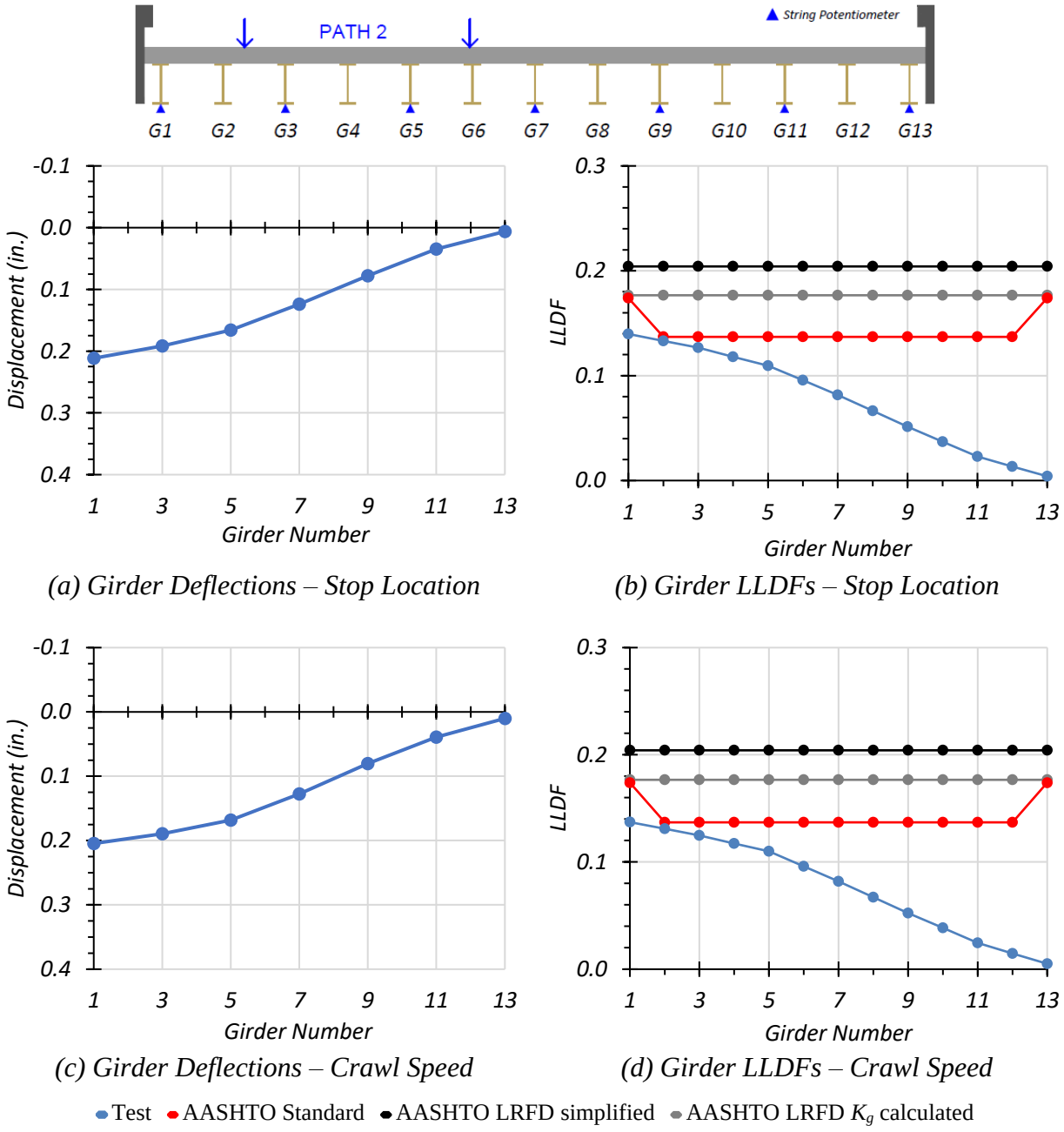

(a) Girder Deflections – Stop Location

(b) Girder LLDFs – Stop Location

(c) Girder Deflections – Crawl Speed

(d) Girder LLDFs – Crawl Speed

Figure 6.23. Static Deflection Results for Path 2 Loading

Middle Path Loading. Table 6.10 shows the measured girder deflections during testing for the stop location test and crawl speed test along the Middle Path. Deflection data for every other girder were recorded; therefore, deflections of the intermediate girders have been interpolated. The associated LLDFs, determined using the measured midspan deflections, are also provided.

Table 6.10. Experimental Midspan Deflections and LLDFs for Middle Path Loading

Girder	G1	G2*	G3	G4*	G5	G6*	G7	G8*	G9	G10*	G11	G12*	G13
Stop Location Test Disp. (in.)	0.075	0.089	0.103	0.119	0.134	0.140	0.145	0.142	0.140	0.125	0.109	0.105	0.100
Stop Location Test LLDF	0.049	0.058	0.068	0.078	0.088	0.091	0.095	0.093	0.092	0.082	0.072	0.069	0.066
Crawl Speed Test Disp. (in.)	0.073	0.087	0.102	0.119	0.136	0.141	0.146	0.142	0.139	0.125	0.111	0.107	0.104
Crawl Speed Test LLDF	0.048	0.057	0.066	0.078	0.089	0.092	0.095	0.093	0.091	0.082	0.072	0.070	0.068
Note: G = girder, Disp. = Displacement, * = displacement results have been interpolated using test results													

Table 6.11 compares the maximum experimental LLDFs based on midspan deflections to those calculated using the *AASHTO Standard Specifications*, the *AASHTO LRFD Specifications* using the simplified stiffness parameter, and the *AASHTO LRFD Specifications* using the analytical stiffness parameter (AASHTO 2002, 2017). Note that the LLDF expressions in the *AASHTO LRFD Specifications* (AASHTO 2017) consider a multiple presence factor m of 1.2 for one-lane loading and 1.0 for two-lane loading. For this reason, the LLDF values computed for interior girders were divided by 1.2 for comparison to the *AASHTO Standard Specifications* LLDFs and measured LLDFs, which are for a one-lane loaded condition. The g_{AASHTO_Std}/g_{test} ratio was always above 1.0, ranging from 1.44 to 2.64. The g_{AASHTO_S}/g_{test} and g_{AASHTO_K}/g_{test} ratios were also always above 1.0, ranging from 1.86 to 3.09. In all cases, the AASHTO estimates are conservative relative to the measured LLDFs for the Middle Path loading.

Table 6.11. LLDF Comparison with AASHTO for Middle Path Loading

Test and Girder Type	AASHTO Standard Specs ($g^m_{AASHTO\_Std}$)	AASHTO LRFD Simplified ($g^m_{AASHTO\_S}$)	AASHTO LRFD K_g Calculated ($g^m_{AASHTO\_K}$)	Test (g^m_{test})	$g^m_{AASHTO\_Std}/g^m_{test}$	$g^m_{AASHTO\_S}/g^m_{test}$	$g^m_{AASHTO\_K}/g^m_{test}$
Stop Location Interior	0.137	0.204	0.177	0.095	1.44	2.15	1.86
Stop Location Exterior	0.174	0.204	0.177	0.066	2.64	3.09	2.68
Crawl Speed Interior	0.137	0.204	0.177	0.095	1.44	2.15	1.86
Crawl Speed Exterior	0.174	0.204	0.177	0.068	2.56	3.00	2.60

Figure 6.24(a) and Figure 6.24(c) show the Middle Path stop location and crawl speed girder deflection profiles. Figure 6.24(b) and Figure 6.24(d) show the Middle Path stop location and crawl speed LLDFs compared to relevant AASHTO values. The governing LLDFs observed during testing are significantly lower when compared to all the LLDFs provided by all three of the AASHTO methods.

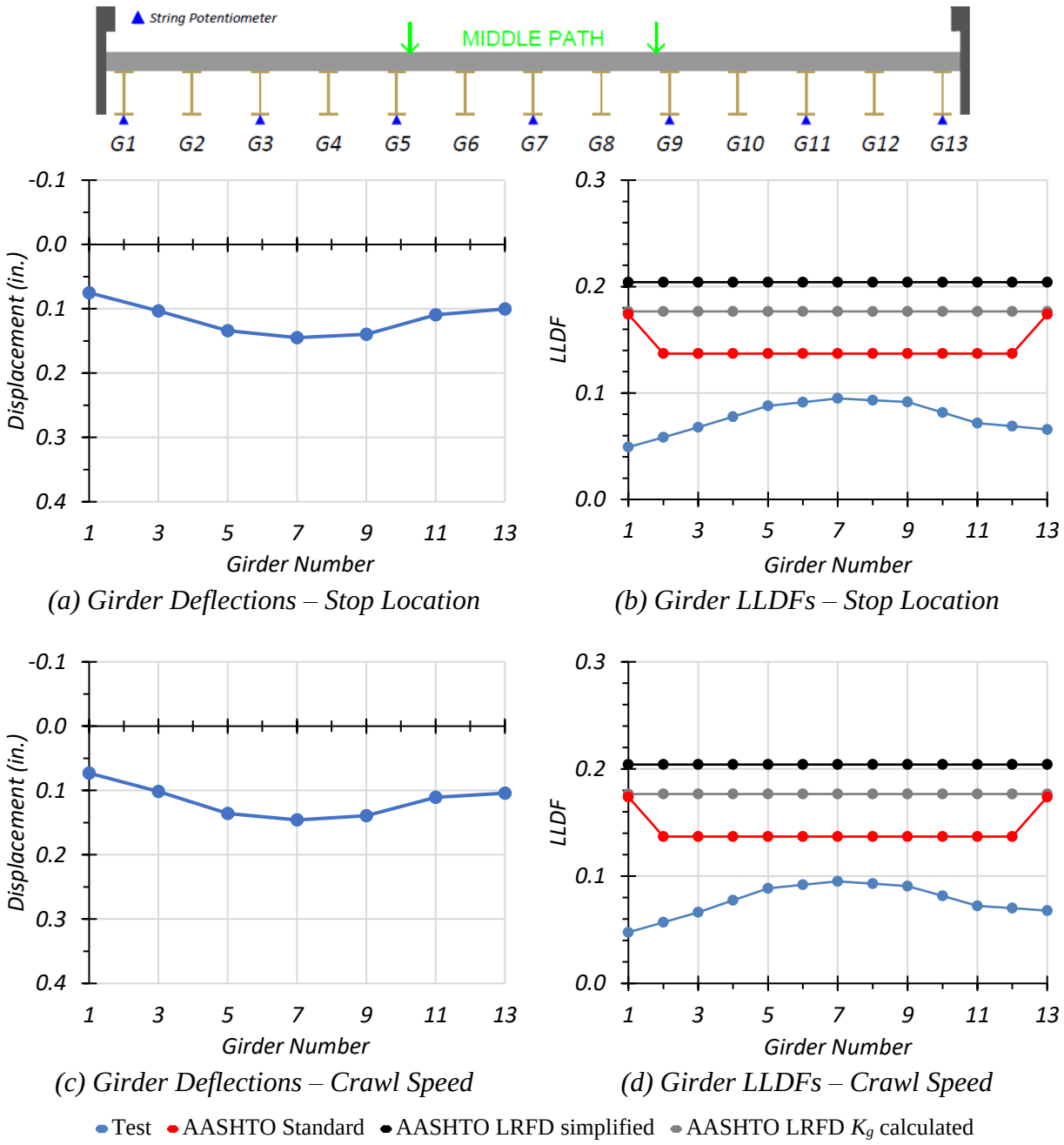

(a) Girder Deflections – Stop Location

(b) Girder LLDFs – Stop Location

(c) Girder Deflections – Crawl Speed

(d) Girder LLDFs – Crawl Speed

Figure 6.24. Static Deflection Results for Middle Path Loading

Comparison of Results Based on Deflection Measurements. The critical LLDF for an exterior girder was 0.195, which was observed during the crawl speed test along Path 1. This figure corresponds to a g_{AASHTO}/g_{test} ratio of 0.89 when using the *AASHTO Standard Specifications*, 1.05 when using the *AASHTO LRFD Specifications* using the simplified stiffness parameter, and 0.91 when using the *AASHTO LRFD Specifications* using the analytical stiffness parameter. The

critical LLDF for an interior girder was 0.164, which was also observed during the crawl speed test along Path 1. This number corresponds to a g_{AASHTO}/g_{test} ratio of 0.84 when using the *AASHTO Standard Specifications*, 1.24 when using the *AASHTO LRFD Specifications* using the simplified stiffness parameter, and 1.08 when using the *AASHTO LRFD Specifications* using the analytical stiffness parameter. During the static load tests along Path 1, the maximum LLDF was 0.186 for the stop location test while increasing to 0.195 for the crawl speed test. During the static load tests along Path 2, the maximum LLDF was 0.140 for the stop location test while decreasing to 0.134 for the crawl speed test. During the static load tests along Middle Path, the maximum LLDF of 0.095 for the stop location test remained the same for the crawl speed test.

Only the *AASHTO Standard Specifications* LLDFs (AASHTO 2002) produced lower values than the LLDFs observed during field testing, which occurred during Path 1 loading. However, for Path 2 loading and Middle Path loading, the *AASHTO Standard Specifications* LLDFs were conservative. Both LLDF methods in the *AASHTO LRFD Specifications* (AASHTO 2017) were always conservative for every load case, except for exterior girders during Path 1 loading. TxDOT is currently using the *AASHTO Standard Specifications* to determine LLDFs for Bridge SM-5. Since these LLDFs are usually conservative and only slightly unconservative in some cases, it is unlikely that the LLDFs could be improved for this bridge.

6.6.2 Dynamic Load Tests on Bridge SM-5

6.6.2.1 Dynamic Amplification

Maximum Girder Strains. From the results of the static and dynamic tests for each path, the increases in strains and deflections at the midspan due to the moving vehicle were examined. Figure 6.25, Figure 6.26, and Figure 6.27 show the maximum midspan strains observed for dynamic testing along Path 1, Path 2, and the Middle Path, respectively, plotted with the strains observed for the same alignments (paths) under static loading. Figure 6.28 shows the strain values and compares them to the appropriate static load case.

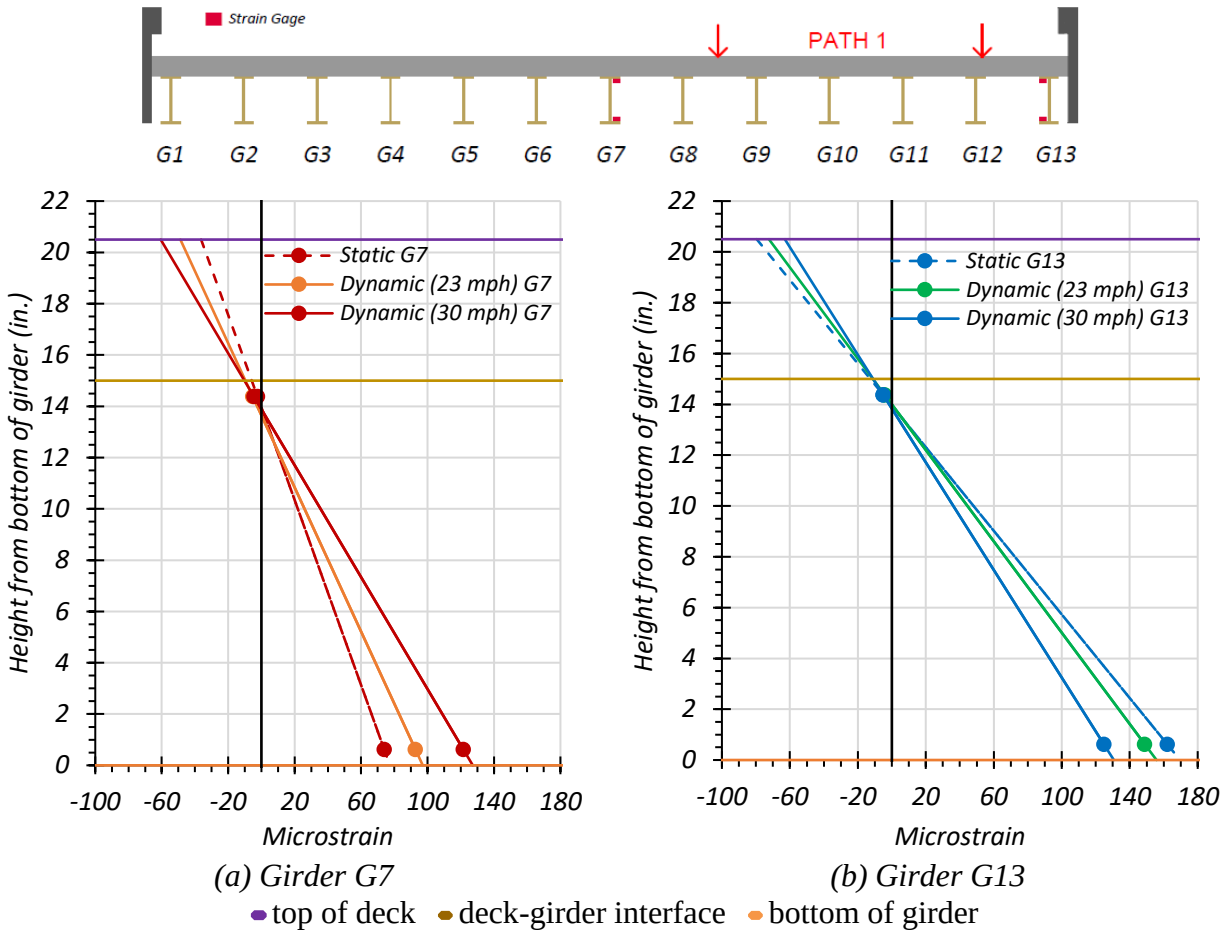

Figure 6.25. Maximum Strains for Static and Dynamic Tests for Path 1 Loading

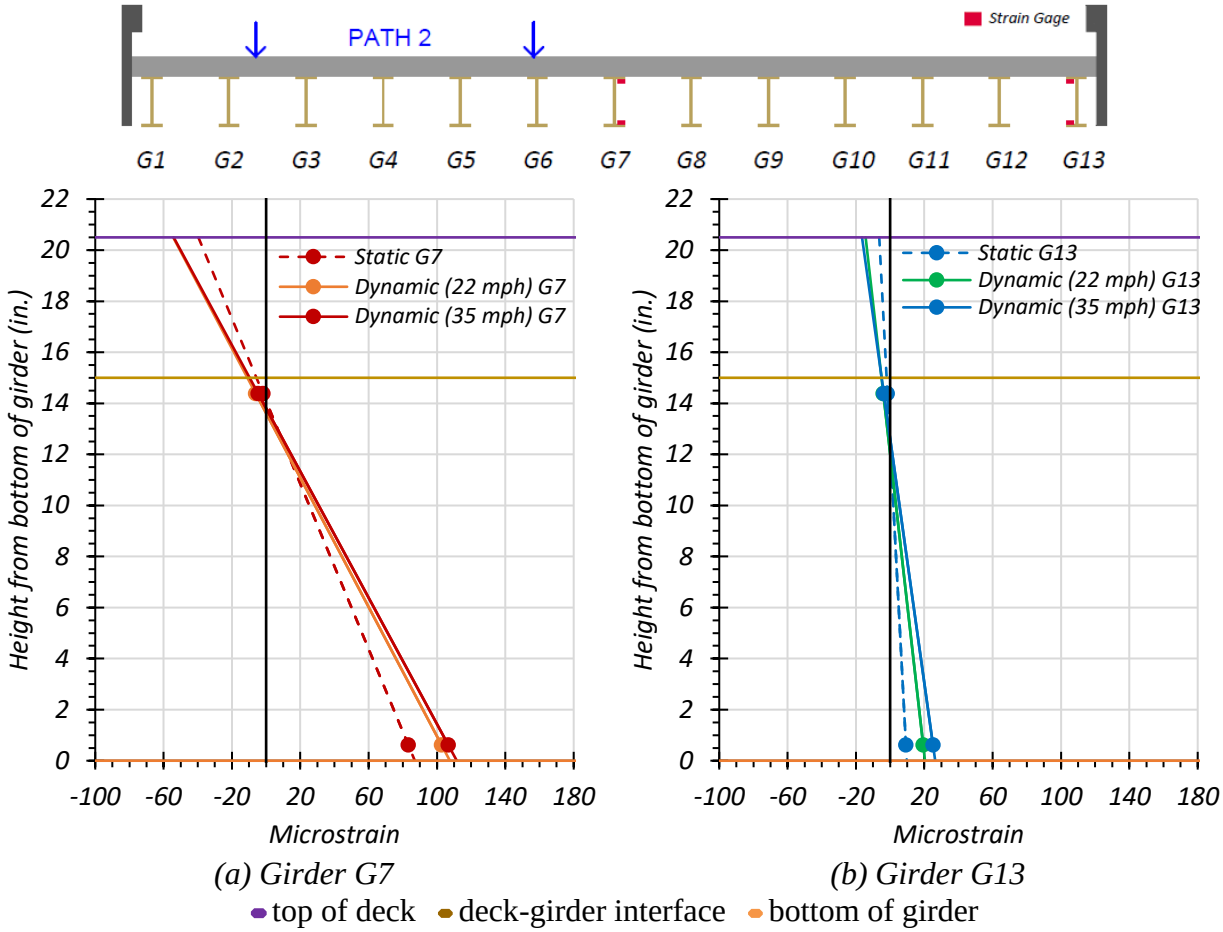

Figure 6.26. Maximum Strains for Static and Dynamic Tests for Path 2 Loading

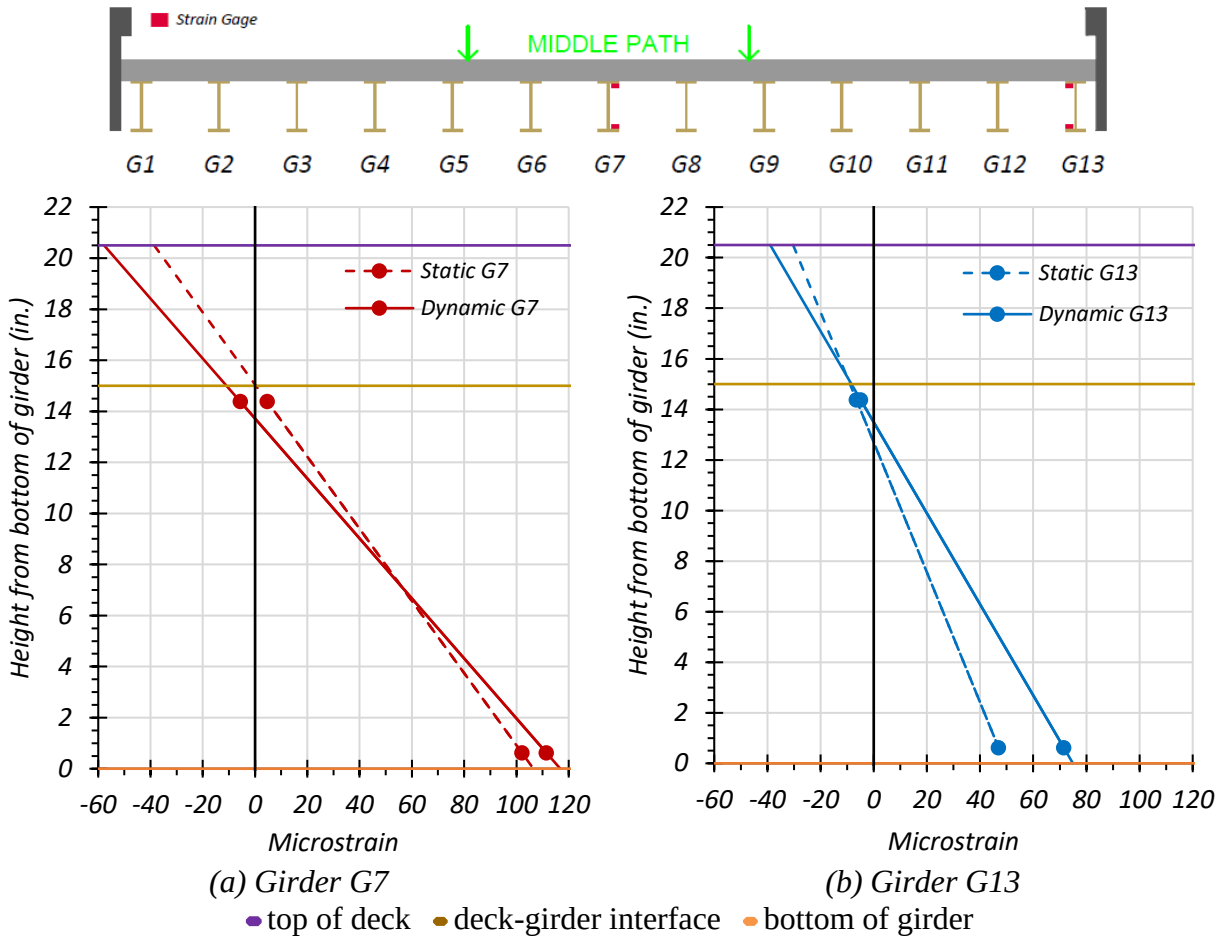

Figure 6.27. Maximum Strains for Static and Dynamic Tests for Middle Path Loading

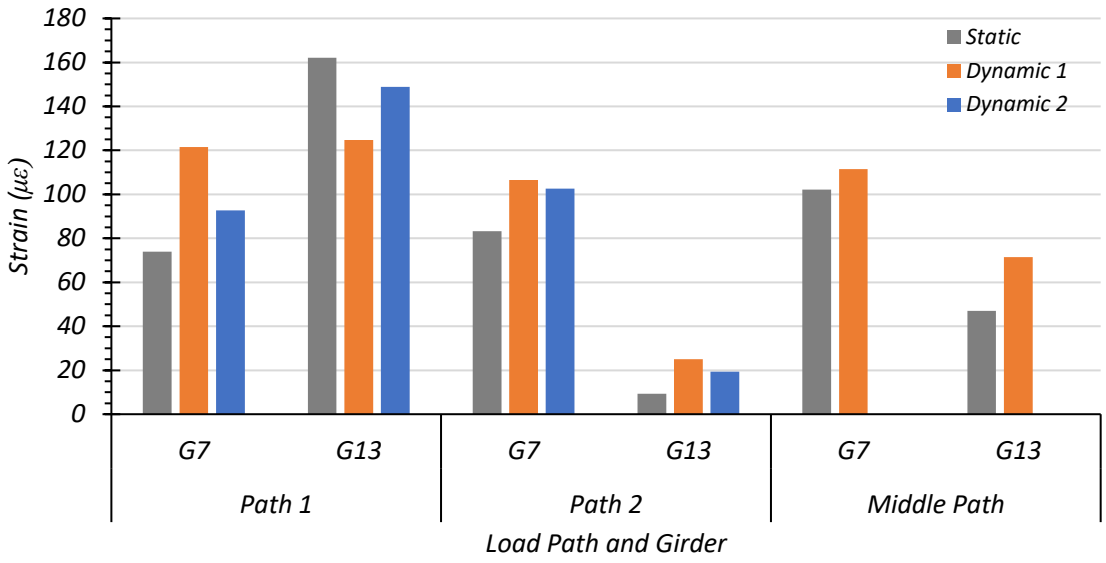

Note:

- *Path 1: Dynamic 1 = 23 mph, Dynamic 2 = 30 mph*
- *Path 2: Dynamic 1 = 22 mph, Dynamic 2 = 35 mph*
- *Middle Path: Dynamic 1 = 34 mph*

Figure 6.28. Comparison of Maximum Strains for Static and Dynamic Tests

The dynamic impact factor given by the *AASHTO Standard Specifications* for this bridge is 30 percent, while the *AASHTO LRFD Specifications* specifies an impact factor of 33 percent. The average dynamic impact factor for all girders based on the strain values observed during testing was 45 percent, indicating that for this bridge the dynamic impact factor can be higher than specified by AASHTO. However, this result could be misleading. If a girder experiences a very low amount of strain under static loading, a small increase in strain under dynamic loading could cause a large percent difference to occur, which is the case for Girder G13 under Path 2 loading. It sees an increase in strain from 9.24 microstrain during static loading to 25.06 microstrain during Dynamic 1 loading, which corresponds to a 171 percent difference in strain. However, 25.06 microstrain corresponds to a stress of only 0.73 ksi. Such a large percent difference for a girder that is carrying very little load significantly skews the average dynamic factor in this case.

For only Girder G7, which is not skewed by having small strain increases on top of small static strain values, the average dynamic amplification is 30.1 percent. This value is almost the same as the AASHTO specified values. An examination of Girder G13 under Path 1 loading—its controlling load case—revealed that the dynamic strain decreases by 8.2 percent for Dynamic 1

and 23.0 percent for Dynamic 2. Removing the cases that are insignificant for load rating gives values for dynamic amplification that are much more typical.

The dynamic effect seems to be more significant for an interior girder, as shown by the large dynamic increases in Girder G7 under Path 1 and Path 2 loading. Although Girder G13 experienced larger strains during load testing, this girder had a decrease in maximum strain during dynamic loading. Because Load Path 1 was quite close to the guardrail, the driver might not have felt comfortable driving or have been able to drive along Path 1 perfectly at higher speeds.

Maximum Girder Deflections at the Midspan. Figure 6.29, Figure 6.30, and Figure 6.31 show the girder deflection time histories for the dynamic load cases along Path 1, Path 2, and the Middle Path, respectively, for each dynamic loading test. Table 6.12 provides the maximum measured girder deflections for the stop location load case and for each dynamic load case. Figure 6.32 shows the static and dynamic maximum deflection values and compares them. Figure 6.33 shows the measured deflections for each dynamic load cases as a ratio to the stop location deflection.

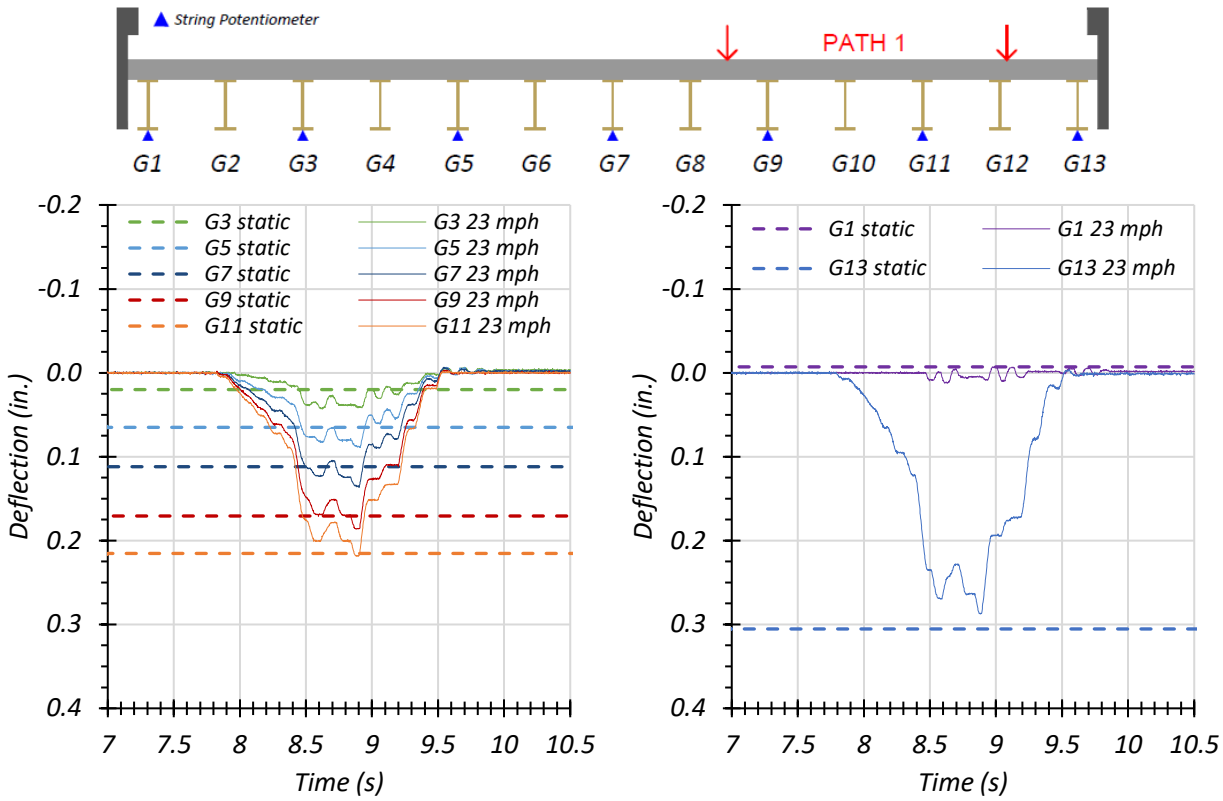

(a) Deflection Time Histories – Dynamic (23 mph)

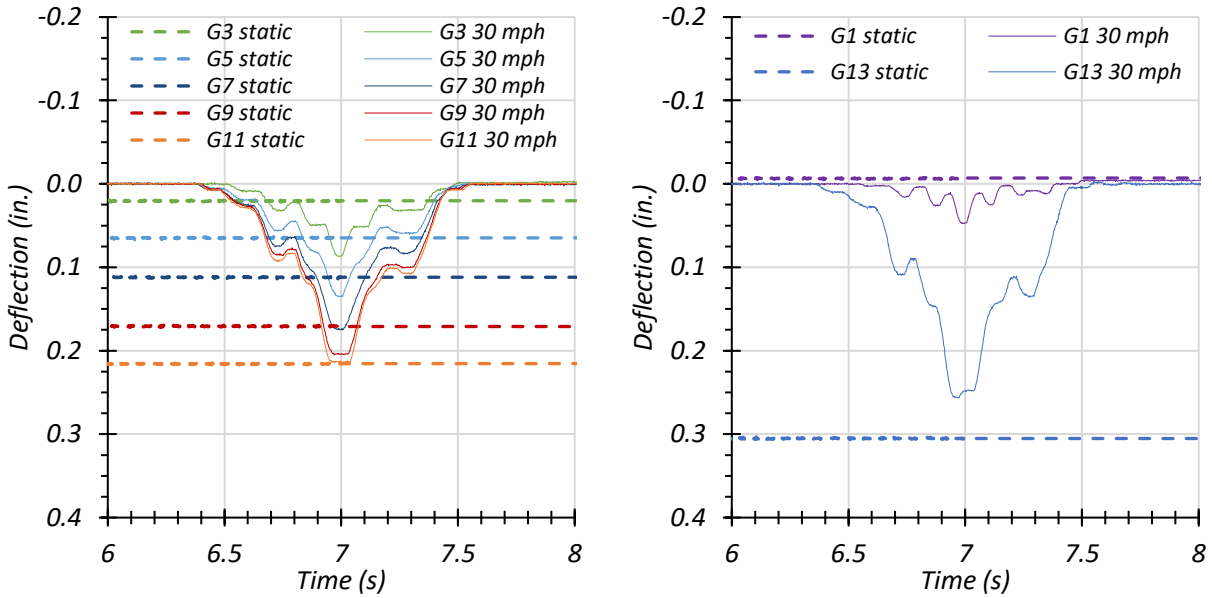

(b) Deflection Time Histories – Dynamic (30 mph)

Figure 6.29. Midspan Deflections for Static and Dynamic Tests for Path 1 Loading

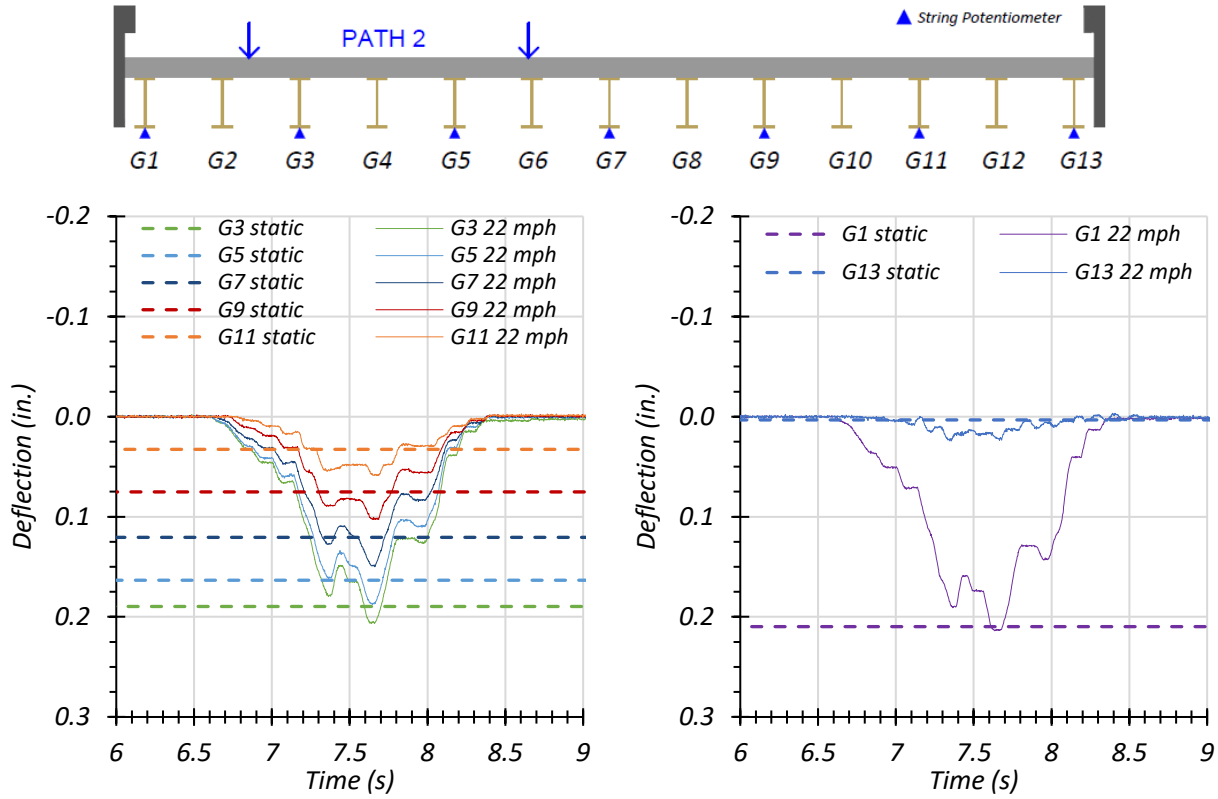

(a) Deflection Time Histories – Dynamic (22 mph)

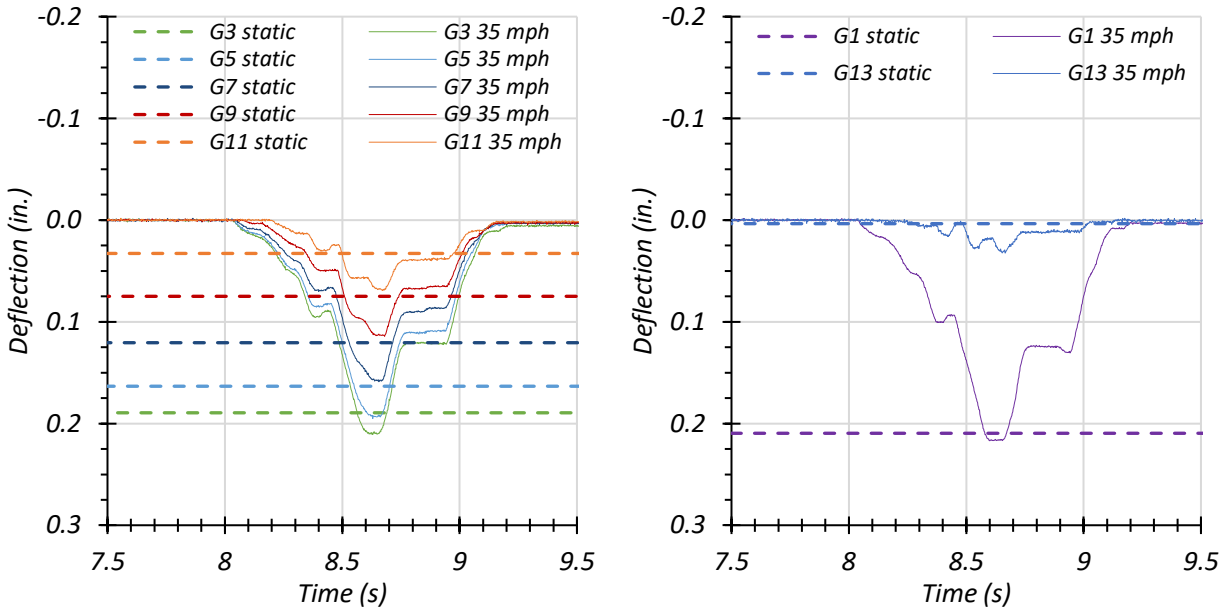

(b) Deflection Time Histories – Dynamic (35 mph)

Figure 6.30. Midspan Deflections for Static and Dynamic Tests for Path 2 Loading

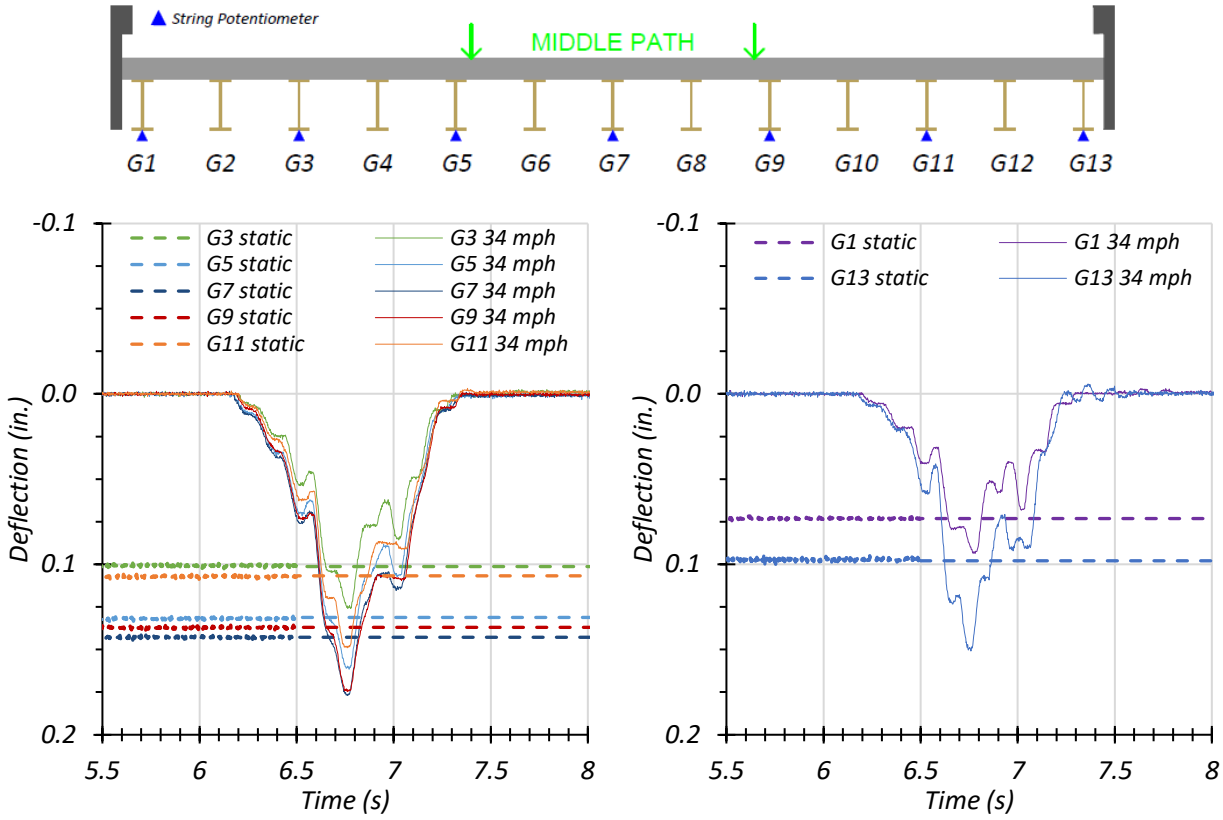

Figure 6.31. Midspan Deflections for Static and Dynamic (34 mph) Tests for Middle Path Loading

Table 6.12. Maximum Midspan Deflections for Static and Dynamic Tests

Load Scenario	Girder Displacement (in.)						
	G1	G3	G5	G7	G9	G11	G13
Path 1 Static	-0.009	0.023	0.067	0.114	0.173	0.218	0.307
Path 1 Dynamic (23 mph)	0.012	0.043	0.089	0.137	0.186	0.219	0.288
Path 1 Dynamic (30 mph)	0.048	0.087	0.135	0.175	0.205	0.214	0.257
Maximum Dynamic Amplification	**659%**	**280%**	**101%**	**53.5%**	**18.8%**	**0.4%**	**-6.4%**
Path 2 Static	0.212	0.192	0.166	0.124	0.078	0.035	0.006
Path 2 Dynamic (22 mph)	0.214	0.207	0.188	0.150	0.103	0.059	0.024
Path 2 Dynamic (35 mph)	0.217	0.211	0.195	0.159	0.114	0.069	0.033
Maximum Dynamic Amplification	**2.5%**	**9.9%**	**17.7%**	**28.5%**	**46.9%**	**101%**	**428%**
Middle Static	0.075	0.103	0.134	0.145	0.140	0.109	0.100
Middle Dynamic (34 mph)	0.094	0.126	0.162	0.177	0.175	0.149	0.151
Maximum Dynamic Amplification	**24.7%**	**22.0%**	**20.5%**	**22.2%**	**25.0%**	**36.3%**	**50.3%**

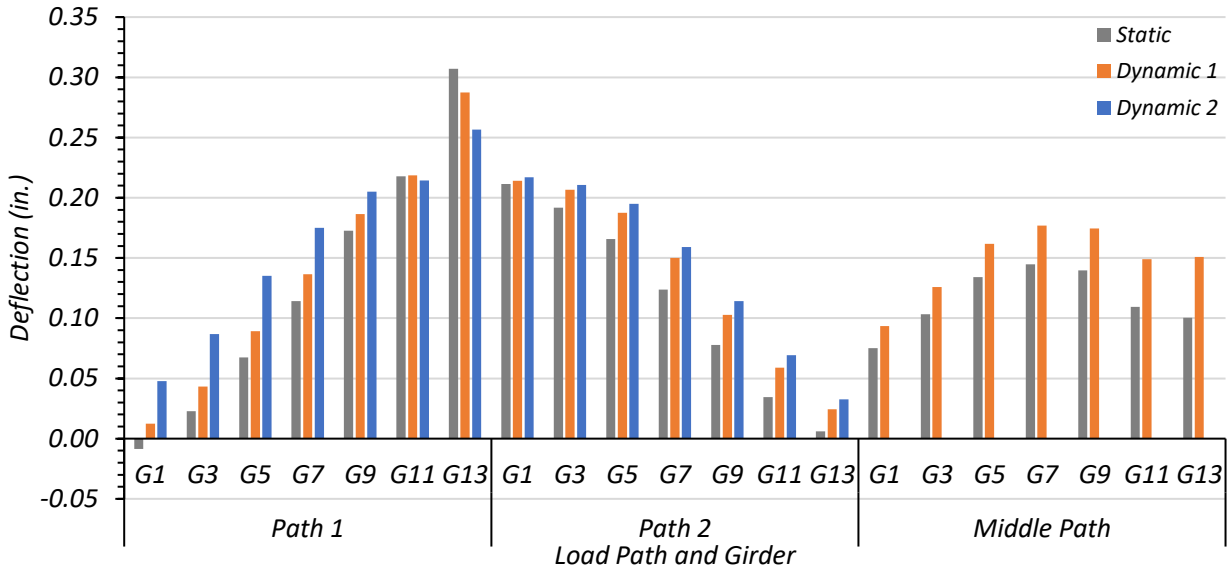

Note:

- *Path 1: Dynamic 1 = 23 mph, Dynamic 2 = 30 mph*
- *Path 2: Dynamic 1 = 22 mph, Dynamic 2 = 35 mph*
- *Middle Path: Dynamic 1 = 34 mph*

Figure 6.32. Comparison of Maximum Midspan Deflections for Static and Dynamic Tests

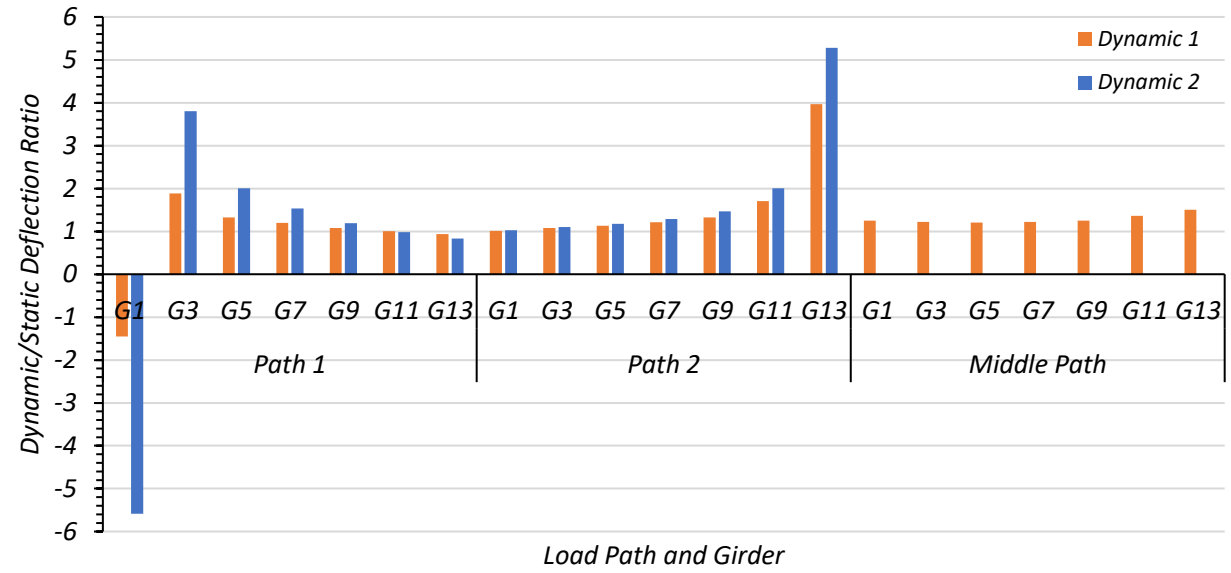

Note:

- *Path 1: Dynamic 1 = 23 mph, Dynamic 2 = 30 mph*
- *Path 2: Dynamic 1 = 22 mph, Dynamic 2 = 35 mph*
- *Middle Path: Dynamic 1 = 34 mph*

Figure 6.33. Maximum Midspan Dynamic Deflections to Static Deflections Ratios

The dynamic impact factor given by the *AASHTO Standard Specifications* for this bridge is 30 percent, while the dynamic impact factor given by the *AASHTO LRFD Specifications* is 33 percent. The average dynamic impact factor for all girders based on the deflection values observed during testing was 78 percent. However, this result could be misleading because many girders had very minimal static deflections. A small numerical increase in deflection would cause a large increase percent difference between the static and dynamic case, which is the case for many of the girders that were on the opposite side of the bridge from the testing load case, meaning they were experiencing minimal amounts of load and therefore would not be controlling. For example, during Path 2 loading, the controlling girder based on LLDFs was found to be Girder G1. It experienced a stop location deflection of 0.212 in. and a maximum dynamic deflection of 0.217 in. during Dynamic 2, corresponding to a dynamic amplification of 2.5 percent. On the opposite side of the bridge, Girder G1 experiences a stop location deflection of 0.006 in. and a maximum dynamic deflection of 0.033 in. during Dynamic 2, corresponding to a dynamic amplification of 428 percent. This large value puts more weight on the dynamic amplification of a girder that is not controlling and significantly skews the average dynamic amplification value.

For only Girder G7, which is not skewed by having small deflection increases on top of small static deflection values, the average dynamic amplification is 29.1 percent, which is almost the same as the AASHTO specified values. The average dynamic amplification under Middle Path loading for the seven girders whose deflections were measured was 28.7 percent, slightly under the AASHTO values. An examination of Girder G13 under Path 1 loading—its controlling load case—revealed that the dynamic strain decreases by 6.4 percent for Dynamic 1 and 16.5 percent for Dynamic 2. Removing the cases that are insignificant for load rating gives values for dynamic amplification that are much more typical.

During Path 1 loading, the maximum percent increase in deflection for Girder G7 was 53.5 percent during Dynamic 2 loading. The maximum percent increase in deflection in Girder G13 was -6.4 percent during Dynamic 1 loading.

During Path 2 loading, the maximum percent increase in deflection for Girder G7 was 28.5 percent during Dynamic 2 loading. The maximum percent increase in deflection in Girder G13 was 428.3 percent during Dynamic 2 loading; however, it is worth noting that Girder G13 experiences very minimal deflection during Path 2 loading, which may explain the large dynamic effect.

During Middle Path loading, the maximum percent increase in deflection for Girder G7 was 22.2 percent during Dynamic 1 loading. The maximum percent increase in deflection in Girder G13 was 50.3 percent during Dynamic 1 loading.

In conclusion, Figure 6.32 and Figure 6.33 show that while large dynamic amplifications are possible, for the girders that are most heavily loaded along a particular path, the dynamic amplifications are close to the AASHTO values, and sometime even below them. In some cases, the most heavily loaded girders actually feel a decrease in effect under dynamic loading.

6.6.2.2 ***Dynamic Characteristics of the Bridge***

Data obtained from the accelerometers during dynamic tests and the sledgehammer tests were filtered, and a fast Fourier transform (FFT) was performed that allowed for determination of the first three natural frequencies of the bridge as 7.57 Hz, 9.03 Hz, and 17.58 Hz. For each natural frequency, the amplitude and phase angle of each accelerometer were used to develop the mode shape. Figure 2.17 shows a longitudinal section and a transverse section at the midspan of the mode shape produced by the first natural frequency of Bridge SM-5. Figure 6.35 shows a longitudinal section and a transverse section at the midspan of the mode shape produced by the second natural frequency of the bridge. Figure 6.36 shows a longitudinal section and a transverse section at the midspan of the mode shape produced by the third natural frequency of the bridge.

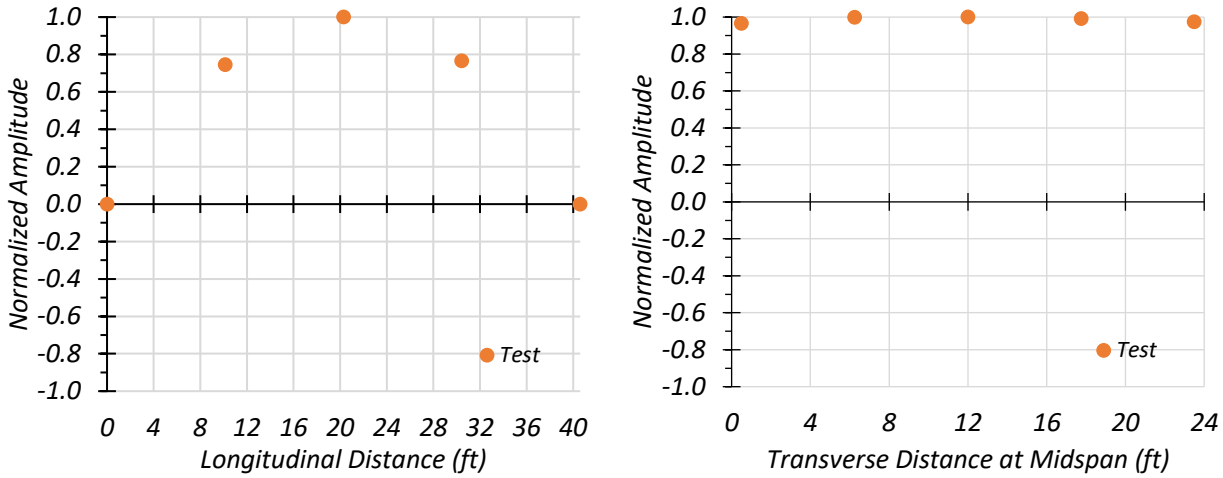

(a) Longitudinal Section *(b) Transverse Section*

Figure 6.34. First Mode Shape of Bridge SM-5 (f_1 = 7.57 Hz)

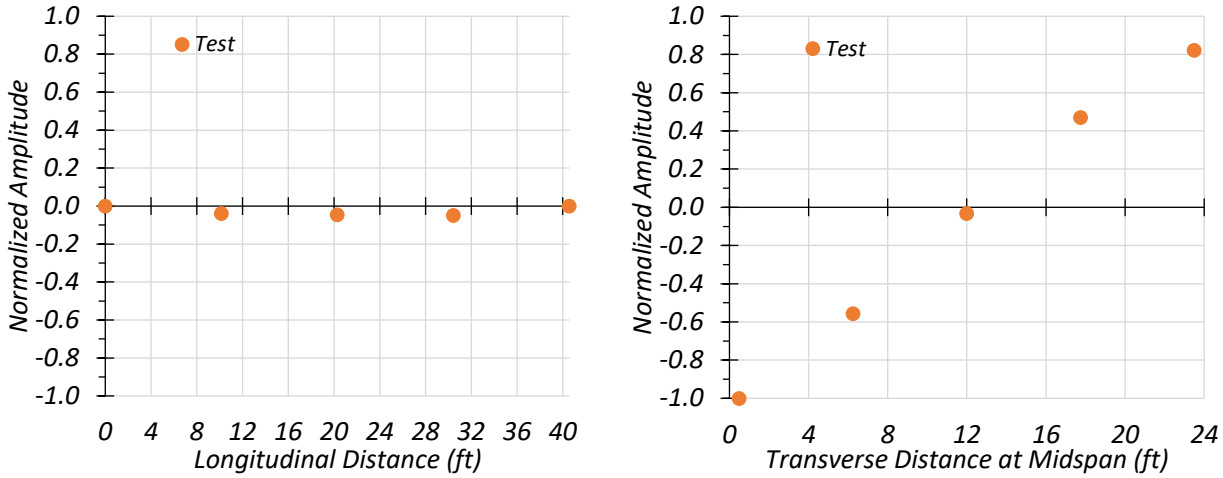

(a) Longitudinal Section *(b) Transverse Section*

Figure 6.35. Second Mode Shape of Bridge SM-5 (f_2 = 9.03 Hz)

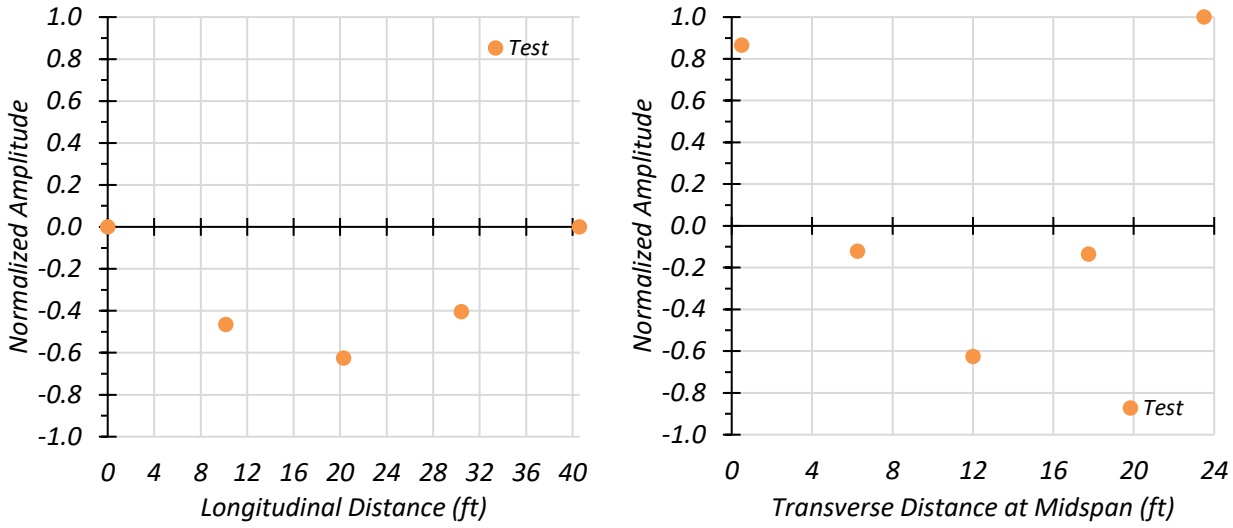

(a) Longitudinal Section *(b) Transverse Section*

Figure 6.36. Third Mode Shape of Bridge SM-5 (f_3 = 17.58 Hz)

6.6.3 Computer Vision

During testing, a video camera was set up on a tripod on the side of the bridge near exterior Girder G13. The camera had a frame size of 1280 pixels by 720 pixels and a sampling frequency of 30 Hz. It was placed near the midspan of the bridge so that the girders were perpendicular to the camera's line of sight. Each load test was recorded, and computer vision was used on each Path 1 load test to measure the deflection experienced in Girder G13.

The computer vision algorithm compares the sub-window of the initial frame in the video to the same sub-window in the following frames of the video. The user selects the pixel width and height of this initial sub-window. The user also defines a reference distance that the algorithm corresponds to a number of pixels. The algorithm then finds the location of the displaced sub-window in the frames following the initial frame. The algorithm finds the minimum sum of the squared difference between the location of the first sub-window and the location of the subsequent sub-window, thereby calculating the displacement of the objects in the original sub-window. A lowpass Butterworth filter was used to smooth the deflection signal output by the program. For all load cases, a 25 pixel by 25 pixel sub-window was used for computer vision.

The results from the computer vision were compared with the deflections recorded by the string potentiometer on Girder G13. For Bridge SM-5, computer vision was performed on three of the six Path 1 tests. The three tests for which computer vision were performed include (1) Test 1—

Path 1—static with the engine running, (2) Test 3—Path 1—crawl at 5 mph, and (3) Test 7—Path 1—dynamic at 23 mph.

Figure 6.37 shows the deflection over time using computer vision and the deflection measured with the Girder G13 string potentiometer for the Path 1 static load test with the engine running. The cutoff frequency used for filtering was 0.75 Hz. The maximum deflection given by the string potentiometer is 0.307 in., while the maximum deflection given by computer vision is 0.248 in. Computer vision underestimated the deflection value by 0.059 in. and differed from the string potentiometer by 21.3 percent.

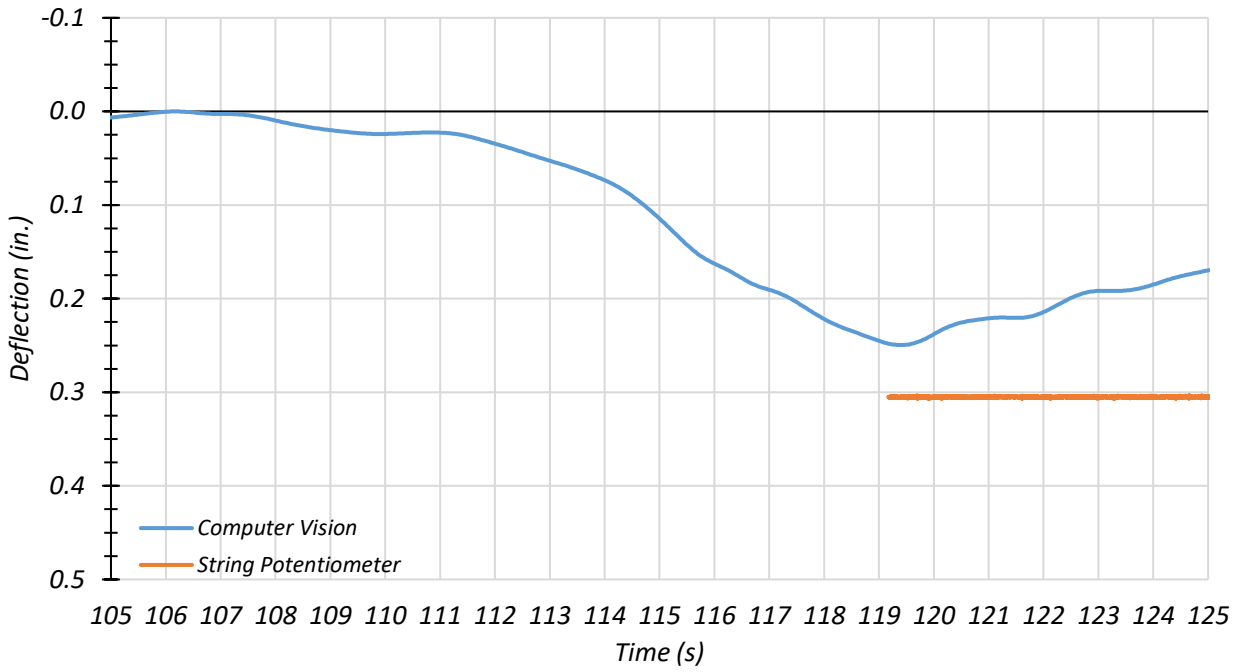

Figure 6.37. Girder G13 Midspan Deflections for Path 1—Static with Engine Running Test

Figure 6.38 shows the deflection over time using computer vision and the Girder G13 string potentiometer for the Path 1 crawl speed test at 5 mph. The cutoff frequency used for filtering was 0.75 Hz. The maximum deflection given by the string potentiometer is 0.299 in., while the maximum deflection given by computer vision is 0.298 in. Computer vision underestimated the deflection value by 0.001 in. and differed from the string potentiometer by 0.3 percent. Computer vision matched the string potentiometer measurements very well for this load test.

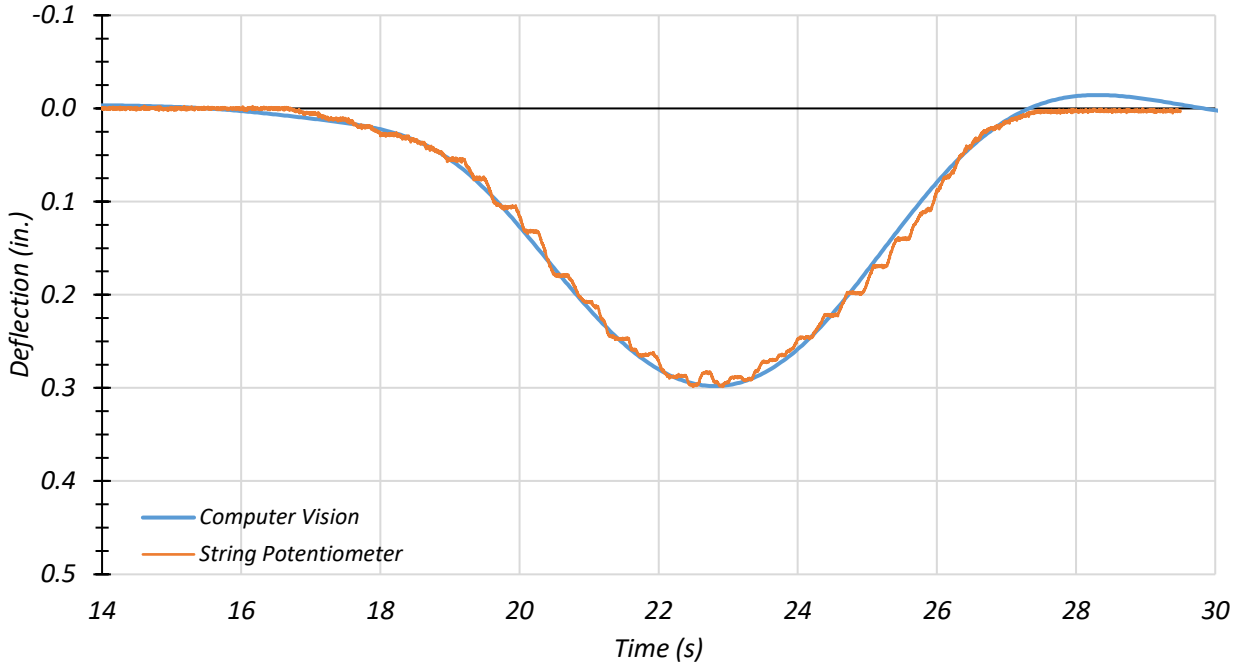

Figure 6.38. Girder G13 Midspan Deflections for Path 1—Crawl Speed Test at 5 mph

Figure 6.39 shows the deflection over time using computer vision and the Girder G13 string potentiometer for the Path 1 dynamic test at 23 mph. The cutoff frequency used for filtering was 1.5 Hz. The maximum deflection given by the string potentiometer is 0.288 in., while the maximum deflection given by computer vision is 0.265 in. Computer vision underestimated the deflection value by 0.023 in. and differed from the string potentiometer by 8.3 percent. Computer vision matched the string potentiometer reasonably well for this test.

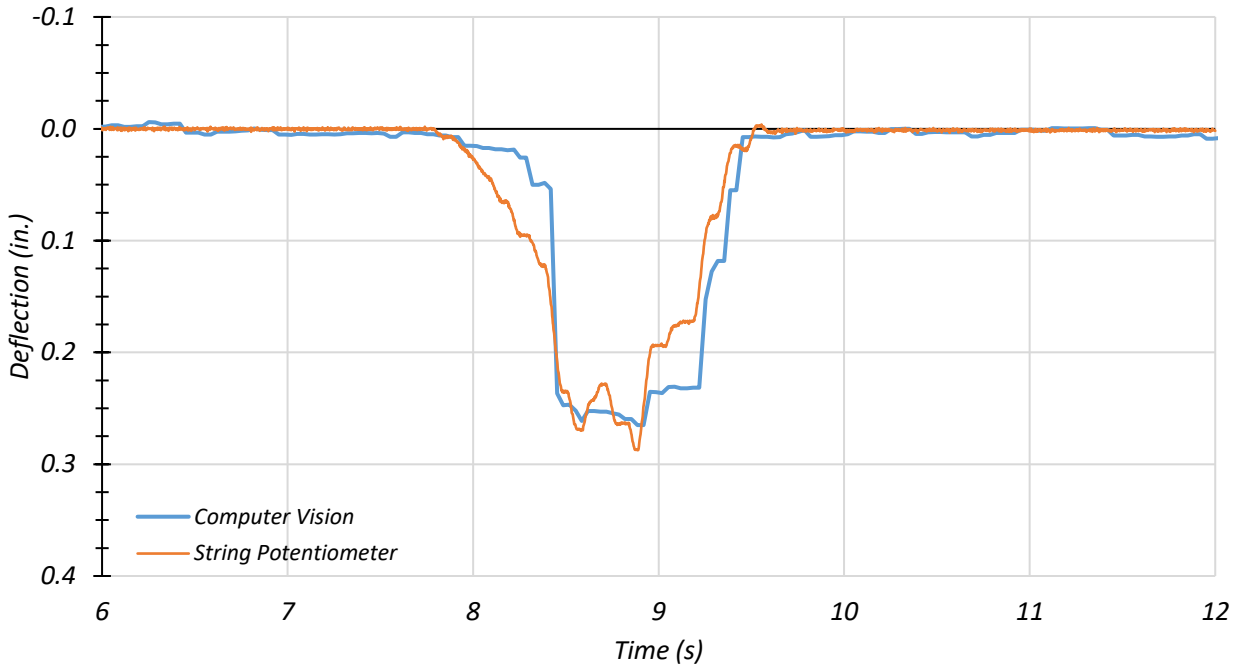

Figure 6.39. Girder G13 Midspan Deflections for Path 1—Dynamic Test at 23 mph

The testing of Bridge SM-5 indicated that computer vision has the potential to be used to provide deflections during bridge load testing without the need for targets. It could be used to confirm that a bridge is behaving compositely when estimated composite and non-composite deflections are known. For future bridge tests in this report, computer vision is used along with the other methods. The process of using computer vision was improved based on the lessons learned from the first test, such as camera resolution and camera placement.

6.7 FEM MODEL UPDATING AND CALIBRATION

6.7.1 General

Following the load testing, the original FEM model developed for SM-5 was modified to evaluate appropriate modeling parameters based on a comparison to the test results. The models are described first and then compared to the corresponding field measurements in Section 6.6.

*6.7.1.1 **Modulus of Elasticity***

Before the FEM model was updated, a sensitivity study was performed to understand the effect of changes in the MOE of concrete on the model analysis. Table 6.13 shows the effect of changing

the MOE value on the modal frequencies of the bridge and the midspan deflection, West End curvature, and East End curvature of the girders. Figure 6.40 shows this change for each output parameter graphically. Of note, the original MOE value used during Task 4 of this project was 2850 ksi, corresponding to concrete with an f_c' of 2.5 ksi, which is closest to the MOE value of 3000 examined in the sensitivity study. The MOE determined from NDE field measurements was 4836 ksi, corresponding to concrete with an f_c' of 7.2 ksi, which is closest to the MOE value of 5000 examined in the sensitivity study.

Table 6.13. Effect of Modulus of Elasticity Value on Selected FEM Results

MOE (ksi)	Modal Frequency (Hz)		Midspan Deflection (in.)		West End Curvature		East End Curvature	
	1st Mode	2nd Mode	G7	G13	G7	G13	G7	G13
3000	11.83	12.31	0.064	0.107	7.02E-06	1.14E-05	7.72E-06	1.27E-05
4000	12.23	12.82	0.059	0.099	6.64E-06	1.10E-05	7.37E-06	1.24E-05
5000	12.51	13.22	0.055	0.094	6.34E-06	1.07E-05	7.09E-06	1.21E-05
6000	12.74	13.55	0.052	0.09	6.14E-06	1.05E-05	6.89E-06	1.18E-05

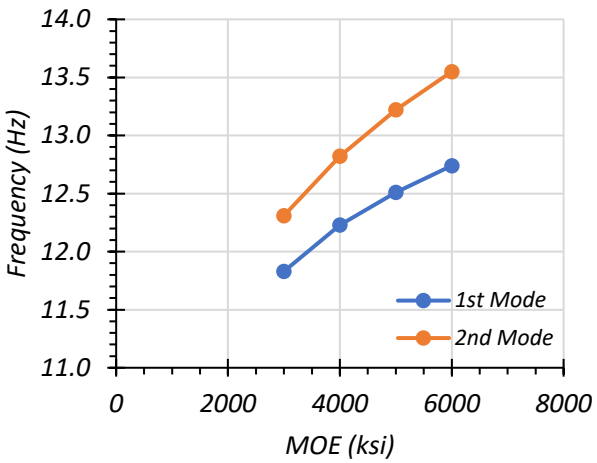

(a) Effect on Modal Frequency

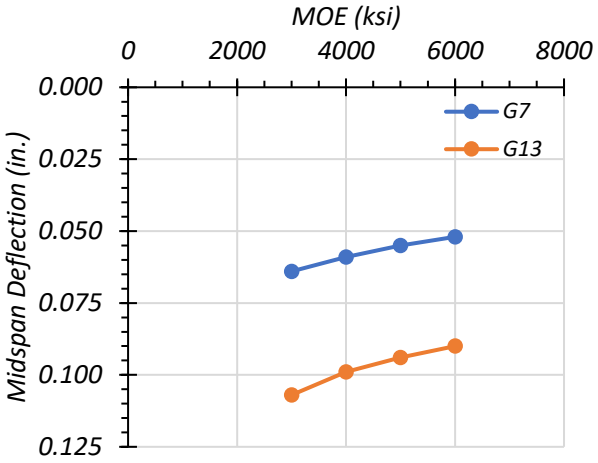

(b) Effect on Midspan Deflection

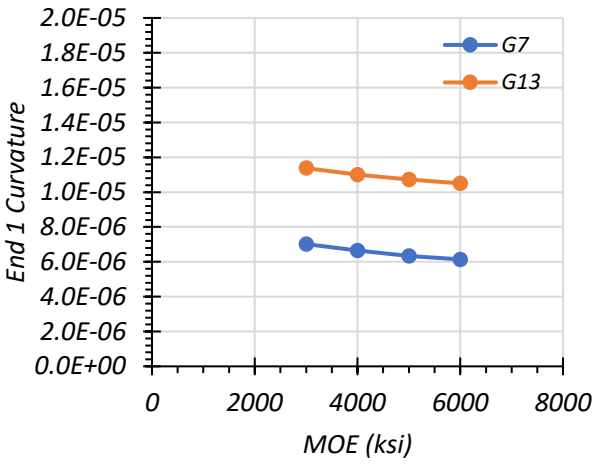

(c) Effect on West End Curvature

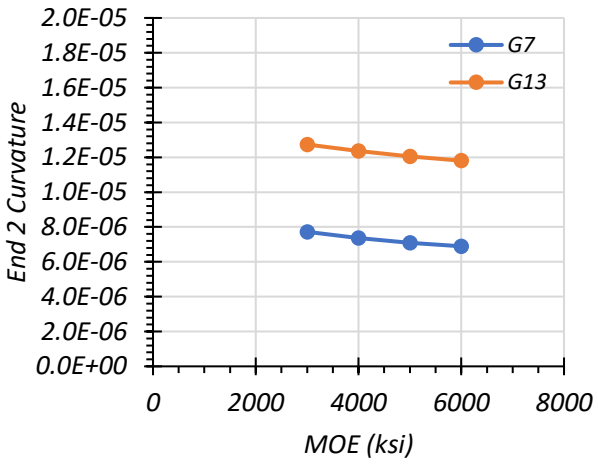

(d) Effect on East End Curvature

Figure 6.40. Effect of Modulus of Elasticity Value on Selected FEM Results

6.7.2 Updated FEM Models

Two updated FEM models were developed based on the original FEM model for Bridge SM-5. The original model was modified to reflect the updated dimensions and in situ concrete compressive strength discussed in Section 6.3. The two updated FEM models were (1) a model assuming no composite action between the steel girders and concrete deck, and (2) a model assuming fully composite action between the girders and deck. Both models assume roller boundary conditions at both ends of every girder, except for one end of a single girder that has a pinned support to resist any lateral forces.

The two updated models use the field-measured dimensions of the bridge, which includes changing the centerline to centerline of bearing span length from 40 ft 2 in. given in the inspection reports to 40 ft 7 in. measured in the field. These models also use the minimum f_c' of 7.2 ksi found using the NDE tests described in Subsection 6.3.2. This measurement is an increase in f_c' from the 2.5 ksi used in load rating calculations that are based on the age of the bridge when the concrete deck strength is unknown (TxDOT 2018a). The increase in f_c' corresponds to an increase in computed concrete MOE from 2850 ksi to 4836 ksi. Table 6.14 shows the results from the fully composite and fully non-composite simply supported FEM models with updated geometric and material properties, along with selected field-test results. It can be seen that the test results tend to be closer to the fully composite updated FEM model. The modal frequencies and midspan deflections are closer to the composite case but can be matched more closely. Some end restraint was observed during field testing as well, which is not accounted for in the updated FEM models. It is important to note that TxDOT currently assumes fully non-composite action when load rating Bridge SM-5 (TxDOT 2018a).

Table 6.14. Selected FEM Results for Updated FEM Models

Model	Modal Frequency (Hz)		Midspan Deflection (in.)		West End Curvature		East End Curvature	
	1st Mode	2nd Mode	G7	G13	G7	G13	G7	G13
Non-Composite	3.78	4.87	0.349	0.627	0.00E+00	0.00E+00	0.00E+00	0.00E+00
Composite	6.28	7.17	0.131	0.245	0.00E+00	0.00E+00	0.00E+00	0.00E+00
Field Test	7.57	9.03	0.145	0.307	1.50E-06	5.41E-06	3.01E-07	9.02E-07

6.7.3 Model Calibration Process

In addition to the two models discussed above, a third FEM model was developed for Bridge SM-5 that took into account the measured end fixity and composite action observed during testing. The goal of the development of this calibrated FEM model was to create a model that more closely represents the measured bridge response. The calibrated model also uses the updated geometric properties and concrete MOE described in the previous section.

With respect to support conditions, the vertical translational degree of freedom is fully restrained at all girder ends for the model since no bearing pads are present at the abutments. Partial

end fixity was created in the model by including horizontal springs at the nodes located at the bottom flange of each girder and at the deck nodes. Horizontal springs were also added between the bottom surface of the deck and the top girder flanges at each common node location to model partial composite action.

Based on the load tests, five main input parameters were identified in order to study their effect on the FEM results. These parameters were the interior girder end spring stiffness on the first abutment, the exterior girder end spring stiffness on the first abutment, the interior girder end spring stiffness on the second abutment, the exterior girder end spring stiffness on the second abutment, and the spring stiffness for partial composite action. Initially, the spring stiffness value required for each parameter was set as fully fixed, and the value required for the springs to be fully free were found. Next, each individual parameter was methodically changed while keeping all of the other parameters the same in order to see the effect of that parameter on the FEM results. Based on this parametric study, a spring stiffness value was chosen for each input parameter to begin the process of refining the final calibrated model.

6.7.4 Calibrated FEM Model Results

6.7.4.1 ***West End Interior Girder Stiffness Spring***

The first parameter identified for calibration was the longitudinal support spring stiffness in translation for each interior girder at Abutment (End) 1.

Table 6.15 shows the effect of changing the West End interior girder spring stiffness value on the modal frequencies of the bridge, the midspan deflections of middle Girder G7 and exterior Girder G13, and the West End and East End curvatures of Girders G7 and G13. Figure 6.41 shows this change for each output parameter graphically. The Girder G13 results are obtained from the Path 1 stop location load test, Girder G7 results are obtained from the Middle Path stop location load test, and the test modal frequencies are obtained from the sledgehammer test at the midspan along the centerline of the bridge. For the West End interior girder stiffness spring, the desired test result for matching is the Girder G7 West End curvature. Based on the sensitivity study, the spring stiffness value that most closely matches is 500 kip/in.

Table 6.15. Effect of West End Interior Girder Stiffness Value on Selected FEM Results

Stiffness Value (kip/in.)	Modal Frequency (Hz)		Midspan Deflection (in.)		West End Curvature (in^{-1})		East End Curvature (in^{-1})	
	1st Mode	2nd Mode	G7	G13	G7	G13	G7	G13
0	10.71	12.67	0.069	0.098	4.01E-07	1.36E-05	7.92E-06	1.20E-05
500	11.33	12.96	0.063	0.094	**1.78E-06**	1.26E-05	7.45E-06	1.17E-05
5000	12.78	13.76	0.052	0.085	4.64E-06	1.04E-05	6.57E-06	1.08E-05
10,000	13.09	13.96	0.050	0.083	5.14E-06	9.90E-06	6.39E-06	1.07E-05
20,000	13.28	14.09	0.049	0.082	5.44E-06	9.58E-06	6.29E-06	1.06E-05
40,000	13.39	14.17	0.048	0.081	5.62E-06	9.43E-06	6.24E-06	1.05E-05
Test	7.57	9.03	0.145	0.307	**1.50E-06**	5.41E-06	3.01E-07	9.02E-07

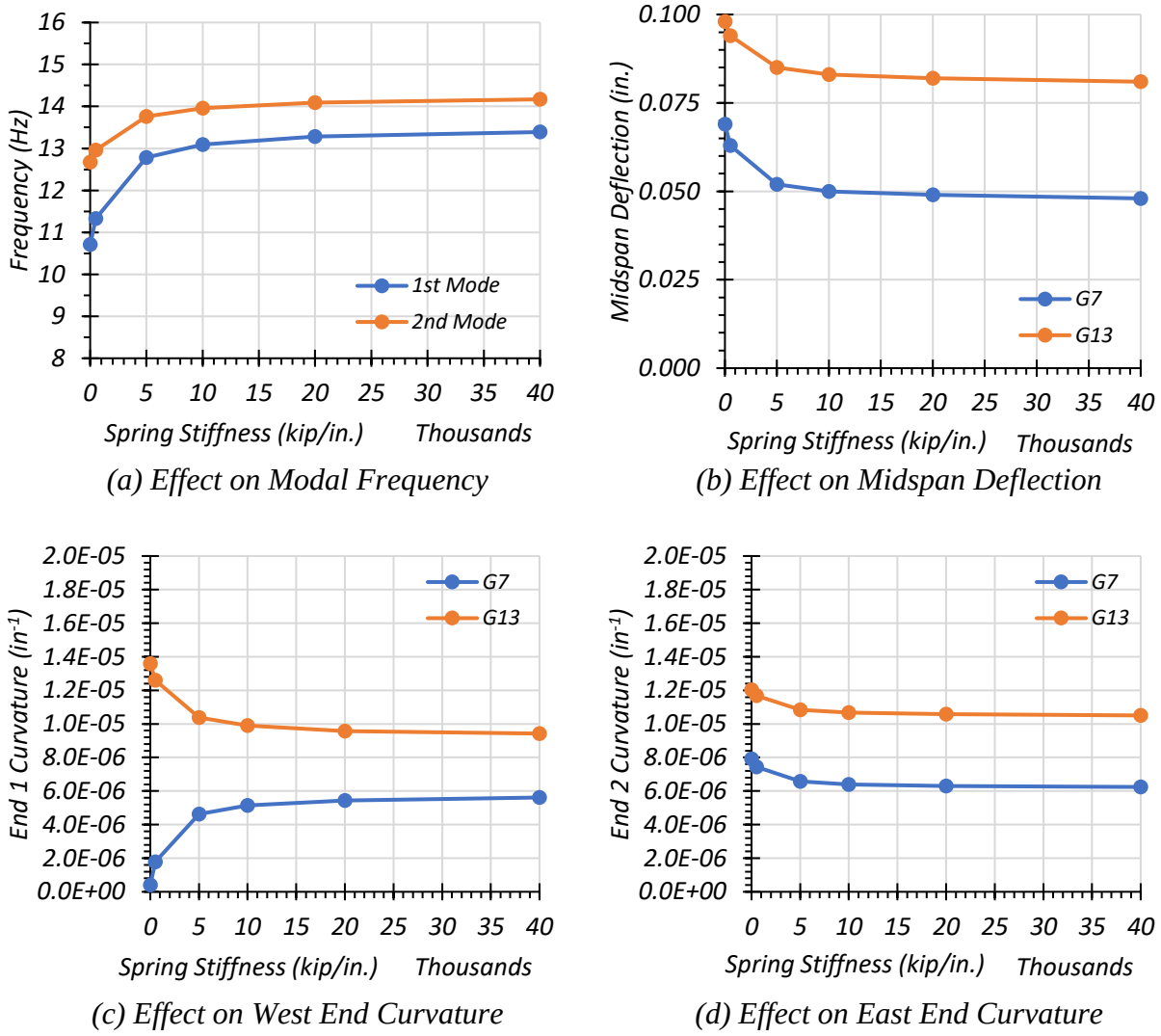

(a) Effect on Modal Frequency

(b) Effect on Midspan Deflection

(c) Effect on West End Curvature

(d) Effect on East End Curvature

Figure 6.41. Effect of West End Interior Girder Stiffness Value on Selected FEM Results

*6.7.4.2 **West End Exterior Girder Stiffness Spring***

The second parameter identified for calibration is the longitudinal support spring stiffness in translation for an exterior girder at West End. Table 6.16 shows the effect of changing the West End exterior girder spring stiffness value on the modal frequencies of the bridge, the midspan deflections of middle Girder G7 and exterior Girder G13, and the West End and East End curvatures of Girders G7 and G13. Figure 6.42 shows this change for each output parameter graphically. The Girder G13 results are obtained from the Path 1 stop location load test, Girder G7 results are obtained from the Middle Path stop location load test, and the test modal frequencies are obtained from the sledgehammer test at the midspan along the centerline of the bridge. For the

West End exterior girder stiffness spring, the desired test results to match were for the Girder G13 West End curvature. Based on the sensitivity study, the spring stiffness value providing the best match is 2500 kip/in.

Table 6.16. Effect of West End Exterior Girder Stiffness Value on Selected FEM Results

Stiffness Value (kip/in.)	Modal Frequency (Hz)		Midspan Deflection (in.)		West End Curvature (in^{-1})		East End Curvature (in^{-1})	
	1st Mode	2nd Mode	G7	G13	G7	G13	G7	G13
0	13.08	13.40	0.048	0.090	5.62E-06	8.27E-07	6.24E-06	1.14E-05
2500	13.25	13.80	0.049	0.085	5.62E-06	**5.89E-06**	6.24E-06	1.08E-05
3000	13.26	13.83	0.049	0.085	5.62E-06	6.27E-06	6.24E-06	1.08E-05
5000	13.30	13.94	0.049	0.084	5.62E-06	7.22E-06	6.24E-06	1.07E-05
10,000	13.35	14.05	0.048	0.083	5.62E-06	8.27E-06	6.24E-06	1.06E-05
20,000	13.38	14.12	0.048	0.082	5.62E-06	9.00E-06	6.24E-06	1.05E-05
40,000	13.39	14.17	0.048	0.081	5.62E-06	9.43E-06	6.24E-06	1.05E-05
Test	7.57	9.03	0.145	0.307	1.50E-06	**5.41E-06**	3.01E-07	9.02E-07

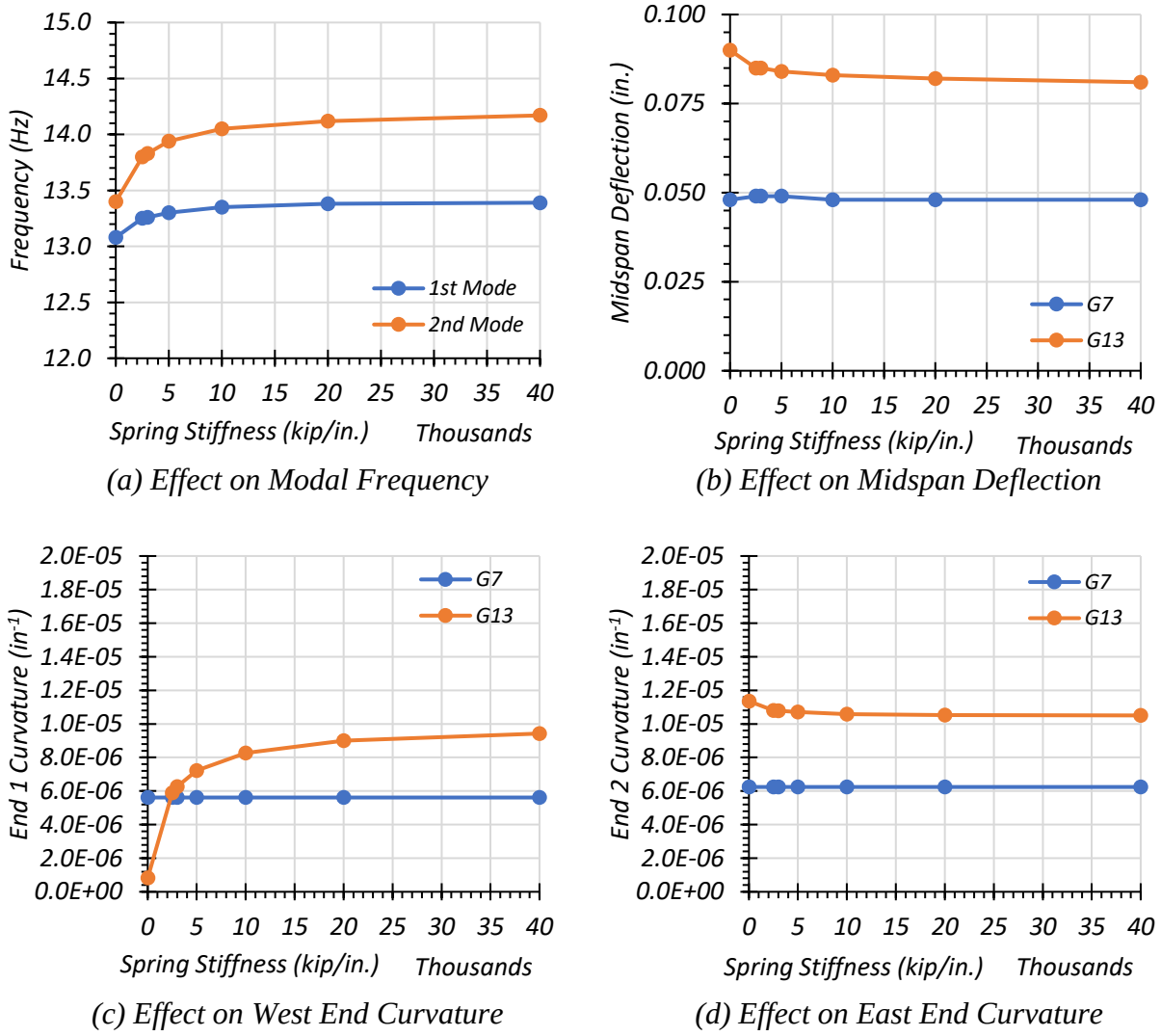

(a) Effect on Modal Frequency

(b) Effect on Midspan Deflection

(c) Effect on West End Curvature

(d) Effect on East End Curvature

Figure 6.42. Effect of West End Exterior Girder Stiffness Value on Selected FEM Results

6.7.4.3 East End Interior Girder Stiffness Spring

The third parameter identified for calibration was the longitudinal support spring stiffness in translation for an interior girder at East End. Table 6.17 shows the effect of changing the East End interior girder spring stiffness value on the modal frequencies of the bridge, the midspan deflection, and the West End and East End curvatures of the girders. Figure 6.43 shows this change for each output parameter graphically. The Girder G13 results are obtained from the Path 1 stop location load test, Girder G7 results are obtained from the Middle Path stop location load test, and the test modal frequencies are obtained from the sledgehammer test at the midspan along the centerline of the bridge. For the East End interior girder stiffness spring, the desired test results to

match were for the Girder G7 East End curvature. Based on the sensitivity study, the spring stiffness value providing the closest match is 0 kip/in. Since this result corresponds to a fully free spring condition, only two iterations of the sensitivity study were performed.

Table 6.17. Effect of East End Interior Girder Stiffness Value on Selected FEM Results

Stiffness Value (kip/in.)	Modal Frequency (Hz)		Midspan Deflection (in.)		West End Curvature (in^{-1})		East End Curvature (in^{-1})	
	1st Mode	2nd Mode	G7	G13	G7	G13	G7	G13
0	10.71	12.67	0.072	0.101	7.55E-06	1.12E-05	**5.26E-07**	1.53E-05
40,000	13.39	14.17	0.048	0.081	5.62E-06	9.43E-06	6.24E-06	1.05E-05
Test	7.57	9.03	0.145	0.307	1.50E-06	5.41E-06	**3.01E-07**	9.02E-07

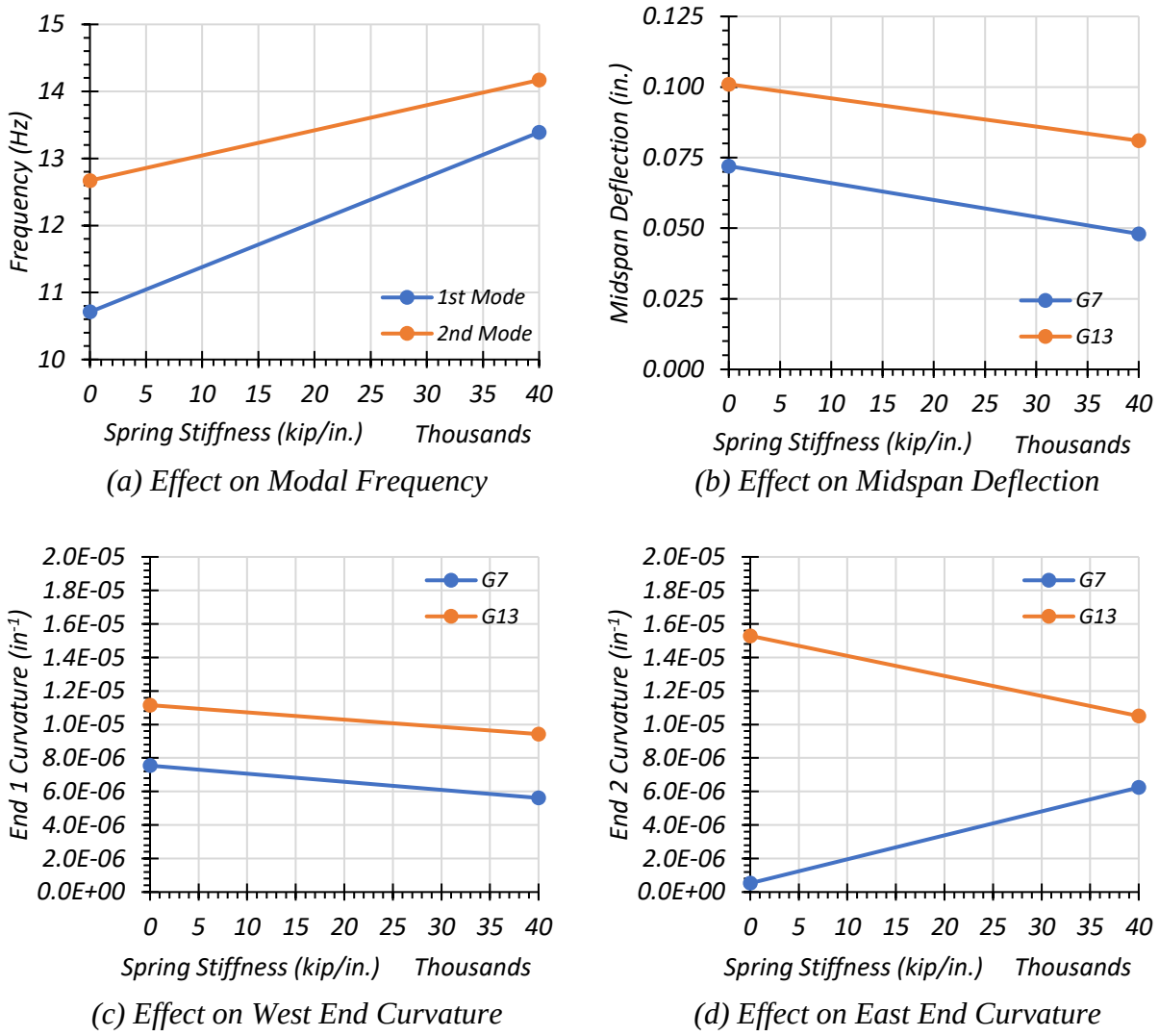

(a) Effect on Modal Frequency

(b) Effect on Midspan Deflection

(c) Effect on West End Curvature

(d) Effect on East End Curvature

Figure 6.43. Effect of East End Interior Girder Stiffness Value on Selected FEM Results

6.7.4.4 East End Exterior Girder Stiffness Spring

The fourth parameter identified for calibration was the longitudinal support spring stiffness in translation for an exterior girder at East End. Table 6.18 shows the effect of changing the East End exterior girder spring stiffness value on the modal frequencies of the bridge, the midspan deflection, and the West End and East End curvatures of the girders. Figure 6.44 shows this change for each output parameter graphically. The Girder G13 results are obtained from the Path 1 stop location load test, GG7 results are obtained from the Middle Path stop location load test, and the test modal frequencies are obtained from the sledgehammer test at the midspan along the centerline of the bridge. For the East End exterior girder stiffness spring, the desired test results to match

were for the Girder G13 East End curvature. Based on the sensitivity study, the spring stiffness value providing the closest match is 0 kip/in.

Table 6.18. Effect of East End Exterior Girder Stiffness Value on Selected FEM Results

Stiffness Value (kip/in.)	Modal Frequency (Hz)		Midspan Deflection (in.)		West End Curvature (in^{-1})		East End Curvature (in^{-1})	
	1st Mode	2nd Mode	G7	G13	G7	G13	G7	G13
0	13.08	13.40	0.048	0.091	5.54E-06	1.02E-05	6.09E-06	**1.43E-06**
100	13.09	13.43	0.048	0.091	5.62E-06	1.01E-05	6.24E-06	2.41E-06
500	13.14	13.53	0.048	0.089	5.62E-06	1.00E-05	6.24E-06	3.46E-06
5000	13.30	13.94	0.048	0.084	5.62E-06	9.63E-06	6.24E-06	8.00E-06
10,000	13.35	14.05	0.048	0.083	5.62E-06	9.53E-06	6.24E-06	9.22E-06
20,000	13.38	14.12	0.048	0.082	5.62E-06	9.45E-06	6.24E-06	1.00E-05
40,000	13.39	14.17	0.048	0.081	5.62E-06	9.43E-06	6.24E-06	1.05E-05
Test	7.57	9.03	0.145	0.307	1.50E-06	5.41E-06	3.01E-07	**9.02E-07**

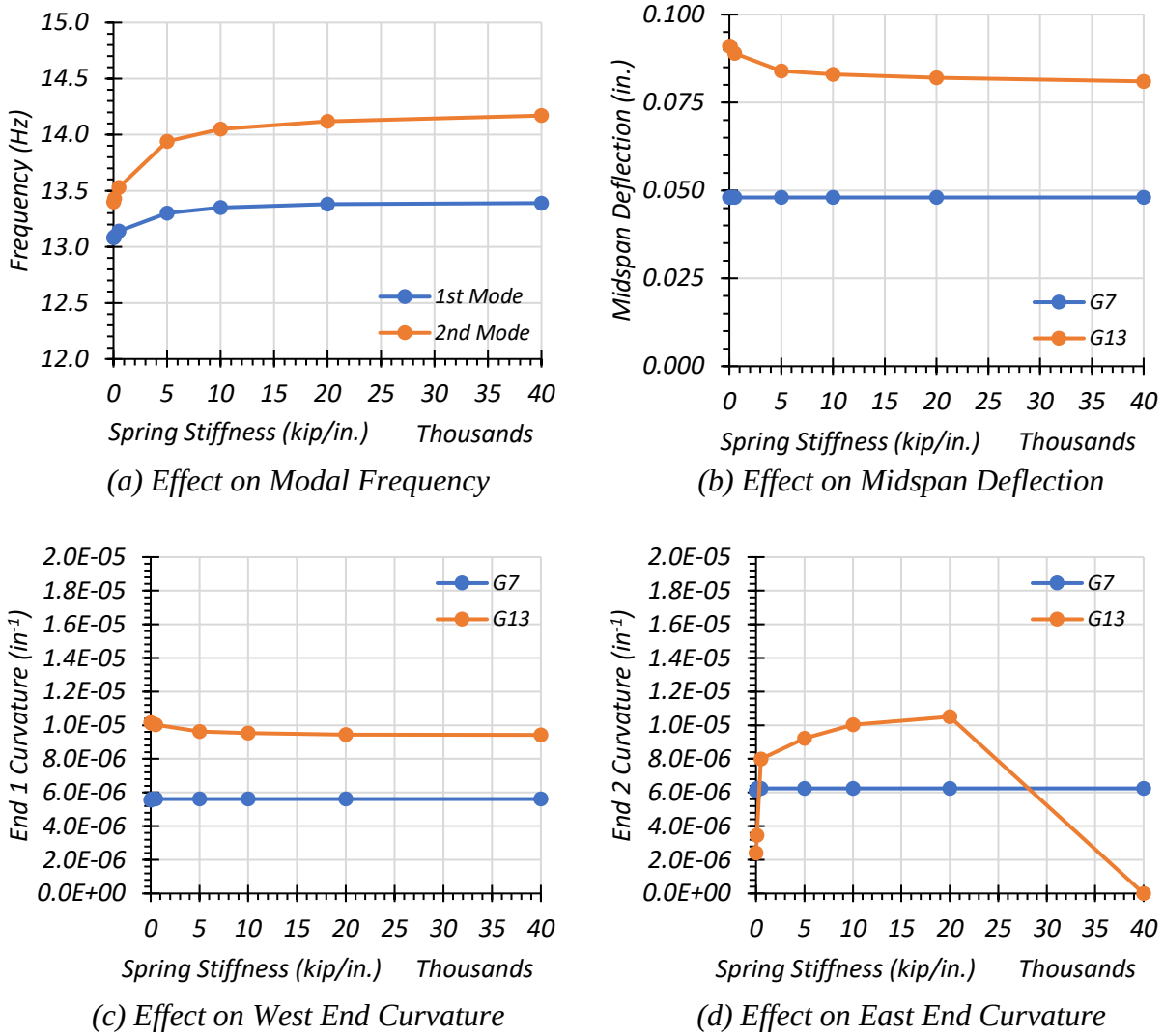

(a) Effect on Modal Frequency

(b) Effect on Midspan Deflection

(c) Effect on West End Curvature

(d) Effect on East End Curvature

Figure 6.44. Effect of East End Exterior Girder Stiffness Value on Selected FEM Results

6.7.4.5 ***Composite Spring Stiffness***

The fifth parameter identified for calibration was the composite spring stiffness between the deck and the girders. Table 6.19 shows the effect of changing the composite spring stiffness value on the modal frequencies of the bridge, the midspan deflection, the West End curvature, and the East End curvature of the girders. Figure 6.45 shows this change for each output parameter graphically. The Girder G13 results are obtained from the Path 1 stop location load test, Girder G7 results are obtained from the Middle Path stop location load test, and the test modal frequencies are obtained from the sledgehammer test at the midspan along the centerline of the bridge.

It is important to note that before performing the composite spring sensitivity analysis, stiffness values were chosen for the springs at the ends of the girders. These values were selected based on the results of the sensitivity study that most closely matched the test results. These values were 500 kip/in. for the West End interior girders, 3000 kip/in. for the West End exterior girders, 0 kip/in. for the East End interior girders, and 100 kip/in. for the East End exterior girders. The reason 100 kip/in. was chosen for the East End exterior girders was to provide a close match to the bottom flange strain measured in the girder. These values were all kept constant while performing the composite spring sensitivity analysis. Of note, a partial composite spring stiffness value of zero would be fully non-composite (10 was used because modal results cannot be obtained when the stiffness value is zero). Full composite is represented by an infinite spring stiffness.

Table 6.19. Effect of Composite Spring Stiffness Value on Selected FEM Results

Stiffness Value (kip/in.)	Modal Frequency (Hz)		Midspan Deflection (in.)		West End Curvature (in^{-1})		East End Curvature (in^{-1})	
	1st Mode	2nd Mode	G7	G13	G7	G13	G7	G13
10	5.07	6.65	0.154	0.274	9.12E-06	2.42E-05	4.54E-06	9.88E-06
100	6.77	7.86	0.148	0.264	8.00E-06	2.21E-05	4.24E-06	9.35E-06
250	6.93	8.09	0.141	0.251	7.32E-06	2.08E-05	3.76E-06	8.47E-06
500	7.14	8.31	0.134	0.237	6.62E-06	1.91E-05	3.21E-06	7.34E-06
1000	7.41	8.60	0.125	0.219	5.19E-06	1.72E-05	2.01E-06	5.89E-06
2500	7.78	9.01	0.115	0.197	4.46E-06	1.51E-05	1.73E-06	4.44E-06
7500	8.12	9.38	0.106	0.180	3.58E-06	1.35E-05	1.15E-06	3.36E-06
15,000	8.24	9.52	0.103	0.174	3.16E-06	1.29E-05	7.77E-07	2.96E-06
30,000	8.31	9.60	0.102	0.171	3.13E-06	1.26E-05	9.02E-07	2.91E-06
Infinite	8.39	9.70	0.100	0.167	2.98E-06	1.23E-05	8.77E-07	2.48E-06
Test	7.57	9.03	0.145	0.307	1.50E-06	5.41E-06	3.01E-07	9.02E-07

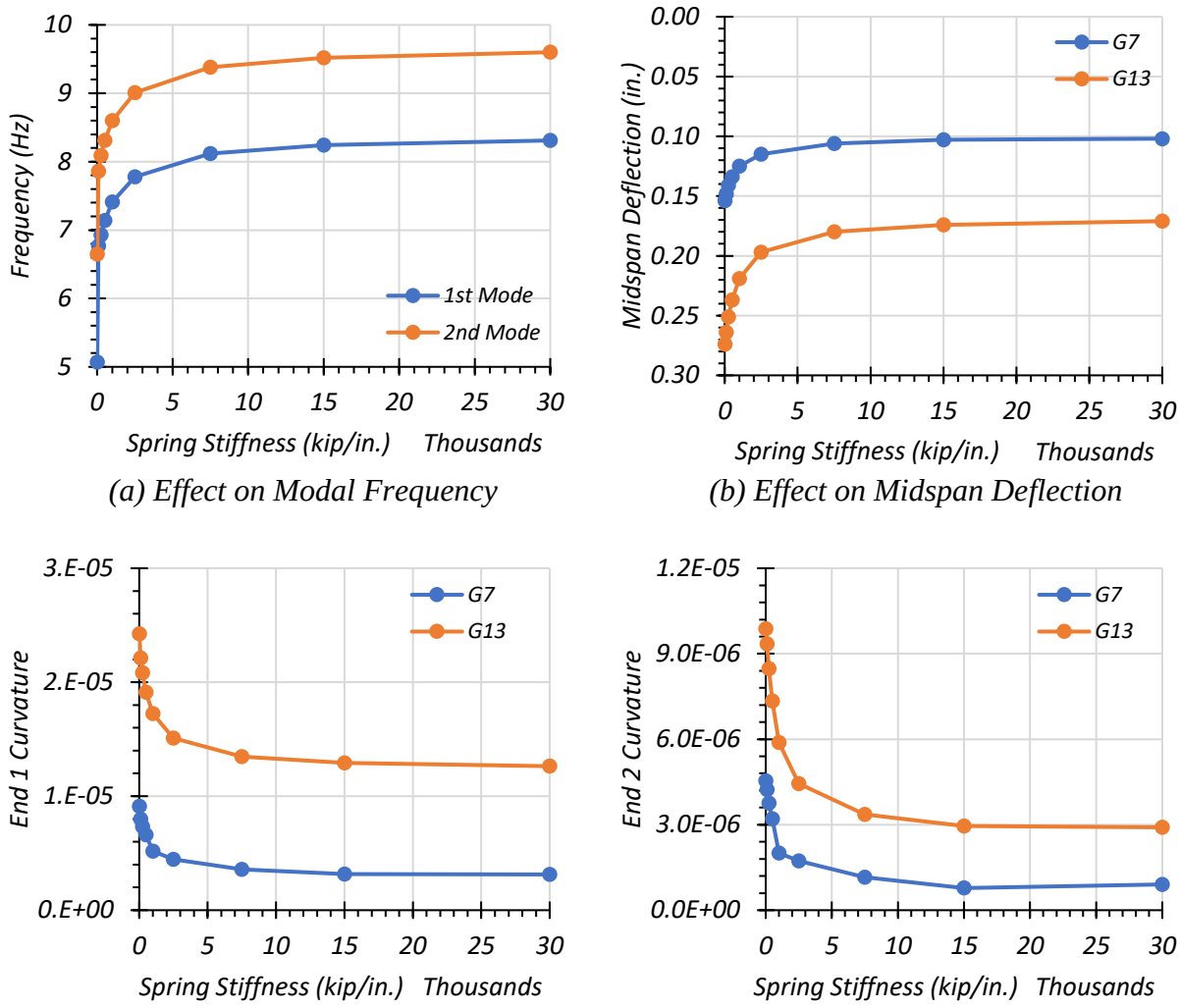

(a) Effect on Modal Frequency

(b) Effect on Midspan Deflection

(c) Effect on West End Curvature

(d) Effect on East End Curvature

Figure 6.45. Effect of Composite Spring Stiffness Value on Selected FEM Results

*6.7.4.6 **Final Calibration***

Based on the results of the individual sensitivity studies, values were selected for each parameter to begin the final model calibration. In the refinement of the final calibrated model, each input parameter was slightly adjusted in order to get as close as possible to representing the test results. During the refinement process, a small amount of horizontal stiffness in the transverse direction at the bearing supports was added to the springs to achieve a closer match with the test results. The longitudinal stiffness of the springs attached to the deck nodes was also reduced to half of that attached to the bottom flange nodes for the same reason, and this could help if there is more

restraint in the bottom of the girders than in the deck for the in situ bridge. Table 6.20 shows the selected spring stiffness values for all parameters in the final calibrated Bridge SM-5 model.

Table 6.20. Selected Spring Stiffness Parameters for Bridge SM-5 Calibration (kip/in.)

Partial Composite	West End Longitudinal Bottom		East End Longitudinal Bottom		West End Transverse		East End Transverse		West End Longitudinal Top		East End Longitudinal Top	
	G7	G13	G7	G13	G7	G13	G7	G13	G7	G13	G7	G13
7500	500	1500	0	50	50	150	250	150	250	750	0	25

Figure 6.46 shows the calibrated model with the end fixity springs and the horizontal deck partial composite springs. Table 6.21 shows the output for selected major parameters for the calibrated FEM model and for the field tests performed on Bridge SM-5. It is important to note that the Girder G13 results come from the Path 1 stop location load case and that the Girder G7 results come from the Middle Path stop location load case. This calibrated model was also used in comparison with the field-test results.

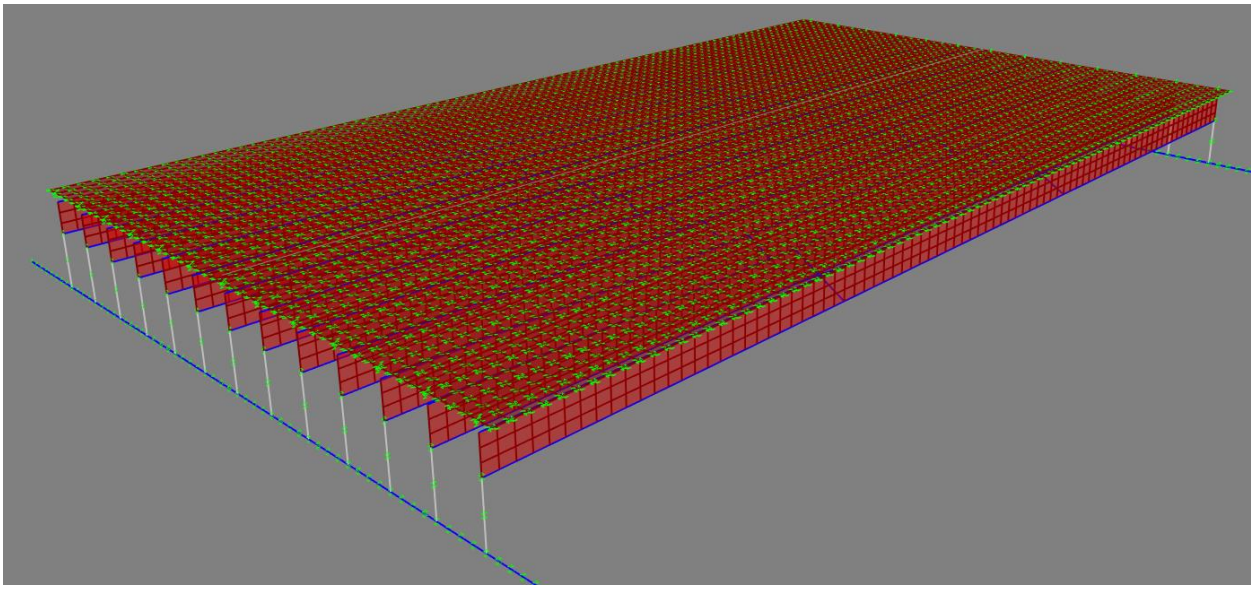

Figure 6.46. Calibrated FEM Model for Bridge SM-5

Table 6.21. Results of SM-5 Model Calibration

Analyzed Parameter	Calibrated FEM Output		Test Result		Updated FEM Composite with End Fixity Output	
	G7	G13	G7	G13	G7	G13
Midspan Deflection (in.)	0.148	0.271	0.145	0.307	0.127	0.230
West End Bottom Flange Strain (με)	−19.0	−64.1	−19.3	−66.2	−20.7	−68.6
East End Bottom Flange Strain (με)	−2.1	−10.7	−1.0	−11.4	−2.1	−10.0
West End Top Flange Strain (με)	1.4	7.2	1.4	8.3	1.2	4.5
East End Top Flange Strain (με)	0.0	0.0	3.1	1.0	0.0	0.0
Midspan Bottom Flange Strain (με)	88.6	156.6	102.1	162.1	85.3	151.9
First Modal Frequency (Hz)	6.54		7.57		7.03	
Second Modal Frequency (Hz)	7.78		9.03		7.48	

Because Bridge SM-5 was observed to be acting almost fully composite in the field, a final FEM model was created with the same support conditions as the calibrated model, but with fully fixed composite springs. This procedure was done to observe if a fully composite model with end fixity would also produce results comparable to the test data. These results are included in Table 6.21. It can be seen that while the end strains and midspan strains matched fairly well with the test results, the midspan deflections are further away from the test results than the calibrated model deflections. The Girder G13 deflection in the fully composite, end fixity model is 28.7 percent different than the test deflections. For this reason, the calibrated model with end fixity and slightly partial composite action was used from this point on.

6.7.5 Dynamic Characteristics of the Bridge

Data obtained from the accelerometers during dynamic tests and the sledgehammer tests were filtered, and an FFT analysis was performed, which allowed for determination of the first three natural frequencies of the bridge as 7.57 Hz, 9.03 Hz, and 17.58 Hz. For each natural frequency, the amplitude and phase angle of each accelerometer were used to develop the mode shape. These modes shapes obtained from testing were compared to the mode shapes obtained from the calibrated FEM model. Figure 6.47 shows a longitudinal section and a transverse section at the midspan of the mode shape produced by the first natural frequency of Bridge SM-5. Figure 6.48 shows a longitudinal section and a transverse section at the midspan of the mode shape produced

by the second natural frequency of the bridge. Figure 6.49 shows a longitudinal section and a transverse section at the midspan of the mode shape produced by the third natural frequency of the bridge. In some cases, the magnitudes of the mode shapes produced by the calibrated FEM model are slightly different from the test mode shapes. However, in general, the calibrated model does a reasonably good job of predicting the mode shape.

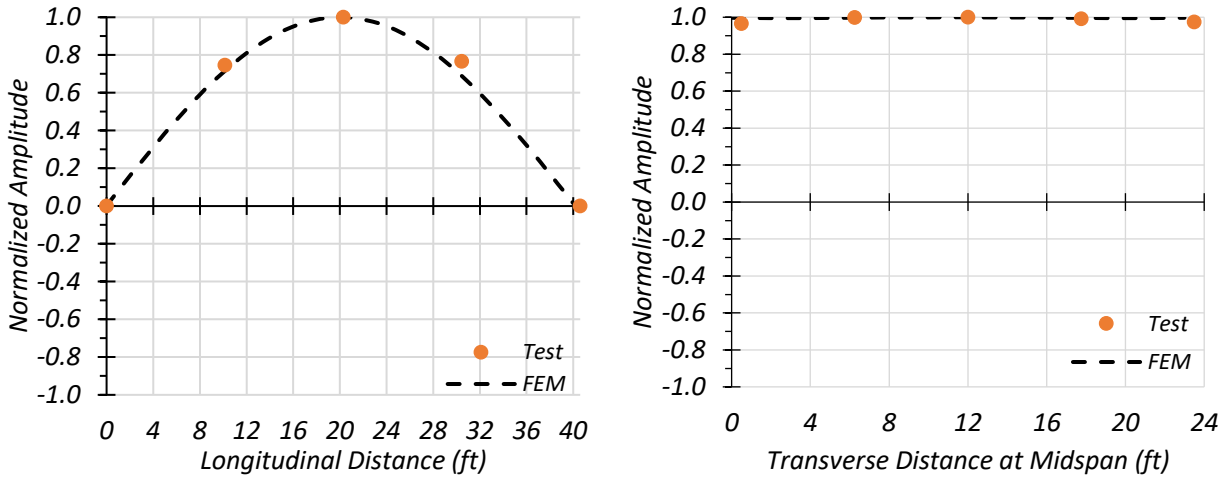

(a) Longitudinal Section *(b) Transverse Section*

Figure 6.47. Comparison of First Mode Shape of Bridge SM-5

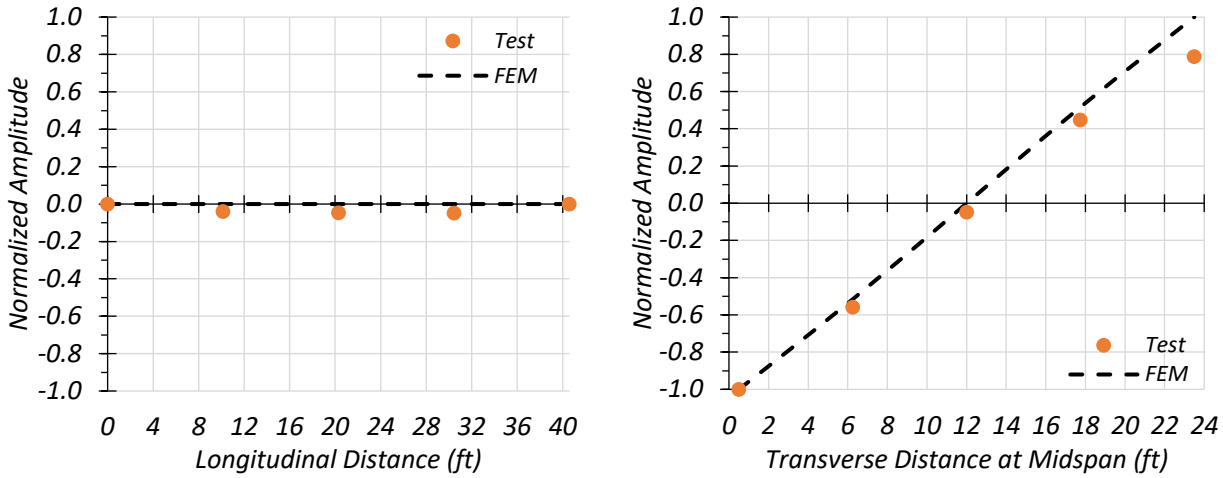

(a) Longitudinal Section *(b) Transverse Section*

Figure 6.48. Comparison of Second Mode Shape of Bridge SM-5

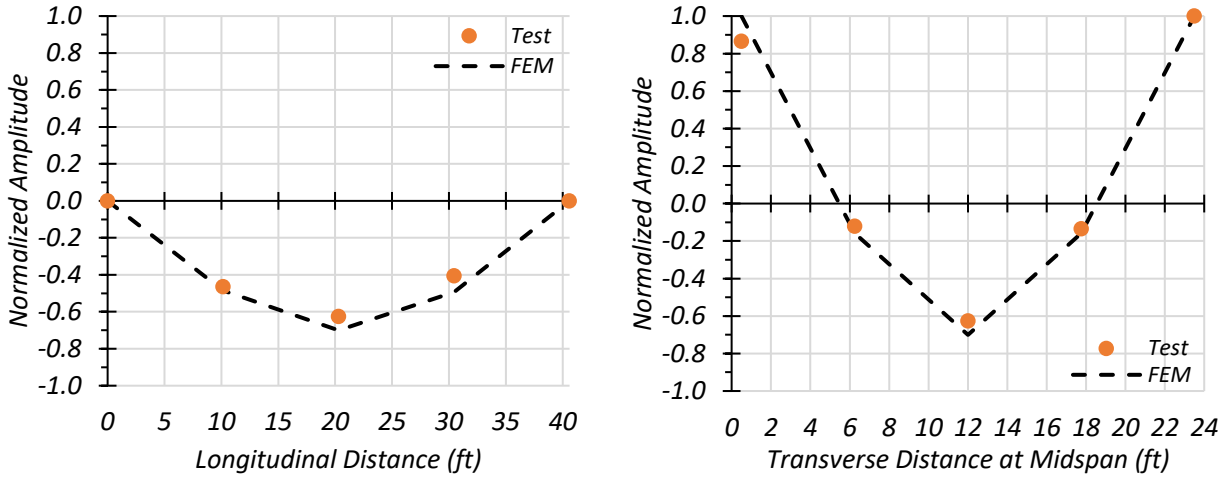

(a) Longitudinal Section *(b) Transverse Section*

Figure 6.49. Comparison of Third Mode Shape of Bridge SM-5

The natural frequencies of Bridge SM-5 observed during testing were compared to the natural frequencies produced by FEM. Table 6.22 shows the test and FEM natural frequencies. The frequencies observed during testing are much closer to those of the composite FEM bridge than those of the non-composite FEM bridge. They are also closer to the calibrated FEM model frequencies than to the updated composite FEM frequencies, but only slightly.

Table 6.22. Bridge SM-5 Test and FEM Natural Frequencies for First Two Mode Shapes

Frequency	Test (Hz)	Updated FEM Composite (Hz)	Updated FEM Non-Composite (Hz)	Calibrated FEM (Hz)
1st Natural Frequency	7.57	6.44	3.83	6.54
2nd Natural Frequency	9.03	7.45	5.10	7.78

6.8 COMPARISON OF TEST RESULTS AND FEM PREDICTIONS

6.8.1 Strain Measurements and Composite Action

Composite action can be determined by reviewing the strain diagrams over the section depth. Some information is available from the measured results to evaluate the composite behavior between the concrete deck and steel girders. A number of strain plots are provided in this section, in which the measured strain values are shown by a colored dot symbol. The colored line connecting two dot symbols represents the strain diagram at this cross section based on the assumption that plane sections remain plane. The dashed colored line represents the extrapolation of the observed strain diagram, assuming composite action, since it was observed that the deck and girder exhibited significant composite action. The black and gray dotted lines show the composite and non-composite strain diagrams obtained from the updated FEM models, and the purple dotted line shows the strain diagram obtained from the calibrated FEM model. The blue plot shows the strain results for the west end, the red plot shows the strain results for the east end, and the green plot shows the strain results for the midspan of the girder.

*6.8.1.1 **Interior Girder G7***

Figure 6.50 through Figure 6.52 provide plots of the measured strains for interior Girder G7 during static load testing and compare the midspan strain diagram to those diagrams obtained through the updated and calibrated FEM models. The strains measured for Girder G7 during the Path 1 static tests are shown in Figure 6.50 and compared with values obtained from the FEM updated and calibrated models. Figure 6.50(a) shows the maximum strains observed during the stop location test for Girder G7 at each end of the girder. Figure 6.50(b) shows the FEM comparison for the stop location test for Girder G7 at the midspan. Figure 6.50(c) shows the maximum strains observed

during the crawl speed test for Girder G7 at each end of the girder. Figure 6.50(d) shows the FEM comparison for the crawl speed test for Girder G7 at the midspan.

The strains measured for Girder G7 during the Path 2 static tests are shown in Figure 6.51 and compared with values obtained from the FEM updated and calibrated models. Figure 6.51(a) shows the maximum strains observed during the stop location test for Girder G7 at each end of the girder. Figure 6.51(b) shows the FEM comparison for the stop location test for Girder G7 at the midspan. Figure 6.51(c) shows the maximum strains observed during the crawl speed test for Girder G7 at each end of the girder. Figure 6.51(d) shows the FEM comparison for the crawl speed test for Girder G7 at the midspan.

The strains measured for Girder G7 during the Middle Path static tests are shown in Figure 6.52 and compared with values obtained from the FEM updated and calibrated models. Figure 6.52(a) shows the maximum strains observed during the stop location test for Girder G7 at each end of the girder. Figure 6.52(b) shows the FEM comparison for the stop location test for Girder G7 at the midspan. Figure 6.52(c) shows the maximum strains observed during the crawl speed test for Girder G7 at each end of the girder. Figure 6.52(d) shows the FEM comparison for the crawl speed test for Girder G7 at the midspan.

Both the calibrated FEM model and the updated fully composite FEM model strain diagrams at the midspan compare well with the midspan strain diagram observed during testing. Either model would likely be a good candidate to use to conduct a load rating analysis. The updated fully composite FEM model tends to be slightly closer to the test value when looking at bottom flange strain; however, it is also important to note that the calibrated FEM model takes into account the fixity at the ends of the girders, and the updated fully composite FEM model does not.

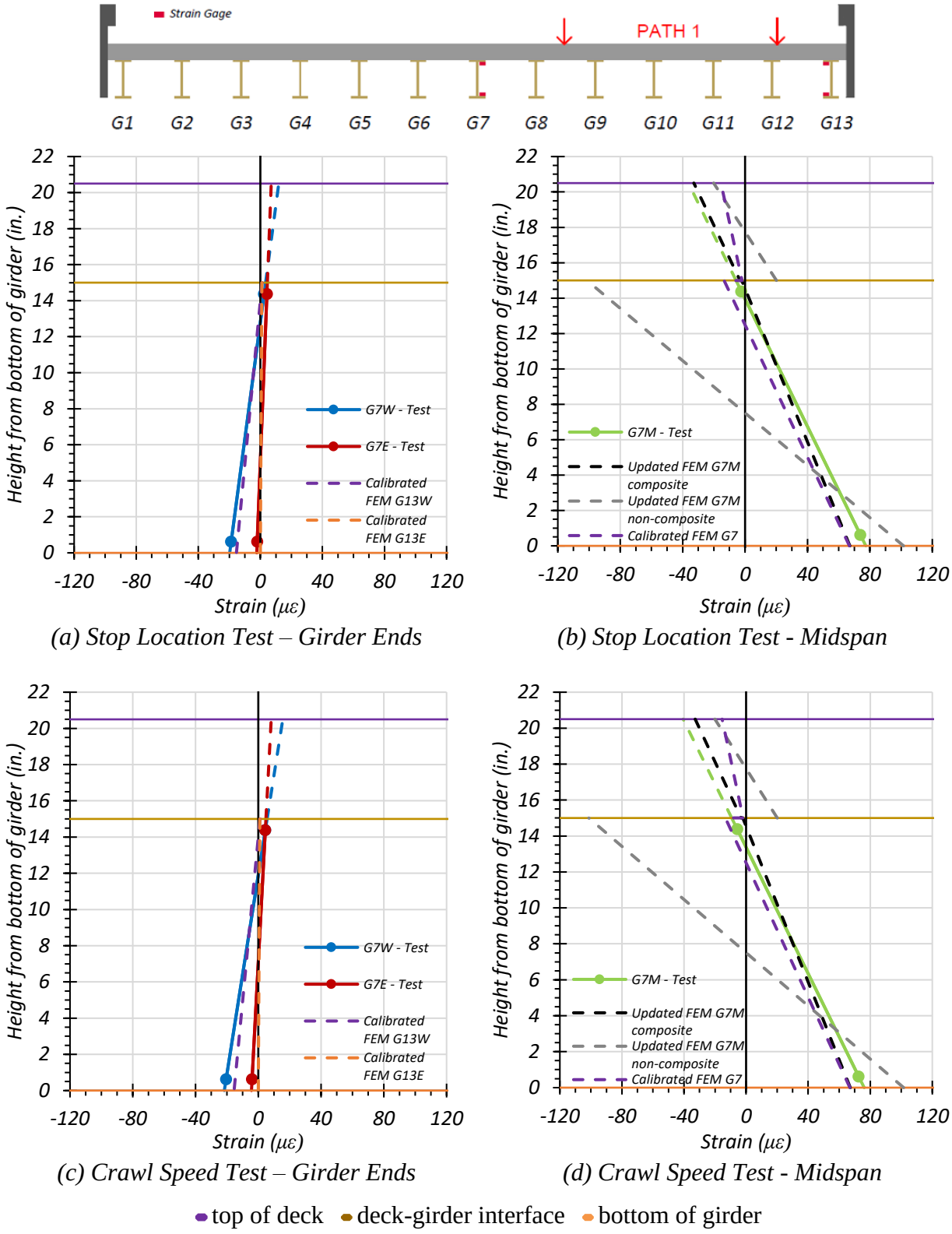

(a) Stop Location Test – Girder Ends

(b) Stop Location Test - Midspan

(c) Crawl Speed Test – Girder Ends

(d) Crawl Speed Test - Midspan

Figure 6.50. Static Strains for Girder G7—Path 1

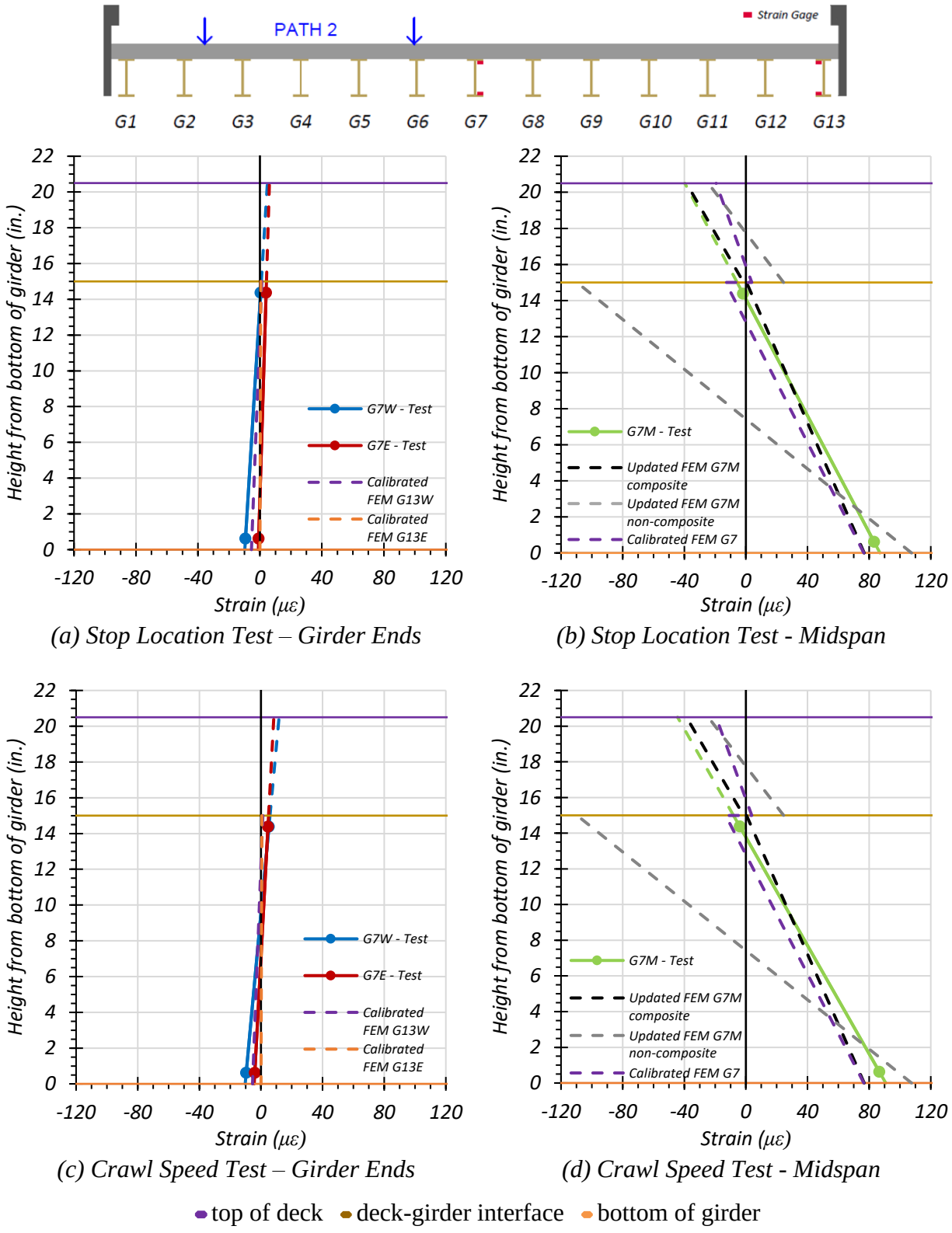

(a) Stop Location Test – Girder Ends

(b) Stop Location Test - Midspan

(c) Crawl Speed Test – Girder Ends

(d) Crawl Speed Test - Midspan

Figure 6.51. Static Strains for Girder G7—Path 2

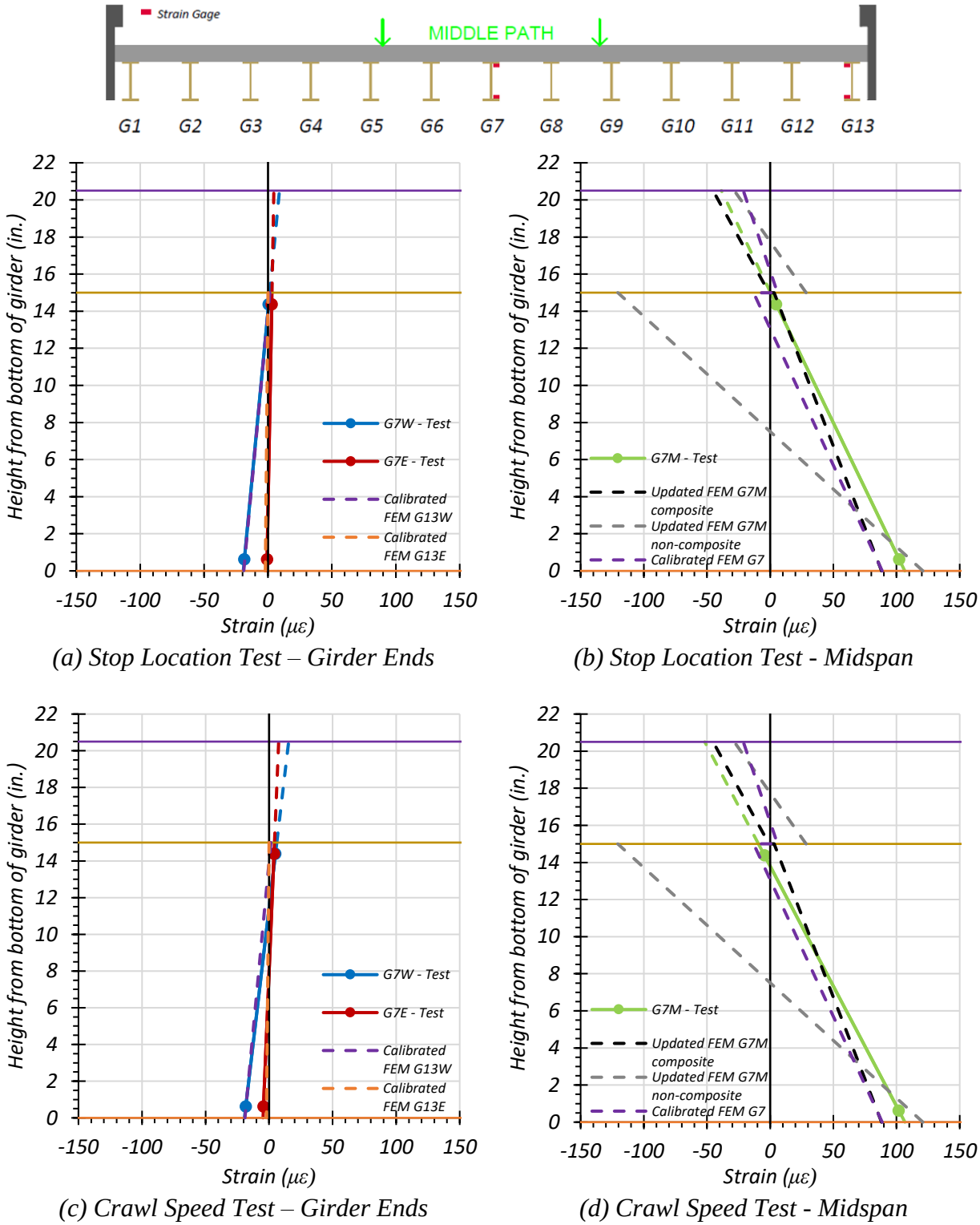

(a) Stop Location Test – Girder Ends

(b) Stop Location Test - Midspan

(c) Crawl Speed Test – Girder Ends

(d) Crawl Speed Test - Midspan

Figure 6.52. Static Strains for Girder G7—Middle Path

6.8.1.2 ***Exterior Girder G13***

Figure 6.53 through Figure 6.55 provide plots of the measured strains for exterior Girder G13 during static load testing and compare the midspan strain diagram to those obtained through the updated and calibrated FEM models. The strains measured for Girder G13 during the Path 1 static tests are shown in Figure 6.53 and compared with values obtained from the FEM updated and calibrated models. Figure 6.53(a) shows the maximum strains observed during the stop location test for Girder G13 at each end of the girder. Figure 6.53(b) shows the FEM comparison for the stop location test for Girder G13 at the midspan. Figure 6.53(c) shows the maximum strains observed during the crawl speed test for Girder G13 at each end of the girder. Figure 6.53(b) shows the FEM comparison for the crawl speed test for Girder G13 at the midspan.

The strains measured for Girder G13 during the Path 2 static tests are shown in Figure 6.54 and compared with values obtained from the FEM updated and calibrated models. Figure 6.54(a) shows the maximum strains observed during the stop location test for Girder G13 at each end of the girder. Figure 6.54(b) shows the FEM comparison for the stop location test for Girder G13 at midspan. Figure 6.54(c) shows the maximum strains observed during the crawl speed test for Girder G13 at each end of the girder. Figure 6.54(d) shows the FEM comparison for the crawl speed test for Girder G13 at the midspan.

The strains measured for Girder G13 during the Middle Path static tests are shown in Figure 6.55 and compared with values obtained from the FEM updated and calibrated models. Figure 6.55(a) shows the maximum strains observed during the stop location test for Girder G13 at each end of the girder. Figure 6.55(b) shows the FEM comparison for the stop location test for Girder G13 at the midspan. Figure 6.55(c) shows the maximum strains observed during the crawl speed test for Girder GG13 at each end of the girder. Figure 6.55(d) shows the FEM comparison for the crawl speed test for Girder G13 at the midspan.

Both the calibrated FEM model and the updated fully composite FEM model strain diagrams at the midspan compare well with the midspan strain diagram observed during testing. Either model would likely be a good candidate to use to conduct a load rating analysis. The updated fully composite FEM model tends to be slightly closer to the test value when looking at bottom flange strain; however, it is also important to note that the calibrated FEM model takes into account the fixity at the ends of the girders, and the updated fully composite FEM model does not.

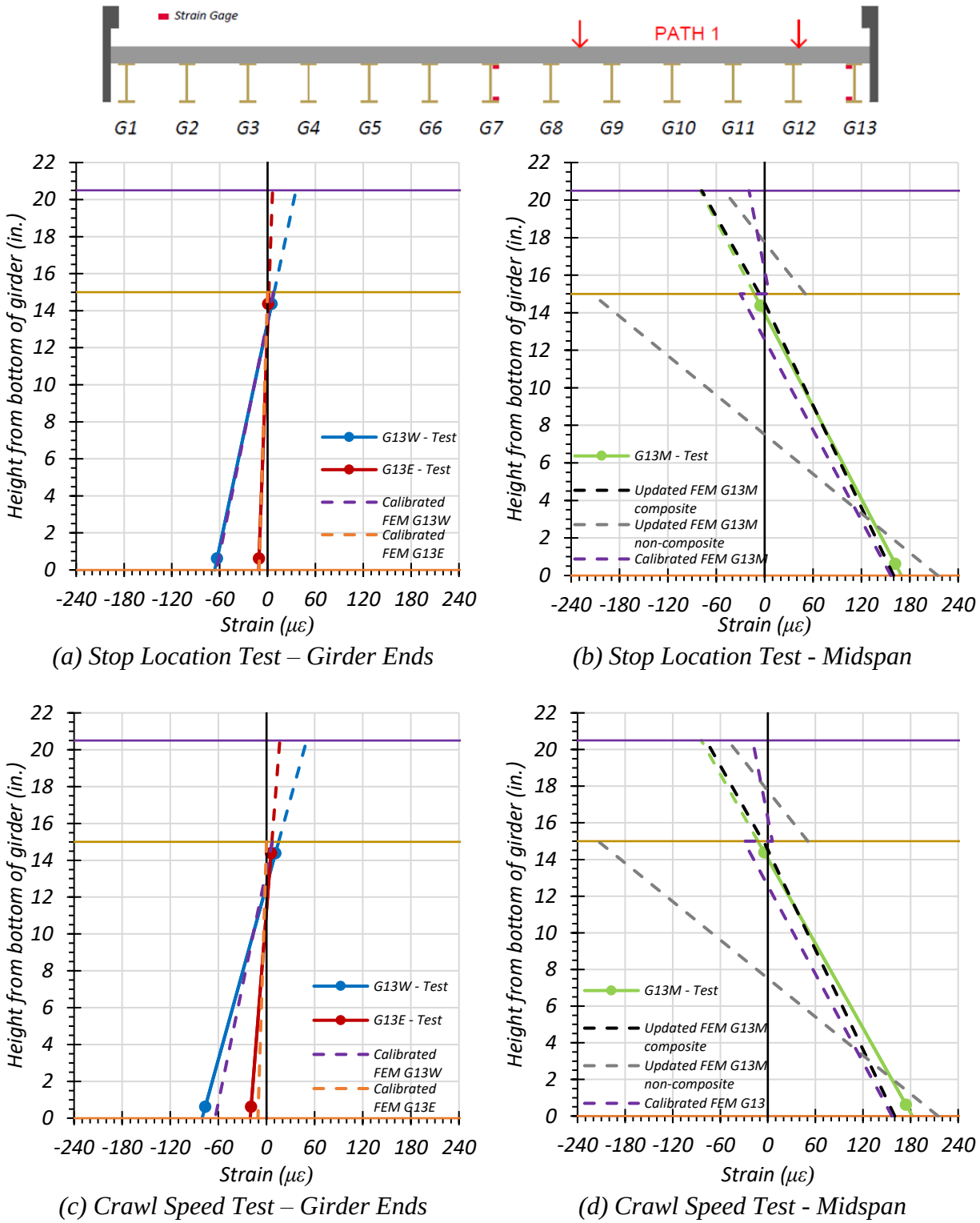

(a) Stop Location Test – Girder Ends

(b) Stop Location Test - Midspan

(c) Crawl Speed Test – Girder Ends

(d) Crawl Speed Test - Midspan

Figure 6.53. Static Strains for Girder G13—Path 1

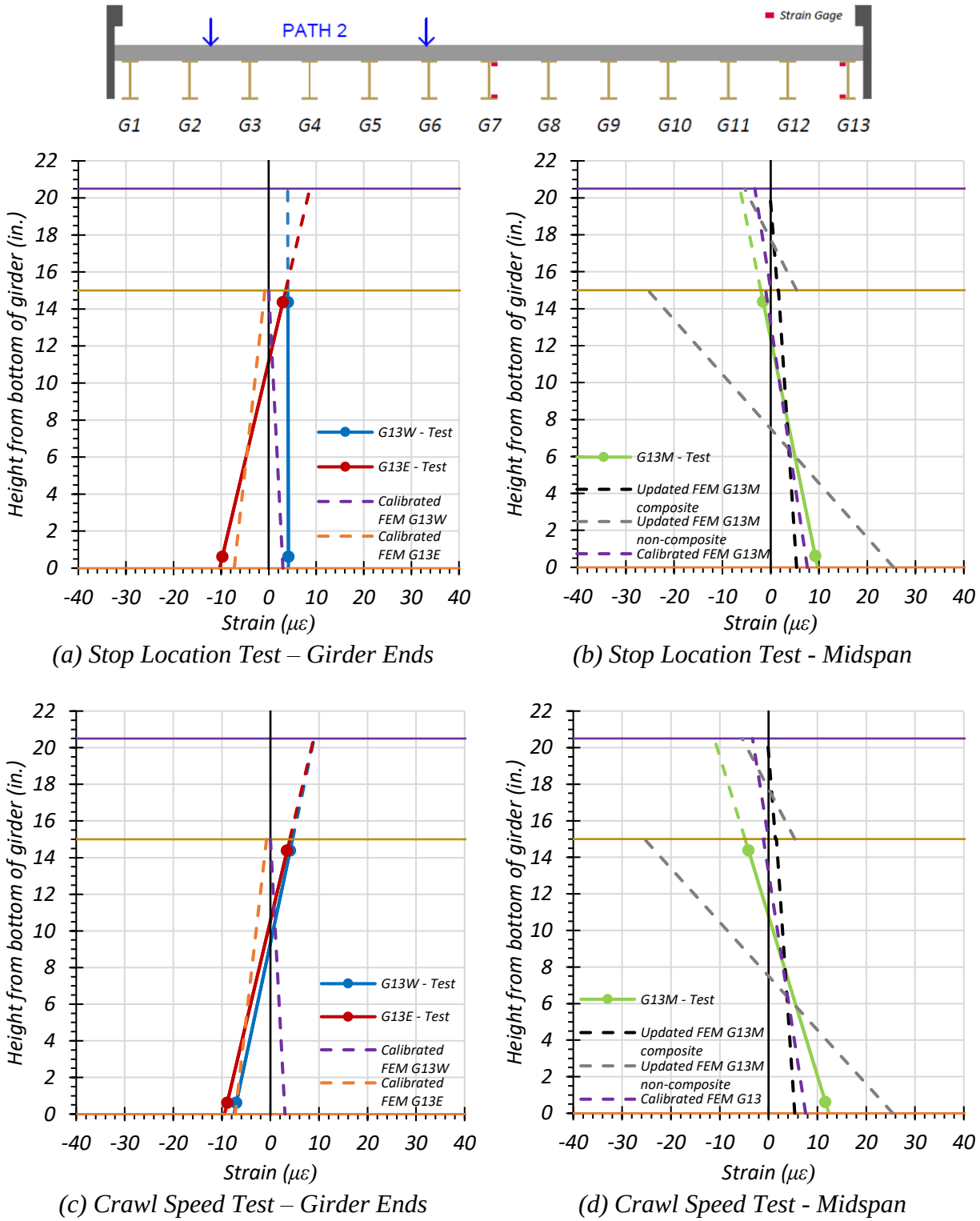

(a) Stop Location Test – Girder Ends

(b) Stop Location Test - Midspan

(c) Crawl Speed Test – Girder Ends

(d) Crawl Speed Test - Midspan

Figure 6.54. Static Strains for Girder G13—Path 2

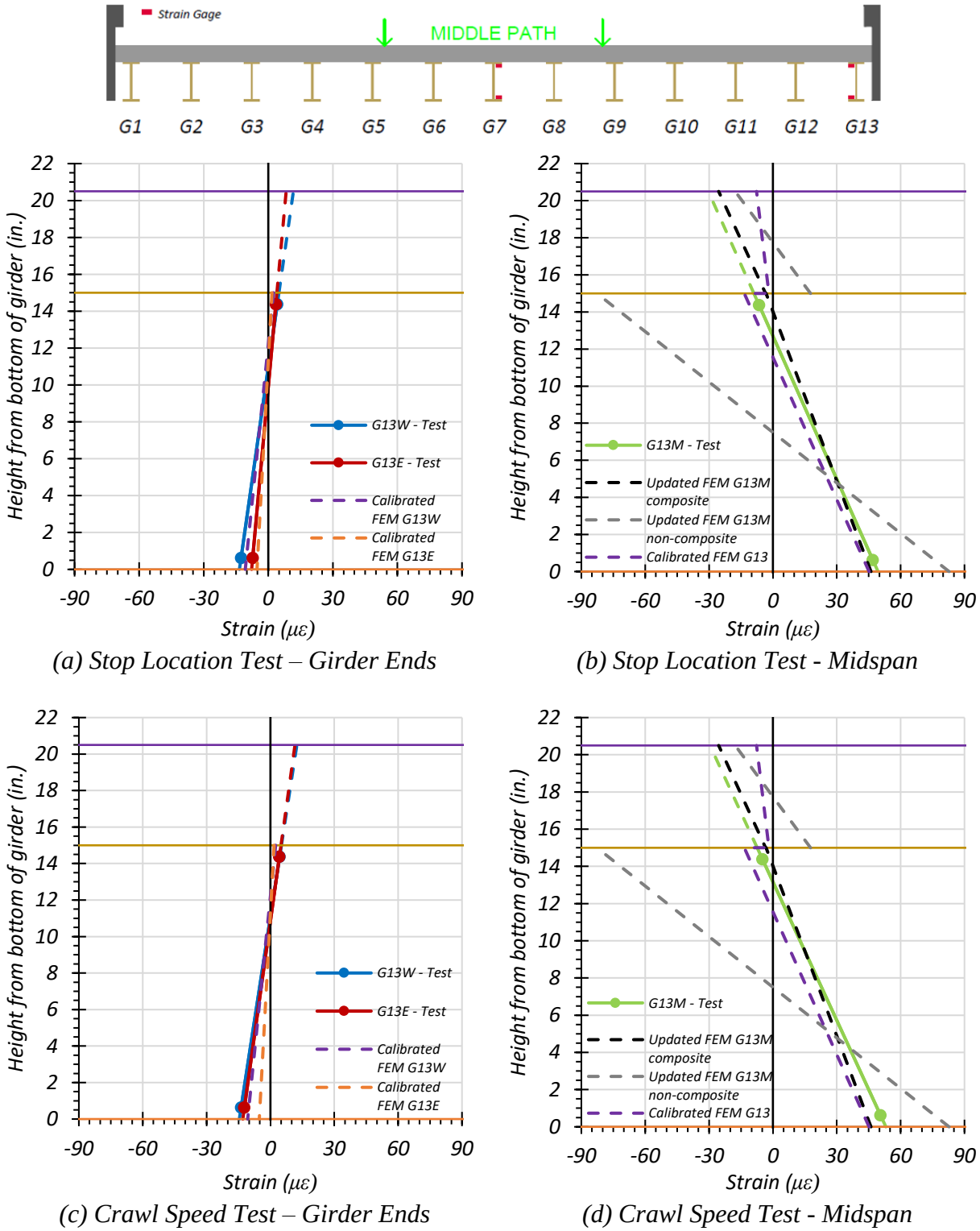

(a) Stop Location Test – Girder Ends

(b) Stop Location Test - Midspan

(c) Crawl Speed Test – Girder Ends

(d) Crawl Speed Test - Midspan

Figure 6.55. Static Strains for Girder G13—Middle Path

*6.8.1.3 **Comparison of Results based on Measured Strains***

The neutral axis locations of Girder G13 and Girder G7 observed during the load tests were compared with the theoretical neutral axis locations calculated using the FEM strain predictions. Table 6.23 shows the neutral axis locations measured for all static load tests and for the three FEM models. Figure 6.56 compares the test neutral axis locations with the non-composite and composite neutral axis locations obtained from FEM. Because the test neutral axis locations are very close to the FEM composite neutral axis locations, Bridge SM-5 is expected to act as almost fully composite.

Table 6.23. Measured and FEM Neutral Axis Locations for All Static Load Tests

Test	G7 Neutral Axis Location (in. from bottom of girder)	G13 Neutral Axis Location (in. from bottom of girder)
Path 1—Stop Location	13.95	13.96
Path 1—Crawl Speed	13.37	14.04
Path 2—Stop Location	14.08	12.39
Path 2—Crawl Speed	13.77	10.79
Middle Path—Stop Location	15.05	12.70
Middle Path—Crawl Speed	13.80	13.17
Theoretical Non—Composite	7.50	7.50
Theoretical Composite	14.28	13.60
FEM Non-Composite	7.50	7.50
FEM Composite	14.83	14.51
FEM Calibrated	13.07	12.56

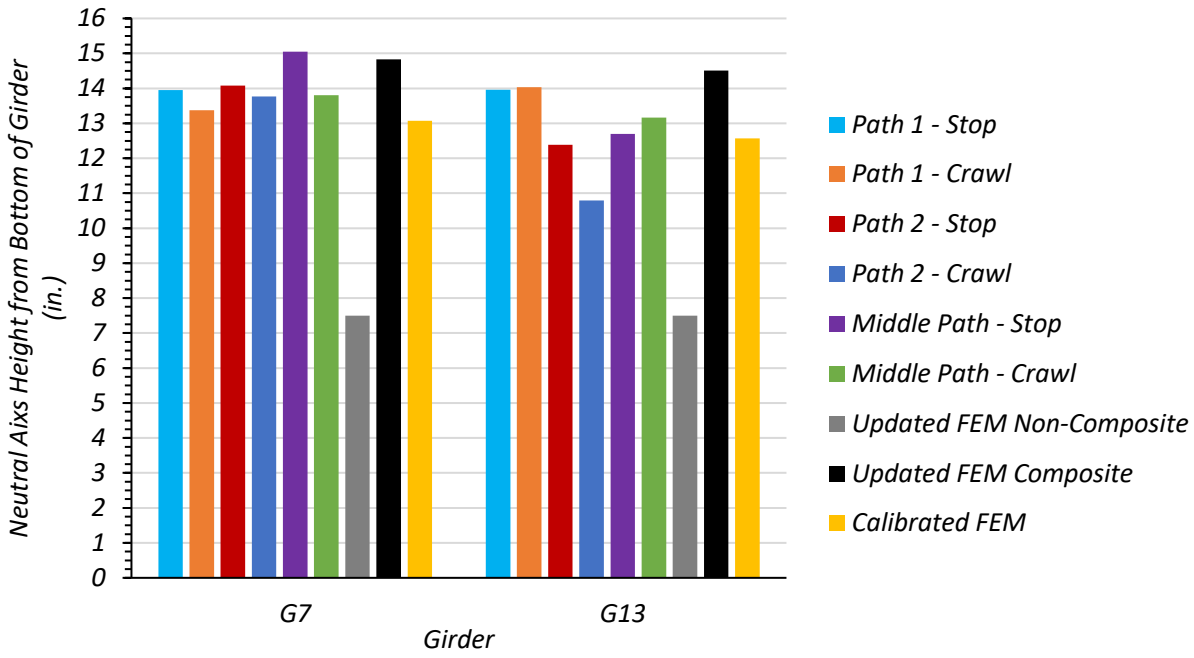

Figure 6.56. Test and FEM Neutral Axis Locations

The maximum bottom flange stresses of Girder G7 and Girder G13 observed during static load tests along each path were compared with the theoretical maximum bottom flange stresses calculated by FEM. Only the stop location tests were used for comparison because FEM performs a step-by-step analysis. Therefore, it would be inappropriate to include dynamic effects in the comparison. Table 6.24 shows the measured bottom flange stress during testing and the FEM non-composite and composite bottom flange stresses for Girder G7. Table 6.25 shows the measured bottom flange stress during testing and the FEM non-composite and composite bottom flange stresses for Girder G13. Figure 6.57 compares the test results with the FEM results. Since the measured bottom flange stresses are close to the expected composite bottom flange stresses for most load cases, Bridge SM-5 is expected to act as at least partially composite.

Table 6.24. Maximum Bottom Flange Stresses from Test and FEM for Girder G7

Load Path	Stop Location Test	Crawl Speed Test	Updated FEM Non-Composite	Updated FEM Composite	Calibrated FEM
Path 1	2.24	2.21	2.94	1.95	1.94
Path 2	2.52	2.63	3.12	2.23	2.22
Middle Path	3.09	3.09	3.51	2.56	2.57

Notes:
1. All stress values are in ksi units.
2. FEM results correspond to the same vehicle longitudinal position as the stop location tests.

Table 6.25. Maximum Bottom Flange Stresses from Test and FEM for Girder G13

Load Path	Stop Location Test	Crawl Speed Test	Updated FEM Non-Composite	Updated FEM Composite	Calibrated FEM
Path 1	4.92	5.29	6.22	4.64	4.54
Path 2	0.28	0.36	0.74	0.16	0.22
Middle Path	1.43	1.54	2.40	1.34	1.31

Notes:
1. All stress values are in ksi units.
2. FEM results correspond to the same vehicle longitudinal position as stop location tests.

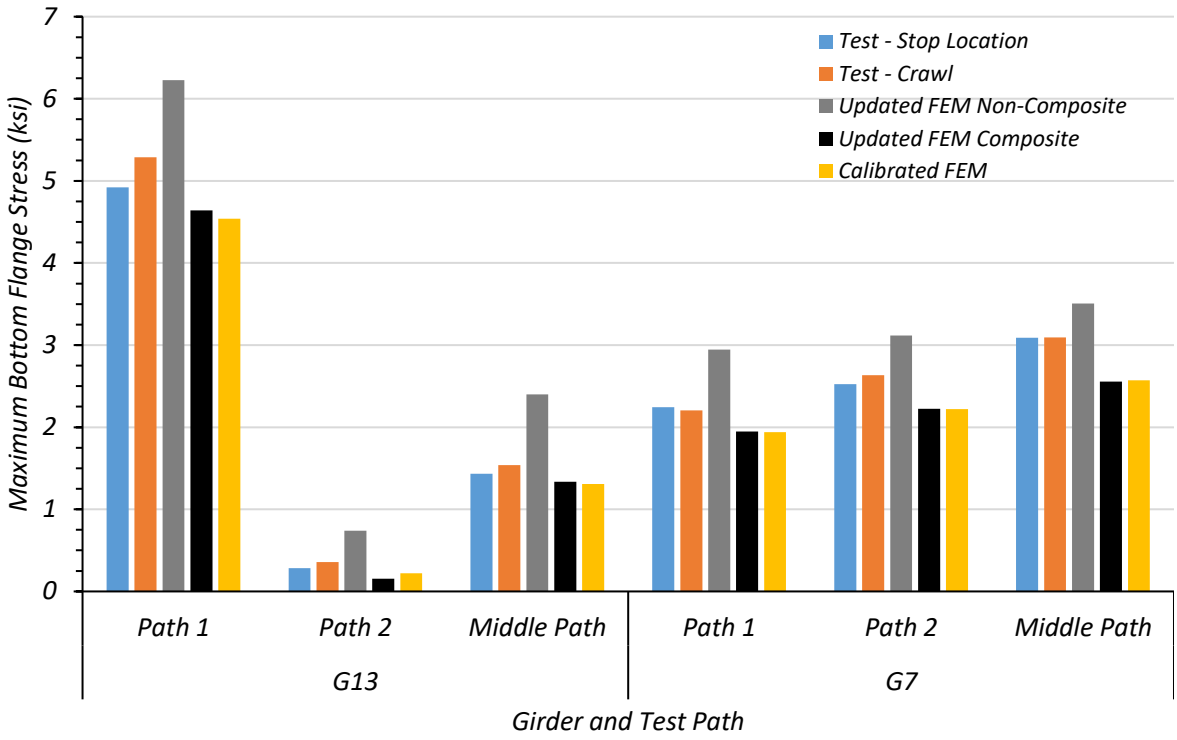

Figure 6.57. Comparison of Maximum Bottom Flange Stresses from Test and FEM

The observed bottom flange stresses tend to match better with the updated composite FEM model and the calibrated FEM model than with the updated non-composite FEM model for most load cases. On average, the updated non-composite FEM model overestimates the bottom flange stress by 34.3 percent.

6.8.2 Deflection Measurements and LLDFs

6.8.2.1 ***Path 1 Loading***

Table 6.26 shows the measured girder deflections during testing for the stop location test and crawl speed test along Path 1. Deflection data for every other girder were recorded; therefore, deflections corresponding to the intermediate girders have been interpolated. The girder displacements determined by the calibrated, updated non-composite, and updated composite FEM models are also shown.

Table 6.26. Experimental and FEM Deflections for Path 1 Loading

Girder	G1	G2*	G3	G4*	G5	G6*	G7	G8*	G9	G10*	G11	G12*	G13
Updated FEM Non-Composite Disp. (in.)	0.047	0.084	0.121	0.164	0.206	0.256	0.306	0.361	0.415	0.467	0.518	0.573	0.627
Updated FEM Composite Disp. (in.)	-0.007	0.009	0.025	0.044	0.062	0.085	0.107	0.131	0.155	0.177	0.198	0.222	0.245
Calibrated FEM Disp. (in.)	-0.004	0.013	0.031	0.051	0.072	0.096	0.121	0.148	0.173	0.197	0.221	0.246	0.271
Stop Location Test Disp. (in.)	-0.009	0.007	0.023	0.045	0.067	0.091	0.114	0.143	0.173	0.195	0.218	0.263	0.307
Crawl Speed Test Disp. (in.)	-0.013	0.002	0.017	0.040	0.063	0.088	0.112	0.142	0.172	0.197	0.222	0.273	0.324
Note: 1 – G = girder, Disp. = Displacement, * = displacement results have been interpolated using test results													

Table 6.27 compares the test LLDFs determined using deflection to those LLDFs obtained by the deflections of the updated non-composite, updated composite, and calibrated FEM models. The updated composite and calibrated FEM models do a better job of estimating the LLDFs than does the updated non-composite model.

Table 6.27. FEM Displacement LLDF Comparison with Test for Path 1 Loading

Test and Girder Type	Updated Non-Composite FEM LLDF (g_{NC})	Updated Composite FEM LLDF (g_C)	Calibrated FEM LLDF (g_{cal})	Test (g_{test})	g_{NC}/g_{test}	g_C/g_{test}	g_{cal}/g_{test}
Stop Location Interior	0.138	0.153	0.150	0.159	0.87	0.96	0.94
Stop Location Exterior	0.151	0.169	0.166	0.186	0.81	0.91	0.89
Crawl Speed Interior	0.138	0.153	0.150	0.164	0.84	0.93	0.91
Crawl Speed Exterior	0.151	0.169	0.166	0.195	0.91	0.87	0.85

Figure 6.58(a) and Figure 6.58(c) show the Path 1 stop location and crawl speed deflections compared to non-composite, composite, and calibrated values obtained from FEM analysis. Figure 6.58(b) and Figure 6.58(d) show the Path 1 stop location and crawl speed LLDFs compared to relevant AASHTO values and to values obtained from calibrated FEM model deflection results

and moment results. Table 6.28 shows the test LLDF values, the displacement and moment LLDF values obtained from the calibrated FEM model, and the LLDF values found using all three AASHTO methods. The test and calibrated model LLDFs are all lower than the prescribed AASHTO LRFD LLDF values and higher than the prescribed AASHTO Standard Specifications LLDF values for interior girders. They are close to the AASHTO Standard Specifications and AASHTO LRFD with calculated stiffness parameter for exterior girders. Using the test deflection values to obtain LLDFs slightly overestimates the LLDF for Girder G13 during Path 1 loading when compared to the calibrated FEM moment LLDFs.

Table 6.28. Experimental, FEM, and AASHTO LLDFs for Path 1 Loading

Girder	G1	G2*	G3	G4*	G5	G6*	G7	G8*	G9	G10*	G11	G12*	G13
Stop Location Test Disp. LLDF	0.005	0.004	0.014	0.027	0.041	0.055	0.069	0.087	0.104	0.118	0.132	0.159	0.186
Crawl Speed Test Disp. LLDF	0.008	0.001	0.010	0.024	0.038	0.053	0.068	0.085	0.103	0.118	0.133	0.164	0.195
Calibrated FEM Disp. LLDF	0.002	0.008	0.019	0.031	0.044	0.059	0.074	0.090	0.106	0.120	0.135	0.150	0.166
Calibrated FEM Moment LLDF	0.001	0.008	0.018	0.028	0.041	0.055	0.073	0.094	0.111	0.122	0.136	0.155	0.159
AASHTO Standard LLDF	0.174	0.137	0.137	0.137	0.137	0.137	0.137	0.137	0.137	0.137	0.137	0.137	0.174
AASHTO LRFD LLDF using simplified stiffness	0.204	0.204	0.204	0.204	0.204	0.204	0.204	0.204	0.204	0.204	0.204	0.204	0.204
AASHTO LRFD LLDF using analytical stiffness	0.177	0.177	0.177	0.177	0.177	0.177	0.177	0.177	0.177	0.177	0.177	0.177	0.177
Note: 1 – G = girder, Disp. = Displacement, * = displacement results have been interpolated using test results													

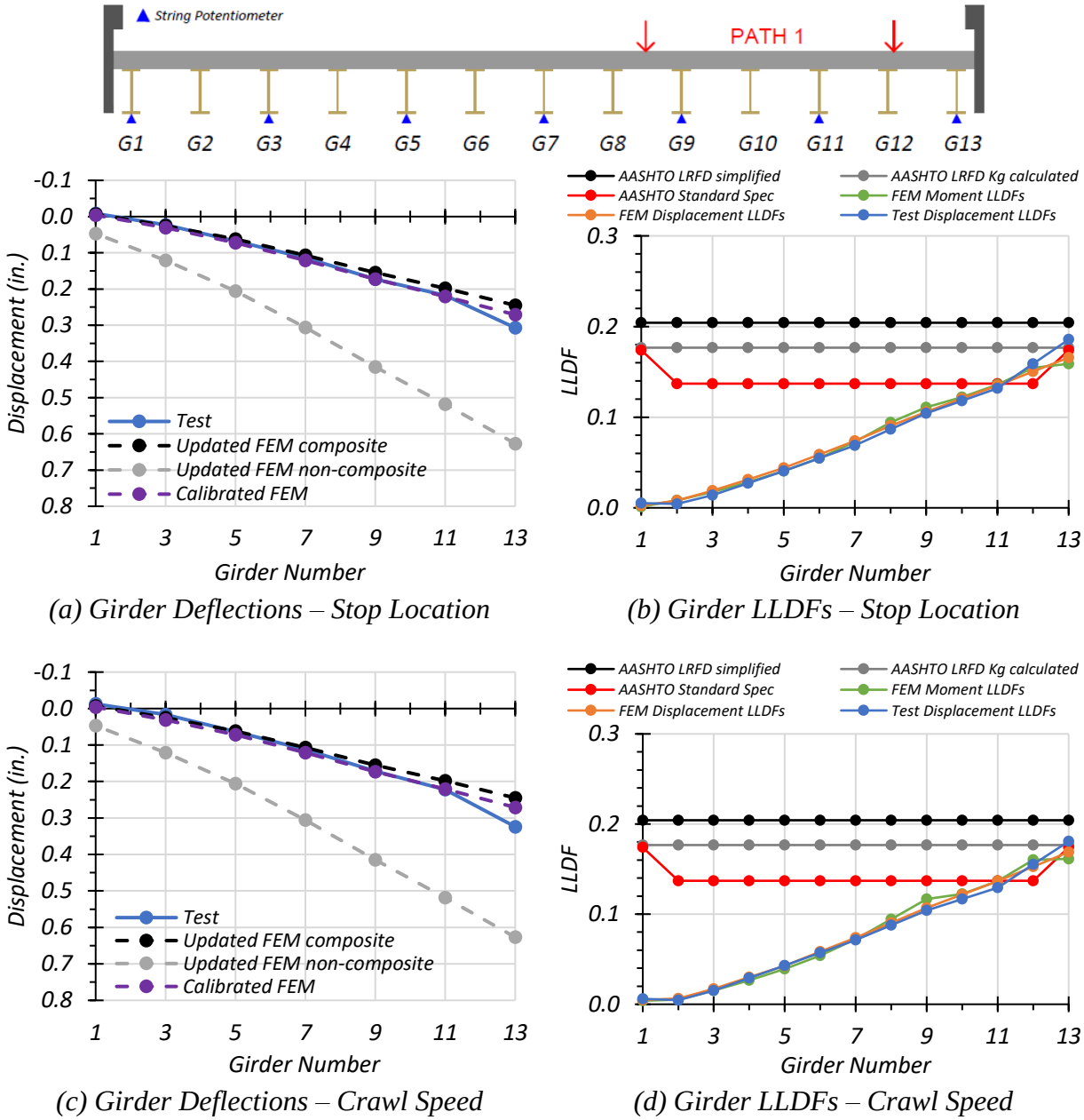

Figure 6.58. Static Deflection Results for Path 1 Loading

6.8.2.2 ***Path 2 Loading***

Table 6.29 shows the measured girder deflections during testing for the stop location test and crawl speed test along Path 2. Deflection data for every other girder were recorded; therefore, deflections corresponding to the intermediate girders have been interpolated. The girder displacements

determined by the calibrated, updated non-composite, and updated composite FEM models are also shown.

Table 6.29. Experimental and FEM Deflections for Path 2 Loading

Girder	G1	G2*	G3	G4*	G5	G6*	G7	G8*	G9	G10*	G11	G12*	G13
Updated FEM Non-Composite Disp. (in.)	0.543	0.510	0.477	0.441	0.404	0.363	0.321	0.277	0.232	0.193	0.153	0.118	0.082
Updated FEM Composite Disp. (in.)	0.206	0.194	0.181	0.166	0.151	0.133	0.115	0.095	0.075	0.057	0.039	0.023	0.007
Calibrated FEM Disp. (in.)	0.229	0.216	0.202	0.186	0.170	0.152	0.131	0.108	0.086	0.066	0.046	0.028	0.011
Stop Location Test Disp. (in.)	0.212	0.202	0.192	0.179	0.166	0.145	0.124	0.101	0.078	0.056	0.035	0.020	0.006
Crawl Speed Test Disp. (in.)	0.205	0.197	0.189	0.179	0.168	0.148	0.127	0.104	0.081	0.060	0.039	0.025	0.010
Note: 1 – G = girder, Disp. = Displacement, * = displacement results have been interpolated using test results													

Table 6.30 compares the test LLDFs determined using deflection to those obtained by the deflections of the updated non-composite, updated composite, and calibrated FEM models. The updated composite and calibrated FEM models do a better job of estimating the LLDFs than the updated non-composite FEM model; however, the calibrated FEM model seems to do the best job.

Table 6.30. FEM Displacement LLDF Comparison with Test for Path 2 Loading

Test and Girder Type	Updated Non-Composite FEM LLDF (g_{NC})	Updated Composite FEM LLDF (g_C)	Calibrated FEM LLDF (g_{cal})	Test (g_{test})	g_{NC}/g_{test}	g_C/g_{test}	g_{cal}/g_{test}
Stop Location Interior	0.124	0.134	0.132	0.133	0.93	1.01	0.99
Stop Location Exterior	0.132	0.143	0.140	0.140	0.94	1.02	1.00
Crawl Speed Interior	0.124	0.134	0.132	0.129	0.94	1.04	1.02
Crawl Speed Exterior	0.132	0.143	0.140	0.134	0.99	1.07	1.04

Figure 6.59(a) and Figure 6.59(c) show the Path 2 stop location and crawl speed deflections compared to non-composite, composite, and calibrated values obtained from FEM analysis. Figure 6.59(b) and Figure 6.59(d) show the Path 2 stop location and crawl speed LLDFs compared to relevant AASHTO values and to values obtained from calibrated FEM deflection results and moment results. Table 6.31 shows the test LLDF values, the displacement and moment LLDF values obtained from the calibrated FEM model, and the LLDF values found using all three AASHTO methods. The test and calibrated model LLDFs are all significantly lower than the prescribed AASHTO LRFD LLDF values and than the AASHTO Standard Specifications LLDF value for exterior girders. They are very close to the prescribed AASHTO Standard Specifications value for interior girders. Using the test deflection values to obtain LLDFs slightly overestimates the LLDF for Girder G1 during Path 2 loading in comparison to the calibrated FEM moment LLDFs.

Table 6.31. Experimental, FEM, and AASHTO LLDFs for Path 2 Loading

Girder	G1	G2*	G3	G4*	G5	G6*	G7	G8*	G9	G10*	G11	G12*	G13
Stop Location Test Disp. LLDF	0.140	0.133	0.127	0.118	0.109	0.096	0.082	0.067	0.051	0.037	0.023	0.013	0.004
Crawl Speed Test Disp. LLDF	0.134	0.129	0.124	0.117	0.110	0.097	0.083	0.068	0.053	0.039	0.026	0.016	0.007
Calibrated FEM Disp. LLDF	0.140	0.132	0.124	0.114	0.104	0.093	0.080	0.066	0.053	0.040	0.028	0.017	0.007
Calibrated FEM Moment LLDF	0.127	0.135	0.128	0.116	0.109	0.100	0.084	0.065	0.050	0.037	0.026	0.016	0.007
AASHTO Standard LLDF	0.174	0.137	0.137	0.137	0.137	0.137	0.137	0.137	0.137	0.137	0.137	0.137	0.174
AASHTO LRFD LLDF using simplified stiffness	0.204	0.204	0.204	0.204	0.204	0.204	0.204	0.204	0.204	0.204	0.204	0.204	0.204
AASHTO LRFD LLDF using analytical stiffness	0.177	0.177	0.177	0.177	0.177	0.177	0.177	0.177	0.177	0.177	0.177	0.177	0.177
Note: 1 – G = girder, Disp. = Displacement, * = displacement results have been interpolated using test results													

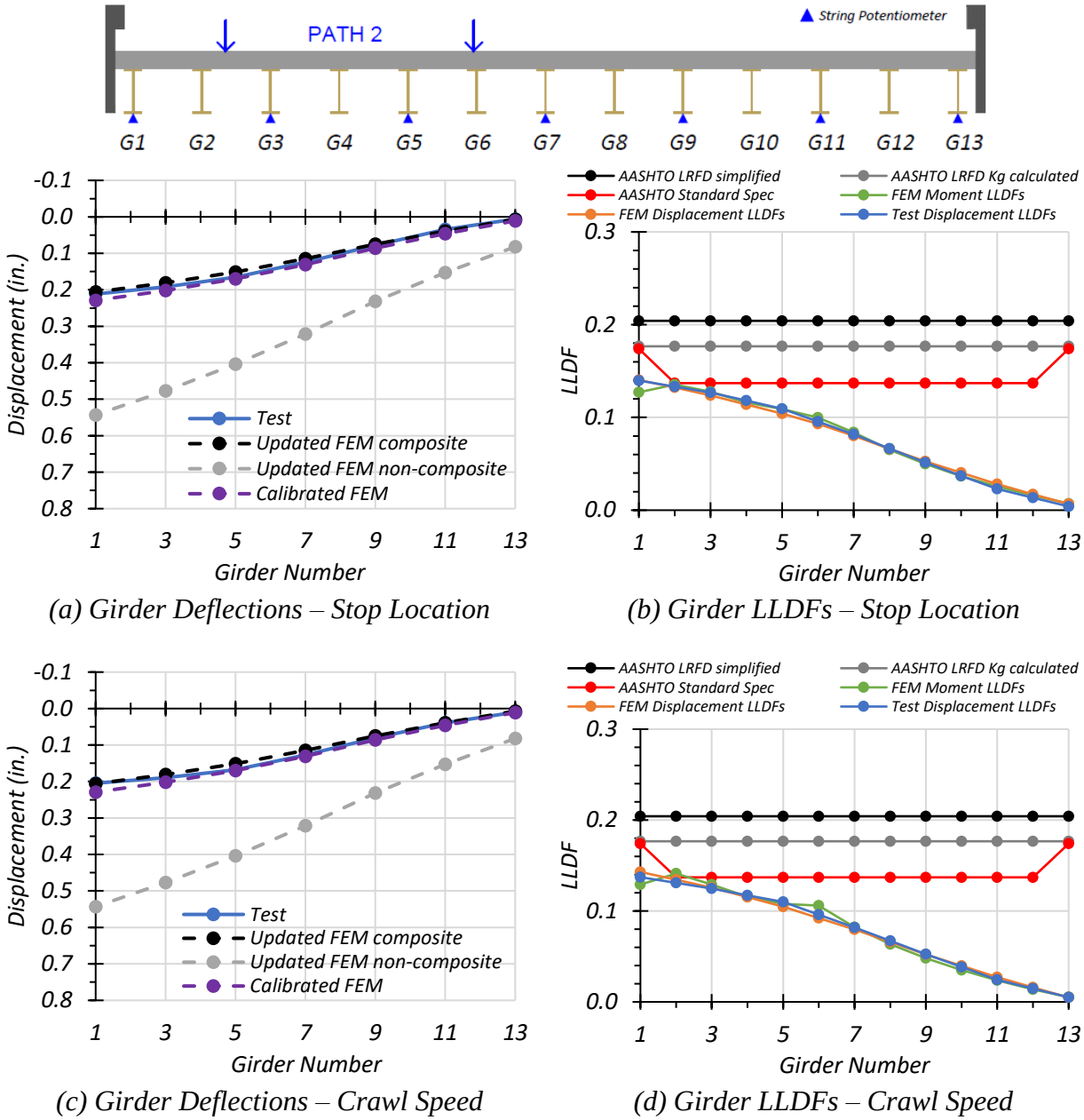

(a) Girder Deflections – Stop Location

(b) Girder LLDFs – Stop Location

(c) Girder Deflections – Crawl Speed

(d) Girder LLDFs – Crawl Speed

Figure 6.59. Static Deflection Results for Path 2 Loading

*6.8.2.3 **Middle Path Loading***

Table 6.32 shows the measured girder deflections during testing for the stop location test and crawl speed test along the Middle Path. Deflection data for every other girder were recorded; therefore, deflections corresponding to the intermediate girders have been interpolated. The girder

displacements determined by the calibrated, updated non-composite, and updated composite FEM models are also shown.

Table 6.32. Experimental and FEM Deflections for Middle Path Loading

Girder	G1	G2*	G3	G4*	G5	G6*	G7	G8*	G9	G10*	G11	G12*	G13
Updated FEM Non-Composite Disp. (in.)	0.267	0.285	0.303	0.321	0.338	0.344	0.349	0.344	0.338	0.321	0.303	0.285	0.267
Updated FEM Composite Disp. (in.)	0.083	0.094	0.105	0.115	0.125	0.128	0.131	0.128	0.125	0.115	0.105	0.094	0.083
Calibrated FEM Disp. (in.)	0.095	0.106	0.119	0.131	0.141	0.147	0.148	0.147	0.141	0.131	0.119	0.106	0.095
Stop Location Test Disp. (in.)	0.075	0.089	0.103	0.119	0.134	0.140	0.145	0.142	0.140	0.125	0.109	0.105	0.100
Crawl Speed Test Disp. (in.)	0.073	0.087	0.102	0.119	0.136	0.141	0.146	0.142	0.139	0.125	0.111	0.107	0.104
Note: 1 – G = girder, Disp. = Displacement, * = displacement results have been interpolated using test results													

Table 6.33 compares the test LLDFs determined using deflection to those obtained by the deflections of the updated non-composite, updated composite, and calibrated FEM models. The updated non-composite FEM model seems to do a better job of estimating the LLDFs than the updated composite and calibrated FEM models.

Table 6.33. FEM Displacement LLDF Comparison with Test for Middle Path Loading

Test and Girder Type	Updated Non-Composite FEM LLDF (g_{NC})	Updated Composite FEM LLDF (g_C)	Calibrated FEM LLDF (g_{cal})	Test (g_{test})	g_{NC}/g_{test}	g_C/g_{test}	g_{cal}/g_{test}
Stop Location Interior	0.086	0.092	0.091	0.095	0.91	0.97	0.96
Stop Location Exterior	0.066	0.058	0.058	0.066	1.00	0.88	0.88
Crawl Speed Interior	0.086	0.092	0.091	0.095	0.91	0.97	0.96
Crawl Speed Exterior	0.066	0.058	0.058	0.068	0.97	0.85	0.85

Figure 6.60(a) and Figure 6.60(c) show the Middle Path stop location and crawl speed deflections compared to non-composite, composite, and calibrated values obtained from FEM analysis. Figure 6.60(b) and Figure 6.60(d) show the Middle Path stop location LLDFs compared to relevant AASHTO values and to values obtained from calibrated FEM deflection results and moment results. Table 6.34 shows the test LLDF values, the displacement and moment LLDF values obtained from the calibrated FEM model, and the LLDF values found using all three AASHTO methods. The test and calibrated model LLDFs are all significantly lower than the prescribed AASHTO LLDF values.

Table 6.34. Experimental, FEM, and AASHTO LLDFs for Middle Path Loading

Girder	G1	G2*	G3	G4*	G5	G6*	G7	G8*	G9	G10*	G11	G12*	G13
Stop Location Test Disp. LLDF	0.049	0.058	0.068	0.078	0.088	0.091	0.095	0.093	0.092	0.082	0.072	0.069	0.066
Crawl Speed Test Disp. LLDF	0.048	0.057	0.066	0.078	0.089	0.092	0.095	0.093	0.091	0.082	0.072	0.070	0.068
Calibrated FEM Disp. LLDF	0.058	0.065	0.073	0.081	0.087	0.090	0.091	0.090	0.087	0.081	0.073	0.065	0.058
Calibrated FEM Moment LLDF	0.046	0.059	0.070	0.084	0.095	0.098	0.097	0.098	0.095	0.084	0.070	0.059	0.046
AASHTO Standard LLDF	0.174	0.137	0.137	0.137	0.137	0.137	0.137	0.137	0.137	0.137	0.137	0.137	0.174
AASHTO LRFD LLDF using simplified stiffness	0.204	0.204	0.204	0.204	0.204	0.204	0.204	0.204	0.204	0.204	0.204	0.204	0.204
AASHTO LRFD LLDF using analytical stiffness	0.177	0.177	0.177	0.177	0.177	0.177	0.177	0.177	0.177	0.177	0.177	0.177	0.177
Note: 1 – G = girder, Disp. = Displacement, * = displacement results have been interpolated using test results													

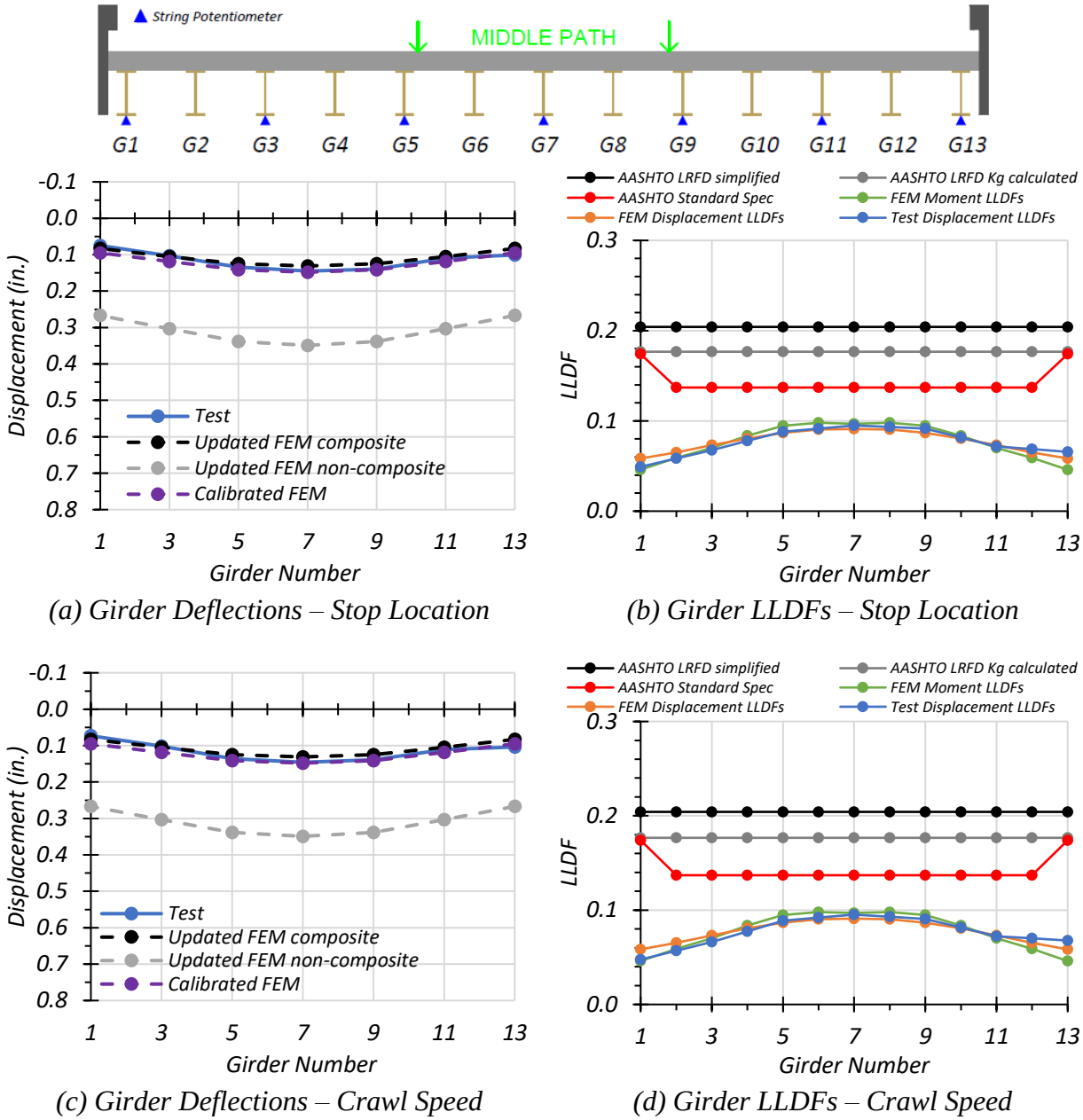

(a) Girder Deflections – Stop Location

(b) Girder LLDFs – Stop Location

(c) Girder Deflections – Crawl Speed

(d) Girder LLDFs – Crawl Speed

Figure 6.60. Static Deflection Results for Middle Path Loading

6.9 SUMMARY AND FINDINGS

6.9.1 Live Load Distribution Factors

6.9.1.1 ***General Findings***

LLDF values computed using FEM deflection results and FEM moment results were compared to ensure that the values obtained using midspan deflection data obtained from testing could be used to calculate experimental LLDFs. The FEM values using both displacements and moments were very close; thus, LLDF values were determined for each load test based on the maximum midspan deflections.

For the Path 1 load cases, the g_{AASHTO}/g_{Test} ratio ranges from 0.86 to 0.94 when considering the *AASHTO Standard Specifications*, from 1.05 to 1.28 when considering the simplified stiffness *AASHTO LRFD Specifications*, and from 0.91 to 1.11 when considering the analytical stiffness *AASHTO LRFD Specifications* (AASHTO 2002, 2017). While the *AASHTO Standard Specifications* produce unconservative results for Path 1 loading, they are not very unconservative, which would likely be made up for within other conservative areas of the load rating process. The LLDFs produced by the *AASHTO LRFD Specifications* are close to the test results at times, ranging from slightly unconservative to slightly conservative.

For the Path 2 load cases, the g_{AASHTO}/g_{Test} ratio ranges from 1.03 to 1.30 when considering the *AASHTO Standard Specifications*, from 1.46 to 1.58 when considering the simplified stiffness *AASHTO LRFD Specifications*, and from 1.26 to 1.37 when considering the analytical stiffness *AASHTO LRFD Specifications* (AASHTO 2002, 2017). In all three methods of determining LLDFs, AASHTO is conservative for Path 2 loading. However, the *AASHTO Standard Specifications* are the least conservative, producing values close to the test values at times.

For the Middle Path load cases, the g_{AASHTO}/g_{Test} ratio ranges from 1.44 to 2.64 when considering the *AASHTO Standard Specifications*, from 2.15 to 3.09 when considering the simplified stiffness *AASHTO LRFD Specifications*, and from 1.86 to 2.68 when considering the analytical stiffness *AASHTO LRFD Specifications* (AASHTO 2002, 2017). In all three methods of determining LLDFs, AASHTO is very conservative for Middle Path loading. No LLDF determined by AASHTO is close to the test value.

Of note, the close girder spacing of Bridge SM-5 (23 in.) deems it out of range for using the AASHTO LRFD Specifications LLDF equations, which require a minimum spacing of 42 in. However, for the sake of comparison, they are included in this study. The *AASHTO LRFD Specifications* indicate that a refined analysis should be performed for girder spacings that are less than the minimum (AASHTO 2017).

TxDOT currently uses the *AASHTO Standard Specifications* LLDFs for load rating of this bridge type and age. Based on the LLDF results observed from load testing, the LLDFs obtained through the *AASHTO Standard Specifications* provide an appropriate level of conservatism for most scenarios without being overly conservative. Therefore, a significant reduction in LLDFs is not available for this particular bridge; thus, this area is not identified as one that can potentially increase the load rating of Bridge SM-5 or similar bridges of this type.

6.9.1.2 ***Consideration of Moment of Inertia Difference Between Girders***

When calculating the LLDFs obtained from the displacements observed during testing, a more accurate method would be to consider the difference in moment of inertia between an interior girder and an exterior girder for cases where the moments of inertia are different. Updated LLDFs can be developed for each girder by taking the deflection multiplied by the moment of inertia of an individual girder and dividing by the sum of the deflection multiplied by the moment of inertia for all girders. Equation (6.1) shows the equation used to obtain an LLDF through this method:

$$LLDF_i = \frac{\Delta_i I_i}{\sum(\Delta_i I_i)} \tag{6.1}$$

where:

$LLDF_i$ = Live load distribution factor for an individual girder
Δ_i = Deflection of the individual girder (in.)
I_i = Moment of inertia of the individual girder (in^4)

Bridge SM-5 has the same steel section for interior and exterior girders (S15x42.9), so under fully non-composite action, only the deflection terms impact the LLDFs as the moment of inertia terms cancel. However, under fully composite action, which the measurements for Bridge SM-5 support, the interior girders and exterior girders have different moments of inertia due to different effective

deck widths (23 in. for interior girders and 17.5 in. for exterior girders). The fully composite interior girder was found to have a moment of inertia of 1329 in^4, and the exterior girder was found to have a moment of inertia of 1231 in^4.

By considering the controlling stop location load case for Girder G13 along Path 1 and using the procedure described above, new LLDFs were developed. The controlling interior girder, Girder G12, experienced a 1.3 percent increase in LLDF from 0.159 to 0.161. The controlling exterior girder, Girder G13, experienced a 6.7 percent decrease in LLDF, from 0.186 to 0.174. Table 6.35 and Figure 6.61 show the LLDFs developed using this method compared to LLDFs determined through the calibrated FEM model displacements, the calibrated FEM model moments, the *AASHTO Standard Specifications*, the *AASHTO LRFD Specifications* using the simplified stiffness parameter, and the *AASHTO LRFD Specifications* using the analytical stiffness parameter (AASHTO 2002, 2017).

Table 6.35. Bridge SM-5 LLDF Comparison Considering Difference in Inertia

Selected Girder LLDFs for Various Methods	Interior Girder G12	Exterior Girder G13
Test Displacement Considering Inertia Difference	0.161	0.174
Test Displacement without Considering Inertia Difference	0.159	0.186
Calibrated FEM Displacements	0.150	0.166
Calibrated FEM Moments	0.160	0.161
AASHTO Standard Specifications	0.137	0.174
AASHTO LRFD Specifications – Simplified	0.204	0.204
AASHTO LRFD Specifications – Analytical	0.177	0.177

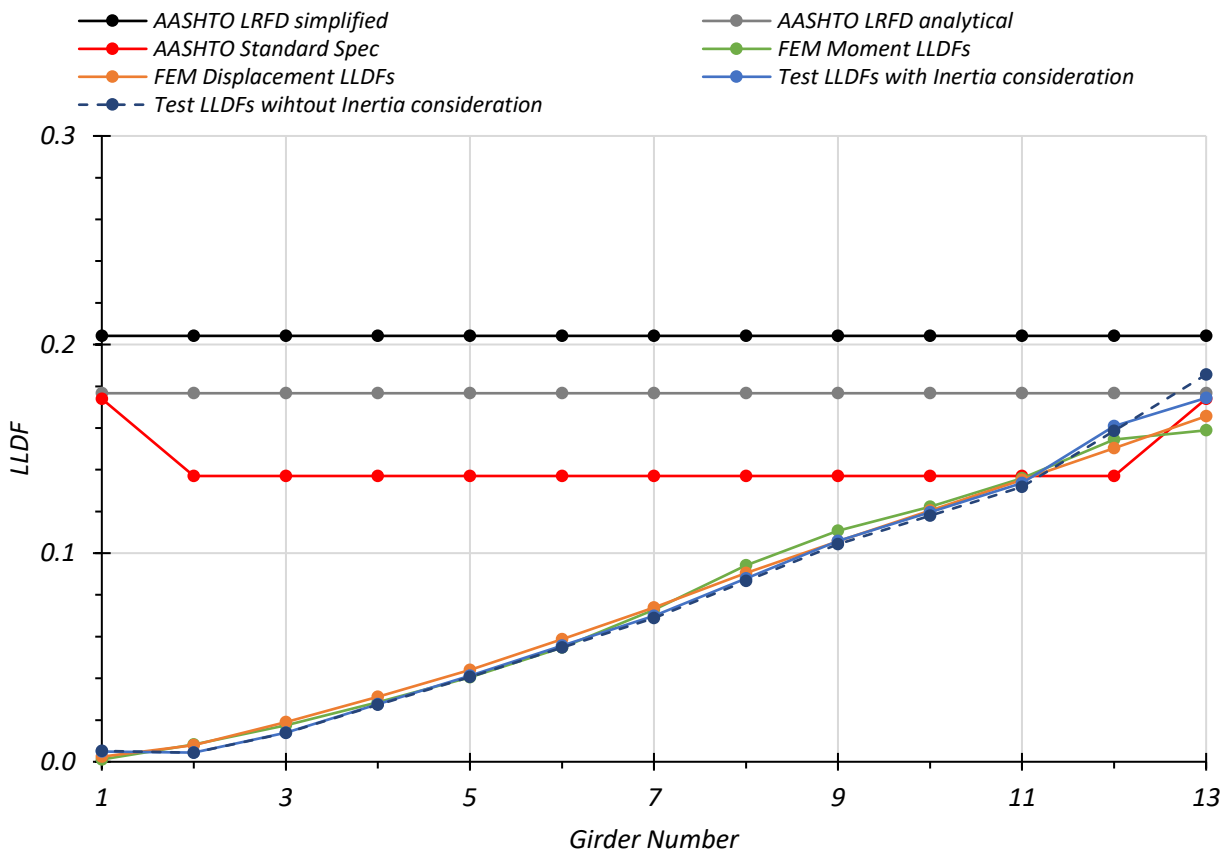

Figure 6.61. Bridge SM-5 LLDF Comparison Considering Difference in Inertia

The consideration of the moment of inertia difference between interior and exterior girders does not cause a significant change in the calculated LLDFs for Bridge SM-5 because the composite interior and exterior girders do not have a significant difference in moment of inertia. The LLDFs calculated without consideration of inertia difference are slightly more conservative, and both methods do a good job of matching the LLDF results from FEM displacements and FEM moments. Both results also match closely to the LLDFs given by the *AASHTO Standard Specifications* (AASHTO 2002). Furthermore, under the initial conservative assumption made during the basic load rating analysis that Bridge SM-5 is non-composite, there would be no difference in the moment of inertia between interior and exterior girders. Therefore, the LLDFs would be calculated based only on displacements. Without conducting a field test, it is difficult to ensure that a bridge exhibits composite behavior. For these reasons, the LLDFs were kept as calculated throughout this chapter, and the difference in moment of inertia between interior and exterior girders under composite action was not considered. However, it is noted that to bound the

possible LLDFs when considering the presence of partial of full composite action, one can consider both the fully non-composite case and the fully composite case.

6.9.2 Composite Action

A large amount of information was obtained from the load tests that suggests Bridge SM-5 is acting as nearly fully composite under the test truck loading. The girder flanges of this bridge are embedded into the concrete deck and therefore suggest the potential for composite action. From the strain gauges attached to the top and bottom flanges of the girders, a strain diagram of an interior and exterior girder was constructed for each load test. Although in some cases the neutral axes shown by these diagrams are slightly lower than that expected for fully composite action, in every case the neutral axis is significantly higher than that expected for non-composite section. It was also determined that, in general, the neutral axis was closer to the fully composite value when the truck was near the girder.

The bottom flange stresses obtained from testing were compared to the expected non-composite and composite bottom flange stresses from FEM analysis. For all load tests, the measured bottom flange stresses were close to the ones obtained from FEM composite model, while being significantly different than the stress values obtained from FEM non-composite model.

The deflection data obtained during the load testing were compared to estimated girder deflection values from FEM considering both non-composite and composite action. In general, the girder deflection profiles seen in the field were much closer to those profiles of the composite FEM model, and in some cases the two almost matched.

Bridge SM-5 is acting as nearly fully composite under live load based on four observations: (1) the top flanges are embedded into the deck slab, and there are no signs of cracking between the girder flanges and deck, (2) the neutral axis locations, (3) the bottom flange stresses, and (4) the girder deflections. Based on a fully composite section assumption, the RFs calculated for Bridge SM-5 in Task 3 were reanalyzed and compared. Table 6.36 shows the Strength I RFs calculated for Bridge SM-5 using the Allowable Stress Rating (ASR), Load Factor Rating (LFR), and Load and Resistance Factor Rating (LRFR) methods considering the fully composite action observed during load tests. The table compares the updated RFs to those calculated in Task 3 of this project and to the current TxDOT RFs. It is important to note that for the ASR ratings, the dead load stresses used are non-composite stresses. When using the LFR method, which is the method

currently used by TxDOT to rate this bridge, the consideration of composite action would allow the posting of this bridge to be removed, per TxDOT's on-system load rating flowchart (TxDOT 2018b). For an almost fully composite girder, as used in the calibrated FEM model, the capacity and load rating would be slightly reduced. However, this reduction would not be expected to significantly affect the load posting determined through TxDOT's previously mentioned flowchart.

For the ASR fully composite RF, the capacity stress was 18.15 ksi for the inventory rating and 24.75 for the operating rating, the dead load stress was 7.72 ksi, the superimposed dead load stress was 0.77 ksi, and the live load stress was 13.11 ksi. For the LFR fully composite RF, the moment capacity was 284.6 kip-ft, the dead load moment was 43.3 kip-ft, and the live load moment was 102.4 kip-ft. For the LRFR fully composite RF, the moment capacity was 284.6 kip-ft, the dead load moment was 43.3 kip-ft, and the live load moment was 207.4 kip-ft.

Table 6.36. Comparison of Bridge SM-5 Composite RFs to Non-Composite RFs for Strength I

Method	TxDOT RF		Task 3 RF		Composite RF		Composite RF/ TxDOT RF		Composite RF/ Task 3 RF	
	Inv.	Oper.	Inv.	Oper.	Inv.	Oper.	Inv.	Oper.	Inv.	Oper.
ASR	-	-	0.46	0.78	0.74	1.24	-	-	1.61	1.59
LFR	0.47	0.79	0.48	0.81	**0.99**	**1.65**	2.11	2.09	2.06	2.04
LRFR	-	-	0.28	0.37	0.60	0.78	-	-	2.14	2.11
Note: TxDOT and Task 3 RFs are calculated for a non-composite section										

6.9.3 Stresses

The maximum bottom flange stresses experienced during loading were quite minimal. The maximum bottom flange stress for Girder G7 was 3.69 ksi from Test 5. The maximum bottom flange stress for Girder G13 was 5.29 ksi from Test 11. For non-composite action, the estimated dead load bottom flange stresses obtained from the calibrated FEM model are 8.53 ksi for Girder G7 and 9.24 ksi for Girder G13.

An ASR load rating can be performed for Bridge SM-5 using this information and the yield strength of 33 ksi taken into account by TxDOT in its load rating calculations (TxDOT 2018a). Equation (6.2) shows the ASR RF equation, with the variables defined as well. The capacity, dead load effect, and live load effect are in terms of stresses:

$$RF = \frac{C - A_1 D}{A_2 L(1 + I)} \quad (6.2)$$

where:

RF	=	Rating Factor for the live load carrying capacity
C	=	Capacity of the member = 0.55**F*$_y$ for inventory, 0.75*F*$_y$ for operating
D	=	Dead load effect on the member (computed as 10.53 ksi for Girder G7 and 11.24 ksi for Girder G13 for the non-composite section)
L	=	Live load effect on the member (determined from test as 3.69 ksi for Girder G7 and 5.29 ksi for Girder G13)
I	=	Impact factor to be used with the live load effect = 0.3
A$_1$	=	Factor for dead loads = 1.0
A$_2$	=	Factor for live load = 1.0

Table 6.37 shows the calculated RFs for Bridge SM-5 using the measured test information and the ASR method. It is important to note that these RFs are for the test vehicle, which was almost exactly at the posted limit, not for the design HS-20 truck. It is also important to note that this method only considers one truck on the bridge, which is marked as two lanes.

Table 6.37. Bridge SM-5 Calculated ASR RF for Test Vehicle Using Measured Results

Girder	Maximum Measured Live Load Stress from Static Load Tests (ksi)	Inventory RF	Operating RF
Interior G7	3.69	2.01	3.38
Exterior G13	5.29	1.30	2.26

6.9.4 Model Calibration and Update

Analysis was performed using the calibrated FEM model of Bridge SM-5 for the HS-20 design vehicle under two-lane loading. This vehicle is used in the ASR and LFR rating methods, which TxDOT uses to perform load ratings of bridges not designed using LRFR (TxDOT 2018b). The maximum dead load bottom flange stresses considering non-composite action were 8.53 ksi for Girder G7 and 9.24 ksi for Girder G13. In the calibrated model, the maximum live load bottom

flange stress on Girder G7 is 9.08 ksi, and the maximum live load bottom flange stress on Girder G13 is 9.22 ksi. With these results, an ASR load rating was performed for Bridge SM-5 for the HS-20 live load.

Table 6.38 shows the ASR HS-20 two-lane RFs for Girder G7 and Girder G13 using the analysis results from the calibrated FEM model. These RFs for Bridge SM-5 allow its posting to be removed based on the TxDOT on-system load posting flowchart (TxDOT 2018b).

Table 6.38. Bridge SM-5 Calculated ASR HS-20 RFs Using Calibrated FEM Model Results

Girder	Inventory RF	Operating RF
Interior G7	0.81	1.37
Exterior G13	0.74	1.29

LFR Strength I RFs can also be developed using the calibrated FEM model of Bridge SM-5. The capacity found using a fully composite section, since Bridge SM-5 was found to essentially be a fully composite bridge, is 284.6 kip-ft for Girder G7 and 277.0 kip-ft for Girder G13. The capacity was calculated using LFD procedures provided in the *AASHTO Standard Specifications* (AASHTO 2002). The non-composite dead load moments were 47.1 kip-ft on Girder G7 and 50.9 kip-ft on Girder G13. In the calibrated FEM model, the controlling live load moments were 62.8 kip-ft on Girder G7 and 59.1 kip-ft on Girder G13 for two-lane HS-20 load paths. An LFR load rating using these results was performed on Bridge SM-5 for the HS-20 live load. Equation (6.3) shows the LFR RF equation, with the variables defined as well. The capacity, dead load effect, and live load effect are moment values:

$$RF = \frac{C - A_1 D}{A_2 L(1 + I)} \tag{6.3}$$

where:

RF = Rating Factor for the live load carrying capacity

C = Capacity of the member (computed to be 284.6 kip-ft for Girder G7 and 277.0 kip-ft for Girder G13)

D = Dead load effect on the member (computed to be 57.1 kip-ft for Girder G7 and 60.9 kip-ft for Girder G13)

L = Live load effect on the member (computed to be 62.8 kip-ft for Girder G7 and 59.1 kip-ft for Girder G13)

I = Impact factor to be used with the live load effect = 0.3

A_1 = Factor for dead loads = 1.3

A_2 = Factor for live load = 2.17 for inventory, 1.3 for operating

Table 6.39 shows the LFR Strength I HS-20 two-lane RFs for Girder G7 and Girder G13 using the analysis results from the calibrated FEM model. These RFs for Bridge SM-5 allow its posting to be removed based on the TxDOT on-system load posting flowchart (TxDOT 2018b), shown in Figure 4.2 in the Volume 1 report (Hueste et al. 2019a).

Table 6.39. Bridge SM-5 Calculated LFR Strength I HS-20 RFs Using Calibrated FEM Model Results

Girder	Inventory RF	Operating RF
Interior G7	1.19	1.98
Exterior G13	1.19	1.98

7 EXPERIMENTAL TESTING OF BRIDGE SC-12

7.1 INTRODUCTION

Nondestructive load testing of Bridge SC-12 was conducted to gather information about the in-situ behavior of the bridge under vehicular loading. The load test results provide evidence of whether partial composite action is present in the structure and provide measurements of the actual live load distribution between girders. Field-measured geometric details and nondestructive material testing results were used for FEM model updating, and the load test results were used to calibrate the FEM model of the bridge, with which refined analysis is conducted. These results help to determine if the bridge posting can be increased or removed.

Various non-destructive material tests were performed on Bridge SC-12. GPR was used to locate steel reinforcing bars in the concrete deck. UPV testing and Original Schmidt Hammer and Silver Schmidt Hammer tests were performed to determine the compressive strength of the concrete deck.

7.2 GENERAL DESCRIPTION OF BRIDGE SC-12

Bridge SC-12 has a deck condition rating of 6 (Satisfactory), a superstructure condition rating of 7 (Good) without beam section loss due to corrosion, and a substructure condition rating of 7 (Good). The girder flexure controls the rating of the bridge, which has an inventory rating of 19 US tons and an operating rating of 32 US tons. Table 7.1 shows the posted loads of Bridge SC-12 for different axle and vehicle configurations. Figure 7.1 shows an elevation view of Bridge SC-12 and a view of the underside of the superstructure. Figure 7.2 shows transverse section details of Bridge SC-12.

Table 7.1. Bridge SC-12 Postings

Configuration	Posting (lbs)
Single Axle	20,000
Tandem Axle	34,000
Single Vehicle	58,000
Combination Vehicle	75,000

(a) Elevation view

(b) Underside view

Figure 7.1. Photographs of Bridge SC-12 (TxDOT 2018a)

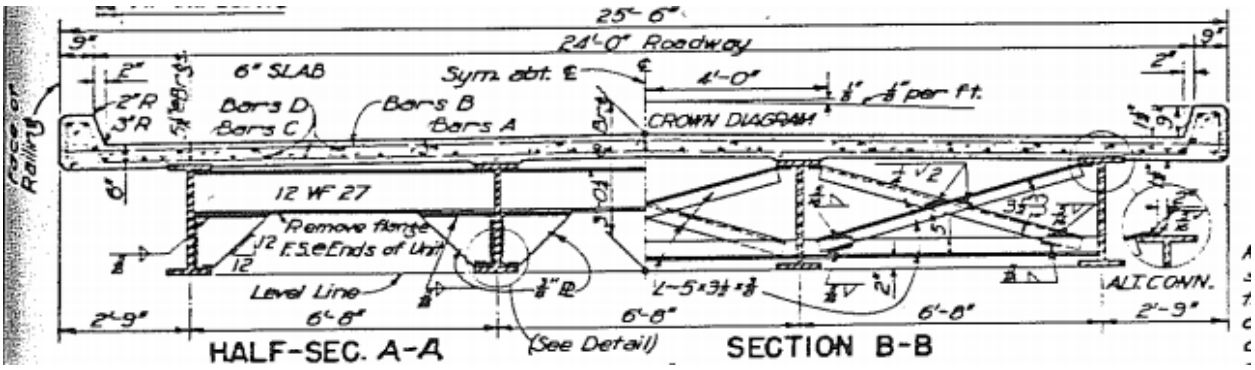

Figure 7.2. Bridge SC-12 Transverse Section (TxDOT 2018a)

7.3 IN-SITU MEASUREMENTS AND OBSERVATIONS AND NDE RESULTS

7.3.1 In-Situ Measurements and Observations

In-situ measurements of the geometric details of Bridge SC-12 were taken during field testing. The only geometric measurement that disputed the measurements given in the as-built drawings was the concrete deck thickness, which is given as 6 in. in the drawings; however, the thickness in the field was measured as 5.75 in. Therefore, the deck thickness was changed to 5.75 in. for future FEM models.

7.3.2 NDE Results

Three different nondestructive material tests were also performed on Bridge SC-12 in order to obtain more information about the concrete deck. The first test performed was a UPV test that measures the time it takes for an ultrasonic wave to travel through a known thickness of concrete, which was conducted in accordance with ASTM C597 standard test method for pulse velocity through concrete (ASTM C597 2016). The compressive strength of the concrete can then be estimated based on the measured velocities. For Bridge SC-12, this test was performed on both the slab and the curb. The measured wave velocities were 4092 m/s for the slab and 3874 m/s for the curb. By considering the wave velocity only and using equations given in Trtnik et al. (2009), the compressive strength can be found as 2.4 ksi for the slab and 1.8 ksi for the curb. However, as stated in Huang et al. (2011), using wave velocity alone is not a reliable method to obtain concrete compressive strength. Therefore, the SonReb method was performed. By using the wave velocity, the rebound number found using the Original Schmidt Hammer, and equations given in Huang et

al. (2011), the concrete compressive strength was found to be 6.3 ksi for the slab and 6.9 ksi for the curb.

The second NDE material test performed on Bridge SC-12 was the Original Schmidt Hammer, which was conducted in accordance with ASTM C805 standard test method for rebound number of hardened concrete (ASTM C805 2018). In this test, a device is pushed against the concrete surface and uses the rebound of a spring-loaded mass to estimate the compressive strength of the concrete. For Bridge SC-12, this test was also performed for both the slab and the curb. The average rebound value produced by ten Original Schmidt Hammer measurements was 43.6 for the slab and 48.7 for the curb. From the conversion chart shown in Figure 7.3, the compressive strength of the slab was determined to be 6.4 ksi and the compressive strength of the curb was determined to be 7.8 ksi.

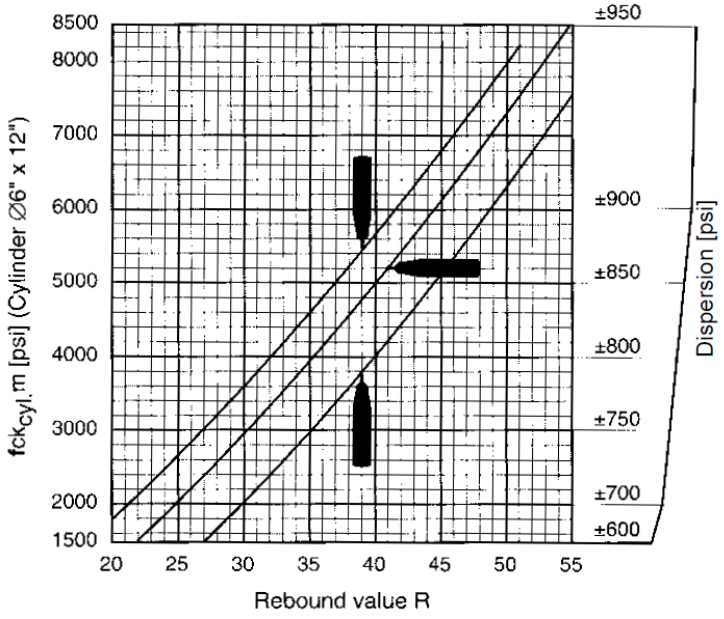

Figure 7.3. Original Schmidt Hammer Conversion Chart (Proceq 2017a)

The third NDE test performed on Bridge SC-12 was the Silver Schmidt Hammer test. The procedure for performing this test is very similar to that of the Original Schmidt Hammer. For Bridge SC-12, the average Q value produced by ten Silver Schmidt Hammer measurements was 54 for the slab and 67 for the curb. Based on the conversion chart shown in Figure 7.4, these results correspond to a compressive strength of 6.25 ksi for the slab and 10.75 ksi for the curb.

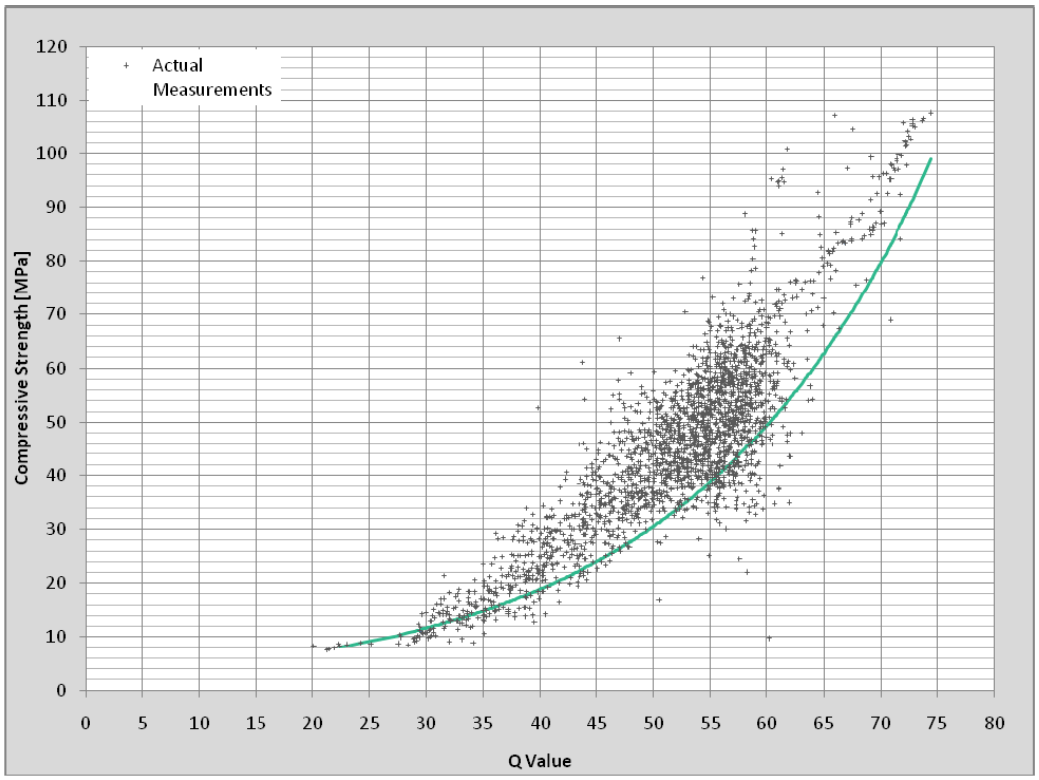

Figure 7.4. Silver Schmidt Hammer Conversion Chart (Proceq 2017b)

Of the three NDE tests performed to measure the compressive strength of the concrete deck, the lowest compressive strength value produced was 6.25 ksi. This value was used in updated FEM models to perform post-test analysis for comparison of other test values.

7.4 DATA ACQUISITION AND INSTRUMENTATION OF BRIDGE SC-12

The instrumentation plan for field testing of Bridge SC-12 was developed based on the objectives of the research project. Three types of instrumentation, including strain gauges, string potentiometers, and accelerometers were installed on the bridge to measure its response during the load tests. Figure 7.5 and Figure 7.6 show the detailed instrumentation plan for Bridge SC-12.

7.4.1 Instrumentation Plan for Bridge SC-12

The installed instrumentation and their locations on the bridge were selected in order to obtain specific data to understand the behavior of the bridge, such as load sharing between girders and composite action, and to determine if the bridge posting can be increased or removed.

Figure 7.5 shows the plan views of the full instrumentation layout for Bridge SC-12 and Figure 7.6 shows cross-section views. Figure 7.7 shows the labeling system used for the instrumentation, and Table 7.2 shows the DAQ system instrumentation labels and corresponding DAQ channels.

Strain gauges were installed on the bottom face of the top flange and the top face of the bottom flange as close as possible to the girder web at three longitudinal locations for an interior girder and an exterior girder. The strain gauges were installed at the midspan location of the main span (Span 2), at $0.4L$ away from the west abutment for the end span (Span 1), and at an average of 5 in. away from the bearing centerline adjacent to the interior pier for the selected interior and exterior girders. This spacing was done to infer moments within the spans and over the interior support. Several goals were identified in determining the instrumentation types and locations, as follows:

- The strain gauge locations were selected to collect data pertaining to the midspan moments and to determine neutral axis values to check for potential composite action.
- The string potentiometer locations were selected to measure midspan deflections and infer experimental LLDFs to compare with the estimated values from the FEM model of Bridge SC-12.
- The accelerometer locations were selected to collect bridge vibration data, allowing for comparison with estimated dynamic properties from the FEM model of the bridge.

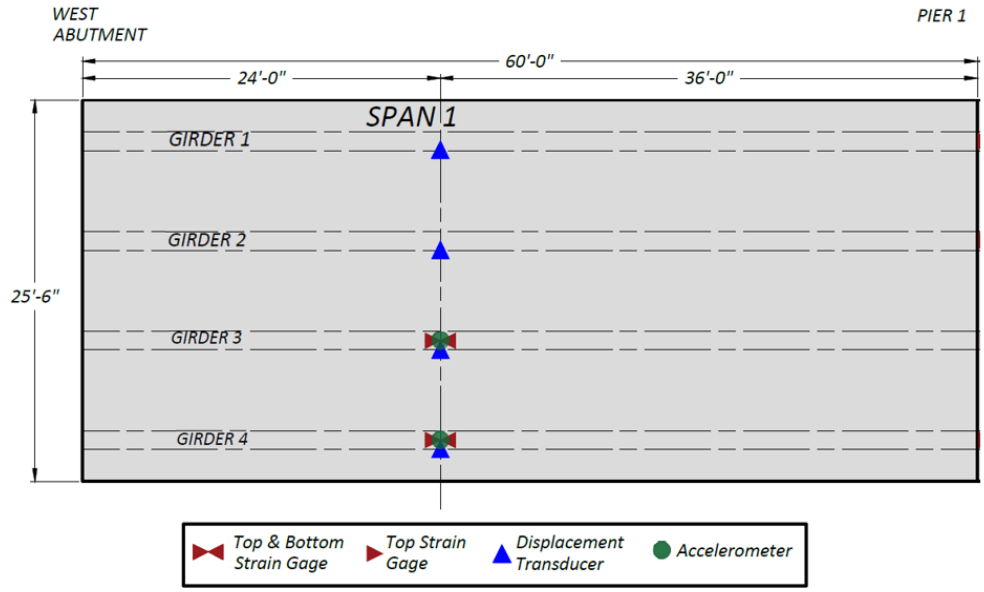

(a) End Span Plan View

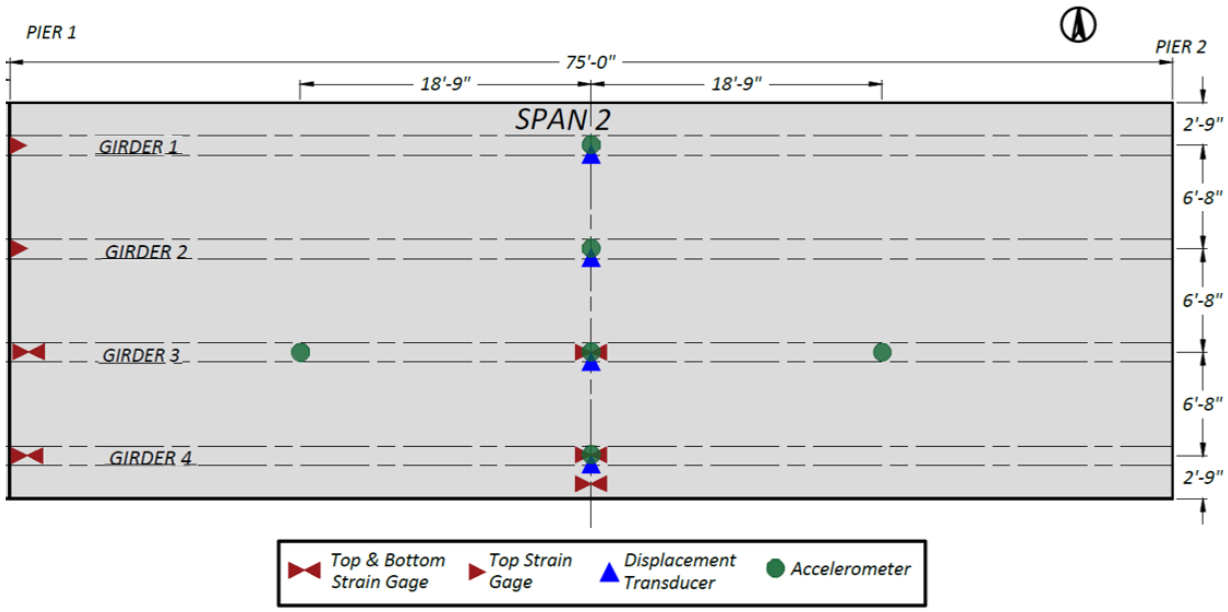

(b) Main Span Plan View

Figure 7.5. Plan View Instrumentation Layout for Bridge SC-12

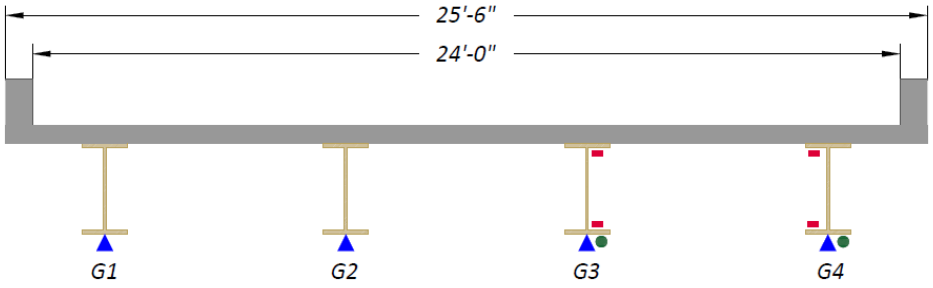

(a) End Span – Section at 0.4L

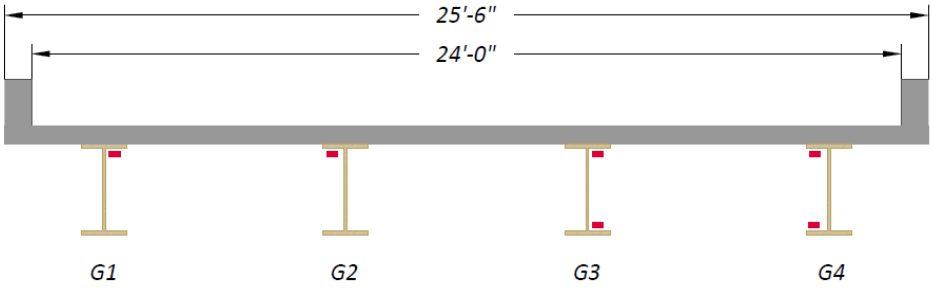

(b) Main Span – Section Adjacent to Interior Pier

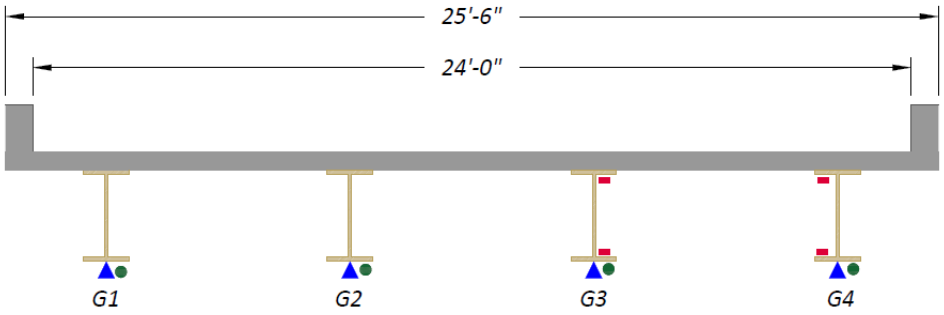

(c) Main Span - Midspan Section

Figure 7.6. Section View Instrumentation Layout for Bridge SC-12

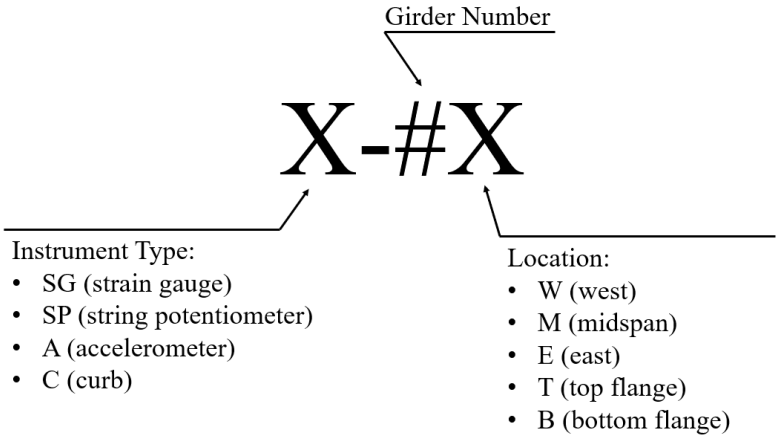

Figure 7.7. Instrumentation Labeling System Used for Bridge SC-12

Table 7.2. Instrumentation Labels for Bridge SC-12

DAQ Box	Channel	Label	Type	DAQ Box	Channel	Label	Type
Strain Book	CH1	SG-4WT	FLA-6	WBK 16-3	CH25	SP-2Mend	SM1-2
	CH2	SG-4WB	FLA-6		CH26	SP-1Mend	SM1-2
	CH3	SG-4MT	FLA-6		CH27	–	–
	CH4	SG-4MB	FLA-6		CH28	–	–
	CH5	SG-4MTend	FLA-6		CH29	–	–
	CH6	SG-4MBend	FLA-6		CH30	–	–
	CH7	SG-3WT	FLA-6		CH31	–	–
	CH8	SG-3WB	FLA-6		CH32	–	–
WBK 16-1	CH9	SG-3MT	FLA-6	WBK 18	CH57	A-4M	4507IEPE
	CH10	SG-3MB	FLA-6		CH58	A-3M	4507IEPE
	CH11	SG-3MTend	FLA-6		CH59	A-2M	4507IEPE
	CH12	SG-3MBend	FLA-6		CH60	A-1M	4507IEPE
	CH13	SG-2WT	FLA-6		CH61	A-3E	4507IEPE
	CH14	SG-1WT	FLA-6		CH62	A-3W	4507IEPE
	CH15	SG-CMT	PL-60		CH63	A-4Mend	4507IEPE
	CH16	SG-CMB	PL-60		CH64	A-3Mend	4507IEPE
WBK 16-2	CH17	–	–				
	CH18	–	–				
	CH19	SP-4M	SM1-2				
	CH20	SP-3M	SM1-2				
	CH21	SP-2M	SM1-2				
	CH22	SP-1M	SM1-2				
	CH23	SP-4Mend	SM1-2				
	CH24	SM-3Mend	SM1-2				

7.4.2 Data Acquisition System and Instrument Details

7.4.2.1 ***Data Acquisition System***

A total of 32 strain gauges (using half-bridge circuits at 16 measurement locations), eight string potentiometers, and eight accelerometers were installed onto Bridge SC-12. Thirty-two channels were used in the DAQ system, which consisted of a Measurement Computing StrainBook main DAQ unit and WBK16 extension modules for recording the strain gauge and string potentiometer data, and a WBK18 extension module for recording accelerometer data. Figure 6.8(a) shows the main box and extensions modules of the DAQ system.

7.4.2.2 ***Strain Gauges***

In order to obtain longitudinal strain data during load testing, 28 Tokyo Measuring Instruments Lab FLA-6-11-3LJCT strain gauges were installed at 14 locations on the steel girders of the bridge. Two strain gauges were installed at each measurement location: a main gauge in the longitudinal direction to obtain longitudinal strain data and a secondary gauge in the transverse direction to compensate for any temperature changes experienced during testing. Figure 7.8 shows a close-up photograph of an installed quarter bridge strain gauge couple. The strain gauges used were selected with ease of installation in mind and because the testing being conducted takes place over the span of a couple of hours. Figure 7.9 shows the strain gauges used during testing. Four Tokyo Measuring Instruments Lab PL-60-11-3LJCT-F concrete strain gauges were used only at two locations, on the curb and at the top of the deck.

Figure 7.8. Close-Up of Strain Gauge Installation

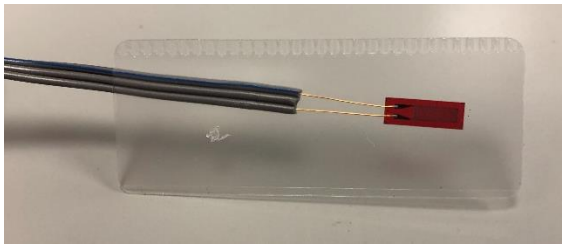

(a) Tokyo Measuring Instruments Lab FLA-6-11-3LJCT Steel Strain Gauge

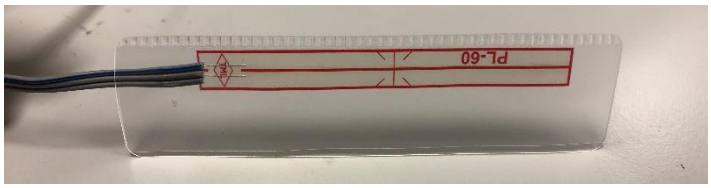

(b) Tokyo Measuring Instruments Lab PL-60-11-3LJCT-F Concrete Strain Gauge

Figure 7.9. Strain Gauges Used during Testing

7.4.2.3 ***String Potentiometers***

A total of eight Celesco SM1-2 string potentiometers, four at the midspan of every girder in the main span and another four at the moment critical position (0.4*L* away from the abutment) in one end span, were installed to obtain girder deflections. All string potentiometers used were Celesco

SM1-2 string potentiometers with a 2.5 in. stroke. Figure 6.8(c) shows the string potentiometers used during testing.

*7.4.2.4 **Accelerometers***

To obtain dynamic properties of the bridge, such as natural frequency and mode shapes, eight Brüel & Kjær IEPE piezoelectric accelerometers were installed on the bridge. Accelerometers were installed in the main span at the midspan on the bottom of every girder, as well as at quarter span locations on the bottom of the third girder. They were installed at 40 percent of the span length in one end span on the bottom of the third and fourth girders. The accelerometers used were selected because their resonance frequency of 18 kHz is much higher than the bridge's natural frequency and because they are highly sensitive and low in mass and size. Figure 6.8(d) shows the accelerometers used during testing.

7.5 LOAD TESTING PROCEDURE FOR BRIDGE SC-12

A comprehensive test program was conducted to evaluate the performance and behavior of Bridge SC-12. The test program consisted of two parts: (1) static load tests, which consisted of stop location tests and crawl speed tests, and (2) dynamic load tests. The testing took place on June 20, 2019.

7.5.1 Test Vehicle

The TxDOT Lampasas Maintenance Office provided an International F-7100 dump truck to be used for the nondestructive testing of Bridge SC-12. It was loaded with asphalt base material such that the rear tandem axles weighed approximately the same as the posted limit of the bridge (posted as 34,000 lb tandem axle). The truck was weighed using portable scales provided by the Texas Department of Public Safety. The wheel loads and wheel and axle spacings of the dump truck used for testing are shown in Figure 7.10.

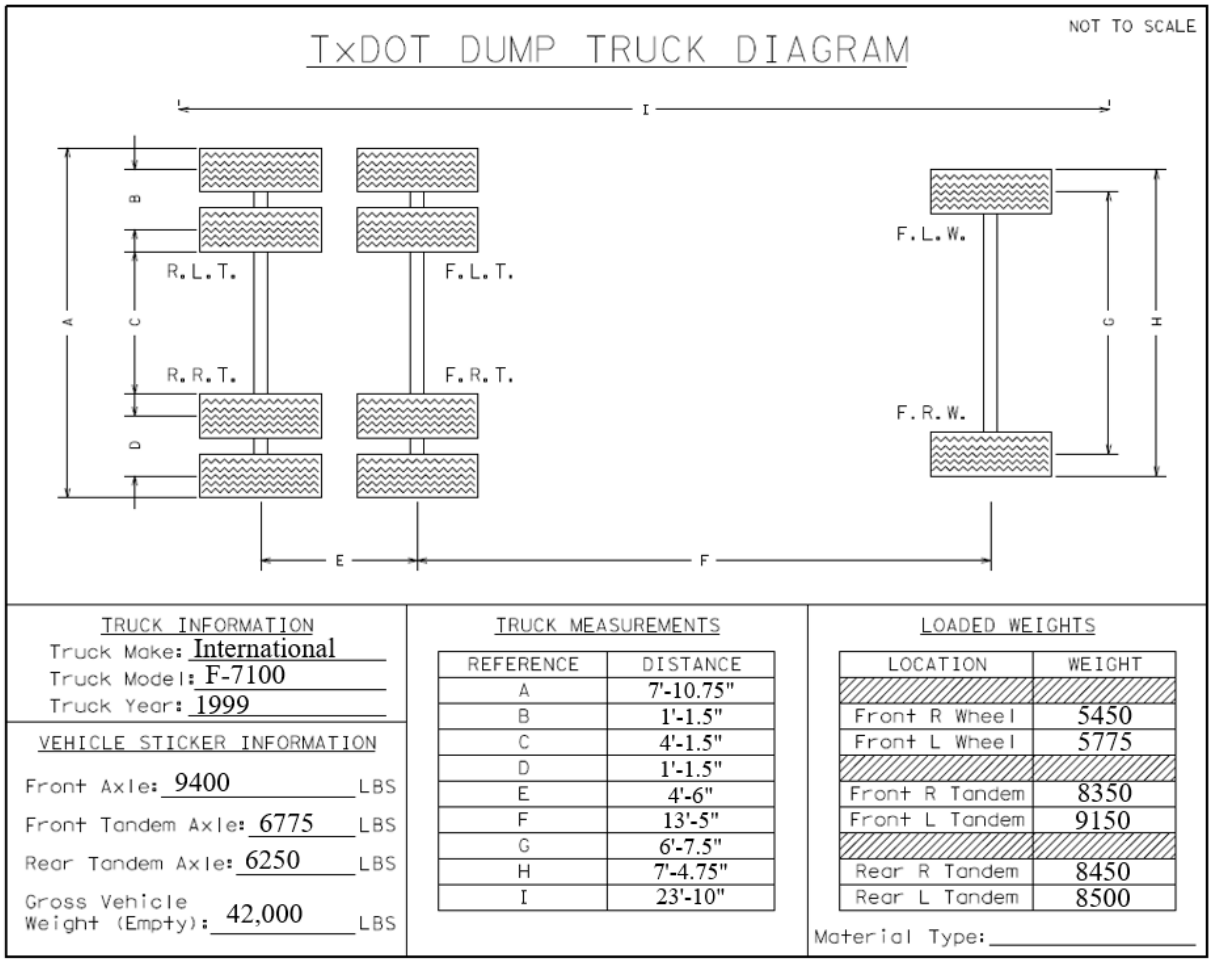

Figure 7.10. Wheel Weights and Spacings of the Loaded Dump Truck

7.5.2 Vehicle Positioning

In order to investigate the transverse load distribution between the bridge girders, three paths were determined that would be used during the testing. The first path, designated Path 1, was at a location such that the centerline of the adjacent rear tires would be 2 ft from the bridge guardrail. The second path, designated Path 2, was in the opposite lane at a location such that the centerline of the adjacent rear tires would be 2 ft from the centerline of the bridge. The third and final path, designated the Middle Path, was at a location such that the truck was straddling the centerline of the bridge. All three testing paths are shown in the bridge cross-section in Figure 7.11.

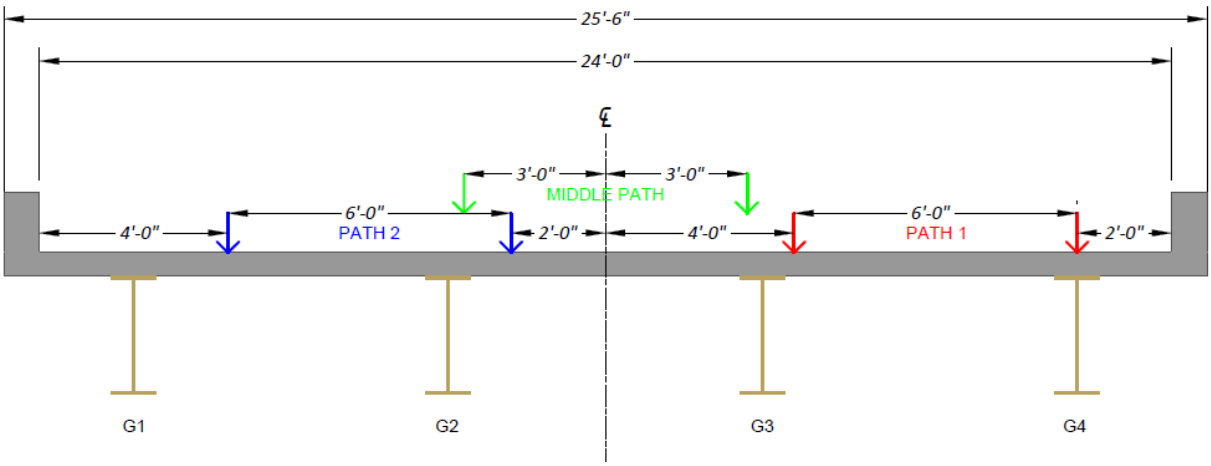

Figure 7.11. Load Test Paths for Bridge SC-12

For the static load tests, the desire was for the truck to be placed approximately at the location at which maximum moment would occur in the girders because the moment LLDFs are one of the key parameters of interest. There were two stop locations for the static load tests, one for the end span and one for the main span. Therefore, the truck was placed such that the front axle was 13 ft 5 in. from the 40 percent span point in the end span and from the midspan in the main span. This resulted in the first rear axle at either 0.4L or at the midspan for the end span and main span, respectively. This longitudinal position was used for the static tests conducted. For the crawl speed tests and the dynamic tests, the truck was run completely across the bridge without stopping.

7.5.3 Test Protocol

7.5.3.1 Static Tests

Two types of static load tests were performed on Bridge SC-12, stop location tests and crawl speed tests. The static stop location load tests began with the truck stopped before entering the bridge to record a reference data file that serves as a baseline. The truck then proceeded onto the bridge and was stopped at the longitudinal moment critical position previously described. Once the truck was stopped, data were recorded for a period of approximately five seconds. This procedure was used for each load path. The static stop location tests along Path 1, Path 2, and the Middle Path were conducted at positive moment critical positions of the end span and the main span, resulting in a total of six stop location tests.

The static crawl speed tests began with the truck stopped before entering the bridge to record a reference data file that serves as a baseline. The truck then proceeded at an idle speed of approximately 2 mph across the full length of the bridge while data were recorded for the entire time. This procedure was used along the three previously described transverse load paths.

*7.5.3.2 **Dynamic Tests***

The dynamic tests began with the truck stopped at some distance away from the bridge. At that time, a reference data file was recorded. The truck then proceeded at a specific speed across the entire length of the bridge while data were recorded during the passage of the vehicle. This procedure was used along each load path. Two different dynamic tests were performed along Path 1 and Path 2. The first dynamic test was performed at approximately 30 mph, and the second dynamic test was performed at 37 mph to 44 mph. Three dynamic tests were performed along the Middle Path at 30 mph, 44 mph, and 57 mph. These speeds were chosen based on a variety of factors, including the speed limit of the road (60 mph), the estimated speed at which a heavy vehicle might drive over the bridge, and the comfort level of the truck driver going at certain speeds along the load paths.

*7.5.3.3 **Impact Tests***

In order to obtain more information about the dynamic properties of the bridge, a sledgehammer was used to strike the top of the bridge deck in nine different locations. The sledgehammer tests were performed at 40 percent of the span length away from the abutment for the end span and at the midspan and quarter span for the main span. The sledgehammer tests were performed at three transverse positions at each of these longitudinal positions: at the north edge, centerline, and south edge of the bridge. Although all the instruments were in place while data were being recorded during these three impact tests, only accelerometer measurements were used to identify dynamic characteristics. The impact excitation may provide a more accurate way of measuring bridge dynamic characteristics because unlike a vehicle excitation, the impact excitation does not introduce additional mass and dynamic interaction with the bridge. Table 7.3 summarizes all the tests that were performed on Bridge SC-12.

Table 7.3. Test Protocol for Bridge SC-12 Testing

Test Number	Test Location	Test Type
1	Path 1—Span 1	Static—Stop Location (Engine Off)
2	Path 1—Span 2	Static—Stop Location (Engine Off)
3	Path 1	Static—Crawl (2 mph)
4	Path 1	Dynamic (30 mph)
5	Path 1	Dynamic (37 mph)
6	Path 2—Span 1	Static—Stop Location (Engine Off)
7	Path 2—Span 2	Static—Stop Location (Engine Off)
8	Path 2	Static—Crawl (2 mph)
9	Path 2	Dynamic (29 mph)
10	Path 2	Dynamic (44 mph)
11	Middle Path—Span 1	Static—Stop Location (Engine Off)
12	Middle Path—Span 2	Static—Stop Location (Engine Off)
13	Middle Path	Static—Crawl (2 mph)
14	Middle Path	Dynamic (30 mph)
15	Middle Path	Dynamic (44 mph)
16	Middle Path	Dynamic (57 mph)
17	Span 1—North Edge	Sledgehammer
18	Span 1—Centerline	Sledgehammer
19	Span 1—South Edge	Sledgehammer
20	Span 2—Midspan—North Edge	Sledgehammer
21	Span 2—Midspan—Centerline	Sledgehammer
22	Span 2—Midspan—South Edge	Sledgehammer
23	Span 2—Quarter span—North Edge	Sledgehammer
24	Span 2—Quarter span—Centerline	Sledgehammer
25	Span 2—Quarter span—South Edge	Sledgehammer

7.5.4 Test Operations

The test program for Bridge SC-12 was conducted from June 18, 2019, to June 20, 2019. This process included all instrumentation installation, load testing, and instrumentation removal.

The clearance height of Bridge SC-12 is approximately 26 ft. Therefore, three-story scaffolding platforms were set up below the bridge to provide a working platform for instrumentation installation. To install strain gauges, an approximately 2 in. by 4 in. area at the desired location of the strain gauge was ground using an angle grinder to remove any loosely bonded adherent such as paint, rust, and oxides. This location was then sanded using 150- and 220-

grit sandpaper to obtain a smooth surface. Conditioner (acetone) was applied repeatedly, and the surface was scrubbed with paper towels until a clean tip was no longer discolored by the scrubbing. Liberally applying acetone brought the surface condition back to an optimum alkalinity of 7.0 to 7.5 pH for ideal bonding of the glue. The strain gauges were then glued using CN adhesive. Figure 7.12(a) shows an example of installed strain gauges on the girders. String potentiometers were attached to either wood posts or small pieces of wood, which were attached to rocks in the streambed or glued to the sloped abutment, respectively. Figure 7.12(c) shows the installation of the string potentiometers in the streambed and on the abutment. The string potentiometers were fixed by attaching fishing wire to metal hooks attached to the girders by using magnets. Accelerometers were attached to the bottom flange of the appropriate girders by magnets. Figure 7.12(b) shows an example of an installed accelerometer and string potentiometer on a girder.

The load testing took place on June 20, 2019. Traffic control was provided by the TxDOT Brownwood District office while the testing took place. The dump truck was loaded and weighed at the TxDOT Lampasas Maintenance Office in the morning, while members of the research team marked the test paths and the static test stop locations on the bridge using chalk. The previously described tests in the test protocol were performed while data from the installed instruments were recorded during each test period. Once the testing was completed, the instrumentation was removed from the bridge, and traffic control ceased. Figure 7.13(a) shows the scaffolding setup for instrumentation installation and Figure 7.13(b) shows the test truck on the bridge during a load test.

(a) Example of Installed Strain Gauges

(b) Example of Installed Accelerometer

(c) Example of an Installed String Potentiometer

Figure 7.12. Installed Instrumentation on Bridge SC-12

(a) Instrumentation of Bridge SC-12

(b) Test Truck at the Stop Location for Path 2 – Span 1

Figure 7.13. Instrumentation and Testing of Bridge SC-12

7.6 TEST RESULTS FOR BRIDGE SC-12

Two types of diagnostic tests were conducted following the guidelines provided in AASHTO MBE (AASHTO 2018): (1) static load tests using stationary loads (avoiding bridge vibrations) to obtain static strains and deflections and infer composite action and LLDFs, and (2) dynamic load tests with moving loads that excite vibrations in the bridge to measure modes of vibration, frequencies, and dynamic amplification.

The data obtained during testing were compiled, processed, and analyzed. Strains were measured using strain gauges, which allowed stresses to be inferred. Deflections were measured using string potentiometers, which were used to infer transverse load distribution. Accelerations were measured using accelerometers, which were processed to obtain natural frequencies and mode shapes of the bridge. Videos taken during testing using computer vision were used to determine deflections and compared with the string potentiometer measurements. NDE results were also compiled to obtain in situ compressive strength of the concrete bridge deck.

Because Bridge SC-12 is three-span continuous, the strain measurements and deflection measurements are presented in two sections: (1) examining end Span 1 data while Span 1 is loaded and (2) examining main Span 2 data while Span 2 is loaded. The stop location test data shown are those data from the same span on which the truck is loaded. The crawl test data shown are the maximum recorded results when the truck is on the specified span.

7.6.1 Static Load Tests on Bridge SC-12 Span 1

Two types of static load tests were conducted: (1) stop location tests by parking the vehicle at the moment critical longitudinal position in each span for each selected path on the bridge, and (2) crawl speed tests by moving the truck at low speeds (approximately 2 mph) along the same predefined paths.

7.6.1.1 Strain Measurements and Composite Action

After obtaining strain gauge data from the load testing, the maximum bottom flange strains were plotted along with their corresponding top flange strains at the same moment in time. In all strain figures, the measured strain values are shown by a colored dot symbol. The colored line connecting two dot symbols represents the strain diagram at this cross-section based on the assumption that the plane section remains plane. The blue plot shows the strain results for the pier location, the red

plot shows the strain results for Span 1, and the green plot shows the strain results for Span 2. It is important to note that all strain values were taken at the same point in time as the maximum bottom flange strain value for the span being considered.

Interior Girder G3. Figure 7.14 through Figure 7.16 provide plots of the measured strains for interior Girder G3 during static load testing. The strains measured for Girder G3 during the Path 1—Span 1 static tests are shown in Figure 7.14. Figure 7.14(a) shows the maximum strains observed during the stop location test for Girder G3 adjacent to the interior pier and midspan of Span 2. Figure 7.14(b) shows the maximum strains observed during the stop location test for Girder G3 at 0.4*L* of Span 1. Figure 7.14(c) shows the maximum strains observed during the crawl speed test for Girder G3 adjacent to the interior pier and midspan of Span 2. Figure 7.14(d) shows the maximum strains observed during the crawl speed test for Girder G3 at 0.4*L* of Span 1. The corresponding observed Span 1 stresses for Girder G3 are 4.49 ksi for the stop location test and 4.42 ksi for the crawl speed test. The observed neutral axis locations at the midspan are 17.77 in. from the bottom of the girder for the stop location test and 17.34 in. from the bottom of the girder for the crawl speed test.

The strains measured for Girder G3 during the Path 2—Span 1 static tests are shown in Figure 7.15. Figure 7.15(a) shows the maximum strains observed during the stop location test for Girder G3 adjacent to the interior pier and midspan of Span 2. Figure 7.15(b) shows the maximum strains observed during the stop location test for Girder G3 at 0.4*L* of Span 1. Figure 7.15(c) shows the maximum strains observed during the crawl speed test for Girder G3 adjacent to the interior pier and midspan of Span 2. Figure 7.15(d) shows the maximum strains observed during the crawl speed test for Girder G3 at 0.4*L* of Span 1. The corresponding observed midspan stresses for Girder G3 are 2.23 ksi for the stop location test and 2.07 ksi for the crawl speed test. The observed neutral axis locations at the midspan are 20.10 in. from the bottom of the girder for the stop location test and 20.51 in. from the bottom of the girder for the crawl speed test.

The strains measured for Girder G3 during the Middle Path static tests are shown in Figure 7.16. Figure 7.16(a) shows the maximum strains observed during the stop location test for Girder G3 adjacent to the interior pier and midspan of Span 2. Figure 7.16(b) shows the maximum strains observed during the stop location test for Girder G3 at 0.4*L* of Span 1. Figure 7.16(c) shows the maximum strains observed during the crawl speed test for Girder G3 adjacent to the interior pier and midspan of Span 2. Figure 7.16(d) shows the maximum strains observed during the crawl

speed test for Girder G3 at 0.4*L* of Span 1. The corresponding observed midspan stresses for Girder G3 are 3.59 ksi for the stop location test and 3.66 ksi for the crawl speed test. The observed neutral axis locations at the midspan are 18.28 in. from the bottom of the girder for the stop location test and 17.61 in. from the bottom of the girder for the crawl speed test.

The live load stress levels for interior Girder G3 when locating the test truck on the three considered paths are relatively low. In addition, the neutral axis locations based on the strain measurements over the section depth at 0.4*L* of Girder G3 indicate that partial composite action between the girder and concrete deck could be taking place. In Span 2, a small negative moment is occurring in Girder G3, and the neutral axis is higher than the theoretical non-composite neutral axis of 14.9 in. from the bottom of the girder.

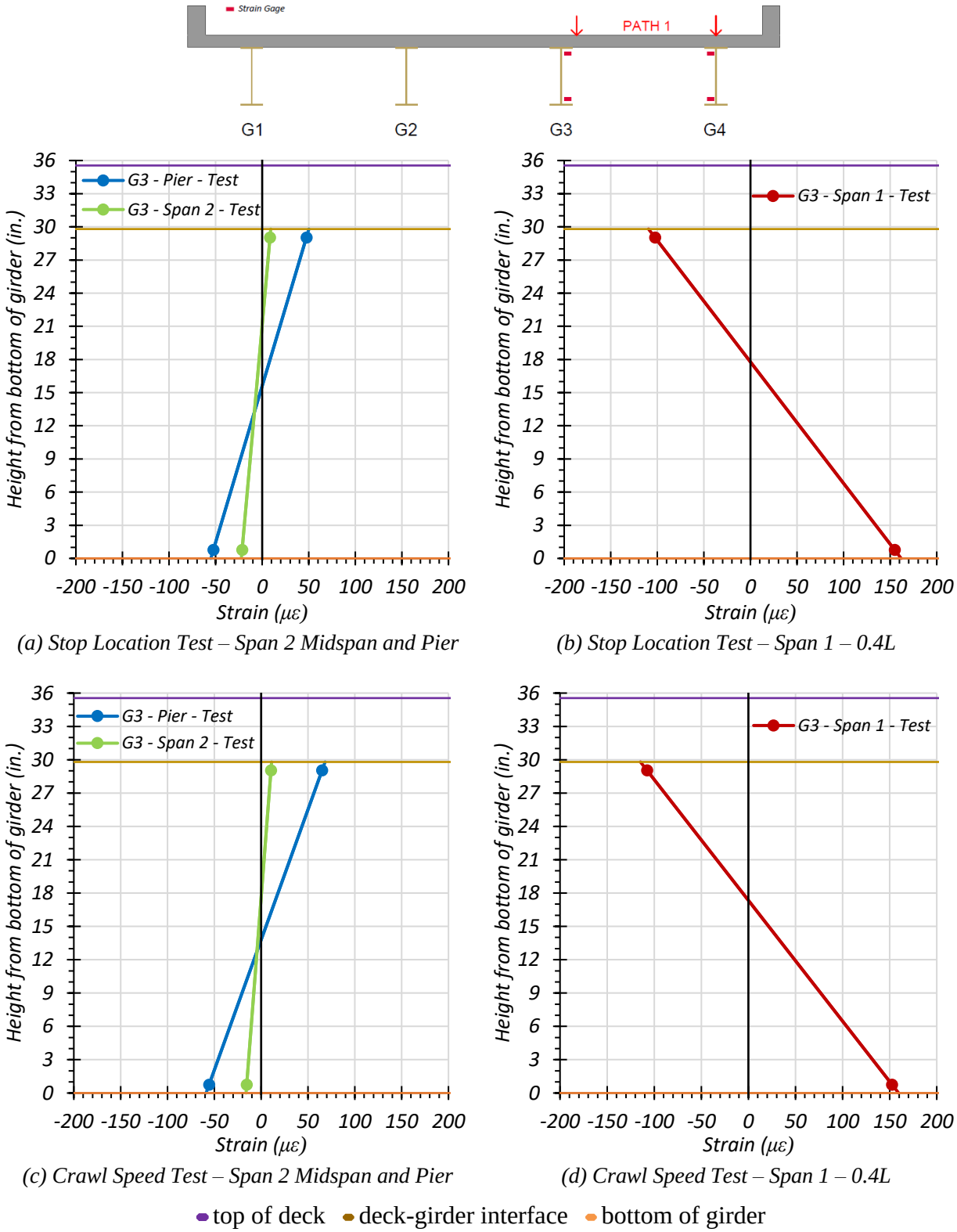

Figure 7.14. Static Strains for Interior Girder G3: Path 1—Span 1

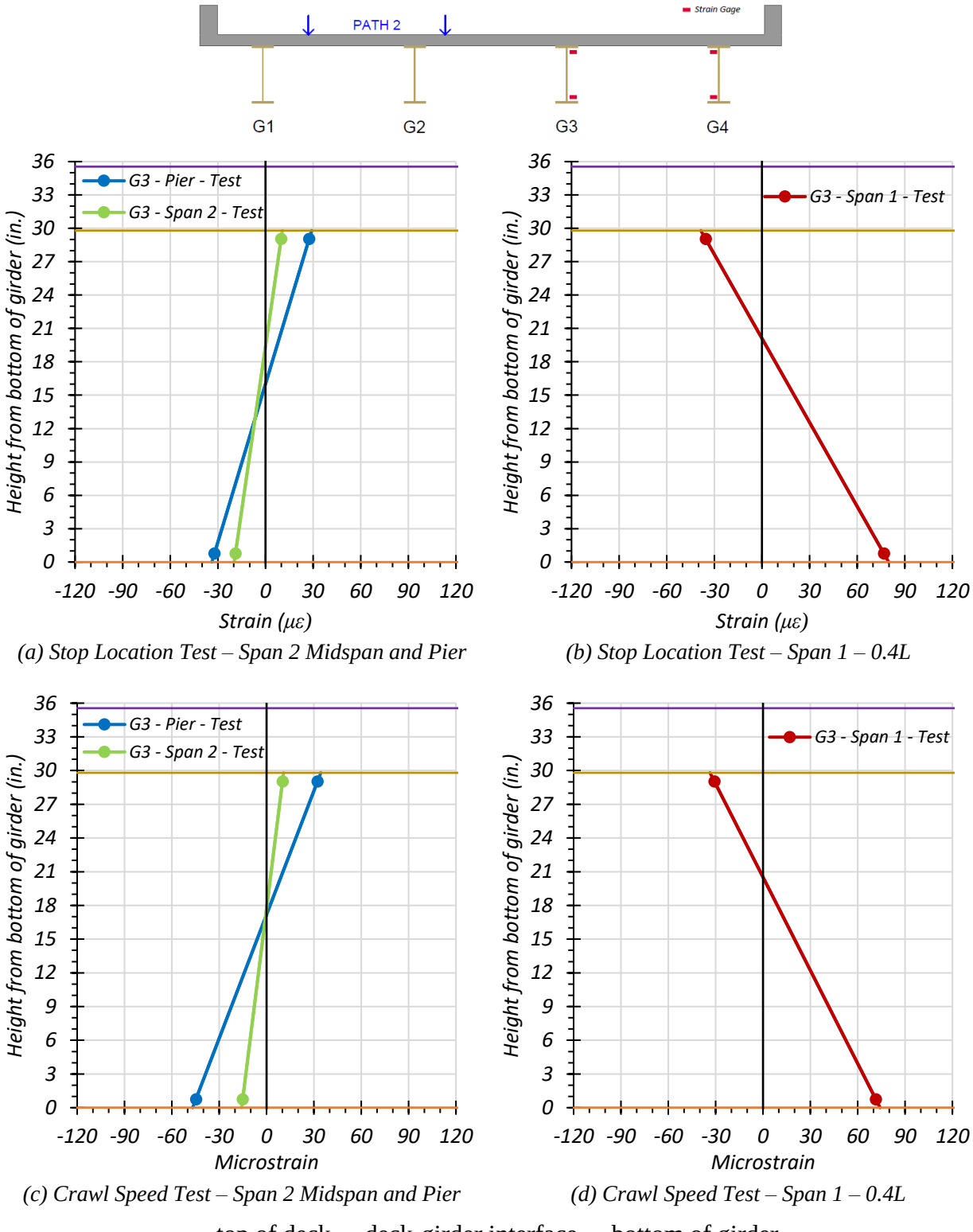

(a) Stop Location Test – Span 2 Midspan and Pier

(b) Stop Location Test – Span 1 – 0.4L

(c) Crawl Speed Test – Span 2 Midspan and Pier

(d) Crawl Speed Test – Span 1 – 0.4L

Figure 7.15. Static Strains for Interior Girder G3: Path 2—Span 1

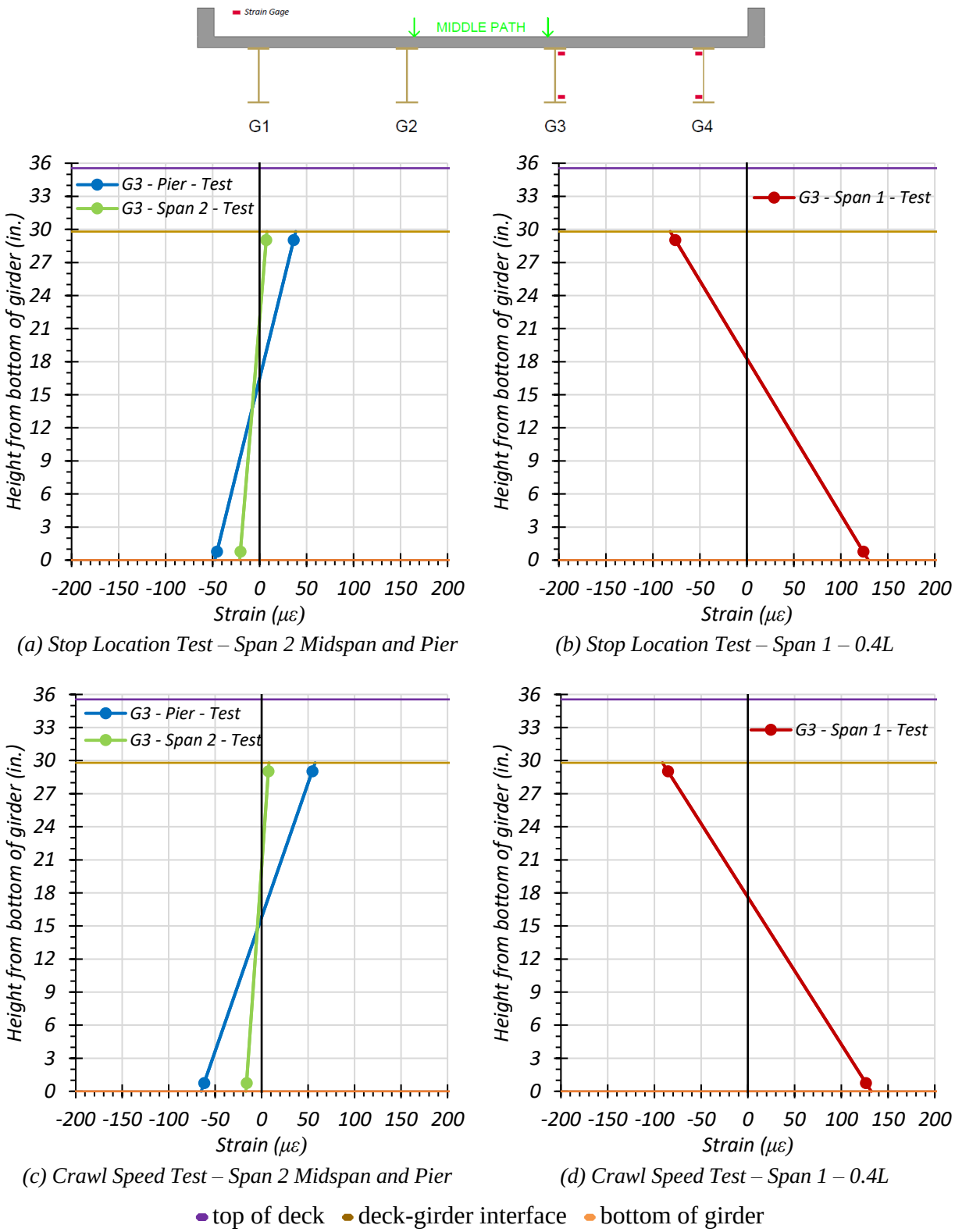

(a) Stop Location Test – Span 2 Midspan and Pier

(b) Stop Location Test – Span 1 – 0.4L

(c) Crawl Speed Test – Span 2 Midspan and Pier

(d) Crawl Speed Test – Span 1 – 0.4L

Figure 7.16. Static Strains for Interior Girder G3: Middle Path—Span 1

Exterior Girder G4. Figure 7.17 through Figure 7.19 provide plots of the measured strains for exterior Girder G4 during static load testing. The strains measured for Girder G4 during the Path 1—Span 1 static tests are shown in Figure 7.17. Figure 7.17(a) shows the maximum strains observed during the stop location test for Girder G4 at the midspan of Span 2 and adjacent to the interior pier. Figure 7.17(b) shows the maximum strains observed during the stop location test for Girder G4 at 0.4*L* of Span 1. Figure 7.17(c) shows the maximum strains observed during the crawl speed test for Girder G4 at the midspan of Span 2 and adjacent to the pier. Figure 7.17(d) shows the maximum strains observed during the crawl speed test for Girder G4 at 0.4*L* of Span 1. The corresponding observed Span 1 stresses for Girder G4 are 5.28 ksi for the stop location test and 5.34 ksi for the crawl speed test. The observed neutral axis locations at 0.4*L* are 17.42 in. from the bottom of the girder for the stop location test and 17.41 in. from the bottom of the girder for the crawl speed test.

The strains measured for Girder G4 during the Path 2—Span 1 static tests are shown in Figure 7.18. Figure 7.18(a) shows the maximum strains observed during the stop location test for Girder G4 adjacent to the interior pier and midspan of Span 2. Figure 7.18(b) shows the maximum strains observed during the stop location test for Girder G4 at 0.4*L* of Span 1. Figure 7.18(c) shows the maximum strains observed during the crawl speed test for Girder G4 adjacent to the interior pier and midspan of Span 2. Figure 7.18(d) shows the maximum strains observed during the crawl speed test for Girder G4 at the 40 percent point of Span 1. The corresponding observed stresses for Girder G4 are 0.67 ksi for the stop location test and 0.43 ksi for the crawl speed test. The observed neutral axis locations at 0.4*L* are 16.50 in. from the bottom of the girder for the stop location test and 15.22 in. from the bottom of the girder for the crawl speed test.

The strains measured for Girder G4 during the Middle Path static tests are shown in Figure 7.19. Figure 7.19(a) shows the maximum strains observed during the stop location test for Girder G4 adjacent to the interior pier and midspan of Span 2. Figure 7.19(b) shows the maximum strains observed during the stop location test for Girder G4 at 0.4*L* of Span 2. Figure 7.19(c) shows the maximum strains observed during the crawl speed test for Girder G4 adjacent to the interior pier and midspan of Span 2. Figure 7.19(d) shows the maximum strains observed during the crawl speed test for Girder G4 at 0.4*L* of Span 1. The corresponding observed stresses for Girder G4 are 2.00 ksi for the stop location test and 2.05 ksi for the crawl speed test. The observed neutral axis

locations at 0.4*L* are 17.65 in. from the bottom of the girder for the stop location test and 16.53 in. from the bottom of the girder for the crawl speed test.

The live load stress levels for interior Girder G4 when locating the test truck on the three considered paths are relatively low. In addition, the neutral axis locations, based on the strain measurements over the section depth at 0.4*L* of Girder G4, indicate that partial composite action between the girder and concrete deck could be taking place. In Span 2, a small negative moment is occurring in Girder G4, and the neutral axis is higher than the theoretical non-composite neutral axis of 14.9 in. from the bottom of the girder.

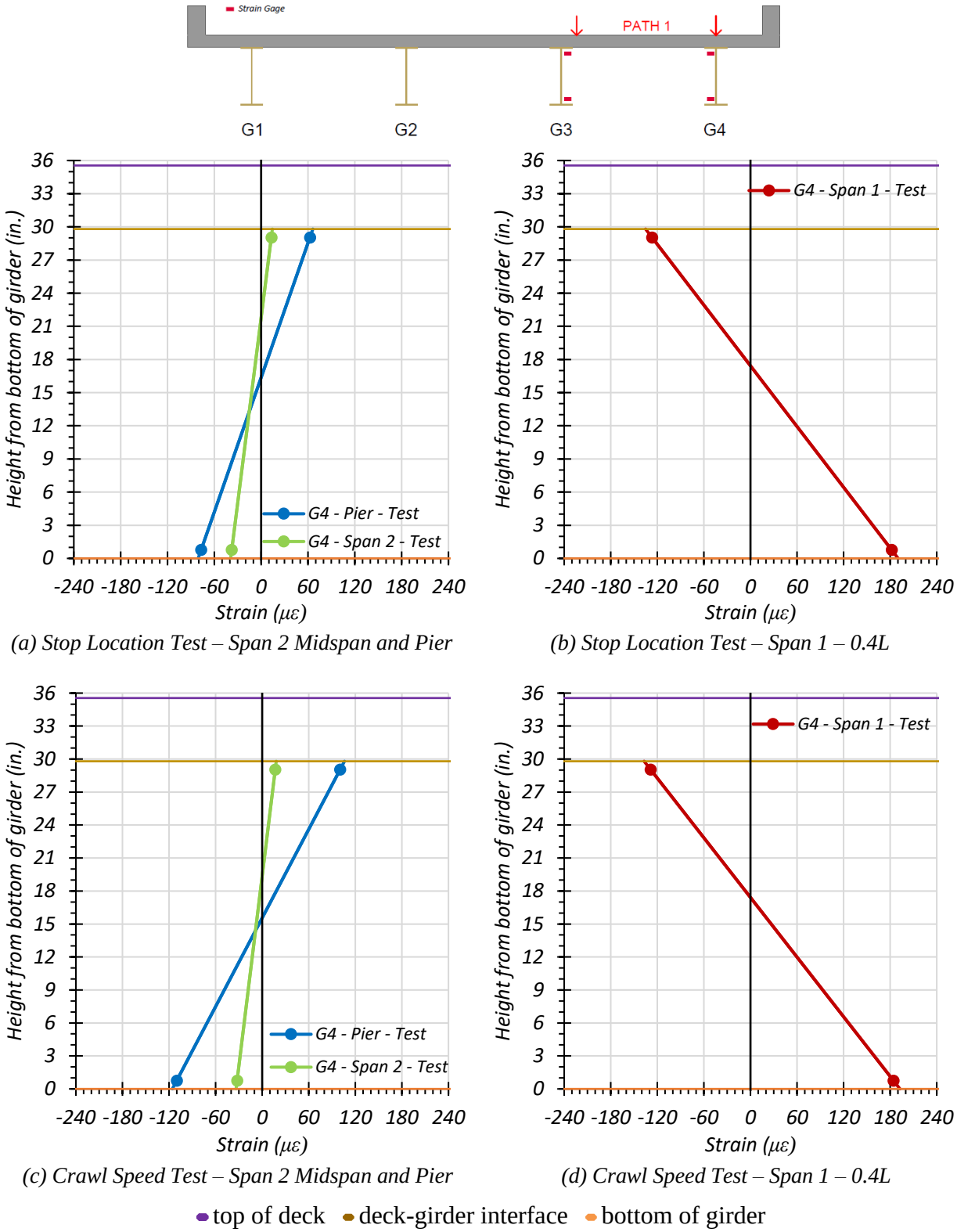

(a) Stop Location Test – Span 2 Midspan and Pier

(b) Stop Location Test – Span 1 – 0.4L

(c) Crawl Speed Test – Span 2 Midspan and Pier

(d) Crawl Speed Test – Span 1 – 0.4L

Figure 7.17. Static Strains for Exterior Girder G4: Path 1—Span 1

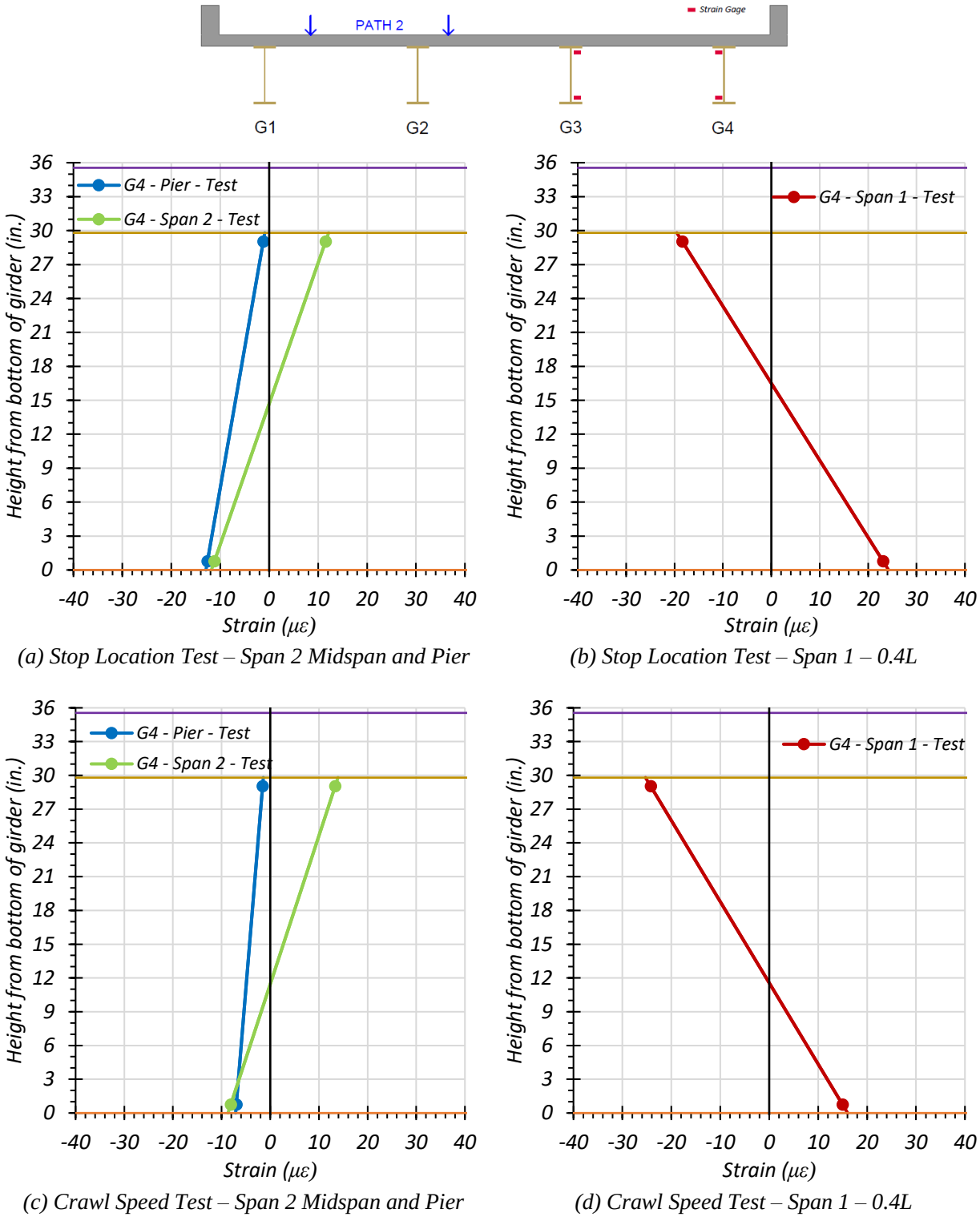

(a) Stop Location Test – Span 2 Midspan and Pier

(b) Stop Location Test – Span 1 – 0.4L

(c) Crawl Speed Test – Span 2 Midspan and Pier

(d) Crawl Speed Test – Span 1 – 0.4L

Figure 7.18. Static Strains for Exterior Girder G4: Path 2—Span 1

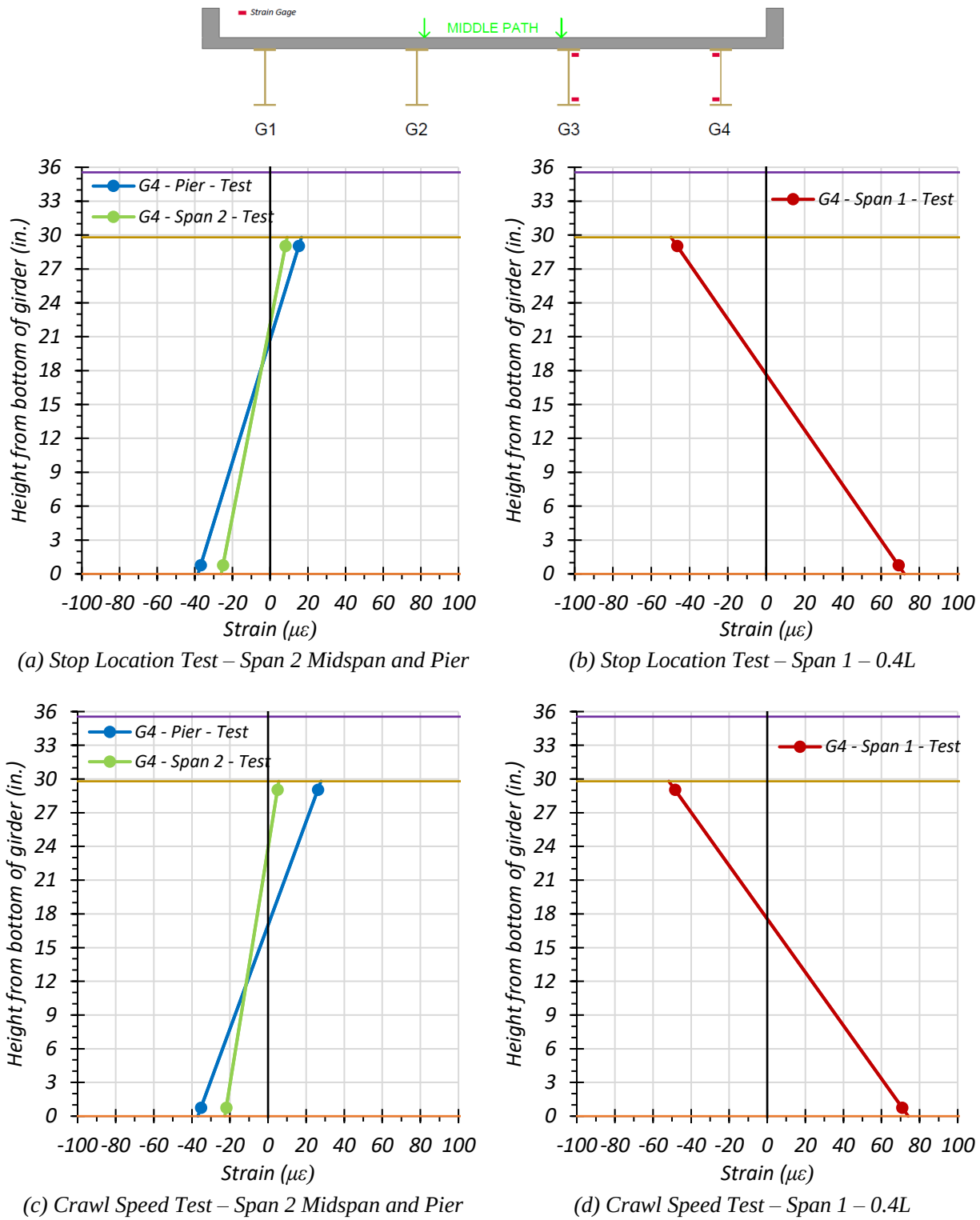

(a) Stop Location Test – Span 2 Midspan and Pier

(b) Stop Location Test – Span 1 – 0.4L

(c) Crawl Speed Test – Span 2 Midspan and Pier

(d) Crawl Speed Test – Span 1 – 0.4L

Figure 7.19. Static Strains for Exterior Girder G4: Middle Path—Span 1

Comparison of Measured Strain Results. Table 7.4 and Figure 7.20 show the neutral axis locations measured for all static load tests in Span 1. The average test neutral axis was 18.60 in. from the bottom of the girder for Girder G3 and 16.79 in. from the bottom of the girder for Girder G4. The neutral axis values based on the strain measurements tend to increase as the loading on the girder increases. The measured values from the test truck loading indicate neutral axis values between the theoretical composite and the theoretical non-composite neutral axes. The theoretical values are based on the parallel axis theorem using the updated geometric material properties determined during testing. These values include an f_c' of 6.25 ksi and a corresponding concrete MOE of 4506 ksi. The effective deck width used for the interior girder and exterior girder is 5 ft 9 in., determined using Article 10.38.3 in the *AASHTO Standard Specifications* (AASHTO 2002). Reinforcing steel is not included in this calculation. The results show that Bridge SC-12 is likely providing some degree of partial composite action between the steel girders and concrete deck for positive bending.

In negative bending, the theoretical non-composite neutral axis is the same as the theoretical non-composite axis in positive bending, 14.90 in. from the bottom of the girder. The theoretical composite neutral axis will be influenced by the presence of reinforcing steel in the deck. The longitudinal reinforcement in the deck is unknown, so for this calculation, transverse bar sizes of #5 bars and spacing of 12.25 in. were used. This process was also detailed in Task 4 of this project as well. The theoretical composite neutral axis in negative bending is also shown in Table 7.4.

Table 7.4. Measured Neutral Axis Locations for All Span 1 Static Load Tests

Test	G3 Neutral Axis Location (in. from bottom of girder)	G4 Neutral Axis Location (in. from bottom of girder)
Path 1—Stop Location	17.77	17.42
Path 1—Crawl Speed	17.34	17.41
Path 2—Stop Location	20.10	16.50
Path 2—Crawl Speed	20.51	15.22
Middle Path—Stop Location	18.28	17.65
Middle Path—Crawl Speed	17.61	16.53
Theoretical Non-Composite	14.90	14.90
Theoretical Composite—Positive Bending	26.11	26.11
Theoretical Composite—Negative Bending	16.66	16.66

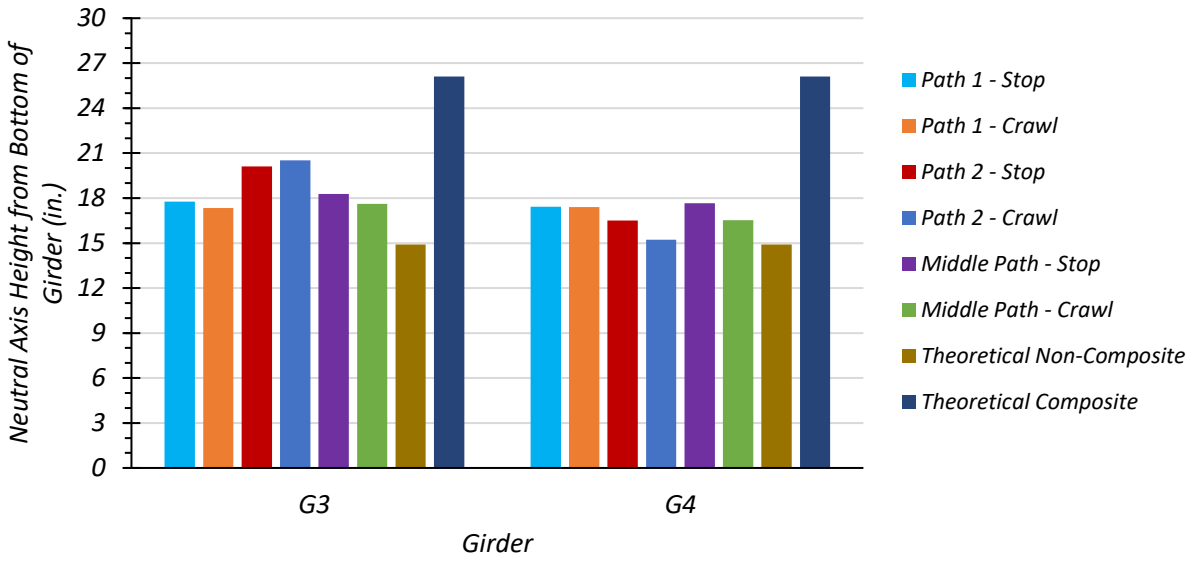

Figure 7.20. Test Neutral Axis Locations for Span 1 Loading

Table 7.5 and Figure 7.21 show the maximum bottom flange stresses observed during Span 1 testing inferred from the measured strains and an assumed elastic modulus for the steel of 29,000 ksi. The maximum tension stress in Girder G4 was 5.58 ksi from the Path 1 crawl speed test. The maximum tension stress in Girder G3 was 4.69 ksi from the Path 1 stop location test.

Table 7.5. Maximum Static Test Bottom Flange Stresses (ksi) for Span 1 Loading

Load Path	Interior Girder G3		Exterior Girder G4	
	Stop Location Test	Crawl Speed Test	Stop Location Test	Crawl Speed Test
Path 1	4.69	4.63	5.52	5.58
Path 2	2.32	2.15	0.70	0.59
Middle Path	3.75	3.83	2.09	2.22

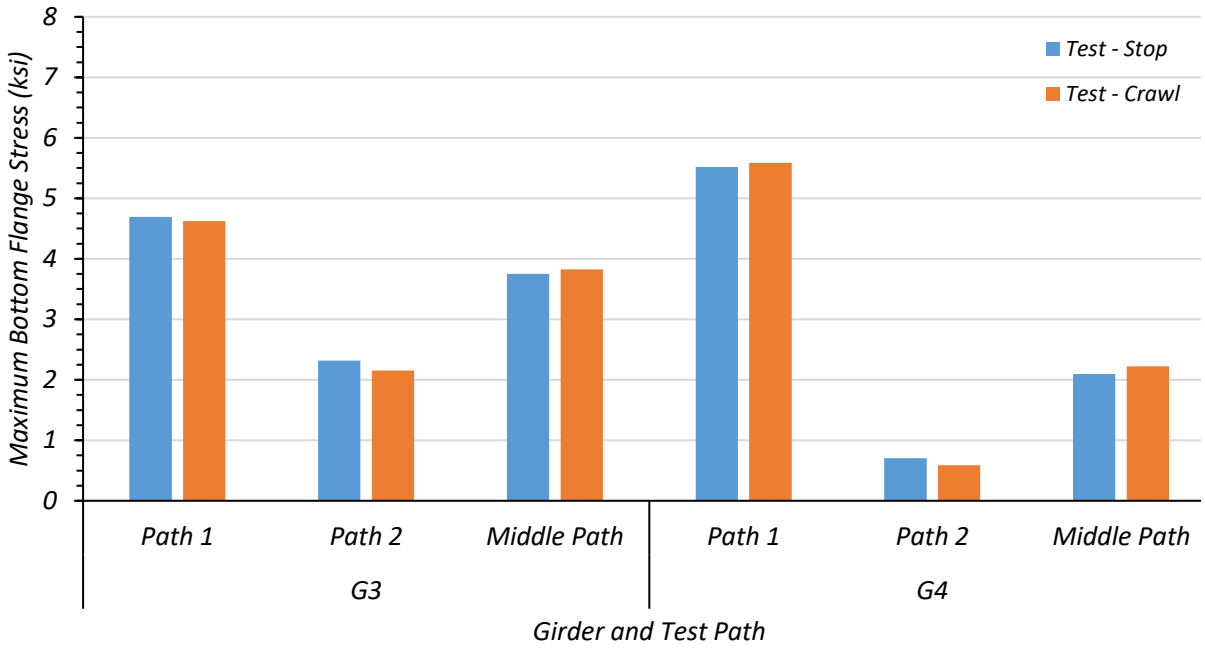

Figure 7.21. Comparison of Maximum Test Bottom Flange Stresses for Span 1 Loading

*7.6.1.2 **Deflection Measurements and LLDFs***

Path 1 Loading. Table 7.6 shows the measured girder deflections at 0.4*L* during testing for the stop location test and crawl speed test along Path 1—Span 1. The associated LLDFs, determined using the measured deflections at 0.4*L*, are also provided.

Table 7.6. Experimental Deflections and LLDFs for Path 1—Span 1 Loading

Description	G1	G2	G3	G4
Stop Location Test Disp. (in.)	0.023	0.176	0.351	0.485
Stop Location Test LLDF	0.023	0.170	0.339	0.468
Crawl Speed Test Disp. (in.)	0.016	0.167	0.342	0.481
Crawl Speed Test LLDF	0.016	0.166	0.340	0.478
Note: 1 – G = girder, Disp. = Displacement 2 – LLDF values are based on 0.4*L* deflections.				

Table 7.7 compares the maximum experimental LLDFs based on deflections at 0.4*L* to those calculated using the *AASHTO Standard Specifications*, the *AASHTO LRFD Specifications* determined using the simplified stiffness parameter, and the *AASHTO LRFD Specifications* determined using the analytical stiffness parameter (AASHTO 2002, 2017). Note that the LLDF expressions in the *AASHTO LRFD Specifications* (AASHTO 2017) consider a multiple presence factor m of 1.2 for one-lane loading and 1.0 for two-lane loading. For this reason, the LLDF values computed for interior girders were divided by 1.2 for comparison to the *AASHTO Standard Specifications* LLDFs and measured LLDFs, which are for a one-lane loaded condition. The maximum g_{AASHTO_Std}/g_{test} ratios are above 1.0, ranging from 1.23 to 1.40. The maximum g_{AASHTO_S}/g_{test} ratios are above 1.0, ranging from 1.11 to 1.41. The maximum g_{AASHTO_K}/g_{test} ratios are also above 1.0, ranging from 1.08 to 1.41. These results indicate all three AASHTO methods to determine LLDFs are conservative for Path 1—Span 1 loading.

Table 7.7. LLDF Comparison with AASHTO for Path 1—Span 1 Loading

Test and Girder Type	AASHTO Standard Specs ($g^m_{AASHTO\_Std}$)	AASHTO LRFD Simplified ($g^m_{AASHTO\_S}$)	AASHTO LRFD K_g Calculated ($g^m_{AASHTO\_K}$)	Test (g^m_{test})	$g^m_{AASHTO\_Std}/g^m_{test}$	$g^m_{AASHTO\_S}/g^m_{test}$	$g^m_{AASHTO\_K}/g^m_{test}$
Stop Location Interior	0.476	0.377	0.368	0.339	1.40	1.11	1.09
Stop Location Exterior	0.589	0.660	0.660	0.468	1.26	1.41	1.41
Crawl Speed Interior	0.476	0.377	0.368	0.340	1.40	1.11	1.08
Crawl Speed Exterior	0.589	0.660	0.660	0.478	1.23	1.38	1.38

Figure 7.22(a) and Figure 7.22(c) show the Path 1—Span 1 stop location and crawl speed test girder deflection profiles at 0.4*L*. Figure 7.22(b) and Figure 7.22(d) show the Path 1—Span 1 stop location and crawl speed LLDFs compared to relevant AASHTO values. The governing LLDFs observed during testing are lower than the LLDFs provided by the *AASHTO Standard Specifications*, the *AASHTO LRFD Specifications* LLDFs using the simplified stiffness parameter, and the *AASHTO LRFD Specifications* LLDFs using the analytical stiffness parameter.

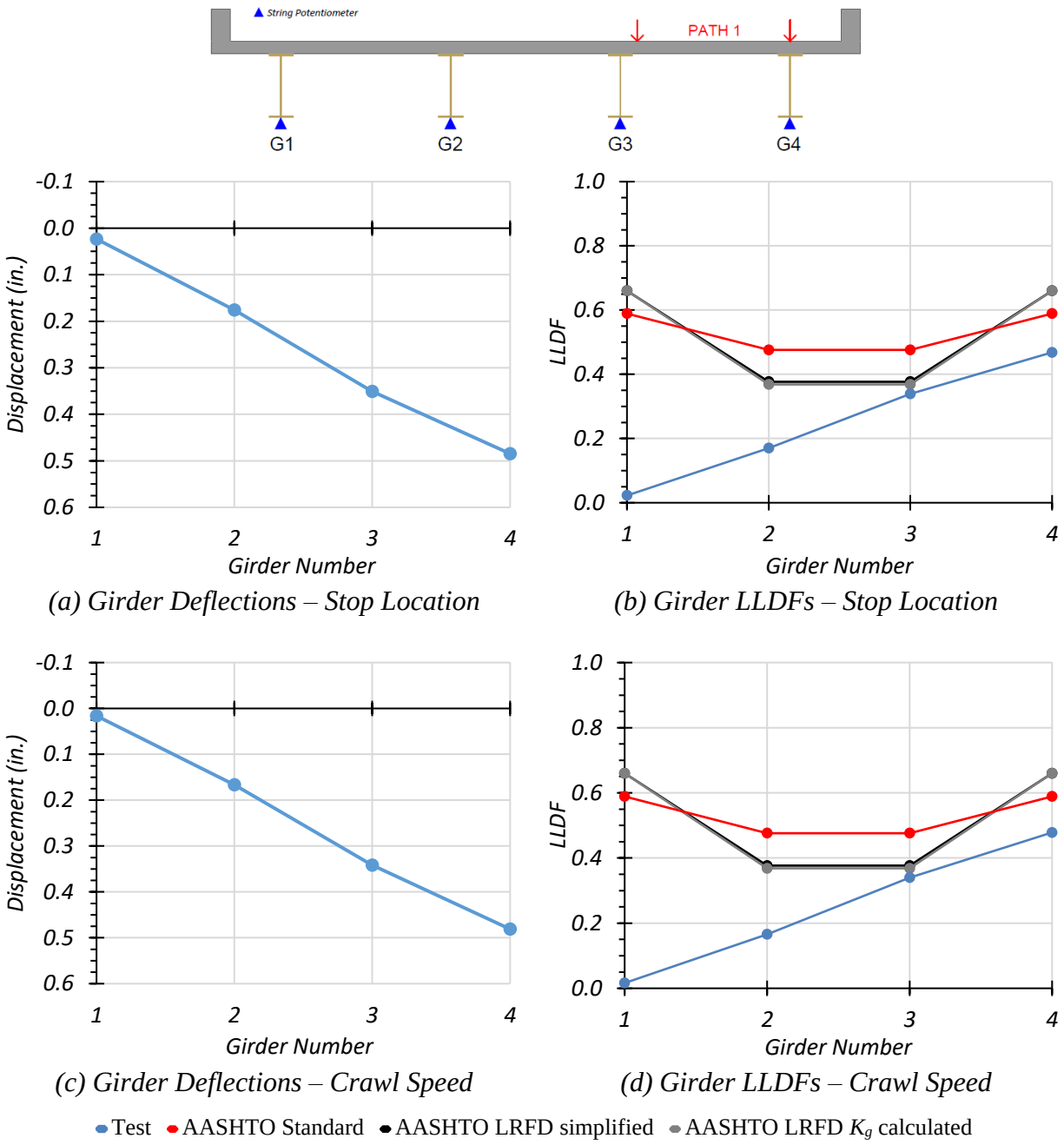

(a) Girder Deflections – Stop Location *(b) Girder LLDFs – Stop Location*

(c) Girder Deflections – Crawl Speed *(d) Girder LLDFs – Crawl Speed*

Figure 7.22. Static Deflection Results for Path 1—Span 1 Loading

Path 2 Loading. Table 7.8 shows the measured girder deflections at 0.4*L* during testing for the stop location test and crawl speed test along Path 2—Span 1. The associated LLDFs, determined using the measured deflections at 0.4*L*, are also provided.

Table 7.8. Experimental Deflections and LLDFs for Path 2—Span 1 Loading

Description	G1	G2	G3	G4
Stop Location Test Disp. (in.)	0.422	0.340	0.198	0.075
Stop Location Test LLDF	0.408	0.328	0.192	0.072
Crawl Speed Test Disp. (in.)	0.413	0.322	0.182	0.061
Crawl Speed Test LLDF	0.423	0.329	0.186	0.063
Note: 1 – G = girder, Disp. = Displacement 2 – LLDF values are based on 0.4*L* deflections.				

Table 7.9 compares the test LLDFs to those calculated using the *AASHTO Standard Specifications*, *AASHTO LRFD Specifications* determined using the simplified stiffness parameter, and *AASHTO LRFD Specifications* determined using the analytical stiffness parameter (AASHTO 2002, 2017). Note that the LLDF expressions in the *AASHTO LRFD Specifications* (AASHTO 2017) consider a multiple presence factor m of 1.2 for one-lane loading and 1.0 for two-lane loading. For this reason, the LLDF values computed for interior girders were divided by 1.2 for comparison to the *AASHTO Standard Specifications* LLDFs and measured LLDFs, which are for a one-lane loaded condition. The maximum g_{AASHTO_Std}/g_{test} ratios are above 1.0, ranging from 1.39 to 1.45. The maximum g_{AASHTO_S}/g_{test} ratios are above 1.0, ranging from 1.15 to 1.62. The maximum g_{AASHTO_K}/g_{test} ratios are also above 1.0, ranging from 1.12 to 1.62. These results indicate all three AASHTO methods to determine LLDFs are conservative for Path 2—Span 1 loading.

Table 7.9. LLDF Comparison with AASHTO for Path 2—Span 1 Loading

Test and Girder Type	AASHTO Standard Specs ($g^m_{AASHTO\_Std}$)	AASHTO LRFD Simplified ($g^m_{AASHTO\_S}$)	AASHTO LRFD K_g Calculated ($g^m_{AASHTO\_K}$)	Test (g^m_{test})	$g^m_{AASHTO\_Std}/g^m_{test}$	$g^m_{AASHTO\_S}/g^m_{test}$	$g^m_{AASHTO\_K}/g^m_{test}$
Stop Location Interior	0.476	0.377	0.368	0.328	1.45	1.15	1.12
Stop Location Exterior	0.589	0.660	0.660	0.408	1.44	1.62	1.62
Crawl Speed Interior	0.476	0.377	0.368	0.329	1.45	1.15	1.12
Crawl Speed Exterior	0.589	0.660	0.660	0.423	1.39	1.56	1.56

Figure 7.23(a) and Figure 7.23(c) show the Path 2—Span 1 stop location and crawl speed test girder deflection profiles at 0.4*L*. Figure 7.23(b) and Figure 7.23(d) show the Path 2—Span 1 stop location and crawl speed LLDFs compared to relevant AASHTO values. The governing LLDFs observed during testing are significantly lower than the LLDFs provided by the *AASHTO Standard Specifications*, the *AASHTO LRFD Specifications* LLDFs using the simplified stiffness parameter, and the *AASHTO LRFD Specifications* LLDFs using the analytical stiffness parameter.

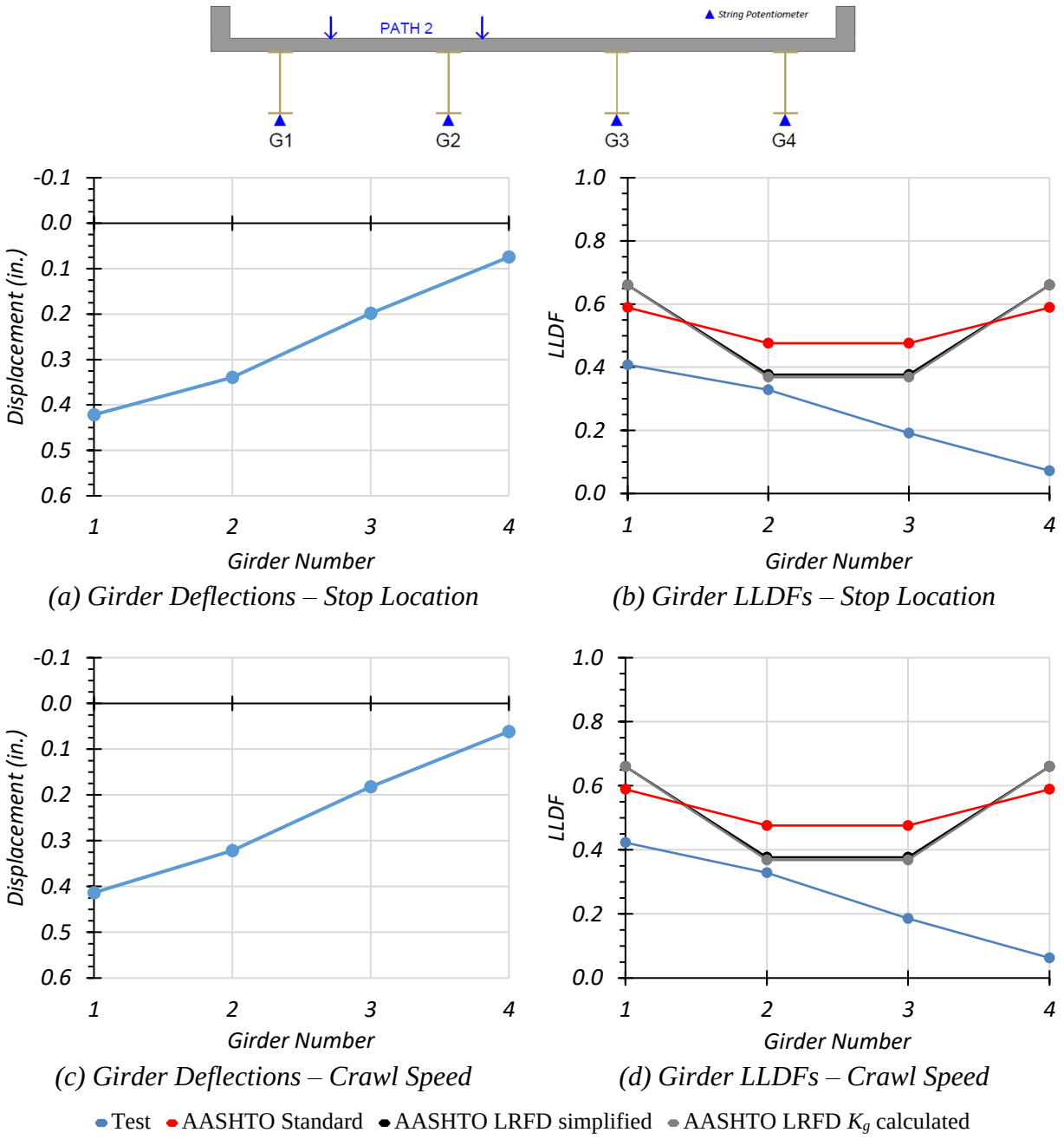

(a) Girder Deflections – Stop Location

(b) Girder LLDFs – Stop Location

(c) Girder Deflections – Crawl Speed

(d) Girder LLDFs – Crawl Speed

Figure 7.23. Static Deflection Results for Path 2—Span 1 Loading

Middle Path Loading. Table 7.10 shows the measured girder deflections at 0.4*L* during testing for the Middle Path—Span 1 stop location and crawl speed tests. The associated LLDFs, determined using the measured deflections at 0.4*L* are also provided.

Table 7.10. Experimental Deflections and LLDFs for Middle Path—Span 1 Loading

Description	G1	G2	G3	G4
Stop Location Test Disp. (in.)	0.217	0.286	0.280	0.203
Stop Location Test LLDF	0.220	0.290	0.284	0.205
Crawl Speed Test Disp. (in.)	0.201	0.278	0.280	0.211
Crawl Speed Test LLDF	0.207	0.287	0.289	0.217
Note: 1 – G = girder, Disp. = Displacement 2 – LLDF values are based on 0.4*L* deflections.				

Table 7.11 compares the test LLDFs to those calculated using the *AASHTO Standard Specifications*, *AASHTO LRFD Specifications* determined using the simplified stiffness parameter, and *AASHTO LRFD Specifications* determined using the analytical stiffness parameter (AASHTO 2002, 2017). Note that the LLDF expressions in the *AASHTO LRFD Specifications* (AASHTO 2017) consider a multiple presence factor m of 1.2 for one-lane loading and 1.0 for two-lane loading. For this reason, the LLDF values computed for interior girders were divided by 1.2 for comparison to the *AASHTO Standard Specifications* LLDFs and measured LLDFs, which are for a one-lane loaded condition. The maximum g_{AASHTO_Std}/g_{test} ratios are above 1.0, ranging from 1.64 to 2.71. The maximum g_{AASHTO_S}/g_{test} ratios are above 1.0, ranging from 1.30 to 3.04. The maximum g_{AASHTO_K}/g_{test} ratios are above 1.0, ranging from 1.27 to 3.04. These results indicate all three of the AASHTO methods to determine LLDFs are conservative for Middle Path—Span 1 loading.

Table 7.11. LLDF Comparison with AASHTO for Middle Path—Span 1 Loading

Test and Girder Type	AASHTO Standard Specs ($g^m_{AASHTO\_Std}$)	AASHTO LRFD Simplified ($g^m_{AASHTO\_S}$)	AASHTO LRFD K_g Calculated ($g^m_{AASHTO\_K}$)	Test (g^m_{test})	$g^m_{AASHTO\_Std}/g^m_{test}$	$g^m_{AASHTO\_S}/g^m_{test}$	$g^m_{AASHTO\_K}/g^m_{test}$
Stop Location Interior	0.476	0.377	0.368	0.290	1.64	1.30	1.27
Stop Location Exterior	0.589	0.660	0.660	0.220	2.68	3.00	3.00
Crawl Speed Interior	0.476	0.377	0.368	0.289	1.65	1.30	1.27
Crawl Speed Exterior	0.589	0.660	0.660	0.217	2.71	3.04	3.04

Figure 7.24(a) and Figure 7.24(c) show the Middle Path—Span 1 stop location and crawl speed test girder deflection profiles at 0.4*L*. Figure 7.24(b) and Figure 7.24(d) show the Middle Path—Span 1 stop location and crawl speed LLDFs compared to relevant AASHTO values. The governing LLDFs observed during testing are significantly lower than the LLDFs provided by the *AASHTO Standard Specifications*, the *AASHTO LRFD Specifications* LLDFs using the simplified stiffness parameter, and the *AASHTO LRFD Specifications* LLDFs using the analytical stiffness parameter.

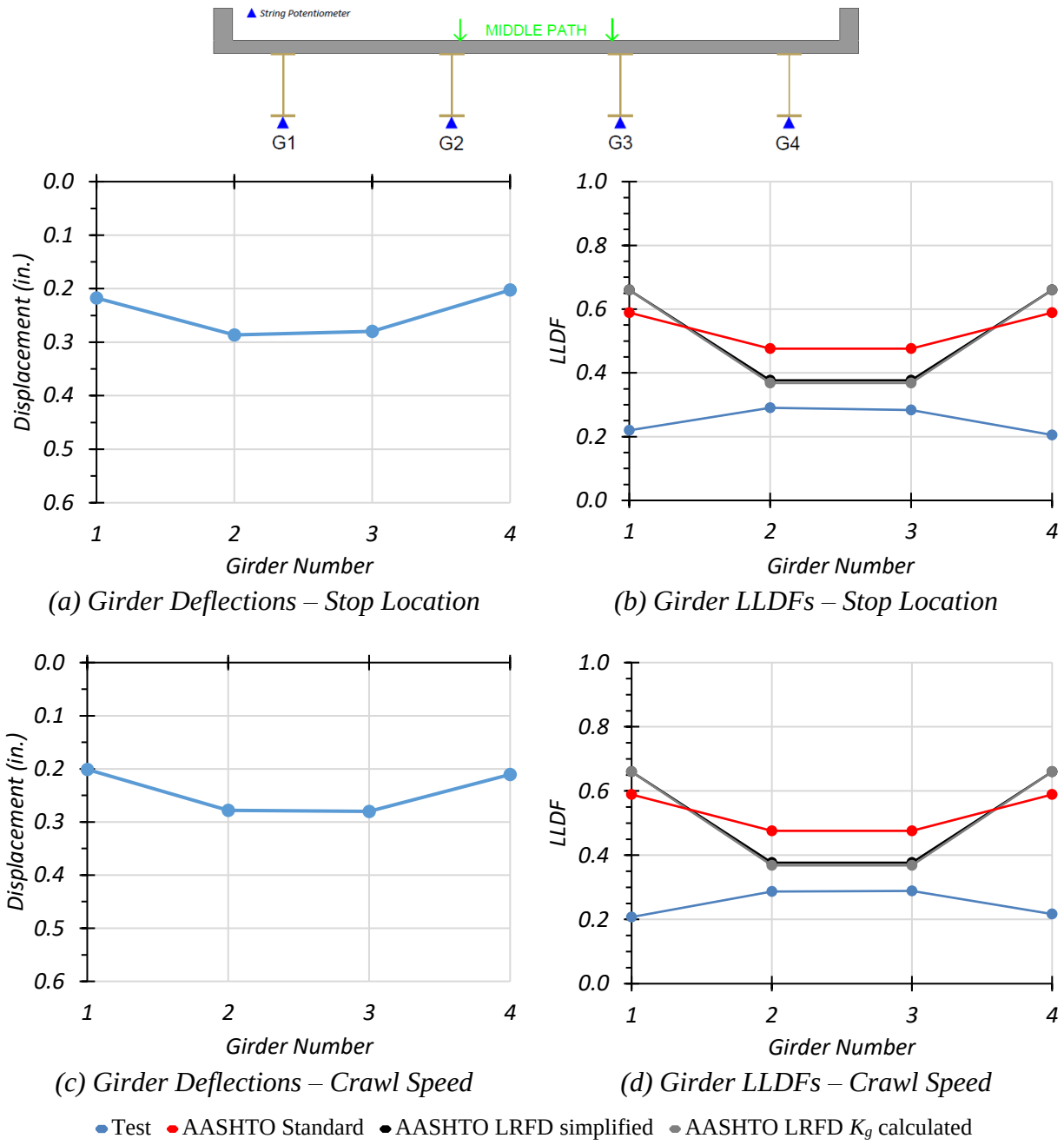

(a) Girder Deflections – Stop Location *(b) Girder LLDFs – Stop Location*

(c) Girder Deflections – Crawl Speed *(d) Girder LLDFs – Crawl Speed*

Figure 7.24. Static Deflection Results for Middle Path—Span 1 Loading

Comparison of Results Based on Deflection Measurements. For Span 1 0.4*L* location deflections, the critical LLDF for an exterior girder was 0.478, which was observed during the crawl speed test along Path 1. This result corresponds to a g_{AASHTO}/g_{test} ratio of 1.22 when using the *AASHTO Standard Specifications*, 1.38 when using the *AASHTO LRFD Specifications* determined using the simplified stiffness parameter, and 1.38 when using the *AASHTO LRFD*

Specifications determined using the analytical stiffness parameter. The critical LLDF for an interior girder was 0.340, which was also observed during the crawl speed test along Path 1. This result corresponds to a g_{AASHTO}/g_{test} ratio of 1.39 when using the *AASHTO Standard Specifications*, 1.11 when using the *AASHTO LRFD Specifications* determined using the simplified stiffness parameter, and 1.08 when using the *AASHTO LRFD Specifications* determined using the analytical stiffness parameter. During the static load tests along Path 1, the maximum LLDF was 0.461 for the stop location test, which increased to 0.478 for the crawl speed test. During the static load tests along Path 2, the maximum LLDF was 0.408 for the stop location test and increased to 0.423 for the crawl speed test. During the static load tests along Middle Path, the maximum LLDF was 0.290 for the stop location test and decreased slightly to 0.289 for the crawl speed test.

Overall, none of the AASHTO methods to determine LLDFs produced lower values than the LLDFs observed during Span 1 testing. The AASHTO methods were always conservative for Bridge SC-12, in most cases by a significant margin. These findings could possibly indicate an area through which the load rating for Bridge SC-12 could improve.

7.6.2 Static Load Tests on Bridge SC-12 Span 2

Two types of static load tests were conducted without introducing any dynamic effects: (1) stop location tests—by parking the vehicle at the moment critical longitudinal position in each span for each selected path on the bridge, and (2) crawl speed tests—by moving the truck at low speeds (around 2 mph) along the same predefined paths.

7.6.2.1 Strain Measurements and Composite Action

Interior Girder G3. Figure 7.25 through Figure 7.27 provide plots of the measured strains for interior Girder G3 during static load testing. The strains measured for Girder G3 during the Path 1—Span 2 static tests are shown in Figure 7.25. Figure 7.25(a) shows the maximum strains observed during the stop location test for Girder G3 at 0.4*L* of Span 1 and the interior pier. Figure 7.25(b) shows the maximum strains observed during the stop location test for Girder G3 at the midspan of Span 2. Figure 7.25(c) shows the maximum strains observed during the crawl speed test for Girder G3 at 0.4*L* of Span 1 and the interior pier. Figure 7.25(d) shows the maximum strains observed during the crawl speed test for Girder G3 at the midspan of Span 2. The

corresponding observed Span 2 stresses for Girder G3 are 4.50 ksi for the stop location test and 4.47 ksi for the crawl speed test. The observed neutral axis locations at the midspan are 19.97 in. from the bottom of the girder for the stop location test and 19.56 in. from the bottom of the girder for the crawl speed test.

The strains measured for Girder G3 during the Path 2—Span 2 static tests are shown in Figure 7.26. Figure 7.26(a) shows the maximum strains observed during the stop location test for Girder G3 at 0.4*L* of Span 1 and the interior pier. Figure 7.26(b) shows the maximum strains observed during the stop location test for Girder G3 at the midspan of Span 2. Figure 7.26(c) shows the maximum strains observed during the crawl speed test for Girder G3 at 0.4*L* of Span 1 and the interior pier. Figure 7.26(d) shows the maximum strains observed during the crawl speed test for Girder G3 at the midspan of Span 2. The corresponding observed midspan stresses for Girder G3 are 2.80 ksi for the stop location test and 2.68 ksi for the crawl speed test. The observed neutral axis locations at the midspan are 15.08 in. from the bottom of the girder for the stop location test and 15.32 in. from the bottom of the girder for the crawl speed test.

The strains measured for Girder G3 during the Middle Path static tests are shown in Figure 7.27. Figure 7.27(a) shows the maximum strains observed during the stop location test for Girder G3 at 0.4*L* of Span 1 and the interior pier. Figure 7.27(b) shows the maximum strains observed during the stop location test for Girder G3 at the midspan of Span 2. Figure 7.27(c) shows the maximum strains observed during the crawl speed test for Girder G3 at 0.4*L* of Span 1 and the interior pier. Figure 7.27(d) shows the maximum strains observed during the crawl speed test for Girder G3 at the midspan of Span 2. The corresponding observed midspan stresses for Girder G3 are 3.86 ksi for the stop location test and 3.86 ksi for the crawl speed test. The observed neutral axis locations at the midspan are 15.88 in. from the bottom of the girder for the stop location test and 15.45 in. from the bottom of the girder for the crawl speed test.

The live load stress levels for interior Girder G3 when locating the test truck on the three considered paths are relatively low. In addition, the neutral axis locations based on the strain measurements over the section depth at the midspan of Girder G3 indicate that partial composite action between the girder and concrete deck could be taking place. In Span 1, a small negative moment is occurring in Girder G3, and the neutral axis is higher than the theoretical non-composite neutral axis of 14.9 in. from the bottom of the girder.

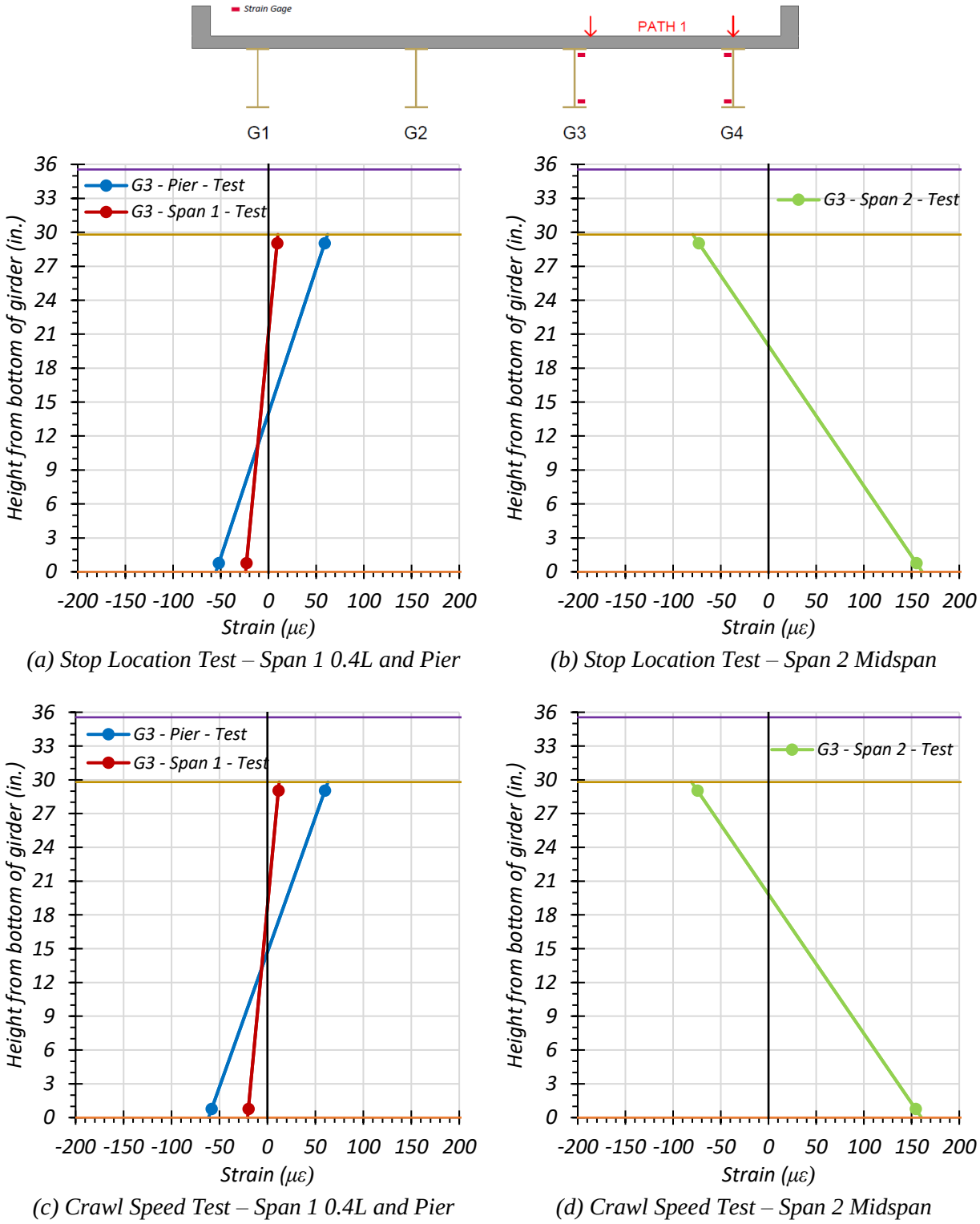

(a) Stop Location Test – Span 1 0.4L and Pier

(b) Stop Location Test – Span 2 Midspan

(c) Crawl Speed Test – Span 1 0.4L and Pier

(d) Crawl Speed Test – Span 2 Midspan

Figure 7.25. Static Strains for Interior Girder G3: Path 1—Span 2

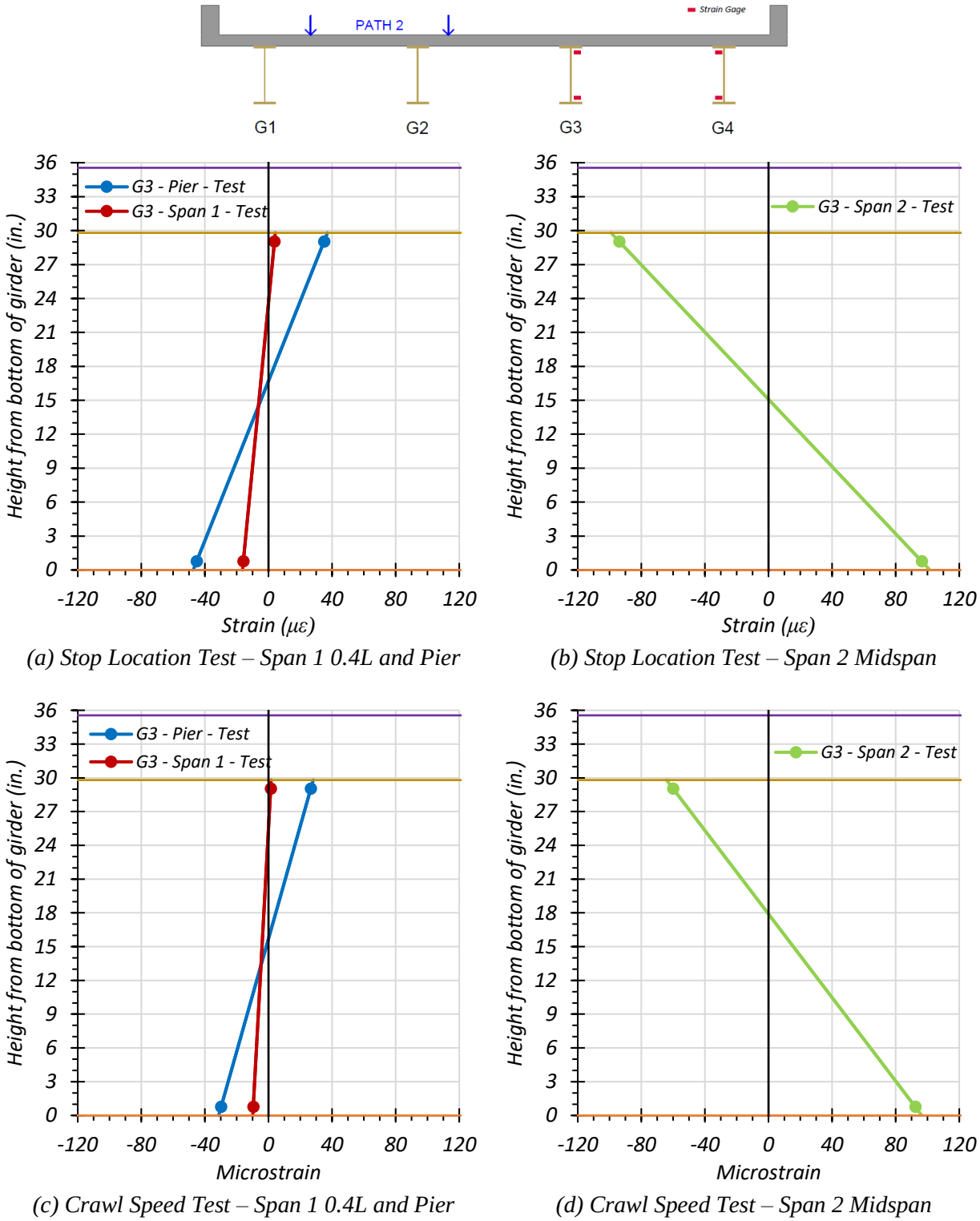

(a) Stop Location Test – Span 1 0.4L and Pier

(b) Stop Location Test – Span 2 Midspan

(c) Crawl Speed Test – Span 1 0.4L and Pier

(d) Crawl Speed Test – Span 2 Midspan

Figure 7.26. Static Strains for Interior Girder G3: Path 2—:Span 2

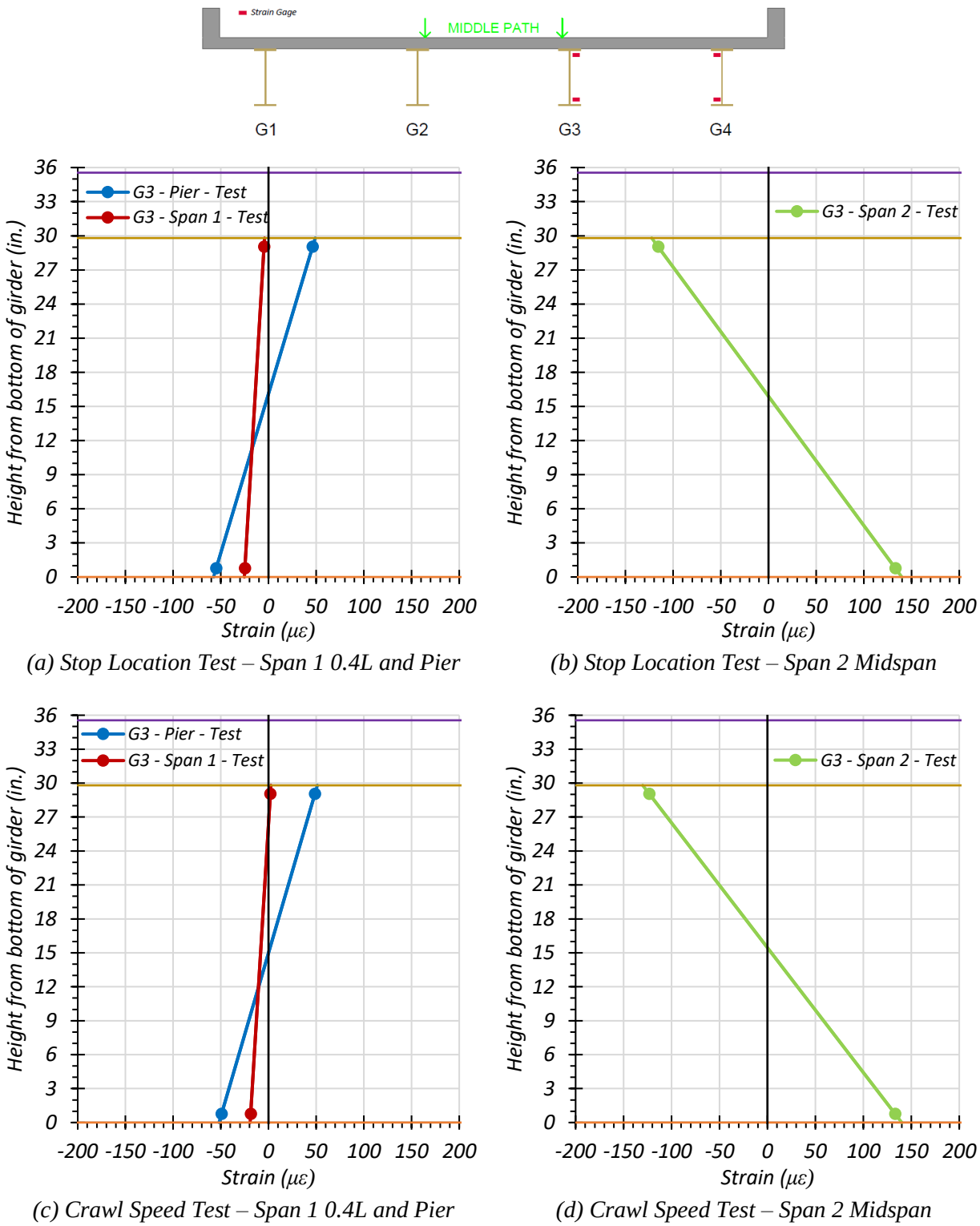

(a) Stop Location Test – Span 1 0.4L and Pier

(b) Stop Location Test – Span 2 Midspan

(c) Crawl Speed Test – Span 1 0.4L and Pier

(d) Crawl Speed Test – Span 2 Midspan

Figure 7.27. Static Strains for Interior Girder G3: Middle Path—Span 2

Exterior Girder G4. Figure 7.28 through Figure 7.30 provide plots of the measured strains for exterior Girder G4 during static load testing. The strains measured for Girder G4 during the Path 1—Span 2 static tests are shown in Figure 7.28. Figure 7.28(a) shows the maximum strains observed during the stop location test for Girder G4 at 0.4*L* of Span 1 and the interior pier. Figure 7.28(b) shows the maximum strains observed during the stop location test for Girder G4 at the midspan of Span 2. Figure 7.28(c) shows the maximum strains observed during the crawl speed test for Girder G4 at 0.4*L* of Span 1 and the interior pier. Figure 7.28(d) shows the maximum strains observed during the crawl speed test for Girder G4 at the midspan of Span 2. The corresponding observed Span 2 stresses for Girder G4 are 6.61 ksi for the stop location test and 6.82 ksi for the crawl speed test. The observed neutral axis locations at the midspan are 19.76 in. from the bottom of the girder for the stop location test and 19.85 in. from the bottom of the girder for the crawl speed test.

The strains measured for Girder G4 during the Path 2—Span 2 static tests are shown in Figure 7.29. Figure 7.29(a) shows the maximum strains observed during the stop location test for Girder G4 at 0.4*L* of Span 1 and the interior pier. Figure 7.29(b) shows the maximum strains observed during the stop location test for Girder G4 at the midspan of Span 2. Figure 7.29(c) shows the maximum strains observed during the crawl speed test for Girder G4 at 0.4*L* of Span 1 and the interior pier. Figure 7.29(d) shows the maximum strains observed during the crawl speed test for Girder G4 at the midspan of Span 2. The corresponding observed midspan stresses for Girder G4 are 0.58 ksi for the stop location test and 0.52 ksi for the crawl speed test.

The strains measured for Girder G4 during the Middle Path static tests are shown in Figure 7.30. Figure 7.30(a) shows the maximum strains observed during the stop location test for Girder G4 at 0.4*L* of Span 1 and the interior pier. Figure 7.30(b) shows the maximum strains observed during the stop location test for Girder G4 at the midspan of Span 2. Figure 7.30(c) shows the maximum strains observed during the crawl speed test for Girder G4 at 0.4*L* of Span 1 and the interior pier. Figure 7.30(d) shows the maximum strains observed during the crawl speed test for Girder G4 at the midspan of Span 2. The corresponding observed midspan stresses for Girder G4 are 2.72 ksi for the stop location test and 2.68 ksi for the crawl speed test. The observed neutral axis locations at the midspan are 34.13 in. from the bottom of the girder for the stop location test and 32.76 in. from the bottom of the girder for the crawl speed test.

The live load stress levels for interior Girder G4 when locating the test truck on the three considered paths are relatively low. In addition, the neutral axis locations based on the strain measurements over the section depth at the midspan of Girder G4 indicate that partial composite action between the girder and concrete deck could be taking place. In Span 1, a small negative moment is occurring in Girder G4, and the neutral axis is higher than the theoretical non-composite neutral axis of 14.9 in. from the bottom of the girder.

During Path 2 loading, the strains at the top and bottom of Girder G4 are very similar. It seems the girder is taking a very small amount of almost only axial load. This element could be due to the girder receiving very little load during Path 2 loading since the truck is on the other side of the bridge and most of the load is likely going to Girders G1 and G2.

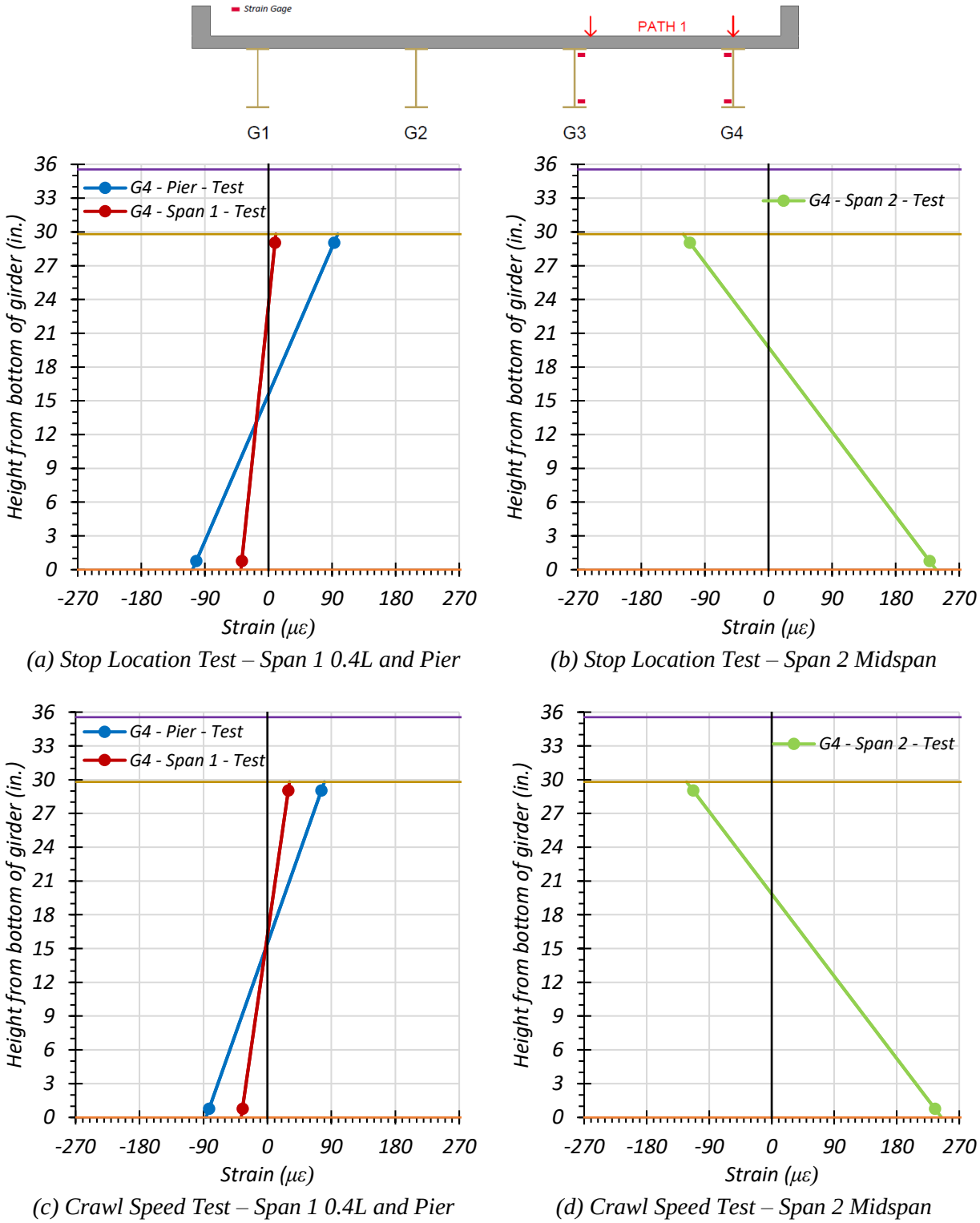

(a) Stop Location Test – Span 1 0.4L and Pier

(b) Stop Location Test – Span 2 Midspan

(c) Crawl Speed Test – Span 1 0.4L and Pier

(d) Crawl Speed Test – Span 2 Midspan

Figure 7.28. Static Strains for Exterior Girder G4: Path 1—Span 2

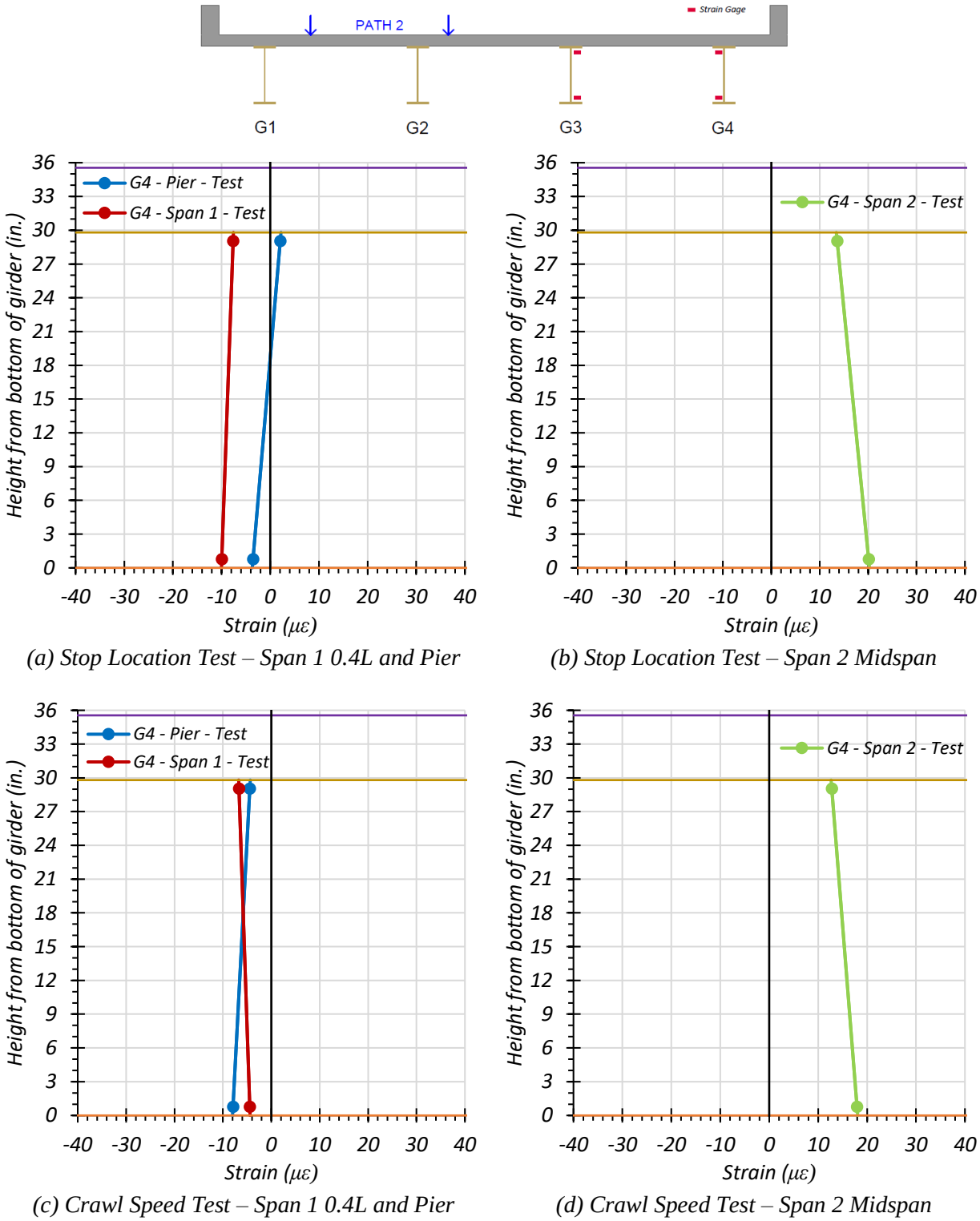

(a) Stop Location Test – Span 1 0.4L and Pier

(b) Stop Location Test – Span 2 Midspan

(c) Crawl Speed Test – Span 1 0.4L and Pier

(d) Crawl Speed Test – Span 2 Midspan

Figure 7.29. Static Strains for Exterior Girder G4: Path 2—Span 2

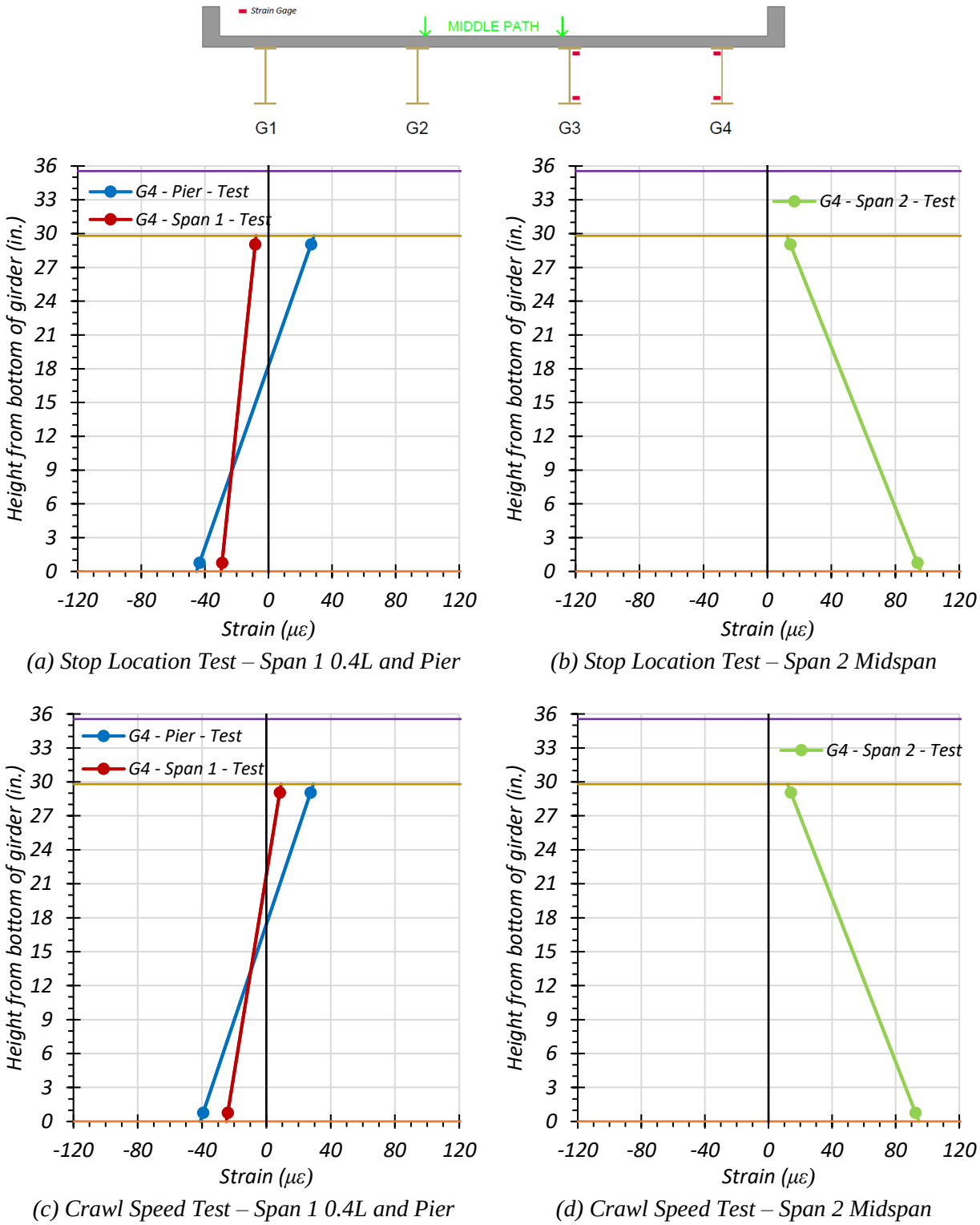

(a) Stop Location Test – Span 1 0.4L and Pier

(b) Stop Location Test – Span 2 Midspan

(c) Crawl Speed Test – Span 1 0.4L and Pier

(d) Crawl Speed Test – Span 2 Midspan

Figure 7.30. Static Strains for Exterior Girder G4: Middle Path—Span 2

Comparison of Measured Strain Results. Table 7.12 and Figure 7.31 show the neutral axis locations measured for all static load tests in Span 2. The average test neutral axis value for Girder G3 was 16.88 in. from the bottom of the girder. The test neutral axis that is most meaningful for Girder G4 is 19.76 in. from the bottom of the girder. The neutral axes based on strain measurements during field testing tend to be somewhere in between the theoretical composite and the theoretical non-composite neutral axes, which are based on the parallel axis theorem using the updated geometric material properties determined during testing. These properties include an f_c' of 6.25 ksi and a corresponding MOE of 4506 ksi. The effective deck width used for an interior girder and for an exterior girder is 69 in., determined using Article 10.38.3 in the *AASHTO Standard Specifications* (AASHTO 2002). Reinforcing steel is not included in this calculation. This result shows that Bridge SC-12 is likely acting as partially composite. The neutral axis locations observed for Girder G4 under Path 2 loading are quite high, which could be because Girder G4 is receiving very minimal load during Path 2 loading.

Table 7.12. Measured Neutral Axis Locations for All Span 2 Static Load Tests

Test	G3 Neutral Axis Location (in. from bottom of girder)	G4 Neutral Axis Location (in. from bottom of girder)
Path 1—Stop Location	19.97	19.76
Path 1—Crawl Speed	19.56	19.85
Path 2—Stop Location	15.08	88.17
Path 2—Crawl Speed	15.32	99.15
Middle Path—Stop Location	15.88	34.13
Middle Path—Crawl Speed	15.45	32.76
Theoretical Non-Composite	14.90	14.90
Theoretical Composite—Positive Bending	26.11	26.11
Theoretical Composite—Negative Bending	16.66	16.66

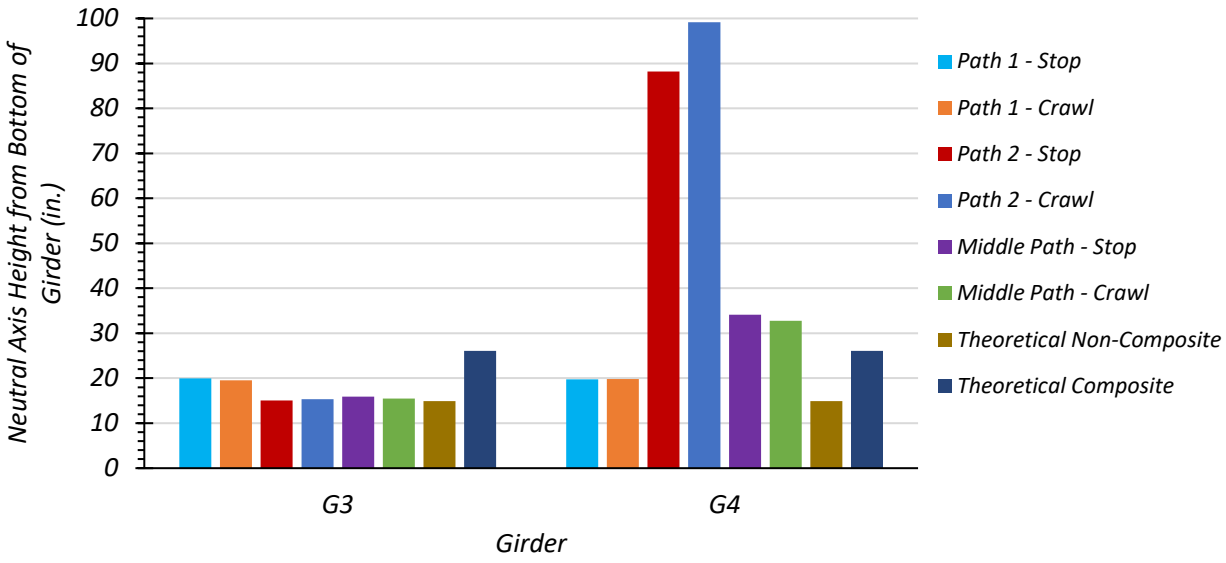

Figure 7.31. Test Neutral Axis Locations for Span 2 Loading

Table 7.13 and Figure 7.32 show the maximum bottom flange stresses observed during Span 2 static testing. The maximum stress in Girder G4 was 7.09 ksi from the Path 1 crawl speed test. The maximum stress in Girder G3 was 4.68 ksi from the Path 1 stop location test. It can be seen that Girder G4 is barely taking any load during the Path 2 load tests, which could explain the unexpectedly high neutral axis values.

Table 7.13. Maximum Test Bottom Flange Stresses (ksi) for Span 2 Loading

Load Path	Interior Girder G3		Exterior Girder G4	
	Stop Location Test	Crawl Speed Test	Stop Location Test	Crawl Speed Test
Path 1	4.68	4.66	6.88	7.09
Path 2	2.94	2.82	0.59	0.52
Middle Path	4.05	4.06	2.78	2.82

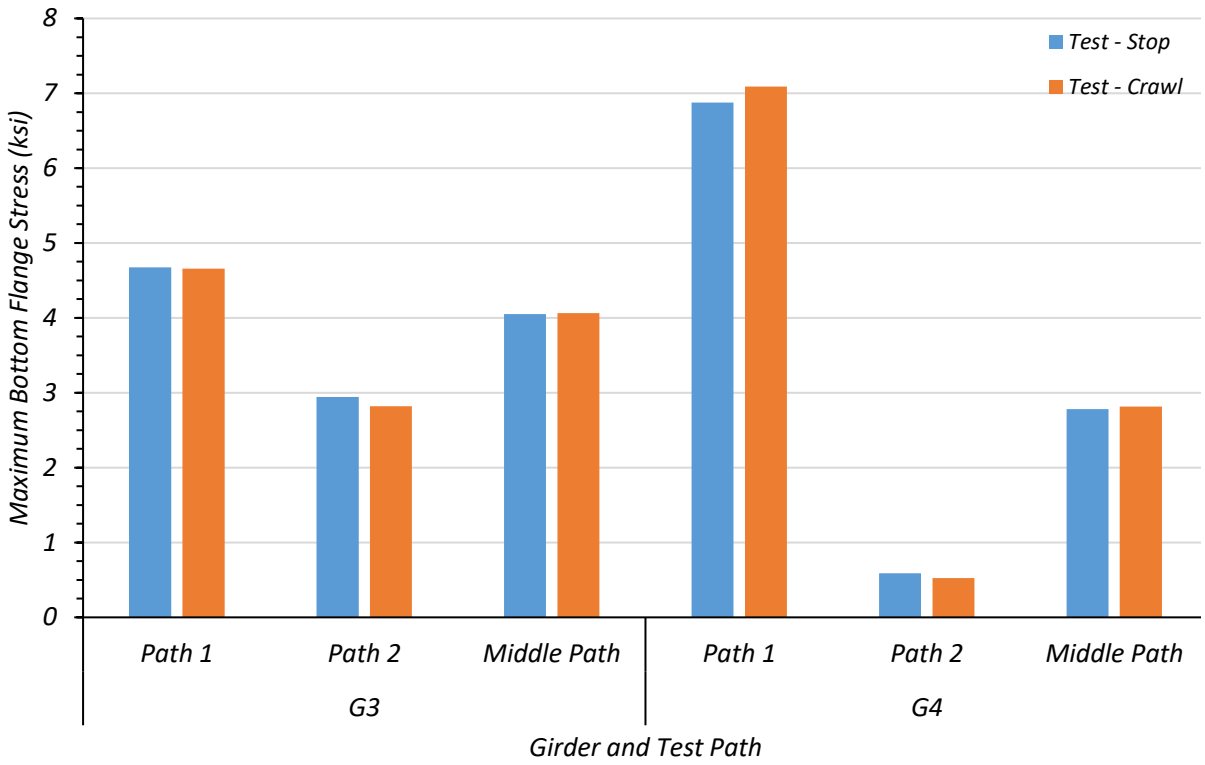

Figure 7.32. Comparison of Test Maximum Bottom Flange Stresses for Span 2 Loading

7.6.2.2 Deflection Measurements and LLDFs

Path 1 Loading. Table 7.14 shows the measured girder deflections during testing for the stop location test and crawl speed test along Path 1—Span 2. The associated LLDFs, determined using the measured midspan deflections, are also provided.

Table 7.14. Experimental Midspan Deflections and LLDFs for Path 1—Span 2 Loading

Girder	G1	G2	G3	G4
Stop Location Test Disp. (in.)	0.049	0.280	0.526	0.755
Stop Location Test LLDF	0.030	0.174	0.327	0.469
Crawl Speed Test Disp. (in.)	0.032	0.260	0.520	0.771
Crawl Speed Test LLDF	0.020	0.164	0.328	0.487
Note: 1 – G = girder, Disp. = Displacement 2 – LLDF values are based on the midspan deflections.				

Table 7.15 compares the test LLDFs to those calculated using the *AASHTO Standard Specifications*, *AASHTO LRFD Specifications* determined using the simplified stiffness parameter, and *AASHTO LRFD Specifications* determined using the analytical stiffness parameter (AASHTO 2002, 2017). Note that the LLDF expressions in the *AASHTO LRFD Specifications* (AASHTO 2017) consider a multiple presence factor m of 1.2 for one-lane loading and 1.0 for two-lane loading. For this reason, the LLDF values computed for interior girders were divided by 1.2 for comparison to the *AASHTO Standard Specifications* LLDFs and measured LLDFs, which are for a one-lane loaded condition. The maximum g_{AASHTO_Std}/g_{test} ratios are above 1.0, ranging from 1.21 to 1.46. The maximum g_{AASHTO_S}/g_{test} ratios are above 1.0, ranging from 1.09 to 1.41. The maximum g_{AASHTO_K}/g_{test} ratios are above 1.0, ranging from 1.04 to 1.41. These results indicate all three of the AASHTO methods to determine LLDFs are conservative for Path 1—Span 2 loading.

Table 7.15. LLDF Comparison with AASHTO for Path 1—Span 2 Loading

Test and Girder Type	AASHTO Standard Specs ($g^m_{AASHTO\_Std}$)	AASHTO LRFD Simplified ($g^m_{AASHTO\_S}$)	AASHTO LRFD K_g Calculated ($g^m_{AASHTO\_K}$)	Test (g^m_{test})	$g^m_{AASHTO\_Std}/g^m_{test}$	$g^m_{AASHTO\_S}/g^m_{test}$	$g^m_{AASHTO\_K}/g^m_{test}$
Stop Location Interior	0.476	0.356	0.342	0.327	1.46	1.09	1.05
Stop Location Exterior	0.589	0.660	0.660	0.469	1.26	1.41	1.41
Crawl Speed Interior	0.476	0.356	0.342	0.328	1.45	1.09	1.04
Crawl Speed Exterior	0.589	0.660	0.660	0.487	1.21	1.36	1.36

Figure 7.33(a) and Figure 7.33(c) show the Path 1—Span 2 stop location and crawl speed test girder deflection profiles. Figure 7.33(b) and Figure 7.33(d) show the Path 1—Span 2 stop location and crawl speed LLDFs compared to relevant AASHTO values. The governing LLDFs observed during testing are significantly lower than the LLDFs provided by the *AASHTO Standard Specifications*, and slightly lower than the *AASHTO LRFD Specifications* LLDFs using the

simplified stiffness parameter, and the *AASHTO LRFD Specifications* LLDFs using the analytical stiffness parameter.

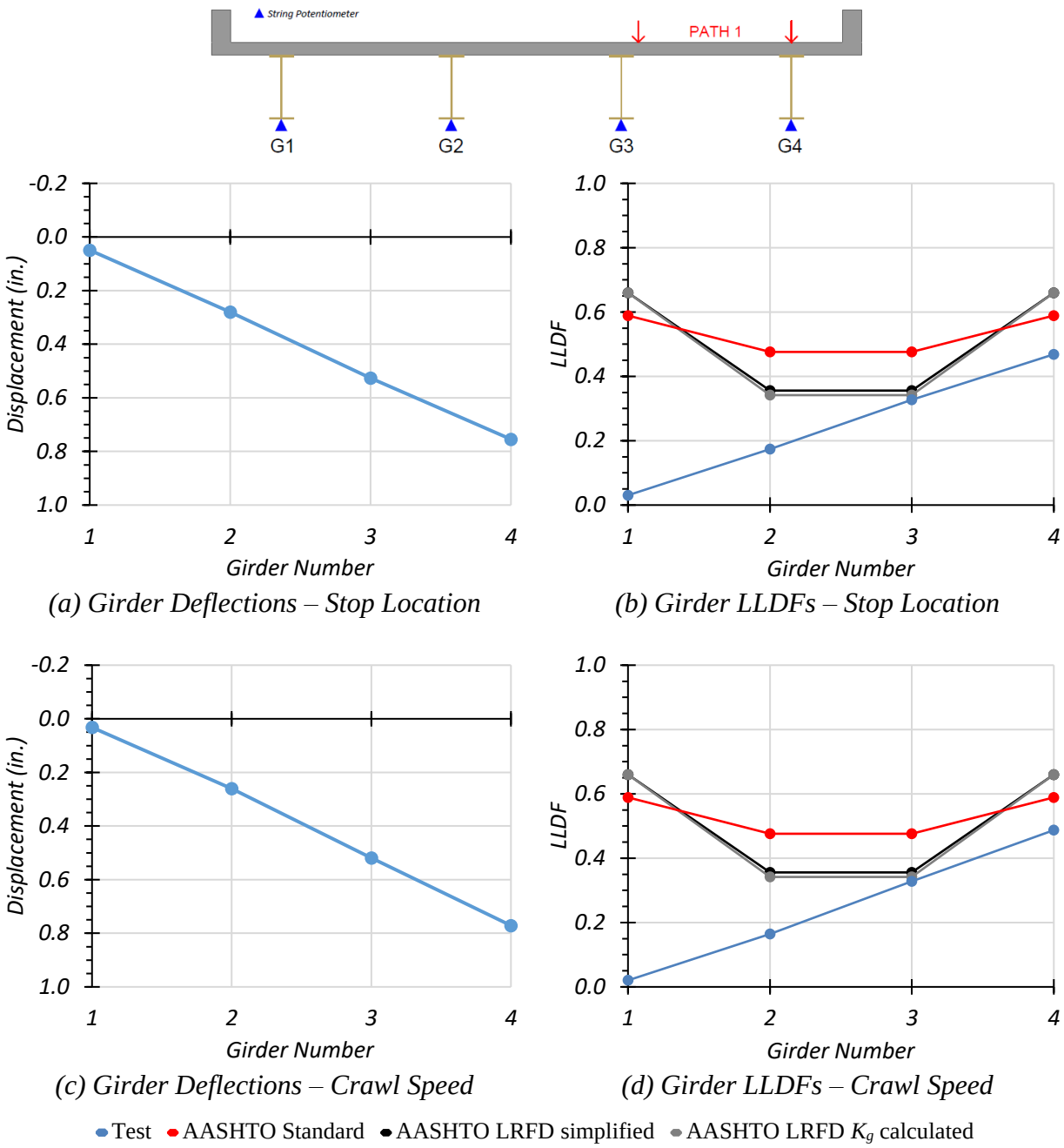

(a) Girder Deflections – Stop Location

(b) Girder LLDFs – Stop Location

(c) Girder Deflections – Crawl Speed

(d) Girder LLDFs – Crawl Speed

Figure 7.33. Static Deflection Results for Path 1—Span 2 Loading

Path 2 Loading. Table 7.16 shows the measured girder deflections during testing for the stop location test and crawl speed test along Path 2—Span 2. The associated LLDFs, determined using the measured midspan deflections, are also provided.

Table 7.16. Experimental Midspan Deflections and LLDFs for Path 2—Span 2 Loading

Description	G1	G2	G3	G4
Stop Location Test Disp. (in.)	0.692	0.556	0.298	0.077
Stop Location Test LLDF	0.427	0.343	0.184	0.047
Crawl Speed Test Disp. (in.)	0.693	0.537	0.279	0.060
Crawl Speed Test LLDF	0.442	0.342	0.178	0.038
Note: 1 – G = girder, Disp. = Displacement 2 – LLDF values are based on the midspan deflections.				

Table 7.17 compares the test LLDFs to those calculated using the *AASHTO Standard Specifications*, *AASHTO LRFD Specifications* determined using the simplified stiffness parameter, and *AASHTO LRFD Specifications* determined using the analytical stiffness parameter (AASHTO 2002, 2017). Note that the LLDF expressions in the *AASHTO LRFD Specifications* (AASHTO 2017) consider a multiple presence factor m of 1.2 for one-lane loading and 1.0 for two-lane loading. For this reason, the LLDF values computed for interior girders were divided by 1.2 for comparison to the *AASHTO Standard Specifications* LLDFs and measured LLDFs, which are for a one-lane loaded condition. The maximum g_{AASHTO_Std}/g_{test} ratios are above 1.0, ranging from 1.33 to 1.39. The maximum g_{AASHTO_S}/g_{test} ratios are above 1.0, ranging from 1.04 to 1.55. The maximum g_{AASHTO_K}/g_{test} ratios are above 1.0, ranging from 1.00 to 1.55. These results indicate all three of the AASHTO methods to determine LLDFs are conservative for exterior girders for Path 2—Span 2 loading. The *AASHTO LRFD Specifications* LLDFs determined using the simplified stiffness parameter, and *AASHTO LRFD Specifications* LLDFs determined using the analytical stiffness parameter match the LLDFs based on measurements for the interior girders, while the *AASHTO Standard Specifications* are conservative (AASHTO 2002, 2017).

Table 7.17. LLDF Comparison with AASHTO for Path 2—Span 2 Loading

Test and Girder Type	AASHTO Standard Specs ($g^m_{AASHTO\_Std}$)	AASHTO LRFD Simplified ($g^m_{AASHTO\_S}$)	AASHTO LRFD K_g Calculated ($g^m_{AASHTO\_K}$)	Test (g^m_{test})	$g^m_{AASHTO\_Std}/g^m_{test}$	$g^m_{AASHTO\_S}/g^m_{test}$	$g^m_{AASHTO\_K}/g^m_{test}$
Stop Location Interior	0.476	0.356	0.342	0.343	1.39	1.04	1.00
Stop Location Exterior	0.589	0.660	0.660	0.427	1.38	1.55	1.55
Crawl Speed Interior	0.476	0.356	0.342	0.342	1.39	1.04	1.00
Crawl Speed Exterior	0.589	0.660	0.660	0.442	1.33	1.49	1.49

Figure 7.34(a) and Figure 7.34(c) show the Path 2—Span 2 stop location and crawl speed test girder deflection profiles. Figure 7.34(b) and Figure 7.34(d) show the Path 2—Span 2 stop location and crawl speed LLDFs compared to relevant AASHTO values. The governing LLDFs observed during testing are significantly lower than the LLDFs provided by the *AASHTO Standard Specifications*, and for the *AASHTO LRFD Specifications* LLDFs using the simplified stiffness parameter and the *AASHTO LRFD Specifications* LLDFs using the analytical stiffness parameter when examining exterior girders. They are the same as the *AASHTO LRFD Specifications* LLDFs using the simplified stiffness parameter and the *AASHTO LRFD Specifications* LLDFs using the analytical stiffness parameter when examining interior girders.

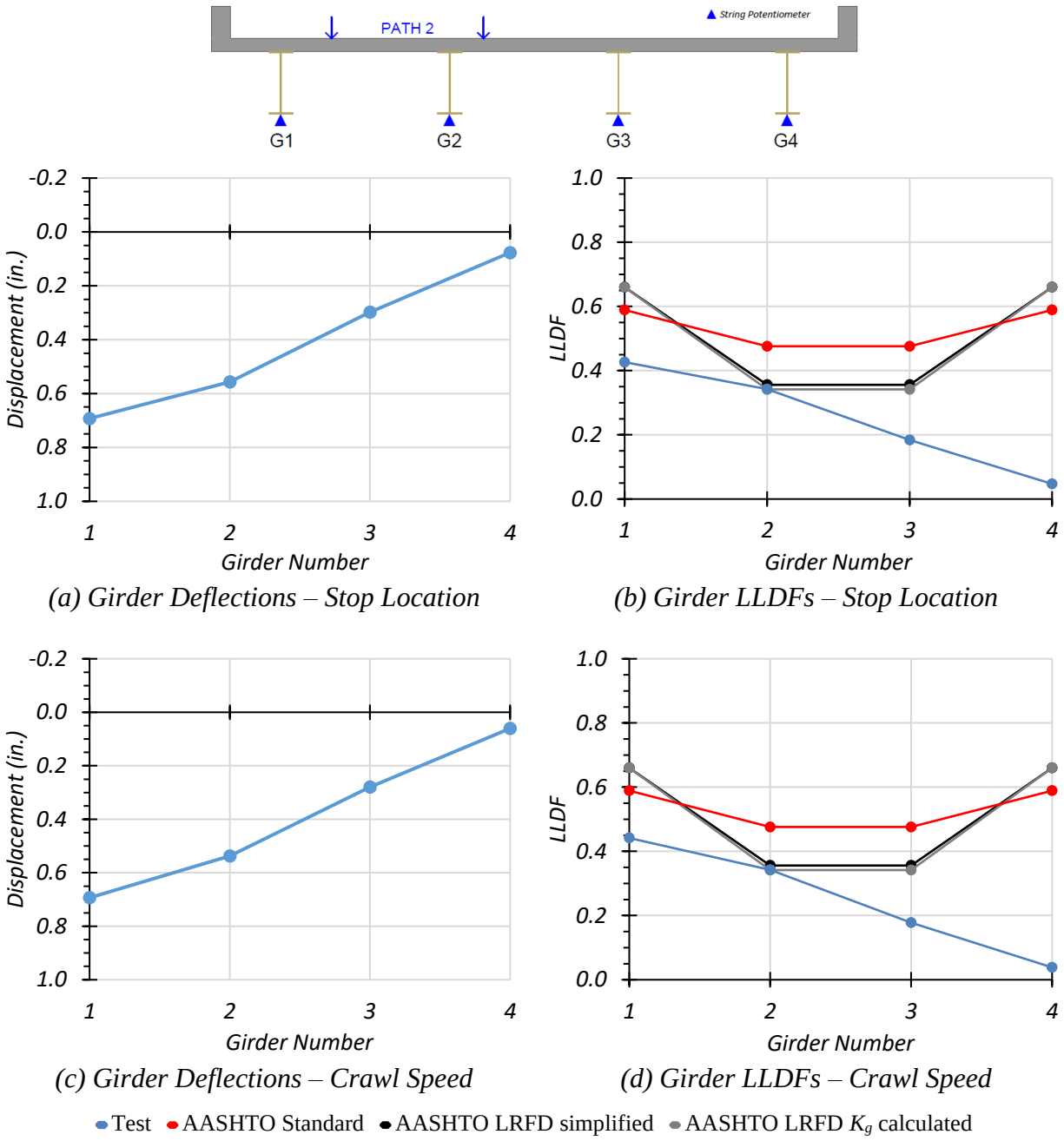

(a) Girder Deflections – Stop Location

(b) Girder LLDFs – Stop Location

(c) Girder Deflections – Crawl Speed

(d) Girder LLDFs – Crawl Speed

Figure 7.34. Static Deflection Results for Path 2—Span 2 Loading

Middle Path Loading. Table 7.18 shows the measured girder deflections during testing for the Middle Path—Span 2 stop location test. The associated LLDFs, determined using the measured midspan deflections, are also provided.

Table 7.18. Experimental Midspan Deflections and LLDFs for Middle Path—Span 2 Loading

Description	G1	G2	G3	G4
Stop Location Test Disp. (in.)	0.328	0.457	0.440	0.353
Stop Location Test LLDF	0.208	0.289	0.279	0.224
Crawl Speed Test Disp. (in.)	0.313	0.444	0.436	0.355
Crawl Speed Test LLDF	0.202	0.287	0.281	0.229
Note: 1 – G = girder, Disp. = Displacement 2 – LLDF values are based on the midspan deflections.				

Table 7.19 compares the test LLDFs to those calculated using the *AASHTO Standard Specifications*, *AASHTO LRFD Specifications* with the simplified stiffness parameter, and *AASHTO LRFD Specifications* with the analytical stiffness parameter (AASHTO 2002, 2017). Note that the LLDF expressions in the *AASHTO LRFD Specifications* (AASHTO 2017) consider a multiple presence factor m of 1.2 for one-lane loading and 1.0 for two-lane loading. For this reason, the LLDF values computed for interior girders were divided by 1.2 for comparison to the *AASHTO Standard Specifications* LLDFs and measured LLDFs, which are for a one-lane loaded condition. The maximum g_{AASHTO_Std}/g_{test} ratios are above 1.0, ranging from 1.65 to 2.63. The maximum g_{AASHTO_S}/g_{test} ratios are above 1.0, ranging from 1.23 to 2.95. The maximum g_{AASHTO_K}/g_{test} ratios are above 1.0, ranging from 1.18 to 2.95. These results indicate all three of the AASHTO methods to determine LLDFs are conservative for Middle Path—Span 2 loading.

Table 7.19. LLDF Comparison with AASHTO for Middle Path—Span 2 Loading

Test and Girder Type	AASHTO Standard Specs ($g^m_{AASHTO\_Std}$)	AASHTO LRFD Simplified ($g^m_{AASHTO\_S}$)	AASHTO LRFD K_g Calculated ($g^m_{AASHTO\_K}$)	Test (g^m_{test})	$g^m_{AASHTO\_Std}/g^m_{test}$	$g^m_{AASHTO\_S}/g^m_{test}$	$g^m_{AASHTO\_K}/g^m_{test}$
Stop Location Interior	0.476	0.356	0.342	0.289	1.65	1.23	1.18
Stop Location Exterior	0.589	0.660	0.660	0.224	2.63	2.95	2.95
Crawl Speed Interior	0.476	0.356	0.342	0.287	1.66	1.24	1.19
Crawl Speed Exterior	0.589	0.660	0.660	0.229	2.57	2.88	2.88

Figure 7.35(a) and Figure 7.35(c) show the Middle Path—Span 2 stop location and crawl speed test girder deflection profiles. Figure 7.35(b) and Figure 7.35(d) show the Middle Path—Span 2 stop location and crawl speed LLDFs compared to relevant AASHTO values. The governing LLDFs observed during testing are significantly lower than the LLDFs provided by the *AASHTO Standard Specifications*, the *AASHTO LRFD Specifications* LLDFs using the simplified stiffness parameter, and the *AASHTO LRFD Specifications* LLDFs using the analytical stiffness parameter.

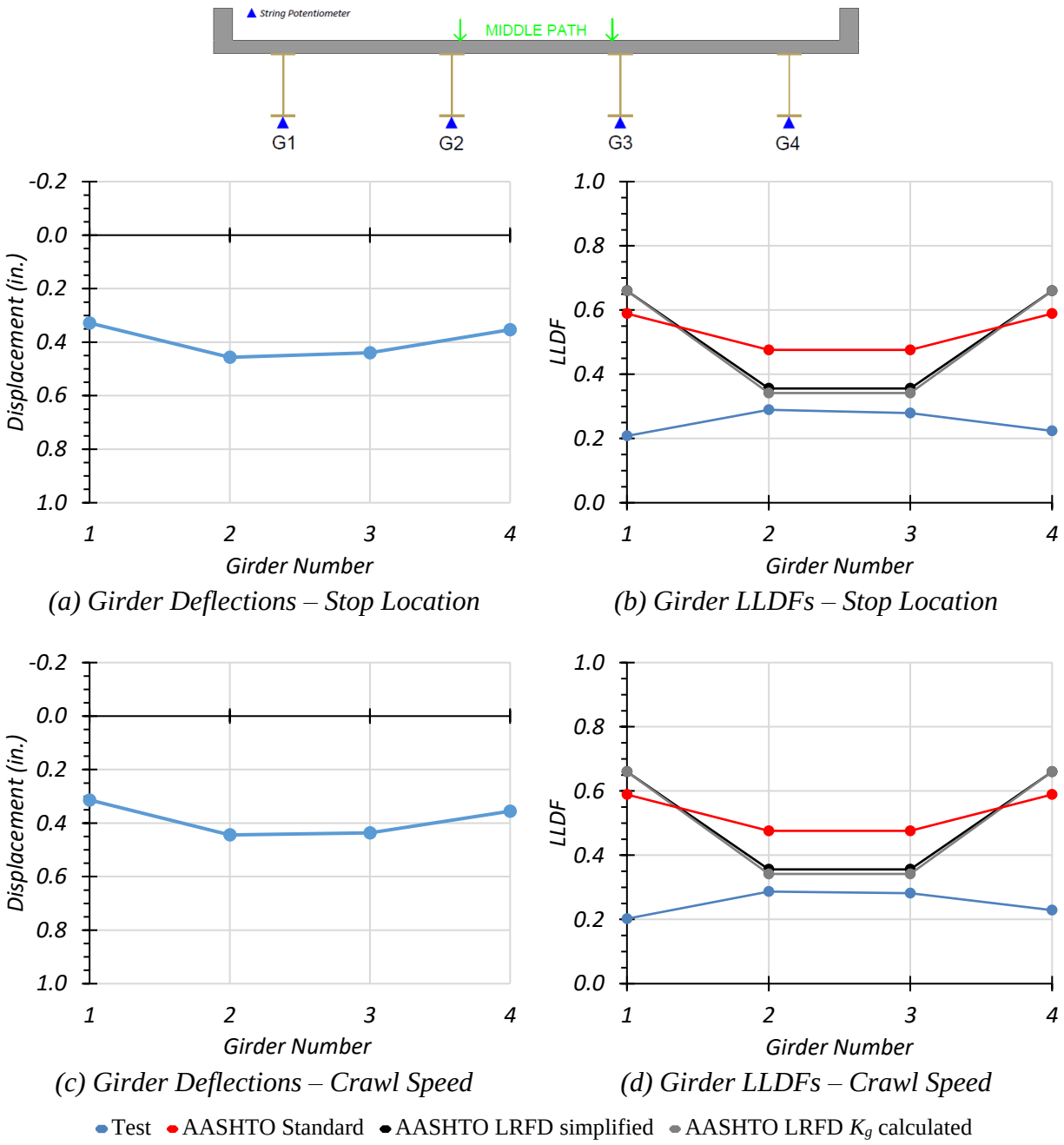

(a) Girder Deflections – Stop Location

(b) Girder LLDFs – Stop Location

(c) Girder Deflections – Crawl Speed

(d) Girder LLDFs – Crawl Speed

Figure 7.35. Static Deflection Results for Middle Path—Span 2 Loading

Comparison of Results Based on Deflection Measurements. For Span 2 midspan deflections, the critical LLDF for an exterior girder was 0.487, which was observed during the crawl speed test along Path 1. This figure corresponds to a g_{AASHTO}/g_{test} ratio of 1.21 when using the *AASHTO Standard Specifications*, 1.36 when using the *AASHTO LRFD Specifications* determined using the simplified stiffness parameter, and 1.36 when using the *AASHTO LRFD*

Specifications determined using the analytical stiffness parameter. The critical LLDF for an interior girder was 0.343, observed during the stop location test along Path 2. This figure corresponds to a g_{AASHTO}/g_{test} ratio of 1.39 when using the *AASHTO Standard Specifications*, 1.04 when using the *AASHTO LRFD Specifications* determined using the simplified stiffness parameter, and 1.00 when using the *AASHTO LRFD Specifications* determined using the analytical stiffness parameter. During the static load tests along Path 1, the maximum LLDF was 0.469 for the stop location test and increased to 0.487 for the crawl speed test. During the static load tests along Path 2, the maximum LLDF was 0.427 for the stop location test and decreased to 0.442 for the crawl speed test. During the static load tests along Middle Path, the maximum LLDF was 0.289 for the stop location test and decreased slightly to 0.287 for the crawl speed test.

Overall, none of the AASHTO methods to determine LLDFs produced lower values than the LLDFs observed during Span 2 testing. The only instance in which an AASHTO method produced nearly identical LLDFs as observed based on test measurements was for interior girders during Path 2 loading when using the *AASHTO LRFD Specifications*. In all other instances AASHTO methods were conservative for Bridge SC-12, and in most cases by a significant margin, possibly indicating an area through which the load rating for Bridge SC-12 could improve.

7.6.3 Pier Location Strains and Negative Moment LLDFS

By using the strain gauges attached to the top flange of each of the four girders at the location adjacent to the interior support within Span 2, negative moment region LLDFs were determined. The strains used for the LLDF calculations were taken from the same point in time as when the critical girder felt the maximum effect during the crawl speed test for each loading path. Only the crawl speed test was examined since it is unknown if the stop location test is the truck location that will produce the maximum negative moment. The crawl speed test covers every possible longitudinal location on the bridge, thereby ensuring that the maximum possible negative moment will be experienced.

Table 7.20 shows the measured pier location strains for the Path 1 crawl test. The associated LLDFs, determined using the measured strains, are also provided.

Table 7.20. Pier Location Experimental Strains and LLDFs for Path 1 Crawl Speed Loading

Description	G1	G2	G3	G4
Test Strain (με)	−2.7	25.9	65.2	100.8
Test LLDF	0.014	0.137	0.345	0.533
Note: 1 – G = girder, Disp. = Displacement 2 – LLDF values are based on the top flange strains.				

Table 7.21 compares the test LLDFs to those calculated using the *AASHTO Standard Specifications, AASHTO LRFD Specifications* determined using the simplified stiffness parameter, and *AASHTO LRFD Specifications* determined using the analytical stiffness parameter. All three g_{AASHTO}/g_{test} ratios were above 1.0 for both interior and exterior girders. For an interior girder, the g_{AASHTO_Std}/g_{test} ratio of 1.38 was most conservative, while the g_{AASHTO_K}/g_{test} ratio of 1.03 was least conservative. For an exterior girder, the g_{AASHTO_S}/g_{test} and g_{AASHTO_K}/g_{test} ratios of 1.24 were most conservative, while the g_{AASHTO_Std}/g_{test} ratio of 1.11 was least conservative.

Table 7.21. Negative Moment Region LLDF Comparison with AASHTO for Path 1 Crawl Speed Loading

Girder Type	AASHTO Standard Specs ($g^m_{AASHTO\_Std}$)	AASHTO LRFD Simplified ($g^m_{AASHTO\_S}$)	AASHTO LRFD K_g Calculated ($g^m_{AASHTO\_K}$)	Test (g^m_{test})	$g^m_{AASHTO\_Std}/g^m_{test}$	$g^m_{AASHTO\_S}/g^m_{test}$	$g^m_{AASHTO\_K}/g^m_{test}$
Interior	0.476	0.366	0.354	0.345	1.38	1.06	1.03
Exterior	0.589	0.660	0.660	0.533	1.11	1.24	1.24

Figure 7.36(a) and Figure 7.36(b) show the Path 1 strain values for each girder and the associated LLDFs compared to relevant AASHTO values. The governing LLDFs observed during testing are lower than the LLDFs provided by the *AASHTO Standard Specifications*, the *AASHTO LRFD Specifications* LLDFs using the simplified stiffness parameter, and the *AASHTO LRFD Specifications* LLDFs using the analytical stiffness parameter. Note that the LLDF expressions in the *AASHTO LRFD Specifications* (AASHTO 2017) consider a multiple presence factor m of 1.2 for one-lane loading and 1.0 for two-lane loading. For this reason, the LLDF values computed for interior girders were divided by 1.2 for comparison to the *AASHTO Standard Specifications* LLDFs and measured LLDFs, which are for a one-lane loaded condition.

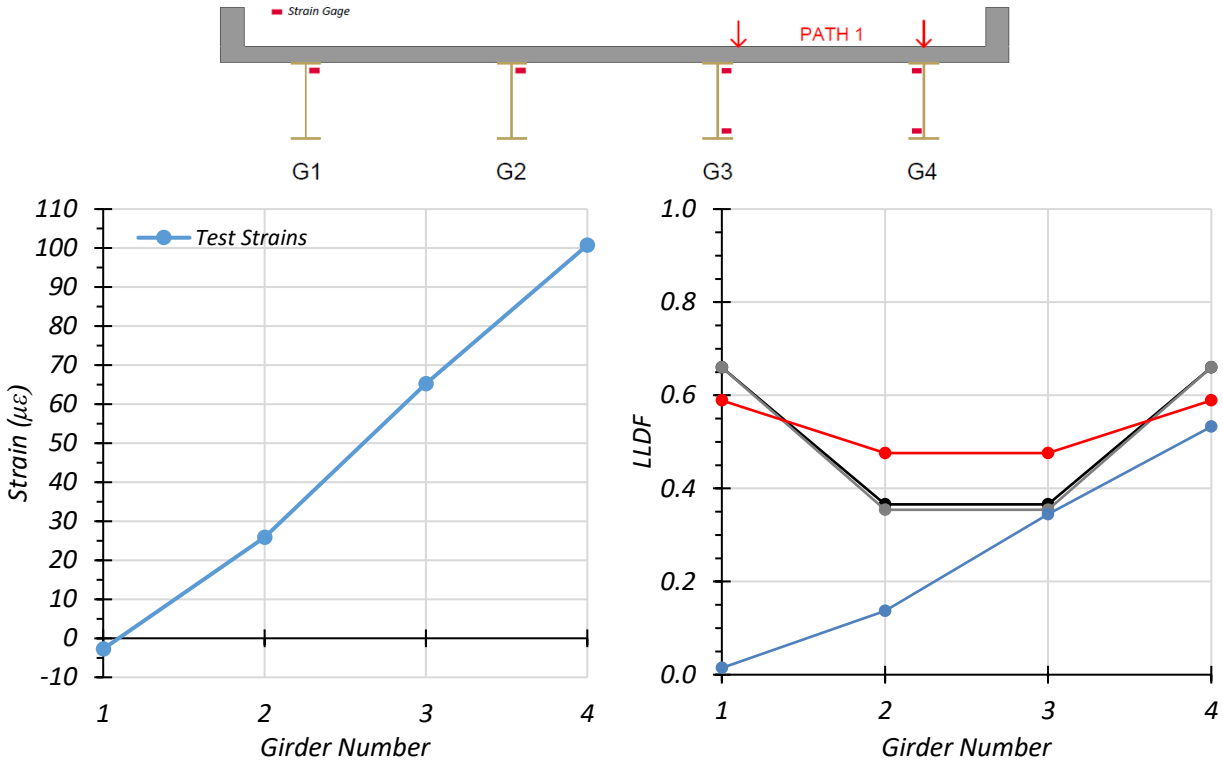

(a) Girder Top Flange Strains *(b) Girder Negative Moment Region LLDFs*

Figure 7.36. Pier Location Results for Path 1 Crawl Speed Loading

Table 7.22 shows the measured pier location strains for the Path 2 crawl test. The associated LLDFs, determined using the measured strains, are also provided.

Table 7.22. Pier Location Experimental Strains and LLDFs for Path 2 Crawl Speed Loading

Description	G1	G2	G3	G4
Test Strain (με)	97.2	70.2	33.1	−3.4
Test LLDF	0.493	0.356	0.168	0.017
Note: 1 – G = girder, Disp. = Displacement 2 – LLDF values are based on the top flange strains.				

Table 7.23 compares the test LLDFs to those calculated using the *AASHTO Standard Specifications*, the *AASHTO LRFD Specifications* with the simplified stiffness parameter, and the *AASHTO LRFD Specifications* with the analytical stiffness parameter. All three g_{AASHTO}/g_{test} ratios were above 1.0 for exterior girders. The LLDF ratio for the *AASHTO Standard Specifications* LLDF was above 1.0 for interior girders, while the *AASHTO LRFD Specifications*

with the simplified stiffness parameter and the *AASHTO LRFD Specifications* with the analytical stiffness parameter were nearly 1.0 . For an interior girder, the g_{AASHTO_Std}/g_{test} ratio of 1.34 was most conservative, while the g_{AASHTO_K}/g_{test} ratio of 0.99 was least conservative. For an exterior girder, the g_{AASHTO_S}/g_{test} and g_{AASHTO_K}/g_{test} ratios of 1.34 were most conservative, while the g_{AASHTO_Std}/g_{test} ratio of 1.19 was least conservative.

Table 7.23. Negative Moment Region LLDF Comparison with AASHTO for Path 2 Crawl Speed Loading

Girder Type	AASHTO Standard Specs ($g^m_{AASHTO\_Std}$)	AASHTO LRFD Simplified ($g^m_{AASHTO\_S}$)	AASHTO LRFD K_g Calculated ($g^m_{AASHTO\_K}$)	Test (g^m_{test})	$g^m_{AASHTO\_Std}/g^m_{test}$	$g^m_{AASHTO\_S}/g^m_{test}$	$g^m_{AASHTO\_K}/g^m_{test}$
Interior	0.476	0.366	0.354	0.356	1.34	1.03	0.99
Exterior	0.589	0.660	0.660	0.493	1.19	1.34	1.34

Figure 7.37(a) and Figure 7.37(b) show the Path 2 strain values for each girder and the associated LLDFs compared to relevant AASHTO values. The governing LLDFs observed during testing are significantly lower than the LLDFs provided by the *AASHTO Standard Specifications*, the *AASHTO LRFD Specifications* LLDFs using the simplified stiffness parameter, and the *AASHTO LRFD Specifications* LLDFs using the analytical stiffness parameter. Note that the LLDF expressions in the *AASHTO LRFD Specifications* (AASHTO 2017) consider a multiple presence factor *m* of 1.2 for one-lane loading and 1.0 for two-lane loading. For this reason, the LLDF values computed for interior girders were divided by 1.2 for comparison to the *AASHTO Standard Specifications* LLDFs and measured LLDFs, which are for a one-lane loaded condition.

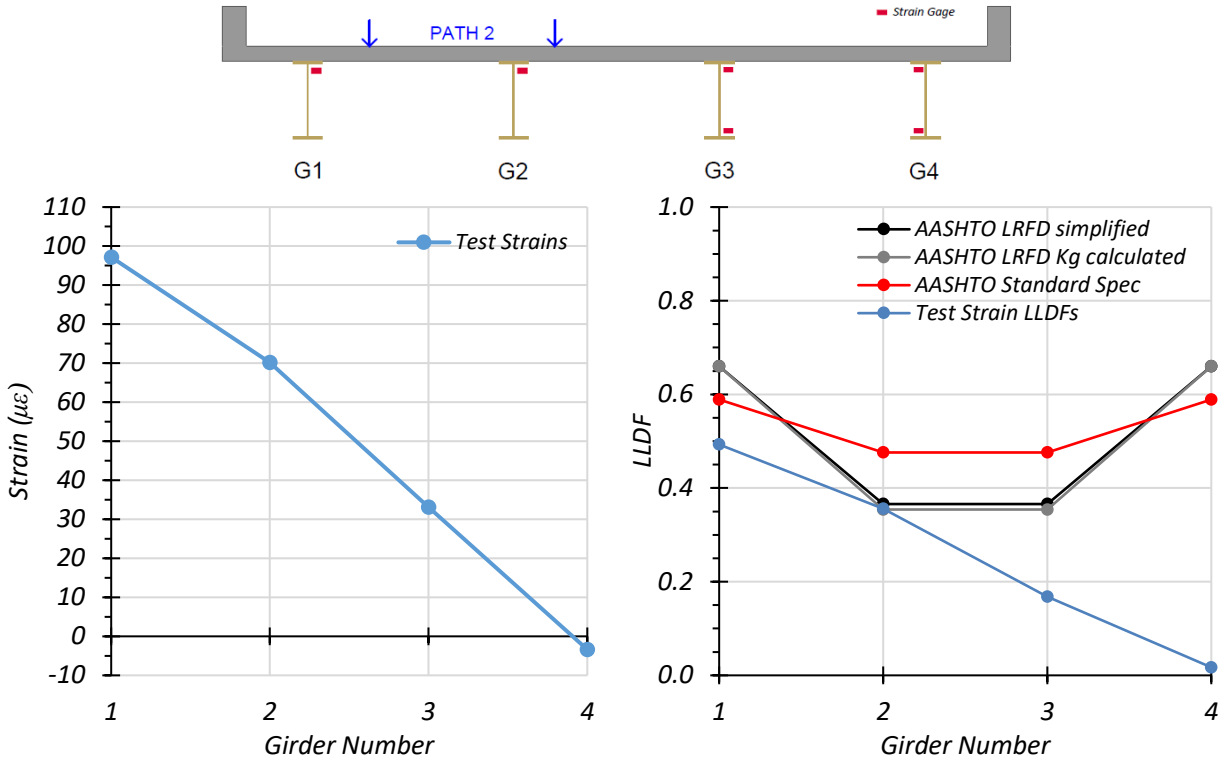

(a) Girder Top Flange Strains *(b) Girder Negative Moment Region LLDFs*

Figure 7.37. Pier Location Results for Path 2 Crawl Speed Loading

Table 7.24 shows the measured pier location strains for the Middle Path crawl test. The associated LLDFs, determined using the measured strains, are also provided.

Table 7.24. Pier Location Experimental Strains and LLDFs for Middle Path Crawl Speed Loading

Description	G1	G2	G3	G4
Test Strain (με)	39.3	55.0	54.6	27.0
Test LLDF	0.223	0.313	0.310	0.154
Note: 1 – G = girder, Disp. = Displacement 2 – LLDF values are based on the top flange strains.				

Table 7.25 compares the test LLDFs to those calculated using the *AASHTO Standard Specifications*, *AASHTO LRFD Specifications* with the simplified stiffness parameter, and *AASHTO LRFD Specifications* with the analytical stiffness parameter. All three g_{AASHTO}/g_{test} ratios were above 1.0 for both interior and exterior girders. For an interior girder, the

g_{AASHTO_Std}/g_{test} ratio of 1.52 was most conservative, while the g_{AASHTO_K}/g_{test} ratio of 1.13 was least conservative. For an exterior girder, the g_{AASHTO_S}/g_{test} and g_{AASHTO_K}/g_{test} ratios of 2.96 were most conservative, while the g_{AASHTO_Std}/g_{test} ratio of 2.64 was least conservative.

Table 7.25. Negative Moment Region LLDF Comparison with AASHTO for Middle Path Crawl Speed Loading

Girder Type	AASHTO Standard Specs ($g^m_{AASHTO\_Std}$)	AASHTO LRFD Simplified ($g^m_{AASHTO\_S}$)	AASHTO LRFD K_g Calculated ($g^m_{AASHTO\_K}$)	Test (g^m_{test})	$g^m_{AASHTO\_Std}/g^m_{test}$	$g^m_{AASHTO\_S}/g^m_{test}$	$g^m_{AASHTO\_K}/g^m_{test}$
Interior	0.476	0.366	0.354	0.313	1.52	1.17	1.13
Exterior	0.589	0.660	0.660	0.223	2.64	2.96	2.96

Figure 7.38(a) and Figure 7.38(b) show the Middle Path strain values for each girder and the associated LLDFs compared to relevant AASHTO values as well as values. The governing LLDFs observed during testing are significantly lower than the LLDFs provided by the *AASHTO Standard Specifications*, the *AASHTO LRFD Specifications* LLDFs using the simplified stiffness parameter, and the *AASHTO LRFD Specifications* LLDFs using the analytical stiffness parameter. Note that the LLDF expressions in the *AASHTO LRFD Specifications* (AASHTO 2017) consider a multiple presence factor m of 1.2 for one-lane loading and 1.0 for two-lane loading. For this reason, the LLDF values computed for interior girders were divided by 1.2 for comparison to the *AASHTO Standard Specifications* LLDFs and measured LLDFs, which are for a one-lane loaded condition.

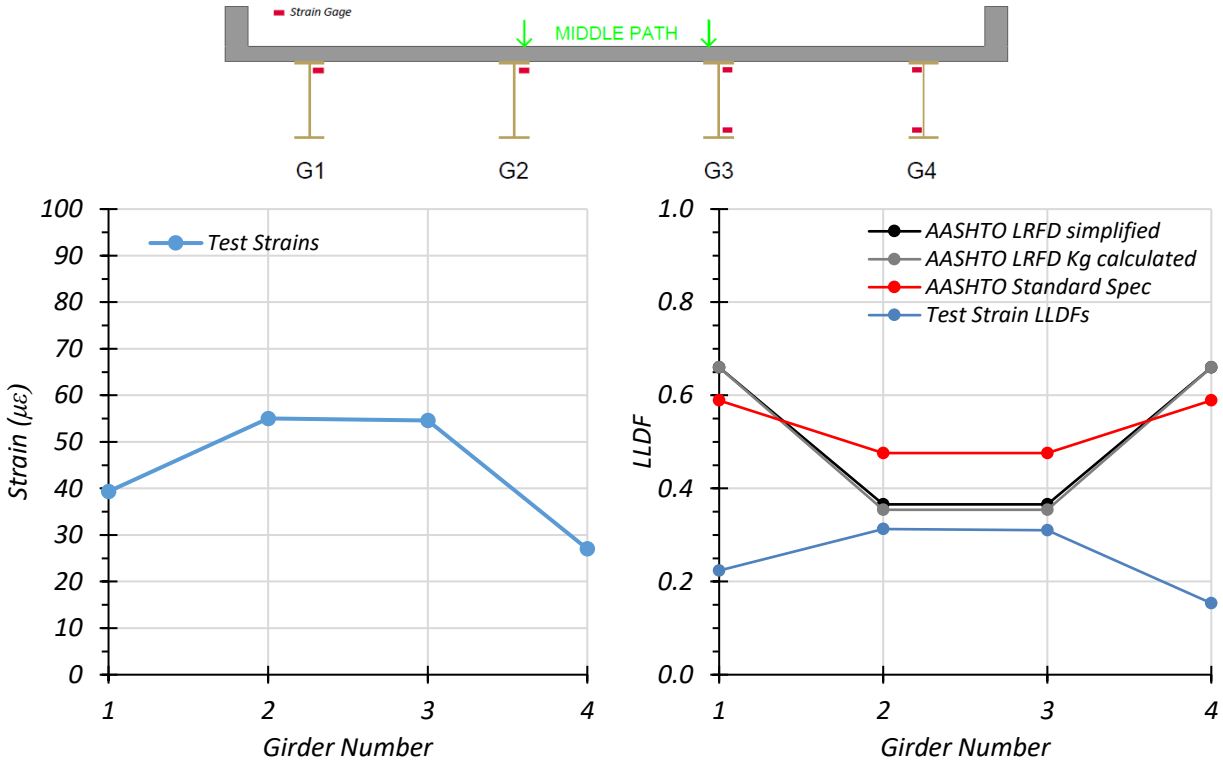

(a) Girder Top Flange Strains *(b) Girder Negative Moment Region LLDFs*

Figure 7.38. Pier Location Results for Middle Path Crawl Speed Loading

In the negative moment region, the critical LLDF for an exterior girder was 0.553, observed during the crawl speed test along Path 1. The critical LLDF for an interior girder was 0.356, observed during the crawl speed test along Path 2. For the critical interior girder, the g_{AASHTO}/g_{test} ratio was 1.34, 1.03, and 0.99 when considering the *AASHTO Standard Specifications*, the *AASHTO LRFD Specifications* with simplified stiffness parameter, and the *AASHTO LRFD Specifications* with analytical stiffness parameter, respectively. For the critical exterior girder, the g_{AASHTO}/g_{test} ratio was 1.11, 1.24, and 1.24 when considering the *AASHTO Standard Specifications*, the *AASHTO LRFD Specifications* with simplified stiffness parameter, and the *AASHTO LRFD Specifications* with analytical stiffness parameter, respectively.

7.6.4 Curb Strains for Bridge SC-12

Strain gauge data were also obtained from gauges attached to the top of the deck and the top of the curb at the midspan of the main span (Span 2). These gauges were used to identify if the curb was

taking any load and thereby participating in the resistance. Figure 7.39 shows the maximum compressive strain for the top of the curb observed during the crawl speed test and the corresponding top of deck strain for all three load paths. The data indicate, specifically for Path 1 and Middle Path loading, the curb is participating in the load carrying of the bridge. Therefore, in future FEM models of Bridge SC-12, the curb is included.

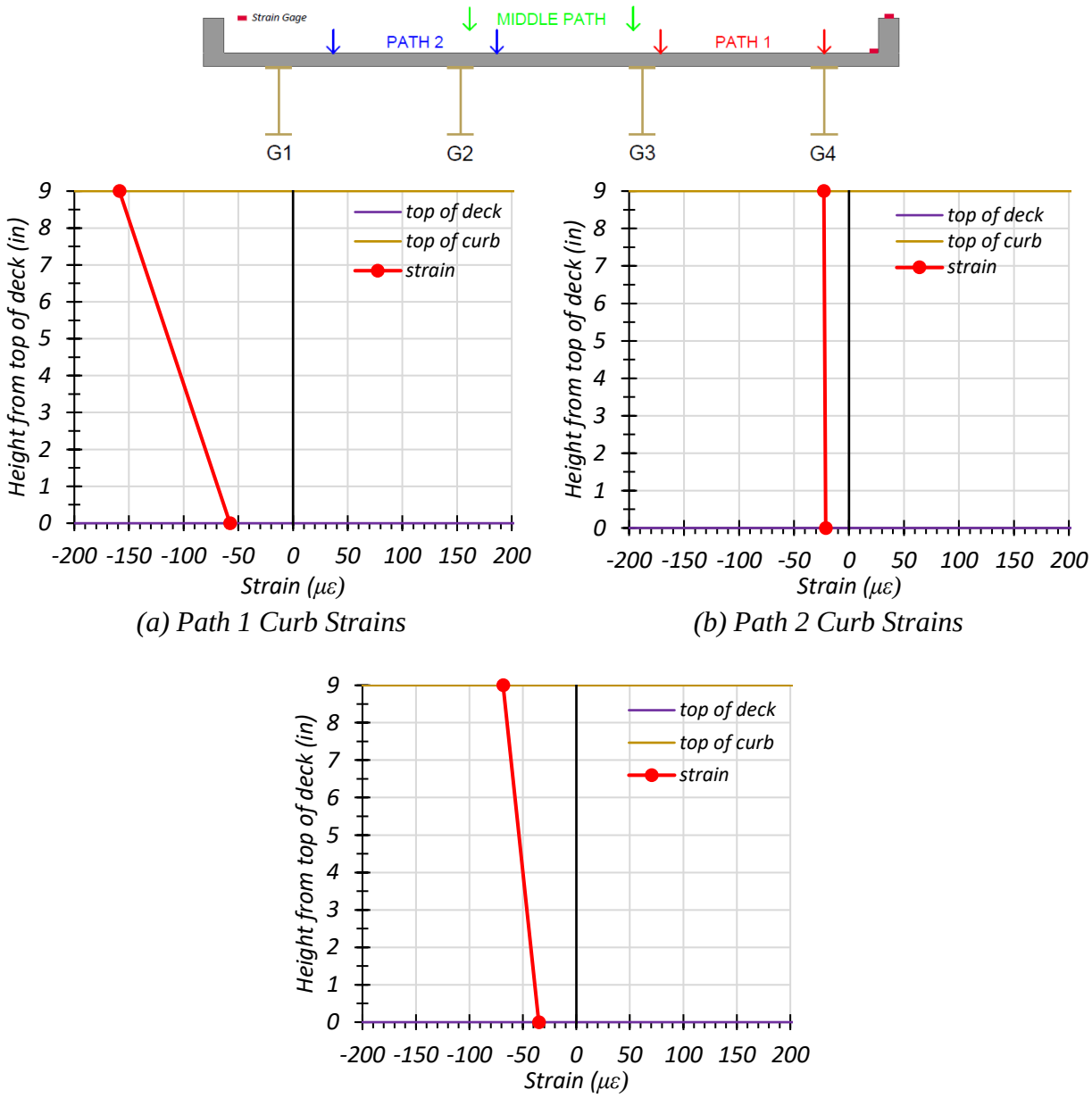

(a) Path 1 Curb Strains

(b) Path 2 Curb Strains

(c) Middle Path Curb Strains

Figure 7.39. Curbs Strains for Loading of All Paths

7.6.5 Dynamic Load Tests on Bridge SC-12

7.6.5.1 Span 1 Dynamic Amplification

Maximum Girder Strains. From the results of the static and dynamic tests for each path, the increases in strains and deflections due to the moving vehicle were examined. Figure 7.40, Figure 7.41, and Figure 7.42 show the maximum Span 1 dynamic strains observed for Path 1, Path 2, and the Middle Path, respectively, plotted with the static strains observed for those paths. Figure 7.43 shows those strain values and compares them to the appropriate static load case for Span 1.

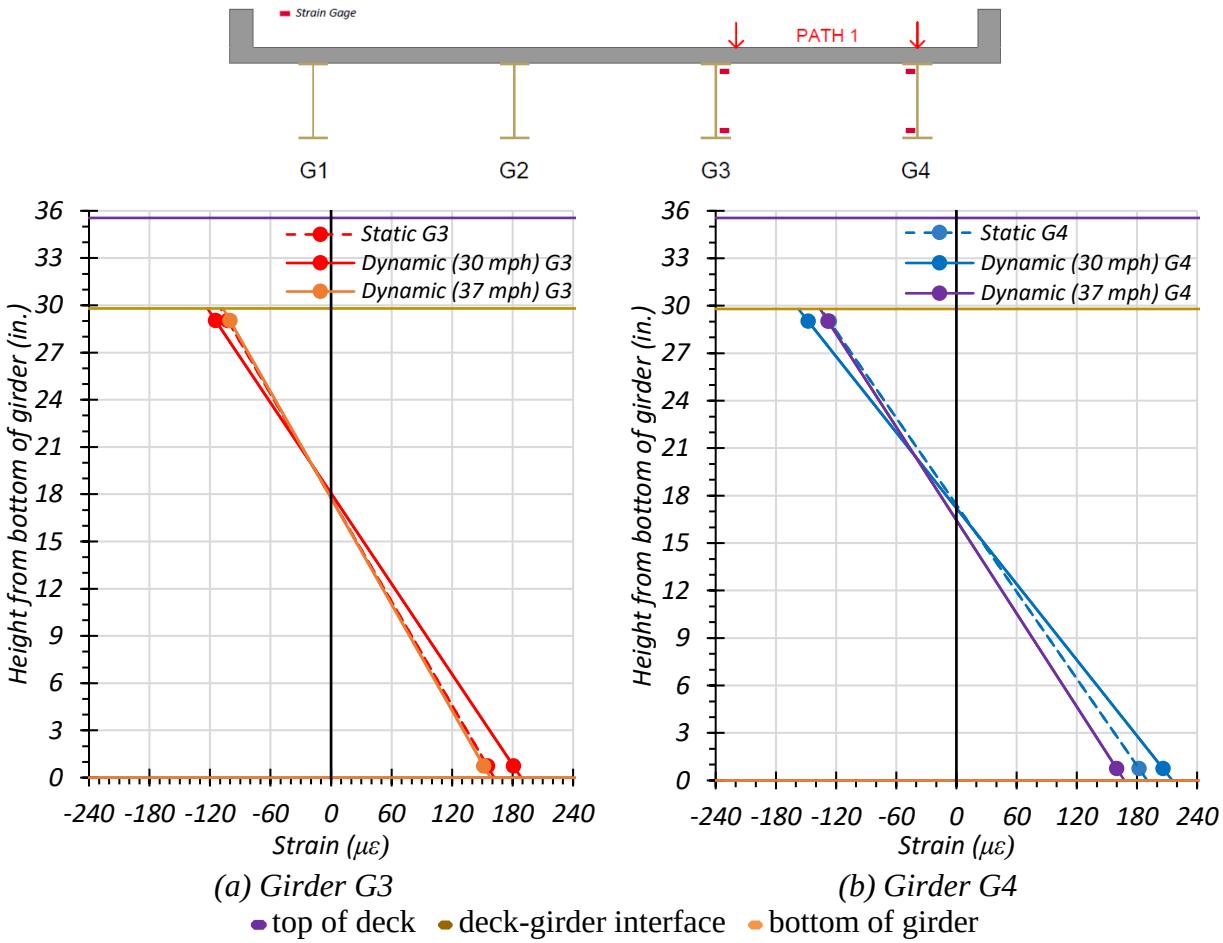

Figure 7.40. Maximum Strains for Static and Dynamic Tests for Path 1—Span 1 Loading

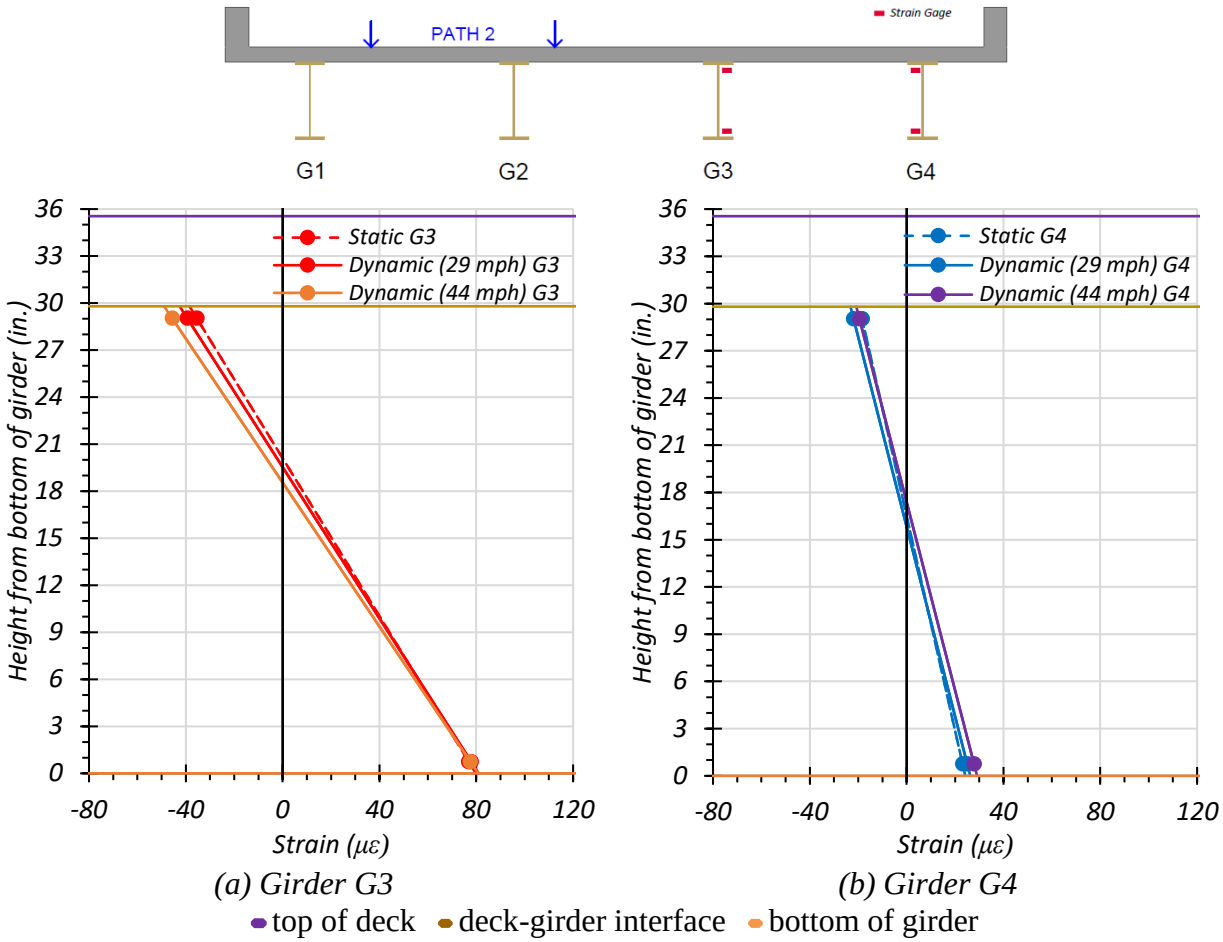

Figure 7.41. Maximum Strains for Static and Dynamic Tests for Path 2—Span 1 Loading

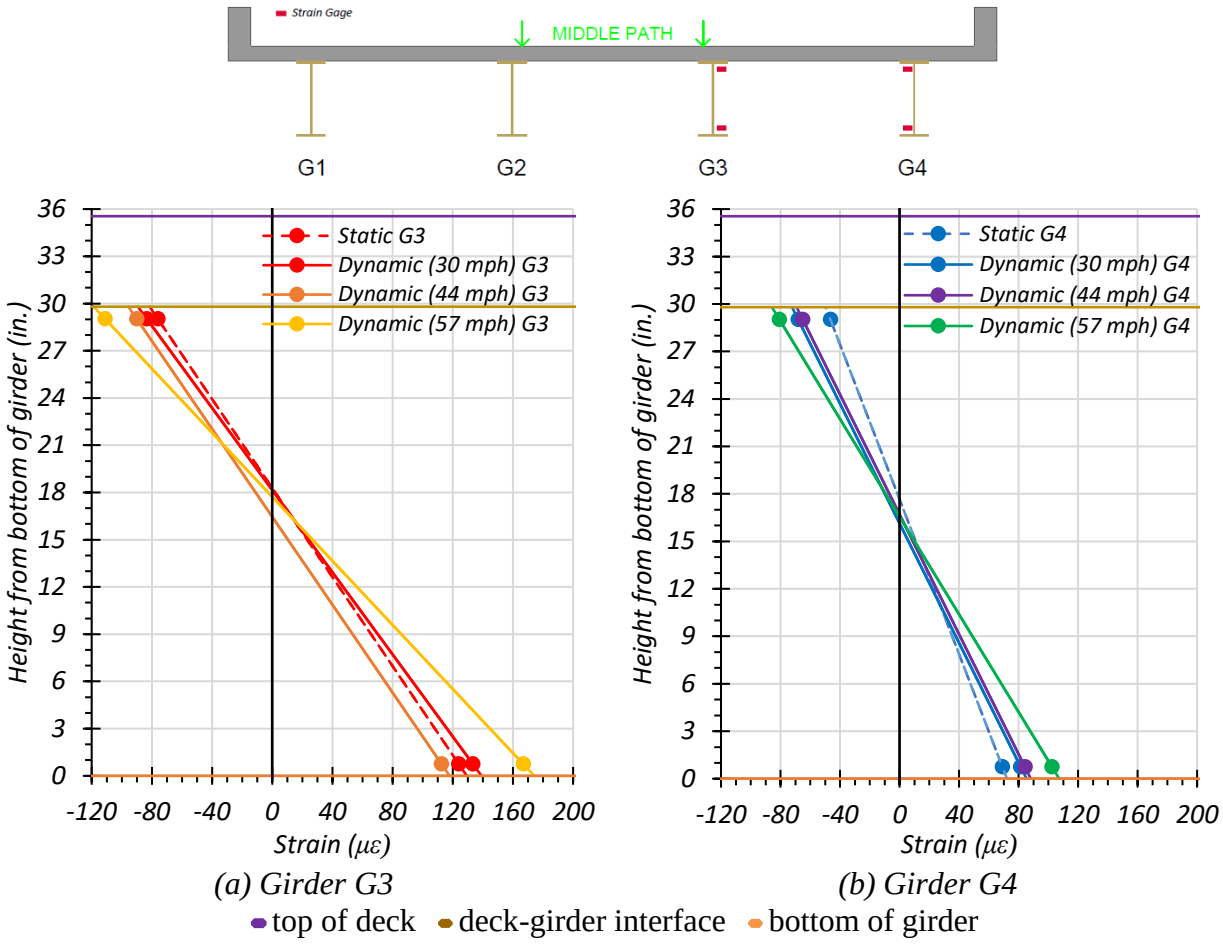

(a) Girder G3 *(b) Girder G4*

top of deck deck-girder interface bottom of girder

Figure 7.42. Maximum Strains for Static and Dynamic Tests for Middle Path—Span 1 Loading

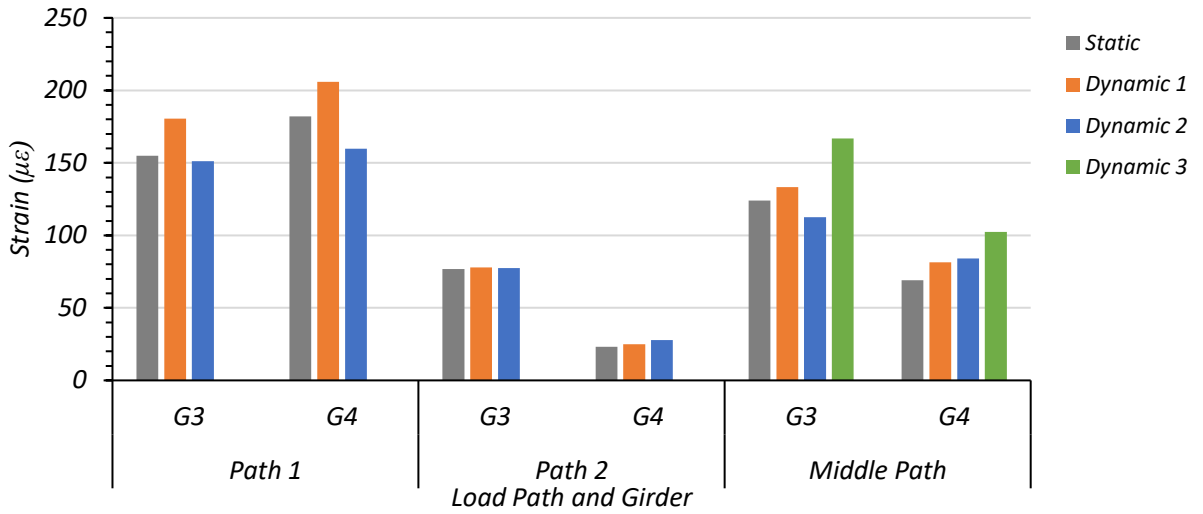

Note:

- *Path 1: Dynamic 1 = 30 mph, Dynamic 2 = 37 mph*
- *Path 2: Dynamic 1 = 29 mph, Dynamic 2 = 44 mph*
- *Middle Path: Dynamic 1 = 30 mph, Dynamic 2 = 44 mph, Dynamic 3 = 57 mph*

Figure 7.43. Comparison of Maximum Bottom Flange Strains for Static and Dynamic Tests in Span 1

The dynamic impact factor given by the *AASHTO Standard Specifications* for Span 1 of Bridge SC-12 is 27 percent, while the dynamic impact factor given by the *AASHTO LRFD Specifications* for Span 1 is 33 percent. The average dynamic impact factor for all girders for Span 1 based on the strain values observed during testing was 12 percent. The impact factor is more significant for the girders providing the majority of the load resistance, which is seen through the strain increase in Girders G3 and G4 for Dynamic 1 and in Girder G3 for Dynamic 3. However, both Girders G3 and G4 were essentially unaffected by the dynamic impact during Path 2 loading.

Maximum Girder Deflections. Figure 7.44, Figure 7.45, Figure 7.46, and Figure 7.47 show the Span 1 girder deflection time histories for the dynamic load cases along Path 1, Path 2, and the Middle Path, respectively, for each dynamic loading. Table 7.26 shows the maximum measured girder deflections for the stop location load case and for each dynamic load case. Figure 7.48 shows the Span 1 static and dynamic maximum deflection values and compares them. Figure 7.49 shows the dynamic effect based on deflection as a ratio to the static deflection.

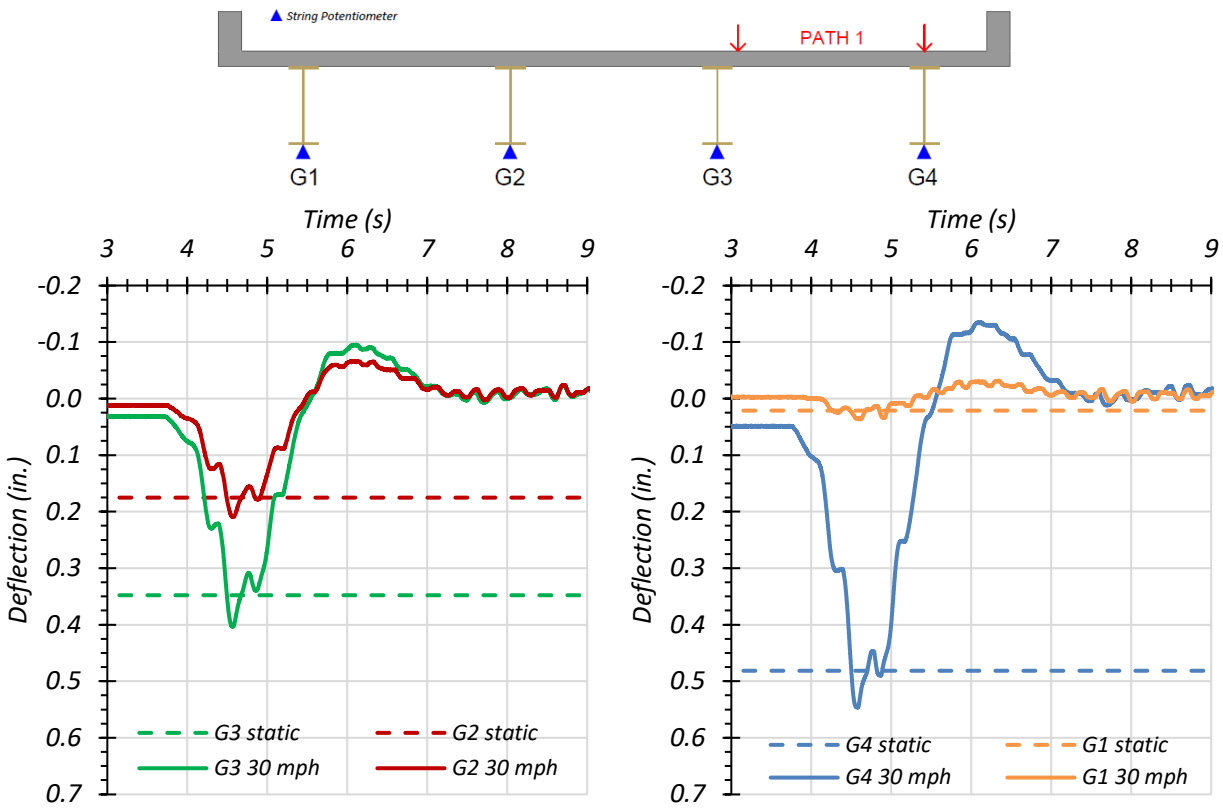

(a) Deflection Time Histories – Dynamic (30 mph)

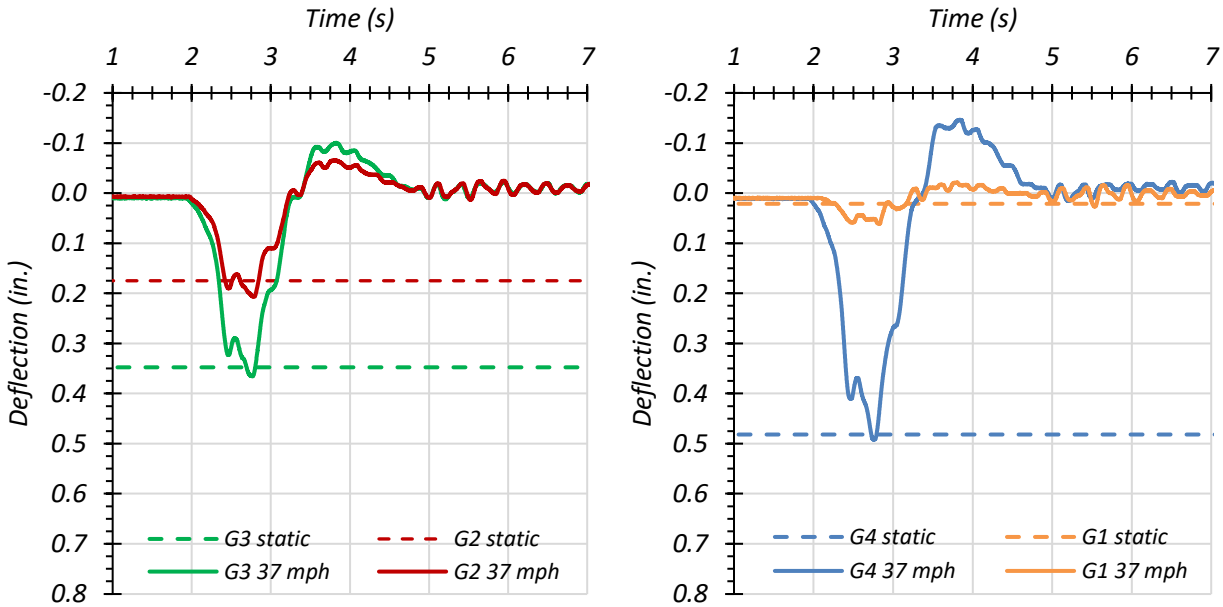

(b) Deflection Time Histories – Dynamic (37 mph)

Figure 7.44. Midspan Deflections for Static and Dynamic Tests for Path 1—Span 1 Loading

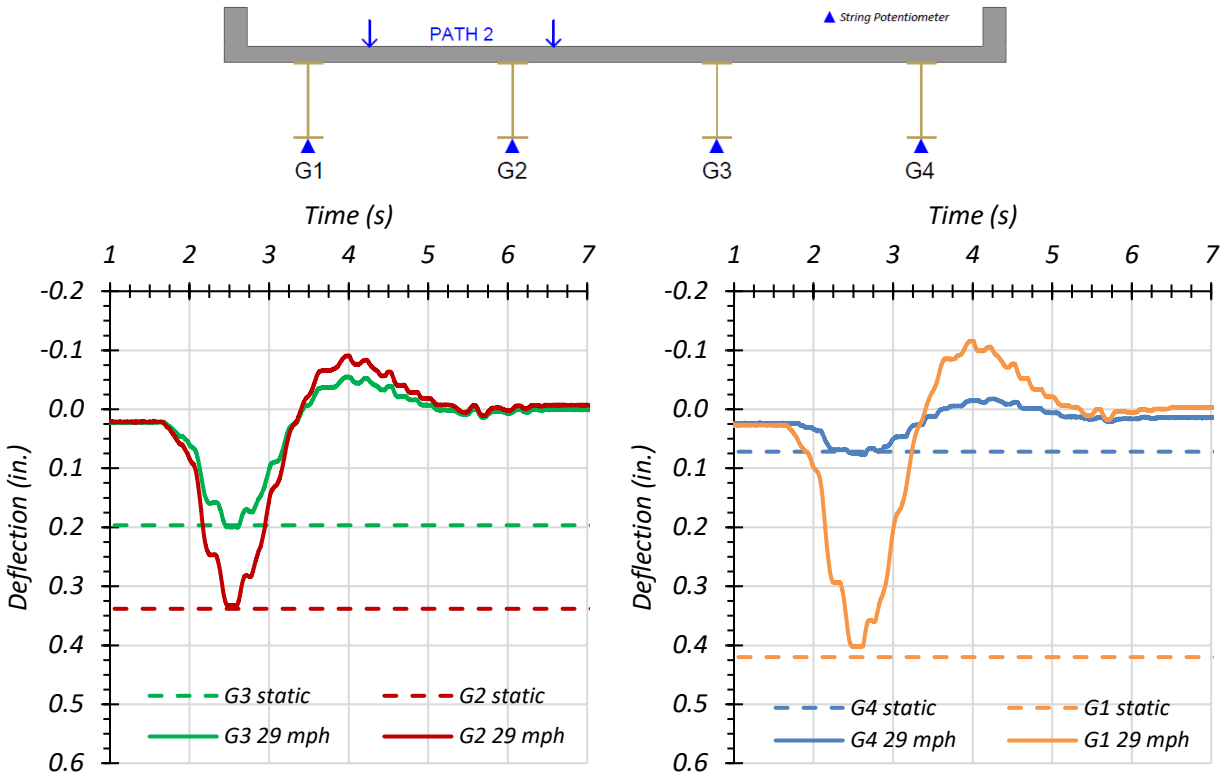

(a) Deflection Time Histories – Dynamic (29 mph)

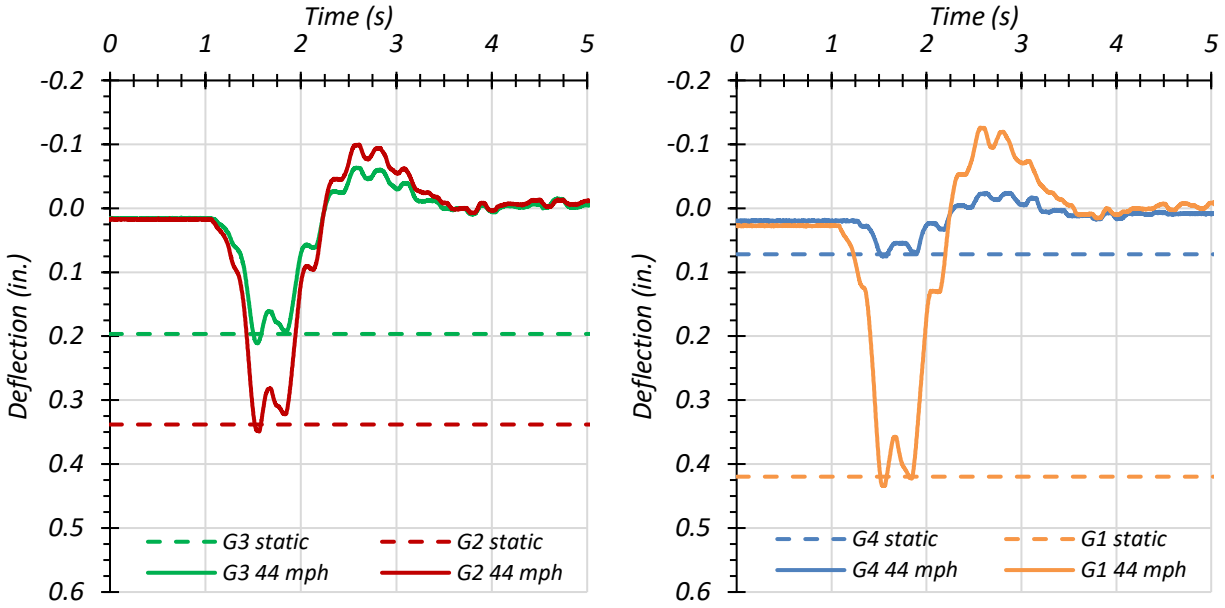

(b) Deflection Time Histories – Dynamic (44 mph)

Figure 7.45. Midspan Deflections for Static and Dynamic Tests for Path 2—Span 1 Loading

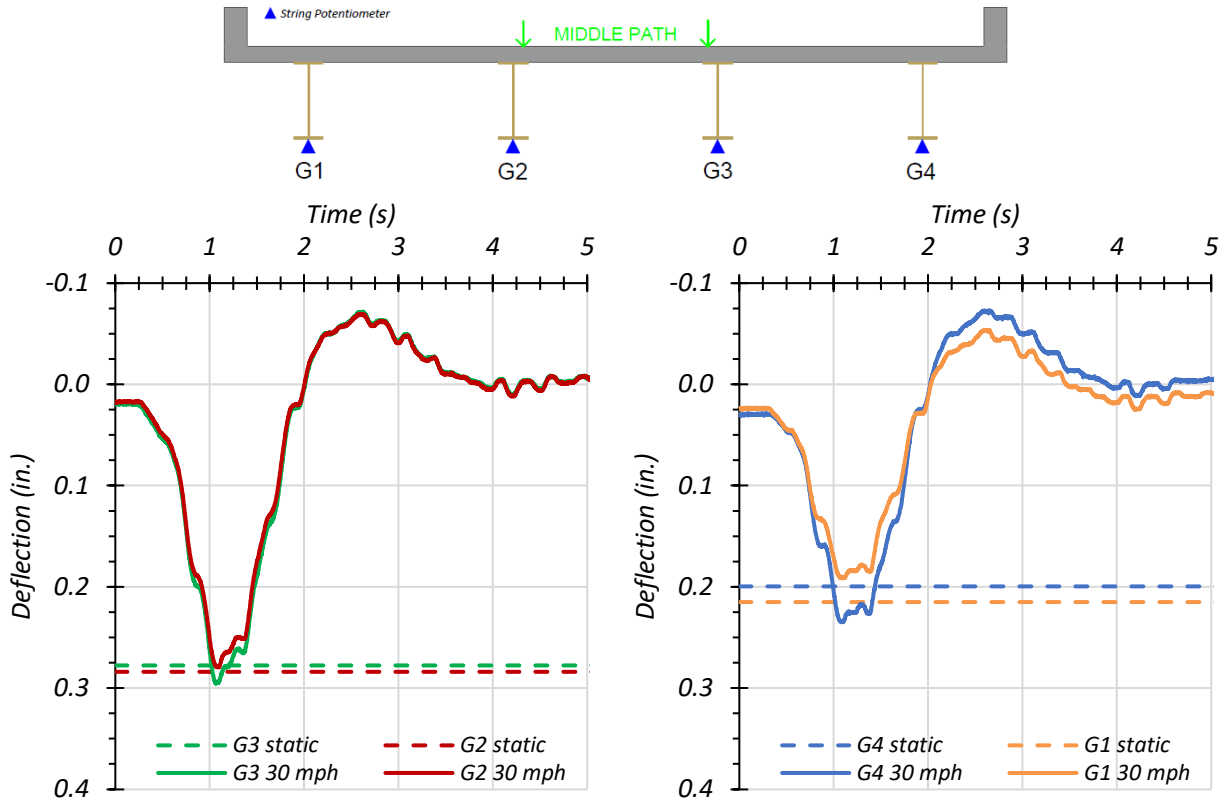

(a) Deflection Time Histories – Dynamic (30 mph)

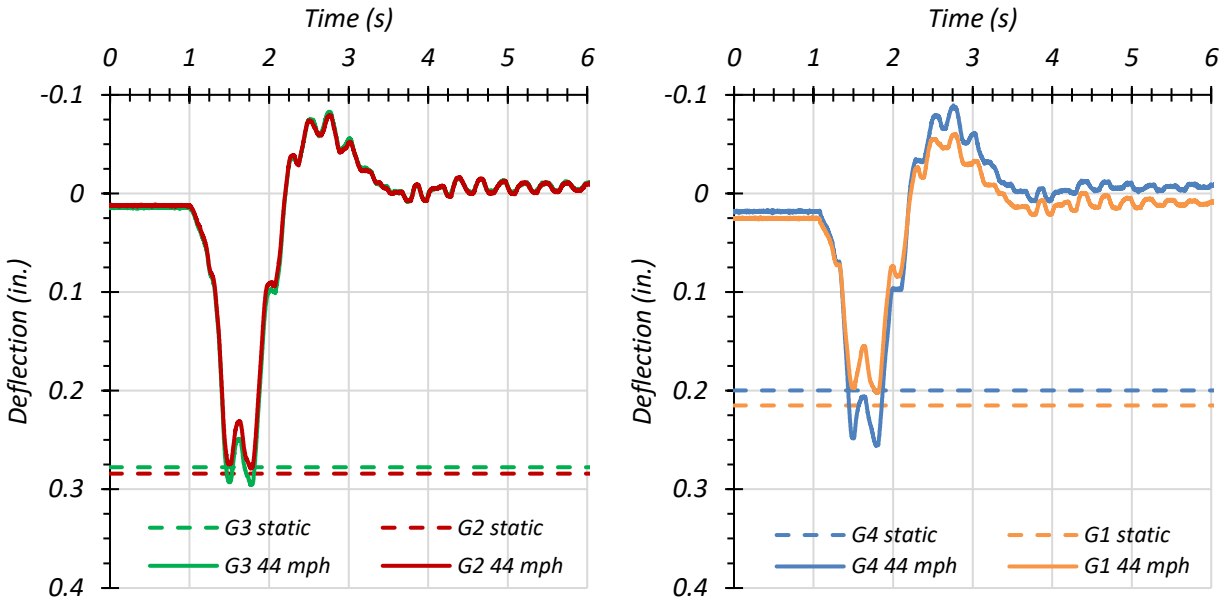

(b) Deflection Time Histories – Dynamic (44 mph)

Figure 7.46. Midspan Deflections for Static and Dynamic Tests for Middle Path—Span 1 Loading

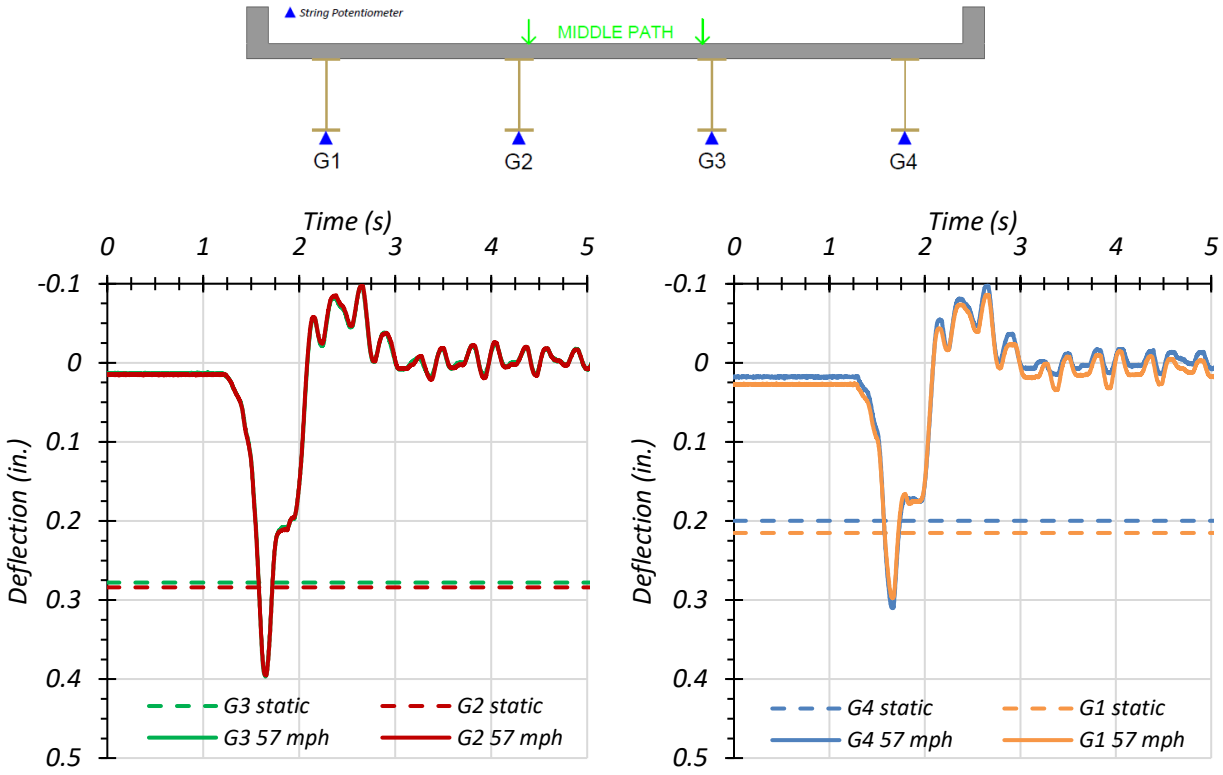

Figure 7.47. Midspan Deflections for Static and Third Dynamic Test for Middle Path—Span 1 Loading

Table 7.26. Maximum Span 1 Deflections for Static and Dynamic Tests

Load Scenario	Girder Displacement (in.)			
	G1	G2	G3	G4
Path 1 Static	0.023	0.176	0.351	0.485
Path 1 Dynamic (30 mph)	0.037	0.209	0.404	0.546
Path 1 Dynamic (37 mph)	0.061	0.207	0.366	0.492
Maximum Dynamic Amplification	**161.4%**	**19.0%**	**15.1%**	**12.8%**
Path 2 Static	0.422	0.340	0.198	0.075
Path 2 Dynamic (29 mph)	0.403	0.334	0.201	0.077
Path 2 Dynamic (44 mph)	0.434	0.349	0.211	0.076
Maximum Dynamic Amplification	**3.0%**	**2.8%**	**6.5%**	**3.7%**
Middle Static	0.217	0.286	0.280	0.203
Middle Dynamic (30 mph)	0.217	0.280	0.296	0.235
Middle Dynamic (44 mph)	0.202	0.279	0.296	0.256
Middle Dynamic (57 mph)	0.298	0.395	0.397	0.310
Maximum Dynamic Amplification	**37.1%**	**38.0%**	**41.8%**	**53.2%**

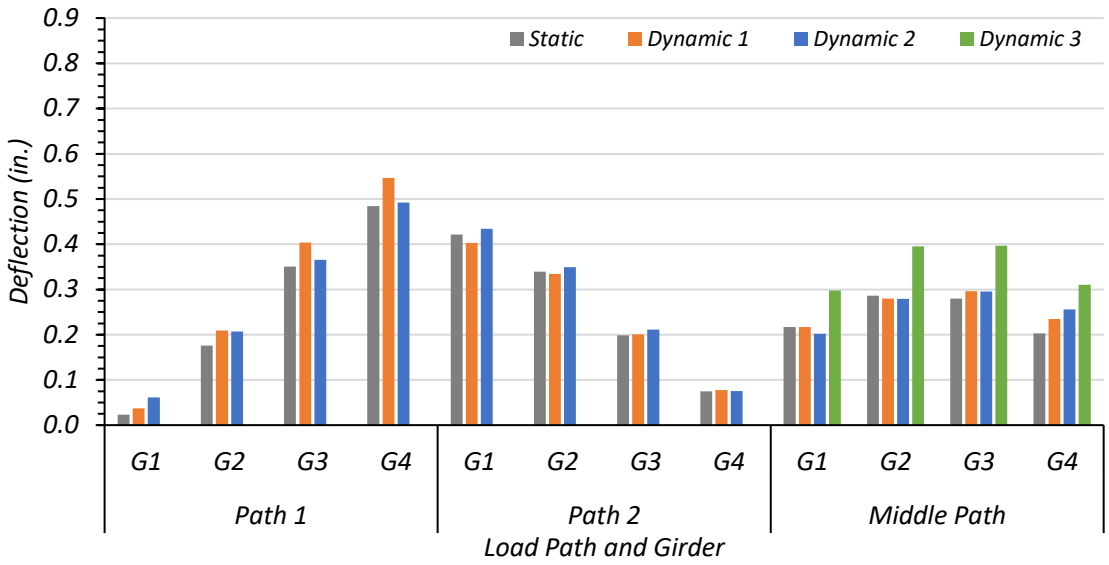

Note:

- *Path 1: Dynamic 1 = 30 mph, Dynamic 2 = 37 mph*
- *Path 2: Dynamic 1 = 29 mph, Dynamic 2 = 44 mph*
- *Middle Path: Dynamic 1 = 30 mph, Dynamic 2 = 44 mph, Dynamic 3 = 57 mph*

Figure 7.48. Comparison of Maximum Span 1 Deflections for Static and Dynamic Tests

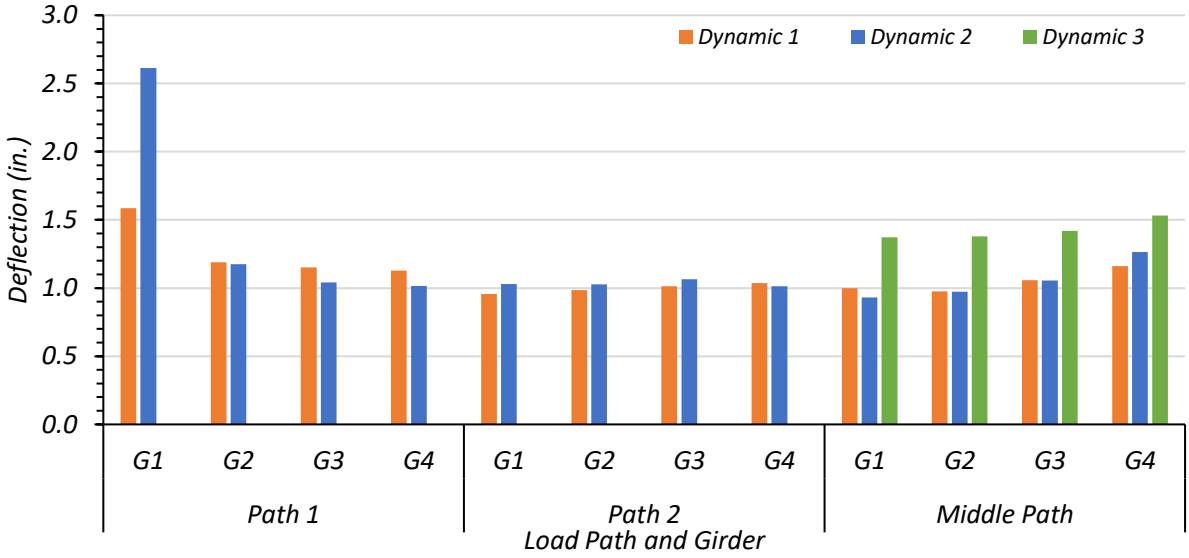

Note:

- *Path 1: Dynamic 1 = 30 mph, Dynamic 2 = 37 mph*
- *Path 2: Dynamic 1 = 29 mph, Dynamic 2 = 44 mph*
- *Middle Path: Dynamic 1 = 30 mph, Dynamic 2 = 44 mph, Dynamic 3 = 57 mph*

Figure 7.49. Ratio of Maximum Span 1 Dynamic Deflection to Static Deflection

The dynamic impact factor given by the *AASHTO Standard Specifications* for Span 1 of Bridge SC-12 is 27 percent, while the dynamic impact factor given by the *AASHTO LRFD Specifications* for this bridge is 33 percent. The average dynamic impact factor for all girders for Span 1 based on the deflection values observed during testing was 18 percent.

During Path 1 loading, the maximum percent increase in deflection for Girder G3 was 15.1 percent during Dynamic 2 loading. The maximum percent increase in deflection in Girder G4 was 12.8 percent during Dynamic 2 loading.

During Path 2 loading, the maximum percent increase in deflection for Girder G3 was 6.5 percent during Dynamic 2 loading. The maximum percent increase in deflection in Girder G4 was 3.7 percent during Dynamic 1 loading.

During Middle Path loading, the maximum percent increase in deflection for Girder G3 was 41.8 percent during Dynamic 3 loading. The maximum percent increase in deflection in Girder G4 was 53.2 percent during Dynamic 3 loading.

*7.6.5.2 **Span 2 Dynamic Amplification***

Maximum Girder Strains. Based on the results of the static and dynamic tests for each path, the increases in strains and deflections due to the moving vehicle were examined. Figure 7.50, Figure 7.51, and Figure 7.52 show the maximum Span 2 dynamic strains observed for Path 1, Path 2, and the Middle Path, respectively, plotted with the static strains observed for those paths. Figure 7.53 shows those strain values and compares them to the appropriate static load case for Span 2.

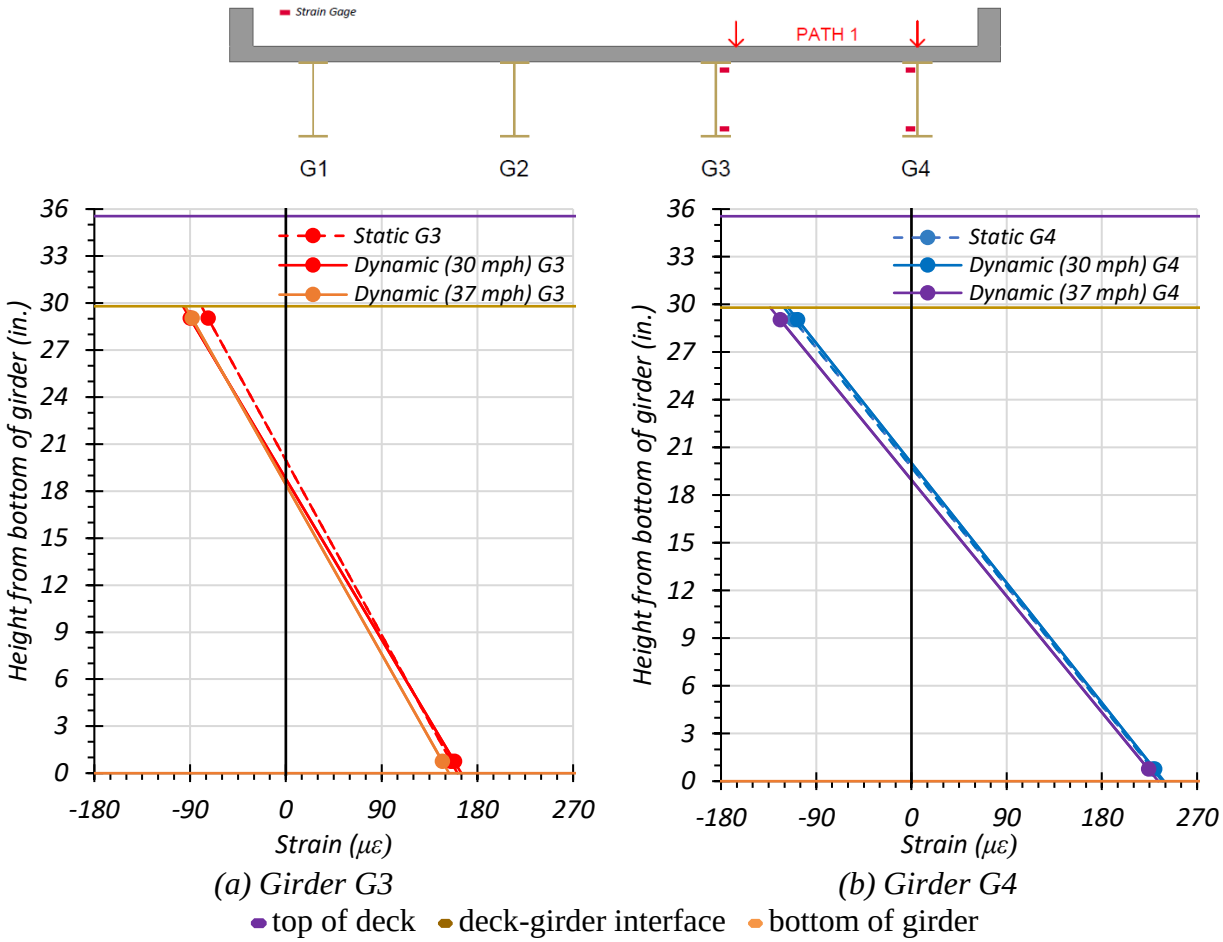

Figure 7.50. Maximum Strains for Static and Dynamic Tests for Path 1—Span 2 Loading

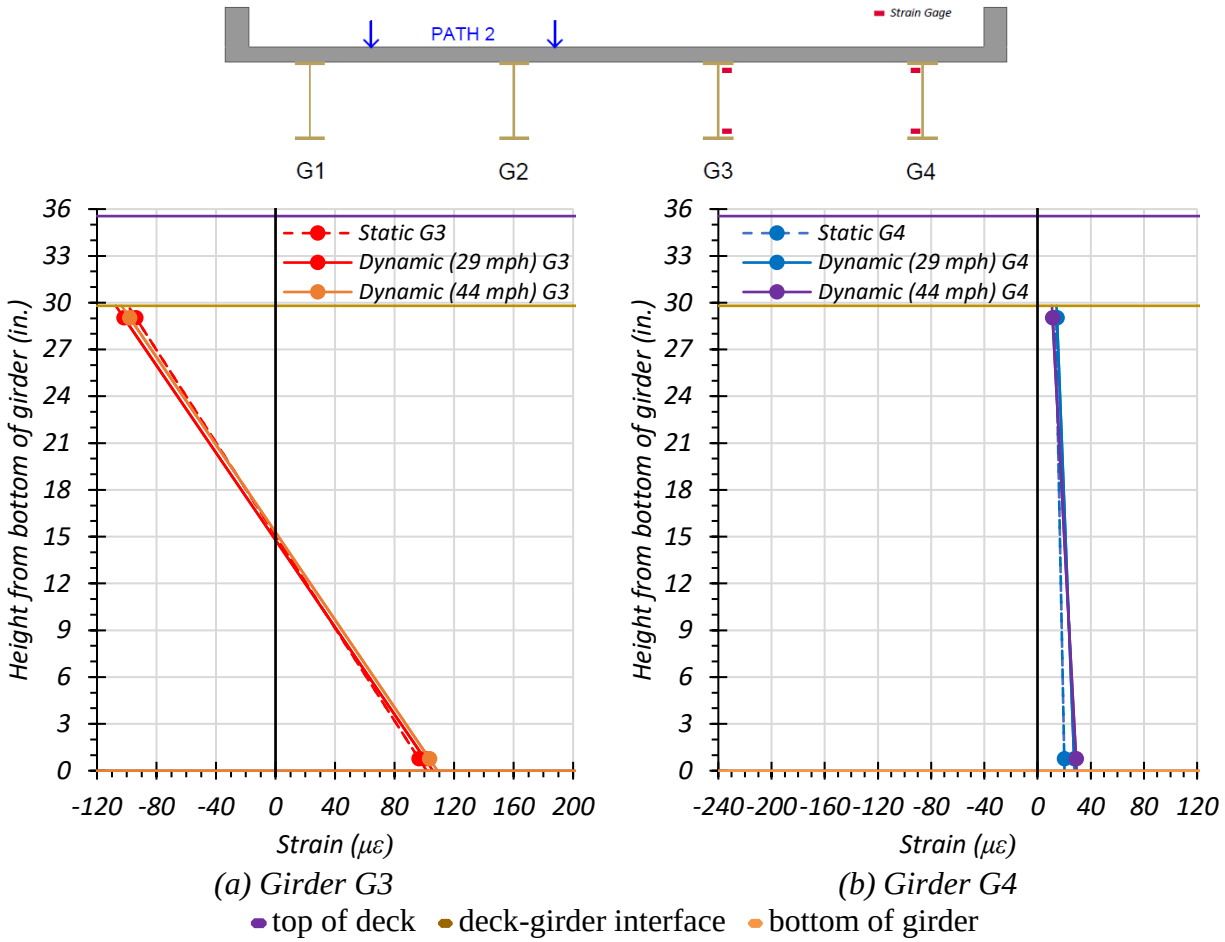

Figure 7.51. Maximum Strains for Static and Dynamic Tests for Path 2—Span 2 Loading

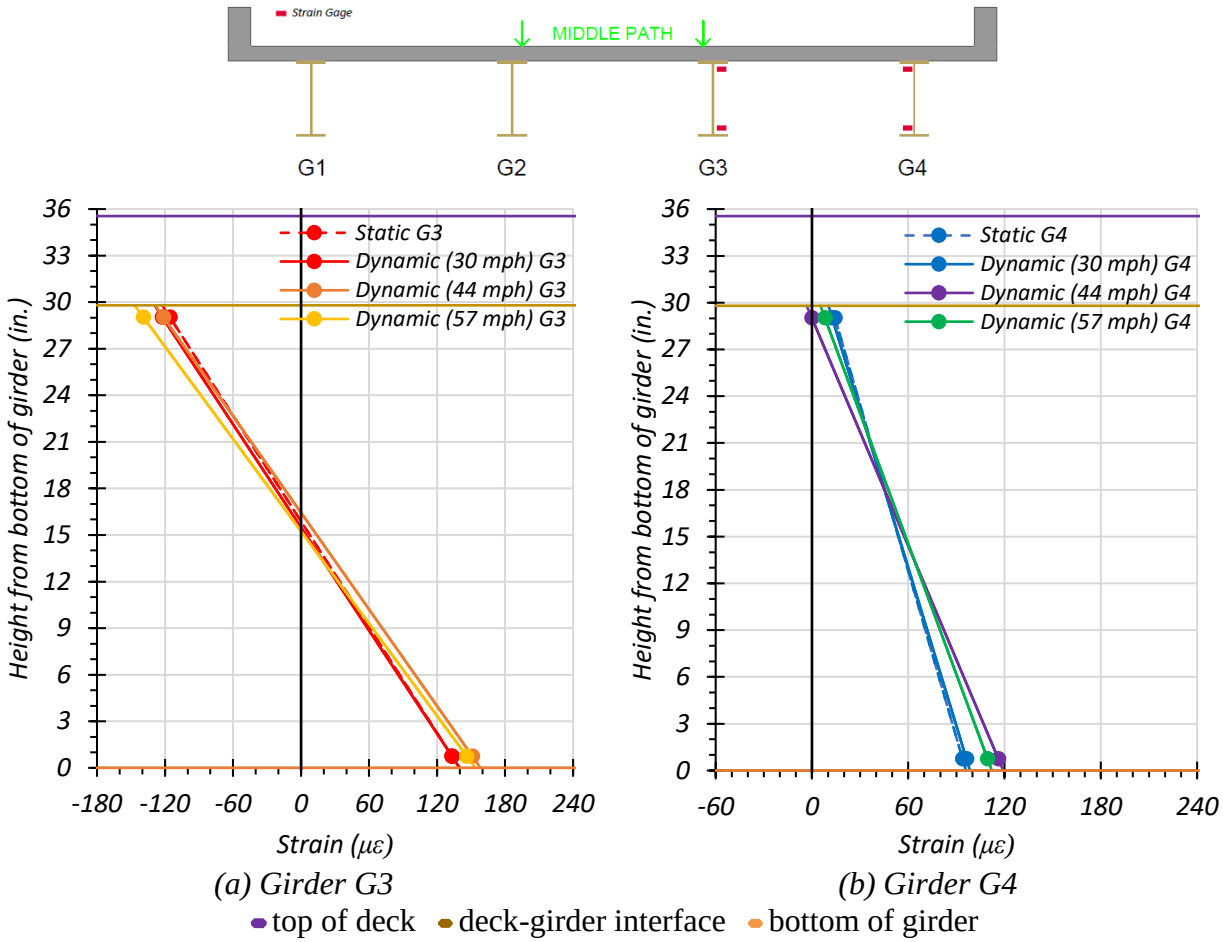

Figure 7.52. Maximum Strains for Static and Dynamic Tests for Middle Path—Span 2 Loading

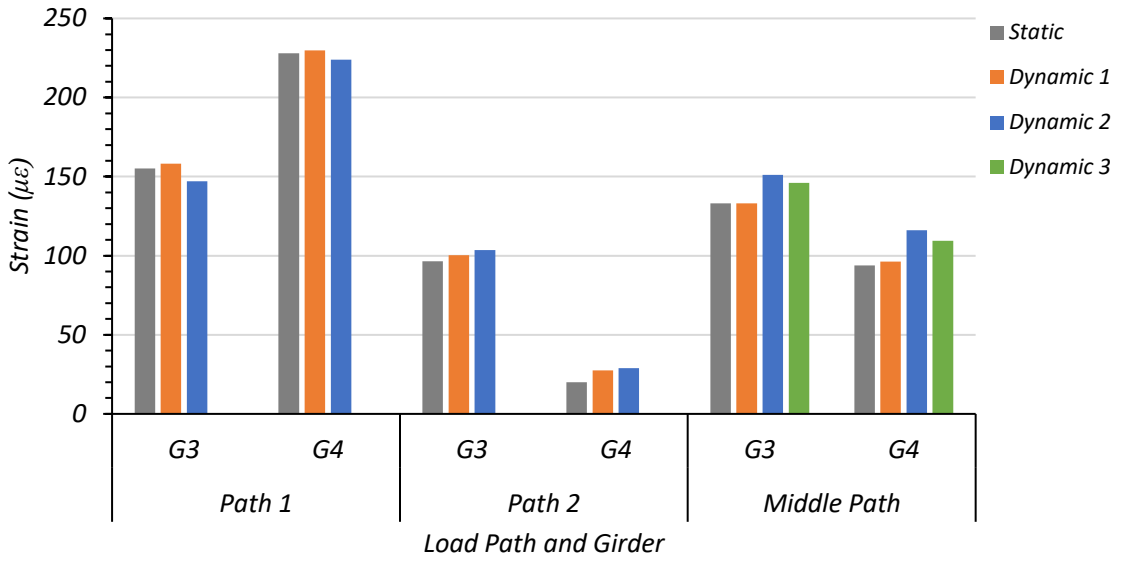

Note:

- *Path 1: Dynamic 1 = 30 mph, Dynamic 2 = 37 mph*
- *Path 2: Dynamic 1 = 29 mph, Dynamic 2 = 44 mph*
- *Middle Path: Dynamic 1 = 30 mph, Dynamic 2 = 44 mph, Dynamic 3 = 57 mph*

Figure 7.53. Comparison of Maximum Bottom Flange Strains for Static and Dynamic Tests in Span 2

The dynamic impact factor given by the *AASHTO Standard Specifications* for Span 2 of Bridge SC-12 is 25 percent. The dynamic impact factor given by the *AASHTO LRFD Specifications* for this bridge is 33 percent. The average dynamic impact factor for all girders for Span 2 based on the strain values observed during testing was 11 percent. The dynamic impact factor is less significant for Span 2 than Span 1. Both Path 1 and Path 2 loading produced fairly insignificant dynamic effects for Girder G3 and Girder G4, and in some cases these girders saw decreases in strain under dynamic load. However, the Middle Path loading did produce noticeable dynamic effects on both Girder G3 and G4 for Dynamic 2 and Dynamic 3 loading.

Maximum Girder Deflections. Figure 7.54, Figure 7.55, Figure 7.56, and Figure 7.57 show the Span 2 girder deflection time histories for the dynamic load cases along Path 1, Path 2, and the Middle Path, respectively, for each dynamic loading. Table 7.27 shows the maximum measured girder deflections for the stop location load case and for each dynamic load case. Figure 7.58 shows the Span 2 static and dynamic maximum deflection values and compares them. Figure 7.59 shows the dynamic effect based on deflection as a ratio to the static deflection.

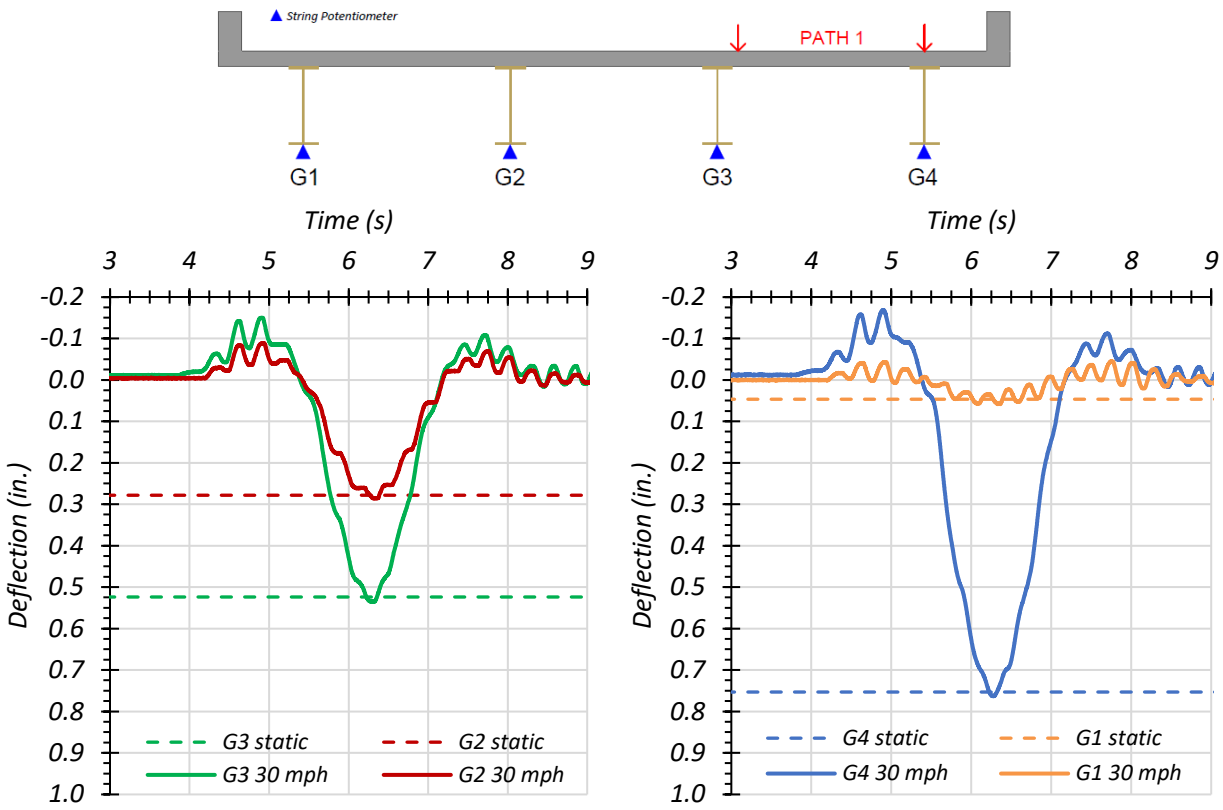

(a) Deflection Time Histories – Dynamic (30 mph)

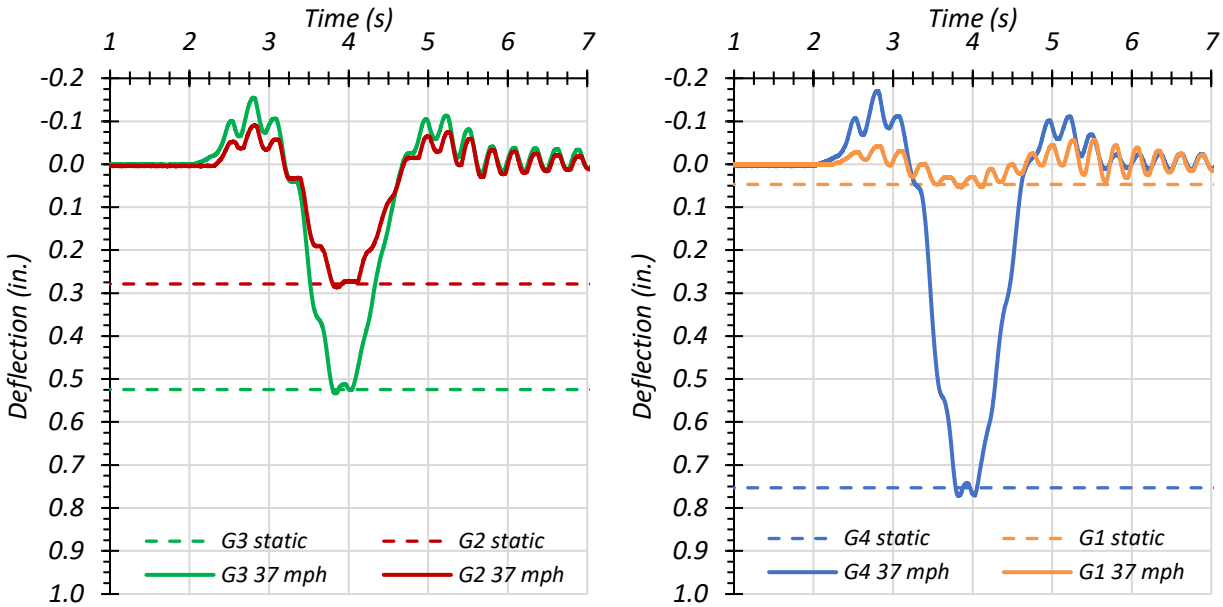

(b) Deflection Time Histories – Dynamic (37 mph)

Figure 7.54. Midspan Deflections for Static and Dynamic Tests for Path 1—Span 2 Loading

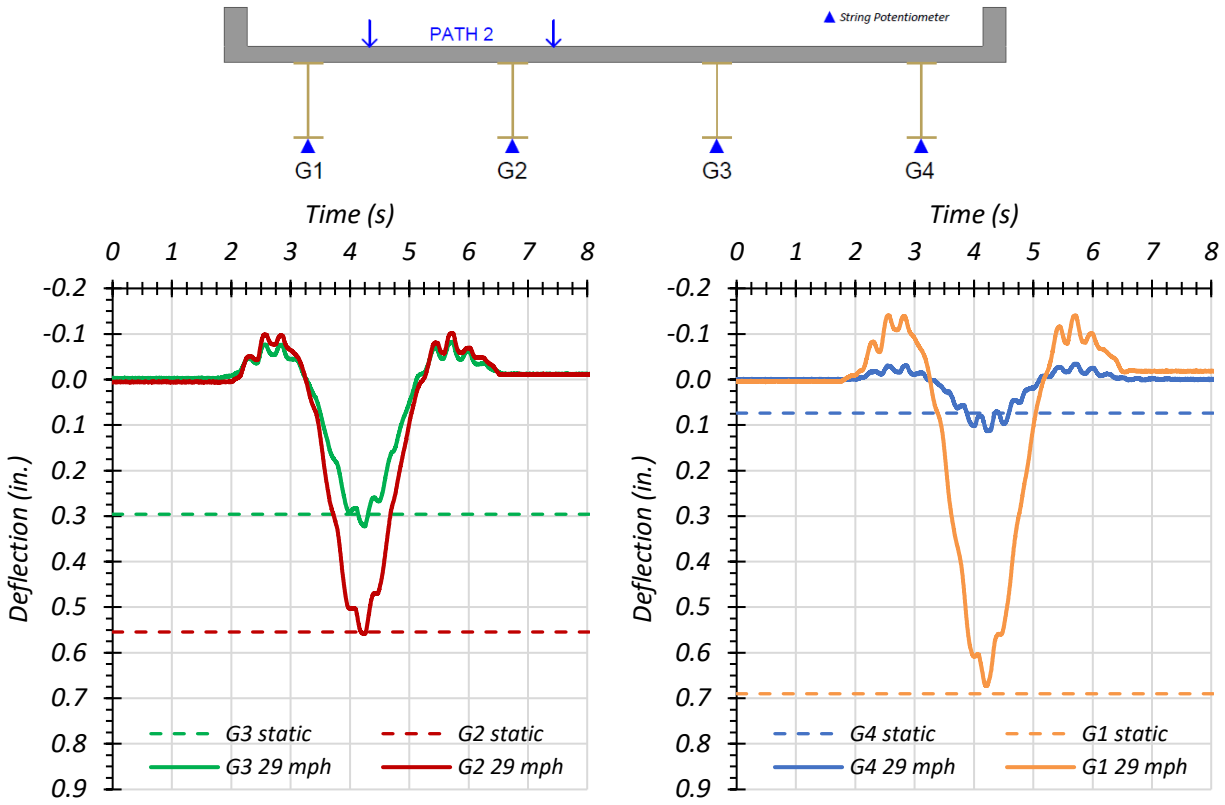

(a) Deflection Time Histories – Dynamic (29 mph)

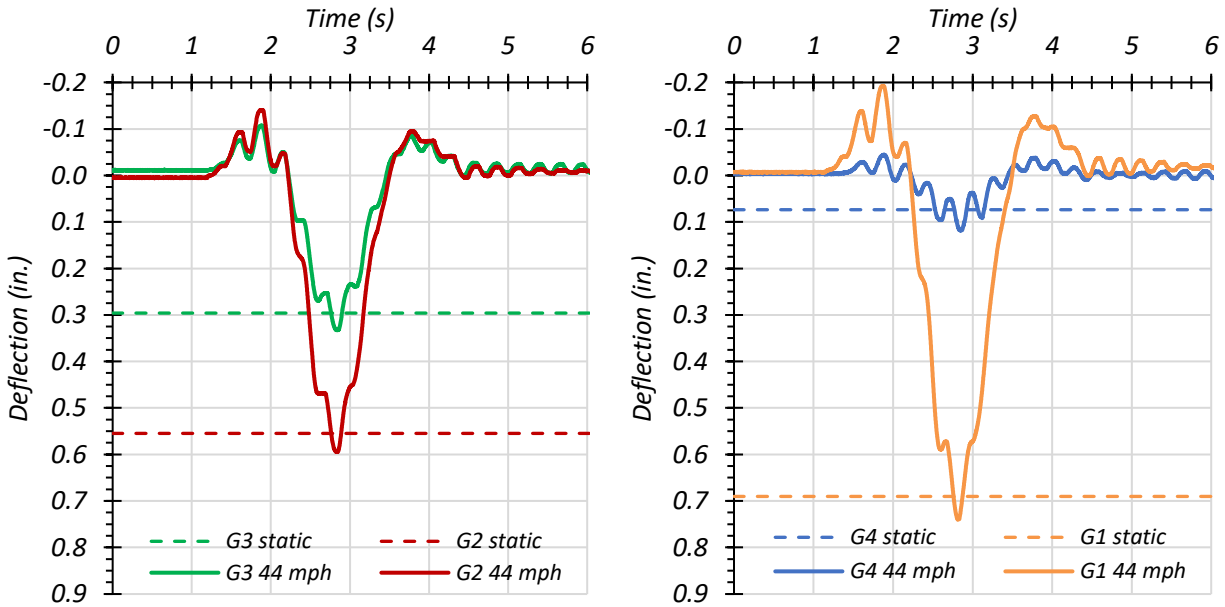

(b) Deflection Time Histories – Dynamic (44 mph)

Figure 7.55. Midspan Deflections for Static and Dynamic Tests for Path 2—Span 2 Loading

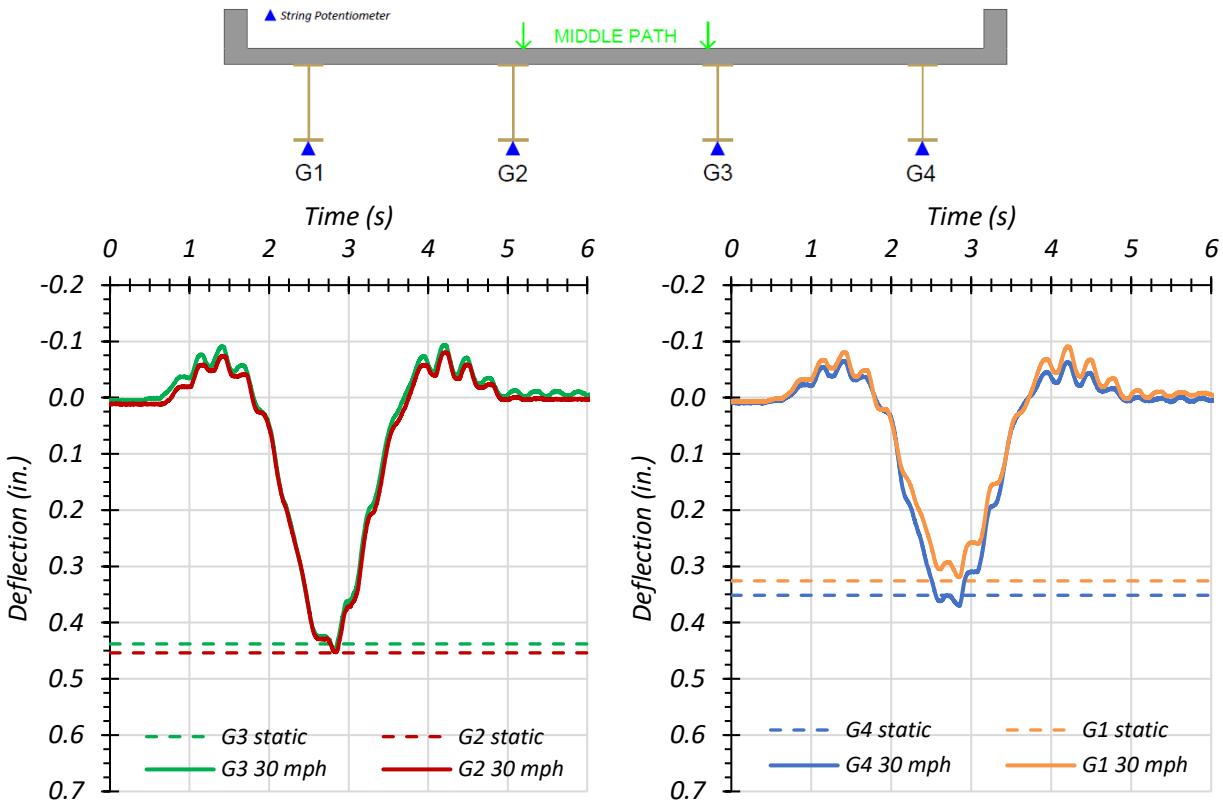

(a) Deflection Time Histories – Dynamic (30 mph)

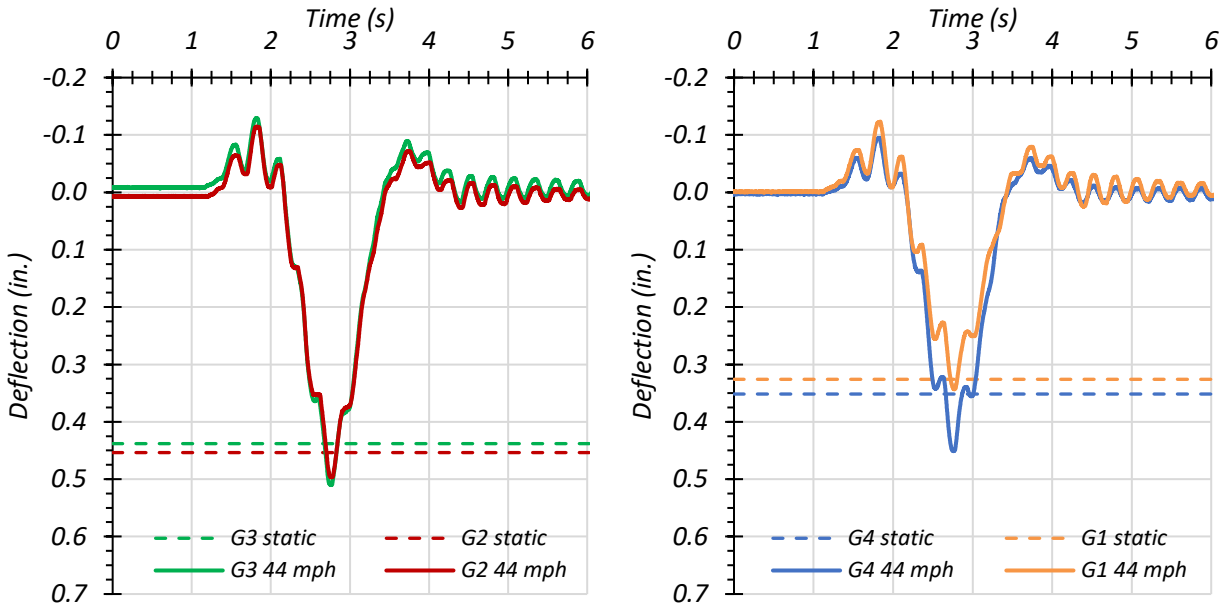

(b) Deflection Time Histories – Dynamic (44 mph)

Figure 7.56. Midspan Deflections for Static and Dynamic Tests for Middle Path—Span 2 Loading

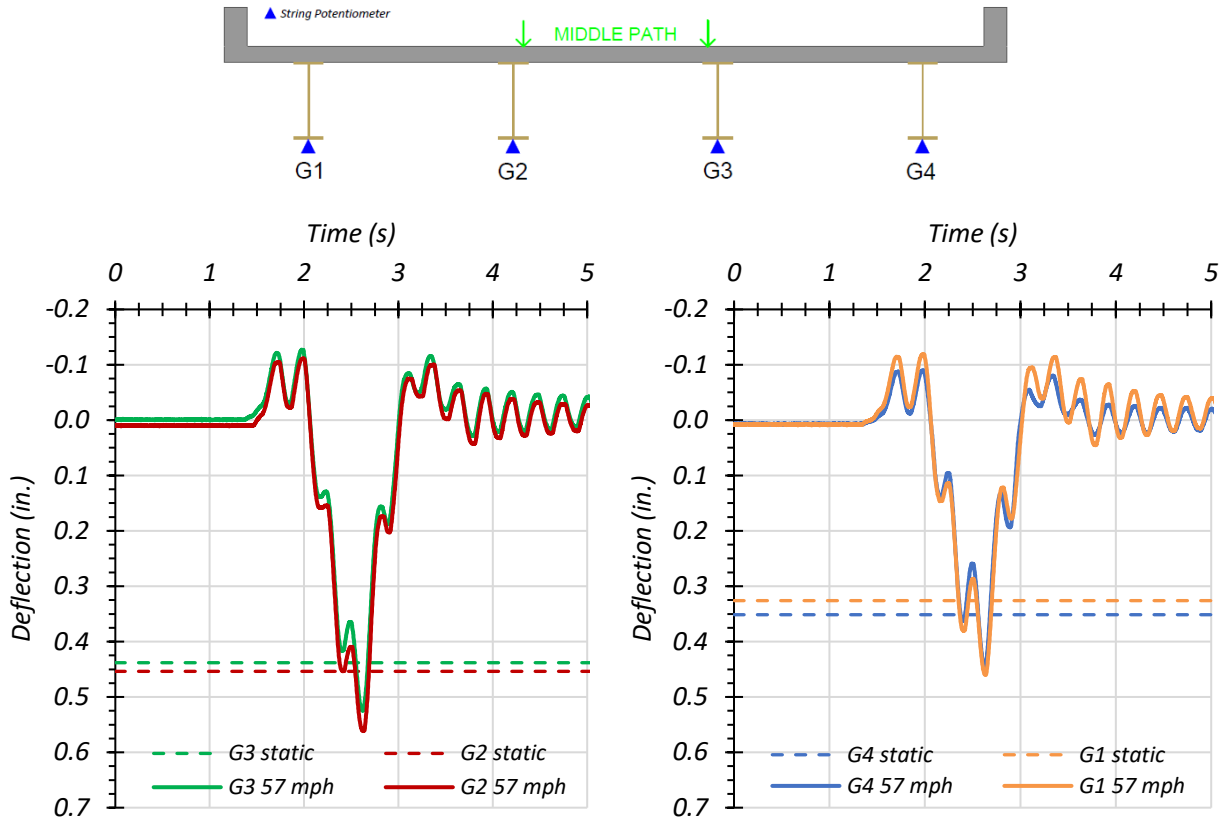

Figure 7.57. Midspan Deflections for Static and Third Dynamic Test for Middle Path—Span 2 Loading

Table 7.27. Maximum Span 2 Deflections for Static and Dynamic Tests

Load Scenario	Girder Displacement (in.)			
	G1	G2	G3	G4
Path 1 Static	0.049	0.280	0.526	0.755
Path 1 Dynamic (30 mph)	0.058	0.286	0.536	0.764
Path 1 Dynamic (37 mph)	0.054	0.287	0.533	0.772
Maximum Dynamic Amplification	**19.0%**	**2.2%**	**1.8%**	**2.3%**
Path 2 Static	0.692	0.556	0.298	0.077
Path 2 Dynamic (29 mph)	0.673	0.559	0.322	0.113
Path 2 Dynamic (44 mph)	0.740	0.595	0.333	0.119
Maximum Dynamic Amplification	**6.9%**	**6.9%**	**11.8%**	**55.1%**
Middle Static	0.328	0.457	0.440	0.353
Middle Dynamic (30 mph)	0.328	0.453	0.446	0.370
Middle Dynamic (44 mph)	0.343	0.497	0.510	0.451
Middle Dynamic (57 mph)	0.460	0.562	0.525	0.444
Maximum Dynamic Amplification	**40.2%**	**23.0%**	**19.4%**	**27.9%**

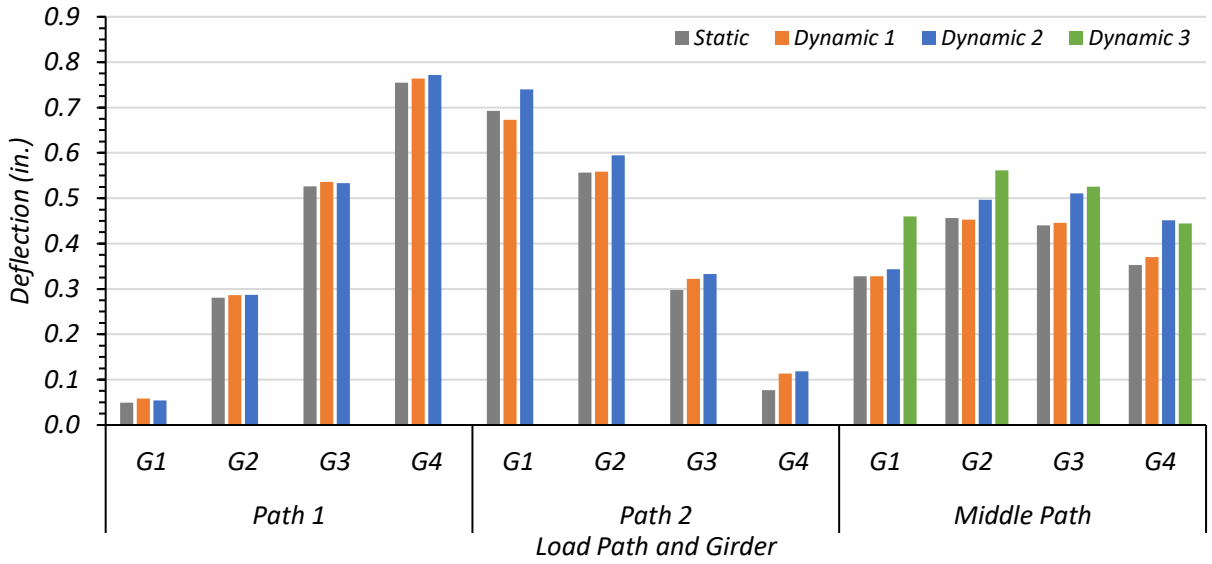

Note:

- *Path 1: Dynamic 1 = 30 mph, Dynamic 2 = 37 mph*
- *Path 2: Dynamic 1 = 29 mph, Dynamic 2 = 44 mph*
- *Middle Path: Dynamic 1 = 30 mph, Dynamic 2 = 44 mph, Dynamic 3 = 57 mph*

Figure 7.58. Comparison of Maximum Span 2 Deflections for Static and Dynamic Tests

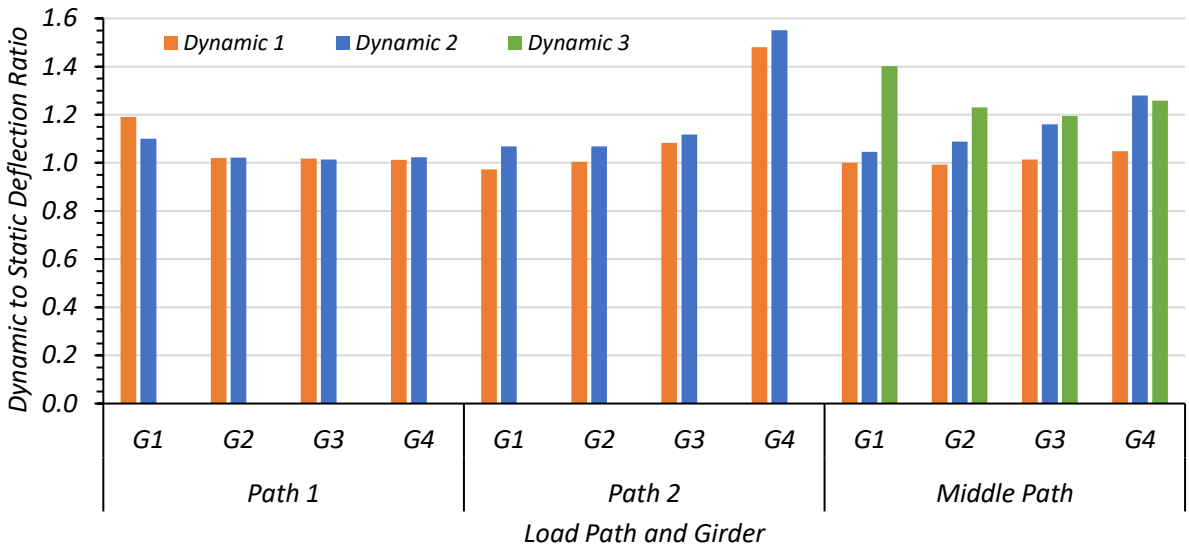

Note:

- *Path 1: Dynamic 1 = 30 mph, Dynamic 2 = 37 mph*
- *Path 2: Dynamic 1 = 29 mph, Dynamic 2 = 44 mph*
- *Middle Path: Dynamic 1 = 30 mph, Dynamic 2 = 44 mph, Dynamic 3 = 57 mph*

Figure 7.59. Ratio of Maximum Span 2 Dynamic Deflection to Static Deflection

The dynamic impact factor given by the *AASHTO Standard Specifications* for Span 2 of Bridge SC-12 is 25 percent while the dynamic impact factor given by the *AASHTO LRFD Specifications* for this bridge is 33 percent. The average dynamic impact factor for all girders for Span 2 based on the deflection values observed during testing was 12 percent.

During Path 1 loading, the maximum percent increase in deflection for Girder G3 was 1.8 percent during Dynamic 2 loading. The maximum percent increase in deflection in Girder G4 was 2.3 percent during Dynamic 2 loading.

During Path 2 loading, the maximum percent increase in deflection for Girder G3 was 11.8 percent during Dynamic 1 loading. The maximum percent increase in deflection in Girder G4 was 55.1 percent during Dynamic 2 loading; however, Girder G4 experienced very minimal deflection during Path 2 loading, which may explain the large dynamic effect.

During Middle Path loading, the maximum percent increase in deflection for Girder G3 was 19.4 percent during Dynamic 3 loading. The maximum percent increase in deflection in Girder G4 was 27.9 percent during Dynamic 2 loading.

7.6.5.3 ***Dynamic Characteristics of the Bridge***

Data obtained from the accelerometers during dynamic tests and the sledgehammer tests were filtered, and an FFT analysis was performed, which determined the first two natural frequencies of the bridge as 3.78 Hz and 6.71 Hz. For each natural frequency, the amplitude and phase angle of each accelerometer were used to develop the mode shape. Figure 7.60 shows a cut through the longitudinal centerline of the bridge and a transverse section of both spans for the mode shape produced by the first natural frequency of Bridge SC-12. Figure 7.61 shows a longitudinal section and a transverse section of both spans for the mode shape produced by the second natural frequency of the bridge. Figure 7.62 shows a longitudinal section and a transverse section of both spans for the mode shape produced by the second natural frequency of the bridge.

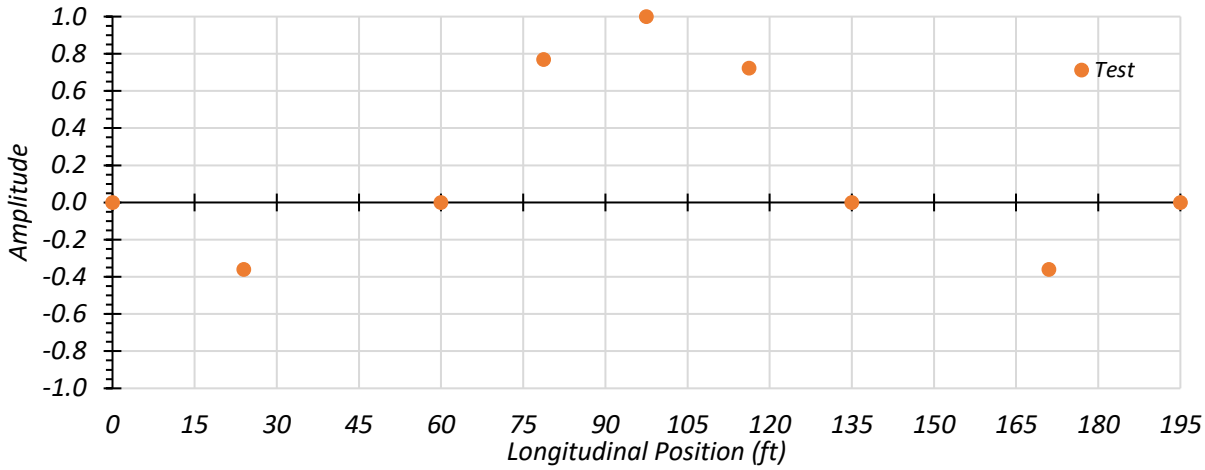

(a) Longitudinal Section

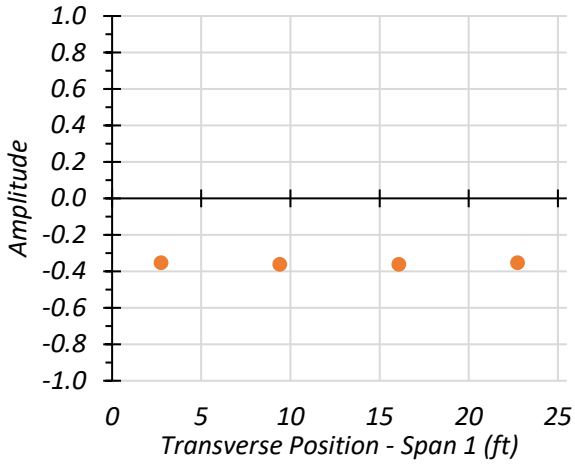

(b) Transverse Section – Span 1

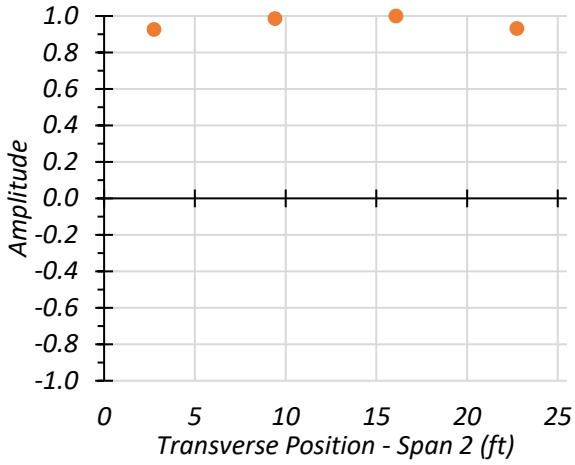

(c) Transverse Section – Span 2

Figure 7.60. First Mode Shape of Bridge SC-12 (f_1 = 3.78 Hz)

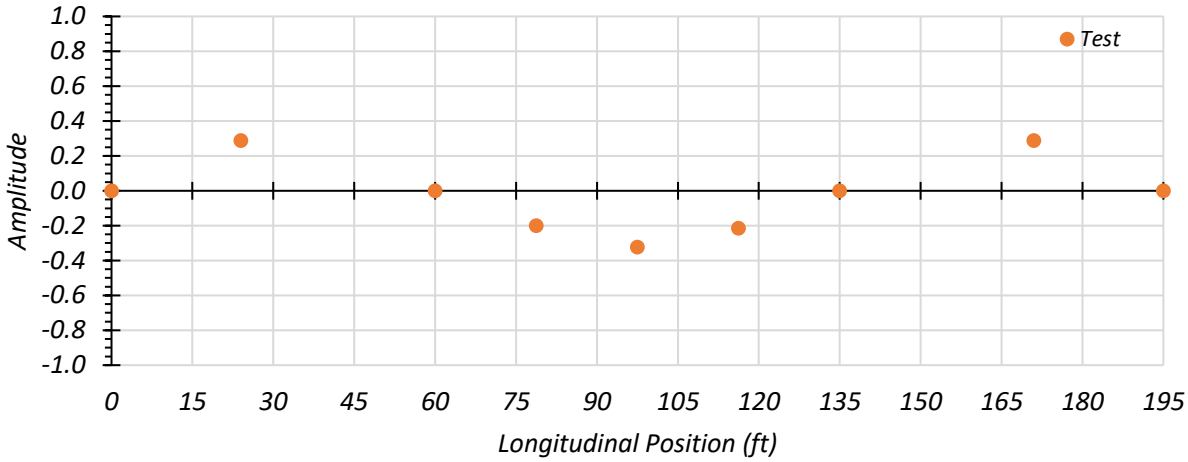

(a) Longitudinal Section

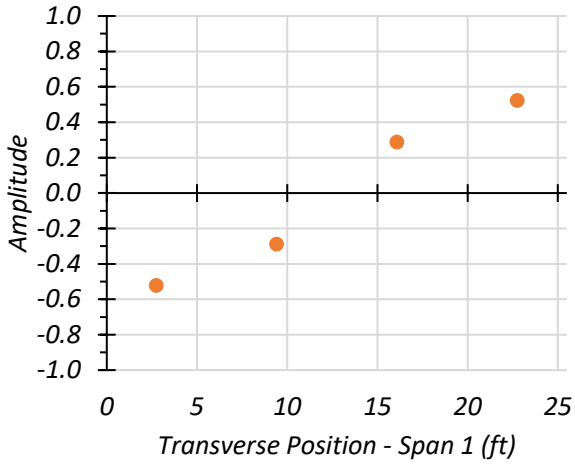

(b) Transverse Section – Span 1

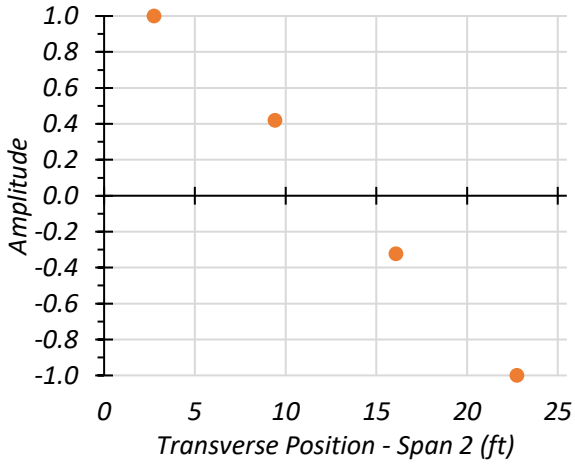

(c) Transverse Section – Span 2

Figure 7.61. Second Mode Shape of Bridge SC-12 (f_2 = 6.71 Hz)

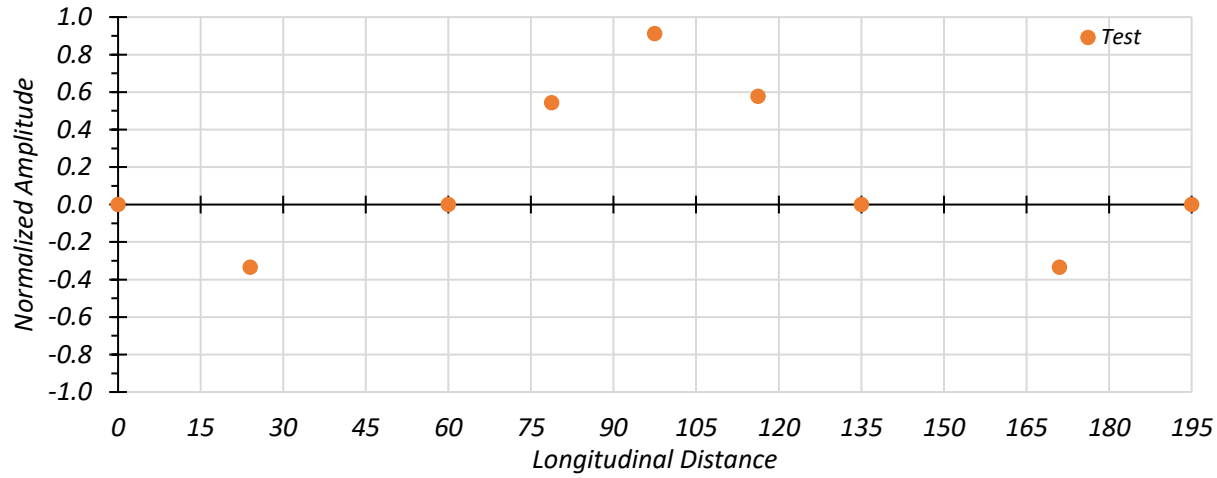

(a) Longitudinal Section

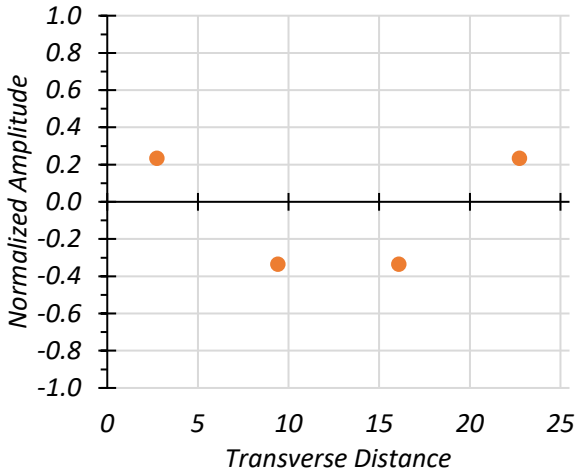

(b) Transverse Section – Span 1

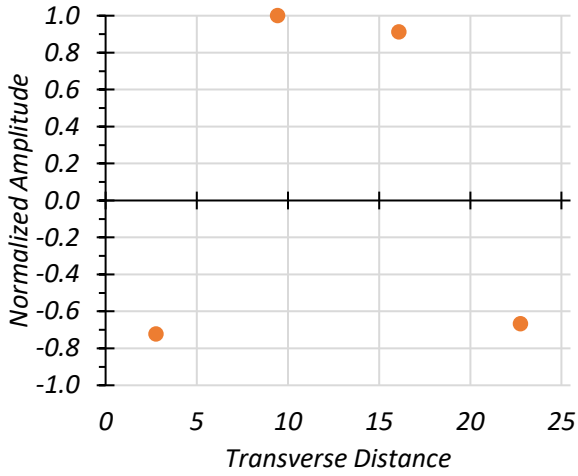

(c) Transverse Section – Span 2

Figure 7.62. Third Mode Shape of Bridge SC-12 (f_3 = 11.23 Hz)

7.6.6 Computer Vision

During testing, a video camera was set up on a tripod on the side of the bridge near exterior Girder G4 at the center of Span 2. The camera had a frame size of 1280 pixels by 720 pixels and a sampling frequency of 30 Hz. An iPhone camera was set up on a tripod on the side of the bridge near exterior Girder G1 at 0.4*L* of Span 1. The iPhone camera had a frame size of 3840 pixels by 2160 pixels and a sampling frequency of 60 Hz. The cameras were placed so that the girders were perpendicular to the camera's line of sight. Each load test was recorded, and computer vision was

used on each Path 1 load test to measure the deflection experienced in Girder G4 and on each Path 2 load test to measure the deflection experienced in Girder G1.

The computer vision algorithm compares the sub-window of the initial frame in the video to the same sub-window in the following frames of the video. The user selects the pixel width and height of this initial sub-window. The user also defines a reference distance that the algorithm corresponds to a number of pixels. The algorithm then finds the location of the displaced sub-window in the frames following the initial frame. The algorithm finds the minimum sum of the squared difference between the location of the first sub-window and the location of the subsequent sub-window, thereby calculating the displacement of the objects in the original sub-window. A lowpass Butterworth filter was used to smooth the deflection signal output by the program. For all Path 1 load cases, the video camera was used, and a 20 pixel by 20 pixel sub-window was used for computer vision. For all Path 2 load cases, the iPhone camera was used, and a 100 pixel by 100 pixel sub-window was used for computer vision.

The results from the computer vision were compared with the deflections recorded by the corresponding string potentiometers. For Bridge SC-12, computer vision was performed on all five of the Path 1 tests. The algorithm was applied to three of the five Path 2 load tests. The camera drifted slightly while recording for two Path 2 stop location tests, rendering the computer vision ineffective; therefore, those results are not included.

*7.6.6.1 **Maximum Effect Girders***

Figure 7.63 shows the Span 2 midspan deflection over time using computer vision and the Girder G4 string potentiometer for the Path 1—Span 1 stop location test. The cutoff frequency used for filtering was 0.75 Hz. The maximum deflection given by the string potentiometer is 0.107 in. upwards, while the computer vision does not give a result that is meaningful.

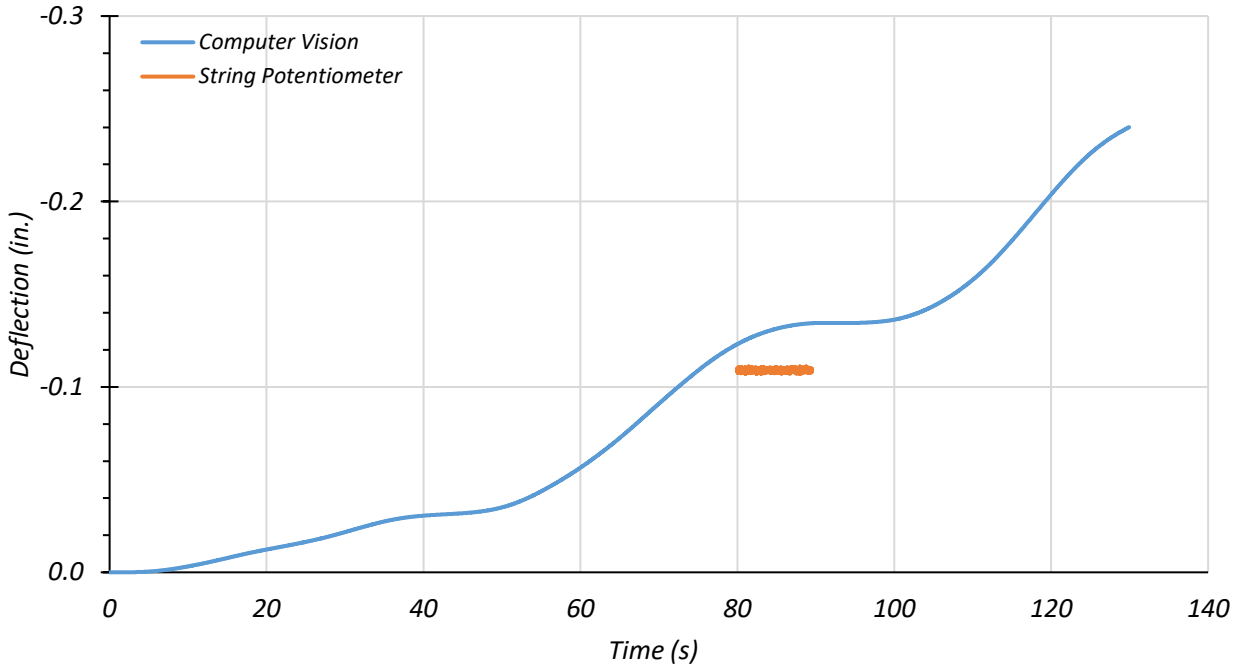

Figure 7.63. Girder G4: Span 2 Deflections for Path 1—Span 1 Stop Location

Figure 7.64 shows the Span 2 midspan deflection over time using computer vision and the Girder G4 string potentiometer for the Path 1—Span 2 stop location test. The cutoff frequency used for filtering was 0.75 Hz. The maximum deflection given by the string potentiometer is 0.755 in., while the maximum deflection given by computer vision is 0.635 in. Computer vision underestimated the deflection value by 0.120 in. and had a 17.3 percent difference with the string potentiometer.

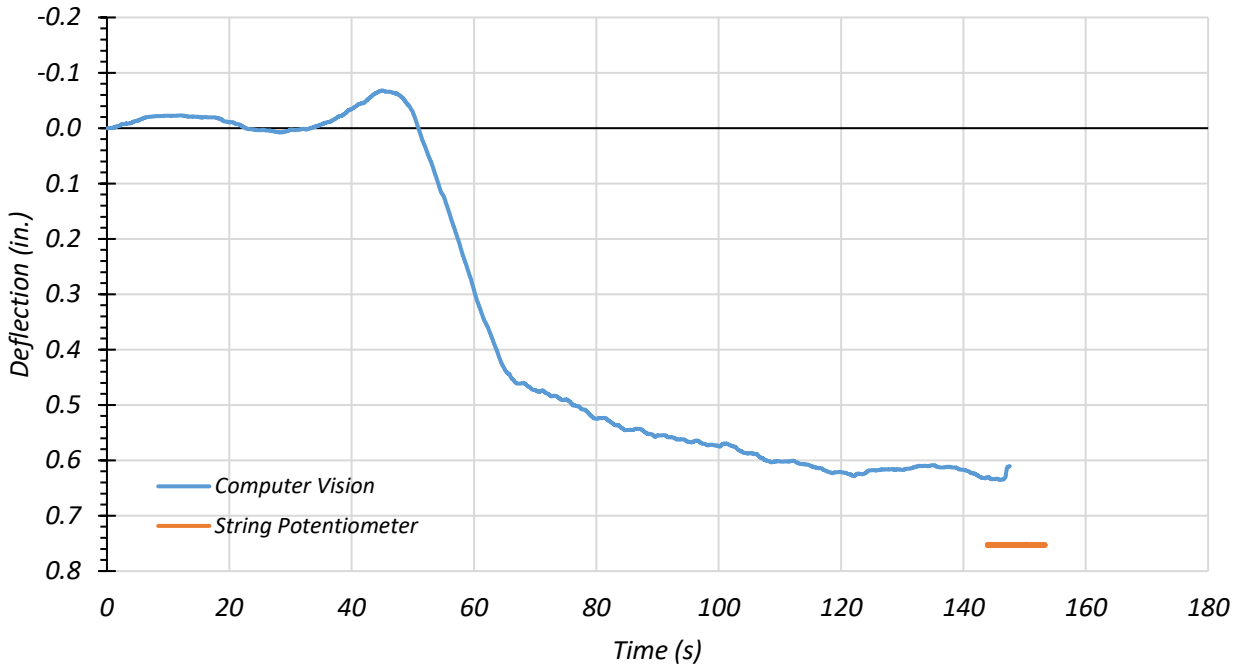

Figure 7.64. Girder G4: Span 2 Deflections for Path 1—Span 2 Stop Location

Figure 7.65 shows the Span 2 midspan deflection over time using computer vision and the Girder G4 string potentiometer for the Path 1 crawl speed test at 2 mph. The cutoff frequency used for filtering was 1.5 Hz. The maximum deflection given by the string potentiometer is 0.771 in., while the maximum deflection given by computer vision is 0.705 in. Computer vision underestimated the deflection value by 0.066 in. and had an 8.9 percent difference with the string potentiometer.

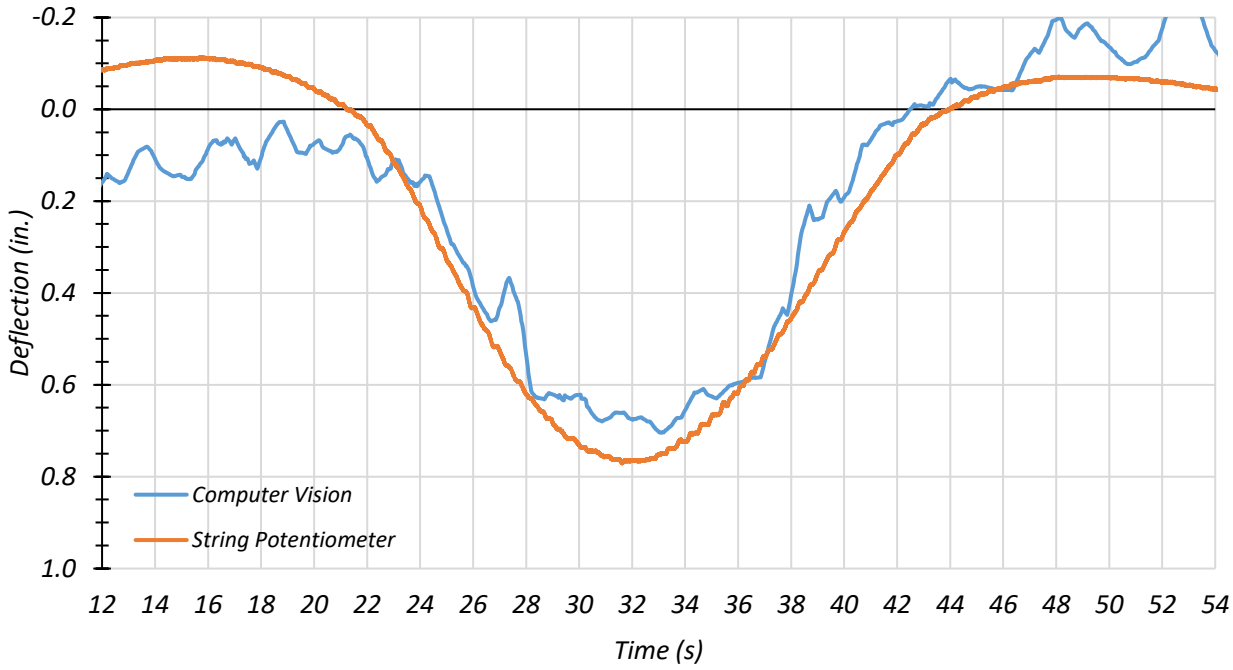

Figure 7.65. Girder G4: Span 2 Deflections for Path 1—Crawl Speed Test

Figure 7.66 shows the Span 2 midspan deflection over time using computer vision and the Girder G4 string potentiometer for the Path 1 dynamic test at 30 mph. The cutoff frequency used for filtering was 1.5 Hz. The maximum deflection given by the string potentiometer is 0.776 in., while the maximum deflection given by computer vision is 0.750 in. Computer vision underestimated the deflection value by 0.026 in. and had a 3.4 percent difference with the string potentiometer. The computer vision deflection value matches the string potentiometer well for this test.

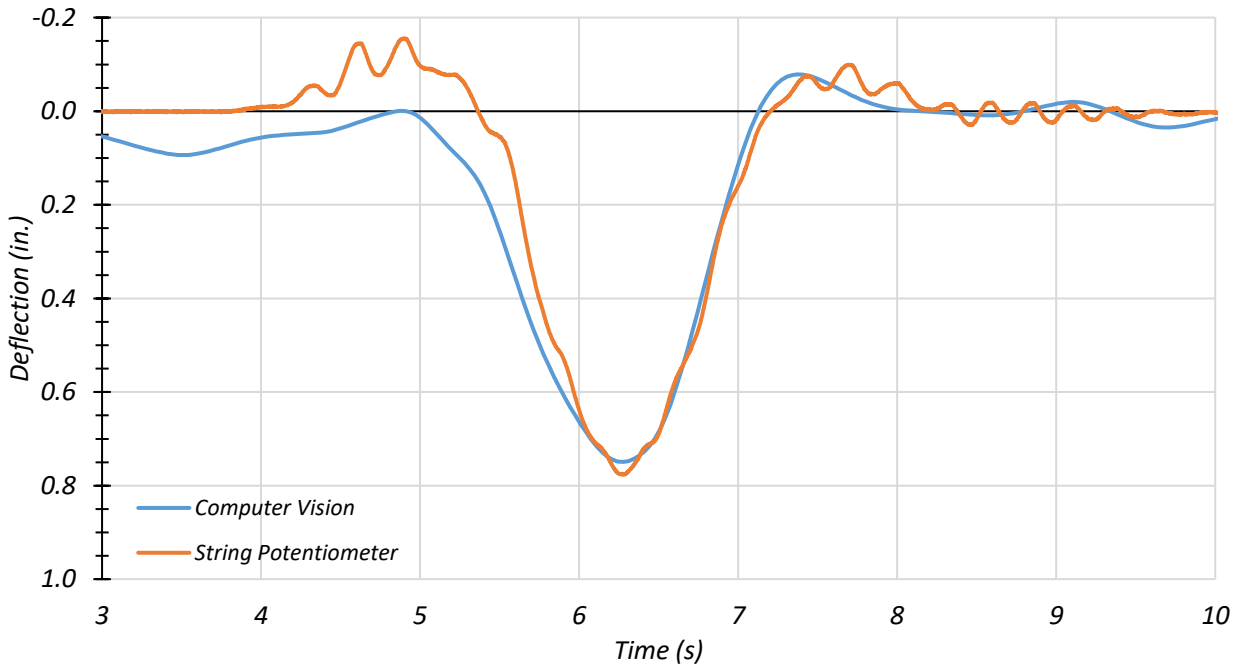

Figure 7.66. Girder G4: Span 2 Deflections for Path 1—Dynamic Test at 30 mph

Figure 7.67 shows the Span 2 midspan deflection over time using computer vision and the Girder G4 string potentiometer for the Path 1 dynamic test at 37 mph. The cutoff frequency used for filtering was 1.5 Hz. The maximum deflection given by the string potentiometer is 0.772 in., while the maximum deflection given by computer vision is 0.617 in. Computer vision underestimated the deflection value by 0.155 in. and had a 22.3 percent difference with the string potentiometer.

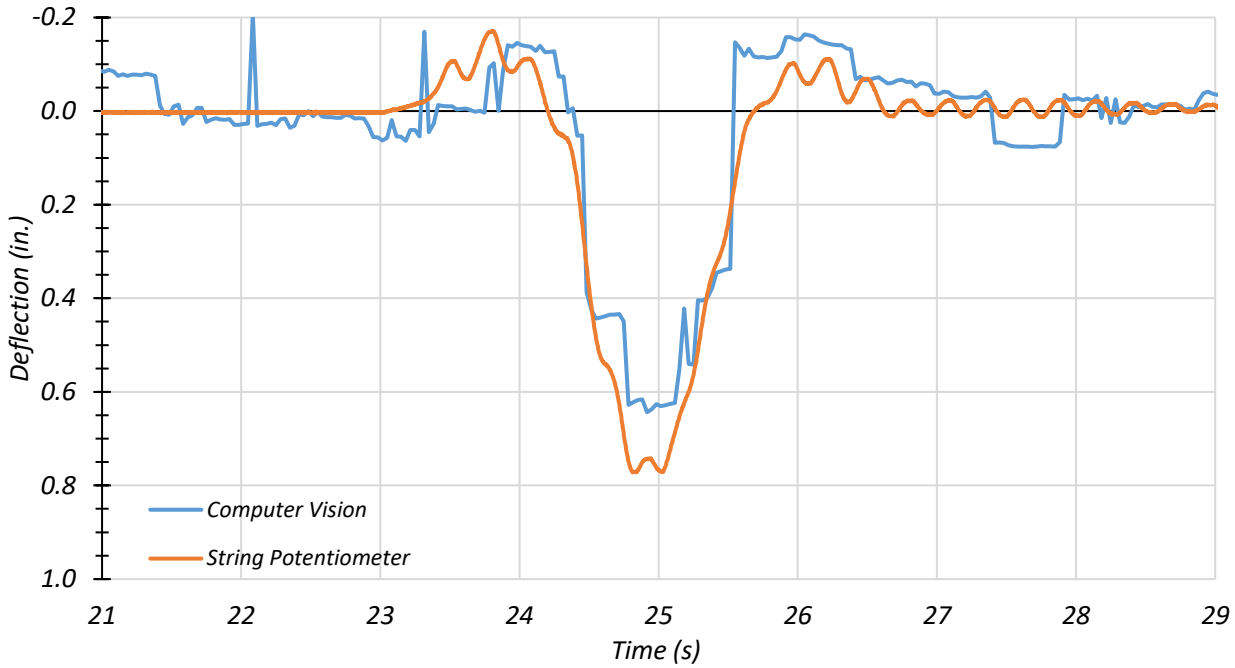

Figure 7.67. Girder G4: Span 2 Deflections for Path 1—Dynamic Test at 37 mph

Figure 7.68 shows the Span 1 midspan deflection over time using computer vision and the Girder G1 string potentiometer for the Path 2 crawl speed test at 2 mph. The cutoff frequency used for filtering was 1.5 Hz. The maximum deflection given by the string potentiometer is 0.413 in., while the maximum deflection given by computer vision is 0.546 in. Computer vision overestimated the deflection value by 0.133 in. and had a 27.7 percent difference with the string potentiometer.

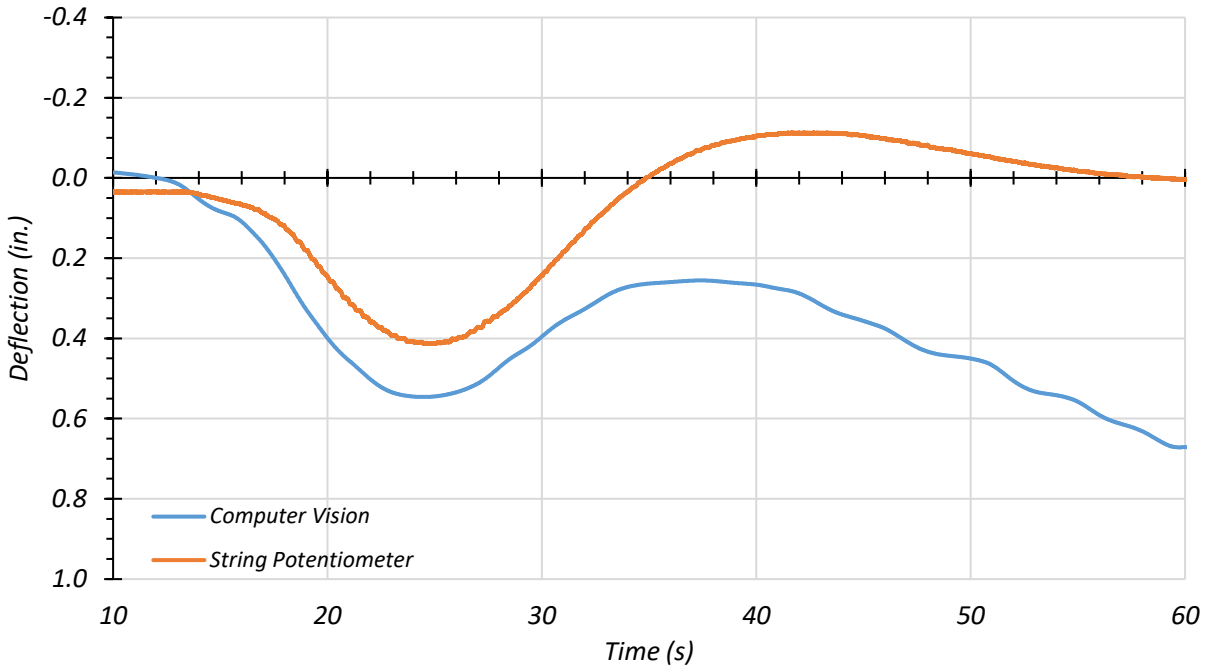

Figure 7.68. Girder G1: Span 1 Deflections for Path 2—Crawl Speed Test

Figure 7.69 shows the Span 1 midspan deflection over time using computer vision and the Girder G1 string potentiometer for the Path 2 dynamic test at 29 mph. The cutoff frequency used for filtering was 0.45 Hz. The maximum deflection given by the string potentiometer is 0.403 in., while the maximum deflection given by computer vision is 0.381 in. Computer vision underestimated the deflection value by 0.022 in. and had a 5.6 percent difference with the string potentiometer. The computer vision deflection value matches the string potentiometer well for this test.

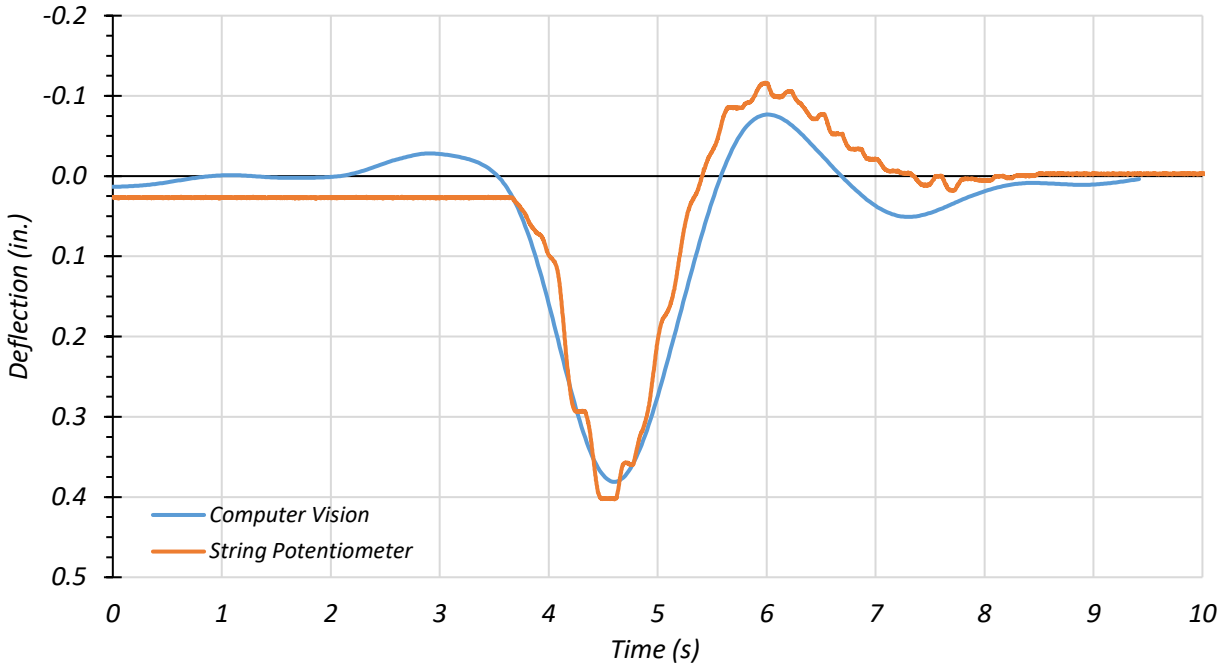

Figure 7.69. Girder G1: Span 1 Deflections for Path 2—Dynamic Test at 29 mph

Figure 7.70 shows the Span 1 midspan deflection over time using computer vision and the Girder G1 string potentiometer for the Path 2 dynamic test at 44 mph. The cutoff frequency used for filtering was 6 Hz. The maximum deflection given by the string potentiometer is 0.434 in., while the maximum deflection given by computer vision is 0.421 in. Computer vision underestimated the deflection value by 0.013 in. and had a 3.0 percent difference with the string potentiometer. The computer vision deflection value matches the string potentiometer well for this test.

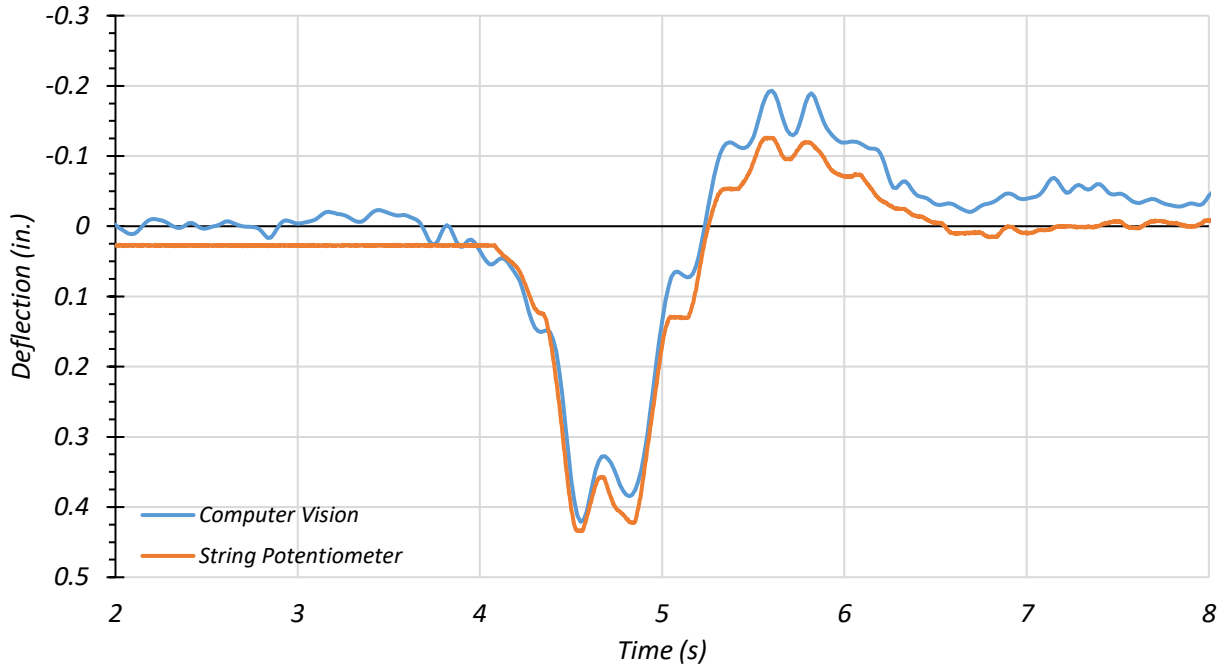

Figure 7.70. Girder G1: Span 1 Deflections for Path 2—Dynamic Test at 44 mph

The testing of Bridge SC-12 demonstrates that computer vision has the potential to be used to provide deflections during bridge load testing without the need for targets. More specifically, computer vision seems to be quite accurate for dynamic load tests.

*7.6.6.2 **Interior Girders***

Computer vision was also used to investigate the deflection of the two interior girders during two load tests: (1) the Path 1 dynamic test at 30 mph, and (2) the Path 2 dynamic test at 29 mph. Computer vision had difficulty capturing the furthest exterior girder for each test.

Figure 7.71 shows the Span 2 midspan deflection over time using computer vision and the Girder G3 string potentiometer for the Path 1 dynamic test at 30 mph. The cutoff frequency used for filtering was 3 Hz. The maximum deflection given by the string potentiometer is 0.546 in., while the maximum deflection given by computer vision is 0.513 in. Computer vision underestimated the deflection value by 0.033 in. and had a 6.2 percent difference with the string potentiometer. The computer vision deflection value matches the string potentiometer well for this test.

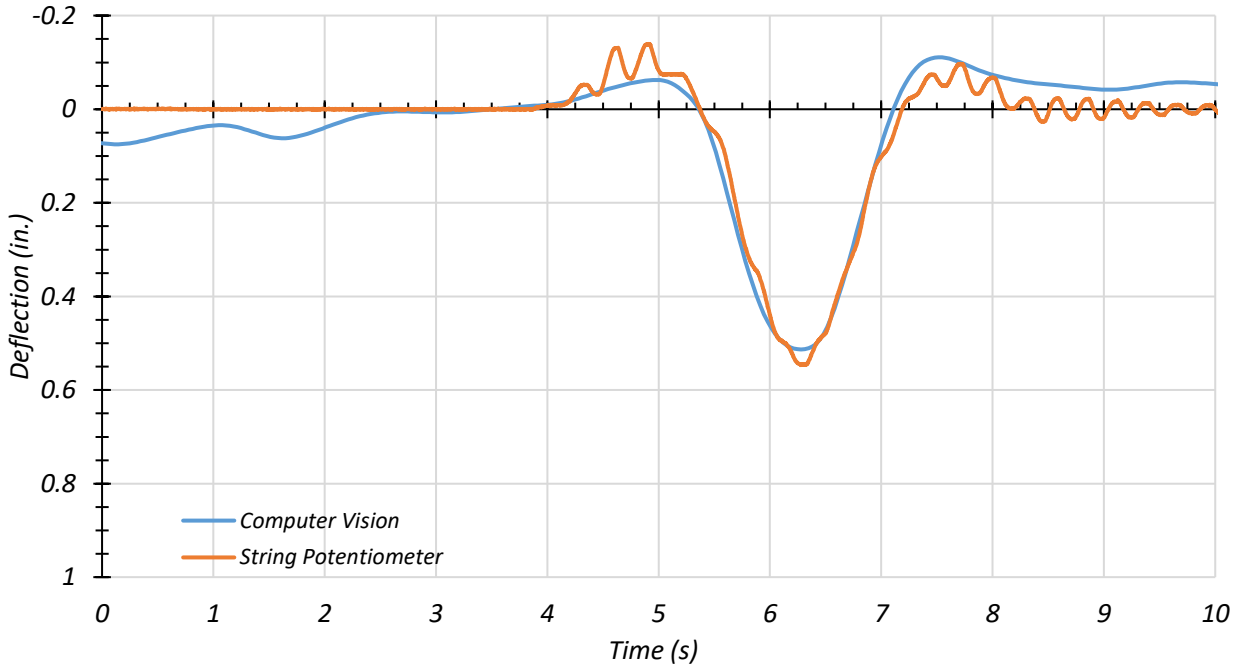

Figure 7.71. Girder G3: Span 2 Deflections for Path 1—Dynamic Test at 30 mph

Figure 7.72 shows the Span 2 midspan deflection over time using computer vision and the Girder G2 string potentiometer for the Path 1 dynamic test at 30 mph. The cutoff frequency used for filtering was 3 Hz. The maximum deflection given by the string potentiometer is 0.290 in., while the maximum deflection given by computer vision is 0.244 in. Computer vision underestimated the deflection value by 0.046 in. and had a 17.2 percent difference with the string potentiometer.

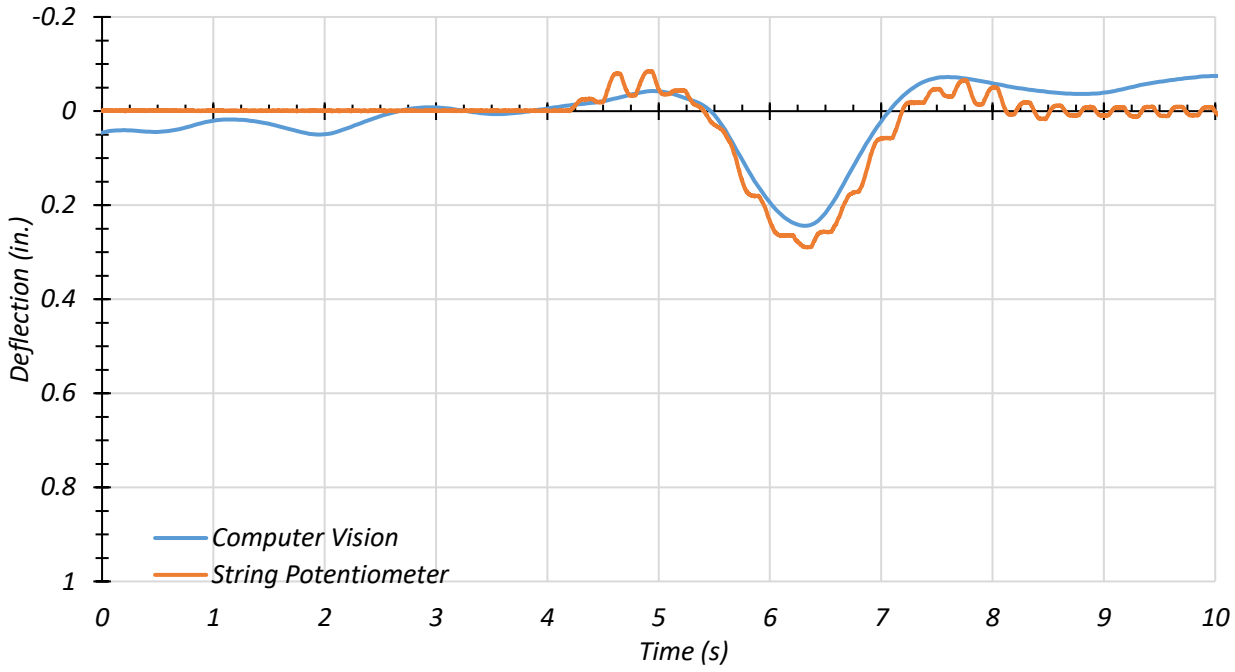

Figure 7.72. Girder G2: Span 2 Deflections for Path 1—Dynamic Test at 30 mph

Figure 7.73 shows the Span 1 midspan deflection over time using computer vision and the Girder G2 string potentiometer for the Path 2 dynamic test at 29 mph. The cutoff frequency used for filtering was 3 Hz. The maximum deflection given by the string potentiometer is 0.334 in., while the maximum deflection given by computer vision is 0.317 in. Computer vision underestimated the deflection value by 0.017 in. and had a 5.2 percent difference with the string potentiometer.

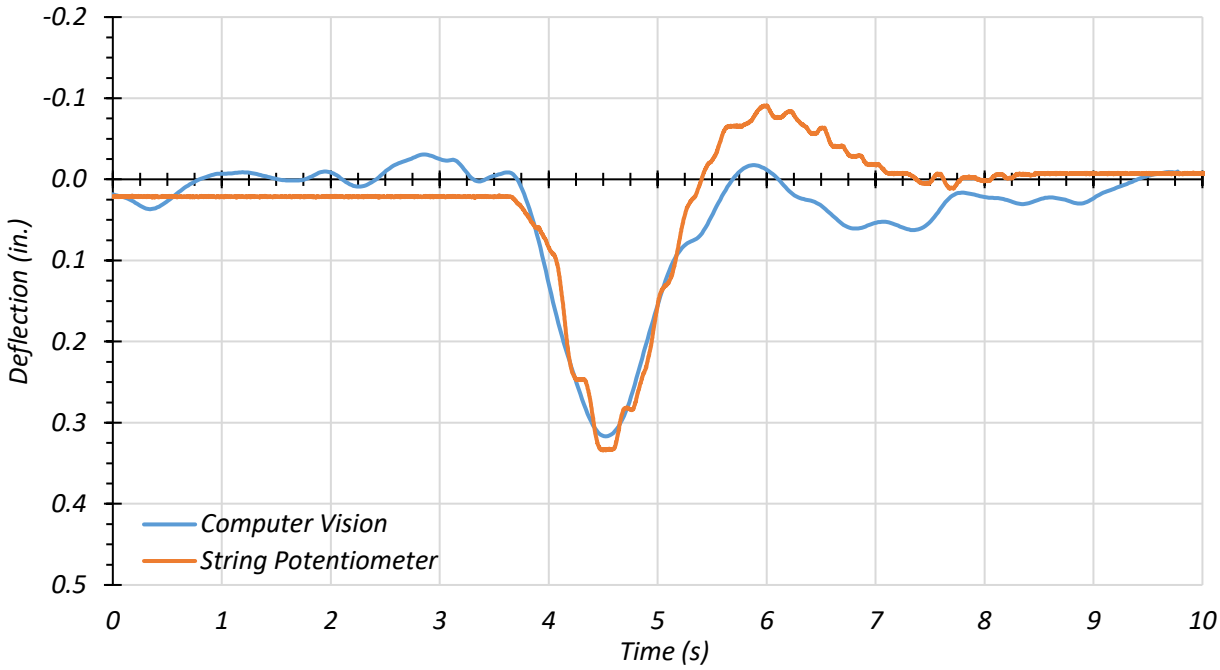

Figure 7.73. Girder G2: Span 1 Deflections for Path 2—Dynamic Test at 29 mph

Figure 7.74 shows the Span 1 midspan deflection over time using computer vision and the Girder G3 string potentiometer for the Path 2 dynamic test at 29 mph. The cutoff frequency used for filtering was 3 Hz. The maximum deflection given by the string potentiometer is 0.201 in., while the maximum deflection given by computer vision is 0.205 in. Computer vision overestimated the deflection value by 0.004 in. and had a 2.0 percent difference with the string potentiometer.

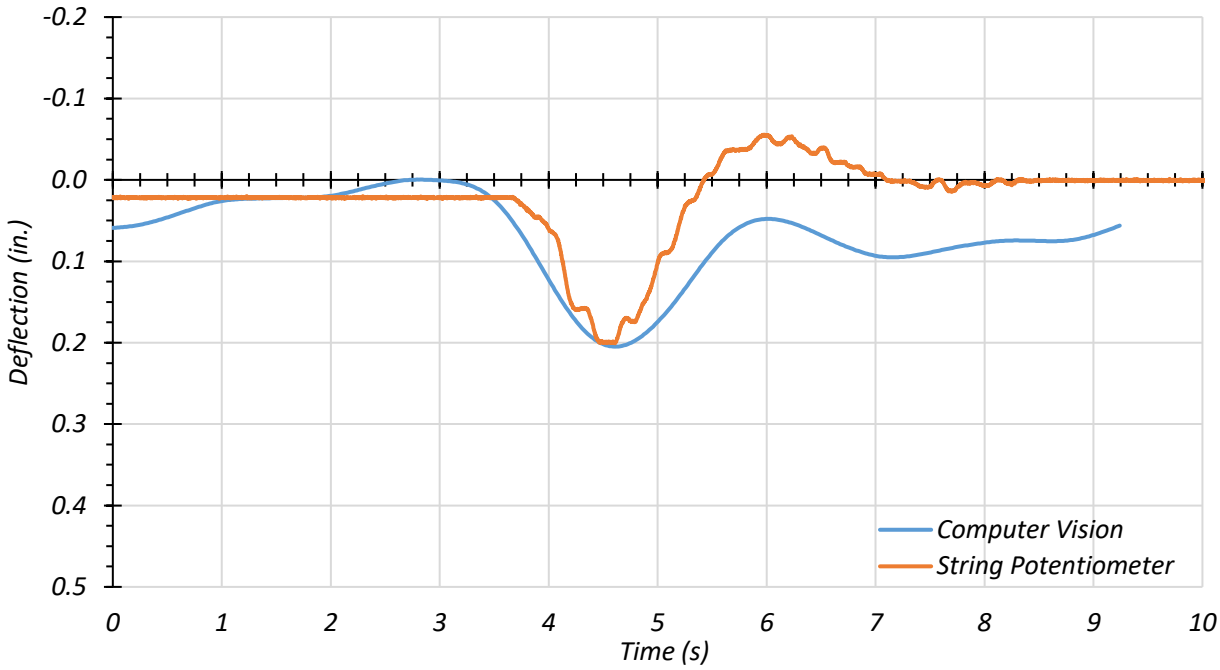

Figure 7.74. Girder G3: Span 1 Deflections for Path 2—Dynamic Test at 29 mph

The testing of Bridge SC-12 demonstrates that computer vision has the potential to be used to provide deflections during bridge load testing without the need for targets, which includes capturing the deflections of interior girders. More specifically, computer vision seems to be quite accurate for dynamic load tests.

7.7 FEM MODEL UPDATING AND CALIBRATION

7.7.1 General

Following the load testing, the original FEM model developed for Bridge SC-12 was modified to evaluate appropriate modeling parameters based on a comparison of the test results. The models are described first and then compared to the corresponding field measurements in Section 7.6.

7.7.2 Updated FEM Models

Two FEM models were developed to reflect the updated dimensions and in situ concrete compressive strength discussed in Section 7.3: (1) an updated model assuming no composite action between the steel girders and concrete deck, and (2) an updated model assuming fully composite

action between the girders and deck. Both models assume roller boundary conditions at both ends of every girder, except for one end of a single girder that has a pinned support to resist any lateral forces.

The two updated models use the field-measured dimensions of the bridge, including changing the deck thickness from the 6 in. given in the as-built drawings to the 5.75 in. measured in the field. These models also use the minimum f_c' of 6.25 ksi found using the NDE tests described in Subsection 7.3. This figure is an increase in f_c' from the 2.5 ksi that is assumed in load rating calculations, based on the age of the bridge, when the concrete deck strength is unknown (TxDOT 2018a). The increase in f_c' corresponds to an increase in computed concrete MOE from 2850 ksi to 4506 ksi. Table 7.28 shows the results from the fully composite and fully non-composite simply supported FEM models with updated material properties, along with selected field-test results. The results from the field testing seem to show that the bridge is behaving somewhere in between fully composite and fully non-composite. It is worth noting that TxDOT currently assumes fully non-composite behavior to load rate this bridge (TxDOT 2018a).

Table 7.28. Selected FEM Results for Updated FEM Models

Model	Modal Frequency (Hz)		Span 1 Deflection (in.)		Span 2 Deflection (in.)		Span 1 Curvature (in^{-1})		Span 2 Curvature (in^{-1})	
	1st Mode	2nd Mode	G3	G4	G3	G4	G3	G4	G3	G4
Non-Composite	3.14	6.07	0.641	0.672	0.672	0.928	2.42E-05	3.65E-05	2.52E-05	3.85E-05
Composite	4.20	6.97	0.236	0.331	0.352	0.495	1.12E-05	1.28E-05	1.15E-05	1.64E-05
Field Test	3.78	6.71	0.351	0.485	0.526	0.755	1.92E-05	2.31E-05	1.70E-05	2.53E-05

7.7.3 Calibrated FEM Model Process

In addition to the two models discussed above, a third FEM model was developed for Bridge SC-12 that took into account the measured composite action observed during testing. The goal in the development of this calibrated FEM model was to create a model that more closely represents the measured bridge response. The calibrated model also uses the updated geometric properties and concrete MOE described in the previous section.

Partial composite action was created in the model by inserting horizontal springs at the nodes between the bottom surface of the deck and the top flanges of the girders. As shown in the original model development, the reduction of stiffness of the concrete deck in the negative moment regions due to cracking can affect bridge behavior. Although no cracking in the deck was noticed during field testing due to the asphalt overlay, this bridge has been in service for a long period of time. It is expected that the deck is experiencing cracking near the interior supports. For this reason, the stiffness of the deck near the interior supports was reduced in the calibrated FEM model. The procedure for this reduction is explained in the model development for Bridge SC-12 reported earlier.

Initially the horizontal spring stiffness values required for a fully composite structure and a fully non-composite structure were found. Then, the stiffness parameter was methodically increased while keeping all other parameters the same in order to view the effect that partial composite behavior has on the results of the analysis. Based on this parametric study, a spring stiffness value was chosen for each input parameter to begin the process of refining the final calibrated model.

7.7.4 Calibrated FEM Model Results

7.7.4.1 ***Composite Spring Stiffness***

Table 7.29 shows the effect of changing the composite spring stiffness value on the modal frequencies of the bridge, the Span 1 and Span 2 deflections, and the Span 1 and Span 2 curvatures. Figure 7.75 shows this change for each output parameter graphically. Both Girder G3 and Girder G4 results are obtained from the Path 1 stop location load tests since these were found to be controlling, and the test modal frequencies are obtained from the sledgehammer test at the midspan of Span 2 along the centerline of the bridge.

Table 7.29. Effect of Composite Spring Stiffness Value on Selected FEM Results

Model (kip/in.)	Modal Frequency (Hz)		Span 1 Deflection (in.)		Span 2 Deflection (in.)		Span 1 Curvature (in^{-1})		Span 2 Curvature (in^{-1})	
	1st Mode	2nd Mode	G3	G4	G3	G4	G3	G4	G3	G4
Infinite	4.20	6.97	0.236	0.331	0.352	0.495	1.12E-05	1.28E-05	1.15E-05	1.64E-05
1500	3.84	6.79	0.291	0.391	0.422	0.575	1.44E-05	1.61E-05	1.44E-05	1.98E-05
1000	3.77	6.76	0.303	0.404	0.438	0.592	1.56E-05	1.68E-05	1.57E-05	2.07E-05
500	3.67	6.70	0.325	0.428	0.466	0.624	1.69E-05	1.81E-05	1.73E-05	2.19E-05
250	3.58	6.63	0.347	0.454	0.496	0.660	1.83E-05	1.95E-05	1.86E-05	2.34E-05
150	3.51	6.57	0.364	0.475	0.518	0.690	1.93E-05	2.06E-05	1.96E-05	2.45E-05
5	3.14	6.07	0.641	0.672	0.672	0.928	2.42E-05	3.65E-05	2.52E-05	3.85E-05
Test	3.78	6.71	0.351	0.485	0.526	0.755	1.92E-05	2.31E-05	1.70E-05	2.53E-05

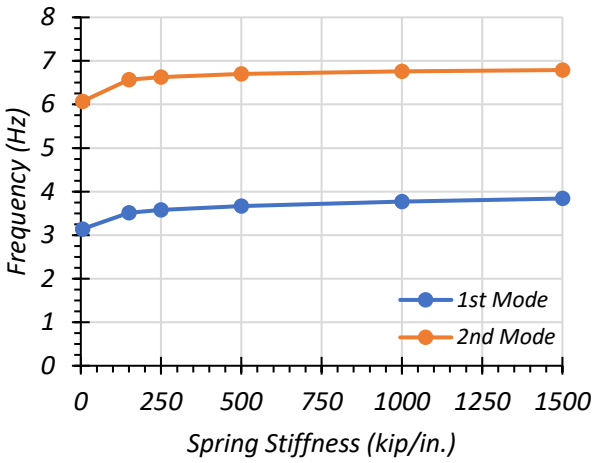

(a) Effect on Modal Frequency

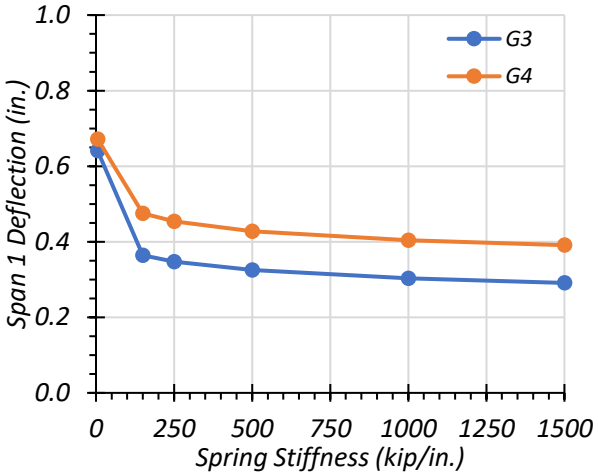

(b) Effect on Span 1 Deflection

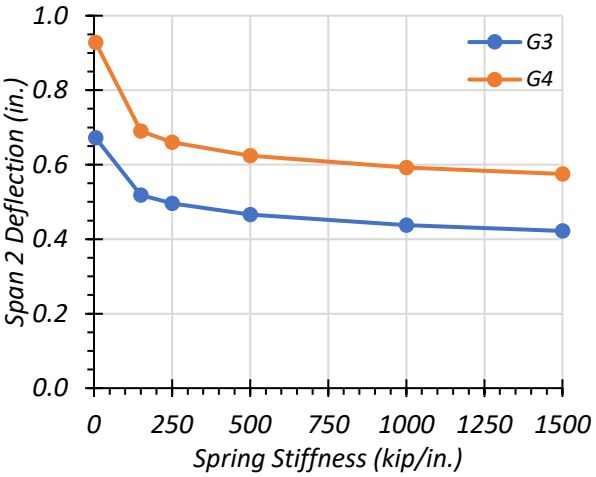

(c) Effect on Span 2 Deflection

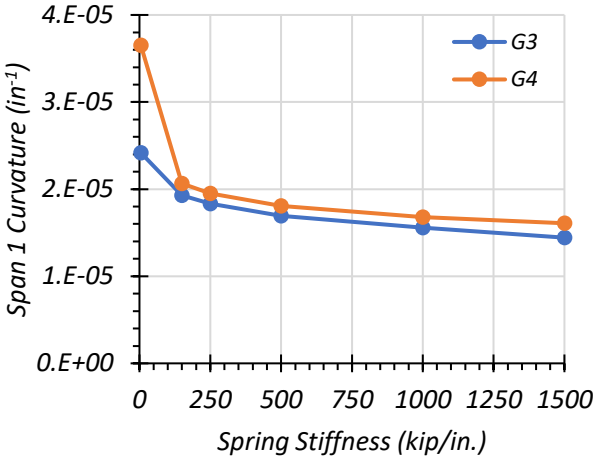

(d) Effect on Span 1 Curvature

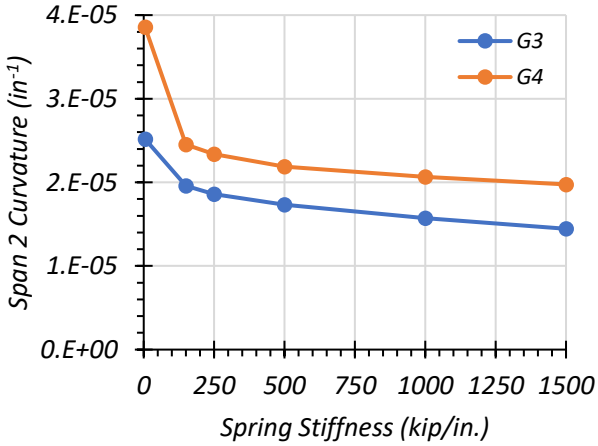

(e) Effect on Span 2 Curvature

Figure 7.75. Effect of Composite Spring Stiffness Value on Selected FEM Results

7.7.4.2 ***Final Calibration***

In the refinement of the final calibrated model, the partial composite spring stiffness was slightly adjusted in order to get as close as possible to representing the test results. In addition, the final calibrated model uses different spring stiffness values for the interior and exterior girders. The stiffness values used in the final model are 200 kip/in. for the interior girders and 100 kip/in. for the exterior girders. Table 7.30 provides the final partial composite horizontal spring stiffness values used for each girder in the calibrated SC-12 model.

Table 7.30. Partial Composite Horizontal Spring Stiffness Values for Calibrated SC-12 Model

Girder	G1	G2	G3	G4
Spring Stiffness (kip/in.)	100	200	200	100

The analysis of the model for each iteration of the calibration process was compared to selected test measurements. Table 7.31 shows the output for selected major parameters for the final calibrated FEM model and for the field tests performed on Bridge SC-12. It is important to note that the results for both girders come from the Path 1 stop location load tests because Path 1 is the controlling load case for both girders. Figure 7.76 shows the final calibrated model with the partial composite horizontal stiffness springs. This calibrated model was also used in comparison with the field-test results.

Table 7.31. Results of SC-12 Model Calibration

Parameter	Calibrated FEM Output		Test Result	
	G3	G4	G3	G4
Span 1 Deflection (in.)	0.369	0.490	0.351	0.485
Span 2 Deflection (in.)	0.526	0.720	0.526	0.755
Span 1 Top Flange Strain (με)	−111.6	−99.8	−102.4	−126.9
Span 1 Bottom Flange Strain (με)	150.5	191.3	161.7	190.3
Span 2 Top Flange Strain (με)	−99.1	−104.9	−73.1	−111.4
Span 2 Bottom Flange Strain (με)	163.4	239.9	161.4	237.2
First Modal Frequency	3.50		3.78	
Second Modal Frequency	6.07		6.71	

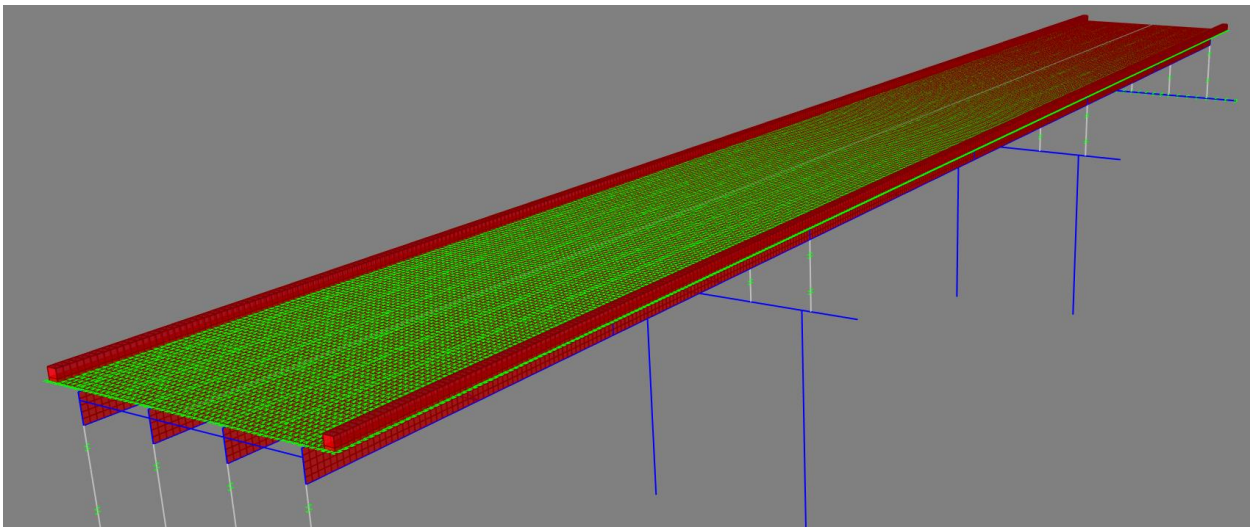

Figure 7.76. Bridge SC-12 Calibrated Model

7.7.5 Dynamic Characteristics of the Bridge

The dynamic characteristics of the bridge were analyzed as part of the model calibration process. Data obtained from the accelerometers during dynamic tests and the sledgehammer tests were filtered, and an FFT was performed. This process allowed for determination of the first two natural frequencies of the bridge. The calibrated model produced a first modal frequency of 3.50 Hz, compared to a test first modal frequency of 3.78 Hz. The calibrated model produced a second modal frequency of 6.07 Hz, compared to a test first modal frequency of 6.71 Hz. For each natural frequency, the amplitude and phase angle of each accelerometer were used to develop the mode shape. These mode shapes were compared to the calibrated FEM model. Figure 7.77 shows the comparison for a longitudinal section and a transverse section of both spans for the mode shape produced by the first natural frequency of Bridge SC-12. Figure 7.78 shows the comparison for a longitudinal section and a transverse section of both spans for the mode shape produced by the second natural frequency of the bridge. For the third mode shape observed during testing, the modal frequencies presented in the FEM program do not go as high in magnitude. In addition, the shape of the third mode seen during testing could not be matched with a mode shape presented by the FEM model. Therefore, it could not be compared. There are some slight differences between magnitudes of the mode shapes developed by the test results and the mode shapes developed by the calibrated FEM model. However, in general, the calibrated model mode shapes fit the test mode shapes well.

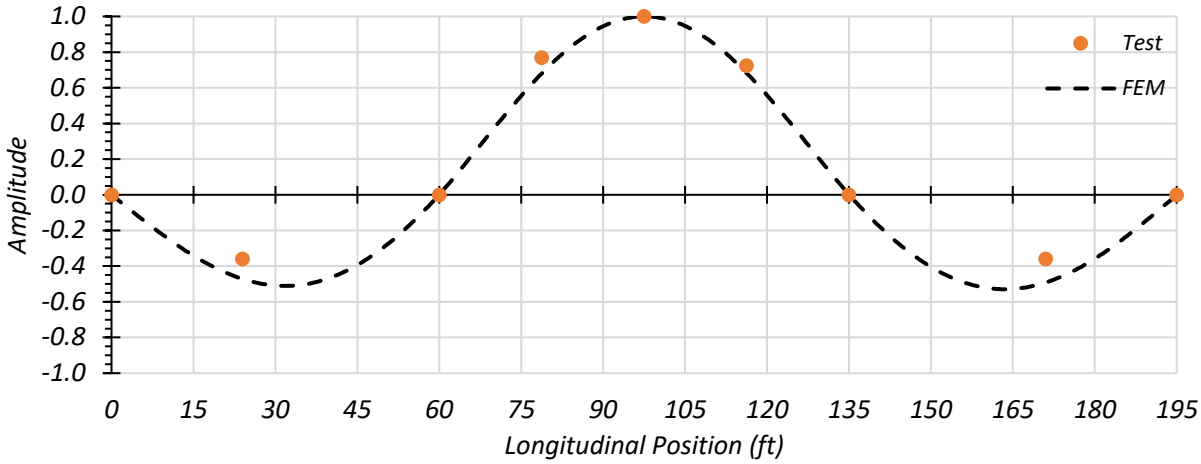

(a) Longitudinal Section

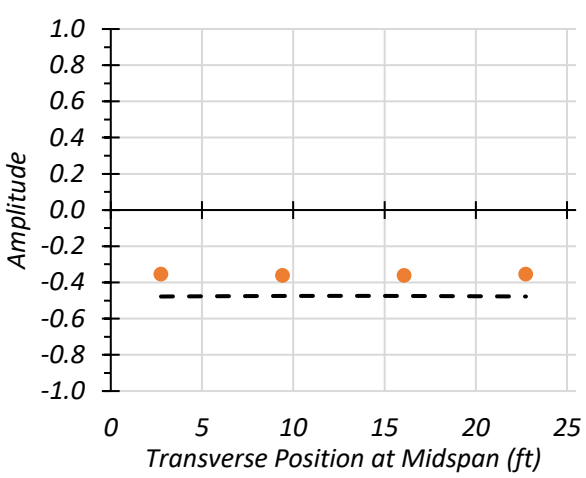

(b) Transverse Section – Span 1

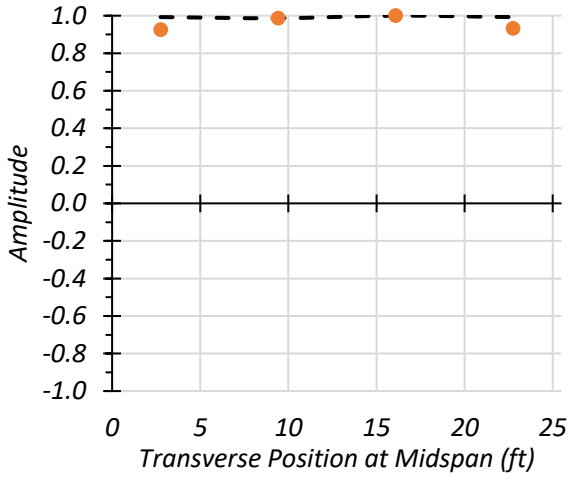

(c) Transverse Section – Span 2

Figure 7.77. Comparison of First Mode Shape of Bridge SC-12

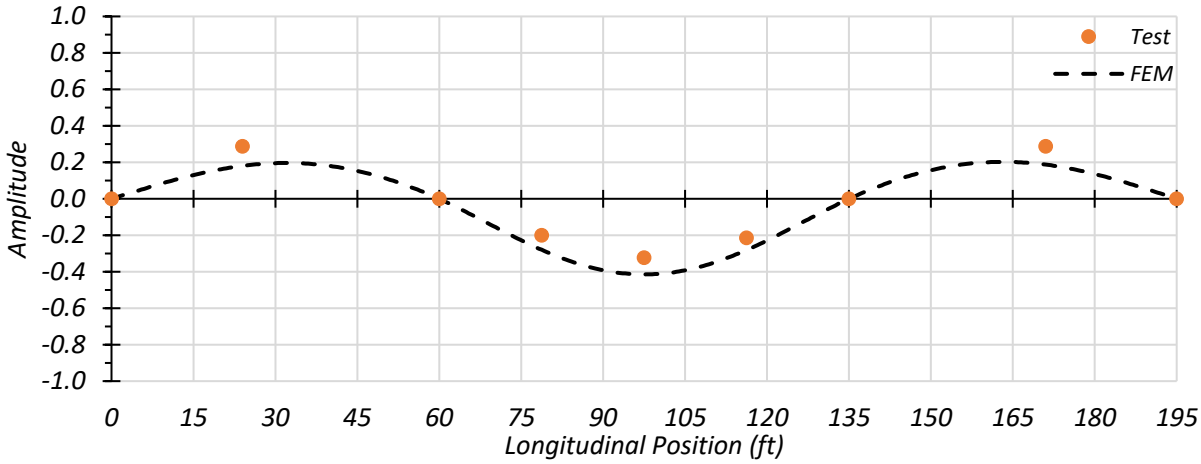

(a) Longitudinal Section

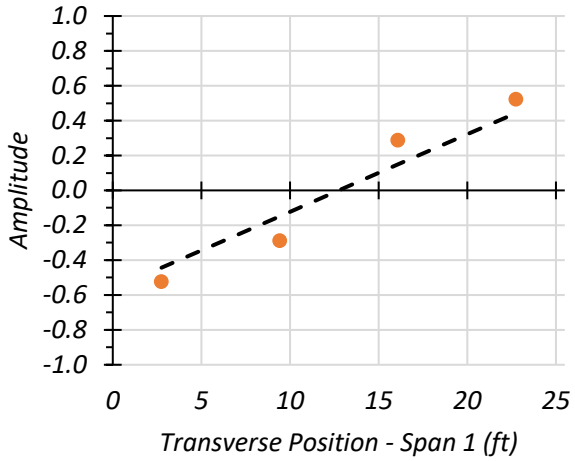

(b) Transverse Section – Span 1

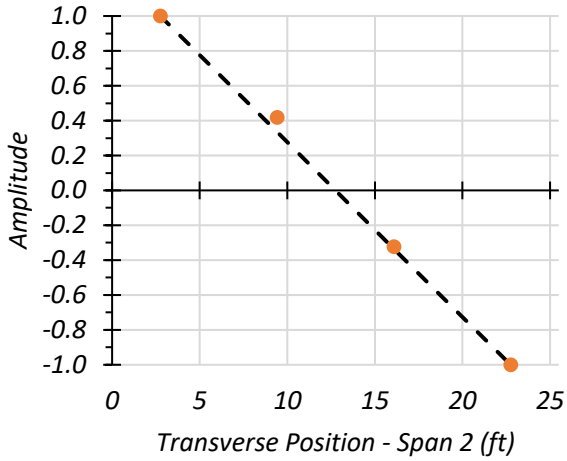

(c) Transverse Section – Span 2

Figure 7.78. Comparison of Second Mode Shape of Bridge SC-12

The natural frequencies of Bridge SC-12 observed during testing were compared to the natural frequencies produced by FEM. Table 7.32 shows the test and FEM natural frequencies. The first natural frequency is close to the calibrated FEM first natural frequency; however, it is closer to the first natural frequency of the updated composite FEM model. The test second frequency matches better with the calibrated FEM model second frequency.

Table 7.32. Bridge SM-5 Test and FEM Natural Frequencies for First Two Mode Shapes

Frequency	Test (Hz)	Updated FEM Non-Composite (Hz)	Updated FEM Composite (Hz)	Calibrated FEM (Hz)
1st Natural Frequency	3.78	2.52	3.85	3.50
2nd Natural Frequency	6.71	2.96	8.35	6.07

7.8 COMPARISON OF TEST RESULTS AND FEM PREDICTIONS

7.8.1 Static Load Tests on Bridge SC-12 Span 1

Two types of static load tests were conducted without introducing any dynamic effects: (1) stop location tests—by parking the vehicle at moment critical longitudinal position in each span for each selected path on the bridge, and (2) crawl speed tests—by moving the truck at low speeds (around 2 mph) along the same predefined paths.

7.8.1.1 Strain Measurements and Composite Action

Partial composite action can be determined by reviewing the strain diagrams over the section depth. Some information is available from the measured results to evaluate the composite behavior between the concrete deck and steel girders. A number of strain plots are provided in this section, wherein measured strain values are shown by a colored dot symbol. The colored line connecting two dot symbols represents the strain diagram at this cross-section based on the assumption that plane sections remain plane. In the plots for the loaded span, the black and gray dotted lines show the composite and non-composite strain diagrams obtained from the updated FEM models, and the purple dotted line shows the strain diagram obtained from the calibrated FEM model. The blue plot shows the strain results for the pier location, the red plot shows the strain results for Span 1, and the green plot shows the strain results for Span 2. The orange dotted line and the purple dotted line in (a) and (c) of the figures represent the calibrated FEM model results for the unloaded span and the pier, respectively.

Interior Girder G3. Figure 7.79 through Figure 7.81 provide plots of the measured strains for interior Girder G3 during static load testing and compare the midspan strain diagram to those obtained through the updated and calibrated FEM models. The strains measured for Girder G3

during the Path 1—Span 1 static tests are shown in Figure 7.79 and compared with values obtained from the FEM updated and calibrated models. Figure 7.79(a) shows the FEM comparison for the stop location test for Girder G3 adjacent to the interior pier and midspan of Span 2. Figure 7.79(b) shows the FEM comparison for the stop location test for Girder G3 at 0.4*L* of Span 1. Figure 7.79(c) shows the FEM comparison for the crawl speed test for Girder G3 adjacent to the interior pier and midspan of Span 2. Figure 7.79(d) shows the FEM comparison for the crawl speed test for Girder G3 at 0.4*L* of Span 1.

The strains measured for Girder G3 during the Path 2—Span 1 static tests are shown in Figure 7.80 and compared with values obtained from the FEM updated and calibrated models. Figure 7.80(a) shows the FEM comparison for the stop location test for Girder G3 adjacent to the interior pier and midspan of Span 2. Figure 7.80(b) shows the FEM comparison for the stop location test for Girder G3 at 0.4*L* of Span 1. Figure 7.80(c) shows the FEM comparison for the crawl speed test for Girder G3 adjacent to the interior pier and midspan of Span 2. Figure 7.80(d) shows the FEM comparison for the crawl speed test for Girder G3 at 0.4*L* of Span 1.

The strains measured for Girder G3 during the Middle Path static tests are shown in Figure 7.81 and compared with values obtained from the FEM updated and calibrated models. Figure 7.81(a) shows the FEM comparison for the stop location test for Girder G3 adjacent to the interior pier and midspan of Span 2. Figure 7.81(b) shows the FEM comparison for the stop location test for Girder G3 at 0.4*L* of Span 1. Figure 7.81(c) shows the FEM comparison for the crawl speed test for Girder G3 adjacent to the interior pier and midspan of Span 2. Figure 7.81(d) shows the FEM comparison for the crawl speed test for Girder G3 at 0.4*L* of Span 1.

The calibrated model compares well with the Path 1 and Middle Path loading strain diagrams but does not compare quite as well with the Path 2 loading strain diagram. This result is likely due to Girder G3 not receiving much load during Path 2 loading because the truck is closer to Girders G1 and G2.

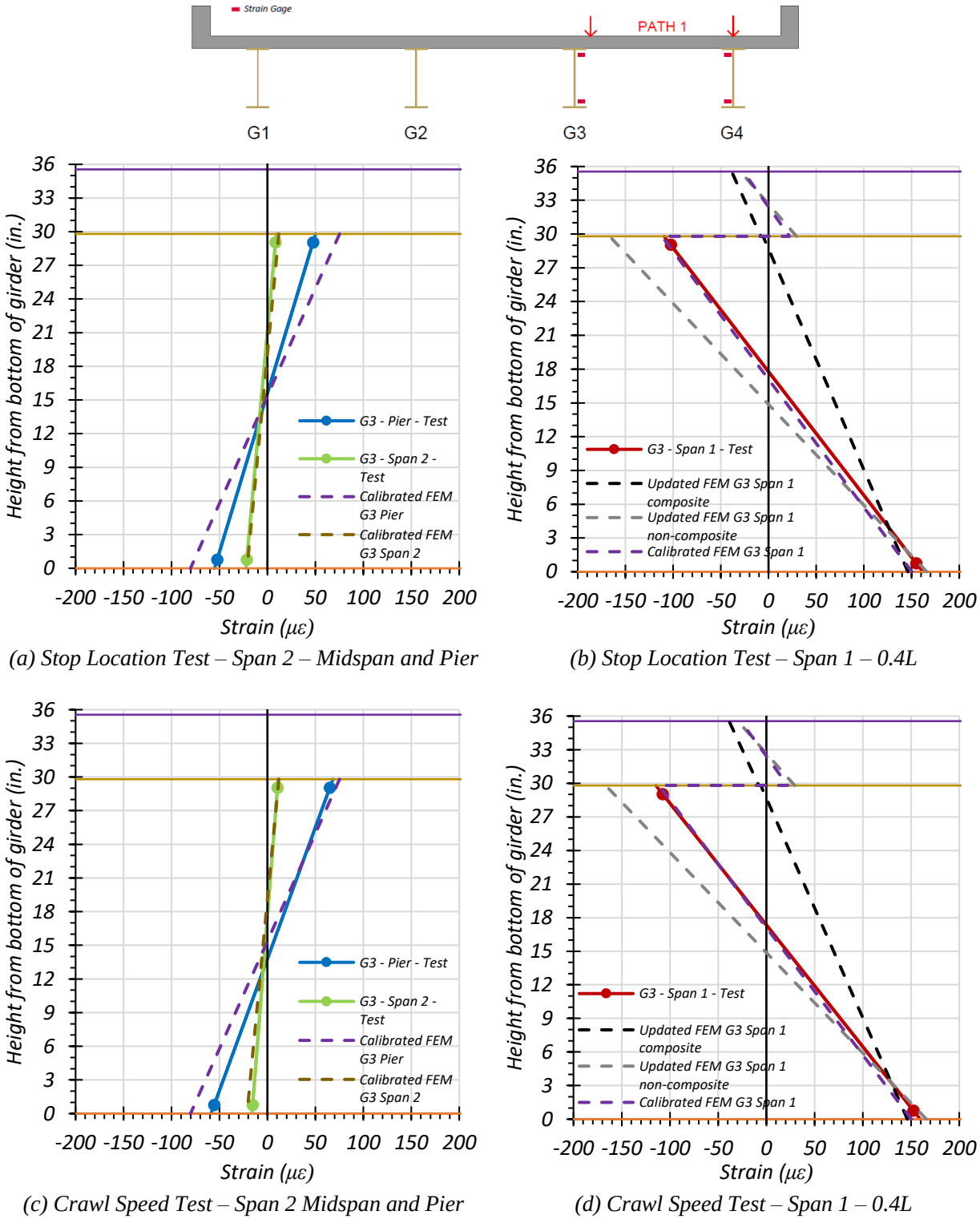

(a) Stop Location Test – Span 2 – Midspan and Pier

(b) Stop Location Test – Span 1 – 0.4L

(c) Crawl Speed Test – Span 2 Midspan and Pier

(d) Crawl Speed Test – Span 1 – 0.4L

Figure 7.79. Static Strains for Interior Girder G3: Path 1—Span 1

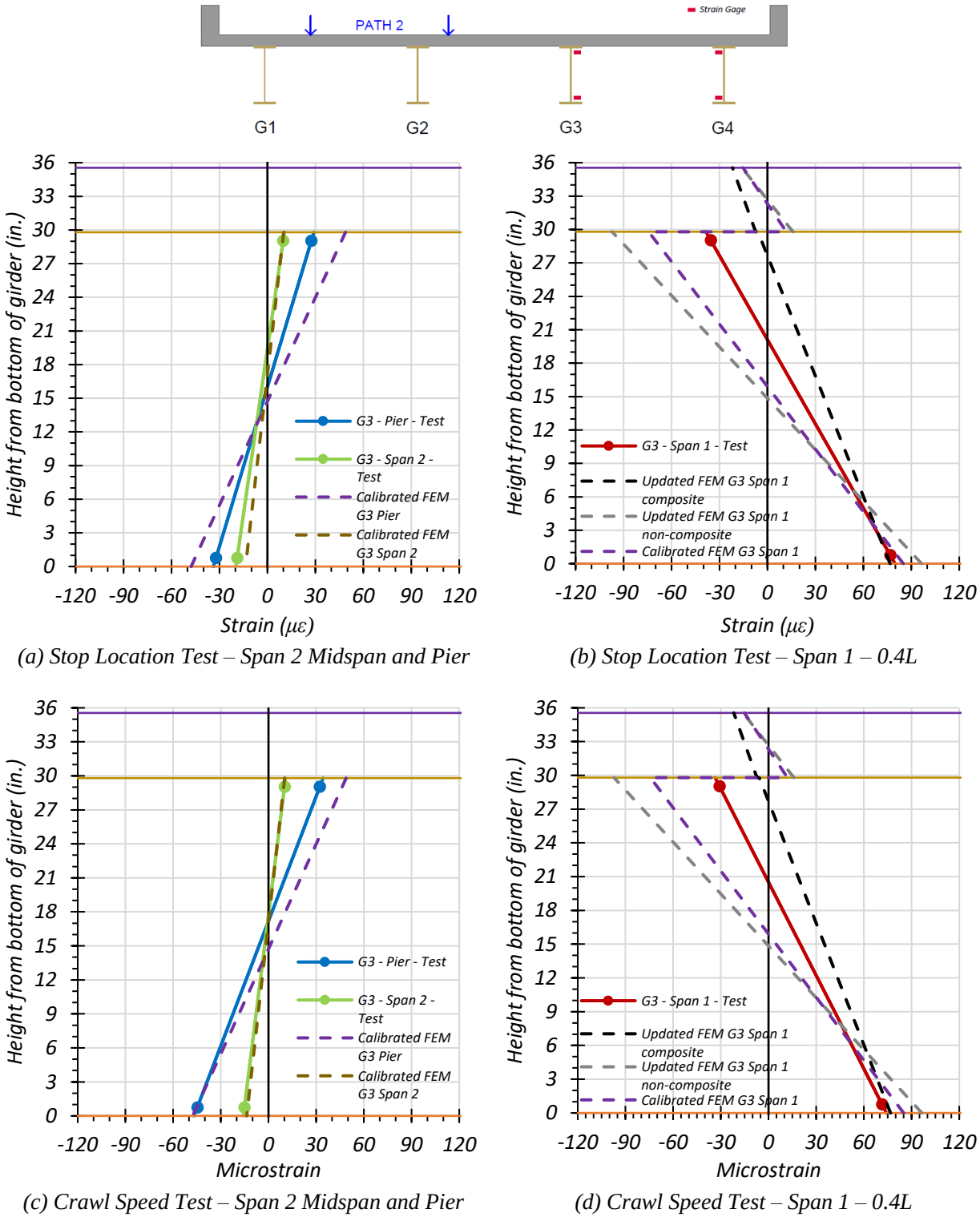

(a) Stop Location Test – Span 2 Midspan and Pier

(b) Stop Location Test – Span 1 – 0.4L

(c) Crawl Speed Test – Span 2 Midspan and Pier

(d) Crawl Speed Test – Span 1 – 0.4L

Figure 7.80. Static Strains for Interior Girder G3: Path 2—Span 1

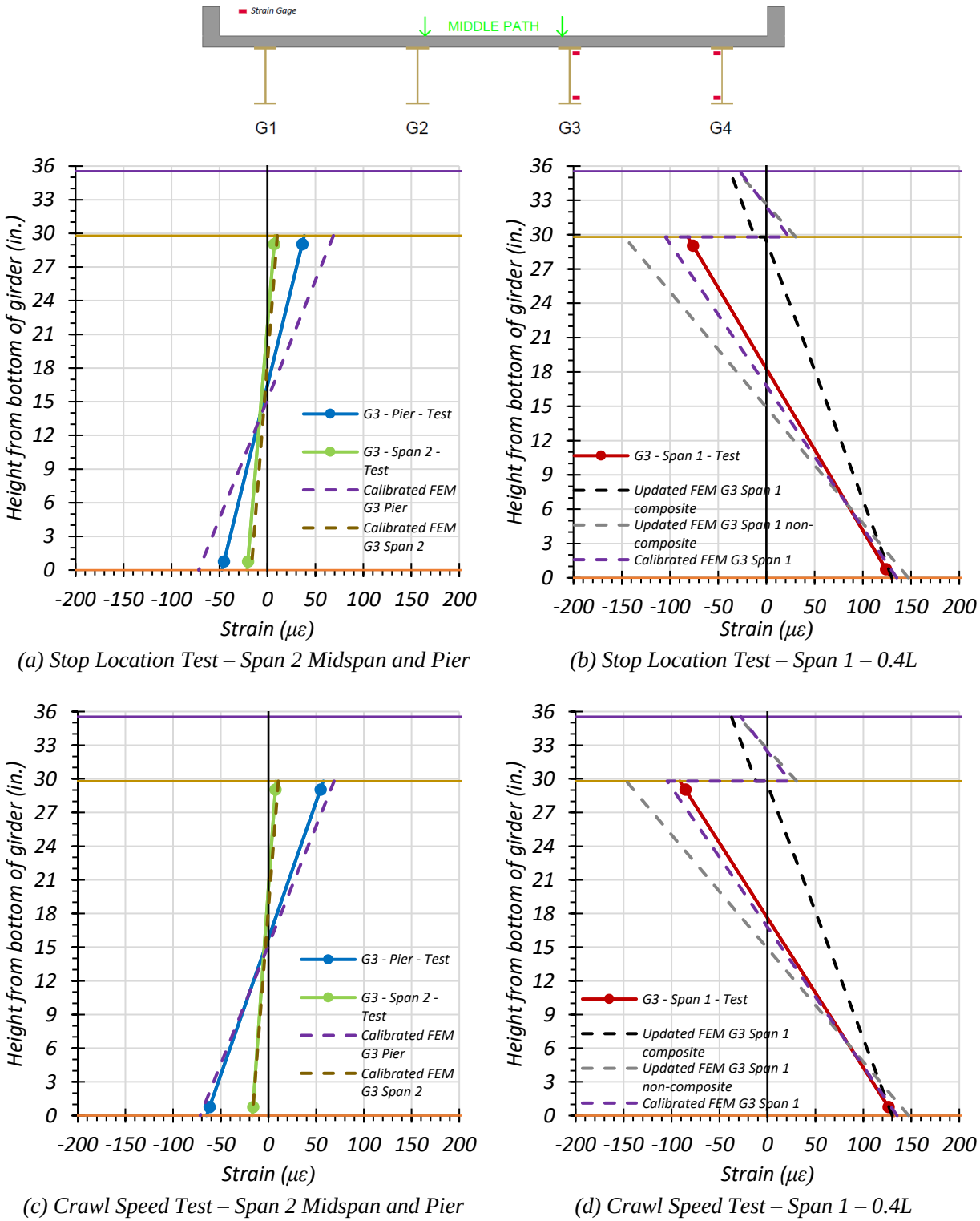

(a) Stop Location Test – Span 2 Midspan and Pier

(b) Stop Location Test – Span 1 – 0.4L

(c) Crawl Speed Test – Span 2 Midspan and Pier

(d) Crawl Speed Test – Span 1 – 0.4L

Figure 7.81. Static Strains for Interior Girder G3: Middle Path—Span 1

Exterior Girder G4. Figure 7.82 through Figure 7.84 provide plots of the measured strains for exterior Girder G4 during static load testing and compare the midspan strain diagram to those obtained through the updated and calibrated FEM models. The strains measured for Girder G4 during the Path 1—Span 1 static tests are shown in Figure 7.82 and compared with values obtained from the FEM updated and calibrated models. Figure 7.82(a) shows the FEM comparison for the stop location test for Girder G4 adjacent to the interior pier and midspan of Span 2. Figure 7.82(b) shows the FEM comparison for the stop location test for Girder G4 at 0.4*L* of Span 1. Figure 7.82(c) shows the FEM comparison for the crawl speed test for Girder G4 adjacent to the interior pier and midspan of Span 2. Figure 7.82(d) shows the FEM comparison for the crawl speed test for Girder G4 at 0.4*L* of Span 1.

The strains measured for Girder G4 during the Path 2—Span 1 static tests are shown in Figure 7.83 and compared with values obtained from the FEM updated and calibrated models. Figure 7.83(a) shows the FEM comparison for the stop location test for Girder G4 adjacent to the interior pier and midspan of Span 2. Figure 7.83(b) shows the FEM comparison for the stop location test for Girder G4 at 0.4*L* of Span 1. Figure 7.83(c) shows the FEM comparison for the crawl speed test for Girder G4 adjacent to the interior pier and midspan of Span 2. Figure 7.83(d) shows the FEM comparison for the crawl speed test for Girder G4 at 0.4*L* of Span 1.

The strains measured for Girder G4 during the Middle Path static tests are shown in Figure 7.84 and compared with values obtained from the FEM updated and calibrated models. Figure 7.84(a) shows the FEM comparison for the stop location test for Girder G4 adjacent to the interior pier and midspan of Span 2. Figure 7.84(b) shows the FEM comparison for the stop location test for Girder G4 at 0.4*L* of Span 1. Figure 7.84(c) shows the FEM comparison for the crawl speed test for Girder G4 adjacent to the interior pier and midspan of Span 2. Figure 7.84(d) shows the FEM comparison for the crawl speed test for Girder G4 at 0.4*L* of Span 1.

The calibrated model compares well with the Path 1 loading strain diagrams but does not compare quite as well with the Path 2 and Middle Path loading strain diagrams, which is likely due to Girder G4 not receiving significant load during Path 2 loading and Middle Path loading because the truck is closer to Girders G1 and G2 under Path 2 loading and to Girders G2 and G3 under Middle Path loading.

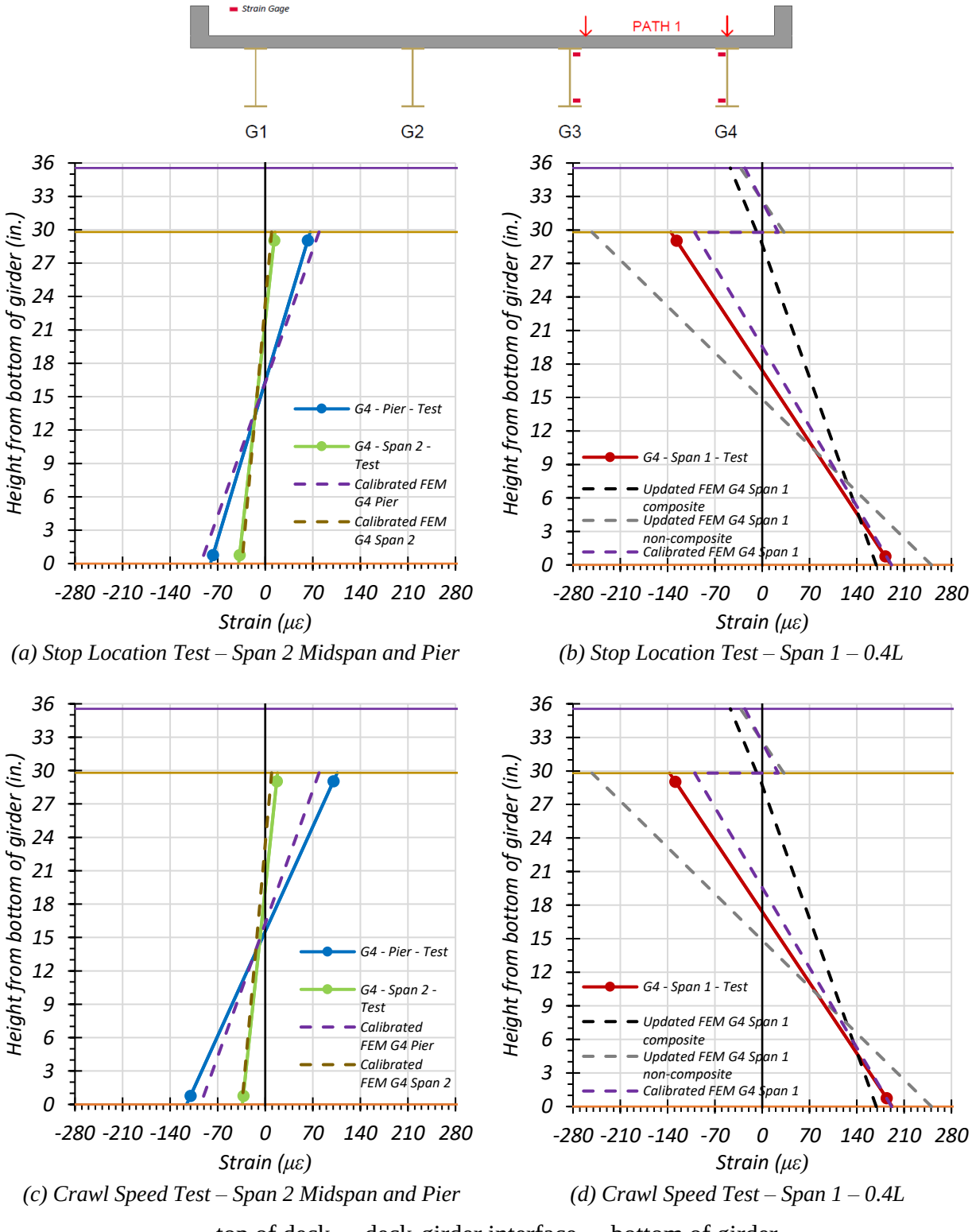

(a) Stop Location Test – Span 2 Midspan and Pier

(b) Stop Location Test – Span 1 – 0.4L

(c) Crawl Speed Test – Span 2 Midspan and Pier

(d) Crawl Speed Test – Span 1 – 0.4L

Figure 7.82. Static Strains for Exterior Girder G4: Path 1—Span 1

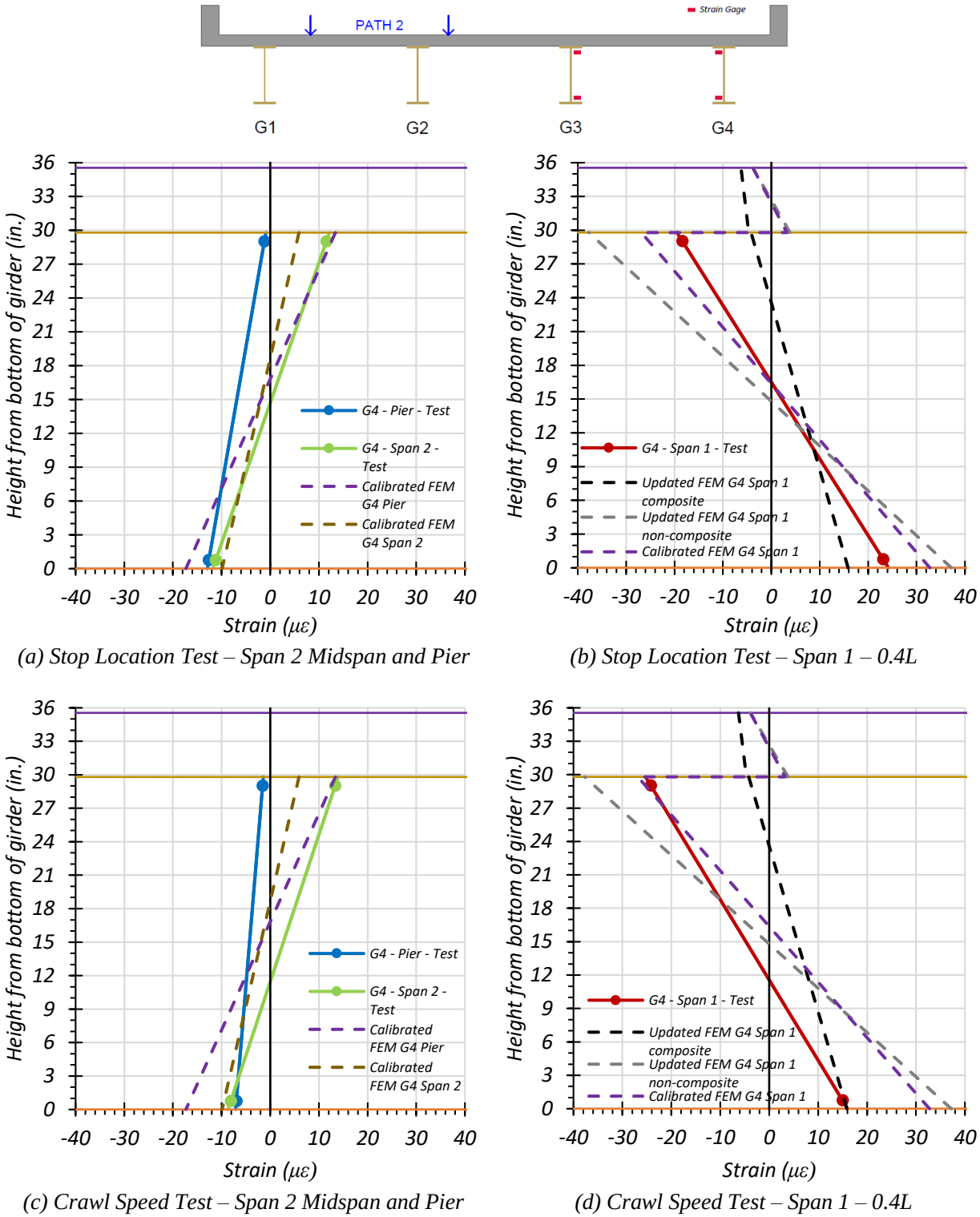

(a) Stop Location Test – Span 2 Midspan and Pier

(b) Stop Location Test – Span 1 – 0.4L

(c) Crawl Speed Test – Span 2 Midspan and Pier

(d) Crawl Speed Test – Span 1 – 0.4L

Figure 7.83. Static Strains for Exterior Girder G4: Path 2—Span 1

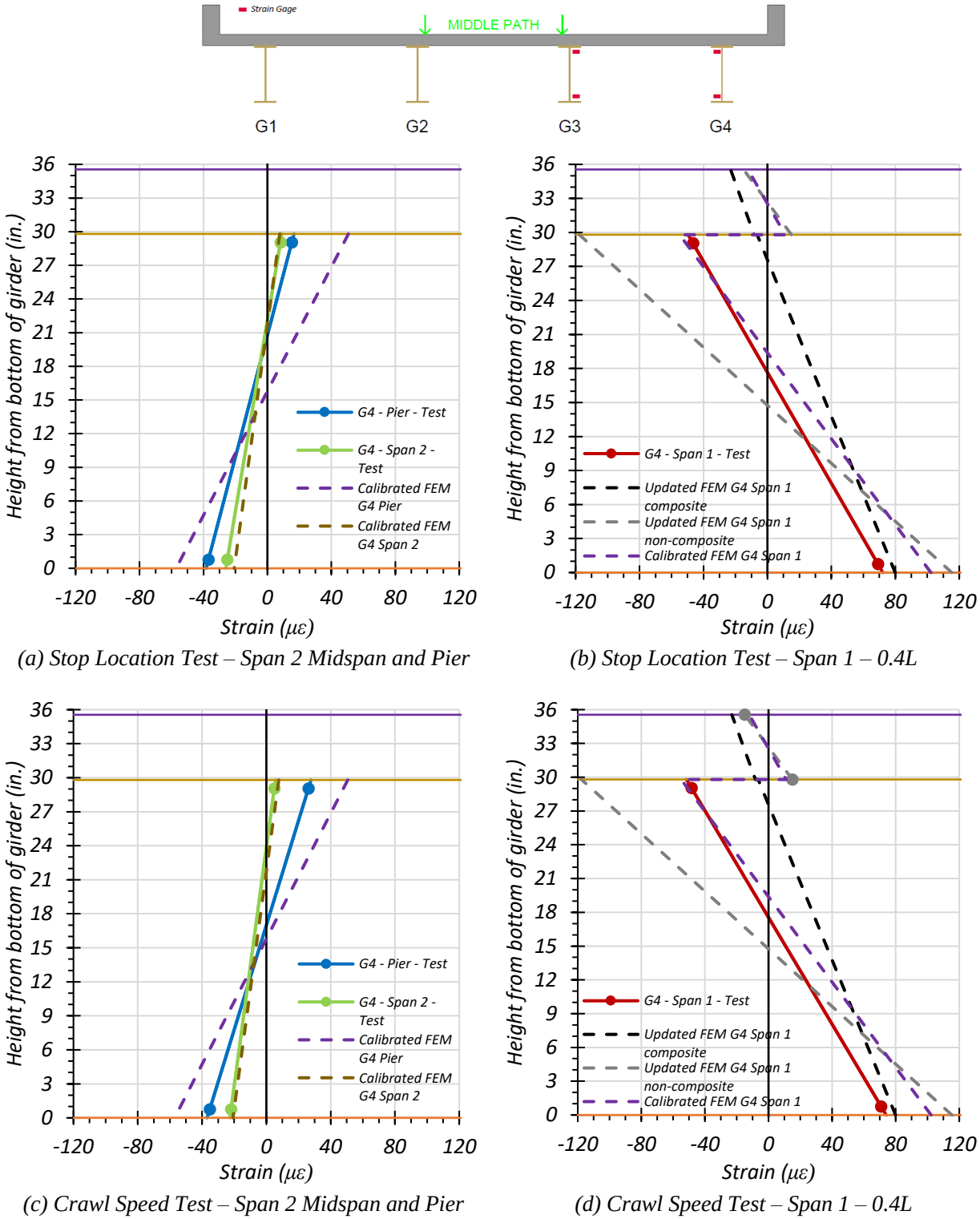

(a) Stop Location Test – Span 2 Midspan and Pier

(b) Stop Location Test – Span 1 – 0.4L

(c) Crawl Speed Test – Span 2 Midspan and Pier

(d) Crawl Speed Test – Span 1 – 0.4L

Figure 7.84. Static Strains for Exterior Girder G4: Middle Path—Span 1

Comparison of Measured Strain Results. The neutral axis locations of Girder G3 and Girder G4 observed during the load tests were compared with the theoretical neutral axis locations calculated using the FEM strain predictions. Table 7.33 shows the neutral axis locations measured for all static load tests and for the three FEM models. Figure 7.85 compares the test neutral axis locations with the non-composite and composite neutral axis locations obtained from FEM. Since the test neutral axis locations are in between the estimated composite neutral axis locations and non-composite neutral axis locations, Bridge SC-12 appears to exhibit partial composite action between the concrete deck and steel girders.

Table 7.33. Measured and FEM Neutral Axis Locations for All Span 1 Static Load Tests under Positive Bending at 0.4*L* Location

Test	G3 Neutral Axis Location (in. from bottom of girder)	G4 Neutral Axis Location (in. from bottom of girder)
Path 1—Stop Location	17.77	17.42
Path 1—Crawl Speed	17.34	17.41
Path 2—Stop Location	20.10	16.50
Path 2—Crawl Speed	20.51	15.22
Middle Path—Stop Location	18.28	17.65
Middle Path—Crawl Speed	17.61	16.53
Theoretical Non-Composite	14.90	14.90
Theoretical Composite	26.11	26.11
FEM Non-Composite	14.90	14.90
FEM Composite	28.69	28.73
FEM Calibrated	17.10	19.57

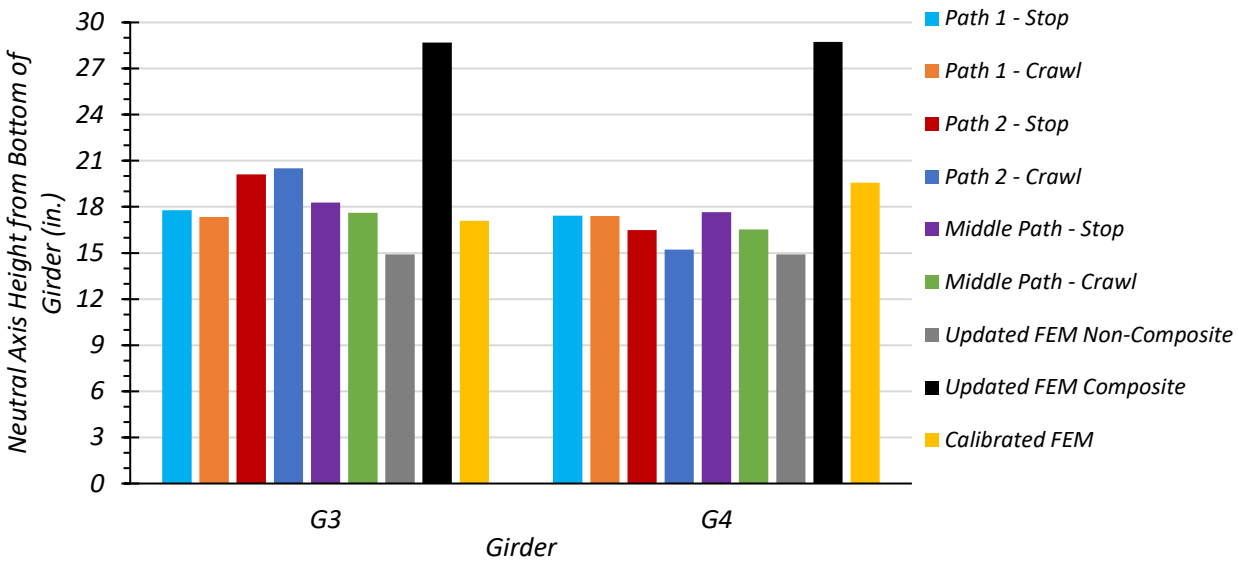

Figure 7.85. Test and FEM Neutral Axis Locations for Span 1 Loading

The maximum bottom flange stresses of Girder G3 and Girder G4 observed during Span 1 static load tests along each path were compared with the theoretical maximum bottom flange stresses calculated by FEM. Only the static tests were used for comparison because FEM performs a multistep static analysis. Therefore, it would be inappropriate to include dynamic effects in the comparison. Table 7.34 and Table 7.35 show the maximum bottom flange stresses observed during testing and the FEM non-composite, composite, and calibrated bottom flange stresses. Figure 7.86 compares the test results with the FEM results.

Table 7.34. Maximum Girder G3 Bottom Flange Stresses from Test and FEM for Span 1 Loading

Load Path	Stop Location Test	Crawl Speed Test	Updated FEM Non-Composite	Updated FEM Composite	Calibrated FEM
Path 1	4.69	4.63	5.42	4.31	4.77
Path 2	2.32	2.15	3.13	2.19	2.57
Middle Path	3.75	3.83	4.68	3.49	3.91

Notes:
1. All stress values are in ksi units
2. FEM results correspond to the same vehicle longitudinal position as stop location tests

Table 7.35. Maximum Girder G4 Bottom Flange Stresses from Test and FEM for Span 1 Loading

Load Path	Stop Location Test	Crawl Speed Test	Updated FEM Non-Composite	Updated FEM Composite	Calibrated FEM
Path 1	5.52	5.58	7.37	5.74	5.58
Path 2	0.70	0.59	1.2	0.45	0.74
Middle Path	2.09	2.22	3.14	2.23	2.48

Notes:
1. All stress values are in ksi units
2. FEM results correspond to the same vehicle longitudinal position as stop location tests

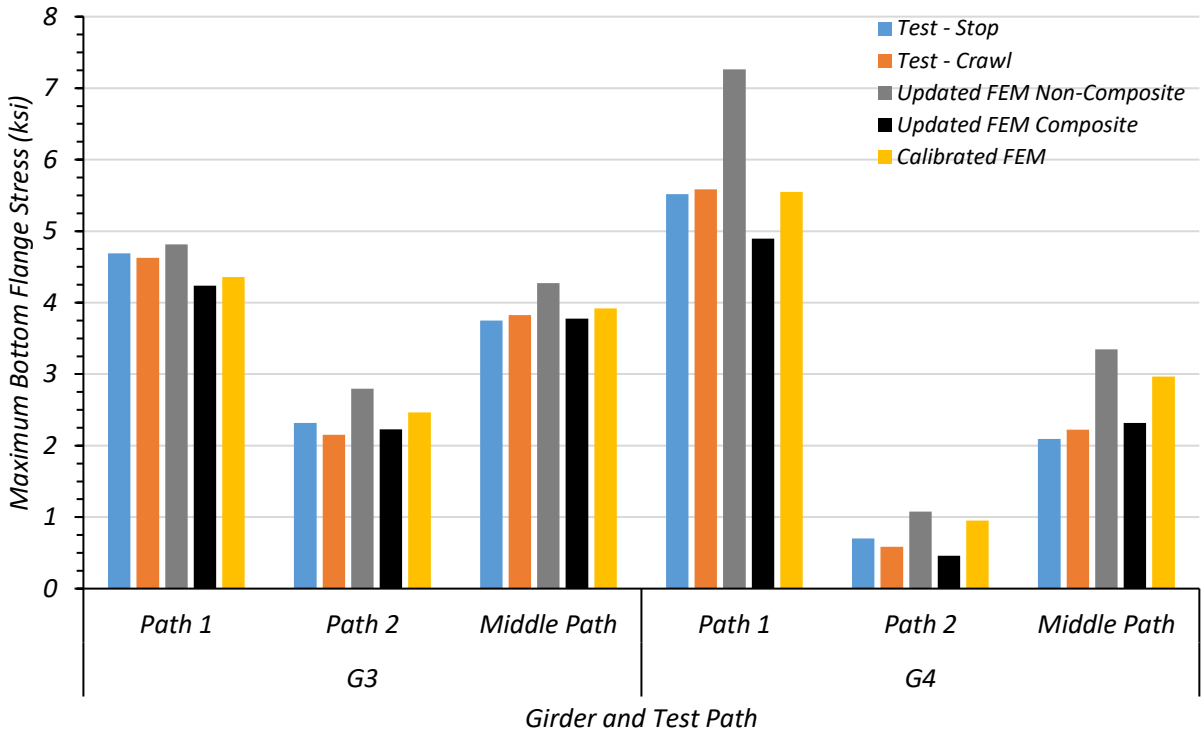

Figure 7.86. Comparison of Maximum Bottom Flange Stresses from Test and FEM for Span 1 Loading

7.8.1.2 Deflection Measurements and LLDFs

Path 1 Loading. Table 7.36 shows the measured girder deflections during testing for the stop location test and crawl speed test along Path 1—Span 1. The girder displacements determined by the calibrated, updated non-composite, and updated composite FEM models are also shown.

Table 7.36. Experimental and FEM Deflections for Path 1—Span 1 Loading

Description	G1	G2	G3	G4
Updated FEM Non-Composite Disp. (in.)	0.062	0.255	0.468	0.641
Updated FEM Composite Disp. (in.)	0.010	0.114	0.236	0.331
Calibrated FEM Disp. (in.)	0.061	0.210	0.369	0.485
Stop Location Test Disp. (in.)	0.023	0.176	0.351	0.485
Crawl Speed Test Disp. (in.)	0.016	0.167	0.342	0.481
Note: 1. G = girder, Disp. = Displacement				

Table 7.37 compares the test LLDFs determined using deflection to those obtained by the deflections of the updated non-composite, updated composite, and calibrated FEM models. All three models do a good job of estimating the LLDF; however, the updated composite model is consistently closest to the test results.

Table 7.37. FEM Displacement LLDF Comparison with Test for Path 1—Span 1 Loading

Test and Girder Type	Updated Non-Composite FEM LLDF (g_{NC})	Updated Composite FEM LLDF (g_C)	Calibrated FEM LLDF (g_{cal})	Test (g_{test})	g_{NC}/g_{test}	g_C/g_{test}	g_{cal}/g_{test}
Stop Location Interior	0.328	0.342	0.328	0.351	0.93	0.97	0.93
Stop Location Exterior	0.450	0.479	0.431	0.485	0.93	0.99	0.89
Crawl Speed Interior	0.328	0.342	0.328	0.342	0.96	1.00	0.96
Crawl Speed Exterior	0.450	0.479	0.431	0.481	0.94	0.99	0.90

Figure 7.87(a) and Figure 7.87(c) show the Path 1—Span 1 stop location and crawl speed deflections compared to non-composite, composite, and calibrated values obtained from FEM analysis. Figure 7.87(b) and Figure 7.87(d) show the Path 1—Span 1 stop location and crawl speed LLDFs compared to relevant AASHTO values and values obtained from calibrated FEM deflection results and moment results. Table 7.38 shows the test LLDF values, the displacement and moment LLDF values obtained from the calibrated FEM model, and the LLDF values found

using all three AASHTO methods. The test and calibrated model LLDFs are all significantly lower than the prescribed AASHTO LLDF values for exterior girders. They are lower than the *AASHTO Standard Specifications* values and close to the *AASHTO LRFD Specifications* values for interior girders.

Table 7.38. Experimental, FEM, and AASHTO LLDFs for Path 1—Span 1 Loading

Description	G1	G2	G3	G4
Stop Location Test Disp. LLDF	0.023	0.170	0.339	0.468
Crawl Speed Test Disp. LLDF	0.016	0.166	0.340	0.478
Calibrated FEM Disp. LLDF	0.054	0.187	0.328	0.431
Calibrated FEM Moment LLDF	0.025	0.155	0.347	0.473
AASHTO Standard LLDF	0.589	0.476	0.476	0.589
AASHTO LRFD LLDF using simplified stiffness	0.660	0.377	0.377	0.660
AASHTO LRFD LLDF using analytical stiffness	0.660	0.368	0.368	0.660

Note:
1. G = girder, Disp. = Displacement

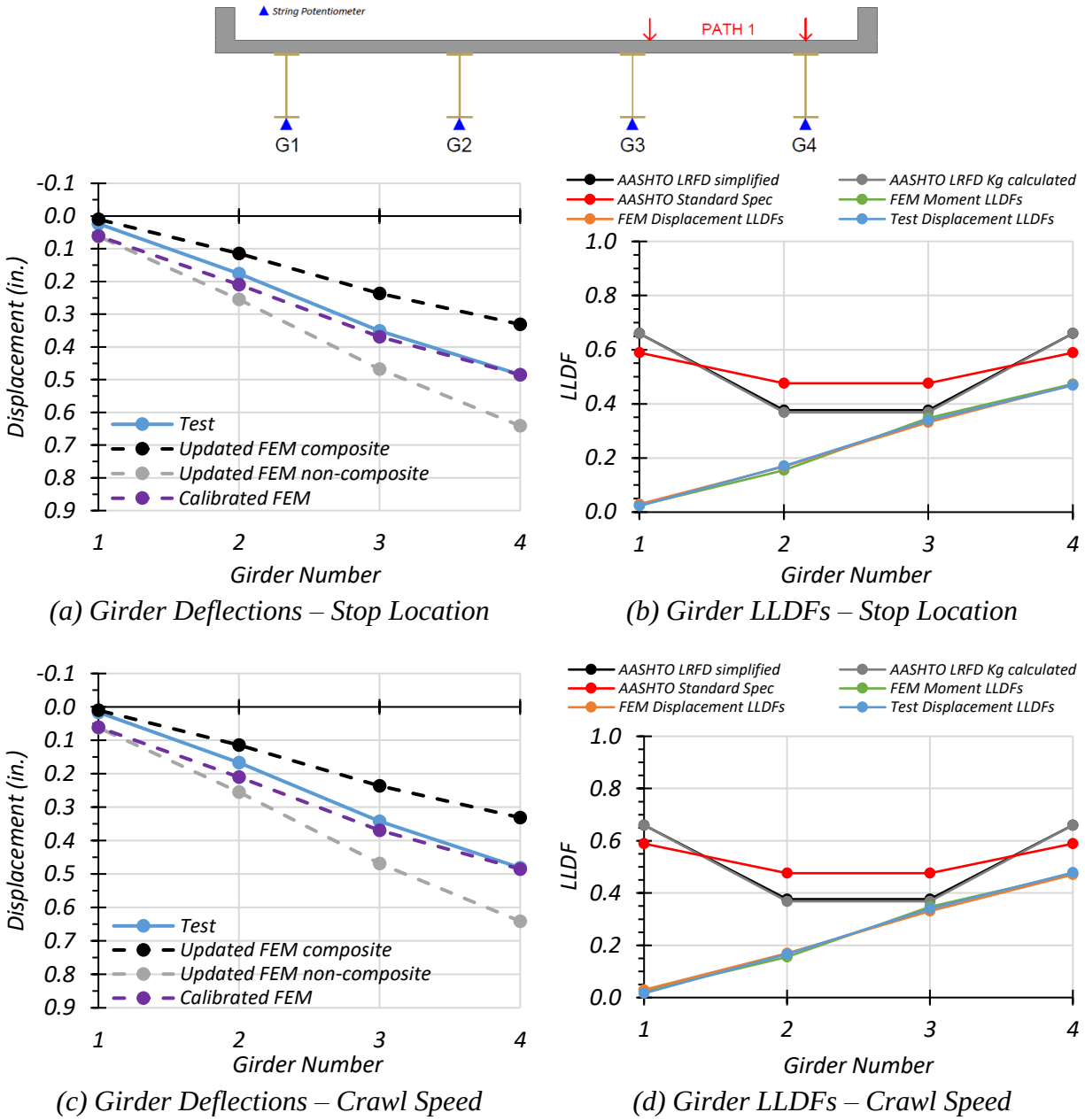

(a) Girder Deflections – Stop Location

(b) Girder LLDFs – Stop Location

(c) Girder Deflections – Crawl Speed

(d) Girder LLDFs – Crawl Speed

Figure 7.87. Static Deflection Results for Path 1—Span 1 Loading

Path 2 Loading. Table 7.39 shows the measured girder deflections during testing for the stop location test and crawl speed test along Path 2—Span 1. The girder displacements determined by the calibrated, updated non-composite, and updated composite FEM models are also shown.

Table 7.39. Experimental and FEM Deflections for Path 2—Span 1 Loading

Description	G1	G2	G3	G4
Updated FEM Non-Composite Disp. (in.)	0.573	0.465	0.288	0.106
Updated FEM Composite Disp. (in.)	0.291	0.236	0.138	0.032
Calibrated FEM Disp. (in.)	0.435	0.369	0.236	0.094
Stop Location Test Disp. (in.)	0.422	0.340	0.198	0.075
Crawl Speed Test Disp. (in.)	0.413	0.322	0.182	0.061
Note: 1. G = girder, Disp. = Displacement				

Table 7.40 compares the test LLDFs determined using deflection to those obtained by the deflections of the updated non-composite, updated composite, and calibrated FEM models. All three models do a good job of estimating the test LLDF; however, the calibrated model is somewhat unconservative for the exterior girder.

Table 7.40. FEM Displacement LLDF Comparison with Test for Path 2—Span 1 Loading

Test and Girder Type	Updated Non-Composite FEM LLDF (g_{NC})	Updated Composite FEM LLDF (g_C)	Calibrated FEM LLDF (g_{cal})	Test (g_{test})	g_{NC}/g_{test}	g_C/g_{test}	g_{cal}/g_{test}
Stop Location Interior	0.325	0.339	0.325	0.328	0.99	1.03	0.99
Stop Location Exterior	0.400	0.418	0.384	0.408	0.98	1.02	0.94
Crawl Speed Interior	0.325	0.339	0.325	0.329	0.99	1.03	0.99
Crawl Speed Exterior	0.400	0.418	0.384	0.423	0.95	0.99	0.91

Figure 7.88(a) and Figure 7.88(c) show the Path 2—Span 1 stop location and crawl speed deflections compared to non-composite, composite, and calibrated values obtained from FEM analysis. Figure 7.88(b) and Figure 7.88(d) show the Path 2—Span 1 stop location and crawl speed LLDFs compared to relevant AASHTO values and values obtained from calibrated FEM deflection results and moment results. Table 7.41 shows the test LLDF values, the displacement and moment LLDF values obtained from the calibrated FEM model, and the LLDF values found

using all three AASHTO methods. The test and calibrated model LLDFs are all significantly lower than the prescribed AASHTO LLDF values for exterior girders. They are lower than the *AASHTO Standard Specifications* values and close to the *AASHTO LRFD Specifications* values for interior girders.

Table 7.41. Experimental, FEM, and AASHTO LLDFs for Path 2—Span 1 Loading

Description	G1	G2	G3	G4
Stop Location Test Disp. LLDF	0.422	0.340	0.198	0.075
Crawl Speed Test Disp. LLDF	0.413	0.322	0.182	0.061
Calibrated FEM Disp. LLDF	0.384	0.325	0.208	0.083
Calibrated FEM Moment LLDF	0.414	0.349	0.185	0.053
AASHTO Standard LLDF	0.589	0.476	0.476	0.589
AASHTO LRFD LLDF using simplified stiffness	0.66	0.377	0.377	0.66
AASHTO LRFD LLDF using analytical stiffness	0.66	0.368	0.368	0.66

Note:
1. G = girder, Disp. = Displacement

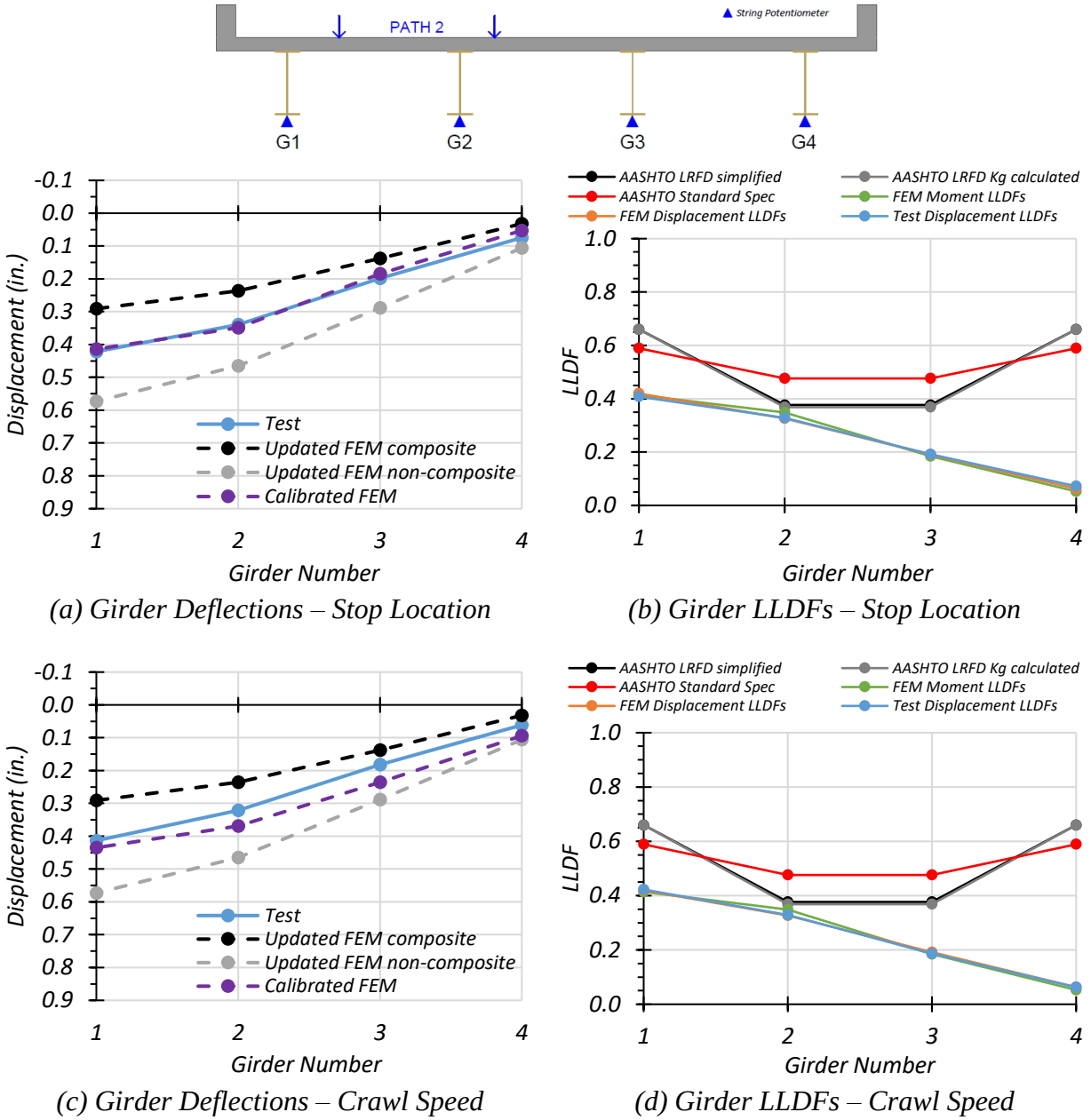

(a) Girder Deflections – Stop Location

(b) Girder LLDFs – Stop Location

(c) Girder Deflections – Crawl Speed

(d) Girder LLDFs – Crawl Speed

Figure 7.88. Static Deflection Results for Path 2—Span 1 Loading

Middle Path Loading. Table 7.42 shows the measured girder deflections during testing for the Middle Path—Span 1 stop location test. The girder displacements determined by the calibrated, updated non-composite, and updated composite FEM models are also shown.

Table 7.42. Experimental and FEM Deflections for Middle Path—Span 1 Loading

Description	G1	G2	G3	G4
Updated FEM Non-Composite Disp. (in.)	0.314	0.408	0.408	0.314
Updated FEM Composite Disp. (in.)	0.142	0.206	0.206	0.142
Calibrated FEM Disp. (in.)	0.246	0.330	0.330	0.246
Stop Location Test Disp. (in.)	0.217	0.286	0.280	0.203
Crawl Speed Test Disp. (in.)	0.201	0.278	0.280	0.211
Note: 1. G = girder, Disp. = Displacement				

Table 7.43 compares the test LLDFs determined using deflection to those obtained by the deflections of the updated non-composite, updated composite, and calibrated FEM models. All three models do a good job of estimating the test LLDF; however, the updated composite model is somewhat unconservative for the exterior girder.

Table 7.43. FEM Displacement LLDF Comparison with Test for Middle Path—Span 1 Loading

Test and Girder Type	Updated Non-Composite FEM LLDF (g_{NC})	Updated Composite FEM LLDF (g_C)	Calibrated FEM LLDF (g_{cal})	Test (g_{test})	g_{NC}/g_{test}	g_C/g_{test}	g_{cal}/g_{test}
Stop Location Interior	0.283	0.296	0.286	0.290	0.98	1.02	0.99
Stop Location Exterior	0.217	0.204	0.214	0.220	0.99	0.93	0.97
Crawl Speed Interior	0.283	0.296	0.286	0.289	0.98	1.02	0.99
Crawl Speed Exterior	0.217	0.204	0.214	0.217	1.00	0.94	0.99

Figure 7.89(a) and Figure 7.89(c) show the Middle Path—Span 1 stop location and crawl speed deflections compared to non-composite, composite, and calibrated values obtained from FEM analysis. Figure 7.89(b) and Figure 7.89(d) show the Middle Path—Span 1 stop location and crawl speed LLDFs compared to relevant AASHTO values and values obtained from calibrated FEM deflection results and moment results. Table 7.44 shows the test LLDF values, the displacement and moment LLDF values obtained from the calibrated FEM model, and the LLDF

values found using all three AASHTO methods. The test and calibrated model LLDFs are all significantly lower than the prescribed AASHTO LLDF values.

Table 7.44. Experimental, FEM, and AASHTO LLDFs for Middle Path—Span 1 Loading

Description	G1	G2	G3	G4
Stop Location Test Disp. LLDF	0.220	0.290	0.284	0.205
Crawl Speed Test Disp. LLDF	0.207	0.287	0.289	0.217
Calibrated FEM Disp. LLDF	0.214	0.286	0.286	0.214
Calibrated FEM Moment LLDF	0.197	0.303	0.303	0.197
AASHTO Standard LLDF	0.589	0.476	0.476	0.589
AASHTO LRFD LLDF using simplified stiffness	0.66	0.377	0.377	0.66
AASHTO LRFD LLDF using analytical stiffness	0.66	0.368	0.368	0.66

Note:
1. G = girder, Disp. = Displacement

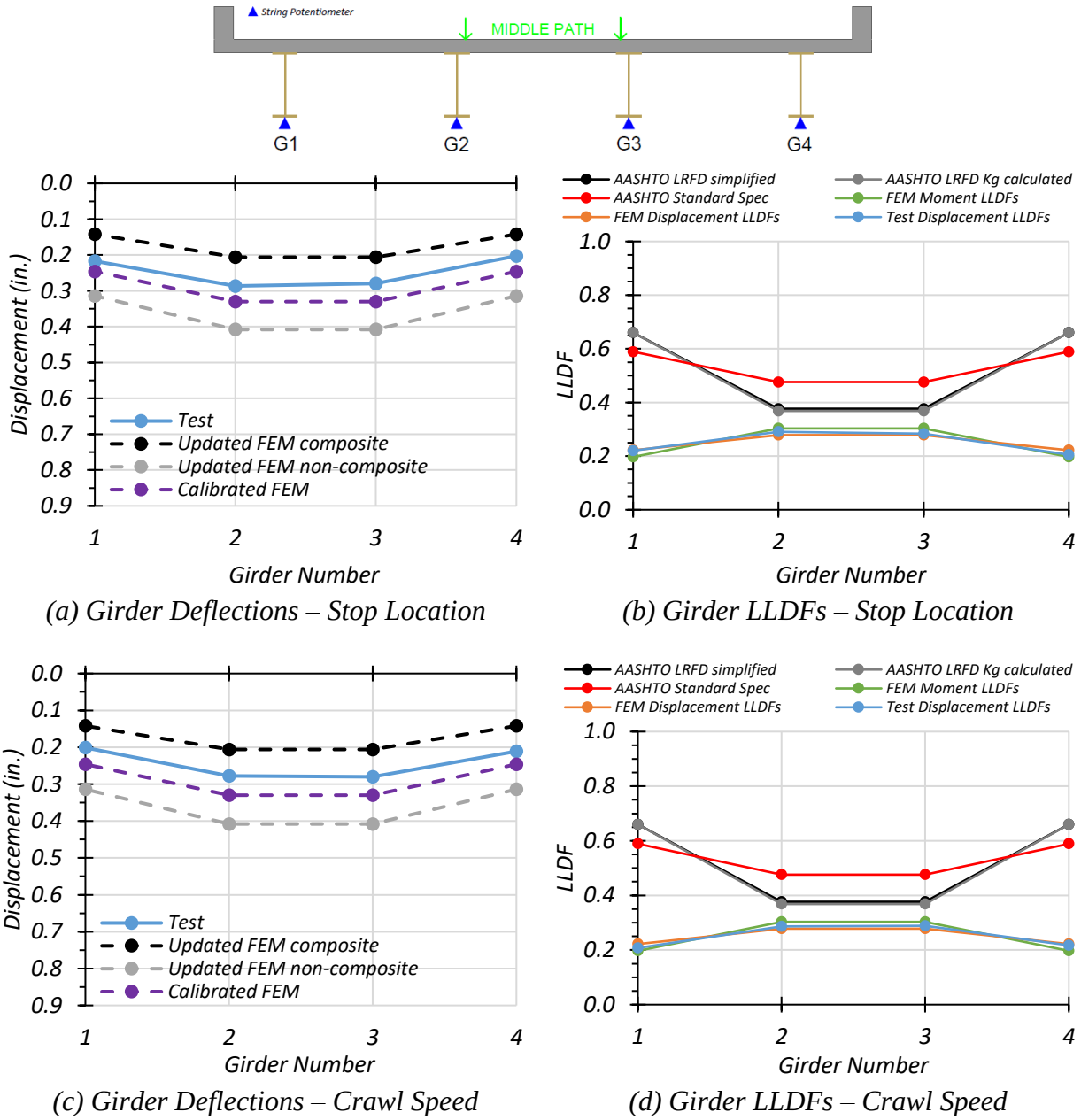

(a) Girder Deflections – Stop Location

(b) Girder LLDFs – Stop Location

(c) Girder Deflections – Crawl Speed

(d) Girder LLDFs – Crawl Speed

Figure 7.89. Static Deflection Results for Middle Path—Span 1 Loading

7.8.2 Static Load Tests on Bridge SC-12 Span 2

Two types of static load tests were conducted without introducing any dynamic effects: (1) stop location tests—by parking the vehicle at the moment critical longitudinal position in each span for each selected path on the bridge, and (2) crawl speed tests—by moving the truck at low speeds (around 2 mph) along the same predefined paths.

7.8.2.1 Strain Measurements and Composite Action

Interior Girder G3. Figure 7.90 through Figure 7.92 provide plots of the measured strains for interior Girder G3 during static load testing and compare the midspan strain diagram to those obtained through the updated and calibrated FEM models. The strains measured for Girder G3 during the Path 1—Span 2 static tests are shown in Figure 7.90 and compared with values obtained from the FEM updated and calibrated models. Figure 7.90(a) shows the FEM comparison for the stop location test for Girder G3 at 0.4*L* of Span 1 and the interior pier. Figure 7.90(b) shows the FEM comparison for the stop location test for Girder G3 at the midspan of Span 2. Figure 7.90(c) shows the FEM comparison for the crawl speed test for Girder G3 at 0.4*L* of Span 1 and the interior pier. Figure 7.90(d) shows the FEM comparison for the crawl speed test for Girder G3 at the midspan of Span 2.

The strains measured for Girder G3 during the Path 2—Span 2 static tests are shown in Figure 7.91 and compared with values obtained from the FEM updated and calibrated models. Figure 7.91(a) shows the FEM comparison for the stop location test for Girder G3 at 0.4*L* of Span 1 and the interior pier. Figure 7.91(b) shows the FEM comparison for the stop location test for Girder G3 at the midspan of Span 2. Figure 7.91(c) shows the FEM comparison for the crawl speed test for Girder G3 at 0.4*L* of Span 1 and the interior pier. Figure 7.91(d) shows the FEM comparison for the crawl speed test for Girder G3 at the midspan of Span 2.

The strains measured for Girder G3 during the Middle Path static tests are shown in Figure 7.92 and compared with values obtained from the FEM updated and calibrated models. Figure 7.92(a) shows the FEM comparison for the stop location test for Girder G3 at 0.4*L* of Span 1 and the interior pier. Figure 7.92(b) shows the FEM comparison for the stop location test for Girder G3 at the midspan of Span 2. Figure 7.92(c) shows the FEM comparison for the crawl speed test for Girder G3 at 0.4*L* of Span 1 and the interior pier. Figure 7.92(d) shows the FEM comparison for the crawl speed test for Girder G3 at the midspan of Span 2.

The calibrated model compares well with the Path 1 and Middle Path loading strain diagrams but does not compare quite as well with the Path 2 loading strain diagram, which is likely due to Girder G3 not receiving much load during Path 2 loading because the truck is closer to Girders G1 and G2.

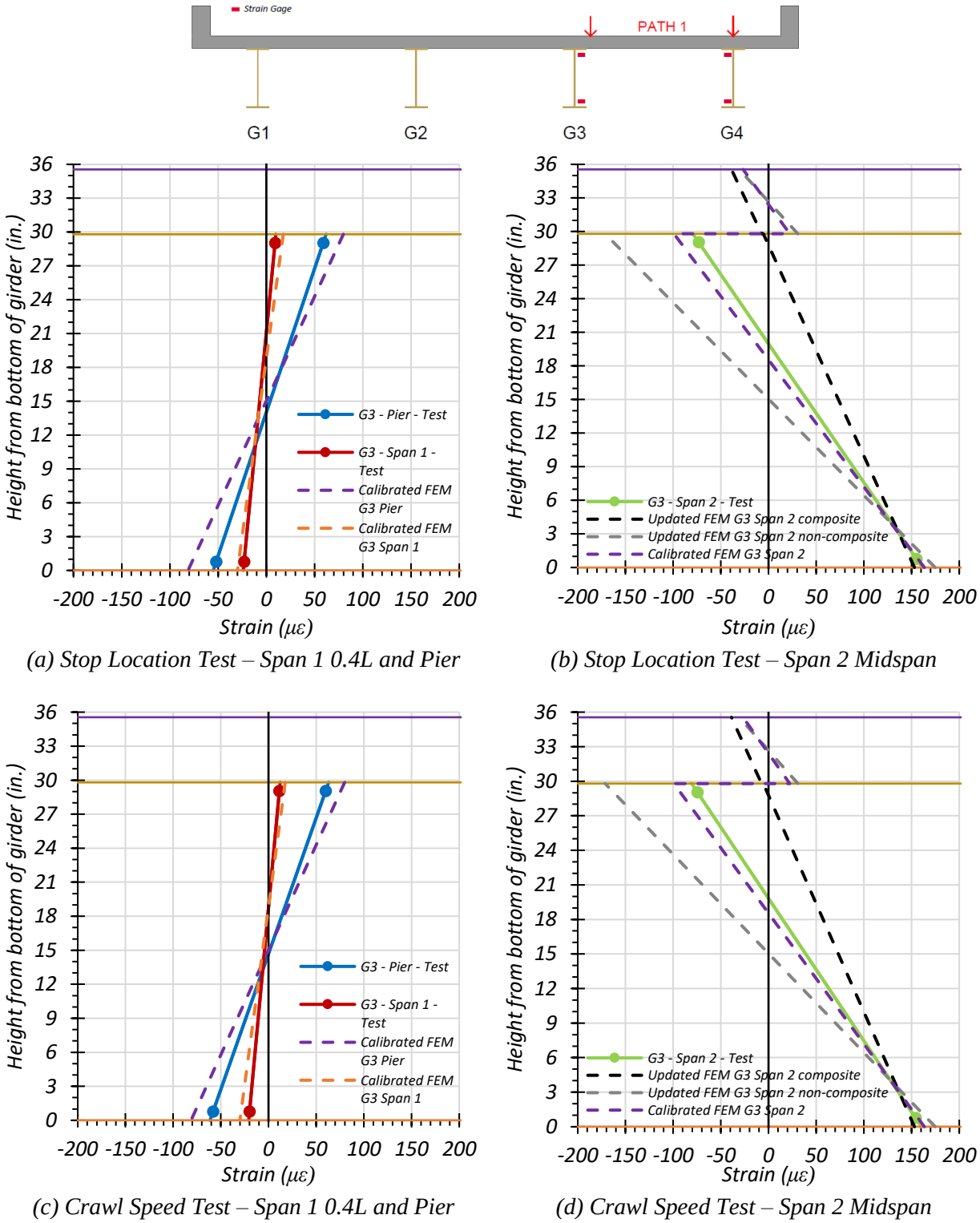

(a) Stop Location Test – Span 1 0.4L and Pier

(b) Stop Location Test – Span 2 Midspan

(c) Crawl Speed Test – Span 1 0.4L and Pier

(d) Crawl Speed Test – Span 2 Midspan

Figure 7.90. Static Strains for Interior Girder G3: Path 1—Span 2

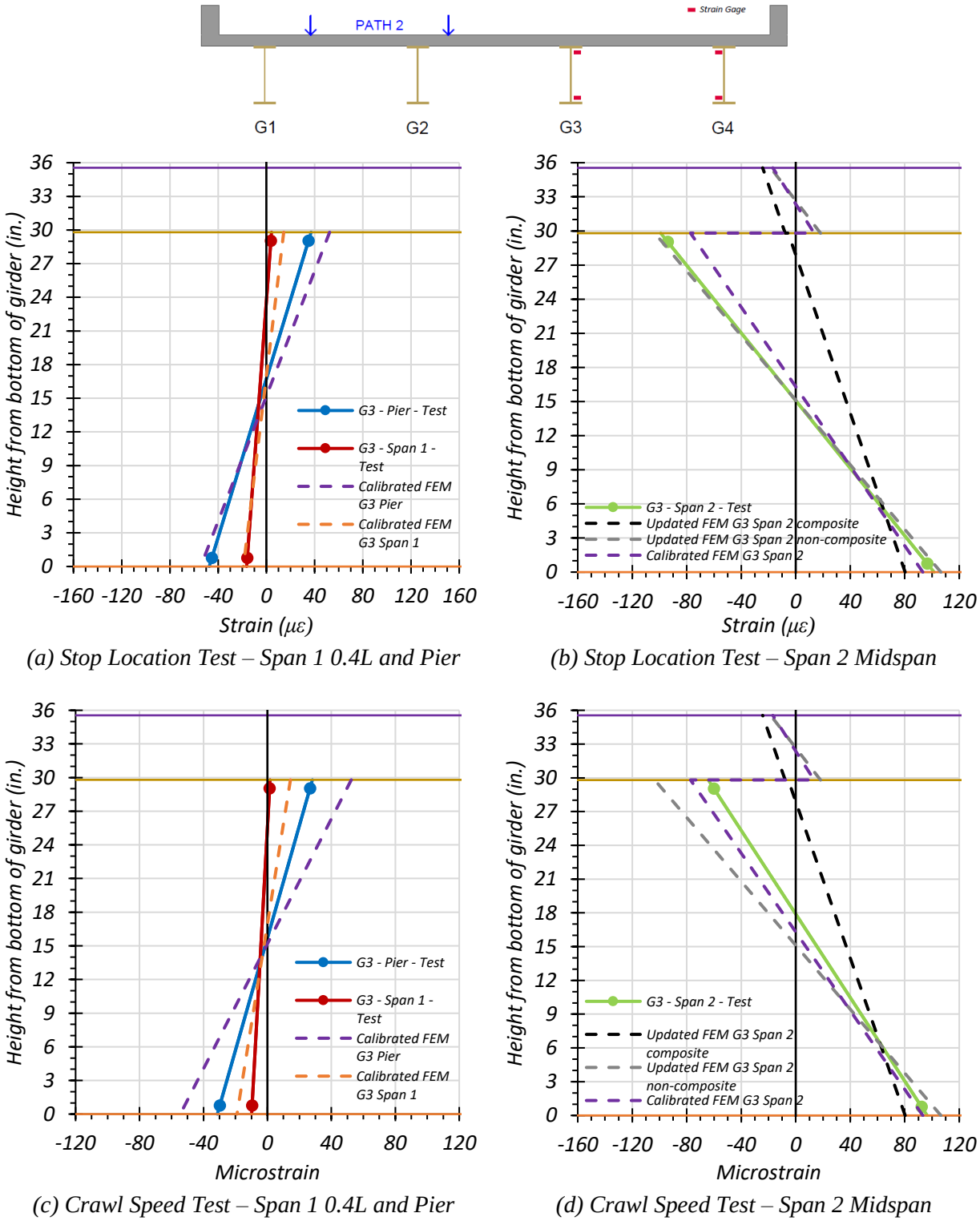

(a) Stop Location Test – Span 1 0.4L and Pier

(b) Stop Location Test – Span 2 Midspan

(c) Crawl Speed Test – Span 1 0.4L and Pier

(d) Crawl Speed Test – Span 2 Midspan

Figure 7.91. Static Strains for Interior Girder G3: Path 2—Span 2

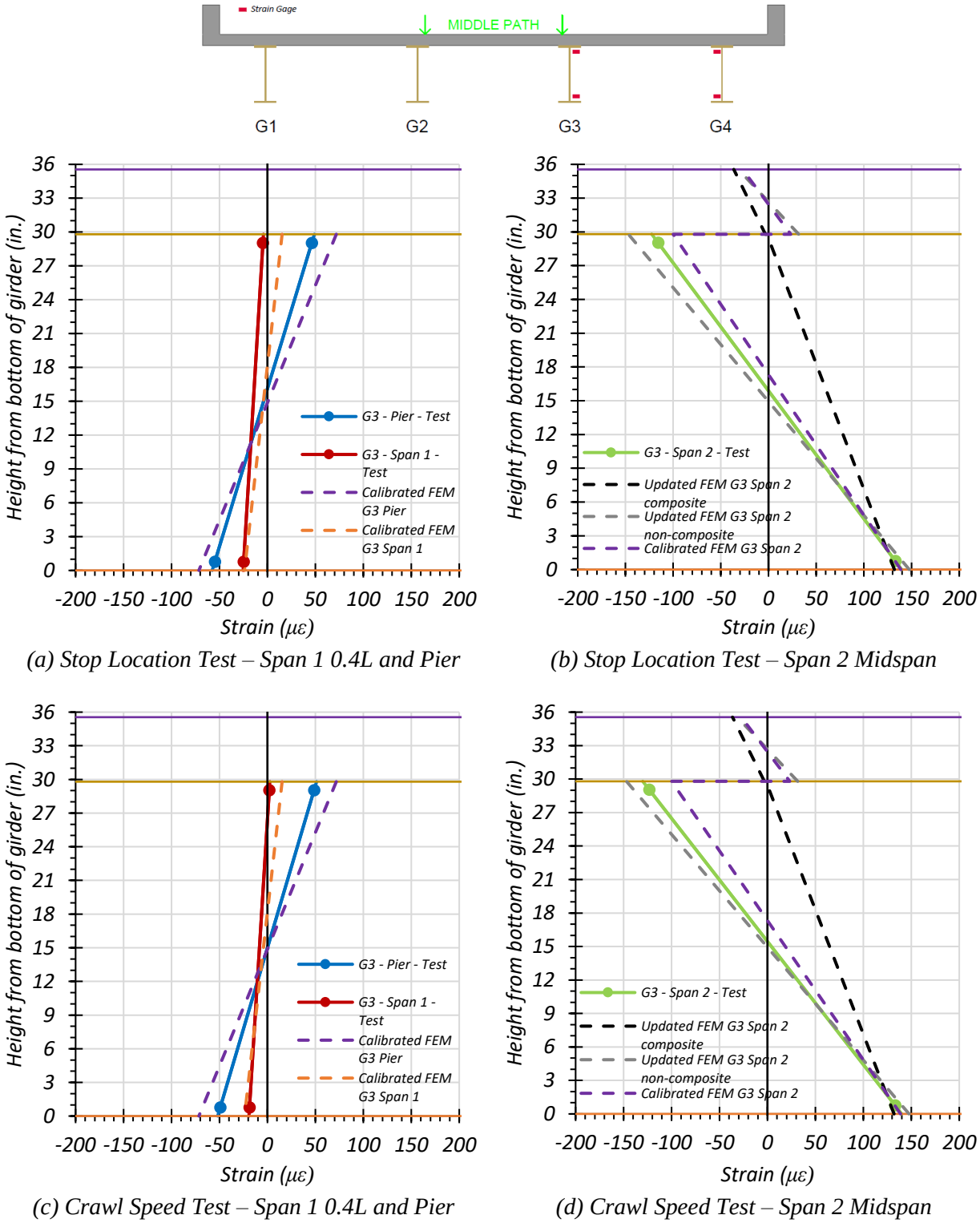

(a) Stop Location Test – Span 1 0.4L and Pier

(b) Stop Location Test – Span 2 Midspan

(c) Crawl Speed Test – Span 1 0.4L and Pier

(d) Crawl Speed Test – Span 2 Midspan

Figure 7.92. Static Strains for Interior Girder G3: Middle Path—Span 2

Exterior Girder G4. Figure 7.93 through Figure 7.95 provide plots of the measured strains for exterior Girder G4 during static load testing and compare the midspan strain diagram to those obtained through the updated and calibrated FEM models. The strains measured for Girder G4 during the Path 1—Span 2 static tests are shown in Figure 7.93 and compared with values obtained from the FEM updated and calibrated models. Figure 7.93(a) shows the FEM comparison for the stop location test for Girder G4 at 0.4*L* of Span 1 and the interior pier. Figure 7.93(b) shows the FEM comparison for the stop location test for Girder G4 at the midspan of Span 2. Figure 7.93(c) shows the FEM comparison for the crawl speed test for Girder G4 at 0.4*L* of Span 1 and the interior pier. Figure 7.93(d) shows the FEM comparison for the crawl speed test for Girder G4 at the midspan of Span 2.

The strains measured for Girder G4 during the Path 2—Span 2 static tests are shown in Figure 7.94 and compared with values obtained from the FEM updated and calibrated models. Figure 7.94(a) shows the FEM comparison for the stop location test for Girder G4 at 0.4*L* of Span 1 and the interior pier. Figure 7.94(b) shows the FEM comparison for the stop location test for Girder G4 at the midspan of Span 2. Figure 7.94(c) shows the FEM comparison for the crawl speed test for Girder G4 at 0.4*L* of Span 1 and the interior pier. Figure 7.94(d) shows the FEM comparison for the crawl speed test for Girder G4 at the midspan of Span 2.

The strains measured for Girder G4 during the Middle Path static tests are shown in Figure 7.95 and compared with values obtained from the FEM updated and calibrated models. Figure 7.95(a) shows the FEM comparison for the stop location test for Girder G4 at 0.4*L* of Span 1 and the interior pier. Figure 7.95(b) shows the FEM comparison for the stop location test for Girder G4 at the midspan of Span 2. Figure 7.95(c) shows the FEM comparison for the crawl speed test for Girder G4 at 0.4*L* of Span 1 and the interior pier. Figure 7.95(d) shows the FEM comparison for the crawl speed test for Girder G4 at the midspan of Span 2.

The calibrated model compares well with the Path 1 loading strain diagrams but does not compare quite as well with the Path 2 and Middle Path loading strain diagrams, which is likely due to Girder G4 not receiving much load during Path 2 loading and Middle Path loading because the truck is closer to Girders G1 and G2 under Path 2 loading and to Girders G2 and G3 under Middle Path loading.

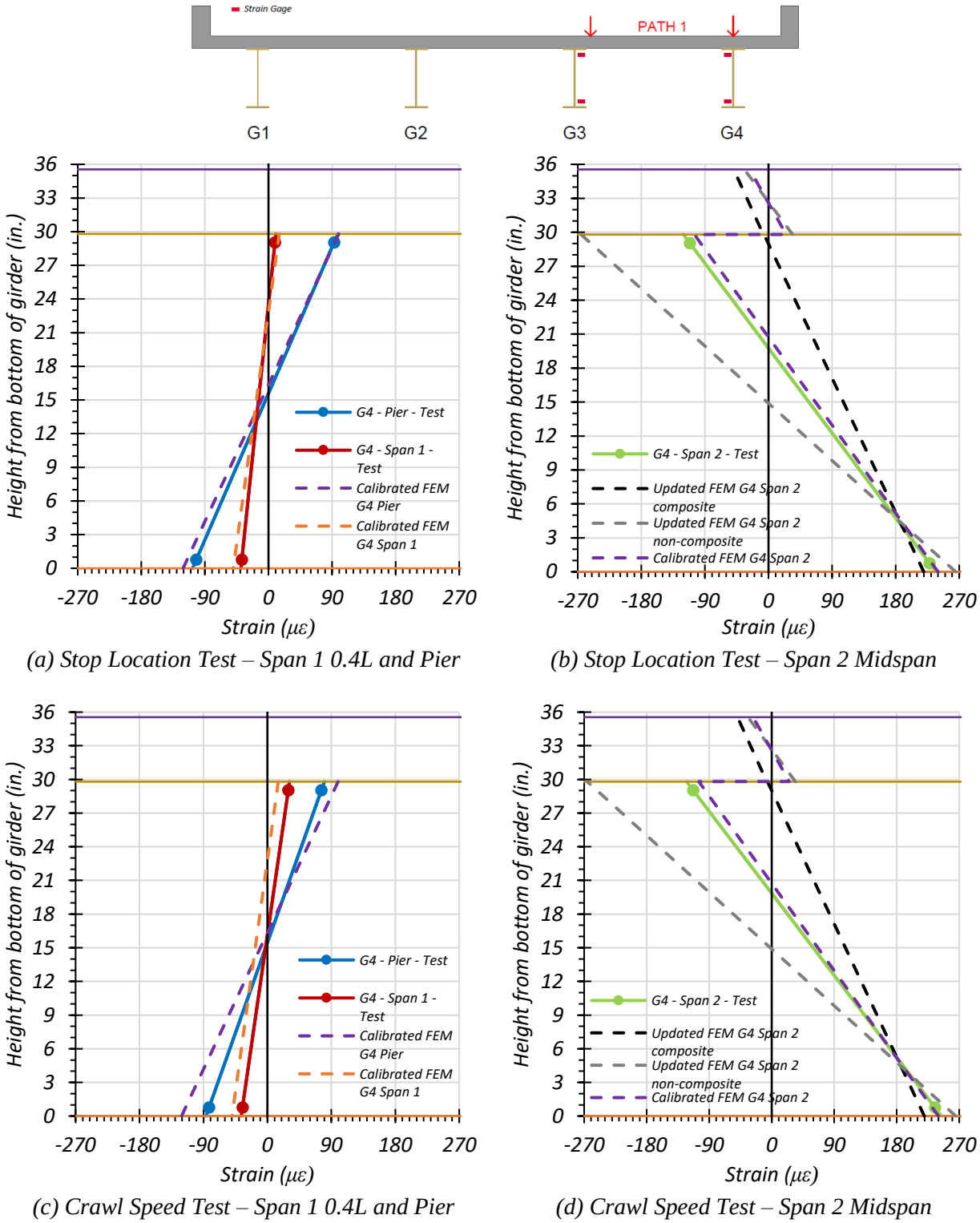

(a) Stop Location Test – Span 1 0.4L and Pier

(b) Stop Location Test – Span 2 Midspan

(c) Crawl Speed Test – Span 1 0.4L and Pier

(d) Crawl Speed Test – Span 2 Midspan

Figure 7.93. Static Strains for Exterior Girder G4: Path 1—Span 2

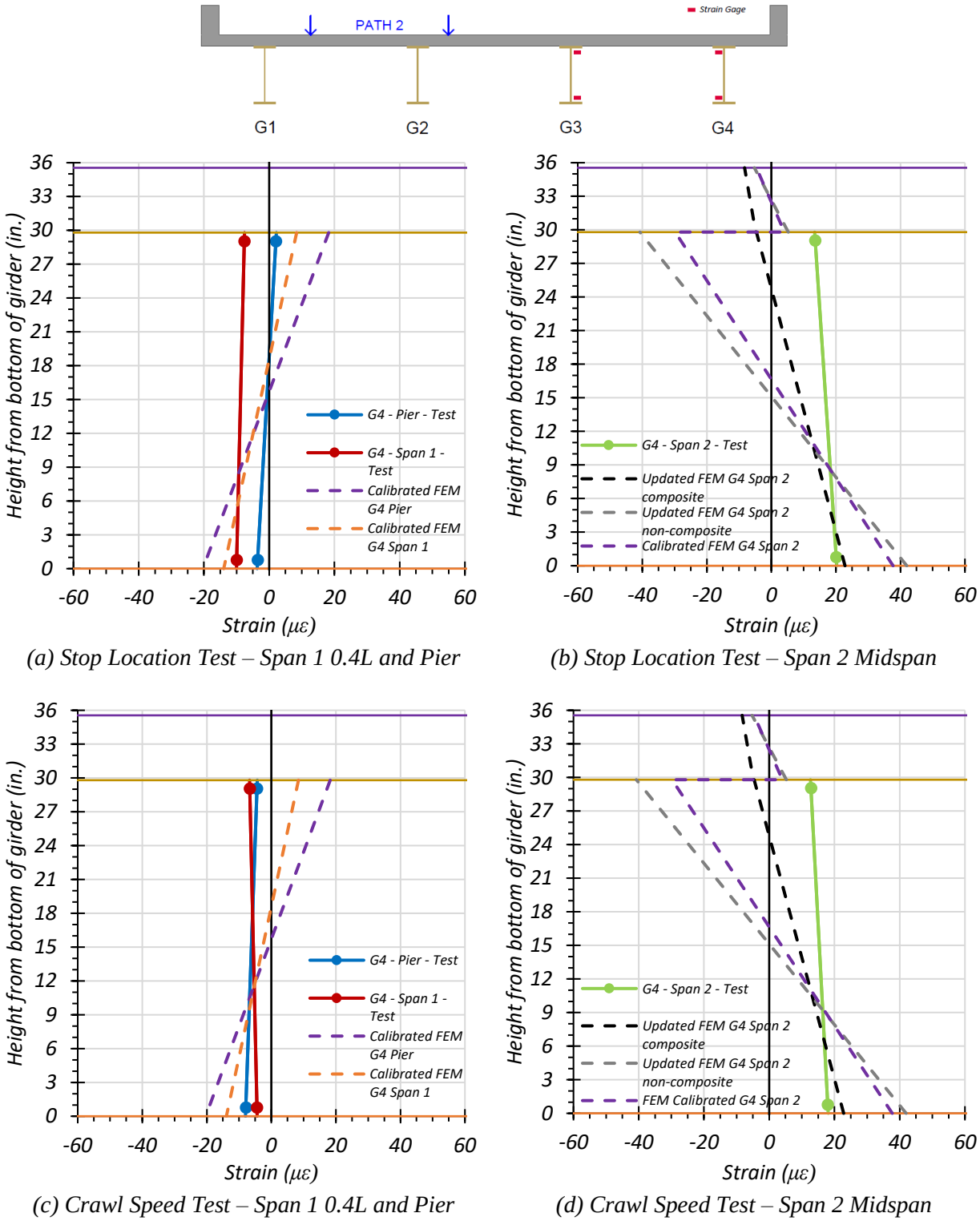

(a) Stop Location Test – Span 1 0.4L and Pier

(b) Stop Location Test – Span 2 Midspan

(c) Crawl Speed Test – Span 1 0.4L and Pier

(d) Crawl Speed Test – Span 2 Midspan

Figure 7.94. Static Strains for Exterior Girder G4: Path 2—Span 2

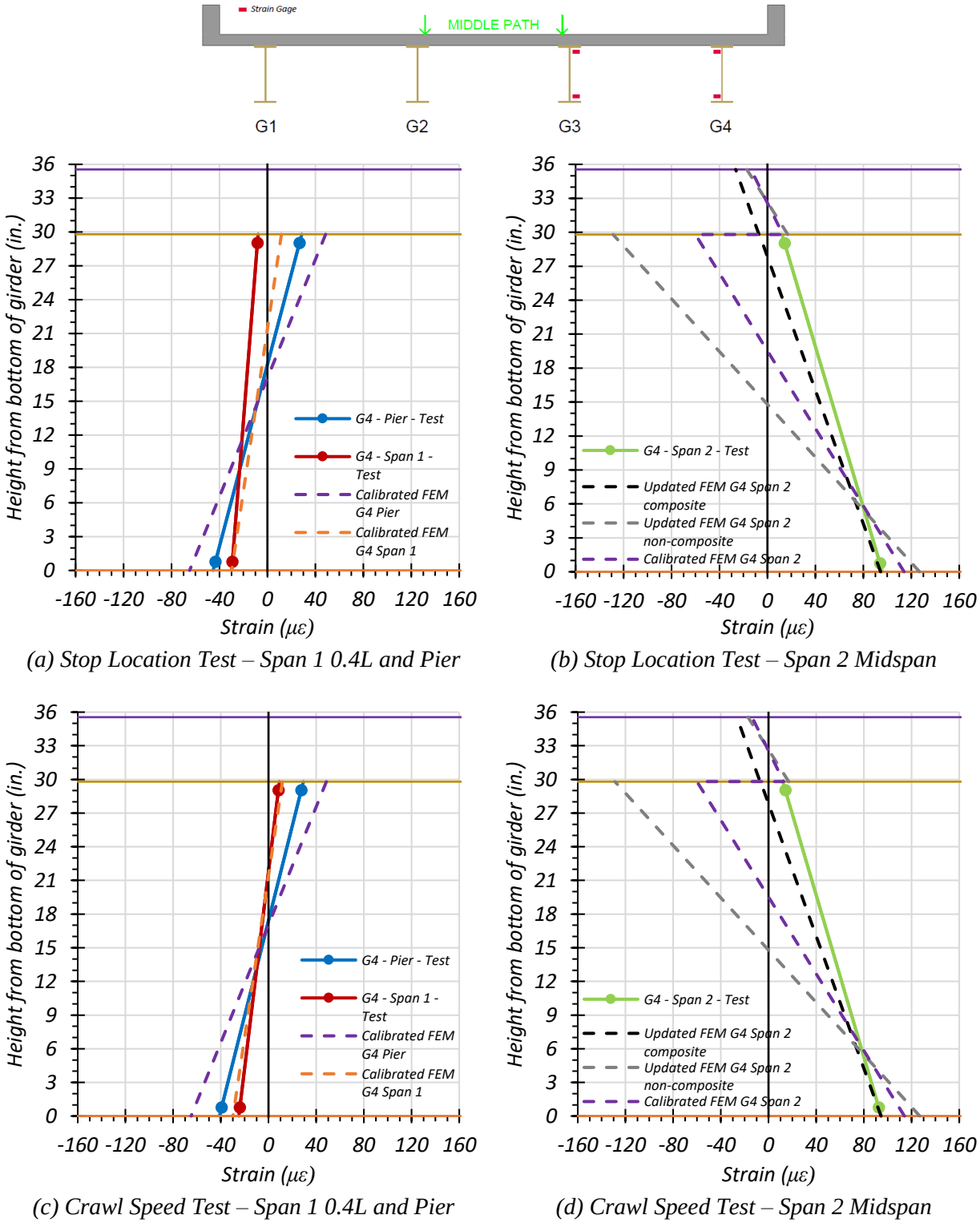

(a) Stop Location Test – Span 1 0.4L and Pier

(b) Stop Location Test – Span 2 Midspan

(c) Crawl Speed Test – Span 1 0.4L and Pier

(d) Crawl Speed Test – Span 2 Midspan

Figure 7.95. Static Strains for Exterior Girder G4: Middle Path—Span 2

Comparison of Measured Strain Results. The neutral axis locations of Girder G4 and Girder G3 observed during the load tests were compared with the theoretical neutral axis locations calculated using the FEM strain predictions. Table 7.45 shows the neutral axis locations measured for all static load tests and for the three FEM models. Figure 7.96 compares the test neutral axis locations with the non-composite and composite neutral axis locations obtained from FEM. Since the test neutral axis locations are in between the estimated composite neutral axis locations and non-composite neutral axis locations, Bridge SC-12 appears to be acting as partially composite.

Table 7.45. Measured and FEM Neutral Axis Locations for All Span 2 Static Load Tests

Test	G3 Neutral Axis Location (in. from bottom of girder)	G4 Neutral Axis Location (in. from bottom of girder)
Path 1—Stop Location	19.97	19.76
Path 1—Crawl Speed	19.56	19.85
Path 2—Stop Location	15.08	88.17
Path 2—Crawl Speed	15.32	99.15
Middle Path—Stop Location	15.88	34.13
Middle Path—Crawl Speed	15.45	32.76
Theoretical Non-Composite	14.90	14.90
Theoretical Composite	26.11	26.11
FEM Non-Composite	14.90	14.90
FEM Composite	28.79	28.97
FEM Calibrated	18.55	20.73

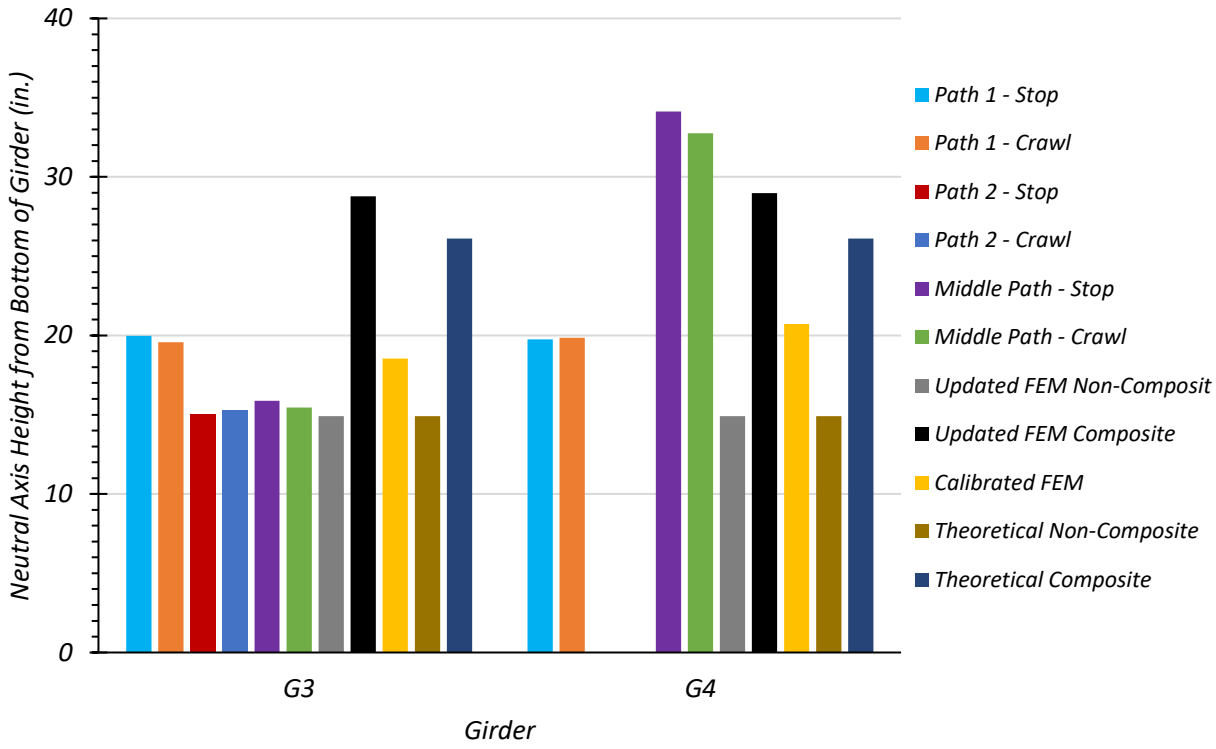

Figure 7.96. Test and FEM Neutral Axis Locations for Span 2 Loading

The maximum bottom flange stresses of Girder G4 and Girder G3 observed during Span 2 static load tests along each path were compared with the theoretical maximum bottom flange stresses calculated by FEM. Only the stop location tests were used for comparison because FEM performs a multistep static analysis. Therefore, it would be inappropriate to include dynamic effects in the comparison. Table 7.46 and Table 7.47 show the maximum bottom flange stresses observed during testing and the FEM non-composite, composite, and calibrated bottom flange stresses. Figure 7.97 compares the test results with the FEM results. In general, the stresses observed during testing fall in between the expected composite and non-composite stresses.

Table 7.46. Maximum Girder G3 Bottom Flange Stresses from Test and FEM for Span 2 Loading

Load Path	Stop Location Test	Crawl Speed Test	Updated FEM Non-Composite	Updated FEM Composite	Calibrated FEM
Path 1	4.68	4.66	5.59	3.98	4.59
Path 2	2.94	2.82	3.35	2.27	2.90
Middle Path	4.05	4.06	4.77	3.73	4.23

Notes:
1. All stress values are in ksi units
2. FEM results correspond to the same vehicle longitudinal position as stop location tests

Table 7.47. Maximum Girder G4 Bottom Flange Stresses from Test and FEM for Span 2 Loading

Load Path	Stop Location Test	Crawl Speed Test	Updated FEM Non-Composite	Updated FEM Composite	Calibrated FEM
Path 1	6.88	7.09	7.64	6.33	6.85
Path 2	0.59	0.52	1.42	0.59	0.94
Middle Path	2.78	2.82	3.78	2.23	3.10

Notes:
1. All stress values are in ksi units
2. FEM results correspond to the same vehicle longitudinal position as stop location tests

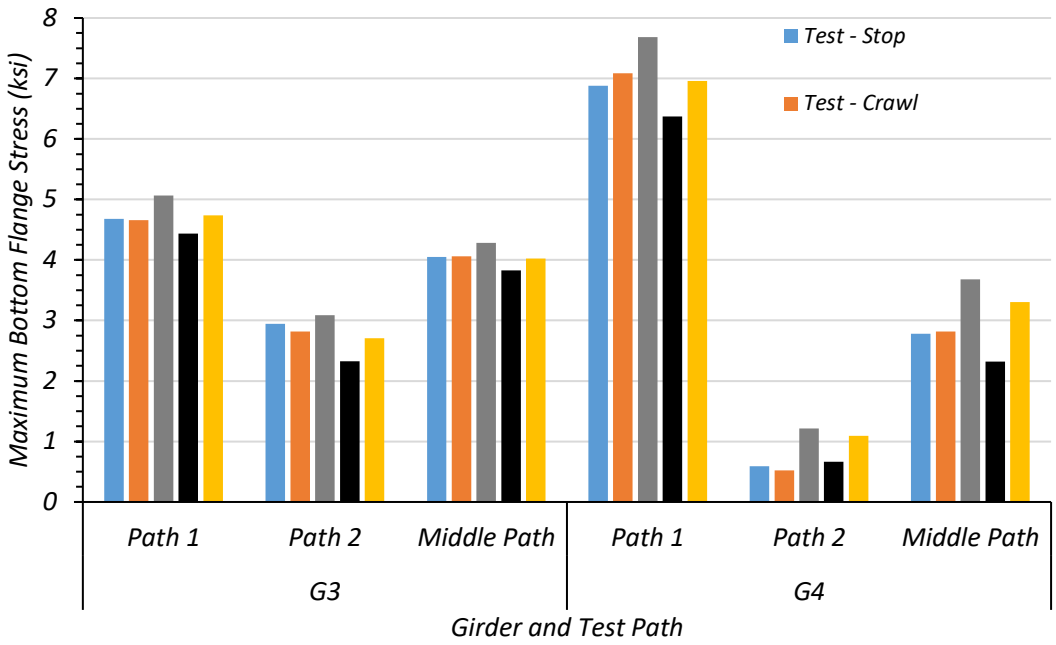

Figure 7.97. Comparison of Maximum Bottom Flange Stresses from Test and FEM for Span 2 Loading

7.8.2.2 Deflection Measurements and LLDFs

Path 1 Loading. Table 7.48 shows the measured girder deflections during testing for the stop location test and crawl speed test along Path 1—Span 2. The girder displacements determined by the calibrated, updated non-composite, and updated composite FEM models are also shown.

Table 7.48. Experimental and FEM Deflections for Path 1—Span 2 Loading

Description	G1	G2	G3	G4
Updated FEM Non-Composite Disp. (in.)	0.098	0.376	0.672	0.928
Updated FEM Composite Disp. (in.)	0.025	0.180	0.352	0.495
Calibrated FEM Disp. (in.)	0.065	0.276	0.511	0.720
Stop Location Test Disp. (in.)	0.049	0.280	0.526	0.755
Crawl Speed Test Disp. (in.)	0.032	0.260	0.520	0.771
Note: 1. G = girder, Disp. = Displacement				

Table 7.49 compares the test LLDFs determined using deflection to those obtained by the deflections of the updated non-composite, updated composite, and calibrated FEM models. All

three models do a good job of estimating the LLDF; however, the calibrated model is somewhat unconservative for exterior girders.

Table 7.49. FEM Displacement LLDF Comparison with Test for Path 1—Span 2 Loading

Test and Girder Type	Updated Non-Composite FEM LLDF (g_{NC})	Updated Composite FEM LLDF (g_C)	Calibrated FEM LLDF (g_{cal})	Test (g_{test})	g_{NC}/g_{test}	g_C/g_{test}	g_{cal}/g_{test}
Stop Location Interior	0.324	0.335	0.325	0.327	0.99	1.02	0.99
Stop Location Exterior	0.447	0.471	0.458	0.469	0.95	1.00	0.98
Crawl Speed Interior	0.324	0.335	0.325	0.328	0.99	1.02	0.99
Crawl Speed Exterior	0.447	0.471	0.458	0.487	0.92	0.97	0.94

Figure 7.98(a) and Figure 7.98(c) show the Path 1—Span 2 stop location and crawl speed deflections compared to non-composite, composite, and calibrated values obtained from FEM analysis. Figure 7.98(b) and Figure 7.98(d) show the Path 1—Span 2 stop location and crawl speed LLDFs compared to relevant AASHTO values as well as to values obtained from calibrated FEM deflection results and moment results. Table 7.50 shows the test LLDF values, the displacement and moment LLDF values obtained from the calibrated FEM model, and the LLDF values found using all three AASHTO methods. The test and calibrated model LLDFs are all significantly lower than the prescribed AASHTO LLDF values for exterior girders. They are significantly lower than the *AASHTO Standard Specifications* LLDF values and close to the *AASHTO LRFD Specifications* values for interior girders.

Table 7.50. Experimental, FEM, and AASHTO LLDFs for Path 1—Span 2 Loading

Description	G1	G2	G3	G4
Stop Location Test Disp. LLDF	0.030	0.174	0.327	0.469
Crawl Speed Test Disp. LLDF	0.020	0.164	0.328	0.487
Calibrated FEM Disp. LLDF	0.041	0.176	0.325	0.458
Calibrated FEM Moment LLDF	0.032	0.166	0.335	0.467
AASHTO Standard LLDF	0.589	0.476	0.476	0.589
AASHTO LRFD LLDF using simplified stiffness	0.660	0.356	0.356	0.660
AASHTO LRFD LLDF using analytical stiffness	0.660	0.342	0.342	0.660

Note:
1. G = girder, Disp. = Displacement

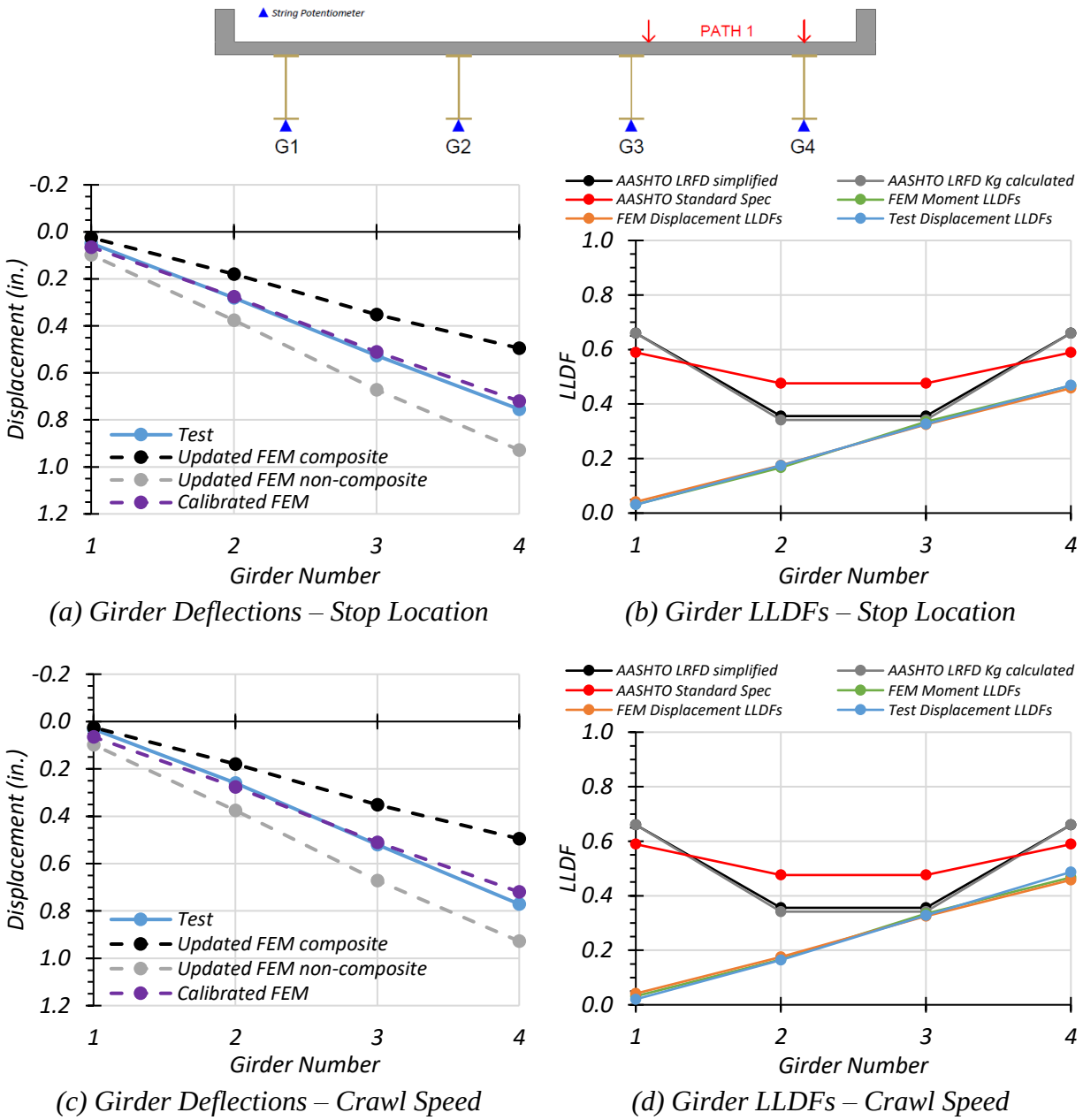

(a) Girder Deflections – Stop Location

(b) Girder LLDFs – Stop Location

(c) Girder Deflections – Crawl Speed

(d) Girder LLDFs – Crawl Speed

Figure 7.98. Static Deflection Results for Path 1—Span 2 Loading

Path 2 Loading. Table 7.51 shows the measured girder deflections during testing for the stop location test and crawl speed test along Path 2—Span 2. The girder displacements determined by the calibrated, updated non-composite, and updated composite FEM models are also shown.

Table 7.51. Experimental and FEM Deflections for Path 2—Span 2 Loading

Description	G1	G2	G3	G4
Updated FEM Non-Composite Disp. (in.)	0.835	0.662	0.418	0.166
Updated FEM Composite Disp. (in.)	0.441	0.347	0.206	0.061
Calibrated FEM Disp. (in.)	0.635	0.520	0.339	0.145
Stop Location Test Disp. (in.)	0.692	0.556	0.298	0.077
Crawl Speed Test Disp. (in.)	0.693	0.537	0.279	0.060
Note: 1. G = girder, Disp. = Displacement				

Table 7.52 compares the test LLDFs determined using deflection to those obtained by the deflections of the updated non-composite, updated composite, and calibrated FEM models. All three models do a good job of estimating the LLDF; however, the updated composite model does a slightly better job than the calibrated model and the updated non-composite model.

Table 7.52. FEM Displacement LLDF Comparison with Test for Path 2—Span 2 Loading

Test and Girder Type	Updated Non-Composite FEM LLDF (g_{NC})	Updated Composite FEM LLDF (g_C)	Calibrated FEM LLDF (g_{cal})	Test (g_{test})	g_{NC}/g_{test}	g_C/g_{test}	g_{cal}/g_{test}
Stop Location Interior	0.318	0.329	0.317	0.343	0.93	0.96	0.92
Stop Location Exterior	0.401	0.418	0.387	0.427	0.94	0.98	0.91
Crawl Speed Interior	0.318	0.329	0.317	0.342	0.93	0.96	0.93
Crawl Speed Exterior	0.401	0.418	0.387	0.442	0.91	0.95	0.88

Figure 7.99(a) and Figure 7.99(c) show the Path 2—Span 2 stop location and crawl speed deflections compared to non-composite, composite, and calibrated values obtained from FEM analysis. Figure 7.99(b) and Figure 7.99(d) show the Path 2—Span 2 stop location and crawl speed LLDFs compared to relevant AASHTO values as well as to values obtained from calibrated FEM deflection results and moment results. Table 7.53 shows the test LLDF values, the displacement and moment LLDF values obtained from the calibrated FEM model, and the LLDF values found

using all three AASHTO methods. The test and calibrated model LLDFs are all significantly lower than the prescribed AASHTO LLDF values for exterior girders. They are significantly lower than the *AASHTO Standard Specifications* LLDF values and close to the *AASHTO LRFD Specifications* LLDF values for interior girders.

Table 7.53. Experimental, FEM, and AASHTO LLDFs for Path 2—Span 2 Loading

Description	G1	G2	G3	G4
Stop Location Test Disp. LLDF	0.427	0.343	0.184	0.047
Crawl Speed Test Disp. LLDF	0.442	0.342	0.178	0.038
Calibrated FEM Disp. LLDF	0.387	0.317	0.207	0.088
Calibrated FEM Moment LLDF	0.415	0.332	0.191	0.063
AASHTO Standard LLDF	0.589	0.476	0.476	0.589
AASHTO LRFD LLDF using simplified stiffness	0.660	0.356	0.356	0.660
AASHTO LRFD LLDF using analytical stiffness	0.660	0.342	0.342	0.660

Note:
1. G = girder, Disp. = Displacement

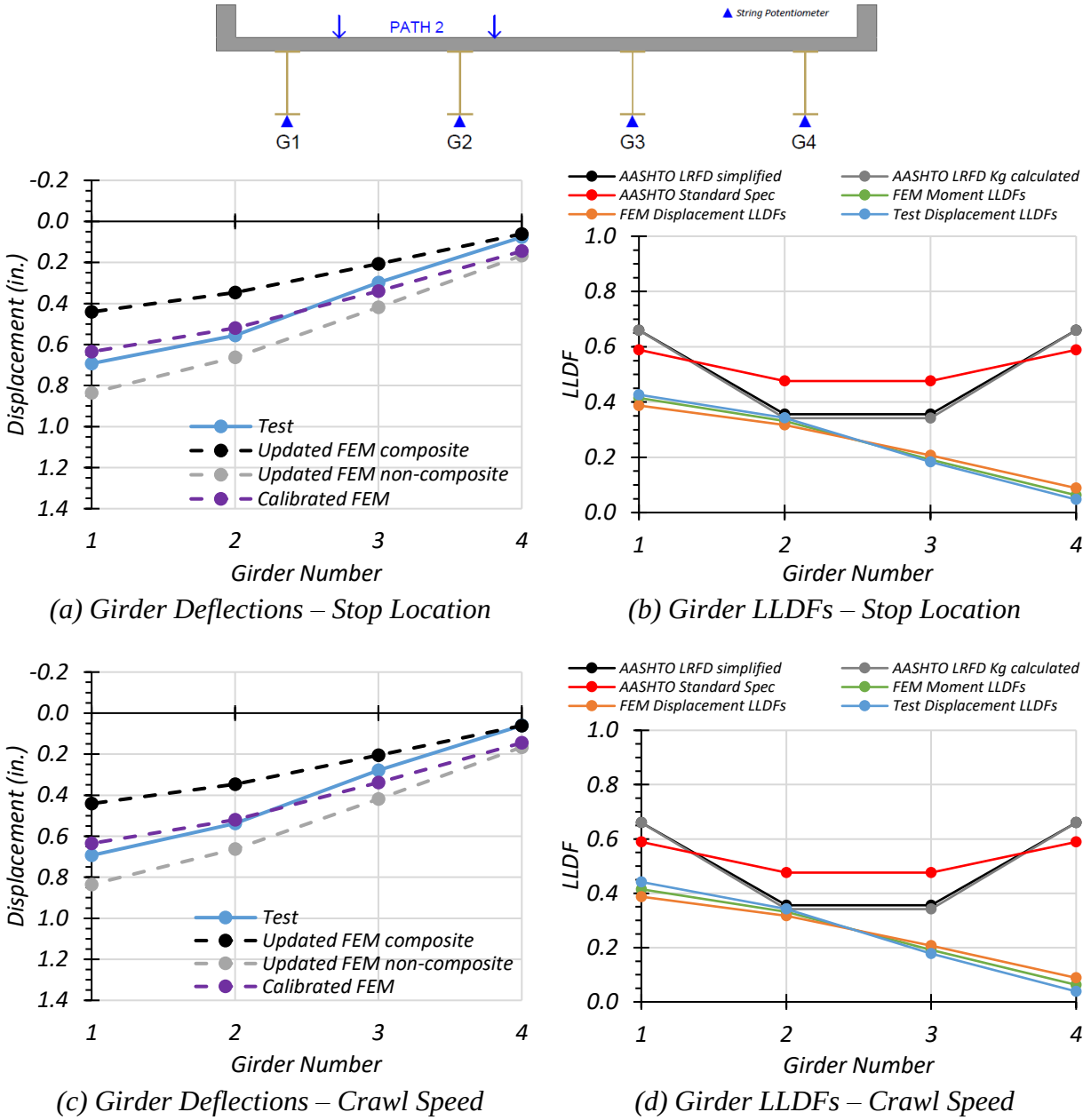

(a) Girder Deflections – Stop Location

(b) Girder LLDFs – Stop Location

(c) Girder Deflections – Crawl Speed

(d) Girder LLDFs – Crawl Speed

Figure 7.99. Static Deflection Results for Path 2—Span 2 Loading

Middle Path Loading. Table 7.54 shows the measured girder deflections during testing for the Middle Path—Span 2 stop location test. The girder displacements determined by the calibrated, updated non-composite, and updated composite FEM models are also shown.

Table 7.54. Experimental and FEM Deflections for Middle Path—Span 2 Loading

Description	G1	G2	G3	G4
Updated FEM Non-Composite Disp. (in.)	0.474	0.573	0.573	0.474
Updated FEM Composite Disp. (in.)	0.231	0.300	0.300	0.231
Calibrated FEM Disp. (in.)	0.371	0.460	0.460	0.371
Stop Location Test Disp. (in.)	0.328	0.457	0.440	0.353
Crawl Speed Test Disp. (in.)	0.313	0.444	0.436	0.355
Note: 1. G = girder, Disp. = Displacement				

Table 7.55 compares the test LLDFs determined using deflection to those obtained by the deflections of the updated non-composite, updated composite, and calibrated FEM models. All three models do a good job of estimating the LLDF.

Table 7.55. FEM Displacement LLDF Comparison with Test for Middle Path—Span 2 Loading

Test and Girder Type	Updated Non-Composite FEM LLDF (g_{NC})	Updated Composite FEM LLDF (g_C)	Calibrated FEM LLDF (g_{cal})	Test (g_{test})	g_{NC}/g_{test}	g_C/g_{test}	g_{cal}/g_{test}
Stop Location Interior	0.274	0.282	0.277	0.289	0.95	0.98	0.96
Stop Location Exterior	0.226	0.218	0.223	0.224	1.01	0.97	1.00
Crawl Speed Interior	0.274	0.282	0.277	0.287	0.95	0.98	0.97
Crawl Speed Exterior	0.226	0.218	0.223	0.229	0.99	0.95	0.97

Figure 7.100(a) and Figure 7.100(c) show the Middle Path—Span 2 stop location and crawl speed deflections compared to non-composite, composite, and calibrated values obtained from FEM analysis. Figure 7.100(b) and Figure 7.100(d) show the Middle Path—Span 2 stop location and crawl speed LLDFs compared to relevant AASHTO values as well as to values obtained from calibrated FEM deflection results and moment results. Table 7.56 shows the test LLDF values, the displacement and moment LLDF values obtained from the calibrated FEM model, and the LLDF

values found using all three AASHTO methods. The test and calibrated model LLDFs are all lower than the prescribed AASHTO LLDF values.

Table 7.56. Experimental, FEM, and AASHTO LLDFs for Middle Path—Span 2 Loading

Description	G1	G2	G3	G4
Stop Location Test Disp. LLDF	0.208	0.289	0.279	0.224
Crawl Speed Test Disp. LLDF	0.202	0.287	0.281	0.229
Calibrated FEM Disp. LLDF	0.223	0.277	0.277	0.223
Calibrated FEM Moment LLDF	0.211	0.289	0.289	0.211
AASHTO Standard LLDF	0.589	0.476	0.476	0.589
AASHTO LRFD LLDF using simplified stiffness	0.660	0.356	0.356	0.660
AASHTO LRFD LLDF using analytical stiffness	0.660	0.342	0.342	0.660

Note:
1. G = girder, Disp. = Displacement

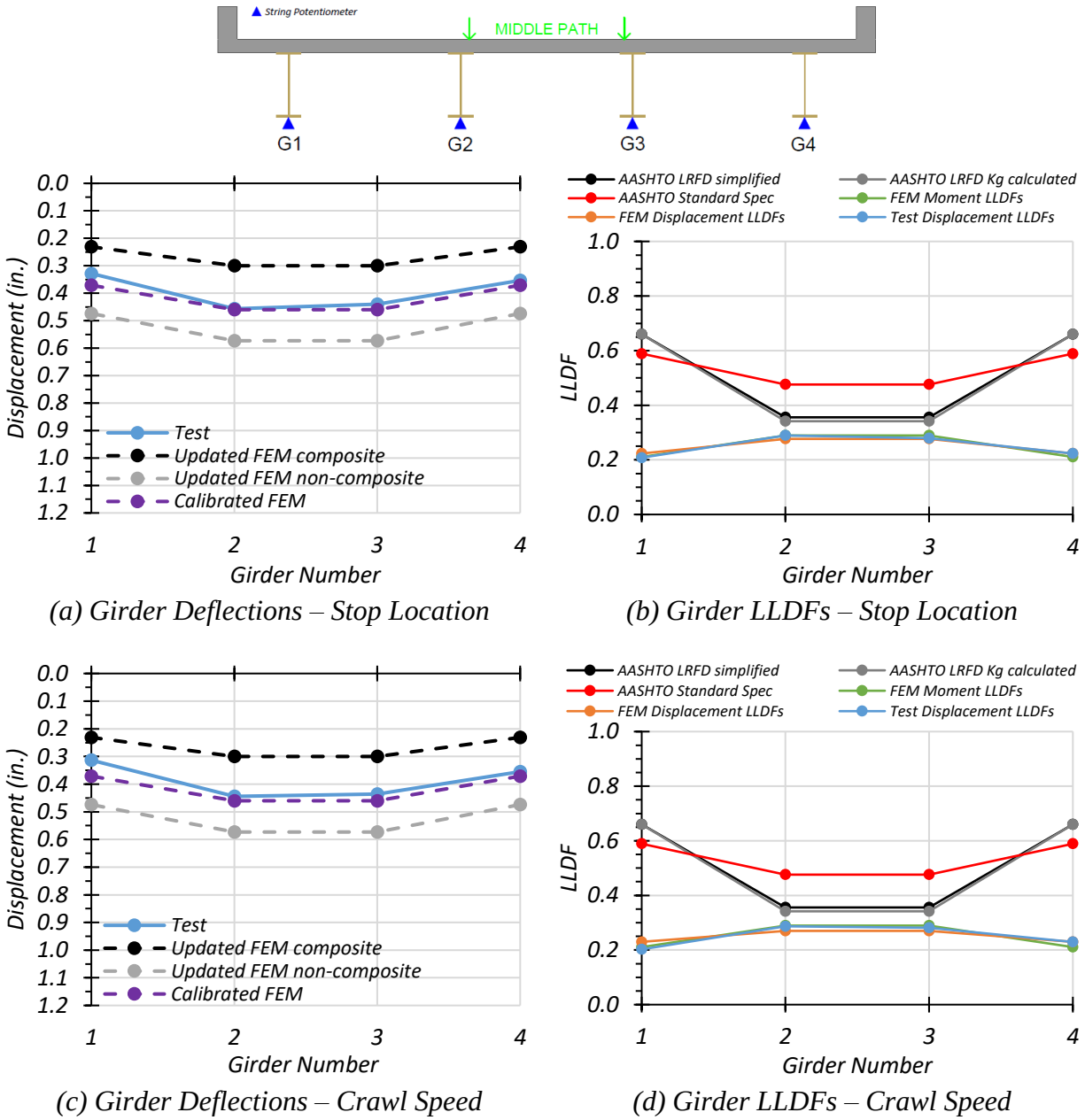

(a) Girder Deflections – Stop Location

(b) Girder LLDFs – Stop Location

(c) Girder Deflections – Crawl Speed

(d) Girder LLDFs – Crawl Speed

Figure 7.100. Static Deflection Results for Middle Path—Span 2 Loading

7.9 SUMMARY AND FINDINGS

7.9.1 Live Load Distribution Factors

7.9.1.1 ***General Findings***

LLDF values computed using FEM deflection results and FEM moment results were compared to ensure that the values were close, thereby allowing the deflection data obtained from testing to be used to calculate experimental LLDFs. The FEM values were deemed very close (within 2.0 percent) for the controlling load case; thus, LLDF values were determined for each load test based on the maximum span deflections.

For the Path 1 load cases, the g_{AASHTO}/g_{Test} ratio ranges from 1.21 to 1.46 when considering the *AASHTO Standard Specifications*, from 1.09 to 1.41 when considering the simplified stiffness *AASHTO LRFD Specifications*, and from 1.04 to 1.41 when considering the analytical stiffness *AASHTO LRFD Specifications* (AASHTO 2002, 2017). The *AASHTO Standard Specifications* method of determining LLDFs for this bridge is significantly conservative for Path 1 loading. The *AASHTO LRFD Specifications* methods of determining LLDFs for this bridge range from slightly conservative to significantly conservative for Path 1 loading.

For the Path 2 load cases, the g_{AASHTO}/g_{Test} ratio ranges from 1.33 to 1.45 when considering the *AASHTO Standard Specifications*, from 1.04 to 1.62 when considering the simplified stiffness *AASHTO LRFD Specifications*, and from 1.00 to 1.62 when considering the analytical stiffness *AASHTO LRFD Specifications* (AASHTO 2002, 2017). The *AASHTO Standard Specifications* method of determining LLDFs for this bridge is significantly conservative for Path 2 loading. The *AASHTO LRFD Specifications* methods of determining LLDFs for this bridge range from very close to significantly conservative for Path 2 loading.

For the Middle Path load cases, the g_{AASHTO}/g_{Test} ratio ranges from 1.64 to 2.71 when considering the *AASHTO Standard Specifications*, from 1.23 to 3.04 when considering the simplified stiffness *AASHTO LRFD Specifications*, and from 1.18 to 3.04 when considering the analytical stiffness *AASHTO LRFD Specifications* (AASHTO 2002, 2017). The *AASHTO Standard Specifications* method of determining LLDFs for this bridge is significantly conservative for Middle Path loading. The *AASHTO LRFD Specifications* methods of determining LLDFs for this bridge range from conservative to significantly conservative for Middle Path loading.

7.9.1.2 ***Consideration of Moment of Inertia Difference Between Girders***

When calculating the LLDFs obtained from the displacements observed during testing, a more accurate method is to consider the difference in moment of inertia between an interior girder and an exterior girder in the case that the moments of inertia are different. Updated LLDF can be developed for each girder by taking the deflection multiplied by the moment of inertia of an individual girder and dividing by the sum of the deflection multiplied by the moment of inertia for all girders. Equation (7.1) shows the equation used to obtain an LLDF through this method:

$$LLDF_i = \frac{\Delta_i I_i}{\sum(\Delta_i I_i)} \tag{7.1}$$

where:

$LLDF_i$ = Live load distribution factor for an individual girder

Δ_i = Deflection of the individual girder (in.)

I_i = Moment of inertia of the individual girder (in^4)

Bridge SC-12 has the same steel section for interior and exterior girders (W30x108), so under fully non-composite action only, the deflection affects the calculation of the LLDFs. However, under partial composite action, which Bridge SC-12 exhibited based on field testing, the interior girders and exterior girders have different moments of inertia due to different effective deck widths. For an interior girder, the effective deck width is 72 in. For an exterior girder, the effective deck width is 56.5 in. and also includes a 10 in. wide by 9 in. tall curb. Based on the field-measured displacements, and by considering fully composite action, Bridge SC-12 LLDFs were recomputed to obtain an upper and lower bound for the LLDFs. The fully composite interior girder was found to have a moment of inertia of 11,300 in^4, and the fully exterior girder was found to have a moment of inertia of 13,250 in^4.

By considering the controlling stop location load case for Girder G4 along Path 1 and in Span 2 and by using the procedure described above, new LLDFs were developed. The controlling interior girder, Girder G3, experienced an 8.3 percent decrease in LLDF—from 0.327 to 0.301. The controlling exterior girder, Girder G4, experienced a 7.6 percent increase in LLDF—from 0.469 to 0.506. Table 7.57 and Figure 7.101 show the LLDFs developed using this method compared to LLDFs determined through the calibrated FEM displacements, the calibrated FEM

moments, the *AASHTO Standard Specifications*, the *AASHTO LRFD Specifications* using the simplified stiffness parameter, and the *AASHTO LRFD Specifications* using the analytical stiffness parameter (AASHTO 2002, 2017).

Table 7.57. Bridge SC-12 LLDF Comparison Considering Difference in Inertia

Selected Girder LLDFs for Various Methods	Interior Girder G3	Exterior Girder G4
Test Displacement Considering Inertia Difference	0.301	0.506
Test Displacement without Considering Inertia Difference	0.327	0.469
Calibrated FEM Displacements	0.325	0.458
Calibrated FEM Moments	0.335	0.467
AASHTO Standard Specifications	0.476	0.589
AASHTO LRFD Specifications – Simplified	0.356	0.660
AASHTO LRFD Specifications – Analytical	0.342	0.660

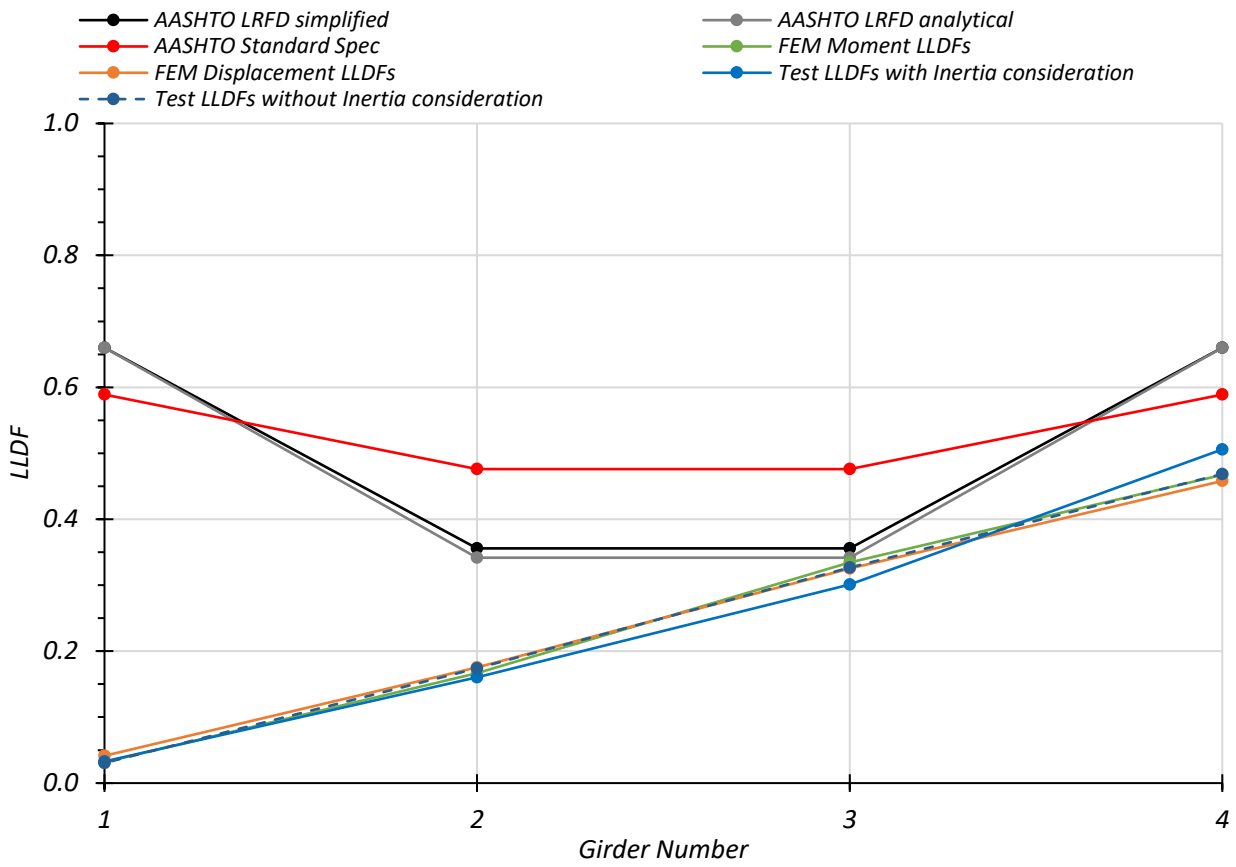

Figure 7.101. Bridge SC-12—Span 2 LLDF Comparison Considering Difference in Inertia

The consideration of the moment of inertia difference between interior and exterior girders does not cause a significant change in calculated LLDFs for Bridge SC-12 because the composite interior and exterior girders do not have a significant difference in the updated moments of inertia. The LLDFs calculated based on displacements alone do a good job of matching the LLDF results from FEM displacements and FEM moments. Both results also remain below the LLDFs given by the *AASHTO Standard Specifications* (AASHTO 2002), which are proposed to be applied for this bridge. Furthermore, under the initial conservative assumption made during the basic load rating analysis that Bridge SC-12 is non-composite, there would be no difference in the moment of inertia between interior and exterior girders. Therefore, the LLDFs would be calculated based only on displacements. Without conducting a field test, the presence of partial composite action cannot be determined. The updated LLDFs were calculated considering the inertia difference based on fully composite action. Therefore, the LLDFs for the partially composite Bridge SC-12 would be

between the two values shown based on the test displacements. For these reasons, the LLDFs were kept as calculated throughout this chapter, and the difference in moment of inertia between interior and exterior girders under composite action was not considered further. However, it is noted that to bound the possible LLDFs when considering the presence of partial or full composite action, one can consider both the fully non-composite case and the fully composite case.

7.9.2 Composite Action

Some data obtained during testing suggest Bridge SC-12 is acting as partially composite. By using the strain gauges attached to the top and bottom flanges of the girders, a strain diagram of an interior and exterior girder was determined for each load test. The updated non-composite FEM model neutral axis is located 14.9 in. from the bottom of the girder. The updated composite FEM model neutral axis is 28.3 in. from the bottom of the girder for an exterior girder and 28.6 in. from the bottom of the girder for an interior girder. The median test neutral axis was determined to be 18.71 in. from the bottom of the girder for an exterior girder and 17.69 in. from the bottom of the girder for an interior girder; these values lie between the model values determined based on non-composite and fully composite behavior.

The bottom flange stresses obtained from testing were also compared to the expected non-composite and composite bottom flange stresses from the updated FEM analysis. It was found that the stresses also varied between the non-composite and fully composite stress values.

The deflection data obtained during the load testing were compared to the estimated girder deflection values from the FEM model analysis and considered both non-composite and fully composite girder behavior. For the Path 1—Span 2 stop location test, the maximum deflection measured in Girder G4 was 0.755 in., which was between the FEM composite deflection of 0.509 in. and the FEM non-composite deflection of 1.121 in. For the Path 2—Span 2 stop location test, the maximum deflection measured in Girder G4 was 0.692 in., which was also between the FEM composite deflection of 0.451 in. and the FEM non-composite deflection of 1.007 in. For the Middle Path—Span 2 stop location test, the maximum deflection measured in Girder G4 was 0.457 in., which was again between the FEM composite deflection of 0.291 in. and the FEM non-composite deflection of 0.671 in.

The measured neutral axes during the critical static load tests for Span 2 was 19.77 in. from the bottom of Girder G3 and 19.81 in. from the bottom of Girder G4. The theoretical non-

composite neutral axis is 14.90 in. from the bottom of the girder, and the theoretical composite neutral axis is 26.11 in. from the bottom of the girder. The neutral axis locations observed during the critical load tests were used in a load rating analysis. Because the TxDOT RF for this bridge is found for an interior girder in positive bending, the interior girder positive moment RFs calculated for Bridge SC-12 during the basic load rating were reanalyzed and compared. Table 7.58 shows the Strength I RFs calculated for Bridge SC-12 using the ASR, LFR, and LRFR methods and considering the partial composite action observed during load tests. It compares these RFs values to those calculated for an interior girder considering positive bending in Task 3 of this project and to the current TxDOT RFs. It is important to note that for the ASR ratings, the dead load stresses are based on the non-composite section. It is also important to note that these results consider all of the same bridge characteristics used in the basic load rating analysis, not any updated parameters from FEM analysis or from load testing.

For the ASR partial composite, positive-moment-region RF, the capacity stress was 18.15 ksi for the inventory level and 24.75 for the operating level, the dead load stress was 5.12 ksi, the superimposed dead load stress was 1.62 ksi, and the live load stress was 16.43 ksi. For the LFR partial composite, positive-moment-region RF, the moment capacity was 1357.0 kip-ft, the dead load moment was 177.0 kip-ft, and the live load moment was 503.0 kip-ft. For the LRFR partial composite, positive-moment-region RF, the moment capacity was 1357.0 kip-ft, the dead load moment was 177.0 kip-ft, and the live load moment was 625.8 kip-ft.

Table 7.58. Comparison of Bridge SC-12 Interior Girder Positive Moment Partial Composite RFs to Non-Composite RFs for Strength I

Method	TxDOT RF		Task 3 RF		Partial Composite RF		Partial Composite RF/ TxDOT RF		Partial Composite RF/ Task 3 RF	
	Inv.	Oper.	Inv.	Oper.	Inv.	Oper.	Inv.	Oper.	Inv.	Oper.
ASR	–	–	0.59	0.89	0.70	1.10	–	–	1.19	1.24
LFR	0.55	0.93	0.55	0.92	**1.03**	**1.72**	1.87	1.85	1.87	1.87
LRFR	–	–	0.60	0.78	1.02	1.33	–	–	1.70	1.71
Note: TxDOT and Task 3 RFs are calculated for a non-composite section										

To determine the ratio of compressive force in the concrete deck for partial composite action to compressive force in the concrete deck for fully composite action, Equation C-I3-4 in the *AISC Steel Construction Manual* (AISC 2013), shown in Equation (7.2), was examined:

$$I_{equiv} = I_s + \sqrt{\frac{\sum Q_n}{C_f}}(I_{tr} - I_s) \tag{7.2}$$

where:

I_{equiv} = Equivalent partial composite moment of inertia = 7271 in^4

I_s = Moment of inertia for the structural steel section = 4460 in^4

I_{tr} = Moment of inertia for the fully composite uncracked transformed section = 10,417 in^4

ΣQ_n = Maximum force transferred across the deck-girder interface (kip)

C_f = Compressive force in concrete slab for fully composite beam (kip)

By solving for the $\frac{\sum Q_n}{C_f}$, the ratio of compressive force in the concrete deck for partial composite action to compressive force in the concrete deck for fully composite action is determined to be 0.22. In determining the nominal moment capacity of the partially composite section, the compressive force in the deck was multiplied by this ratio. This process produced the same neutral axis location observed during field testing. Next, moments of the components of the cross section were summed about the neutral axis to obtain a nominal moment capacity. The components of the cross-section included the bottom flange in tension, the web in tension, the web in compression, the top flange in compression, and the portion of the concrete deck in compression. It is also worth noting that the partial composite moment capacity was equal to the non-composite moment capacity plus 47 percent of the difference between the non-composite and composite moment capacities, which corresponds to the value produced by $\sqrt{\frac{\sum Q_n}{C_f}}$.

7.9.3 Stresses

The maximum bottom flange stresses experienced during static loading were used to perform a stress analysis on the bridge. The maximum bottom flange stress in the positive moment region

for Girder G3 was 4.69 ksi, from Test 1. The maximum bottom flange stress in the positive moment region for Girder G4 was 7.09 ksi, from Test 3. In the updated FEM model, the estimated non-composite dead load bottom flange stresses in the positive moment region are 6.24 ksi for interior Girder G3 and 7.19 ksi for exterior Girder G4.

The maximum bottom flange stress in the negative moment region for Girder G3 was -2.06 ksi, from Test 5. The maximum bottom flange stress in the negative moment region for Girder G4 was -3.42 ksi, also from Test 5. Using the calibrated FEM model, the estimated non-composite dead load bottom flange stresses in the negative moment region were found to be -9.37 ksi for Girder G3 and -10.29 ksi for Girder G4.

An ASR load rating can be performed for Bridge SC-12 by using both this information and the yield strength of 33 ksi taken by TxDOT in its load rating calculations (TxDOT 2018a). Equation (7.3) shows the ASR RF equation, and the capacity, dead load effect, and live load effect are in terms of stresses:

$$RF = \frac{C - A_1 D}{A_2 L(1 + I)} \tag{7.3}$$

where:

RF	=	Rating Factor for the live load carrying capacity
C	=	Capacity of the member = $0.55F_y$ for inventory, $0.75F_y$ for operating
D	=	Dead load effect on the member
L	=	Live load effect on the member
I	=	Impact factor to be used with the live load effect = 0.25
A_1	=	Factor for dead loads = 1.0
A_2	=	Factor for live load = 1.0

Table 7.59 shows the calculated RFs for Bridge SC-12 using the measured test information and the ASR method. It is important to note that these RFs are for a single test vehicle that was almost exactly at the posted limit, not for the design HS-20 truck. It is also important to note that these data only consider one truck on the bridge, which is marked for two lanes.

Table 7.59. Bridge SC-12 Calculated ASR One-Lane Test Vehicle RFs Using Test Results

Girder	Positive Moment Region			Negative Moment Region		
	Maximum Measured Live Load Stress from Static Load Tests (ksi)	Inventory RF	Operating RF	Maximum Measured Live Load Stress from Static Load Tests (ksi)	Inventory RF	Operating RF
Interior G3	4.69	2.03	3.16	−2.06	3.41	5.97
Exterior G4	7.09	1.24	1.98	−3.42	1.84	3.38

7.9.4 Model Calibration and Update

By using the calibrated FEM model of Bridge SC-12, analysis was performed for the HS-20 design vehicle. This vehicle is used in the ASR and LFR rating methods, which TxDOT uses to perform load ratings of bridges not designed using LRFR (TxDOT 2018b). The maximum live load bottom flange stress in the positive moment region for interior Girder G3 was 10.31 ksi. The maximum live load bottom flange stress in the positive moment region for exterior Girder G4 was 10.92 ksi. Using the calibrated FEM model, the estimated non-composite dead load bottom flange stresses in the positive moment region were found to be 6.24 ksi for Girder G3 and 7.19 ksi for Girder G4.

The maximum live load bottom flange stress in the negative moment region for Girder G3 was -7.66 ksi. The maximum live load bottom flange stress in the negative moment region for Girder G4 was -8.65 ksi. Using the calibrated FEM model, the estimated non-composite dead load bottom flange stresses in the negative moment region were found to be -9.37 ksi for Girder G3 and -10.29 ksi for Girder G4.

An ASR load rating using these results was performed for Bridge SC-12 for the HS-20 live load. Table 7.60 shows the ASR HS-20 RFs for Girder G4 and Girder G3 using the analysis results from the calibrated FEM model. A load rating using the calibrated FEM model for the HS-20 vehicle would allow the posting of Bridge SC-12 to be removed, per TxDOT's on-system load rating flowchart (TxDOT 2018b).

Table 7.60. Bridge SC12 Calculated ASR HS-20 RFs Using Calibrated FEM Model Results

Girder	Positive Moment Region		Negative Moment Region	
	Inventory RF	Operating RF	Inventory RF	Operating RF
G3	0.92	1.44	0.92	1.61
G4	0.80	1.29	0.73	1.34

LFR Strength I RFs can also be developed using the calibrated FEM model of Bridge SC-12. The positive moment capacity found using a partially composite section with the same neutral axis locations, as observed during testing, is 1357.0 kip-ft for Girder G3 and 1357.0 kip-ft for Girder G4. The capacity was calculated using LFD procedures provided in the *AASHTO Standard Specifications* (AASHTO 2002). By using the updated FEM model, researchers found the non-composite positive dead load moments to be 158.3 kip-ft on Girder G3 and 171.2 kip-ft on Girder G4. Using the calibrated FEM model, the controlling positive live load moments were found to be 290.3 kip-ft on Girder G3 and 299.4 kip-ft on Girder G4 for two-lane HS-20 load paths.

The negative moment capacity found using a non-composite section is -1081.0 kip-ft for Girder G3 and -1081.0 kip-ft for Girder G4. Using the calibrated FEM model, the non-composite negative dead load moments were found to be -306.9 kip-ft on Girder G3 and -337.0 kip-ft on Girder G4. Using the calibrated FEM model, the controlling negative live load moments were found to be -250.9 kip-ft on Girder G3 and -283.3 kip-ft on Girder G4 for two-lane HS-20 load paths.

An LFR load rating analysis using these results was performed for Bridge SC-12 for the HS-20 live load. Equation (7.4) shows the LFR RF equation with the variables defined as well. The capacity, dead load effect, and live load effect are moment values:

$$RF = \frac{C - A_1 D}{A_2 L(1 + I)} \tag{7.4}$$

where:

RF = Rating Factor for the live load carrying capacity

C = Capacity of the member

D = Dead load effect on the member

L = Live load effect on the member

I = Impact factor to be used with the live load effect = 0.25

A_1 = Factor for dead loads = 1.3

A_2 = Factor for live load = 2.17 for inventory, 1.3 for operating.

Table 7.61 shows the LFR Strength I HS-20 two-lane RFs for Girder G3 and Girder G4 using the analysis results from the calibrated FEM model. These RFs for Bridge SC-12 allow its posting to be removed based on the TxDOT on-system load posting flowchart (TxDOT 2018b), shown in Figure 4.2 in the Volume 1 report (Hueste et al. 2019a).

Table 7.61. Bridge SC-12 Calculated LFR Strength I HS-20 RFs Using Calibrated FEM Model Results

Girder	Positive Moment Region				Negative Moment Region			
	Capacity (kip-ft)	Live Load Demand (kip-ft)	Inventory RF	Operating RF	Capacity (kip-ft)	Live Load Demand (kip-ft)	Inventory RF	Operating RF
Interior G3	1357.0	290.3	1.46	2.44	−1081.0	−250.9	1.00	1.67
Exterior G4	1357.0	299.4	1.40	2.33	−1081.0	−283.3	0.84	1.40

8 EXPERIMENTAL TESTING OF BRIDGE CM-5

8.1 INTRODUCTION

In a previous task, basic load rating evaluation of 14 simple-span concrete multi-girder (CM) bridges was conducted, and an FEM model of a typical load-posted concrete multi-girder bridge was developed using the commercial software package CSiBridge. The selected simple-span concrete multi-girder bridge, CM-5, was load tested in the field. The purpose of the load test was to capture the actual in situ behavior of the bridge, such as the presence of partial fixity at the ends and the measured live load distribution between girders. The results from the field tests were used to calculate the experimental LLDFs for the individual bridge girders. The FEM model was also updated to include field measurements, nondestructive measures of concrete strength, and any observed end fixity in order to more accurately model the bridge.

Several nondestructive evaluation methods were used to identify the concrete compressive strength and the layout of the reinforcing bars. The results of NDE tests were used to update the FEM model of the bridge to represent the actual concrete compressive strength and reinforcement layout if it is different than the reinforcement details provided in the structural drawings. Because of the absence of structural drawings for this specific bridge, the measured bridge geometry and reinforcement details were compared to the standard drawing for this bridge type provided on the TxDOT website titled “CG 30'-4" Spans” (TxDOT 2005).

In addition to conventional measuring devices, such as string potentiometers, strain gauges, and accelerometers, two cameras mounted on a tripod was also used to record the bridge response during each load test. An image analysis algorithm was used to determine the displacements from the unloaded bridge image and loaded bridge image. A thorough investigation of the field-test results and the results from the updated and calibrated FEM model is then used to determine a refined load rating for the bridge.

8.2 GENERAL DESCRIPTION OF BRIDGE CM-5

Bridge CM-5 carries CR 119 and traverses Small Creek near Caldwell, Texas, approximately 2.5 mi east of State Highway 36. It has a deck condition rating of 7 (Good), a superstructure condition rating of 7 (Good), and a substructure condition rating of 5 (Fair). The flexural resistance of the

concrete pan girders controls the rating of the bridge, which has an inventory rating of 26 US tons and an operating rating of 36 US tons. The bridge is posted for a 24,000 lbs tandem axle. Figure 4.1 shows photographs of an elevation view and an underside view of Bridge CM-5. Figure 4.2 shows a longitudinal section detail obtained from TxDOT inspection reports (TxDOT 2018a).

(a) Elevation view

(b) Underside view

Figure 8.1. Photographs of Bridge CM-5 (TxDOT 2018a)

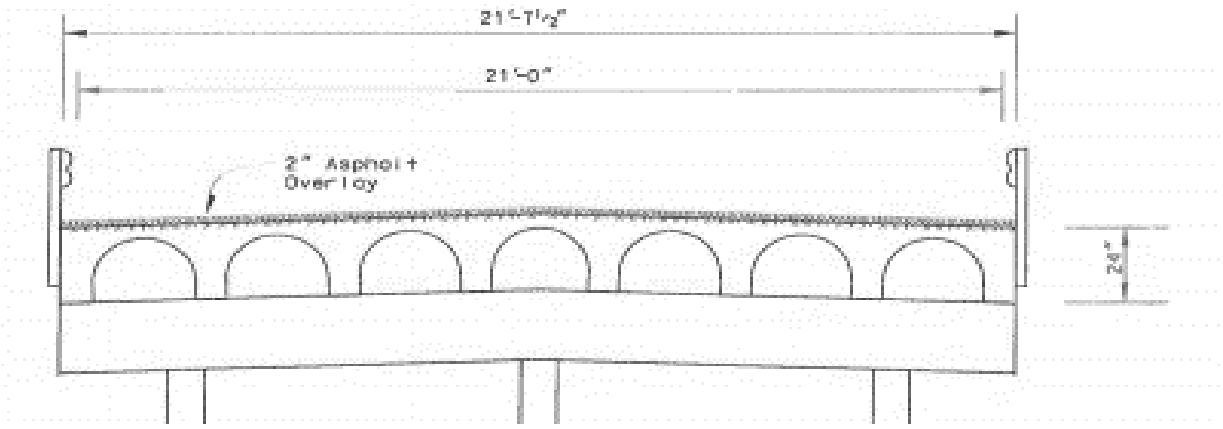

Figure 8.2. Longitudinal Section of Bridge CM-5 (TxDOT 2018a)

8.3 IN-SITU MEASUREMENTS AND OBSERVATIONS AND NDE RESULTS

8.3.1 In-Situ Measurements and Observations

The as-built geometric details were measured to confirm the values given in the standard structural drawings. The bridge measured 30 ft in length, and the total roadway width measured 21 ft 7 in. wide. The abutments were approximately 28 ft 4 in. apart. The bridge has eight pan girders, and the external girders were 24 in. deep. The exterior girders were 7 in. wide at the bottom of the web, while the interior girders were 6.875 in. wide at the bottom of the web.

8.3.2 NDE Results

The in-situ concrete compressive strength of Bridge CM-5 was determined onsite using a rebound number test and a UPV test. The UPV test uses the speed and time needed for an ultrasonic pulse to pass through a known concrete thickness to determine the compressive strength, which was conducted in accordance with ASTM C597 standard test method for pulse velocity through concrete (ASTM C597 2016).

The compressive strength of concrete was determined through a rebound number test using two different instruments, an Original Schmidt Hammer and a Silver Schmidt Hammer, and was conducted in accordance with ASTM C805 standard test method for rebound number of hardened concrete (ASTM C805 2018). The surface over which these tests were conducted was first ground using an angle grinder with a masonry grinding wheel. The surface was further smoothened with

the help of a grinding stone. An indicator solution of phenolphthalein in ethanol was applied to the clean surface to check for carbonation of concrete. Concrete carbonation can affect the result obtained from these tests. If the indicator solution did not turn purple, the surface was further ground to reach the non-carbonated layer. Ten rebound number readings were obtained for both Schmidt Hammers by pushing against the surface. The maximum and minimum rebound numbers were ignored, and the average of the remaining eight rebound numbers was calculated. The average rebound number for the Original Schmidt Hammer was 45.4. This number corresponds to a concrete compressive strength of approximately 7 ksi using the conversion curve in Figure 6.4. In this test, the hammer was pushed vertically downward.

The Silver Schmidt Hammer uses the same principle and directly gives the compressive strength of concrete when within the range of the instrument. This test was carried out three times and yielded different compressive strength values of 8.1 ksi, 7.0 ksi, and 7.8 ksi. The average of these values is approximately 7.6 ksi. Figure 6.5 provides the conversion chart used for Silver Schmidt Hammer rebound values.

A UPV test was also used to determine the compressive strength of concrete on site. In this test, an ultrasonic pulse was passed through the concrete slab between the pan girders, and the time taken for it to travel through the thickness was measured. The concrete depth measured 7.25 in. The test was repeated three times, and the travel times for the pulse were 48.8 μs, 44.4 μs, and 46.8 μs, with an average travel time of 46.6 μs. This figure corresponds to an average wave velocity of 3952 m/s. By using the equation provided by Trtnik et al. (2009), the compressive strength of concrete was calculated from the average wave velocity to be 1.63 ksi. This measured compressive strength of concrete is smaller than the other NDE measurements, which may be due to interference from the reinforcement during the measurement. Huang et al. (2011) remarked that UPV alone does not provide an accurate measure of the compressive strength of concrete and suggest using a combination of the wave speed and rebound number. The concrete compressive strength was calculated to be 6.6 ksi using the average wave velocity and the rebound number obtained from the Original Schmidt Hammer test using equations provided in Huang et al. (2011).

Table 8.1 summarizes the concrete compressive strength results obtained with the NDE tests.

Table 8.1. Concrete Compressive Strengths from NDE Tests

Test	Concrete Compressive Strength (ksi)
Schmidt Hammer Test	7.0
Silver Schmidt Hammer Test	7.6
UPV*	1.63
SonReb*	6.6
*The measured wave velocity was inaccurate due to possible interference of reinforcement	

The SonReb test provides the smallest measured value for the compressive strength of concrete (6.6 ksi). However, this measurement uses the average wave velocity measured by the UPV test, which was found to be inaccurate due to possible interference of reinforcement. Thus, the smallest compressive strength measured using the Original Schmidt Hammer Test and Silver Schmidt Hammer Test was used (7 ksi), and the corresponding estimated MOE was adopted for the concrete in the updated FEM models.

Information regarding the steel reinforcement, such as spacing and cover, was also determined on site using GPR. The spacing of the transverse slab reinforcement was irregular, ranging from 9 in. and 13 in., with an average spacing of approximately 10.8 in. A single layer of longitudinal reinforcement was located at 3 in. and another layer at 21 in. from the bottom of the girder. This information could not be verified due to the absence of structural drawings for Bridge CM-5.

8.4 DATA ACQUISITION AND INSTRUMENTATION FOR BRIDGE CM-5

The bridge instrumentation plan was developed to capture the maximum response of the bridge when subjected to the different vehicle loading scenarios. The instruments used to measure the response of the bridge included strain gauges, string potentiometers, and accelerometers that were connected to the DAQ system to digitally record the measured data.

8.4.1 Instrumentation Plan for Bridge CM-5

The instrumentation plan for Bridge CM-5, along with the cross-sectional views, is shown in Figure 8.3. The labeling system used in the instrumentation plan is explained in Figure 6.7. The instrumentation labels for the DAQ system are tabulated in Table 8.2.

The measured bridge response is used to identify the actual bridge behavior and live load distribution and any potential areas of opportunity to increase or remove the load posting. Several goals were identified in determining the instrumentation types and locations, as follows:

- The data collected from the strain gauges are used to determine the neutral axis position of the girders and any unintended partial fixity of the girders at the supports.
- The midspan deflection data collected by the string potentiometers are used to infer experimental moment LLDFs to compare with the estimated values from the FEM model of Bridge CM-5 and the AASHTO LLDFs.
- The accelerometers collect vibration data used to compute the dynamic properties of the bridge.

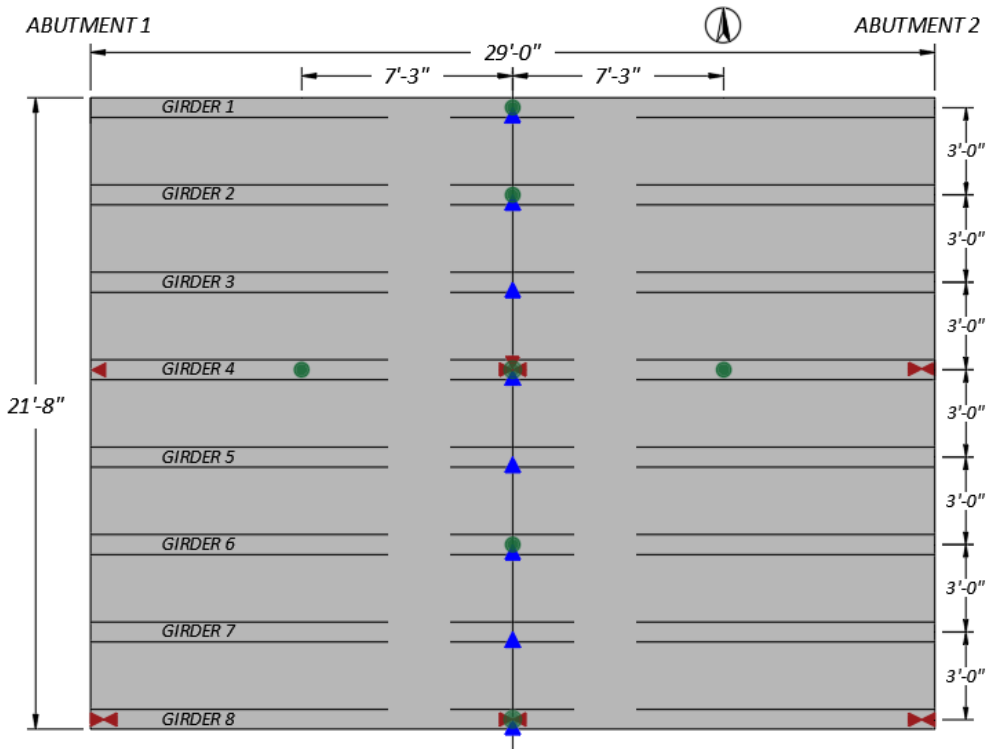

(a) Plan View

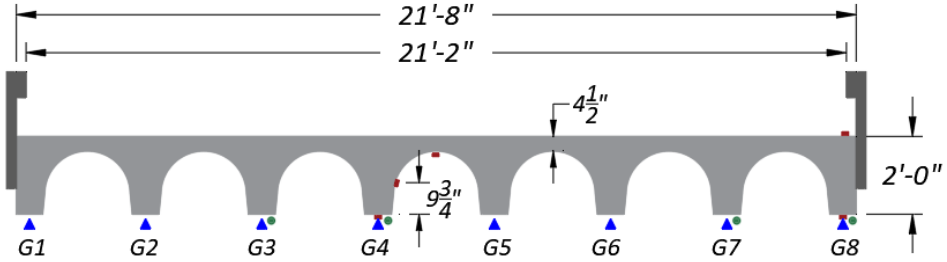

(b) Midspan Section

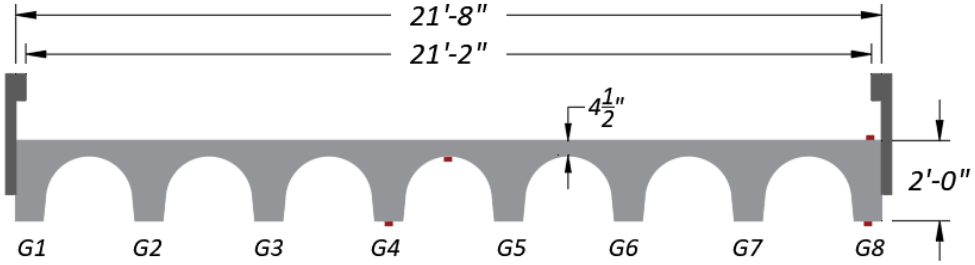

(c) End Section

Figure 8.3. Instrumentation Plan for Bridge CM-5

Table 8.2. Instrumentation Labels for Bridge CM-5

DAQ Box	Channel	Label	Type	DAQ Box	Channel	Label	Type
Strain Book	CH1	SG-8WT	PL-60	WBK 16-3	CH25	SP-2M	SM1-2
	CH2	SG-8WB	PL-60		CH26	SP-1M	SM1-2
	CH3	SG-8MT	PL-60		CH27	–	–
	CH4	SG-8MB	PL-60		CH28	–	–
	CH5	SG-8ET	PL-60		CH29	–	–
	CH6	SG-8EB	PL-60		CH30	–	–
	CH7	SG-4Mm	PL-60		CH31	–	–
	CH8	SG-4WB	PL-60		CH32	–	–
WBK 16-1	CH9	SG-4MT	PL-60	WBK 18	CH57	A-8M	4507 IEPE
	CH10	SG-4MB	PL-60		CH58	A-6M	4507 IEPE
	CH11	SG-4ET	PL-60		CH59	A-4M	4507 IEPE
	CH12	SG-4EB	PL-60		CH60	A-2M	4507 IEPE
	CH13	–	–		CH61	A-4W	4507 IEPE
	CH14	–	–		CH62	A-4E	4507 IEPE
	CH15	–	–		CH63	A-1M	4507 IEPE
	CH16	–	–		CH64	-	
WBK 16-2	CH17	–	–				
	CH18	–	–				
	CH19	SP-8M	SM1-2				
	CH20	SP-7M	SM1-2				
	CH21	SP-6M	SM1-2				
	CH22	SP-5M	SM1-2				
	CH23	SP-4M	SM1-2				
	CH24	SP-3M	SM1-2				

Notes:
1. Refer to Figure 6.7 for explanation of the labeling system used.
2. “m” refers to the location at the mid-height of the pan girder

8.4.2 Data Acquisition System and Instrument Details

A total of 24 strain gauges (using half-bridge circuits at 12 measurement locations), eight string potentiometers, and seven accelerometers were installed on Bridge CM-5. Twenty-seven channels in the DAQ system were used. The strain gauges and string potentiometers were connected via cables to the main box (Measurement Computing StrainBook) and WBK16 extension module boxes. The accelerometer data were collected by the additional WBK18 extension module box. The DAQ system is further described in Section 6.4.2.

8.4.2.1 ***Strain Gauges***

A pair of strain gauges were installed at 12 measurement locations on the bridge to capture the strain profile at the midspan and at the ends of the selected interior girder and exterior girder. The strain gauge type used in Bridge CM-5 was Tokyo Measuring Instruments Lab PL-60-11-3LJCT strain gauge. The main gauge was installed in the longitudinal direction, while the temperature compensation gauge was installed transverse to the main gauge. Figure 8.4 shows a close-up of the installation of the concrete strain gauges. Strain gauges were installed along the bottom of the girder at six different locations on two girders. Gauges were also installed on top of the slab at three locations along an exterior girder. Gauges were installed at the midspan and at an average of 6 in. from the bearing centerline at each abutment for both an exterior and an interior girder. The strains obtained from these gauges were used to determine the location of the neutral axis of the girder sections and identify the presence of partial end fixity at the supports.

Figure 8.4. Close-Up of Strain Gauge Installation

*8.4.2.2 **String Potentiometers***

Eight string potentiometers were installed at the midspan of each girder to record the midspan deflections during the vehicular load tests. Celesco SM1-2 string potentiometers having a 2.5 in. stroke were used at all eight locations.

*8.4.2.3 **Accelerometers***

A total of seven Brüel & Kjær IEPE accelerometers were installed—five accelerometers at the midspan of every other girder and two accelerometers at quarter spans along an interior girder—to record the dynamic vibrations of the bridge during the dynamic load tests. The recorded vibrations were used to obtain the frequencies and the mode shapes of the bridge. The piezoelectric accelerometers are light, compact, and sensitive; they have a resonance frequency of 18 kHz, which is much higher than the bridge's natural frequency.

8.5 LOAD TESTING PROCEDURE FOR BRIDGE CM-5

A comprehensive test program was conducted to evaluate the performance and behavior of Bridge CM-5. The test program consisted of two parts: (1) static load tests, which consisted of stop location tests and crawl speed tests, and (2) dynamic load tests. The nondestructive vehicular load testing of Bridge CM-5 was conducted on April 18, 2019.

8.5.1 Test Vehicle

The vehicle used for the load testing was a Sterling LT 9500 dump truck provided by the TxDOT Caldwell Office. The dump truck was loaded with base material to match the rear tandem axle weight to the posted load limit (posted at 24,000 lbs tandem axle). The truck axle configuration and its empty and loaded weights are shown in Figure 8.5.

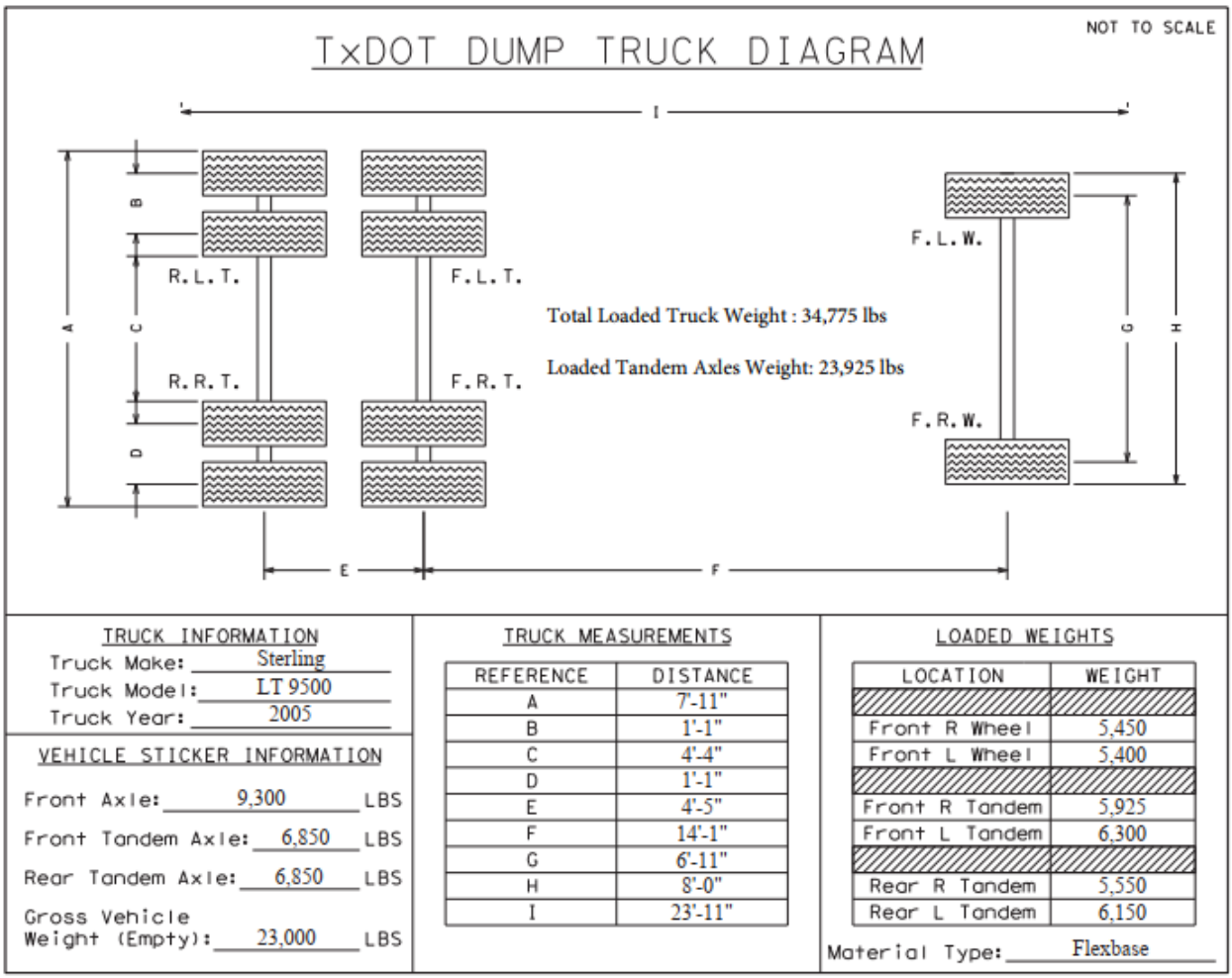

Figure 8.5. Wheel Weights and Spacing of the Loaded Dump Truck Used

8.5.2 Vehicle Positioning

Three transverse paths were defined across the bridge to create critical transverse loading positions for exterior and interior girders. The minimum allowable clearances from the barrier and centerline of the bridge, as outlined in *AASHTO Standard Specifications* (AASHTO 2002) and *AASHTO LRFD Specifications* (AASHTO 2017), were adhered to when defining the paths. Figure 8.6 shows a schematic of the loading paths across the transverse section of Bridge CM-5. Path 1 corresponds to the location where the centerline of the adjacent rear tires of the dump truck was located 2 ft from the face of the bridge guardrail. Path 2 is defined along the second lane, where the centerline of the adjacent rear tires is located 2 ft from the centerline of the bridge. A third path was defined

along the centerline of the bridge, called Middle Path, where the dump truck ran along the center of the bridge.

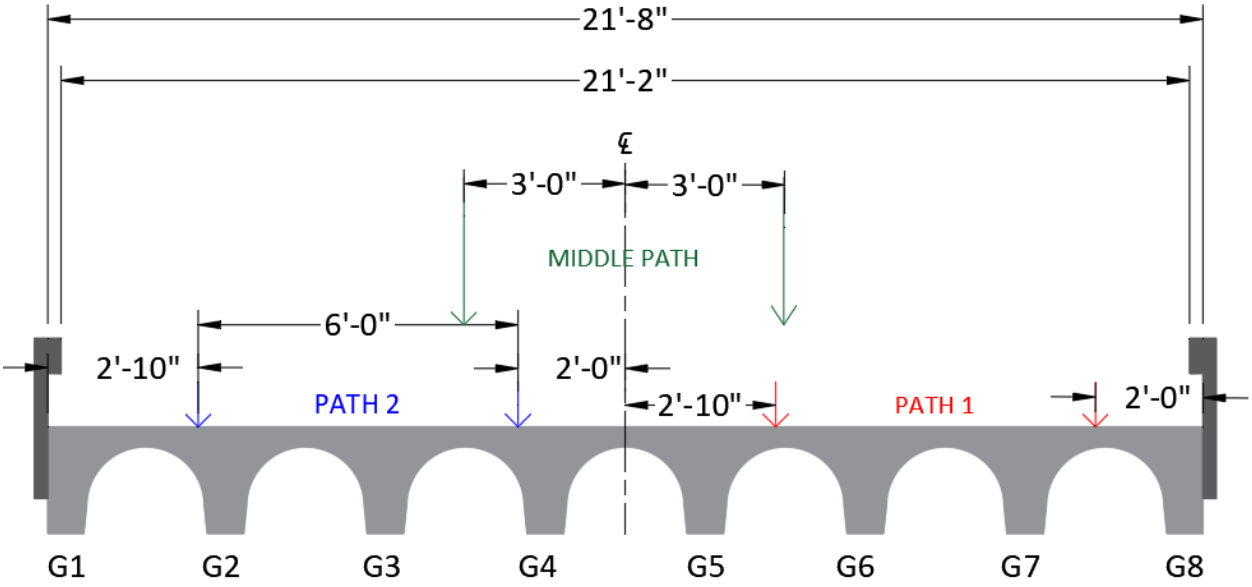

Figure 8.6. Test Paths for Bridge CM-5

8.5.3 Test Protocol

Bridge CM-5 was subjected to static, crawl speed, and dynamic tests. Impact tests were also conducted to capture the dynamic properties of the bridge. Table 8.3 lists the test protocol carried out for proof testing of Bridge CM-5. In the following sections, details regarding each test are outlined.

Table 8.3. Test Protocol for Bridge CM-5

Test Number	Load Position	Test Type
1	Path 1	Static—Stop Location
2	Path 1	Static—Crawl Speed
3	Path 1	Dynamic (31 mph)
4	Path 1	Dynamic (41 mph)
5	Path 2	Static—Stop Location
6	Path 2	Static—Crawl Speed
7	Path 2	Dynamic (30 mph)
8	Path 2	Dynamic (40 mph)
9	Middle Path	Static—Stop Location
10	Middle Path	Static—Crawl Speed
11	Middle Path	Dynamic (29 mph)
12	Middle Path	Dynamic (40 mph)
13	North	Sledgehammer
14	Middle Path	Sledgehammer
15	South	Sledgehammer

*8.5.3.1 **Static Tests***

The static load tests conducted on Bridge CM-5 were of two types: (1) a stop location test, and (2) a crawl speed test. For each stop location test along Path 1, Path 2, and the Middle Path, reference data were recorded prior to the bridge being loaded. The truck was positioned on the bridge such that the maximum bending moment would be obtained in the girder closest to the wheel line. This effect was achieved when the two rear tandem axles of the truck were located equidistant from the centerline of the bridge. Because of the short span of Bridge CM-5, the front axle of the truck was off the bridge for each static test. Once the truck was positioned and the engine was turned off, data for the loaded bridge were recorded.

Reference files were recorded for each crawl speed test along the same paths prior to the truck moving over the bridge. The data were recorded while the truck passed over the entire span of the bridge at an idle speed of 2–3 mph.

*8.5.3.2 **Dynamic Tests***

Prior to each dynamic test, reference files for the unloaded bridge were recorded. The truck was accelerated up a predetermined speed and then passed over the entire span of the bridge while

maintaining the speed. The corresponding data were recorded. The dynamic tests were carried out at two different speeds. The first test for each path was conducted at a speed of 30 mph, and the second test was carried out at a speed of 40 mph. The speed limit for the road on which the bridge was located was noted to be 45 mph.

8.5.3.3 ***Impact Tests***

To obtain information related to the dynamic properties of Bridge CM-5, a sledge hammer was used to strike the top of the bridge deck at three different transverse positions at the midspan to excite different modes of the bridge. The recorded vibration data were used to determine the dynamic properties of the bridge. The tests were carried out at three midspan locations (north side of the bridge, transverse center of the bridge, and south side of the bridge).

8.5.4 Test Operations

The testing schedule for Bridge CM-5 spanned from April 16, 2019, to April 18, 2019, and included all instrumentation installation, load testing, and instrumentation removal.

The clearance height to the underside of the bridge was approximately 8 ft. Thus, there was no need for scaffolding. All instrumentation was installed on the underside of the bridge during the first two days with the help of stepladders. The installation locations were marked as per the instrumentation plan. An angle grinder with a masonry grinding wheel was used to grind an approximately 4 in. by 4 in. area at locations where the strain gauges were to be installed. The surface was made smooth with the help of 150- and 220-grit sandpaper and then cleaned with acetone. The surface was repeatedly cleaned with acetone until a clean tip was no longer discolored by the scrubbing. Liberally applying acetone brings the surface pH back to an optimum alkalinity of 7.0 to 7.5 pH, ideal for bonding of the glue. Any microscopic gaps or cracks on the concrete surface were filled with the application of an epoxy. Once the epoxy dried, the surface was sandpapered and cleaned with acetone, as previously described. The strain gauges were installed onto the surface with the help of suitable adhesive after the surface dried.

For the string potentiometer installation, eight wooden posts were hammered into the stream bed, and the string potentiometers were screwed onto the posts. Metal hooks were installed on the bottom of each pan girder at the midspan, and fishing wires were attached from the hooks

to the string potentiometers. Accelerometers were also attached to the metal plates glued onto the pan girders. Figure 8.7 shows the installed instrumentation for Bridge CM-5.

The nondestructive load tests were conducted on the April 18, 2019. The designated paths were marked on the bridge with washable spray paint. The DAQ system was set up, and the cables from all instrumentation were attached to the DAQ boxes. The dump truck was loaded to approximately the posted load limit at the TxDOT Caldwell Maintenance Office (Figure 8.8 (a)). The 15 tests listed in the test protocol were carried out and the corresponding data recorded. Figure 8.8(b) shows the set-up for Test 5. After the completion of all tests, all the instruments were removed.

(a) Installed Strain Gauges

(b) Installed Accelerometer

(c) Installed String Potentiometers

Figure 8.7. Installed Instrumentation for Bridge CM-5

(a) Dump Truck Weighing Operation

(b) Static Test along Path 2

Figure 8.8. Testing of Bridge CM-5

8.6 TEST RESULTS FOR BRIDGE CM-5

The data recorded during the diagnostic tests were processed, analyzed, and filtered for noise, if required. Strain gauge data were used to determine the strain profile and stresses within the section. String potentiometers recorded the deflections across the bridge, from which the LLDF for each girder was calculated. The dynamic properties of the bridge, such as natural frequencies and mode shapes, were obtained from the data recorded by the accelerometers. An image analysis algorithm was used to determine the deflections from the videos of each test. These results are provided in the following sections.

8.6.1 Static Load Tests on Bridge CM-5

The stop location test and crawl speed test were the two static tests conducted on Bridge CM-5. During the stop location test, the truck was positioned on the bridge such that the maximum bending moment would be obtained in the girder closest to the wheel line. During the crawl speed test, the truck passed over the entire span of the bridge at a crawl speed of approximately 2–3 mph.

*8.6.1.1 **Strain Measurements***

The strain gauge data for each test were compiled. For the stop location test, the maximum strain occurring at each strain gauge location was obtained. For the crawl speed test, the maximum bottom strain in the girder closest to the location of the truck and the corresponding time at which it occurred were first obtained. All other strain values were extracted for that specific time. It should be noted that the tensile strains are taken to be positive, and the compressive strains are negative. The neutral axis location for each girder was determined from the strain profile at the midspan.

Note that the strain values obtained from the bottom strain gauge attached at the midspan of Girder G4 are very high and seem to indicate an issue with the gauge. These values have been shown in the following graphs with a green dot but were not used for calculating the neutral axis depth. By using the assumption that plane sections remain plane, a linear trend was adopted between the top strain (below the slab) and mid-height strain at Girder G4, and this line was extended to determine the neutral axis depth at the midspan of Girder G4 (shown as a dashed green line in the following graphs).

Interior Girder G4—Path 1 Loading. Strain profiles corresponding to the top and bottom strains for interior Girder G4 under static tests along Path 1 are provided in Figure 8.9.

The strain profiles at the west and east ends of Girder G4 are shown in Figure 8.9(a) for the stop location test and Figure 8.9(c) for the crawl speed test. It can be seen that the bottom strain at both the west and east ends of Girder G4 are compressive for the stop location test and crawl speed test, indicating some degree of end fixity is present. The bottom strains obtained from the stop location test are slightly less than those obtained from the crawl speed test, which may be due to the truck stop location not being exactly at the moment critical position.

The strain profiles at the midspan of Girder G4 are shown in Figure 8.9(b) for the stop location test and Figure 8.9(d) for the crawl speed test. The neutral axis depth at the midspan was found to be 10.40 in. from the bottom of Girder G4 using the strain profile obtained from the stop location test and 10.65 in. from the bottom of Girder G4 using the strain profile obtained from the crawl speed test. The neutral axis depth calculated using the strain profile obtained from the crawl speed test is slightly higher than the one obtained from the stop location test. This result could also be due to the stop location test being slightly different from the moment critical position for absolute maximum moment.

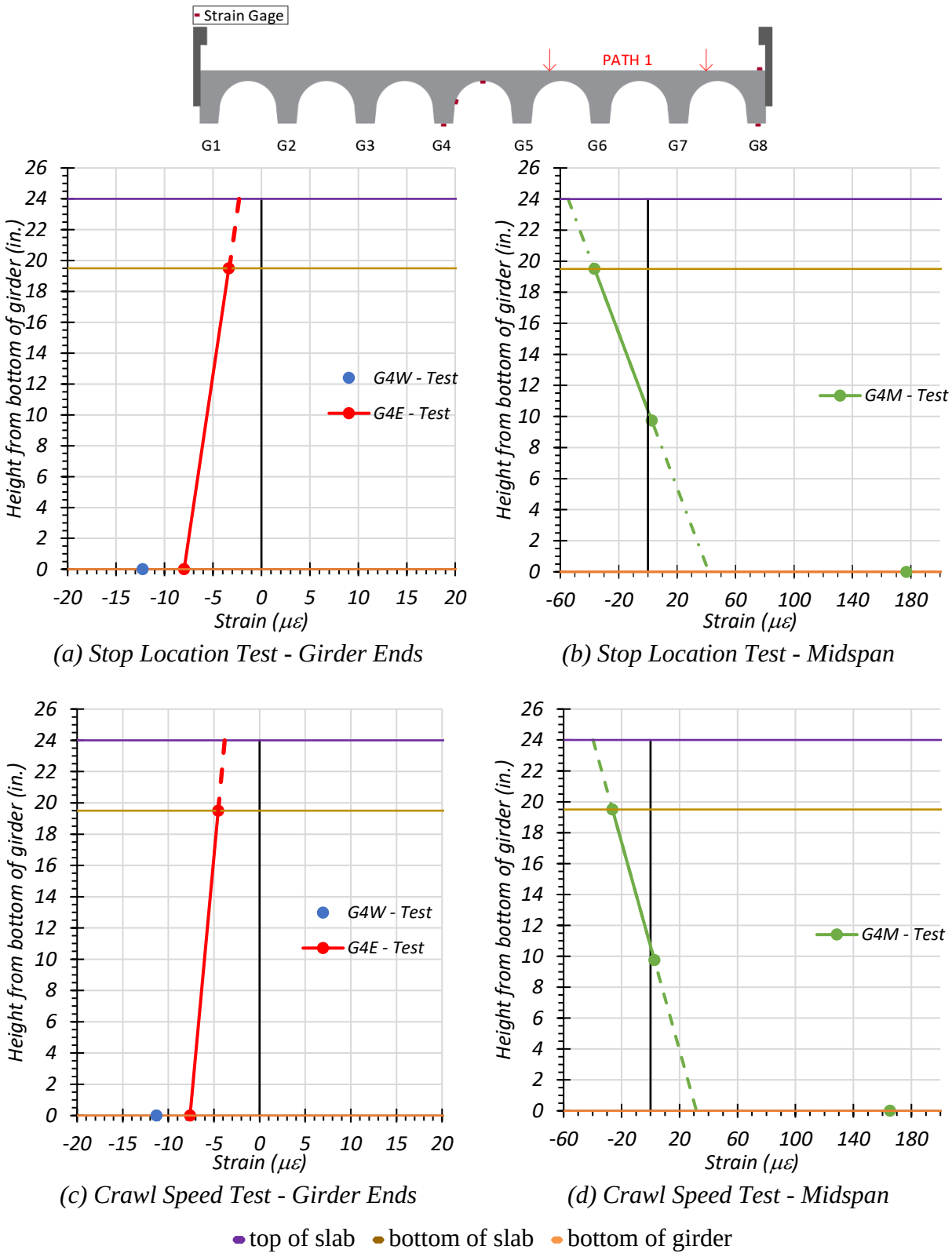

Figure 8.9. Static Strains for Interior Girder G4—Path 1

Interior Girder G4—Path 2 Loading. Strain profiles corresponding to the top and bottom strains for interior Girder G4 under static tests along Path 2 are provided in Figure 8.10.

The strain profile at the west and east ends of Girder G4 is shown in Figure 8.10(a) for the stop location test and Figure 8.10(c) for the crawl speed test. The bottom strain for both the west and east ends of Girder G4 are compressive for the stop location test and crawl speed test, indicating some degree of end fixity is present. The bottom strains obtained from the crawl speed test are slightly less, which may be due to the truck stop location not being exactly at the moment critical position.

The strain profile at the midspan of Girder G4 is shown in Figure 8.10(b) for the stop location test and Figure 8.10(d) for the crawl speed test. The neutral axis depth at the midspan was found to be 9.37 in. from the bottom of Girder G4 using the strain profile obtained from the stop location test and 10.23 in. from the bottom of Girder G4 using the strain profile obtained from the crawl speed test. The neutral axis depth calculated using the strain profile obtained from the crawl speed test is slightly higher than the one obtained from the stop location test. This result could be due to the stop location test being slightly different from the moment critical position for absolute maximum moment.

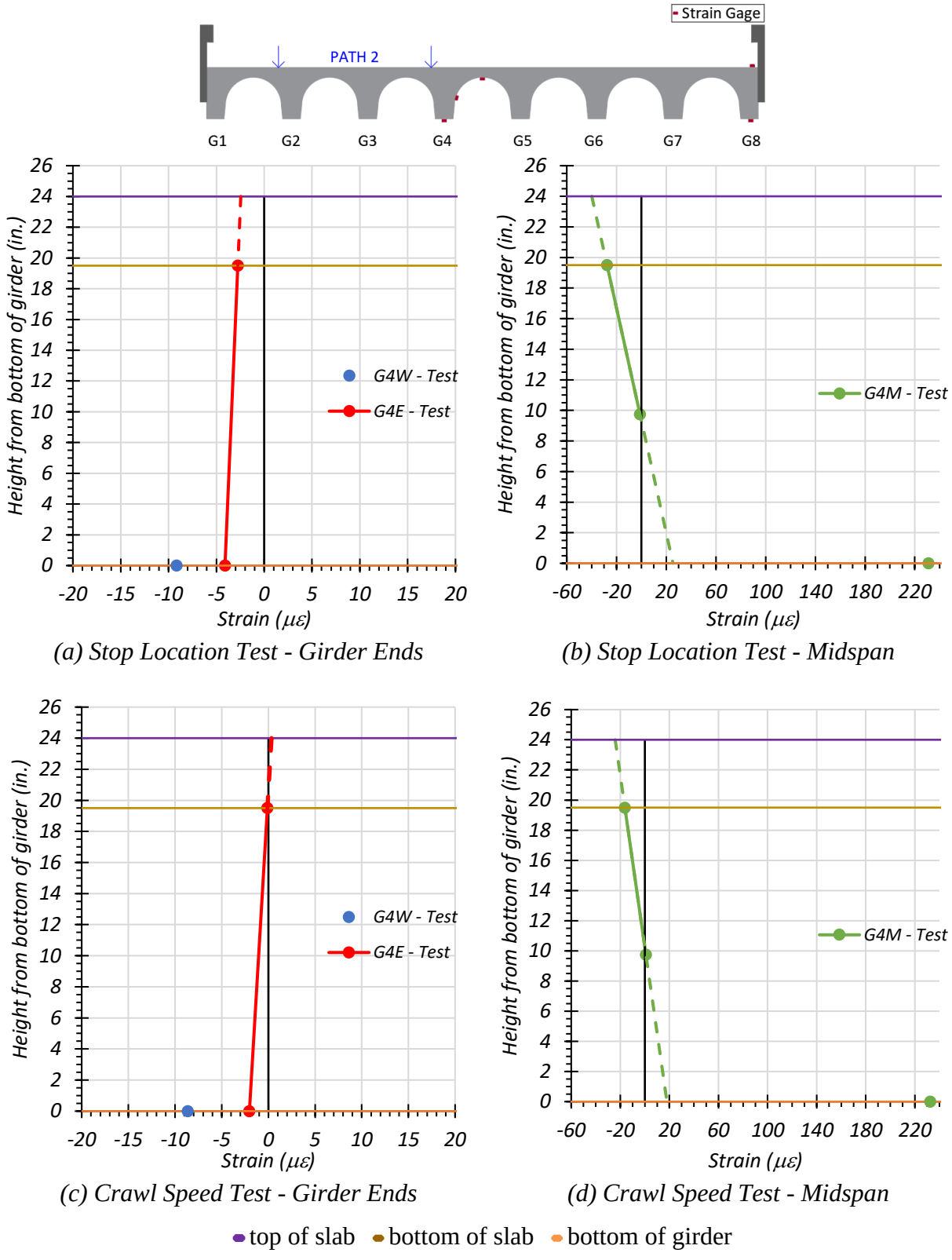

(a) Stop Location Test - Girder Ends

(b) Stop Location Test - Midspan

(c) Crawl Speed Test - Girder Ends

(d) Crawl Speed Test - Midspan

Figure 8.10. Static Strains for Interior Girder G4—Path 2

Interior Girder G4—Middle Path Loading. Strain profiles corresponding to the top and bottom strains for interior Girder G4 under static tests along the Middle Path are provided in Figure 8.11.

The strain profiles at the west and east ends of Girder G4 are shown in Figure 8.11(a) for the stop location test and Figure 8.11(c) for the crawl speed test. It can be seen that the bottom strain at both the west and east ends of Girder G4 are compressive for the stop location test and crawl speed test, indicating some degree of end fixity is present. The bottom strains obtained from the stop location test and crawl speed test are very similar.

The strain profiles at the midspan of Girder G4 are shown in Figure 8.11(b) for the stop location test and Figure 8.11(d) for the crawl speed test. The neutral axis depth at the midspan was found to be 10.01 in. from the bottom of Girder G4 using the strain profile obtained from the stop location test and 10.24 in. from the bottom of Girder G4 using the strain profile obtained from the crawl speed test. The neutral axis depth calculated using the strain profile obtained from the crawl speed test is slightly higher than the one obtained from the stop location test. This result could also be due to the stop location test being slightly different from the moment critical position for absolute maximum moment.

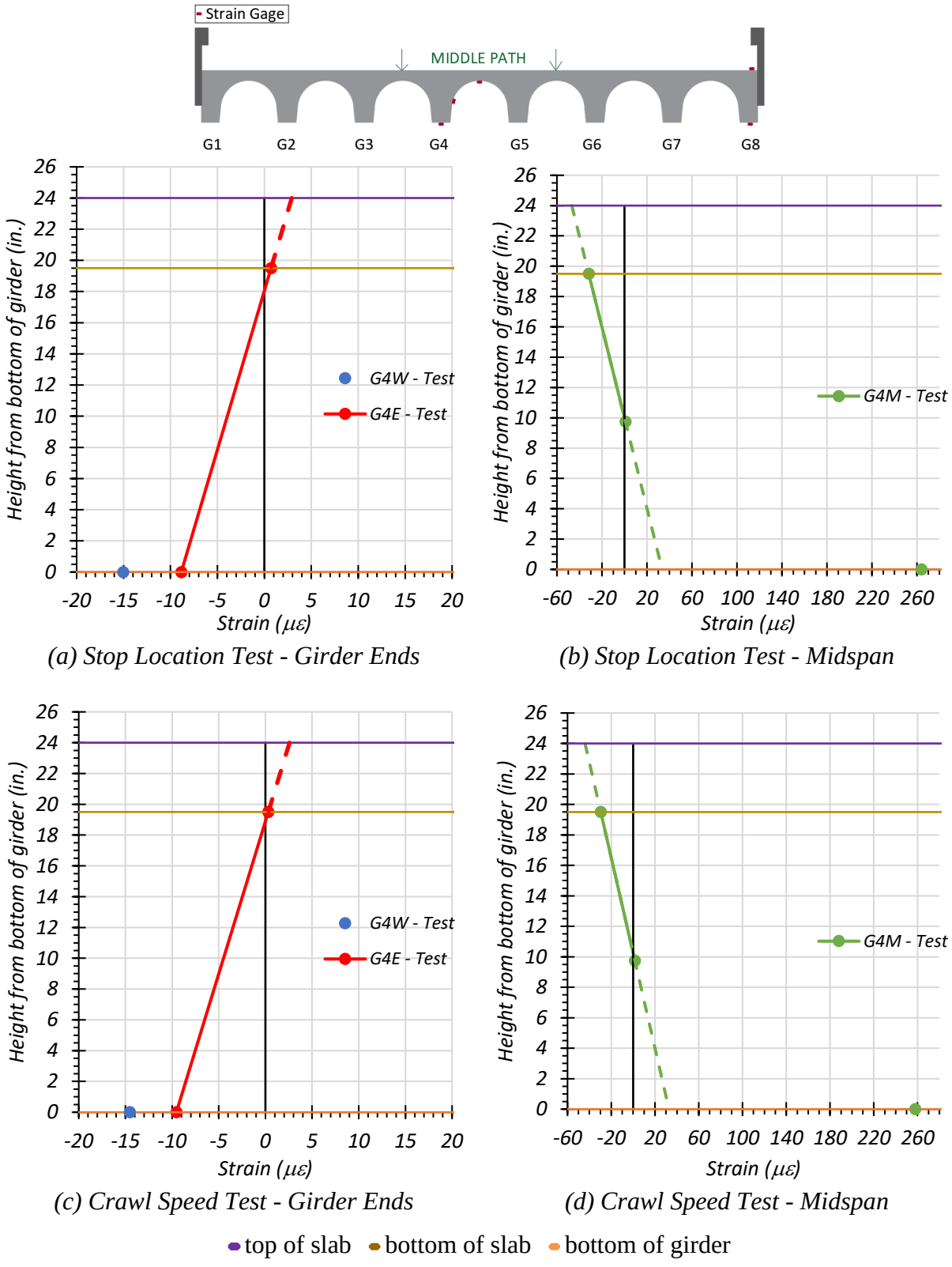

(a) Stop Location Test - Girder Ends

(b) Stop Location Test - Midspan

(c) Crawl Speed Test - Girder Ends

(d) Crawl Speed Test - Midspan

Figure 8.11. Static Strains for Interior Girder G4—Middle Path

Exterior Girder G8—Path 1 Loading. Strain profiles corresponding to the top and bottom strains for exterior Girder G8 under static tests along Path 1 are provided in Figure 8.12.

The strain profiles at the west and east ends of Girder G8 are shown in Figure 8.12(a) for the stop location test and Figure 8.12(c) for the crawl speed test. The bottom strains for the west end of Girder G8 are compressive for both the stop location test and crawl speed test, indicating some degree of end fixity is present. For both the stop location test and crawl speed test, the bottom strains at the east end of Girder G8 are small negative values (< 5 με), which indicates the absence of significant partial restraint at this end. The bottom strains obtained from the crawl speed test were slightly higher than those obtained from the stop location test for the west end of Girder G8. The difference in strain values for the stop location test and crawl speed test may be due to the truck stop location not being exactly at the moment critical position.

The strain profiles at the midspan of Girder G8 are shown in Figure 8.12(b) for the stop location test and Figure 8.12(d) for the crawl speed test. The neutral axis depth at the midspan was found to be 15.02 in. from the bottom of Girder G8 using the strain profile obtained from the stop location test and 14.37 in. from the bottom of Girder G8 using the strain profile obtained from the crawl speed test. The neutral axis depth calculated using the strain profile obtained from the crawl speed test is slightly higher than the one obtained from the stop location test. This result could also be due to the stop location test being slightly different from the moment critical position for absolute maximum moment.

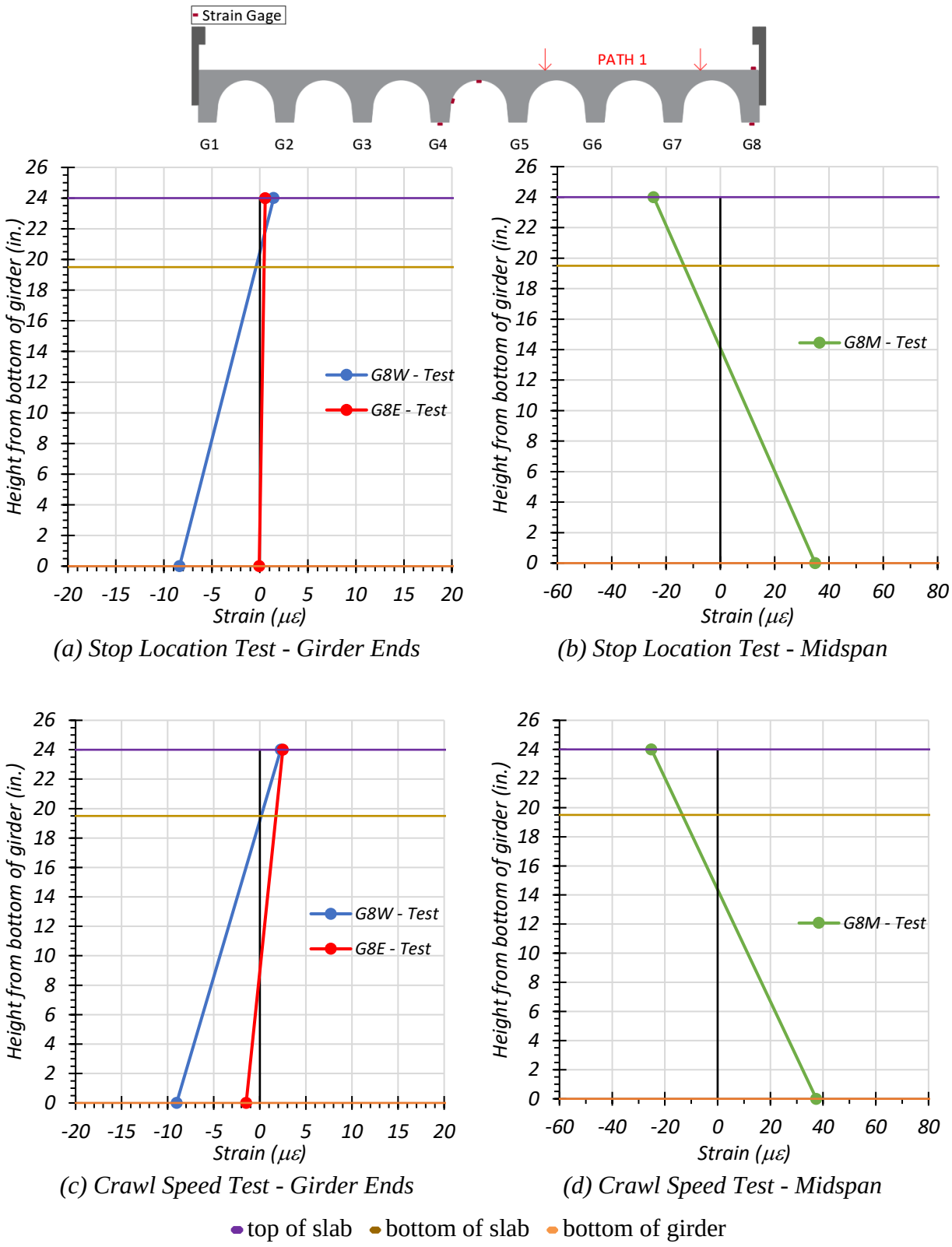

(a) Stop Location Test - Girder Ends

(b) Stop Location Test - Midspan

(c) Crawl Speed Test - Girder Ends

(d) Crawl Speed Test - Midspan

top of slab bottom of slab bottom of girder

Figure 8.12. Static Strains for Exterior Girder G8—Path 1

Exterior Girder G8—Path 2 Loading. Strain profiles corresponding to the top and bottom strains for exterior Girder G8 under static tests along Path 2 are provided in Figure 8.13.

The strain profiles at the west and east ends of Girder G8 are shown in Figure 8.13(a) for the stop location test and Figure 8.13(c) for the crawl speed test. The bottom strains for both the west and east ends of Girder G8 were positive, indicating the absence of significant partial restraint. The bottom strains at both ends for the stop location test and crawl speed test are very similar.

The strain profiles at the midspan of Girder G8 are shown in Figure 8.13(b) for the stop location test and Figure 8.13(d) for the crawl speed test. The neutral axis depth at the midspan was found to be 19.06 in. from the bottom of Girder G8 using the strain profile obtained from the stop location test and 17.96 in. from the bottom of Girder G8 using the strain profile obtained from the crawl speed test. The neutral axis depth calculated using the strain profile obtained from the crawl speed test is slightly higher than the one obtained from the stop location test. This result could also be due to the stop location test being slightly different from the moment critical position for absolute maximum moment.

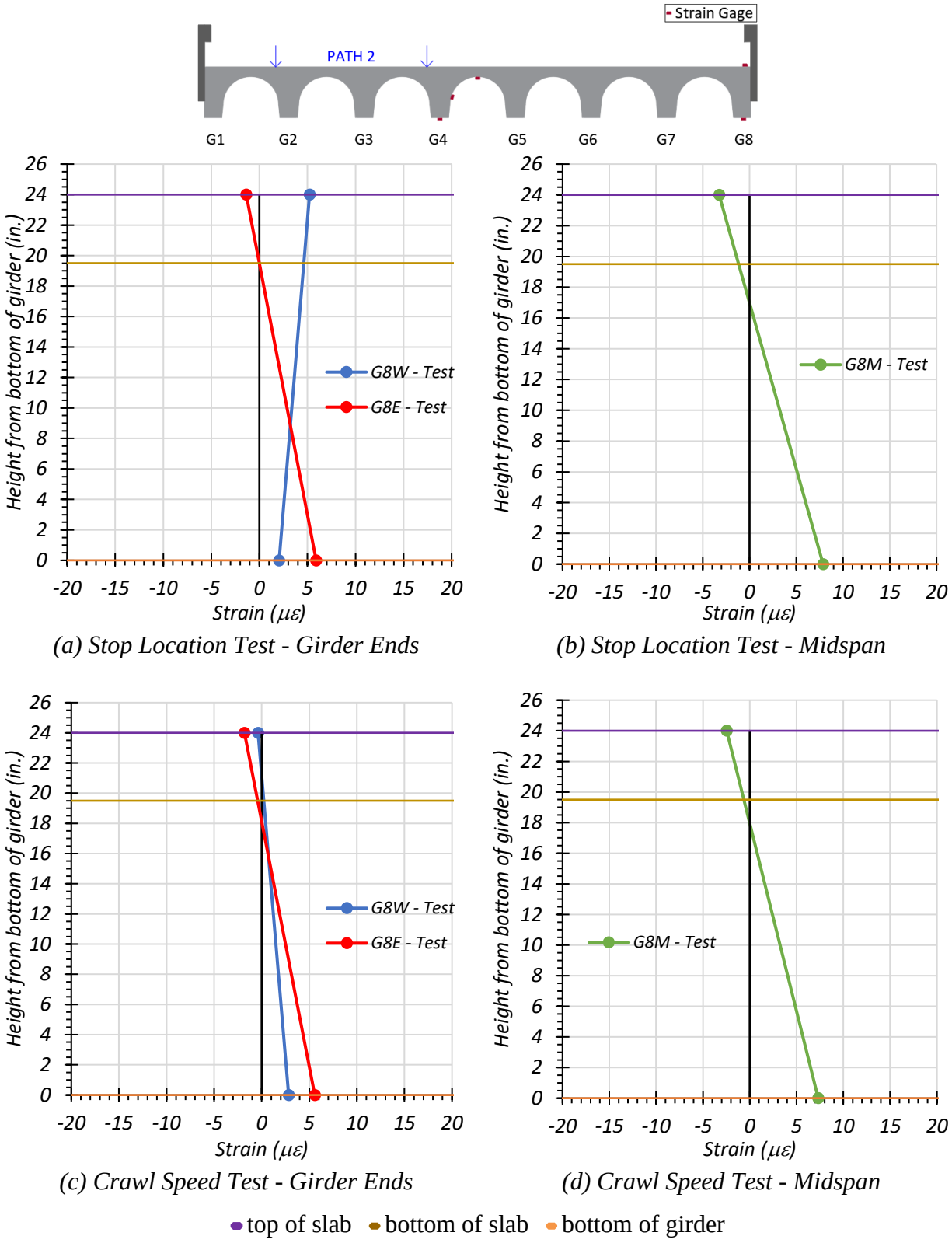

Figure 8.13. Static Strains for Exterior Girder G8—Path 2

Exterior Girder G8—Middle Path Loading. Strain profiles corresponding to the top and bottom strains for exterior Girder G8 under static tests along the Middle Path are provided in Figure 8.14.

The strain profiles at the west and east ends of Girder G8 are shown in Figure 8.14(a) for the stop location test and Figure 8.14(c) for the crawl speed test. The bottom strains for both the west and east ends of Girder G8 were positive, indicating the absence of significant partial restraint. The bottom strain at the west end for the crawl speed test was higher than the one obtained from the stop location test. The bottom strain at the east end for the crawl speed test was smaller than the one obtained from the stop location test.

The strain profiles at the midspan of Girder G8 are shown in Figure 8.14(b) for the stop location test and Figure 8.14(d) for the crawl speed test. The neutral axis depth at the midspan was found to be 14.73 in. from the bottom of Girder G8 using the strain profile obtained from the stop location test and 14.50 in. from the bottom of Girder G8 using the strain profile obtained from the crawl speed test. The neutral axis depth calculated using the strain profile obtained from the crawl speed test is slightly higher than the one obtained from the stop location test. This result could also be due to the stop location test being slightly different from the moment critical position for absolute maximum moment.

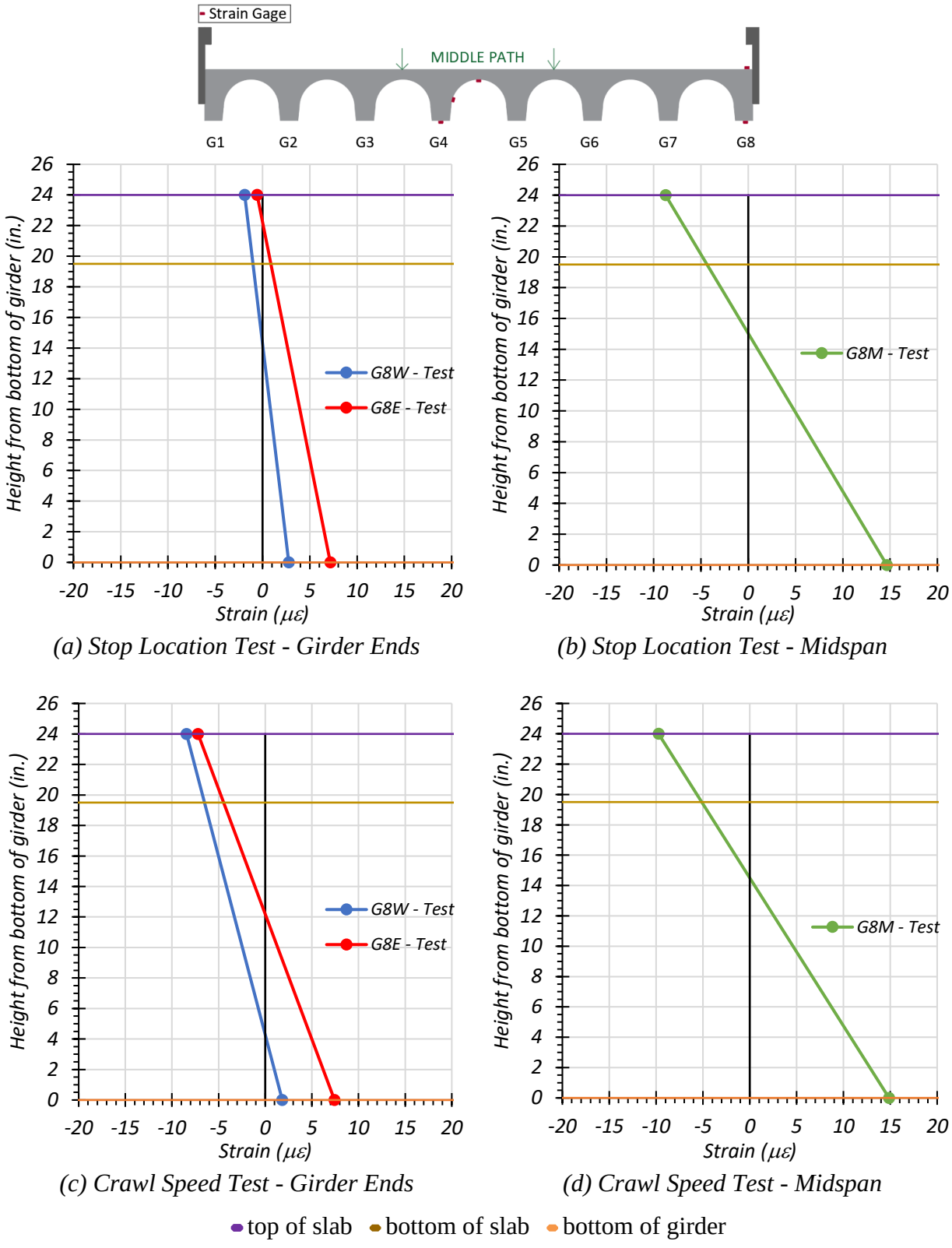

(a) Stop Location Test - Girder Ends

(b) Stop Location Test - Midspan

(c) Crawl Speed Test - Girder Ends

(d) Crawl Speed Test - Midspan

Figure 8.14. Static Strains for Exterior Girder G8—Middle Path

Comparison of Measured Strain Results. Theoretical calculations to determine the neutral axis depth for a cracked and uncracked concrete section were carried out for both an exterior and interior girder. A typical transverse section, along with the reinforcement information from the standard drawings, is provided in Figure 8.15. A single layer of bottom reinforcement consisting of two #11 bars was considered based on GPR measurements taken during the test. The girders were spaced at 3 ft center-to-center intervals. The *AASHTO Standard Specifications* define the effective flange width as the minimum of a quarter of the span length, the center-to-center spacing of the girders, and 12 times the slab thickness. Thus, the effective width of the interior girder was taken to be 3 ft and the effective width of the exterior girder was 1 ft 9.5 in. The MOE for concrete was calculated using the following equation, which is valid for normal weight concrete with a unit weight between 0.09 and 0.155 kcf and a design compressive strength up to 15.0 ksi:

$$E_c = 33{,}000 K_1 w_c^{1.5} \sqrt{f_c'} \quad (8.1)$$

where:

E_c = Elastic modulus of concrete, ksi

K_1 = Correction factor for source of aggregate, to be taken as 1.0 unless determined by physical test

w_c = Unit weight of concrete, kcf

f_c' = Compressive strength of concrete, ksi

The MOE for concrete was calculated to be 5072 ksi based on the measured f_c' of 7 ksi. The theoretical position of the neutral axis depth for an uncracked concrete section was determined to be 15.21 in. from the bottom of the interior girder and 14.05 in. from the bottom of the exterior girder. For a cracked concrete section, the neutral axis depth was calculated to be 19.91 in. from the bottom of the interior girder and 18.87 in. from the bottom of the exterior girder.

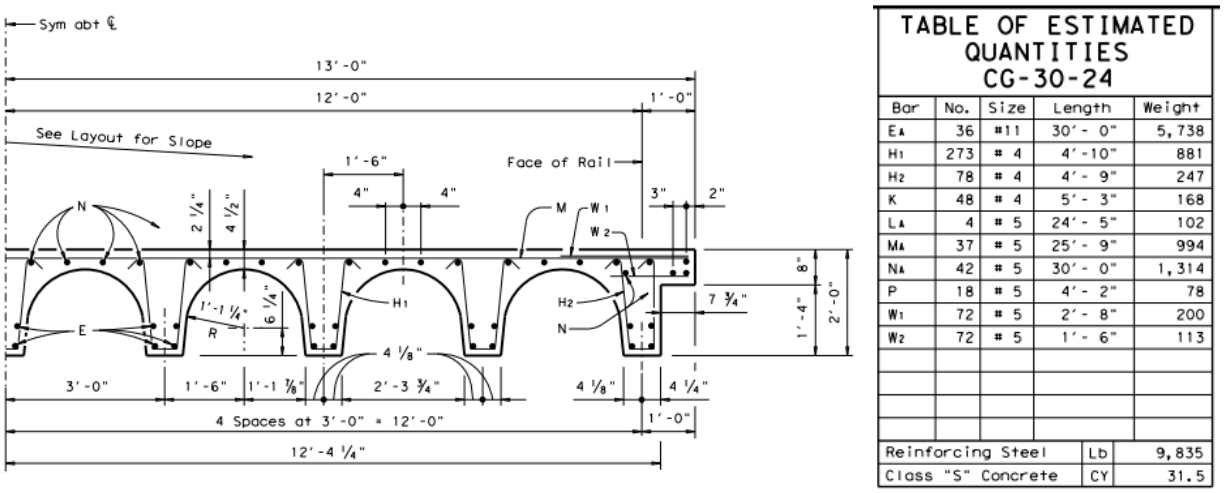

TABLE OF ESTIMATED QUANTITIES
CG-30-24

Bar	No.	Size	Length	Weight
EA	36	#11	30'- 0"	5,738
H1	273	# 4	4'-10"	881
H2	78	# 4	4'- 9"	247
K	48	# 4	5'- 3"	168
LA	4	# 5	24'- 5"	102
MA	37	# 5	25'- 9"	994
NA	42	# 5	30'- 0"	1,314
P	18	# 5	4'- 2"	78
W1	72	# 5	2'- 8"	200
W2	72	# 5	1'- 6"	113
Reinforcing Steel			Lb	9,835
Class "S" Concrete			CY	31.5

Figure 8.15. Transverse Section Typical to Pan Girder Bridges (TxDOT 2005)

Table 8.4 lists the midspan neutral axes corresponding to all the different tests. Figure 8.16 compares the neutral axes obtained from the static tests with the FEM neutral axis for both Girders G8 and G4. The neutral axes determined from the tests are closer to the theoretical uncracked neutral axis for both Girders G4 and G8.

Table 8.4. Measured Neutral Axis Locations for All Static Load Tests

Test	G4 Neutral Axis Location (in. from bottom of girder)	G8 Neutral Axis Location (in. from bottom of girder)
Path 1—Stop Location	10.40	15.02
Path 1—Crawl Speed	10.65	14.37
Path 2—Stop Location	9.37	19.06
Path 2—Crawl Speed	10.23	17.96
Middle Path—Stop Location	10.01	14.73
Middle Path—Crawl Speed	10.24	14.50
Theoretical Uncracked	14.05	15.21
Theoretical Cracked	19.91	18.87

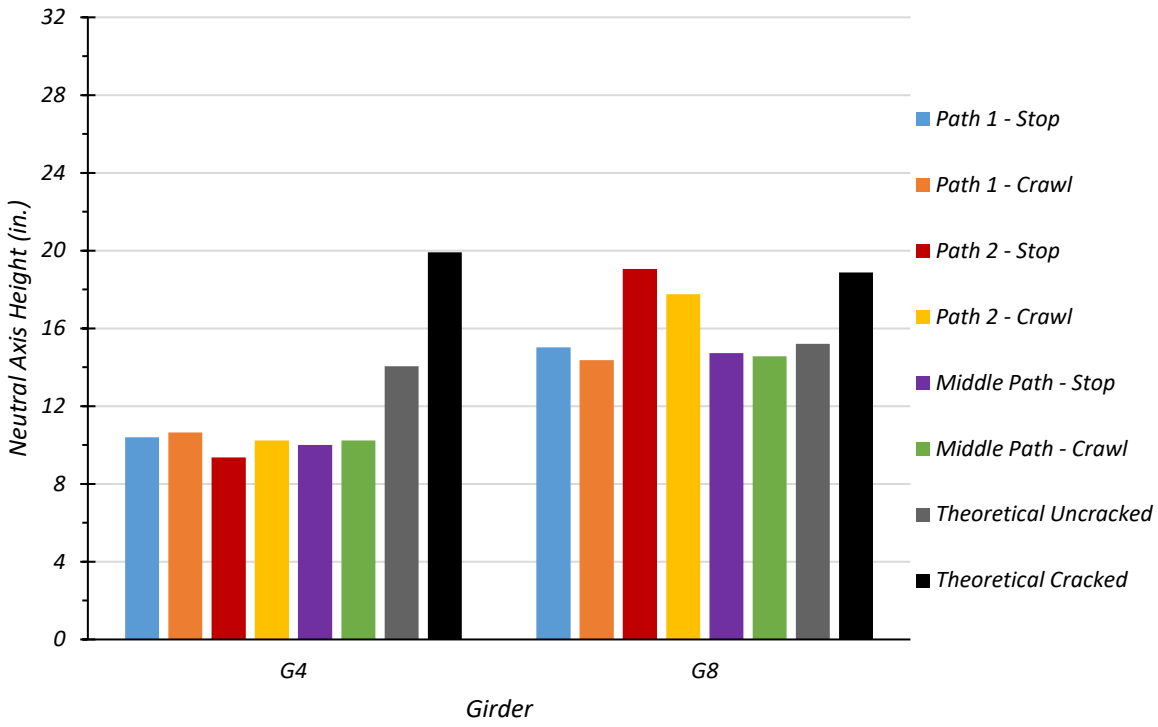

Figure 8.16. Test Neutral Axis Locations at the Midspan

*8.6.1.2 **Deflection Measurements and LLDFs***

All instrumentation for the bridge was installed the afternoon before the test day. Heavy rain fell that night, and the water level in the stream below the bridge rose. The string potentiometers, which were attached to wooden stakes driven into the bed of the stream, were covered with plastic bags for protection. However, some string potentiometers may have been exposed to water, which could be the reason why the string potentiometers at Girder G2 and G4 show lower displacements for all static tests. The measured deflections for all girders and the corresponding LLDFs are presented in this section.

Path 1 Loading. The deflection for each girder was recorded over a period of time for each test. The maximum downward deflection for each girder was obtained. The corresponding LLDF for each girder was calculated using Equation (8.2).

$$LLDF = \frac{\Delta_i I_i}{\sum \Delta_i I_i} \tag{8.2}$$

where:

$LLDF$ = Live load distribution factor

Δ_i = Maximum vertical deflection of girder *i*, in.

I_i = Cracked moment of inertia of girder *i*, in^4

The measured deflection for all girders and the LLDFs for the stop location test and crawl speed test along Path 1 are provided in Table 8.5. For both the stop location test and crawl speed test, the maximum exterior girder deflection was observed in Girder G8, and the maximum interior girder deflection was observed in G6. These results were due to the close proximity of these girders to the wheel lines. The corresponding LLDF for Girder G8 was 0.184 for the stop location test and 0.191 for the crawl speed test. G6 had an LLDF of 0.218 for the stop location test and 0.222 for the crawl speed test.

A comparison of the LLDFs calculated from the test data and those calculated using the approximate equations in the *AASHTO Standard Specifications* (AASHTO 2002) and *AASHTO LRFD Specifications* (AASHTO 2017) with the simplified and analytical stiffness parameter is provided in Table 8.6. Note that the LLDF expressions in the *AASHTO LRFD Specifications* (AASHTO 2017) consider a multiple presence factor m of 1.2 for one-lane loading and 1.0 for two-lane loading. For this reason, the LLDF values computed for interior girders were divided by 1.2 for comparison to the *AASHTO Standard Specifications* LLDFs and measured LLDFs, which are for a one-lane loaded condition. The AASHTO standard LLDF is slightly unconservative with a ratio of 0.95 for Girder G8 and slightly conservative with a ratio of 1.06 for Girder G6, in comparison to the test LLDF obtained for the stop location test. The AASHTO LRFD LLDFs are slightly unconservative with a ratio of 0.95 for Girder G8 and more conservative with a ratio of 1.32 for Girder G6, in comparison to the LLDFs obtained for the stop location test.

Figure 8.17(a) and (c) show stop location test and crawl speed test measured deflections for each girder, respectively. A comparison of the test LLDFs with those LLDFs calculated from the *AASHTO Standard Specifications* is shown in Figure 8.17 (b) and (d) for stop location test and crawl speed test, respectively.

Table 8.5. Experimental Deflections and LLDFs for Path 1 Loading

Girder	G1	G2	G3	G4	G5	G6	G7	G8
Stop Location Test Disp. (in.)	0.006	0.002	0.014	0.016	0.034	0.041	0.040	0.037
Stop Location Test LLDF	0.032	0.012	0.076	0.088	0.180	0.218	0.210	0.184
Crawl Speed Test Disp. (in.)	0.004	0.003	0.014	0.015	0.033	0.041	0.041	0.038
Crawl Speed Test LLDF	0.019	0.013	0.074	0.079	0.180	0.222	0.221	0.191
Note: 1 – G = girder, Disp. = Displacement 2 – LLDF values are based on the midspan deflections.								

Table 8.6. LLDF Comparison with AASHTO for Path 1 Loading

Test and Girder Type	AASHTO Standard Specs ($g^m_{AASHTO\_Std}$)	AASHTO LRFD Simplified ($g^m_{AASHTO\_S}$)	AASHTO LRFD K_g Calculated ($g^m_{AASHTO\_K}$)	Test (g^m_{test})	$g^m_{AASHTO\_Std}/g^m_{test}$	$g^m_{AASHTO\_S}/g^m_{test}$	$g^m_{AASHTO\_K}/g^m_{test}$
Stop Location Interior	0.231	0.287	0.283	0.218	1.06	1.32	1.30
Stop Location Exterior	0.174	0.174	0.174	0.184	0.95	0.95	0.95
Crawl Speed Interior	0.231	0.287	0.283	0.222	1.04	1.29	1.27
Crawl Speed Exterior	0.174	0.174	0.174	0.191	0.91	0.91	0.91

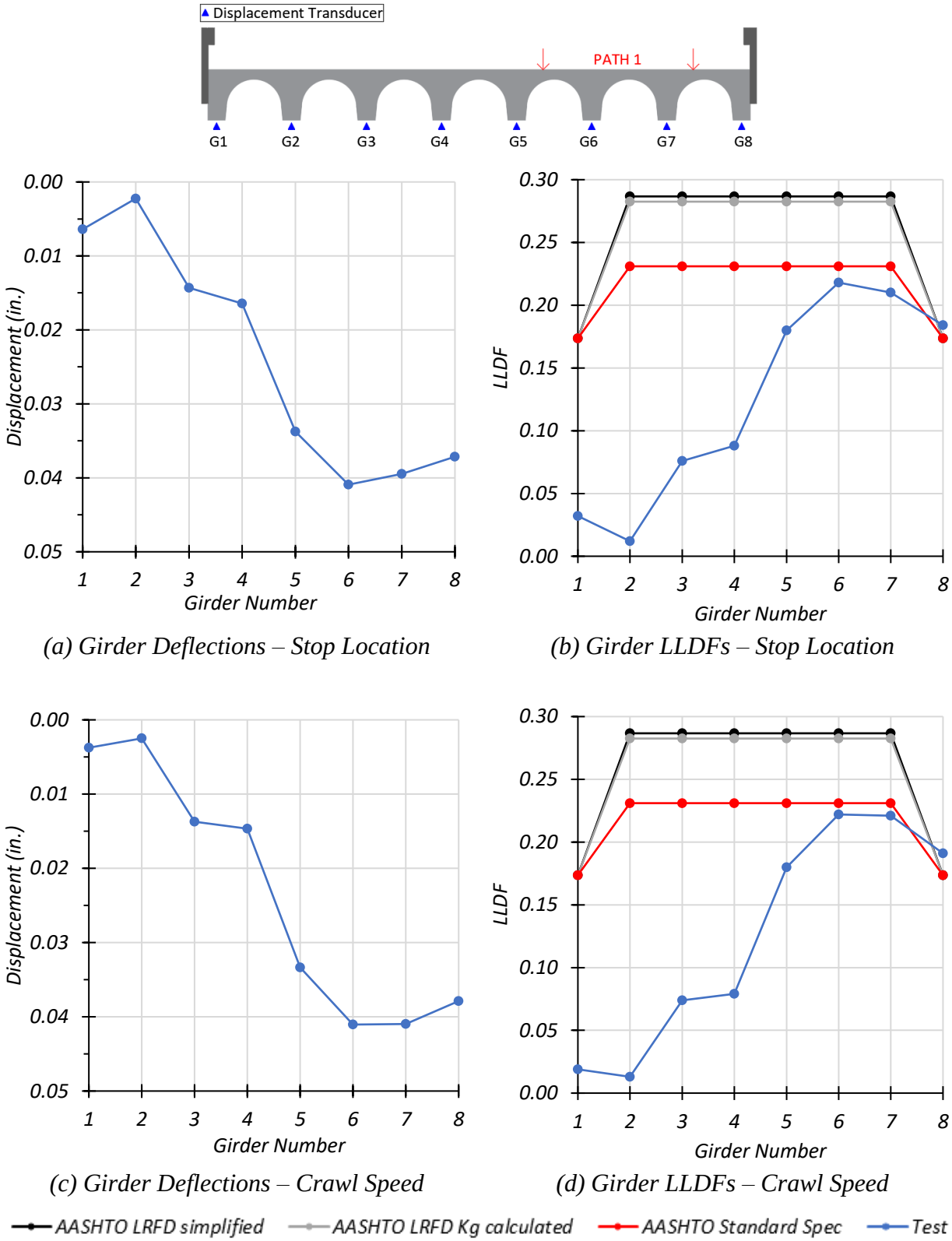

(a) Girder Deflections – Stop Location

(b) Girder LLDFs – Stop Location

(c) Girder Deflections – Crawl Speed

(d) Girder LLDFs – Crawl Speed

Figure 8.17. Static Deflection Results for Path 1 Loading

Path 2 Loading. The measured deflections for all girders and the LLDFs for the stop location test and crawl speed test along Path 2 are provided in Table 8.7. For both the stop location test and crawl speed test, the maximum exterior girder deflection was observed in Girder G1, and the maximum interior girder deflection was observed in Girder G3. These results were due to the close proximity of these girders to the wheel lines. The corresponding LLDF for Girder G1 was 0.164 for the stop location test and 0.187 for the crawl speed test. Girder G3 had an LLDF of 0.224 for the stop location test and 0.221 for the crawl speed test.

A comparison of the LLDFs calculated from the test data and those calculated using the approximate equations in the *AASHTO Standard Specifications* (AASHTO 2002) and *AASHTO LRFD Specifications* (AASHTO 2017) with the simplified and analytical stiffness parameter is provided in Table 8.8. Note that the LLDF expressions in the *AASHTO LRFD Specifications* (AASHTO 2017) consider a multiple presence factor m of 1.2 for one-lane loading and 1.0 for two-lane loading. For this reason, the LLDF values computed for interior girders were divided by 1.2 for comparison to the *AASHTO Standard Specifications* LLDFs and measured LLDFs, which are for a one-lane loaded condition. The AASHTO standard LLDF is slightly conservative, with a ratio of 1.06 for Girder G1 and 1.03 for Girder G3, in comparison to the test LLDF obtained for the stop location test. The AASHTO LRFD LLDF is more conservative, with a ratio of 1.06 for Girder G1 and 1.28 for Girder G3, in comparison to the test LLDF obtained for the stop location test.

Figure 8.18(a) and (c) show static and crawl test measured deflections for each girder, respectively. A comparison of the test LLDFs with those calculated from the *AASHTO Standard Specifications* are shown in Figure 8.18(b) and (d) for static and crawl tests, respectively.

Table 8.7. Experimental Deflections and LLDFs for Path 2 Loading

Girder	G1	G2	G3	G4	G5	G6	G7	G8
Stop Location Test Disp. (in.)	0.030	0.032	0.038	0.024	0.026	0.015	0.006	0.003
Stop Location Test LLDF	0.164	0.186	0.224	0.141	0.149	0.086	0.034	0.016
Crawl Speed Test Disp. (in.)	0.033	0.031	0.036	0.022	0.023	0.014	0.005	0.003
Crawl Speed Test LLDF	0.187	0.187	0.221	0.135	0.141	0.083	0.030	0.015
Note: 1 – G = girder, Disp. = Displacement 2 – LLDF values are based on the midspan deflections.								

Table 8.8. LLDF Comparison with AASHTO for Path 2 Loading

Test and Girder Type	AASHTO Standard Specs ($g^m_{AASHTO\_Std}$)	AASHTO LRFD Simplified ($g^m_{AASHTO\_S}$)	AASHTO LRFD K_g Calculated ($g^m_{AASHTO\_K}$)	Test (g^m_{test})	$g^m_{AASHTO\_Std}/g^m_{test}$	$g^m_{AASHTO\_S}/g^m_{test}$	$g^m_{AASHTO\_K}/g^m_{test}$
Stop Location Interior	0.231	0.287	0.283	0.224	1.03	1.28	1.26
Stop Location Exterior	0.174	0.174	0.174	0.164	1.06	1.06	1.06
Crawl Speed Interior	0.231	0.287	0.283	0.221	1.05	1.30	1.28
Crawl Speed Exterior	0.174	0.174	0.174	0.187	0.93	0.93	0.93

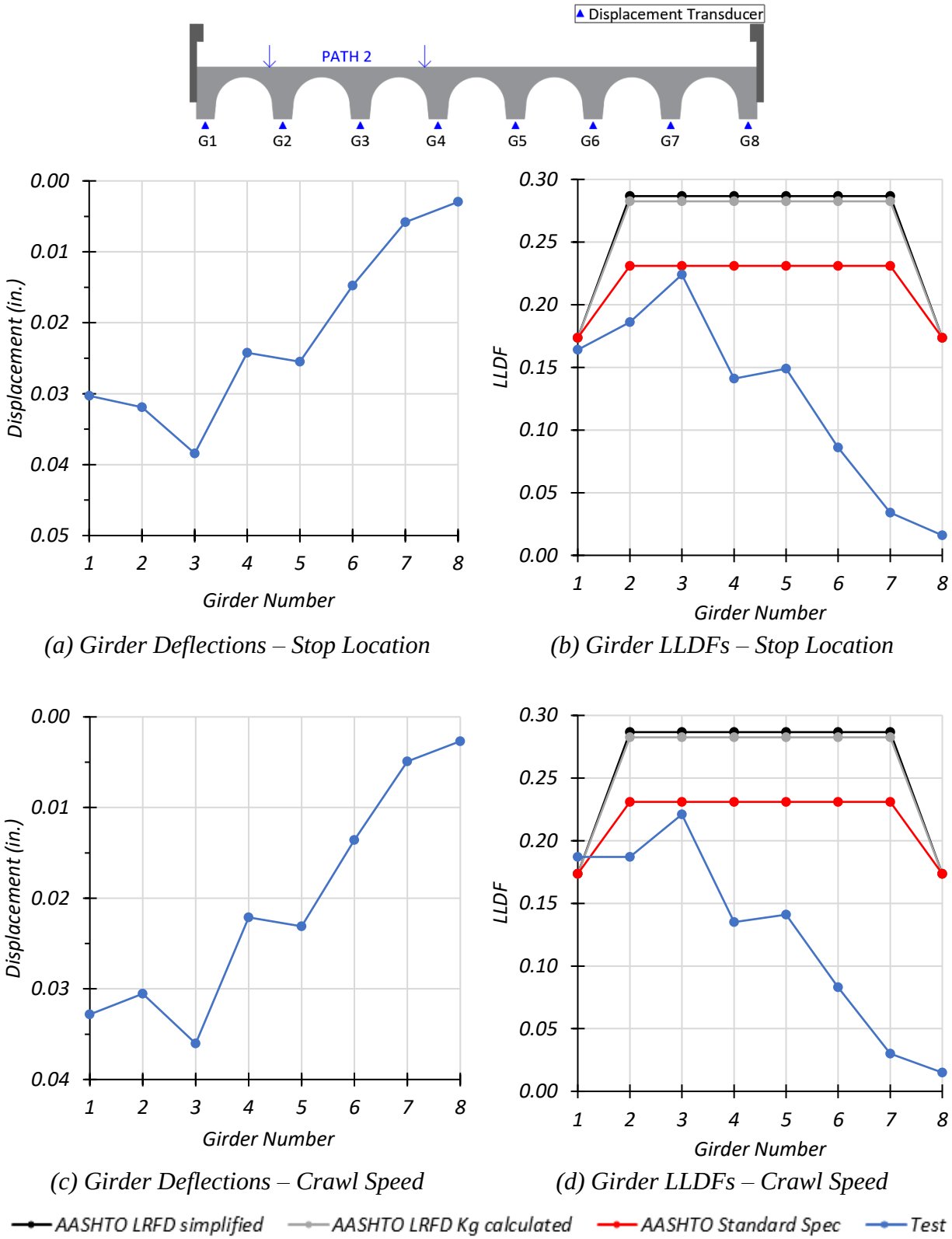

(a) Girder Deflections – Stop Location

(b) Girder LLDFs – Stop Location

(c) Girder Deflections – Crawl Speed

(d) Girder LLDFs – Crawl Speed

Figure 8.18. Static Deflection Results for Path 2 Loading

Middle Path Loading. The measured deflection for all girders and the LLDFs for the stop location test and crawl speed test along the Middle path are provided in Table 8.9. For both the stop location test and crawl speed test, the maximum exterior girder deflection was observed in Girder G1, and the maximum interior girder deflection was observed in G5. These results were due to the close proximity of these girders to the wheel lines. The corresponding LLDF for Girder G1 was 0.076 for the stop location test and 0.069 for the crawl speed test. G5 had an LLDF of 0.195 for the stop location test and 0.197 for the crawl speed test.

A comparison of the LLDFs calculated from the test data and those calculated using the approximate equations in the *AASHTO Standard Specifications* (AASHTO 2002) and *AASHTO LRFD Specifications* (AASHTO 2017) with the simplified and analytical stiffness parameter is provided in Table 8.10. Note that the LLDF expressions in the *AASHTO LRFD Specifications* (AASHTO 2017) consider a multiple presence factor m of 1.2 for one-lane loading and 1.0 for two-lane loading. For this reason, the LLDF values computed for interior girders were divided by 1.2 for comparison to the *AASHTO Standard Specifications* LLDFs and measured LLDFs, which are for a one-lane loaded condition. The AASHTO standard LLDF is highly conservative, with a ratio of 2.29 for Girder G1, and slightly conservative, with a ratio of 1.20 for G5, in comparison to the test LLDF obtained for the stop location test. The AASHTO LRFD LLDF is highly conservative, with a ratio of 2.29 for Girder G1 and 1.47 for G5, in comparison to the test LLDF obtained for the stop location test.

Figure 8.19(a) and (c) show static and crawl test measured deflections for each girder, respectively. A comparison of the test LLDFs with those calculated from the *AASHTO Standard Specifications* are shown in Figure 8.19(b) and (d) for static and crawl tests, respectively.

Table 8.9. Experimental Deflections and LLDFs for Middle Path Loading

Girder	G1	G2	G3	G4	G5	G6	G7	G8
Stop Location Test Disp. (in.)	0.015	0.016	0.033	0.026	0.036	0.030	0.018	0.013
Stop Location Test LLDF	0.076	0.085	0.179	0.141	0.195	0.163	0.097	0.064
Crawl Speed Test Disp. (in.)	0.013	0.015	0.030	0.025	0.035	0.028	0.019	0.012
Crawl Speed Test LLDF	0.069	0.084	0.172	0.143	0.197	0.159	0.109	0.065
Note: 1 – G = girder, Disp. = Displacement 2 – LLDF values are based on the midspan deflections.								

Table 8.10. LLDF Comparison with AASHTO for Middle Path Loading

Test and Girder Type	AASHTO Standard Specs ($g^m_{AASHTO\_Std}$)	AASHTO LRFD Simplified ($g^m_{AASHTO\_S}$)	AASHTO LRFD K_g Calculated ($g^m_{AASHTO\_K}$)	Test (g^m_{test})	$g^m_{AASHTO\_Std}/g^m_{test}$	$g^m_{AASHTO\_S}/g^m_{test}$	$g^m_{AASHTO\_K}/g^m_{test}$
Stop Location Interior	0.231	0.287	0.283	0.195	1.20	1.47	1.45
Stop Location Exterior	0.174	0.174	0.174	0.076	2.29	2.29	2.29
Crawl Speed Interior	0.231	0.287	0.283	0.197	1.18	1.46	1.44
Crawl Speed Exterior	0.174	0.174	0.174	0.069	2.52	2.52	2.52

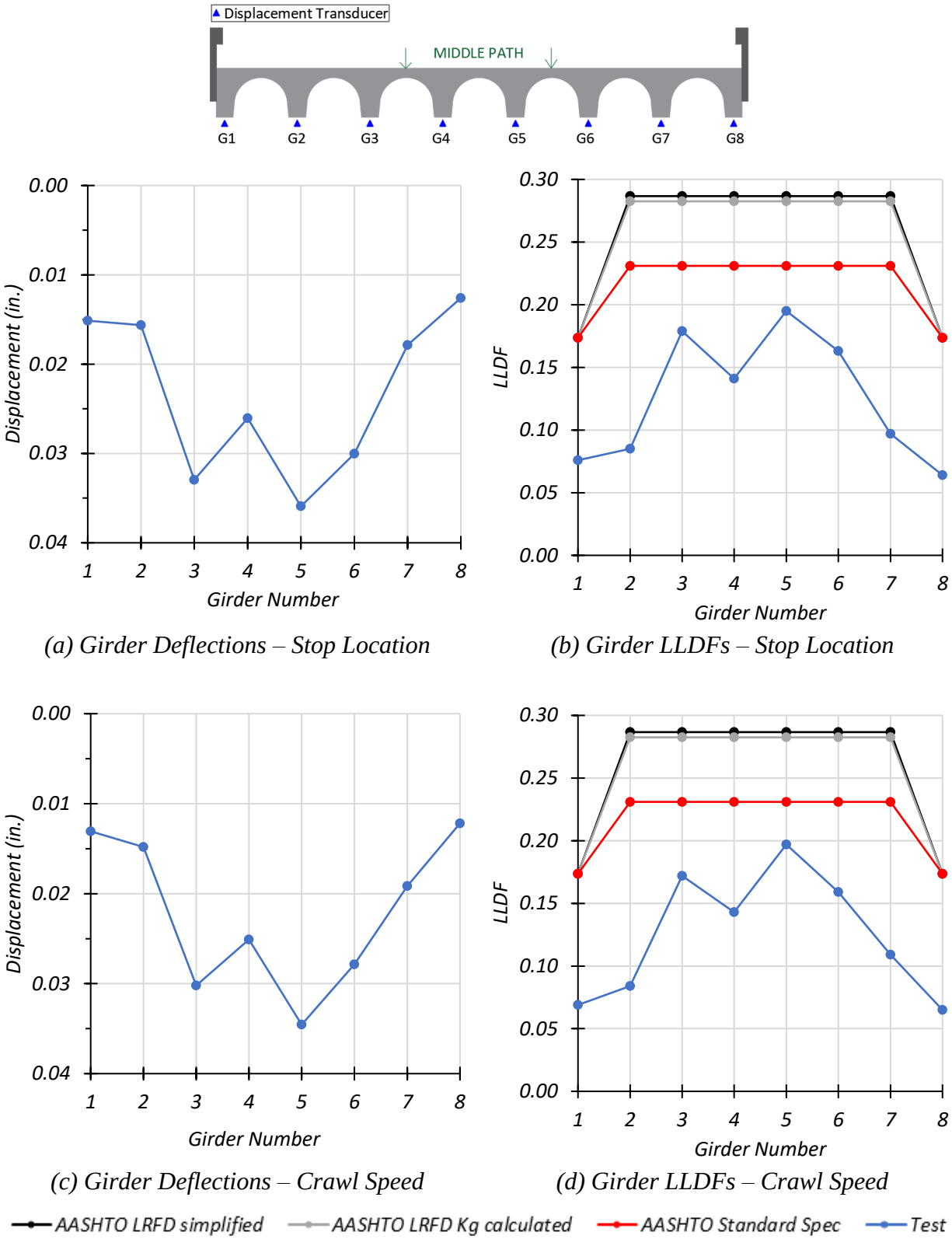

(a) Girder Deflections – Stop Location

(b) Girder LLDFs – Stop Location

(c) Girder Deflections – Crawl Speed

(d) Girder LLDFs – Crawl Speed

Figure 8.19. Static Deflection Results for Middle Path Loading

Comparison of Results based on Deflection Measurements. The maximum LLDF for exterior Girder G8 under the stop location test along Path 1 was 0.184. The maximum LLDF based on deflection measurements increased to 0.191 for the same girder during the crawl speed test along Path 1. The maximum LLDF for the exterior Girder G1 under the stop location test along Path 2 was 0.164. This value increased to 0.187 for the same girder during the crawl speed test along Path 2. The maximum LLDF for the exterior Girder G1 under the stop location test along the Middle Path was 0.076. This value decreased to 0.069 for the same girder during the crawl speed test along the Middle Path. Figure 8.20 provides a bar chart showing the maximum deflection and LLDF for each loading path. The critical LLDF for the exterior girder was noted to be 0.191, which corresponds to the crawl speed test along Path 1.

Similar observations were noted for the interior girders. The maximum LLDF for interior Girder G6 under the stop location test along Path 1 was 0.218. The maximum LLDF based on deflection measurements increased to 0.222 for the same girder during the crawl speed test along Path 1. The maximum LLDF for interior Girder G3 under the stop location test along Path 2 was 0.224. This value decreased to 0.221 for the same girder during the crawl speed test along Path 2. The maximum LLDF for interior Girder G5 under the stop location test along the Middle Path was 0.195. This value increased to 0.197 for the same girder during the crawl speed test along the Middle Path. The critical LLDF for the exterior girder was noted to be 0.224, which corresponds to the stop location test along Path 2.

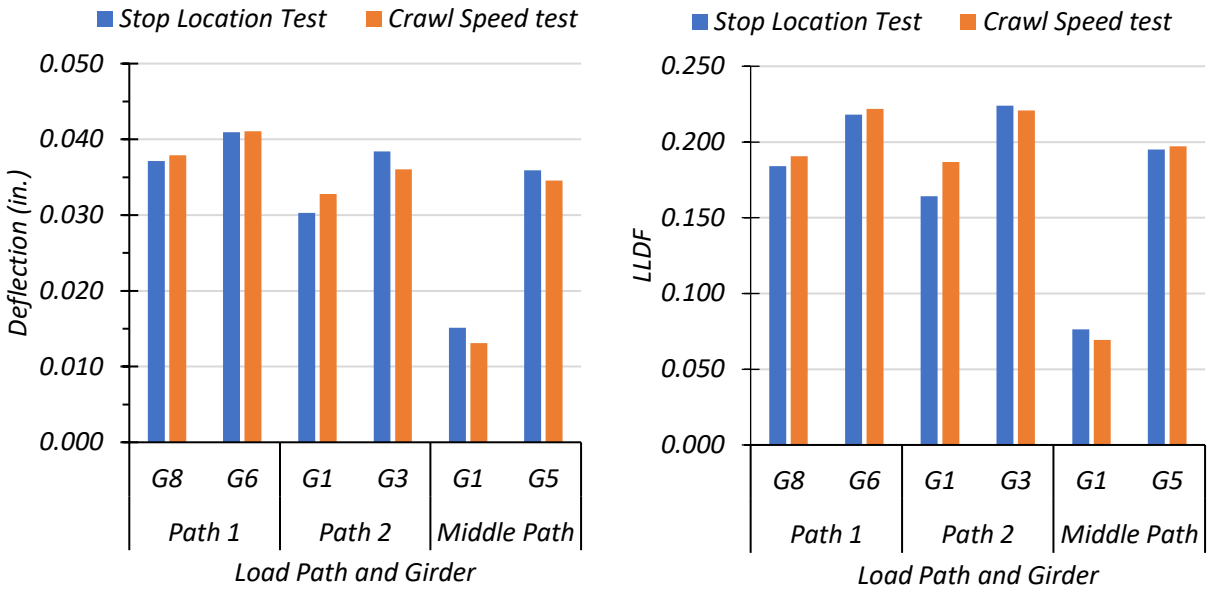

(a) Deflection *(b) LLDF*

Figure 8.20. Comparison of Maximum Deflections and LLDFs for Static Tests

Table 8.11 compares the LLDFs for the controlling interior and exterior girders with the AASHTO LLDFs for both the stop location test and crawl speed test. The *AASHTO Standard Specifications* provide LLDFs that are slightly conservative for the controlling interior girder and slightly unconservative for the controlling exterior girder. However, the LLDFs recommended by the *AASHTO LRFD Specifications* are slightly more conservative for the controlling interior girder and slightly unconservative for the controlling exterior girder.

Table 8.11. LLDF Comparison with AASHTO for Controlling Load Paths

Test and Girder Type	AASHTO Standard Specs ($g^m_{AASHTO\_Std}$)	AASHTO LRFD Simplified ($g^m_{AASHTO\_S}$)	AASHTO LRFD K_g Calculated ($g^m_{AASHTO\_K}$)	Test (g^m_{test})	$g^m_{AASHTO\_Std}/g^m_{test}$	$g^m_{AASHTO\_S}/g^m_{test}$	$g^m_{AASHTO\_K}/g^m_{test}$
Stop Location G3	0.231	0.287	0.283	0.224	1.03	1.28	1.26
Stop Location G8	0.174	0.174	0.174	0.184	0.95	0.95	0.95
Crawl Speed G3	0.231	0.287	0.283	0.221	1.05	1.30	1.28
Crawl Speed G8	0.174	0.174	0.174	0.191	0.91	0.91	0.91

Note: 1 – G8 is the controlling exterior girder under Path 1 loading.
2 – G3 is the controlling interior girder under Path 2 loading.

8.6.2 Dynamic Load Tests on Bridge CM-5

8.6.2.1 Dynamic Amplification

Maximum Girder Strains. The dynamic amplification of strains for Girders G4 and G8 were obtained by comparing the dynamic test results with the static stop location results. Plots of the strain profiles for Girders G4 and G8 obtained from the static tests and dynamic tests for Path 1, Path 2, and Middle Path are shown in Figure 8.21, Figure 8.22, and Figure 8.23, respectively. Figure 8.24 compares the dynamic strains for Girders G4 and G8 with the static values.

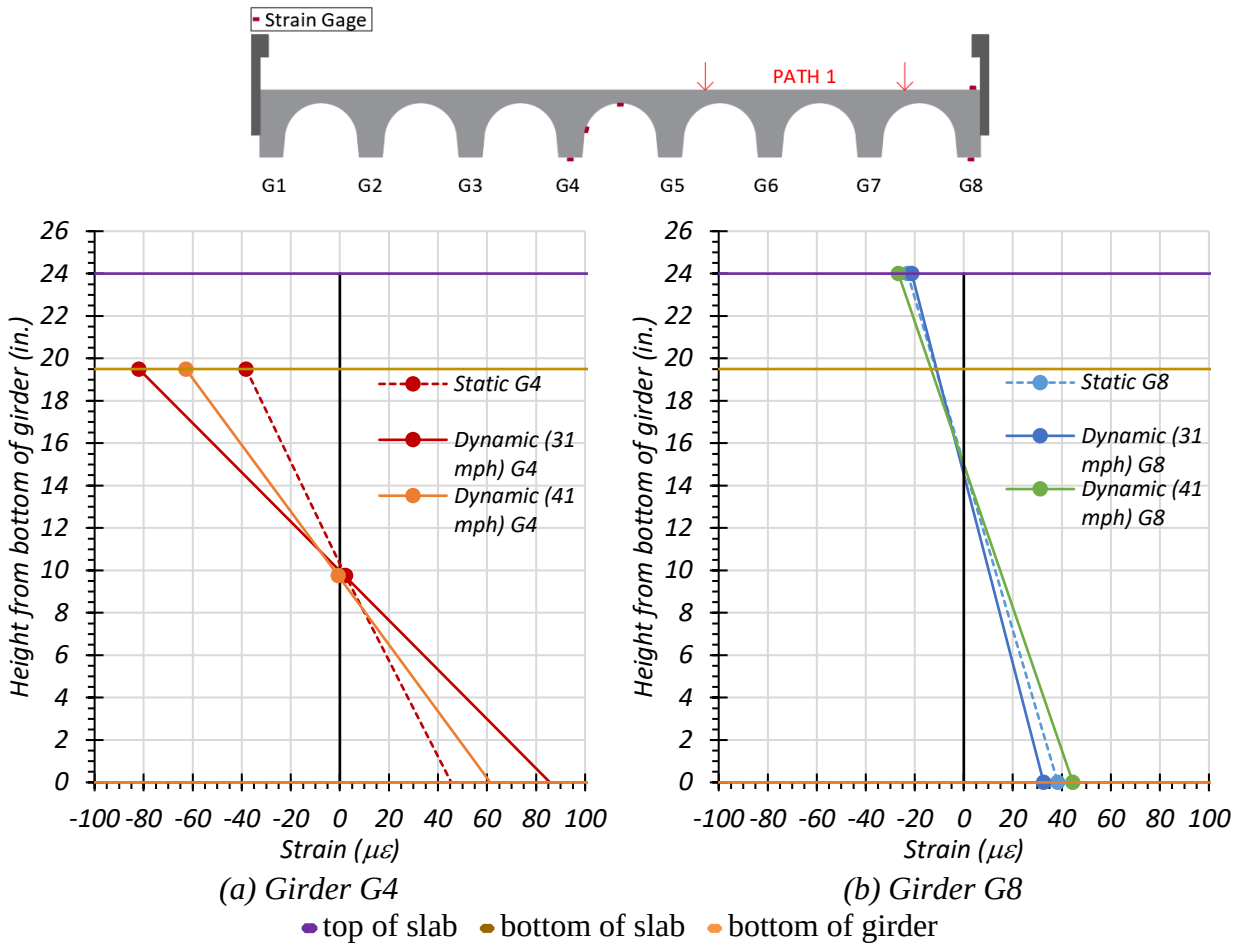

Figure 8.21. Maximum Strains for Static and Dynamic Tests for Path 1 Loading

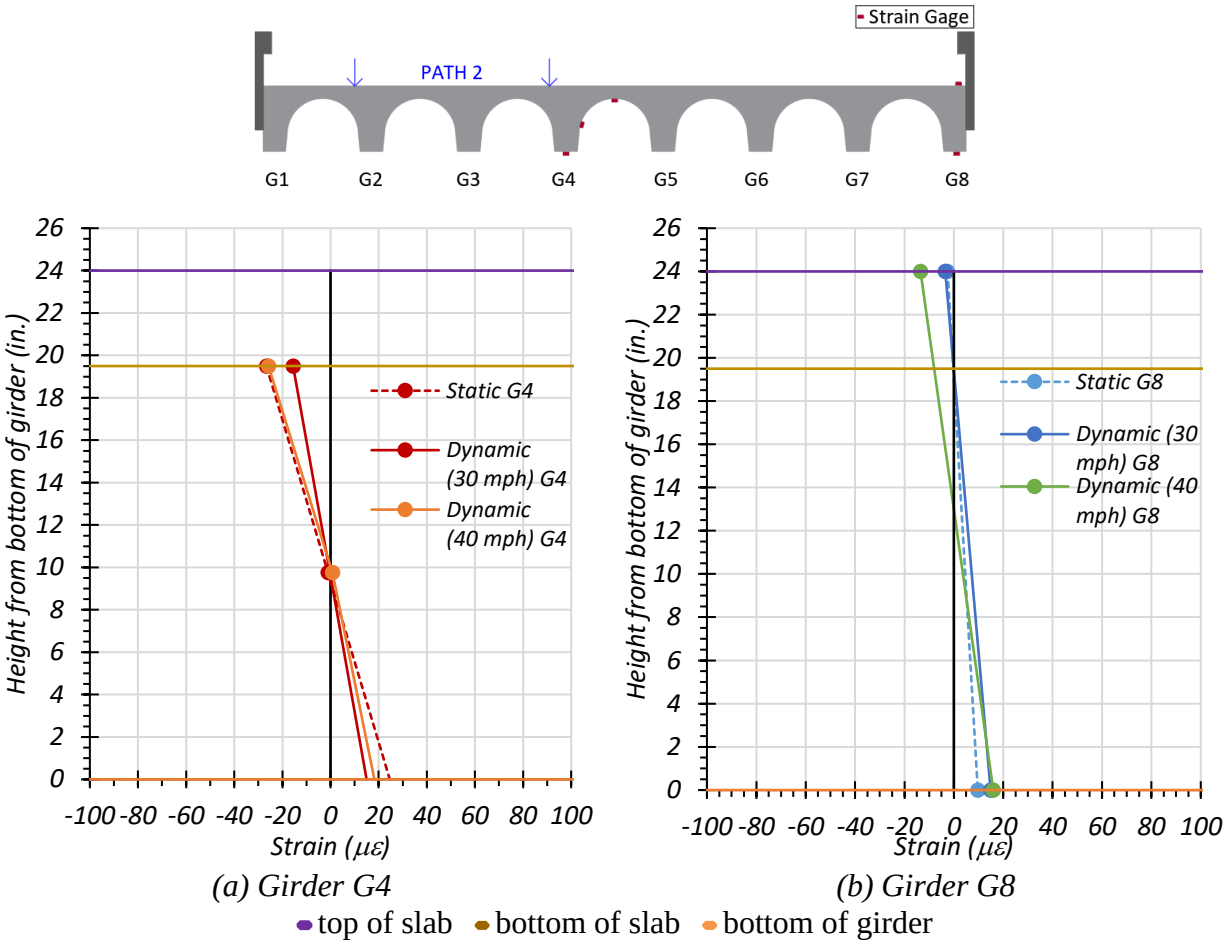

Figure 8.22. Maximum Strains for Static and Dynamic Tests for Path 2 Loading

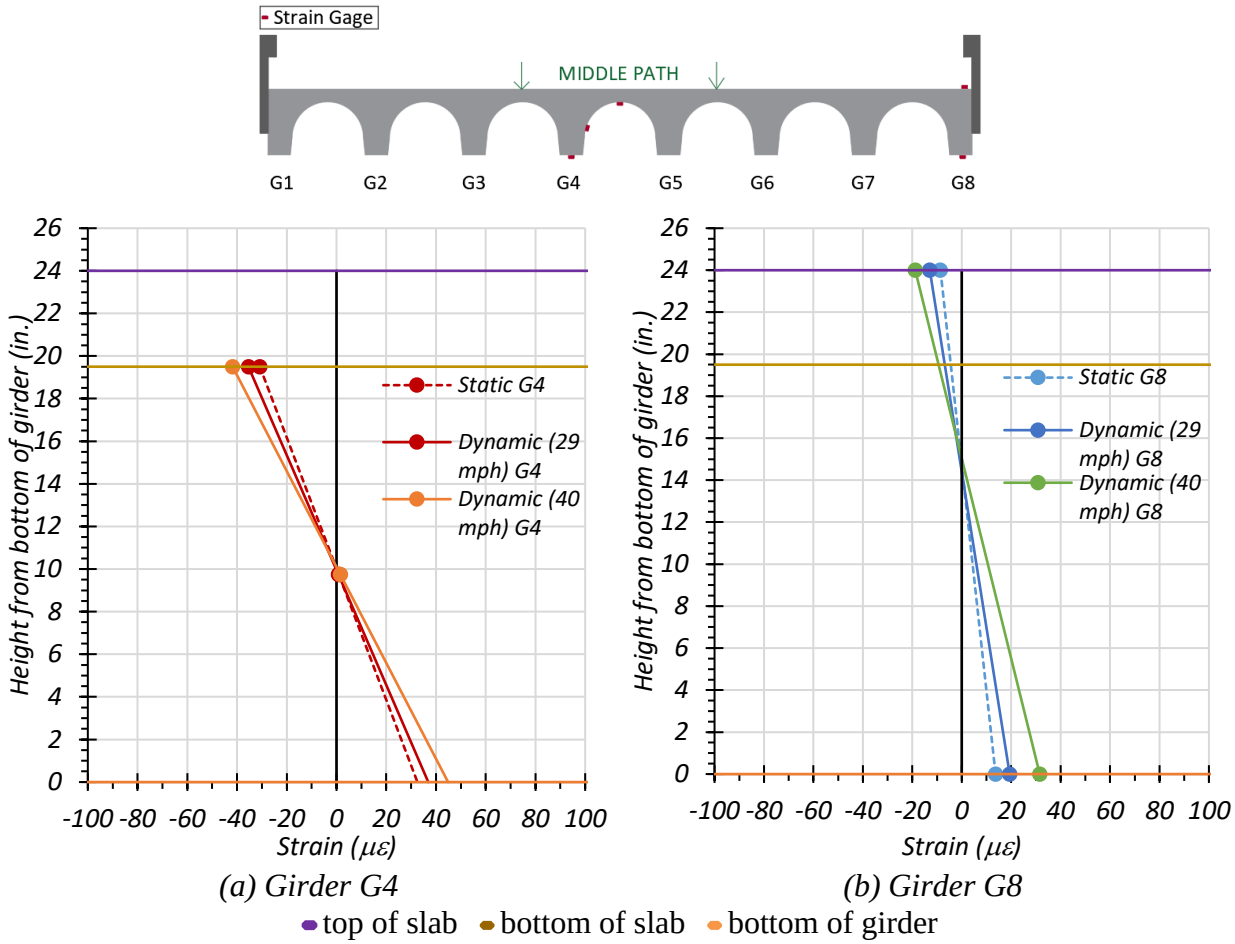

Figure 8.23. Maximum Strains for Static and Dynamic Tests for Middle Path Loading

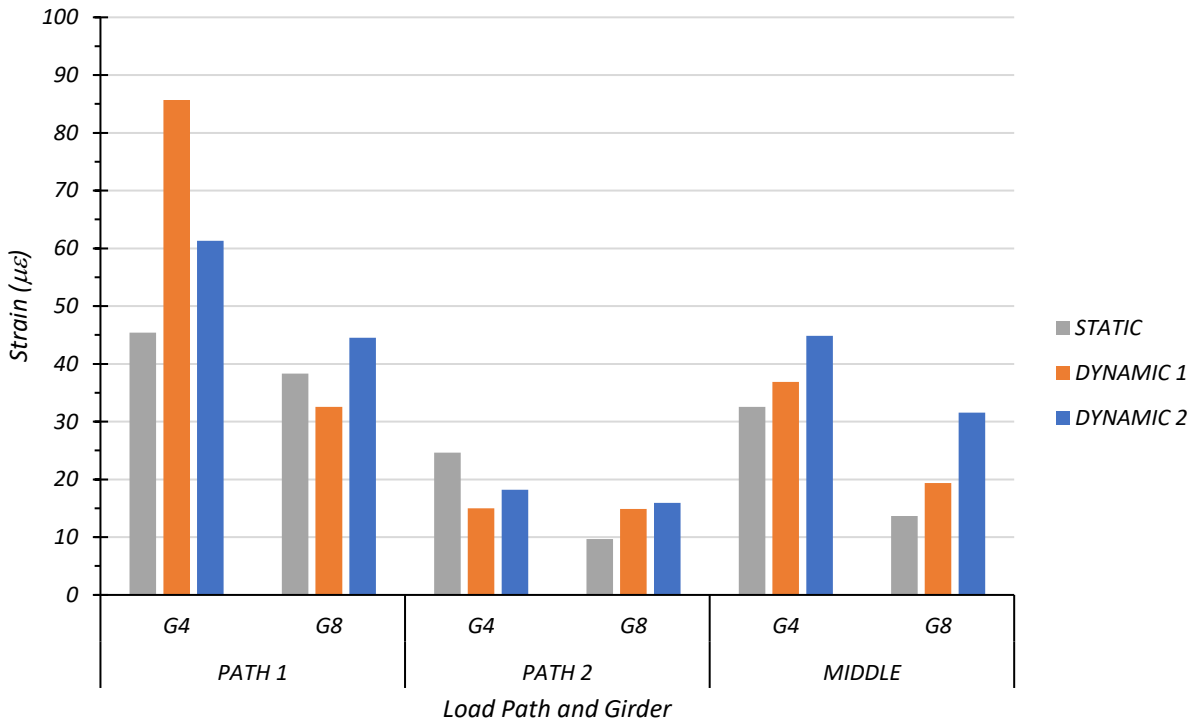

Note:

- *Path 1: Dynamic 1 = 31 mph, Dynamic 2 = 41 mph*
- *Path 2: Dynamic 1 = 30 mph, Dynamic 2 = 40 mph*
- *Middle Path: Dynamic 1 = 29 mph, Dynamic 2 = 40 mph*

Figure 8.24. Comparison of Maximum Strains for Static and Dynamic Tests

For Bridge CM-5, the average dynamic impact factor for the exterior girder was 49 percent, while the one for the interior girder was 18 percent. These figures were calculated based on the maximum bottom strains recorded during testing. *AASHTO Standard Specifications* call for a dynamic impact factor of 30 percent, and *AASHTO LRFD Specifications* stipulate this factor to be 33 percent. Thus, for Bridge CM-5, the dynamic impact factor is higher than the one specified by AASHTO for the exterior girders. However, it is lower for the interior girders.

Maximum Girder Deflections. Dynamic amplification can also be obtained by comparing the dynamic deflections with the static deflections. Deflection time history plots for each girder for static tests and Dynamic 1 and Dynamic 2 tests are provided in Figure 8.25, Figure 8.26, and Figure 8.27 for Path 1, Path 2, and the Middle Path, respectively. It should be noted that the static data were recorded for a shorter time period than the two dynamic data. The maximum deflection for each girder under static and dynamic tests for Path 1, Path 2, and the Middle path is tabulated

in Table 8.12. Figure 8.28 compares the dynamic deflections for each girder with the static deflections. Figure 8.29 shows the measured deflections for each dynamic load case as a ratio to the stop location deflection.

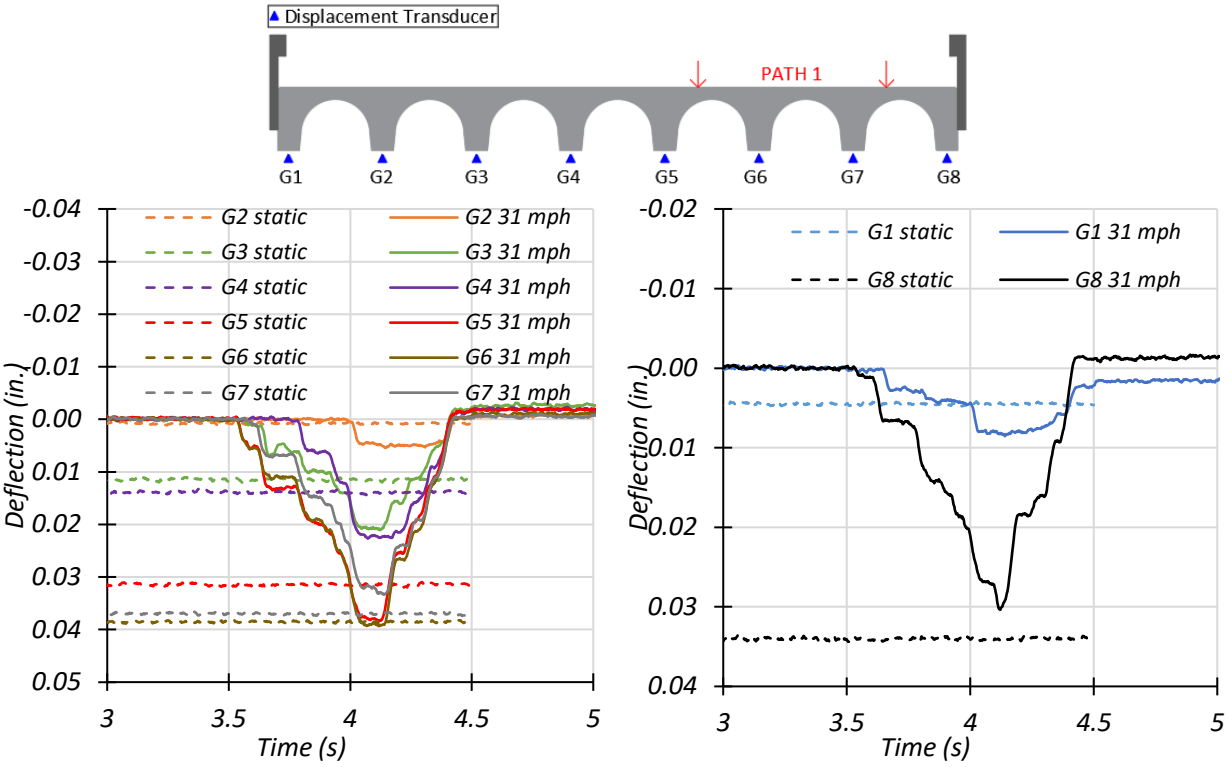

(a) Interior Girder Deflection Time Histories – Dynamic (31 mph)

(b) Exterior Girder Deflection Time Histories – Dynamic (31 mph)

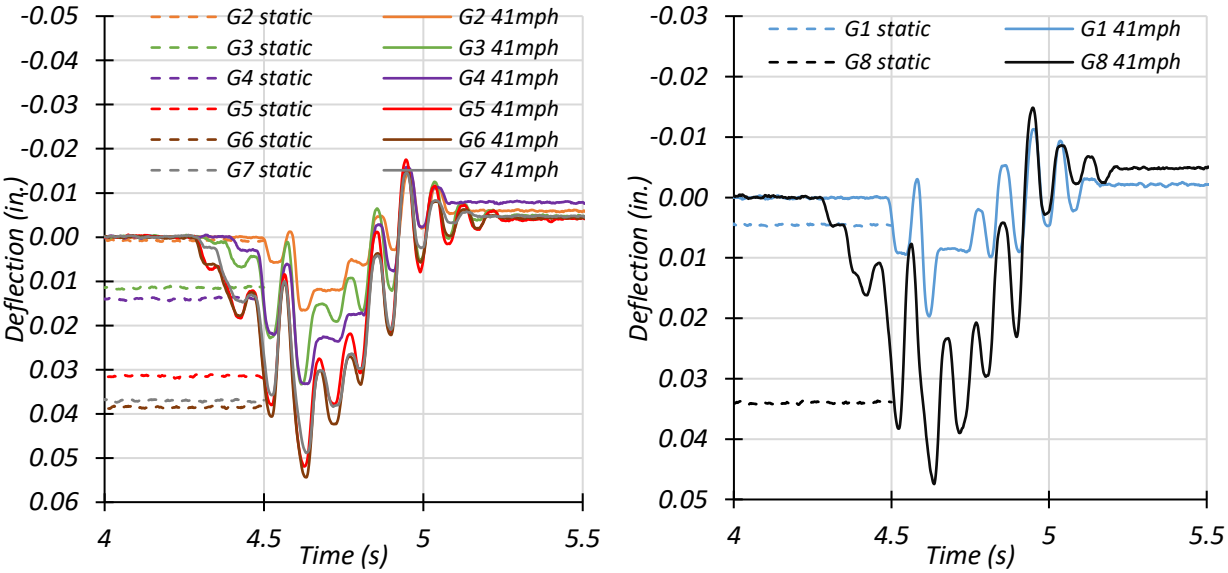

(c) Interior Girder Deflection Time Histories – Dynamic (41 mph)

(d) Exterior Girder Deflection Time Histories – Dynamic (41 mph)

Figure 8.25. Midspan Deflections for Static and Dynamic Tests for Path 1 Loading

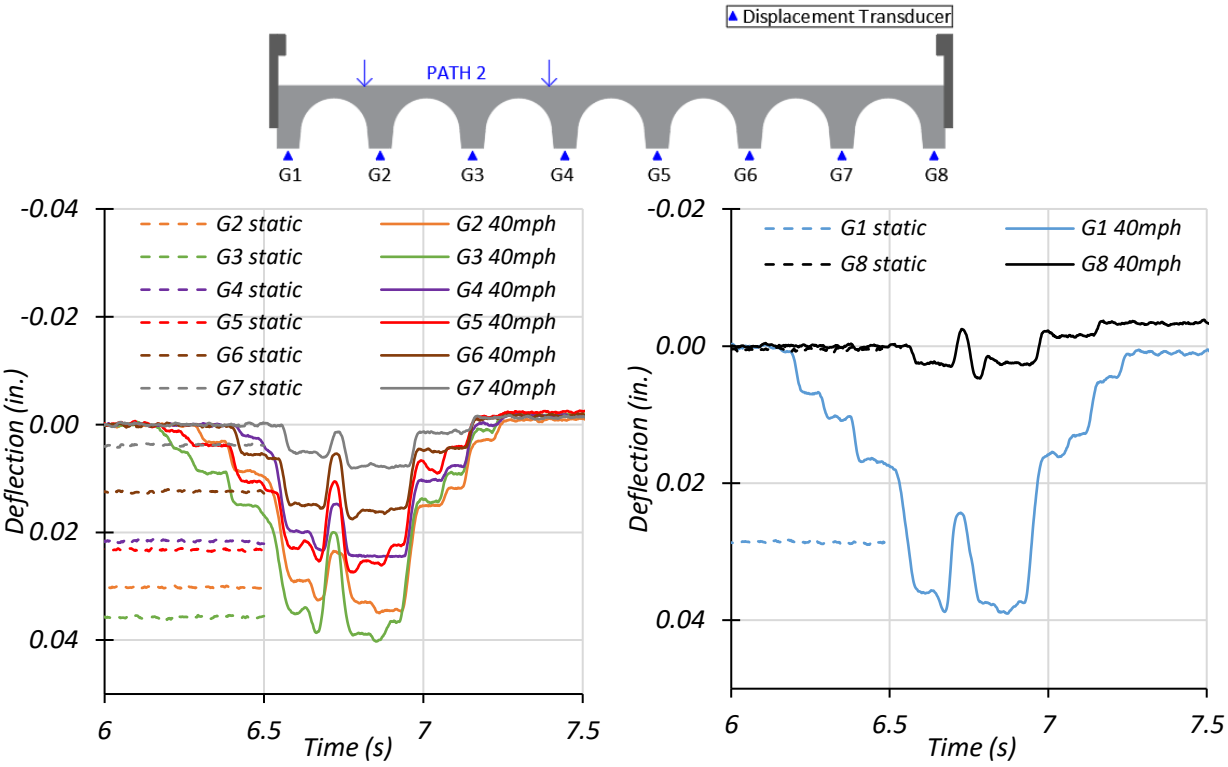

(a) Interior Girder Deflection Time Histories – Dynamic (30 mph)

(b) Exterior Girder Deflection Time Histories – Dynamic (30 mph)

(c) Interior Girder Deflection Time Histories – Dynamic (40 mph)

(d) Exterior Girder Deflection Time Histories – Dynamic (40 mph)

Figure 8.26. Midspan Deflections for Static and Dynamic Tests for Path 2 Loading

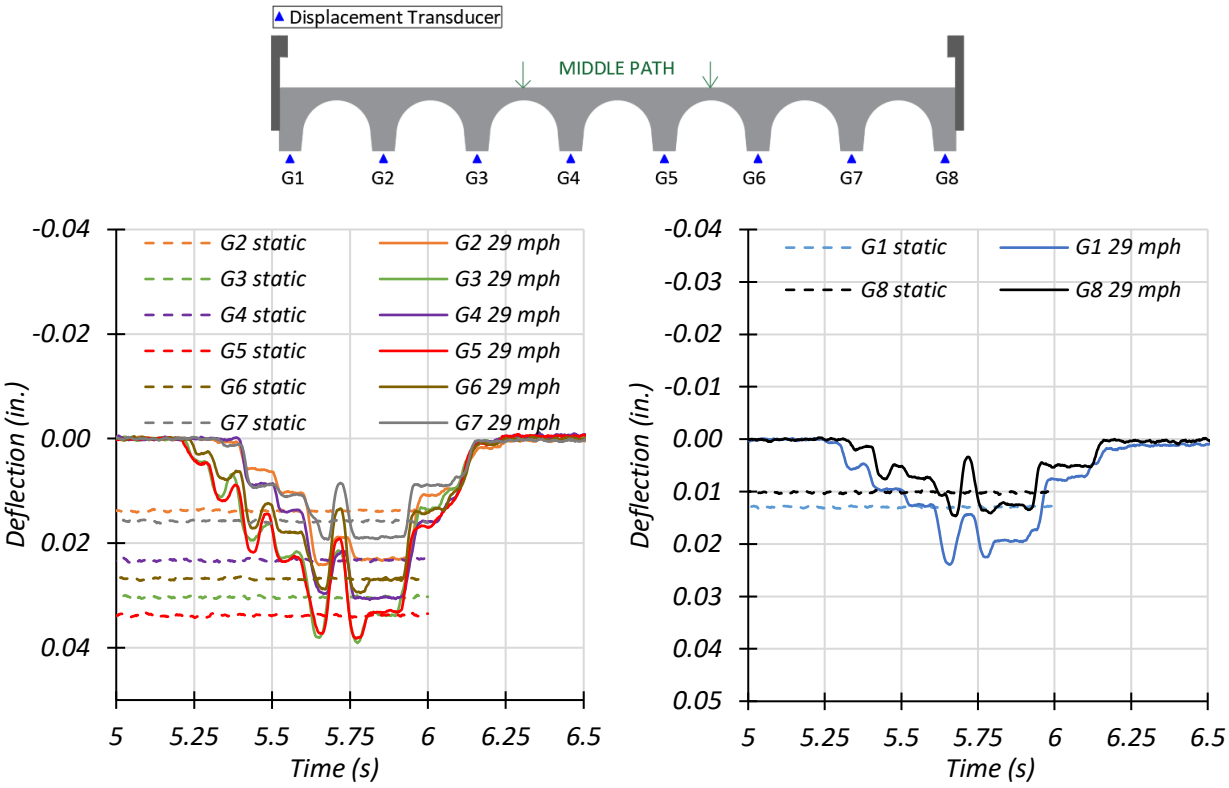

(a) (a) Interior Girder Deflection Time Histories – Dynamic (29 mph)

(b) Exterior Girder Deflection Time Histories – Dynamic (29 mph)

(c) Interior Girder Deflection Time Histories – Dynamic (40 mph)

(d) Exterior Girder Deflection Time Histories – Dynamic (40 mph)

Figure 8.27. Midspan Deflections for Static and Dynamic Tests for Middle Loading

Table 8.12. Maximum Midspan Deflections for Static and Dynamic Tests

	Loading	G1	G2	G3	G4	G5	G6	G7	G8
Girder Displacement (in.)	Path 1 Static	0.006	0.002	0.014	0.016	0.034	0.041	0.040	0.037
	Path 1 Dynamic (31 mph)	0.010	0.006	0.022	0.024	0.039	0.040	0.034	0.031
	Path 1 Dynamic (41 mph)	0.018	0.017	0.032	0.033	0.052	0.055	0.049	0.048
	Max. Path 1 Amplification						35%		30%
Girder Displacement (in.)	Path 2 Static	0.030	0.032	0.038	0.024	0.026	0.015	0.006	0.003
	Path 2 Dynamic (30 mph)	0.040	0.036	0.041	0.025	0.028	0.018	0.009	0.005
	Path 2 Dynamic (40 mph)	0.046	0.042	0.049	0.031	0.031	0.020	0.011	0.009
	Max. Path 2 Amplification	50%		28%					
Girder Displacement (in.)	Middle Static	0.015	0.016	0.033	0.026	0.036	0.030	0.018	0.013
	Middle Dynamic (29 mph)	0.025	0.025	0.040	0.032	0.039	0.030	0.020	0.015
	Middle Dynamic (40 mph)	0.021	0.020	0.037	0.032	0.044	0.041	0.031	0.027
	Max. Middle Path Amplification	62%				22%			

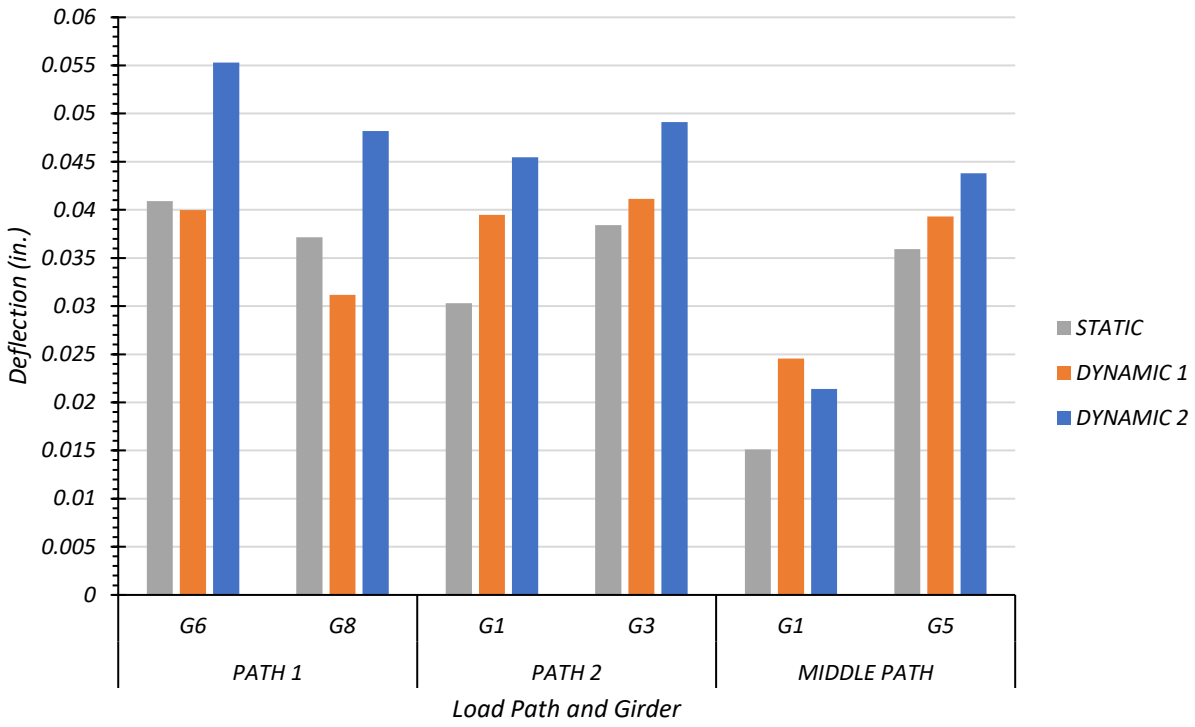

Note:

- *Path 1: Dynamic 1 = 31 mph, Dynamic 2 = 41 mph*
- *Path 2: Dynamic 1 = 30 mph, Dynamic 2 = 40 mph*
- *Middle Path: Dynamic 1 = 29 mph, Dynamic 2 = 40 mph*

Figure 8.28. Static and Dynamic Deflection Comparison for Critical Girders

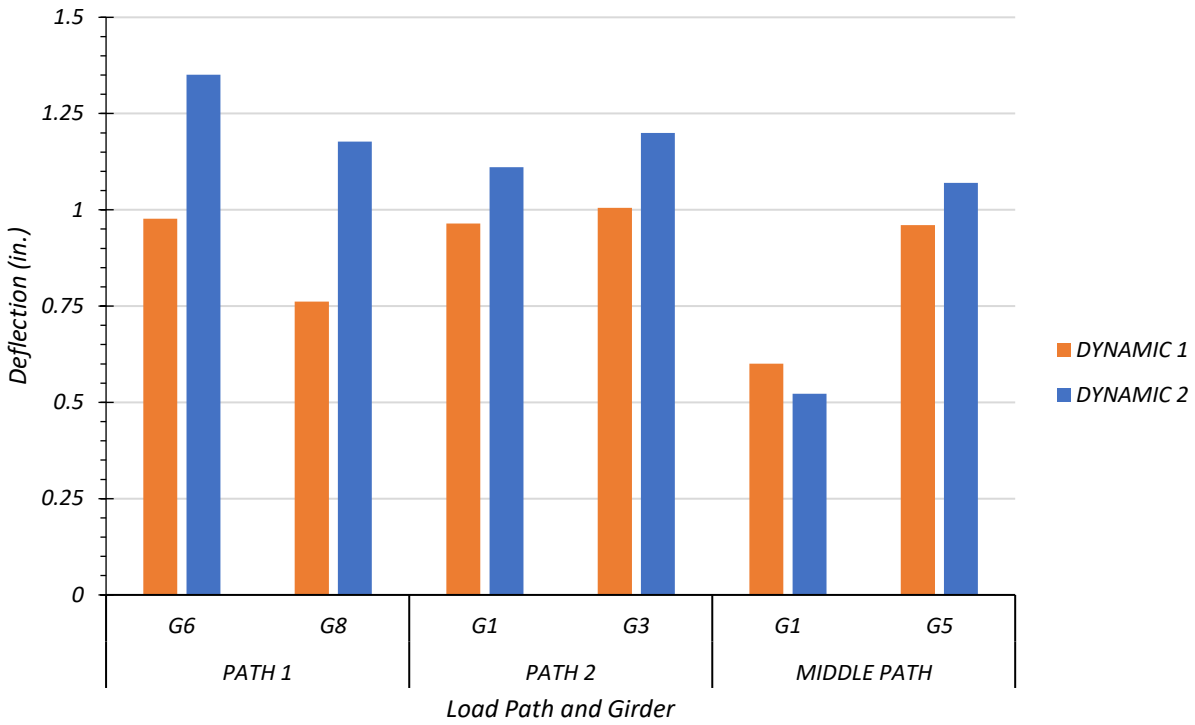

Note:

- *Path 1: Dynamic 1 = 31 mph, Dynamic 2 = 41 mph*
- *Path 2: Dynamic 1 = 30 mph, Dynamic 2 = 40 mph*
- *Middle Path: Dynamic 1 = 29 mph, Dynamic 2 = 40 mph*

Figure 8.29. Maximum Midspan Dynamic Deflections to Static Deflections Ratios

For Bridge CM-5, the average dynamic impact factor for the exterior girder was 47 percent, while the one for the interior girder was 28 percent. These measurements were determined based on the maximum deflections recorded during testing. *AASHTO Standard Specifications* call for a dynamic impact factor of 30 percent, and *AASHTO LRFD Specifications* stipulate this factor to be 33 percent. Thus, for Bridge CM-5, the dynamic impact factor is higher than the one specified by AASHTO for the exterior girders. However, it is lower for the interior girders.

The maximum deflection obtained for an interior girder during the static test, Dynamic 1 test, and Dynamic 2 test along Path 1 was for Girder G6. The deflection reduced by 2 percent for Dynamic 1 loading and increased by 35 percent for Dynamic 2 loading in comparison to the static test results. The maximum deflection obtained for an exterior girder during the static test, Dynamic 1 test, and Dynamic 2 test along Path 1 was for Girder G8. The deflection reduced by 16 percent

for Dynamic 1 loading and increased by 35 percent for Dynamic 2 loading in comparison to the static test results.

The maximum deflection obtained for an interior girder during the static test, Dynamic 1 test, and Dynamic 2 test along Path 2 was for Girder 3. The deflection increased by 7 percent for Dynamic 1 loading and by 28 percent for Dynamic 2 loading in comparison to the static test results. The maximum deflection obtained for an exterior girder during the static test, Dynamic 1 test, and Dynamic 2 test along Path 2 was for Girder G1. The deflection increased by 30 percent for Dynamic 1 loading and by 50 percent for Dynamic 2 loading in comparison to the static test results.

The maximum deflection obtained for an interior girder during the static test, Dynamic 1 test, and Dynamic 2 test along the Middle Path was for Girder G5. The deflection increased by 9 percent for Dynamic 1 loading and by 22 percent for Dynamic 2 loading in comparison to the static test results. The maximum deflection obtained for an exterior girder during the static test, Dynamic 1 test, and Dynamic 2 test along the Middle Path was for Girder G8. The deflection increased by 21 percent for Dynamic 1 loading and by 115 percent for Dynamic 2 loading in comparison to the static test results.

*8.6.2.2 **Dynamic Characteristics of Bridge***

The data recorded by the accelerometers for the dynamic tests and impact (sledgehammer tests) were filtered using a low pass filter and analyzed to determine the dynamic characteristics of the bridge. By using the FFT approach, the first three natural frequencies of the bridge were determined to be 11.84 Hz, 16.60 Hz, and 25.15 Hz. The mode shape across the longitudinal and transverse section for each natural frequency was developed using the corresponding amplitude and phase angle for each accelerometer. Because the bridge has an even number of girders, the accelerometer common to both the longitudinal section and transverse section is located at Girder G4, 15 ft longitudinally and 12.44 ft transversely. The mode shape along the longitudinal section and transverse section for the first natural frequency is shown in Figure 8.30. Figure 8.31 provides the mode shape along the longitudinal section and transverse section for the second natural frequency. The mode shape along the longitudinal section and transverse section for the third natural frequency is shown in Figure 8.32.

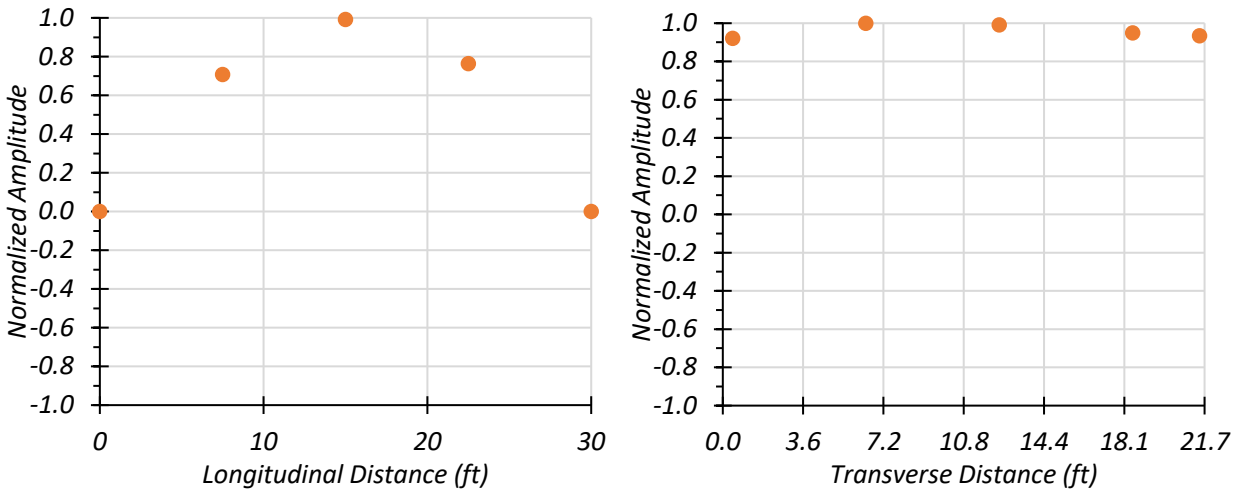

(a) Longitudinal Section *(b) Transverse Section*

Figure 8.30. Measured Mode Shape 1 for Bridge CM-5 (f_1 = 11.84 Hz)

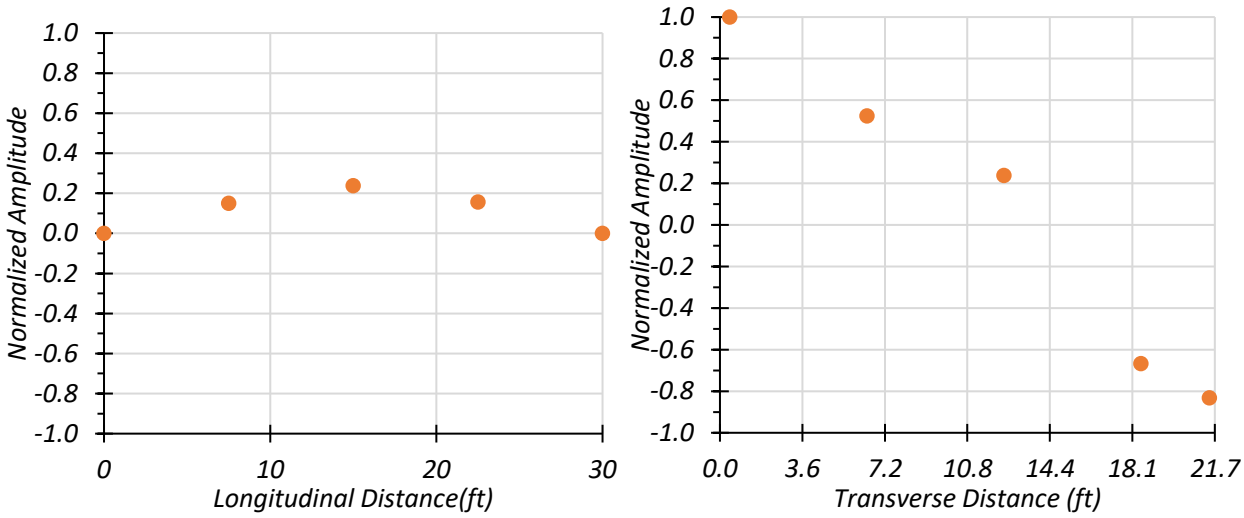

(a) Longitudinal Section *(b) Transverse Section*

Figure 8.31. Measured Mode Shape 2 for Bridge CM-5 (f_2 = 16.60 Hz)

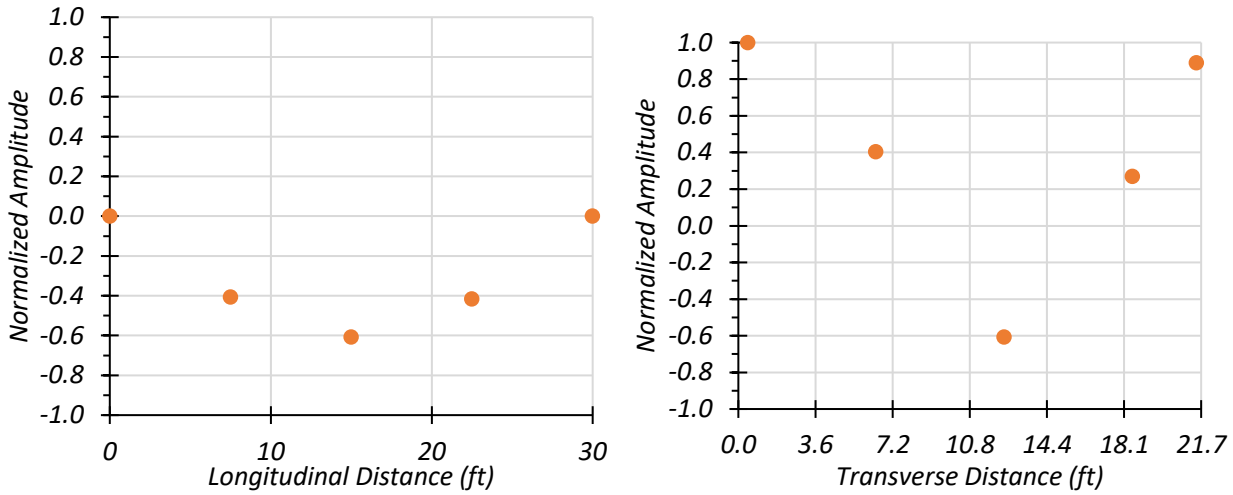

(a) Longitudinal Section *(b) Transverse Section*

Figure 8.32. Measured Mode Shape 3 for Bridge CM-5 (f_3 = 25.15 Hz)

8.6.3 Computer Vision

The possibility of determining bridge deflection from video recordings of the bridge during a truck pass was evaluated during the testing of Bridge CM-5. Two cameras, a Sony HDR-CX405 video camera and an iPhone 8, were mounted on tripods and set up on either side of the bridge. These cameras were used to record the bridge during each test. The video resolution of the video camera was 1440 pixels by 1080 pixels, while that of the iPhone was 3840 pixels by 2160 pixels. Two images of the bridge as it is unloaded and loaded were extracted from the videos using a computer algorithm. The displacement measurement between the images was obtained using an image analysis algorithm comparing one sub-window of the unloaded bridge image with several sub-windows of the loaded bridge image. The window size used in all these tests were 50 pixels by 50 pixels, and its location on the image was selected such that it covered an area of high contrast. All signals were filtered to remove the noise associated with the data, such as unintended vibration of the cameras. Depending on the level of noise, a high pass, a low pass, or a band pass filter may be used.

The three tests for which computer vision was performed include the following: (1) Test 2—Path 1 Crawl Test, (2) Test 3—Path 1 Dynamic at 31 mph, and (3) Test 7—Path 1 Dynamic at 30 mph.

The time history plot of deflection obtained from the computer vision analysis was plotted along with the corresponding deflection obtained from the string potentiometer to compare the results. Figure 8.33 shows the time history plot for exterior Girder G8 during the crawl test along Path 1. The image data obtained from the iPhone camera were filtered using a low pass filter to remove any noise in the data due to vibration of the bridge during testing. The maximum deflection obtained from the computer vision analysis was 0.0372 in., while the string potentiometer recorded the maximum deflection as 0.0361 in. The deflection obtained from computer vision was 5 percent lower than the deflection obtained from the string potentiometer.

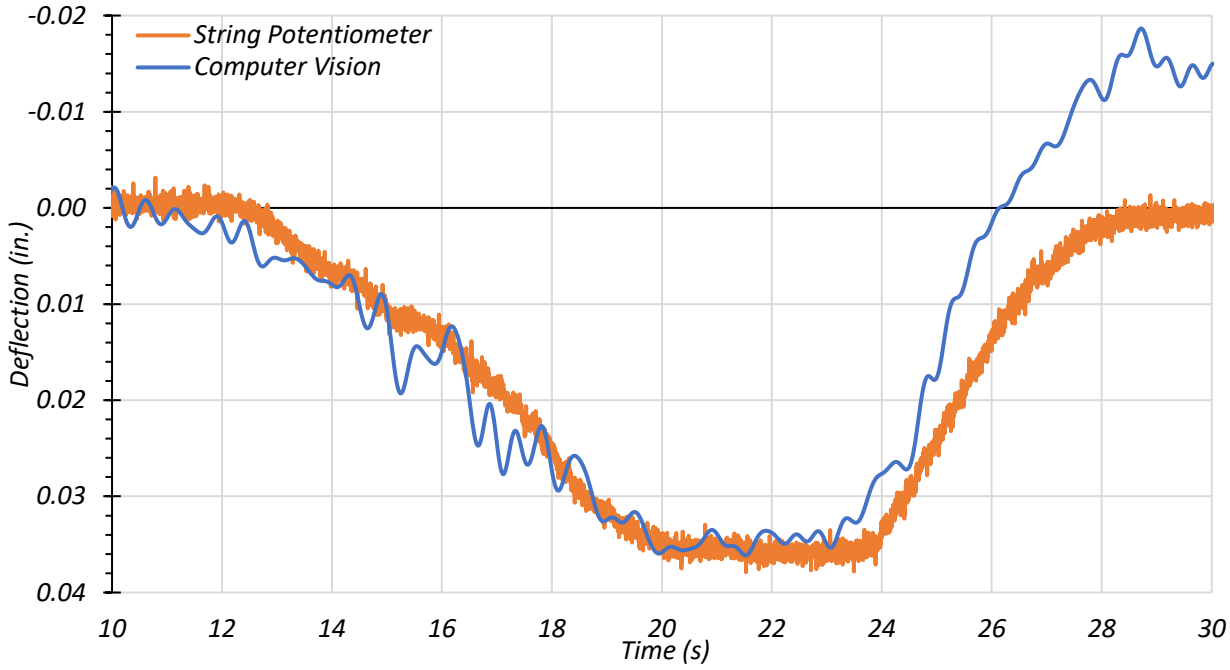

Figure 8.33. Girder G8 Midspan Deflections for Path 1 Crawl Test

The time history deflection plot for Girder G8 during the dynamic test at 31 mph along Path 1 is presented in Figure 8.34. A similar low pass filter was also applied to this image data obtained from the iPhone camera. The maximum deflection obtained from the computer vision analysis was 0.0370 in., while the string potentiometer recorded the maximum deflection as 0.0312 in. The deflection obtained from computer vision was 19 percent higher than that the deflection obtained from the string potentiometer.

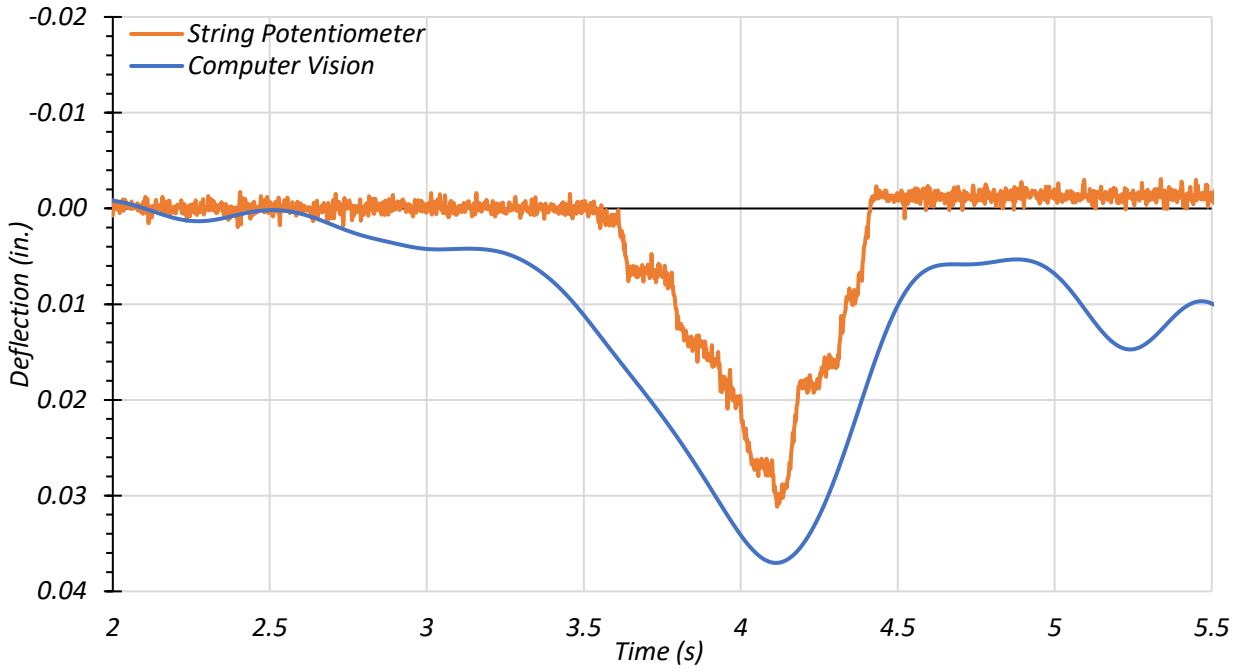

Figure 8.34. Girder G8 Midspan Deflections for Path 1 Dynamic Test at 31 mph

Figure 8.35 shows the time history plot for exterior Girder G1 during the dynamic test at 30 mph along Path 2. For this test, the image data obtained from the video camera were filtered using a low pass filter. The maximum deflection obtained from the computer vision analysis was 0.0376 in., while the string potentiometer recorded the maximum deflection as 0.0395 in. The deflection obtained from computer vision was 5 percent lower than the deflection obtained from the string potentiometer.

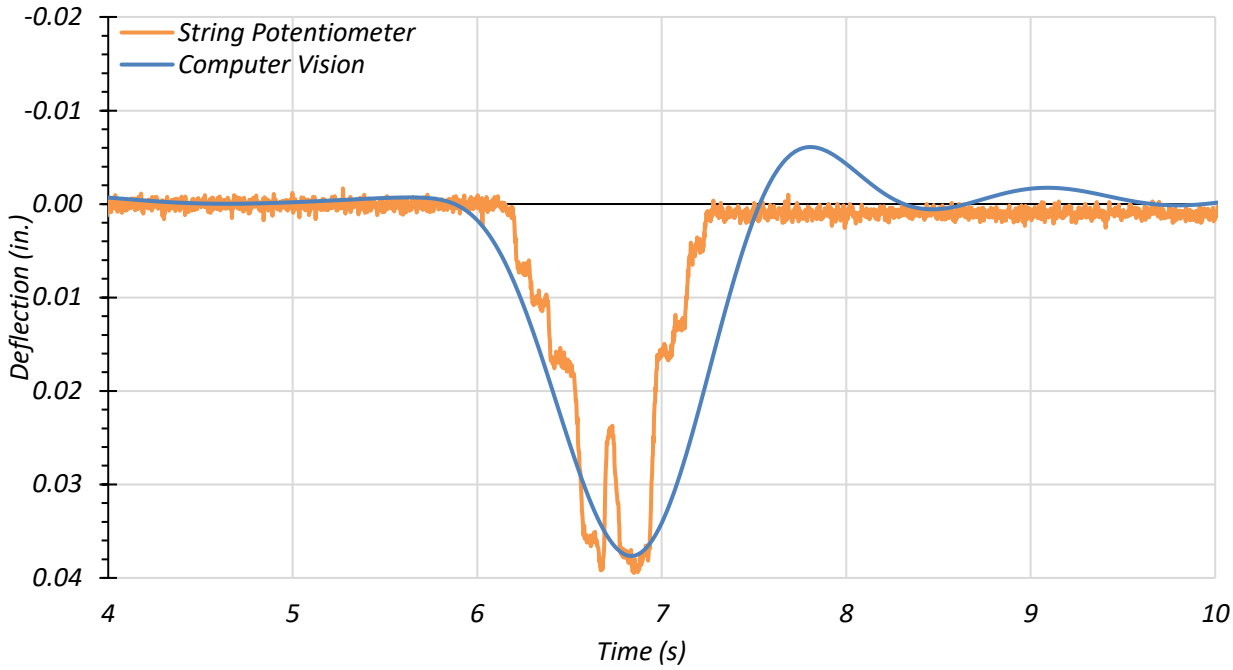

Figure 8.35. Girder G1 Midspan Deflections for Path 2 Dynamic Test at 30 mph

8.7 FEM MODEL UPDATE AND CALIBRATION

8.7.1 General

The original FEM model for Bridge CM-5 was revised to determine appropriate modeling parameters based on comparison to test data. The FEM model update was carried out in two steps: (1) a material property update based on NDE tests, and (2) an end fixity update based on model calibration.

8.7.2 Updated FEM Model

The concrete compressive strength for Bridge CM-5 was taken as 7 ksi based on the NDE tests, as explained in Section 8.3.2. This measurement is higher than the initial f_c' of 4 ksi. The MOE for Bridge CM-5 was increased by 10 percent because (1) the tangent stiffness is higher than the secant stiffness, whereas MOE is calculated based on secant stiffness; and (2) empirical equations typically provide lower bound values in order to be conservative. The MOE for concrete increased from 3834 ksi to 5579 ksi. The FEM model was updated to incorporate the measured f_c' and the measured bridge geometric information noted in Section 8.3. The pan girder bottom width was

reduced from 8.35in. to 7in. The boundary conditions of the updated model were kept the same as the initial FEM model in which both ends of each girder were modeled with roller supports. The results obtained from this updated FEM model are compared with the experimental results in the following sections.

Table 8.13. Selected FEM Results for Updated FEM Model

Model	Modal Frequency (Hz)		Midspan Deflection (in.)		Strain (με)									
					West Top		West Bot		Mid Top	Mid Bot	East Top		East Bot	
	1st	2nd	G4	G8	G4	G8	G4	G8	G8	G8	G4	G8	G4	G8
Updated	11.7	14.8	0.05	0.06	−3.7	−7.6	0	−0.4	−44.2	68.3	−3.6	−7.3	0	17.9
Field Test	11.8	16.6	0.04	0.03	–	−3.8	−11.2	−4.8	−33.0	38.3	−3.2	−5.2	−5.7	3.2

8.7.3 Model Calibration Process

The updated FEM model for Bridge CM-5 was calibrated for cracked concrete properties and end fixity at the abutments. The model developed from this process can capture the true behavior of the bridge more accurately.

During the installation of the instrumentation, it was noted that the interior pan girders were cracked in the web. The updated FEM model was calibrated to incorporate cracked concrete properties by (1) reducing the MOE, and (2) using non-linear material properties. The MOE was reduced by a factor equal to the ratio of the cracked moment of inertia and gross moment of inertia of the section. This ratio was calculated to be 0.386 for the exterior girder and 0.336 for the interior girder. Three cases were considered for the reduced MOE approach. The first case used the respective reduced MOE for the interior girders and exterior girders with simply supported end conditions. The second case used the same properties as the first except with pin-pin end conditions. The third case used reduced MOE for the interior girders while using the gross MOE for the exterior girders for pin-pin end conditions. Another procedure used to consider the cracked behavior of concrete was the nonlinear Mander model for concrete. Two different values for concrete tensile strength were considered: 10 percent of measured concrete compressive strength

and 1 percent of measured concrete compressive strength. These analyses were carried out for simply supported end conditions, pin-pin end conditions and roller-roller end conditions.

Four input parameters were identified for calibrating the above material-calibrated FEM model of Bridge CM-5 to determine the true end fixities. These parameters were (1) the west end of all interior girders, (2) the west end of both exterior girders, (3) the east end of all interior girders, and (4) the east end of both exterior girders. The vertical translational degree of freedom was fully restrained for all girders. Horizontal springs were introduced at the bottom of the girders and at nodes at the top of the concrete slab. The horizontal spring stiffness was modified to provide partial fixities at the ends. Roller supports were considered to be the lower bound for the horizontal spring stiffness, and pin supports were the upper bound. The corresponding upper and lower bound spring stiffnesses were determined. The effect of each input parameter on the analysis results was studied by gradually varying one parameter at a time. The results from this parametric study are presented in the following sections.

8.7.4 Calibrated FEM Model Results

In this section, the influence on the analysis results of changing each input parameter identified earlier is presented. The calibration of the model was carried out based on experimental results obtained from the static test carried out on Bridge CM-5, which are provided in Table 8.14. It should be noted that Girder G8 results come from the Path 1 stop location test and that Girder G4 results come from the Middle Path stop location test.

Table 8.14. Experimental Results for Calibration of Bridge CM-5

Modal Frequency (Hz)		Midspan Deflection (in.)		Strain (με)									
				West Top		West Bot		Mid Top	Mid Bot	East Top		East Bot	
1st Mode	2nd Mode	G4	G8	G4	G8	G4	G8	G8	G8	G4	G8	G4	G8
11.8	16.6	0.04	0.03	–	−3.8	−11.2	−4.8	−33.0	38.3	−3.2	−5.2	−5.7	3.2

8.7.4.1 Modulus of Elasticity

The MOE was modified to account for the cracks observed in the pan girders. The end supports were also modified to study the cumulative effect. These results are summarized and presented in Table 8.15.

Table 8.15. Effect of Modulus of Elasticity Value on Selected FEM Results

Case	West end Fixity	East end Fixity	Modal Frequency (Hz)		Midspan Deflection (in.)		West Curvature		East Curvature	
			1st Mode	2nd Mode	G4	G8	G4	G8	G4	G8
Test			11.8	16.6	0.04	0.03	–	0.36E-06	0.10E-06	0.35E-06
1(a)	Pin	Roller	7.13	12.86	0.15	0.18	2.10E-06	0.53E-06	2.00E-06	0.47E-06
1(b)	Pin	Pin	10.99	12.17	0.06	0.09	0.40E-06	1.07E-06	0.44E-06	0.96E-06
1(c)	Pin	Pin	10.99	12.17	0.06	0.09	5.89E-06	6.23E-06	5.61E-06	1.25E-06
2(a)	Pin	Pin	18.96	21.00	0.02	0.03	9.22E-06	6.23E-06	2.67E-06	1.30E-06
2(b)	Pin	Roller	12.30	22.19	0.04	0.06	1.54E-06	0.50E-06	1.44E-06	0.43E-06
2(c)	Roller	Roller	12.53	15.45	0.04	0.06	0.35E-06	0.36E-06	0.18E-06	0.32E-06
2(d)	Roller	Roller	12.53	15.45	0.04	0.06	0.20E-06	0.34E-06	0.18E-06	1.09E-06

Case 1(a) & 1(b): Both exterior and interior girders with reduced MOE
Case 1(c): Interior girders with reduced MOE, exterior girders with gross MOE
Case 2(a) – 2(c): Nonlinear Mander model for concrete with $f_t = 0.10f_c'$
Case 2(d): Nonlinear Mander model for concrete with $f_t = 0.01f_c'$

The nonlinear Mander model with $f_t = 0.01f_c'$ for concrete provided agreeable results to the experimental results. The following calibration was carried out using Case 2(d) listed in the table above.

*8.7.4.2 **West End Interior Girder Stiffness Spring***

The fixity at the west end of the interior girder was determined by changing the support to a roller (only vertical translation restrained) and a pin (all three translations restrained). The second modal frequency, the top and bottom strain at the midspan of Girder G8 and the bottom strain at the east end of Girder G8, for the roller support is slightly closer to the test results. Thus, the boundary condition for the west end of the interior girders was found to be closer to the roller support, as shown in Table 8.16.

Table 8.16. Effect of West End Interior Girder Boundary Condition on Selected FEM Results

Boundary condition	Modal Frequency (Hz)		Midspan Deflection (in.)		Strain (με)									
					West Top		West Bot		Mid Top	Mid Bot	East Top		East Bot	
	1st	2nd	G4	G8	G4	G8	G4	G8	G8	G8	G4	G8	G4	G8
Test	11.8	16.6	0.04	0.03	–	−3.8	−11.2	−4.8	−33.0	38.3	−3.2	−5.2	−5.7	3.2
Pin	12.3	18.5	0.04	0.06	−1.8	−7.9	−4.1	0.0	−44.3	70.2	−3.0	−7.6	0.0	19.0
Roller	12.5	15.5	0.04	0.06	−3.8	−7.9	0.0	0.0	−42.8	68.7	−3.5	−7.8	0.0	18.6

*8.7.4.3 **West End Exterior Girder Stiffness Spring***

The fixity at the west end of the exterior girder was determined by changing the support to roller (only vertical translation restrained) and pin (all three translations restrained). The first modal frequency, the second modal frequency, the top and bottom strain at the midspan of Girder G8, and the bottom strain at the east end of Girder G8 for the pin support are slightly closer to the test results. Therefore, the boundary condition for the west end of the exterior girders was found to be closer to the pin support, as shown in Table 8.17.

Table 8.17. Effect of West End Exterior Girder Boundary Condition on Selected FEM Results

Boundary condition	Modal Frequency (Hz)		Midspan Deflection (in.)		Strain (με)									
					West Top		West Bot		Mid Top	Mid Bot	East Top		East Bot	
	1st	2nd	G4	G8	G4	G8	G4	G8	G8	G8	G4	G8	G4	G8
Test	11.8	16.6	0.04	0.03	–	−3.8	−11.2	−4.8	−33.0	38.3	−3.2	−5.2	−5.7	3.2
Pin	12.3	16.7	0.04	0.06	−3.7	−8.1	0.0	0.0	−43.9	71.3	−3.5	−7.7	0.0	18.8
Roller	12.5	15.5	0.04	0.06	−3.8	−7.9	0.0	0.0	−42.8	68.7	−3.5	−7.8	0.0	18.6

*8.7.4.4 **East End Interior Girder Stiffness Spring***

The fixity at the east end of the interior girder was determined by changing the support to roller (only vertical translation restrained) and pin (all three translations restrained). The second modal frequency, the top and bottom strain at the midspan of Girder G8, and the bottom strain at the east end of Girder G8 for the roller support are slightly closer to the test results. Consequently, the boundary condition for the east end of the interior girders was found to be closer to the roller support, as shown in Table 8.18.

Table 8.18. Effect of East End Interior Girder Boundary Condition on Selected FEM Results

Boundary condition	Modal Frequency (Hz)		Midspan Deflection (in.)		Strain (με)									
					West Top		West Bot		Mid Top	Mid Bot	East Top		East Bottom	
	1st	2nd	G4	G8	G4	G8	G4	G8	G8	G8	G4	G8	G4	G8
Test	11.8	16.6	0.04	0.03	–	−3.8	−11.2	−4.8	−33.0	38.3	−3.2	−5.2	−5.7	3.2
Pin	12.3	18.5	0.04	0.06	−3.8	−7.9	0.0	0.0	−43.9	71.1	−2.3	−7.4	−4.0	18.4
Roller	12.5	15.5	0.04	0.06	−3.8	−7.9	0.0	0.0	−42.8	68.7	−3.5	−7.8	-0.0	18.6

*8.7.4.5 **East End Exterior Girder Stiffness Spring***

The fixity at the east end of the exterior girder was determined by changing the support to roller (only vertical translation restrained) and pin (all three translations restrained). The first modal frequency, the second modal frequency, and the top and bottom strain at the midspan of Girder G8 for the pin support are slightly closer to the test results. Thus, the boundary condition for the east end of the exterior girders was found to be closer to the roller support, as shown in Table 8.19.

Table 8.19. Effect of East End Exterior Girder Boundary Condition on Selected FEM Results

Boundary condition	Modal Frequency (Hz)		Midspan Deflection (in.)		Strain (με)									
					West Top		West Bot		Mid Top	Mid Bot	East Top		East Bot	
	1st	2nd	G4	G8	G4	G8	G4	G8	G8	G8	G4	G8	G4	G8
Test	11.8	16.6	0.04	0.03	–	−3.8	−11.2	−4.8	−33.0	38.3	−3.2	−5.2	−5.7	3.2
Pin	12.3	16.7	0.04	0.06	−3.9	−8.0	−0.1	0.0	−43.2	71.5	−3.4	−7.6	−0.0	20.1
Roller	12.5	15.5	0.04	0.06	−3.8	−7.9	0.0	0.0	−42.8	68.7	−3.5	−7.8	−0.0	18.6

*8.7.4.6 **Final Calibration***

The individual parametric studies suggested that both the west and east ends of the exterior and interior girders are similar to a pin support. The final model calibration was initiated with these end fixities. Each input parameter was gradually adjusted till the FEM results were close to the experimental results. During calibration, horizontal stiffness in the transverse direction was also introduced at the supports to ensure better match with the test results. The final calibration model uses a spring stiffness of 500 kip/in./in. for the west end of interior girders, 400 kip/in./in. for the west end of exterior girders, 400 kip/in./in. for the east end of interior girders, and 5000 kip/in./in. for the east end of exterior girders. The final calibrated model parameters are presented in Table 8.20.

Table 8.20. Final Calibrated Model Parameters

Concrete Model	Stiffness Value (kip/in.)			
	West End Interior Girder	West End Exterior Girder	East End Interior Girder	East End Exterior Girder
Nonlinear Mander Model with $f_t = 0.01 f_c'$	500	400	400	5000

The calibrated model for Bridge CM-5, along with the end fixity springs, is shown in Figure 8.36. The results obtained from the calibrated FEM model and the test results are tabulated in Table 8.21. In the following sections, the results from this calibrated model are compared with the experimental results.

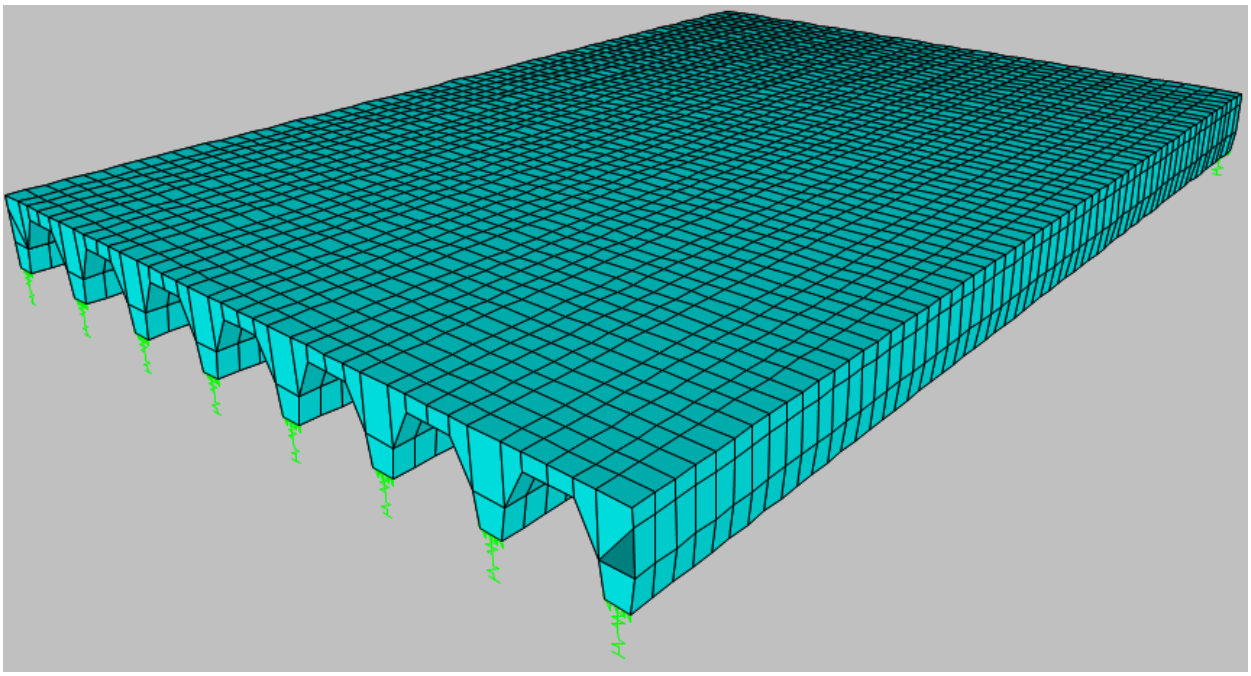

Figure 8.36. Calibrated FEM Model for Bridge CM-5

Table 8.21. Results of CM-5 Model Calibration

Results	Modal Frequency (Hz)		Midspan Deflection (in.)		Strain (με)								
					West Top		West Bot		Mid Bot	East Top		East Bot	
	1st	2nd	G4	G8	G4	G8	G4	G8	G8	G4	G8	G4	G8
Test	11.8	16.6	0.04	0.03	–	−3.8	−11.2	−4.8	38.3	−3.2	−5.2	−5.7	3.2
Calibrated FEM	13.7	16.9	0.04	0.05	−2.3	−6.3	−4.8	−5.5	58.1	−2.8	−5.2	−1.3	7.0

8.8 COMPARISON OF TEST RESULTS AND FEM PREDICTIONS

8.8.1 Strain Measurements

Interior Girder G4. The maximum top and bottom strains for interior Girder G4 under static tests along Path 1 are compared with the calibrated FEM results in Figure 8.37. For the stop location test, the strain profile along the west and east ends of Girder G4 is shown in Figure 8.37(a), and the strain profile at the midspan of Girder G4 is shown in Figure 8.37(b). For the crawl speed test, the strain profile along the west and east ends of Girder G4 is shown in Figure 8.37(c), and the strain profile at the midspan of Girder G4 is shown in Figure 8.37(d).

The maximum top and bottom strains for interior Girder G4 under static tests along Path 2 are compared with the calibrated FEM results in Figure 8.38. For the stop location test, the strain profile along the west and east ends of Girder G4 is shown in Figure 8.38(a), and the strain profile at the midspan of Girder G4 is shown in Figure 8.38(b). For the crawl speed test, the strain profile along the west and east ends of Girder G4 is shown in Figure 8.38(c), and the strain profile at the midspan of Girder G4 is shown in Figure 8.38(d).

The maximum top and bottom strains for interior Girder G4 under static tests along the Middle Path are compared with the calibrated FEM results in Figure 8.39. For the stop location test, the strain profile along the west and east ends of Girder G4 is shown in Figure 8.39(a), and the strain profile at the midspan of Girder G4 is shown in Figure 8.39(b). For the crawl speed test, the strain profile along the west and east ends of Girder G4 is shown in Figure 8.39(c), and the strain profile at the midspan of Girder G4 is shown in Figure 8.39(d).

It should be noted that the strain values obtained from the bottom strain gauge on Girder G4 were very high compared to both the updated and calibrated FEM model results. Additionally,

the top strain gauge for Girder G4 was not attached in line with the bottom strain gauge. The true strain at the top of Girder G4 may be different from the one obtained during testing. However, the updated and calibrated FEM strains at the midspan of Girder G4 were quite similar. The variation in the observed strain values at the ends and the midspan of Girder G4 may be attributed to noise in the strain data obtained from testing.

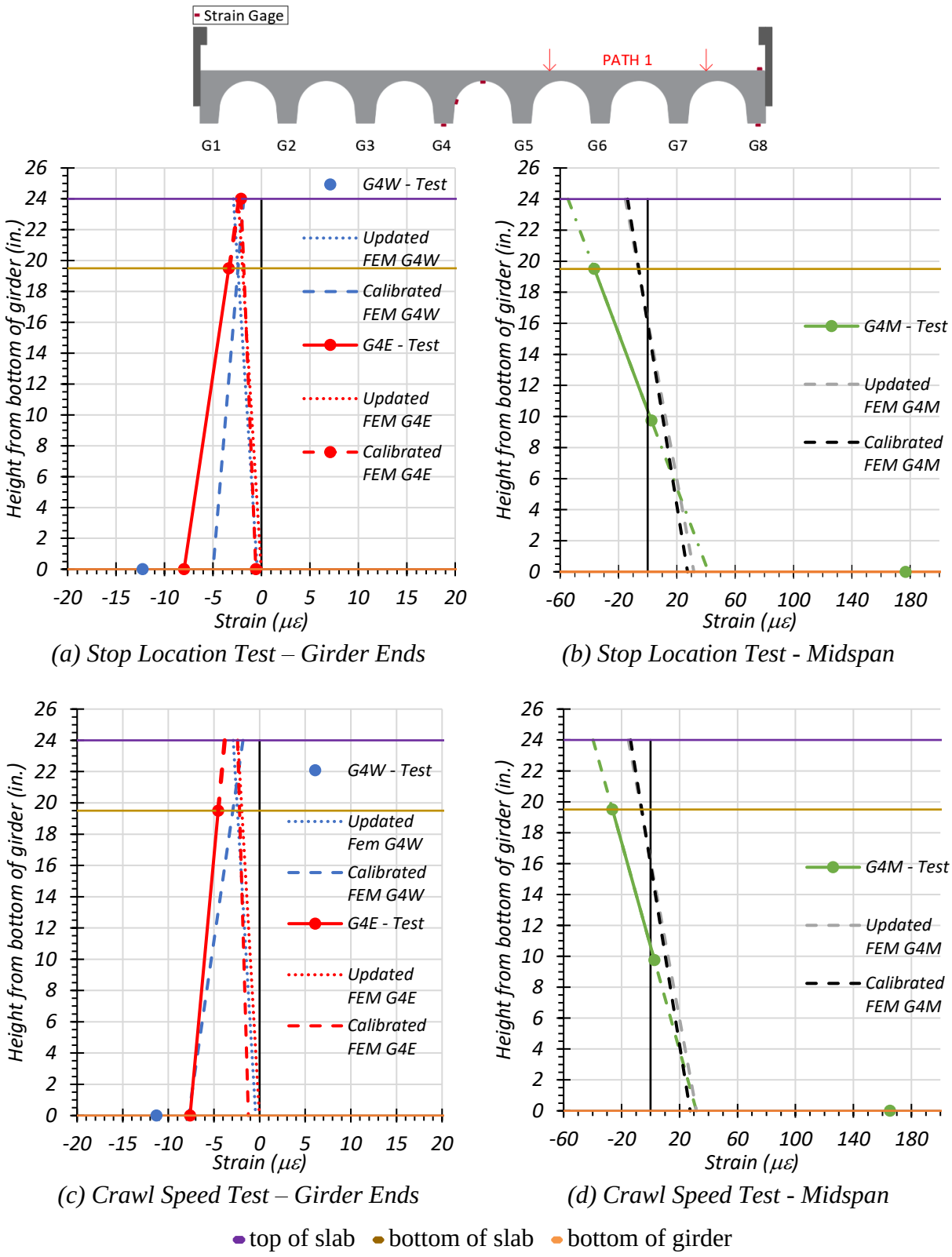

(a) Stop Location Test – Girder Ends

(b) Stop Location Test - Midspan

(c) Crawl Speed Test – Girder Ends

(d) Crawl Speed Test - Midspan

top of slab bottom of slab bottom of girder

Figure 8.37. Comparison of Static Strains for G4 with FEM Results—Path 1

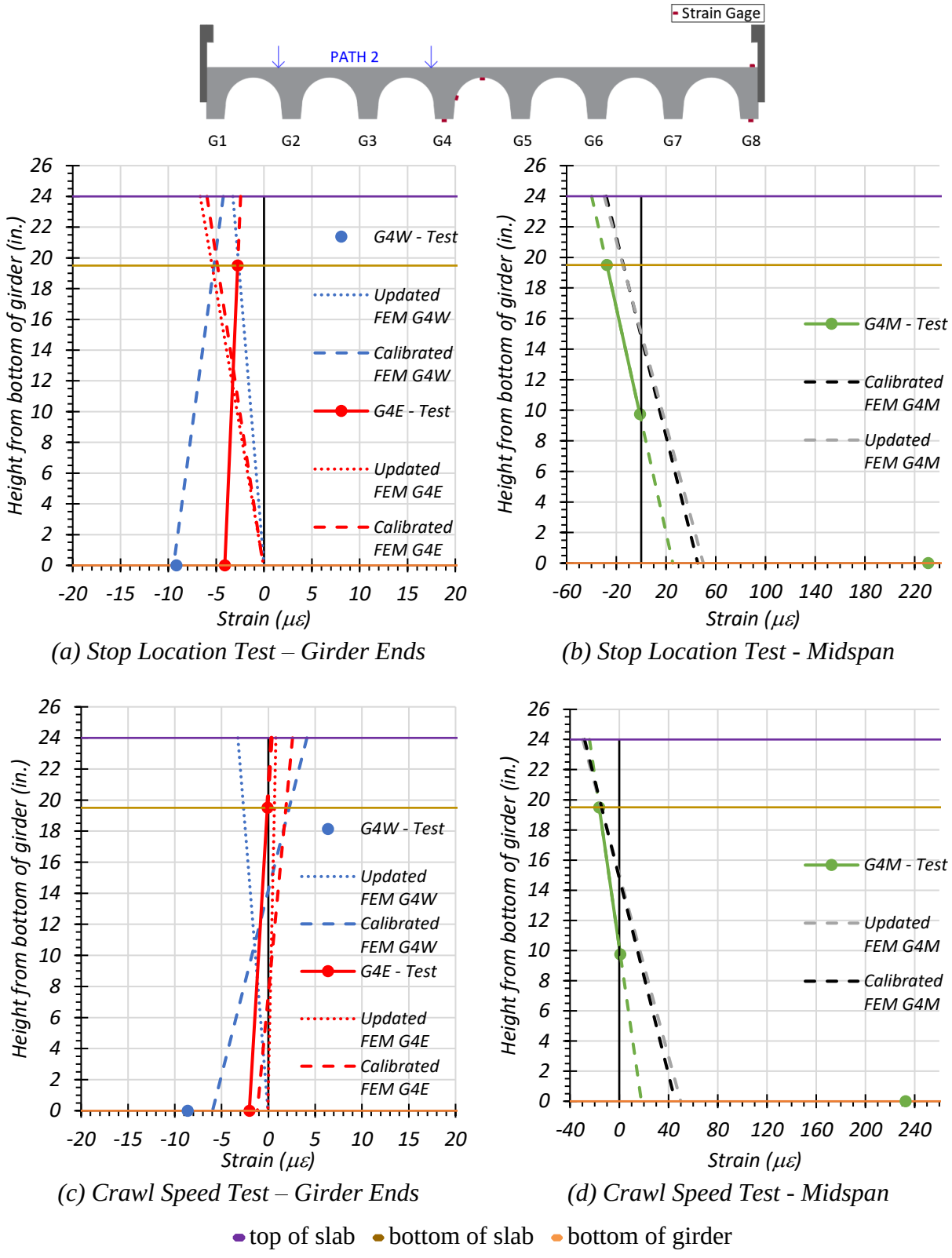

(a) Stop Location Test – Girder Ends

(b) Stop Location Test - Midspan

(c) Crawl Speed Test – Girder Ends

(d) Crawl Speed Test - Midspan

Figure 8.38. Comparison of Static Strains for G4 with FEM Results—Path 2

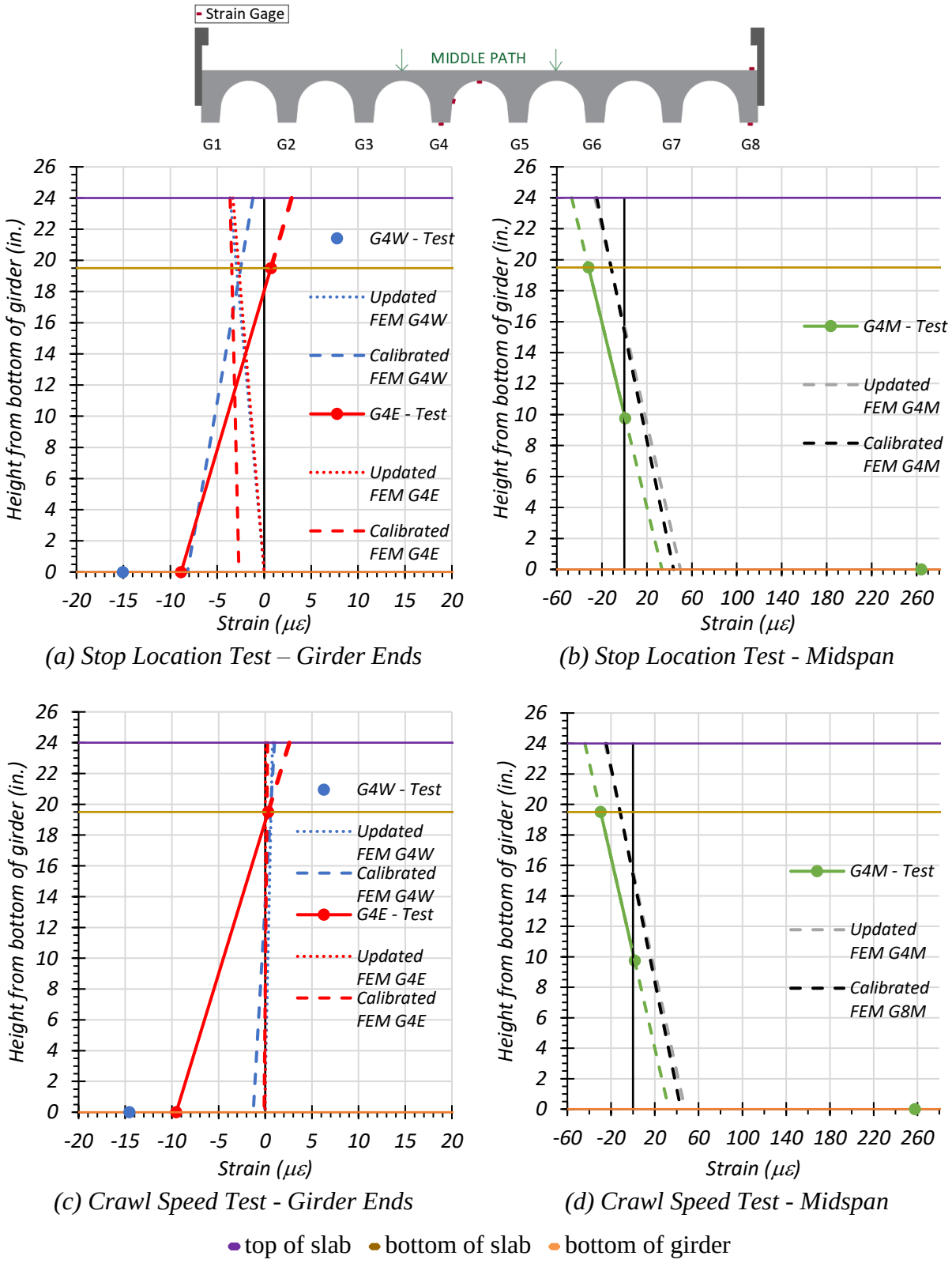

(a) Stop Location Test – Girder Ends

(b) Stop Location Test - Midspan

(c) Crawl Speed Test - Girder Ends

(d) Crawl Speed Test - Midspan

Figure 8.39. Comparison of Static Strains for G4 with FEM Results—Middle Path

Exterior Girder G8. The maximum top and bottom strains for exterior Girder G8 under static tests along Path 1 are compared with the calibrated FEM results in Figure 8.40. For the stop location test, the strain profile along the west and east ends of Girder G8 is shown in Figure 8.40(a), and the strain profile at the midspan of Girder G8 is shown in Figure 8.40(b). For the crawl speed test, the strain profile along the west and east ends of Girder G8 is shown in Figure 8.40(c), and the strain profile at the midspan of Girder G8 is shown in Figure 8.40(d).

The maximum top and bottom strains for the exterior Girder G8 under static tests along Path 2 are compared with the calibrated FEM results in Figure 8.41. For the stop location test, the strain profile along the west and east ends of Girder G8 is shown in Figure 8.41(a), and the strain profile at the midspan of Girder G8 is shown in Figure 8.41(b). For the crawl speed test, the strain profile along the west and east ends of Girder G8 is shown in Figure 8.41(c), and the strain profile at the midspan of Girder G8 is shown in Figure 8.41(d).

The maximum top and bottom strains for the exterior Girder G8 under static tests along the Middle Path are compared with the calibrated FEM results in Figure 8.42. For the stop location test, the strain profile along the west and east ends of Girder G8 is shown in Figure 8.42(a), and the strain profile at the midspan of Girder G8 is shown in Figure 8.42(b). For the crawl speed test, the strain profile along the west and east ends of Girder G8 is shown in Figure 8.42(c), and the strain profile at the midspan of Girder G8 is shown in Figure 8.42(d).

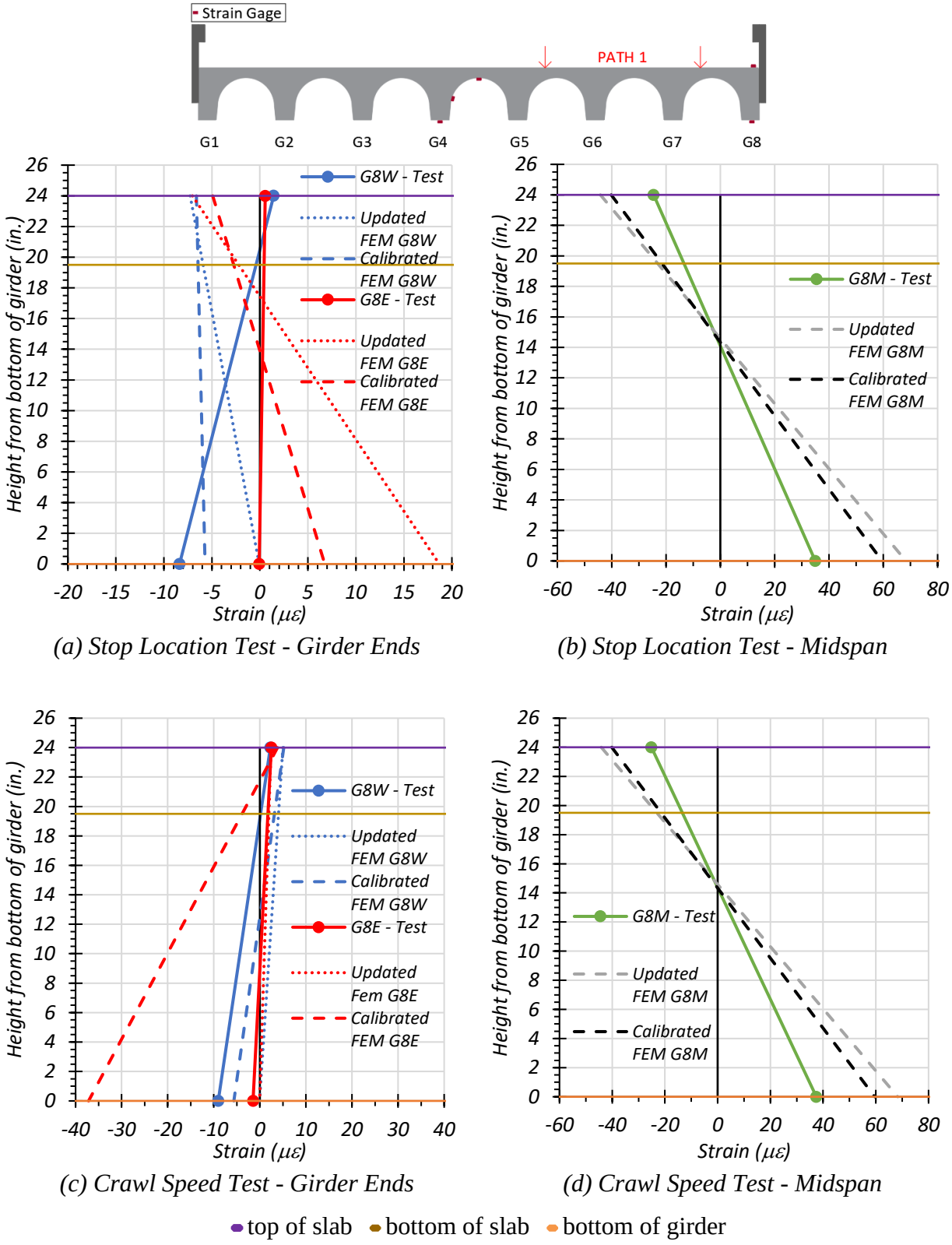

(a) Stop Location Test - Girder Ends

(b) Stop Location Test - Midspan

(c) Crawl Speed Test - Girder Ends

(d) Crawl Speed Test - Midspan

Figure 8.40. Comparison of Static Strains for G8 with FEM Results—Path 1

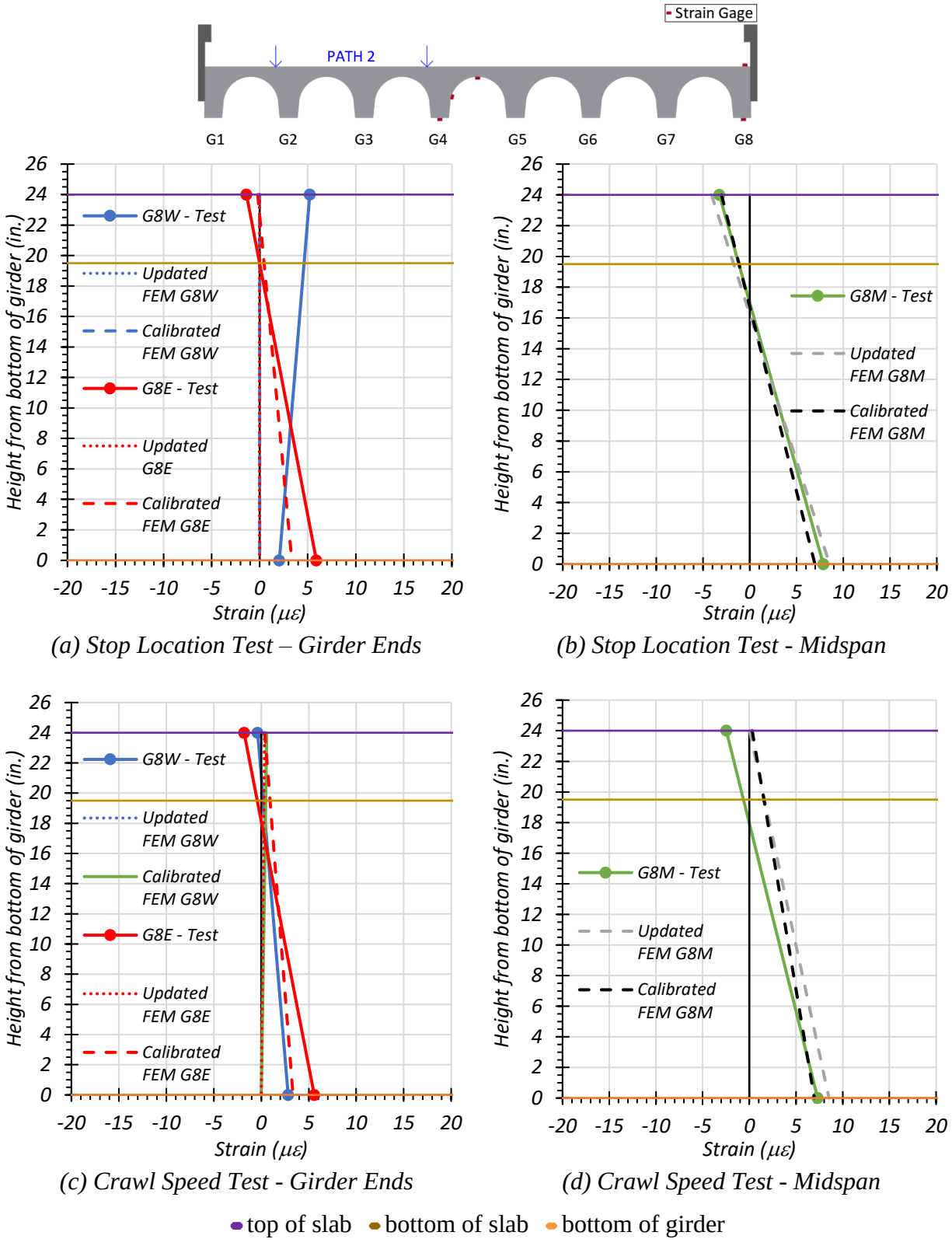

(a) Stop Location Test – Girder Ends

(b) Stop Location Test - Midspan

(c) Crawl Speed Test - Girder Ends

(d) Crawl Speed Test - Midspan

Figure 8.41. Comparison of Static Strains for G8 with FEM Results—Path 2

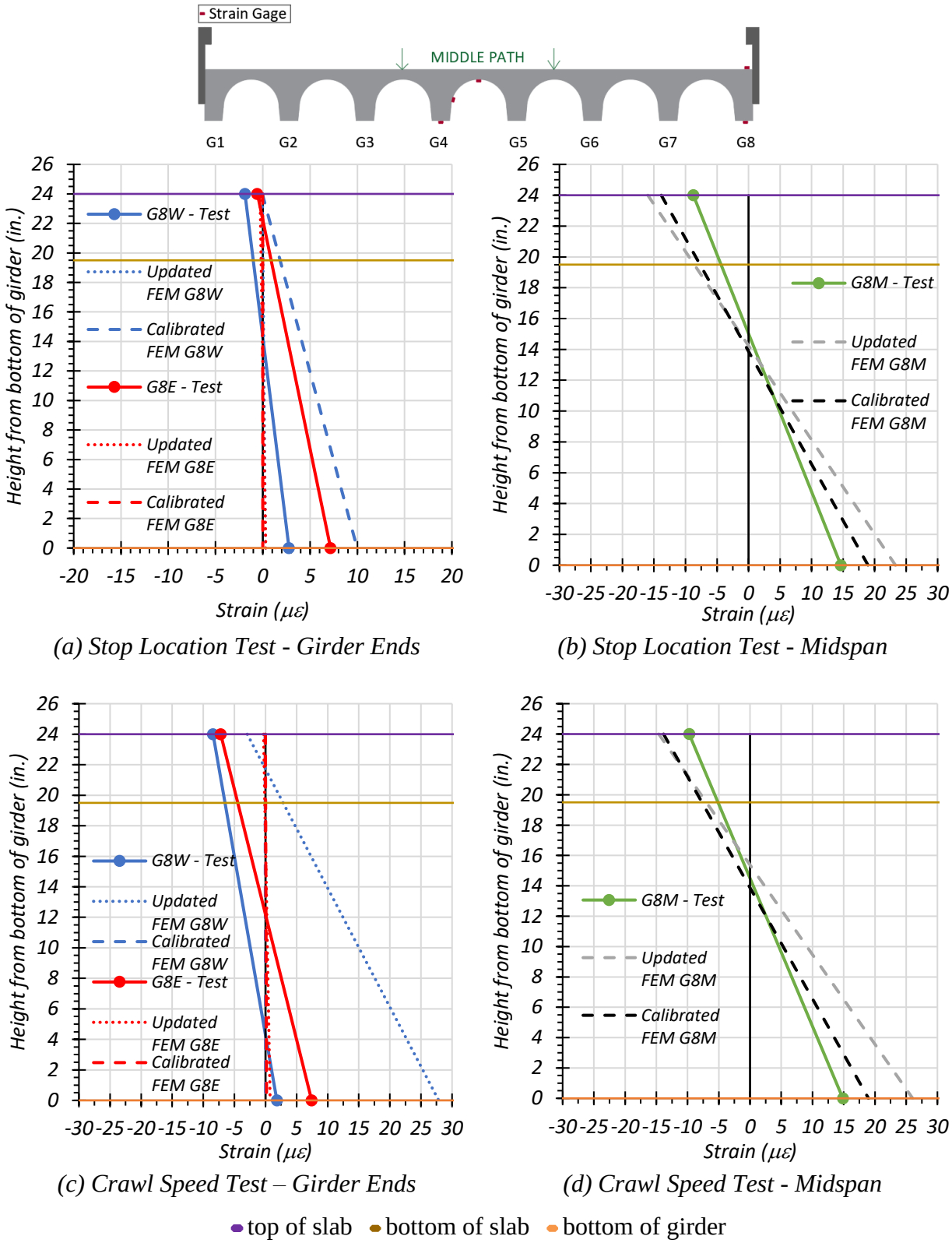

(a) Stop Location Test - Girder Ends

(b) Stop Location Test - Midspan

(c) Crawl Speed Test – Girder Ends

(d) Crawl Speed Test - Midspan

Figure 8.42. Comparison of Static Strains for G8 with FEM Results—Middle Path

Comparison of Results based on Measured Strains. The neutral axis location for each girder is determined from the strain profile at the midspan. The neutral axis positions obtained from Girder G4 were consistently high when compared to those positions obtained from Girder G8, which may be because of cracks that were noticed in Girder G4.

Table 8.22 lists the neutral axes corresponding to all the different tests. Figure 8.43 compares the neutral axes obtained from the static tests with the FEM neutral axis for both Girders G4 and G8. As previously observed, the neutral axis location is closest to the theoretical uncracked section.

Table 8.22. Comparison of Neutral Axis Locations with FEM Results for All Static Load Tests

Test	G4 Neutral Axis Location (in. from bottom of girder)	G8 Neutral Axis Location (in. from bottom of girder)
Path 1—Stop Location	10.40	15.02
Path 1 – Crawl Speed	10.65	14.37
Path 2 – Stop Location	9.37	19.06
Path 2 – Crawl Speed	10.23	17.96
Middle Path – Stop Location	10.01	14.73
Middle Path – Crawl Speed	10.24	14.50
Updated FEM	15.74	14.24
Calibrated FEM	15.38	13.87
Theoretical Uncracked	14.05	15.21
Theoretical Cracked	19.91	18.87

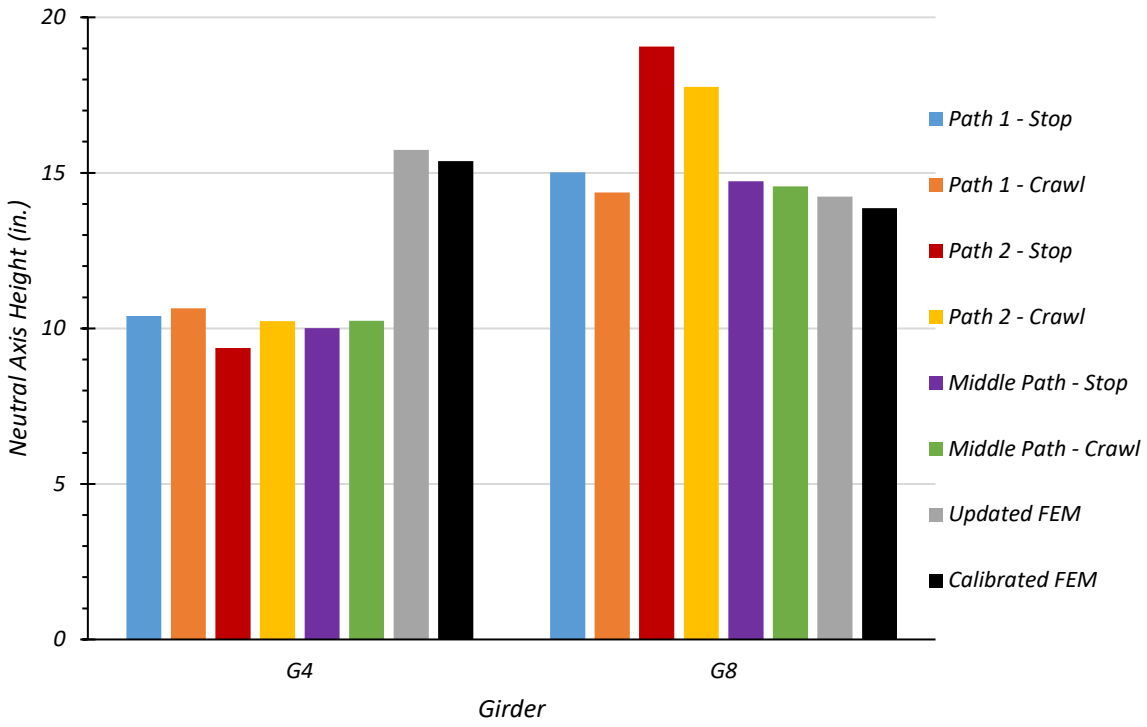

Figure 8.43. Test and Calibrated FEM Neutral Axis Locations

8.8.2 Deflection Measurements

In the following sections, the measured deflections are compared with the FEM results. As noted earlier, the string potentiometers at Girders G2 and G4 show lower displacements for all static tests. Although these results are presented in the following plots, the accuracy of the updated and calibrated FEM models are checked independent of these deflections.

Path 1 Loading. The measured maximum downward deflection for each girder under the static test and crawl speed test along Path 1 is compared with those deflections obtained from the updated and calibrated FEM models in Figure 8.44(a) and (c), respectively. A comparison of the test LLDFs with those LLDFs calculated from the *AASHTO Standard Specifications* (AASHTO 2002) and updated and calibrated FEM models is shown in Figure 8.44(b) and (d) for static and crawl tests, respectively. The updated FEM overestimates the deflection by 59 percent for the stop location test and 55 percent for the crawl speed test along Path 1. The calibrated model provided a better estimation of the observed deflections during static tests along Path 1, with a maximum overestimation of 33 percent for the stop location test and 26 percent for the crawl speed test.

Correspondingly, the displacement-based LLDFs obtained from the calibrated FEM closely model the measured load distribution within the bridge.

Table 8.23 compares the static test deflections for each girder with the updated and calibrated FEM deflections. A comparison of the test LLDFs with the FEM displacement LLDFs is provided in Table 8.24. The LLDFs calculated from the test results and calibrated FEM displacements are tabulated along with the LLDFs obtained from the three AASHTO methods in Table 8.25.

Table 8.23. Experimental and FEM Deflections for Path 1 Loading

Girder	G1	G2	G3	G4	G5	G6	G7	G8
Updated FEM	0.005	0.010	0.017	0.027	0.039	0.047	0.053	0.059
Calibrated FEM	0.004	0.008	0.014	0.023	0.033	0.039	0.045	0.048
Stop Location Test Disp. (in.)	0.006	0.002	0.014	0.016	0.034	0.041	0.040	0.037
Crawl Speed Test Disp. (in.)	0.004	0.003	0.014	0.015	0.033	0.041	0.041	0.038
Note: 1 – G = Girder, Disp. = Displacement								

Table 8.24. FEM Displacement LLDF Comparison with Test for Path 1 Loading

Test and Girder Type	Updated FEM LLDF (g_{FEM})	Calibrated FEM LLDF (g_{cal})	Test (g_{test})	g_{FEM}/g_{test}	g_{cal}/g_{test}
Stop Location Interior	0.212	0.208	0.218	0.97	0.95
Stop Location Exterior	0.218	0.226	0.184	1.18	1.23
Crawl Speed Interior	0.212	0.208	0.222	0.95	0.94
Crawl Speed Exterior	0.218	0.226	0.191	1.14	1.18

Table 8.25. Experimental, FEM, and AASHTO LLDFs for Path 1 Loading

Girder	G1	G2	G3	G4	G5	G6	G7	G8
Stop Location Test LLDF	0.032	0.012	0.076	0.088	0.180	0.218	0.210	0.184
Crawl Speed Test LLDF	0.019	0.013	0.074	0.079	0.180	0.222	0.221	0.191
Calibrated FEM Disp. LLDF	0.016	0.037	0.066	0.107	0.155	0.185	0.208	0.226
AASHTO Standard LLDF	0.174	0.231	0.231	0.231	0.231	0.231	0.231	0.174
AASHTO LRFD LLDF using simplified stiffness	0.174	0.287	0.287	0.287	0.287	0.287	0.287	0.174
AASHTO LRFD LLDF using analytical stiffness	0.174	0.283	0.283	0.283	0.283	0.283	0.283	0.174
Note: 1 – G = Girder, Disp. = Displacement 2 – LLDF values are based on the midspan deflections.								

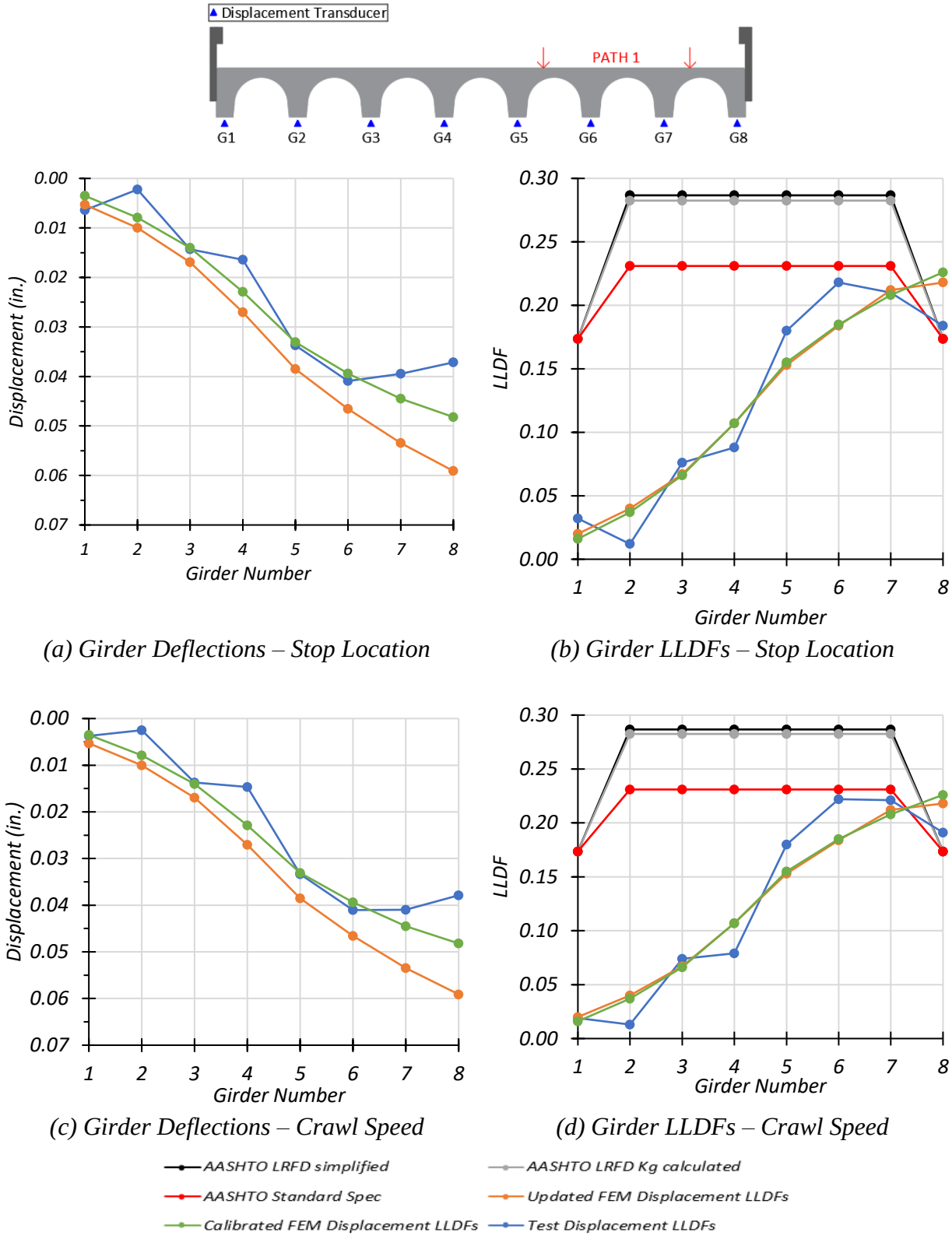

(a) Girder Deflections – Stop Location

(b) Girder LLDFs – Stop Location

(c) Girder Deflections – Crawl Speed

(d) Girder LLDFs – Crawl Speed

Figure 8.44. Comparison of Static Deflection Results with FEM for Path 1 Loading

Path 2 Loading. The measured maximum downward deflection for each girder under the static test and crawl speed test along Path 2 is compared with those deflections obtained from the updated and calibrated FEM models in Figure 8.45(a) and (c), respectively. A comparison of the test LLDFs with those LLDFs calculated from the *AASHTO Standard Specifications* and updated and calibrated FEM models is shown in Figure 8.45(b) and (d) for static and crawl tests, respectively. The updated FEM overestimates the deflection by 100 percent for both the stop location test and the crawl speed test along Path 2. The calibrated model provided a better estimation of the observed deflections during static tests along Path 2, with a maximum underestimation of 67 percent for the stop location test and an overestimation of 80 percent for the crawl speed test. Consequently, the displacement LLDFs obtained from the calibrated FEM closely model the true load distribution within the bridge.

Table 8.26 compares the static test deflections for each girder with the updated and calibrated FEM deflections. A comparison of the test LLDFs with the FEM displacement LLDFs is provided in Table 8.27. The LLDFs calculated from the test results and calibrated FEM displacements are tabulated along with the LLDFs obtained from the three AASHTO methods in Table 8.28.

Table 8.26. Experimental and FEM Deflections for Path 2 Loading

Girder	G1	G2	G3	G4	G5	G6	G7	G8
Updated FEM	0.054	0.051	0.046	0.039	0.029	0.019	0.011	0.006
Calibrated FEM	0.044	0.043	0.039	0.034	0.025	0.016	0.009	0.005
Stop Location Test Disp. (in.)	0.030	0.032	0.038	0.024	0.026	0.015	0.006	0.003
Crawl Speed Test Disp. (in.)	0.033	0.031	0.036	0.022	0.023	0.014	0.005	0.003
Note: 1 – G = Girder, Disp. = Displacement								

Table 8.27. FEM Displacement LLDF Comparison with Test for Path 2 Loading

Test and Girder Type	Updated FEM LLDF (g_{FEM})	Calibrated FEM LLDF (g_{cal})	Test (g_{test})	g_{FEM}/g_{test}	g_{cal}/g_{test}
Stop Location Interior	0.204	0.204	0.224	0.91	0.91
Stop Location Exterior	0.198	0.193	0.164	1.21	1.18
Crawl Speed Interior	0.204	0.204	0.221	0.92	0.92
Crawl Speed Exterior	0.198	0.193	0.187	1.06	1.03

Table 8.28. Experimental, FEM, and AASHTO LLDFs for Path 2 Loading

Girder	G1	G2	G3	G4	G5	G6	G7	G8
Stop Location Test LLDF	0.174	0.184	0.221	0.139	0.147	0.085	0.034	0.017
Crawl Speed Test LLDF	0.187	0.187	0.221	0.135	0.141	0.083	0.030	0.015
Calibrated FEM Disp. LLDF	0.193	0.204	0.185	0.161	0.118	0.075	0.045	0.016
AASHTO Standard LLDF	0.231	0.231	0.231	0.231	0.231	0.231	0.231	0.231
AASHTO LRFD LLDF using simplified stiffness	0.238	0.344	0.344	0.344	0.344	0.344	0.344	0.238
AASHTO LRFD LLDF using analytical stiffness	0.238	0.339	0.339	0.339	0.339	0.339	0.339	0.238

Note: 1 – G = Girder, Disp. = Displacement
2 – LLDF values are based on the midspan deflections.

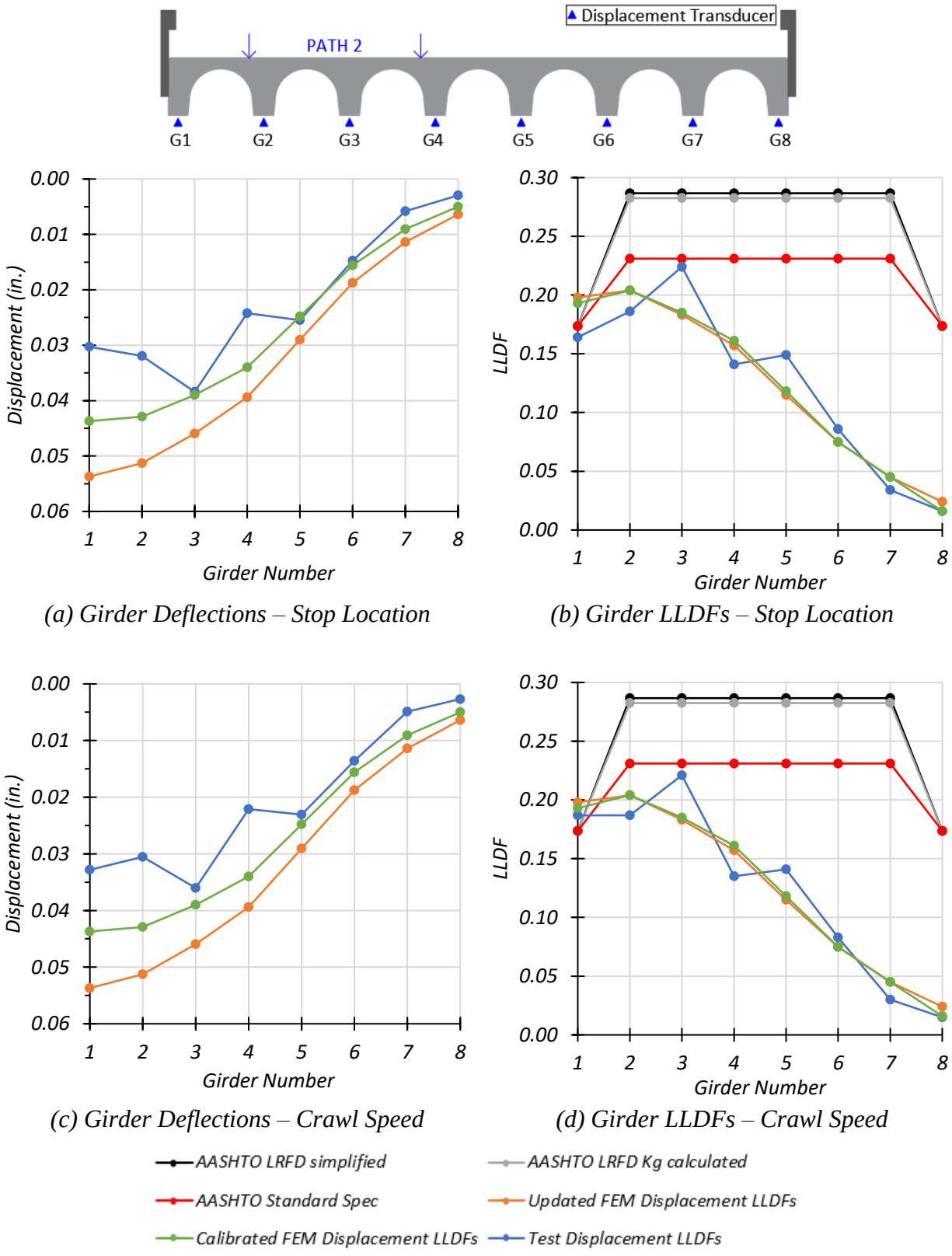

(a) Girder Deflections – Stop Location

(b) Girder LLDFs – Stop Location

(c) Girder Deflections – Crawl Speed

(d) Girder LLDFs – Crawl Speed

Figure 8.45. Comparison of Static Deflection Results with FEM for Path 2 Loading

Middle Path Loading. The measured maximum downward deflection for each girder under the static test and crawl speed test along the Middle Path is compared with those measurements obtained from the calibrated FEM model in Figure 8.46(a) and (c) respectively. A comparison of the test LLDFs with those calculated from the *AASHTO Standard Specifications* and updated and calibrated FEM models are shown in Figure 8.46(b) and (d) for static and crawl tests, respectively. The LLDFs calculated using FEM displacements were similar to the LLDFs obtained using FEM bending moments. The calibrated model provided a better estimation of the observed deflections during static tests along the Middle Path. The updated FEM overestimates the deflection by 62 percent for the stop location test and by 75 percent for the crawl speed test along the Middle Path. The calibrated model provided a better estimation of the observed deflections during static tests along the Middle Path, with a maximum underestimation of 33 percent for the stop location test and a maximum overestimation of 33 percent for the crawl speed test. Thus, the displacement LLDFs obtained from the calibrated FEM closely model the true load distribution within the bridge.

Table 8.29 compares the static test deflections for each girder with the updated and calibrated FEM deflections. A comparison of the test LLDFs with the FEM displacement LLDFs is provided in Table 8.30. The LLDFs calculated from the test results and calibrated FEM displacements are tabulated along with the LLDFs obtained from the three AASHTO methods in Table 8.31.

Table 8.29. Experimental and FEM Deflections for Middle Path Loading

Girder	G1	G2	G3	G4	G5	G6	G7	G8
Updated FEM	0.021	0.028	0.037	0.040	0.040	0.037	0.028	0.021
Calibrated FEM	0.017	0.024	0.032	0.035	0.035	0.032	0.024	0.016
Stop Location Test Disp. (in.)	0.015	0.016	0.033	0.026	0.036	0.030	0.018	0.013
Crawl Speed Test Disp. (in.)	0.013	0.015	0.030	0.025	0.035	0.028	0.019	0.012
Note: 1 – G = Girder, Disp. = Displacement								

Table 8.30. FEM Displacement LLDF Comparison with Test for Middle Path Loading

Test and Girder Type	Updated FEM LLDF (g_{FEM})	Calibrated FEM LLDF (g_{cal})	Test (g_{test})	g_{FEM}/g_{test}	g_{cal}/g_{test}
Stop Location Interior	0.162	0.167	0.195	0.83	0.86
Stop Location Exterior	0.078	0.074	0.076	1.03	0.99
Crawl Speed Interior	0.162	0.167	0.197	0.82	0.85
Crawl Speed Exterior	0.078	0.074	0.069	1.13	1.07

Table 8.31. Experimental, FEM, and AASHTO LLDFs for Middle Path Loading

Girder	G1	G2	G3	G4	G5	G6	G7	G8
Stop Location Test LLDF	0.076	0.085	0.179	0.141	0.195	0.163	0.097	0.064
Crawl Speed Test LLDF	0.069	0.084	0.172	0.143	0.197	0.159	0.109	0.065
Calibrated FEM Disp. LLDF	0.074	0.111	0.150	0.167	0.167	0.150	0.111	0.069
AASHTO Standard LLDF	0.231	0.231	0.231	0.231	0.231	0.231	0.231	0.231
AASHTO LRFD LLDF using simplified stiffness	0.238	0.344	0.344	0.344	0.344	0.344	0.344	0.238
AASHTO LRFD LLDF using analytical stiffness	0.238	0.339	0.339	0.339	0.339	0.339	0.339	0.238

Note: 1 – G = Girder, Disp. = Displacement
2 – LLDF values are based on the midspan deflections.

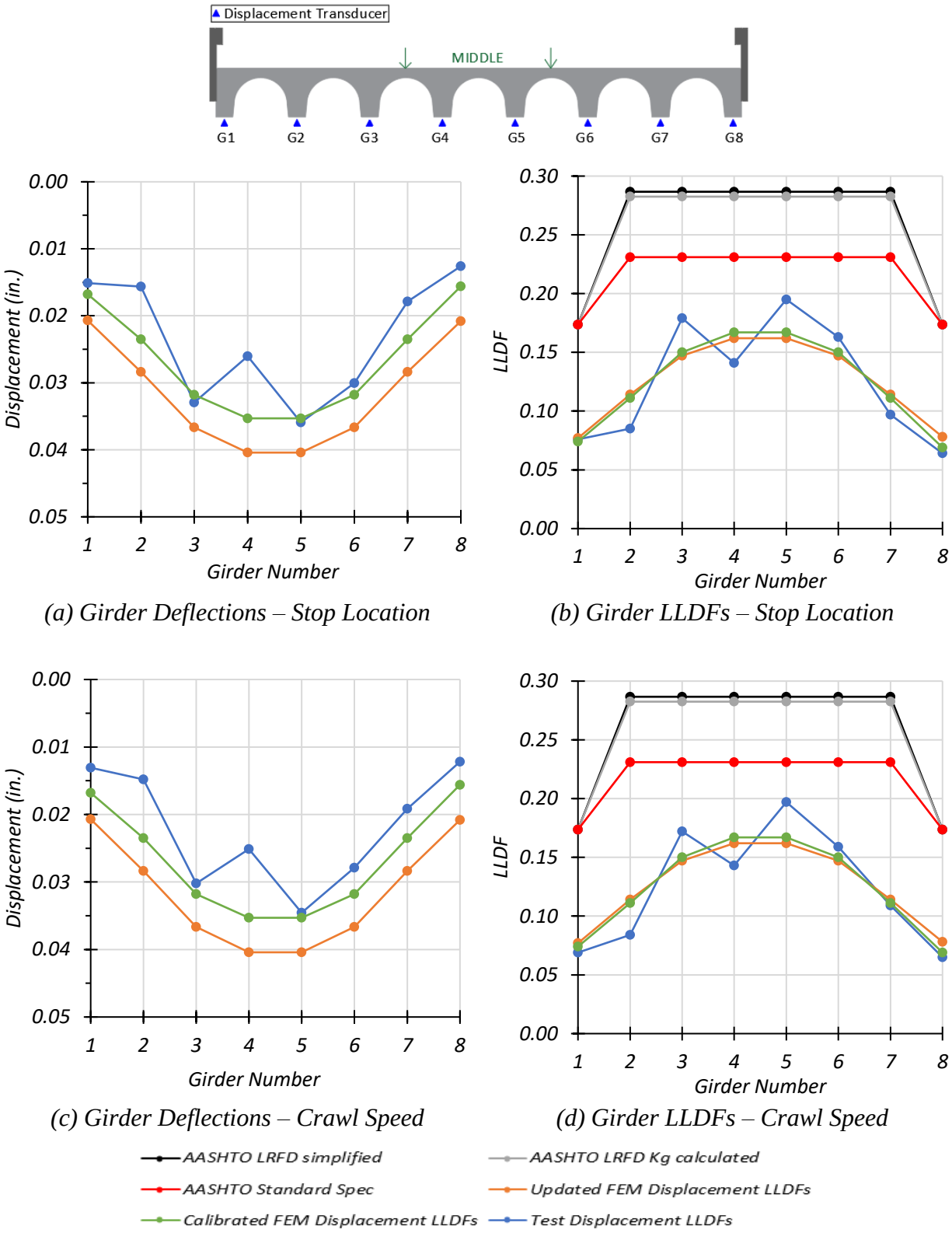

(a) Girder Deflections – Stop Location

(b) Girder LLDFs – Stop Location

(c) Girder Deflections – Crawl Speed

(d) Girder LLDFs – Crawl Speed

Figure 8.46. Comparison of Static Deflection Results with FEM for Middle Path Loading

8.8.3 Dynamic Characteristics of Bridge

The dynamic characteristics of the bridge obtained from the accelerometer data were compared with the updated and calibrated FEM results. The mode shape along the longitudinal section and transverse section for the first natural frequency compared to the updated FEM and calibrated FEM is shown in Figure 8.47. Figure 8.48 provides the mode shape along the longitudinal section and transverse section for the second natural frequency compared to the updated FEM and calibrated FEM. The mode shape along the longitudinal section and transverse section for the third natural frequency compared to the updated FEM and calibrated FEM is shown in Figure 8.49.

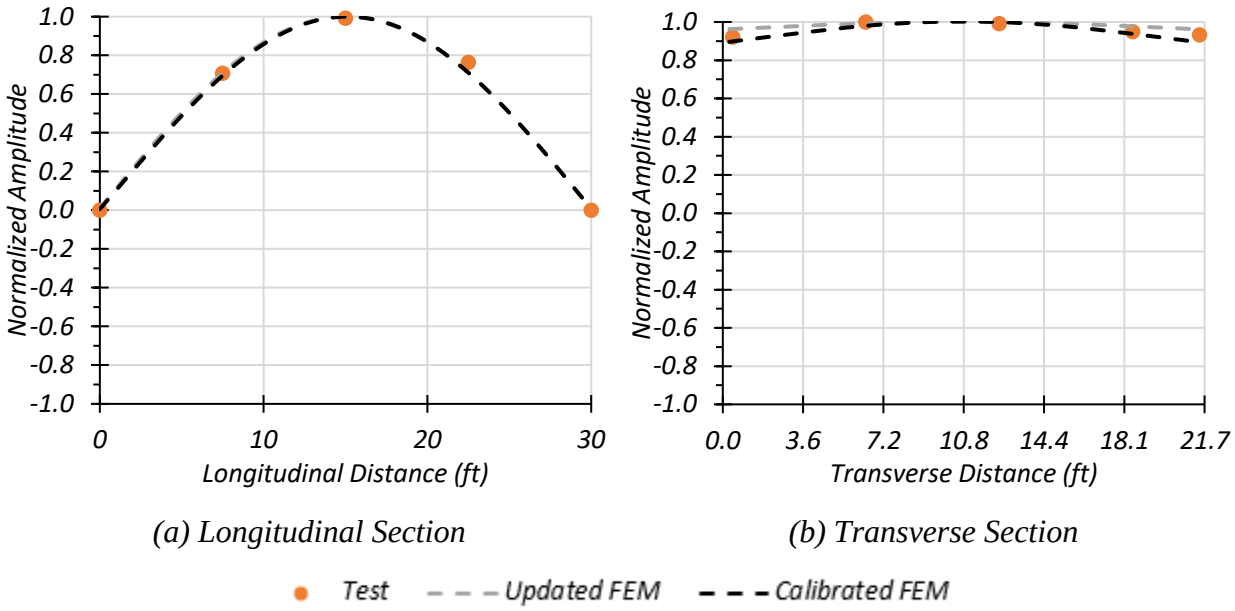

(a) Longitudinal Section *(b) Transverse Section*

Figure 8.47. Mode Shape 1: Comparison of Experimental and FEM Results

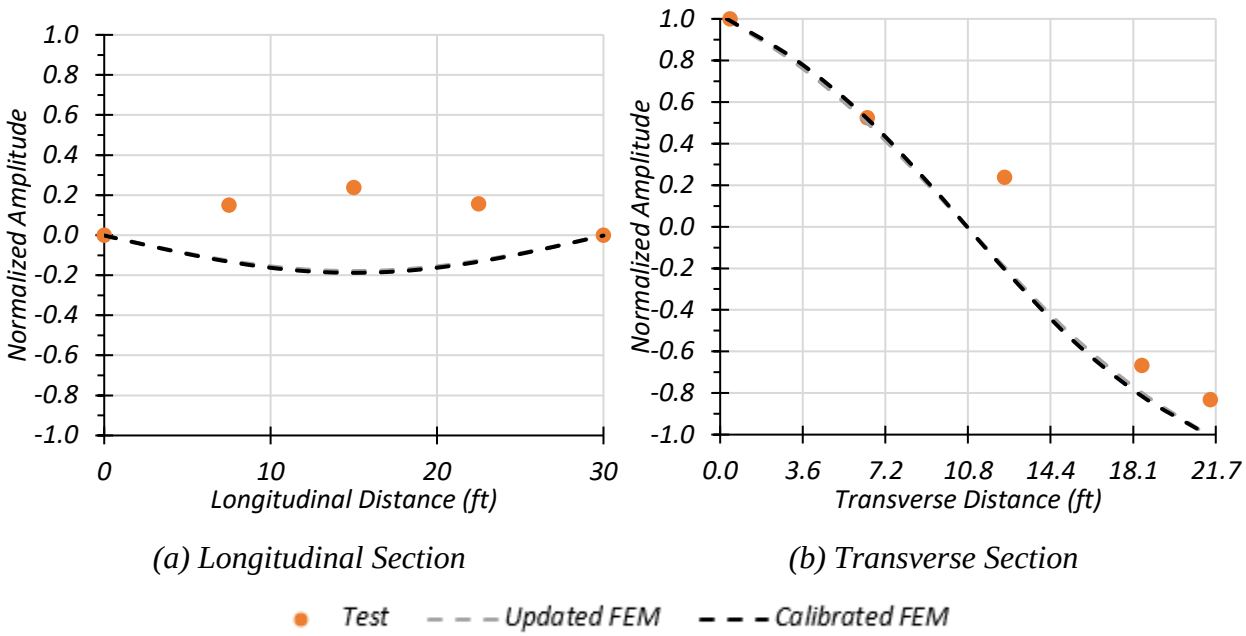

Figure 8.48. Mode Shape 2: Comparison of Experimental and FEM Results

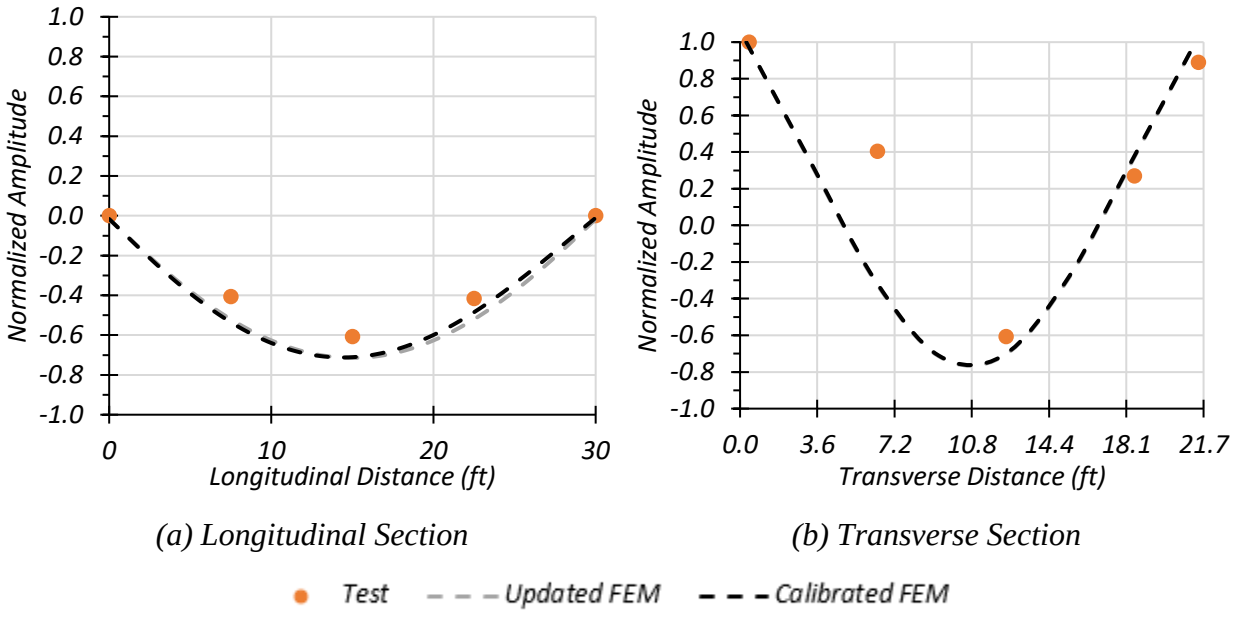

Figure 8.49. Mode Shape 3: Comparison of Experimental and FEM Results

The natural frequencies obtained from the FEM model and those frequencies observed during the testing of Bridge CM-5 are provided in Table 8.32. The first, second, and third natural frequencies obtained from the calibrated FEM model were closer to those frequencies obtained from the tests.

Table 8.32. Bridge CM-5 Test and FEM Natural Frequencies

Frequency	Test (Hz)	Updated FEM (Hz)	Calibrated FEM (Hz)
1st Natural Frequency	11.84	11.95	13.74
2nd Natural Frequency	16.60	14.73	16.94
3rd Natural Frequency	25.15	22.51	24.62

8.9 SUMMARY AND FINDINGS

8.9.1 Live Load Distribution Factors

The LLDFs calculated based on deflections compared well with those LLDFs calculated from bending moments obtained from the FEM model. Thus, the experimental LLDFs for each test were calculated from the deflections obtained at the midspan of the bridge.

In Section 8.6.1.2, the experimental LLDFs were compared with the FEM LLDFs and those LLDFs calculated using the approximate equations in the *AASHTO Standard Specifications* (AASHTO 2002) and in the *AASHTO LRFD Specifications* (AASHTO 2017) with the simplified and analytical stiffness parameter. The *AASHTO Standard Specifications* and *AASHTO LRFD Specifications* provide conservative LLDFs for all girders. The *AASHTO LRFD Specifications* provide slightly conservative estimates for the exterior girder but are conservative for the interior girder.

Currently, TxDOT load rates simple-span concrete pan girder bridges using the *AASHTO Standard Specifications'* LLDFs. These LLDFs were not highly conservative when compared with the experimental LLDFs. Consequently, refining the LLDFs would not significantly increase the load limit for such bridge types.

8.9.2 Updated Material Properties

The material strength of concrete comes into play in the calculation of the RF. The 28-day concrete compressive strength of concrete for Bridge CM-5 was taken to be 4.0 ksi according to the standard

drawing provided on the TxDOT website titled “CG 30'-4" Spans” (TxDOT 2005). The section also shows a doubly reinforced section. However, NDE tests revealed that the actual concrete compressive strength was 7.0 ksi and that the section has only one layer of tensile reinforcement. Table 8.33 provides a comparison of the updated RFs calculated using the in-situ compressive strength of concrete with the originally calculated RFs. For the LFR approach, increasing the material strength by 75 percent does not significantly increase the RFs. Because of the poor condition rating of the substructure (Item 60 < 6), TxDOT’s Off-System Load Rating flowchart (TxDOT 2018b) does not allow the posting to be removed. According to the flowchart, the bridge should be posted at inventory level with an inspection frequency of less than 2 years.

Table 8.33. Comparison of Bridge CM-5 Material Updated RFs to Original RFs

Rating Factor	Basic Load Rating	Load Rating with Measured Material Properties	Measured Material Properties/Basic Load Rating
Inventory	1.17	1.20	1.03
Operating	1.96	2.01	1.03

8.9.3 Calibrated FEM Model

Calibrating the simply supported FEM model with the experimental results showed that some degree of end restraint is present. The bending moment corresponding to the HS-20 design truck is obtained from the calibrated FEM model, which includes the effect of the updated MOE of the concrete, more accurate live load distribution, and updated boundary conditions due to slight end restraint, and this value is used to determine the updated RFs. Table 8.34 provides a comparison of the updated RFs with the original RFs for a simply supported bridge. Only the LFR results are shown in the table because this was the method used by TxDOT to load rate Bridge CM-5. Although the effect of the updated MOE of the concrete coupled with slight end restraint should reduce the midspan moment, the LLDFs from the refined FEM analysis indicate a higher midspan moment as compared to approximate LLDFs from the *AASHTO Standard Specifications*; thereby, reducing the RFs in comparison to the basic load rating analysis. Despite the reduction in the RFs from the refined load rating analysis, both the inventory RF and operating RF is greater than 1.0.

However, due to the poor condition rating of the substructure (Item 60 < 6), TxDOT's Off-System Load Rating Flowchart (TxDOT 2018b) does not allow the posting to be removed. According to the flowchart, the bridge should be posted at inventory level with an inspection frequency of less than 2 years.

Table 8.34. Comparison of Calibrated FEM RFs to Original RFs for Bridge CM-5

Rating Factor	Basic Load Rating	Load Rating with Calibrated FEM Live Load	Calibrated FEM Live Load /Basic Load Rating
Inventory	1.17	1.14	0.97
Operating	1.96	1.91	0.97

9 EXPERIMENTAL TESTING OF BRIDGE CS-9

9.1 INTRODUCTION

In the previous tasks, a basic load rating evaluation of 23 simple-span concrete slab bridges was conducted, and an FEM model of a typical load-posted bridge was developed using the commercial software package CSiBridge. The selected simple-span concrete slab bridge, CS-9, was load tested in the field. The purpose of the load test was to capture the in-situ behavior of the bridge, including the effects of any potential fixity at the bridge ends and the equivalent strip width over which the vehicular loads are distributed. The results from the field tests are used to determine the transverse load distribution between curbs and the slab region. Any observed end fixity was also incorporated into the FEM model to more accurately model the in-situ boundary conditions of the bridge.

Several nondestructive evaluation methods were used to identify the concrete compressive strength and the layout of the reinforcing bars. The results of the NDE tests were used to update the FEM model of the bridge to represent the measured concrete compressive strength and to confirm that no observed differences exist in the reinforcement layout as compared to the reinforcement details provided in the structural drawings.

In addition to conventional measuring devices, such as string potentiometers, strain gauges, and accelerometers, two cameras mounted on tripods recorded the bridge response during each load test. An image analysis algorithm was used to determine the displacements from the unloaded bridge image and loaded bridge image. A thorough investigation of the field-test results and the results from the updated and calibrated FEM models is used to determine potential updates to the load posting of the bridge and implications for load postings for similar bridge structures.

9.2 GENERAL DESCRIPTION OF BRIDGE CS-9

Bridge CS-9 carries FM 216 and traverses Flag Creek near Walnut Springs, Texas, approximately 7.0 mi north of FM 927. It has a deck condition rating of 6 (Satisfactory), a superstructure condition rating of 6 (Satisfactory), and a substructure condition rating of 6 (Satisfactory). The flexural resistance of the concrete slab controls the rating of the bridge, which has an inventory gross load rating of 16 US tons and an operating gross load rating of 33.7 US tons. The bridge is posted for a 28,000 lbs tandem axle. Figure 5.2 shows an elevation view and an underside view of Bridge CS-

9. Figure 5.1 shows a transverse section detail obtained from TxDOT inspection reports (TxDOT 2018a).

(a) Elevation View

(b) Underside View

Figure 9.1. Photographs of Bridge CS-9 (TxDOT 2018a)

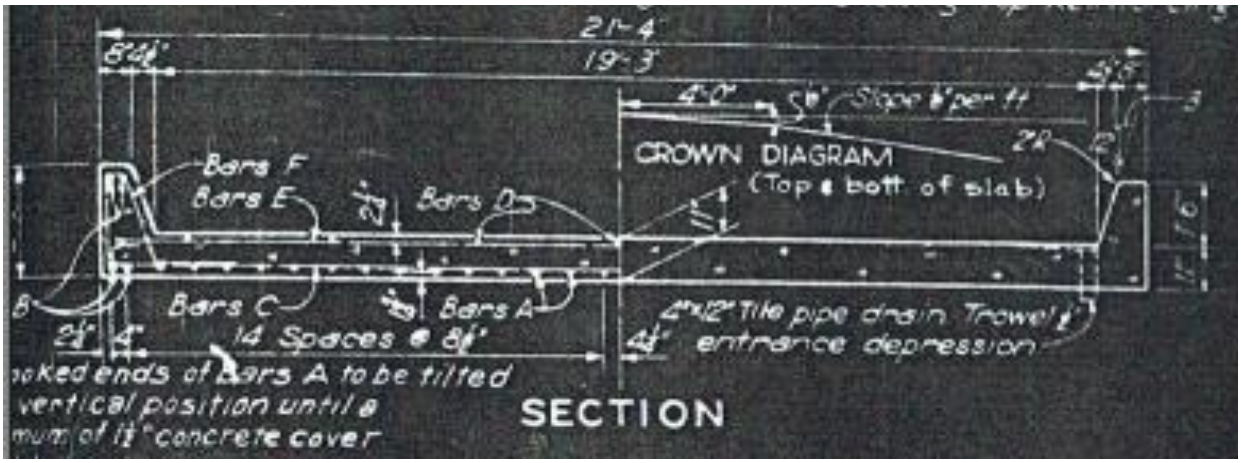

Figure 9.2. Transverse Section of Bridge CS-9 (TxDOT 2018a)

9.3 IN-SITU MEASUREMENTS AND OBSERVATIONS AND NDE RESULTS

9.3.1 Nondestructive Evaluation Results

The as-built geometric details were measured to confirm the values provided in the structural drawings. The bridge measured 25 ft in length, and the total width measured 21 ft 3 in. wide. The total depth from the top of curb to the bottom of the slab was 2 ft 5 in. These measurements agreed with the structural drawings of the bridge.

9.3.2 Nondestructive Evaluation Results

The in-situ concrete compressive strength of Bridge CS-9 was determined on site using nondestructive test methods. Two different rebound number test instruments, the Original Schmidt Hammer and the Silver Schmidt Hammer, were utilized and testing was conducted in accordance with the ASTM C805 standard test method for rebound number of hardened concrete (ASTM C805 2018). The surface over which these tests were conducted was first ground smooth using an angle grinder with a masonry grinding wheel. The surface was made smoother using a grinding stone. An indicator solution of phenolphthalein in ethanol was applied to the clean surface to check for carbonation of the concrete. Concrete carbonation can affect the results obtained from these tests. If the indicator solution did not turn purple, the surface was further ground to reach the non-carbonated layer. Ten rebound number readings were obtained for both Schmidt Hammer tests by pushing against the surface. As per the Original Schmidt Hammer operating instructions, the

highest and lowest rebound numbers were removed, and the average of the remaining eight rebound numbers was calculated. The Silver Schmidt Hammer was developed in accordance with the ASTM C805 guidelines. This test was carried out at two locations on the bridge near the southwest end of the bridge—on the top of a curb and on the side face of the bridge. The average rebound number for the Original Schmidt Hammer was 46.1 on the top of the curb and 41.5 on the side of the bridge. This number corresponds to a concrete compressive strength of approximately 7 ksi on the top of the curb and 5.2 ksi on the side of the bridge based on the conversion curve in Figure 6.4. In this test, the hammer was pushed vertically down on the top of the curb and horizontally onto the surface on the side of the bridge.

The Silver Schmidt Hammer uses the same principle and directly gives the compressive strength of concrete when within the applicable range. This test was carried out two times on the top of the curb and yielded concrete compressive strength values of 7.3 ksi and 5.2 ksi. Another region tested was the side of the bridge, where the concrete compressive strength value was observed to be 9 ksi. The average of these values is approximately 7.2 ksi. Figure 6.5 provides the conversion chart used for Silver Schmidt Hammer rebound values. Table 9.1 summarizes the concrete compressive strength results obtained from the NDE tests. Note that the UPV test could not be performed on this bridge due to the absence of a parallel surface for the curbs and a thick asphalt layer on the slab.

Table 9.1. Concrete Compressive Strengths from NDE Tests

Test	**Concrete Compressive Strength (ksi)**	
	Top of Curb	North Side of Bridge
Schmidt Hammer Test	7.0	5.2 (min.)
Silver Schmidt Hammer Test	6.25	9.0

The lowest concrete compressive strength obtained from the NDEs was noted to be approximately 5.2 ksi. As a result, this strength and the corresponding MOE were adopted in the updated FEM models.

9.4 DATA ACQUISITION AND INSTRUMENTATION FOR BRIDGE CS-9

The bridge instrumentation plan was developed to capture the maximum response of the bridge when subjected to different vehicle loading scenarios. The instruments used to measure the

response of the bridge included strain gauges, string potentiometers, and accelerometers, all of which were connected to the DAQ system to digitally record the data.

9.4.1 Instrumentation Plan for Bridge CS-9

The instrumentation plan was developed to record the response of the bridge when subjected to different loading scenarios. The instrumentation plan for Bridge CS-9 and cross-sectional views are shown in Figure 9.3. The labeling system used in the instrumentation plan is explained in Figure 6.7. The instrumentation labels for the DAQ system are listed in Table 9.2.

The measured bridge response is used to identify the in-situ bridge behavior and live load distribution, which is critical to determine potential areas of opportunity to increase or remove the load posting. Several goals were identified in determining the instrumentation types and locations, as follows:

- The data collected from the strain gauges are used to determine the neutral axis position within the curb and slab sections and any unintended partial fixity at the supports.
- The midspan deflection data collected by the string potentiometers are used to infer experimental moment LLDFs that can be compared to the effective width values used for design and the estimated values from the FEM model of Bridge CS-9 and the AASHTO specifications.
- The accelerometers collect vibration data that are used to compute the dynamic properties of the bridge. These data are useful for model calibration and evaluation of the impact factor.

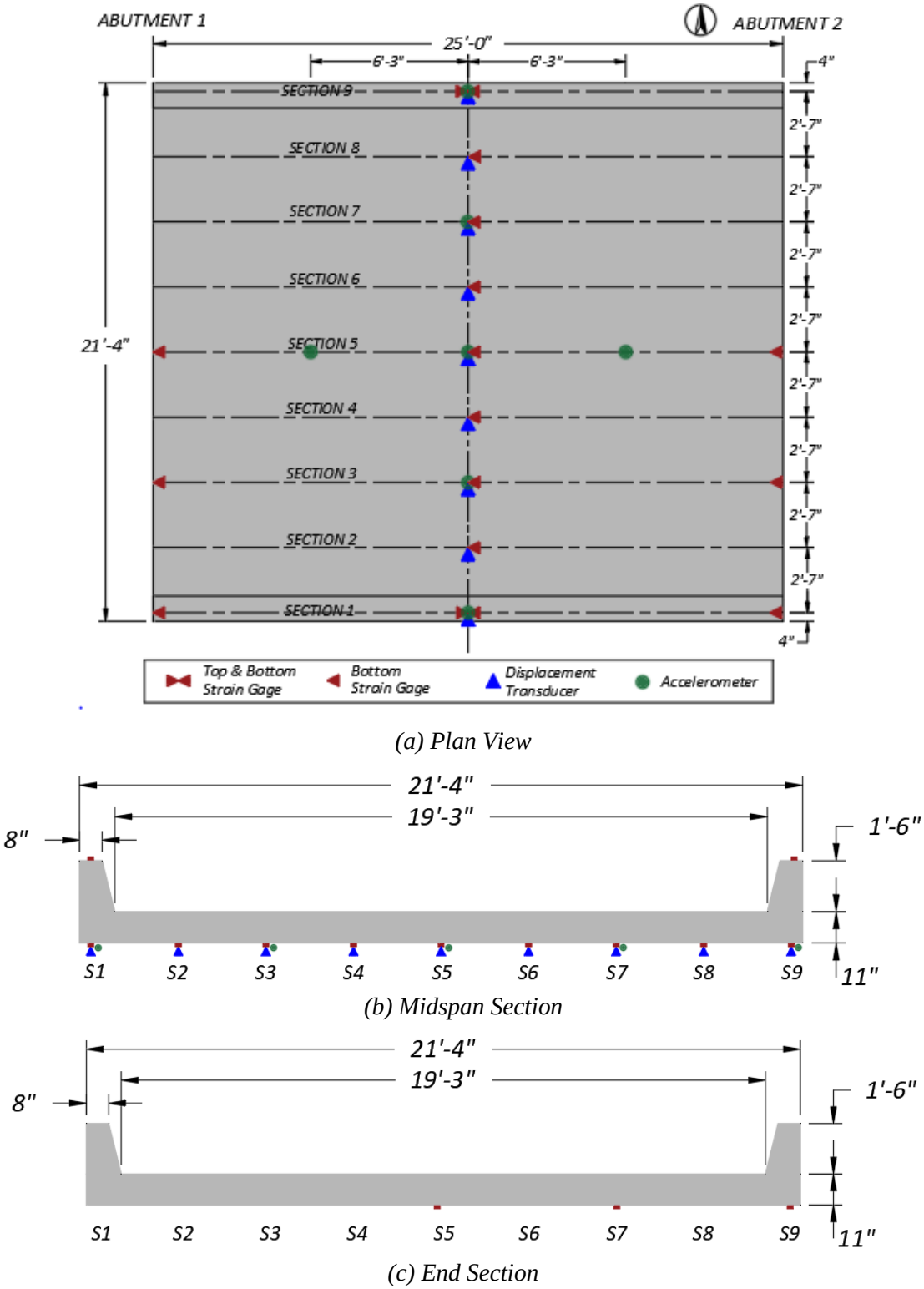

(a) Plan View

(b) Midspan Section

(c) End Section

Figure 9.3. Instrumentation Plan for Bridge CS-9

Table 9.2. Instrumentation Labels for Bridge CS-9

DAQ Box	Channel	Label	Type	DAQ Box	Channel	Label	Type
Strain Book	CH1	SG-9MB	PL-60	WBK 16-3	CH25	SP-3M	SM1-2
	CH2	SG-8MB	PL-60		CH26	SP-2M	SM1-2
	CH3	SG-7MB	PL-60		CH27	SP-1M	SM1-2
	CH4	SG-6MB	PL-60		CH28	–	–
	CH5	SG-5MB	PL-60		CH29	–	–
	CH6	SG-4MB	PL-60		CH30	–	–
	CH7	SG-3MB	PL-60		CH31	–	–
	CH8	SG-2MB	PL-60		CH32	–	–
WBK 16-1	CH9	SG-1MB	PL-60	WBK 18	CH57	A-9M	4507 IEPE
	CH10	SG-9MT	PL-60		CH58	A-7M	4507 IEPE
	CH11	SG-1MT	PL-60		CH59	A-5M	4507 IEPE
	CH12	SG-9WB	PL-60		CH60	A-3M	4507 IEPE
	CH13	SG-7WB	PL-60		CH61	A-5W	4507 IEPE
	CH14	SG-5WB	PL-60		CH62	A-5E	4507 IEPE
	CH15	SG-9EB	PL-60		CH63	-	
	CH16	SG-7EB	PL-60		CH64	-	
WBK 16-2	CH17	SG-5EB	PL-60				
	CH18	–	–				
	CH19	SP-9M	SM1-2				
	CH20	SP-8M	SM1-2				
	CH21	SP-7M	SM1-2				
	CH22	SP-6M	SM1-2				
	CH23	SP-5M	SM1-2				
	CH24	SP-4M	SM1-2				

Note: Refer to Figure 6.7 for explanation of the labeling system used

9.4.2 Data Acquisition System and Instrument Details

A total of 34 strain gauges (using half-bridge circuits at 17 measurement locations), nine string potentiometers, and seven accelerometers were installed on Bridge CS-9. Thirty-three channels in the DAQ system were used. The strain gauges and string potentiometers were connected via cables to the main box (Measurement Computing StrainBook) and WBK16 extension module boxes. The accelerometer data were collected by the additional WBK18 extension module box. The DAQ system is further described in Section 6.4.2.

*9.4.2.1 **Strain Gauges***

A pair of strain gauges were installed at 17 measurement locations on the bridge to accurately capture the strain profile at the midspan and at the ends of the bridge near the supports. The strain

gauge types used in Bridge CS-9 are Tokyo Measuring Instruments Lab PL-60-11-3LT and PL-60-11-3LJCT-F strain gauges. The main gauge was installed in the longitudinal direction, while the temperature compensation gauge was installed transverse to the main gauge. Figure 9.4 shows a close-up of the installation of the concrete strain gauges. Strain gauges were installed along the bottom of the slab at nine different locations. Gauges were also installed on top of both curbs at the midspan. Strain gauges were installed at the midspan and at an average of 6 in. from the bearing centerline at each abutment. The strains obtained from these gauges were used to determine the location of the neutral axis across the section and identify unintended end fixity at the supports.

Figure 9.4. Close-Up of Strain Gauge Installation

9.4.2.2 ***String Potentiometers***

Nine string potentiometers were installed at the midspan to record the midspan deflections during the vehicular load tests. Celesco SM1-2 string potentiometers having a 2.5 in. stroke were used at all nine locations.

*9.4.2.3 **Accelerometers***

A total of seven Brüel & Kjær IEPE accelerometers were installed—five accelerometers at the midspan and two accelerometers at quarter spans along the center of the bridge—to record the dynamic vibrations of the bridge during the dynamic load tests. The recorded vibrations were used to obtain the frequencies and the mode shapes of the bridge. The piezoelectric accelerometers are light, compact, and sensitive and have a resonance frequency of 18 kHz, which is much higher than the natural frequency of the bridge.

9.5 LOAD TESTING PROCEDURE FOR BRIDGE CS-9

A comprehensive test program was conducted to evaluate the performance and behavior of Bridge CS-9. The test program included two phases: (1) static load tests, which consisted of stop location tests and crawl speed tests, and (2) dynamic load tests. The vehicular load testing of Bridge CS-9 was conducted on May 22, 2019.

9.5.1 Test Vehicle

The vehicle used in the load testing was a 2006 Sterling dump truck provided by the TxDOT Bosque Office. The dump truck was loaded with base material to match the rear tandem axle weight to the load posting limit of a 28,000 lbs tandem axle. The truck configuration and its empty and loaded weights are shown in Figure 9.5.

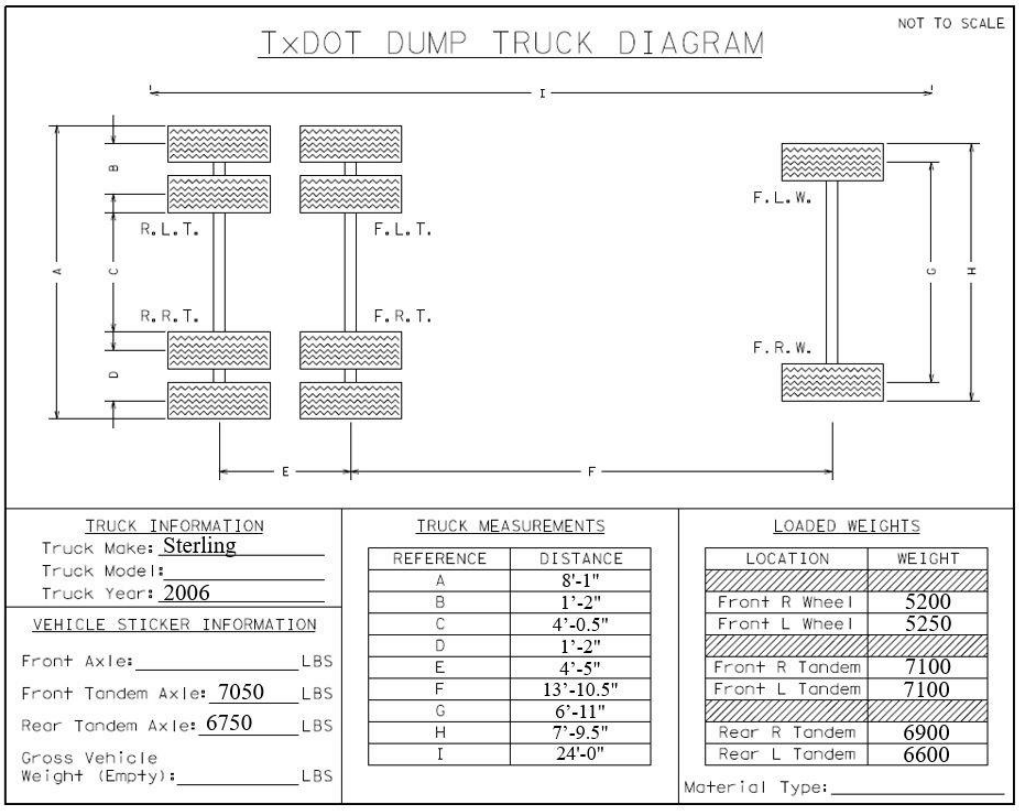

Figure 9.5. Wheel Weights and Spacing of the Loaded Dump Truck

9.5.2 Vehicle Positioning

Three transverse paths were defined across the bridge to create critical transverse loading positions for the bridge. The minimum allowable clearances from the curb and centerline of the bridge, as outlined in *AASHTO Standard Specifications* (AASHTO 2002) and *AASHTO LRFD Specifications* (AASHTO 2017), were adhered to when defining the paths. Figure 9.6 shows a schematic of the loading paths across the transverse section of the bridge. Path 1 corresponds to the location where the centerline of the adjacent rear wheel of the dump truck is located 2 ft away from the face of the curb. Path 2 is defined along the second lane, where the centerline of the adjacent rear wheel is located 1 ft 10 in. from the centerline of the bridge. Because of the narrow width of the bridge, the minimum clearance of 2 ft from the centerline could not be met. A third path was defined along the centerline of the bridge, called Middle Path, where the dump truck ran along the center of the bridge with the wheel lines equidistant from the bridge centerline.

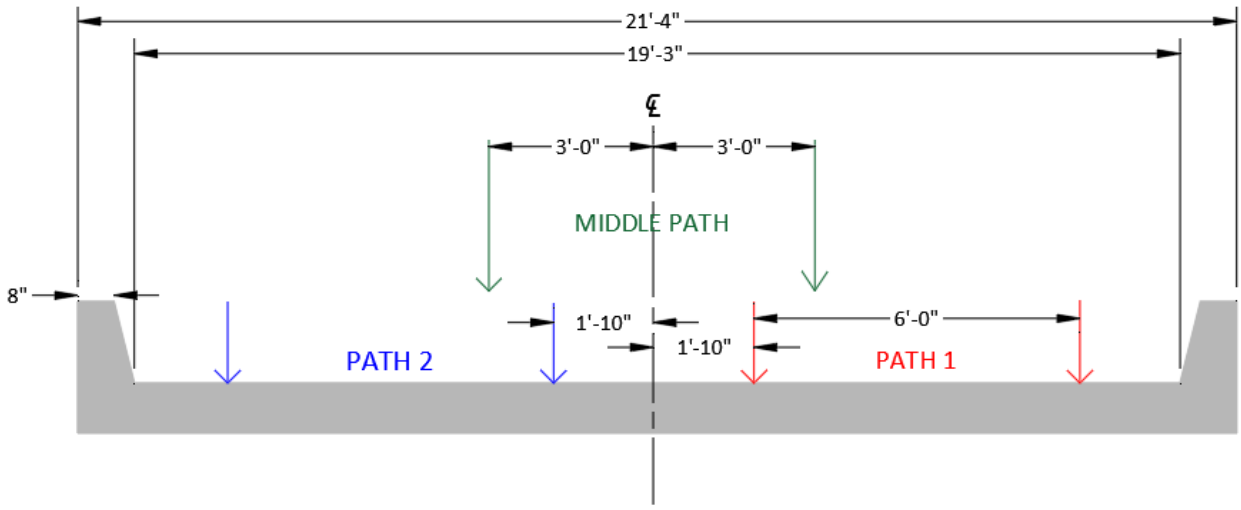

Figure 9.6. Load Test Paths for Bridge CS-9

9.5.3 Test Protocol

Bridge CS-9 was subjected to static, crawl speed, and dynamic tests. Sledge hammer tests were also conducted to capture the dynamic properties of the bridge. In the following sections, details regarding each test are outlined. Table 9.3 lists the test protocol carried out for load testing of Bridge CS-9.

Table 9.3. Test Protocol for Bridge CS-9

Test Number	Load Position	Test Type
1	Path 1	Static—Stop Location (Engine running)
2	Path 1	Static—Crawl Speed
3	Path 1	Dynamic (31 mph)
4	Path 1	Dynamic (41 mph)
5	Path 2	Static—Stop Location (Engine running)
6	Path 2	Static—Crawl Speed
7	Path 2	Dynamic (30 mph)
8	Path 2	Dynamic (40 mph)
9	Middle Path	Static—Stop Location (Engine running)
10	Middle Path	Static—Crawl Speed
11	Middle Path	Dynamic (29 mph)
12	Middle Path	Dynamic (40 mph)
13	Path 1	Static—Stop Location (Engine off)
14	Path 2	Static—Stop Location (Engine off)
15	Middle Path	Static—Stop Location (Engine off)
16	Middle Path	Dynamic (20 mph)
17	Middle Path	Dynamic (59 mph)
18	North	Sledgehammer
19	Middle Path	Sledgehammer
20	South	Sledgehammer
21	Northwest	Sledgehammer
22	Midwest	Sledgehammer
23	Southwest	Sledgehammer
24	Northeast	Sledgehammer
25	Mideast	Sledgehammer
26	Southeast	Sledgehammer
27	North Curb Middle	Sledgehammer
28	South Curb Middle	Sledgehammer

9.5.3.1 ***Static Tests***

The static load tests conducted on Bridge CS-9 were of two types: (1) a stop location test, and (2) a crawl speed test. For each static test along Path 1, Path 2, and the Middle Path, reference data were recorded prior to the bridge being loaded. The truck was positioned on the bridge such that the maximum bending moment would be obtained at the midspan of the bridge. This moment was achieved when the rear tandem and front tandem axles of the truck were located equidistant from

the midspan location of the bridge. Because of the short span of Bridge CS-9, the front axle of the truck was off the bridge for each static test. Once the truck was positioned and the engine was turned off, data for the loaded bridge were recorded.

Reference files prior to the truck crawling at a slow speed over the bridge were recorded for each test. Next, the data were recorded while the truck passed over the entire span of the bridge at an idle speed of 2–3 mph.

9.5.3.2 ***Dynamic Tests***

Prior to each test, reference files for the unloaded bridge were recorded. The truck picked up a predetermined speed and passed over the entire span of the bridge while maintaining the speed. The corresponding data were recorded. The dynamic tests were carried out at two different speeds. The first test for each path was conducted for a speed of 30 mph, and the second test was carried out for a speed of 45 mph. Additional dynamic tests were conducted along the middle path at 20 mph and 60 mph. The speed limit for the road on which the bridge was located was 65 mph.

9.5.3.3 ***Impact Tests***

A sledge hammer was used to hit the deck of the bridge three times at 11 different transverse positions to excite different modes of the bridge. The recorded vibration data were used to determine the dynamic properties of Bridge CS-9. The impact tests were carried out at three midspan locations (at the north side of the bridge, at the transverse center of the bridge, and at the south side of the bridge); at the same three locations along the west end of the bridge; at the same three locations along the east end of the bridge; and at the midspans of both curbs.

9.5.4 Test Operations

The testing schedule for Bridge CS-9 spanned from May 20, 2019, to May 22, 2019, and included all instrumentation installation, load testing, and instrumentation removal.

The clearance height to the underside of the bridge was approximately 12 ft. Thus, scaffolding was not needed. All instrumentation was installed on the underside of the bridge during the first two days with the use of stepladders. The installation locations were marked as per the instrumentation plan. An angle grinder with a masonry grinding wheel was used to grind an approximately 4 x 4 in. area at locations where the strain gauges were to be installed. The surface

was made smooth using 150- and 220-grit sandpaper and then cleaned with acetone. The surface was repeatedly cleaned with acetone applied to paper towels until a clean tip was no longer discolored by the scrubbing. Liberally applying acetone brings the surface pH back to an optimum alkalinity of 7.0 to 7.5 pH, ideal for bonding of the glue. Any microscopic gaps or cracks on the concrete surface were filled with the application of an epoxy. Once the epoxy dried, the surface was again made smooth with sandpaper and cleaned with acetone, as previously described. The strain gauges were installed onto the surface with a suitable adhesive after the surface dried.

For string potentiometers, nine wooden posts were hammered into the ground and the string potentiometers were screwed onto the posts. Metal hooks were installed on the underside of the slab at the midspan, and fishing line was attached from the hooks to the string potentiometers. Accelerometers were attached to metal plates glued onto the bottom of the slab at selected locations. Figure 9.7 shows the installed instrumentation for Bridge CS-9.

The nondestructive load tests were conducted on May 22, 2019. The designated paths were marked on the bridge with duct tape. The DAQ system was set up, and the cables from all instrumentation was attached to the DAQ boxes. The dump truck was loaded approximately to the posted load limit at the Bosque TxDOT maintenance office. The 28 tests listed in the test protocol were carried out, and the corresponding data were recorded. Figure 9.8(a) and Figure 9.8(b) shows the set-up for Test 1 and Test 5, respectively. After testing was completed, all instruments were removed.

(a) Installed Strain Gauges

(b) Installed Accelerometer

(c) Installed String Potentiometers

Figure 9.7. Installed Instrumentation for Bridge CS-9

(a) Static Test along Path 1

(b) Dump Truck Positioned for Static Test along Path 2

Figure 9.8. Testing of Bridge CS-9

9.6 TEST RESULTS FOR BRIDGE CS-9

The data recorded during the load test was processed, analyzed, and filtered for noise, if necessary. The slab was divided into nine transverse sections, and the corresponding data were recorded. Strain gauge data were used to determine the strain profile within the section depth. String potentiometers recorded the deflections across the bridge width, from which the lateral distribution of load was determined. The dynamic properties of the bridge, such as natural frequencies and mode shapes, were obtained from the vibration data recorded by the accelerometers. An image analysis algorithm was used to determine the deflections from the videos recorded during each test. These results are provided in the following sections.

9.6.1 Static Load Tests on Bridge CS-9

Two types of static load tests were performed on Bridge CS-9—stop location tests and crawl speed tests. During the stop location tests, the truck was positioned on the bridge such that the maximum bending moment would be obtained at the midspan. This procedure was carried out twice: once with the engine running and a second time with the engine turned off. During the crawl speed test, the truck passed over the entire span of the bridge at an idle speed of approximately 2–3 mph.

*9.6.1.1 **Strain Measurements***

The strain gauge data for each test were compiled. For the stop location test, the maximum strain occurring at each strain gauge location was obtained. For the crawl speed test, the maximum bottom strain in the transverse section and the corresponding time at which this strain occurs was first obtained. All other strain values were extracted for that specific time. It should be noted that the tensile strains are taken to be positive, and the compressive strains are negative. The neutral axis location for each exterior section was determined from the strain profile at the midspan. Top strain gauges could not be installed at the midspan of the bridge for the interior slab sections due to the thick layer of asphalt. It should be noted that the strain values obtained from the bottom strain gauge attached at the midspan of the transverse Section S5 were very high and may indicate an issue with the gauge.

Exterior Sections 1 and 9—Path 1 Loading. Strain profiles corresponding to the top and bottom strains for exterior Sections S1 and S9 under static tests along Path 1 are provided in Figure 9.9.

The strain profiles at the midspan of Section S1 are shown in Figure 9.9(a) for the stop location test and Figure 9.9(c) for the crawl speed test. The neutral axis depth at the midspan of the curb was 12.55 in. from the bottom face using the strain profile obtained from the stop location test and 14.56 in. from the bottom face using the strain profile obtained from the crawl speed test. The neutral axis depth calculated using the strain profile obtained from the crawl speed test is slightly higher than the one obtained from the stop location test. This result could be due to the stop location test being slightly different from the moment critical position for the absolute maximum moment. Moreover, the transverse location of the truck may be slightly different between the stop location test and crawl speed test.

The strain profiles at the west end, midspan, and east end of Section S9 are shown in Figure 9.9(b) for the stop location test and Figure 9.9(d) for the crawl speed test. The strain at the west and east ends of Section S9 are compressive for both the stop location test and crawl speed test, indicating some degree of end fixity present. The difference at the end strains for both tests may be due to the truck stop location not being exactly at the moment critical position. The neutral axis depth at the midspan of the curb was 5.79 in. from the bottom of S9 using the strain profile obtained from the stop location test and 4.96 in. from the bottom of S9 using the strain profile obtained from the crawl speed test.

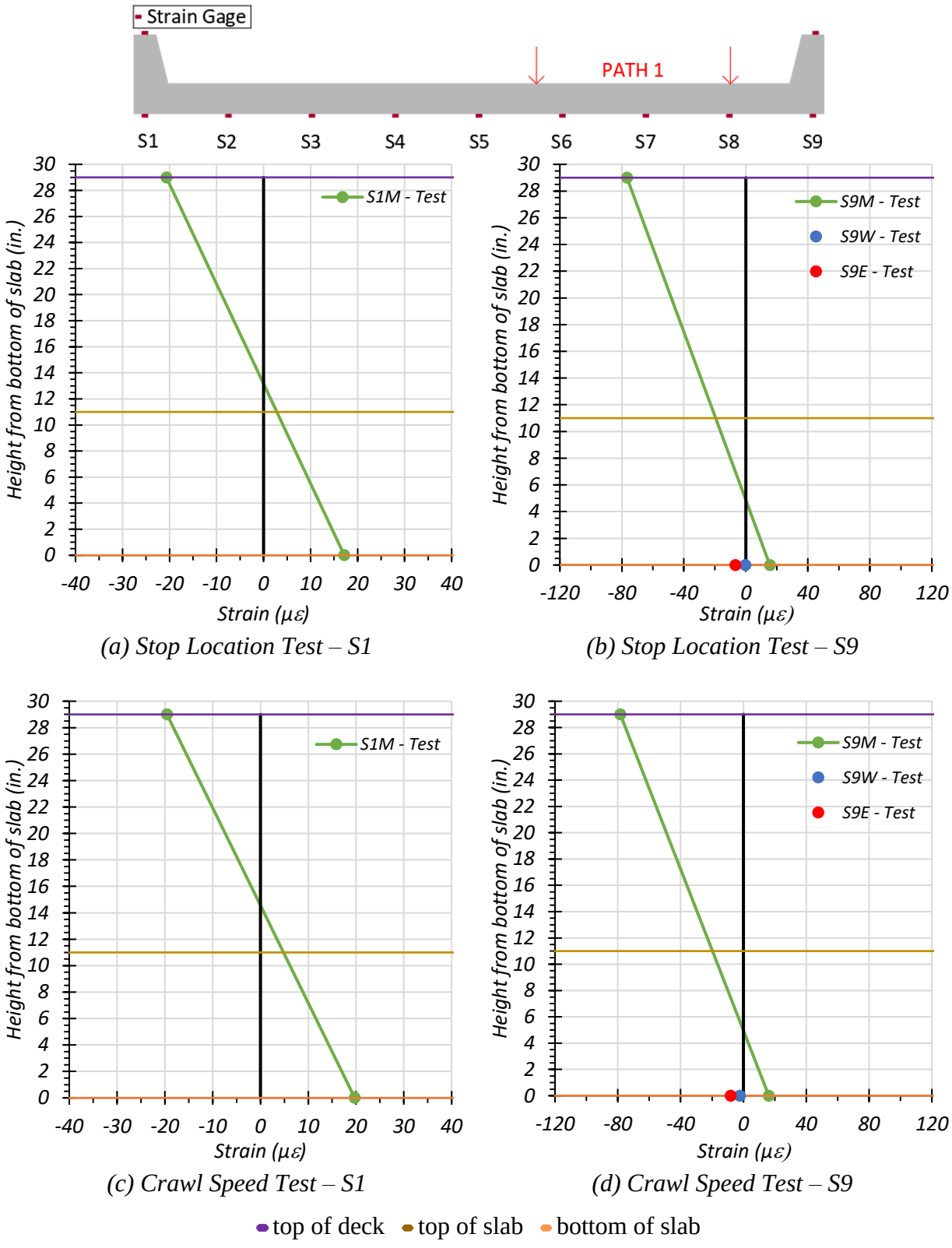

Figure 9.9. Static Strains for Exterior Sections—Path 1

Exterior Sections 1 and 9—Path 2 Loading. Strain profiles corresponding to the top and bottom strains for exterior Sections S1 and S9 under static tests along Path 2 are provided in Figure 9.10.

The strain profiles at the midspan of Section S1 are shown in Figure 9.10(a) for the stop location test and Figure 9.10(c) for the crawl speed test. The neutral axis depth at the midspan of the curb was 13.28 in. from the bottom using the strain profile obtained from the stop location test and 13.50 in. from the bottom using the strain profile obtained from the crawl speed test. The neutral axis depth calculated using the strain profile obtained from the crawl speed test is slightly higher than the one obtained from the stop location test. This result could also be due to the stop location test being slightly different from the moment critical position for the absolute maximum moment. Moreover, the transverse location of the truck may be slightly different between the stop location test and crawl speed test.

The strain profiles at the west end, midspans, and east end of Section S9 are shown in Figure 9.10(b) for the stop location test and Figure 9.10(d) for the crawl speed test. The strain at the east ends of Section S9 are compressive for both the stop location test and crawl speed test, indicating some degree of end fixity is present. However, the strain at the west end is tensile for the stop location test and compressive for the crawl speed test. The difference at the end strains for both tests may be due to the truck stop location not being exactly at the moment critical position. The neutral axis depth at the midspan of the curb was 4.71 in. from the bottom of Section S9 using the strain profile obtained from the stop location test and 4.56 in. from the bottom of Section S9 using the strain profile obtained from the crawl speed test.

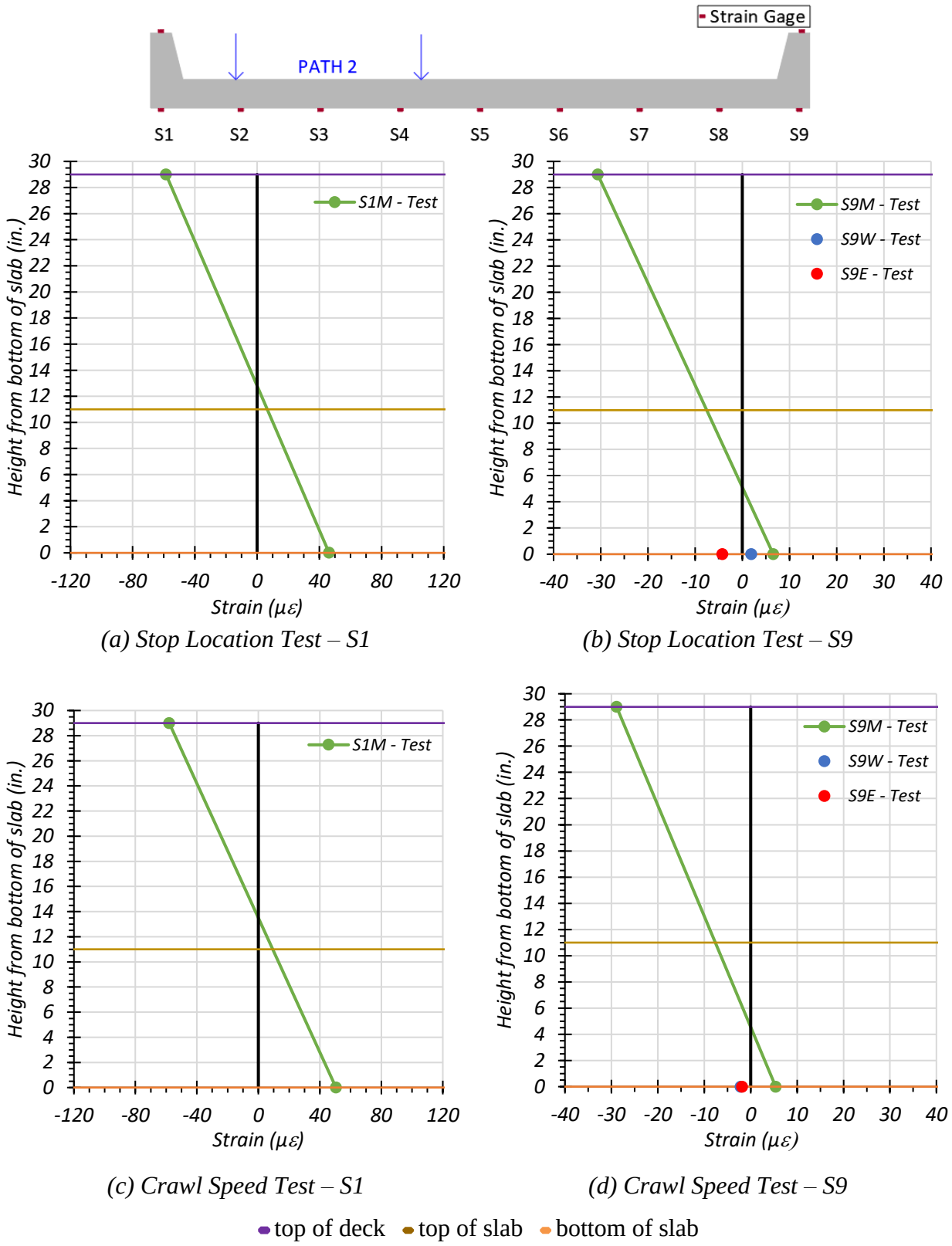

(a) Stop Location Test – S1

(b) Stop Location Test – S9

(c) Crawl Speed Test – S1

(d) Crawl Speed Test – S9

Figure 9.10. Static Strains for Exterior Sections—Path 2

Exterior Sections 1 and 9—Middle Path Loading. Strain profiles corresponding to the top and bottom strains for exterior Sections S1 and S9 under static tests along the Middle Path are provided in Figure 9.11.

The strain profiles at the midspan of Section S1 are shown in Figure 9.11(a) for the stop location test and Figure 9.11(c) for the crawl speed test. The neutral axis depth at the midspan of the curb was 13.57 in. from the bottom of Section S1 using the strain profile obtained from the stop location test and 12.95 in. from the bottom of Section S1 using the strain profile obtained from the crawl speed test. The neutral axis depth calculated using the strain profile obtained from the stop location test is slightly higher than the one obtained from the crawl speed test. This result could be due to the stop location test being slightly different from the moment critical position for the absolute maximum moment. Moreover, the transverse location of truck may be slightly different between the stop location test and crawl speed test.

The strain profiles at the west end, midspan, and east end of Section S9 are shown in Figure 9.11(b) for the stop location test and Figure 9.11(d) for the crawl speed test. The strain at the west end of S9 is tensile for both the stop location test and crawl speed test, indicating the absence of any significant end restraint. The bottom strain at the east end of Section S9 is compressive for both the stop location test and crawl speed test, indicating some degree of end fixity is present. The difference at the end strains for both tests may be due to the truck stop location not being exactly at the moment critical position. The neutral axis depth at the midspan of the curb was 5.23 in. from the bottom of S9 using the strain profile obtained from the stop location test and 4.63 in. from the bottom of S9 using the strain profile obtained from the crawl speed test.

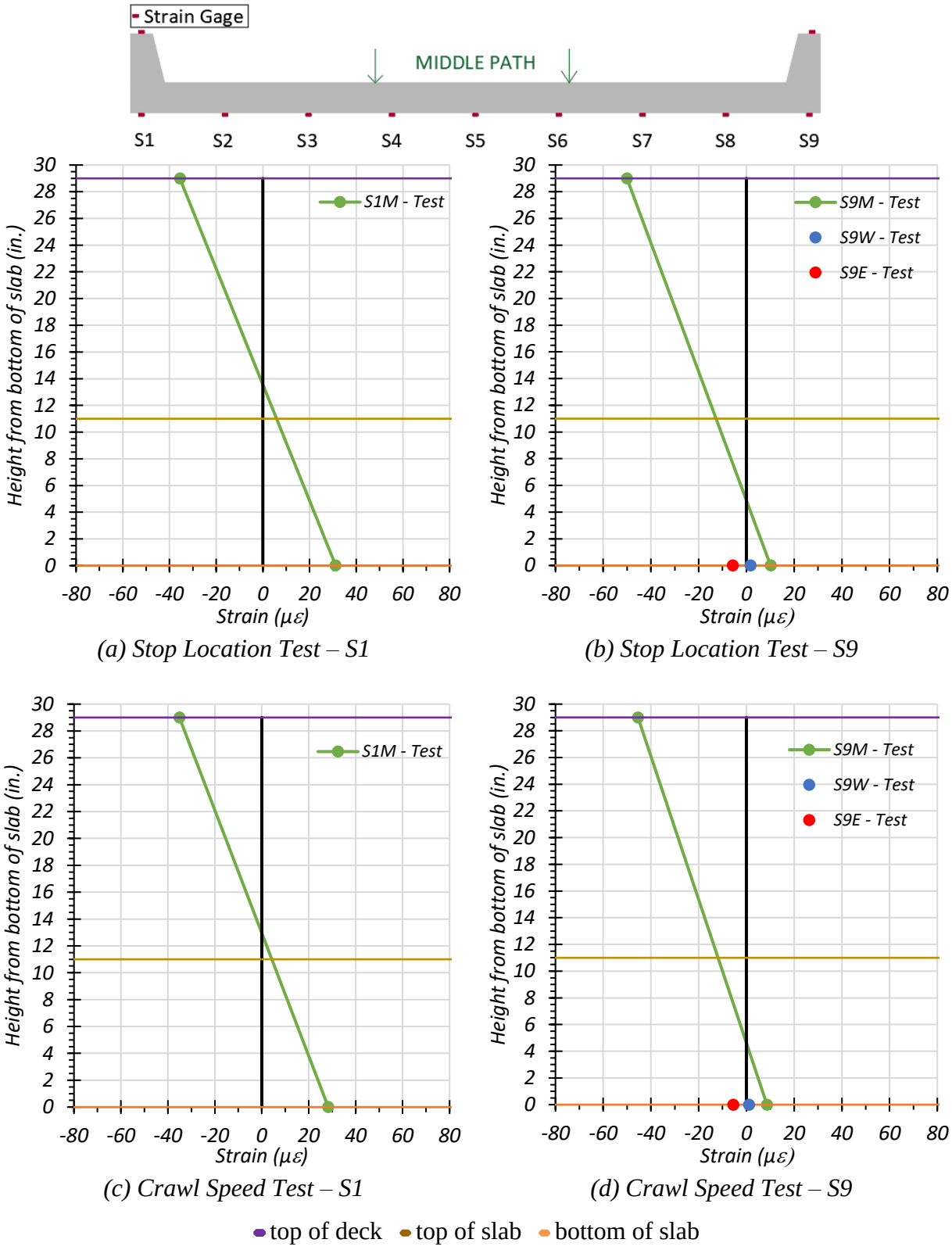

(a) Stop Location Test – S1

(b) Stop Location Test – S9

(c) Crawl Speed Test – S1

(d) Crawl Speed Test – S9

Figure 9.11. Static Strains for Exterior Sections—Middle Path

Comparison of Measured Strain Results. Theoretical calculations to determine the neutral axis depth for a cracked and uncracked concrete section were carried out for both an exterior and interior transverse section. A typical transverse section, along with the reinforcement information from the structural drawings, is provided in Figure 9.12. The curbs consisted of two 1.25 in. square-bottom reinforcing bars, while the bottom reinforcement in the slab consisted of #8 bars at 8.5 in. centers. The MOE for concrete was calculated using the following equation, valid for normal weight concrete with unit weights between 0.09 and 0.155 kcf and design compressive strength up to 15.0 ksi, according to Article 8.7 in the *AASHTO Standard Specifications* (AASHTO 2002):

$$E_c = 33{,}000 K_1 w_c^{1.5} \sqrt{f_c'} \quad (9.1)$$

where:

E_c = Elastic modulus of concrete, ksi

K_1 = Correction factor for source of aggregate, to be taken as 1.0 unless determined by physical test

w_c = Unit weight of concrete, kcf

f_c' = Compressive strength of concrete, ksi

The MOE for concrete was calculated to be 4809 ksi based on the measured f_c' of 5.2 ksi. The theoretical position of the neutral axis depth was determined to be 13.33 in. from the bottom for the curb and 5.50 in. from the bottom of the slab for an uncracked concrete section. For a cracked concrete section, the neutral axis depth was calculated to be 21.43 in. from the bottom of the curb and 8.29 in. from the bottom of the slab.

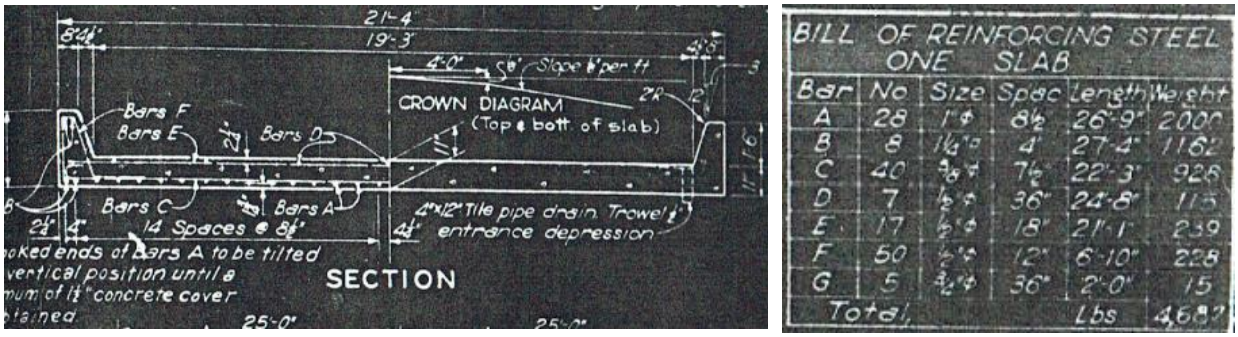

Figure 9.12. Transverse Section of Bridge CS-9 (TxDOT 2005)

Table 9.4 lists the midspan neutral axes corresponding to the various load tests. Figure 9.13 compares the neutral axes obtained from the static tests with the theoretical neutral axis for both Sections S1 and S9. The neutral axes determined from the tests tend to be closer to the theoretical uncracked neutral axis for Section S1. However, the neutral axis depth is lower for the transverse section S9, which may be due to the stiffness of Section S9 being smaller compared to Section S1.

Table 9.4. Measured Neutral Axis Locations for Exterior Sections—Static Load Tests

Test	S1 Neutral Axis Location (in. from bottom of slab)	S9 Neutral Axis Location (in. from bottom of slab)
Path 1—Stop Location	15.80	5.79
Path 1—Crawl Speed	14.56	4.96
Path 2—Stop Location	12.59	6.17
Path 2—Crawl Speed	13.50	4.56
Middle Path—Stop Location	13.53	5.78
Middle Path—Crawl Speed	12.95	4.63
Theoretical Uncracked	13.33	
Theoretical Cracked	21.43	

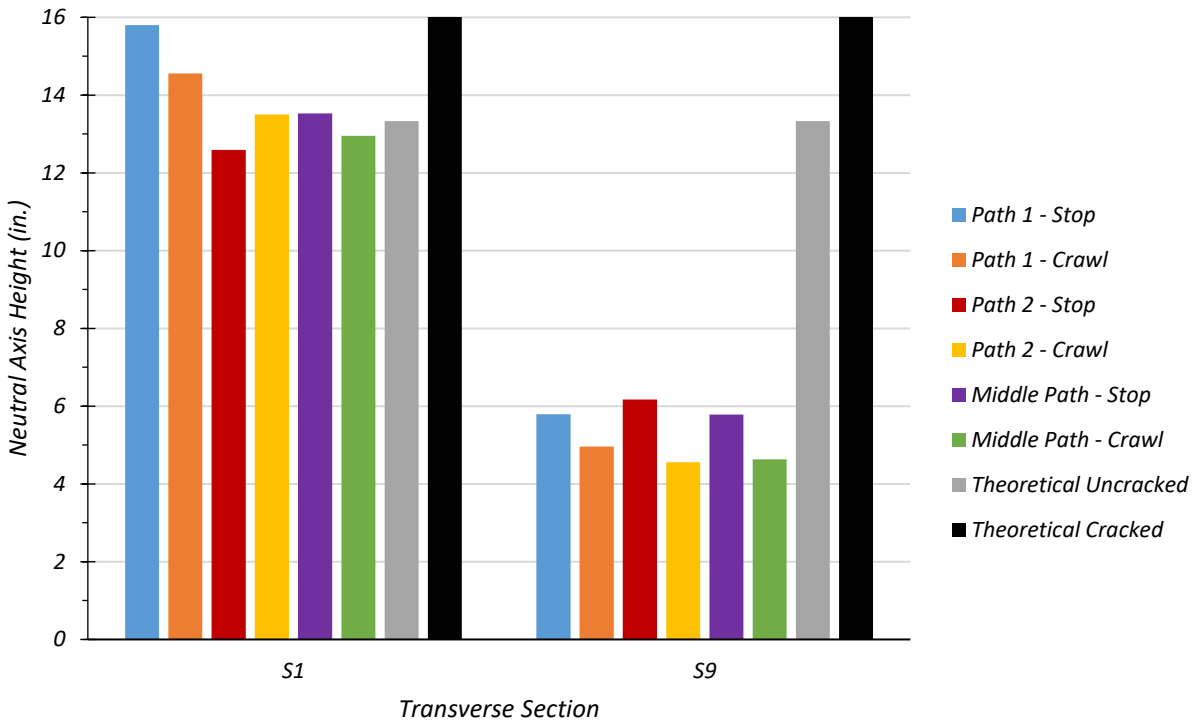

Figure 9.13. Test Neutral Axis Locations

Because of very large compressive strain values (around $-200\,\mu\varepsilon$) obtained from transverse Section S5, which indicates a gauge issue leading to errors in the measured strains, these strain values have not been plotted in the following figures. Figure 9.14 shows the distribution of strain across the bottom of the bridge width for Path 1 loading. Each point represents a strain gauge location at the center of the corresponding section (S1, S2, etc.). The strain distribution across the bottom of the bridge for Path 2 loading is shown in Figure 9.15. Figure 9.16 shows the bottom strain distribution across the bridge width for Middle Path loading. As anticipated, the strains obtained from the crawl speed test were generally higher than those strains obtained from the stop location test. However, the strain obtained for the Section S6 is compressive for both the stop location test and crawl speed test for Path 1 and Middle Path loading, an unexpected result. The strains obtained at Section S4 are consistently high for all loading paths. Because the recorded strains for Section S4 are inconclusive, they are presented with black open circles in the following plots.

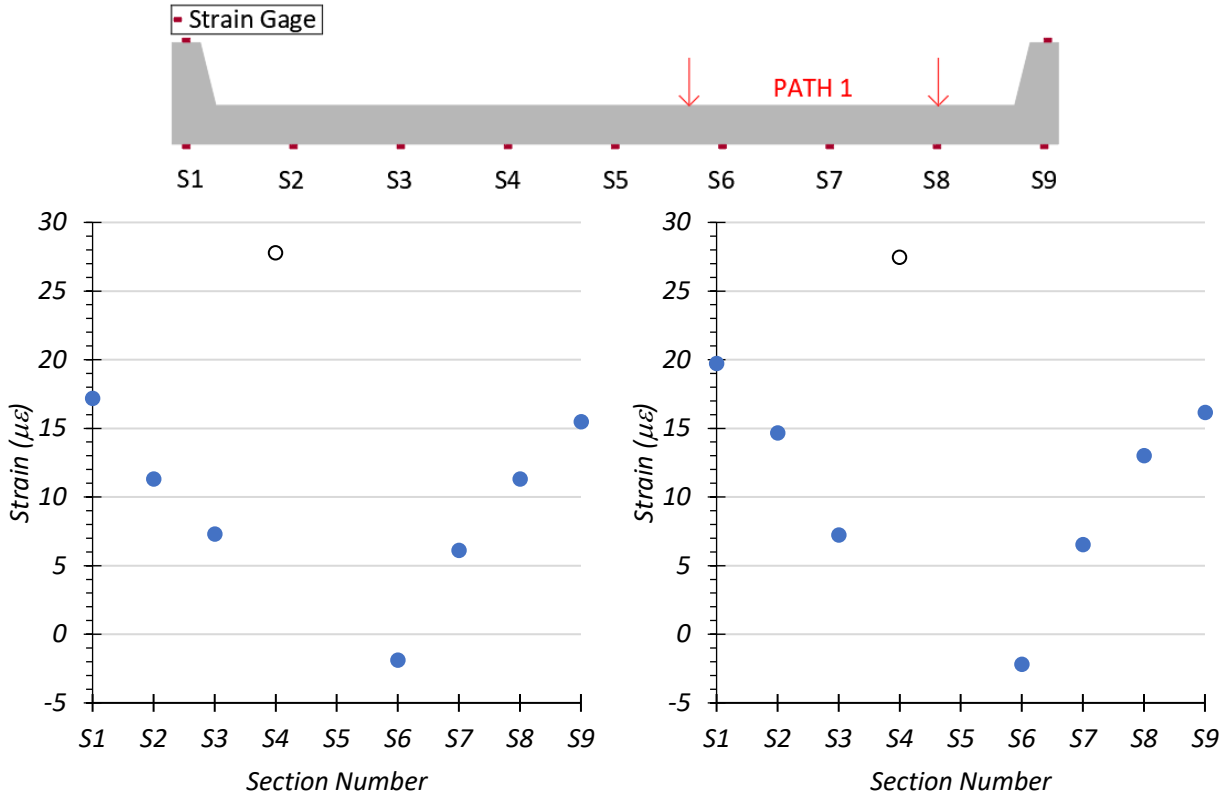

(a) Stop Location Test *(b) Crawl Speed Test*

Figure 9.14. Static Strains across Bridge Width—Path 1

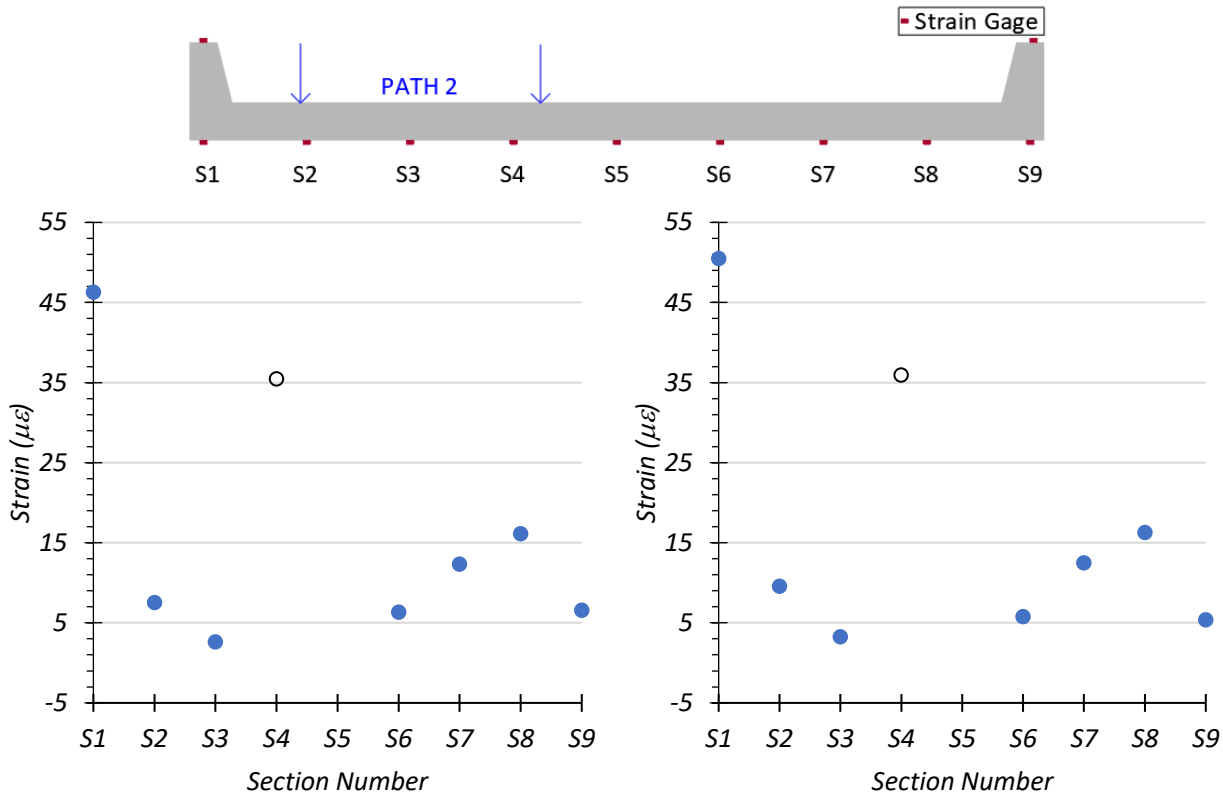

(a) Stop Location Test *(b) Crawl Speed Test*

Figure 9.15. Static Strains across Bridge Width—Path 2

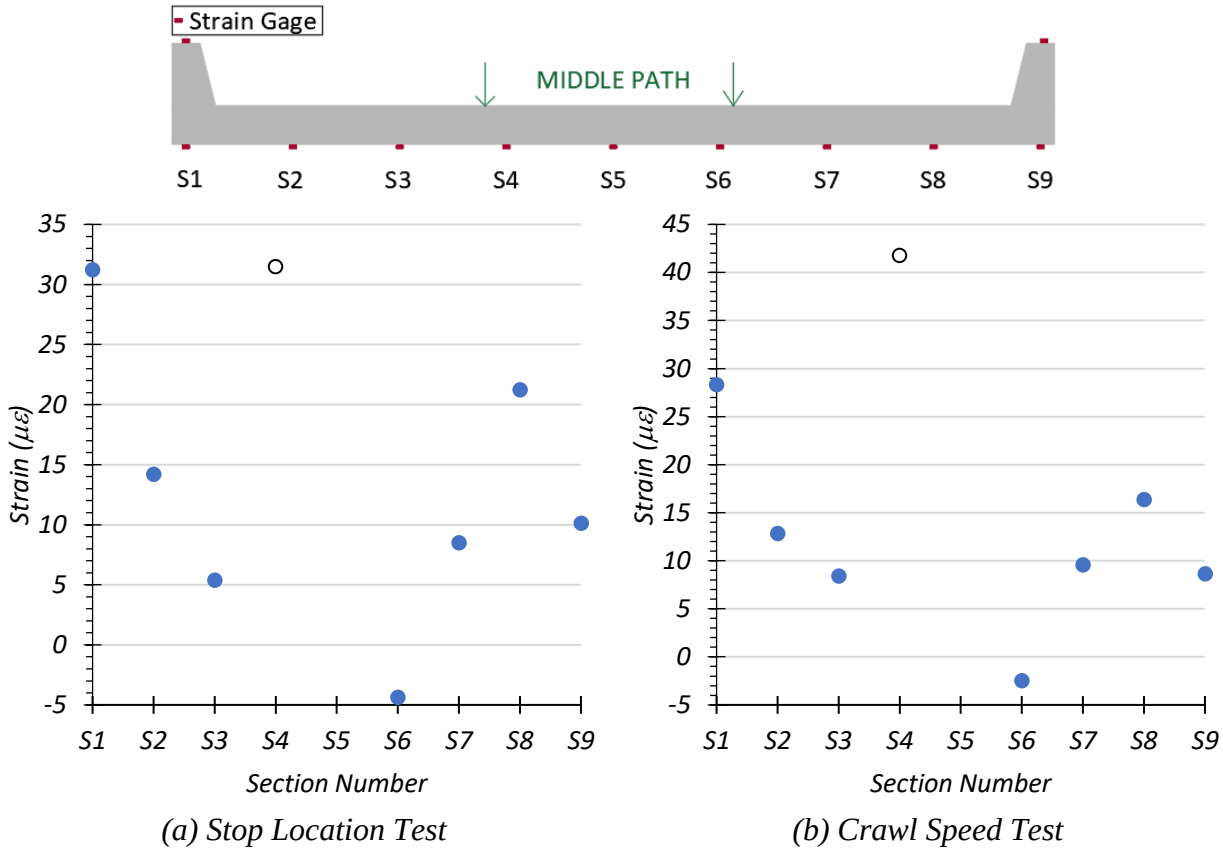

Figure 9.16. Static Strains across Bridge Width—Middle Path

No significant trends can be observed from the plots of the distribution of strain measured across the bottom of the bridge width at the midspan for the different loading scenarios. The measured strains were deemed to provide insufficient information to determine LLDFs with an acceptable level of confidence. In general, the use of bonded gauges can be influenced by cracks at or near a gauge. In the case of an existing bridge, this can be difficult to avoid, particularly when placing gauges in key locations, as for this test. In the following section, LLDFs are calculated using the recorded deflections.

9.6.1.2 ***Deflection Measurements and LLDFs***

The deflection for each transverse section was recorded over a period of time for each test. The maximum downward deflection for each section was obtained. The corresponding LLDF for each section was calculated using Equation (9.2):

$$LLDF = \frac{\Delta_i I_i}{\sum \Delta_i I_i} \tag{9.2}$$

where:

$LLDF$ = Live load distribution factor

Δ_i = Maximum vertical deflection of section *i*, in.

I_i = Cracked moment of inertia of section *i*, in^4

The equivalent width for the slab portion was calculated as the width of the transverse section $W_{Section}$ divided by the maximum LLDF of the slab sections (S2 through S8), as shown in Equation (9.3). The interior transverse sections were each 2 ft 7 in. wide.

$$E = \frac{W_{Section}}{LLDF_{max}} \tag{9.3}$$

Path 1 Loading. Measured deflections for each section for the stop location test and crawl test are shown in Figure 9.17(a) and (b), respectively. The measured deflection for all transverse sections and the LLDFs for the stop location test and crawl speed test along Path 1 are provided in Table 9.5. For both the stop location test and crawl speed test, the maximum exterior section deflection was observed at Section S9, and the maximum interior section deflection was observed at Section S6. This result was due to the close proximity of these sections to the wheel lines. The corresponding LLDF for Section S9 was 0.602 for the stop location test and 0.593 for the crawl speed test. Section S6 had an LLDF of 0.052 for the stop location test and 0.050 for the crawl speed test.

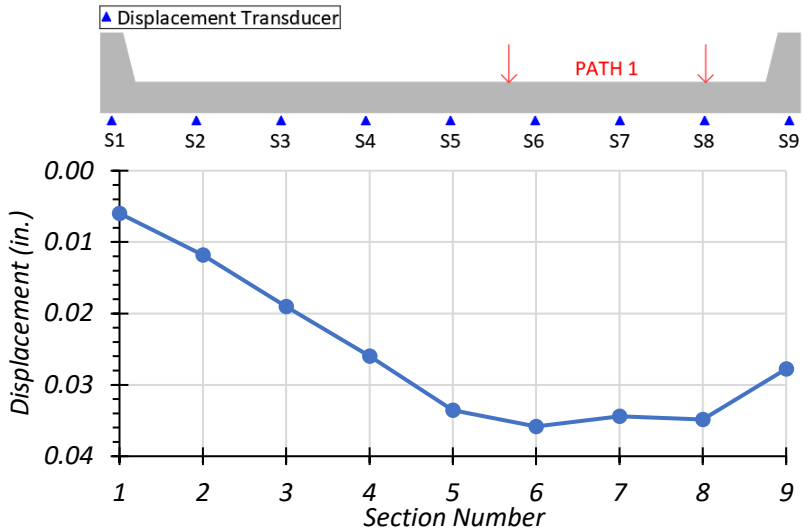

(a) Stop Location Test

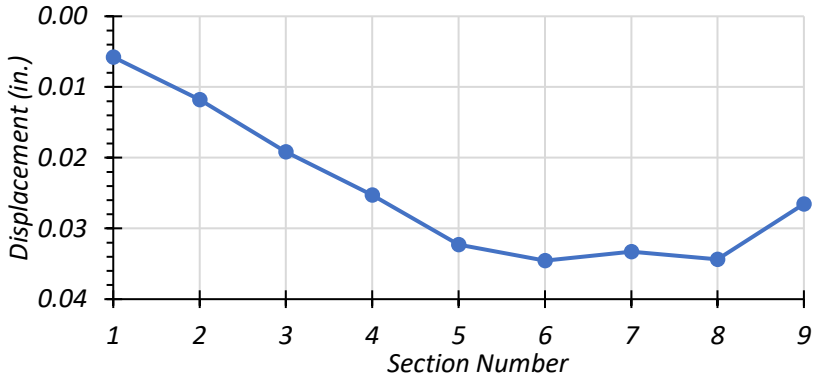

(b) Crawl Speed Test

Figure 9.17. Static Deflection Results for Path 1 Loading

Table 9.5. Experimental Deflections and LLDFs for Path 1 Loading

Section	S1	S2	S3	S4	S5	S6	S7	S8	S9
Stop Location Test Disp. (in.)	0.006	0.011	0.019	0.028	0.035	0.039	0.035	0.036	0.029
Stop Location Test LLDF	0.122	0.015	0.026	0.037	0.048	0.052	0.047	0.049	0.602
Crawl Speed Test Disp. (in.)	0.006	0.012	0.019	0.025	0.032	0.035	0.033	0.034	0.027
Crawl Speed Test LLDF	0.129	0.017	0.028	0.037	0.047	0.050	0.048	0.050	0.593

Note: 1 – S = Section, Disp. = Displacement
2 – LLDF values are based on the midspan deflections.

The LLDFs computed based on the full bridge width result in very large equivalent width values (50–52 ft). Therefore, the IB346 concept (discussed further in Section 9.6.1.3) of defining the L-curb for integral curb and slab bridges is used. Table 9.6 tabulates the step-by-step calculations for the equivalent width of the interior slab section for the stop location test. The IB346 concept of the L-curb (curb section plus 4*h* of the slab) is introduced in this table by considering the combined effect of Sections S1 and S2 and Sections S8 and S9. The bottom width of the curb is 12.5 in., and the thickness of the slab is 11 in. Thus, the total width of the L-curb section is 56.5 in. The deflection for the left L-curb is calculated at the section centroid (23 in. from the bridge edge) by linearly interpolating between the deflections for Sections S1 and S2. This approach is also applied to the right L-curb by interpolating between Sections S8 and S9. The moment of inertias of the cracked L-curb sections and the interior slab section are presented in the table. The LLDFs are calculated using Equation (9.2). The factor *g* refers to the proportion of the total live load taken by each component, the L-curb sections, and the mid-slab section. Equation (9.3) is used to calculate the equivalent width for the interior slab portion. For the stop location test, the maximum LLDF for the interior slab portion is 0.153, and the corresponding equivalent width is 16.88 ft. The corresponding results for the crawl speed test are presented in Table 9.7. The maximum LLDF for the crawl speed test for the interior slab portion is 0.145, and the equivalent width is 17.83 ft. The equivalent width calculated from the crawl speed test is higher than the width obtained from the stop location test; therefore, the stop location result is more conservative.

Table 9.6. Experimental Deflections, LLDFs, and Equivalent Width for Stop Location Test along Path 1 Using L-Curbs

Section	**S1+S2 (Left L-curb)**		**S3**	**S4**	**S5**	**S6**	**S7**	**S8+S9 (Right L-curb)**	
Width (ft)	4.708		2.083	2.583	2.583	2.583	2.083	4.708	
Δ (in.)	0.006	0.011	0.019	0.028	0.035	0.039	0.035	0.036	0.029
	0.009		0.019	0.028	0.035	0.039	0.035	0.034	
I_i (in^4)	14,925		6682	6682	6682	6682	6682	14,925	
$I_i\Delta$ (in^5)	139.03		127.23	183.85	234.39	257.55	231.90	508.80	
LLDF	0.083		0.076	0.109	0.139	0.153	0.138	0.302	
g	0.083		0.615					0.302	
E (ft)	–		16.88					–	

Table 9.7. Experimental Deflections, LLDFs, and Equivalent Width for Crawl Speed Test along Path 1 Using L-Curbs

Section	S1+S2 (Left L-curb)		S3	S4	S5	S6	S7	S8+S9 (Right L-curb)	
Width (ft)	4.708		2.083	2.583	2.583	2.583	2.083	4.708	
Δ (in.)	0.006	0.012	0.019	0.025	0.032	0.035	0.033	0.034	0.027
	0.010		0.019	0.025	0.032	0.035	0.033	0.032	
I_i (in^4)	14,925		6682	6682	6682	6682	6682	14,925	
$I_i\Delta$ (in^5)	149.39		128.09	168.89	215.82	230.88	222.47	477.97	
LLDF	0.094		0.080	0.106	0.135	0.145	0.140	0.300	
g	0.094		0.606					0.300	
E (ft)	–		17.83					–	

Path 2 Loading. Measured deflections for each section for the stop location test and crawl test are shown in Figure 9.18(a) and (b), respectively.The measured deflections for all transverse sections and the corresponding computed LLDFs for the stop location test and crawl test along Path 2 are provided in Table 9.8. For both the stop location test and crawl speed test, the maximum exterior section deflection was observed at Section S1, and the maximum interior section deflection was observed at Section S4. This result was due to the close proximity of these sections to the wheel lines. The corresponding LLDF for Section S9 was 0.598 for the stop location test and 0.621 for the crawl speed test. Section S4 had an LLDF of 0.053 for the stop location test and 0.054 for the crawl speed test.

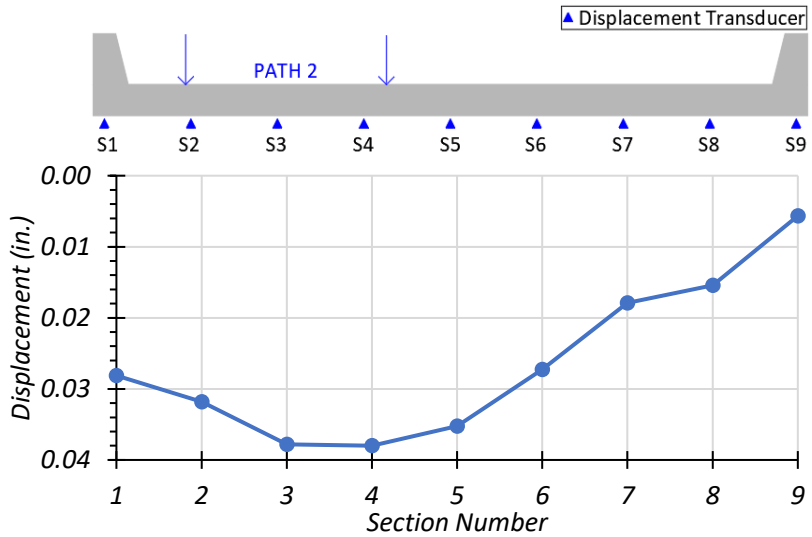

(a) Stop Location Test

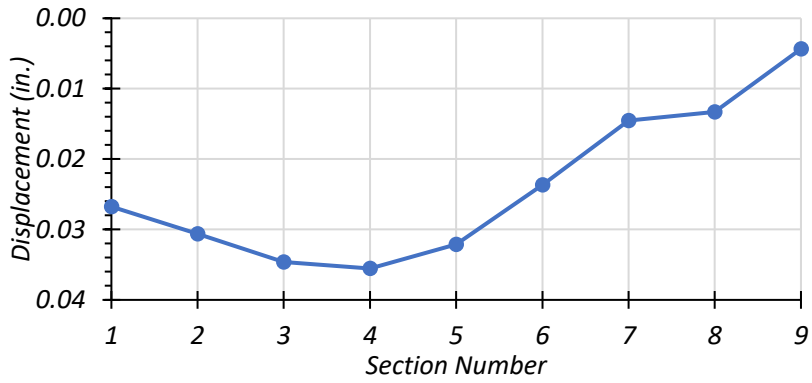

(c) Crawl Speed Test

Figure 9.18. Static Deflection Results for Path 2 Loading

Table 9.8. Experimental Deflections and LLDFs for Path 2 Loading

Section	S1	S2	S3	S4	S5	S6	S7	S8	S9
Stop Location Test Disp. (in.)	0.028	0.032	0.038	0.038	0.035	0.027	0.018	0.015	0.006
Stop Location Test LLDF	0.598	0.044	0.052	0.053	0.049	0.038	0.025	0.021	0.120
Crawl Speed Test Disp. (in.)	0.027	0.031	0.035	0.036	0.032	0.024	0.015	0.013	0.004
Crawl Speed Test LLDF	0.621	0.046	0.052	0.054	0.049	0.036	0.022	0.020	0.101
Note: 1 – S = Section, Disp. = Displacement 2 – LLDF values are based on the midspan deflections.									

Table 9.9 tabulates the step-by-step calculations for the equivalent width of the interior slab section for the stop location test using the IB346 definition of L-curbs. The corresponding results for the crawl speed test are presented in Table 9.10. The equivalent width calculated from the crawl speed test is smaller than the width obtained from the stop location test, which could be due to the stop location test being slightly different from the moment critical position for the absolute maximum moment. Moreover, the transverse location of the truck may be slightly different between the stop location test and crawl speed test.

Table 9.9. Experimental Deflections, LLDFs, and Equivalent Width for Stop Location Test along Path 2 Using L-Curbs

Section	**S1+S2 (Left L-curb)**		**S3**	**S4**	**S5**	**S6**	**S7**	**S8+S9 (Right L-curb)**	
Width (ft)	4.708		2.083	2.583	2.583	2.583	2.083	4.708	
Δ (in.)	0.028	0.032	0.038	0.038	0.035	0.027	0.018	0.015	0.006
	0.031		0.038	0.038	0.035	0.027	0.018	0.013	
I_i (in^4)	14925		6682	6682	6682	6682	6682	14925	
$I_i\Delta$ (in^5)	458.56		252.69	253.90	235.50	182.20	119.50	186.75	
LLDF	0.271		0.150	0.150	0.139	0.108	0.071	0.111	
g	0.271		0.618					0.111	
E (ft)	–		17.19					–	

Table 9.10. Experimental Deflections, LLDFs, and Equivalent Width for Crawl Speed Test along Path 2 Using L-Curbs

Section	**S1+S2 (Left L-curb)**		**S3**	**S4**	**S5**	**S6**	**S7**	**S8+S9 (Right L-curb)**	
Width (ft)	4.708		2.083	2.583	2.583	2.583	2.083	4.708	
Δ (in.)	0.027	0.031	0.035	0.036	0.032	0.024	0.015	0.013	0.004
	0.029		0.035	0.036	0.032	0.024	0.015	0.011	
I_i (in^4)	14925		6682	6682	6682	6682	6682	14925	
$I_i\Delta$ (in^5)	439.78		231.20	237.51	214.68	158.17	97.17	158.93	
LLDF	0.286		0.150	0.154	0.140	0.103	0.063	0.103	
g	0.286		0.611					0.103	
E (ft)	–		16.72					–	

Middle Path Loading. Measured deflections for each section for the stop location test and crawl speed test are plotted in Figure 9.19(a) and (b), respectively. The measured deflections for all transverse sections and the LLDFs for the stop location test and crawl test along the Middle Path are provided in Table 9.11. For both the stop location test and crawl speed test, the maximum exterior section deflection was observed at Section S1, and the maximum interior section deflection was observed at Section S5. This result was due to the close proximity of these sections to the wheel lines. The corresponding LLDF for Section S1 was 0.341 for the stop location test and 0.348 for the crawl speed test. Section S5 has a corresponding LLDF of 0.057 for the stop location test and 0.058 for the crawl speed test.

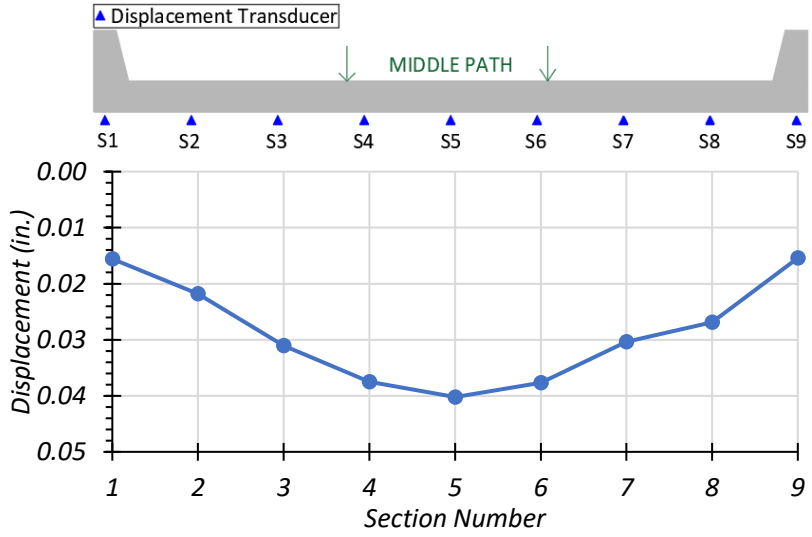

(a) Stop Location Test

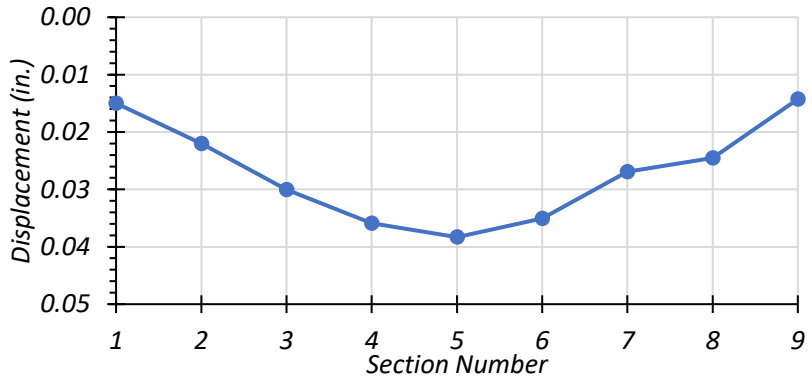

(c) Crawl Speed Test

Figure 9.19. Static Deflection Results for Middle Path Loading

Table 9.11. Experimental Deflections and LLDFs for Middle Path Loading

Section	S1	S2	S3	S4	S5	S6	S7	S8	S9
Stop Location Test Disp. (in.)	0.016	0.022	0.031	0.037	0.040	0.038	0.030	0.027	0.015
Stop Location Test LLDF	0.341	0.031	0.044	0.053	0.057	0.054	0.043	0.038	0.338
Crawl Speed Test Disp. (in.)	0.015	0.022	0.030	0.036	0.038	0.035	0.027	0.024	0.014
Crawl Speed Test LLDF	0.348	0.033	0.045	0.054	0.058	0.053	0.041	0.037	0.331
Note: 1 – S = Section, Disp. = Displacement 2 – LLDF values are based on the midspan deflections.									

Table 9.12 tabulates the step-by-step calculation for the equivalent width of the interior slab section for the stop location test using the IB346 definition of L-curbs. The corresponding results for the crawl speed test are presented in Table 9.13. The equivalent width calculated from the crawl speed test is slightly smaller than the width obtained from the stop location test.

Table 9.12. Experimental Deflections, LLDFs, and Equivalent Width for Stop Location Test along Middle Path Using L-Curbs

Section	S1+S2 (Left L-curb)		S3	S4	S5	S6	S7	S8+S9 (Right L-curb)	
Width (ft)	4.708		2.083	2.583	2.583	2.583	2.083	4.708	
Δ (in.)	0.016	0.022	0.031	0.037	0.040	0.038	0.030	0.027	0.015
	0.020		0.0310	0.0375	0.0402	0.0377	0.0303	0.023	
I_i (in^4)	14,925		6682	6682	6682	6682	6682	14,925	
$I_i\Delta$ (in^5)	297.83		207.35	250.42	268.77	251.92	202.78	350.14	
LLDF	0.163		0.113	0.137	0.147	0.138	0.111	0.191	
g	0.163		0.646					0.191	
E (ft)	–		17.58					–	

Table 9.13. Experimental Deflections, LLDFs, and Equivalent Width for Crawl Speed Test along Middle Path Using L-Curbs

Section	S1+S2 (Left L-curb)		S3	S4	S5	S6	S7	S8+S9 (Right L-curb)	
Width (ft)	4.708		2.083	2.583	2.583	2.583	2.083	4.708	
Δ (in.)	0.015	0.022	0.030	0.036	0.038	0.035	0.027	0.024	0.014
	0.020		0.0300	0.0359	0.0383	0.0351	0.0269	0.021	
I_i (in^4)	14,925		6682	6682	6682	6682	6682	14,925	
$I_i\Delta$ (in^5)	297.29		200.64	239.78	256.08	234.23	179.88	320.28	
LLDF	0.172		0.116	0.139	0.148	0.136	0.104	0.185	
g	0.172		0.643					0.185	
E (ft)	–		17.43					–	

Summary of Deflection Results. The string potentiometer at Section S7 showed consistently low deflections for all static tests along Path 1, Path 2, and the Middle Path, which suggests that there may be an error with the string potentiometer and the corresponding results recorded. This potential error will be further evaluated using the calibrated FEM model.

The measured deflections were similar between the stop location test and crawl speed test along Path 1 loading. The equivalent width calculated for the stop location test was 5 percent smaller than the width calculated for the crawl speed test.

For Path 2 loading, the measured deflections were slightly smaller for the crawl speed test when compared to the stop location test. The equivalent width calculated for the static load was 3 percent higher than the width calculated for the crawl speed test.

The measured deflections were similar for both the stop location test and crawl speed test for the Middle Path loading. The equivalent width calculated for the static load was less than 2 percent higher than the width calculated for the crawl speed test.

The maximum LLDFs for the different loading scenarios are provided in Table 9.14. The maximum LLDF for the L-curbs is obtained from Path 1 loading, and the maximum LLDF for the mid-slab portion is obtained from the Middle Path loading.

Table 9.14. Maximum Moment LLDFs for Stop Location and Crawl Speed Tests

Loading	LLDF						
	S1+S2 (Left L-curb)	**S3**	**S4**	**S5**	**S6**	**S7**	**S8+S9 (Right L-curb)**
Path 1 Stop Location	0.083	0.076	0.109	0.139	0.153	0.138	0.302
Path 1 Crawl Speed	0.094	0.080	0.106	0.135	0.145	0.140	0.300
Max. Path 1 LLDF	0.094	0.615					0.302
Path 2 Stop Location	0.271	0.150	0.150	0.139	0.108	0.071	0.111
Path 2 Crawl Speed	0.286	0.150	0.154	0.140	0.103	0.063	0.103
Max. Path 2 LLDF	0.286	0.618					0.111
Middle Path Stop Location	0.163	0.113	0.137	0.147	0.138	0.111	0.191
Middle Path Crawl Speed	0.172	0.116	0.139	0.148	0.136	0.104	0.185
Max. Middle Path LLDF	0.172	0.646					0.191

*9.6.1.3 **Comparison of Experimental Results with Illinois Bulletin 346***

In the following section, the live load distributions obtained from the recorded deflections are compared with the IB346 recommended load distribution to the L-curb sections and the mid-slab region.

Illinois Bulletin 346. TxDOT uses the IB346 (Jenson et al. 1943) approach to load rate concrete slab bridges with integral curbs and/or beams. IB346 provides equations to determine the bending moment in the curbs and the slab portion of the bridge. IB346 suggests that the curb moment be reduced by 25 percent to account for the vehicle load being shifted in the transverse direction. IB346 equations are provided for wheel loads. Therefore, they are converted to total axle (two wheels) distributions in this report to be consistent with the LLDF definition used throughout the report. In the absence of any distributed live load on the bridge, the moment in the curbs due to the truck load is calculated using Equation (9.4):

$$M_{curb} = 0.75 C_1 \frac{Pa}{4} \tag{9.4}$$

where:

$$C_1 = \left(\frac{12}{2.5 + G}\right)\frac{\left(4 - \frac{v}{a}\right)}{\left(4 + 28\ \left(\frac{v}{a}\right)\right)}$$

$$G = \frac{ah^3}{12I}$$

M_{curb} = Moment shared by a single curb, kip-ft

G = Dimensionless stiffness factor, ratio of slab stiffness to curb stiffness

I = Moment of inertia of curb gross section outside the roadway width, ft^4

h = Slab thickness, ft

v = Axle width, center-to-center of truck tires, ft

P = Magnitude of a rear axle load (one wheels), kip

a = Span of bridge from center-to-center of bearing areas, ft

The bending moment applied to the slab region, M_{slab} (between the curb faces), is calculated according to Equation (9.7). The average moment in the slab, $M_{slab,avg.}$, is calculated by dividing the total slab moment by the width of the slab between the curb faces, as shown in Equation (9.8):

$$M_{slab} = (m - 1.5C_1)\frac{Pa}{4} \quad (9.5)$$

$$M_{slab,avg.} = \frac{M_{slab}}{b} \quad (9.6)$$

where:

b = Width of bridge between curb faces, ft

m = Number of wheel lines (m = 2 for one truck loading)

For the geometry of Bridge CS-9, G was calculated to be 1.49, I was calculated to be 1.03 ft^4, h was 0.92 ft, and the truck axle width was 6.92 ft. Thus, C_1 was calculated to be 0.92.

IB346 considers an L-shaped composite section comprising the curb and adjoining slab of width 4*h* for designing the curbs, where *h* is the slab thickness, as shown in Figure 9.20. Therefore, the moment demand for the curb is calculated for the L-shaped curb, and the slab moment is calculated for the remaining part of the mid-slab portion.

The bending moment applied to the composite curb section (L-shaped), M_{L-curb}, is calculated according to Equation (9.7) from IB346. The average moment in the slab, $M_{slab,avg}$, is calculated by dividing the total slab moment by the width of the slab between the L-shaped curb sections, as shown in Equation (9.8):

$$M_{L-curb} = M_{curb} + 4h\frac{M_{slab}}{b} \tag{9.7}$$

$$M_{mid-slab,avg} = \frac{M_{slab}}{(b - 8h)} \tag{9.8}$$

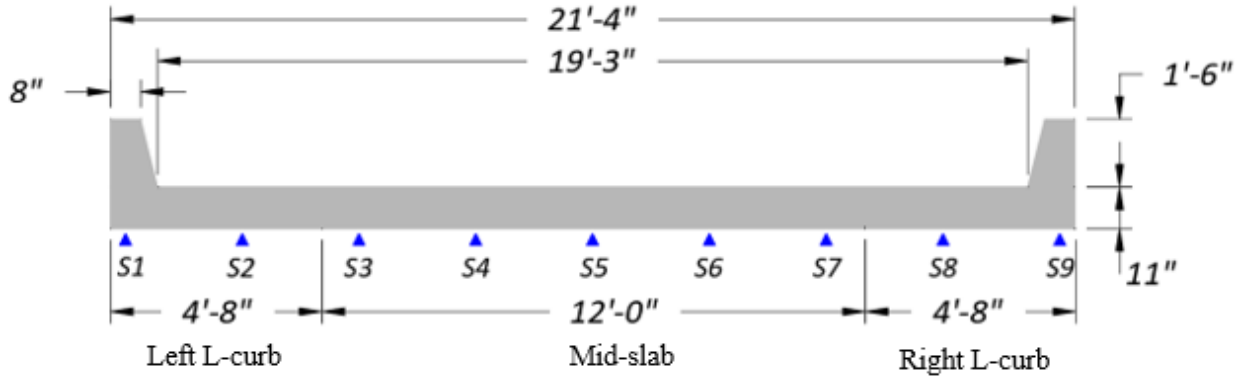

Figure 9.20. Typical Curb Cross-Section for Capacity Calculations

The moment distribution to one of the L-curbs can be calculated as the ratio of the curb moment to the total truck moment, as shown in Equation (9.9):

$$g_{L-curb} = \frac{M_{L-curb}}{M_{Total}} \tag{9.9}$$

The moment distributed to the slab portion can be calculated as the difference between the total minus the moment share of the two curbs, as shown in Equation (9.10):

$$g_{mid-slab} = 1 - 2g_{L-curb} \quad (9.10)$$

The term g may be defined as the distribution of the total moment to the bridge components—curbs and slab. It is the ratio of the moment taken by the bridge component to the total moment taken by the bridge. The distribution of the bending moment across Bridge CS-9 is presented in Table 9.15. As expected, the curbs attract a higher moment than the slab. The average moment per unit width of the slab is 2.16 kip-ft/ft.

Table 9.15. Distribution of Bending Moment across Bridge CS-9 Using IB346

Description	Left L-Curb	Mid-Slab	Right L-Curb
Moment (kip-ft)	54.94	25.75	54.94
g	0.405	0.190	0.405

Table 9.16 calculates the distribution of bending moment across Bridge CS-9 using cracked section properties of the curb. The use of the cracked section leads to a decreased contribution to the L-curbs and an increased contribution to the mid-slab.

Table 9.16. Distribution of Bending Moment across Bridge CS-9 Using IB346 with Cracked Section Properties

Description	Left L-Curb	Mid-Slab	Right L-Curb
Moment (kip-ft)	50.89	33.84	50.89
g	0.375	0.249	0.375

Experimental LLDFs Using Deflections. The maximum LLDFs for one-lane loading calculated for the different components for all static test types is shown in Table 9.17. As anticipated, the LLDF is highest in a component when the truck is located nearest to it. For the left L-curb, the truck is running along Path 2, while for the right L-curb, the truck is running along Path 1.

Table 9.17. Maximum Experimental One-Lane LLDFs for Static Tests

Load Path	$LLDF$		
	Left L-Curb	**Mid-Slab**	**Right L-Curb**
Path 1	0.094	0.615	0.302
Path 2	0.286	0.618	0.111
Middle Path	0.172	0.646	0.191
Max.	0.286	0.646	0.302

Table 9.18 compares the distribution across the slab bridge for the experimental results and IB346 calculations for one-lane loading. The slightly asymmetric distribution to the two curbs may be attributed to the test truck not being positioned exactly at the bridge center and/or the two curbs having different amounts of cracking that lead to different cracked-section moment of inertia values. The results indicate that IB346 underestimates the distribution of moment to the mid-slab region but gives a conservative estimate of the L-curb moment.

Table 9.18. Comparison of Experimental and IB346 One-Lane LLDFs

Description	g		
	Left L-Curb	**Mid-Slab**	**Right L-Curb**
Test	0.286	0.646	0.302
IB346	0.405	0.190	0.405
IB346/Test	1.416	0.294	1.341
IB346 (cracked)	0.375	0.249	0.375
IB346 (cracked)/Test	1.311	0.385	1.242

The two-lane loading LLDFs for the experimental tests were determined from the sum of the deflections obtained from Path 1 and Path 2 loading. The IB346 bending moments for the two-lane loaded case are calculated by increasing the number of wheel lines, m, used in Equation (9.8), to 4. The LLDFs for the experimental tests and IB346 method are shown in Table 9.19.

Table 9.19. Two-Lane LLDFs for Experimental Tests and IB346

Description	$LLDF$		
	Left L-Curb	**Mid-Slab**	**Right L-Curb**
Stop Location Test	0.354	1.233	0.413
Crawl Speed Test	0.376	1.217	0.407
IB346	0.596	0.808	0.596
IB346 (cracked)	0.566	0.868	0.566

The comparison of the maximum distribution of the live load across the slab bridge for the experimental results and IB346 calculations for two-lane loading is shown in Table 9.20. The ratio IB346/Test for the mid-slab component for a two-lane LLDF is more than two times higher than the one-lane LLDF. Similar to the one-lane comparison, the results indicate that IB346 underestimates the distribution of moment to the mid-slab region but gives a conservative estimate of the L-curb moment.

Table 9.20. Comparison of Experimental and IB346 Two-Lane LLDFs

Description	g		
	Left L-Curb	**Mid-Slab**	**Right L-Curb**
Test	0.376	1.233	0.413
IB346	0.596	0.808	0.596
IB346/Test	1.585	0.655	1.443
IB346 (cracked)	0.566	0.868	0.566
IB346 (cracked)/Test	1.505	0.704	1.370

Modification to Illinois Bulletin 346 Method. The IB346 approach defines an L-shaped curb section that incorporates a slab length equal to four times the thickness of the slab. Because the measured results indicated that the relative curb stiffness is high, a modification to this approach was considered using a 45-degree projection of the curb height onto the slab portion. This approach is similar to that used for the Equivalent Frame Method outlined in Section 8.11 of ACI 318-14 (ACI Committee 318 2014). The portion of the slab to be included with the beam and/or curb is shown in Figure 9.21.

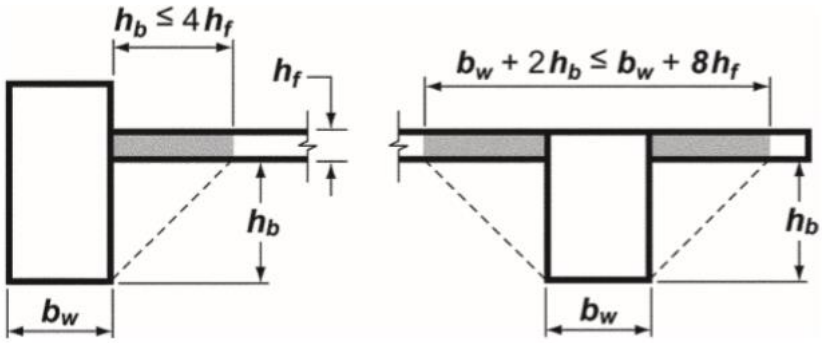

Figure 9.21. Slab Portion to be included with the Beam and/or Curb (ACI Committee 318 2014)

A comparison of the LLDFs calculated using the modified IB346 approach with the experimental values is provided in Table 9.21. The modified approach provides a better estimate of the distribution of moment to the curbs and slab, especially for the two-lane loaded scenario; however, it is still unconservative for the slab region.

Table 9.21. Comparison of Experimental and Modified IB346 LLDFs

Loading	Description	*g*		
		Left L-Curb	Mid-Slab	Right L-Curb
One-lane	Test	0.286	0.646	0.302
	Modified IB346	0.364	0.271	0.364
	Modified IB346/Test	1.273	0.420	1.205
Two-lane	Test	0.376	1.233	0.413
	Modified IB346	0.423	1.154	0.423
	Modified IB346/Test	1.125	0.936	1.024

9.6.1.4 ***Comparison of Experimental Moment LLDFs in Slab Region with Methods from Literature***

The test LLDFs and equivalent width values for the concrete slab bridge are compared with the recommended values from the *AASHTO Standard Specifications* (AASHTO 2002) and *AASHTO LRFD Specifications* (AASHTO 2017) and two other methods from the literature. Both AASHTO specifications provide equations for the equivalent width of the slab over which a single truck load is to be distributed for slab bridges. The *AASHTO Standard Specifications* and the *AASHTO LRFD Specifications* expressions are provided in Equation (9.11) and Equation (9.12), respectively. Note

that the *AASHTO Standard Specifications* and *AASHTO LRFD Specifications* equations for calculating equivalent slab width do not consider concrete slab bridges with integral curbs.

$$\text{AASHTO Standard:} \quad E = 2(4 + 0.06S) \tag{9.11}$$

$$\text{AASHTO LRFD:} \quad E = 10.0 + 5.0\sqrt{L_1 W_1} \tag{9.12}$$

where:

S = Effective span length, ft

L_1 = Modified span length, ft (minimum of actual span or 60 ft)

W_1 = Modified edge-to-edge width of bridge, ft (minimum of actual width or 60 ft for multi-lane loading, or 30 ft for single-lane loading)

Amer et al. (1999) considered both concrete slab bridges without integral curbs and concrete slab bridges with integral curbs in their study. They proposed the following equation for the equivalent width. In the presence of integral edge beams, a factor C_{edge} should be multiplied by the value from Equation (9.14):

$$E = 6.89 + 0.23L \leq \frac{W}{N_L} \tag{9.13}$$

$$C_{edge} = 1.0 + 0.5\left(\frac{d_1}{3.28} - 0.15\right) \geq 1.0 \tag{9.14}$$

where:

E = Equivalent width for a truck load, ft

L = Span length, ft

W = Bridge width, ft

N_L = Number of design lanes

d_1 = Edge beam depth above slab thickness, ft

Jones and Shenton (2012) recommended Equation (9.15) for the determination of the equivalent width for a single-lane bridge. This equation is similar to the equivalent width equation provided in the *AASHTO LRFD Specifications* (AASHTO 2017); however, the coefficient in the

second term is 5.8 rather than 5.0. Slab bridges with integral curbs were not considered in this study.

$$E = 10.0 + 5.8\sqrt{L_1 W_1} \tag{9.15}$$

Path 1 Loading. A comparison of the equivalent widths calculated from the test data for the interior slab portion, based on defining curb sections, to those widths calculated using the approximate equations in the *AASHTO Standard Specifications* (AASHTO 2002) and *AASHTO LRFD Specifications* (AASHTO 2017) is provided in Table 9.22. Comparisons with studies such as Amer et al. (1999) and Jones and Shenton (2012) are also presented. The equivalent width calculated using the approach recommended by Amer et al. (1999) is closer to the width determined from the static tests. All other methods provided conservative equivalent widths. It should be noted that the equivalent widths calculated using the approximate equations in the *AASHTO Standard Specifications* (AASHTO 2002) and *AASHTO LRFD Specifications* (AASHTO 2017) do not consider slab bridges with integral curbs. Similarly, Jones and Shenton (2012) did not consider bridges with integral curbs. Amer et al. (1999) considered bridges similar to the one tested.

Table 9.22. Equivalent Width (ft) Comparison for Interior Slab for Path 1 Loading

Test	Test (E^m_{Test})	Amer et al. (E^m_{Amer})	Jones and Shenton* ($E^m_{Jones\ \&\ Shenton}$)	AASHTO* (E^m_{AASHTO})	AASHTO LRFD* (E^m_{LRFD})
Stop Location	16.9	14.6	12.0	11.0	10.5
Crawl Speed	17.8	14.6	12.0	11.0	10.5
Note: * Methods do not consider the effect of integral curbs.					

A comparison of the test equivalent widths to widths calculated from the *AASHTO Standard Specifications* and *AASHTO LRFD Specifications* (AASHTO 2002) and studies such as Amer et al. (1999) and Jones and Shenton (2012) is shown in Figure 9.22(a) and (b) for the stop location and crawl tests, respectively.

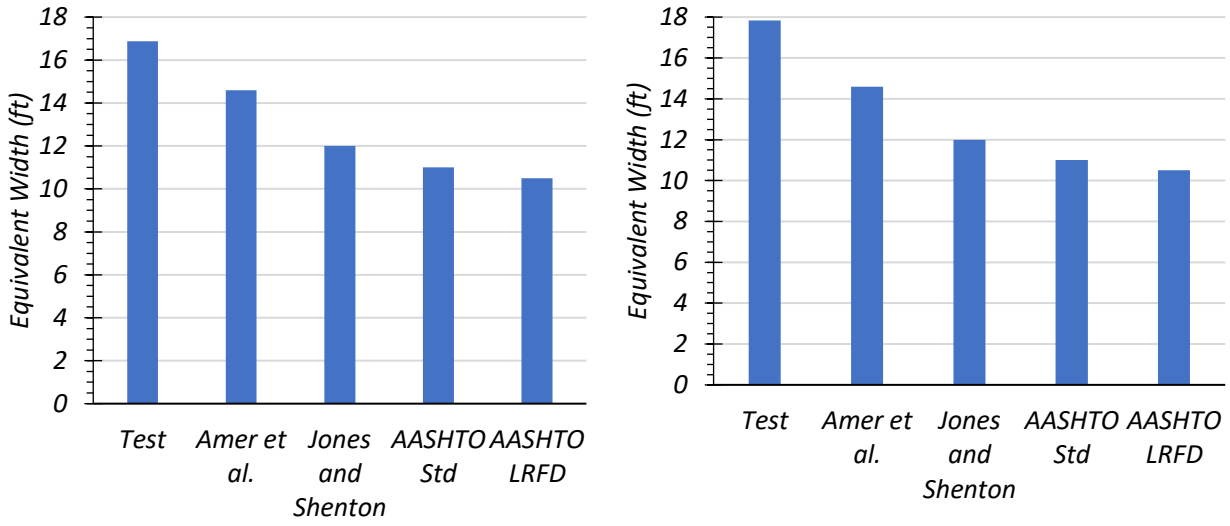

(a) Stop Location Test *(b) Crawl Speed Test*

Figure 9.22. Comparison of Test Equivalent Width with Methods in the Literature for Path 1 Loading

Path 2 Loading. A comparison of the equivalent widths calculated from the test data for the interior slab portion, based on defining curb sections, to those calculated using the approximate equations in the *AASHTO Standard Specifications* (AASHTO 2002) and *AASHTO LRFD Specifications* (AASHTO 2017) is provided in Table 9.23. Comparisons with studies such as Amer et al. (1999) and Jones and Shenton (2012) are also presented. The equivalent width calculated using the approach proposed by Amer et al. (1999) was closer to the width determined from the static tests. All other approaches provided conservative equivalent widths.

Table 9.23. Equivalent Width (ft) Comparison for Interior Slab for Path 2 Loading

Test	Test (E^m_{Test})	Amer et al. (E^m_{Amer})	Jones and Shenton* ($E^m_{Jones\ \&\ Shenton}$)	AASHTO* (E^m_{AASHTO})	AASHTO LRFD* (E^m_{LRFD})
Stop Location	17.2	14.6	12.0	11.0	10.5
Crawl Speed	16.7	14.6	12.0	11.0	10.5
Note: * Methods do not consider the effect of integral curbs.					

A comparison of the test equivalent widths to those calculated from the *AASHTO Standard Specifications* (AASHTO 2002) and *AASHTO LRFD Specifications* (AASHTO 2017) and studies

such as Amer et al. (1999) and Jones and Shenton (2012) is shown in Figure 9.23(a) and (b) for the stop location test and crawl speed test, respectively.

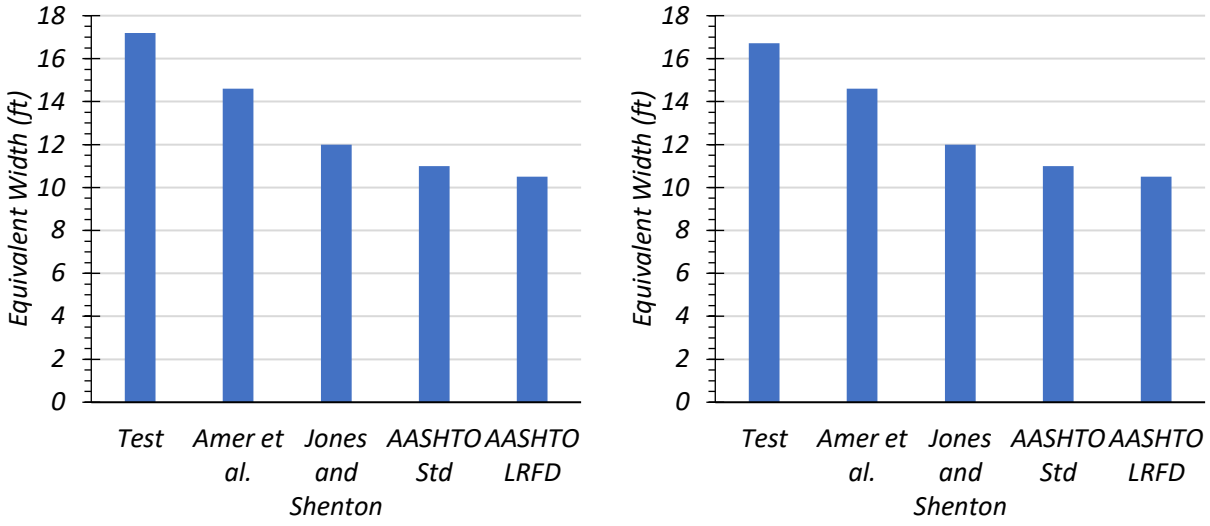

(a) Stop Location Test *(b) Crawl Speed Test*

Figure 9.23. Comparison of Test Equivalent Width with Methods in the Literature for Path 2 Loading

Middle Path Loading. A comparison of the equivalent widths calculated from the test data for the interior slab portion, based on defining curb sections, to those calculated using the approximate equations in the *AASHTO Standard Specifications* (AASHTO 2002) and *AASHTO LRFD Specifications* (AASHTO 2017) is provided in Table 9.24. Comparisons with studies such as Amer et al. (1999) and Jones and Shenton (2012) are also presented. The equivalent width calculated using the approach recommended by Amer et al. (1999) is closer to the width determined from the static tests. All other methods provided conservative equivalent widths.

Table 9.24. Equivalent Width (ft) Comparison for Interior Slab for Middle Path Loading

Test	Test (E^m_{Test})	Amer et al. (E^m_{Amer})	Jones and Shenton* ($E^m_{Jones\ \&\ Shenton}$)	AASHTO* (E^m_{AASHTO})	AASHTO LRFD* (E^m_{LRFD})
Stop Location	17.6	14.6	12.0	11.0	10.5
Crawl Speed	17.4	14.6	12.0	11.0	10.5
Note: * Methods do not consider the effect of integral curbs.					

A comparison of the test equivalent widths to those calculated from the *AASHTO Standard Specifications* (AASHTO 2002) and *AASHTO LRFD Specifications* (AASHTO 2017) and studies such as Amer et al. (1999) and Jones and Shenton (2012) is shown in Figure 9.24(a) and (b) for the stop location test and crawl speed test, respectively.

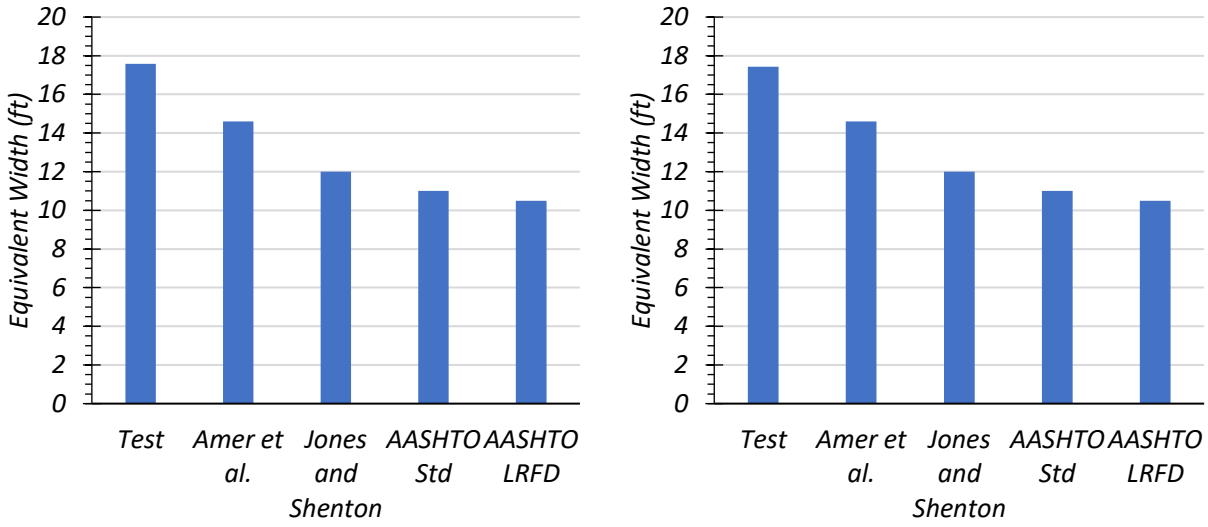

(a) Stop Location Test *(b) Crawl Speed Test*

Figure 9.24. Comparison of Test Equivalent Width with Methods in the Literature for Middle Path Loading

Summary of Comparisons. The equivalent widths calculated using the approximate equations in the *AASHTO Standard Specifications* (AASHTO 2002) and *AASHTO LRFD Specifications* (AASHTO 2017) appear to be quite conservative for integral curb bridges such as Bridge CS-9. Similarly, Jones and Shenton (2012) did not consider bridges with integral curbs, and their equivalent widths are conservative. Amer et al. (1999) considered bridges similar to the one tested (having integral edge beams), and the equivalent width calculated using their equation was 13 percent more conservative than the width determined for the Middle Path stop location test equivalent width.

TxDOT currently uses the IB346 approach to determine the distribution of moment per ft width in the interior slab section and for design of the curbs. The IB346 methods and other methods from literature are compared to the measured values in the following section.

Mid-slab Live Load Distribution per foot. The per ft distribution of the live load, $g_{per\ foot}$, is considered for the mid-slab component for both the experimental tests and the IB346 methodology. This distribution is calculated by dividing g for the mid-slab section by the width of the mid-slab component (11.92 ft), as shown in Equation (9.16):

$$g_{per\ foot} = \frac{g}{W_{mid-slab}} \tag{9.16}$$

The g and $g_{per\ foot}$ for the different experimental tests and IB346 for one-lane loading are shown in Table 9.25.

Table 9.25 Experimental and IB346 Moment LLDFs in Slab Region for One-Lane Loaded

Test/Method	g	$g_{per\ foot}$
Stop Location (Path 1)	0.615	0.052
Crawl Speed (Path 1)	0.606	0.051
Stop Location (Path 2)	0.618	0.052
Crawl Speed (Path 2)	0.611	0.051
Stop Location (Middle Path)	0.646	0.054
Crawl Speed (Middle Path)	0.643	0.054
IB346	0.190	0.016
IB346 (cracked)	0.249	0.021

The $g_{per\ foot}$ for the *AASHTO Standard Specifications* (AASHTO 2002), *AASHTO LRFD Specifications* (AASHTO 2017), Amer et al. (1999), and Jones and Shenton (2012) is defined as the inverse of the equivalent width. Table 9.26 provides this information.

Table 9.26. Moment LLDFs in Slab Region with Different Methods for One-Lane-Loaded

Approach	E **(ft)**	$g_{per\ foot}$
Amer et al.	14.6	0.068
Jones and Shenton*****	12.0	0.083
AASHTO*****	11.0	0.091
AASHTO LRFD*****	10.5	0.096
Note: * Methods do not consider the effect of integral curbs.		

Figure 9.25 compares the one-lane $g_{per\ foot}$ factor calculated for the experimental tests and the different methods in the literature. IB346, when considering both uncracked and cracked sections, is highly unconservative for the mid-slab section, while *AASHTO Standard Specifications* (AASHTO 2002), *AASHTO LRFD Specifications* (AASHTO 2017), Amer et al. (1999), and Jones and Shenton (2012) ranges from being conservative to highly conservative for this bridge type.

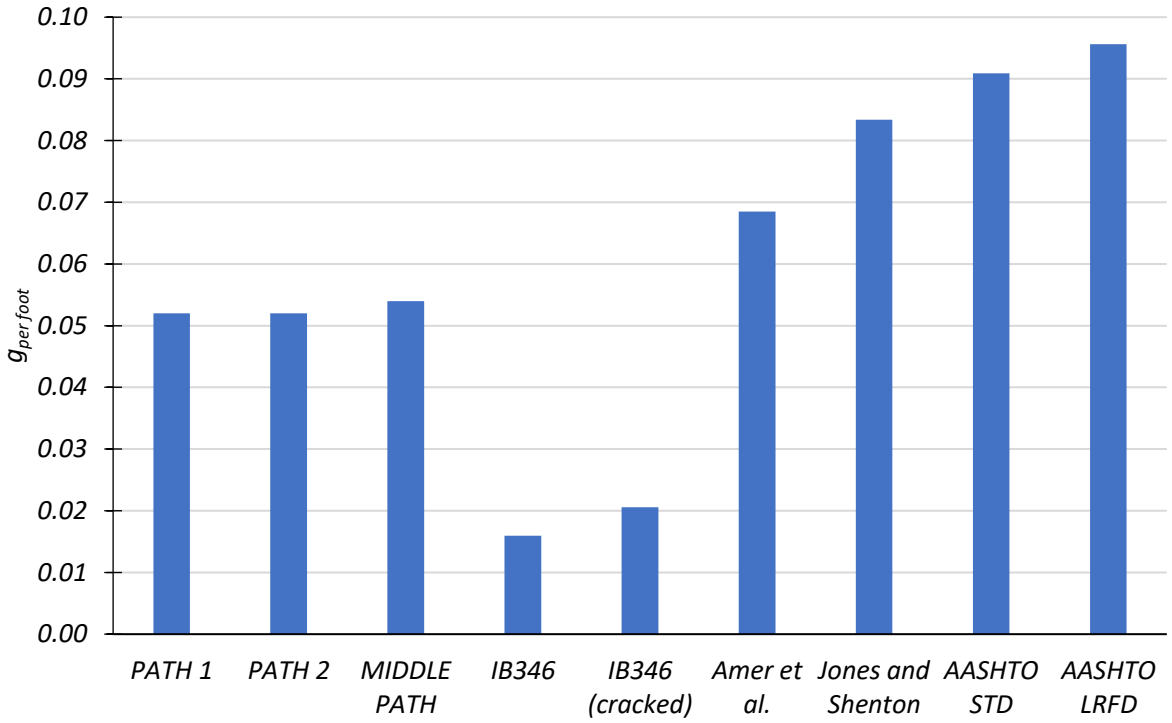

Figure 9.25. Comparison of Experimental Moment LLDFs in Slab Region with Different Methods in the Literature for One-Lane-Loaded

Similar calculations were carried out for the two-lane loading scenario. The two-lane loading LLDFs for the field tests were determined from the sum of the deflections obtained from Path 1 and Path 2 loading. The IB346 bending moments for a two-lane loaded case is calculated by increasing the number of wheel lines, m, used in Equation (9.8), to 4. Table 9.27 provides the g and $g_{per\ foot}$ for the experimental test and IB346 for two-lane loading.

Table 9.27. Experimental and IB346 Moment LLDFs in Slab Region for Two-Lane-Loaded

Test/Method	g	$g_{per\ foot}$
Stop Location (Path 1+2)	1.233	0.104
Crawl Speed (Path 1+2)	1.217	0.102
IB346	0.808	0.068
IB346 (cracked)	0.868	0.073

The equivalent width for two-lane (or more) loading for the *AASHTO LRFD Specifications* (AASHTO 2017) is provided in Equation (9.17). Equation (9.18) provides the corresponding equivalent width recommended by Jones and Shenton (2012). Note that these equations do not consider concrete slab bridges with integral curbs.

$$\text{AASHTO LRFD (AASHTO 2017):} \quad E = 84.0 + 1.44\sqrt{L_1 W_1} \tag{9.17}$$

$$\text{Jones and Shenton (2012):} \quad E = 84.0 + 2.06\sqrt{L_1 W_1} \tag{9.18}$$

where:

L_1 = Modified span length, ft (minimum of actual span or 60 ft)

W_1 = Modified edge-to-edge width of bridge, ft (minimum of actual width or 60 ft for multi-lane loading, or 30 ft for single-lane loading)

Table 9.28 provides the g and $g_{per\ foot}$ for the experimental test and IB346 for two-lane loading. Figure 9.26 compares the two-lane $g_{per\ foot}$ factor calculated for the experimental tests and the different approaches found in the literature. Similar to the one-lane loading, IB346 for uncracked and cracked sections is unconservative for the slab demand, while the approach by Jones and Shenton (2012) is slightly unconservative for this bridge type. In fact, *AASHTO LRFD Specifications* provides a reasonably good estimate of the $g_{per\ foot}$ factor in comparison to the experimental results.

Table 9.28. Moment LLDFs in Slab Region with Different Methods for Two-Lane-Loaded

Test/Method	E (ft)	$g_{per\ foot}$
Amer et al.	14.6	0.068
Jones and Shenton	11.0	0.091
AASHTO Standard Specifications	11.0	0.091
AASHTO LRFD Specifications	9.8	0.102

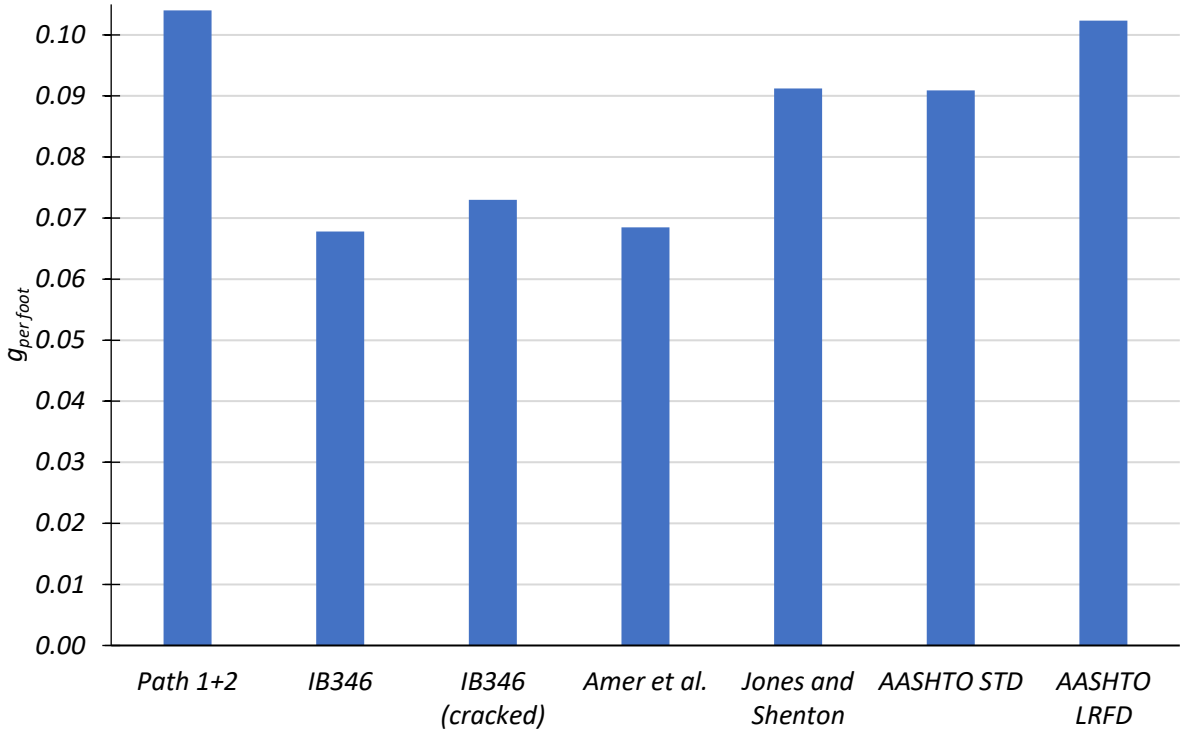

Figure 9.26. Comparison of Experimental Moment LLDFs in Slab Region with Different Methods in the Literature for Two-Lane Loading

9.6.2 Dynamic Load Tests on Bridge CS-9

In this section of the report, results from the dynamic tests undertaken along Path 1, Path 2, and the Middle Path are presented.

9.6.2.1 Dynamic Amplification

The dynamic amplification of the bridge is considered by comparing the magnifications in the strain values and deflections from the stop location test to the dynamic test.

Maximum Section Strains. The dynamic amplification of strains for transverse Sections S1 and S9 were obtained by comparing the dynamic test results with the static stop location results. Plots of the strain profiles for Sections S1 and S9 obtained from the stop location tests and dynamic tests for Path 1, Path 2, and the Middle Path are shown in Figure 9.27, Figure 9.28, and Figure 9.29, respectively. Figure 9.30 compares the dynamic strains for Section S1 and S9 with the stop location values.

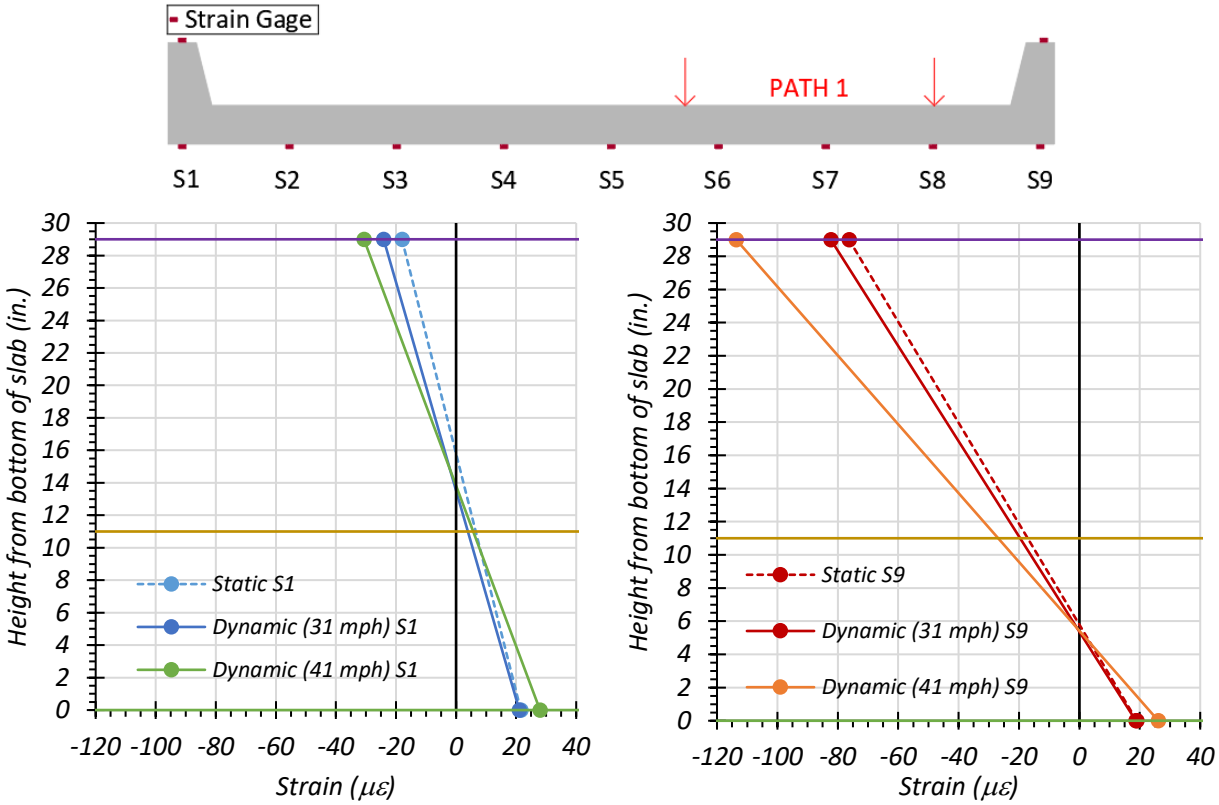

Figure 9.27. Maximum Strains for Static and Dynamic Tests for Path 1 Loading

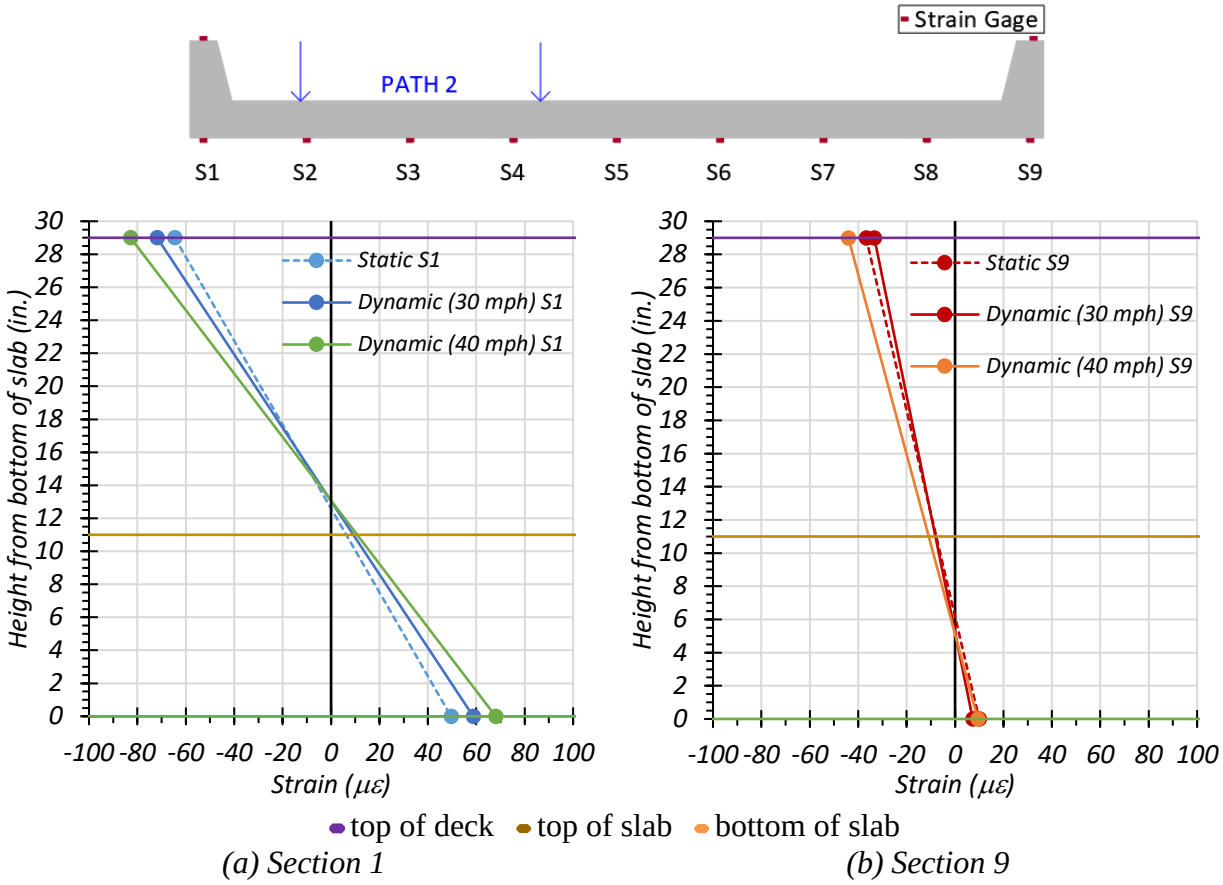

(a) Section 1 *(b) Section 9*

Figure 9.28. Maximum Strains for Static and Dynamic Tests for Path 2 Loading

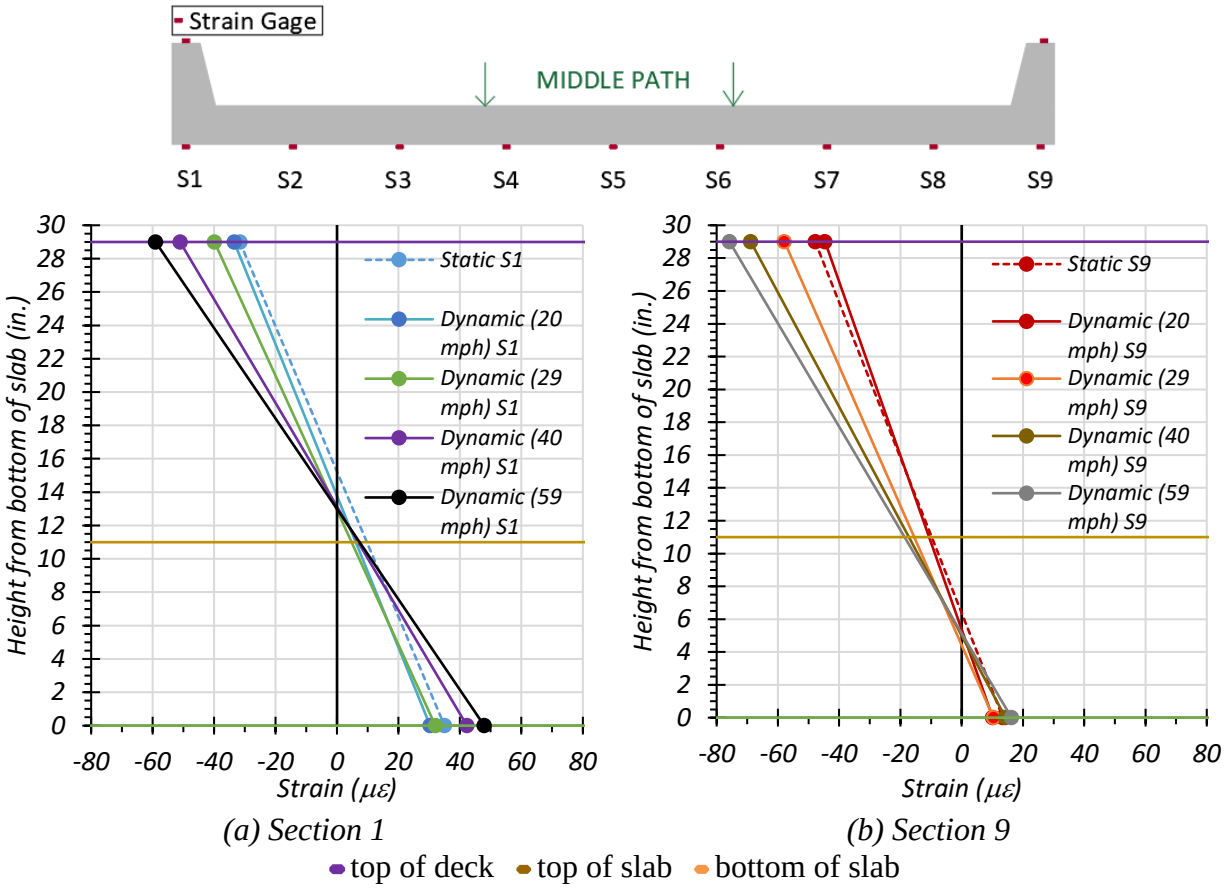

Figure 9.29. Maximum Strains for Static and Dynamic Tests for Middle Path Loading

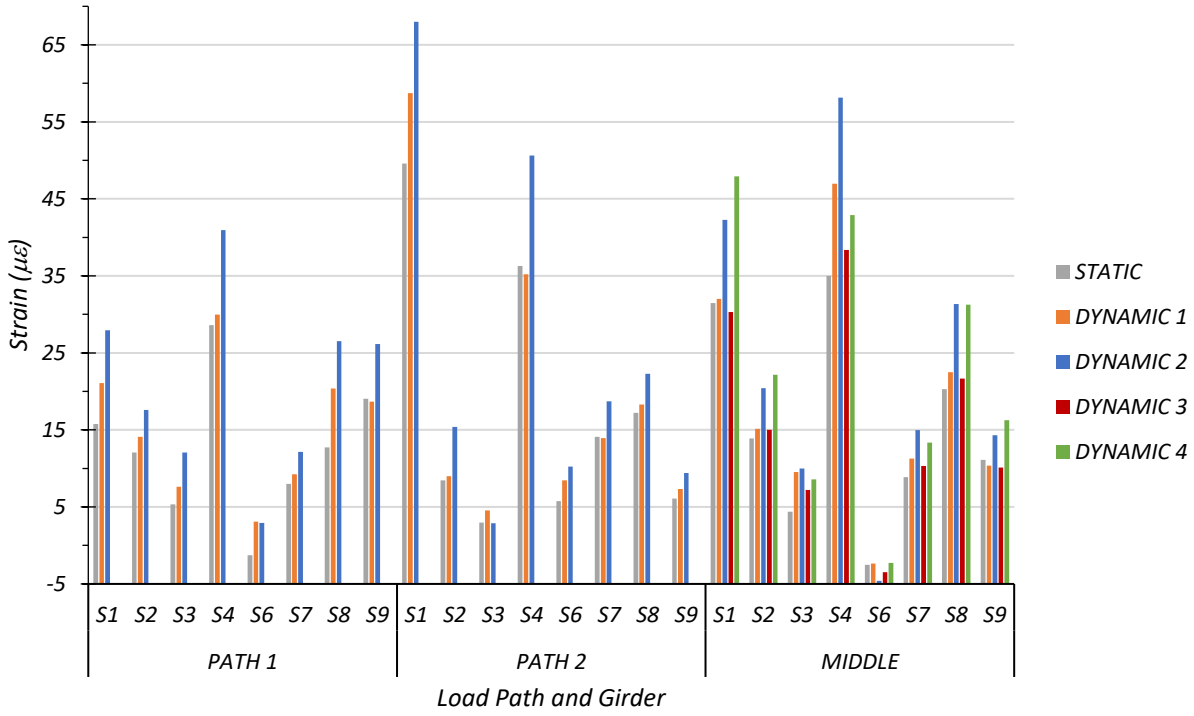

Note:

- *Path 1: Dynamic 1 = 31 mph, Dynamic 2 = 41 mph*
- *Path 2: Dynamic 1 = 30 mph, Dynamic 2 = 40 mph*
- *Middle Path: Dynamic 1 = 20 mph, Dynamic 2 = 29 mph, Dynamic 3 = 40 mph, Dynamic 4 = 59 mph*

Figure 9.30. Comparison of Maximum Bottom Strains for Static and Dynamic Tests

For Bridge CS-9, the average dynamic impact factor for the exterior section was 36 percent, while the average dynamic impact factor for the interior section was 49 percent. These percentages were calculated based on the maximum strains recorded during testing. The *AASHTO Standard Specifications* calls for a dynamic impact factor of 30 percent, and *AASHTO LRFD Specifications* stipulates this factor to be 33 percent. Thus, for Bridge CS-9, the average dynamic impact factor for the exterior and interior sections is approximately 10 to 50 percent higher than what is specified by AASHTO. This result suggests that the maximum impact can be greater than the specified values in AASHTO both in the exterior and interior sections of this integral curb slab bridge, but particularly for the slab section, which often governs the load rating.

The maximum strains for each section under static and dynamic tests for Path 1, Path 2, and Middle Path loading are tabulated in Table 9.29. Figure 9.31 compares the dynamic strains for each section with the corresponding static strains. Figure 9.32 shows the measured strains for the controlling dynamic load cases as a ratio to the stop location strain.

The maximum strain obtained for an interior section during the static, Dynamic 1, and Dynamic 2 tests along Path 1 was for Section S3. The strain increased by 43 percent for the Dynamic 1 loading and by 126 percent for Dynamic 2 loading in comparison to the static test results. The maximum strain obtained for an exterior section during the static, Dynamic 1, and Dynamic 2 tests along Path 1 was for S9. The strain decreased by 2 percent for Dynamic 1 loading and increased by 37 percent for the Dynamic 2 loading in comparison to the static test results.

The maximum strain obtained for an interior section during the static, Dynamic 1, and Dynamic 2 tests along Path 2 was for Section S2. The strain increased by 7 percent for the Dynamic 1 test and by 82 percent for the Dynamic 2 test in comparison to the static test results. The maximum strain obtained for an exterior section during the static, Dynamic 1, and Dynamic 2 tests along Path 2 was for Section S1. The strain decreased by 3 percent for Dynamic 1 loading and increased by 39 percent for Dynamic 2 loading in comparison to the static test results.

The maximum strains obtained for an interior section during the static and dynamic tests along the Middle Path were for Section S3. The strain increased by 117 percent for Dynamic 1 loading, increased by 127 percent for Dynamic 2 loading, increased by 64 percent for Dynamic 3 loading, and increased by 96 percent for Dynamic 4 loading in comparison to the static test results. The maximum strains obtained for an exterior section during the static and dynamic tests along the Middle Path were measured for Section S1. The strain increased by 2 percent for Dynamic 1 loading, increased by 34 percent for Dynamic 2 loading, decreased by 4 percent for Dynamic 3 test, and increased by 52 percent for Dynamic 4 loading in comparison to the static test results.

Table 9.29. Maximum Midspan Strains for Static and Dynamic Tests

	Loading	S1	S2	S3	S6	S7	S8	S9
Bottom Strain (με)	Path 1 Static	15.78	12.06	5.33	-1.27	7.99	12.75	19.03
	Path 1 Dynamic (31 mph)	21.07	14.09	7.60	3.11	9.24	20.36	18.68
	Path 1 Dynamic (41 mph)	27.95	17.58	12.06	2.91	12.16	26.54	26.13
	Max. Path 1 Amplification	–	–	126%	–	–	–	37%
Bottom Strain (με)	Path 2 Static	49.58	8.45	2.95	5.73	14.10	17.23	6.09
	Path 2 Dynamic (30 mph)	58.73	9.00	4.56	8.47	13.95	18.29	7.32
	Path 2 Dynamic (40 mph)	68.01	15.37	2.87	10.24	18.69	22.30	9.41
	Max. Path 2 Amplification	37%	82%	–	–	–	–	–
Bottom Strain (με)	Middle Static	31.47	13.91	4.39	-2.51	8.87	20.30	11.10
	Middle Dynamic (20 mph)	32.01	15.13	9.54	-2.36	11.26	22.51	10.37
	Middle Dynamic (29 mph)	42.28	20.43	9.99	-4.62	14.97	31.34	14.32
	Middle Dynamic (40 mph)	30.30	15.01	7.19	-3.48	10.32	21.65	10.12
	Middle Dynamic (59 mph)	47.91	22.16	8.58	-2.27	13.34	31.27	16.28
	Max. Middle Path Amplification	52%	–	127%	–	–	–	–

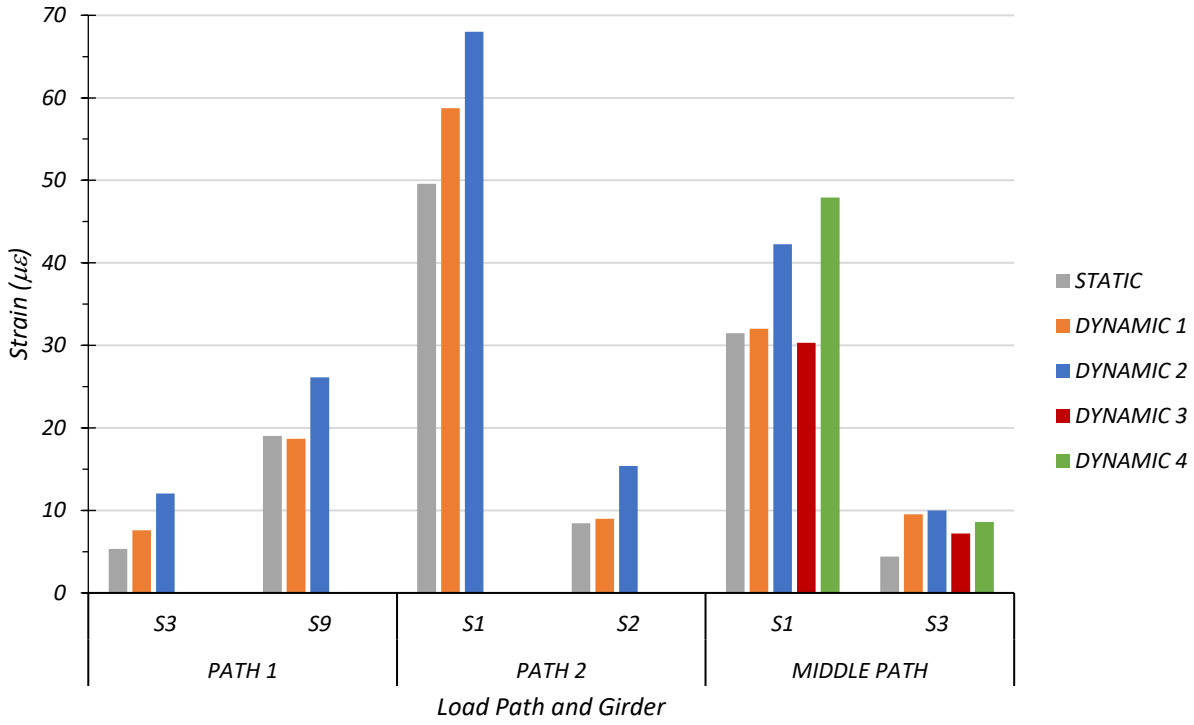

Note:

- *Path 1: Dynamic 1 = 31 mph, Dynamic 2 = 41 mph*
- *Path 2: Dynamic 1 = 30 mph, Dynamic 2 = 40 mph*
- *Middle Path: Dynamic 1 = 20 mph, Dynamic 2 = 29 mph, Dynamic 3 = 40 mph, Dynamic 4 = 59 mph*

Figure 9.31. Static and Dynamic Strain Comparison

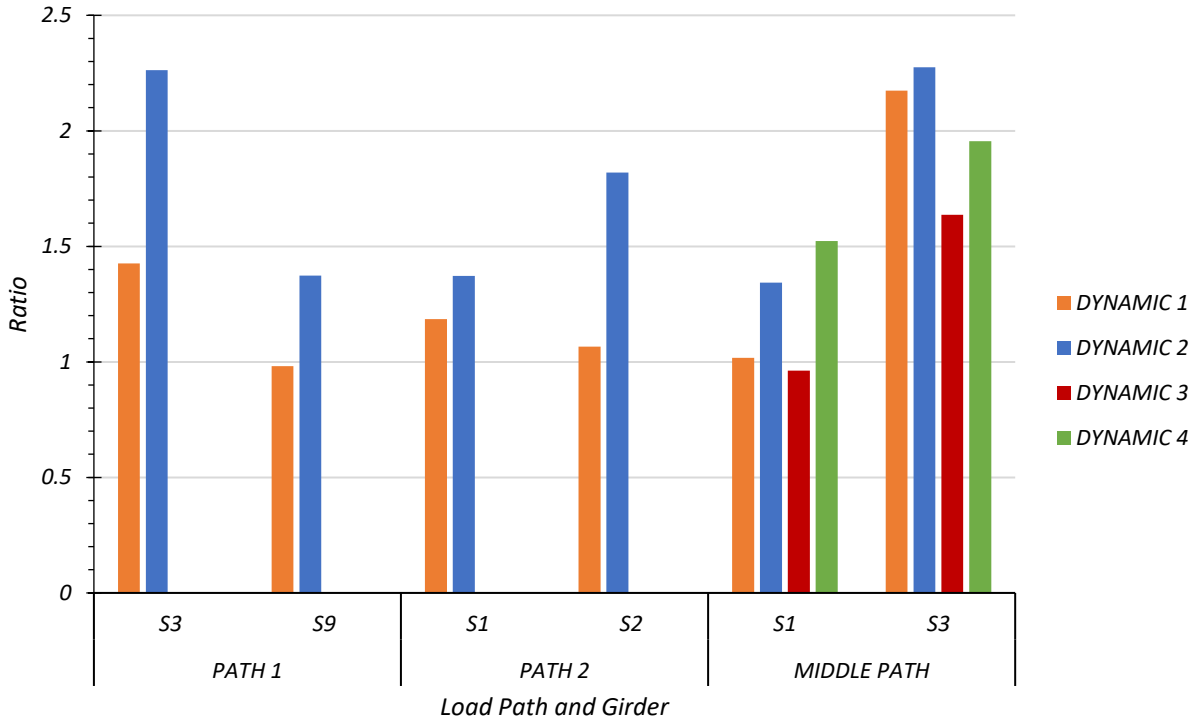

Note:

- *Path 1: Dynamic 1 = 31 mph, Dynamic 2 = 41 mph*
- *Path 2: Dynamic 1 = 30 mph, Dynamic 2 = 40 mph*
- *Middle Path: Dynamic 1 = 20 mph, Dynamic 2 = 29 mph, Dynamic 3 = 40 mph, Dynamic 4 = 59 mph*

Figure 9.32. Maximum Midspan Dynamic Strains to Static Strains Ratios

Maximum Section Deflections. Dynamic amplification can also be obtained by comparing the dynamic deflections with the static deflections. Deflection time history plots for each section for the static test and for Dynamic 1 and Dynamic 2 tests are provided in Figure 9.33 and Figure 9.34 for Path 1 and Path 2, respectively. Figure 9.35plots the same information for the Middle Path, including Dynamic 3 and Dynamic 4 test results. The static data provided in the following graphs were filtered using the moving average approach over 100 points to remove noise. The sampling rate for the string potentiometers was 500 samples per second.

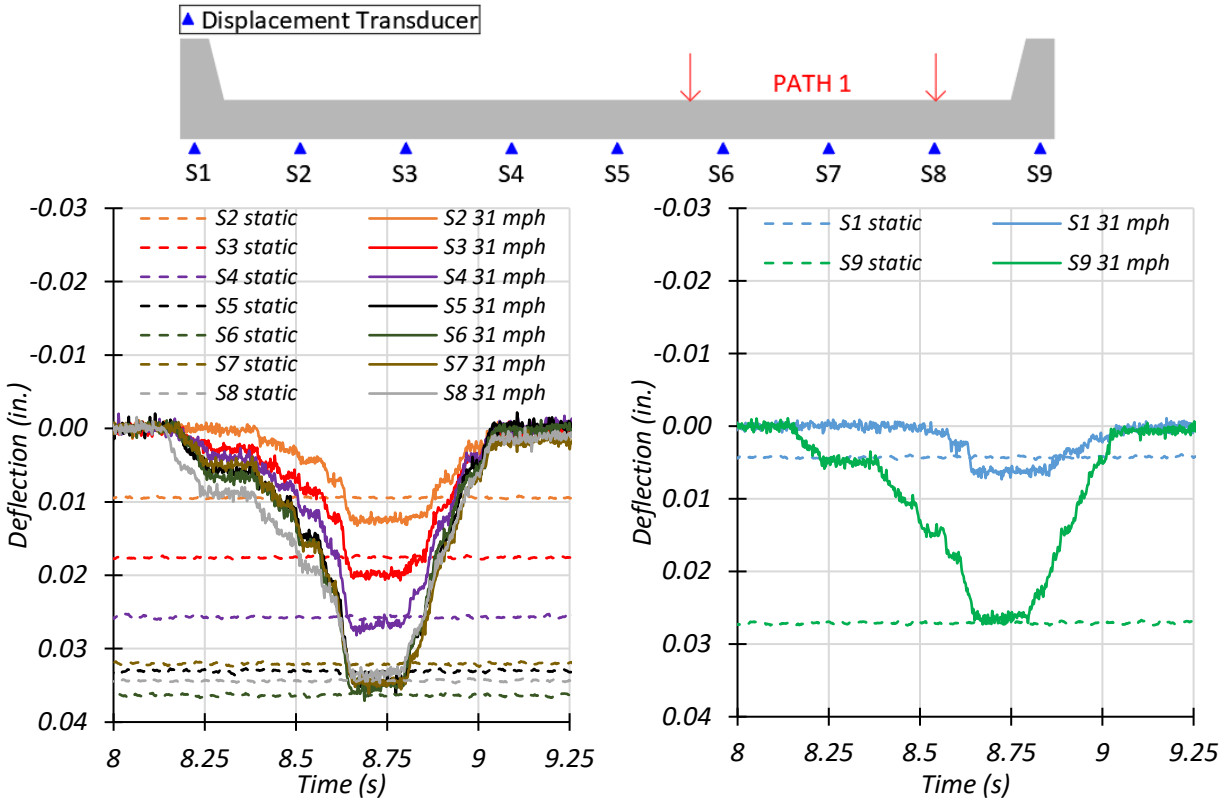

(a) Deflection Time Histories – Dynamic 1 (31 mph)

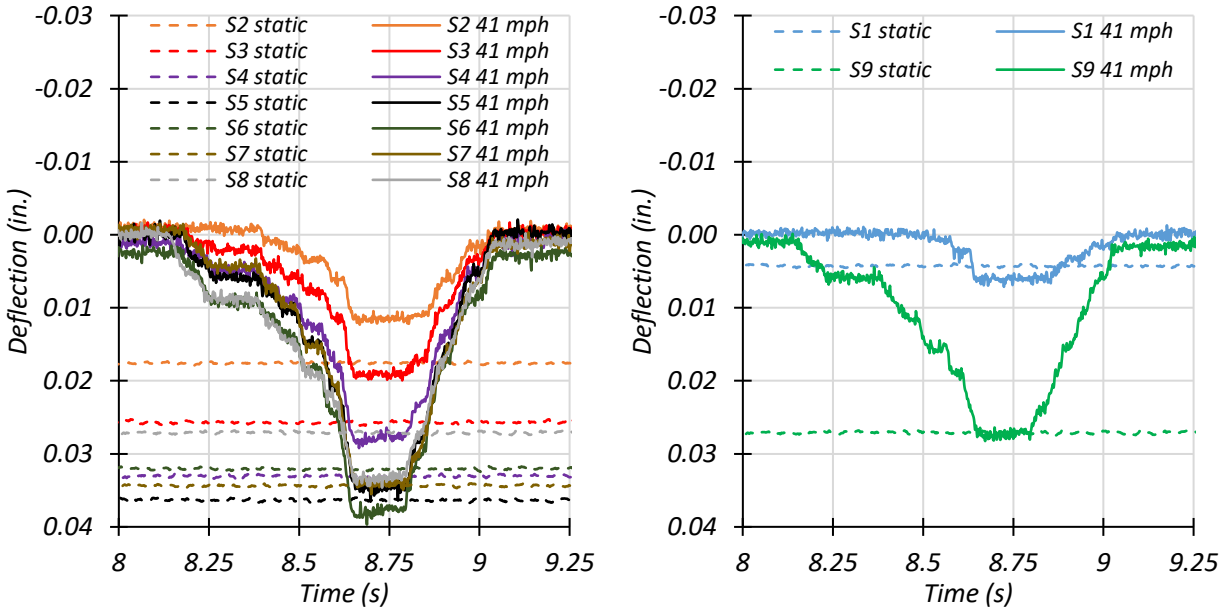

(b) Deflection Time Histories – Dynamic 2 (41 mph)

Figure 9.33. Midspan Deflections for Static and Dynamic Tests for Path 1 Loading

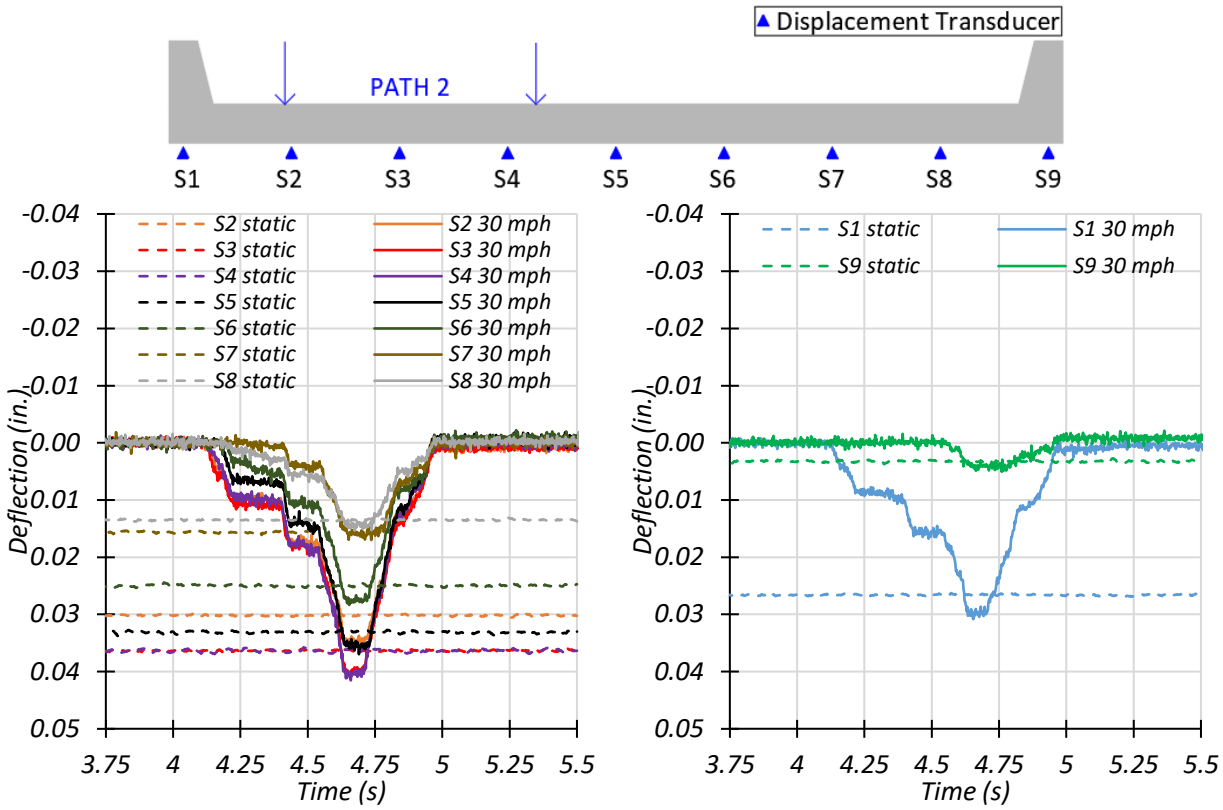

(a) Deflection Time Histories – Dynamic 1 (30 mph)

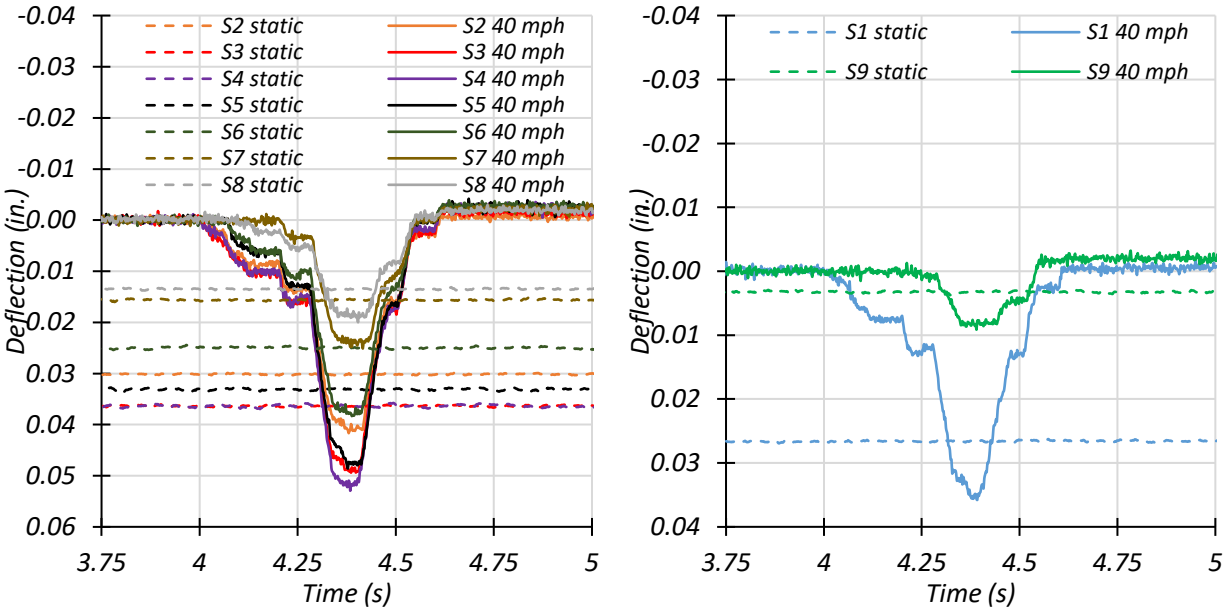

(b) Deflection Time Histories – Dynamic 2 (40 mph)

Figure 9.34. Midspan Deflections for Static and Dynamic Tests for Path 2 Loading

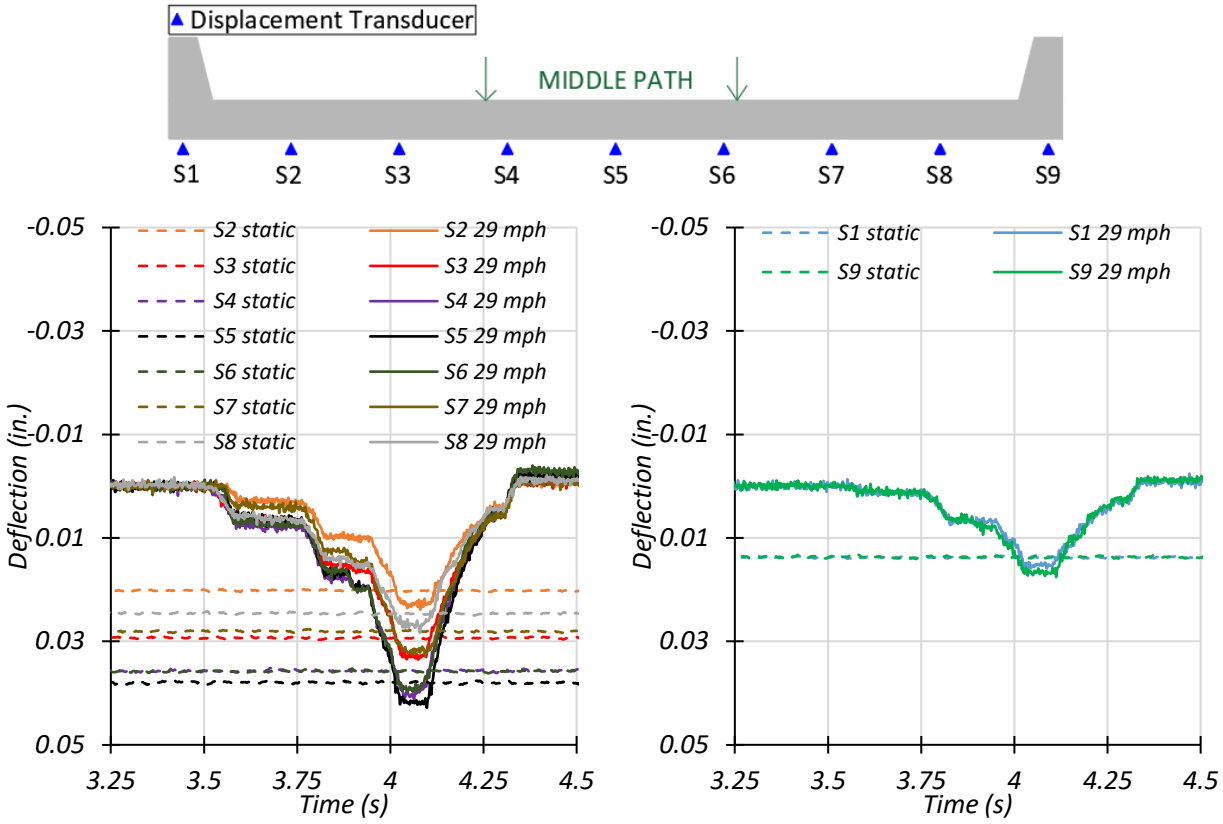

(a) Deflection Time Histories – Dynamic 1 (29 mph)

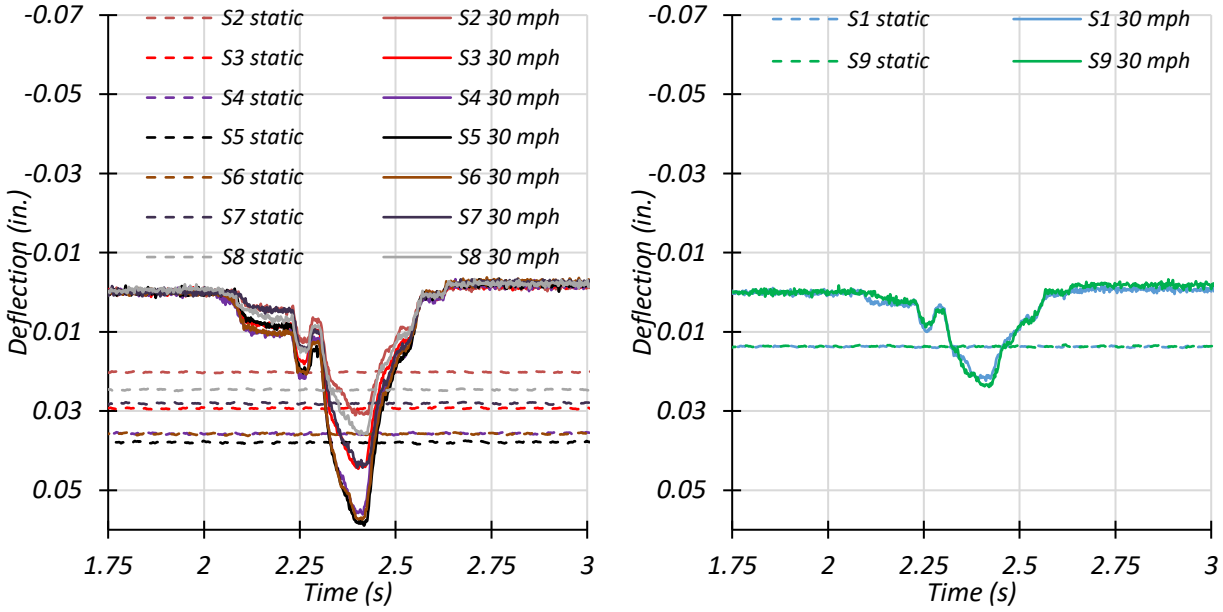

(b) Deflection Time Histories – Dynamic 2 (40 mph)

Figure 9.35. Midspan Deflections for Static and Dynamic Tests for Middle Path Loading

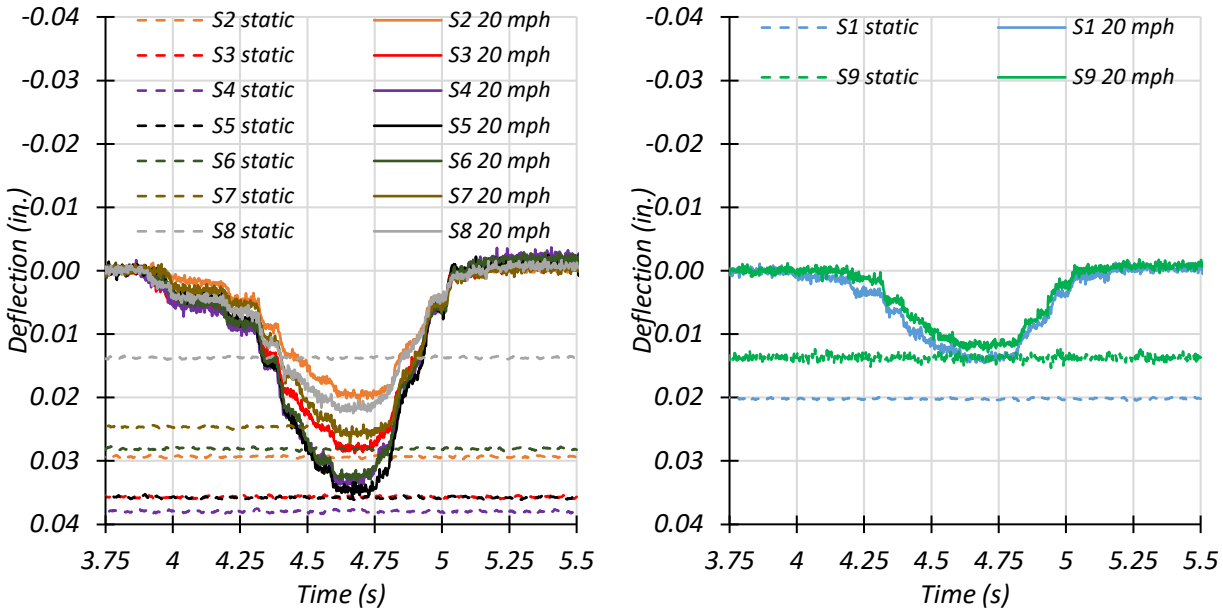

(c) Deflection Time Histories – Dynamic 3 (20 mph)

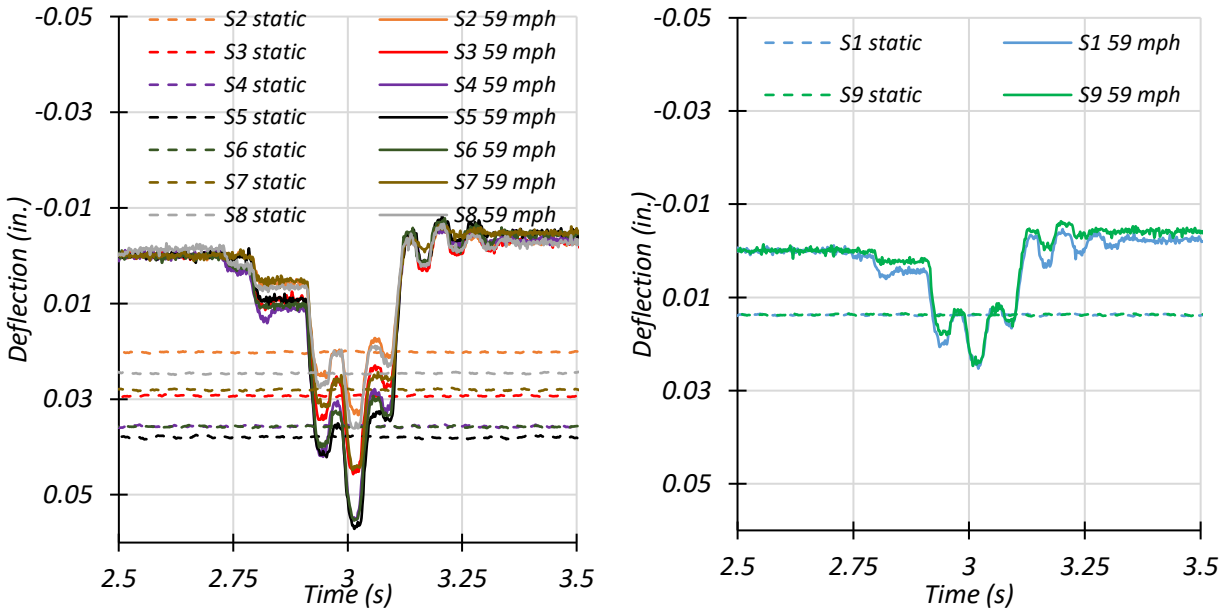

(d) Deflection Time Histories – Dynamic 4 (59 mph)

Figure 9.35. Midspan Deflections for Static and Dynamic Tests for Middle Path Loading (Continued)

The maximum deflections for each section under static and dynamic tests for Path 1, Path 2, and Middle Path loadings are tabulated in Table 9.30. Figure 9.36 compares the dynamic deflections for each section with the corresponding static deflections. Figure 9.37 shows the

measured deflections for the controlling dynamic load cases as a ratio to the stop location deflection.

Table 9.30. Maximum Midspan Deflections for Static and Dynamic Tests

	Loading	S1	S2	S3	S4	S5	S6	S7	S8	S9
Section Displacement (in.)	Path 1 Static	0.006	0.012	0.019	0.026	0.034	0.036	0.034	0.035	0.028
	Path 1 Dynamic (31 mph)	0.007	0.013	0.021	0.028	0.036	0.037	0.036	0.035	0.027
	Path 1 Dynamic (41 mph)	0.007	0.012	0.020	0.029	0.037	0.040	0.036	0.035	0.028
	Max. Path 1 Amplification	–	–	–	–	–	11%	–	–	0%
Section Displacement (in.)	Path 2 Static	0.028	0.032	0.038	0.038	0.035	0.027	0.018	0.015	0.006
	Path 2 Dynamic (30 mph)	0.031	0.036	0.041	0.042	0.037	0.028	0.017	0.015	0.005
	Path 2 Dynamic (40 mph)	0.036	0.042	0.049	0.053	0.049	0.038	0.025	0.020	0.009
	Max. Path 2 Amplification	29%	–	–	39%	–	–	–	–	–
Section Displacement (in.)	Middle Static	0.016	0.022	0.031	0.037	0.040	0.038	0.030	0.027	0.015
	Middle Dynamic (20 mph)	0.015	0.021	0.029	0.035	0.036	0.033	0.027	0.022	0.013
	Middle Dynamic (29 mph)	0.016	0.024	0.033	0.042	0.043	0.040	0.033	0.028	0.018
	Middle Dynamic (40 mph)	0.022	0.031	0.045	0.056	0.059	0.057	0.044	0.036	0.024
	Middle Dynamic (59 mph)	0.025	0.033	0.046	0.055	0.057	0.055	0.045	0.036	0.025
	Max. Middle Path Amplification	–	–	–	–	48%	–	–	–	67%

The maximum dynamic impact factor for the exterior section was 48 percent, and for the interior section it was 67 percent. For Bridge CS-9, the average dynamic impact factor for the exterior section was 32 percent, while the factor for the interior section was 33 percent. These percentages were calculated based on the maximum deflections recorded during testing. The

AASHTO Standard Specifications call for a dynamic impact factor of 30 percent, and *AASHTO LRFD Specifications* stipulates this factor to be 33 percent. Thus, based on the deflection data for Bridge CS-9, the average dynamic impact factor for the exterior and interior sections is within the range specified by AASHTO. However, as shown in the table for specific tests, the maximum impact can be greater than the specified values in AASHTO both in the exterior and interior sections of this integral curb slab bridge.

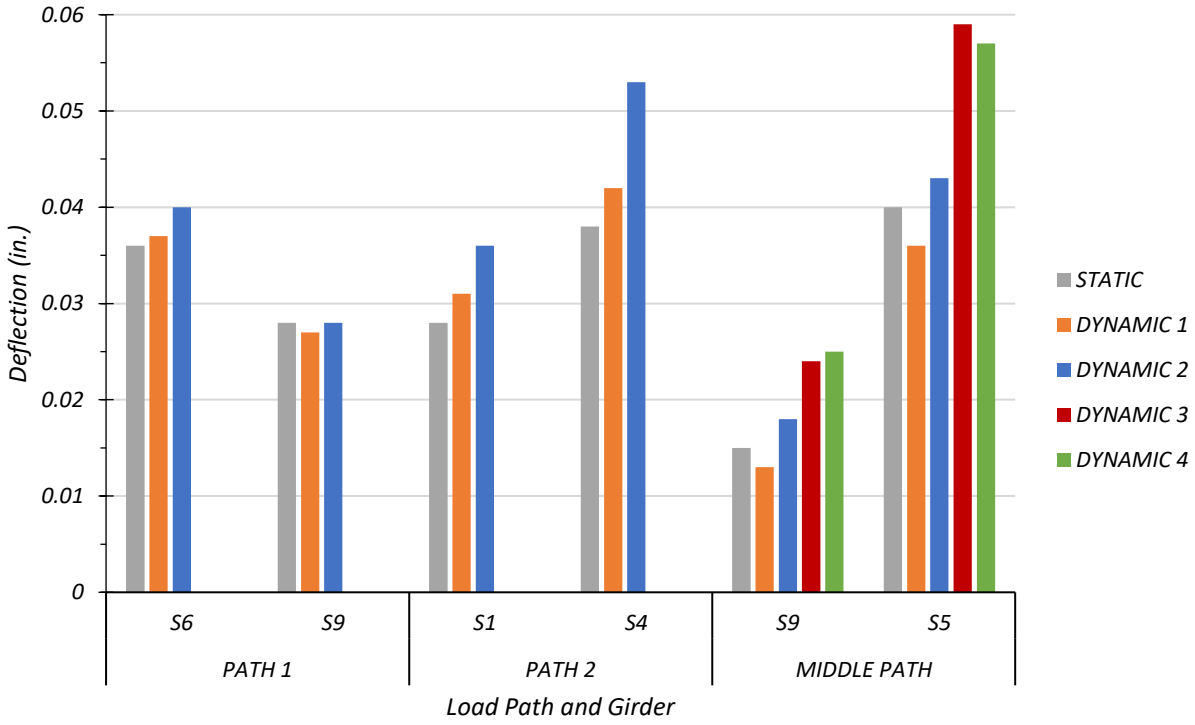

Note:

- *Path 1: Dynamic 1 = 31 mph, Dynamic 2 = 41 mph*
- *Path 2: Dynamic 1 = 30 mph, Dynamic 2 = 40 mph*
- *Middle Path: Dynamic 1 = 20 mph, Dynamic 2 = 29 mph, Dynamic 3 = 40 mph, Dynamic 4 = 59 mph*

Figure 9.36. Static and Dynamic Deflection Comparison

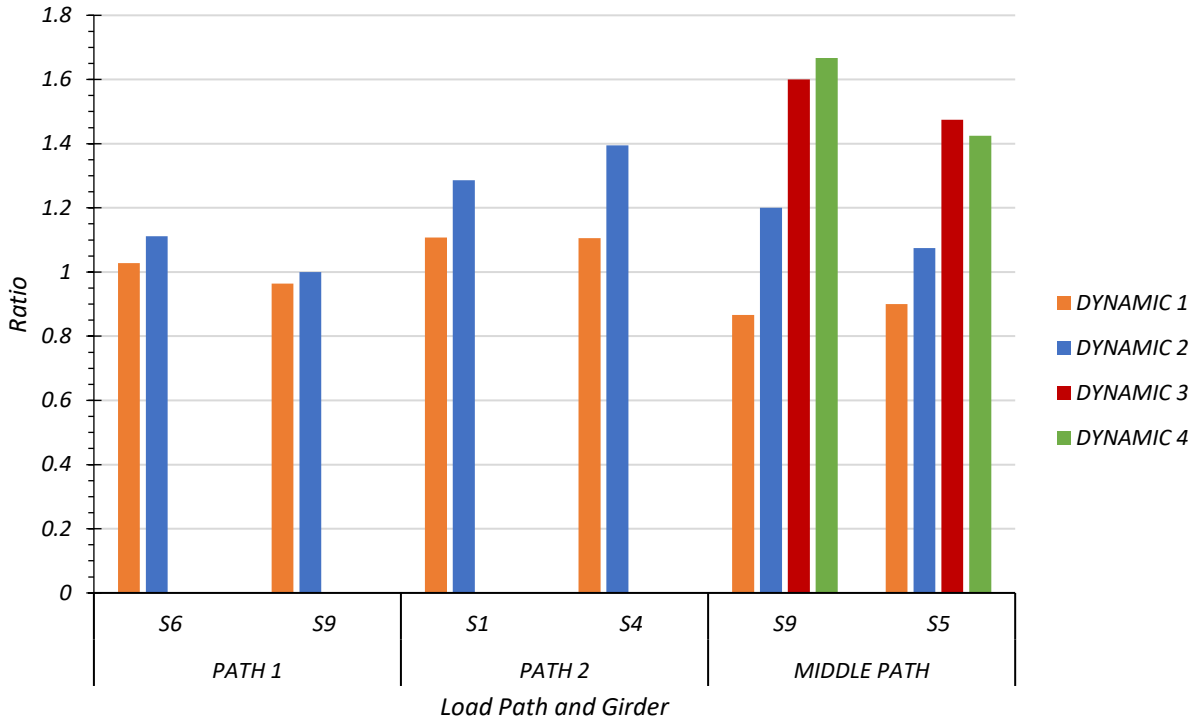

Note:

- *Path 1: Dynamic 1 = 31 mph, Dynamic 2 = 41 mph*
- *Path 2: Dynamic 1 = 30 mph, Dynamic 2 = 40 mph*
- *Middle Path: Dynamic 1 = 20 mph, Dynamic 2 = 29 mph, Dynamic 3 = 40 mph, Dynamic 4 = 59 mph*

Figure 9.37. Maximum Midspan Dynamic Deflections to Static Deflections Ratios

The maximum impact factor for the interior section is 48 percent for Section S5 during the Middle Path loading scenario. The maximum impact factor for the exterior section is 67 percent for Section S9 for the same loading scenario.

*9.6.2.2 **Dynamic Characteristics of Bridge***

The vibration data recorded by the accelerometers for the dynamic tests and impact tests were filtered using a low pass filter and analyzed to determine the dynamic characteristics of the bridge. The impact test was explained in detail in Section 9.5.3.3. By using the FFT approach, the first three natural frequencies of the bridge were determined to be 14.65 Hz, 22.46 Hz, and 37.11 Hz. The mode shapes across the longitudinal and transverse section for each natural frequency were developed using the corresponding amplitude and phase angle for each accelerometer. The accelerometer common to both the longitudinal section and transverse section is at 12.5 ft

longitudinally and 10.7 ft transversely. The mode shape along the longitudinal section and transverse section for the first natural frequency is shown in Figure 9.38. Figure 9.39 provides the mode shape along the longitudinal section and transverse section for the second natural frequency. The mode shape along the longitudinal section and transverse section for the third natural frequency is shown in Figure 9.40.

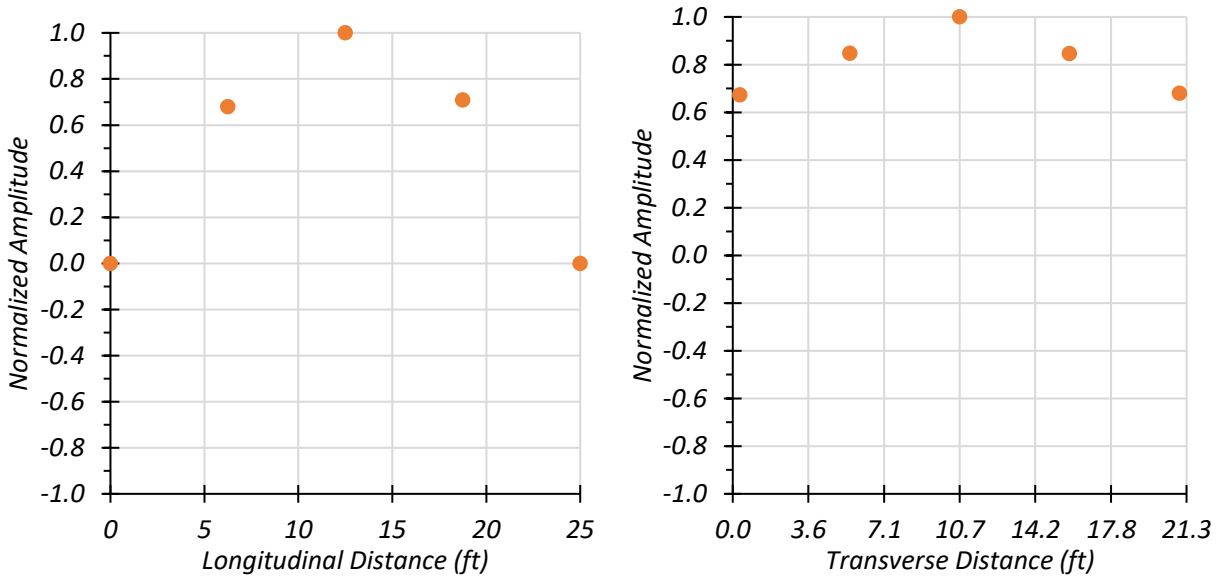

(a) Longitudinal Section *(b) Transverse Section*

Figure 9.38. Measured Mode Shape 1 for Bridge CS-9 (f_1 = 14.65 Hz)

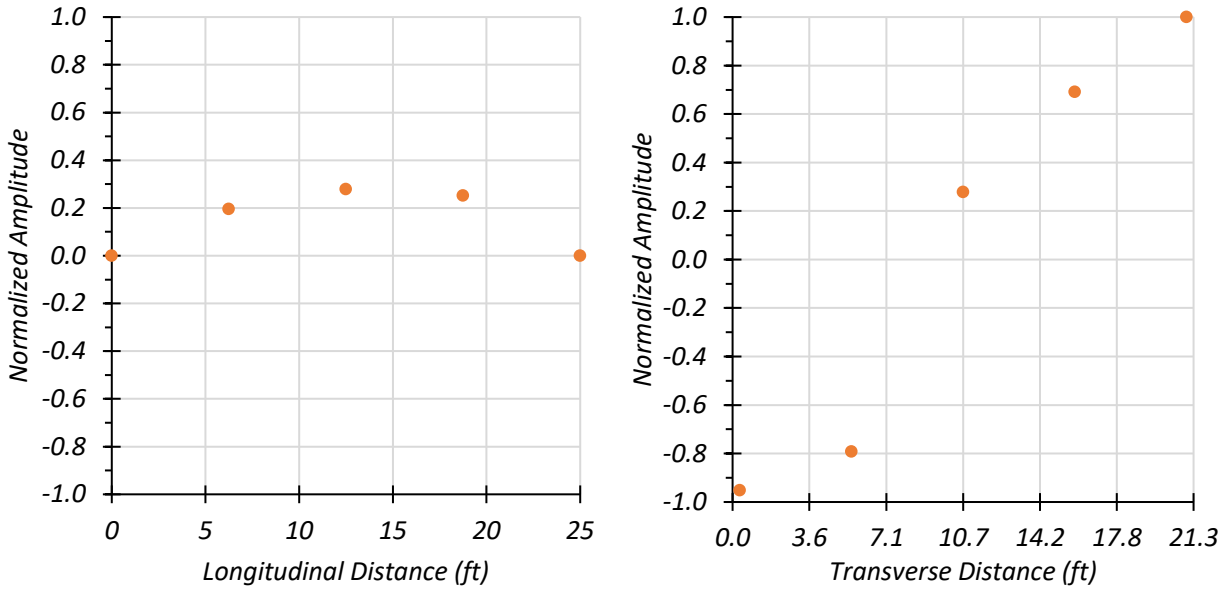

(a) Longitudinal Section *(b) Transverse Section*

Figure 9.39. Measured Mode Shape 2 for Bridge CS-9 (f_2 = 22.46 Hz)

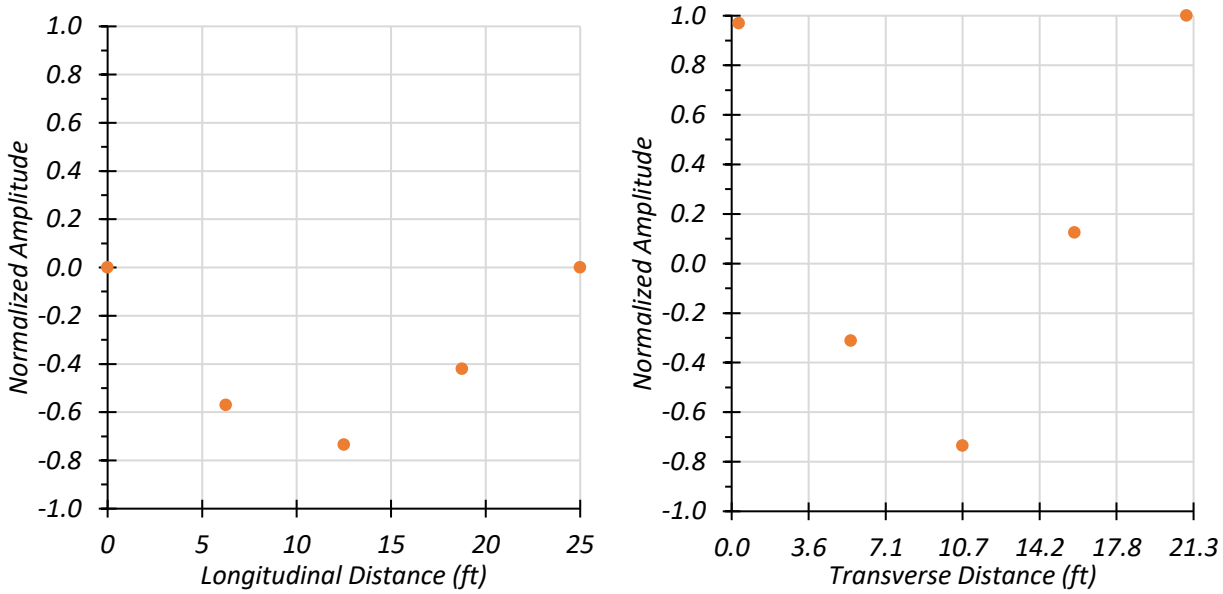

(a) Longitudinal Section *(b) Transverse Section*

Figure 9.40. Measured Mode Shape 3 for Bridge CS-9 (f_3 = 37.11 Hz)

9.6.3 Computer Vision

The possibility of determining bridge deflections from video recordings of the bridge during a truck pass was evaluated during testing of Bridge CS-9. Two cameras, a Sony HDR-CX405 video camera and an iPhone 8, were mounted on tripods and set up on either side of the bridge. These cameras were used to record the bridge during each test. The video resolution of the video camera was 1440 pixels by 1080 pixels, while that of the iPhone was 3840 pixels by 2160 pixels. Two images of the bridge as it is unloaded and loaded were extracted from the videos using a computer vision algorithm. The displacement measurements between the images were obtained using an image analysis algorithm comparing one sub-window of the unloaded bridge image with several sub-windows of the loaded bridge image. The window size used in all these tests were 50 pixels by 50 pixels, and its location on the image was selected such that it covered an area of high contrast. All signals were filtered using a band pass filter to remove the noise associated with the data, such as unintended vibration of the cameras. Depending on the level of noise, a high pass, a low pass, or a band pass filter may be used.

The time history plot of deflection obtained from the computer vision analysis was plotted along with the corresponding deflection obtained from the string potentiometer to compare the results. Figure 9.41 shows the time history plot for the exterior Section S9 during the crawl speed test along Path 1. The image data obtained from the video camera were filtered using a low pass filter to remove any noise in the data due to vibration of the bridge during testing. The maximum deflection obtained from the computer vision analysis was 0.0331 in., while the string potentiometer recorded the maximum deflection as 0.0265 in. The deflection obtained from computer vision was 25 percent higher than the deflection obtained from the string potentiometer.

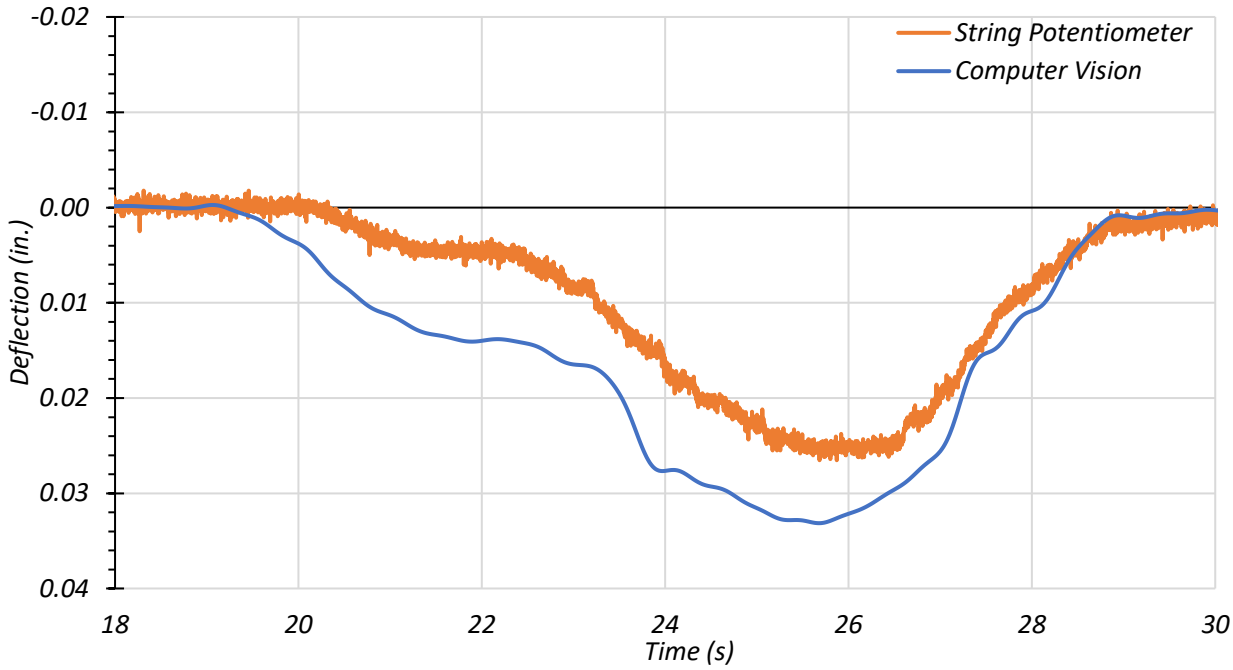

Figure 9.41. Section 9 Midspan Deflections for Path 1—Crawl Test

The time history deflection plot for the exterior Section S9 during the dynamic test at 31 mph along Path 1 is presented in Figure 9.42. A similar low pass filter was also applied to the image data obtained from the video camera. The maximum deflection obtained from the computer vision analysis was 0.0329 in., while the string potentiometer recorded the maximum deflection as 0.0273 in. The deflection obtained from computer vision was 21 percent higher than the deflection obtained from the string potentiometer.

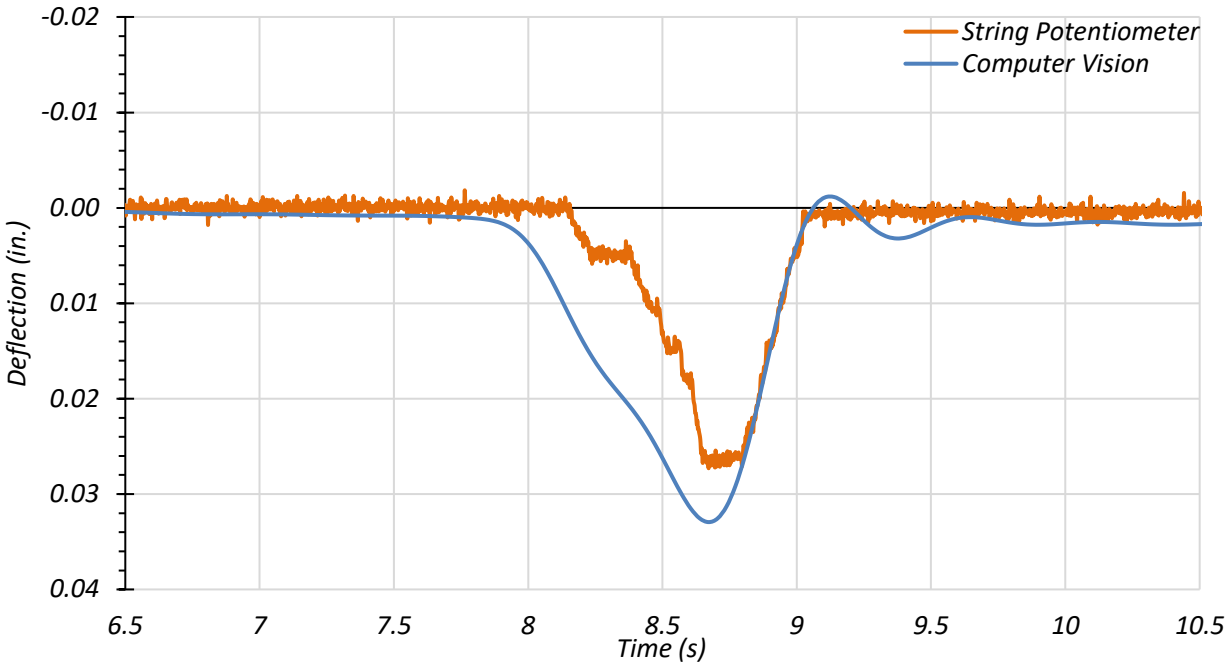

Figure 9.42. Section 9 Midspan Deflections for Path 1—Dynamic Test at 31 mph

Figure 9.43 shows the time history plot for the exterior Section S9 during the dynamic test at 41 mph along Path 1. For this test, the image data obtained from the video camera were filtered using a low pass filter. The maximum deflection obtained from the computer vision analysis was 0.0281 in., while the string potentiometer recorded the maximum deflection as 0.0273 in. The deflection obtained from computer vision was 3 percent higher than the deflection obtained from the string potentiometer.

In this section, several selected results obtained from the computer vision analysis are presented. The aim of this analysis was to determine the feasibility of this approach to determine the deflection of the bridge under vehicular loading from a video/image in comparison to measurements using string potentiometers. The deflections associated with this bridge are very small (multiple of 1/100 of an in.), which may be the reason for some of the variations observed in the percentage difference. However, this approach seems to provide reasonable deflection measurements for this bridge.

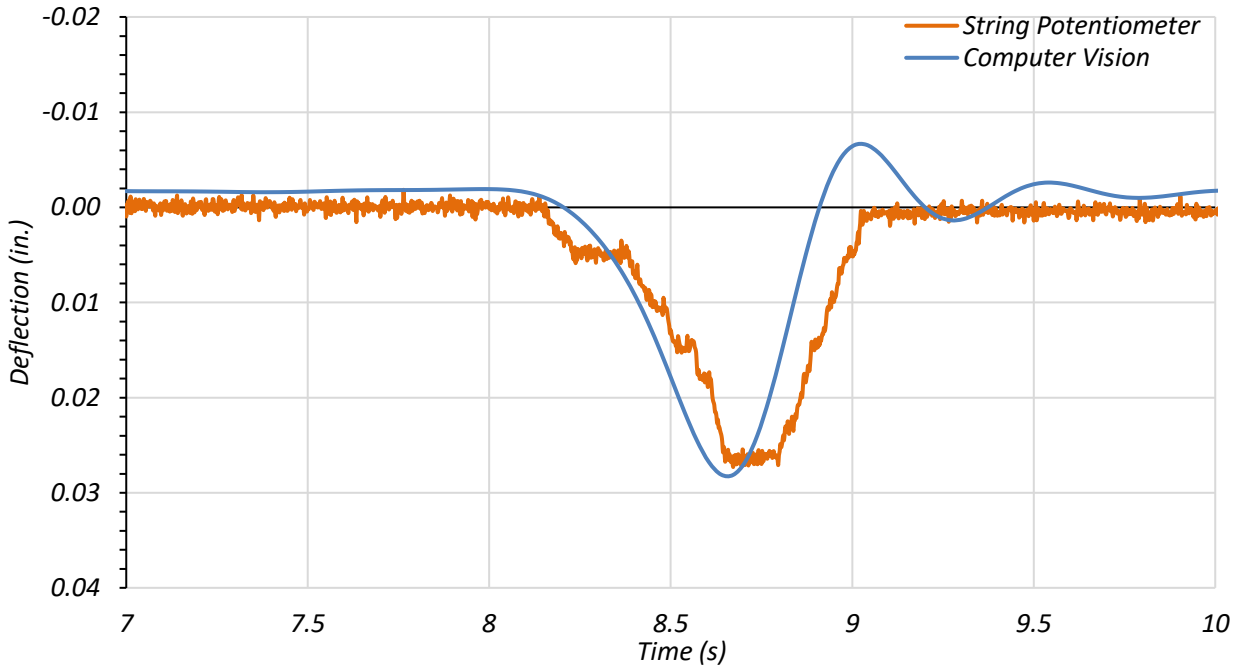

Figure 9.43. Section 9 Midspan Deflections for Path 1—Dynamic Test at 41 mph

9.7 FEM MODEL UPDATE AND CALIBRATION

9.7.1 General

The initial FEM model for Bridge CS-9 was revised to determine appropriate modeling parameters based on comparison to test data. The FEM model update was carried out in two steps: (1) a concrete material property update based on NDE tests, and (2) an end fixity update based on model calibration.

9.7.2 Updated FEM Model

The concrete compressive strength for Bridge CS-9 was determined to be 5.2 ksi from the NDE tests, as discussed in Section 9.3.2. This measurement is higher than the initial f_c' taken to be 2.5 ksi for the initial FEM model that was created prior to field testing. Therefore, the MOE was updated using $f_c' = 5.2$ ksi. In addition, the updated MOE for Bridge CM-5 was increased by 10 percent because (1) empirical code equations calculate MOE using a secant stiffness, which is smaller than the tangent stiffness, and (2) empirical code equations typically provide lower bound values to be conservative. As a result, the MOE of concrete increased from 3031 ksi to 4809 ksi.

The FEM model was updated to incorporate the MOE based on the measured f_c' and the measured bridge geometries noted in Section 9.3. The end conditions of the updated model were kept the same as the initial FEM model; both ends were modeled with roller supports, except that one end of one exterior section was modeled as a pin, and the end of the other exterior section was restrained both vertically and longitudinally. This configuration ensured that the model was restrained in all degrees of freedom. Table 9.31 provides a few selected results from the updated FEM model and compares the results to measurements from the field test. The results obtained from this updated FEM model are further compared with the experimental results in the following sections.

Table 9.31. Selected FEM Results for Updated FEM Model

Model or Test	Modal Frequency (Hz)		Midspan Deflection (in.)		Strain (με)					
					West Bottom		Mid Top	Mid Bottom	East Bottom	
	1st	2nd	S1	S5	S5	S9	S1	S1	S5	S9
Field Test	14.65	22.46	0.040	0.029	−11.23	3.44	49.58	−64.58	−39.37	−3.33
Original Model	11.57	14.30	0.067	0.053	−0.01	23.59	59.15	−111	0.00	−0.03
Updated Model	11.57	15.38	0.061	0.059	0.00	20.24	53.39	−133	0.00	−0.01

9.7.3 Model Calibration Process

The updated FEM model for Bridge CS-9 discussed in the previous subsection was further calibrated for end fixity at the abutments and to include cracked section properties. The model developed from this calibration process is intended to more closely represent the measured behavior of the bridge.

The updated FEM model was modified to incorporate cracked concrete section properties by using nonlinear material properties based on the Mander model for concrete (Mander et al. 1988). Two different values for concrete tensile strength were considered: 10 percent of the measured concrete compressive strength and 1 percent of the measured concrete compressive strength. These analyses were carried out for simply supported end conditions, pin-pin end conditions, and roller-roller end conditions.

Four input parameters were identified for calibrating the above updated FEM model of Bridge CS-9 to determine the appropriate end fixities. These parameters were as follows: (1) west end of all interior sections, (2) west end of both exterior sections, (3) east end of all interior

sections, and (4) east end of both exterior sections. The vertical translational degree of freedom was fully restrained for all sections. Horizontal springs were introduced at the bottom nodes of the sections of the concrete slab bridge. The horizontal spring stiffness was modified to provide partial fixities at the ends. The influence of introducing horizontal springs at the top nodes of the concrete slab was also considered. Roller supports were considered to be the lower bound for the horizontal spring stiffness, and pin supports were the upper bound. The corresponding upper and lower bound spring stiffness was determined. The effect of each input parameter on the analysis results was studied by gradually varying one parameter at a time. The results from this parametric study are presented in the following sections.

9.7.4 Calibrated FEM Model Results

In this section, the influence of changing each selected input parameter on the analysis results is presented. The calibration of the model was conducted using experimental results obtained for the static tests carried out on Bridge CS-9, as provided in Table 9.32. It should be noted that Section S9 results are obtained from the Path 1 stop location test, Section S1 results from the Path 2 stop location test, and Section S5 results from the Middle Path stop location test.

Table 9.32. Experimental Results for Calibration of Bridge CS-9

Modal Frequency (Hz)		Midspan Deflection (in.)		Strain (με)					
				West Bottom		Mid Top	Mid Bottom	East Bottom	
1st	2nd	S1	S5	S5	S9	S1	S1	S5	S9
14.65	22.46	0.029	0.040	−11.23	3.44	−64.57	49.58	−39.37	−3.33

*9.7.4.1 **Modulus of Elasticity***

The MOE was modified to account for the cracks observed in the slab bridge with integral curbs. The end supports were also modified to study the cumulative effect. These results are summarized and presented in Table 8.15.

Table 9.33. Effect of Modulus of Elasticity Value on Selected FEM Results

Case	West Fixity	East Fixity	Modal Frequency (Hz)		Midspan Deflection (in.)		Strain (με)					
							West Bot		Mid Top	Mid Bot	East Bot	
			1st	2nd	S1	S5	S5	S9	S1	S1	S5	S9
Test	Pin	Roller	14.65	22.46	0.029	0.040	-11.23	3.44	−64.57	49.58	−39.37	−3.33
1(a)	Pin	Pin	14.50	20.75	0.042	0.043	−8.84	0.32	−112	35.29	−9.72	−4.98
1(b)	Pin	Roller	11.64	17.18	0.061	0.059	0.00	18.15	−135	54.67	0.00	−0.01
1(c)	Roller	Roller	11.66	18.15	0.061	0.059	0.00	19.84	−136	55.94	0.00	0.00
1(d)	Roller	Roller	14.50	20.75	0.042	0.043	−5.35	3.16	−112	36.00	−13.06	−18.04
Case 1(a) – (c): Nonlinear Mander model for concrete with $f_t = 10\% f_c'$ Case 1(d): Nonlinear Mander model for concrete with $f_t = 1\% f_c'$												

The nonlinear Mander model, with $f_t = 1\% f_c'$ for concrete, which was intended to represent the presence of existing cracks, provided agreeable results to the experimental results. The following calibration is carried out using Case 1(d) listed in Table 8.15.

*9.7.4.2 **West End Interior Section Stiffness Spring***

The effect of changing the boundary condition at the west end of the interior sections was determined by changing the support to roller (only vertical translation restrained) and pin (all three translations restrained) while keeping the boundary conditions for the west end exterior sections and the east end as rollers. The second modal frequency and the bottom strain at the midspan for Section S1 for the pin support are close to the test results. Thus, the boundary condition for the west end of the interior sections was found to be closer to the pin support, as shown in Table 9.34.

Table 9.34. Effect of West End Interior Section Fixity on Selected FEM Results

West End Interior Sections	Modal Frequency (Hz)		Midspan Deflection (in.)		Strain (με)					
					West Bottom		Mid Top	Mid Bottom	East Bottom	
Support	1st	2nd	S1	S5	S5	S9	S1	S1	S5	S9
Test	14.65	22.46	0.029	0.040	−11.23	3.44	−64.57	49.58	−39.37	−3.33
Pin	12.87	21.20	0.047	0.050	0.00	16.84	−99.1	46.09	0.00	−0.02
Roller	13.03	20.32	0.048	0.050	0.00	16.79	−63.58	27.28	0.00	−0.02

9.7.4.3 West End Exterior Section Stiffness Spring

The effect of changing the boundary condition at the west end of the exterior transverse sections was determined by changing the support to roller (only vertical translation restrained) and pin (all three translations restrained) while keeping the boundary conditions for the west end interior sections and the east end as rollers. The second modal frequency and the bottom strain at the midspan of Section S1 for the pin support are close to the test results. Therefore, the boundary condition for the west end of the exterior sections was found to be closer to the pin support, as shown in Table 9.35.

Table 9.35. Effect of West End Exterior Section Fixity on Selected FEM Results

West End Exterior Section	Modal Frequency (Hz)		Midspan Deflection (in.)		Strain (με)					
					West Bottom		Mid Top	Mid Bottom	East Bottom	
Support	1st	2nd	S1	S5	S5	S9	S1	S1	S5	S9
Test	14.65	22.46	0.029	0.040	−11.23	3.44	−64.57	49.58	−39.37	−3.33
Pin	12.82	21.50	0.047	0.050	0.00	16.20	−102	46.58	0.00	−0.02
Roller	13.03	20.32	0.048	0.050	0.00	16.79	−63.58	27.28	0.00	−0.02

9.7.4.4 East End Interior Section Stiffness Spring

The effect of changing the boundary condition at the east end of the interior transverse sections was determined by changing the support to roller (only vertical translation restrained) and pin (all three translations restrained) while keeping the boundary conditions for the east end exterior sections and west end as rollers. The second modal frequency and the bottom strain at the midspan of Section S1 for the pin support are close to the test results. Thus, the boundary condition for the east end of the interior sections was found to be closer to the pin support, as shown in Table 9.36.

Table 9.36. Effect of East End Interior Section Fixity on Selected FEM Results

East End Interior Section	Modal Frequency (Hz)		Midspan Deflection (in.)		Strain (με)					
					West Bottom		Mid Top	Mid Bottom	East Bottom	
Support	1st	2nd	S1	S5	S5	S9	S1	S1	S5	S9
Test	14.65	22.46	0.029	0.040	−11.23	3.44	−64.57	49.58	−39.37	−3.33
Pin	12.86	21.20	0.047	0.050	0.00	17.07	−102	46.77	0.00	−0.02
Roller	13.03	20.32	0.048	0.050	0.00	16.79	−63.58	27.28	0.00	−0.02

9.7.4.5 East End Exterior Section Stiffness Spring

The fixity at the east end of the exterior section was determined by changing the support to roller (only vertical translation restrained) and pin (all three translations restrained) while keeping the boundary conditions for the east end interior sections and west end as rollers. The second modal frequency and the bottom strain at the midspan of Section S1 for the pin support are close to the test results. Thus, the fixity was found to be closer to the pin support, as shown in Table 9.37.

Table 9.37. Effect of East End Exterior Section Fixity on Selected FEM Results

East End Exterior Section	Modal Frequency (Hz)		Midspan Deflection (in.)		Strain (με)					
					West Bottom		Mid Top	Mid Bottom	East Bottom	
Support	1st	2nd	S1	S5	S5	S9	S1	S1	S5	S9
Test	14.65	22.46	0.029	0.040	−11.23	3.44	−64.57	49.58	−39.37	−3.33
Pin	12.82	21.50	0.047	0.050	0.00	17.29	−102	47.54	0.00	−0.02
Roller	13.03	20.32	0.048	0.050	0.00	16.79	−63.58	27.28	0.00	−0.02

9.7.4.6 Final Calibration

The individual parametric studies suggested that both ends of the bridge supports are similar to a pin support. The final model calibration was initiated with these end conditions. Each input parameter was gradually adjusted until the FEM results were close to the experimental results. The model was analyzed with different end stiffness values ranging from 50 kip/in. to 15,000 kip/in. The final calibrated model parameters are presented in Table 9.38. In this study, *pinned* indicates

an infinitely stiff spring at the support providing restraint in all three translational directions. It should be noted that no horizontal springs were provided to restrain the top nodes of the slab.

Table 9.38. Final Calibrated Model Parameters

Concrete Properties		**Stiffness Value (kip/in.)**			
f_c' **(ksi)**	E_c **(ksi)**	**West End Interior Sections**	**West End Exterior Sections**	**East End Interior Sections**	**East End Exterior Sections**
5.2	4809	Pinned	Pinned	Pinned	500

The calibrated model for Bridge CS-9, along with the end fixity springs, is shown in Figure 9.44. The results obtained from the calibrated FEM model and the test results are tabulated in Table 9.39. In the following sections, the results from this calibrated model are compared with the experimental results.

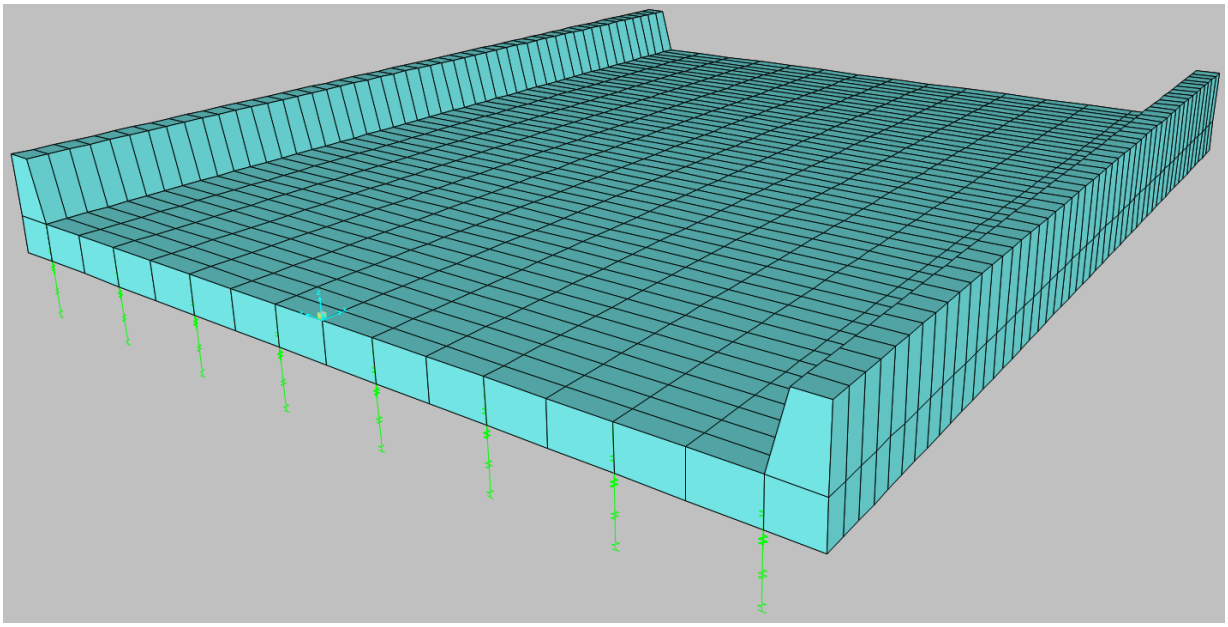

Figure 9.44. Calibrated FEM Model for Bridge CS-9

Table 9.39. Results of CS-9 Model Calibration

Results	Modal Frequency (Hz)		Midspan Deflection (in.)		Strain (με)					
					West Bottom		Mid Top	Mid Bottom	East Bottom	
	1st	2nd	S1	S5	S5	S9	S1	S1	S5	S9
Test	14.65	22.46	0.029	0.040	−11.23	3.44	−64.57	49.58	−39.37	−3.33
Calibrated	16.66	23.11	0.032	0.034	−6.63	3.40	−76.64	31.92	−17.29	−1.89

9.8 COMPARISON OF TEST RESULTS AND FEM PREDICTIONS

9.8.1 Strain Measurements

The maximum top and bottom strains for exterior Sections S1 and S9 under static tests along Path 1 are compared with the updated and calibrated FEM results in Figure 9.45. Figure 9.45(a) and (c) provide strain profiles for Section S1 for the stop location test and crawl speed test, respectively. The top strain obtained from the updated FEM model was 107 percent higher and the bottom strain was 25 percent lower than the test values for the static test. The maximum variation obtained from the calibrated FEM model was 16 percent higher for the top strain and 73 percent lower for the bottom strain in comparison to the test results. The corresponding strain profiles for Section S9 are provided in Figure 9.45(b) and (d) for static tests. Here, the maximum variation observed in the

updated FEM model was 42 percent higher for the top strain and 268 percent higher for the bottom strain when compared to the test results. The calibrated model was 2 percent higher than the recorded top strain and 88 percent higher than the recorded bottom strain. These differences may be due to the similar stiffnesses considered for the two curbs, while the experimental measurements indicated some difference.

The maximum top and bottom strains for exterior Sections S1 and S9 under static tests along Path 2 are compared with the updated and calibrated FEM results in Figure 9.46. Figure 9.46(a) and (c) provide strain profiles for Section S1 for the stop location test and the crawl speed test, respectively. The top strain obtained from the updated FEM model was 93 percent higher and the bottom strain was 20 percent higher than the test values for the static test. The maximum variation obtained from the calibrated FEM model was 32 percent higher for the top strain and 36 percent lower for the bottom strain in comparison to the test results. The corresponding strain profiles for Section S9 are provided in Figure 9.46(b) and (d) for static tests. The maximum variation observed in the updated FEM model was 21 percent higher for the top strain and 182 percent higher for the bottom strain when compared to the test results. The calibrated model was 49 percent lower than the recorded top strain and 31 percent lower than the recorded bottom strain.

Figure 9.47 compares the strain profiles obtained from Sections S1 and S9 during the static test along the Middle Path with the updated and calibrated FEM results. Figure 9.47 (a) and (c) provide strain profiles for Section S1 for the stop location test and crawl speed test, respectively. The top strain obtained from the updated FEM model was 95 percent higher and the bottom strain was 24 percent higher than the test values for the static test. The maximum variation obtained from the calibrated FEM model was 26 percent higher for the top strain and 55 percent lower for the bottom strain in comparison to the test results. The corresponding strain profiles for Section S9 are provided in Figure 9.46(b) and (d) for static tests. The maximum variation observed in the updated FEM model was 44 percent higher for the top strain and 318 percent higher for the bottom strain when compared to the test results. The calibrated model was 24 percent lower than the recorded top strain and 92 percent higher than the recorded bottom strain.

The calibrated FEM model overall matches better with the test results than does the updated FEM model. The calibration was conducted using test strains obtained from the curb sections. It should be noted that the FEM models consider both curbs to have similar stiffnesses. However,

experimental results indicate otherwise, which may be the reason the strains obtained from the calibrated FEM models do not match the test values. As highlighted in Section 9.6.1.1, there is a lack of confidence in some measured strain values. Consequently, the FEM models were also calibrated against recorded deflections and dynamic characteristics of the bridge.

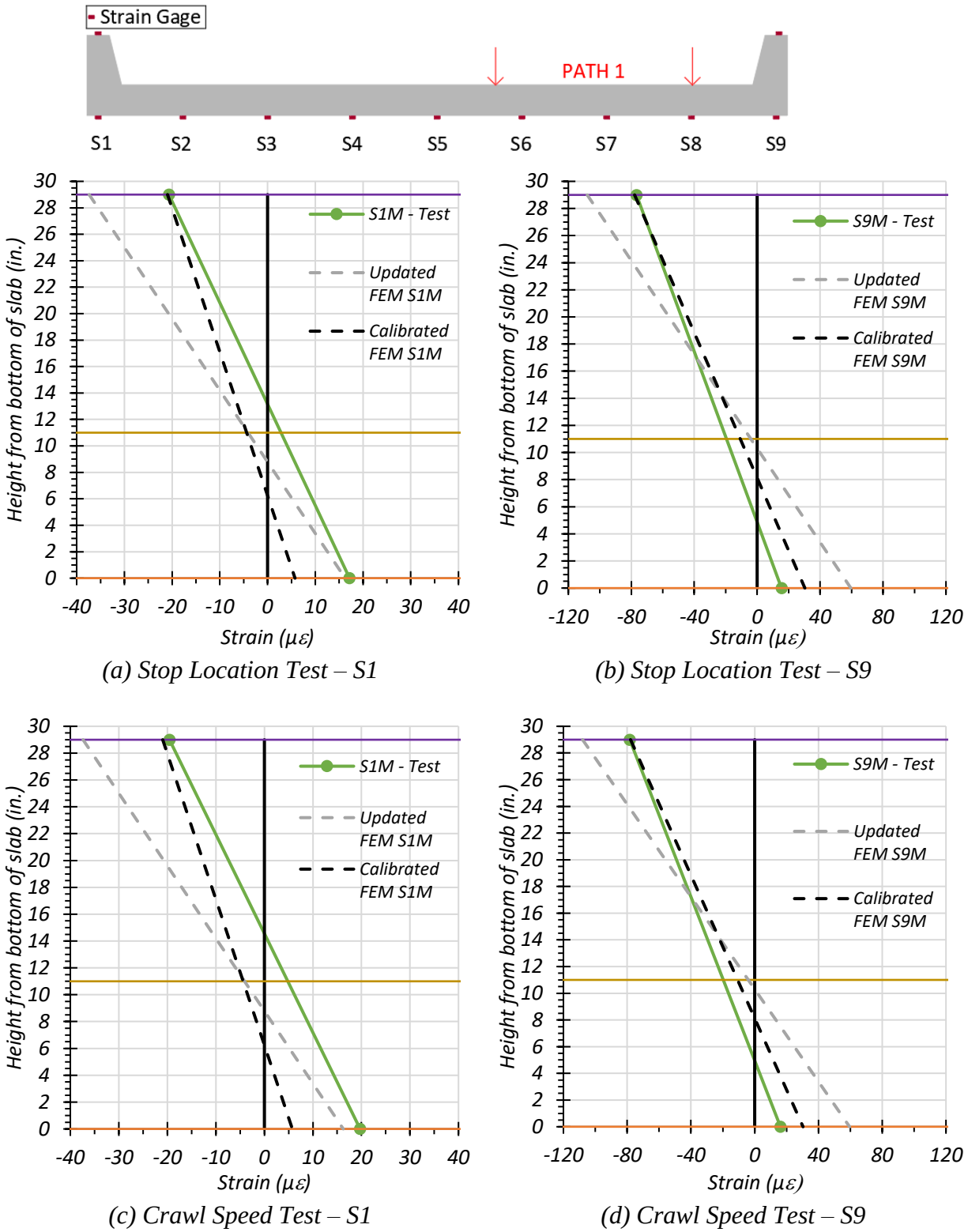

(a) Stop Location Test – S1

(b) Stop Location Test – S9

(c) Crawl Speed Test – S1

(d) Crawl Speed Test – S9

Figure 9.45. Comparison of Static Strains with FEM Results—Path 1

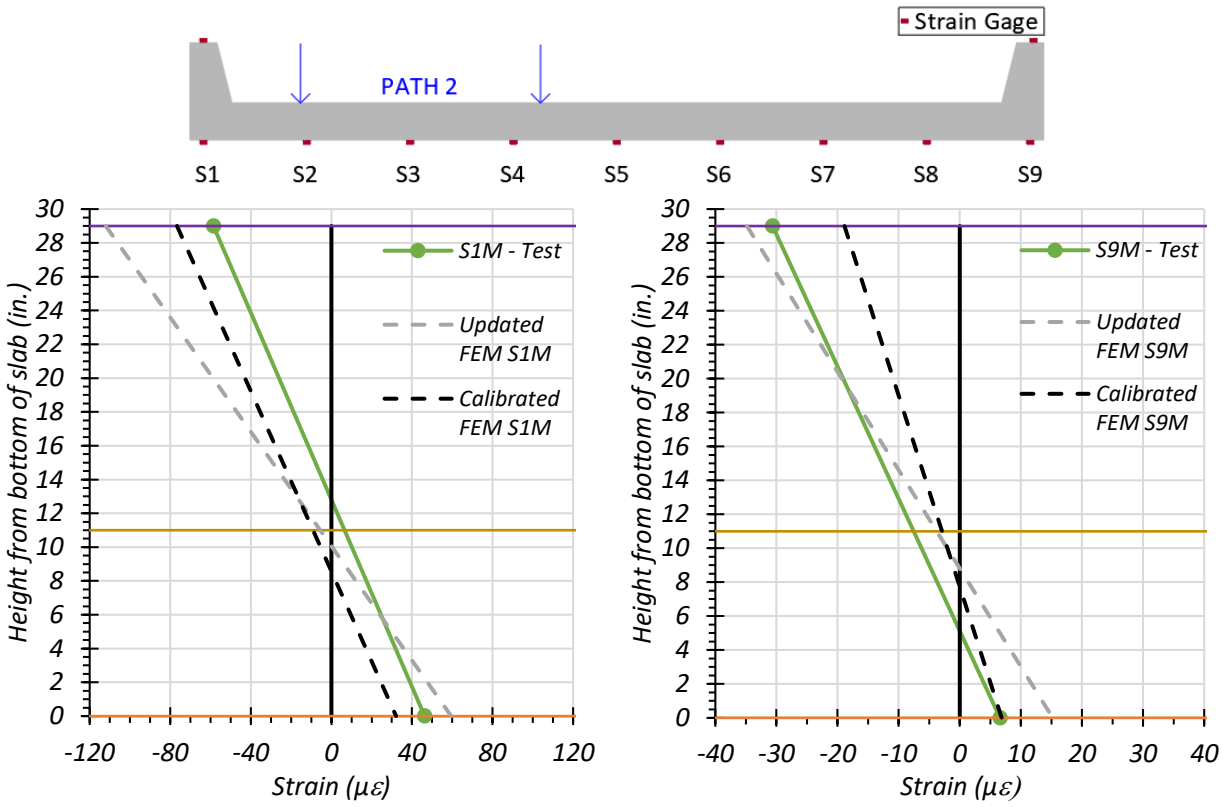

(a) Stop Location Test – S1

(b) Stop Location Test – S9

(c) Crawl Speed Test – S1

(d) Crawl Speed Test – S9

Figure 9.46. Comparison of Static Strains with FEM Results—Path 2

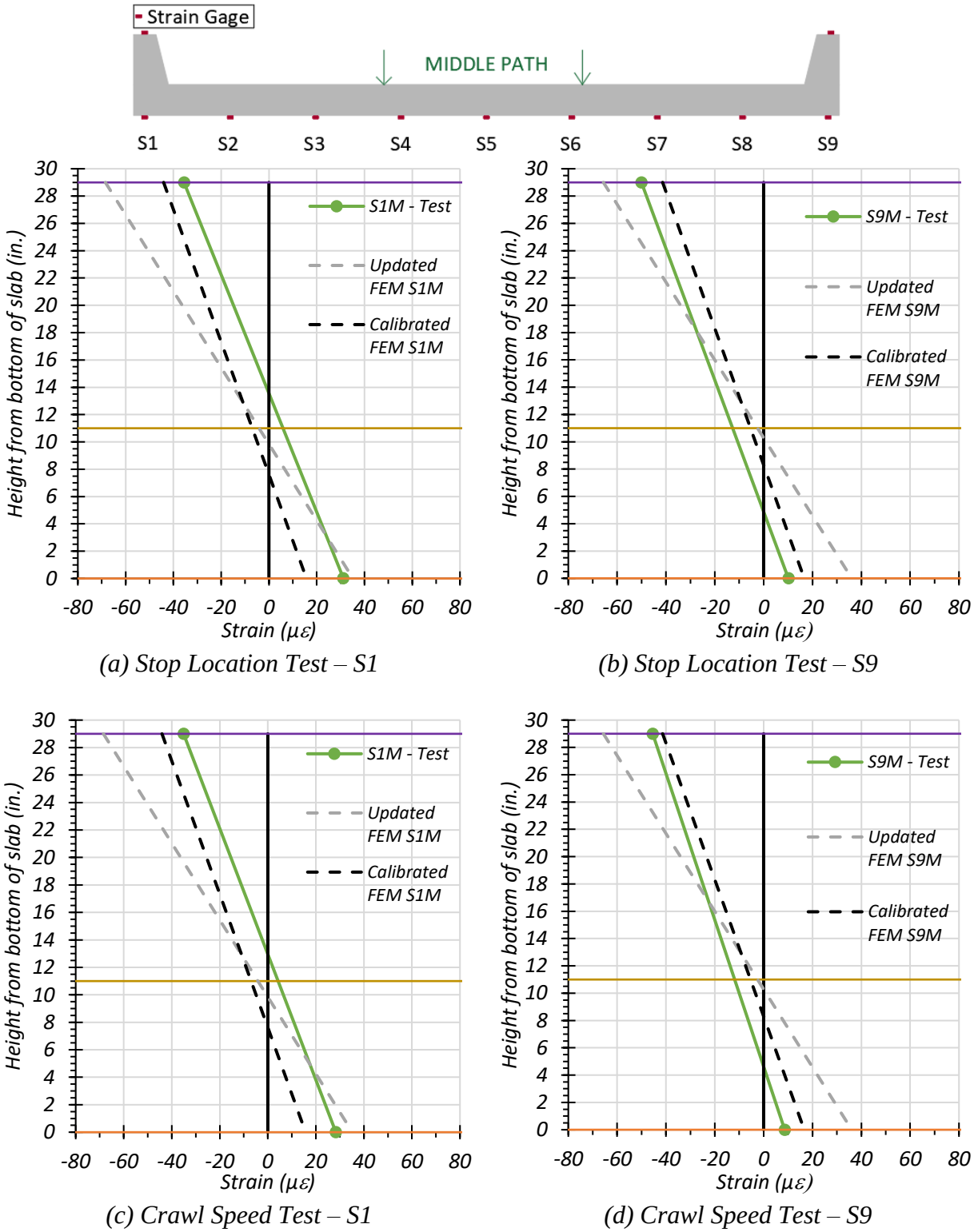

(a) Stop Location Test – S1

(b) Stop Location Test – S9

(c) Crawl Speed Test – S1

(d) Crawl Speed Test – S9

Figure 9.47. Comparison of Static Strains with FEM Results—Middle Path

Comparison of Results Based on Measured Strains. The neutral axis location for each transverse section is determined from the strain profile at the midspan.

Table 9.40 lists the neutral axes corresponding to all the different tests. Figure 9.48 compares the neutral axes obtained from the static tests with the FEM neutral axis for both Section S1 and S9. The test results show that the stiffness of Section S9 may be less than that of Section S1. The FEM models considered the same stiffness for both the sections. Additionally, the calibrated FEM model considers cracked concrete properties for the bridge.

Table 9.40. Measured Neutral Axis Locations for All Static Load Tests

Test	S1 Neutral Axis Location (in. from bottom of slab)	S9 Neutral Axis Location (in. from bottom of slab)
Path 1 – Stop Location	15.80	5.79
Path 1 – Crawl Speed	14.56	4.96
Path 2 – Stop Location	12.59	6.17
Path 2 – Crawl Speed	13.50	4.56
Middle Path – Stop Location	13.53	5.78
Middle Path – Crawl Speed	12.95	4.63
Updated FEM	9.85	10.61
Calibrated FEM	7.62	8.57
Theoretical Uncracked	13.33	
Theoretical Cracked	21.43	

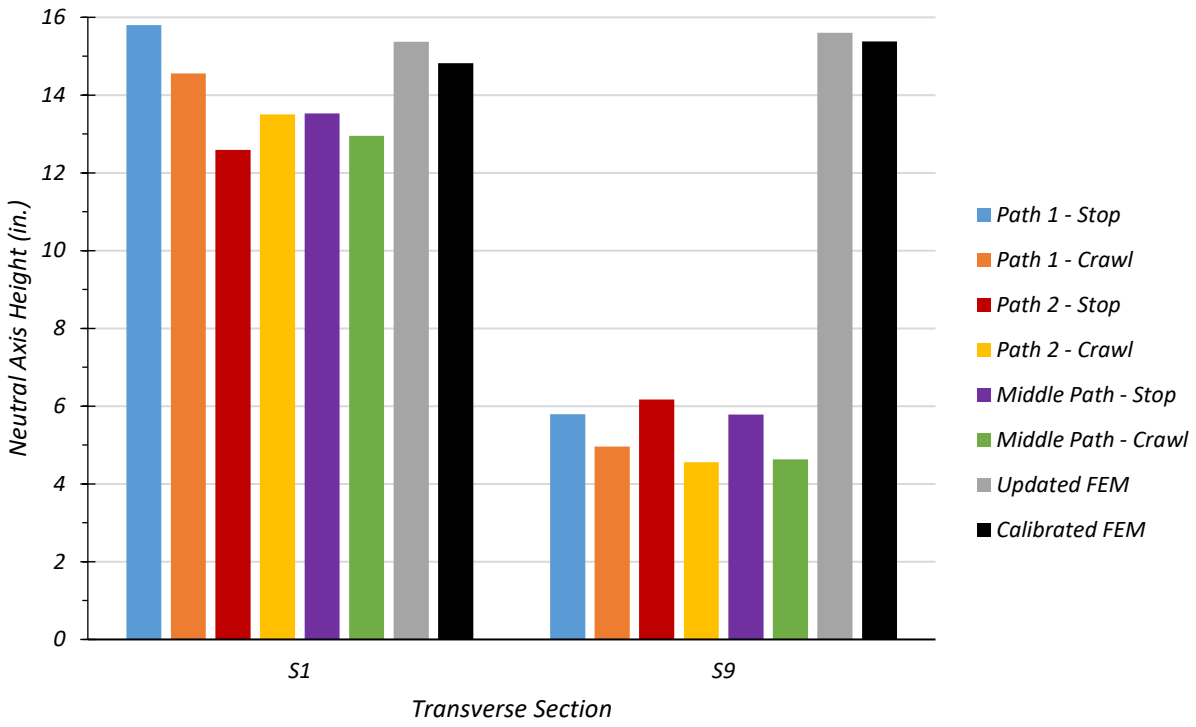

Figure 9.48. Test Neutral Axis Locations

9.8.2 Deflection Measurements

In this section, the deflections measured during load testing are compared with the updated and calibrated FEM results.

Path 1 Loading. The measured maximum downward deflection for each section under the static test and crawl speed test along Path 1 was compared with those obtained from the updated and calibrated FEM models in Figure 9.49(a) and (b), respectively. The updated FEM model overestimates the deflection by over 200 percent for both the stop location test and crawl speed test along Path 1. The calibrated FEM model provides a better estimation of the observed deflections during static tests along Path 1, with a maximum overestimation of 10 percent for the stop location test and 33 percent for the crawl speed test. It should be noted that the FEM models were developed considering the same stiffness for both the curbs. However, the test results show that the stiffness was smaller for the curb at Section S9 as compared to the one at Section S1.

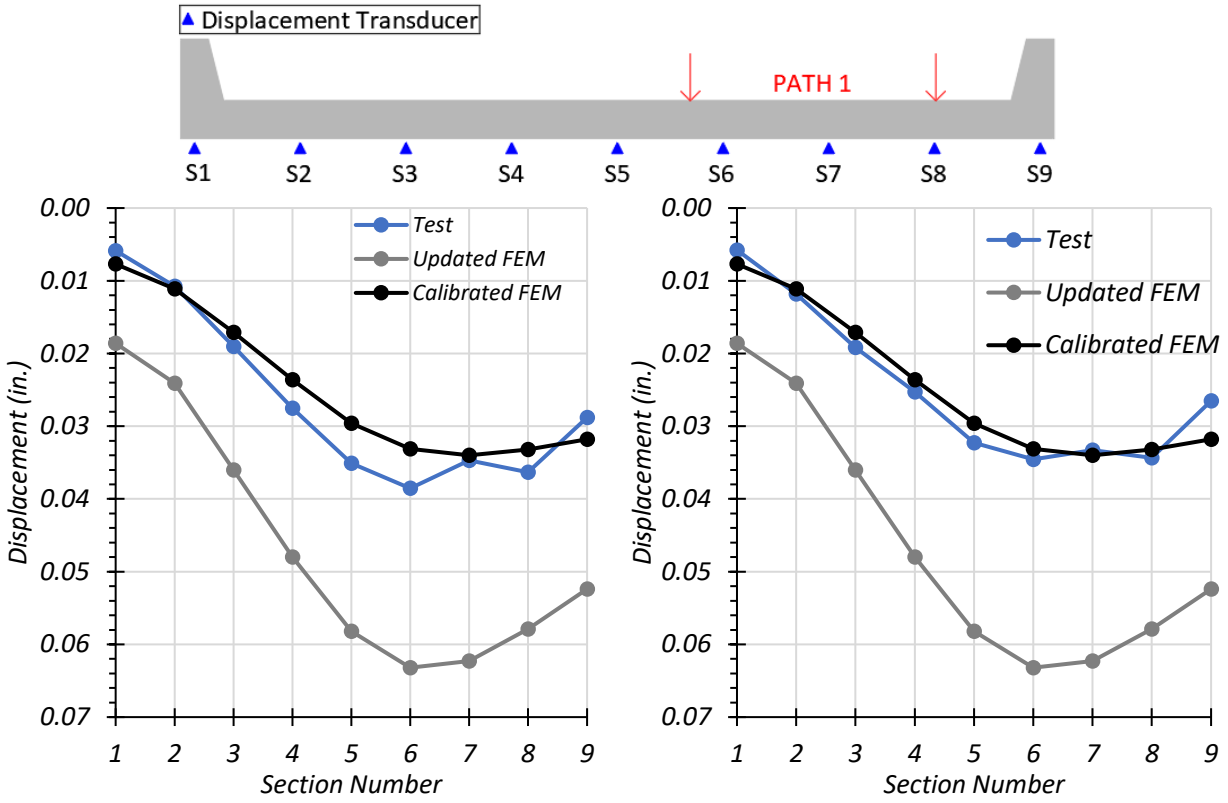

(a) Section Deflections – Stop Location *(b) Section Deflections – Crawl Speed*

Figure 9.49. Comparison of Static Deflection Results with FEM for Path 1 Loading

Based on a similar approach used to determine the equivalent width of the slab using the test data (Section 9.6.1.2), the step-by-step calculations for the equivalent width of the interior slab section for the stop location test for the calibrated FEM model are provided in Table 9.41.

Table 9.41. Calibrated FEM Deflections, LLDFs, and Equivalent Width for Stop Location Test along Path 1 Using L-Curbs

Section	S1+S2 (Left L-curb)		S3	S4	S5	S6	S7	S8+S9 (Right L-curb)	
Width (ft)	4.708		2.083	2.583	2.583	2.583	2.083	4.708	
Δ (in.)	0.008	0.011	0.017	0.024	0.030	0.033	0.034	0.033	0.032
	0.010		0.017	0.024	0.030	0.033	0.034	0.033	
I_i (in^4)	14,925		6682	6682	6682	6682	6682	14,925	
$I_i\Delta$ (in^5)	150.59		114.27	157.70	197.80	221.19	227.20	489.30	
LLDF	0.097		0.073	0.101	0.127	0.142	0.146	0.314	
g	0.097		0.589					0.314	
E (ft)	–		17.72					–	

A comparison of the calibrated FEM results with the Path 1 test results are shown in Table 9.42. The calibrated FEM results provide a $g_{per\ foot}$ value that is 3.8 percent lower than the experimental test value.

Table 9.42. Comparison of Calibrated FEM Results with Test Results for Path 1

Method	Section	S1+S2 (Left L-curb)	Mid-slab	S8+S9 (Right L-curb)
Test	g	0.083	0.615	0.302
	$g_{per\ foot}$	–	0.052	–
	E (ft)	–	16.88	–
Calibrated FEM	g	0.097	0.589	0.314
	$g_{per\ foot}$	–	0.050	–
	E (ft)	–	17.72	–

Path 2 Loading. The measured maximum downward deflection for each section under the static test and crawl speed test along Path 2 is compared with those deflections obtained from the updated and calibrated FEM models in Figure 9.50(a) and (b), respectively. The updated FEM overestimates the deflection along Path 2 by 70 percent for the stop location test and by 300 percent for the crawl speed test. The calibrated model provides a better estimation of the observed deflections during static tests along Path 2, with a maximum overestimation of 47 percent for the stop location test and 91 percent for the crawl speed test. It should be noted that these percent differences may seem high due to the low strain values obtained from the bridge testing.

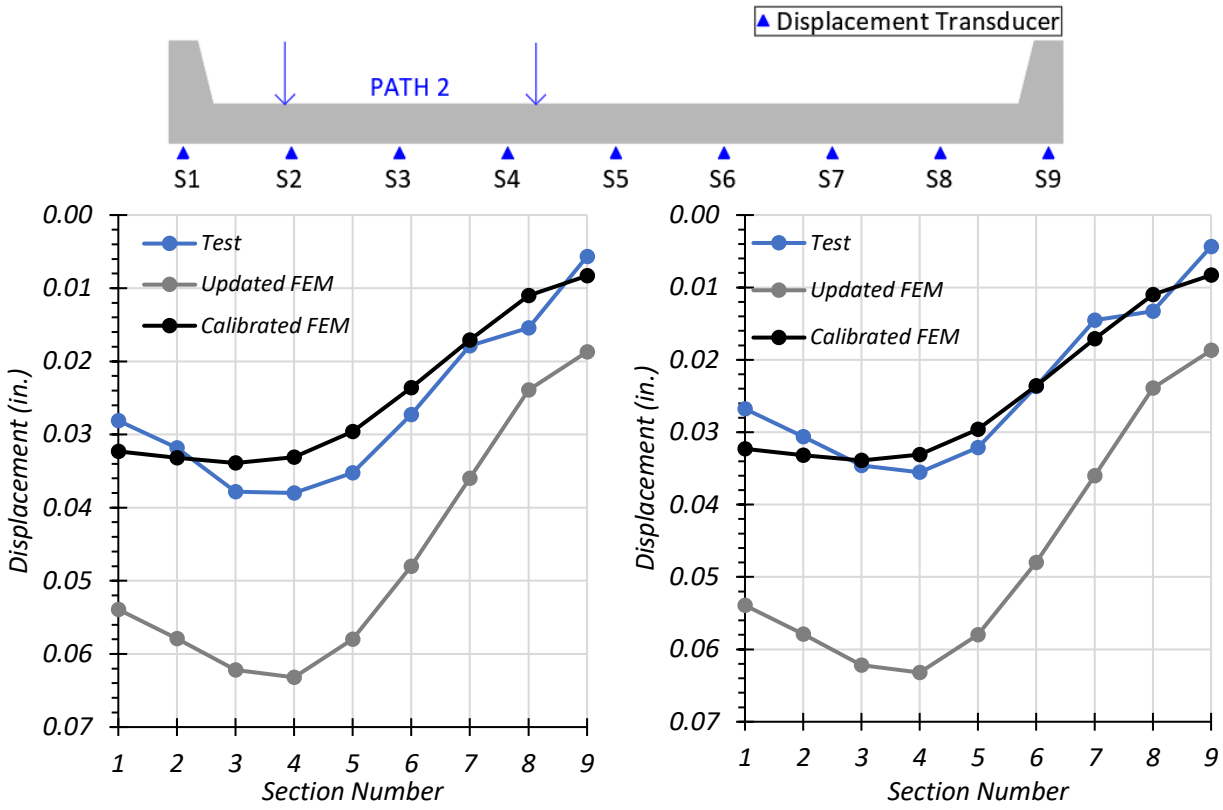

(a) Section Deflections – Stop Location *(b) Section Deflections – Crawl Speed Test*

Figure 9.50. Comparison of Static Deflection Results with FEM for Path 2 Loading

The step-by-step calculations for the equivalent width of the interior slab section for the stop location test for the calibrated FEM model are provided in Table 9.43.

Table 9.43. Calibrated FEM Deflections, LLDFs, and Equivalent Width for Stop Location Test along Path 2 Using L-Curbs

Section	S1+S2 (Left L-curb)		S3	S4	S5	S6	S7	S8+S9 (Right L-curb)	
Width (ft)	4.708		2.083	2.583	2.583	2.583	2.083	4.708	
Δ (in.)	0.032	0.033	0.034	0.033	0.030	0.024	0.017	0.011	0.008
	0.033		0.034	0.033	0.030	0.024	0.017	0.010	
I_i (in^4)	14,925		6682	6682	6682	6682	6682	14,925	
$I_i\Delta$ (in^5)	491.51		226.53	221.19	197.80	157.70	114.27	152.20	
LLDF	0.315		0.145	0.142	0.127	0.101	0.073	0.097	
g	0.315		0.588					0.097	
E (ft)	–		17.80					–	

A comparison of the calibrated FEM results with the Path 1 test results are shown in Table 9.44. The calibrated FEM results provide a $g_{per\ foot}$ value that is 5.8 percent lower than the experimental test value.

Table 9.44. Comparison of Calibrated FEM Results with Test Results for Path 2

Method	Section	S1+S2 (Left L-curb)	Mid-slab	S8+S9 (Right L-curb)
Test	g	0.271	0.618	0.111
	$g_{per\ foot}$	–	0.052	–
	E (ft)	–	17.19	–
Calibrated FEM	g	0.315	0.588	0.097
	$g_{per\ foot}$	–	0.049	–
	E (ft)	–	17.80	–

Middle Path Loading. The measured maximum downward deflection for each girder under the static test and crawl speed test along the Middle Path is compared with those deflections obtained from the calibrated FEM model in Figure 9.51(a) and (b), respectively. The updated FEM overestimates the deflection along the Middle Path by 117 percent for the stop location test and by 125 percent for the crawl speed test. The calibrated model provides a better estimation of the observed deflections during static tests along the Middle Path, with a maximum overestimation of 20 percent for the stop location test and 28 percent for the crawl speed test.

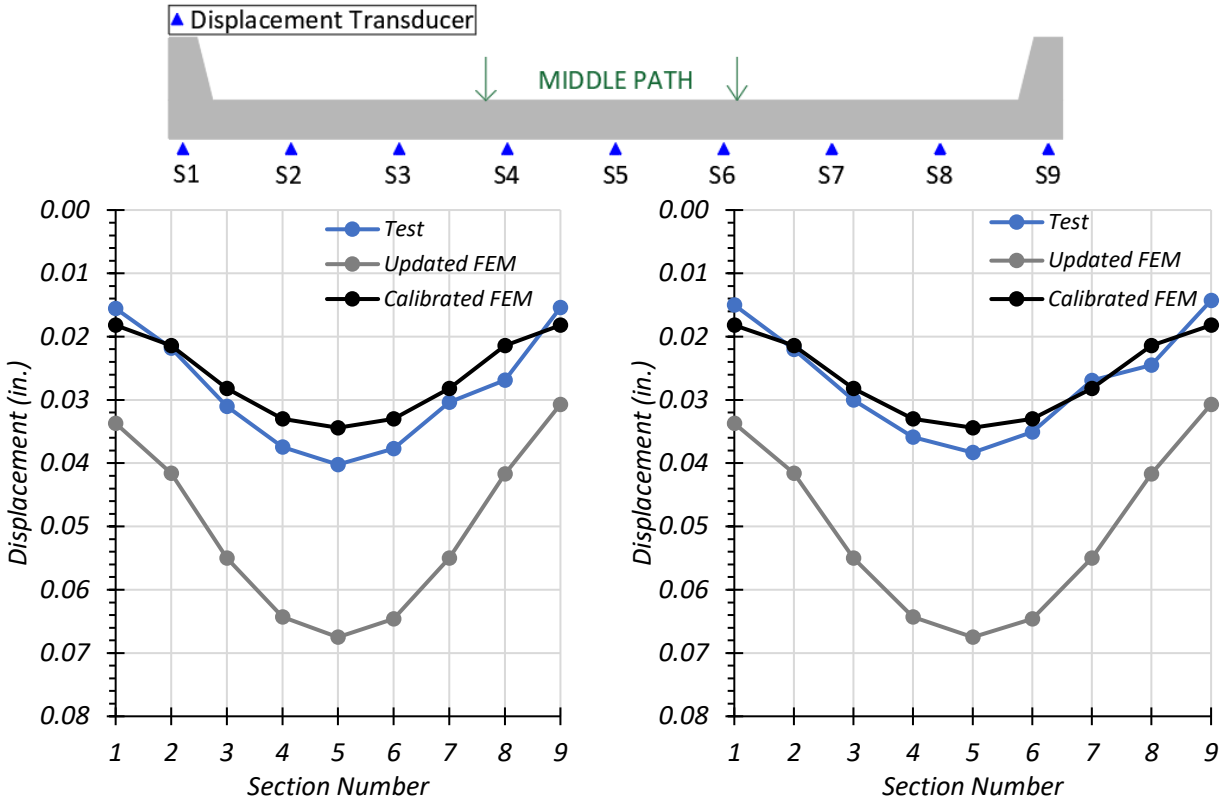

(a) Section Deflections – Stop Location *(b) Section Deflections – Crawl Speed Test*

Figure 9.51. Comparison of Static Deflection Results with FEM for Middle Path Loading

The step-by-step calculations for the equivalent width of the interior slab section for the stop location test for the calibrated FEM model are provided in Table 9.45.

Table 9.45. Calibrated FEM Deflections, LLDFs, and Equivalent Width for Stop Location Test along Middle Path Using L-Curbs

Section	**S1+S2 (Left L-curb)**		**S3**	**S4**	**S5**	**S6**	**S7**	**S8+S9 (Right L-curb)**	
Width (ft)	4.708		2.083	2.583	2.583	2.583	2.083	4.708	
Δ (in.)	0.018	0.021	0.028	0.033	0.034	0.033	0.028	0.021	0.018
	0.020		0.028	0.033	0.034	0.033	0.028	0.020	
I_i (in^4)	14,925		6682	6682	6682	6682	6682	14,925	
$I_i\Delta$ (in^5)	305.20		188.44	220.52	229.87	220.52	188.44	305.20	
LLDF	0.184		0.114	0.133	0.139	0.133	0.114	0.184	
g	0.184		0.632					0.184	
E (ft)	–		18.63					–	

A comparison of the calibrated FEM results with the Path 1 test results are shown in Table 9.46. The calibrated FEM results provide a $g_{per\ foot}$ value that is 1.9 percent lower than the experimental test value.

Table 9.46. Comparison of Calibrated FEM Results with Test Results for Middle Path

Method	Section	S1+S2 (Left L-curb)	Mid-slab	S8+S9 (Right L-curb)
Test	g	0.163	0.646	0.191
	$g_{per\ foot}$	–	0.054	–
	E (ft)	–	17.58	–
Calibrated FEM	g	0.184	0.632	0.184
	$g_{per\ foot}$	–	0.053	–
	E (ft)	–	18.63	–

Two-lane Loading. The deflection results for the stop location test along Path 1 plus Path 2 were used to calculate the equivalent width of the interior slab section and the $g_{per\ foot}$. The deflections obtained from FEM analysis along with the calculated LLDF and equivalent width results are presented in Table 9.47.

Table 9.47. Calibrated FEM Bending Moment, LLDFs and Equivalent Width for Stop Location Test for Two-lane Loading using L-Curbs

Section	S1+S2 (Left L-curb)		S3	S4	S5	S6	S7	S8+S9 (Right L-curb)	
Width (ft)	4.708		2.083	2.583	2.583	2.583	2.083	4.708	
Δ (in.)	0.040	0.044	0.051	0.057	0.060	0.057	0.051	0.044	0.040
	0.043		0.0510	0.0570	0.0600	0.0570	0.0510	0.043	
I_i (in^4)	14,925		6682	6682	6682	6682	6682	14,925	
$I_i\Delta$ (in^5)	638.96		340.80	380.90	400.94	380.90	340.80	638.96	
LLDF	0.409		0.218	0.244	0.257	0.244	0.218	0.409	
g	0.409		1.181					0.409	
E (ft)	–		10.06					–	

Comparison with Test and Other Methods. Live load moment distribution across the bridge width was calculated using FEM deflection predictions for the same three paths (path 1, path 2, and middle path) that were used during field testing. The envelope of these three loading paths was used to identify the controlling moment distribution to the left L-curb, middle slab and

right L-curb. The calculated FEM displacement-based LLDF results are compared with the envelope of the LLDF results obtained from the field testing along the same three paths using measured displacements. Table 9.48 provides a comparison of the LLDFs and equivalent width results from the FEM with the test results and other methods in the literature. The calibrated FEM results estimates a $g_{per\ foot}$ value that is 2 percent lower than the test result.

Table 9.48. LLDFs and Equivalent Widths from FEM, Test and Different Methods from the Literature for One-Lane-Loaded Case

Method	Section	S1+S2 (Left L-curb)	Mid-slab	S8+S9 (Right L-curb)
Test	g	0.271	0.646	0.302
	$g_{per\ foot}$	-	0.054	-
	E (ft)	-	17.58	-
Calibrated FEM	g	0.315	0.632	0.314
	$g_{per\ foot}$	-	0.053	-
	E (ft)	-	18.63	-
IB346	g	0.405	0.190	0.405
	$g_{per\ foot}$	-	0.016	-
Amer et al.	$g_{per\ foot}$	-	0.069	-
	E (ft)	-	14.60	-
Jones and Shenton*	$g_{per\ foot}$	-	0.083	-
	E (ft)	-	12.00	-
AASHTO STD*	$g_{per\ foot}$	-	0.091	-
	E (ft)	-	11.00	-
AASHTO LRFD*	$g_{per\ foot}$	-	0.096	-
	E (ft)	-	10.50	-
Note: * Approaches do not consider the effect of integral curbs.				

Table 9.49 provides a comparison of the LLDF and equivalent width results from calibrated FEM results with the two lane-loaded test results and other methods from the literature. The calibrated FEM results provide a $g_{per\ foot}$ value that is 5 percent smaller than the experimental test value.

Table 9.49. Comparison of Calibrated FEM Results with Test Results for Two-lane Loading

Method	Section	S1+S2 (Left L-curb)	Mid-slab	S8+S9 (Right L-curb)
Test	g	0.354	1.233	0.413
	$g_{per\ foot}$	-	0.104	-
	E (ft)	-	9.27	-
Calibrated FEM	g	0.409	1.181	0.409
	$g_{per\ foot}$	-	0.099	-
	E (ft)	-	10.06	-
IB346	g	0.596	0.808	0.596
	$g_{per\ foot}$	-	0.068	-
Amer et al.	$g_{per\ foot}$	-	0.069	-
	E (ft)	-	14.60	-
Jones and Shenton*	$g_{per\ foot}$	-	0.091	-
	E (ft)	-	11.00	-
AASHTO STD*	$g_{per\ foot}$	-	0.091	-
	E (ft)	-	11.00	-
AASHTO LRFD*	$g_{per\ foot}$	-	0.102	-
	E (ft)	-	9.80	-

Note: * Approaches do not consider the effect of integral curbs.

For the mid-slab region between the L-Curbs, the displacement-based FEM LLDFs are in good agreement with the displacement-based test LLDFs, FEM values only slightly underestimate. The LLDFs for the curbs calculated using the IB346 approach are conservative in comparison to the test measurements and FEM predictions. However, the distribution of live load across the mid-slab portion between L-curbs according to IB346 is unconservative in comparison to the test results for both one-lane and two-lane loading scenario. The Amer et al. (1999) approach for estimating the proportion of moment resisted by the mid-slab portion provides a good moment estimate for one-lane loading, while the *AASHTO LRFD Specifications* provide a better estimate of the proportion of moment demand in the mid-slab portion for two-lane loading. These methods should be adopted if they provide a higher moment estimate in comparison to IB346 method.

9.8.3 Dynamic Characteristics of Bridge

The dynamic characteristics of the bridge obtained from the accelerometer data were compared with the updated and calibrated FEM results. The mode shape along the longitudinal section and transverse section for the first natural frequency compared to the updated FEM and calibrated FEM is shown in Figure 9.52. Figure 9.53 provides the mode shape along the longitudinal section and transverse section for the second natural frequency compared to the updated FEM and calibrated FEM. The mode shape along the longitudinal section and transverse section for the third natural frequency compared to the updated FEM and calibrated FEM is shown in Figure 9.54.

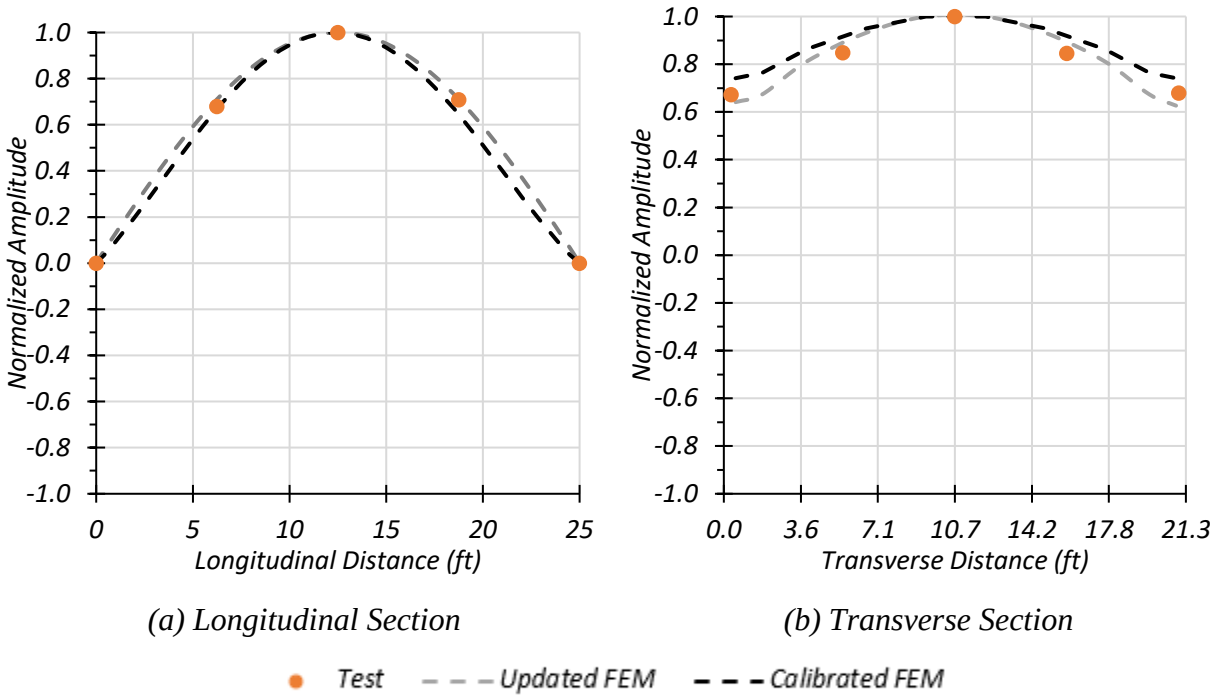

(a) Longitudinal Section *(b) Transverse Section*

Figure 9.52. Mode Shape 1: Comparison of Experimental and FEM Results

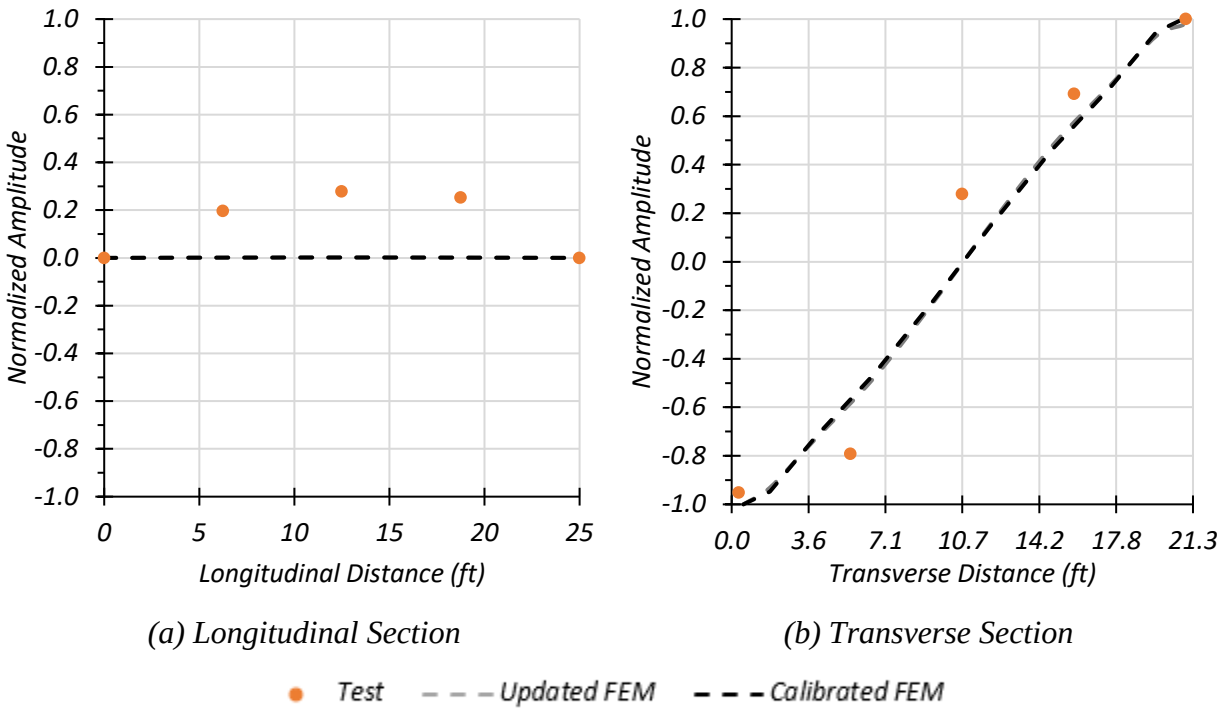

(a) Longitudinal Section *(b) Transverse Section*

Figure 9.53. Mode Shape 2: Comparison of Experimental and FEM Results

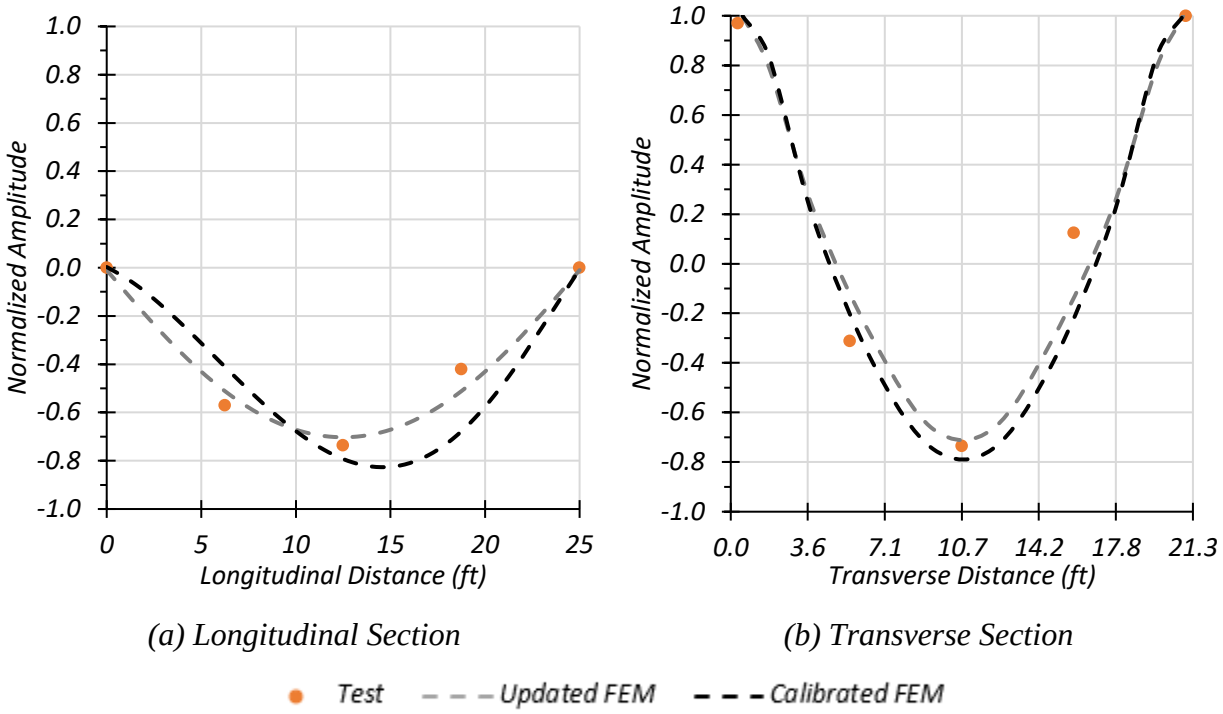

Figure 9.54. Mode Shape 3: Comparison of Experimental and FEM Results

The natural frequencies obtained from the FEM model and those frequencies observed during testing of Bridge CS-9 are provided in Table 9.50. The first, second, and third natural frequencies obtained from the calibrated FEM model are closer to those frequencies obtained from the tests.

Table 9.50. Bridge CS-9 Test and FEM Natural Frequencies

Frequency	Test (Hz)	Updated FEM (Hz)	Calibrated FEM (Hz)
1st Natural Frequency	14.65	13.03	16.66
2nd Natural Frequency	22.46	20.32	23.11
3rd Natural Frequency	37.11	35.83	37.43

9.9 SUMMARY AND FINDINGS

The equivalent widths calculated based on deflections were compared with those widths recommended by *AASHTO Standard Specifications* (AASHTO 2002) and *AASHTO LRFD Specifications* (AASHTO 2017). Both the *AASHTO Standard Specifications* and *AASHTO LRFD Specifications* provide quite conservative equivalent widths for the interior slab portion. A

comparison was conducted of the test equivalent widths to those widths calculated from studies such as Amer et al. (1999) and Jones and Shenton (2012). The studies were also found to provide conservative equivalent widths.

Currently, TxDOT load rates simple-span concrete slab bridges with integral curbs using IB346 (Jenson et al. 1943) recommendations for load distribution. Table 9.51 compares the distribution of the live load based on the field measurements with distributions obtained using the IB346 approach.

Table 9.51. Comparison of Experimental Moment LLDFs in Slab Region with Methods in the Literature

Loading	Test/Method	g	$g_{per\ foot}$
One-lane	Stop Location (Path 1)	0.615	0.052
	Stop Location (Path 2)	0.618	0.052
	Stop Location (Middle Path)	0.646	0.054
	Calibrated FEM (Path 1)	0.589	0.050
	Calibrated FEM (Path 2)	0.588	0.049
	Calibrated FEM (Middle Path)	0.632	0.053
	IB346	0.190	0.016
	Amer et al.	-	0.068
	AASHTO LRFD	-	0.096
Two-lane	Stop Location (Path 1+2)	1.233	0.104
	Calibrated FEM (Path 1+2)	1.181	0.099
	IB346	0.808	0.068
	Amer et al.	-	0.068
	AASHTO LRFD	-	0.102

The IB346 prediction for the live load distribution to the interior slab region is unconservative when compared to the test results and FEM predictions for both the one-lane and two-lane loading scenario. The approach by Amer et al. (1999) gave a good estimate for the interior slab section for determining the demand for one-lane loading; however, the *AASHTO LRFD Specifications* provide a better estimate of the moment demand in the interior slab section for two-lane loading.

Table 9.52 shows that the IB346 prediction for the live load distribution to the L-curb sections is conservative when compared to the test results and FEM predictions for both the one-

lane and two-lane loading scenario. Therefore, it is recommended to continue using the IB346 approach to determine moment demands in the L-curb sections of concrete slab bridges with integral curbs.

Table 9.52. Comparison of Experimental and IB346 Moment LLDFs

Loading	Load Path	$LLDF$		
		Left L-Curb	Mid-Slab	Right L-Curb
One-lane	Path 1	0.094	0.615	0.302
	Path 2	0.286	0.618	0.111
	Middle Path	0.172	0.646	0.191
	IB346	0.405	0.190	0.405
Two-lane	Stop Location Test	0.354	1.233	0.413
	Crawl Speed Test	0.376	1.217	0.407
	IB346	0.596	0.808	0.596

Areas of opportunity for this type of bridge include updating the capacity using the actual material strength and considering any unintended end fixity. The 28-day concrete compressive strength of concrete for Bridge CS-9 was specified to be 2.5 ksi in the structural drawings. However, NDE tests revealed that the actual concrete compressive strength was 5.2 ksi. Table 9.53 provides a comparison of the updated RFs calculated using the in-situ compressive strength of concrete with the originally calculated RFs. As expected, doubling the material strength does not significantly increase the RFs governed by flexure. The increased material strength still provides an operating RF smaller than 1.0. Thus, based on TxDOT's on-system load rating flowchart (TxDOT 2018b), for a bridge with a condition rating greater than 5 for all components and an operating RF less than 1.0, the bridge should be posted at inventory level with an inspection frequency of less than 2 years.

Table 9.53. Comparison of Material Updated and Original RFs for Bridge CS-9

Rating Factor	**Basic Load Rating**	**Load Rating with Measured Material Properties**	**Measured Material Properties/Basic Load Rating**
Inventory	0.42	0.45	1.07
Operating	0.92	0.97	1.05

Calibrating the simply supported FEM model based on load test results in the field showed that there is some degree of end fixity present. The bending moment corresponding to the HS-20 design truck is obtained from the calibrated FEM model, which includes the effect of updated MOE of the concrete, more accurate live load distribution, and updated boundary conditions due to slight end restraint, and this value is used to determine the updated RFs. Table 9.54 provides a comparison of the updated RFs with the original RFs for a simply supported bridge. Only the LFR results are shown in the table because it was the method used to load rate Bridge CS-9. Although the updated inventory RF is less than 1.0, based on TxDOT's on-system load rating flowchart (TxDOT 2018b), for a bridge with a condition rating greater than 5 for all components and an operating RF greater than 1.0, the load posting can be removed.

Table 9.54. Comparison of Calibrated FEM and Original RFs for Bridge CS-9

Rating Factor	Basic Load Rating	Load Rating with Calibrated FEM Live Load	Calibrated FEM Live Load /Basic Load Rating
Inventory	0.42	0.56	1.33
Operating	0.92	1.27	1.38

10 SUMMARY AND CONCLUSIONS

This research project quantifies and characterizes the population of load-posted bridges in Texas and identifies areas of opportunity, including using more accurate material properties and information from bridge inspections, refined modeling, and load testing, in which more precise verification of acceptable load levels can be determined. The Volume 1 report (Hueste et al. 2019a) fully documents a review of the state-of-the-practice and state-of-the-art for load rating of existing bridges, a review and synthesis of the bridge characteristics of load-posted bridges in Texas, and the basic load rating analysis for selected representative bridges to identify the controlling limit states and areas of opportunities that likely lead to a reduced operating load for typical bridge structures.

This Volume 2 report presents the refined analysis procedures and results for more accurate LLDF predictions, fully documents the field testing and measured results, and discusses FEM model updating and calibration for the selected typical bridge types. The findings and areas of opportunities identified through field testing and refined modeling have been further evaluated in terms of potential implications for refined load ratings. Note that the bridges considered in this research were selected as representative bridges among the SSLO bridges in Texas, and the findings are relevant for the particular geometries considered. General applicability of the findings should be considered in a case by case basis.

10.1 REFINED ANALYSIS FOR MORE ACCURATE PREDICTION OF LOAD DISTRIBUTION

Refined analysis of the four selected typical bridge structures have been conducted using three-dimensional linear finite element models, which allow for a more realistic prediction of live load distribution and resulting LLDFs. The estimated LLDF values are compared to the applicable AASHTO LLDF formulas to identify whether they provide a good estimate for selected typical bridge geometries. The effect of the composite action on the LLDFs has also been evaluated. The following conclusions have been drawn for different bridge types.

10.1.1 Simple-Span Steel Multi-Girder Bridges (Bridge SM-5 and SM-21)

Based on the results of the refined analysis, the following conclusions have been drawn for LLDFs of the considered simple-span steel multi-girder bridges.

1. The FEM analysis of the selected simple-span steel multi-girder bridges has shown that, in general, the current LLDF equations given in the *AASHTO Standard Specifications* (AASHTO 2002) provide accurate, slightly conservative LLDF values in flexure for the selected bridges. Therefore, using this analysis will likely not significantly affect the load rating of this bridge type.
2. For the shear LLDF values obtained from the FEM analysis, the ratios of the *AASHTO Standard Specifications* LLDF to FEM LLDF g_{AASHTO}/g_{FEM} for shear range from 0.59 to 1.44, producing a larger variation in results. In order to better capture the wide range, the shear LLDFs of certain bridges could be updated relative to the *AASHTO Standard Specifications*. However, the shear RFs for the larger group of selected bridges are already quite high; thus, refining the shear LLDF is not expected to significantly change the limiting RFs and corresponding load postings.
3. The FEM analysis of the selected simple-span steel multi-girder bridges has shown that, in general, the current LLDF equations given in the *AASHTO LRFD Specifications* (AASHTO 2017) provide conservative exterior girder LLDF values and fairly accurate interior girder moment LLDF values for the selected bridges. The LLDF predictions from FEM analysis are only slightly conservative for one-lane loaded cases. However, for two-lane loaded cases they are significantly conservative. Using more accurate LLDFs for two-lane-loaded cases would likely help increase the LRFR ratings.
4. For the shear LLDF values obtained from the FEM analysis, the ratios of the AASHTO LRFD LLDF to FEM LLDF g_{AASHTO}/g_{FEM} for shear range from 1.31 to 3.24, again producing very conservative results. The shear LLDFs could be updated based on refined analysis in order to improve the LRFR shear RFs for this bridge type.
5. No significant difference in LLDF predictions exists when analyzing the bridge as fully composite versus fully non-composite. Although the LLDF values estimated from the FEM analysis are very similar, it was observed that the composite action significantly reduces the induced stresses, which would allow an increase in the flexural resistance of the section.

10.1.2 Continuous Steel Multi-Girder Bridge (Bridge SC-12)

Based on the results of the refined analysis, the following conclusions have been drawn for LLDFs of the considered continuous steel multi-girder bridge.

1. The FEM analysis has shown that, in general, the current LLDF equations in the *AASHTO Standard Specifications* (AASHTO 2002) provide conservative LLDF predictions in positive flexure and shear for the selected continuous steel multi-girder bridge. Although the AASHTO predictions are conservative, but generally not overly conservative, possible changes to the LLDFs are not likely to significantly affect the LFR load ratings of this bridge type.
2. In general, the current LLDF equations in the *AASHTO LRFD Specifications* (AASHTO 2017) provide fairly accurate LLDF predictions in positive and negative flexure and shear for the selected continuous steel multi-girder bridge.
3. The LLDFs obtained from FEM analysis using both composite and non-composite bridge behavior were found to be very similar; however, the non-composite bridge model seemed to exhibit more uniform LLDF profiles across the bridge transverse section. In addition, it is known that composite action significantly affects the positive moment capacity of the bridge, which was observed from the reduction in stresses for the composite bridge model.

10.1.3 Simple-Span Concrete Multi-Girder Bridge (Bridge CM-5)

Based on the results of the refined analysis, the following conclusions have been drawn for LLDFs of the considered simple-span concrete multi-girder bridge.

1. In general, the moment and shear LLDF formulas in the *AASHTO Standard Specifications* (AASHTO 2002) provide accurate and slightly conservative predictions for the selected simple-span concrete multi-girder bridge. Therefore, using refined analysis for more accurate LLDF estimation is not expected to significantly affect the LFR rating for this bridge type.
2. The moment and shear LLDF equations in the *AASHTO LRFD Specifications* (AASHTO 2017) provide highly conservative LLDF estimates for the selected simple-span concrete multi-girder bridge. Therefore, using refined analysis for more accurate LLDF prediction would likely lead to increased LRFR ratings.

10.1.4 Simple-Span Concrete Slab Bridge with Integral Curbs (Bridge CS-9)

Based on the results of the refined analysis, the following conclusions have been drawn for LLDFs of the considered simple-span concrete slab bridge.

1. The equivalent widths for the interior slab portion calculated using the empirical equations in the *AASHTO Standard Specifications* (AASHTO 2002) and the *AASHTO LRFD Specifications* (AASHTO 2017) are conservative in comparison to the equivalent widths obtained from the FEM bending moment results. This difference is due to the presence of the integral curbs for this bridge type, which is not reflected in the AASHTO equations for equivalent width.
2. The IB346 (Jenson et al. 1943) currently used by TxDOT for integral curb slab bridges was reviewed. For the one-lane-loaded case, the bending moments for the curb and slab calculated using the simplified approach outlined in IB346 are less than the estimated bending moments using the FEM model, with the curb moment being very similar and the slab moment being much lower. For the two-lane-loaded case, the calculated moments using IB346 are conservative for the curb and unconservative for the interior slab portion in comparison to the FEM predictions. The IB346 moment estimate for the slab portion is unconservative because IB346 calculates the average slab moment, while the FEM provides the maximum moment, which is higher around the wheel lines.

10.2 LOAD TESTING, MODEL UPDATING AND CALIBRATION, AND REFINED LOAD RATINGS

A comprehensive field-test program was conducted for the four selected bridges to more accurately measure the transverse live load distribution, identify any potential composite action and end fixity, and obtain dynamic characteristics of the tested bridges. The test results have been used for updating and calibrating the FEM models, which are then used to determine more accurate flexural and shear force effects. The field-test results and FEM predictions from the calibrated models are reviewed with respect to the potential implications and opportunities for load rating these bridges and similar bridge structures. The following subsections provide the summary and findings for the different bridge types.

10.2.1 Simple-Span Steel Multi-Girder Bridge (Bridge SM-5)

Based on the results of the refined analysis, the following conclusions have been drawn for LLDFs of the considered simple-span steel multi-girder bridge

1. The LLDF values obtained from the formulas in the *AASHTO Standard Specifications* (AASHTO 2002) are slightly unconservative for the Path 1 loading and slightly conservative for the other loading paths in comparison to the test results. The LLDFs calculated using the equations in the *AASHTO LRFD Specifications* (AASHTO 2017) range from being conservative to overly conservative.
2. TxDOT currently uses the *AASHTO Standard Specifications* LLDFs for load rating bridges of this type and age. Based on the LLDF results observed from load testing, the LLDFs obtained through the *AASHTO Standard Specifications* provide an appropriate level of conservatism for most scenarios without being overly conservative. Therefore, a significant reduction in LLDFs is not expected for this particular bridge; thus, similar to simple-span multi-girder bridges, this area is not seen as potentially increasing the load rating.
3. The strain measurements indicate that the neutral axis is significantly higher, as measured from the bottom of the girder section, than expected for a non-composite section and is nearly the same as the theoretical value for a fully composite section.
4. For all load tests, the measured bottom flange stress values are close to those values obtained from the FEM composite model, while being significantly less than the stress values obtained from the FEM non-composite model.
5. The girder deflection values measured in the field are much closer to those of the composite FEM model, and in some cases the values are nearly identical.
6. The operating and inventory rating factors calculated based on a fully composite section assumption using LFR or LRFR methods are more than twice the rating factors calculated based on a non-composite section assumption. When using the LFR method, which is the method currently used by TxDOT to rate this bridge, the consideration of composite action would allow the posting of this bridge to be removed, per TxDOT's on-system load rating flowchart (TxDOT 2018b).
7. The operating and inventory rating factors were also calculated using more accurate predictions for the load effects from the calibrated FEM model, which can take into account the combined effect of more accurate LLDFs, partial composite action, and partial end

fixity. Both the ASR and LFR rating factors indicate that the load posting for Bridge SM-5 can be removed based on the TxDOT on-system load posting flowchart (TxDOT 2018b).

10.2.2 Continuous Steel Multi-Girder Bridge (Bridge SC-12)

Based on the results of the refined analysis, the following conclusions have been drawn for LLDFs of the considered continuous steel multi-girder bridge.

1. Moment LLDF values calculated from the equations provided in the *AASHTO Standard Specifications* (AASHTO 2002) and the *AASHTO LRFD Specifications* (AASHTO 2017) were overly conservative in comparison to the measured values for exterior girders. Therefore, more accurate LLDF values obtained from load testing or refined modeling may potentially increase the load rating of Bridge SC-12 or similar bridges of this type. However, the *AASHTO LRFD Specifications* (AASHTO 2017) did provide fairly accurate LLDF estimations for Bridge SC-12.
2. The measured neutral axes during the critical static load tests for Span 2 were 19.77 in. from the bottom of the interior girder and 19.81 in. from the bottom of the exterior girder. The theoretical non-composite neutral axis is 14.90 in. from the bottom of the girder, and the theoretical composite neutral axis is 26.11 in. from the bottom of the girder. These strain measurements indicate partial composite action.
3. The deflection data obtained during the load testing were compared to the estimated girder deflection values from the FEM analysis considering both non-composite and fully composite girder behavior. For the Path 1—Span 2 stop location test, the maximum deflection measured in the exterior girder was 0.755 in., which was between the FEM predictions for fully composite deflection of 0.509 in. and non-composite deflection of 1.121 in.
4. The rating factor for an interior girder positive moment region was calculated considering partial composite action based on the field-measured neutral axis value and compared with the rating factor that was previously calculated using a non-composite section assumption. The consideration of partial composite action increases the ASR rating factor by approximately 20 percent, increases the LFR rating factor by approximately 90 percent, and increases the LRFR rating factor by about 70 percent.

5. The rating factors were also calculated using the load effects obtained from the calibrated FEM model, which can take into account the combined effect of more accurate LLDFs and partial composite action. Both the ASR and LFR HS-20 rating factors for Bridge SC-12 allow its posting to be removed based on the TxDOT on-system load posting flowchart (TxDOT 2018b).

10.2.3 Simple-Span Concrete Multi-Girder Bridge (Bridge CM-5)

Based on the results of the refined analysis, the following conclusions have been drawn for LLDFs of the considered simple-span concrete multi-girder bridge.

1. The *AASHTO Standard Specifications* (AASHTO 2002) provide slightly conservative LLDF predictions for moment in both the interior and exterior girders in comparison to the LLDFs calculated from field measurements.
2. The *AASHTO LRFD Specifications* (AASHTO 2017) provide slightly conservative LLDF estimates for moment in exterior girders but are overly conservative for moment LLDFs in interior girders.
3. Currently, TxDOT load rates simple-span concrete pan girder bridges using the *AASHTO Standard Specifications* LLDFs. Because moment LLDFs from *AASHTO Standard Specifications* (AASHTO 2002) were found to be only slightly conservative in comparison to LLDFs obtained from test measurements, refining the LLDFs would not significantly increase the load rating for Bridge CM-5 or similar bridges of this type.
4. Using the updated concrete compressive strength of 7 ksi rather than the 4 ksi design compressive strength value did not significantly increase the rating factor for Bridge CM-5. Note that the updated material properties considered only the in-situ concrete strength based on the NDE material testing, while keeping the steel yield strength the same as the design value. Using a higher steel strength based on mill certificate data or laboratory testing of extracted bars would likely have a more pronounced effect on the rating factors.
5. Inventory and operating HS-20 rating factors based on the LFR method were calculated using the load effects obtained from the calibrated FEM model, which can take into account the combined effect of more accurate LLDFs and partial end fixity. The revised rating factors were found to be more than two times higher than the basic load ratings that assume simply supported boundary conditions and use approximate LLDFs. Although the

superstructure has both inventory and operating RFs greater than 1.0, the poor condition rating of the substructure (Item 60 < 6) resulted in the load posting of this bridge.

10.2.4 Simple-Span Concrete Slab Bridge with Integral Curbs (Bridge CS-9)

Based on the results of the refined analysis, the following conclusions have been drawn for LLDFs of the considered simple-span concrete slab bridge.

1. Both the *AASHTO Standard Specifications* (AASHTO 2002) and *AASHTO LRFD Specifications* (AASHTO 2017) provide quite conservative equivalent width predictions for the interior slab portion in comparison to the test results obtained using the displacement results. As noted earlier, this difference is due to the presence of the integral curbs for this bridge, which is not reflected in the AASHTO equations for equivalent width.
2. The equivalent width values calculated from studies such as Amer et al. (1999), which include the influence of integral curbs in slab bridges, and Jones and Shenton (2012) were also found to provide conservative equivalent width estimates in comparison to the test equivalent widths.
3. Currently, TxDOT load rates simple-span concrete slab bridges with integral curbs using IB346 (Jenson et al. 1943) recommendations for load distribution. The moment demands for the curbs calculated using the IB346 approach are conservative in comparison to the test measurements. Continuing to use the IB346 approach to determine moment demands for the L-curb sections in concrete slab bridges with integral curbs is recommended. However, the distribution of live load across the interior slab portion according to IB346 is unconservative in comparison to the test results for both one-lane and two-lane loading scenario. The Amer et al. (1999) approach for estimating the proportion of moment resisted by the interior slab sections provides a good moment estimate for one-lane loading, while the *AASHTO LRFD Specifications* provide a better estimate of the proportion of moment demand in the slab portion for two-lane loading. These methods should be adopted if they provide a higher moment estimate in comparison to IB346 method.
4. Increasing the in-situ concrete compressive strength to 5.2 ksi based on NDE testing slightly improves the HS-20 rating factors using the LFR method. Although the increase is not significant for Bridge CS-9, it provides an operating RF greater than 1.0. Based on TxDOT's on-system load rating flowchart (TxDOT 2018b), for a bridge with a condition

rating greater than 5 for the different components and an operating RF greater than 1.0, the load posting can be removed.

5. Inventory and operating HS-20 rating factors based on the LFR method were calculated using the load effects obtained from the calibrated FEM model, which can take into account the more accurate transverse live load distribution and partial end restraint. The load effects from refined analysis result in an inventory rating factor that is around 30 percent higher and an operating rating factor that is around 40 percent higher in comparison to the basic load rating factors that are based on simply supported boundary conditions. Although the inventory RF is less than 1.0, based on TxDOT's on-system load rating flowchart (TxDOT 2018b), for a bridge with a condition rating greater than 5 for the different components and an operating RF greater than 1.0, the load posting can be removed.

REFERENCES

AASHTO (2002). "Standard Specifications for Highway Bridges, 17th Edition." American Association of State Highway and Transportation Officials, Washington, DC.

AASHTO (2017). "AASHTO LRFD Bridge Design Specifications, 8th Edition." American Association of State Highway and Transportation Officials, Washington, DC.

AASHTO (2018). "Manual for Bridge Evaluation, 3rd Edition." American Association of State Highway and Transportation Officials, Washington, DC.

ACI Committee 318 (2014). "Building Code Requirements for Structural Concrete and Commentary." American Concrete Institute, Farmington Hills, MI.

AISC (2013). "Steel Construction Manual, 14th Edition." American Institute of Steel Construction, Chicago, IL.

Amer, A., Arockiasamy, M., and Shahawy, M. (1999). "Load Distribution of Existing Solid Slab Bridges Based on Field Tests." ASCE *Journal of Bridge Engineering*, 4(3), 189-193.

ASTM C597 (2016). "Standard Test Method for Pulse Velocity Through Concrete." ASTM International, West Conshohocken, PA, 4.

ASTM C805 (2018). "Standard Test Method for Rebound Number of Hardened Concrete." ASTM International, West Conshohocken, PA.

Barnard, T., Hovell, C. G., Sutton, J. P., Mouras, J. M., Neuman, B. J., Samaras, V. A., Kim, J., Williamson, E. B., and Frank, K. H. (2010). "Modeling the Response of Fracture Critical Steel Box-Girder Bridges." *Report No. FHWA/TX-10/9-5498*, Center for Transportation Research at the Univ. of Texas at Austin, 1, Austin, TX.

Computers and Structures Inc. (2019). CSiBridge, Integrated 3-D Bridge Analysis, Design and Rating, version 20, Computers and Structures Inc., Berkeley, CA.

Davids, W. G., Poulin, T. J., and Goslin, K. (2013). "Finite-Element Analysis and Load Rating of Flat Slab Concrete Bridges." *ASCE Journal of Bridge Engineering*, 18(10), 946-956.

Huang, Q., Gardoni, P., and Hurlebaus, S. (2011). "Predicting Concrete Compressive Strength Using Ultrasonic Pulse Velocity and Rebound Number." ACI *Materials Journal*, 108(4), 403-412.

Hueste, M. B., Mander, J. B., Terzioglu, T., Jiang, D., and Petersen-Gauthier, J. (2015). "Spread Prestressed Concrete Slab Beam Bridges." FHWA/TX-15/0-6722-1, Texas Department of Transportation, Austin, TX, 406.

Hueste, M. B., Hurlebaus, S., Mander, J., Paal, S., Terzioglu, T., Stieglitz, M., and Kabir, N. (2019a). "Development of a Strategy to Address Load-Posted Bridges through Reduction in Uncertainty in Load Ratings—Volume 1: Basic Load Rating." FHWA/TX-19/0-6955-R1-Vol1, Texas Department of Transportation, Austin, TX, 524.

Hueste, M. B., Hurlebaus, S., Mander, J., Paal, S., Terzioglu, T., Stieglitz, M., and Kabir, N. (2019b). "Development of a Strategy to Address Load-Posted Bridges through Reduction in Uncertainty in Load Ratings—Volume 3: Refined Load Rating Guidelines." FHWA/TX-19/0-6955-R1-Vol3, Texas Department of Transportation, Austin, TX, 200.

Hurlebaus, S., Mander, J. B., Terzioglu, T., Boger, N. C., and Fatima, A. (2018). "Fracture Critical Steel Twin Tub Girder Bridges: Technical Report." FHWA/TX-18/0-6937-R1, Texas Department of Transportation, Austin, TX, 474.

Jenson, V. P., Kluge, R. W., and Williams, C. B. (1943). "Highway Slab-Bridges with Curbs: Laboratory Tests and Proposed Design Method." *Bulletin Series No. 346*, University of Illinois, Urbana-Champaign, IL, 1-65.

Jones, B. P., and Shenton, H. W. (2012). "Effective Width of Concrete Slab Bridges in Delaware." Delaware Center for Transportation, University of Delaware, Newark, DE, 1-82.

Mander, J. B., Priestley, M. J. N., and Park, R. (1988). "Theoretical Stress-Strain Model for Confined Concrete." ASCE *Journal of Structural Engineering*, 114(8), 1804-1826.

MCC (2014). "StrainBook/616 User`s Manual." Norton, MA, Measurement Computing, <https://www.mccdaq.com/pdfs/manuals/strainbook_616.pdf>. (July 15, 2014).

NBI (2016). "National Bridge Inventory (NBI)." Federal Highway Administration, Washington, DC, <https://www.fhwa.dot.gov/bridge/nbi/ascii.cfm>, September 2017.

Proceq (2017a). "Original Schmidt Concrete Test Hammer Operating Instructions." *Model N/NR: Conversion Curves Based on the Average Compressive Strength of a Cylinder and the Rebound Value R*, Proceq SA, Schwerzenbach, Switzerland.

Proceq (2017b). "Silver Schmidt Operating Instructions." Proceq SA, Schwerzenbach, Switzerland.

Puckett, J. A., Huo, S. X., Jablin, M., and Mertz, D. R. (2011). "Framework for Simplified live load distribution-factor computations." ASCE *Journal of Bridge Engineering*, 16(6), 777-791.

RISA Tech Inc. (2016). RISA-Structural Engineering Software for Analysis & Design, version 15, RISA Tech, Inc, Foothill Ranch, CA.

Trtnik, G., Kavčič, F., and Turk, G. (2009). "Prediction of concrete strength using ultrasonic pulse velocity and artificial neural networks." *Ultrasonics*, 49(1), 53-60.

TxDOT (2001). "Rate Spreadsheet User Guide." Texas Department of Transportation, Bridge Division, Austin, TX, 33.

TxDOT (2005). "Bridge Standards." *Concrete Slab and Girder Spans - 24 ft Roadway*, Texas Department of Transportation, Austin, TX.

TxDOT (2018a). "InspecTech Inspection Records." Bentley Systems and Texas Department of Transportation, Austin, TX, June 2018.

TxDOT (2018b). "Bridge Inspection Manual." *Ratings and Load Posting*, Texas Department of Transportation, Austin, TX.